Mathematical Problems in Engineering

Operations Research in Engineering Problems: Potential Applications and Perspectives

Lead Guest Editor: Mohammad Yazdi
Guest Editors: Noorbakhsh Amiri Golilarz and Samuel Yousefi

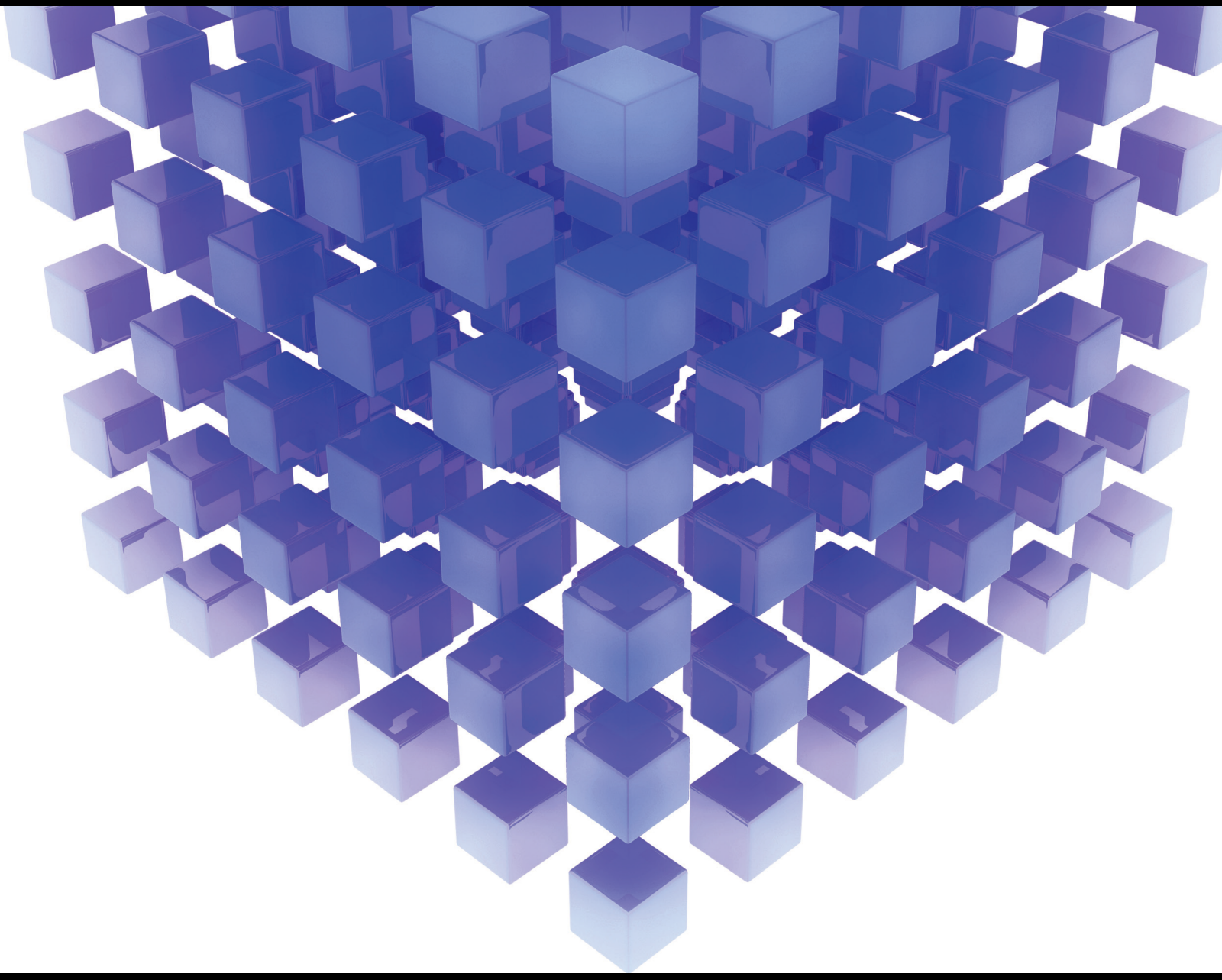

Operations Research in Engineering Problems: Potential Applications and Perspectives

Mathematical Problems in Engineering

Operations Research in Engineering Problems: Potential Applications and Perspectives

Lead Guest Editor: Mohammad Yazdi
Guest Editors: Noorbakhsh Amiri Golilarz and Samuel Yousefi

Contents

Contents

Contents

Hindawi
Mathematical Problems in Engineering
Volume 2022, Article ID 6162829, 14 pages
https://doi.org/10.1155/2022/6162829

Research Article

Quantitative Risk Analysis on Rail Transportation of Hazardous Materials

Iraj Mohammadfam,[1] **Esmaeil Zarei**,[2] **Mohammad Yazdi**,[3] **and Kamran Gholamizadeh**[1]

[1]*Center of Excellence for Occupational Health, Occupational Health and Safety Research Center, School of Public Health, Hamadan University of Medical Sciences, Hamadan, Iran*
[2]*Centre for Risk, Integrity and Safety Engineering (C-RISE), Faculty of Engineering and Applied Science, Memorial University of Newfoundland, St. John's, Newfoundland A1B 3X5, Canada*
[3]*Department of Process Engineering, Faculty of Engineering and Applied Science, Memorial University of Newfoundland, St. John's, Newfoundland A1B 3X5, Canada*

Correspondence should be addressed to Kamran Gholamizadeh; kamrangholamizade1373@gmail.com

Received 19 May 2021; Revised 11 September 2021; Accepted 24 December 2021; Published 8 March 2022

Academic Editor: Alessandro Della Corte

The hazardous nature of the chemical materials is of significant concern in the economic viability of rail transportation globally. The potential risks of these materials to cause severe health impairments and catastrophic accidents have been widely studied and reported. Moreover, several models have been employed for assessing the risks associated with transporting hazardous materials by rail. However, a more holistic, quantitative, and robust model should incorporate more potential risk-triggered criteria, especially those causing severe health loss and devastating consequences like vapor cloud explosion. This study develops a risk assessment model by incorporating potential health risk factors and the obstacle circumstances. The potential risk factors are population density, route distance from residential areas, and the availability of sensitive third parties for health consequences. The proposed model utilizes Bayesian networks for causality modeling of the material release scenarios and fuzzy set theory for estimating the health effects and severity impact coefficient. Finally, individual risk curves and safe distances from the railway are developed. A real rail system for gasoline transportation in Tehran is investigated to evaluate the model's effectiveness. The study provides panoramic leverages for risk-managed decision-making for safely transporting hazardous material by rail.

1. Introduction

Rail transport is an effective mode for transporting materials, with an estimate of about a million shipments conducted annually in the USA [1]. Statistical data show that 10% of all materials were transported via a railway network in 2014 in Iran [2]. Despite the lower share of the rail network in materials' transportation, statistical data show that a significant percentage of hazardous chemicals is transported using this network [3, 4].

Annually, consignments consisting of petroleum products and other hazardous materials result in accidents at localities whose level of emergency preparedness is next to nothing [5, 6]. Although rail accidents rarely occur, they are more severe than road accidents, mainly due to the high volume of the hazardous materials transported [7]. For example, a postcollision train crash of Graniteville, USA, in January 2005 resulted in over 100 casualties, displacement of about 5400 populated a residential area, and loss of $ 6.9 million worth of economic ventures [8]. Also, the Neyshabur accident in Iran in 2004 is one of the biggest railway accidents related to the transportation of chemicals, in which railway wagons carrying a load of dangerous goods exploded. The accident killed more than 720 people and destroyed residential areas within a radius of 10 km [9].

A practical and effective technique of managing accidents in railway networks globally should involve timely identification, assessment, and evaluation of potential hazards and the attendant risks [1]. In addition, such a technique should have the capability to effectively reduce the probability of occurrence [7]. The Federal Railroad Administration (FRA) has attempted to categorize rail accidents according to the significant causative factors such as the track, equipment, human, signals, and other causes [10]. Several techniques such as the conventional risk assessment [10–12], human error analysis [13], optimal routing [14], economic impact assessment [15], environmental impacts [16], and accident statistical analysis [10, 17, 18] have been deployed through various studies to identify the major causative factors of rail accidents.

Previous studies have shown that the quantitative risk analysis (QRA) approach can be used as a reliable and high-precision technique for determining safety zones on transportation routes [19–21] and hazardous material storages [22, 23]. For example, Ahmadi et al. used the new Fuzzy-Bayesian network approach for risk assessment in the process industries [24]. The work of Gooijer et al. also used a new quantitative risk assessment approach to determine the safe construction distance around the process industries [25]. Gonzalez Dan et al. used the Monte Carlo simulation method to assess the quantitative risk of human error in the process industries [26]. Moreover, Guo et al. used the Copula-based Bayesian network (BN) technique to investigate the fault tree analysis (FT) uncertainty for the examination of quantitative risk in process systems [27]. In addition, the new fuzzy approach was used by Miri Lavasani et al. to assess the oil and gas industries [28]. Dormohammadi et al. used the QRA approach to model the potential safety risks and consequences of LPG [23]. Other recent QRA studies were on hydrogen release [29, 30] and the dynamic QRA on hydrogen infrastructure [31].

However, new fuzzy-based approaches have shown enhanced integrity and support for various aspects of risk assessment. For instance, Li et al. used the Fuzzy-BN approach to assess the risk of road transport conveying combustible materials [32]. Moreover, in the field of fuzzy inferences and fuzzy analytical hierarchy process (FAHP), An et al. [33] evaluated the quantitative risk of the railway network. Furthermore, a quantitative risk assessment approach was employed by Hassan et al. to assess the risk of ammonium transportation in the rail network [34]. Leitner assessed the risk of rail transportation in the field of scenario-based assessment [35]. However, for the modeling-based risk assessment approach, Paltrinieri et al. assessed the quantitative risk of the dangerous goods transported through railway routes [36]. Furthermore, Zhang et al. used a quantitative approach to determine critical nodes in railway routes [37].

Generally, both the semiquantitative and qualitative methods have been widely applied; however, they are plagued by a poor level of accuracy [38]. Conversely, quantitative methods are more valid due to the low level of uncertainty [39–43]. More often than none for accurate modeling [20, 37], the quantitative risk assessment of the rail network is usually based on equipment failures [33, 44] and human error [45–47]. The Bayesian network is one of the new methods in risk assessment, which is widely used due to its ability to interrelate the nonlinear relationships between parameters and, as a result, enhance the level of computational accuracy [48]. Meanwhile, conventional applications of BN have been criticized for employing crisp probabilities in assessing uncertainty; assigning fuzzy probabilities in BN has been found to produce more accurate findings in risk and safety analysis of critical systems [49, 50]. Providentially, a robust assessment of the potential health hazards with the attendant risks could be reliably achieved with high accuracy by imbibing in the assessment tool the effects of the causative agents viz-a-viz population density, distance from residential zones, and the critical points. Therefore, this current study presents a comprehensive and quantitative BN-fuzzy set theory (BN-FST) risk assessment tool for modeling the transportation of petroleum via railway networks under uncertainty. The specific research objectives are fashioned as follows: (i) determining the probability of chemical leakage from trucks, (ii) describing the leakage process and emission of materials using equations, and (iii) modeling the health and safety effects of chemical leakage.

The paper proceeds as follows. In Section 2, the proposed methodology and the case study are fully described and demonstrated, findings are presented in Section 3, and, finally, the discussion and conclusion are provided in Sections 4 and 5, respectively.

2. Materials and Methods

The proposed methodology in the present study is illustrated in Figure 1. The occurrence probability of chemical material release and the potential consequences are predicted under uncertainty in the first step. Concurrently, the severity of the latter is being estimated as described in the next step. After that a severity impact coefficient (SIC) is defined to modify the estimated health risk for the critical points in the case study. Finally, individual health and explosion risks are estimated. Each of these steps is explained in the following sections.

2.1. Estimating the Probability of Consequences

2.1.1. The Causes-Consequences Modeling. The cause-consequences analysis of material leakage from rail cars is performed at the initial step using the Bowtie (BT) method. This method is suitable for identifying the effects of causes on the occurrence of events and how events turn into consequences by considering the effects of safety barriers [51]. This method is closely linked to Event Tree Analysis (ET) and FT methods [52]. At the onset, the views of safety experts on specific issues about the history of by rail accidents with chemical materials consignments are collected and collated. These views help identify primary and intermediate events causing the leakage from the rail cars. It also provides some data on the possibility of each event per year. In this process, the opinions of 20 safety and railway experts are employed, and finally, the quantitative probabilities are

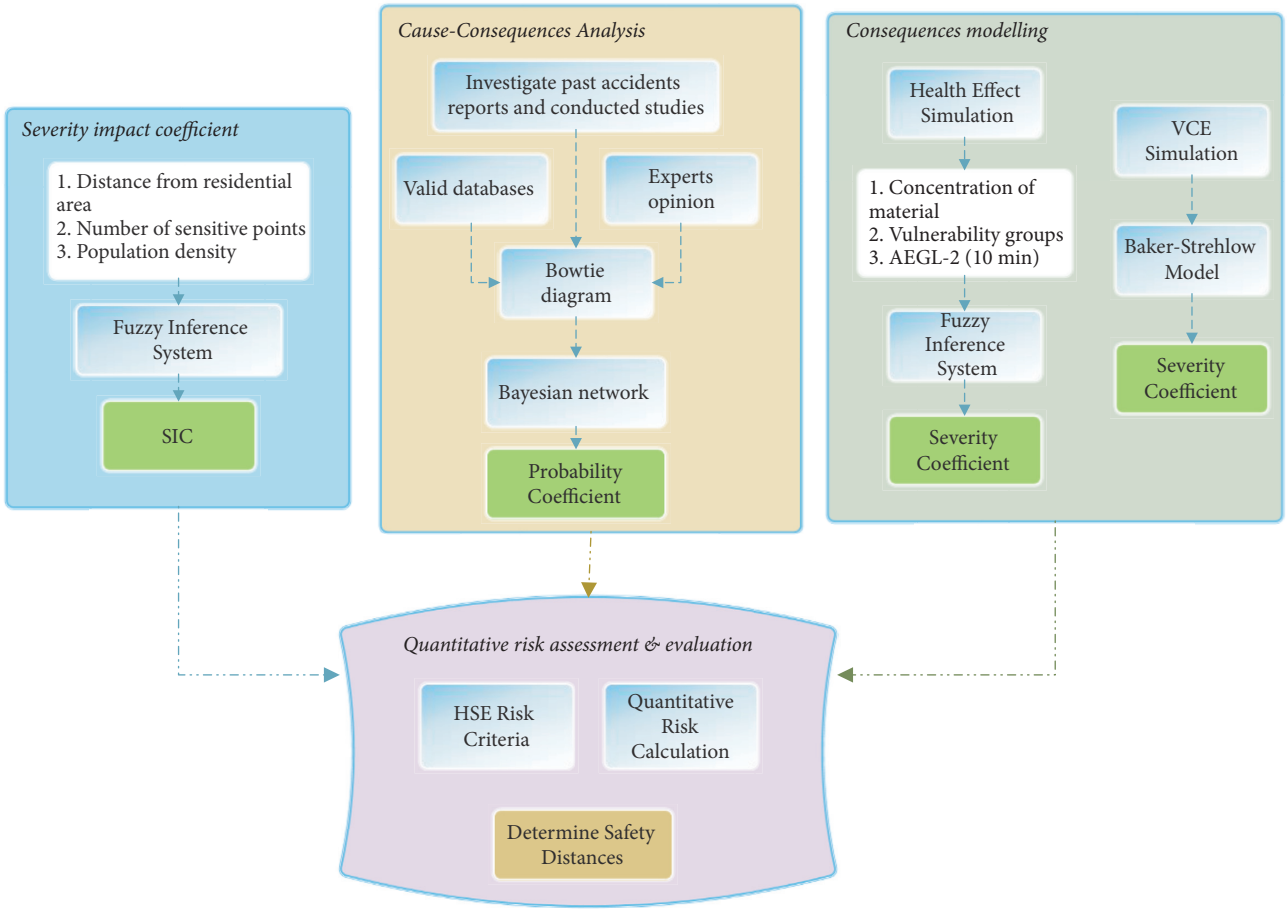

Figure 1: The proposed framework to quantitative risk analysis of hazardous material transportation.

calculated using the FAHP method. Given the prevalent conditions of time and location of the incidence, the probable factors of occurrence, types, and probability of consequences can be deduced. Figure 1 depicts the causes of events on the left and the outcomes on the right [53, 54].

2.1.2. Bayesian Network Modeling. BN was applied to quantitative modeling of cause-effect scenarios under uncertainty [6]. This study performed the BN analysis because it provides a noncyclic graph that presents a set of random variables. The associations between them are assessed using conditional probability tables (CPT). Nodes (random variables) and arcs (possible relationships) form the basis of this network, whose main task is to display nonlinear relationships between parameters. Bayes theory is the main foundation of this network, and it is presented in Equation (1). In this equation, A and B are events and $P(B) \neq 0$; moreover, $P(A \mid B)$ is the probability of A occurring when B is true, and also, $P(B \mid A)$ is the probability of B occurring when A is true. In the same vein, $P(A)$ and $P(B)$ are likelihood of A and B, which is known as marginal probability. In addition, this network is applied to determine the most concrete outcomes of leakage; and to this end, material leakage (TE) as the evidence node and the essential items influencing leakage are selected [43, 55–57]:

$$P(A|B) = \frac{P(B|A)P(A)}{P(B)}. \tag{1}$$

2.2. Estimating the Severity of Consequences

2.2.1. Modeling of VCE. The Baker-Strehlow (BS) method simulated vapor cloud explosion (VCE) of petroleum products' leakage from the rail cars. The BS method was first introduced in a 1996 paper by Baker et al. [58] and was developed based on obstructed regions. According to recent studies, this method is more accurate than other models (such as multienergy and TNT methods) [59]. The main reason for selecting BS is its capability to assess the explosion pressure using all the factors influencing overpressure and flame propagation speed [4]. This consequently leads to the determination of the explosion blast intensity by assessing the propagating of the flame front, fuel reactivity, and obstacle density. Accordingly, the BS method can determine cloud dimensions and evaluate the energy of the explosion. This method is applied in the next step to measure the overpressure as a function of the scaled distance using flame speed as an effective parameter as suggested by [60].

The vapor cloud can be estimated from the leaked liquid state (flammable liquid pool). The quantity of vapor forming

the vapor cloud is the product of the liquid's evaporation rate and the time of inflammable, which is the time span between the leakages and the explosion. It should be noted that the simulation calculations are performed based on 80% leakage. First, taking into account the weight of the material leaking from the reservoir, the density of the vapor of the material, and the material to oxygen molecular ratio (based on the chemical reaction of combustion), the volume of vapor of the leaked material is calculated using the following equation:

$$V\left(m^3\right) = \left(\frac{m}{\rho}\right)R, \tag{2}$$

where m is the weight of the material leaked from the reservoir (kg), ρ is the density of the vapor of the material (kg/m^{vl}), and R is the material to molecular oxygen ratio. The cloud radius, R (m), is obtained from the cloud volume V (m^3), considered that a hemisphere is calculated using the following equation:

$$R = \left(\frac{3v}{2\pi}\right)^{1/3}. \tag{3}$$

From the reference tables [60], the flame speed (Mj) is calculated based on the flame expansion (1D, 2D, or 3D), fuel reactivity (high, medium, or low reactivity), and obstacle density. For example, when the flame is free to expand in three dimensions, the reactivity of the material is considered to be high, and the density of obstacles is medium. The flame speed is then equal to 0.153 Mj. Conversely, the scaled distance (r') is calculated using the following equation:

$$r' = x\left(\frac{E}{P_a}\right)^{-\left(\frac{1}{3}\right)}, \tag{4}$$

where P_a (MP$_a$) is the ambient pressure (= 0.1 MPa), and x (m) is the distance from the center of the explosion. Using combustion heat ΔHc (MJ/kg), cloud volume V (m^3), density ρ_m (kg/m^3), and reaction stoichiometry ratio of material to oxygen (R), the energy of the explosion E (MJ) is E (MJ) is the total energy of the explosion is calculated using the following equation:

$$E = V\left[\Delta H_c \times \rho \times \left(\frac{1}{R}\right)\right]. \tag{5}$$

Finally, considering the scaled distance (r'), flame speed (Mj), and reference diagrams, the size of explosion pressure (bar) is determined.

Then, using Equation (6), the fatality probit of the VCE is estimated as [61]

$$Y = -77.1 + 6.91 \ln P, \tag{6}$$

where Y is the fatality probit of the VCE, and P is the overpressure (N/m^2). Finally, the probability of VCE fatality or the severity coefficient is estimated using equation (7) (based on the probit model):

$$\Pr(Y = 1lX) = \phi\left(X^T\beta\right), \tag{7}$$

where φ was the distribution function.

2.2.2. Modeling the Toxicological Consequences. In the fuzzy set theory, verbal expressions (linguistic terms) introduce numerical intervals. The output of the fuzzy set is a numerical index, but to design it, the numerical intervals must first be specified as verbal codes in the fuzzy toolbox. From a verbal expression, L represented by a numerical interval {0.0, 0.5, 1.0}, the numerical output is estimated according to the fuzzy inference rules. The philosophy of using a fuzzy set in quantifying experts' opinions is based on this principle [62]. To model the potential health consequences, a fuzzy set theory is applied. Accordingly, crisp linguistic variables are changed into fuzzy numbers through the fuzzy rules, and defuzzification operations are applied to obtain the fuzzy output numbers [63].

The system used three input parameters, including the concentration of the leaked chemicals, the rate of vulnerability in population, and toxicological characteristics of the released material. This system was first used by Gholamizadeh et al. [64, 65] to assess the toxicological consequences of chemical road transport. The desired output is the severity exposure coefficient calculated using the parameters above. Equation (8) is used to determine the airborne concentration of the substance [66]:

$$c(x, y, z) = \frac{Q}{2\pi u\sigma_y\sigma_z}e^{-y^2/2\sigma_y^2}\left\{e^{-(z-H)^2/2\sigma_z^2} + e^{-(z-H)^2/2\sigma_z^2}\right\}, \tag{8}$$

where C is the airborne concentration (g/m^3), Q is the output flow rate at the moment of leakage (g/s), U is the local wind speed (m/s), H is the respiratory point height (m), Z is the substance leakage height (m), σ_y is the dispersion in the y-axis (m), and σ_z is the dispersion in the z-axis (m). The relationships and the classification of materials stability are used to assess the last two parameters σ_y and σ_z. Then, based on the opinions of toxicology and safety experts, age, lifestyle, and specific situations (such as pregnancy), the levels of exposure are categorized into several groups.

Acute exposure is considered an essential item in evaluating accidents and chemicals' leakage. For this purpose, the AEGL-2 (10 min) parameter is selected as an item representing all the features of the hazardous material (HM) in both mild and acute exposures [67]. Eighty if-then rules are set and applied with the three input variables and experts' opinions. Therefore, a Mamdani set (fuzzy inputs and outputs) was designed, and a defuzzification technique based on the "center of area" was used. Researchers have used this fuzzy technique for risk assessment [68, 69].

2.3. SIC Estimation. The extent of exposure is determined by the region's population density where the hazards are released. The severity of the effects of the accident is expected to be lower for a sparsely populated region than for a densely populated region. Therefore, a new item SIC is added to Equation (9) and used for normalization. Accordingly, a

standard questionnaire is designed to estimate the average number of people in 2500 m^2 during peak times when a significant number of people are present, and the route distance to residential points is measured. The sensitive points are determined based on the experts' opinions. Considering all parameters, the quantitative input and output items are evaluated using the Sugeno set (fuzzy inputs but numerical outputs) [70]. This system helps to determine this coefficient related to the nodes. Tables 1 and 2 illustrate the fuzzy system developed to assess the toxicological effects and SIC, respectively.

2.4. Quantitative Risk Assessment and Evaluation. In this step, the quantitative risk is calculated based on the probability of the specified parameter (P), severity (S), and SCI using Equation (9). It is noteworthy that safety distances are calculated based on the geometric average of the SIC on the railway route, and the node with the highest geometric mean of SIC is considered in the following equation:

$$\text{Risk} = P \times [SIC \times SS]. \tag{9}$$

The individual risk (IR) levels are evaluated according to the UK's health and safety executive (HSE) that divides the risk at the border of three levels of "broadly acceptable" (1.00E-6/year), "tolerable" (1.00E-5/year), and "unacceptable" (1.00E-4/year) [71] using Equation (9) [5]. The safe construction distances are determined based on these criteria. Safety philosophy tells us that when assessing and evaluating risk and determining safe distances, the most severe condition should be considered a criterion [65]. Accordingly, the safe distances are calculated based on the most severe cases, the most dangerous study node, and the "high obstacles" state.

2.5. Case Study Description. In consultation with the experts working in Tehran Petroleum Products Distribution Company, the route of gasoline fuel transportation from Tehran Railway to "Shahr-e-Ray" Railway is selected for the stu11111111 dy. The selected transport route is presented in Figure 2. This route is 8.5 km long and passes through residential areas in the south of Tehran. High traffic points, high accident areas, and critical and congested areas are selected. The specifications of the gasoline carriage are presented in Table 3. This fuel does not damage the health of exposed people [72]. The case study assumed that the atmospheric conditions are stable with a wind speed of 360 m/h.

3. Results

3.1. The Results of Probability Prediction

3.1.1. Bowtie Results. BT results show that defects in rail car compartments and packaging (containers, etc.) are identified as some of the main causes of HM release. Finally, 29 root causes (BE) and 19 intermediate causes (IE) for material release are identified. The specifications of each of the causes and their classical probabilities are presented in Table 3. Moreover, Figure 3 shows the general ET regarding HM leakage. If the flammable HM is released, a pool of fire occurs when there is an immediate ignition source; in addition, if the emergency response team does not respond at the right time, and given the right conditions, continuous material leakage could lead to dispersion. The dispersion of any chemical product can cause vapor cloud and health damage in the absence of ignition.

Moreover, if being a delay in the ignition and the environment congested, VCE is expected to occur due to inhalation of the vapor. On the other hand, flash fire is expected if there are no sources of delayed ignition in the open-space environment. In this regard, Table 4 shows the probabilities (per calendar year) of the parameters related to this diagram.

3.1.2. BN Results. Figure 4 demonstrates the ET diagram related to the HM leakage. In addition, the numerical results are presented in Table 5. Accordingly, the probability of Hazmat leakage is 1.18E-2 or once every 84 years (Table 5). The railway line studied has been operated for 11 years without any significant leakages; accurate statistics of rail accidents in the study area are scarce. Mirabadi et al. [6] regarding the influencing causes of rail accidents between 1994 and 2005 revealed that human error, locomotive defects, and defects in rail cars had the most significant impact on rail accidents in Tehran. This existing study corroborates the results of the present study. Moreover, the quantitative probabilities of health damage (per working year), VCE, flash fire, and pool fire are 2.40E-3, 3.80E-2, 2.50E-3, and 2.50E-3, respectively. In addition, the probability of successful containment is obtained as a 6.00E-4/working year.

3.2. The Results of Severity Estimation

3.2.1. VCE Modeling Results. The radii of the rail car's explosion are calculated as shown in Figure 5. This further reveals the overpressure is caused by VCE in three states of obstacles in retrospect of the distance from the point of explosion. The chart shows that VCE pressure in the "high obstacles" state is significantly different from other states. Under the mentioned conditions, VCE pressure is 3.72 bar (372500 N/m2) when it is three meters away from the leakage point, and it is 1.20 bar (12000 N/m2) and 0.10 bar (10000 N/m2), respectively, in the "medium obstacles" and "low obstacles" conditions.

The severity coefficient of VCE is presented in Figure 6. As shown in this figure, the probability of fatality for the population exposed to VCE in the "high obstacles" state is 100% (severity coefficient = 1) at a distance up to 37 meters away from the explosion point. In the "medium obstacles" state, at a distance of 3 meters away from the leakage point, the probability of fatality for the exposed population is coming 10% (severity coefficient = 0.1). In the "low obstacles" state, the probability of fatality at all distances becomes zero (severity coefficient = 0).

Table 1: The details of fuzzy set system related to toxicological effects.

Level of factor	Airborne concentration of the substance	LT*	Vulnerability groups (age)	LT	AEGL-2 (10 min) (ppm)	LT	Toxicological effect	LT
1	<NOAEL of material	L	18 to 34	L	>1000	L	Low	L
2	<IDLH of material	LM	34 to 54	LM	500 to 100	LM	Low-moderate	LM
3	<LC50 of material	M	11 to 18 and 54 to74	MH	100 to 500	MH	Moderate	M
4	<Lethal dose of material	MH	Sensitive group<11>74	H	<100	H	Moderate-high	MH
5	>Lethal dose of material	H					High	H

*LT: linguistic term, L: low, LM: low-moderate, M: moderate, MH: moderate-high, H: high.

Table 2: The details of fuzzy set system related to severity impact coefficient (SIC).

Level of factor	Number of people in 2500 m^2 (person)	LT*	Route distance to residential points (m)	LT	Number of critical points	LT	SIC**	LT
1	<10	L	>40	L	0	L	Low	L
2	10 to 50	LM	30 to 40	LM	1	LM	Low-moderate	LM
3	50 to 100	MH	20 to30	MH	2 and 3	MH	Moderate-high	MH
4	>100	H	<20	H	3>	H	High	H

*LT: linguistic term, **SIC: severity impact coefficient, L: low, LM: low-moderate, M: moderate, MH: moderate-high, H: high.

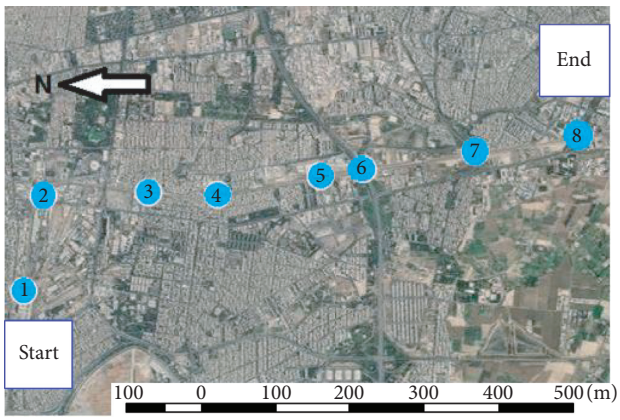

Figure 2: Study nodes in the selected rail system.

Table 3: The properties of transported material.

Material	Volume (m^3)	Stability class	AEGL-2 10 min (mg/m3)	Lc50 (g/m3)	IDLH (g/m3)	Reactivity level	Heat combustion (mj/kg)
Gasoline	65	Relatively stable		300	38.24	High	45.5

IDLH: immediately dangerous to life or health, AEGL-2: acute exposure guideline levels, LC: lethal concentration.

3.2.2. Toxicological Modeling Results. Based on the dispersion and the classifications in the fuzzy set, the airborne concentration of gasoline vapor at the dispersion area is 0.07 g/m^3. It should be noted that this amount is meager; thus, it is classified as the *L* level of the fuzzy system. This concentration is well below the toxicological indices of gasoline. Other cases are analyzed via the FL based on the ages of the population and the toxicological characteristics of gasoline. Table 6 shows the results of the case study using this system.

It is observed that no information is available on AEGL-2 *e* or the NOAEL (no observed adverse effect level) of gasoline, and the level of AEGL-2 gasoline *L* is taken into account. Going by the results, if gasoline is released, the concentration of gasoline vapor will be lower than the NOAEL. Consequently, the radius is not affected by different parts due to the concentration deficit at the leakage point. The graph reveals that the exposure severity decreases as it moves away from the leakage point. Hence, the vulnerability of any individual will be determined by the exposure coefficient.

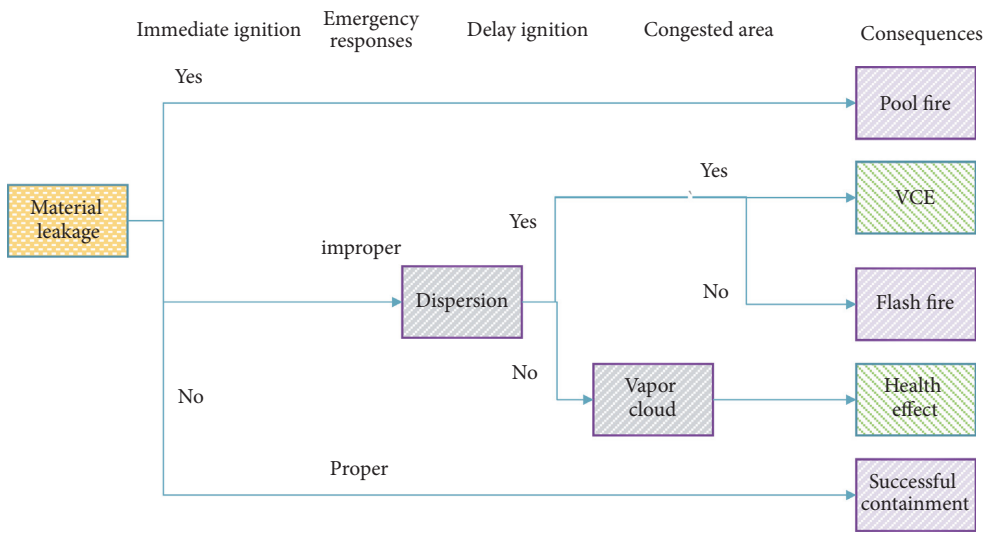

Figure 3: Event tree (ET) diagram related to the hazardous material (HM) leakage.

Table 4: Basic and intermediate causes in BT and BN diagram and the corresponding probability.

Event	BT probability (calendar year)	BN probability (calendar year)	Event	BT probability (calendar year)	BN probability (calendar year)
Basic event			Failure to connect rail cars	7.00*E*-3	6.00*E*-2
Defects in radio communication signals	1.00*E*-2	8.60*E*-2	Malfunction in terminal monitoring system	4.00*E*-3	4.00*E*-3
Fault in the emergency brake system	6.00*E*-3	1.00*E*-4	Burnout of material containers	3.00*E*-3	3.00*E*-3
Wheels broken	8.00*E*-4	6.00*E*-3	Holes in the body of the container	3.00*E*-3	3.00*E*-3
Intentional error in leaving the train	2.00*E*-3	1.70*E*-2	Intermediate event		
Operator inexperience	8.00*E*-3	6.90*E*-2	Accident	1.07*E*-1	8.84*E*-1
High-speed train	1.00*E*-2	8.60*E*-2	Defect in rail car body	1.50*E*-2	1.29*E*-1
Lack of familiarity with the route of transport of materials	1.00*E*-4	1.00*E*-4	Defects in packaging materials	2.40*E*-5	1.00*E*-4
Fault in rail connections	2.00*E*-3	1.70*E*-2	Exit train from rails	3.61*E*-2	3.07*E*-1
Rail fracture	4.00*E*-3	3.40*E*-2	Train collision with another train	7.17*E*-2	5.99*E*-1
Error in the route monitoring system	5.50*E*-3	4.70*E*-2	Planning error	2.35*E*-2	2.01*E*-1
Error in line adjustment by the operator	3.00*E*-3	2.60*E*-2	Operator error	1.82*E*-2	1.56*E*-1
Error in the route monitoring system	8.00*E*-3	3.90*E*-2	Inappropriate weather conditions	8.00*E*-3	6.9*E*-2
Operator error in timing	7.00*E*-3	6.00*E*-2	A technical defect in train	1.60*E*-2	1.37*E*-1
Operator inexperience	8.00*E*-3	6.90*E*-2	Railway defect	6.00*E*-3	1.05*E*-2
Operator fatigue	1.00*E*-3	8.06*E*-2	Error in setting lines	8.50*E*-3	7.30*E*-2
Lack of familiarity with the route of transport of materials	2.00*E*-4	2.00*E*-3	Error in scheduling	1.50*E*-2	1.29*E*-1
Intentional error in train collision with another train	1.00*E*-5	1.00*E*-5	A technical defect in train	1.00*E*-2	8.60*E*-2
Dusty railway	6.00*E*-3	5.00*E*-2	Operator error	2.01*E*-2	1.72*E*-2
Foggy railway	2.00*E*-3	1.70*E*-2	Railway defect	6.00*E*-3	5.20*E*-2
Defects in radio communication signals	1.00*E*-2	8.60*E*-2	Defects in train wheels	4.80*E*-6	1.00*E*-6
Fault in the emergency brake system	6.00*E*-3	5.20*E*-2	Unintentional error in leaving the train	1.81*E*-2	1.55*E*-1

Table 4: Continued.

Event	BT probability (calendar year)	BN probability (calendar year)	Event	BT probability (calendar year)	BN probability (calendar year)
Fault in rail connections	2.00*E*-3	1.70*E*-2	Unintentional crash on the train with another train	1.82*E*-2	1.56*E*-2
Rail fracture	4.00*E*-3	3.40*E*-2	Defects in the body of containers carrying materials	6.00*E*-3	6.00*E*-3
Leakage of the rail car body	3.00*E*-3	2.60*E*-2	Top event		
Wreckage of rail car body	5.00*E*-3	4.30*E*-2	Material leakage	1.225*E*-1	1.16*E*-1

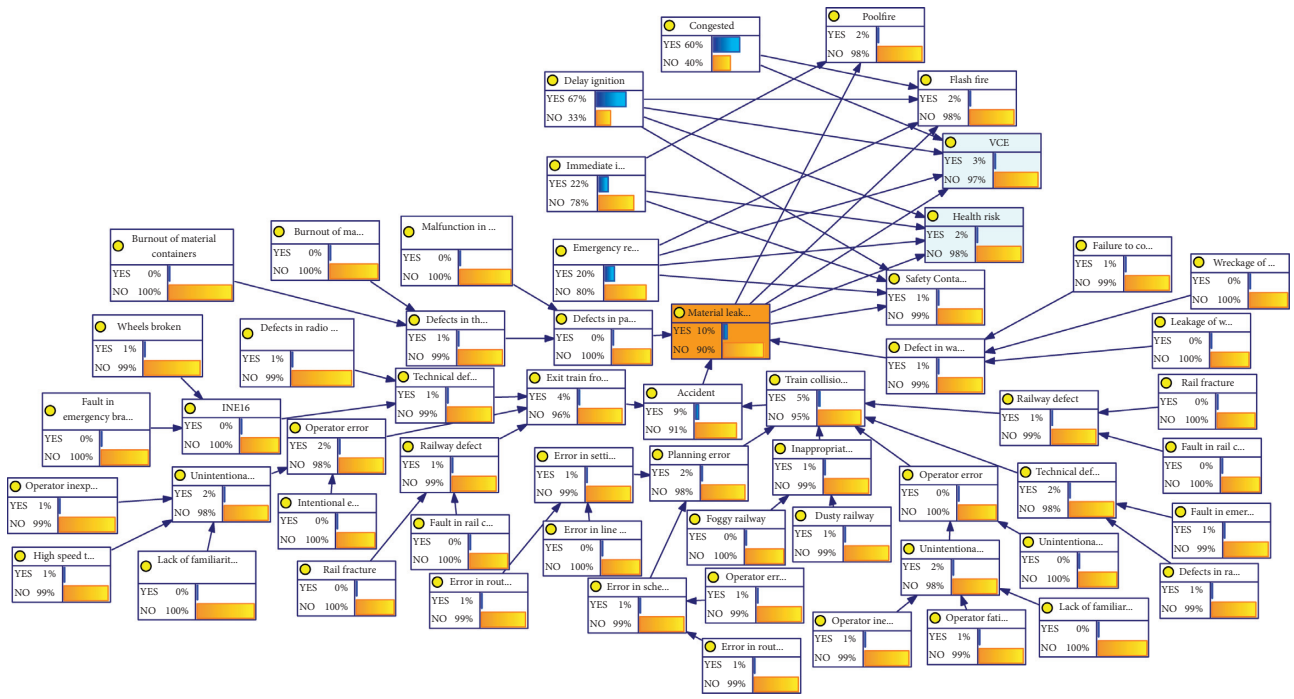

Figure 4: Bayesian network model of gasoline leakage.

Table 5: The barriers and consequences related to material leakage from rail cars.

Barrier	Probability (working year)*	Consequences	BT probability (working year)	BN probability (working year)
Material leakage	1.18*E*-2	Pool fire	7.90*E*-3	2.50*E*-3
Immediate ignition	6.70*E*-1	Flash fire	1.00*E*-3	2.50*E*-3
Delay ignition	2.20*E*-1	VCE	1.50*E*-3	3.80*E*-2
Proper emergency responses	2.00*E*-1	Health risk	4.70*E*-3	2.40*E*-3
Congested area	6.00*E*-1	Safe containment	3.80*E*-3	6.00*E*-4

*Working year = calendar year×0.119.

3.3. SIC Estimation Results. In this section, eight study nodes are evaluated. The final scores (rank) of all the selected nodes are presented in Figure 7. Based on the results, node 5, with a coefficient of 1.50, has the highest, and node 6, with a SIC of 1.15, has the lowest coefficient. So, node 5 is considered a basic node in calculating QRA.

3.4. QRA Results. Based on the BN results, the health and safety simulations, and the determined SICs, the individual quantitative risks in the health and safety consequences are calculated using Equation (8). Figures 8–10 show the final findings of the quantitative VCE and toxicology risk assessment. The risk also approached zero at 55 m. Therefore, safe construction distance should be determined based on node 5 and age group 4. As presented in Figure 8, the individual risk of fatality due to VCE at a distance of 3 meters away from the leakage point is 8.49E-3 per working year. Figure 9 also shows that the individual risk of fatality from a VCE at a distance of 3 meters away from the leakage point is 8.49E-2 per working year. The trend of decreasing risk relative to the distance in the "medium density" state is abnormal due

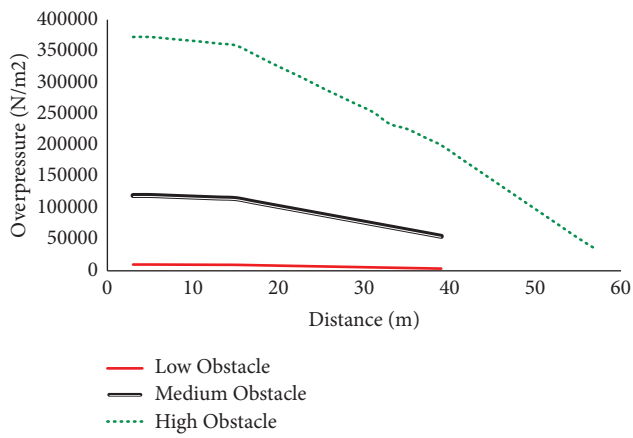

Figure 5: VCE overpressure at different distances from the leakage point.

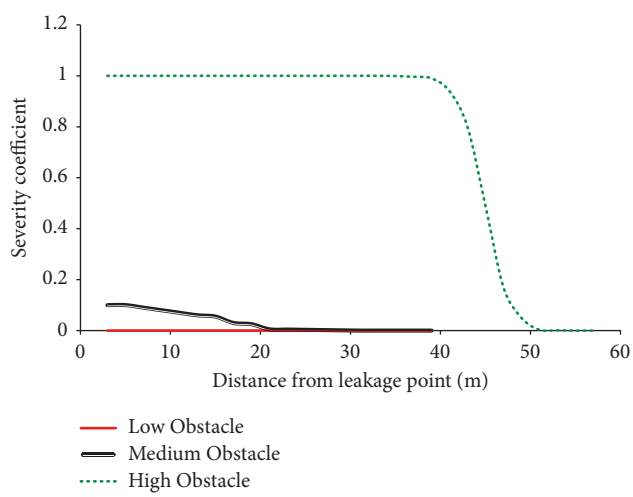

Figure 6: VCE severity at different distances from the leakage point.

Table 6: Severity coefficient of exposure to gasoline vapor in different age groups using FIS.

Groups	Vulnerability class	Severity coefficient
1	Age range: 18–34	0.08
2	Age range: 35–54	0.12
3	Age range: 11–17 and 55–74	0.2
4	Pregnant women, persons with underlying illness, age range: ≥75 and ≤10	0.5

to reference diagrams adopted for the BS method. Conversely, Figure 10 shows a significant difference between the risk of irreversible health damage between age group 4 and other groups. Based on this, it was found that the risk faced by group 4 is 1.78E-3 and group 1 is 2.85E-4 per working year. These risks were calculated based on the SIC of node 5.

The risk map is plotted based on the results of Equation (8) (see Figure 11, considering the most severe cases = node 5

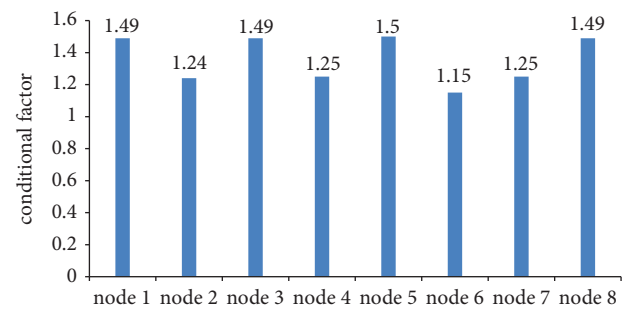

Figure 7: Severity impact coefficient (SIC) in the studied nodes.

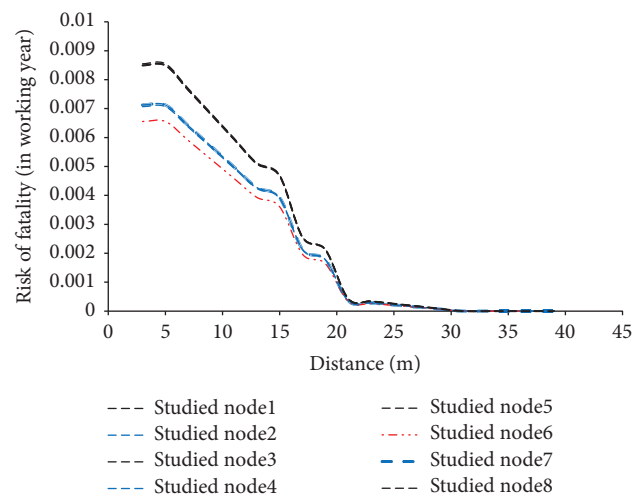

Figure 8: Individual severity of VCE based on the "medium obstacles" level.

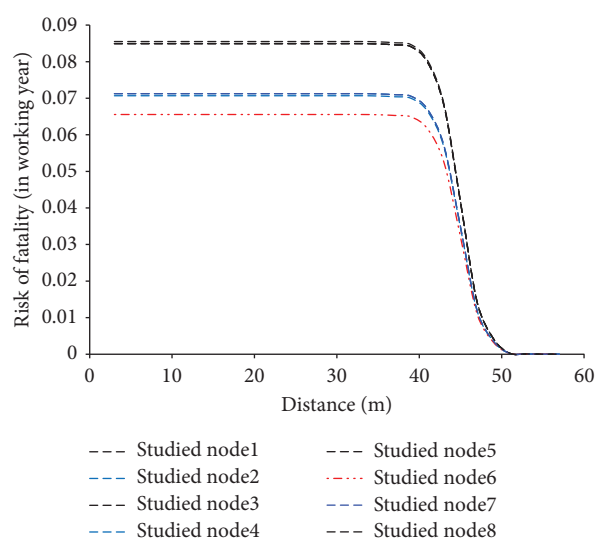

Figure 9: Individual risk of VCE based on the "medium obstacles" level.

and the "high obstacles" state in the BS method). Based on the three criteria mentioned above, at 50.00, 53.00, and 54.50 meters away from the leakage point, the individual

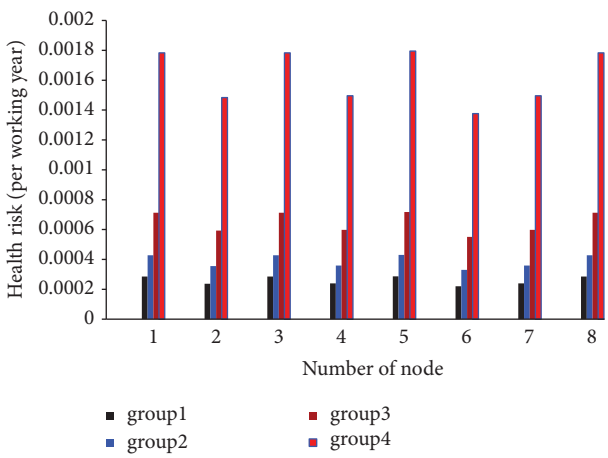

Figure 10: Health risk in different age groups in the selected study nodes.

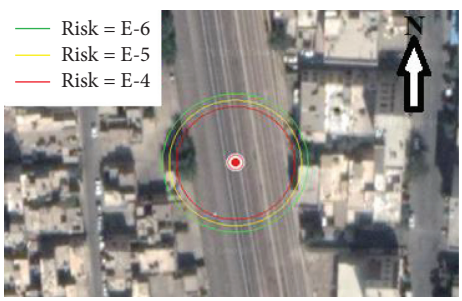

Figure 11: Explosion risk map based on the three criteria in node 5.

risks (per working year) are obtained as 1.00E-4, 1.00E-5, and 1.00E-6, respectively. It should be noted that given the low amount of health risk in the case studied, the risk map is plotted based on the risk of VCE.

4. Discussion

In the present study, the QRA related to the consequences of the leakage of petroleum products in railway transport is conducted using BN and FL systems. The BN is used to estimate the quantitative probability of gasoline release and possible consequences such as toxicological effects and VCE. In addition, a combination of equations is used to simulate the VCE. Furthermore, a fuzzy set is applied to simulate and evaluate the severity of toxicological consequences and estimate the SIC of the studied nodes.

The proposed model indicates that BN can be used as a proper tool in improving the accuracy of the probabilistic findings related to cause-consequences analysis. This assertion has been posited by Khakzad et al. [51]. The present study shows that considering the nonlinear relationships between influential parameters produced higher accuracy than the BT method; this is also in conformity with the previous work of Zarei et al. [43] and Aliabadi et al. [6]. In addition, the present study corroborates the findings of Papazoglou et al. [73] that a direct relationship exists between the heat of combustion and overpressure. Moreover, our findings proved that a direct relationship between the distance from the point of explosion and the probability of mortality is consistent with Azhar et al. [61]. The proposed hybrid equation can also simulate explosions in petroleum liquids. Thus, the results indicate that the probit (the probit function is the quantitative function associated with the standard normal distribution) of mortality must be used to determine the recommended safe distances. Nevertheless, a different approach by Chakrabarti [21] where pressure from the explosion point was used to determine safe distances is used as the basis for comparing the proposed study.

On the other hand, in the study of Jahangiri et al. [74], the factor of "National Fire Protection Association (NFPA) 704" [75] was considered as the only influential factor in transportation risk. However, in the present study, the equations related to estimating airborne concentration and the fuzzy set theory based on the vulnerability of community groups are used. In designing the fuzzy system for simulating the toxicological effects, we were tried to consider all the influencing factors. For instance, in compiling the approach by Azar et al. [76] in designing this system, the main factor of acute exposure, namely AEGL-2 (10 min), is considered as one of the systems' inputs. In line with Milovanović et al.' [77], chemical characteristics and the sensitivity class of the exposed peoples are equally considered. The findings show that group 4 should be considered the base group in determining the safe distance. Our approach in this regard is in line with the approach of Huang et al. [78].

In analyzing technical and human factors, the results obtained can be compared with similar studies. Our results show inexperience as one of the major causes of rail accidents. This is consistent with the findings of Kyriakidis et al. [79] who reported that familiarity was one of the main causes (15.4% of accidents) of rail accidents. The ability to properly monitor the system and skills required for performing routine settings and repairs are identified as the most vital parts of the human factor. It is found that the level of monitoring and accuracy in repairs and detection of defects with a failure rate = 8.00E-3 is higher than what was reported by Singh et al. [80] with a failure rate = 1.00E-2. In line with the study conducted by Rose et al. [45], Baysari et al. [81], as well as Kim et al. [47], BT analysis of the proposed study shows that human factors directly impacted the technical failure rate of the equipment. Therefore, the defects in the maintenance of the equipment directly impact the defect rate of the brake and wheel systems of the rail cars. These systems are identified as the safest technical part of the rail cars because of the good level of monitoring and maintenance. This level is higher than the level calculated by Kumar et al. [82] with a Brake system failure rate = 0.20 and Singh et al. [80] study with a wheel failure rate = 0.039.

Contrary to Oggero et al. [12], BN is used instead of ET to estimate the consequence probability. This improved the accuracy of probability calculations. Although Marsh et al. [83] used the Bayesian network to model rail events, root causes and possible BN consequences are further considered in this study. Contrary to the study conducted by Liu et al. [10], who cited railroad fractures as the main cause of

accidents (from 2001 to 2010), this study identified radio communication defects and unauthorized speeds as the main causes of accidents in rail cars. The divergent results can be attributed to Iran's other monitoring and surveillance systems and other countries.

The study of Andrew and Dunnett [84] on the statistics of rail accidents in Europe showed that radio communication failure is one of the significant causes of rail accidents. However, the present study adopts a new approach for quantitative risk assessment of petroleum products transport in the rail network. It, therefore, shows that gasoline could not cause health damage in healthy groups of the community. Adequate preventive measures should be taken to protect the vulnerable group 4, as stated in this study. The authors suggest that moving residential areas out of the dangerous zones can be a beneficial sure in this regard.

Although the radius of health effects on gasoline leakage was not obtained, the authors strongly believe that in the transportation of all liquid HM, the approach of this study can be used to assess the risk of toxicological effects. The findings show that residential areas, roads, and pedestrian crossings should be constructed over 54 meters away from railway networks. In addition, our findings show that Hazmat transportation during the day when there is less pedestrian or vehicle traffic (00 : 00 to 05 : 00 am) is the more appropriate option to decrease the risk of hazardous incidents. Moreover, looking at the equations used in VCE simulation, it can be seen that the volume of the reservoirs has the most significant impact on the overpressure. Therefore, the authors suggest that the reservoirs' volume should be reduced as much as conceivable. For example, if the volume of the tanks decreases by 50 percent, at 11 meters from the center of the explosion, we can see a 25% reduction in the radius of the vapor cloud and a reduction of 1,000 N/m^2 in the overpressure. This reduction can decrease the risk significantly by 18%. Future studies can focus on optimizing the routes based on the proposed method and utilizing other simulation systems such as genetic algorithms and dynamic analysis.

5. Conclusion

Rail transporting of hazardous materials has led to severe accident occurrences. These potential accidents pose severe risks to humans and the environment. Therefore, a risk assessment should be conducted to ensure that potential hazards are adequately identified and controlled. To this end, the present research has developed a concerted model to assess the safety and health risks of Hazmat transporting in railway systems. The proposed model used the BNs to develop a quantitative cause-consequences modeling beginning from the root events. Several factors contributing to health and safety risks are included in the risk function developed using the fuzzy set theory. This operation deals with the epistemic uncertainty in estimating the severity parameter and provides a precise risk prediction. The proposed risk model can analyze the possible risks and safely design transporting routes and third parts such as transporting rules. This research focuses on VCE as the worst safety consequence, while other types of fire and explosion, such as pool fire and flash fire, occur only when released into the atmosphere.

Moreover, the health concerns and safety characteristics of other hazards that may be different from gasoline are investigated in the present study. Finally, domino effects in rail transportation of chemical materials in terms of VCE and BLEVE can impose significant risks. These are not modeled in the current research. Hence, this can be posed as new opportunities for future investigations.

Data Availability

In this study, the data used in the Bayesian network were obtained through the fuzzy hierarchical analysis (FHA) and using the opinions of safety and rail experts. Parameters affecting material leakage as well as parameters affecting the fuzzy systems used were identified and classified by reviewing past studies and using the opinions of experts. This content is described in the text of the article quite clearly. All of these data can be found in the text of the study.

Conflicts of Interest

The authors declare that they have no conflicts of interest.

Acknowledgments

The authors would like to thank the Tehran Petroleum Products Distribution Company for their cooperation and HUMS for financial support. This study has been supported by Hamadan University of Medical Sciences, grant no. 9803282465.

References

[1] X. Liu, T. Turla, and Z. Zhang, "Accident-cause-specific risk analysis of rail transport of hazardous materials," *Transportation Research Record: Journal of the Transportation Research Board*, vol. 2672, no. 10, pp. 176–187, 2018.

[2] H. Kalantari and I. Razini, "Railway transport market ranking and target markets offer," *Journal of Commerce*, vol. 21, no. 81, pp. 149–180, 2016.

[3] P. E. Dept, *Hazmat Transportation by Rail: An Unfair Liability*, Association of American Railroads, Washington, DC, USA, 2009.

[4] E. Zarei, K. Gholamizadeh, F. Khan, and N. Khakzad, "A dynamic domino effect risk analysis model for rail transport of hazardous material," *Journal of Loss Prevention in the Process Industries*, vol. 74, Article ID 104666, 2022.

[5] I. Mohammadfam, M. N. Abdullah, and K. Gholamizadeh, "Developing a comprehensive technique for investigating hazmat transport accidents," *Journal of Failure Analysis and Prevention*, vol. 21, no. 4, pp. 1362–1373, 2021.

[6] M. M. Aliabadi and K. Gholamizadehx, "Locating urban CNG stations using quantitative risk assessment: using the Bayesian network," *Safety and Reliability*, vol. 40, 2021.

[7] X. Liu, M. R. Saat, and C. P. L. Barkan, "Integrated risk reduction framework to improve railway hazardous materials transportation safety," *Journal of Hazardous Materials*, vol. 260, pp. 131–140, 2013.

[8] U. S. N. T. S. B. Ntsb, "Collision of norfolk southern freight train 192 with standing norfolk southern local train P22 with subsequent hazardous materials release at Graniteville, South Carolina. 490 LíEnfant plaza, S.W. Washington, D.C. 20594: railroad accident report," Report No.: NTSB/RAR-05/04 Contract No.: PB2005-916304, Washington, DC, USA, 2005.

[9] S. Ghazinoory and A. S. Kheirkhah, "Transportation of hazardous materials in Iran: a strategic approach for decreasing accidents," *Transport*, vol. 23, no. 2, pp. 104–111, 2008.

[10] X. Liu, M. R. Saat, and C. P. L. Barkan, "Analysis of causes of major train derailment and their effect on accident rates," *Transportation Research Record: Journal of the Transportation Research Board*, vol. 2289, no. 1, pp. 154–163, 2012.

[11] T. S. Glickman and E. Erkut, "Assessment of hazardous material risks for rail yard safety," *Safety Science*, vol. 45, no. 7, pp. 813–822, 2007.

[12] A. Oggero, R. M. Darbra, M. Muñoz, E. Planas, and J. Casal, "A survey of accidents occurring during the transport of hazardous substances by road and rail," *Journal of Hazardous Materials*, vol. 133, no. 1-3, pp. 1–7, 2006.

[13] S. Reinach and A. Viale, "Application of a human error framework to conduct train accident/incident investigations," *Accident Analysis & Prevention*, vol. 38, no. 2, pp. 396–406, 2006.

[14] R. Bubbico, S. Di Cave, and B. Mazzarotta, "Risk analysis for road and rail transport of hazardous materials: a GIS approach," *Journal of Loss Prevention in the Process Industries*, vol. 17, no. 6, pp. 483–488, 2004.

[15] M. Verma, "A cost and expected consequence approach to planning and managing railroad transportation of hazardous materials," *Transportation Research Part D: Transport and Environment*, vol. 14, no. 5, pp. 300–308, 2009.

[16] M. R. Saat, C. J. Werth, D. Schaeffer, H. Yoon, and C. P. L. Barkan, "Environmental risk analysis of hazardous material rail transportation," *Journal of Hazardous Materials*, vol. 264, pp. 560–569, 2014.

[17] A. W. Evans, "Fatal train accidents on Europe's railways: 1980-2009," *Accident Analysis & Prevention*, vol. 43, no. 1, pp. 391–401, 2011.

[18] H. B. Spraggins, "The case for rail transportation of hazardous materials," *Journal of Management and Marketing Research*, vol. 3, no. 1, pp. 88–95, 2010.

[19] U. K. Chakrabarti and J. K. Parikh, "Route risk evaluation on class-2 hazmat transportation," *Process Safety and Environmental Protection*, vol. 89, no. 4, pp. 248–260, 2011.

[20] U. K. Chakrabarti and J. K. Parikh, "Applying HAZAN methodology to hazmat transportation risk assessment," *Process Safety and Environmental Protection*, vol. 90, no. 5, pp. 368–375, 2012.

[21] U. K. Chakrabarti and J. K. Parikh, "A societal risk study for transportation of class-3 hazmats - a case of Indian state highways," *Process Safety and Environmental Protection*, vol. 91, no. 4, pp. 275–284, 2013.

[22] E. Zarei, M. J. Jafari, and N. Badri, "Risk assessment of vapor cloud explosions in a hydrogen production facility with consequence modeling," *Journal of Research in Health Sciences*, vol. 13, no. 2, pp. 181–187, 2013.

[23] A. Dormohammadi, E. Zarei, M. B. Delkhosh, and A. Gholami, "Risk analysis by means of a QRA approach on a LPG cylinder filling installation," *Process Safety Progress*, vol. 33, no. 1, pp. 77–84, 2014.

[24] O. Ahmadi, S. B. Mortazavi, H. A. Mahabadi, and M. H. Pouri, "Development of a dynamic quantitative risk assessment methodology using fuzzy DEMATEL-BN and leading indicators," *Process Safety and Environmental Protection*, vol. 142, 2020.

[25] L. Gooijer, N. Cornil, and C. L. Lenoble, "An international comparison of four quantitative risk assessment approaches-A benchmark study based on a fictitious LPG plant," *Process Safety and Environmental Protection*, vol. 90, no. 2, pp. 101–107, 2012.

[26] J. R. González Dan, A. Guix, V. Martí, J. Arnaldos, and R. M. Darbra, "Monte Carlo simulation as a tool to show the influence of the human factor into the quantitative risk assessment," *Process Safety and Environmental Protection*, vol. 102, pp. 441–449, 2016.

[27] C. Guo, F. Khan, and S. Imtiaz, "Copula-based Bayesian network model for process system risk assessment," *Process Safety and Environmental Protection*, vol. 123, pp. 317–326, 2019.

[28] S. M. Miri Lavasani, Z. Yang, J. Finlay, and J. Wang, "Fuzzy risk assessment of oil and gas offshore wells," *Process Safety and Environmental Protection*, vol. 89, no. 5, pp. 277–294, 2011.

[29] I. Mohammadfam and E. Zarei, "Safety risk modeling and major accidents analysis of hydrogen and natural gas releases: a comprehensive risk analysis framework," *International Journal of Hydrogen Energy*, vol. 40, no. 39, Article ID 13653, 2015.

[30] M. J. Jafari, E. Zarei, and N. Badri, "The quantitative risk assessment of a hydrogen generation unit," *International Journal of Hydrogen Energy*, vol. 37, no. 24, Article ID 19241, 2012.

[31] E. Zarei, F. Khan, and M. Yazdi, "A dynamic risk model to analyze hydrogen infrastructure," *International Journal of Hydrogen Energy*, vol. 46, no. 5, pp. 4626–4643, 2021.

[32] Y. Li, D. Xu, and J. Shuai, "Real-time risk analysis of road tanker containing flammable liquid based on fuzzy Bayesian network," *Process Safety and Environmental Protection*, vol. 134, pp. 36–46, 2020.

[33] M. An, W. Lin, and A. Stirling, "Fuzzy-reasoning-based approach to qualitative railway risk assessment," *Proceedings of the Institution of Mechanical Engineers - Part F: Journal of Rail and Rapid Transit*, vol. 220, no. 2, pp. 153–167, 2006.

[34] C. R. C. Hassan, B. Puvaneswaran, A. R. Aziz, M. N. Zalina, F. C. Hung, and N. M. Sulaiman, "Quantitative risk assessment for the transport of ammonia by rail," *Process Safety Progress*, vol. 29, no. 1, pp. 60–63, 2010.

[35] B. Leitner, "A general model for railway systems risk assessment with the use of railway accident scenarios analysis," *Procedia Engineering*, vol. 187, pp. 150–159, 2017.

[36] N. Paltrinieri, G. Landucci, M. Molag, S. Bonvicini, G. Spadoni, and V. Cozzani, "Risk reduction in road and rail LPG transportation by passive fire protection," *Journal of Hazardous Materials*, vol. 167, no. 1-3, pp. 332–344, 2009.

[37] Z. Zhang, X. Li, and H. Li, "A quantitative approach for assessing the critical nodal and linear elements of a railway infrastructure," *International Journal of Critical Infrastructure Protection*, vol. 8, pp. 3–15, 2015.

[38] M. Yazdi and E. Zarei, "Uncertainty handling in the safety risk analysis: an integrated approach based on fuzzy fault tree analysis," *Journal of Failure Analysis and Prevention*, vol. 18, no. 2, pp. 392–404, 2018.

[39] R. Ferdous, F. Khan, R. Sadiq, P. Amyotte, and B. Veitch, "Fault and event tree analyses for process systems risk analysis: uncertainty handling formulations," *Risk Analysis*, vol. 31, no. 1, pp. 86–107, 2011.

[40] A. S. Markowski and A. Kotynia, ""Bow-tie" model in layer of protection analysis," *Process Safety and Environmental Protection*, vol. 89, no. 4, pp. 205–213, 2011.

[41] A. Mentes and I. H. Helvacioglu, "An application of fuzzy fault tree analysis for spread mooring systems," *Ocean Engineering*, vol. 38, no. 2-3, pp. 285–294, 2011.

[42] Ö Uğurlu, E. Köse, U. Yıldırım, and E. Yüksekyıldız, "Marine accident analysis for collision and grounding in oil tanker using FTA method," *Maritime Policy & Management*, vol. 42, no. 2, pp. 163–185, 2015.

[43] E. Zarei, A. Azadeh, N. Khakzad, M. M. Aliabadi, and I. Mohammadfam, "Dynamic safety assessment of natural gas stations using Bayesian network," *Journal of Hazardous Materials*, vol. 321, pp. 830–840, 2017.

[44] M. An, S. Huang, and C. J. Baker, "Railway risk assessment - the fuzzy reasoning approach and fuzzy analytic hierarchy process approaches: a case study of shunting at Waterloo depot," *Proceedings of the Institution of Mechanical Engineers - Part F: Journal of Rail and Rapid Transit*, vol. 221, no. 3, pp. 365–383, 2007.

[45] J. A. Rose and C. Bearman, "Making effective use of task analysis to identify human factors issues in new rail technology," *Applied Ergonomics*, vol. 43, no. 3, pp. 614–624, 2012.

[46] N. Rhayma, P. Bressolette, P. Breul, M. Fogli, and G. Saussine, "A probabilistic approach for estimating the behavior of railway tracks," *Engineering Structures*, vol. 33, no. 7, pp. 2120–2133, 2011.

[47] D. S. Kim, D. H. Baek, and W. C. Yoon, "Development and evaluation of a computer-aided system for analyzing human error in railway operations," *Reliability Engineering & System Safety*, vol. 95, no. 2, pp. 87–98, 2010.

[48] S. Kwag, A. Gupta, and N. Dinh, "Probabilistic risk assessment based model validation method using Bayesian network," *Reliability Engineering & System Safety*, vol. 169, pp. 380–393, 2018.

[49] E. Zarei, N. Khakzad, V. Cozzani, and G. Reniers, "Safety analysis of process systems using Fuzzy Bayesian Network (FBN)," *Journal of Loss Prevention in the Process Industries*, vol. 57, pp. 7–16, 2019.

[50] E. Zarei, M. Yazdi, R. Abbassi, and F. Khan, "A hybrid model for human factor analysis in process accidents: FBN-HFACS," *Journal of Loss Prevention in the Process Industries*, vol. 57, pp. 142–155, 2019.

[51] N. Khakzad, F. Khan, and P. Amyotte, "Dynamic risk analysis using bow-tie approach," *Reliability Engineering & System Safety*, vol. 104, pp. 36–44, 2012.

[52] F. Aqlan and E. Mustafa Ali, "Integrating lean principles and fuzzy bow-tie analysis for risk assessment in chemical industry," *Journal of Loss Prevention in the Process Industries*, vol. 29, pp. 39–48, 2014.

[53] H. Abdo, M. Kaouk, J.-M. Flaus, and F. Masse, "A safety/security risk analysis approach of Industrial Control Systems: a cyber bowtie - combining new version of attack tree with bowtie analysis," *Computers & Security*, vol. 72, pp. 175–195, 2018.

[54] R. W. McLeod and P. Bowie, "Bowtie Analysis as a prospective risk assessment technique in primary healthcare," *Policy and Practice in Health and Safety*, vol. 16, no. 2, pp. 177–193, 2018.

[55] N. Khakzad, F. Khan, and P. Amyotte, "Safety analysis in process facilities: comparison of fault tree and Bayesian network approaches," *Reliability Engineering & System Safety*, vol. 96, no. 8, pp. 925–932, 2011.

[56] N. Khakzad, F. Khan, and P. Amyotte, "Dynamic safety analysis of process systems by mapping bow-tie into Bayesian network," *Process Safety and Environmental Protection*, vol. 91, no. 1-2, pp. 46–53, 2013.

[57] W. Premchaiswadi, *Bayesian Networks*, BoD–Books on Demand, United Kingdom, 2012.

[58] Q. A. Baker, M. J. Tang, E. A. Scheier, and G. J. Silva, "Vapor cloud explosion analysis," *Process Safety Progress*, vol. 15, no. 2, pp. 106–109, 1996.

[59] C. Chen, N. Khakzad, and G. Reniers, "Dynamic vulnerability assessment of process plants with respect to vapor cloud explosions," *Reliability Engineering & System Safety*, vol. 200, Article ID 106934, 2020.

[60] M. J. Assael and K. E. Kakosimos, *Fires, Explosions, and Toxic Gas Dispersions: Effects Calculation and Risk Analysis*, CRC Press, Boca Raton, FL, USA, 2010.

[61] S. S. Azhar, M. Abdul Rah, M. Saari, K. F. Hafiz, and D. Suhardy, "Risk assessment study for storage explosive," *American Journal of Applied Sciences*, vol. 3, no. 1, pp. 1685–1689, 2006.

[62] I. Mohammadfam and K. Gholamizadeh, "Assessment of security risks by FEMA and fuzzy FEMA methods, A case study: combined cycle power plant," *Journal of Occupational Hygiene Engineering*, vol. 8, no. 2, pp. 15–23, 2021.

[63] B. Baranidharan and B. Santhi, "DUCF: distributed load balancing Unequal Clustering in wireless sensor networks using Fuzzy approach," *Applied Soft Computing*, vol. 40, pp. 495–506, 2016.

[64] K. Gholamizadeh, I. Mohammadfam, and O. Kalatpour, "Evaluation of the health consequences in Chemicals road transport accidents: using a fuzzy approach," *Journal of Occupational Hygiene Engineering*, vol. 6, no. 3, pp. 1–7, 2019.

[65] I. Mohammadfam, O. Kalatpour, and K. Gholamizadeh, "Quantitative assessment of safety and health risks in hazmat road transport using a hybrid approach: a case study in tehran," *ACS Chemical Health & Safety*, vol. 27, no. 4, pp. 240–250, 2020.

[66] J. J. Peirce, R. Weiner, R. Matthews, and P. A. Vesilind, *Environmental Engineering*, Butterworth-Heinemann, Oxford, UK, 2003.

[67] N. R. Council, *Acute Exposure Guideline Levels for Selected Airborne Chemicals*, National Academies Press, Washington, DC, USA, 2003.

[68] F. Camastra, A. Ciaramella, V. Giovannelli et al., "A fuzzy decision system for genetically modified plant environmental risk assessment using Mamdani inference," *Expert Systems with Applications*, vol. 42, no. 3, pp. 1710–1716, 2015.

[69] A. Jamshidi, A. Yazdani-Chamzini, S. H. Yakhchali, and S. Khaleghi, "Developing a new fuzzy inference system for pipeline risk assessment," *Journal of Loss Prevention in the Process Industries*, vol. 26, no. 1, pp. 197–208, 2013.

[70] A. Benzaouia and A. E. Hajjaji, *Advanced Takagi-Sugeno Fuzzy Systems*, Springer, Manhattan, NY, USA, 2016.

[71] J. Dawson, K. Bruce, and D. John, *Corrosion Risk Assessment and Safety Management for Offshore Processing Facilities*HSE Books, London, UK, 2001.

[72] Human Health Effects Of Fuel Oil No, "2 US National Library of Medicine: toxicology data network(TOXNET)," 2019.

[73] I. A. Papazoglou, P. Saravanos, I. Giakoumatos, and O. N. Aneziris, "Quantified risk assessment for plants producing and storing explosives," *International Journal of Automation and Computing*, vol. 3, no. 2, pp. 184–191, 2006.

[74] M. Jahangiri and H. Jamshidi, "Chemical transportation risk assessment in the pass leading to amirkabir terminal at shiraz city," *Iran Occupational Health*, vol. 13, no. 4, pp. 23–30, 2016.

[75] N. F. P. Association, *NFPA 704 Standard System for the Identification of the Hazards of Materials for Emergency Response 2007 Edition*, Technical report, NFPA, Quincy, 2009.

[76] A. Azar, M. Safarzadeh, and A. Ehsani, "Assessment of hazardous materials transportation on country roads case study: fars road network," *Rahavar Journal*, vol. 8, no. 16, pp. 7–20, 2012.

[77] B. Milovanović, V. D. Jovanović, P. Živanović, and S. Žeželj, "Methodology for establishing the routes for transportation of dangerous goods on the basis of the risk level-Case study: city of Belgrade," *Scientific Research and Essays*, vol. 7, no. 1, pp. 38–50, 2012.

[78] X. Huang, X. Wang, J. Pei, M. Xu, X. Huang, and Y. Luo, "Risk assessment of the areas along the highway due to hazardous material transportation accidents," *Natural Hazards*, vol. 93, no. 3, pp. 1181–1202, 2018.

[79] M. Kyriakidis, K. T. Pak, and A. Majumdar, "Railway accidents caused by human error," *Transportation Research Record: Journal of the Transportation Research Board*, vol. 2476, no. 1, pp. 126–136, 2015.

[80] S. Singh, R. Kumar, A. Barabadi, and S. Kumar, "Human error quantification of railway maintenance tasks of disc brake unit," *Lecture Notes in Engineering and Computer Science*, vol. 2212, 2014.

[81] M. T. Baysari, A. S. McIntosh, and J. R. Wilson, "Understanding the human factors contribution to railway accidents and incidents in Australia," *Accident Analysis & Prevention*, vol. 40, no. 5, pp. 1750–1757, 2008.

[82] S. Singh and R. Kumar, "Evaluation of human error probability of disc brake unit assembly and wheel set maintenance of railway bogie," *Procedia Manufacturing*, vol. 3, pp. 3041–3048, 2015.

[83] W. Marsh and G. Bearfield, "Using Bayesian networks to model accident causation in the UK railway industry," in *Probabilistic Safety Assessment and Management*Springer, London, UK, 2004.

[84] J. D. Andrews and S. J. Dunnett, "Event-tree analysis using binary decision diagrams," *IEEE Transactions on Reliability*, vol. 49, no. 2, pp. 230–238, 2000.

Hindawi
Mathematical Problems in Engineering
Volume 2021, Article ID 5092480, 15 pages
https://doi.org/10.1155/2021/5092480

Research Article

A New Moth-Flame Optimization Algorithm for Discounted {0-1} Knapsack Problem

Tung Khac Truong

Faculty of Information Technology, Van Lang University, Ho Chi Minh City, Vietnam

Correspondence should be addressed to Tung Khac Truong; tung.tk@vlu.edu.vn

Received 25 May 2021; Revised 6 June 2021; Accepted 18 June 2021; Published 1 November 2021

Academic Editor: Mohammad Yazdi

The discounted {0–1} knapsack problem may be a kind of backpack issue with gathering structure and rebate connections among things. A moth-flame optimization algorithm has shown good searchability combined with an effective solution presentation designed for the discounted {0-1} knapsack problem. A new encoding scheme used a shorter length binary vector to help reduce the search domain and speed up the computing time. A greedy repair procedure is used to help the algorithm have fast convergence and reduce the gap between the best-found solution and the optimal solution. The experience results of 30 discounted {0-1} knapsack problem instances are used to evaluate the proposed algorithm. The results demonstrate that the proposed algorithm outperforms the two binary PSO algorithms and the genetic algorithm in solving 30 DKP01 instances. The Wilcoxon rank-sum test is used to support the proposed declarations.

1. Introduction

The knapsack problem is a well-known problem in combinatorial optimization. There are many variants of knapsack problems such as 0-1 knapsack problem, multidimensional knapsack problem, change-making problem, generalized assignment problem, bin-packing problem, and discounted {0-1} knapsack problem (DKP01). Among the knapsack variants, the discounted {0-1} knapsack problem is new. The DKP01 is first introduced by Guldan in [1]. This problem has an important role within the modern commerce real world. It could be a portion of numerous key issues such as venture decision-making, mission determination, and budget control. A correct calculation based on energetic programming for the DKP01 is, to begin with, proposed in [1]. An approach that combined dynamic programming with the center of the DKP01 to unravel it is considered in [2]. Two calculations based on approximate methods for DKP01 are named FirEGA and SecEGA in [3].

DKP01 can be presented as follows:

$$\text{maximize } f(X) = \sum_{i=0}^{n-1} \left(x_{3i}p_{3i} + x_{3i+1}p_{3i+1} + x_{3i+2}p_{3i+2}\right), \tag{1}$$

$$\text{subject to} \quad x_{3i} + x_{3i+1} + x_{3i+2} \le 1, \quad i \in \{0, \ldots, n-1\}, \tag{2}$$

$$\left(x_{3i}w_{3i} + x_{3i+1}w_{3i+1} + x_{3i+2}w_{3i+2}\right) \le C, \tag{3}$$

$$x_{3i}, x_{3i+1}, x_{3i+2} \in \{0, 1\}, \quad \forall i \in \{1, 2, \ldots, n-1\}, \tag{4}$$

where x_{3i}, x_{3i+1}, and x_{3i+2} represent whether the items $3i, 3i+1$, and $3i+2$ are put into the a knapsack; $x_j = 0$ indicates the item $j\,(j = 0, 1, \ldots, 3n-1)$ is not in knapsack, while $x_j = 1$ indicates the item j is in the knapsack. It is worth noting that a binary vector $X = (x_0, x_1, \ldots, x_{3n-1}) \in \{0, 1\}^{3n}$ is a potential solution of DKP01. Only if X meets both (2) and (3), it is a feasible solution of DKP01. n is the number of groups, each group has three items, and each item has its profit and weight. The item is collected for knapsack aims to maximized profit while the weight capacity

does not excess C. Each group does not contain more than one item.

Lately, they moreover had a point-by-point consideration of the calculations of the DKP01 and proposed greenhorn deterministic calculation and estimation calculations. A modern correct calculation and two guess calculations with an eager repair administrator were proposed to illuminate DKP01 [4]. A calculation based on PSO is named GBPSO utilizing discrete molecule swarm optimization [5]. An evolution algorithm combines with ring theory to solve DKP01 [6], binary moth search algorithm [7], and a teaching-learning-based optimization algorithm [8].

Moth-flame optimization is first proposed in [9] and it is successfully used to solve many optimization problems such as a quantum-behaved simulated annealing algorithm-based moth-flame optimization method [10], an efficient task scheduling approach using moth-flame optimization algorithm for cyber-physical system applications in fog computing [11], a hybrid Harris hawks-moth-flame optimization algorithm including fractional-order chaos maps and evolutionary population dynamics [12], a differential moth-flame optimization algorithm for mobile sink trajectory [13], LVCI approach for optimal allocation of distributed generations and capacitor banks in distribution grids based on moth-flame optimization algorithm [14], real challenging constrained engineering optimization problems [15], parameters extraction of the three diode models for the multicrystalline solar cell [16], Alzheimer's disease diagnosis [17], profit maximization with integration of wind farm [18], and MFO with rolling mechanism to forecast the electricity consumption of inner Mongolia [19].

This research proposed a new moth-flame optimization (MFO) and a new encoding scheme for DKP01. A successful 0-1 vector with 2∗dimensional length is utilized for a solution combined with MFO. This advantageous solution present is first used by Truong [20]. The experience results on 30 discounted {0-1} knapsack problem (DKP01) instances are used to evaluate the proposed algorithm. The results demonstrate that the proposed algorithm outperforms the two binary PSO algorithms and genetic algorithm in solving 30 DKP01 instances:

(i) Moth-flame optimization algorithm has shown good searchability combined with an effective solution presentation designed to the discounted {0-1} knapsack problem.

(ii) A new encoding scheme used a shorter length binary vector to help reduce the search domain and speed up the computing time.

(iii) A greedy repair procedure is used to help the algorithm have fast convergence and reduce the gap between the best-found solution and the optimal solution.

The rest of this paper is organized in the following order: Section 2 presents related works. Section 3 proposes moth-flame optimization algorithm for DKP01. The simulated results of the proposed algorithms are presented in Section 4. We conclude this paper and suggest potential future work in Section 5.

2. Related Works

2.1. Particle Swarm Optimization. The PSO conducts its search utilizing a swarm of particles; a swarm of particles is arbitrarily made initially [21, 22]. The standard atom swarm optimizer keeps up a swarm of atoms that talk to the potential courses of action for the issue at hand. Suppose that the look space is D-dimensional and the position of ith particle of the swarm can be portrayed utilizing a D-dimensional vector, $x_i = (x_{i1}, \ldots, x_{id}, \ldots, x_{iD})$. The velocity of the particle x_i is described by a D-dimensional vector $v_i = (v_{i1}, \ldots, v_{id}, \ldots, v_{iD})$. The last best position of ith particle is named $p_i = (p_{i1}, \ldots, p_{id}, \ldots, p_{iD})$. In substance, the heading of each atom is updated concurring to its claim flying encounter as well as to that of the finest atom inside the swarm. The basic PSO calculation can be portrayed as

$$\begin{aligned} v_{i,d}^{k+1} &= w \cdot v_{i,d}^{k} + c_1 \cdot r_1^k \cdot \left(p_{i,d}^k - x_{i,d}^k\right) + c_2 \cdot r_2^k \cdot \left(p_{g,d}^k - x_{i,d}^k\right), \\ x_{i,d}^{k+1} &= x_{i,d}^k + v_{i,d}^{k+1}, \end{aligned} \tag{5}$$

where $v_{i,d}^k$ is dth dimension velocity of particle i in cycle k; $x_{i,d}^k$ is the dth dimension position of particle i in cycle k; $p_{i,d}^k$ is the dth dimension position of personal best ($p$best) of particle i in cycle k; $p_{g,d}^k$ is the dth dimension position of global best particle (g_{best}) in cycle k; w is the inertia weight; c_1 is the cognitive weight and c_2 is a social weight; and r_1 and r_2 are two random values uniformly distributed in the range of [0, 1] [23].

2.2. Moth-Flame Optimization Algorithm. Mirjalili [9] proposed MFO in 2015 as a nature-inspired optimization algorithm that simulates the actions of individuals in a swarm of moths (search agents) that have unique night navigation methods. In the MFO algorithm, the candidate solutions are assumed to be search agents. In order to model how individuals move in a spiral, the m-by-d matrix namely M is used, where m stands for the number of search agents and d for the number of dimensions. It is assumed that, for each entity, there is an array for storing the value of the objective function as an m-by-one matrix, namely, OM.

The flame, which is defined in an m-by-d matrix called F, is also an important part of this algorithm. It is assumed that there is a way to store F's fitness value as OF in an array. When using the MFO algorithm, F can be thought of as M's best location in the search space. To mathematically model this action, each search agent's location is modified as follows:

$$M_i = S\left(M_i, F_j\right), \tag{6}$$

where M_i is the ith search agent and F_j is the jth best position found so far, and S indicates the logarithmic spiral function which is updated as follows:

Table 1: $2*n$ length binary encoding scheme.

No.	$2*n$ length binary vector	Meaning
1	00	No item of the group is chosen
2	01	The first item of the group is chosen
3	10	The second item of the group is chosen
4	11	The third item of the group is chosen

Table 2: $3*n$ length binary encoding scheme.

No.	$3*n$ length binary vector	Meaning
1	000	No item of the group is chosen
2	001	The first item of the group is chosen
3	010	The second item of the group is chosen
4	011	Violate constraint (2)
5	100	The third item of the group is chosen
6	101	Violate constraint (2)
7	110	Violate constraint (2)
8	111	Violate constraint (2)

$$S\left(M_i, F_j\right) = D_i e^{cr} \cos(2\pi r) + F_j, \tag{7}$$

where r is a random number in $[-1, 1]$, c is a constant that defines the shape of the logarithmic spiral, and D_i factor is the distance of the ith search agent for the jth flame, which is calculated as follows:

$$D_i = \left|F_j - M_i\right|. \tag{8}$$

M is required to use only one of the F to change its location in this algorithm, and an adaptive mechanism for the number of F is suggested as follows:

$$\text{flame no.} = \text{round}\left(N - \frac{t(N-1)}{T}\right), \tag{9}$$

where t is the current iteration number, N is the maximum number of flames, and T is the maximum iteration number.

3. The Proposed MFO for DKP01

3.1. Solution Presentation. Currently, there are two methods for presenting a solution: one uses a binary vector with a length equal to the dimensional of the problem which is $3*n$ [3, 7, 24, 25], and the other uses an integer vector with a length equal to the number of groups n [8].

The solution [20] is presented in this paper using a new binary encode scheme with a length of $2*n$. This encoding scheme has the benefit of being shorter in length and automatically satisfying constraint 2. In Table 1, a new binary encoding scheme is introduced. When compared with the previous solution presentation shown in Table 2, it has two disadvantages: it uses a longer vector to present a solution and there are four violate solutions in each scheme.

3.2. Repair Function. Constraint 2 is automatically satisfied by the current encoding scheme. A new repair based on the concept in [3] is proposed to manage restriction 3 and increase the consistency of the solution.

The benefit of this repair technique is that it strikes a balance between CPU time consumption and the avoidance of local optima. The profit-to-weight ratios are p_i/w_i ($i = 1, 2, \ldots, n$) so that they are not increasing. It means that

$$\frac{p_i}{w_i} \geq \frac{p_j}{w_j}, \quad \text{for } i < j. \tag{10}$$

This repair operator consists of two phases. The first phase (called repair phase) examines each variable in an increasing order of p_j/w_j and drops an item from knapsack if feasibility is violated. The first phase (called optimization phase) examines each variable in an increasing order of p_j/w_j and add an item to knapsack as long as feasibility is not violated. The repair phase aims to obtain a feasible solution from an infeasible solution, whilst the optimization phase seeks to improve the fitness of a feasible solution. The details of this repair operator can be found in [20].

The overall pseudocode of the MFO algorithms for DKP01 is given in Algorithm 1.

3.3. Binary Moth-Flame Optimization Algorithm. The MFO algorithm was designed for real domain. To solve DKP01, MFO is used to redesign a search in a binary domain. Equations (11)–(13) are used to convert real vectors to binary vectors:

$$X(i, j) = \begin{cases} 0, & \text{if rand}() \geq \text{TF}(M(i, j)), \\ 1, & \text{if rand}() < \text{TF}(M(i, j)), \end{cases} \tag{11}$$

where TF (.) are the transforming functions of the probability as the following expressions:

```
Input: initial parameters
Output: optimal solution
Initialize search agents M
t = 1;
while t ≤ T do
    Update flame no. by equation (9)
    Generate binary X matrix by equation (11);
    Apply repair operator on X and assign its fitness to OM;
    if t = = 1 then
        F = sort (M_1);
        OF = sort (OM_1);
    else
        F = sort (M_{t-1}, M_t);
        OF = sort (OM_{t-1}, OM_t);
    for i = 1:m do
        for j = 1:d do
            Calculate D by equation (8);
            Update M (i, j) by equations (6) and (7);
    t = t + 1.
```

Algorithm 1: The overall pseudocode MFO algorithm for DKP01.

$$\mathrm{TF}_1(M(i,j)) = \frac{1}{1+e^{-2M(i,j)}}, \tag{12}$$

$$\mathrm{TF}_2(M(i,j)) = \frac{1}{1+e^{-M(i,j)}}. \tag{13}$$

In this section, we proposed 2 binary algorithms based on MFO named MFO1 and MFO2. MFO1 and MFO2 use transfer function TF_1 (equation (12)) and TF_2 (equation (13)), respectively. They use formula (11) to compute binary vector X.

4. Simulation Results

In this paper, the experience results of MFO1 and MFO2 algorithms are compared to find out the best one to solve DKP01 among them. The proposed algorithms are used to compare the results of three algorithms took from [6] named as SecEGA and two PSO algorithms took from Truong [20]. The PSO1 and PSO2 algorithms are BSPO7 and BPSO8 taken from Truong [20], respectively. 30 DKP01 test instances include 10 weakly correlated instances (denoted as WDKP1–WDKP10), 10 inverse strongly correlated instances (denoted as IDKP1–IDKP10), and 10 strongly correlated instances (denoted as SDKP1–SDKP10) [3].

All experiments of the proposed algorithms are running on a Laptop ASUS with an Intel (R) Core (TM) i5-8250u CPU-1.6 GHz and 8 GB DDR4 memory. The operating system is Microsoft Windows 10. The programming language is MATLAB, version R2016a.

In MFO, the number of moths is set to 50, and the search domain is the interval [1, 10]. The parameters of SecEGA are shown in [6]. The population size of SecEGA is set to 50, and the iteration is set equal to the dimension of the DKP01. For a fair comparison, the parameters for two PSO algorithms are set as the number of particles equal to 50, C_1 and C_2 are set to 2, w is linearly decreased from 0.9 to 0.4, the maximum number of iterations is set equal to the dimension of DKP01, and the stopping criterion is satisfied when the maximum number of iterations is reached. For all algorithms, the max iteration is set equal to $2 * n$. The Gap is calculated by

$$\mathrm{Gap} = \frac{|\mathrm{OPT} - \mathrm{Average}|}{\mathrm{OPT}} 100\%. \tag{14}$$

In this section, the short terms Best, Average, Worst, and StdDev are best, average, worst, and standard deviation of 30 independent runs, respectively.

Tables 3–5 summarizes the comparison among PSO1, PSO2, MFO2, SecEGA, and MFO1 based on the 6 different performance criteria on 30 independent runs including Best, Average, Worst, StdDev, the Gap, and Average rank. The MFO1 is better than PSO1, PSO2, MFO2, and SecEGA in Best, Average, and Worst for the instances of SDKP, UDKP, and WDKP except for instances of IDKP. The algorithm MFO1 archived the best rank on Average results.

The results showed that MFO1 is the best one among the 5 algorithms. Table 6 summarizes the average rank of the 5 algorithms on 30 instances. The result showed that MFO1

Table 3: Comparison of PSO1, PSO2, SecEGA, MFO1, and MFO2 on IDKP1–IDKP10.

Instance	OPT	Algorithm	Best	Average	Worst	StdDev	Gap	Rank
		PSO1	69471	68980	68252	288.0	1.6	4
		PSO2	69530	69117	68376	237.2	1.4	3
IDKP1	70106	SecEGA	68 663	68000	67 369	328.4	3.0	5
		MFO1	70106	70106	70106	0.0	0.0	1
		MFO2	70106	70104	70090	4.9	0.0	2
		PSO1	116710	116212	115370	354.2	1.7	4
		PSO2	117200	116516	115700	337.3	1.5	3
IDKP2	118268	SecEGA	114 434	113385	112 307	7446.7	4.1	5
		MFO1	118268			0.0	0.0	1
		MFO2	118268	118251	118230	19.3	0.0	2
		PSO1	234290	233653	232350	420.4	0.5	3
		PSO2	234390	232600	232600	389.6	0.4	4
IDKP3	234804	SecEGA	220 096	217982	216 313	835.8	7.2	5
		MFO1	234770	234748	234740	7.7	0.0	1
		MFO2	234700	234544	234360	92.3	0.1	2
		PSO1	280540	279714	277810	578.1	1.0	4
		PSO2	280770	279858	279110	486.7	1.0	3
IDKP4	282591	SecEGA	263 238	260425	258 922	933.4	7.8	5
		MFO1	282590	282587	282570	5.8	0.0	1
		MFO2	282470	282210	281940	132.1	0.1	2
		PSO1	333140	331595	329340	748.8	1.2	4
		PSO2	332710	331896	329280	691.2	1.1	3
IDKP5	335584	SecEGA	309 573	306878	304 881	907.2	8.6	5
		MFO1	335580	335580	335580	0.0	0.0	1
		MFO2	335280	335000	334780	107.2	0.2	2
		PSO1	450290	449287	447540	681.7	0.7	4
		PSO2	450880	449350	447890	683.3	0.7	3
IDKP6	452463		414 090	411367	408 788	1099.3	9.1	5
		MFO1	452430	452415	452390	9.7	0.0	1
		MFO2	451750	451293	450990	198.3	0.3	2
		PSO1	483180	481656	478830	944.5	1.5	3
		PSO2	483170	481578	479910	1034.9	1.5	4
IDKP7	489149	SecEGA	451 528	444316	442 133	1280.3	9.2	5
		MFO1	489150	489132	489120	9.7	0.0	1
		MFO2	488520	487889	487030	288.1	0.3	2
		PSO1	523300	520939	517720	1480.0	2.4	4
		PSO2	526240	521844	519190	1540.0	2.2	3
IDKP8	533841	SecEGA	490 494	481831	478 035	2215.7	9.7	5
		MFO1	533840	533825	533820	6.3	0.0	1
		MFO2	533050	532345	531940	284.3	0.3	2
		PSO1	515680	511908	507210	1937.0	3.1	4
		PSO2	516550	512575	509090	1727.0	2.9	3
IDKP9	528144	SecEGA	489 661	477001	471 848	3656.2	9.7	5
		MFO1	528140	528136	528120	7.2	0.0	1
		MFO2	527140	526734	526370	205.8	0.3	2
		PSO1	563960	560214	556100	2204.1	3.6	4
		PSO2	566670	562000	559540	1950.2	3.3	3
IDKP10	581244	SecEGA	535 541	521604	516 445	4265.1	10.3	5
		MFO1	581240	581233	581230	4.5	0.0	1
		MFO2	580620	579589	578870	365.0	0.3	2

Table 4: Comparison of PSO1, PSO2, SecEGA, MFO1, and MFO2 on SDKP1–SDKP10.

Instance	OPT	Algorithm	Best	Average	Worst	StdDev	Gap	Rank
SDKP1	94459	PSO1	94219	93874	93489	184.3	33.9	4
		PSO2	94205	93999	93703	130.5	34.1	3
		SecEGA	89 769	88832	87463	594.9	6.0	5
		MFO1	94286	94274	94258	12.6	34.5	1
		MFO2	94286	94222	94121	43.2	34.4	2
SDKP2	160805	PSO1	160280	159531	158810	360.1	34.9	4
		PSO2	160090	159617	159030	307.4	35.0	3
		SecEGA	153 821	152059	150753	489.4	5.4	5
		MFO1	159980	159895	159800	47.3	35.2	1
		MFO2	159840	159667	159390	93.9	35.0	2
SDKP3	238248	PSO1	237340	236389	235320	440.2	0.7	3
		PSO2	237300	236428	235620	371.4	0.7	1
		SecEGA	224 997	223580	221918	543.4	6.2	5
		MFO1	236530	236404	236310	51.8	0.7	2
		MFO2	236140	235855	235600	128.8	0.4	4
SDKP4	340027	PSO1	337960	337013	335880	585.0	19.3	1
		PSO2	337860	336811	335890	508.3	19.2	3
		SecEGA	318 510	315513	313 747	851.1	7.2	5
		MFO1	336980	336865	336800	39.0	19.2	2
		MFO2	336390	335989	335730	172.9	18.9	4
SDKP5	463033	PSO1	459780	458216	456130	728.5	36.5	3
		PSO2	459420	458086	456840	615.1	36.5	4
		SecEGA	420 238	416964	413 933	1291.7	10.0	5
		MFO1	460190	460096	460010	45.5	37.1	1
		MFO2	459240	458554	458240	225.4	36.6	2
SDKP6	466097	PSO1	462350	460874	459340	677.1	1.9	2
		PSO2	462000	460989	459690	602.6	1.9	1
		SecGA	430 738	427304	425 504	1031.1	8.3	5
		MFO1	461000	460862	460750	64.3	1.9	3
		MFO2	460060	459245	458780	226.8	1.5	4
SDKP7	620446	PSO1	614510	612746	610360	1059.2	25.3	4
		PSO2	614780	612902	610930	928.1	25.3	3
		SecEGA	561 224	556083	552 007	1926.3	10.4	5
		MFO1	615900	615756	615630	69.2	25.9	1
		MFO2	613930	613268	612870	281.1	25.4	2
SDKP8	670697	PSO1	663730	661988	659770	984.4	24.0	4
		PSO2	664250	662529	660340	992.7	24.1	2
		SecEGA	611 644	606263	603 774	1446.9	9.6	5
		MFO1	664750	664590	664450	76.0	24.5	1
		MFO2	662910	662053	661640	303.5	24.0	3
SDKP9	739121	PSO1	731830	730283	727770	1058.9	38.3	3
		PSO2	732320	730619	728570	1060.1	38.3	2
		SecEGA	674 885	667900	664 580	1614.0	9.6	5
		MFO1	731630	731502	731360	68.3	38.5	1
		MFO2	728790	728306	727650	315.5	37.9	4
SDKP10	765317	PSO1	756580	755021	753220	806.2	29.9	2
		PSO2	757430	754798	752470	1402.8	29.9	3
		SecEGA	708 935	695557	691 994	2956.1	9.1	5
		MFO1	756190	755966	755650	120.7	30.1	1
		MFO2	753740	753027	752270	336.6	29.6	4

Table 5: Comparison of PSO1, PSO2, SecEGA, MFO1, and MFO2 on WDKP1–WDKP10.

Instance	OPT	Algorithm	Best	Average	Worst	StdDev	Gap	Rank
WDKP1	83098	PSO1	82998	82764	82465	140.5	18.1	4
		PSO2	83002	82797	82549	125.7	18.1	3
		SecEGA	80014	79022	78096	473.7	4.9	5
		MFO1	82962	82894	82848	22.5	18.2	1
		MFO2	82950	82862	82798	34.8	18.2	2
WDKP2	138215	PSO1	137880	137278	136770	254.2	16.1	4
		PSO2	137860	137381	136780	247.2	16.2	3
		SecEGA	133315	132276	131337	415.6	4.3	5
		MFO1	137920	137873	137850	22.0	16.6	1
		MFO2	137890	137795	137720	40.7	16.5	2
WDKP3	256616	PSO1	256160	255362	254210	422.3	8.8	4
		PSO2	255990	255386	254670	356.3	8.8	3
		SecEGA	238331	235721	234025	873.6	8.1	5
		MFO1	255970	255891	255820	28.4	9.0	1
		MFO2	255660	255463	255260	90.0	8.8	2
WDKP4	315657	PSO1	314790	313860	313010	434.8	11.1	4
		PSO2	314750	314108	313390	399.3	11.2	3
		SecEGA	293640	290851	288764	950.1	7.9	5
		MFO1	315040	314980	314930	28.0	11.5	1
		MFO2	314630	314400	314190	125.6	11.3	2
WDKP5	428490	PSO1	426910	425683	424470	701.9	26.8	4
		PSO2	426680	425736	424520	501.1	26.9	3
		SecEGA	393617	390014	387992	1059.8	9.0	5
		MFO1	427710	427666	427620	23.0	27.4	1
		MFO2	427260	426687	426270	214.5	27.1	2
WDKP6	466050	PSO1	463690	462092	460590	641.3	2.1	4
		PSO2	463350	462284	460930	583.1	2.2	3
		SecGA	429208	425112	423269	1058.4	8.8	5
		MFO1	464880	464819	464760	28.9	2.7	1
		MFO2	463820	463485	463080	203.2	2.4	2
WDKP7	547683	PSO1	544700	542724	538860	1154.9	11.0	4
		PSO2	544730	542765	539860	922.5	11.0	3
		SecEGA	501557	496134	493845	1230.9	9.4	5
		MFO1	546500	546425	546380	29.8	11.7	1
		MFO2	545300	544705	544110	295.4	11.4	2
WDKP8	576959	PSO1	572530	570187	567530	1216.6	6.8	4
		PSO2	571870	570226	568570	825.3	6.8	3
		SecEGA	530971	523203	520350	2157.1	9.3	5
		MFO1	575590	575463	575360	45.5	7.8	1
		MFO2	574520	573672	572880	299.1	7.5	2
WDKP9	650660	PSO1	643950	641272	638210	1501.3	21.4	4
		PSO2	645140	641658	638230	1502.3	21.5	3
		SecEGA	598343	586770	583854	2315.5	9.8	5
		MFO1	648760	648672	648600	35.9	22.8	1
		MFO2	647040	646510	646030	268.1	22.4	2
WDKP10	678967	PSO1	672380	668923	666420	1429.2	15.1	3
		PSO2	671880	668830	665740	1553.1	15.1	4
		SecEGA	620230	606215	609964	3090.9	10.7	5
		MFO1	677450	677388	677330	34.5	16.5	1
		MFO2	676110	675115	674680	284.2	16.2	2

Table 6: Average rank of PSO1, PSO2, SecEGA, MFO1, and MFO2 on 30 instances.

Algorithms	Mean rank of 10 IDKP instances	Mean rank of 10 SDKP instances	Mean rank of 10 WDKP instances
PSO1	3.8	3.0	3.9
PSO2	3.2	2.5	3.1
SecEGA	4.5	4.5	4.5
MFO1	1.0	1.4	1.0
MFO2	2.0	3.1	2.0

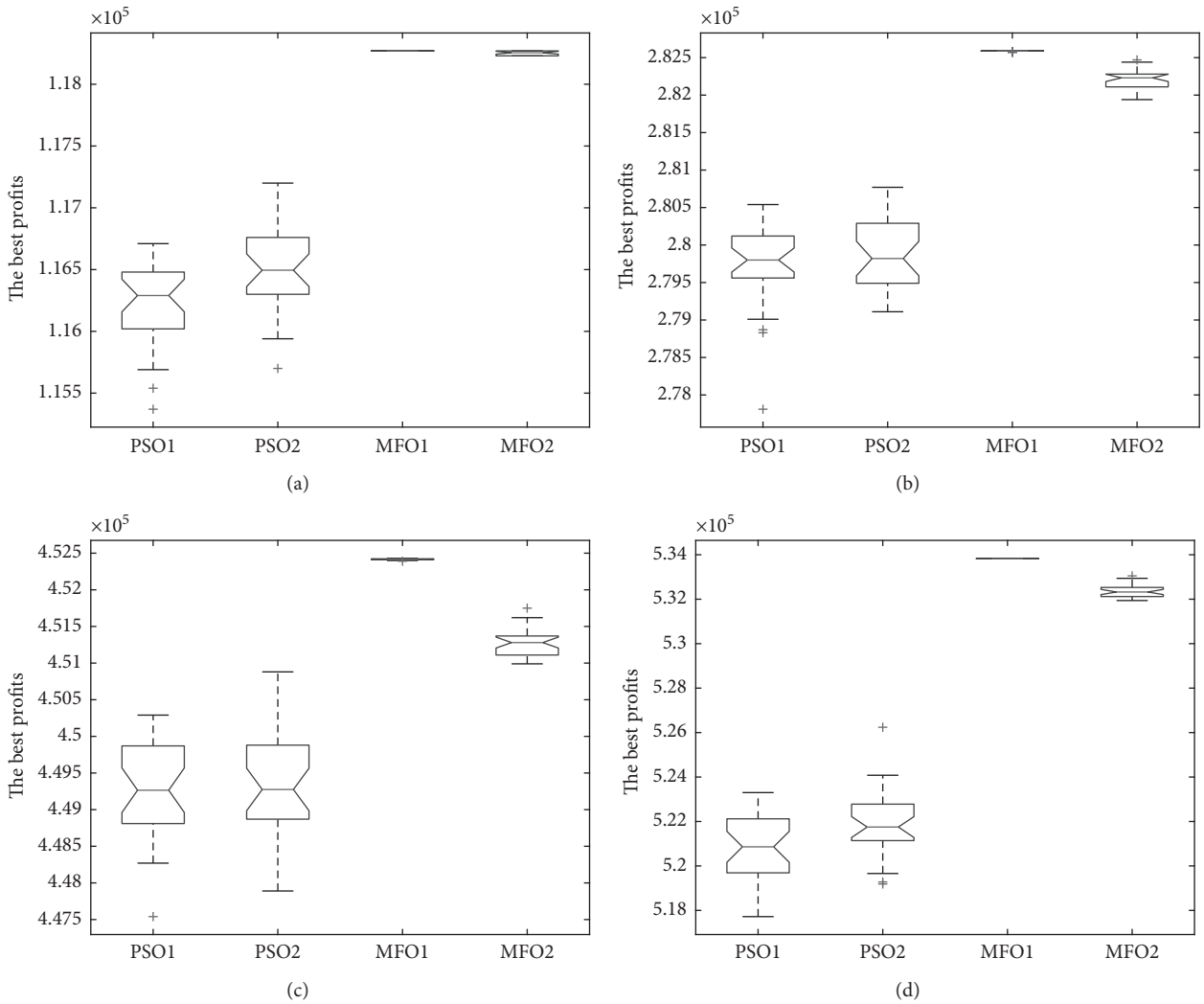

Figure 1: Box plot of four algorithms on IDKP instances. (a) IDKP2. (b) IDKP4. (c) IDKP6. (d) IDKP8.

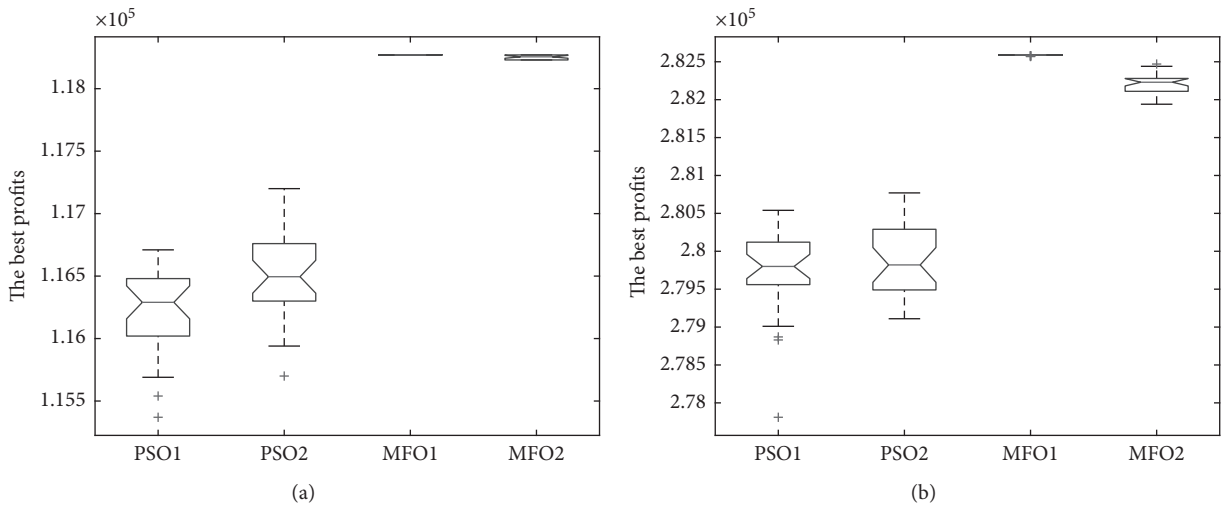

Figure 2: Continued.

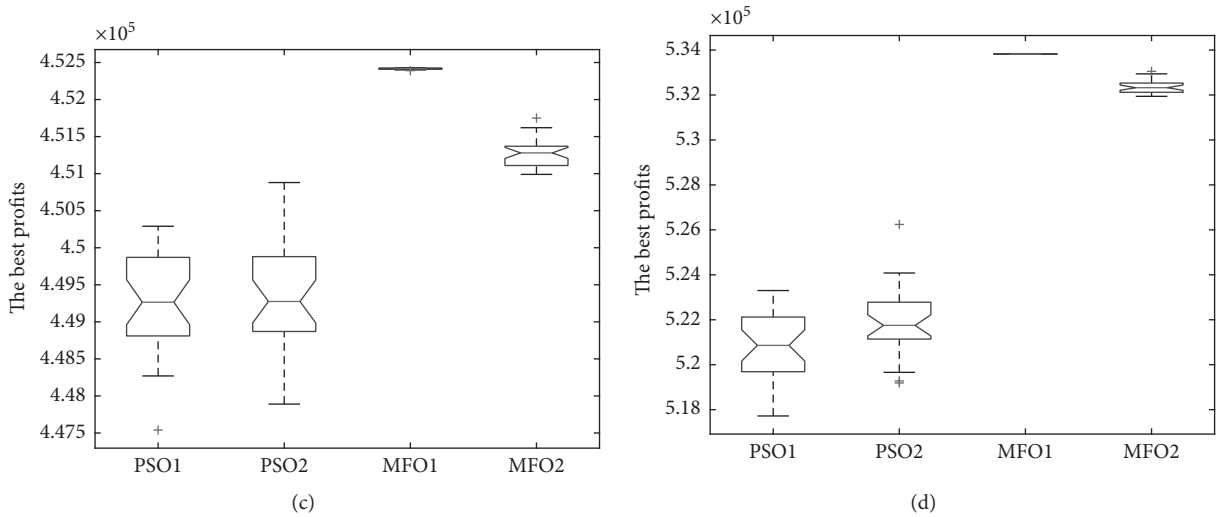

Figure 2: Box plot of four algorithms on WDKP instances. (a) WDKP2. (b) WDKP4. (c) WDKP6. (d) WDKP8.

achieved the average best rank in all the three test instances on average mean rank. Figure 1 demonstrates the boxplot of the four algorithms on IDKP instances: IDKP2, IDKP4, IDKP6, and IDKP8. Figure 2 demonstrates the boxplot of the four algorithms on WDKP instances: WDKP2, WDKP4, WDKP6, and WDKP8. Figure 3 demonstrates the boxplot of the four algorithms on SDKP instances: SDKP2, SDKP4, SDKP6, and SDKP8. These box plot figures showed that MFO1 obtained the best result.

Figure 4 demonstrates the convergence curves of the four algorithms on IDKP instances: IDKP2, IDKP4, IDKP6, and IDKP8. Figure 5 demonstrates the convergence curves of the four algorithms on WDKP instances: WDKP2, WDKP4, WDKP6, and WDKP8. Figure 6 demonstrates the convergence curves of the four algorithms on SDKP instances: SDKP2, SDKP4, SDKP6, and SDKP8. These convergence curves demonstrated that MFO1 has faster convergence than group algorithms PSO1, PSO2, and MFO2.

Therefore, the performance of MFO1 is better than that of the other algorithm for the DKP01 problem. From the above comparison, MFO1 showed far better result than those of PSO1, PSO2, MFO2, and SecEGA. The evidence supports that MFO1 is a potential method for solving DKP01.

4.1. Wilcoxon Rank Sum Test. With the observable measures, I am ready to prove beyond a shadow of a doubt that the outcomes are not the product of chance. The nonparametric Wilcoxon statistical test is used and the calculated p values are reported as metrics of significance as well. Any p values <0.05 evidence the statistical significant superiority of the

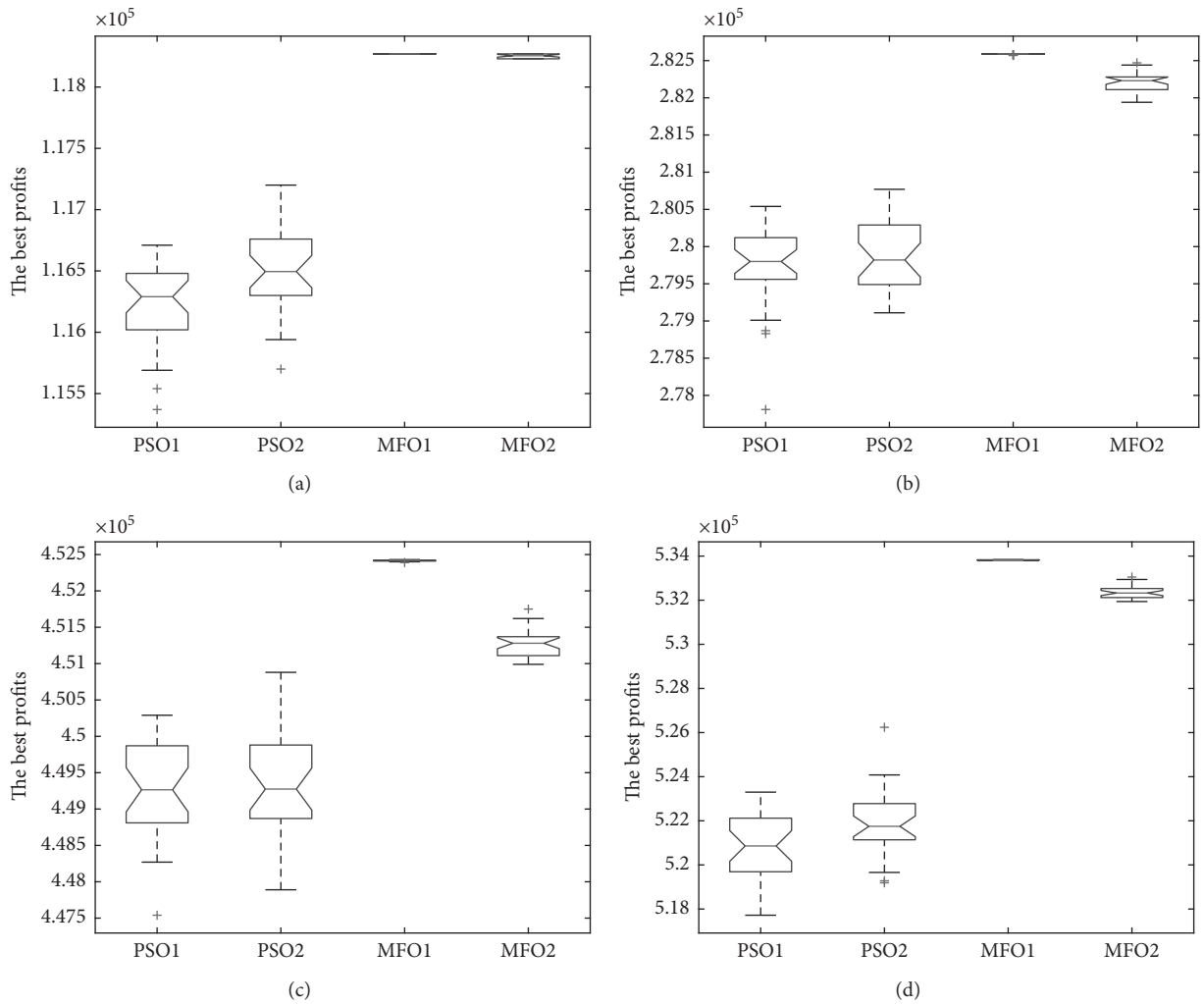

Figure 3: Box plot of four algorithms on SDKP instances. (a) SDKP2. (b) SDKP4. (c) SDKP6. (d) SDKP8.

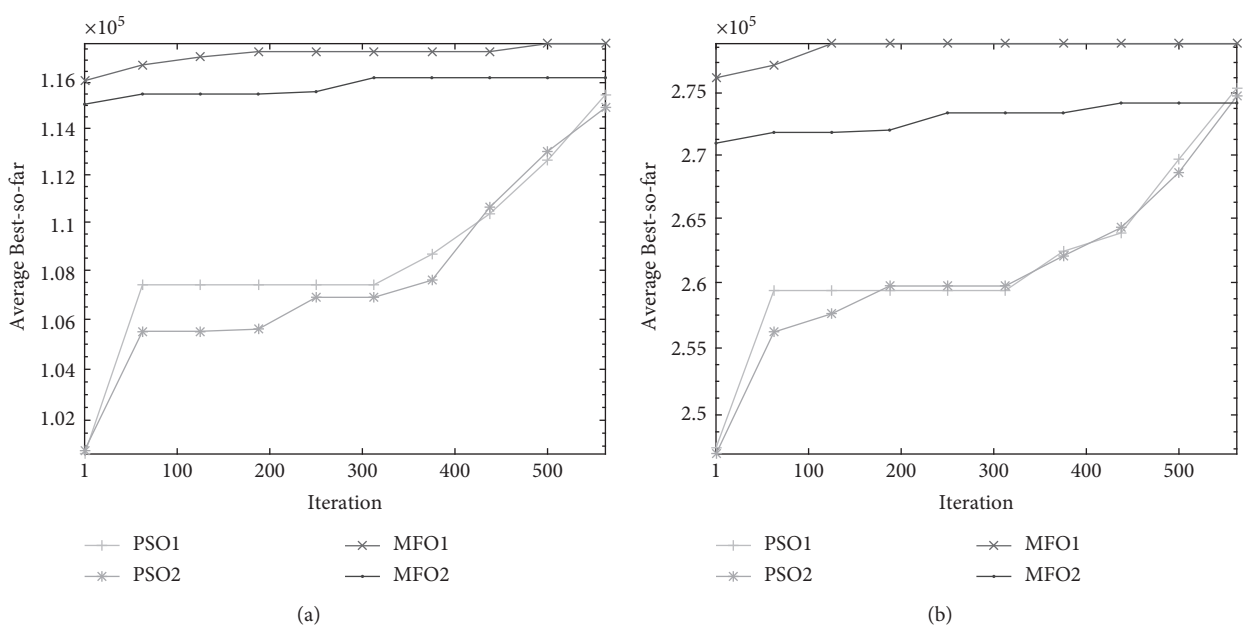

Figure 4: Continued.

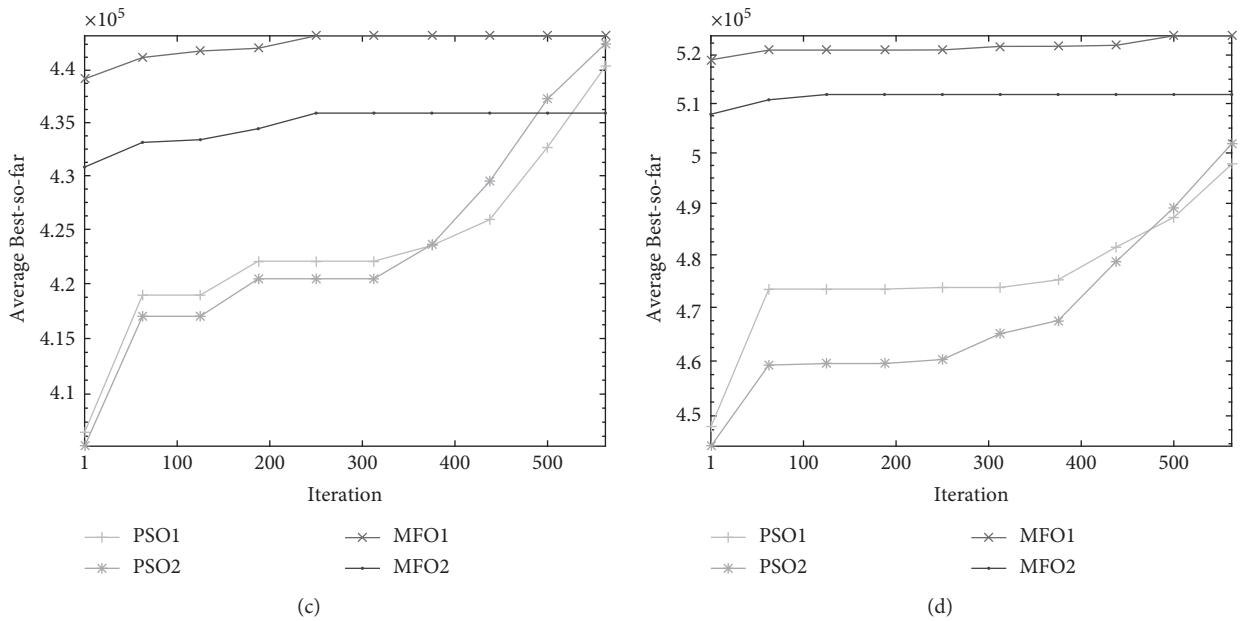

Figure 4: Convergence curves of four algorithms on IDKP instances. (a) IDKP2. (b) IDKP4. (c) IDKP6. (d) IDKP8.

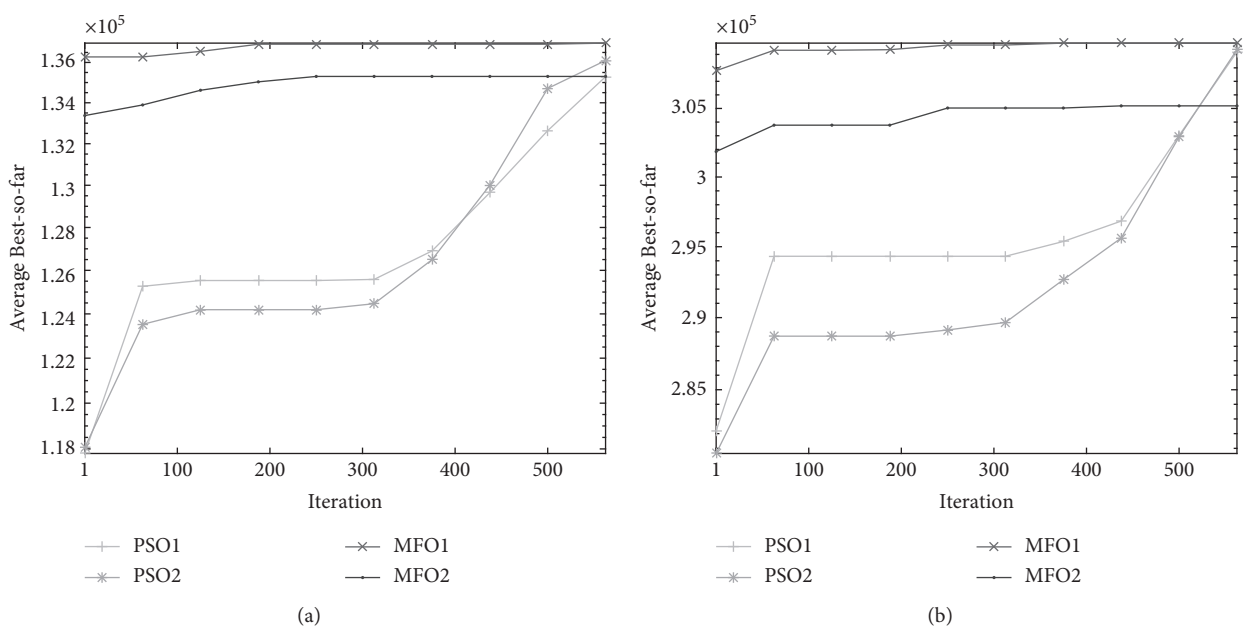

Figure 5: Continued.

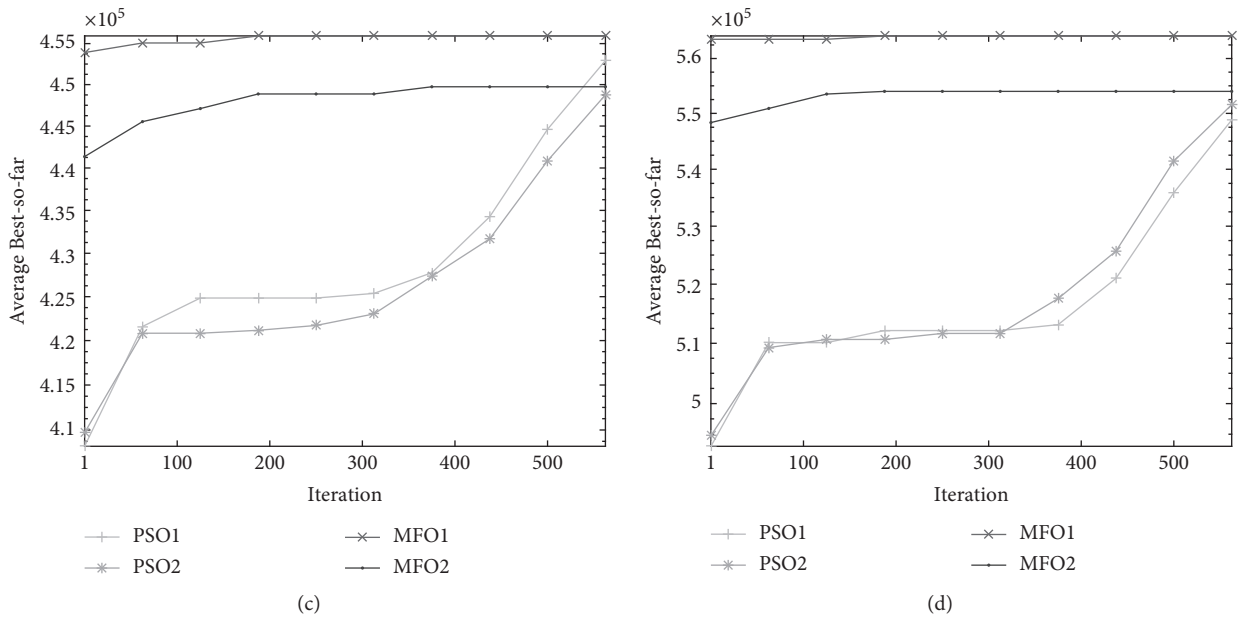

Figure 5: Convergence curves of four algorithms on WDKP instances. (a) WDKP2. (b) WDKP4. (c) WDKP6. (d) WDKP8.

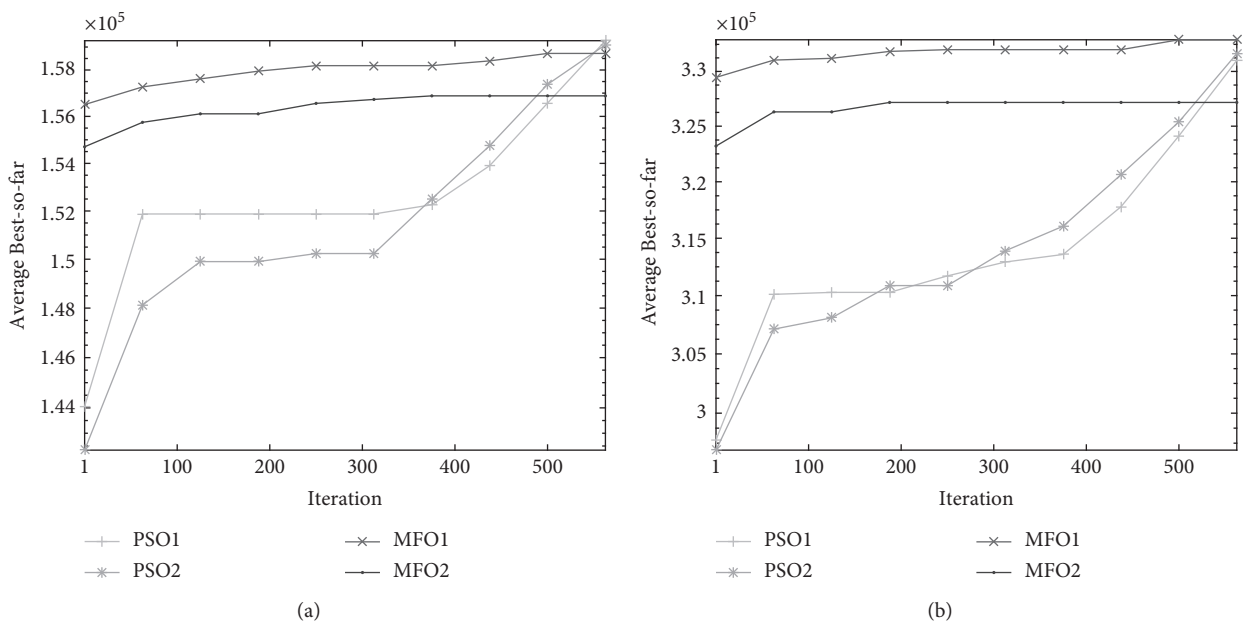

Figure 6: Continued.

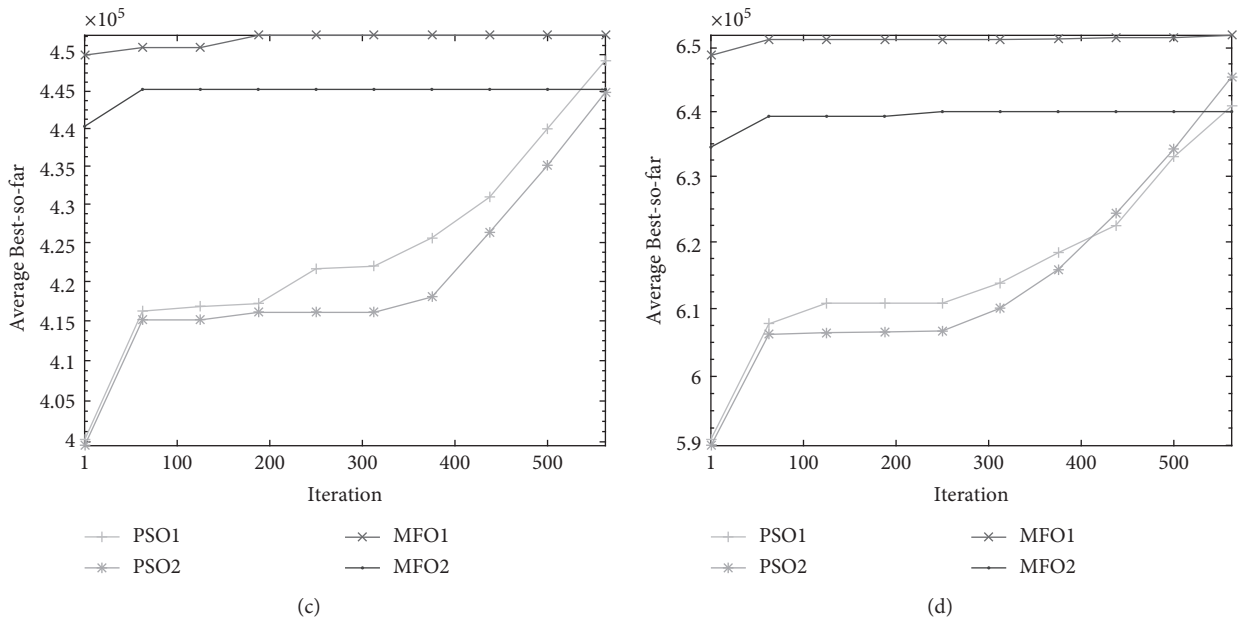

Figure 6: Convergence curves of four algorithms on SDKP instances. (a) SDKP2. (b) SDKP4. (c) SDKP6. (d) SDKP8.

Table 7: p values of the Wilcoxon rank-sum test over 30 runs.

Instance	**MFO2**	**PSO1**	**PSO2**
IDKP1	**0.081404**	$1.21E-12$	$1.21E-12$
IDKP2	$1.14E-05$	$1.21E-12$	$1.21E-12$
IDKP3	$1.86E-11$	$1.87E-11$	$1.87E-11$
IDKP4	$6.34E-12$	$6.42E-12$	$6.42E-12$
IDKP5	$1.2E-12$	$1.21E-12$	$1.21E-12$
IDKP6	$1.23E-11$	$1.24E-11$	$1.24E-11$
IDKP7	$2.25E-11$	$2.25E-11$	$2.25E-11$
IDKP8	$1.45E-11$	$1.45E-11$	$1.45E-11$
IDKP9	$7.77E-12$	$7.8E-12$	$7.8E-12$
IDKP10	$8.84E-12$	$8.87E-12$	$8.87E-12$
SDKP1	$4.45E-07$	$2.11E-11$	$2.11E-11$
SDKP2	$5.56E-11$	$4.32E-06$	0.000351
SDKP3	$2.89E-11$	**0.482158**	**0.578909**
SDKP4	$2.76E-11$	0.030575	0.109566
SDKP5	$2.93E-11$	$2.94E-11$	$2.94E-11$
SDKP6	$2.95E-11$	**0.164345**	**0.26713**
SDKP7	$2.96E-11$	$2.97E-11$	$2.97E-11$
SDKP8	$2.96E-11$	$2.96E-11$	$2.96E-11$
SDKP9	$2.97E-11$	$3.91E-08$	0.000431
SDKP10	$2.99E-11$	$1.02E-06$	$3.36E-05$
WDKP1	$2.68E-05$	0.000774	0.000401
WDKP2	$2.19E-10$	$1.87E-10$	$8.09E-11$
WDKP3	$2.21E-11$	$2.41E-07$	$6.25E-10$
WDKP4	$2.71E-11$	$2.74E-11$	$2.73E-11$
WDKP5	$2.86E-11$	$2.87E-11$	$2.87E-11$
WDKP6	$2.87E-11$	$2.86E-11$	$2.88E-11$
WDKP7	$2.85E-11$	$2.85E-11$	$2.85E-11$
WDKP8	$2.9E-11$	$2.92E-11$	$2.92E-11$
WDKP9	$2.83E-11$	$2.84E-11$	$2.83E-11$
WDKP10	$2.92E-11$	$2.93E-11$	$2.93E-11$

$p > 0.05$ is indicated in bold.

results when comparing MFO1 with MFO2, PSO1, and PSO2. After all, the statistical results for 30 instances are provided in Table 7.

5. Conclusion

A moth-flame optimization algorithm that showed good searchability is combined with an effective solution presentation designed to the discounted {0-1} knapsack problem. A new encoding scheme used a shorter length binary vector to help reduce the search domain and speed up the computing time. A greedy repair procedure is used to help the algorithm have fast convergence and reduce the gap between the best-found solution and th eoptimal solution. The simulation results of 30 DKP01 instances showed that the proposed algorithms are better than the two particle swarm optimization algorithms and one genetic algorithm. In the future, some variants of the moth-flame optimization algorithm are considered for study for the discounted {0-1} knapsack problem.

Data Availability

The data used to support the findings of this study are included within the article or are made publicly available to the research community at https://www.researchgate.net/publication/336126537_Four_kinds_of_D0-1KP_instances.

Conflicts of Interest

The author declares that there are no conflicts of interest regarding the publication of this paper.

Acknowledgments

The author thanks Van Lang University for supporting this work.

References

[1] B. Guldan, *Heuristic and Exact Algorithms for Discounted Knapsack Problems*, University of Erlangen-Nürnberg, Erlangen, Germany, 2007.

[2] A. Rong, J. R. Figueira, and K. Klamroth, "Dynamic programming based algorithms for the discounted {0-1} knapsack problem," *Applied Mathematics and Computation*, vol. 218, no. 12, pp. 6921–6933, 2012.

[3] Y. He, X. Wang, W. Li, X. Zhang, and Y. Chen, "Research on genetic algorithms for discounted 0–1 knapsack problem," *Chinese Journal of Computers*, vol. 39, no. 12, pp. 2614–2630, 2016.

[4] Y.-C. He, X.-Z. Wang, Y.-L. He, S.-L. Zhao, and W.-B. Li, "Exact and approximate algorithms for discounted {0-1} knapsack problem," *Information Sciences*, vol. 369, pp. 634–647, 2016.

[5] J. Kenedy and R. Eberhart, "A discrete binary version of the particle swarm optimization," *Computational cybernatics and simulation*, vol. 5, no. 1, pp. 4104–4108, 1997.

[6] Y. He, X. Wang, and S. Gao, "Ring theory-based evolutionary algorithm and its application to $D\{0\text{-}1\}$ KP," *Applied Soft Computing*, vol. 77, pp. 714–722, 2019.

[7] Y. H. Feng and G. G. Wang, "Binary moth search algorithm for discounted 0-1 knapsack problem," *IEEE Access*, vol. 6, pp. 10708–10719, 2018.

[8] C. Wu, J. Zhao, Y. Feng, and M. Lee, "Solving discounted {0-1} knapsack problems by a discrete hybrid teaching-learning-based optimization algorithm," *Applied Intelligence*, vol. 50, no. 6, pp. 1872–1888, 2020.

[9] S. Mirjalili, "Moth-flame optimization algorithm: a novel nature-inspired heuristic paradigm," *Knowledge-Based Systems*, vol. 89, pp. 228–249, 2015.

[10] C. Yu, A. A. Heidari, and H. Chen, "A quantum-behaved simulated annealing algorithm-based moth-flame optimization method," *Applied Mathematical Modelling*, vol. 87, pp. 1–19, 2020.

[11] M. Ghobaei-Arani, A. Souri, F. Safara, and M. Norouzi, "An efficient task scheduling approach using moth-flame optimization algorithm for cyber-physical system applications in fog computing," *Transactions on Emerging Telecommunications Technologies*, vol. 31, no. 2, Article ID e3770, 2020.

[12] M. Abd Elaziz, D. Yousri, and S. Mirjalili, "A hybrid harris hawks-moth-flame optimization algorithm including fractional-order chaos maps and evolutionary population dynamics," *Advances in Engineering Software*, vol. 154, Article ID 102973, 2021.

[13] S. Sapre and S. Mini, "A differential moth flame optimization algorithm for mobile sink trajectory," *Peer-to-Peer Networking and Applications*, vol. 14, no. 1, pp. 44–57, 2021.

[14] M. A. Tolba, A. A. Z. Diab, V. N. Tulsky, and A. Y. Abdelaziz, "LVCI approach for optimal allocation of distributed generations and capacitor banks in distribution grids based on moth-flame optimization algorithm," *Electrical Engineering*, vol. 100, no. 3, pp. 2059–2084, 2018.

[15] N. Jangir, M. H. Pandya, I. N. Trivedi, R. Bhesdadiya, P. Jangir, and A. Kumar, "Moth-flame optimization algorithm for solving real challenging constrained engineering optimization problems," in *Proceedings of the 2016 IEEE Students' Conference on Electrical, Electronics and Computer Science (SCEECS)*, pp. 1–5, IEEE, Bhopal, India, March 2016.

[16] D. Allam, D. A. Yousri, and M. B. Eteiba, "Parameters extraction of the three diode model for the multi-crystalline solar cell/module using moth-flame optimization algorithm," *Energy Conversion and Management*, vol. 123, pp. 535–548, 2016.

[17] G. I. Sayed, A. E. Hassanien, T. M. Nassef, and J.-S. Pan, "Alzheimer's disease diagnosis based on moth flame optimization," in *Proceedings of the International Conference on Genetic and Evolutionary Computing*, pp. 298–305, Springer, Fuzhou, China, November 2016.

[18] S. Gope, S. Dawn, A. K. Goswami, and P. K. Tiwari, "Profit maximization with integration of wind farm in contingency constraint deregulated power market using moth flame optimization algorithm," in *Proceedings of the 2016 IEEE Region 10 Conference (TENCON)*, pp. 1462–1466, IEEE, Singapore, November 2016.

[19] H. Zhao, H. Zhao, and S. Guo, "Using GM (1, 1) optimized by MFO with rolling mechanism to forecast the electricity consumption of inner Mongolia," *Applied Sciences*, vol. 6, no. 1, p. 20, 2016.

[20] T. K. Truong, "Different transfer functions for binary particle swarm optimization with a new encoding scheme for discounted 0-1 knapsack problem," *Mathematical Problems in Engineering*, vol. 2021, Article ID 2864607, 17 pages, 2021.

[21] R. Eberhart and J. Kennedy, "A new optimizer using particle swarm theory," in *Proceedings of the MHS'95 Sixth International Symposium on Micro Machine and Human Science*, pp. 39–43, IEEE, Nagoya, Japan, October 1995.

[22] J. Kennedy and R. Eberhart, "Particle swarm optimization," in *Proceedings of the ICNN'95 - International Conference on Neural Networks*, vol. 4, pp. 1942–1948, Perth, Australia, December 1995.

[23] Z. Li and N. Li, "A novel multi-mutation binary particle swarm optimization for 0/1 knapsack problem," in *Proceedings of the 2009 Chinese Control and Decision Conference*, pp. 3042–3047, Guilin, China, June 2009.

[24] Y. Feng, G. G. Wang, W. Li, and N. Li, "Multi-strategy monarch butterfly optimization algorithm for discounted {0-1} knapsack problem," *Neural Computing & Applications*, vol. 30, no. 10, pp. 3019–3036, 2018.

[25] H. Zhu, Y. He, X. Wang, and E. C. C. Tsang, "Discrete differential evolutions for the discounted {0-1} knapsack problem," *International Journal of Bio-Inspired Computation*, vol. 10, no. 4, p. 219, 2017.

Hindawi
Mathematical Problems in Engineering
Volume 2021, Article ID 9281961, 17 pages
https://doi.org/10.1155/2021/9281961

Research Article

Finite Element Analysis of the Effect of Dental Implants on Jaw Bone under Mechanical and Thermal Loading Conditions

Dorsa Darvish, Siamak Khorramymehr, and Mohammad Nikkhoo

Department of Biomedical Engineering, Science and Research Branch, Islamic Azad University, Tehran, Iran

Correspondence should be addressed to Siamak Khorramymehr; s.khorramymehr@srbiau.ac.ir

Received 13 July 2021; Accepted 10 September 2021; Published 4 October 2021

Academic Editor: Mohammad Yazdi

Dental implants have been studied over the years to replace missing teeth. One of the conditions for the success of implants is their stability and resistance under the applied forces and minimal tension in the surrounding bone. The purpose of this dissertation is numerical and three-dimensional analysis of jaws with implants under mechanical and thermal loading by the finite element method. For this purpose, implant simulations (including ceramic crown, titanium root, and jaw bone) under dynamic and thermal load have been performed in Abacus software. In this simulation, it is considered that the jawbone is composed of two areas, one area is the superficial bone tissue (cortical) and the other part is the spongy tissue. Implants are usually made of different metals or ceramics with a bone-like structure that are compatible with body tissues. Implants are currently made of titanium metal. Therefore, titanium metal has been used for modeling implants in this dissertation. The implant crown is also considered as a ceramic material. In the simulation, the effect of stresses imposed by the implant on the jawbone is performed. In this simulation, mechanical force is applied to the upper part of the implant and force enters the jawbone through the implant, which causes tension at the junction of the implant to the jawbone. To investigate the effect of thermal loads, different temperature conditions are considered by considering the decrease in temperature and increase in temperature on the tooth surface and its effect on the implant and the jaw bone. After validation and ensuring the accuracy of the modeling, it has been observed that, with increasing mechanical load, the stresses created in all parts of the ceramic coating, titanium implants, and jawbone have increased. It is also observed that the stress created in the titanium implant due to the application of negative heat flux was about twice as much as the stress created due to the application of positive heat flux.

1. Introduction

Given the importance of the human body and the importance and impact of the type and properties of implants in the jaw, as well as its impact on human body function, choosing the best parameters both in terms of mechanical properties and biocompatibility (compatibility with the human body) is essential. Also, the function of dental implants and its effect on the jaw bone is affected by mechanical and thermal loads, which is also important and necessary to study this issue.

Therefore, by modeling and analyzing the effect of dental implants on the jaw bone in terms of mechanical and thermal loading, as well as considering different properties for the implant, it is possible to have a detailed study on its performance, which is very important [1–3].

We may lose one or more of our teeth for a variety of reasons. Not having one or more teeth can cause problems such as loss of beauty. There are several alternatives to missing teeth, among which dental implants are the best choice. However, various reasons, such as the inability to withstand the forces and torques and the intolerance of high temperatures, can lead to failure in the implantation process. A dental implant is a titanium screw that replaces a missing tooth by being inserted into the jawbone. Dental implants can be one-piece or two-piece, with the crown and root joined by a screw. Dental implants are an alternative to shaven-tooth bridge prostheses, and the primary goal of introducing this therapy (dental implant) is to ensure that no teeth will be shaved or damaged in the future owing to the bridge base.

Oguz et al. [4] studied the static, dynamic, and fatigue behavior of dental implants using the finite element method. In this study, a dynamic load is applied to the occlusal surface for 5 seconds and the fatigue life is calculated based on Goodman, Soderbergh, and Gerber criteria. They found that von Mises maximum stress in dynamic loading is greater than static loading. Kong et al. [5] investigated the effect of thread change in maximum stress on bone and implants through finite element analysis. The results showed that the thread pitch plays an important role in the strength of the implant under axial load. Djebbae et al. and Tian et al. [6, 7] obtained the stress distribution in dentures by the finite element method. The amount of stress, especially at the junction of the implant bone, was examined. They found that force and direction of loading have a large effect on the amount of stress. Huang et al. and Dorogoy et al. [8, 9] used 11 different finite element models to study the stress distribution and slip of implants. The contact of the surfaces is of frictional type. The results show that, in fast-loading implants, especially in off-axis loads, the stress on the bone around the implant is very high. As the number of threads and the contact surface of the bone and implant increase, the stress distribution and slip of the implant and bone surface decrease. Guan et al. and Yazdi [10, 11] performed dynamic modeling and simulation of the dental implant placement process using the finite element method. In this study, by examining the effect of different placement depths on spongy bone and dense bone, it was found that increasing the placement depth increases the amount of stress in dense bone. The authors of [12–14] presented finite element analysis of thermal implants exposed to heat. In this study, by observing the results of thermal stresses, it can be seen that thermal stresses have small values, and it is also due to small temperature changes in the complex. The highest stress is related to the abutment, which is also caused by the stiffening torque. The authors in [15, 16] reviewed the mechanical design requirements of dental implants and found that compressive loading stabilizes the implant in the jawbone and tensile loading of the implant loosens and shear loading causes the implant to fail. Creating rough surfaces also improves the adhesion between the implant and the bone. Using the finite element method, the authors of [17, 18] studied the influence of the tooth and jaw bone-implant contact model on maximum implant stress. The largest stress can occur in the neck area of the implant and in the connection points with the dense bone under oblique loading, according to the stress distribution. The authors of [19, 20] used the finite element method to undertake static and dynamic analysis of dental implants that Abacus specialist software was used in this investigation. Modeling geometry, specifying material characteristics, boundary conditions, contact conditions, loading, and elementing for bone-implant simulation were all done in Abacus program. There will be two analyses, each with a distinct force. The ceramic cap is subjected to a force of 100 Newtons at a 45-degree angle during static analysis. All modeling phases are inserted into dynamic analysis with a force of 400 Newtons in 0.01 seconds, identical to static analysis. In static analysis, the highest von Mises stress was 82.5 MPa, but in dynamic analysis, it was 770.2 MPa. In contrast to dynamic analysis, the maximum stress in static analysis is lower. Dynamic analysis allows for a smaller maximum displacement than static analysis. The authors of [21, 22] used finite element simulation to evaluate the biomechanical behavior of mini-implants under real-world working settings. Stress analysis of two distinct quality of the D2 and D3 jawbone around three types of mini-implants was performed using the finite element method in this study due to the relevance of placing short implants in confined spaces between the edentulous region. Three varieties of Osteocare, Dio, and Dentis mini-implants were included in this experimental investigation. The highest component of the abutment was loaded with a vertical force of 100 N and a lateral force of 100 N at a 45-degree angle.

ABAQUS software was used to analyze stress levels in the mini-implant and surrounding bone. The findings revealed that the amount of von Mises stress in D3 bone for all implants is higher than D2 bone and that the level of stress in the cortical bone is higher than the spongy bone. Furthermore, all the systems studied had identical stress distributions in the cortical bone. Additionally, the initial implant thread caused the most stress in the implant's neck, but the Osteocare mini-implant created less tension in the bone. The topology optimization technique in dental implants was examined using Abacus software by [23–25]. This article discusses how to use Abacus software to optimize dental implant architecture. One of the types of optimization in Abacus software is topology optimization. Topological optimization is a mathematical method for determining the best material distribution shape for a structure in a given space. Optimization minimizes the weight of the material, resulting in lower assembly costs and time. The authors of [26–28] used the finite element approach to simulate the mechanical performance of dental implants comprised of memory materials. A sample of existing dental implants, as well as a portion of the jawbone, were modeled in Abacus software and statically assessed for this purpose. Finally, the implant's level of stress was compared to that of other implants made of standard materials. The results show that when the memory implant was utilized, the stress values in the implant were lower than when the nickel-titanium implant was used. The amount of stress transferred from the nitinol implant to the nickel-titanium implant to the jawbone was also fewer in the regions which were subjected to increased force and stress. The authors of [29, 30] used the finite element approach to investigate the effect of geometric and mechanical features on the stress distribution of the dental implant system. The findings demonstrate that the angle and step of fastening are critical in boosting implant stability and minimizing bone stress.

Over the years, dental implants have been researched as a way to replace missing teeth. One of the requirements for implant success is their stability and resistance to applied stresses, as well as minimum tension in the surrounding bone. The goal of this work is to use the finite element method to perform numerical and three-dimensional analysis of jaws with implants under mechanical and thermal loading. Implant simulation (containing ceramic crown, titanium root, and jaw bone) is performed in Abacus program under dynamic and thermal load for this purpose. The jawbone is divided into two sections in this simulation: the superficial bone tissue (cortical) and the spongy tissue. Implants are typically made of metals or ceramics that have a

bone-like structure and are compatible with bodily tissues. Currently, titanium metal is used to make implants [31]. As a result, in this article, titanium metal is used to simulate the implant. A ceramic substance is also used to make the implant crown. The effect of implant-induced strains on the jawbone is simulated in this simulation. Mechanical force is given to the top section of the implant and force is applied to the jawbone through the implant in this simulation, resulting in strains and concentrations of stresses at the implant-jawbone junction. Different temperature settings are investigated to investigate the effect of thermal stresses, including temperature decreases and increases, on the tooth surface, as well as their effect on the implant and the jaw bone. High temperature tolerance can arise when drilling the jawbone or when drinking hot liquids, according to the findings of this study. As a result, the goal of this research is to use the finite element method to conduct a numerical and three-dimensional analysis of jaws with implants under mechanical and thermal loads. Thus, we derive the stress distribution, strain, and displacement in the implant and jawbone by modeling the set of implants and jawbone while considering mechanical and thermal loads, and we investigate the effect of various parameters on them.

2. Research Method

2.1. Modelling Software. The study approach involves modeling the geometric model of the jaw bone in Solidwork's software in two states: cortical and spongy. SolidWorks software is also used to construct the geometric model of the implant set and its cover, which is then inserted in the bone. The boundary and force properties and conditions are determined after importing the designed geometric models into the Abaqus analytical software, and the model is then evaluated and examined after meshing. Mechanical and thermal loads are applied to the model in this finite element study, and the heat load due to drinking hot and cold drinks is applied to the whole surface of the ceramic coating in the form of heat flux per unit area. The size of the element converges to improve the accuracy of the simulation findings. The outcomes of modeling this research are also compared to the results of valid articles for validation. The jaw and the implant are presumed to be in perfect contact in this study and that there is no slippage between them. In fact, the bone and the titanium implant are joined, to use medical terminology. The step is utilized directly or implicitly in the analysis, which is dynamic. The simulation approach is offered after the stages of modeling and specifying the required problem in this program are accomplished step by step in different modules of Abacus software.

2.2. Create a Geometric Model. The first stage in issue software modeling is to develop a geometric model of the problem's pieces. The geometry of the ceramic crown, titanium root, and jawbone, as depicted in Figures 1–3, is initially modeled for this purpose. These parts' modeling is three-dimensional and adaptable.

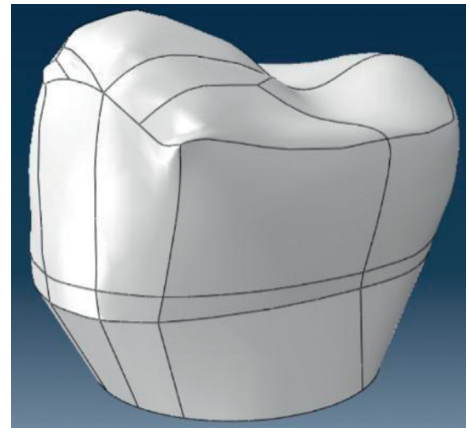

Figure 1: Geometric modeling of a ceramic crown.

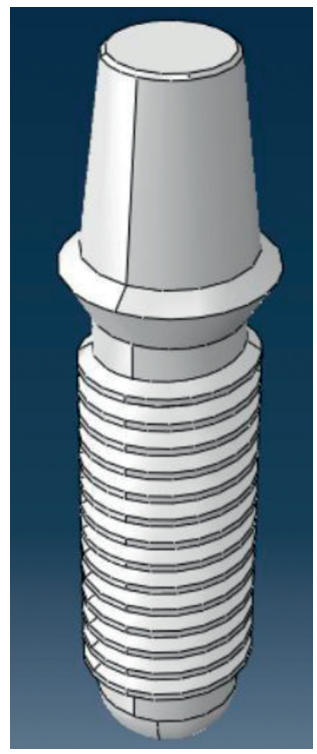

Figure 2: Geometric modeling of titanium root.

2.3. Definition of Material Properties. The crown of the implant is constructed of ceramic, while the root is composed of titanium Ti6Al4V metal, and the jawbone is divided into two groups: cortical and spongy. As a result, mechanical properties such as density, Young's modulus, Poisson's ratio, and plasticity qualities, as well as thermal properties such as specific heat, are determined for each of the materials mentioned. The Drucker–Prager plastic model is combined with the ductile damage model to create the ceramic material for the implant crown. The metal root of the implant is likewise subjected to Johnson Cook's damage model. The jawbone has also benefited from Johnson Cook's elastic and plastic characteristics. Table 1 shows the mechanical properties of implant components.

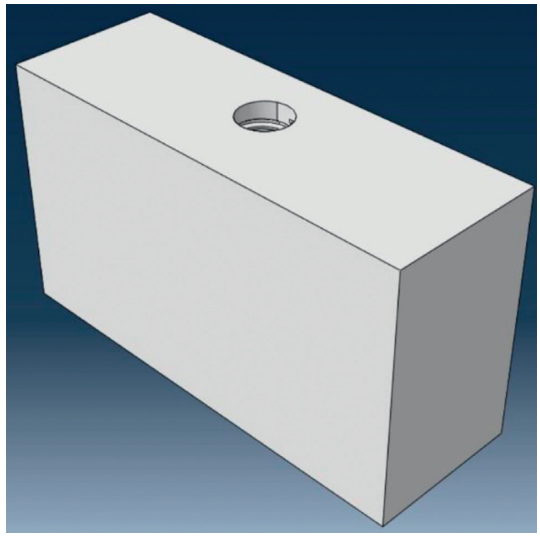

Figure 3: Geometric modeling of the jawbone.

Table 1: Mechanical properties of implant components.

Piece	Identity	Density (kg/m³)	Modulus of elasticity (GPa)	Poisson's ratio (Γ)	Surrender strength (MPa)
Ceramic coating	Porclain	2450	70	0/19	500
Implant	Ti6Al4V metal	4500	110	0/35	800

Table 2 shows the mechanical properties of bone components.

Table 3 shows the thermal properties of the model components.

2.4. Assembly of Parts. Different pieces of the model, including as the ceramic crown, titanium root, and jawbone, are positioned adjacent to each other and their relative positions are defined for this reason. Figure 4 depicts the model parts being put together.

2.5. Define the Type of Analysis. The analysis is classified as linked temp-displacement. This problem clearly considers the type of solver. This solution examines the governing equation system using the element diagonal mass matrix and the law of explicit integration. Figure 5 depicts the software's definition of this type of analysis for massive transformations.

2.6. Define Boundary Conditions and Loadings. The jawbone's lateral surfaces are considered joint support in this article. The upper surface of the ceramic crown has also been subjected to two forms of loading: mechanical and thermal. The entire upper surface of the ceramic crown is paired with a reference point on the same surface in order to establish mechanical and thermal loading, and then, the intended loads are applied to this point. On the upper surface of the crown, a compressive force is exerted. Three distinct values for the amount of compressive force have been evaluated in various analyses to investigate the effect of the amount of force on the behavior of the dental implant. A heat flux is delivered to the upper surface of the ceramic crown to provide a thermal burden. Three distinct values for the amount of heat flow have been investigated in various analyses to investigate the effect of heat flux on the behavior of dental implants. As a result, Abacus software is used to define the above boundary conditions and loads. The articular support on the lateral sides of the jawbone is defined in Figure 6.

Figure 7 shows the application of mechanical load as a compressive force to the upper surface of the crown.

The application of heat flux is seen in Figure 8. It is worth noting that the starting temperature and surrounding environment are both 27 degrees Celsius.

2.7. Meshing. The mesh of the model parts in the form of hexagonal meshes with an element size of 0.2 mm is taken into account. Temperature-displacement coupling elements, explicit library, and quadratic geometric order are among the elements in its family, with a total of 1,986,000 elements. In Section 3, we will look into mesh independence for this amount of elements. The model set correlation is depicted in Figure 9.

3. Analysis of Results

3.1. Check the Independence of the Mesh. The simulation results for numerous different element sizes were explored to ensure that the results from the elements and meshes were independent. For varying sizes of model elements, Table 4 indicates the maximum output stress values in the ceramic coating.

Table 2: Mechanical properties of bone components [28].

Gxy = 4850	Uxy = 0.3 Uyx = 0.3	Ex = 12600		
Gyz = 5700	Uyz = 0.253 Uzy = 0.39	Ey = 12600	$\rho = 1700$	Cortical bone
Gxz = 5700	Uxz = 0.253 Uzx = 0.39	Ez = 19400		
Gxy = 68	Uxy = 0.055 Uyx = 0.01	Ex = 1148		
Gyz = 68	Uyz = 0.01 Uzy = 0.055	Ey = 270	$\rho = 270$	Sponge bone
Gxz = 434	Uxz = 0.322 Uzx = 0.322	Ez = 1148		

Table 3: Thermal properties of model components.

Piece	Thermal expansion coefficient	Thermal conductivity coefficient	Specific heat
Ceramic coating	9/5	5	920
Implant	8/6	6/7	523
Sponge bone	0/031	0/3	1440
Cortical bone	0/028	0/58	1300

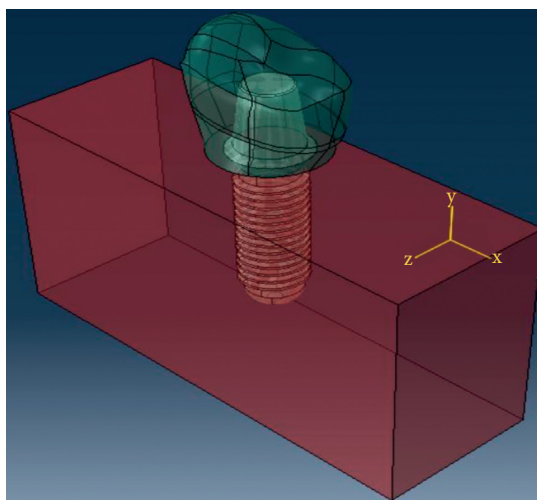

Figure 4: Assembly of model parts.

As can be observed, the results are nearly consistent from element sizes equal to 0.2 mm onwards, indicating that the analysis findings are reliable and that the solution has attained convergence with a high degree of accuracy. The findings are also shown to be independent of the number and size of elements and meshes when using this element size. As a result, various findings have been derived using this element's size.

3.2. Validation. A comparison was done between the results of the current work and the results connected to Niroumand and Jafari in order to validate and evaluate the accuracy of the modeling and numerical solution method. Table 5 shows the maximal von Mises stress of the current investigation and compares it to the results of robust and extensive research for this goal. These values are provided for the model's various components. The stresses in the table are measured in megapascals.

Because there is a small discrepancy between the results of this study and the results of Niroumand and Jafari's publication, it is concluded that the current modeling is accurate and legitimate.

3.3. Stress Results. For three distinct loads, Figure 10 depicts the stress distribution in the ceramic coating area (2500 N, 5000N, and7500).

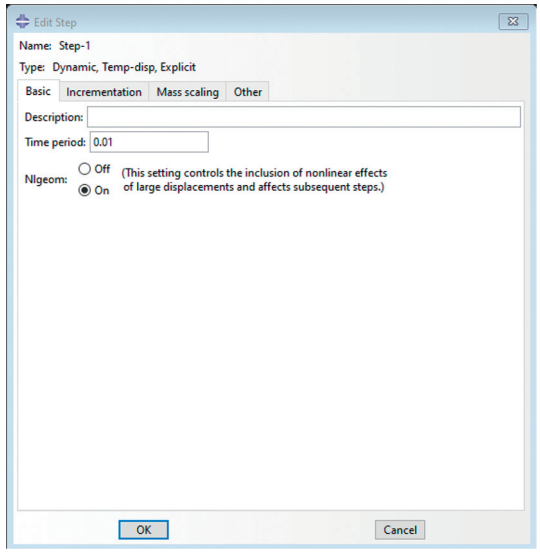

Figure 5: A displacement-temperature coupling with large deformations is defined as the kind of analysis.

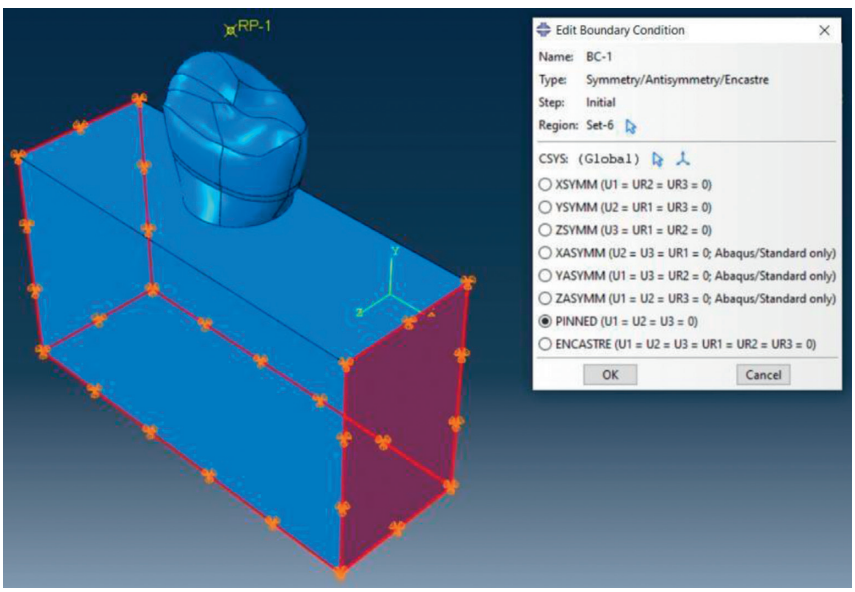

Figure 6: Definition of the articular support on the lateral surfaces of the jawbone.

The stress distribution in the titanium implant region for three distinct loads is shown in Figure 11 (2500 N, 5000 N, and 7500 N).

Figure 12 depicts the distribution of stress in the bone under three different loads (2500 N, 5000N, and 7500 N).

3.4. Strain Results. Figure 13 shows the strain distribution in the ceramic coating section for three different loads (2500 N, 5000N, and 7500).

The strain distribution in the titanium implant part for three distinct loads is shown in Figure 14 (2500 N, 5000 N, and 7500 N).

Figure 15 shows the strain distribution in the bone for three different loads (2500 N, 5000 N, and 7500 N).

3.5. Deformation Results. Figure 16 shows the deformation distribution in the ceramic coating section for three different loads (2500 N, 5000 N, and 7500).

Figure 17 shows the deformation distribution in the titanium implant section for three different loads (2500 N, 5000 N, and 7500 N).

Figure 18 shows the distribution of deformation in the bone for three different loads (2500 N, 5000 N, and 7500 N).

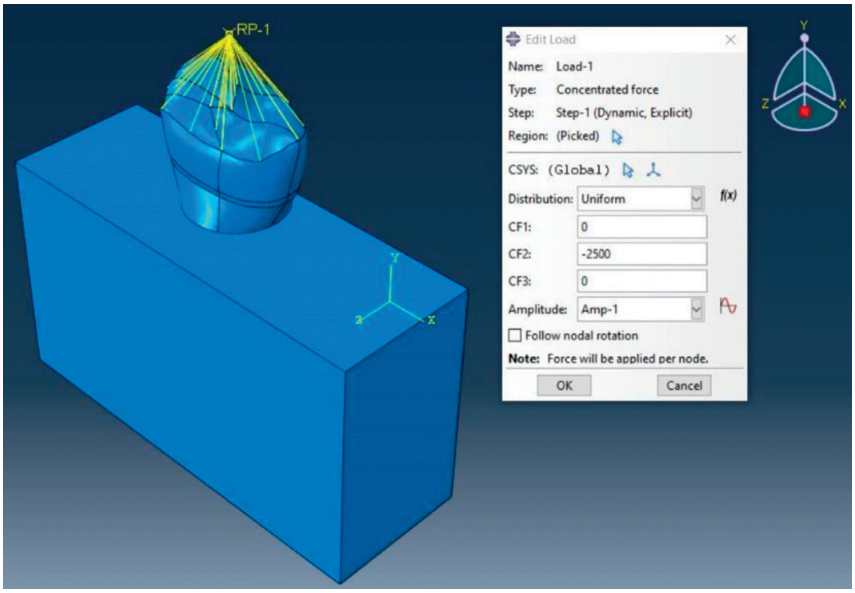

Figure 7: Definition of mechanical load as compressive force to the upper surface of the crown.

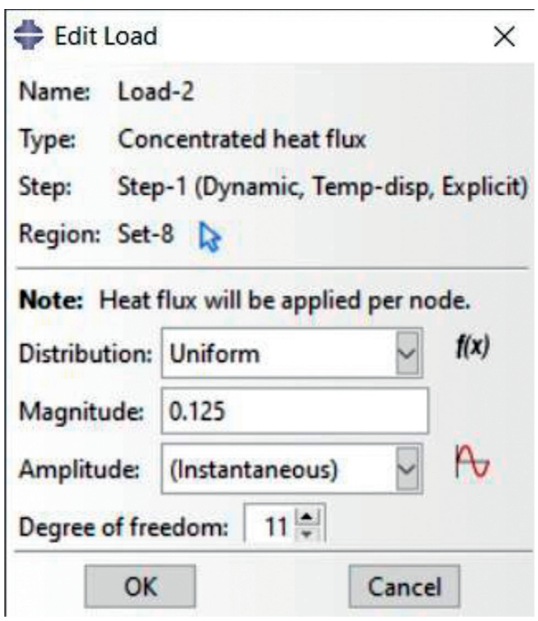

Figure 8: Applying heat flux.

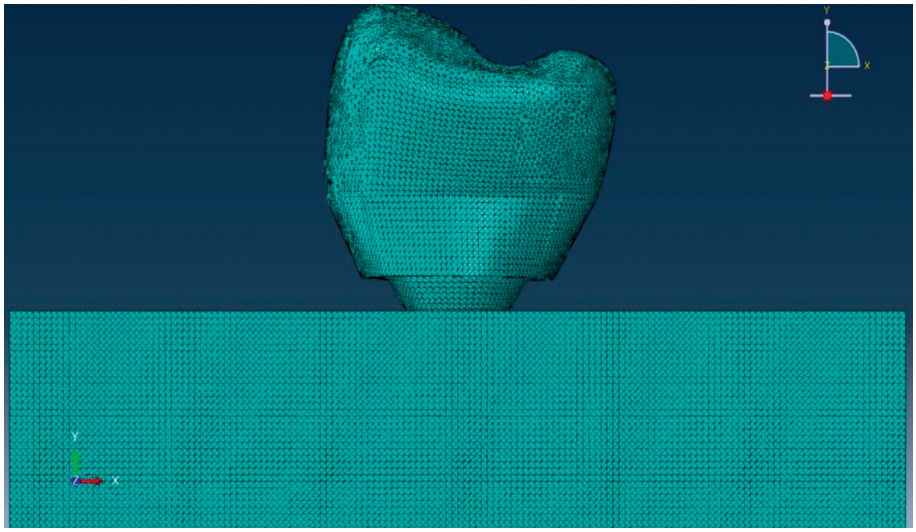

Figure 9: Modeling mesh set.

Table 4: Maximum output stress values in the ceramic coating section for different element sizes.

Element size (mm)	Maximum output stress (MPa)
2	48.83
1	48.29
0.5	47.95
0.2	47.76
0.1	47.68
0.05	47.65

Table 5: Maximum output stress values for different element sizes.

Different model components	Existence research	Niroumand and Jafari research	Percentage error
Implant	85.01	80.72	5.32
Sponge bone	2.33	2.22	4.86
Cortical bone	30.60	29.12	5.07

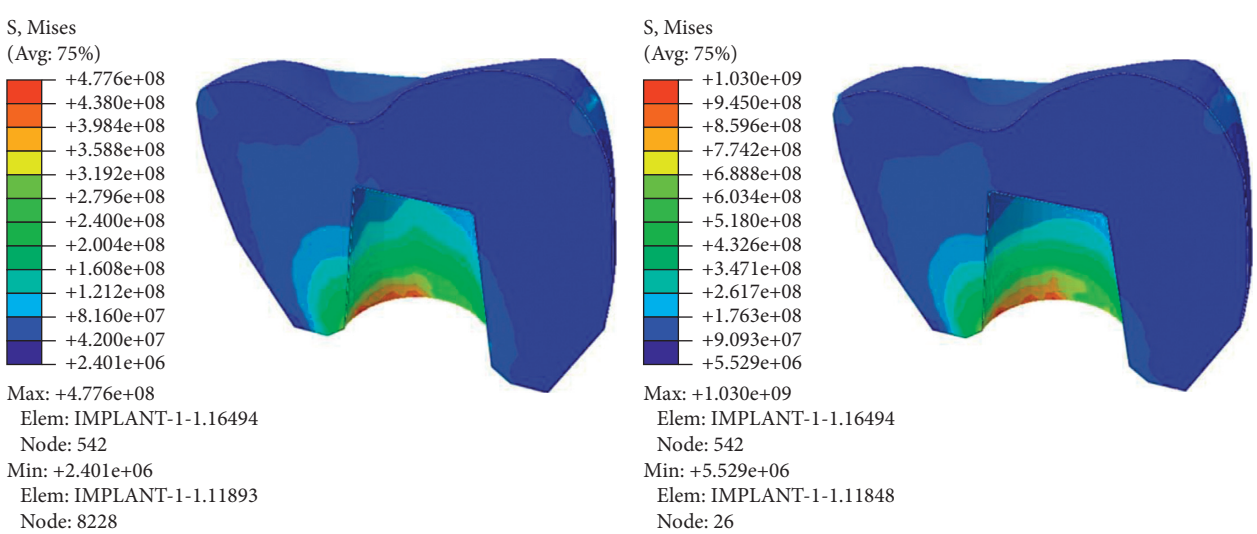

(a) (b)

Figure 10: Continued.

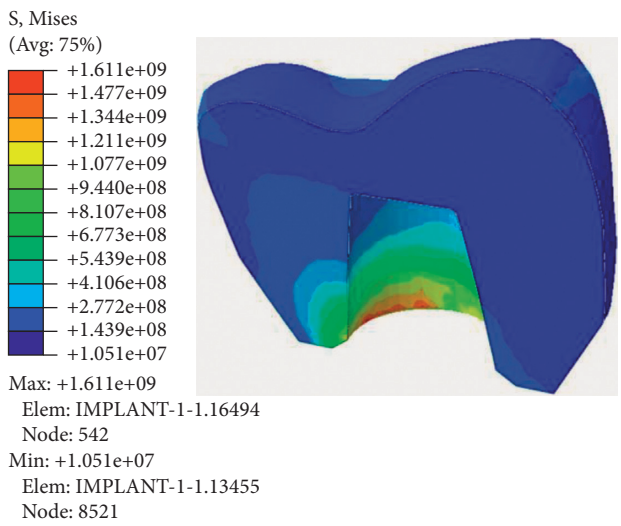

(c)

Figure 10: The stress distribution in the ceramic coating portion for loads of 2500, 5000, and 7500 N.

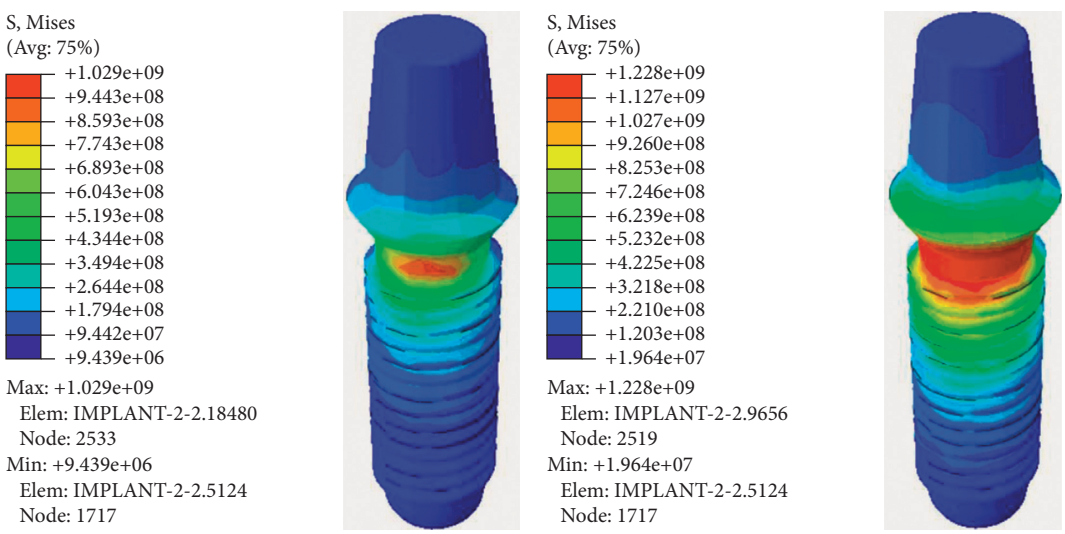

(a) (b)

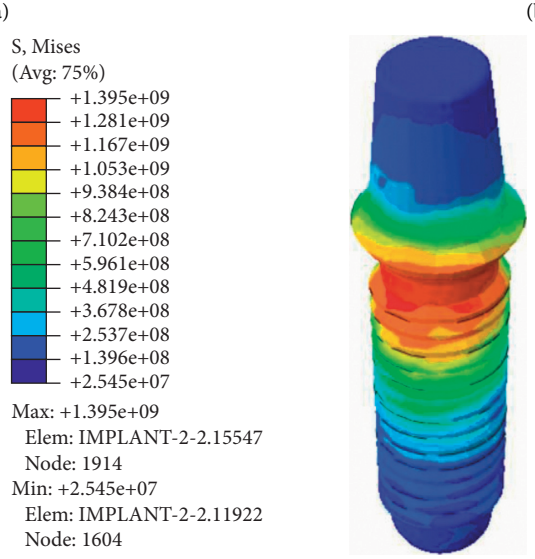

(c)

Figure 11: Stress distribution in the titanium implant section for loads: (a) 2500, (b) 5000, and (c) 7500 N.

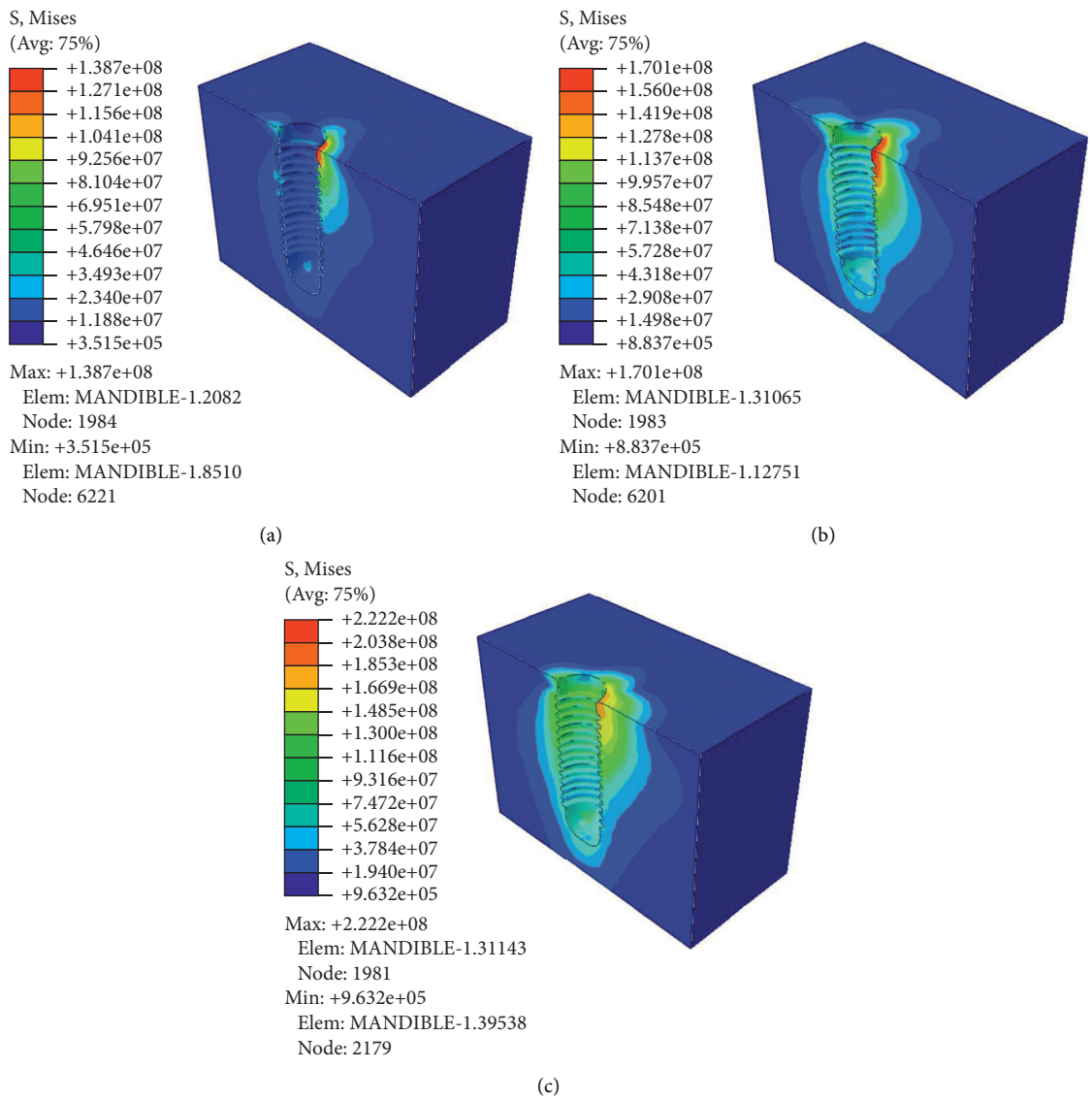

Figure 12: The distribution of stress in the bone segment for loads of 2500, 5000, and 7500 N.

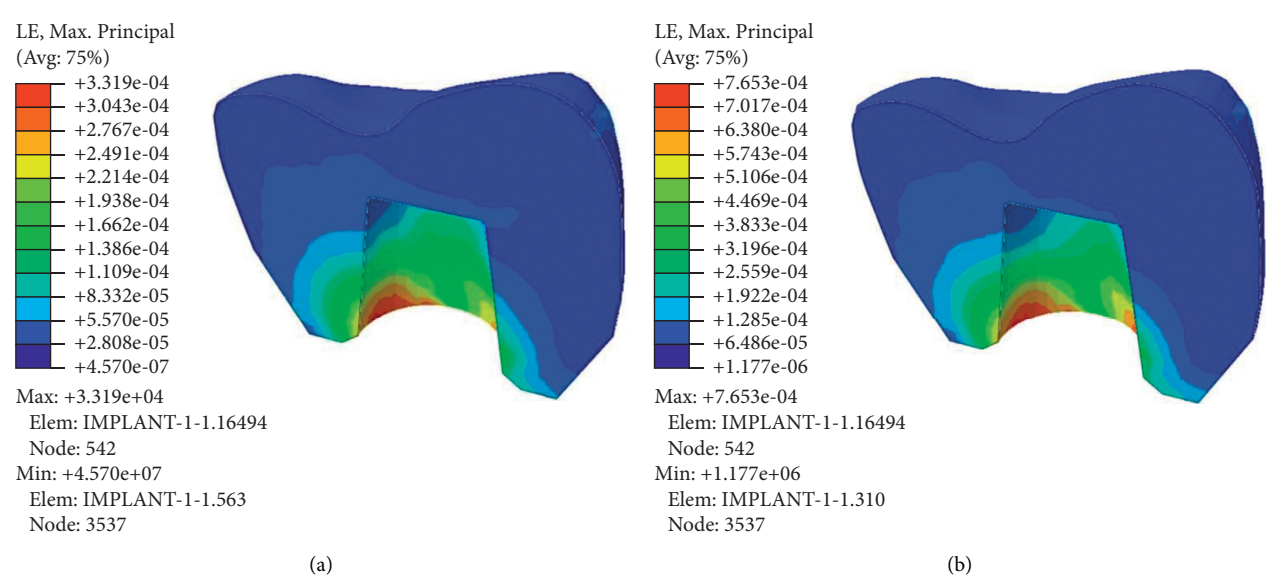

Figure 13: Continued.

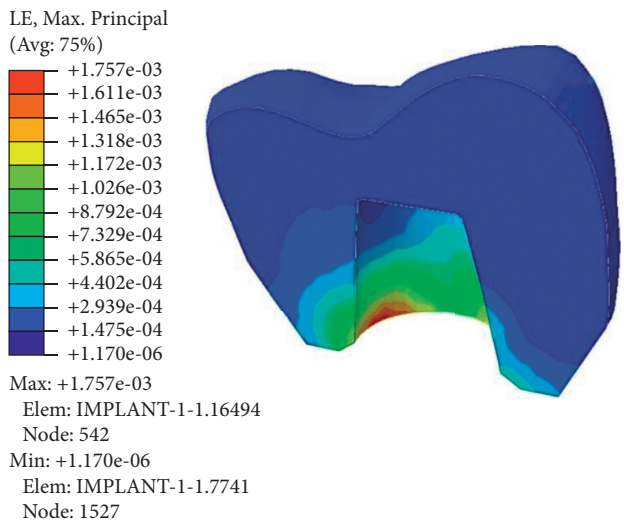

(c)

Figure 13: Strain distribution in the ceramic coating section for loads: (a) 2500, (b) 5000, and (c) 7500 N.

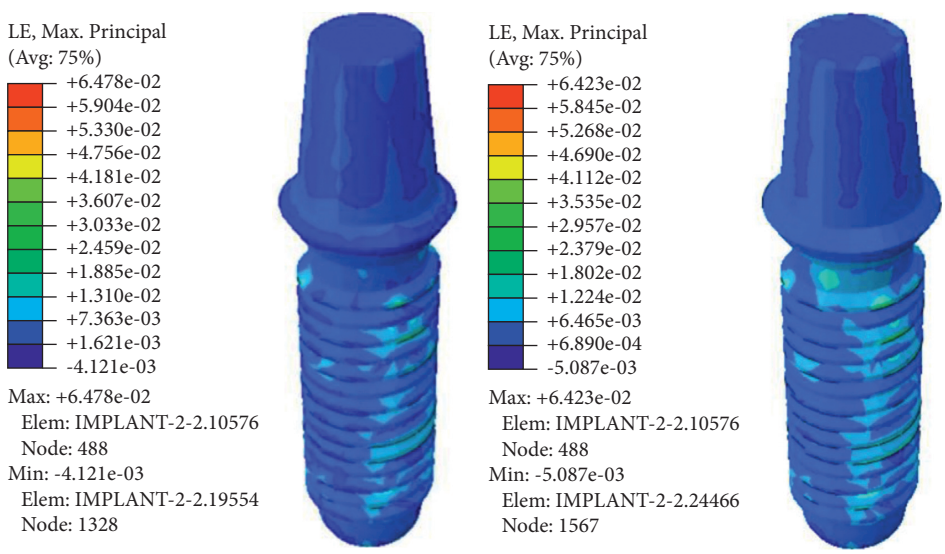

(a) (b)

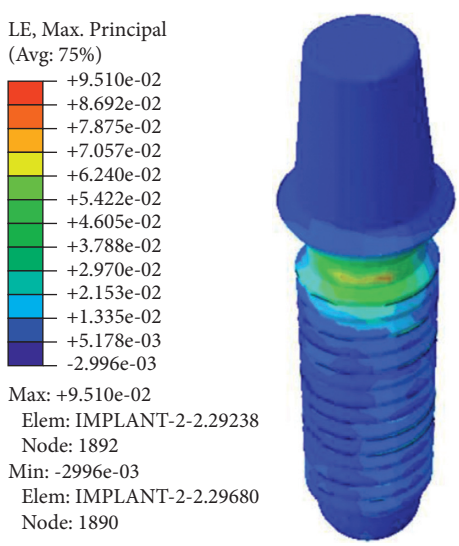

(c)

Figure 14: Strain distribution in the titanium implant section for loads: (a) 2500, (b) 5000, and (c) 7500 N.

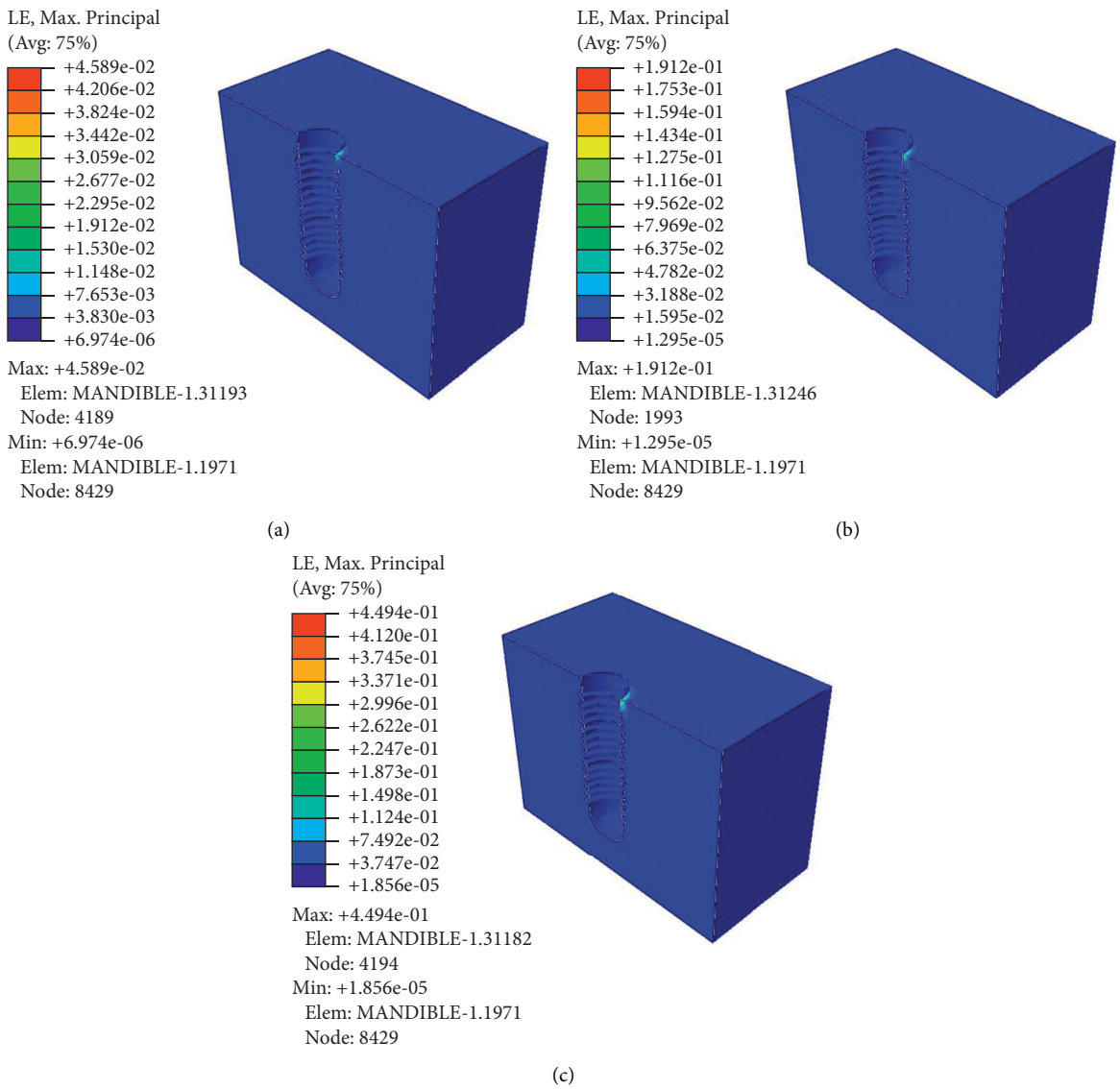

Figure 15: Strain distribution in the bone section for loads: (a) 2500, (b) 5000, and (c) 7500 N.

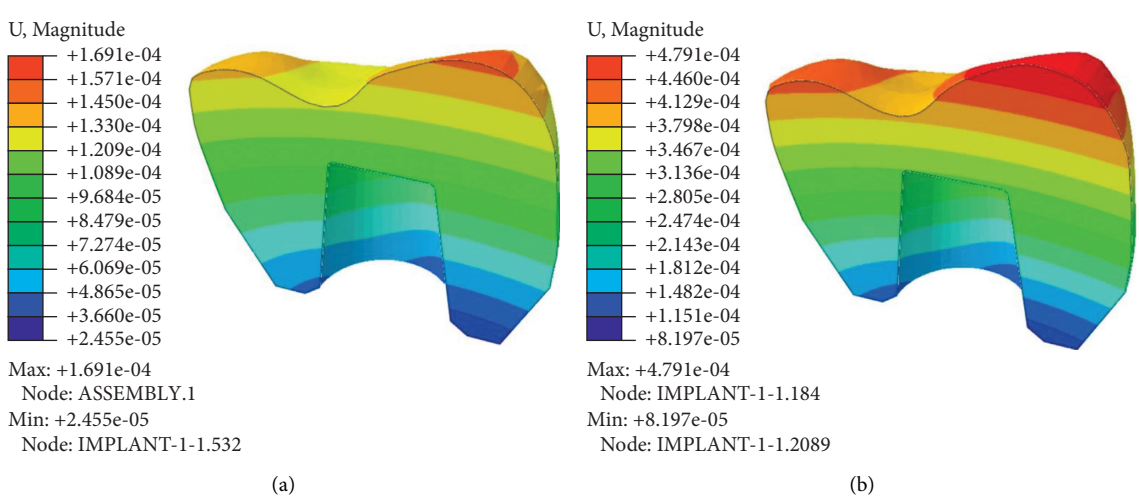

Figure 16: Continued.

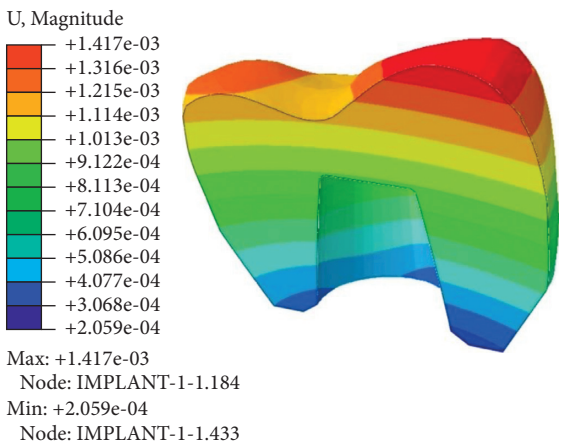

(c)

Figure 16: Deformation distribution in the ceramic coating section for loads: (a) 2500, (b) 5000, and (c) 7500 N.

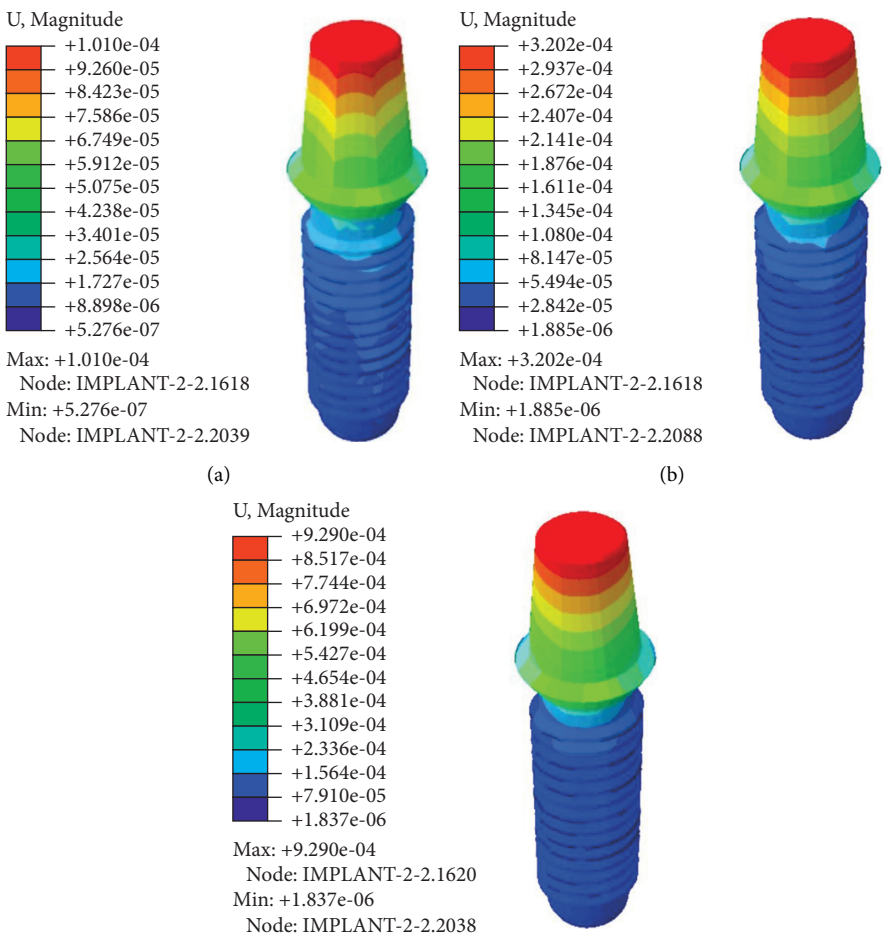

Figure 17: Distribution in the titanium implant section for loads: (a) 2500, (b) 5000, and (c) 7500 N.

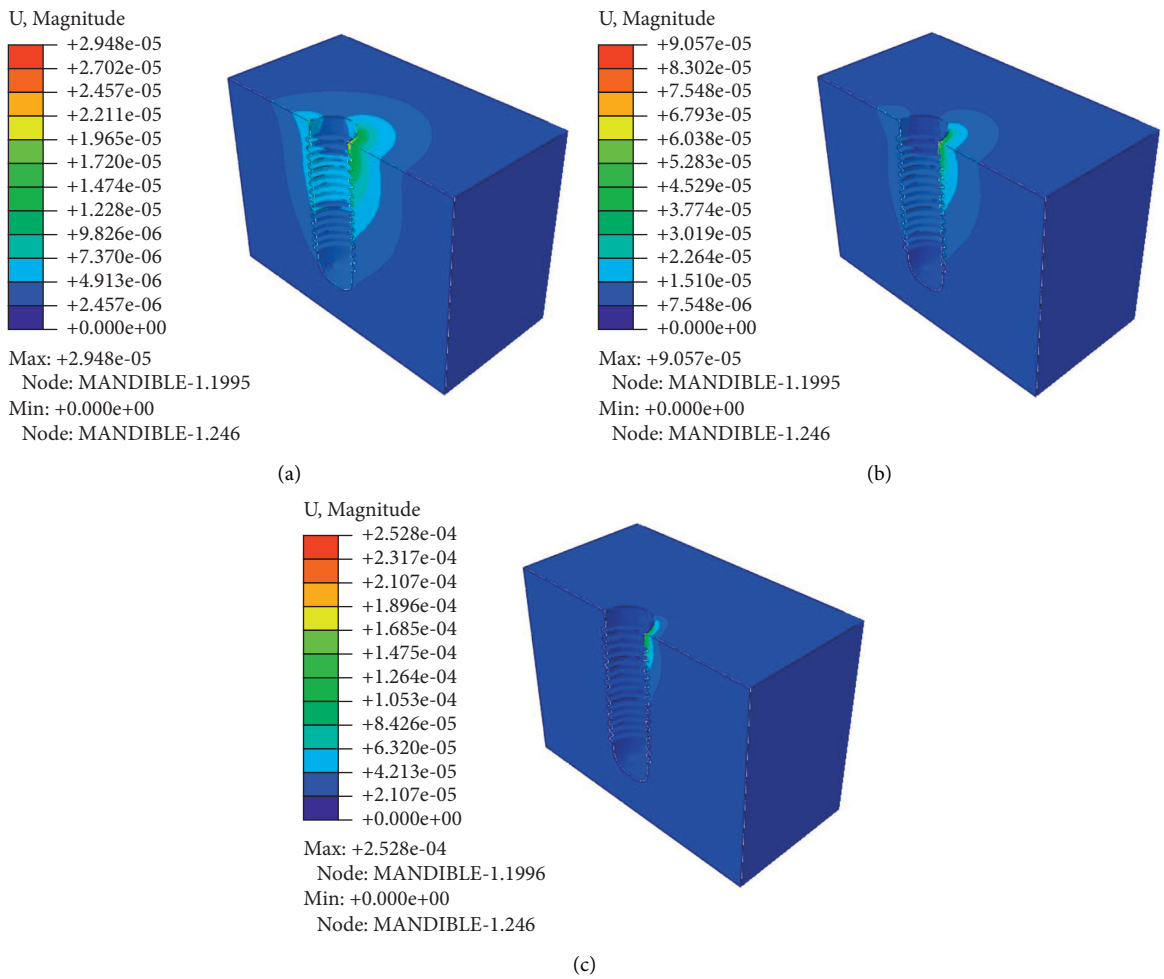

Figure 18: Bone deformation distribution for (a) 2500, (b) 5000, and (c) 7500 N loads.

Table 6: Temperature values in different parts of the model, due to the application of negative and positive heat flux.

Model parts	Minimum temperature due to negative flux (Celsius)	Maximum temperature due to positive flux (Celsius)
Ceramic coating	23.48	48.5
Titanium implants	30.58	42.73
Sponge bone	34.65	39.3
Cortical bone	31.58	41.9

Table 7: Maximum stress values in different parts of the model due to negative and positive heat flux.

Model parts	Maximum stress due to negative flux (MPa)	Maximum stress due to positive flux (MPa)
Ceramic coating	2.355	2.420
Titanium implants	5.455	2.835
Sponge bone	0.03011	0.03208
Cortical bone	1.064	1.063

3.6. Investigating the Effect of Heat Flux. Table 6 shows the temperature values in different parts of the model, due to the application of negative and positive heat flux.

Table 7 shows the maximum stress values caused by negative and positive heat flux in various regions of the model.

4. Conclusion

Over the years, dental implants have been researched as a way to replace missing teeth. One of the requirements for implant success is their stability and resistance to applied stresses, as well as minimum tension in the surrounding

bone. The goal of this work is to use the finite element method to perform numerical and three-dimensional analysis of jaws with implants under mechanical and thermal loading. Implant simulations (containing ceramic crowns, titanium roots, and jawbone) under dynamic and thermal load were done in Abacus program for this purpose, and the following results were found after validation and assuring the reliability of modeling:

(1) The strains induced in all components of the ceramic covering, titanium implants, and jawbone have increased as the mechanical load has grown. It is worth noting that the stress levels shown are related to the von Mises result stress, which may be calculated using the equation below:

$$\sigma^* = \frac{1}{\sqrt{2}}\left[(\sigma xx - \sigma yy)^2 + (\sigma xx - \sigma zz)^2 + (\sigma yy - \sigma zz)^2\right]^{0.5}. \quad (1)$$

(2) The highest levels of stress were seen in the titanium implant at varied loads, whereas the lowest quantities were observed in the jawbone due to the stress distribution.

(3) The strains caused in all regions of the ceramic covering, titanium implants, and jawbone have grown as the mechanical load has increased. It should be emphasized that the reported strain values are related to the elastic strain corresponding to the sum of all strain terms, as determined by the equation below:

$$\varepsilon^* = \frac{1}{\sqrt{2(1+\nu)}}\left[(\varepsilon xx - \varepsilon yy)^2 + (\varepsilon xx - \varepsilon zz)^2 + (\varepsilon yy - \varepsilon zz)^2\right]^{0.5}. \quad (2)$$

(4) It was discovered that, under different loads, the maximum values of strain occurred in the titanium implant and the lowest amount occurred in the ceramic covering due to the strain distribution.

(5) As the mechanical stress on the ceramic coating, titanium implants, and jawbone increases, deformations in all portions of the ceramic coating, titanium implants, and jawbone rise. It is worth noting that the values of the presented deformations are related to the result's deformation.

(6) The maximum amount of distortion occurred in the ceramic covering under varied weights, while the lowest amount occurred in the jawbone, owing to the deformation distribution.

(7) It has been noticed that, due to the effects of positive and negative heat flux, the temperature of the high surface of the ceramic coating that is exposed to the current has increased to 48.5°C when positive heat flux is applied and has reduced to 23.48°C when negative heat flux is applied. Furthermore, due to positive heat flow, the temperature of the titanium implant increased to 42.73°C and reduced to 30.58°C due to negative heat flux.

(8) When positive heat flux was applied to the jaw bone, the temperature of the spongy part of the bone rose to 39.30°C, and when negative heat flux was applied, the temperature of the spongy part of the bone rose to 34.65°C. Due to the positive heat flux, the temperature of the cortical section of the bone increased to 41.90°C and reduced to 31.58°C.

(9) In thermal analysis of the implant and bone set, the maximum temperature transferred to the bone tissue through the implant is investigated. How much heat has reached the bone tissue and the contact surface of the implant with the bone? With some proteins denaturing at 42°C and above, as well as exposing the bone to 47°C for 1 minute, rising bone temperature can have fatal consequences. As a result of the findings of this study, it may be regulated that conditions of detrimental effects on bone tissue do not exist in patients with dental implants.

(10) When comparing the maximum stress values in different regions of the model, it was discovered that the stress caused by negative and positive heat flux in the ceramic covering, sponge bone, and cortical bone is about equivalent. While the stress induced in the titanium implant by negative heat flow was roughly twice that created by positive heat flux. This is due to the temperature gradient in the two circumstances being different. In the negative flux mode, the temperature gradient in the implant was around 7°, while in the positive flux mode, it was about 5°.

4.1. Suggestions. In this study, finite element analysis of the effect of dental implants on the jawbone under mechanical and thermal loading conditions and its results are presented. The following are suggestions for research in this area:

(1) Considering different contact models in modeling the placement of implants on the jawbone

(2) Examining different types of implants with different geometry and materials and comparing their performance

(3) Optimizing the performance of dental implants according to various geometric and physical parameters

Data Availability

The data used to support the findings of this study are included within the article.

Conflicts of Interest

The authors declare that they have no conflicts of interest.

References

[1] C. Santiuste, M. Rodríguez-Millán, E. Giner, and H. Miguélez, "The influence of anisotropy in numerical modeling of orthogonal cutting of cortical bone," *Composite Structures*, vol. 116, pp. 423–431, 2014.

[2] T. Achour, A. Merdji, B. Bachir Bouiadjra, B. Serier, and N. Djebbar, "Stress distribution in dental implant with elastomeric stress barrier," *Materials and Design*, vol. 32, no. 1, pp. 282–290, 2011.

[3] A. Merdji, B. Bachir Bouiadjra, T. Achour, B. Serier, B. Ould Chikh, and Z. O. Feng, "Stress analysis in dental prosthesis," *Computational Materials Science*, vol. 49, no. 1, pp. 126–133, 2010.

[4] K. Oguz, E. Yuzbasiogu, and F. Erzincanh, "Static, dynamic and fatigue behaviors of dental implant using finite element method," *Advances in Engineering Software*, vol. 37, pp. 649–658, 2006.

[5] L. kong and Y. Zhao, K. Hu, D. Li, H. Zhou, Z. Wu, and B. Liu, Selection of the implant thread pitch for optimal biomechanical properties: a three-dimensional finite element analysis," *Advances in Engineering Software*, vol. 40, no. 7, pp. 474–478, 2009.

[6] N. Djebbae, B. Serier, B. Bachir Bouiadjra, S. Benbarek, and A. Drari, "Analysis of the effect of load direction on the stress distribution in dental implant," *Materials and Design*, vol. 31, 2009.

[7] K. Tian, J. Chen, L. Han, J. Yang, W. Huang, and D. Wu, "Angled abutments result in increased or decreased stress on surrounding bone of single-unit dental implants: a finite element analysis," *Medical Engineering and Physics*, vol. 34, no. 10, pp. 1526–1531, 2012.

[8] H.-L. Huang, J.-T. Hsu, L.-J. Fuh, D.-J. Lin, and M. Y. C. Chen, "Biomechanical simulation of various surface roughnesses and geometric designs on an immediately loaded dental implant," *Computers in Biology and Medicine*, vol. 40, no. 5, pp. 525–532, 2010.

[9] A. Dorogoy, D. Rittel, K. Shemtov-Yona, and R. Korabi, "Modeling dental implant insertion," *Journal of the mechanical behavior of biomedical materials*, vol. 68, pp. 42–50, 2017.

[10] H. Guan, R. C. van Staden, N. W. Johnson, and Y.-C. Loo, "Dynamic modelling and simulation of dental implant insertion process-a finite element study," *Finite Elements in Analysis and Design*, vol. 47, no. 8, pp. 886–897, 2011.

[11] M. Yazdi, "Ignorance-aware safety and reliability analysis: a heuristic approach," *Quality and Reliability Engineering*, vol. 36, 2019.

[12] M. Reza Khalili, B. Ziaie, and M. Kazemi, "Finite element analysis for dental implants subjected to thermal loads," *Journal of Dental Medicine-Tehran University of Medical Sciences*, vol. 26, no. 4, pp. 270–280, 2014.

[13] J. N. Reddy, *An Introduction to the Finite Element Method*, McGraw-Hill, New York, NY, USA, Third ed. edition, 2006.

[14] K. Wong, A. Boyde, and P. G. T. Howell, "A model of temperature transients in dental implants," *Biomaterials*, vol. 22, no. 20, pp. 2795–2797, 2001.

[15] L.-J. Fuh, J.-T. Hsu, H.-L. Huang, M. Y. Chen, and Y.-W. Shen, "Biomechanical investigation of thread designs and interface conditions of zirconia and titanium dental implants with bone: three-dimensional numeric analysis," *The International Journal of Oral & Maxillofacial Implants*, vol. 28, no. 2, pp. e64–e71, 2013.

[16] P. Papaspyridakos, M. Mokti, C.-J. Chen, G. I. Benic, G. O. Gallucci, and V. Chronopoulos, "Implant and prosthodontic survival rates with implant fixed complete dental prostheses in the edentulous mandible after at least 5 years: a systematic review," *Clinical Implant Dentistry and Related Research*, vol. 16, no. 5, pp. 705–717, 2014.

[17] M. R. Niroomand and F. Jafari Maryaki, "Investigation on the effect of the contact model between dental implants and jaw bone on the maximum stress of implant using finite element method," *Journal of Mechanics Enginnering*, vol. 46, pp. 275–280, 2017.

[18] F.K. MohammadYazdi and R.R. RouzbehAbbassi, "Improved DEMATEL methodology for effective safety management decision-making," *Safety Science*, vol. 127, Article ID 104705, 2020.

[19] R. C. van Staden, H. Guan, N. W. Johnson, and Y.-C. Loo, "Performance evaluation of bone– implant system during implantation process: dynamic modelling and analysis," *Springer Series in Biomaterials Science and Engineering*, Springer, Berlin, Germany, pp. 45–69, 2017.

[20] T. Berglundh, L. Persson, and B. Klinge, "A systematic review of the incidence of biological and technical complications in implant dentistry reported in prospective longitudinal studies of at least 5 years," *Journal of Clinical Periodontology*, vol. 29, pp. 197–212, 2002.

[21] S. H. Chang, S. R. Huang, S. F. Huang, and C. L. Lin, "Mechanical response comparison in an implant overdenture retained by ball attachments on conventional regular and mini dental implants: a finite element analysis," *Computer Methods in Biomechanics and Biomedical Engineering*, vol. 19, pp. 911–21, Article ID 911921, 2016.

[22] V. Chappuis, R. Buser, U. Brägger, M. M. Bornstein, G. E. Salvi, and D. Buser, "Long-term outcomes of dental implants with a titanium plasma-sprayed surface: a 20-year prospective case series study in partially edentulous patients," *Clinical Implant Dentistry and Related Research*, vol. 15, no. 6, pp. 780–790, 2013.

[23] Z. Zhang, J. Chen, E. Li, W. Li, M. Swain, and Q. Li, "Topological design of all-ceramic dental bridges for enhancing fracture resistance," *International Journal for Numerical Methods in Biomedical Engineering*, vol. 32, Article ID e02749, 2016.

[24] M. Yazdi, N. A. Golilarz, A. Nedjati, and K. A. Adesina, "An improved lasso regression model for evaluating the efficiency of intervention actions in a system reliability analysis," *Neural Computing and Applications*, vol. 33, 2021.

[25] I. B. Babuska, O. Uday, and E. John, "Generalized finite element methods: main ideas, results, and perspective," *International Journal of Computational Methods*, vol. 1, no. 1, pp. 67–103, 2004.

[26] A. A. Solghar, A. Ali, and R. Mehrabi, "Simulation of mechanical behavior of dental implant made of shape memory alloy using the finite element method," *Journal of Mashhad Dental School*, vol. 43, no. 3, pp. 242–252, 2019.

[27] G. Molnár and A. Gravouil, "2D and 3D Abaqus implementation of a robust staggered phase-field solution for modeling brittle fracture," *Finite Elements in Analysis and Design*, pp. 27–38, 2017.

[28] T. Nagasao, M. Kobayashi, Y. Tsuchiya, T. Kaneko, and T. Nakajima, "Finite element analysis of the stresses around fixtures in various reconstructed mandibular models-Part II (effect of horizontal load)," *Journal of Cranio-Maxillofacial Surgery*, vol. 31, no. 3, pp. 168–175, 2003.

[29] N. Prabhu, N. Naik, and V. Patil, "A study on effect of geometric patterns and material onstress distribution in dental implant system: a 3-dimensional finite element analysis"," *International Journal of Mechanical and Production*, vol. 9, pp. 743–752, 2020.

[30] J. Ao, T. Li, Y. Liu et al., "Optimal design of thread height and width on an immediately loaded cylinder implant: a finite element analysis," *Computers in Biology and Medicine*, vol. 40, no. 8, pp. 681–686, 2010.

[31] P.-I. Brånemark, U. Breine, R. Adell, B. O. Hansson, J. Lindström, and Å. Ohlsson, "Intra-osseous anchorage of dental prostheses:I. Experimental studies," *Scandinavian Journal of Plastic and Reconstructive Surgery*, vol. 3, no. 2, pp. 81–100, 1969.

Hindawi
Mathematical Problems in Engineering
Volume 2021, Article ID 1473917, 12 pages
https://doi.org/10.1155/2021/1473917

Research Article

Implementation of MCDM-Based Integrated Approach to Identifying the Uncertainty Factors on the Constructional Project

Raana Bagheri,[1] **Zahra Borouji**,[2] **Seyed Behnam Razavian**,[3] **Mohammad Mahdi Keshvari**,[3] **Farzad Sharifi**,[4] **and Sara Sharifi**[5]

[1]*Department of Management, Science & Technology, Amirkabir University of Technology (Tehran Polytechnic), Tehran, Iran*
[2]*Department of Architecture, Faculty of Architecture, Dr. Shariaty Technical and Vocational University, Tehran, Iran*
[3]*Department of Industrial Management, Binaloud Institute of Higher Education, Mashhad, Iran*
[4]*Department of Industrial Engineering, Yazd University, Yazd, Iran*
[5]*Department of Industrial Management, Yazd University, Yazd, Iran*

Correspondence should be addressed to Raana Bagheri; raana_bagheri@aut.ac.ir

Received 7 July 2021; Revised 30 July 2021; Accepted 13 August 2021; Published 3 September 2021

Academic Editor: Mohammad Yazdi

Presently, environmental management for companies emphasizing environmental protection has become one of the most critical issues for customers, shareholders, governments, employees, competitors, and global pressures requiring organizations to produce environmentally-friendly products and services. This challenge has created a new concept called green supply chain management in business, which combines environmental thinking with the supply chain. Selection of suppliers by considering risk criteria is a category that has attracted the attention of a large number of researchers in order to select the best suppliers according to uncertain factors. In this research, we aim to select a green supplier considering risk factors using a new MCDM approach under uncertainty. For this selection problem, HF-MAIRCA, a new multicriteria sorting method for many alternatives, has been developed. This is used for sorting the alternatives into predefined, ordered supplier categories. This sorting method can be applied to different environmental problems that have a large number of alternatives. As a result of Iran's case study, the result shows that materials flexibility and materials quality are essential criteria for green supplier selection.

1. Introduction

Supply chain management is a serious and fundamental matter to take into account [1–4]. Companies use SCM to effectively provide reliable, flexible, and cheaper products to maintain their competitiveness [5–8]. The process of selecting the right supplier that can meet the customer's needs in terms of quality, price, and punctuality is one of the essential elements in creating a supply chain [9–12]. The selection of the right supplier is critical to a company's manufacturing and distribution operations [13–16]. An abundance of seasoned companies asserts that supplier recruitment is crucial for a business [17–20]. Choosing the wrong suppliers will result in significant financial losses for the business [21–24]. Reducing production costs is a critical skill in today's hypercompetitive market. By identifying suppliers who will meet the organization's needs, a significant reduction in production costs can be realized, and the company's competitiveness will be enhanced [25–28]. A large portion of the final product cost is included in raw materials and components in almost all industries [15, 29–31].

Increasing environmental concerns attract the attention of governments [32–35], customers, and organizations [36–46]. These worries made them define some environmental perquisites in their line of products; since most of the materials and components of products come from external suppliers, having a keen eye on environmental criteria in the supply chain process seems necessary [8, 47–49]. Due to the increasing environmental hazards caused by industrial activities, paying more attention to this issue and making sustainable processes are vital. Green supply chain

management considers the effects of human toxicology and integrates environmental concerns into supply chain management [50–53]. No company today can give up supply chain management and expect its survival [54–57].

Assessment and selection of a decent supplier are among the main tasks in making a sustainable supply chain, which is a significant concern for conserving the environment [58–61].

Construction industry is one of today's essential industries to consider [62–65]. Since Iran's construction companies depend on a stable supply chain, implementing a green supply chain is essential [8, 66–68]. It is possible to implement green supply chain management in the construction industry to manage their natural resource consumption [4, 36, 69, 70]. Additionally, it can help the construction process as a whole be more efficient. Green supply chain management in the construction industry has previously been shown to benefit the business. This product may benefit the organization in several ways, including reducing production costs, protecting the environment, and making a significant contribution to sustainable development. Recruiting a green contractor is a crucial part of supply chain management. It has long-term environmental impacts [71–74].

Choosing a green supplier is a multicriteria decision-making problem [48, 75, 76]. The primary purpose of this study is to identify and prioritize the items for choosing green suppliers in the construction industry and then to rank suppliers based on the items identified using a new approach [25, 77–79].

Many MCDM methods have been introduced for supplier selection. One method to be named is the VIKORSORT [80] method which evaluates the green supplier based on the formula of multicriteria sorting method.

The suppliers got candidates based on AHP Sort II with the type 2 fuzzy distance method in a robust supplier selection problem [81, 82]. Unfortunately, the construction project risk in the supplier selection process has not been considered in previous articles. SC operations are exposed to a variety of risks as a result of globalization. Risky constraints surround the supply chain projects. These emerging constraints should be looked at like a strategic issue that needs to be addressed by SC managers.

Analysis of the green supplier performance and its impact on uncertain variables is essential in choosing effective suppliers. Having said this, it is necessary to have a risk-based supplier selection and sorting method.

It can be stated that there is no feasible approach on integrated multicriteria decision-making methods for sorting green suppliers based on the uncertainty in the construction projects. In order to fill this gap, this study proposes a new multicriteria method based on MAIRCA. This article is based on two principles: first, a MAIRCA-based method called hesitant fuzzy MAIRCA and, second, using the proposed method to rank green suppliers based on the uncertainty of their construction projects.

In this research, we seek to develop a new integrated model of entropy-MAIRCA based on hesitant fuzzy set to select a green supplier in the construction industry under uncertainty.

2. Literature Review

2.1. Green Supply Chain. A world with rising greenhouse gas emissions and rising global temperatures is confronted with various global issues such as global warming, pollution, and various other environmental threats [83]. The discovery of these problems could result in the extinction of the human race. Due to this, environmental preservation programs quickly became essential priorities in business due to their ability to lead to organizational innovation [84, 85]. One hand focused on profitability and the other hand on minimizing or eliminating waste. This location played a vital role in the development of the green supply chain. The Michigan State University Industrial Research Association launched green supply chain management in 1996. It is a new environmental protection management model [85, 86]. All stages of raw materials, product design and manufacturing, product sales and transportation, product use, and product recycling are all involved in the "green supply chain management" strategy from a product life cycle perspective. Reducing the negative environmental impacts while utilizing optimal resources and energy is possible by implementing supply chain management and green technology [87, 88].

The greening of the supply chain is the process throughout the supply chain to consider environmental criteria or considerations. Supply chain management that is green uses all aspects of design, supply chain selection, and green, from conception to completion, as tools for integrating supply chain management with environmental requirements [89, 90].

The concept of sustainable or green supply chain integration encompasses environmentally sustainable practices employed in the traditional supply chain [88]. This may include selecting suppliers and purchasing material, the design of products, the production of products, and the management of final distribution and disposal [85]. Rather than attempting to soften the impact of business and supply chain operations, the green supply chain involves providing value in the form of product or service improvement, plus/or product or service creation, via the operations of the entire supply chain [87, 91–93]. The main goal of the green supply chain is to reduce pollution in the air, water, and waste [37, 38, 70, 94]. However, while attempting to meet this goal, companies can also reduce waste manufacturing, reuse, and recycling, manufacturing costs, asset efficiency, image building, and customer satisfaction [39–41, 95]. The benefits of green supply chain areas are shown in Figure 1.

2.2. Green Supplier Selection. The increase of production level from corporations is an unintended consequence of industrial booming and has continued up until today [96]. The adverse effects of later events have led the production processes to adopt new strategies in the environmental management field to maintain their position. One solution is to conflate the greenness issues in supply chains, which will significantly affect the performance of suppliers [83, 85, 86, 88]. Therefore, evaluating and selecting a green supplier are a strategic decision to maintain a competitive market and social position for companies [50, 97].

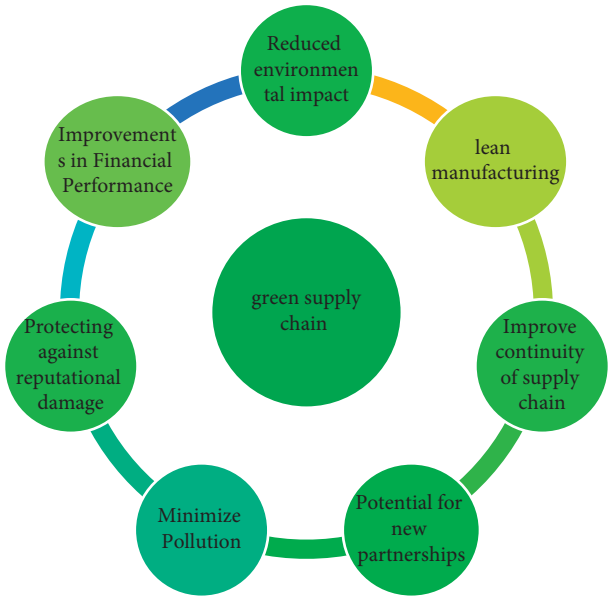

Figure 1: The benefits of green supply chain.

There is much literature evaluating and selecting green suppliers, but there is relatively limited research on evaluating and selecting a green supplier at risk. Recently, research on the evaluation and selection of green suppliers has attracted many academic and industrial sectors [93].

Researchers have developed various tools and techniques for supplier selection, most of which are multicriteria decision-making techniques. An integrated green supplier selection approach is introduced with the ANP process and improved gray relationship analysis [4, 14, 42–46, 48, 49, 63–65, 98–101]. A case study of the food industry to select a green supplier using fuzzy group multicriteria decision-making methods has undergone investigation [16]. Green supplier selection was made using the AHP-entropy-TOPSIS framework [102]. Using the TODIM multicriteria group decision method, a green supplier was selected in the type 2 interval fuzzy environment [103]. In [29], the green supplier selection modeling is done to integrate the DANP model with the VIKOR model.

Artificial intelligence can be a valuable tool for supplier selection. An "intelligent agent" is a system that, by knowing its surroundings, increases its chances of success after analysis [37, 38]. Artificial intelligence in the industry today: due to the spread of knowledge and more complex decision-making process, the use of information systems, especially artificial intelligence systems in decision making, has become more important [39–42]. The spread of knowledge in the field of technology and industry and the complexity of environmental decisions—in other words, human life—has attracted the attention of experts for the use of decision support systems in environmental affairs [43, 44].

Also, in some green supplier articles, multicriteria decision-making and other methods were performed. For example, in [13], artificial neural networks and MADA methods were used in a combined model to select the green supplier. An integrated QFD-MCDM framework was demonstrated for green supplier selection [14]. Selection and evaluation of green suppliers were made using the DEA method [67]. Selection and evaluation of green suppliers were made by combining ANP and IPA methods to achieve sustainable management for the green supply chain [62]. Evaluation and selection of green suppliers were made using cloud model theory and QUALIFLEX method [104].

2.3. Green Supply Chain in the Construction Industry. Many conductive kinds of research have undergone investigation on supplier selection in construction projects. In improving the quality of life in urban environments, the building sector has a significant impact. The greening of the supply chain is a significant challenge and needs to be addressed adequately in the building industry. Paper [26] seeks to select green suppliers for building projects in public universities in Iran through the rough theory of multicriteria decision models. In [27], a new approach is demonstrated for the dynamic decision-making multicriterion choice of green suppliers for construction projects in the time sequences presented. Sustainable development is one of the most undeniable preconditions for resource conservation and balances the performance of a complete supply chain in various regions. Given the complexity of sustainable development and supply chain, different decisions have to be made daily, which requires various substantial parameters to be considered. In [24], a new hybrid MCDM model, which includes COPRAS, ARAS, WASPAS, SAW, and MABAC, is developed to evaluate and select suppliers in a supply chain for construction companies.

During the last decade, supply chain management for construction managers has become a new challenge to obtain the appropriate material and budget on time. In [105], the choice evaluation for the supplier was carried out by the ANP method for building materials such as cladding and roof constructions.

Choosing a supplier as a strategic decision plays a significant role in issues that have attracted the attention of researchers [4, 63]. Suppliers are the first part of the chain, and any failure in this tire will continue in the chain, and its effect will be intensified until the end. It is impossible to produce high-quality, low-cost products or services without having proper decent suppliers in today's competitive world [24, 105]. From the decision-making point of view, different and conflicting criteria must be taken account of, making supplier selection much more ambiguous. In today's open world economy, it is essential to both develop the product and expand supplier lines simultaneously; evaluating and selecting suppliers are a must [75, 96].

Reducing production costs is a crucial law of survival in today's highly competitive environment [106]. The selection of appropriate providers can considerably reduce costs and enhance the organization's competitiveness; that is why in most industries the cost of raw materials and product components engages a large portion of the company's liquidity for the product to take over the market [89]. Increasing concerns about environmental warnings have attracted the attention of governments, customers, and organizations. They discovered the importance of meeting environmental requirements in their productions since most of the materials and components come from external suppliers [90]. Hence, it is crucial to pay attention to environmental criteria in the procurement process. Making a supply chain green is an opportunity for those concerned about sustainable consumption issues and environmental practices [90, 107]. Since most of the materials and components of products are supplied from external suppliers, it is essential to pay attention to environmental criteria in the procurement process. Making a supply chain green is an opportunity for those concerned about sustainable consumption issues and environmental business practices [95, 108–110].

3. Research Methodology

3.1. Hesitant Fuzzy Set. The inherent complexity of natural objects and human inability to fully comprehend such things pose significant problems when it comes to making decisions that rely on information [64, 111]. Most of the issues and challenges faced by decision makers and planners are multi-objective, which adds to the analytical difficulties [4, 65]. Many of the simplifications of the past—for example, that in a given decision only the minimum or maximum cost or benefit is essential—are not acceptable today, and it is necessary to confront the actual situation as much as possible with the methods and utilize more progressive approaches [98, 99]. These methods take a more comprehensive look at issues such as the multiplicity of futures, the multiplicity of goals, the changing attitudes towards risk, and, most importantly, the inevitable balances [100, 101]. Fuzzy sets (FS) were developed by the mathematician Lotfi Zadeh [95] to deal with real-life decisions that are complicated due to the inherent uncertainty. Decision making was aided by fuzzy sets, which Zadeh pioneered in 1965. Afterward, as the progression of decision-making science has progressed, various fuzzy sets have been developed [93]. Torra first proposed the hesitant fuzzy sets concept in 2011.

In contrast to classic fuzzy sets, which have more significant disadvantages, hesitant fuzzy sets have more significant advantages [83]. While applying the classical methods, we have discovered a subtle error that led to a problem with membership values. Thus, we have become motivated to look into hesitation fuzzy sets because this issue has been solved by defining a list of possible values. This issue has been dealt with. By establishing a membership degree as a measurement of the hesitant fuzzy decision-making methods, interval-assignment is less accurate than membership, indicating that hesitant fuzzy methods of decision making are more accurate than other methods [112].

Definition 1 (see [69]). A fuzzy set with an affiliation function mF is in a reference set like X with [0, 1] values such as

$$\mu_F\colon X \longrightarrow [0,1]. \tag{1}$$

Atanassov defined the concept of Intuitive Fuzzy Set (IFS) after introducing the function of fuzzy sets in the decision-making process to express decision-makers preferences more precisely.

Let h, $h1$, and $h2$ be three HFEs; then [111, 112],

$$\begin{aligned}
&(1)\, h^{\lambda} = \bigcup_{\gamma\in h}\left\{\gamma^{\lambda}\right\};\\
&(2)\, \lambda h = \bigcup_{\gamma\in h}\left\{1-(1-\gamma)^{\lambda}\right\};\\
&(3)\, \widetilde{h}_1 \cup \widetilde{h}_2 = \bigcup_{\gamma_1\in\widetilde{h}_1,\gamma_2\in\widetilde{h}_2 \mathrm{Max}\{\gamma_1,\gamma_2\}};\\
&(4)\, \widetilde{h}_1 \cap \widetilde{h}_2 = \bigcup_{\gamma_1\in\widetilde{h}_1,\gamma_2\in\widetilde{h}_2 \mathrm{Min}\{\gamma_1,\gamma_2\}};\\
&(5)\, h_1 \oplus h_2 = \bigcup_{\gamma_1\in h_1,\gamma_2\in h_2 \{\gamma_1+\gamma_2-\gamma_1\gamma_2\}};\\
&(6)\, h_1 \otimes h_2 = \bigcup_{\gamma_1\in h_1,\gamma_2\in h_2 \{\gamma_1\gamma_2\}}.
\end{aligned} \tag{2}$$

Definition 2 (see [69]). If the reference set $X = \{x1, x2, \ldots, xn\}$, the intuitionist fluid set A is defined as the following in the reference set X:

$$A = \left\{\langle x_i, \mu(x_i), \nu(x_i)\rangle | x_i \in X\right\}. \tag{3}$$

Moreover, in the following conditions for all values are membership function and nonmembership function in the [0, 1] interval:

$$0 \le \mu(x_i) + \nu(x_i) \le 1. \tag{4}$$

For set A, we have $\pi_A(x_i)$, which is the uncertainty x_i value:

$$\pi_A(x_i) = 1 - \mu(x_i) - \nu(x_i). \tag{5}$$

Definition 3 (see [69]). A hesitant fluid element, such as H in A, is an HFS function defined as a h subset when an interviewing reference setting [0, 1] is applied. The hesitant fluid set is the generalization of intuitionist fluids. Xu and Xia define this set as follows to make it comfortable:

$$H = \{\langle x_i, h(x_i)\rangle | x_i \in X\}, \tag{6}$$

where $h(x_i)$ is a set of various interval values [0, 1]. $h(x_i)$ is referred to as the hesitant HFE element.

Definition 4 (see [93]). If the X reference set is $h(x) = \{\mu 1, \alpha 2, \ldots, \mu 1\}$, then the HFE mean of $h(x)$ is defined by the following formula for a set of possible values of μm k ($k = 1, 2, \ldots, l$) and 1 is the value for $h(x)$. Consider the following:

$$\overline{h}(x) = \frac{1}{l}\sum_{k=1}^{l}\gamma_k. \tag{7}$$

A definition of value operator and variance operator is required to compare the rules of hesitant fuzzy elements.

Definition 5 (see [69]). The value operator per HFE is the following:

$$s(h) = \frac{1}{l_h}\sum_{\gamma \varepsilon h}\gamma. \tag{8}$$

It is clear that, if $s(h1) > s(h2)$ are $h1 > h2$ and the two values are the same $s(h1) = s(h2)$, then $h1 = h2$.

When two values are compared, it does not matter if one is hesitant or fuzzy because the value operator is the same for both. Moreover, the variance operator is defined as a supplementary concept.

Definition 6 (see [69]). The formula for each HFE is the following:

$$v_1(h) = \frac{1}{l_h}\sqrt{\sum_{\gamma_i,\gamma_j \in h}\left(\gamma_i - \gamma_j\right)^2}. \tag{9}$$

For both HFE elements such as $h1$ and $h2$, if $v1(h1) > v1(h2)$, then $h1 < h2$.

3.2. The Proposed Model (Hesitant Fuzzy Entropy-MAIRCA)

3.2.1. Uncertainty Entropy Method. The entropy procedure is a method of weighting. The weighting method of uncertainty and hesitant fuzzy is a new method of weighing the criteria in a situation where experts' assessment for different reasons is possible, such as many experts, and the problem needs to be weighed under uncertainty.

The following steps are taken in this way [69]:

Step 1: use the following formula to calculate the hesitant fuzzy score Sij on the Expert Opinions matrix:

$$s\left(h_E(x)\right) = \sum_{j=1}^{l\left(h_E(x)\right)}\frac{h_E^{\sigma(j)}(x)}{l\left(h_E(x)\right)}. \tag{10}$$

Step 2: the computation of the normalized matrix S is calculated based on the computation in the previous step:

$$s'_{ij} = \frac{s_{ij}}{\sum_{i=1}^{m} s_{ij}}. \tag{11}$$

Step 3: with the use of De Luca–Termini entropy under hesitant fuzzy sets, we have

$$E_j = -\frac{1}{m \ln 2}\sum_{i=1}^{m}\left(s'_{ij}\ln s'_{ij} + \left(1 - s'_{iy}\right)\ln\left(1 - s'_y\right)\right), \quad j = 1, 2, \ldots, n. \tag{12}$$

Step 4: a formula that describes the weight of the features is

$$w_j = \frac{1 - E_j}{\sum_{j-1}^{n}\left(1 - E_j\right)}, \quad j = 1, 2, \ldots, n. \tag{13}$$

W_J is the subcriteria's weight.

3.2.2. HF-MAIRCA Method. This method is done in six steps [97, 113].

Step 1: form a decision matrix H (see Table 1).

Step 2: determine the distance between two hesitant fuzzy elements through the following formula:

$$d\left(h_M, h_N\right) = \frac{1}{l}\sum_{k=1}^{l}\left|h_M^{\sigma(k)} - h_N^{\sigma(k)}\right|. \tag{14}$$

Now, the following formulas will be used to calculate the value and variance operators of hesitant fuzzy sets:

$$s(h) = \frac{1}{l_h}\sum_{\gamma \varepsilon h}\gamma. \tag{15}$$

Step 3: determine the hesitant fuzzy priority based on the choice of options (P_{Sh}).

When deciding on the work process, the decision maker is unbiased. He is unenthusiastic about any of the available options. People often make a faulty assumption when they assume that the decision maker ignores the probabilities associated with each option. Since each m option can be visually equivalent, the decision maker must decide based on this equation.

$$P_{Sh_i} = \frac{1}{m},$$

$$\sum_{i=1}^{m} P_{sh} = 1, \tag{16}$$

$$i = 1, 2, \ldots, m.$$

Table 1: Decision matrix.

	C_1	C_2	...	C_n
A_1	H_{11}	H_{12}	...	H_{1n}
A_2	H_{21}	H_{22}	...	H_{2n}
...	...	...	...	...
A_m	H_{m1}	H_{m2}	...	H_{mn}

M specifies the total number of options in the above relation. In the context of decision analysis, we assume that the decision maker is risk-neutral concerning the probabilities listed. When it comes to this particular option, all preferences are equivalent; i.e., all P_{Sh} are equal.

Step 3: calculate the theoretical evaluation matrix elements (T_p).

Theoretical evaluation matrix (T_p), in the format $n * m$, is the total criteria number, and m is the total option number. As a coefficient of preference as P_{Sh} options and as a weight, the elements of the theoretical evaluation matrix ($tpij$) are calculated as follows:

$$T_p = \begin{array}{c} \\ P_{A_1} \\ P_{A_2} \\ \cdots \\ P_{A_m} \end{array} \begin{array}{c} \begin{array}{cccc} w_1 & w_1 & \cdots & w_n \end{array} \\ \begin{bmatrix} t_{p11} & t_{p12} & \cdots & t_{p1n} \\ t_{p21} & t_{p22} & \cdots & t_{p2n} \\ \cdots & \cdots & \cdots & \cdots \\ t_{pm1} & t_{pm2} & \cdots & t_{pmn} \end{bmatrix} \end{array} = \begin{array}{c} \\ P_{A_1} \\ P_{A_2} \\ \cdots \\ P_{A_m} \end{array} \begin{array}{c} \begin{array}{cccc} w_1 & w_1 & \cdots & w_n \end{array} \\ \begin{bmatrix} P_{A_1 w_1} & P_{A_1 w_2} & \cdots & P_{A_1 w_n} \\ P_{A_2 w_1} & P_{A_2 w_2} & \cdots & P_{A_2 w_n} \\ \cdots & \cdots & \cdots & \cdots \\ P_{A_m w_1} & P_{A_m w_2} & \cdots & P_{A_m w_n} \end{bmatrix} \end{array}. \tag{17}$$

Since the decision maker for the initial selection of options is neutral, all preferences (P_{Ai}) are equal. Then, the above equation can be shown in the following equation:

$$T_p = P_{A_i} \begin{array}{c} \begin{array}{cccc} w_1 & w_1 & \cdots & w_n \end{array} \\ [t_{p1} \quad t_{p2} \quad \cdots \quad t_{pn}] \end{array} = P_{A_i} \begin{array}{c} \begin{array}{cccc} w_1 & w_1 & \cdots & w_n \end{array} \\ [P_{A_1 w_1} \quad P_{A_i w_2} \quad \cdots \quad t_{A_i w_n}] \end{array}. \tag{18}$$

Step 4: determine the accurate evaluation equation.

The computation of the elements of the actual assessment matrix (Tr) is carried out by multiplying the theoretical evaluation matrix (TP) elements by the following equations and the elements of the initial deciding matrix (X). The first equation is positive, and the second equation is negative.

$$\begin{aligned} t_{rij} &= t_{pij}\left(\frac{x_{ij} - x_i^-}{x_i^+ - x_i^-}\right), \\ t_{rij} &= t_{pij}\left(\frac{x_{ij} - x_i^+}{x_i^- - x_i^+}\right). \end{aligned} \tag{19}$$

Step 5: calculate the total gap matrix (G).

The G matrix elements are calculated as the difference (distance) between theoretical (t_{pij}) and real (t_{rij}) estimates which are expressed in the following equation. If g_{ij} tends to be zero, a theoretical (t_{pij}) and real evaluation (t_{rij}) option with the most negligible difference is chosen. In other words, if the theoretical assessment is equal to the actual assessment in the Ci criterion, compared to the Ci criterion, the Ai option is the best.

$$G = T_p - T_r = \begin{bmatrix} g_{11} & g_{12} & \cdots & g_{1n} \\ g_{21} & g_{22} & \cdots & g_{2n} \\ \cdots & \cdots & \cdots & \cdots \\ g_{m1} & g_{m2} & \cdots & g_{mn} \end{bmatrix} = \begin{bmatrix} t_{p11} - t_{r11} & t_{p12} - t_{r12} & \cdots & t_{p1n} - t_{r1n} \\ t_{p21} - t_{r21} & t_{p22} - t_{r22} & \cdots & t_{p2n} - t_{r2n} \\ \cdots & \cdots & \cdots & \cdots \\ t_{pm1} - t_{rm1} & t_{pm2} - t_{rm2} & \cdots & t_{pmn} - t_{rmn} \end{bmatrix}. \tag{20}$$

Table 2: Criteria for green supplier selection in construction projects.

Criteria	Main criteria	Subcriteria
Green supplier selection in construction projects	C1: building materials information	C11: materials C12: materials flexibility C13: materials quality
	C2: green business operation	C21: emergency response capability C22: green logistics C23: financial capability
	C3: potential for sustainable cooperation	C31: the desire for green cooperation
	C4: green technology capability	C41: green certifications C42: ecodesign of materials C43: green production

Table 3: S values.

C11	C12	C13	C21	C22	C23	C31	C41	C42	C43	
0/51	0/52	0/48	0/22	0/23	0/34	0/94	0/5	0/23	0/38	
0/49	0/95	0/69	0/32	0/58	0/48	0/98	0/41	0/37	0/5	*sij*
0/94	0/13	0/86	0/45	0/64	0/27	0/81	0/4	0/76	0/12	
0/26	0/63	0/43	0/67	0/83	0/6	0/45	0/22	0/53	0/42	
2/200	2/230	2/460	1/660	2/280	1/690	3/180	1/530	1/890	1/420	Sum *Sij*

Table 4: S' values.

C11	C12	C13	C21	C22	C23	C31	C41	C42	C43	
0/153614	0/166666667	0/15286624	0/078014	0/075658	0/158139535	0/227603	0/252525	0/069697	0/122581	
−0/14759	0/304487179	0/21974522	0/113475	0/190789	0/223255814	0/237288	0/207071	0/112121	0/16129	$s'ij$
0/283133	0/041666667	0/27388535	0/159574	0/210526	0/125581395	0/196126	0/20202	0/230303	0/03871	
0/078313	0/201923077	0/13694268	0/237589	0/273026	0/279069767	0/108959	0/111111	0/160606	0/135484	

Table 5: Weight of criteria.

C11	C12	C13	C21	C22	C23	C31	C41	C42	C43	
−0/42893	−0/45056121	−0/4276488	−0/27389	−0/26803	−0/43657189	−0/53636	−0/56509	−0/25285	−0/37204	$s' \ln s' + 1 - s' \ln 1 - s'$
−0/41851	−0/61461847	−0/5265853	−0/35372	−0/48737	−0/53099796	−0/54793	−0/51005	−0/35093	−0/4418	
−0/59589	−0/17320521	−0/5870851	−0/43896	−0/51465	−0/37789996	−0/49498	−0/50319	−0/53964	−0/16382	
−0/27463	−0/50305684	−0/3993745	−0/54828	−0/58625	−0/5920726	−0/34433	−0/34883	−0/44067	−0/39668	
−2/59347	−2/54030114	−2/6213229	−2/62005	−2/55419	−2/57746201	−2/62967	−2/62754	−2/60469	−2/54146	Sum
0/597664	0/585410298	0/60408169	0/603788	0/58861	0/593973989	0/606004	0/605514	0/600248	0/585678	*Ej*
0/402336	0/414589702	0/39591831	0/396212	0/41139	0/406026011	0/393996	0/394486	0/399752	0/414322	$1 - Ej$
0/099859	0/102900646	0/09826643	0/098339	0/102107	0/100775148	0/097789	0/097911	0/099218	0/102834	*wj*

Table 6: Cumulative decision matrix.

w	0/099859	0/102900	0/09826	0/098339	0/102107	0/100775	0/097789	0/097911	0/099218	0/102834	0/099859
Type	+	+	+	+	+	+	+	+	+	+	+
	C11	C12	C13	C21	C22	C23	C31	C41	C42	C43	C11
GT	3/187	3/354	0/004	0/020	3/187	4/864	3/452	0/003	2/254	3/198	3/187
TR	0/005	3/574	2/325	3/354	3/017	3/147	4/110	3/574	2/325	3/147	0/005
WM	2/325	2/254	2/325	0/020	4/149	4/864	4/187	3/157	3/354	3/547	2/325
BA	5/000	4/864	4/190	3/190	4/864	4/980	5/000	4/864	4/190	3/190	5/000

Table 7: *tp* values.

tp	EX1	EX2	EX3	EX4	EX5	EC1	EC2	EC3	S1	S2	S3
GT	0/024965	0/025725	0/024565	0/024585	0/025527	0/025194	0/024447	0/024478	0/024805	0/025709	0/024965
TR	0/024965	0/025725	0/024565	0/024585	0/025527	0/025194	0/024447	0/024478	0/024805	0/025709	0/024965
WM	0/024965	0/025725	0/024565	0/024585	0/025527	0/025194	0/024447	0/024478	0/024805	0/025709	0/024965
BA	0/024965	0/025725	0/024565	0/024585	0/025527	0/025194	0/024447	0/024478	0/024805	0/025709	0/024965

Table 8: Values of *tr*.

tr	EX1	EX2	EX3	EX4	EX5	EC1	EC2	EC3	S1	S2	S3
GT	0/015904	0/010842	0	0/024585	0/023177	0/001594	0	0	0	0/022431	0/015904
TR	0	0/01301	0/013621	0	0/025527	0/025194	0/010392	0/017981	0/00091	0/025709	0
WM	0/011596	0	0/013621	0/024583	0/009882	0/001594	0/011608	0/015881	0/014093	0	0/011596
BA	0/024965	0/025725	0/024565	0/001209	0	0	0/024447	0/024478	0/024805	0/022945	0/024965

Table 9: Calculation of the total gap matrix *G*.

tp − *tr*	C11	C12	C13	C21	C22	C23	C31	C41	C42	C43	C11
GT	0/009061	0/014883	0/024565	0	0/00235	0/023599	0/024447	0/024478	0/024805	0/003278	0/009061
TR	0/024965	0/012715	0/010944	0/024585	0	0	0/014056	0/006496	0/023895	0	0/024965
WM	0/013368	0/025725	0/010944	1/52E-06	0/015645	0/023599	0/01284	0/008596	0/010711	0/025709	0/013368
BA	0	0	0	0/023375	0/025527	0/025194	0	0	0	0/002764	0

Table 10: Ranking alternatives.

Alternatives	*Q*	Rank
GT	0/151465	4
TR	0/117655	2
WM	0/147139	3
BA	0/07686	1

Step 6: calculate the sum of the final values of the total gap (Q).

Based on the following equation, we get the final values for each option which are ranked based on those options. The lower the final values for an option, the higher the ranking.

$$Q_i = \sum_{j=1}^{n} g_{ij}, \quad i = 1, 2, \ldots, m. \tag{21}$$

4. Case Study

Our case study is Aria Asak Construction Company in Iran. The company is about 40 years old and has four leading suppliers (abbreviation of alternatives name company: A1: GT, A2: TR, A3: WM, and A4: BA). In the construction industry, the contractor determines the suppliers of goods and services they use for the project, and the clients then select the contractor. Construction, a project-based business, presents significant environmental risks, and green supply chain management (GSCM) is critical in construction. To successfully implement a project, suppliers aligned with the project objective should be selected for the contractor. The following supply chain management practices help protect the environment: buying green, managing green, marketing green, and reverse logistics, known as reverse logistics by GSCM. A green supply chain is a functional networking pattern in the building industry, which covers the major construction areas, such as construction, as core and infrastructure components, capital flow, information flow, and knowledge flow, and is an aid for the entire lifecycle of the construction project. The selection criteria of green suppliers in this section describe how the qualifications of suppliers in green building technologies, social factors in the construction industry, and environmental capabilities meet the standards required to become a green supplier. Our approach to the selection of the green supplier in building projects includes four main criteria (for example, the price of building materials, the recovery of green, and waste) and ten subcriteria (e.g., building materials information, green business operation, potential for sustainable cooperation, and green technology capability). Table 2 presents criteria for green supplier selection in construction projects.

5. Findings

In the first step, we first obtain the weight of the subcriteria (see Tables 3–6).

First, we calculate S for the decision matrix.

In the next step, we calculate the value of S'.

Now we get the values of E and $1 - E$ and use them to get the weight of the criteria.

Now that the weight of the subcriteria has been obtained, the options are ranked. Using the method, we have the following.

Now because we have 4 options, the value of Ph is 0.25. So by multiplying the matrix values by the cumulative decision in Ph, the values of tp are obtained (Table 7).

Now, considering that all the criteria are positive, the values of tr are obtained (Table 8).

Finally, the total gap matrix is obtained by subtracting the theoretical evaluation matrix and the real evaluation matrix in Table 9.

This value indicates which option is better in each subcriterion. In general, the value of $tp - tr$ in each criterion for each option is zero, so that, under that criterion, that option is better. For example, according to the first column in the system status criterion (C11), the fourth option, BA, is the best option. GT is also the best option in the option of not depending on the criteria C21. WM is not a good option in any of the criteria. Now the result of the overall ranking is as described in Table 10.

6. Conclusion

Carbon emissions reduction has been widely agreed upon across the globe. Healthier and more comfortable living conditions are the direct result of constructing green buildings and a reduction in greenhouse gas emissions in the construction industry. Green building materials are essential for constructors because they can be used to build environmentally-friendly structures while at the same time helping to preserve the environment. GSCM has also become an inevitable option for construction companies due to the market and government pressure. One of the most critical aspects of project construction is to employ green vendors. In this research, we seek to develop a new integrated model of entropy-MAIRCA based on hesitant fuzzy set to select a green supplier in the construction industry under uncertainty. For future research, it is suggested to examine the challenges of the green supply chain in developing countries. It is also suggested to extend other methods of multicriteria decision making like KEMIRA into the MCDM-sorting method in the construction project in developed countries.

Data Availability

There are no available data for this study.

Conflicts of Interest

The authors declare that they have no conflicts of interest.

References

[1] B. Wu, C. Jin, A. Monfort, and D. Hua, "Generous charity to preserve green image? exploring linkage between strategic donations and environmental misconduct," *Journal of business research*, vol. 131, pp. 839–850, 2021.

[2] Y.-Y. Jin, L.-H. Xie, and H.-B. Yang, "Locally upper bounded poset-valued maps and stratifiable spaces," *Topology and Its Applications*, vol.1, Article ID 107517, 2020, In press.

[3] B. Li, R. Liang, W. Zhou, H. Yin, H. Gao, and K. Cai, "LBS meets blockchain:an efficient method with security preserving trust in SAGIN," *IEEE Internet of Things Journal*, vol. 1, p. 1, 2021.

[4] H. Yuan, Z. Wang, Y. Shi, and J. Hao, "A dissipative structure theory-based investigation of a construction and demolition waste minimization system in China," *Journal of Environmental Planning and Management*, vol. 60, pp. 1–27, 2021.

[5] X. Li, Z. Li, T. Jia, P. Yan, D. Wang, and G. Liu, "The sense of community revisited in Hankow, China: combining the impacts of perceptual factors and built environment attributes," *Cities*, vol. 111, Article ID 103108, 2021.

[6] J. Li, Z. Hu, V. Shi, and Q. Wang, "Manufacturer's encroachment strategy with substitutable green products," *International Journal of Production Economics*, vol. 235, Article ID 108102, 2021.

[7] Z. Zhang, S. Liu, and B. Niu, "Coordination mechanism of dual-channel closed-loop supply chains considering product quality and return," *Journal of Cleaner Production*, vol. 248, Article ID 119273, 2020.

[8] S. Sun, M. Zhou, W. Lu, and A. Davarpanah, "Application of symmetry law in numerical modeling of hydraulic fracturing by finite element method," *Symmetry*, vol. 12, no. 7, p. 1122, 2020.

[9] T. F. Liao, "Hybrid modulation strategy for reactive compensation of PV gridconnected inverter," *Intelligent Automation & Soft Computing*, vol. 25, no. 4, pp. 695–704, 2019.

[10] L. Zhao, W. Wang, and W. Zhang, "SEM-based research on influence factors of energy conservation in operation and maintenance of construction project," *Intelligent Automation & Soft Computing*, vol. 25, no. 4, pp. 705–713, 2019.

[11] L. Olatomiwa, S. Mekhilef, S. Shamshirband, and D. Petković, "Adaptive neuro-fuzzy approach for solar radiation prediction in Nigeria," *Renewable and Sustainable Energy Reviews*, vol. 51, pp. 1784–1791, 2015.

[12] A. Mohammadzadeh, O. Castillo, S. S. Band, and A. Mosavi, "A novel fractional-order multiple-model type-3 fuzzy control for nonlinear systems with unmodeled dynamics," *International Journal of Fuzzy Systems*, pp. 1–19, 2021.

[13] R. J. Kuo, Y. C. Wang, and F. C. Tien, "Integration of artificial neural network and MADA methods for green supplier selection," *Journal of Cleaner Production*, vol. 18, no. 12, pp. 1161–1170, 2010.

[14] S. H. Hashemi, A. Karimi, and M. Tavana, "An integrated green supplier selection approach with analytic network process and improved grey relational analysis," *International Journal of Production Economics*, vol. 159, pp. 178–191, 2015.

[15] M. Yazdani, P. Chatterjee, E. K. Zavadskas, and S. H. Zolfani, "Integrated QFD-MCDM framework for green supplier selection," *Journal of Cleaner Production*, vol. 142, pp. 3728–3740, 2017.

[16] N. Banaeian, H. Mobli, B. Fahimnia, I. E. Nielsen, and M. Omid, "Green supplier selection using fuzzy group decision making methods: a case study from the agri-food industry," *Computers & Operations Research*, vol. 89, pp. 337–347, 2018.

[17] R. Habibifar, A. A. Lekvan, and M. Ehsan, "A risk-constrained decision support tool for EV aggregators participating in energy and frequency regulation markets," *Electric Power Systems Research*, vol. 185, Article ID 106367, 2020.

[18] R. Naderi, M. S. Nikabadi, A. A. Tabriz, and M. S. Pishvaee, "Supply chain sustainability improvement using exergy analysis," *Computers & Industrial Engineering*, vol. 154, Article ID 107142, 2021.

[19] M. S. Nikabadi, H. Shambayati, and N. Ataei, "Selection of resilient supply portfolio under disruption risks in supply chain," *International Journal of Industrial and Systems Engineering*, vol. 37, no. 4, pp. 432–462, 2021.

[20] J. Wang, Y. Gao, X. Yin, F. Li, and H. J. Kim, "An enhanced PEGASIS algorithm with mobile sink support for wireless sensor networks," *Wireless Communications and Mobile Computing*, vol. 2018, Article ID 9472075, 9 pages, 2018.

[21] Z. Liao, J. Wang, S. Zhang, J. Cao, and G. Min, "Minimizing movement for target coverage and network connectivity in mobile sensor networks," *IEEE Transactions on Parallel and Distributed Systems*, vol. 26, no. 7, pp. 1971–1983, 2014.

[22] S. Nosratabadi, A. Mosavi, S. Shamshirband, E. Kazimieras Zavadskas, A. Rakotonirainy, and K. W. Chau, "Sustainable business models: a review," *Sustainability*, vol. 11, no. 6, p. 1663, 2019.

[23] J. Zhang, X. Jin, J. Sun, J. Wang, and A. K. Sangaiah, "Spatial and semantic convolutional features for robust visual object tracking," *Multimedia Tools and Applications*, vol. 79, no. 21, pp. 15095–15115, 2020.

[24] B. Matić, S. Jovanović, D. K. Das et al., "A new hybrid MCDM model: sustainable supplier selection in a construction company," *Symmetry*, vol. 11, no. 3, p. 353, 2019.

[25] I. Inayat, S. S. Salim, S. Marczak, M. Daneva, and S. Shamshirband, "A systematic literature review on agile requirements engineering practices and challenges," *Computers in Human Behavior*, vol. 51, pp. 915–929, 2015.

[26] P. Shojaei, "Rough MCDM model for green supplier selection in Iran: a case of university construction project," *Built Environment Project and Asset Management*, vol. 10, no. 3, 2020.

[27] S. Yin, B. Li, H. Dong, and Z. Xing, "A new dynamic multicriteria decision-making approach for green supplier selection in construction projects under time sequence," *Mathematical Problems in Engineering*, vol. 2017, Article ID 7954784, 13 pages, 2017.

[28] M. Younesi Heravi, A. Yeganeh, and S. B. Razavian, "Using fuzzy approach in determining critical parameters for optimum safety functions in mega projects (case study: Iran's construction industry)," in *Frontiers in Nature-Inspired Industrial Optimization*, pp. 183–200, Springer, Berlin, Germany, 2022.

[29] T. C. Kuo, C. W. Hsu, and J. Y. Li, "Developing a green supplier selection model by using the DANP with VIKOR," *Sustainability*, vol. 7, no. 2, pp. 1661–1689, 2015.

[30] M. Rezaei, F. Farahanipad, A. Dillhoff, R. Elmasri, and V. Athitsos, "Weakly-supervised hand part segmentation from depth images," in *Proceedings of the 14th PErvasive Technologies Related to Assistive Environments Conference*, pp. 218–225, Corfu, Greece, June 2021.

[31] V. Torra, "Hesitant fuzzy sets," *International Journal of Intelligent Systems*, vol. 25, no. 6, pp. 529–539, 2010.

[32] M. R. Mahmoudi, D. Baleanu, S. N. Qasem, A. Mosavi, and S. S. Band, "Fuzzy clustering to classify several time series models with fractional Brownian motion errors," *Alexandria Engineering Journal*, vol. 60, no. 1, pp. 1137–1145, 2021.

[33] Z. Liu, A. Mohammadzadeh, H. Turabieh, M. Mafarja, S. S. Band, and A. Mosavi, "A new online learned interval type-3 fuzzy control system for solar energy management systems," *IEEE Access*, vol. 9, pp. 10498–10508, 2021.

[34] C. Mi, Y. Huang, C. Fu, Z. Zhang, O. Postolache, and A. Authors, "Vision-based measurement: actualities and developing trends in automated container terminals," *IEEE Instrumentation and Measurement Magazine*, vol. 24, no. 4, pp. 65–76, 2021.

[35] M. Nabavi, V. Nazarpour, A. H. Alibak, A. Bagherzadeh, and S. M. Alizadeh, "Smart tracking of the influence of alumina nanoparticles on the thermal coefficient of nanosuspensions: application of LS-SVM methodology," *Applied Nanoscience*, vol. 11, pp. 2113–2128, 2021.

[36] M. Shafiei Nikabadi and S. B. Razaviyan, "Identification and ranking of effective indicators on the loyalty of the charities in Iranian charities using fuzzy Delphi and structural interpretative equation," *Quarterly Journal of Socio-Cultural Development Studies*, vol. 6, no. 3, pp. 59–79, 2018.

[37] S. S. Kalantari and A. A. Taleizadeh, "Mathematical modelling for determining the replenishment policy for deteriorating items in an EPQ model with multiple shipments," *International Journal of Systems Science: Operations & Logistics*, vol. 7, no. 2, pp. 164–171, 2020.

[38] A. Chapnevis, I. Güvenç, and E. Bulut, "Traffic shifting based resource optimization in aggregated IoT communication," in *Proceedings of the 2020 IEEE 45th Conference on Local Computer Networks (LCN)*, pp. 233–243, IEEE, Sydney, Australia, November 2020.

[39] M. Masoumnezhad, M. Rajabi, A. Chapnevis et al., "An approach for the global stability of mathematical model of an infectious disease," *Symmetry*, vol. 12, no. 11, p. 1778, 2020.

[40] S. Arasteh, M. Mahdavi, P. N. Bideh, S. Hosseini, and A. Chapnevis, "Security analysis of two key based watermarking schemes based on QR decomposition," in *Proceedings of the Electrical Engineering (ICEE), Iranian Conference on*, pp. 1499–1504, IEEE, Mashhad, Iran, May 2018.

[41] A. Chapnevis and B. Sadeghiyan, "A secure two-party computation protocol for intersection detection between two convex hulls," 2020, https://arxiv.org/abs/2011.00319.

[42] H. Safari-Katesari, S. Y. Samadi, and S. Zaroudi, "Modelling count data via copulas," *Statistics*, vol. 54, no. 6, pp. 1–27, 2020.

[43] H. Safari-Katesari and S. Zaroudi, "Analysing the impact of dependency on conditional survival functions using copulas," *Statistics in Transition New Series*, vol. 22, no. 1, pp. 217–226, 2021.

[44] H. Safari-Katesari and S. Zaroudi, "Count copula regression model using generalized beta distribution of the second kind," *Statistics in Transition New Series*, vol. 21, no. 2, pp. 1–12, 2020.

[45] H. S. Katesari and S. Zarodi, "Effects of coverage choice by predictive modeling on frequency of accidents," *Caspian Journal of Applied Sciences Research*, vol. 5, no. 3, 2016.

[46] H. S. Katesari and B. F. Vajargah, "Testing adverse selection using frank copula approach in Iran insurance markets," *The Journal of Mathematics and Computer Science*, vol. 15, no. 2, pp. 154–158, 2015.

[47] M. Zhu, L. Yu, X. Zhang, and A. Davarpanah, "Application of implicit pressure-explicit saturation method to predict filtrated mud saturation impact on the hydrocarbon reservoirs formation damage," *Mathematics*, vol. 8, no. 7, p. 1057, 2020.

[48] Z. Xiong, N. Xiao, F. Xu et al., "An equivalent exchange based data forwarding incentive scheme for socially aware networks," *Journal of Signal Processing Systems*, vol. 93, no. 2, pp. 249–263, 2021.

[49] H. Zhao and S. Guo, "Selecting green supplier of thermal power equipment by using a hybrid MCDM method for sustainability," *Sustainability*, vol. 6, no. 1, pp. 217–235, 2014.

[50] H. Gao, Y. Ju, E. D. S. Gonzalez, and W. Zhang, "Green supplier selection in electronics manufacturing: an approach based on consensus decision making," *Journal of Cleaner Production*, vol. 245, Article ID 118781, 2020.

[51] T. E. Simos and C. Tsitouras, "Evolutionary derivation of Runge–Kutta pairs for addressing inhomogeneous linear problems," *Numerical Algorithms*, vol. 87, pp. 511–525, 2020.

[52] H. Zhang and Y. Cui, "A model combining a Bayesian network with a modified genetic algorithm for green supplier selection," *Simulation*, vol. 95, no. 12, pp. 1165–1183, 2019.

[53] B. H. Li, Y. Liu, A. M. Zhang, W. H. Wang, and S. Wan, "A survey on blocking technology of entity resolution," *Journal of Computer Science and Technology*, vol. 35, no. 4, pp. 769–793, 2020.

[54] X. Hu, J. Xie, W. Cai, R. Wang, and A. Davarpanah, "Thermodynamic effects of cycling carbon dioxide injectivity in shale reservoirs," *Journal of Petroleum Science and Engineering*, vol. 195, Article ID 107717, 2020.

[55] W. Li, J. Y. Guo, M. Yazdi, A. Nedjati, and K. A. Adesina, "Supportive emergency decision-making model towards sustainable development with fuzzy expert system," *Neural Computing & Applications*, vol. 1, pp. 1–9, 2021.

[56] G. J. Jiang, H. X. Chen, H. H. Sun, M. Yazdi, A. Nedjati, and K. A. Adesina, "An improved multicriteria emergency decision-making method in environmental disasters," *Soft Computing*, vol. 25, pp. 1–29, 2021.

[57] J. Zhang, M. Wang, Y. Tang et al., "Angular velocity measurement with improved scale factor based on a wideband-tunable optoelectronic oscillator," *IEEE Transactions on Instrumentation and Measurement*, vol. 70, 2021.

[58] A. Davarpanah, B. Mirshekari, T. J. Behbahani, and M. Hemmati, "Integrated production logging tools approach for convenient experimental individual layer permeability measurements in a multi-layered fractured reservoir," *Journal of Petroleum Exploration and Production Technology*, vol. 8, no. 3, pp. 743–751, 2018.

[59] D. Petković, Ž. Ćojbašić, V. Nikolić et al., "Adaptive neuro-fuzzy maximal power extraction of wind turbine with continuously variable transmission," *Energy*, vol. 64, pp. 868–874, 2014.

[60] C. Zhang, A. Ali, and L. Sun, "Investigation on low-cost friction-based isolation systems for masonry building structures: experimental and numerical studies," *Engineering Structures*, vol. 243, Article ID 112645, 2021.

[61] R. M. Nejad, F. Berto, G. Wheatley, M. Tohidi, and W. Ma, "On fatigue life prediction of Al-alloy 2024 plates in riveted joints," *Structures*, vol. 33, pp. 1715–1720, 2021.

[62] C. C. Chung, L. C. Chao, and S. J. Lou, "The establishment of a green supplier selection and guidance mechanism with the ANP and IPA," *Sustainability*, vol. 8, no. 3, p. 259, 2016.

[63] R. K. Mavi, "Green supplier selection: a fuzzy AHP and fuzzy ARAS approach," *International Journal of Services and Operations Management*, vol. 22, no. 2, pp. 165–188, 2015.

[64] J. Zhao, J. Liu, J. Jiang, and F. Gao, "Efficient deployment with geometric analysis for mmwave UAV communications," *IEEE Wireless Communications Letters*, vol. 9, no. 7, pp. 1115–1119, 2020.

[65] Q. Jiang, F. Shao, W. Lin, K. Gu, G. Jiang, and H. Sun, "Optimizing multistage discriminative dictionaries for blind image quality assessment," *IEEE Transactions on Multimedia*, vol. 20, no. 8, pp. 2035–2048, 2017.

[66] M. Yazdani, P. Chatterjee, D. Pamucar, and M. D. Abad, "A risk-based integrated decision-making model for green supplier selection: a case study of a construction company in Spain," *Kybernetes*, vol. 49, no. 4, 2019.

[67] I. Dobos and G. Vörösmarty, "Green supplier selection and evaluation using DEA-type composite indicators," *International Journal of Production Economics*, vol. 157, pp. 273–278, 2014.

[68] H. Jafari, M. Nazari, and S. Shamshirband, "Optimization of energy consumption in wireless sensor networks using density-based clustering algorithm," *International Journal of Computers and Applications*, vol. 43, no. 1, pp. 1–10, 2021.

[69] M. S. Nikabadi and S. B. Razavian, "A hesitant fuzzy model for ranking maintenance strategies in small and medium-sized enterprises," *International Journal of Productivity and Quality Management*, vol. 29, no. 4, pp. 558–592, 2020.

[70] M. Rezaei and N. Naderi, "Persian signature verification using fully convolutional networks," 2019, https://arxiv.org/abs/1909.09720.

[71] H. M. W Chen, S. Y. Chou, Q. D. Luu, and T. H. K. Yu, "A fuzzy MCDM approach for green supplier selection from the economic and environmental aspects," *Mathematical Problems in Engineering*, vol. 2016, Article ID 8097386, 10 pages, 2016.

[72] J. Liu, Y. Liu, and X. Wang, "An environmental assessment model of construction and demolition waste based on system dynamics: a case study in Guangzhou," *Environmental Science and Pollution Research*, vol. 27, no. 30, pp. 37237–37259, 2020.

[73] S. Xu, J. Wang, W. Shou, T. Ngo, A. M. Sadick, and X. Wang, "Computer vision techniques in construction: a critical review," *Archives of Computational Methods in Engineering*, vol. 28, no. 2, pp. 1–15, 2020.

[74] R. Liang and H. Y. Chong, "A hybrid group decision model for green supplier selection: a case study of megaprojects," *Engineering Construction and Architectural Management*, vol. 26, no. 8, 2019.

[75] W. Song, Z. Chen, A. Liu et al., "A study on green supplier selection in dynamic environment," *Sustainability*, vol. 10, no. 4, p. 1226, 2018.

[76] J. Liu, Y. Yi, and X. Wang, "Exploring factors influencing construction waste reduction: a structural equation modeling approach," *Journal of Cleaner Production*, vol. 276, Article ID 123185, 2020.

[77] A. Davarpanah, "Parametric study of polymer-nanoparticles-assisted injectivity performance for axisymmetric two-phase flow in EOR processes," *Nanomaterials*, vol. 10, no. 9, p. 1818, 2020.

[78] F. Bahramian, A. Akbari, M. Nabavi, S. Esfandi, E. Naeiji, and A. Issakhov, "Design and tri-objective optimization of an energy plant integrated with near-zero energy building including energy storage: an application of dynamic simulation," *Sustainable Energy Technologies and Assessments*, vol. 47, no. 1, Article ID 101419, 2021.

[79] A. Davarpanah, R. Shirmohammadi, B. Mirshekari, and A. Aslani, "Analysis of hydraulic fracturing techniques: hybrid fuzzy approaches," *Arabian Journal of Geosciences*, vol. 12, no. 13, pp. 1–8, 2019.

[80] L. Demir, M. E. Akpınar, C. Araz, and M. A. Ilgın, "A green supplier evaluation system based on a new multicriteria sorting method: VIKORSORT," *Expert Systems with Applications*, vol. 114, pp. 479–487, 2018.

[81] Z. Xu, J. Qin, J. Liu, and L. Martinez, "Sustainable supplier selection based on AHPSort II in interval type-2 fuzzy environment," *Information Sciences*, vol. 483, pp. 273–293, 2019.

[82] H. Karimmaslak, B. Najafi, S. S. Band, S. Ardabili, F. Haghighat-Shoar, and A. Mosavi, "Optimization of performance and emission of compression ignition engine fueled with propylene glycol and biodiesel–diesel blends using artificial intelligence method of ANN-GA-RSM," *Engineering Applications of Computational Fluid Mechanics*, vol. 15, no. 1, pp. 413–425, 2021.

[83] M. Yazdani, Z. Wen, H. Liao, A. Banaitis, and Z. Turskis, "A grey combined compromise solution (CoCoSo-G) method for supplier selection in construction management," *Journal of Civil Engineering and Management*, vol. 25, no. 8, pp. 858–874, 2019.

[84] A. Chapnevis, İ. Güvenç, L. Njilla, and E. Bulut, "Collaborative trajectory optimization for outage-aware cellular-enabled UAVs," in *Proceedings of the 2021 IEEE 93rd Vehicular Technology Conference (VTC2021-Spring)*, pp. 1–6, IEEE, Helsinki, Finland, April 2021.

[85] H. W. Lo, J. J. Liou, H. S. Wang, and Y. S. Tsai, "An integrated model for solving problems in green supplier selection and order allocation," *Journal of Cleaner Production*, vol. 190, pp. 339–352, 2018.

[86] Q. Wu, L. Zhou, Y. Chen, and H. Chen, "An integrated approach to green supplier selection based on the interval type-2 fuzzy best-worst and extended VIKOR methods," *Information Sciences*, vol. 502, pp. 394–417, 2019.

[87] B. Bathaei, *The Architectural System of Persian Enclosed Garden: Recognition & Recreating of the Concept of Persian Garden*, LAP LAMBERT Academic Publishing, Sunnyvale, CA, USA, 2020.

[88] M. Igarashi, L. de Boer, and A. M. Fet, "What is required for greener supplier selection? a literature review and conceptual model development," *Journal of Purchasing and Supply Management*, vol. 19, no. 4, pp. 247–263, 2013.

[89] M. K. Buniya, I. Othman, R. Y. Sunindijo, A. F. Kineber, E. Mussi, and H. Ahmad, "Barriers to safety program implementation in the construction industry," *Ain Shams Engineering Journal*, vol. 12, no. 1, pp. 65–72, 2021.

[90] D. D. Camacho, P. Clayton, W. J. O'Brien et al., "Applications of additive manufacturing in the construction industry–a forward-looking review," *Automation in Construction*, vol. 89, pp. 110–119, 2018.

[91] B. Bathaei, "Persian enclosed garden: recognition & recreation of the Persian garden," *Revista Şcolii Doctorale de Urbanism*, vol. 1, no. 1, pp. 53–56, 2016.

[92] B. Bathaei, *Process Analysis of Environmental Perception of Persian Garden Based on Psychological Theory of Environment*, Editura Universitar "Ion Mincu", Bucharest, Romania, 2016.

[93] B. Bathaei, "Change is of the essence, regenerating of brown fields (landscape revitalization of Tehran's brick kilns)," in *Proceedings of the 2nd International Conference on Architecture, Structure and Civil Engineering (ICASCE'16)*, London, UK, March 2016.

[94] B. Bathaei, "Achieving sustainable city by the concept of Persian garden," *Acta Technica Napocensis: Civil Engineering & Architecture*, vol. 61, no. 3, 2018.

[95] S. H. Mafuku, "Greening the construction industry in Zimbabwe," *The Sustainability Ethic in the Management of the Physical, Infrastructural and Natural Resources of Zimbabwe*, p. 361, Langaa RPCIG, Bamenda, Cameroon, 2019.

[96] S. A. S. Haeri and J. Rezaei, "A grey-based green supplier selection model for uncertain environments," *Journal of Cleaner Production*, vol. 221, pp. 768–784, 2019.

[97] L. Gigović, D. Pamučar, Z. Bajić, and M. Milićević, "The combination of expert judgment and GIS-MAIRCA analysis for the selection of sites for ammunition depots," *Sustainability*, vol. 8, no. 4, p. 372, 2016.

[98] M. A. Medvedeva, T. E. Simos, and C. Tsitouras, "Exponential integrators for linear inhomogeneous problems," *Mathematical Methods in the Applied Sciences*, vol. 44, no. 1, pp. 937–944, 2021.

[99] M. A. Medvedeva, T. E. Simos, and C. Tsitouras, "Sixth-order, P-stable, Numerov-type methods for use at moderate accuracies," *Mathematical Methods in the Applied Sciences*, vol. 44, no. 8, pp. 6923–6930, 2021.

[100] T. E. Simos and C. Tsitouras, "Explicit, ninth order, two step methods for solving inhomogeneous linear problems $x''(t) = \Lambda x(t) + f(t)$," *Applied Numerical Mathematics*, vol. 153, pp. 344–351, 2020.

[101] M. A. Medvedeva, T. E. Simos, and C. Tsitouras, "Variable step-size implementation of sixth-order Numerov-type methods," *Mathematical Methods in the Applied Sciences*, vol. 43, no. 3, pp. 1204–1215, 2020.

[102] G. Graham, J. Freeman, and T. Chen, "Green supplier selection using an AHP-entropy-TOPSIS framework," *Supply Chain Management*, vol. 20, no. 3, pp. 327–340, 2015.

[103] J. Qin, X. Liu, and W. Pedrycz, "An extended TODIM multicriteria group decision making method for green supplier selection in interval type-2 fuzzy environment," *European Journal of Operational Research*, vol. 258, no. 2, pp. 626–638, 2017.

[104] K. Q. Wang, H. C. Liu, L. Liu, and J. Huang, "Green supplier evaluation and selection using cloud model theory and the qualiflex method," *Sustainability*, vol. 9, no. 5, p. 688, 2017.

[105] A. E. Cengiz, O. Aytekin, I. Ozdemir, H. Kusan, and A. Cabuk, "A multicriteria decision model for construction material supplier selection," *Procedia Engineering*, vol. 196, pp. 294–301, 2017.

[106] O. Babalola, E. O. Ibem, and I. C. Ezema, "Implementation of lean practices in the construction industry: a systematic review," *Building and Environment*, vol. 148, pp. 34–43, 2019.

[107] M. Ahmed, M. J. Thaheem, and A. Maqsoom, "Barriers and opportunities to greening the construction supply chain management," *Benchmarking: An International Journal*, vol. 27, no. 3, 2019.

[108] A. Oke, D. Aghimien, C. Aigbavboa, and C. Musenga, "Drivers of sustainable construction practices in the Zambian construction industry," *Energy Procedia*, vol. 158, pp. 3246–3252, 2019.

[109] A. A. Lekvan, R. Habibifar, M. Moradi, M. Khoshjahan, S. Nojavan, and K. Jermsittiparsert, "Robust optimization of renewable-based multi-energy micro-grid integrated with flexible energy conversion and storage devices," *Sustainable Cities and Society*, vol. 64, Article ID 102532, 2021.

[110] A. Davarpanah and B. Mirshekari, "A mathematical model to evaluate the polymer flooding performances," *Energy Reports*, vol. 5, pp. 1651–1657, 2019.

[111] M. Xia and Z. Xu, "Hesitant fuzzy information aggregation in decision making," *International Journal of Approximate Reasoning*, vol. 52, no. 3, pp. 395–407, 2011.

[112] R. M. Rodriguez, L. Martinez, and F. Herrera, "Hesitant fuzzy linguistic term sets for decision making," *IEEE Transactions on Fuzzy Systems*, vol. 20, no. 1, pp. 109–119, 2011.

[113] I. Badi and M. Ballem, "Supplier selection using the rough BWM-MAIRCA model: a case study in pharmaceutical supplying in Libya," *Decision Making: Applications in Management and Engineering*, vol. 1, no. 2, pp. 16–33, 2018.

Hindawi
Mathematical Problems in Engineering
Volume 2021, Article ID 2764558, 12 pages
https://doi.org/10.1155/2021/2764558

Research Article

A Decomposition-Based Multiobjective Optimization Evolutionary Algorithm with Adaptive Weight Generation Strategy

Guo-Zhong Fu, Tianda Yu, Wei Li, Qiang Deng, and Bo Yang

Science and Technology on Reactor System Design Technology Laboratory, Nuclear Power Institute of China, Chengdu 610213, China

Correspondence should be addressed to Guo-Zhong Fu; guo-zhongfu@hotmail.com

Received 17 June 2021; Revised 9 August 2021; Accepted 12 August 2021; Published 2 September 2021

Academic Editor: Mohammad Yazdi

Multiobjective evolutionary algorithm based on decomposition (MOEA/D) is the seminal framework of multiobjective evolutionary algorithms (MOEAs). To alleviate the nonuniformly distributed solutions generated by a fixed set of evenly distributed weight vectors in the presence of nonconvex and disconnected problems, an adaptive vector generation mechanism is proposed. A coevolution strategy and a vector generator are synergistically cooperated to remedy the weight vectors. Optimal weight vectors are generated to replace the useless weight vectors to assure that optimal solutions are distributed evenly. Experiment results indicate that this mechanism is efficient in improving the diversity of MOEA/D.

1. Introduction

Multiobjective optimization problems (MOPs), different from the single-objective optimization problems (SOPs), have more than one objective function, and the objective functions conflict with each other. In the optimization process, the relationship between the objective function values is partially ordered. The optimization cannot be selected by simply comparing the values. The optimized solution of MOPs is a set of mutually compromised solutions, i.e., Pareto optimal solution set (PS) [1–5]. The performance metrics of the PS are diversity and convergence. Also, the multiobjective optimization supports simplify the design of products and their several key performances like efficiency, reliability, availability, and lifetime cost-saving [6–11].

Conventional analytical algorithms aggregate multiple objective functions into one, which can be solved by the analytical method. However, these algorithms can only obtain one optimized solution at each iteration. Only by running multiple times and setting different single "composite" objective functions can we obtain enough Pareto optimal solutions. At the same time, since the optimization process of each iteration is independent of each other, the information in the iteration process cannot be shared, requiring complex computations [12]. Furthermore, these algorithms are problem-dependent. Different aggregation strategies would be only applicable for specific MOP problems. An evolutionary algorithm (EA) is a population-based and problem-independent optimization algorithm. It poses computers the ability to solve complex optimization in the absence of gradient information and obtains a set of optimization solutions in parallel at each iteration. Multiobjective evolutionary algorithms (MOEA) have become an important branch in the field of EA and evolutionary multiobjective optimization (EMO) research. The iconic research on employing EA to solve MOPs refers to Goldberg, by which the notion of nondominated sorting and niching technique are introduced [13]. It established the nondominated based framework of MOEAs, by which many researches are developed [14–17]. However, most objective optimization problems (MaOPs) with more than 3 objectives, which make it is difficult for nondominated based MOEAs to obtain efficient solutions. Because the portion of nondominated solutions in the whole population increase

dramatically, it would be difficult to discriminate optimized solutions from the population. Relaxed dominance based MOEAs [18–21], preference-based MOEAs [22–24], indicator based MOEAs [25–27], and decomposition based MOEAs [28, 29] are introduced to tackle MaOPs. The decomposition based MOEAs decompose the MOPs into a set of single-objective subproblems with reference to prescribed weight vectors and then optimize these subproblems at the same time. Due to its superiority in strong convergence to the Pareto front and wide scope of adaption in complex MOPs and MaOPs, decomposition based MOEAs have been the research hotspot in EMO. Recently most researches on decomposition based MOEAs are based on the seminal framework of MOEA/D proposed by Zhang and Li [28].

In the preliminary algorithm, MOEA/D assumes that a set of uniformly distributed weight vectors could result in well-distributed solutions. However, Li and Zhang found that different weight vectors could result in different distributed solutions with respect to different optimization problems [30]. Referring to a convex problem illustrated in Figure 1, a set of uniformly distributed weight vectors $\mathbf{w} = \{w_1, w_2, w_3, w_4, w_5, w_6\}$ would result in a set of nonuniformly distributed solutions $\mathbf{s} = \{s_1, s_2, s_3, s_4, s_5, s_6\}$.

Much research has tried to redesign the generation method of weight vectors so that the optimized solutions can be evenly distributed in the target space, thereby enhancing their diversity. So far, representative weight vector generation methods include simplex-lattice [31], double-layer simplex lattice [32], and uniform design [33]. To obtain an optimal solution with uniform distribution, it demands that the Pareto optimal frontier is not of discrete, degenerate, and singular shapes. In view of this, the current research on weight vectors is mainly focused on the adaptive strategy. According to the sparse degree of the optimized solution, the weight vectors are automatically added or deleted to meet the needs of improving diversity. Relevant researchers have developed effective algorithms regarding the adaptive strategy. Jain and Deb proposed an adaptive reference point reduction strategy based on NSGA-III [32] and A-NSGA-III [34]. A-NSGA-III constructs (m-1) simplex lattices of reference points and deletes the reference points around crowded reference points that have no correlation with the optimized solution. Qi et al. [35] proposed an adaptive weight adjustment strategy (MOEAD-AWA). In the optimization process, first assume that the algorithm converges to the real Pareto optimal frontier, periodically delete the crowded weight vector, and add a new weight vector to the sparse area. Cheng et al. [36] adopted two sets of reference vectors to deal with different problems. However, these methods have certain limitations. These algorithms are specifically designed to solve certain problems. Giagkiozis et al. [37] pointed out that the use of adaptive strategies to generate new weight vectors may cause insufficient convergence for the entire evolution process. In view of this, Wang et al. [38] proposed a method PICEA-w based on the coevolution strategy of weight vectors and optimized solutions. By calculating the Chebyshev function values of the optimized solutions with respect to the weight vectors, the optimal solution and the dominant weight vector are selected into the next iteration together. However, the

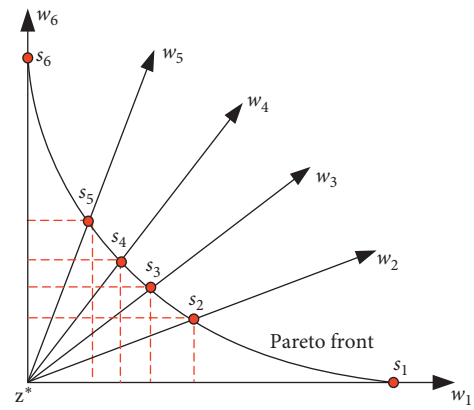

Figure 1: Nonuniformly distributed solutions with respect to uniformly distributed weight vectors.

process of adding weight vectors adopts a randomly generated method and does not make full use of the current solution information. Therefore, based on the coevolution strategy of PICEA-w, this paper introduces an adaptive weight generation mechanism based on MOEA/D (MOEA/D-AW), which adopts the weight vector generation mechanism [35, 39] to make full use of the distribution of the generated solution in the objective space, and reversely guide the addition and deletion of the weight vector.

The remainder of this paper is organized as follows: Section 2 describes the mechanism of PICEA-w. Section 3 introduces the optimized weight generation mechanism and proposes a novel adaptive weight generation based on the coevolution strategy of PICEA-w. Experiment settings are illustrated in Section 4 and experimental results are illustrated in Section 5. Finally, Section 6 concludes this paper.

2. Description of PICEA-W

2.1. Basic Procedure of PICEA-W. The pseudocode of PICEA-w is illustrated in Algorithm 1. 5 functions involved in PICEA-w are illustrated in Table 1.

Brief introductions of the functions involved in Table 1 are listed below (refer to the original research [38] for details),

2.1.1. weightGenerator. Function weightGenerator is used to generate N_w weight vectors $\mathbf{w}_j = \{w_1, \ldots, w_i, w_M\}$, $j = 1, 2, \ldots, N_w$. We define the weight vector $\mathbf{w}_j$ in the following form:

$$w_1 = 1 - \sqrt[M-1]{\text{rand}}$$
$$w_i = \left(1 - \sum_{k=1}^{i-1} w_k\right)\left(1 - \sqrt[M-1]{\text{rand}}\right) : w_M = 1 - \sum_{j=1}^{i-1} w_k, \quad (1)$$

where N_w is the number of weight vectrors, rand is a random number between 0 and 1, and M is the number of objectives.

2.1.2. updateA. Function *updateA* is used to upgrade the nondominated solutions in A. When the size of A surpasses A size, it will execute function *trimA* to make sure that the size of A remains A size.

Inputs: Number of population N, initial population S, N_w weight vectors $W = \{\mathbf{w}_1, \mathbf{w}_2, \ldots, \mathbf{w}_{N_w}\}$, maximum iteration number $\text{iter}_{\max}$, number of objective functions M, size of archive A A size
Outputs S, W, A, Best F
(1) Best $F \leftarrow \phi$
(2) $S \leftarrow$ initialize $S(N)$
(3) $F\_S \leftarrow \text{obj}(S)$
(4) Best $F \leftarrow$ update A (Best F, F_S)
(5) $W \leftarrow$ weightGenerator (N_w)
(6) **while** iter < $\text{iter}_{\max}$ **do**
(7) $Sc \leftarrow$ genetic Operator (S)
(8) $F\_Sc \leftarrow \text{obj}(Sc)$
(9) (Joint S, Joint F) $\leftarrow$ Union (S, Sc, F_S, F_Sc)
(10) $Wc \leftarrow$ weight Generator (N_w)
(11) $\theta \leftarrow$ theta Configuration (iter, $\pi/2$)
(12) $(S, F\_S, W) \leftarrow$ coEvolve (Joint F, Joint S, Joint W, θ)
(13) Best $F \leftarrow$ update A (Best F, F_S, A size)
(14) **end while**

Algorithm 1: PICEA-w.

Table 1: Functions involved in Algorithm 1.

Name of functions	Description
weightGenerator	Generate random weight vectors
update A	Update archive in accordance with the obtained nondominated solutions
thetaConfiguration	Obtain the value of angle intended for the function *coEvolve*
coEvolve	Obtain new solutions and new weight vectors
trim A	Confine the size of the archive

2.1.3. trimA. Function *trimA* is used to confine the size of A to remain initialized value with reference to the clustering technique in SPEA2 [15].

2.1.4. thetaConfiguration. Function *thetaConfiguration* is used to obtain an angle θ as one of the input parameters of function *coEvolve*, and the θ is generated as follows:

$$\theta = \frac{\pi}{2} \frac{\text{iter}}{\text{iter}_{\max}}, \tag{2}$$

where iter is the current number of iterations and $\text{iter}_{\max}$ is the maximum number of iterations.

2.1.5. coEvolve. Function *coevolve* generates optimized solution S, optimized objective values F_S, and optimized weight vector W by coevolution algorithm with all input parameters which are θ, *JointS*, *JointF* and *JointW*. *JointS* is the joint of parent and offspring solutions at iter, *JointF* is the mapping of *JointS* in the objective space, and *JointW* is the joint of optimized weight vectors and randomly generated weight vectors.

The basic procedure of coevolution in function *coevolve* is listed as follows:

(1) Calculate the angles between each weight vector $\mathbf{w}_j$, $j = 1, 2, \ldots, 2N_w$ in *JointW* and each objective vector $\mathbf{F}_i$, $i = 1, 2, \ldots, 2N$ in *JointF* to obtain a relevant angle vector Φ in the scale of $2N \times 2N_w$ when the angle between $\mathbf{F}_i$ and $\mathbf{w}_j$ is less than θ, $\mathbf{F}_i$, $i = 1, 2, \ldots, 2N$ is regarded as the neighbor of $\mathbf{w}_j$. Any elements in Φ surpassing θ will be treated as inf. The performance of $\mathbf{F}_i$ is evaluated by calculating the Chebyshev scalarizing function of $\mathbf{w}_j$ and $\mathbf{F}_i$. Replace the elements that manifest the neighboring relations in Φ with the Chebyshev scalarizing values to obtain a performance vector P in the scale of $2N \times 2N_w$. Sort the elements of P in descending order by $\mathbf{w}_j$ to obtain a sequence vector $\mathbf{R}$ in the scale of $2N \times 2N_w$ of which 1 represents the best performance.

(2) Choose N $\mathbf{F}_i$ as new F_S based on the sequence vector $\mathbf{R}$. Sort $\mathbf{R}$ in ascending order. The 1st column is marked as the best performance, followed by the 2nd column, and so on. Then, choose the first N $\mathbf{F}_i$ to form a new F_S.

(3) Choose N_w $\mathbf{w}_j$ as new W with reference to the newly obtained $\mathbf{F}_i$ of F_S. If $\mathbf{F}_i$ performs the same with multiple weight vectors, choose the farthest $\mathbf{w}_j$ away from $\mathbf{F}_i$ to be its most optimal weight vector.

2.2. Flaws of PICEA-W. At each iteration, weight vectors are randomly generated in accordance with "(1)." In the evolution, as the distribution of the mapping of obtained solutions in the objective is not fully used, which induces that the weight vector generated in step 10 of Algorithm 1 is very

likely to be the same as the last generation and eventually has a lack of diversity.

3. A Novel Decomposition-Based MOEA with Adaptive Weight Generation (MOEA/D-AW)

3.1. Optimal Weight Generation Strategy. Given a reference point $\mathbf{z}_i^* = (\mathbf{z}_1^*, \mathbf{z}_2^*, \ldots, \mathbf{z}_M^*)$, the optimal weight vector $\mathbf{w} = \{\mathbf{w}_1, \mathbf{w}_2, \ldots, \mathbf{w}_M\}$ can be obtained by calculating the Chebyshev scalarizing functions with respect to $\mathbf{z}_i^*$. The basic procedure is listed as follows:

$$\frac{f_1(s) - \mathbf{z}_1^*}{\mathbf{w}_1} = \frac{f_2(s) - \mathbf{z}_2^*}{\mathbf{w}_2} = \cdots = \frac{f_M(s) - \mathbf{z}_M^*}{\mathbf{w}_M}. \quad (3)$$

Meanwhile, as $\mathbf{w}_1 + \mathbf{w}_2 + \cdots + \mathbf{w}_M = 1$, the optimal weight vector can be expressed as follows:

$$\mathbf{w} = (\mathbf{w}_1, \ldots, \mathbf{w}_M) = \left(\frac{f_1(s) - \mathbf{z}_1^*}{\sum_{i=1}^{M} f_i(s) - \mathbf{z}_i^*}, \ldots, \frac{f_M(s) - \mathbf{z}_M^*}{\sum_{i=1}^{M} f_i(s) - \mathbf{z}_i^*} \right). \quad (4)$$

3.2. Basic Idea of the Proposed Algorithm. MOEA/D-AW makes full use of the current solutions to update the weight vectors instead of a set of fixed weight vectors to improve the diversity of the solutions. Different from PICEA-w, the coevolution strategy is amended by replacing the weight generation mechanism shown in "(1)" with that of "(4)."

3.3. Detailed Description. The pseudocode of MOEA/D is illustrated in Algorithm 2. Firstly, an evenly distributed weight vector is generated by means of that proposed by Das and Dennis [31], $W \leftarrow \{\mathbf{w}_1, \mathbf{w}_2, \ldots, \mathbf{w}_N\}$. N subproblems $p_i, i = 1, 2, \ldots, N$ are determined by $\mathbf{w}_i, i = 1, 2, \ldots, N$ to form the initialized population $P^0 = \{p_1^0, p_2^0, \ldots, p_N^0\}$. The ideal point z_0^* in step 3 of Algorithm 2 is determined by minimizing all populations in each objective.

The adaptive weight generation mechanism is manifested in Step 7 of Algorithm 2 with reference to a combination and revision of Step 10 to 12 in Algorithm 1. The weight generation is embedded in function *coEvolve*, once the weight vector with respect to P_i^{iter} could not be its neighbor, the optimal weight vector generated by "(4)" would replace the current one, and then the subproblems in the next iteration would also be updated. The diversity of the solutions is ensured by updating the weight vectors (Algorithms 3 and 4).

As Differential Evolution (DE) operator outstands in convergence with respect to most cases [40], it is used to generate offspring.

4. Experiment Settings

4.1. Test Problems. In this paper, 8 problems from the Walking Fish Group (WFG) test suite [41] invoked in 2-, 4-, 7-objective instances are introduced to test our proposed algorithm and other competitors. The WFG parameters k and l are set to be 18 and 14. The attributes of these problems include nonseparable/separable, unimodal/multimodal, biased (polynomial, flat, parameter dependent)/unbiased, convex/concave, connected/disconnected, etc. Note that the decision variables in WFGs are $z_i = [0, 2i], i = 1, 2, \ldots, n$. Hereinafter, WFG$m$-$n$ referrers to the test problem WFGm with n objectives.

4.2. Performance Metrics. In this paper, 1 qualitative performance metric (Median Attainment Surface [42]) and 4 quantitative performance metrics are included, which are Hypervolume (HV) [16], Inverted Generational Distance (IGD) [43], Generational Distance (GD) [44], and Pure Diversity (PD) [45]. The Median Attainment Surface could intuitively indicate the diversity and convergence of obtained solutions in the objective space (normally less than 3 objectives). HV and IGD are the most widely used metrics that could evaluate the diversity and convergence simultaneously. A greater value of HV and a smaller value of IGD both indicate that the solutions perform better. At the same time, a smaller value of GD and a larger value of PD indicates better performance in convergence and diversity, respectively. Note that the PD metric could assess the diversity of solutions not only in the dimensions of spread and uniformity but also dissimilarity.

4.3. Competitor MOEAs. To evaluate the performance of the proposed MOEA/D-AW, 4 recent published outstanding MOEAs, which are Reference Vector Guided Evolutionary Algorithm (RVEAa) [36], A-NSGA-III [34], Preference Inspired Coevolutionary Algorithm Using Goals (PICEA-g) [46], and Ensemble Fitness Ranking with Ranking Restriction Scheme (EFR-RR) [47], are introduced to be compared with.

In Reference Vector Guided Evolutionary Algorithm (RVEA), a set of evenly distributed reference vectors is prescribed to divide the objective space into the same number of subspaces as that of reference vectors. At each iteration, RVEA combines the parent and the offspring to obtain the next generation based on the elitism strategy of NSGA-II [17]. Angle-Penalized Distance (APD) is introduced to balance the performance of RVEA in diversity and convergence. APD is calculated with reference to the number of iterations so that RVEA could be more inclined to converge at the early iterations while spreading at the final iterations. In the presence of the performance degeneration of RVEA in dealing with irregular Pareto fronts, RVEAa introduces a strategy that could adaptively regenerate the reference vector to alleviate the degeneration. Specifically, after subpopulations are generated by the reference vectors, the reference vectors with respect to empty subpopulations are replaced to be random unit vectors that are ranged from the maximum and minimum objective values of the current translated population.

A-NSGA-III is the adaptive version of NSGA-III which is manifested in adaptively adding and reducing reference points. Similar to NSGA-II, at iteration t, NSGA-III first select the nondominance levels $(F_{1,t}, F_{2,t}, \ldots, F_{l-1,t})$ prior to the critical (last) nondominance level $(F_{l,t})$ to construct part

Initialization N: number of population, T: the size of the neighbors, $\text{iter}_{\max}$: maximum number of iteration
(1) Generate an evenly distributed weight vector, $W \leftarrow \{\mathbf{w}_1, \mathbf{w}_2, \ldots, \mathbf{w}_N\}$
(2) Generate an initialized population, $P^0 = \{p_1^0, p_2^0, \ldots, p_N^0\}$ based on W and calculate the corresponding objective functions, $F\_P^0 \leftarrow \text{obj}(P^0)$
(3) Set the initialized ideal point based on P^0
(4) Calculate the T closest weight vectors to $\mathbf{w}_i$ to form the neighbor, $\lambda_i \leftarrow \{\mathbf{w}_i, \mathbf{w}_j, \ldots, \mathbf{w}_T\}$
(5) iter$\leftarrow$1
(6) **while** iter < $\text{iter}_{\max}$ **do**
(7) $(F\_P^{\text{iter}}, P^{\text{iter}}, W) \leftarrow \text{coEvolve}(F\_P^{\text{iter}}, P^{\text{iter}}, W)$
(8) $P^{\text{iter}} \leftarrow \text{GenerateOffspring}(P^{\text{iter}}, DE)$
(9) $F\_P^{\text{iter}} \leftarrow \text{obj}(P^{\text{iter}})$
(10) **end while**
(11) return non-dominated solutions in P

Algorithm 2: MOEA/D-AW.

Inputs DE: the operator, P^{iter}: population at iter
Outputs P^{iter}
(1) **for** $i \leftarrow 1$: N **do**
(2) Randomly pick 3 individuals from the neighbors of p_i^{iter}, use DE operator to generate its offspring u_i^{iter}
(3) $P^{\text{iter}} \leftarrow \text{Update}(u_i^{\text{iter}}, p_i^{\text{iter}})$
(4) **end for**

Algorithm 3: GenerateOffspring.

Inputs u_i^{iter}: offspring, subproblem: p_i^{iter}
Outputs p_i^{iter}: updated subproblem
(1) Based on the weight vector with respect to p_i^{iter}, $\mathbf{w}_i = \{w_1, w_2, \ldots, w_M\}$, calculate the Chebyshev function of u_i^{iter} and the other solutions in p_i^{iter}, $f_{Tch}(u_i^{\text{iter}})$, $f_{Tch}(nox_{i,k}^{\text{iter}})$, $nox_{i,k}^{\text{iter}} \in p_i^{\text{iter}}$, $k = \{1, 2, \ldots, T\}$
(2) **for** $k \leftarrow 1$: T **do**
(3) **if** $f_{Tch}(u_i^{\text{iter}}) < f_{Tch}(nox_{i,k}^{\text{iter}})$ **then**
(4) $nox_{i,k}^{\text{iter}} \leftarrow u_i^{\text{iter}}$
(5) **end if**
(6) **end for**

Algorithm 4: *Update*.

of the next generation (Q_{t+1}), S_t and much efforts are put into choosing remaining populations from $F_{l,t}$. Associate the solutions in S_t with reference points by calculating the closest perpendicular distance between a solution in S_t and an reference line j. Based on the number of associated solutions concerning reference point j, p_j, reference points with minimum p_j are first classified. In the case of $p_j = 0$, choose the population member from $F_{l,t}$ which is closest to reference line j to construct Q_{t+1}; otherwise exclude the reference point j. In the case of $p_j \geq 1$, a randomly chosen member from $F_{l,t}$, if exists, would be included if it is associated with reference point j. Based on NSGA-III, referring to the case of $p_j > 1$, A-NSGA-III adds a corresponding number of reference points according to the number of objectives near the crowed point j and deletes all reference points that $p_j = 0$. By doing this, the ideal state (each $p_j = 1$) could be achieved to obtain an evenly distributed Pareto front.

Based on the coevolution strategy, PICEA-g uses the range of current objective values to construct a set of goal vectors to divide the objective space. It combines the conventional Pareto dominant relationship and fitness calculation based on goal vector. Like that of NSGA-II, it sorts the fitness of the members in the combined population which is constructed by the parent and the offspring to choose the optimal generation.

Based on the Ensemble Fitness Ranking (EFR), EFR-RR introduces a ranking restriction scheme to formulate the outstanding EFR-RR. The fitness evaluation in EFR is barely executed based on the aggregating function, which would result in distant solutions to the weight vectors and poor performance in diversity. In view of this, EFR-RR devised a

ranking restriction scheme under which the solutions could only be sorted by calculating the fitness function formulated with its neighboring weight vectors. A set of diversely distributed solutions can then be obtained in accordance with an evenly distributed weight vector.

The reference vector in RVEAa, A-NSGA-III, and PICEA-g (goal vector in PICEA-g) could be adjusted adaptively based on the current population to obtain a set of more diverse solutions. At the same time, EFR-RR restricts the fitness sorting to be executed between the solution and its neighboring fitness function to obtain a set of more diverse solutions.

4.4. Parameters. The general parameters involved in the experiment are set as follows:

(1) Population size, N

The N in A-NSGA-III, RVEAa, PICEA-g, and EFR-RR are all set to be 100 when dealing with the 2, 4, and 7 objectives WFGs. The N in our proposed MOEA/D-AW is set to be 100, 126, and 210 with respect to the 2, 4, and 7 objectives WFGs, respectively.

(2) Rate of change of penalty function, α, and the frequency of reference vector adaption, fr,in RVEAa

α is set to be 2 and fr is set to be 0.1 in accordance with that of the original research [35].

(3) Number of goals in PICEA-g, N_{goal}

N_{goal} is set to be $N \cdot m/2$, where m the number of objectives in accordance with that of the original research [46].

(4) Number of neighboring weight vectors in EFR-RR, K

K is set to be 2 in accordance with that of the original research [47].

(5) Position parameter, k, and distance parameter, l, in WFGs

k is set to be 18 and l is set to be 14

(6) Mutation and crossover operators

All algorithms adopt the simulated binary crossover (SBX) and polynomial mutation to generate offspring. The distribution index, η_c, and crossover probability, pc, in SBX are set to be 15 and 1.0, respectively. The distribution index, η_m, and the mutation probability, p_m, in polynomial mutation are set to be 20 and 1/32, respectively.

Note that the parameter p in PD is set to be 0.1, suggested by Wang et al.

(7) Termination condition

The maximum number of iterations is set to be 250.

In addition, when calculating the performance metrics, all nondominated solutions are set to be 100.

5. Experimental Results

All algorithms are executed independently for 31 times. The results are developed from 3 aspects: Median Attainment Surface, numerical statistics, and boxplot. Draw the Median Attainment Surface that approximates the Pareto optimal frontal surface obtained after running all the comparison algorithms 31 times, as shown in Figures 2 and 3. The statistical results of the values with respect to HV, IGD, GD, and PD metrics are listed in Tables 2 to 5.

Note that, in each illustration, ANSGAIII represents A-NSGA-III, PICEAg represents PICEA-g, EFRRR represents EFR-RR, and AW represents MOEA/D-AW.

5.1. Median Attainment Surface. We can see the following from Figure 2:

(1) Referring to the discrete and convex WFG2, all algorithms cannot converge to the true Pareto optimal front. RVEAa is inferior to other algorithms in terms of convergence, while all algorithms perform the same in terms of diversity.

(2) Referring to the linear and convex WFG3, all algorithms could converge to the true Pareto optimal front to some extent, while PICEA-g has a certain degree of volatility, and the convergence is slightly worse. In terms of diversity performance, PICEA-g and MOEA/D-AW are superior to other algorithms.

(3) Referring to the multimodal, separable, and convex WFG4, MOEA/D-AW is superior to other algorithms in terms of both convergence and diversity.

(4) Referring to the deceptive, separable, and concave WGF5, all algorithms could converge to the true Pareto optimal front to some extent while PICEA-g has a certain degree of volatility, and the convergence is slightly worse. In terms of diversity performance, PICEA-g and MOEA/D-AW are superior to other algorithms.

We can see the following from Figure 3:

(1) Referring to the nonseparable, unimodal, and concave WFG6, all algorithms could converge to the true Pareto optimal front to some extent while PICEA-g has a certain degree of volatility, and the convergence is slightly worse. In terms of diversity performance, PICEA-g and MOEA/D-AW are superior to other algorithms.

(2) Referring to the separable, unimodal, and concave WFG7, all algorithms cannot converge to the true Pareto optimal front. In terms of diversity performance, EFR-RR is superior to other algorithms.

(3) Referring to the nonseparable, unimodal, and concave WFG8, all algorithms cannot converge to the true Pareto optimal front. EFR-RR and RVEAa are superior to other algorithms in terms of convergence.

(4) Referring to the deceptive, multimodal, nonseparable, and concave WGF9, all algorithms could converge to the true Pareto optimal front to some

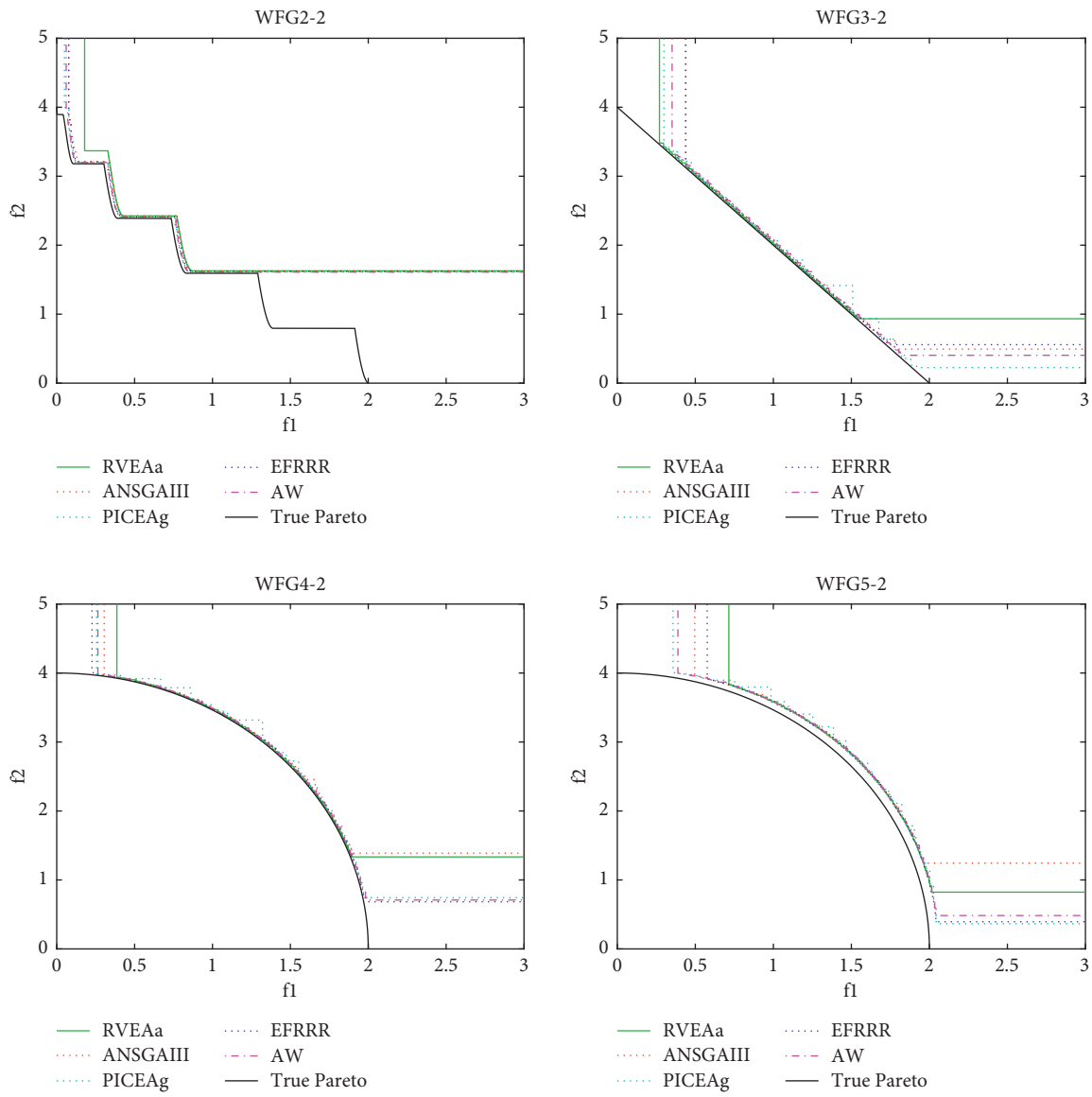

Figure 2: Median attainment surfaces of the 2-objective WFG2 to WFG5.

extent while PICEA-g has a certain degree of volatility, and the convergence is slightly worse. In terms of diversity performance, PICEA-g and MOEA/D-AW are superior to other algorithms.

In all, our proposed MOEA/D-AW and PICEA-g are superior to other algorithms in terms of diversity in most cases, while MOEA/D-AW is superior to PICEA-g in terms of convergence in most cases.

5.2. Statistical Results. Since all algorithms are essentially random search methods, it is difficult to determine whether an algorithm is good or bad based on the results of a single operation. Therefore, in this section, the average statistics of the results of 31 independent operations are compared with respect to different performance metrics. The best performing algorithms in each of these problems are given in bold in Tables 2 to 5.

As shown in Table 2, PICEA-g is slightly superior to other algorithms in terms of HV metric on most WFGs. MOEA/D-AW performs well compared to other algorithms in the 4-objective and 7-objective WFGs, except for being slightly inferior to EFR-RR and PICEA-g.

As shown in Table 3, PICEA-g is superior to other algorithms in terms of IGD metric on most 4- and 7-objective WFGs. The average IGD metric index obtained by MOEA/D-AW on WFG2-7 is superior to other algorithms, and it performs poorly on other test problems. Based on the comparison results in Table 2, the average IGD metric indexes obtained by MOEA/D-AW on most WFGs are mainly limited by its convergence, and it reveals that MOEA/D-AW is superior to other algorithms in terms of diversity.

As shown in Table 4, MOEA/D-AW is superior to other algorithms on WFG3-4, WFG3-7, WFG4-4, WFG4-7, WFG5-7, and WFG6-4, while RVEAa is superior to

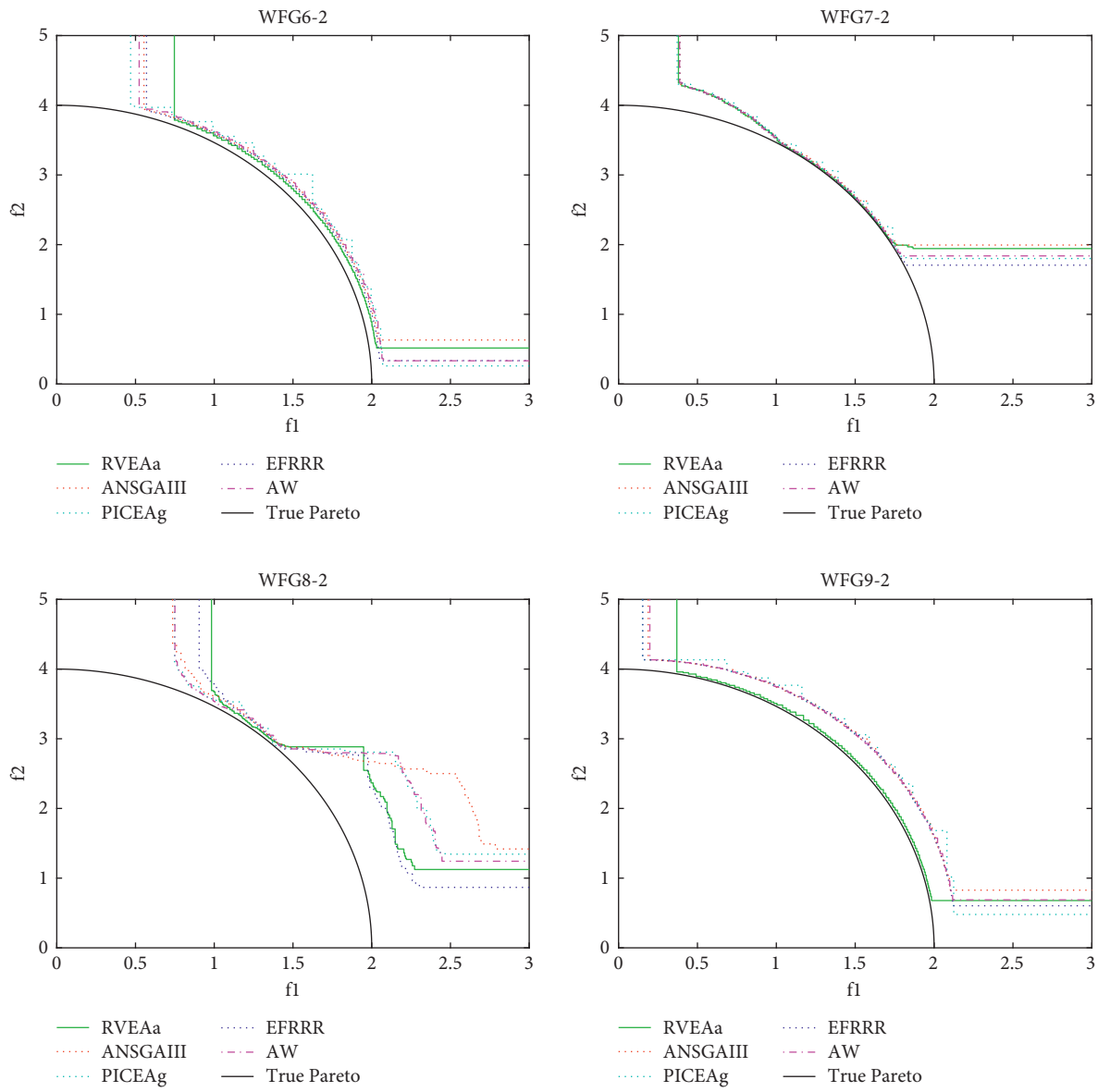

Figure 3: Median attainment surfaces of the 2-objective WFG6 to WFG9.

Table 2: The statistical results (mean) of the HV values obtained by 5 algorithms on WFG2 to WFG9.

	Obj	ANSGAIII	RVEAa	PICEAg	EFRRR	MOEA/D-AW
WFG2	2	0.568387	0.550097	**0.573903**	0.564387	0.570258
	4	0.793419	0.764000	0.805484	**0.819484**	0.808258
	7	0.874677	0.835290	0.884032	0.840258	**0.899903**
WFG3	2	0.571097	0.545677	**0.599936**	0.591290	0.586484
	4	0.328194	0.203710	**0.364419**	0.329484	0.183065
	7	0.089355	0.000000	**0.249419**	0.054839	0.000000
WFG4	2	0.374065	0.384000	0.403097	**0.410258**	0.401710
	4	0.563903	0.619419	0.701194	**0.718032**	0.703032
	7	0.819936	0.713194	0.667677	0.808936	**0.823839**
WFG5	2	0.358323	0.358161	**0.380000**	0.376032	0.368903
	4	0.599968	0.577742	0.695419	**0.697936**	0.670677
	7	**0.790548**	0.652871	0.736645	0.762677	0.782097

Table 2: Continued.

	Obj	ANSGAIII	RVEAa	PICEAg	EFRRR	MOEA/D-AW
WFG6	2	0.352774	0.351419	**0.377226**	0.372161	0.370839
	4	0.613484	0.601355	0.692323	**0.693065**	0.664129
	7	0.794323	0.694419	**0.866516**	0.799742	0.786710
WFG7	2	0.327968	0.334581	0.345548	**0.349742**	0.343419
	4	0.606581	0.615129	**0.744097**	0.706194	0.716194
	7	0.845871	0.718581	0.820613	0.766000	**0.872710**
WFG8	2	0.263581	0.245129	0.254903	0.265387	**0.274645**
	4	0.510323	0.459290	**0.591032**	0.550452	0.570258
	7	0.733419	0.607516	**0.773774**	0.653710	0.706839
WFG9	2	0.356129	0.368161	0.361839	**0.371710**	0.365677
	4	0.571419	0.582323	0.599936	0.594645	**0.608484**
	7	0.680774	0.657742	0.699677	0.653581	**0.703258**

The best results are given in bold.

Table 3: The statistical results (mean) of the IGD values obtained by 5 algorithms on WFG2 to WFG9.

	Obj	ANSGAIII	RVEAa	PICEAg	EFRRR	MOEA/D-AW
WFG2	2	0.027742	0.056307	**0.024923**	0.075312	0.027174
	4	0.318926	0.319134	**0.244438**	0.397874	0.265584
	7	2.478501	2.573738	3.055701	2.932787	**2.236648**
WFG3	2	0.022826	0.029178	0.020397	**0.016903**	0.028081
	4	0.706847	0.618760	**0.018508**	0.226327	1.491903
	7	0.793979	1.865569	**0.008584**	0.482924	3.875040
WFG4	2	0.011243	**0.006770**	0.010859	0.007660	0.011409
	4	0.144125	0.207221	**0.119248**	0.126419	0.158724
	7	0.968558	1.121720	**0.552663**	0.801419	1.055519
WFG5	2	0.068020	**0.064636**	0.064953	0.064900	0.068315
	4	0.246305	0.211099	**0.153042**	0.156273	0.178305
	7	0.991691	1.170598	**0.727007**	0.876354	1.117266
WFG6	2	0.078930	**0.071754**	0.075731	0.076946	0.077206
	4	0.294787	0.269174	0.170637	**0.164501**	0.214040
	7	0.911231	1.239905	**0.596021**	0.712028	1.083449
WFG7	2	0.096721	**0.066667**	0.096891	0.086643	0.088512
	4	0.183409	0.185135	**0.113988**	0.145567	0.142149
	7	0.900902	1.247910	**0.576098**	1.049238	0.963121
WFG8	2	**0.228603**	0.267558	0.239812	0.292829	0.244698
	4	0.441809	0.634984	**0.224257**	0.593517	0.342018
	7	1.103588	1.792134	**0.572861**	1.508154	1.435946
WFG9	2	0.155992	**0.116460**	0.124575	0.123171	0.126931
	4	0.300874	0.270670	**0.234286**	0.246548	0.248221
	7	1.370617	1.507547	**1.093408**	1.396443	1.326873

The best results are given in bold.

other algorithms on the other WFGs. The average PD metric indexes obtained by MOEA/D-AW on the WFGs that RVEAa performs best are not much different from that of RVEAa and are in the same order of magnitude. The obtained results reveal that MOEA/D-AW is superior to other outstanding algorithms in terms of diversity on most problems that are linear, convex, multimodal, separable, deceptive, and concave, which supports the regularities revealed by the obtained results from Tables 2 and 3 and complies to the motivation of the proposed algorithm.

As shown in Table 5, PICEA-g and RVEAa are superior to other algorithms in terms of convergence on most WFGs, while MOEA/D-AW is barely superior to other algorithms on WFG2-4, WFG2-7, and WFG5-4. The gap between the average GD metric indexes obtained by MOEA/D-AW and the best algorithm on other WFGs is not big. The obtained results reveal that the proposed MOEA/D is inferior to other outstanding algorithms in terms of convergence in most cases.

5.3. Further Discussion. In this section, we will discuss why MOEA/D-AW performs badly compared with those outstanding MOEAs in terms of convergence on many occasions.

Table 4: The statistical results (mean) of the PD values obtained by 5 algorithms on WFG2 TO WFG9.

	Obj	ANSGAIII	RVEAa	PICEAg	EFRRR	MOEA/D-AW
WFG2	2	2.59$E-01$	9.97$E-01$	9.93$E-03$	**1.14E + 00**	2.41$E-01$
	4	**1.53E + 04**	1.38$E+04$	5.36$E+02$	2.86$E+03$	5.70$E+03$
	7	1.03$E+06$	**2.84E + 06**	2.84$E+04$	7.31$E+05$	1.54$E+06$
WFG3	2	3.11$E+00$	5.96$E+00$	9.31$E-02$	**8.16E + 00**	3.72$E+00$
	4	1.25$E+03$	1.18$E+04$	2.14$E+01$	2.54$E+01$	**2.12E + 04**
	7	2.30$E+05$	6.21$E+06$	2.18$E+02$	6.22$E+04$	**9.84E + 06**
WFG4	2	3.04$E+00$	**6.17E + 00**	2.98$E-02$	3.22$E+00$	3.09$E+00$
	4	1.14$E+04$	4.37$E+04$	1.27$E+03$	6.25$E+03$	**4.55E + 04**
	7	4.73$E+06$	1.35$E+07$	1.59$E+03$	4.45$E+06$	**1.41E + 07**
WFG5	2	3.61$E+00$	**5.60E + 00**	3.25$E-02$	3.79$E+00$	3.30$E+00$
	4	3.47$E+04$	**4.45E + 04**	1.23$E+03$	1.16$E+04$	3.94$E+04$
	7	9.21$E+06$	1.52$E+07$	1.92$E+04$	6.22$E+06$	**1.53E + 07**
WFG6	2	3.21$E+00$	**4.92E + 00**	4.68$E-$ -02	3.75$E+00$	2.49$E+00$
	4	3.23$E+04$	4.37$E+04$	7.15$E+02$	2.28$E+03$	**4.43E+04**
	7	8.07$E+06$	**1.32E+07**	2.87$E+04$	1.78$E+06$	1.23$E+07$
WFG7	2	2.75$E+00$	**8.02E + 00**	2.16$E-02$	4.16$E+00$	2.20$E+00$
	4	6.31$E+03$	**5.33E + 04**	7.31$E+02$	3.39$E+03$	4.46$E+04$
	7	1.14$E+06$	**2.09E + 07**	3.30$E+04$	5.70$E+06$	9.43$E+06$
WFG8	2	3.82$E-01$	**2.56E + 00**	3.05$E-02$	1.70$E+00$	7.31$E-01$
	4	4.91$E+03$	**5.51E + 04**	4.64$E+02$	5.49$E+03$	3.99$E+04$
	7	1.25$E+06$	**2.06E + 07**	3.49$E+04$	4.41$E+06$	1.72$E+07$
WFG9	2	2.50$E+00$	**5.78E + 00**	2.17$E-02$	3.48$E+00$	3.02$E+00$
	4	4.97$E+04$	**5.98E + 04**	1.01$E+03$	5.65$E+03$	4.45$E+04$
	7	7.87$E+06$	**2.28E + 07**	9.12$E+04$	5.56$E+06$	1.35$E+07$

The best results are given in bold.

Table 5: The statistical results (mean) of the GD values obtained by 5 algorithms on WFG2 to WFG9.

	Obj	ANSGAIII	RVEAa	PICEAg	EFRRR	MOEA/D-AW
WFG2	2	0.002806	0.006392	**0.002599**	0.010613	0.002742
	4	0.033624	0.032956	0.025543	0.056684	**0.021916**
	7	0.183074	0.189915	0.230406	0.331688	**0.161590**
WFG3	2	0.002307	0.002955	0.002062	**0.001708**	0.002825
	4	0.089108	0.062784	**0.002019**	0.033096	0.126013
	7	0.066543	0.138259	**0.000780**	0.056480	0.261087
WFG4	2	0.001170	**0.000721**	0.001142	0.000805	0.001196
	4	0.013677	0.019292	**0.011413**	0.014473	0.012318
	7	0.070404	0.082590	**0.043364**	0.089228	0.070061
WFG5	2	0.006819	**0.006484**	0.006526	0.006517	0.006854
	4	0.022822	0.019645	0.014288	0.017428	**0.013727**
	7	0.070445	0.084546	**0.053274**	0.094565	0.073117
WFG6	2	0.007920	**0.007206**	0.007612	0.007738	0.007751
	4	0.027430	0.024996	**0.015878**	0.018369	0.016379
	7	0.065424	0.089358	**0.044954**	0.078487	0.071123
WFG7	2	0.014487	**0.012465**	0.015652	0.014600	0.014396
	4	0.017162	0.017502	**0.011000**	0.017954	0.011135
	7	0.065801	0.090326	**0.045114**	0.116701	0.064698
WFG8	2	**0.031439**	0.037681	0.034324	0.035284	0.031517
	4	0.054451	0.064436	**0.027970**	0.077218	0.031472
	7	0.080463	0.128387	**0.044472**	0.170342	0.095627
WFG9	2	0.016028	**0.012483**	0.013274	0.013520	0.013388
	4	0.027862	0.025002	0.021662	0.027273	0.018952
	7	0.096764	0.106072	**0.078735**	0.150570	0.085949

The best results are given in bold.

One major reason is about setting the crossover and mutation operators in the algorithm. It can be seen from the obtained results that the SBX operator could generate converged offspring in terms of 2-objective WFGs in the decomposition-based framework, MOEA/D while degenerating in terms of high dimension occasions (WFG4s and WFG7s). The competitors involved in the experiment essentially generate the offspring under the dominance-based framework, which could perform well in terms of convergence in most cases while degenerating in terms of diversity. The DE operator, which is superior in terms of convergence, has been adopted to solve complex problems and is validated to be efficient [30]. In this paper, for the sake of fairness, all algorithms adopt the simulated binary crossover (SBX) and polynomial mutation to generate offspring.

6. Conclusion

In this paper, MOEA/D-AW is proposed to enhance the diversity of decomposition-based MOEAs. The basic idea is to devise a coevolved adaptive weight vector generation mechanism to adjust the evolution during the iteration. The weight vector is updated based on the sparsity of the mapping of the current population in the objective space, deletion of crowed weight vectors, and addition of sparse weight vectors are conducted. Moreover, the mechanism makes full use of the convergence information of the current population, the current utopian point, to generate optimal weight vectors to update the evolution direction.

In the experimental studies, MOEA/D-AW is compared to 4 state-of-the-art MOEAs which are proven to effectively enhance diversity. 8 test instances with up to 7 objectives from WFG2 to WFG9 test suits are introduced for comparison. The results indicate that MOEA/D-AW is superior to other competitor MOEAs in terms of diversity on most test problems while shows a slight disadvantage over other competitors MOEAs in terms of convergence on many objective test problems.

In further studies, many efforts would be carried to devise a more efficient mechanism that would adaptively select different operators based on the spread of the mapping of current solutions in the objective space during the iteration. Also, it has been proven that different operators show different performances in exploration and exploitation in EAs [48].

Data Availability

The raw/processed data required to reproduce these findings cannot be shared at this time as the data also form part of an ongoing study.

Conflicts of Interest

The authors declare that they have no conflicts of interest.

Acknowledgments

This study was supported by funds from Sichuan Science and Technology Program under contract no. 2019ZDZX0001.

References

[1] K. Deb, K. Sindhya, and J. Hakanen, "Multiobjective optimization," in *Decision Sciences: Theory and Practice*CRC Press, Boca Raton, FL, USA, 2016.

[2] T. Xiahou, Y. Liu, and Q. Zhang, "Multiobjective redundancy allocation for multi-state system design under epistemic uncertainty of component states," *Journal of Mechanical Design*, vol. 142, no. 11, 2020.

[3] G.-Z. Fu, H.-Z. Huang, Y.-F. Li, and J. Zhou, "An adaptive hybrid evolutionary algorithm and its application in aero-engine maintenance scheduling problem," *Soft Computing*, vol. 25, no. 8, pp. 6527–6538, 2021.

[4] G.-Z. Fu, H.-Z. Huang, Y.-F. Li, B. Zheng, and T. Jin, "Multiobjective design optimization for a two-stage transmission system under heavy load condition," *Mechanism and Machine Theory*, vol. 122, pp. 308–325, 2018.

[5] G.-Z. Fu, Y.-F. Li, Y. Tao, and H.-Z. Huang, "An interactive preference-based evolutionary algorithm for multi-criteria satisficing optimization," *Journal of Intelligent and Fuzzy Systems*, vol. 34, no. 4, pp. 2503–2511, 2018.

[6] H. Li, Z.-M. Deng, N. A. Golilarz, and C. Guedes Soares, "Reliability analysis of the main drive system of a CNC machine tool including early failures," *Reliability Engineering & System Safety*, vol. 215, Article ID 107846, 2021.

[7] H. Li, A. P. Teixeira, and C. Guedes Soares, "A two-stage Failure Mode and Effect Analysis of offshore wind turbines," *Renewable Energy*, vol. 162, pp. 1438–1461, 2020.

[8] H. Li, C. Guedes Soares, and H.-Z. Huang, "Reliability analysis of a floating offshore wind turbine using Bayesian networks," *Ocean Engineering*, vol. 217, Article ID 107827, 2020.

[9] H. Li, H. Díaz, and C. Guedes Soares, "A failure analysis of floating offshore wind turbines using AHP-FMEA methodology," *Ocean Engineering*, vol. 234, Article ID 109261, 2021.

[10] H. Li, H. Díaz, and C. Guedes Soares, "A developed failure mode and effect analysis for floating offshore wind turbine support structures," *Renewable Energy*, vol. 164, pp. 133–145, 2021.

[11] H. Li, H.-Z. Huang, Y.-F. Li, J. Zhou, and J. Mi, "Physics of failure-based reliability prediction of turbine blades using multi-source information fusion," *Applied Soft Computing*, vol. 72, pp. 624–635, 2018.

[12] K. Miettinen and M. M. Mäkelä, "On scalarizing functions in multiobjective optimization," *OR Spectrum*, vol. 24, no. 2, pp. 193–213, 2002.

[13] D. E. Goldberg, *Genetic Algorithms in Search, Optimization, and Machine Learning*, Addison Wesley Longman Publishing, Boston, MA, USA, 1989.

[14] C. M. Fonseca and P. J. Fleming, "Genetic algorithms for multiobjective optimization: formulation discussion and generalization," in *Proceedings of the Fifth International Conference on Genetic Algorithms*, pp. 416–423, San Francisco, CA, USA, June 1993.

[15] E. Zitzler, M. Laumanns, and L. Thiele, "SPEA2: improving the strength Pareto evolutionary algorithm," in *Proceedings of the EUROGEN 2001, Evolutionary Methods for Design, Optimization and Control With Applications to Industrial Problems,* K. Giannakoglou, D. Tsahalis, J. Periaux, P. Papailou, and T. Fogarty, Eds., pp. 95–100, Athens, Greece, September 2001.

[16] E. Zitzler and L. Thiele, "Multiobjective optimization using evolutionary algorithms—a comparative case study," in *Proceedings of the International Conference on Parallel*

Problem Solving from Nature, pp. 292–301, Amsterdam, Netherlands, September 1998.

[17] K. Deb, A. Pratap, S. Agarwal, and T. Meyarivan, "A fast and elitist multiobjective genetic algorithm: NSGA-II," *IEEE Transactions on Evolutionary Computation*, vol. 6, no. 2, pp. 182–197, 2002.

[18] K. Ikeda, H. Kita, and S. Kobayashi, "Failure of Pareto-based MOEAs: does non-dominated really mean near to optimal?" in *Proceedings of the 2001 Congress on Evolutionary Computation (IEEE Cat. No.01TH8546)*, vol. 2, pp. 957–962, Seoul, Republic of korea, May 2001.

[19] M. Laumanns, L. Thiele, K. Deb, and E. Zitzler, "Combining convergence and diversity in evolutionary multiobjective optimization," *Evolutionary Computation*, vol. 10, no. 3, pp. 263–282, 2002.

[20] K. Deb, M. Mohan, and S. Mishra, "Evaluating the ε-domination based multiobjective evolutionary algorithm for a quick computation of Pareto-optimal solutions," *Evolutionary Computation*, vol. 13, no. 4, pp. 501–525, 2005.

[21] S. Yang, M. Li, X. Liu, and J. Zheng, "A grid-based evolutionary algorithm for many-objective optimization," *IEEE Transactions on Evolutionary Computation*, vol. 17, no. 5, pp. 721–736, 2013.

[22] H. Li and D. Landa Silva, "Evolutionary multiobjective Simulated Annealing with adaptive and competitive search direction," in *Proceedings of the 2008 IEEE Congress on Evolutionary Computation (IEEE World Congress on Computational Intelligence)*, pp. 3311–3318, Hong Kong, China, June 2008.

[23] L. Thiele, K. Miettinen, P. J. Korhonen, and J. Molina, "A preference-based evolutionary algorithm for multiobjective optimization," *Evolutionary Computation*, vol. 17, no. 3, pp. 411–436, 2009.

[24] K. Deb and A. Kumar, "Interactive evolutionary multiobjective optimization and decision-making using reference direction method," in *Proceedings of the Genetic and Evolutionary Computation Conference*, London, UK, uly 2007.

[25] N. Beume, B. Naujoks, and M. Emmerich, "SMS-EMOA: multiobjective selection based on dominated hypervolume," *European Journal of Operational Research*, vol. 181, no. 3, pp. 1653–1669, 2007.

[26] J. Bader and E. Zitzler, "HypE: an algorithm for fast hypervolume-based many-objective optimization," *Evolutionary Computation*, vol. 19, no. 1, pp. 45–76, 2011.

[27] L. While, L. Bradstreet, and L. Barone, "A fast way of calculating exact hypervolumes," *IEEE Transactions on Evolutionary Computation*, vol. 16, no. 1, pp. 86–95, 2012.

[28] Q. Zhang and H. Li, "MOEA/D: a multiobjective evolutionary algorithm based on decomposition," *IEEE Transactions on Evolutionary Computation*, vol. 11, no. 6, pp. 712–731, 2007.

[29] H. Ishibuchi and T. Murata, "A multiobjective genetic local search algorithm and its application to flowshop scheduling," *IEEE Transactions on Systems, Man and Cybernetics, Part C (Applications and Reviews)*, vol. 28, no. 3, pp. 392–403, 1998.

[30] H. Li and Q. Zhang, "Multiobjective optimization problems with complicated Pareto sets, MOEA/D and NSGA-II," *IEEE Transactions on Evolutionary Computation*, vol. 13, no. 2, pp. 284–302, 2009.

[31] I. Das and J. E. Dennis, "Normal-boundary intersection: a new method for generating the Pareto surface in nonlinear multicriteria optimization problems," *SIAM Journal on Optimization*, vol. 8, no. 3, pp. 631–657, 1998.

[32] K. Deb and H. Jain, "An evolutionary many-objective optimization algorithm using reference-point-based nondominated sorting approach, part I: solving problems with box constraints," *IEEE Transactions on Evolutionary Computation*, vol. 18, no. 4, pp. 577–601, 2014.

[33] A. Rodríguez Sánchez, A. Ponsich, A. L. Jaimes, and S. Z. Martínez, "A parallel tabu search heuristic to approximate uniform designs for reference set based MOEAs," in *Evolutionary Multi-Criterion Optimization*, pp. 254–265, Springer International Publishing, Berlin, Germany, 2019.

[34] H. Jain and K. Deb, "An Evolutionary many-objective optimization algorithm using reference-point based nondominated sorting approach, part II: handling constraints and extending to an adaptive approach," *IEEE Transactions on Evolutionary Computation*, vol. 18, no. 4, pp. 602–622, 2014.

[35] Y. Qi, X. Ma, F. Liu, L. Jiao, J. Sun, and J. Wu, "MOEA/D with adaptive weight adjustment," *Evolutionary Computation*, vol. 22, no. 2, pp. 231–264, 2014.

[36] R. Cheng, Y. Jin, M. Olhofer, and B. Sendhoff, "A reference vector guided evolutionary algorithm for many-objective optimization," *IEEE Transactions on Evolutionary Computation*, vol. 20, no. 5, pp. 773–791, 2016.

[37] I. Giagkiozis, R. C. Purshouse, and P. J. Fleming, "Generalized decomposition," in *Proceedings of the International Conference on Evolutionary Multi-Criterion Optimization*, pp. 428–442, Sheffield, UK, March 2013.

[38] R. Wang, R. C. Purshouse, and P. J. Fleming, "Preference-inspired co-evolutionary algorithms using weight vectors," *European Journal of Operational Research*, vol. 243, no. 2, pp. 423–441, 2015.

[39] M. Li and X. Yao, "What weights work for you? adapting weights for any Pareto front shape in decomposition-based evolutionary multiobjective optimisation," *Evolutionary Computation*, vol. 28, no. 2, pp. 227–253, 2020.

[40] S. Das and P. N. Suganthan, "Differential evolution: a survey of the state-of-the-art," *IEEE Transactions on Evolutionary Computation*, vol. 15, no. 1, pp. 4–31, 2011.

[41] S. Huband, L. Barone, L. While, and P. Hingston, "A scalable multiobjective test problem toolkit," in *Proceedings of the Third international conference on Evolutionary Multi-Criterion Optimization*, pp. 280–295, Guanajuato, Mexico, March 2005.

[42] C. M. Fonseca and P. J. Fleming, "An overview of evolutionary algorithms in multiobjective optimization," *Evolutionary Computation*, vol. 3, no. 1, pp. 1–16, 1995.

[43] P. Czyżżak and A. Jaszkiewicz, "Pareto simulated annealing—a metaheuristic technique for multiple-objective combinatorial optimization," *Journal of Multi-Criteria Decision Analysis*, vol. 7, no. 1, pp. 34–47, 1998.

[44] D. A. Van Veldhuizen and G. B. Lamont, *Evolutionary Computation and Convergence to a Pareto Front*, Stanford University, Stanford, CA, USA, 1998.

[45] H. Wang, Y. Jin, and X. Yao, "Diversity assessment in many-objective optimization," *IEEE Transactions on Cybernetics*, vol. 47, no. 6, pp. 1510–1522, 2017.

[46] R. Wang, R. C. Purshouse, and P. J. Fleming, "Preference-inspired coevolutionary algorithms for many-objective optimization," *IEEE Transactions on Evolutionary Computation*, vol. 17, no. 4, pp. 474–494, 2013.

[47] Y. Yuan, H. Xu, B. Wang, B. Zhang, and X. Yao, "Balancing convergence and diversity in decomposition-based many-objective optimizers," *IEEE Transactions on Evolutionary Computation*, vol. 20, no. 2, pp. 180–198, 2016.

[48] M. Črepinšek, S.-H. Liu, and M. Mernik, "Exploration and exploitation in evolutionary algorithms: a survey," *ACM Computing Surveys*, vol. 45, no. 3, pp. 1–33, 2013.

Hindawi
Mathematical Problems in Engineering
Volume 2021, Article ID 4236572, 15 pages
https://doi.org/10.1155/2021/4236572

Research Article

Implementation of Computer-Based Vision Technology to Consider Visual Form of Ceramic Mural Art

Dazhuang Li [1] **and Emad Saadi Alkathir** [2]

[1] *Faculty of Humanities and Arts, Macau University of Science and Technology, Macau 999078, China*
[2] *Department of Computer Engineering, Pardis Branch, Islamic Azad University, Tehran, Iran*

Correspondence should be addressed to Dazhuang Li; lidazhuang311@163.com and Emad Saadi Alkathir; e.alkathir@gmail.com

Received 15 July 2021; Revised 9 August 2021; Accepted 12 August 2021; Published 30 August 2021

Academic Editor: Mohammad Yazdi

As one of the cultural forms of human beings, ceramic murals transcend the dimension of time and space and transcend the single cognition of materialism in the sense of purely material materials. The emergence of computer vision technology has also provided conditions for developing ceramic murals in terms of concepts and technical forms. This article first studies the visual communication language research in ceramic mural art, at the same time comprehensively analyzes the design principles of ceramic mural art, and interprets the visual form of ceramic mural art from the perspective of actual projects in the thesis; then, it boldly analyzes the future of ceramic mural art Development trend. Finally, this article analyzes the composition in ceramic mural art, the graphics in ceramic mural art, the color in ceramic mural art, the scale in ceramic mural art, the lighting in ceramic mural art, and the design principles in ceramic mural art. The experimental results show that there are significant differences in the artistic design principles of ceramic murals ($P < 0.05$), and there are significant differences in the artistic design principles of ceramic murals ($P < 0.05$). Therefore, the artistic design principles of modern ceramic murals should mainly follow elegant and prominent forms.

1. Introduction

The birth of reinforced concrete has completely changed people's living environment and public space, making people's buildings more compact for indoor use and significantly reducing the threat to human life from natural disasters such as earthquakes and fires [1–13]. However, cold concrete buildings also make the public space environment and living environment monotonous, making them lose their personal and regional characteristics [14–26]. The development of modern Chinese ceramic murals is relatively slow [27–39]. As western artists increasingly use ceramic murals to decorate public places and environments, they have achieved good results [40–52]. The development of household ceramic murals is very rapid, and many ceramic murals with high artistic value are accepted by the public [52–58]. As an essential means of decorating public spaces, ceramic murals have attracted more and more attention. The research on ceramic murals can create a harmonious public space environment that meets people's material and spiritual needs [59–62]. It has become a hot topic of discussion and research and is of great significance to art and engineering [63–67]. Ebnali et al. propose an augmented reality computer vision-based technique in order to communicate automation reliability in partially automated driving vehicles. Digital image processing with augmented reality help to reduce the reaction time, which improve users' safety while the system is on the lower reliability mode [68]. In [69], the authors propose a deep-learning/computer-vision-based method for the analysis of the human hand, which automatically detects and segments out different hand semantic parts such as fingers from the input image. The proposed method learns to perform the task without the need for any segmentation labels at the training time.

With the development of urbanization and the rapid development of the construction industry, more and more public environments need decorative design, enabling ceramic artists to participate in the environmental art of public

spaces, thereby linking art and technology, and art and design are approaching. Chen et al. proposed that the rule of form applied to ceramic mural design has important practical significance. He mainly discusses the application of the plane composition, three-dimensional composition, color composition, and texture effect in the design of ceramic murals through the analysis and research of the beauty rules of the form and the design of ceramic murals [70]. Kiedrowski believes that constitutional art is a widely influential art form in modern visual art. It enriches the formal language of modern mural design and broadens the expression of visual aesthetics, which has an important influence on the development of modern murals [71]. Wang et al. pointed out that the objective life of the society determines the art of each era at that time. Once society changes, the art that reflects this era cannot fail to produce corresponding changes. The old art has become history as a product of the previous era, and new art will also emerge with the development of the times [72]. In [73], the author proposed using two image processing techniques (Canny edge detection and Hough line transform) combined with the Mask R-CNN model to measure the depth of flood in images of traffic signs. In [74], the author proposed using the Canny edge detection and Hough transform image processing techniques combined with $A*$ search route optimization and distance decay function to determine the shortest flood-free route for citizens transiting in flood events.

The history of Chinese ceramics is the largest globally, and Chinese translation can show that ceramics are significant to China. At present, ceramic murals have been widely used in architectural environment decoration worldwide, but for China, it needs to be developed and improved. Compared with the development of ceramic murals globally, the development of ceramic murals in China is still in its infancy, but artists increasingly use the decoration of ceramic murals in public places. By interpreting the status quo of visual communication, A H T helps readers create artworks with a unique artistic vision and a clearer understanding of visual communication phenomena in society [75]. Xi et al. introduced the development process of Chinese subway mural art, summarized valuable experiences from the historical development and creation, and analyzed the future development prospects of Chinese subway mural art [76]. Rosario introduces a group of famous contemporary ceramic artists and their works, outlines their art forms and style characteristics, and demonstrates the form characteristics of ceramic murals in the public environment in the form of case appreciation and analysis [77]. This research proposal has enabled ceramic art to reach a certain level, but ceramic art has not been fully reflected in practical applications, and its practicability is not high.

Ceramic mural art is a kind of visual art that can reflect the urban culture and humanistic spirit. It is an art form with both aesthetics and functionality. The research of this subject starts with the universality of ceramic mural art, analyzes the ceramic mural art in major domestic cities, summarizes the language and design principles of visual communication, and summarizes the visual communication form suitable for ceramic mural art. The innovation of this paper is to compare the edge detection operators in the experimental part, analyze the advantages and disadvantages of each edge detection operator, and choose the edge detection operator suitable for ceramic mural image detection. Finally, the optimal threshold is obtained through the iterative threshold segmentation method, and the image is binarized, the roundness index is used to distinguish the genuine and the inferior products, and finally, the classification is realized.

2. Visual Form of Ceramic Mural Art Based on Computer Vision Technology

2.1. Digital Image Processing Technology

2.1.1. Digital Image Processing Technology. With the rapid development of computer technology, digital image processing technology will continue to mature. The current decline in the cost of computer equipment, the expansion of broadband Internet communications on the Internet, the proliferation of image digitization and imaging equipment, and the implementation of low-cost digital image processing systems have created unprecedented opportunities for the continuous development of digital processing technology [78, 79].

2.1.2. Digital Image Processing, Recognition, and Understanding. Image processing is the use of computer systems to process digital images for various purposes. Image processing in time aims to improve image quality and use people as objects to improve people's visual effects. In image editing, the input image quality is poor, and the output image quality is higher [80, 81]. There is also a type of image processing that uses machines as objects. The purpose of processing is to allow the machine or computer to recognize the target, which is called image recognition automatically.

2.1.3. Main Research Contents of Digital Image Processing. The recently studied waveform transformation has good detection characteristics in time and frequency and has many practical applications in image processing. Image enhancement and restoration aim to enhance the image quality to highlight the region of interest in the image. Although many edge extraction and region segmentation methods have been studied, no practical method applies to various images. Therefore, the research on image segmentation continues to deepen, which is also one of the hotspots of current image processing research [82, 83].

2.1.4. Process of Ceramic Mural Art Image Processing. The digital camera images are stored as "frames" in the memory, and the application can export and process any "frame" data at any time. The primary task of a digital image processing system is to use a specific algorithm to determine the required information from a specific "frame" of the

image. There are usually many methods to achieve the goal, but the results and efficiency obtained using different algorithms may be very different [84, 85]. The basic process of processing ceramic mural art images is shown in Figure 1.

2.2. Image Processing Technology of Ceramic Murals. First of all, ceramic murals have a horizontal extension of the architectural space. Due to the structural layout of the entire building, some building spaces may be relatively small. Usually, hanging a bright mirror on the wall of the room will make people have a visual illusion, feeling that the size of the room has doubled. In the same way, artists can create a sensory ideal space environment through various sensory effects of ceramic murals [86]. The artist makes full use of the space changes, starting from the content of the ceramic mural itself, using light and dark contrast, virtual and real contrast, size contrast, etc., to make full use of the visual illusion of the human eye to achieve the purpose of extending the architectural space.

Secondly, ceramic murals have a horizontal contraction effect on the architectural space. The narrow architectural space environment makes people feel anxious, so people yearn for a spacious space, which makes people feel comfortable. However, things must be reversed; too empty and open space will also make people feel lonely and indifferent. This kind of "spaciousness" has turned into a disadvantage [87]. Artists can change people's feelings of overly spacious space environment through human visual senses. People's attention is attracted by the contrast of different forms of ceramic murals and the expression of the proportions of the ceramic murals. People's visual focus will be on the ceramic murals as soon as they enter the space environment, ignoring other environmental factors. To successfully achieve these, one must be familiar with the overall public space environment, understand people's psychology, and be good at discovering the central point of people's vision. Among them, image preprocessing, edge detection, filtering, and image binarization are required, specifically as follows:

(1) Image preprocessing: the first step of image processing is generally to preprocess the image. Image preprocessing mainly completes the fair compensation and smoothing of the target image. Its ultimate goal is to provide as adequate image data as possible for subsequent processing:

$$\Delta = d\left(1 + \frac{1}{M}\right),$$
$$d_2 = \frac{l_1 + l_2}{l_1} d_1, \tag{1}$$
$$\Delta d_2 = \frac{l_1 + l_2}{l_1} \Delta d_1.$$

For a target composed of an infinite number of points, a superposition of countless enlarged ring holes is formed on the image surface. These superimposed ring holes are called coded images [88]. Suppose the target function is $o(x, y)$, $h(x, y)$ is the point spread function of the annular coded aperture system, and $n(x, y)$ is the irrelevant noise function of the system, then the image function $i(x, y)$ formed by the coded aperture camera is as follows:

$$i(x, y) = o(x, y) * h(x, y) + n(x, y). \tag{2}$$

In the formula, $*$ is the convolution symbol, and the Fourier transform of the above formula can obtain the frequency spectrum distribution as follows:

$$I(u, v) = O(u, v)H(u, v) + N(u, v),$$
$$O'(u, v) = H^{-1}(u, v)I(u, v) = O(u, v) + H^{-1}(u, v)N(u, v). \tag{3}$$

However, in many problems, H has a zero point or has a small value in some areas; that is, there is a singular or ill-conditioned problem, or there is no inverse transformation, or has a severe amplification effect on noise, so the inverse filtering method is beneficial in practical applications [89].

(2) Edge detection: the gradient $f(x, y)$ in the direction of θ along $\gamma$is defined as follows:

$$\frac{\partial f}{\partial \gamma} = \frac{\partial f}{\partial x}\frac{\partial x}{\partial \gamma} + \frac{\partial f}{\partial y}\frac{\partial y}{\partial \gamma} = f_x \cos\theta + f_y \sin\theta. \tag{4}$$

The condition for obtaining the maximum value of $\partial f/\partial \gamma$ is $(\partial(\partial f/\partial \gamma)/\partial \theta) = 0$, namely:

$$-f_x \sin\theta_g + f_y \cos\theta_g = 0,$$
$$\theta_g = \arctan\frac{f_y}{f_x}, \tag{5}$$
$$g = \left(\frac{\partial f}{\partial \gamma}\right)_{\max} = \sqrt{f_x^2 + f_y^2}.$$

The maximum gradient g is the image edge detection value.

(3) Filter: filtering is to find a filter with a transfer function of $H_w(u, v)$, so that the mean square error between the recovered target estimate $o'(x, y)$ and the real $o(x, y)$ is the smallest, namely:

$$E\left\{\left[o(x, y) - o'(x, y)\right]^2\right\} = \min,$$
$$H_w(u, v) = \frac{H^*(u, v)}{|H(u, v)|^2 + S_n(u, v)/S_o(u, v)}. \tag{6}$$

Among them $H^*(u, v)$ is the complex conjugate of the transfer function of the coded aperture imaging system, and $S_o(u, v)$ and $S_n(u, v)$ are the power spectral density of the target image and noise,

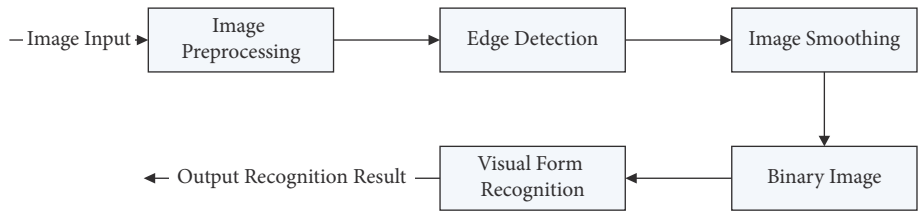

Figure 1: Flowchart of ceramic mural art image processing.

respectively; then the recovered target estimate is as follows:

$$O'(u,v) = H_w(u,v) \cdot I(u,v) = \frac{H^*(u,v) \cdot I(u,v)}{|H(u,v)|^2 + S_n(u,v)/S_o(u,v)}. \tag{7}$$

For calculation convenience, $S_n(u,v)/S_o(u,v)$ it can be set to a particular empirical value ε according to the different processing objects, namely:

$$H_w(u,v) = \frac{H^*(u,v)}{|H(u,v)|^2 + \varepsilon},$$
$$O'(u,v) = \frac{H^*(u,v)}{|H(u,v)|^2 + \varepsilon} \cdot I(u,v) \approx O(u,v) + N'(u,v). \tag{8}$$

Do the inverse Fourier transform of the above formula, and the reconstructed target image is obtained as follows:

$$o'(x,y) \approx o(x,y) + n'(x,y). \tag{9}$$

(4) Binary image: the greater the variance between the background and the foreground, the more significant the difference between the two parts, so when the variance between the two parts reaches the maximum, this threshold T is the best threshold of the maximum variance method [68]. The variance between the two groups is expressed as follows:

$$\delta^2(T) = \omega_0(\mu_1 + \mu)^2 + \omega_1(\mu_2 + \mu)^2 = \omega_0\omega_1(\mu_2 - \mu_1)$$
$$= \frac{[\mu\omega(T) - \mu(T)]^2}{\omega(t)[1 - \mu(T)]}. \tag{10}$$

Among them μ_2 are the probabilities generated by the two parts and μ is the image's overall gray value [90]. Let $x(t)$ be a square-integrable function, denoted as $x(t) \in L^2(R)$, and $\psi(t)$ is a function called basic wavelet, then:

$$\mathrm{WT}_x(a,k) = \frac{1}{\sqrt{a}} \int_{-\infty}^{+\infty} x(t)\psi^*\left(\frac{1-k}{a}\right)\mathrm{d}t = \langle x(t), \psi_{ok}(t)\rangle. \tag{11}$$

Wavelet transforms called $x(t)$. among them,

$$\psi_{ok}(t) = \frac{1}{\sqrt{a}}\psi\left(\frac{t-k}{a}\right) \tag{12}$$

is the displacement and scale expansion of the basic wavelet. In addition, a is the scale factor and k reflects the displacement. The symbol $\langle x, y\rangle$ represents the inner product, and the equivalent frequency domain representation is as follows:

$$\mathrm{WT}_x(a,k) = \frac{\sqrt{a}}{2\pi} \int_{-\infty}^{+\infty} X(\varpi)\Psi^*(a\varpi)e^{j\varpi\pi}\mathrm{d}\varpi, \tag{13}$$

where $X(\varpi)$ and $\Psi^*(a\varpi)$ are the Fourier transform of $x(t)$ and $\chi(t)$, respectively [91].

2.3. Relationship between Ceramic Murals and Public Space Environment

2.3.1. Ceramic Murals Exist Based on the Public Space Environment. The mural made of ceramic materials alone does not have any meaning and value. The ceramic murals exist for a specific public space environment. Its meaning depends on the overall atmosphere of the public space environment, and its manifestation and physical existence depend on the public space environment [91, 92]. Ceramic murals exist based on the large environment of public space. Since its creation, the ceramic mural has not existed as an independent thing; it exists to embellish or beautify the space. That is to say, ceramic murals must match the public space environment in which they are located. This is necessary for ceramic murals to play a good role in beautifying the public space environment. Regardless of how colorful the ceramic mural works are, if it is in harmony with the environment in which it is just completed, even if it does not look so eye-catching, the overall public space environment after it is embellished will often reach unexpected effect [93].

2.3.2. The Public Space Environment Restricts Ceramic Murals. The public space environment is not only the carrier on which the ceramic murals attach, but it also restricts the ceramic murals. The wall shape of the public space environment will restrict ceramic murals. The previous section has discussed the dependence of the physical existence of ceramic murals on the building walls in the public space environment. The physical form of ceramic murals must first meet the requirements of the public space environment. This is a sufficient condition for ceramic

murals to exist in the public space environment [94, 95]. At the same time, it also caused restrictions on ceramic murals in the public space environment. The shape of the wall in the public space environment is not fixed; it changes with the overall structure of the public space. Its size changes with the size of the entire building structure. It can be a regular rectangle or an irregular arc, a plane, or a three-dimensional structure composed of several planes. The creation of ceramic murals is developed based on these external constraints.

2.3.3. Space Adjustment of Ceramic Murals to the Public Environment. The significance of ceramic murals is to embellish and beautify the public space environment. Successful ceramic mural works will give the finishing touch to the public space environment. The artist uses human visual effects and the expression technique of ceramic murals to even make up for certain flaws in the public space environment. Ceramic murals play a role in the horizontal extension of the architectural space. Due to the influence of the layout of the entire building structure, some building spaces may be relatively small [96, 97]. Usually, hanging a bright mirror on the wall of the room will make people have a visual illusion, feeling that the size of the room has doubled. In the same way, artists can create a sensory ideal space environment through various sensory effects of ceramic murals. The artist makes full use of the space changes, starting from the content of the ceramic mural itself, using light and dark contrast, virtual and real contrast, size contrast, etc., to make full use of the visual illusion of the human eye to achieve the purpose of extending the architectural space.

Successful ceramic murals are an indispensable part of the public space environment. Successful artists are good at using the elements of the architectural space environment to achieve the overall beauty of their ceramic mural art [98–101]. The form and technique of ceramic mural painting itself are only many means to embody the artist's creative ideas. Only by combining the various elements of the architectural space environment and making them a way to express the ideas of ceramic murals can the unity and coordination of ceramic murals and architectural space environment be genuinely achieved [102–107].

2.4. Ceramic Art Applied to Landscape Design. As one of the public language arts, ceramic art has formed a unique image, symbol, and even an ignorant concept into the field of public landscape design due to its unique material properties and historical and cultural properties. The ceramic art involved in this article is mainly from ceramics. The material and language characteristics of the material itself and the application of the abstract language of ceramic art to describe the landscape space are intended to find a way to not only create a dialogue between the ceramic art creator and the public but also create a dialogue between the public landscape space and the public—compatibility language.

3. Visual Form of Ceramic Mural Art Based on Computer Vision Technology

3.1. System Architecture Design. A ceramic mural art detection system was written with VC++ based on much research on image processing applications. The software adopts a modular design, and the image processing functions are classified by function, so it has nothing to do with the software interface. The software interface can call specific image processing functions in various ways and display the images before and after processing in the designated area. The system software mainly completes the following tasks: connecting digital cameras, saving images, image preprocessing, image segmentation processing, image feature extraction and classification, and stepping motor control. The system flow software block diagram is shown in Figure 2.

3.2. Test Subject. This article uses a ceramic mural art vision system based on computer vision technology. It selectively enters 4000 pieces of various ceramic murals and classifies and analyzes them. Each ceramic mural has multiple attributes. Here, we analyze the composition in ceramic mural art, the graphics in ceramic mural art, the color in ceramic mural art, the scale in ceramic mural art, the lighting in ceramic mural art, and the design principles in ceramic mural art. Based on the above six indicators, we designed relevant questionnaires by searching many documents and distributing the questionnaires to the masses. Here we distribute them according to the approximate age groups. Each age group distributes 100 questionnaires. All questions are divided into 5 Levels (beautiful, fair, decent, abstract, and ugly). The questionnaires issued this time are sent back on the spot after they are written. The questionnaire recovery rate is 100%. There are no open questions in all the questionnaires, so the efficiency is 100%.

3.3. Experimental Method. In the preexperiment stage, we need to input extensive sample data and classify and analyze the ceramic mural art visual system based on computer vision technology. We also need to query a large amount of literature data to design-related questionnaires.

In the experimental stage, our experimental object is the artistic visual form of ceramic murals, and the data source is the questionnaire issued and recovered. Here we are issuing questionnaires by age group to reduce significant differences.

In the postexperiment stage, we collected statistics on the collected questionnaires. We followed the composition in ceramic mural art, graphics in ceramic mural art, color in ceramic mural art, scale in ceramic mural art, lighting in ceramic mural art, and the six indicators of design principles in ceramic mural art and related knowledge analyze these data to get a conclusion.

3.4. Data Collection. There are many data standard processing methods, but different data standardization methods will have a particular impact on the evaluation results of the system. For the positive indicator standardization method,

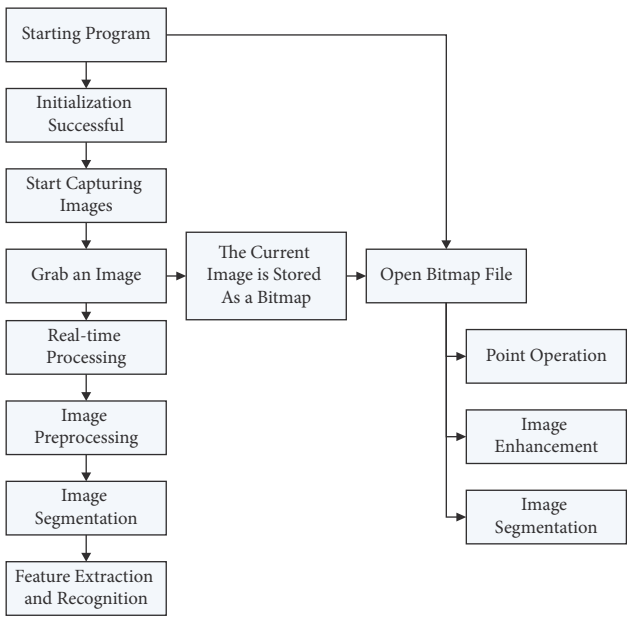

Figure 2: Flowchart of ceramic mural art detection software.

$$y_{ij} = \frac{x_{ij} - \min\{x_{ij}\}}{\max\{x_{ij}\} - \min\{x_{ij}\}}. \tag{14}$$

For negative index standardization methods,

$$y_{ij} = \frac{\max\{x_{ij}\} - x_{ij}}{\max\{x_{ij}\} - \min\{x_{ij}\}}. \tag{15}$$

3.5. Statistical Data Processing Method. SPSS23.0 software was used for data processing, and the count data were expressed in percentage, k is the number of data in this experiment, σ^2 is the variance of all survey results, and $P < 0.05$ indicates that the difference is statistically significant. The formula for calculating reliability is shown in the following equation:

$$a = \frac{k}{k-1}\left(1 - \frac{\sum \sigma_i^2}{\sigma^2}\right). \tag{16}$$

3.6. Evaluation Index System Based on Index Reliability Testing. Reliability refers to the stability and reliability of the questionnaire. This article adopts the α coefficient method created by L. J. Cronbach. Reliability Analysis can obtain the α coefficient in SPSS software. It is generally believed that the α coefficient above 0.8 indicates that the effect of the index set is perfect, and above 0.7 is also acceptable. Here, we analyze the reliability of each type of object, and the reliability index we choose for each type of object is slightly different. The results are shown in Table 1.

It can be seen from Table 1 that the composition in the ceramic mural art, the graphics in the ceramic mural art, the color in the ceramic mural art, the scale in the ceramic mural art, the lighting in the ceramic mural art, and the design principle indicators in the ceramic mural art the influence of the obtained data on this experiment are acceptable ($\alpha > 0.7$). The design principles in the artistic design of modern ceramic murals should mainly follow the principles of graceful form, highlighting regional culture, people-oriented, and green environmental protection. Teachers can reasonably use rational design principles to design ceramic mural art that is more in line with people's aesthetic needs and the development of the times.

3.7. Visual Communication Language in Ceramic Mural Art

3.7.1. Composition of the Ceramic Mural Art. In the composition management of mural paintings, images in multiple spaces simultaneously are often combined on one screen, or images from multiple times in the same space are also combined on one screen, or images from multiple times are combined on one screen. Images and images in multiple spaces are combined on one screen, and the results are shown in Table 2. We make a histogram based on this result, as shown in Figure 3.

Through the paired sample T-test, it can be found that after the experiment, the P value of each age group on the composition score of the ceramic mural art is less than 0.05. There is a significant difference; the P value of each composition index in the ceramic mural art is also less than 0.05. Significant differences explain how to organize the picture structure and form the picture's integrity, and the environment is the most important. These characteristics help the ceramic mural art spread better and better display the charm of the mural art. The specific situation is shown in Figure 3.

3.7.2. Graphics in the Ceramic Mural Art. Graphics are not just a description of the objective world. Designers can use graphics to create a sense of form, produce more profound visual effects, stimulate people's senses, and stimulate people's pursuit of beauty. Graphic language carries a rich accumulation of content and is a highly symbolic visual language. The results are shown in Table 3. We make a bar graph based on this result, as shown in Figure 4.

Through the paired sample T-test, it can be found that after the end of the experiment, there is a significant difference in the P value of each age group on the graphic score of the ceramic mural art, which is less than 0.05; the P value of each index in the ceramic mural art is also less than 0.05. The significant difference explains how to flexibly master the arrangement method of the visual elements of subway murals and how to spread the mural information better and more effectively require the collective efforts of designers. They must have some insights into inheritance and development and persevere in subway murals, going farther and farther on the creative road. The specific situation is shown in Figure 4.

3.7.3. Colors in the Ceramic Mural Art. The application of color symbols tends to pay more attention to its symbolic meaning. The role of symbolic color and human vision will

Table 1: Summary table of reliability test results.

Category	Index combination	Alpha coefficient (α)
Composition of the mural	Centrosymmetric Scattered reconstruction Full belly Geometric segmentation	0.8632
Mural graphics	Specific description Abstract representation Image extension Graphic animation	0.7456
The color of the mural	Warm tones Cool colors Neutral tones	0.7319
Image lighting	Front side light Backlight Top light Natural light	0.8227

Table 2: Data table of composition scoring in ceramic mural art for each age group.

Year	Beautiful	General	Passable	Abstract	Ugly
8–18 years	21	21	29	20	9
19–28 years	16	22	30	28	4
29–38 years	18	24	34	19	5
39–48 years	17	29	28	17	9
Over 49	14	28	36	11	11
P	0.013	0.005	0.005	0.005	0.012

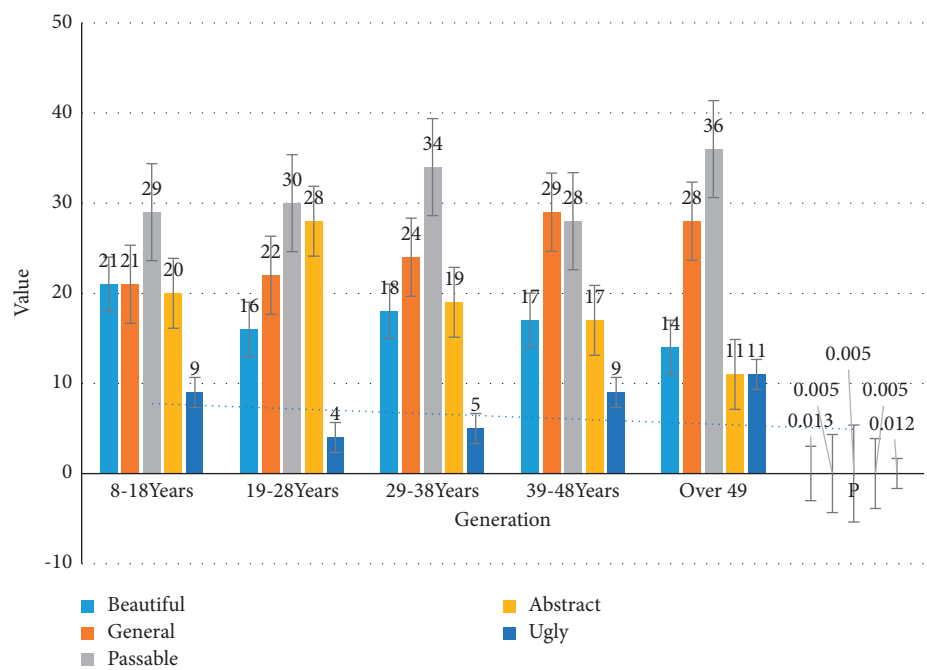

Figure 3: Grading chart of composition in ceramic mural art by age groups.

produce strong psychological induction, stimulating human emotion and imagination. As a form of visual language, the color corresponds to real objects, and human spirit and emotion are connected. The results are shown in Table 4. We make a combination diagram based on this result, as shown in Figure 5.

Through the paired sample T-test, it can be found that after the experiment, the P value of each age group on the color score of ceramic mural art is less than 0.05; there is a significant difference; the P value of each index of the color in ceramic mural art is also less than 0.05. The significant difference shows that only the existence of color contrast can

Table 3: Data table of scoring figures in ceramic mural art by age groups.

Year	Beautiful	General	Passable	Abstract	Ugly
8–18 years	25	28	24	14	9
19–28 years	30	25	27	15	3
29–38 years	19	22	35	19	15
39–48 years	17	18	30	17	18
Over 49	8	30	29	11	22
P	0.001	0.001	0.001	0.001	0.001

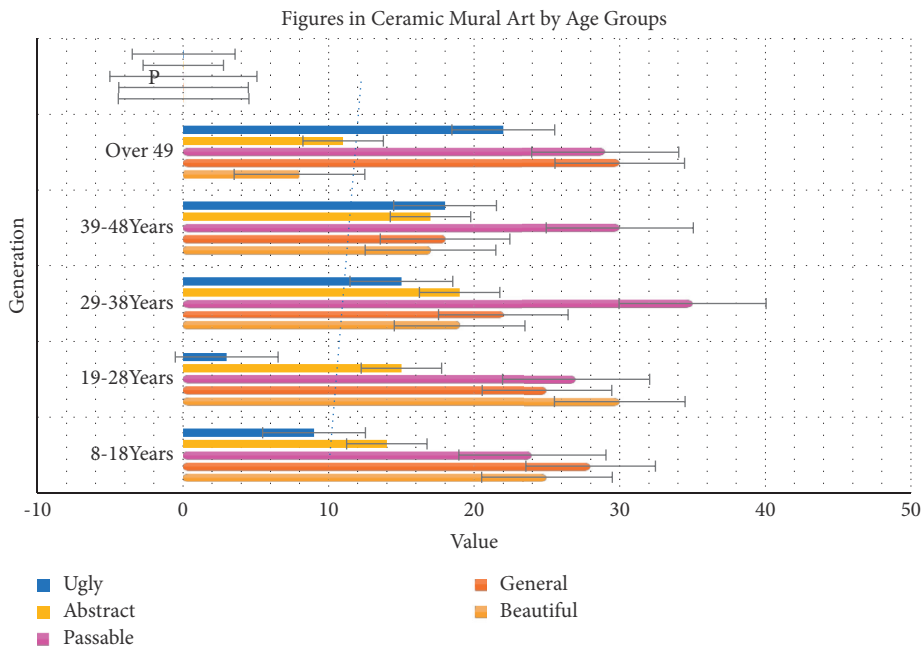

Figure 4: Grading chart of figures in ceramic mural art by age groups.

effectively spread. The strong contrast will quickly attract people's attention, and the weakened contrast can calm people's impetuous mood in the underground space. The specific situation is shown in Figure 5.

3.7.4. Scale in Ceramic Mural Art. The height and width of the subway mural art need to be determined according to the area of the underground space and the height and width of the wall so that the subway mural art is in harmony with the overall environmental space. The importance of scale is based on the other visual communication elements of the subway mural art. Above, the integration of scale and environment is the critical factor of visual aesthetics. The results are shown in Table 5. We make a pie chart based on this result, as shown in Figure 6.

Through the paired sample *T*-test, it can be found that after the experiment, the *P* value of each age group on the scale score of ceramic mural art is less than 0.05 and has a significant difference; the *P* value of each index of the scale in ceramic mural art is also less than 0.05. The significant difference indicates that the scale of ceramic mural art must not only be in harmony with the environmental space, but the ultimate principle is to follow the principle of being people-oriented and fully consider the influence of the scale of the mural on people's psychology so that the subway mural art can indeed act an art enters people's vision and soul. The specific situation is shown in Figure 6.

Table 4: Data table of color scoring in ceramic mural art for each age group.

Year	Beautiful	General	Passable	Abstract	Ugly
8–18 years	21	33	21	13	12
19–28 years	26	27	25	12	10
29–38 years	15	25	30	16	14
39–48 years	17	20	33	10	20
Over 49	10	24	27	18	21
P	0.043	0.037	0.027	0.019	0.044

3.7.5. Lighting in the Ceramic Mural Art. The role of lighting is an indispensable way of expression for subway mural art. The use of light can change the spacing effect, make up for the lack of space, create a space atmosphere, strengthen the environmental characteristics, and locate the characteristics of the place. The results are shown in Table 6. We make a doughnut chart based on this result, as shown in Figure 7.

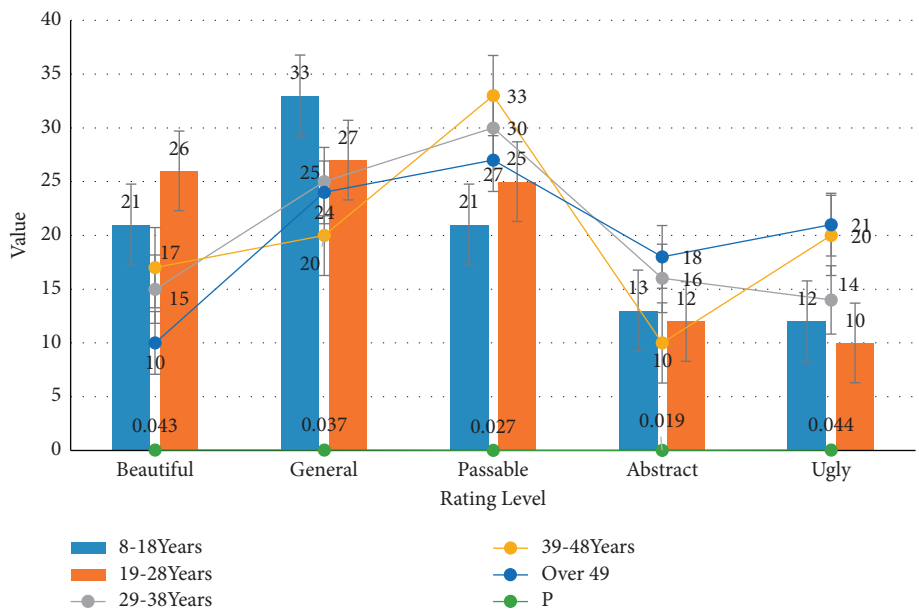

Figure 5: Color grading chart in the ceramic mural art by each age group.

Table 5: Data table of the size scoring in ceramic mural art by age groups.

Year	Beautiful	General	Passable	Abstract	Ugly
8–18 years	2.1	1.97	2.14	1.94	2.09
19–28 years	2.34	27	2.39	2.51	2.51
29–38 years	3.11	3.5	3.17	2.98	3.35
39–48 years	4.5	4.5	3.91	4.45	3.88
Over 49	6.16	5.06	5.18	4.9	4.89
P	0.005	0.005	0.005	0.010	0.019

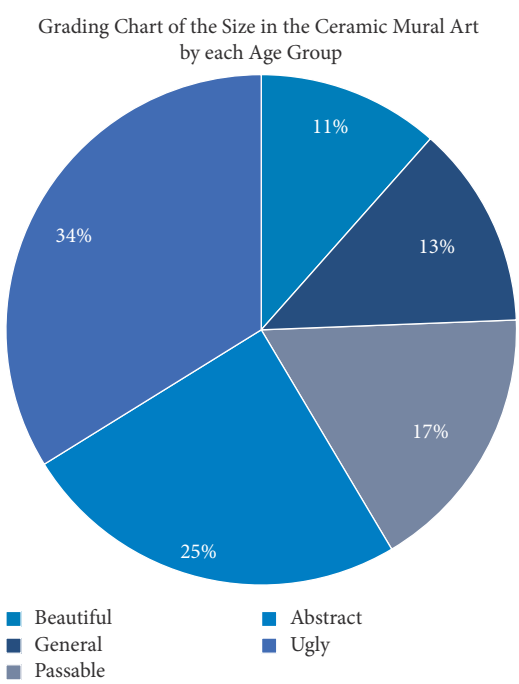

Figure 6: Grading chart of the size in the ceramic mural art by each age group.

Through the paired sample *T*-test, it can be found that after the experiment, the *P* values of the lighting scores in the ceramic mural art are significantly different for each age group to be less than 0.05; the *P* values of the lighting indicators in the ceramic mural art are also less than 0.05. The significant difference shows that the most significant manifestation of the relationship between lighting and space environment is the effect of artificial lighting on the color performance of murals. The combination of light and color of ceramic mural art is complementary, and the use of light for murals must take complete account of the murals' content, color, material, and overall space environment so that the murals can form a harmonious main body and better with the environment. The specific situation is shown in Figure 7.

3.8. Comprehensive Design Principles in Ceramic Mural Art. In the design process, we must first follow the design principles of formal beauty. Secondly, for ceramic mural art, we must highlight the regional cultural characteristics, establish a people-oriented and environmentally friendly design concept, and combine contemporary expression techniques to perfect the ceramic mural art. Spread to the audience. The results are shown in Table 7. We make a bar graph based on this result, as shown in Figure 8.

Figure 8 shows that there are significant differences in the design principles of ceramic mural art ($P < 0.05$), and the indicators of the design principles in ceramic mural art have significant differences ($P < 0.05$), so the modern ceramic mural art design principles should mainly follow the principles of graceful form, highlighting regional culture, people-oriented and green environmental protection, and rationally use rational design principles to design ceramic mural art that is more in line with people's aesthetic needs and the development of the times.

Table 6: Data table of lighting scores in ceramic mural art by age groups.

Rating level	Front side light	Backlight	Top light	Natural light	P
Beautiful	3.23	3.46	2.81	3.04	0.008
General	4.46	4.12	4.48	3.92	0.008
Passable	5.03	4.83	4.95	5.42	0.008
Abstract	5.49	5.45	5.3	5.41	0.004
Ugly	7.4	7.13	7.1	7.36	0.001

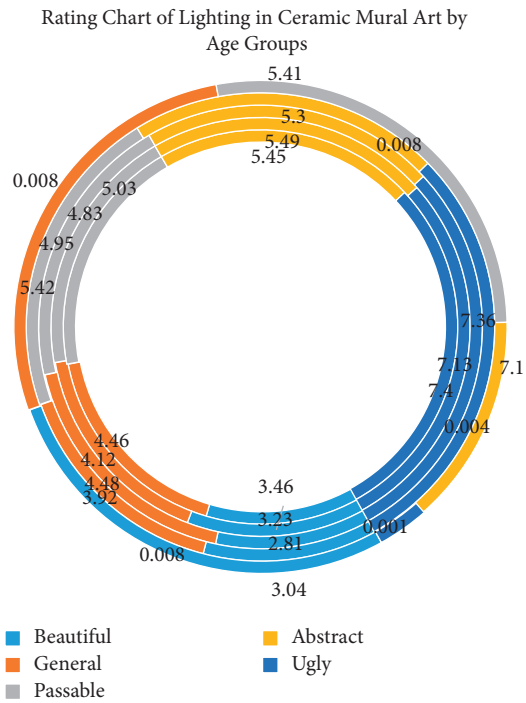

Figure 7: Rating chart of lighting in ceramic mural art by age groups.

Table 7: Comprehensive datasheet of design principles in ceramic mural art.

	Beautiful	General	Passable	Abstract	Ugly	P
Beautiful form	2.2	2.08	2.02	2.04	1.94	0.015
Symmetrical equilibrium	2.34	2.38	2.35	2.62	2.41	0.018
Contrast unity	2.99	3.36	3.33	3.02	2.97	0.005
Rhythm	4.11	4.26	4.35	4.31	4.38	0.001
Scale	5.46	4.81	4.95	5.31	5.22	0.004
Highlight regional culture	5.18	5.01	5.39	5.1	5.38	0.004
People-oriented	7.49	7.25	7.31	7.28	7.04	0.001
Green	8.58	8.14	8.68	8.95	8.06	0.010

4. Discussion

Architecture is the protagonist of public space environmental art, the main body and structural skeleton of public space, and its shape determines the main style of overall space environmental planning. As many new technologies and new materials are constantly being discovered, modern architecture uses these and new material technologies to create new aesthetic concepts. Ceramics is a traditional building material with a history of more than a thousand years. It regains new life through the combination of new technology and new ideas. The unique beauty, texture, color, texture, and potential of ceramics that can be produced without frame requirements and the history, tradition, culture, and other special charms it reflects are becoming more and more popular with artists and the public. This ancient and novel building material gradually becomes a creative material for some architects and artists to express and use. The use of machine vision technology to construct a ceramic mural art vision system can effectively find defects. The system has a simple structure and high-cost performance, which is of great significance in improving the inspection efficiency and reducing the inspectors' labor intensity.

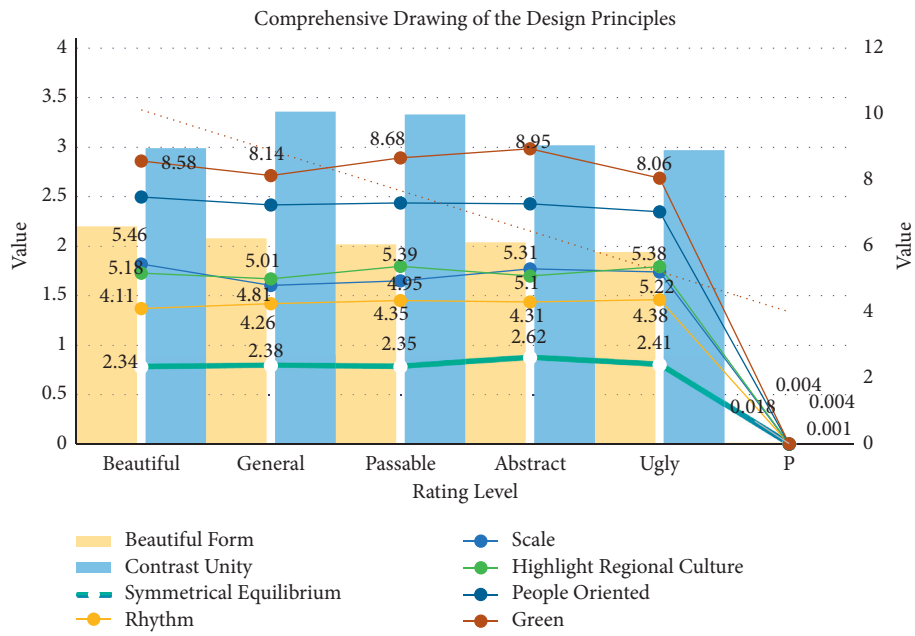

Figure 8: Comprehensive drawing of the design principles in ceramic mural art by various age groups.

Ceramic murals have high requirements for the artist's comprehensive ability. They need to have the most basic artistic ability and innovation ability but also need to have a deeper understanding of the traditional national cultural characteristics of the country and people's aesthetic characteristics. At the same time, they also need to have in-depth research on the characteristics of ceramic materials and have a detailed understanding of the structure of the architectural space environment. Modern ceramic murals must not only make ceramic murals coordinate with the physical structure and functional atmosphere of the public space environment but also help the entire public space environment to coordinate with the local humanistic environment and the entire natural environment, and strive to create a cultural and the social environment; human and natural environment is a unified environmental system. The image processing process that the ceramic mural art image must go through is studied. The median filter is used to smooth the image, which improves the image quality and the sharpness of the image. Through the experimental comparison of various edge detection operators, each edge detection is analyzed. The advantages and disadvantages of the operator and the edge detection operator suitable for ceramic mural art image detection are selected; finally, the optimal threshold is obtained through the iterative threshold segmentation method, the image is binarized, and the roundness index is used to correct the order products are judged and finally classified.

5. Conclusions

The improvement of modern people's aesthetic concepts, the diversification of modern home design styles, and the rise of modern art walls and cultural walls provide a realistic possibility for modern ceramic mural art to intervene in the home environment. The involvement of modern ceramic mural art in the modern home environment manifests the development of modern art and culture—the development of modern economy and technology guarantees modern ceramic mural art to intervene in the home environment. Modern ceramic mural art has deeper cultural connotations in both its art form and its artistic language, and it combines with the home environment space to build a unified art space. It is necessary to completely turn the public's thinking concepts and aesthetic inclination to art, and at the same time, it takes a certain amount of time and practical process. In addition to artistic creativity in artistic creation, ceramic artists should also master and study the various properties of mural materials. They should also have extensive knowledge and experience to explore murals and various objective environments, and people's subjective factors. However, the shortcomings of ceramic art are also reflected, such as lack of creativity and practicality.

Data Availability

There are no available data for this study.

Conflicts of Interest

The authors declare that they have no conflicts of interest.

References

[1] Z. Shen, F. Ding, and Y. Shi, "Digital forensics for recoloring via convolutional neural network," *Computers, Materials & Continua*, vol. 62, no. 1, pp. 1–16, 2020.

[2] S. Wang, T. Yue, and M. Abdel Wahab, "Multiscale analysis of the effect of debris on fretting wear process using a semi-concurrent method," *Computers, Materials & Continua*, vol. 62, no. 1, pp. 17–35, 2020.

[3] M. Abd El-Aziz and A. M. Aly, "Entropy generation for flow and heat transfer of sisko-fluid over an exponentially stretching surface," *Computers, Materials & Continua*, vol. 62, no. 1, pp. 37–59, 2020.

[4] Q. Fan, Y. Zhang, and Z. Wang, "Improved teaching learning based optimization and its application in parameter estimation of solar cell models," *Intelligent Automation & Soft Computing*, vol. 26, no. 1, pp. 1–12, 2020.

[5] M. Abdullah, S. A. Khan, M. Alenez, K. Almustafa, and W. Iqbal, "Application centric virtual machine placements to minimize bandwidth utilization in datacenters," *Intelligent Automation & Soft Computing*, vol. 26, no. 1, pp. 13–25, 2020.

[6] D. Shi, S. Wang, Y. Cai, L. Chen, and C. Yuan, "Model predictive control for nonlinear energy management of a power split hybrid electric vehicle," *Intelligent Automation & Soft Computing*, vol. 26, no. 1, pp. 27–39, 2020.

[7] B. Li, J. Yang, Y. Yang, C. Li, and Y. Zhang, "Sign language/gesture recognition based on cumulative distribution density features using UWB radar," *IEEE Transactions on Instrumentation and Measurement*, vol. 70, pp. 1–13, 2021.

[8] N. Xiao, R. Xinyi, Z. Xiong, F. Xu, X. Zhang, and Q. Xu, "A diversity-based selfish node detection algorithm for socially aware networking," *Journal of Signal Processing Systems*, vol. 93, no. 7, pp. 811–825, 2021.

[9] S. Feng, C. Zuo, L. Zhang, T. Tao, Y. Hu, and W. Yin, "Calibration of fringe projection profilometry: a comparative review," *Optics and Lasers in Engineering*, vol. 143, Article ID 106622, 2021.

[10] G. D. Penna and S. Orefice, "Using spatial relations for qualitative specification of gestures," *Computer Systems Science and Engineering*, vol. 34, no. 6, pp. 325–338, 2019.

[11] H. Chen, A. A. Heidari, H. Chen, M. Wang, Z. Pan, and A. H. Gandomi, "Multi-population differential evolution-assisted harris hawks optimization: framework and case studies," *Future Generation Computer Systems*, vol. 111, pp. 175–198, 2020.

[12] M. Wang and H. Chen, "Chaotic multi-swarm whale optimizer boosted support vector machine for medical diagnosis," *Applied Soft Computing*, vol. 88, Article ID 105946, 2020.

[13] Y. Xu, H. Chen, J. Luo, Q. Zhang, S. Jiao, and X. Zhang, "Enhanced moth-flame optimizer with mutation strategy for global optimization," *Information Sciences*, vol. 492, pp. 181–203, 2019.

[14] X. Zhao, X. Zhang, Z. Cai, and X. Tian, "Chaos enhanced grey wolf optimization wrapped ELM for diagnosis of paraquat-poisoned patients," *Computational Biology and Chemistry*, vol. 78, pp. 481–490, 2019.

[15] C. Li, L. Hou, B. Y. Sharma, and H. Li, "Developing a new intelligent system for the diagnosis of tuberculous pleural effusion," *Computer Methods and Programs in Biomedicine*, vol. 153, pp. 211–225, 2018.

[16] M. Wang, H. Chen, B. Yang, and X. Zhao, "Toward an optimal kernel extreme learning machine using a chaotic moth-flame optimization strategy with applications in medical diagnoses," *Neurocomputing*, vol. 267, pp. 69–84, 2017.

[17] E. Yavuz, R. Yazıcı, M. Cem Kasapba¸sı, and T. Tugay Bilgin, "Improving initial flattening of convex-shaped free-form mesh surface patches using a dynamic virtual boundary," *Computer Systems Science and Engineering*, vol. 34, no. 6, pp. 339–355, 2019.

[18] V. Pandey and P. Saini, "Application layer scheduling in cloud: fundamentals, review and research directions," *Computer Systems Science and Engineering*, vol. 34, no. 6, pp. 357–376, 2019.

[19] C. Liu, K. Li, and K. Li, "A game approach to multi-servers load balancing with load-dependent server availability consideration," *IEEE Transactions on Cloud Computing*, vol. 9, no. 1, pp. 1–13, 2021.

[20] C. Liu, K. Li, K. Li, and R. Buyya, "A new service mechanism for profit optimizations of a cloud provider and its users," *IEEE Transactions on Cloud Computing*, vol. 9, no. 1, pp. 14–26, 2021.

[21] G. Xiao, K. Li, Y. Chen, W. He, A. Y. Zomaya, and T. Li, "CASpMV: a customized and accelerative SpMV framework for the sunway taihulight," *IEEE Transactions on Parallel and Distributed Systems*, vol. 32, no. 1, pp. 131–146, 2021.

[22] M. Duan, K. Li, K. Li, and T. Qi, "A novel multi-task tensor correlation neural network for facial attribute prediction," *ACM Transactions Intelligent Systems and Technology*, vol. 12, no. 1, pp. 3–22, 2021.

[23] J. Feng, Z. Liu, and L. Feng, "Identifying opportunities for sustainable business models in manufacturing: application of patent analysis and generative topographic mapping," *Sustainable Production and Consumption*, vol. 27, pp. 509–522, 2021.

[24] C. Mi, Y. Huang, C. Fu, Z. Zhang, O. Postolache, and A. Authors, "Vision-based measurement: actualities and developing trends in automated container terminals," *IEEE Instrumentation & Measurement Magazine*, vol. 24, no. 4, pp. 65–76, 2021.

[25] P. Wang, L. Wang, H. Leung, and G. Zhang, "Super-resolution mapping based on spatial-spectral correlation for spectral imagery," *IEEE Transactions on Geoscience and Remote Sensing*, vol. 59, no. 3, pp. 2256–2268, 2021.

[26] C. Chen, K. Li, S. G. Teo, X. Zou, K. Li, and Z. Zeng, "Citywide traffic flow prediction based on multiple gated spatio-temporal convolutional neural networks," *ACM Transaction Knowledge Discovery Data*, vol. 14, no. 4, pp. 1–23, 2020.

[27] X. Zhou, K. Li, Z. Yang, Y. Gao, and K. Li, "Efficient approaches to k representative G-skyline queries," *ACM Transactions on Knowledge Discovery Data*, vol. 14, no. 5, pp. 1–27, 2020.

[28] J. Wang, Y. Gao, X. Yin, F. Li, and H. J. Kim, "An enhanced PEGASIS algorithm with mobile sink support for wireless sensor networks," *Wireless Communications and Mobile Computing*, vol. 2018, Article ID 9472075, 9 pages, 2018.

[29] J. Xia, H. Chen, Q. Li, and M. Zhou, "Ultrasound-based differentiation of malignant and benign thyroid nodules: an extreme learning machine approach," *Computer Methods and Programs in Biomedicine*, vol. 147, pp. 37–49, 2017.

[30] H. L. Chen, G. Wang, C. Ma, Z. N. Cai, W. B. Liu, and S. J. Wang, "An efficient hybrid kernel extreme learning machine approach for early diagnosis of parkinson's disease," *Neurocomputing*, vol. 184, pp. 131–144, 2016.

[31] L. Shen, H. Chen, Z. Yu, and W. Kang, "Evolving support vector machines using fruit fly optimization for medical data classification," *Knowledge-Based Systems*, vol. 96, pp. 61–75, 2016.

[32] Z. Liao, J. Wang, S. Zhang, J. Cao, and G. Min, "Minimizing movement for target coverage and network connectivity in

mobile sensor networks," *IEEE Transactions on Parallel and Distributed Systems*, vol. 26, no. 7, pp. 1971–1983, 2014.

[33] J. Wang, Y. Gao, W. Liu, A. K. Sangaiah, and H. J. Kim, "An intelligent data gathering schema with data fusion supported for mobile sink in wireless sensor networks," *International Journal of Distributed Sensor Networks*, vol. 15, no. 3, Article ID 1550147719839581, 2019.

[34] J. Zhang, X. Jin, J. Sun, J. Wang, and A. K. Sangaiah, "Spatial and semantic convolutional features for robust visual object tracking," *Multimedia Tools and Applications*, vol. 79, no. 21, pp. 15095–15115, 2020.

[35] F. Yu, L. Liu, L. Xiao, K. Li, and S. Cai, "A robust and fixed-time zeroing neural dynamics for computing time-variant nonlinear equation using a novel nonlinear activation function," *Neurocomputing*, vol. 350, pp. 108–116, 2019.

[36] X. Zenggang, T. Zhiwen, C. Xiaowen, Z. Xue-min, Z. Kaibin, and Y. Conghuan, "Research on image retrieval algorithm based on combination of color and shape features," *Journal of Signal Processing Systems*, vol. 93, no. 2-3, pp. 139–146, 2019.

[37] L. Wang, Y. Peng, Y. Xie, B. Chen, and Y. Du, "A new iteration regularization method for dynamic load identification of stochastic structures," *Mechanical Systems and Signal Processing*, vol. 156, Article ID 107586, 2021.

[38] T. Zhang, X. Wu, S. M. Shaheen, and J. Rinklebe, "Effects of microorganism-mediated inoculants on humification processes and phosphorus dynamics during the aerobic composting of swine manure," *Journal of Hazardous Materials*, vol. 416, Article ID 125738, 2021.

[39] J. Wang, X. Gu, W. Liu, A. K. Sangaiah, and H. J. Kim, "An empower hamilton loop based data collection algorithm with mobile agent for WSNs," *Human-Centric Computing and Information Sciences*, vol. 9, no. 1, pp. 1–14, 2019.

[40] L. Hu, G. Hong, J. Ma, X. Wang, and H. Chen, "An efficient machine learning approach for diagnosis of paraquat-poisoned patients," *Computers in Biology and Medicine*, vol. 59, pp. 116–124, 2015.

[41] X. Xu and H. L. Chen, "Adaptive computational chemotaxis based on field in bacterial foraging optimization," *Soft Computing*, vol. 18, no. 4, pp. 797–807, 2014.

[42] Y. Zhang, R. Liu, X. Wang, H. Chen, and C. Li, "Boosted binary Harris hawks optimizer and feature selection," *Engineering with Computers*, vol. 1, pp. 1–30, 2020.

[43] W. Li, Z. Chen, X. Gao, W. Liu, and J. Wang, "Multimodel framework for indoor localization under mobile edge computing environment," *IEEE Internet of Things Journal*, vol. 6, no. 3, pp. 4844–4853, 2018.

[44] L. Xiang, X. Shen, J. Qin, and W. Hao, "Discrete multi-graph hashing for large-scale visual search," *Neural Processing Letters*, vol. 49, no. 3, pp. 1055–1069, 2019.

[45] J. Zhang, W. Wang, C. Lu, J. Wang, and A. K. Sangaiah, "Lightweight deep network for traffic sign classification," *Annals of Telecommunications*, vol. 75, no. 7, pp. 369–379, 2020.

[46] S. R. Zhou, J. P. Yin, and J. M. Zhang, "Local binary pattern (LBP) and local phase quantization (LBQ) based on gabor filter for face representation," *Neurocomputing*, vol. 116, pp. 260–264, 2013.

[47] B. Xiong, K. Yang, J. Zhao, W. Li, and K. Li, "Performance evaluation of openflow-based software-defined networks based on queueing model," *Computer Networks*, vol. 102, pp. 172–185, 2016.

[48] J. Wang, Y. Yang, T. Wang, R. S. Sherratt, and J. Zhang, "Big data service architecture: a survey," *Journal of Internet Technology*, vol. 21, no. 2, pp. 393–405, 2020.

[49] S. He, K. Xie, K. Xie, C. Xu, and J. Wang, "Interference-aware multisource transmission in multiradio and multichannel wireless network," *IEEE Systems Journal*, vol. 13, no. 3, pp. 2507–2518, 2019.

[50] D. Zhang, T. Yin, G. Yang, M. Xia, L. Li, and X. Sun, "Detecting image seam carving with low scaling ratio using multi-scale spatial and spectral entropies," *Journal of Visual Communication and Image Representation*, vol. 48, pp. 281–291, 2017.

[51] M. Long, F. Peng, and H. Y. Li, "Separable reversible data hiding and encryption for HEVC video," *Journal of Real-Time Image Processing*, vol. 14, no. 1, pp. 171–182, 2018.

[52] J. Zhang, S. Zhong, T. Wang, H. C. Chao, and J. Wang, "Blockchain-based systems and applications: a survey," *Journal of Internet Technology*, vol. 21, no. 1, pp. 1–14, 2020.

[53] Y. Zhang, "Towards augmented kernel extreme learning models for bankruptcy prediction: algorithmic behavior and comprehensive analysis," *Neurocomputing*, vol. 430, pp. 185–212, 2020.

[54] D. Zhao, "Chaotic random spare ant colony optimization for multi-threshold image segmentation of 2D Kapur entropy," *Knowledge-Based Systems*, vol. 216, Article ID 106510, 2020.

[55] J. Tu, "Evolutionary biogeography-based whale optimization methods with communication structure: towards measuring the balance," *Knowledge-Based Systems*, vol. 212, Article ID 106642, 2020.

[56] Q. Tang, K. Yang, D. Zhou, Y. Luo, and F. Yu, "A real-time dynamic pricing algorithm for smart grid with unstable energy providers and malicious users," *IEEE Internet of Things Journal*, vol. 3, no. 4, pp. 554–562, 2015.

[57] S. He, W. Zeng, K. Xie, H. Yang, M. Lai, and X. Su, "PPNC: privacy preserving scheme for random linear network coding in smart grid," *KSII Transactions on Internet and Information Systems (TIIS)*, vol. 11, no. 3, pp. 1510–1532, 2017.

[58] M. Mortazavi, M. K. M. Nasution, F. Abdolahzadeh, M. Behroozi, and A. Davarpanah, "Sustainable learning environment by mobile-assisted language learning methods on the improvement of productive and receptive foreign language skills: a comparative study for asian universities," *Sustainability*, vol. 13, no. 11, p. 6328, 2021.

[59] M. Mortazavi, F. Tansu Hocanın, and A. Davarpanah, "Application of quantitative computer-based analysis for student's learning tendency on the efficient utilization of mobile phones during lecture hours," *Sustainability*, vol. 12, no. 20, p. 8345, 2020.

[60] A. Davarpanah, "Parametric study of polymer-nanoparticles-assisted injectivity performance for axisymmetric two-phase flow in EOR processes," *Nanomaterials*, vol. 10, no. 9, p. 1818, 2020.

[61] W. Shan, "Double adaptive weights for stabilization of moth flame optimizer: balance analysis, engineering cases, and medical diagnosis," *Knowledge-Based Systems*, vol. 214, Article ID 106728, 2020.

[62] C. Yu, "SGOA: annealing-behaved grasshopper optimizer for global tasks," *Engineering with Computers*, vol. 1, pp. 1–28, 2021.

[63] J. Hu, H. Chen, A. A. Heidari, and M. Wang, "Orthogonal learning covariance matrix for defects of grey wolf optimizer: insights, balance, diversity, and feature selection," *Knowledge-Based Systems*, vol. 213, Article ID 106684, 2021.

[64] A. Davarpanah and B. Mirshekari, "A mathematical model to evaluate the polymer flooding performances," *Energy Reports*, vol. 5, pp. 1651–1657, 2019.

[65] A. Davarpanah, R. Shirmohammadi, B. Mirshekari, and A. Aslani, "Analysis of hydraulic fracturing techniques: hybrid fuzzy approaches," *Arabian Journal of Geosciences*, vol. 12, no. 13, pp. 1–8, 2019.

[66] X. Zhao, D. Li, B. Yang, C. Ma, Y. Zhu, and H. Chen, "Feature selection based on improved ant colony optimization for online detection of foreign fiber in cotton," *Applied Soft Computing*, vol. 24, pp. 585–596, 2014.

[67] H. Yu, W. Li, C. Chen, and J. Liang, "Dynamic gaussian bare-bones fruit fly optimizers with abandonment mechanism: method and analysis," *Engineering with Computers*, vol. 1, pp. 1–29, 2020.

[68] M. Ebnali, R. Fathi, R. Lamb, S. Pourfalatoun, and S. Motamedi, "Using augmented holographic UIs to communicate automation reliability in partially automated driving," in *Proceedings of the AutomationXP@ CHI*, Honolulu, HI, USA, 2020.

[69] M. Rezaei, F. Farahanipad, A. Dillhoff, R. Elmasri, and V. Athitsos, "Weakly-supervised hand part segmentation from depth images," in *Proceedings of the 14th PErvasive Technologies Related to Assistive Environments Conference*, pp. 218–225, Corfu, Greece, June 2021.

[70] Z. Chen, H. Li, Y. Bao, N. Li, and Y. Jin, "Identification of spatio-temporal distribution of vehicle loads on long-span bridges using computer vision technology," *Structural Control and Health Monitoring*, vol. 23, no. 3, pp. 517–534, 2016.

[71] P. Kiedrowski, "Driver's head tracking with pose estimation using computer vision technology under 2D environment," *Advances in Computational Ences and Technology*, vol. 11, no. 11, pp. 887–895, 2018.

[72] Z. Wang, H. Li, and X. Zhang, "Construction waste recycling robot for nails and screws: computer vision technology and neural network approach," *Automation in Construction*, vol. 97, pp. 220–228, 2019.

[73] B. Alizadeh Kharazi, A. H. Behzadan, and A. Behzadan, "Flood depth mapping in street photos with image processing and deep neural networks," *Computers, Environment and Urban Systems*, vol. 88, Article ID 101628, 2021.

[74] A. Kharazi Bahareh, D. Li, Z. Zang, and A. Behzadan, "Feasiblity study of urban flood mapping using traffic signs for route optimization," in *Proceeding of the 28th EG-ICE International Workshop on Intelligent Computing in Engineering*, pp. 572–581, Berlin, Germany, 2021.

[75] H. Tian, T. Wang, Y. Li et al., "Computer vision technology in agricultural automation—a review," *Information Processing in Agriculture*, vol. 7, no. 1, pp. 1–19, 2020.

[76] Q. Xi, Q. Zhang, W. Hu, and W. Xin, "Computer vision-based library management system," *Science & Technology Libraries*, vol. 35, no. 2, pp. 172–182, 2016.

[77] Rosario and Uceda-Sosa, "Computer vision and image processing in intelligent systems and multimedia technologies," *Computing Reviews*, vol. 57, no. 9, p. 535, 2016.

[78] M. T. García-Ordás, E. Alegre, V. González-Castro et al., "A computer vision approach to analyze and classify tool wear level in milling processes using shape descriptors and machine learning techniques," *International Journal of Advanced Manufacturing Technology*, vol. 90, no. 5–8, pp. 1–15, 2016.

[79] Y. Liu, X. Wang, F. Du et al., "Computer vision detection of mold breakout in slab continuous casting using an optimized neural network," *International Journal of Advanced Manufacturing Technology*, vol. 88, no. 1–4, pp. 1–8, 2016.

[80] Y. Liu, X. Wang, F. Du et al., "Computer vision detection of mold breakout in slab continuous casting using an optimized neural network," *International Journal of Advanced Manufacturing Technology*, vol. 88, no. 1, pp. 557–564, 2017.

[81] B. Zhang, L. Zhou, and J. Zhang, "A methodology for obtaining spatiotemporal information of the vehicles on bridges based on computer vision," *Computer-Aided Civil and Infrastructure Engineering*, vol. 34, no. 6, pp. 471–487, 2019.

[82] A. Ray Sarkar, G. Sanyal, and S. Majumder, "Participatory design for selection of icons to represent daily activities of living for a vision-based rehabilitation-cum-assistance system for locked-in patients," *Disability and Rehabilitation: Assistive Technology*, vol. 15, no. 3, pp. 282–291, 2020.

[83] J. Wang, Y. Liu, D. Zhang, H. Peng, and Y. Zhu, "A new computer vision based multi-indentation inspection system for ceramics," *Multimedia Tools and Applications*, vol. 76, no. 2, pp. 2495–2513, 2017.

[84] J. Wang, Y. Liu, D. Zhang et al., "A new computer vision based multi-indentation inspection system for ceramics," *Multimedia Tools and Applications*, vol. 76, no. 2, pp. 1–19, 2016.

[85] A. Brunetti, D. Buongiorno, G. F. Trotta, and V. Bevilacqua, "Computer vision and deep learning techniques for pedestrian detection and tracking: a survey," *Neurocomputing*, vol. 300, pp. 17–33, 2018.

[86] T. Zhe, L. Huang, Q. Wu, J. Zhang, C. Pei, and L. Li, "Inter-vehicle distance estimation method based on monocular vision using 3D detection," *IEEE Transactions on Vehicular Technology*, vol. 69, no. 5, pp. 4907–4919, 2020.

[87] Mihai-Cosmin Iațeșen, "10 creativity and innovation in visual arts through form and space having symbolic value," *Review of Artistic Education*, vol. 14, no. 1, pp. 207–216, 2017.

[88] J. W. Amoroso, J. Marra, C. S. Dandeneau, and K. Brinkman, "Cold crucible induction melter test for crystalline ceramic waste form fabrication: a feasibility assessment," *Journal of Nuclear Materials*, vol. 486, pp. 283–297, 2017.

[89] J. Briales and J. Gonzalez-Jimenez, "A minimal closed-form solution for the perspective three orthogonal angles (P3oA) problem: application to visual odometry," *Journal of Mathematical Imaging and Vision*, vol. 55, no. 3, pp. 266–283, 2016.

[90] W. Long, L. Xia, and X. L. Wang, "A rapid automatic analyzer and its methodology for effective bentonite content based on image recognition technology," *China Foundry*, vol. 13, no. 5, pp. 322–326, 2016.

[91] W. Xing, S. Zhao, and S. Zhang, "Blind identification technology of computer generated image based on texture recognition," *Journal of Computational and Theoretical Nanoscience*, vol. 14, no. 7, pp. 3312–3322, 2017.

[92] S. Satoh, "Image and video technology," *Facial Expression Recognition Using Cascaded Random Forest Based on Local Features*, Springer, vol. 10799, pp. 42–53, Berlin, Germany, 2018.

[93] Y. Wang, S. Wang, Y. Liu et al., "Recognition of group activities based on M-DTCWT and elliptic mahalanobis metrics," in *Communications in Computer and Information Science*, vol. 757, pp. 113–122, Springer, Berlin, Germany, 2018.

[94] H. W. Huang, Q. T. Li, and D. M. Zhang, "Deep learning based image recognition for crack and leakage defects of

metro shield tunnel," *Tunnelling and Underground Space Technology*, vol. 77, pp. 166–176, 2018.

[95] Z. Wang, M. Liu, M. Dong, and L. Wu, "Riemannian alternative matrix completion for image-based flame recognition," *IEEE Transactions on Circuits and Systems for Video Technology*, vol. 27, no. 11, pp. 2490–2503, 2017.

[96] S. H. Shirazi, A. I. Umar, S. Naz, and M. I. Razzak, "Efficient leukocyte segmentation and recognition in peripheral blood image," *Technology & Health Care Official Journal of the European Society for Engineering & Medicine*, vol. 24, no. 3, pp. 335–347, 2016.

[97] Q. Gao, J. Wang, X. Ma, X. Feng, and H. Wang, "CSI-based device-free wireless localization and activity recognition using radio image features," *IEEE Transactions on Vehicular Technology*, vol. 66, no. 11, pp. 10346–10356, 2017.

[98] M. Kumar and Priyanka, "Various image enhancement and matching techniques used for fingerprint recognition system," *International Journal of Information Technology*, vol. 11, no. 4, pp. 767–772, 2019.

[99] H. Ren, J. Zhang, M. Zhu, and M. Liu, "Particle-size analysis of wood fiber and powder based on image processing and recognition," *Journal of Information Technology Research*, vol. 11, no. 3, pp. 105–118, 2018.

[100] W. Tan, B. Yan, and C. Lin, "Beyond visual retargeting: a feature retargeting approach for visual recognition and its applications," *IEEE Transactions on Circuits and Systems for Video Technology*, vol. 28, no. 11, pp. 3154–3162, 2018.

[101] G. Javidannia, M. Bemanian, and M. Mahdavinejad, "Performance oriented design framework for early tall building form development; seismic architecture view," in *Proceedings of the eCAADe38. Cumincad*, Berlin, Germany, September 2020.

[102] G. Javidannia, M. Bemanian, M. Mahdavinejad, S. Nejat, and L. Javidannia, "Generative design workflow for seismic-efficient architectural design of tall buildings; A multi-object optimization approach," in *Proceedings of the SimAUD*, ACM Digital Library, 2021.

[103] M. Rezaei and N. Naderi, "Persian signature verification using fully convolutional networks," 2019, http://arxiv.org/abs/1909.09720.

[104] M. F. Nezhadnaeini, M. Hajivand, M. Abasi, and S. Mohajeryami, "Optimal allocation of distributed generation units based on two different objectives by a novel version group search optimizer algorithm in unbalanced loads system," *Revue Roumaine des Science Techniques*, vol. 61, pp. 338–342, 2016.

[105] M. Abasi, J. Mahmood, A. Saffarian, and S. G. Seifossadat, "A novel complete dynamic and static model of 48-pulse VSC-based GUPFC for parallel transmission lines," *International Journal of Industrial Electronics, Control and Optimization*, vol. 3, no. 4, pp. 447–457, 2020.

[106] M. Abasi, J. Mahmood, A. Saffarian, and S. G. Seifossadat, "Accurate simulation and modeling of the control system and the power electronics of a 72-pulse VSC-based generalized unified power flow controller (GUPFC)," *Electrical Engineering*, vol. 102, no. 6, pp. 1795–1819, 2020.

[107] B. Mafakheri, P. Gonnella, A. Bazzi, B. M. Masini, M. Caggiano, and R. Verdone, "Optimizations for hardware-in-the-loop-based V2X validation platforms," in *Proceedings of the 2021 IEEE 93rd Vehicular Technology Conference (VTC2021-Spring)*, pp. 1–7, IEEE, Helsinki, Finland, April 2021.

Hindawi
Mathematical Problems in Engineering
Volume 2021, Article ID 9982723, 17 pages
https://doi.org/10.1155/2021/9982723

Research Article

Probabilistic Prediction of Unsafe Event in Air Traffic Control Department Based on the Improved Backpropagation Neural Network

Yong Liao, Zhiyang Miao, and Changqi Yang

College of Air Traffic Management, Civil Aviation Flight University of China, Sichuan, Guanghan 618307, China

Correspondence should be addressed to Yong Liao; liaoyong_1234@163.com

Received 27 March 2021; Revised 27 July 2021; Accepted 13 August 2021; Published 27 August 2021

Academic Editor: Samuel Yousefi

Air traffic control is an important tool to ensure the safety of civil aviation. For the departments that do the work of air traffic control, reducing the percentage of unsafe event is the core task of safety management. If the relationship between the percentage of unsafe event and their influencing factors can be effectively clarified, then the probability of unsafe event in some control department can be predicted. So, it is of great importance to improve the level of safety management. To quantitatively estimate the probability of unsafe event, a three-layer BP neural network model is introduced in this paper. First, a probabilistic representation of unsafe event related to air traffic control department is made, and then, the probability of different classes of unsafe events and safe events is taken as the outputs of the BP neural network, the factors influencing occurrence of unsafe event connected with air traffic control is taken as inputs, and the sigmoid function is chosen as activation function for the hidden layer. Based on the error function of neural network, it is proved that the general BP neural network has two drawbacks when used for the training of small probability events, which are as follows: the pattern does not ensure that the sum of probability of all events is equal to one and the relative error between the actual outputs and desired outputs is very large after the training of neural network. The reason proved in this paper is that the occurrence rate of the unsafe event is much smaller than that of the safe event, resulting in each weight in the hide layer being subjected to the desired outputs of the safe event when using the gradient descent method for network training. To address this issue, a new mapping method is put forward to reduce the large difference of the desired outputs between the safe event and unsafe event. It is theoretically proved that the mapping method proposed in this paper can not only improve the training accuracy but also ensure that the sum of probability is equal to one. Finally, a numeric example is given to demonstrate that the method proposed in this paper is effective and feasible.

1. Introduction

China has a large population, vast geographical area, and uneven distribution of natural resources. To promote economic development and improve people's life, the exchange of people and goods among different regions is very frequent. Transportation is the tool to realize the exchange of people and goods, and different transportation modes have different characteristics. Due to the large population and uneven distribution of the population in China, the transportation demands are diverse, and to meet different people's demand, the Chinese government has been committed to building a diversified comprehensive transportation system, creating a comprehensive transportation network integrating railroads, highways, waterways, and civil aviation [1–5].

With the popularization of China's civil aviation from high-end passengers to the public, civil aviation is becoming more and more important in China's comprehensive transportation system. In 2019, China civil aviation completed a total of 129.27 billion ton-kms of freight turnover, 660 million person-times of passengers, and 752.6 million tons of cargo and mail, with growth rates of 7.1%, 7.9%, and 1.9% year-on-year, respectively. With the advantages of safety, speedability, and convenience, civil aviation is winning more and more people's choice, and the share of civil

aviation in passenger transportation reached 32.8%, with a growth rate of 1.5% year-on-year. The number of flights is rising steadily, and Chinese transport airlines completed 4,966,200 takeoffs, with an increase of 5.8% over the previous year [6].

Safety is the primary concern for every mode of transportation. With the increasing in the number of flights, the air routes and airports are becoming more and more congested, and the controllers' workload is constantly increasing, which brings serious challenges to the safety of civil aviation. Air traffic management is an important part to ensure the safety of civil aviation, and the prerequisite for the safety of air traffic management is the safety of air traffic control (ATC), which makes the operation of aircrafts efficient, orderly, and safe. ATC is a service provided by ground-based controllers who direct aircraft on the ground and through controlled airspace, providing advisory services to aircraft in noncontrolled airspace [7]. ATC department is becoming more and more difficult for controllers to direct aircrafts, and the increase of flight volume leads to an increasing possibility of unsafe event and an increasing risk for the operation of the ATC department.

Safe operation has always been the goal pursued by civil aviation and is also the focus of the whole society [8]. There are many factors that influence safety in the ATC department. Air traffic controllers and pilots are crucial in achieving high levels of safety in air traffic operations [9]. The increasing volume of flights and the expanding route network have led to a dramatic increase in the workload of air traffic management, and a gradual increase in the number of ATC unsafe event has had a serious impact on the development of China's civil aviation [10]. Air traffic management systems are typically highly interactive, highly distributed, and complex systems [11]. The changing objective conditions lead to uncertainty, and the issue of ATC safety comes along with various uncertainties in the process of civil aviation transportation [10]. The increase in flight has led to a dramatic increase in demand for airspace, so that various unsafe factors also increase [12]. The contradiction between the capacity of air transport services and demand for transport is becoming more and more prominent. With this come the security risks in air traffic control operations [13]. The limited airspace, manpower, and equipment resources have increased the pressure on air traffic controllers and the probability of unsafe event in air transport has increased [14]. Due to the dynamic and real-time nature of the ATC control operation process, its risk level is higher than other systems, and control factors are more likely to lead to an unsafe event [15]. The risk factors of organization and management in the air traffic control system have a complex influence on flight safety [16].

To improve the safety level of air traffic control, different approaches have been taken in various ways. Safety integrity system is of great significance for modern management, and it is helpful to establish a safety integrity system for ATC [17]. Global networks of satellites for communications, navigation, and surveillance are longer-term solutions to air traffic management [18]. Automation removes some existing sources of human errors, and it can prevent some accident [19]. The construction of a safety culture in air traffic control can protect air traffic controllers [20]. Among the many methods, safety assessment for air traffic control is the commonly used [19, 21, 22].

The Chinese government attaches great importance to civil aviation safety. According to "Rules for Safety Management of Air Traffic Management Operation Department of Civil Aviation" published by the Civil Aviation Administration of China, the operation department of air traffic control of civil aviation shall establish a safety assessment mechanism. However, this document does not put forward specific implementation plan or evaluation method. The reason is that there is no universal risk assessment methodology that can be applied to any situation. So, in the "Regulations for Safety Assessment of Air Traffic management of Civil Aviation" published by the Civil Aviation Administration of China, the Civil Aviation Administration encourages and supports research and innovation on the methods and techniques of safety assessment to make the safety assessment scientific and normative. This document also points out that the safety assessment should choose reasonable methods, based on the conditions, characteristics, and needs of the actual circumstances.

Therefore, the safety assessment in air traffic control has always been an important research topic in civil aviation, and many experts and scholars have made outstanding contributions in this field. For example, Wang and Yao [23] presented a fuzzy Petri net method to assess the risk of air traffic control. Wan and Zhang [24] dealt with the certainty and uncertainty of the assessment system as a whole and establish a risk assessment model based on game theory and set pair analysis (SPA).Yuan et al. [25] believed that there are a lot of uncertainties in air traffic control safety evaluation, such as randomness, imprecision, and ambiguity. They introduced the dempster combination rule to improve it and proposed an ATC safety assessment method based on evidence theory. Yao et al. [26] adopted a fuzzy Petri net and introduced the risk level threshold and analytic hierarchy process to reduce the complexity of the fuzzy Petri net used for ATC safety assessment. Wang and Sun [27] used system theory process analysis (STPA) to identify potential unsafe behaviors of ATC operation system and then used first-order linear temporal logic (LTL) to normalize the identified unsafe behaviors. Finally, they proposed a safety assessment method for the unsafe behaviors. Liao et al. [28], from the perspective of probability theory, proposed a safety probability evaluation method for air traffic control based on Bayesian analysis.

Through a comprehensive analysis about these literature studies, it can be found that most of the current research on unsafe event in the ATC department is focused on safety assessment or risk assessment. ATC safety assessment is mostly based on comprehensive evaluation, that is, taking the whole ATC safety as the research object, establishing corresponding evaluation index, setting the weight of each evaluation index, scoring each evaluation index, and judging which safety level the ATC safety status belongs to by combining the weight of each index and the score of the index on the premise of the given safety level. At present,

most methods of the ATC safety assessment are qualitative assessments on the safety level in the air traffic control department, and there are few quantitative assessments on the probability of unsafe event for some air traffic control department. However, in the field of ground transportation, the application of quantitative methods has been very extensive. For example, Lin et al. used hybrid deep learning model and generative adversarial networks to traffic incident detection [29, 30]. In the field of ground traffic incident detection, the use of various quantitative research methods is very common [31–33]. For the departments that do the work of air traffic control, reducing the percentage of unsafe event in their departments is the core task of safety management. If the relationship between the percentage of unsafe event and their influencing factors can be effectively clarified, then, the probability of unsafe event in some control department can be predicted. In order to quantitatively estimate the probability of unsafe event, a three-layer backpropagation neural network model is introduced in this paper. Considering the training accuracy of the BP neural network is not good when the outputs are small probability event, this paper introduces a corresponding model to improve it.

2. Materials and Methods

2.1. Artificial Neural Networks. An artificial neural network (ANN) is modeled on the brain where neurons are connected in complex patterns to process data from the senses, establish memories, and control the body. Artificial neural networks (ANNs) process data and exhibit some intelligence. It is the piece of a computing system designed to simulate the way the human brain analyzes and processes information [34]. It is the foundation of artificial intelligence (AI) and solves problems that would prove impossible or difficult by human or statistical standards. ANNs have self-learning capabilities that enable them to produce better results as more data become available. Warren McCulloch and Walter Pitts presented the first simple systems, which are the origins of artificial neural networks (ANNs) in the 1940s. They proved that an ANN can learn any arithmetic or logical function [35]. Artificial neural networks have been widely used in various industries and have achieved excellent results [36, 37].

2.2. General Backpropagation Neural Network. There are two types of artificial neural networks, shallow neural network and deep neural network. A shallow neural network has only one hidden layer of neurons that processes inputs and generates outputs. A deep neural network has two or more hidden layers of neurons that process inputs. According to experts [38], shallow neural networks can tackle equally complex problems. So, we use the shallow neural network to solve the problem of predicting probability of unsafe event in the air traffic control department.

Backpropagation is an algorithm that backpropagates the errors from the output nodes to the input nodes. It is the essence of neural net training. It is the method of fine-tuning the weights of a neural network based on the error rate obtained in the previous iteration. It is a standard method of training artificial neural networks. This method helps to calculate the gradient of a loss function with respect to all the weights in the network. BP neural network is described as follows [39–41]. Given a shallow neural network has three layers of neurons that process inputs and generate outputs. this neural network has M inputs in input layer, N outputs in output layer, and K neurons (or nodes) in hidden layer. The input vector in input layer is $X = (x_1, x_m, \ldots, x_M)$, the input vector in hidden layer is $\mathrm{HI} = (hi_1, hi_k, \ldots, hi_K)$, the output vector in hidden layer is $\mathrm{HO} = (ho_1, ho_k, \ldots, ho_K)$, the input vector in output layer is $\mathrm{YI} = (yi_1, yi_n, \ldots, yi_N)$, the output vector in output layer is $\mathrm{YO} = (yo_1, yo_n, \ldots, yo_N)$, the desired output vector is $t = (t_1, t_n, \ldots, t_N)$, the connection weight from the mth node in the input layer to the kth node in the hidden layer is w_{mk}, and the connection weight from the kth node in the hidden layer to the nth node in the output layer is w_{kn}. The bias of each neuron in the hidden layer is b_k, the bias of each neuron in the output layer is b_n, the activation function of the hidden layer is $f_1(\cdot)$, and the activation function of the output layer is $f_2(\cdot)$.

The BP neural network uses the backpropagation algorithm to train networks. Backpropagation algorithm is commonly used in the training of artificial neural networks. The basic idea of the backpropagation algorithm is that the learning process consists of two processes: the forward propagation of the signal and the backward propagation of the error. In the process of forward propagation, the input signals pass from the input layer to the output layer after being handled in the hidden layer. If the actual outputs do not match the desired outputs, then, the process will turn into the backpropagation of error. The model of the BP neural network with one hidden layer is shown in Figure 1.

The input of the kth neuron in the hidden layer is as follows:

$$hi_k = \sum_{m=1}^{M} x_m w_{mk} + b_k. \tag{1}$$

The output of the kth neuron in the hidden layer is as follows:

$$ho_k = f_1(hi_k). \tag{2}$$

The input of the nth neuron in the output layer is as follows:

$$yi_n = \sum_{k=1}^{N} ho_k w_{kn} + b_n. \tag{3}$$

The output of the nth neuron in the output layer is as follows:

$$yo_n = f_2(yi_n). \tag{4}$$

The loss function E between the network outputs and the desired outputs is as follows:

$$E = \frac{1}{2} \sum_{n=1}^{N} (t_n - yo_n)^2. \tag{5}$$

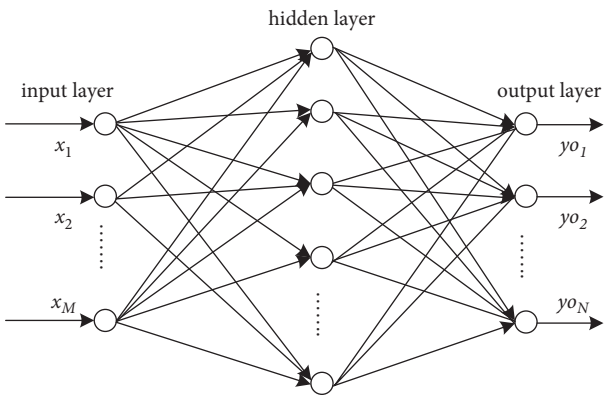

Figure 1: Top structure of the BP neural network.

During network training at a time, the change value of weight in each layer is obtained by gradient descent algorithm as follows:

$$\Delta w_{kn} = \eta ho_n f_2'(yi_n)(t_n - yo_n), \tag{6}$$

$$\Delta w_{mk} = \eta x_m f_1'(hi_k) \sum_{n=1}^{N} (t_n - yo_n) f_2'(yi_n) w_{kn}, \tag{7}$$

where Δw_{mk} represents the change value of weight from the mth node in the input layer to the kth node in the hidden layer. Δw_{kn} represents the change value of weight from the kth node in the hidden layer to the nth node in the output layer. η represents learning rate.

During network training at a time, the change value of biases obtained by gradient descent algorithm is as follows:

$$\Delta b_n = \eta f_2'(yi_n)(t_n - yo_n), \tag{8}$$

$$\Delta b_k = \eta f_1'(hi_k) \sum_{n=1}^{N} (t_n - yo_n) f_2'(yi_n) w_{kn}, \tag{9}$$

where Δb_n represents the change value of the nth bias in the output layer. Δb_k represents the change value of the kth bias in the hidden layer.

BP neural network is widely used in all walks of life because of its strong adaptability, including nonlinear mapping ability, self-learning ability, adaptive ability, generalization ability, fault tolerance ability, and other advantages [39, 42, 43]. At the same time, many scholars have improved the BP neural network considering its shortcomings and deficiencies, which improves the accuracy of the model [44–46]. This paper introduces the BP neural network into the probabilistic prediction of unsafe event in air traffic control department. For the problem of insufficient prediction accuracy of the general BP neural network, this paper proposes an improvement method.

2.3. Modeling Based on the Backpropagation Neural Network. Three problems need to be solved in calculating the probability of ATC unsafe event by using BP neural network: determining the inputs, outputs, and activation function.

2.3.1. Probabilistic Representation of the ATC Event. According to the air traffic management rules of civil aviation in China, ATC unsafe event can be classified into five levels with respect to their severity: accident, serious incident, general incident, serious error, and general error. Each class of unsafe event is strictly defined in this document.

According to the probability theory, this article defines the elementary event as follows. Firstly, the elementary event e_0 is defined as safe event, e_1 represents accident event, e_2 represents the event of serious incident, e_3 represents the event of general incident, e_4 represents serious error event, and e_5 represents general error event. The probability space composed by the elementary event is $\Omega = \{e_0, e_1, e_2, \ldots, e_5\}$. Ψ represents the set of all subsets of Ω, there are a total of 2^6 elements, Ψ is a σ domain, and each subset A in set Ψ is an event. The probability of A is $P(A)$, and then, the probability space of the ATC event can be expressed as (Ω, Ψ, P). Defining the single-valued real function $X(e_i) = i$(i is one of integer form 0 to 6 standing for different ATC event) in the probability space (Ω, Ψ, P), then, X is the random variable about the ATC event. It is known that X is a discrete random variable, which can be seen from the value of X. The probability of different values of X can be expressed in the distribution law. In the set of elementary event defined in this paper, there is a special elementary event e_0, which represents safe event. One important characteristic of probability is the normalization of probabilities, which means that the sum of the probability of all events is equal to one. If we do not consider the safe event e_0, the normalization of the probability will not be satisfied, which will have a bad impact on the accuracy of the prediction.

2.3.2. Outputs of the Backpropagation Neural Network. The outputs are usually the data that the model builder cares about. From the previously mentioned analysis, we are concerned with the probability of an unsafe event occurring in an ATC department. Therefore, the probability of unsafe event should be used as the outputs of the network. In addition to this, as previously mentioned, ensuring the normalization of the probability can improve the prediction accuracy, so the probability of safe event is also included in the outputs. Therefore, using the set of elementary event $\{e_0, e_1, e_2, \ldots, e_5\}$ as the outputs of the network is the most straightforward way. Of course, the outputs can also be adjusted according to the needs of the research purpose. For example, if we only want to know the overall probability of all unsafe events and do not care about which class of unsafe event occurs, we can define event A as $\{e_1, e_2, \ldots, e_5\}$. The outputs of the network are the probability of the event A and the probability of the safe event e_0. That is to say, depending on the actual needs of the research problem, the outputs of the network can be any subset of the set Ω. It should be noted that, in order to satisfy the normalization of probability, the network's output event must be a partition of the set Ω.

2.3.3. Inputs of the Backpropagation Neural Network. The inputs of BP neural network are usually some influencing factors that have an impact on the safety of air traffic

control, including the technical level of the controller, number of conflict points in the controlled airspace, and so on. The essence of determining the inputs is to establish the indicator system that affects the safety of ATC department. The establishment of input indicator system is relatively flexible, which usually needs to meet the following principles: the quantifiability of indicators, moderate number of indicators, and convenient data collection. There are many factors affecting the safety of ATC department, and the relationship among various influencing factors is intricate and complex, so it is very difficult to find the same influencing factors applicable to all different ATC departments. In the safety management of ATC, the analysis method most commonly used and widely recognized by the experts is SHEL model recommend by ICAO [23, 47], as described in Doc 9859 called Safety Management Manual. In this method, the factors affecting ATC safety are divided into four elements: hardware, liveware, environment, and management. The SHEL model provides a holistic overview of the influencing factors affecting ATC department. Therefore, in this paper, the hardware, liveware, environment, and management in the SHEL model are used as the inputs of the neural network. The next question is how to quantify these four inputs. There is no doubt that unsafe acts of human, equipment failures, management loophole, and objective problems in the environment may all lead to unsafe event. So, the number of unsafe acts of human in the ATC department can be used as input data for the liveware. The number of equipment failures in the ATC department can be used as input data for the hardware. The number of problems with management in the ATC department can be used as input data for the management. The number of problems with environment in the ATC department can be used as input data for the environment. Of course, the previously mentioned four inputs can be divided in depth according to the needs of the research. For example, the environment can be divided into the number of hazardous weather and the volume of flights. In short, the inputs of the neural network can be subdivided based on the previously mentioned four indicators in combination with the practical problems.

2.3.4. Activation Function of the Backpropagation Neural Network. BP neural network used in this paper is a three-layer structure, which needs two activation functions. Under normal circumstances, the choice of activation function needs to be determined by the actual problem. When used in probabilistic prediction, it has its particularity; that is, the outputs of the output layer must be in interval (0, 1). Therefore, the output layer chooses the asymmetric sigmoid function as activation function as follows, whose range is also in interval (0, 1):

$$f_2(x) = \frac{1}{\left(1 + e^{-x}\right)}. \tag{10}$$

Considering that the domain of input in output layer may contain negative number, if the activation function of the hidden layer chooses the asymmetric sigmoid function, its output used as the input of the output layer will not cover the domain. Therefore, the symmetric sigmoid function should be a better choice for the hidden layer as follows, whose range is in interval (−1, 1):

$$f_1(x) = \frac{\left(1 - e^{-x}\right)}{\left(1 + e^{-x}\right)}. \tag{11}$$

2.4. Improvement of the BP Neural Network. BP neural network has a good fault-tolerant ability and is widely used in all walks of life. The probability of unsafe event in air traffic control department has its particularity; if we directly apply the BP neural network to probabilistic prediction, it will have a large error in accuracy. So, it needs to be improved.

2.4.1. Problems of the General Backpropagation Neural Network. There are several problems in using general BP neural network directly to predict the probability of unsafe event in the ATC department.

During the training of the network, the outputs do not satisfy the normalization of the probability, which is that the sum of the probability of all network outputs is not equal to one. When the trained network is used for prediction, prediction accuracy may be affected.

There is more than one reason for the previously mentioned problem. For example, the inputs do not fully cover all the influencing factors, the quantization of the inputs is insufficient, and the number of training data is lacking. A few data in the training set is inaccurate, and so on. In short, BP neural network can only approximate a certain function, and errors are inevitable. So, if a constraint is introduced to ensure that the sum of all outputs is equal to one in each training epoch, the problem can be solved.

ATC unsafe events are small probability events. That is, the probability of an unsafe event in the ATC department is very low compared with the probability of safe event. When the connected weight of BP neural network is adjusted, the change of weight is mainly affected by the probability of safe event. This leads to the fact that the training of the whole network is dominated by the error of safe event, which makes the relative error of unsafe event very large. Next, we prove this by starting with the principle of BP neural network.

For the convenience of proof, the case is considered, in which only two outputs are in BP neural network. yo_n is used to represent output, $n = 2$ stands for safe event, and $n = 1$ stands for unsafe event. Since the unsafe event is a small probability event, this means that the desired probability of unsafe event is far less than the desired probability of safe event. For example, in 2020, the rate of unsafe event was 0.0056 per 10,000 flights in Chinese civil aviation. In 2019, the rate of unsafe event was 0.0043 per 10,000 flights in Chinese civil aviation. It is shown as follows:

$$t_1 \ll t_2, \tag{12}$$

where t_1 represents the desired probability of unsafe event and t_2 represents the desired probability of safe event.

The following is obtained from (5):

$$E = \frac{1}{2}\sum_{n=1}^{2}(t_n - yo_n)^2 = \frac{1}{2}\left[t_1^2 + t_2^2 + yo_1^2 + yo_2^2 - 2(t_1 yo_1 + t_2 yo_2)\right]. \tag{13}$$

The following are obtained from (12):

$$t_1 \ll t_2 \Rightarrow t_1 t_1 \ll t_1 t_2, \tag{14}$$

$$t_1 \ll t_2 \Rightarrow t_2 t_1 \ll t_2 t_2. \tag{15}$$

The following is obtained from (14) and (15):

$$t_1^2 \ll t_2^2. \tag{16}$$

In the training process, when the actual outputs of BP neural network yo are close to the target t, there is $yo_1 \ll yo_2$, and the following can be proved, like (16):

$$yo_1^2 \ll yo_2^2. \tag{17}$$

The following apparently hold true:

$$t_1 \ll t_2 \Rightarrow t_1 yo_1 \ll t_2 yo_1, \tag{18}$$

$$yo_1 \ll yo_2 \Rightarrow yo_1 t_2 \ll yo_2 t_2. \tag{19}$$

The following is obtained from (18) and (19):

$$t_1 yo_1 \ll yo_2 t_2. \tag{20}$$

The following can be obtained from (13), (16), (17), and (20):

$$E \approx \frac{1}{2}\left[t_2^2 - 2t_2 yo_2 + yo_2^2\right] \approx \frac{1}{2}(t_2 - yo_2)^2. \tag{21}$$

Bringing (21) into (7) and (9), the following can be obtained:

$$\Delta w_{mk} = \eta x_m f_1'(hi_k)(t_2 - yo_2) f_2'(yi_2) w_{k2}, \tag{22}$$

$$\Delta b_k = \eta f_1'(hi_k)(t_2 - yo_2) f_2'(yi_2) w_{k2}. \tag{23}$$

From (22) and (23), it is easy to find out that the change of weights from the input layer to the hidden layer is mainly determined by the probability of safe event. Therefore, when weight change is based on error, the result for safe event is better, but for unsafe event with small probability is worse.

The general processing method for this situation is to normalize the inputs and outputs, which map the inputs and outputs to the same interval through a function. This method can reduce the difference among the inputs and outputs, reduce errors, and improve the accuracy. After the prediction is made, the outputs can be probability though reverse normalization. However, this method still has following problems.

(1) It still does not guarantee the normalization of probability, and the sum of the all outputs may not be equal to 1.

(2) Different normalized function is going to produce different results. It is hard to say which normalized function is better. Different normalized functions are selected for the same model. This may result in some difference in accuracy. So, it is unclear which normalized function can be trusted.

(3) Normalization destroys the mapping relationship between the original inputs and outputs to some extent. Even if the network training results are good, there may be some loss of precision when facing the new inputs.

For these problems, this paper proposes an improved method of BP neural network, which can not only meet the normalization of probability, but also improve the accuracy of the training of BP neural network.

2.4.2. Improvement of the Backpropagation Neural Network. For a certain input vector, it is assumed that the qth output of the neural network is u_q. Since there is some error in the output, it is assumed that the error of the qth output is ε_q. Then, the true value of the qth output is $u_q + \varepsilon_q$. According to random utility theory [48–50], the probability of the qth output belonging to the qth class of event is as follows:

$$p_q = \mathrm{Prob}\left(u_q + \varepsilon_q > u_z + \varepsilon_z, \forall z \neq q\right) = \mathrm{Prob}\left(\varepsilon_z < \varepsilon_q + u_z - u_q, \forall z \neq q\right), \tag{24}$$

where u_z stands for the zth output of the neural network, and ε_z stands for the error of the zth network output.

Assume that the error ε obeys an independent Gumbel distribution, and its distribution function is shown as follows:

$$F_n(\varepsilon_n) = e^{-e^{-\varepsilon_n}}. \tag{25}$$

Then, its joint distribution $F(\varepsilon_1, \varepsilon_2, \ldots, \varepsilon_n)$ is as follows:

$$F(\varepsilon_1, \varepsilon_2, \ldots, \varepsilon_n) = \prod_{n=1}^{N} e^{-e^{-\varepsilon_n}}. \tag{26}$$

Find the partial derivative of the qth random variable ε_q as follows:

$$\frac{\partial F}{\partial \varepsilon_q} = e^{-\varepsilon_q}\prod_{n=1}^{N} e^{-e^{-\varepsilon_n}}. \tag{27}$$

On substituting (24) into (27) to find its definite integral, the following can be obtained [51–53]:

$$\int_{-\infty}^{+\infty} e^{-\varepsilon_q}\prod_{n=1}^{N} e^{-e^{-(\varepsilon_n + u_z - u_n)}}\,\mathrm{d}\varepsilon_q = \frac{\exp(u_q)}{\sum_{n=1}^{N}\exp(u_n)}. \tag{28}$$

According to the random utility theory, the qth desired output t_q^i corresponding to the ith input vector can be taken as the desired probability of ATC event. So, the following is valid:

$$\frac{\exp\left(u_q^i\right)}{\sum_{n=1}^{N}\exp\left(u_n^i\right)} = t_q^i. \tag{29}$$

If there are N outputs, then, there are N equations like (29), which form an equation set. u_q^i can be obtained by solving the equation set. t_q^i is replaced with u_q^i used for the desired outputs in the training of BP neural network. In the prediction, the network output u is brought into (29), and then, the probability of ATC event can be obtained.

Considering any two network outputs u_p^i and u_q^i corresponds to the ith input vector. According to (29), the following can be obtained:

$$\frac{\exp\left(u_p^i\right)}{\sum_{n=1}^{N}\exp\left(u_n^i\right)} = t_p^i, \tag{30}$$

$$\frac{\exp\left(u_q^i\right)}{\sum_{n=1}^{N}\exp\left(u_n^i\right)} = t_q^i. \tag{31}$$

Equation (30) divided by (31) yields the following:

$$\frac{\exp\left(u_p^i\right)}{\exp\left(u_q^i\right)} = \frac{t_p^i}{t_q^i}. \tag{32}$$

After transformation, the following is obtained:

$$\ln\left[\frac{\exp\left(u_p^i\right)}{\exp\left(u_q^i\right)}\right] = \ln\left(\frac{t_p^i}{t_q^i}\right). \tag{33}$$

Finally, we get the following:

$$u_p^i - u_q^i = \ln\left(\frac{t_p^i}{t_q^i}\right). \tag{34}$$

According to the properties of logarithmic function, when the difference between t_p^i and t_q^i is large, that is, the value of t_p^i/t_q^i is very large or very small, the value of $\ln(yo_p^i/yo_q^i)$will not change too much, and the difference of $|u_p^i - u_q^i|$ will become smaller. For example, if $t_p^i/t_q^i = 100000$, then $\ln(100000) = 11.51293$. Therefore, according to the analysis in Section 2.4.1, replacing t^i with u^i in the training of the network will be more reasonable.

After the training of the network is completed, the ith sample is fed into the neural network and the pth output U_p^i is obtained. On bringing U_p^i into (29), the actual output of the ith input is obtained by the following:

$$T_q^i = \frac{\exp\left(U_q^i\right)}{\sum_{n=1}^{N}\exp\left(U_n^i\right)}. \tag{35}$$

Summing all the equations in (35) yields the following:

$$\sum_{q=1}^{N} T_q^i = \sum_{q=1}^{N}\frac{\exp\left(u_q^i\right)}{\sum_{n=1}^{N}\exp\left(u_n^i\right)} = \frac{\sum_{q=1}^{N}\exp\left(u_q^i\right)}{\sum_{n=1}^{N}\exp\left(u_n^i\right)} = 1. \tag{36}$$

So, the model can satisfy the normalization of probability.

In summary, the outputs of neural network contain all the event which is the partition of probability space, so (36) holds without question.

$$\sum_{n=1}^{N} T_n^i = 1. \tag{37}$$

The equation set formed by (29) has a redundant equation, which can be seen from (36) and (37). N unknown variables cannot be solved by $N-1$ equations. Just let the one u_p^i be zero, and this problem can be solved.

It is difficult to solve the equation set formed by (29) directly. The method of element changing is introduced. Let $x_q^i = \exp(u_q^i)$, and then, (29) is transformed into the following:

$$\frac{x_q^i}{\sum_{n=1}^{N} x_q^i} = t_q^i. \tag{38}$$

If let $u_N^i = 0$, so $x_N^i = 1$. Equation (38) is transformed to the following:

$$\frac{x_q^i}{\left(\sum_{n=1}^{N-1} x_q^i + 1\right)} = t_q^i. \tag{39}$$

The equation set formed by (39) is the linear equations set. Solving it is very simple. After obtaining the solution to the equation set, the u_q^i can be obtained by the following:

$$u_q^i = \ln\left(x_q^i\right). \tag{40}$$

2.4.3. Adjustment of the Improved Backpropagation Neural Network Structure. Since the network output value in the improved BP neural network u_p^i does not need to be limited in this interval (0, 1), the activation function of the output layer $f_2(\cdot)$ can use the linear transfer function as follows to simplify the problem:

$$f_2(x) = x. \tag{41}$$

Then, the change value of weight in the output and hidden layers is obtained by gradient descent algorithm is as follows:

$$\Delta w_{kn} = \eta\left(t_n - yo_n\right)ho_n, \tag{42}$$

$$\Delta v_{mk} = \eta x_m f_1'\left(hi_k\right)\sum_{n=1}^{N}\left(t_n - yo_n\right)w_{kn}. \tag{43}$$

Similarly, during network training at a time, the change value of biases in the output and hidden layers obtained by the gradient descent algorithm is as follows:

$$\Delta b_n = \eta\left(t_n - yo_n\right), \tag{44}$$

$$\Delta b_k = \eta f_1'\left(hi_k\right)\sum_{n=1}^{N}\left(t_n - yo_n\right)w_{kn}. \tag{45}$$

2.5. Scope of Application of the Model. One of the core tasks of air traffic control in civil aviation is to ensure the safety of aircraft and avoid unsafe event. Unfortunately, Murphy's law tells us that absolute security does not exist. That is, it is difficult to succeed in completely avoiding unsafe event. Since it cannot be completely avoided, it must be scientifically confronted. For the department performing air traffic control work, it is very meaningful for air traffic safety management if it can predict the possibility of some unsafe event occurring. In this paper, BP neural network model is introduced into the probability prediction of unsafe event in air traffic control department. There are at least three practical applications:

(1) The improved model in this paper provides a theoretical approach to quantify the probability of unsafe event in ATC department.

As mentioned previously, expert assessment method is mostly used in air traffic control safety research in China at present. In this class of safety assessment method, experts assess the safety situation of air traffic control department based on their own knowledge and experience. There is no doubt that this assessment method plays a positive role in the safety management of air traffic control. However, this kind of evaluation method is mainly based on the qualitative evaluation of experts but has no enough quantitative analysis. At the same time, it is based on the subjective evaluation of experts and has no enough objectivity. In this paper, the neural network model is introduced into the prediction of unsafe event in the ATC department. The historical data are used as the basis to make the evaluation result more objective. The neural network is also a quantitative mathematical model, which is more objective than the qualitative evaluation.

(2)It can be used for the trend analysis of ATC safety development.

For the air traffic control department, the development trend of its risk has a significant impact on air traffic safety management. If the safety risk is increasing, the ATC department needs to invest more manpower, material, and financial resources into the safety management. If the safety risk is decreasing, the investment in safety management can be appropriately reduced according to the actual situation for reducing the cost. The changing trend of the rate of unsafe event reflects the development trend of safety risks to a certain extent. After predicting the probability of unsafe event in the future and combining the past and present rate of unsafe event, the safety risk trend of the ATC department can be judged, and the decision for the safety management of the ATC department can be made.

(3) It provides a method for calculating probabilities for risk assessment.

Risk assessment is a common method for civil aviation safety management. The "Safety Management Manual" prepared and published by International Civil Aviation Organization clearly defines risk as the product of the probability of an unsafe event and the consequences of the unsafe event. The Air Traffic Management Bureau of the Civil Aviation Administration of China has included this method in "Rules for Safety Management of Air Traffic Management Operation Department of Civil Aviation," However, neither the "Safety Management Manual" issued by the International Civil Aviation Organization nor "Rules for Safety Management of Air Traffic Management Operation Department of Civil Aviation," issued by the Civil Aviation Administration of China, give a specific method for calculating the probability of unsafe event. The model proposed in this paper provides a probability calculation method for the risk assessment for ATC department.

3. Numerical Example

The following is a numerical example to illustrate the advantages of the improved BP neural network proposed in this paper compared with other neural networks in the network training about unsafe event in air traffic control department.

3.1. Data. Suppose an air traffic control department wants to know the probability of unsafe event occurring in the next year. As analyzed in Section 2.3.3, four indicators of hardware, liveware, environment, and management related to SHEL model are used as inputs in BP neural network. Taking the unsafe event and safe event as outputs, the number of problems with management in the ATC department is used to quantify the management indicator. The number of problems with environment in the ATC department is used to quantify the environment indicator. The number of unsafe acts of human in the ATC department is used to quantify the liveware indicator. The number of equipment failures in the ATC department is used to quantify the hardware indicator. The occurrence rate of unsafe event is used to quantify the desired output of unsafe event. The occurrence rate of safe event is used to quantify the desired output of safe event. The historical data is as shown in Table 1, in which A_1 represents the safe event, $t(A_1)$ is the desired output of safe event, A_2 represents unsafe event, and $t(A_1)$ is the desired output of unsafe event. The historical data for numerical example is shown in Table 1.

3.2. Modeling. To prove that the model proposed in this paper can improve the prediction accuracy, three types of BP neural network are applied, which are called benchmark model and improved BP neural network. The benchmark model includes general BP neural network and normalized BP neural network. If the accuracy of the improved neural network is higher than the accuracy of the benchmark model used for comparison, it means that the improved neural network is meaningful. Therefore, we need to train the three

Table 1: Historical data for the numerical example.

No.	Liveware	Software	Hardware	Environment	$t(A_1)$	$t(A_2)$	$t(A_1)+t(A_2)$
1	2	8	8	8	0.999095	0.000905	1
2	2	1	7	10	0.999328	0.000672	1
3	1	6	7	10	0.999206	0.000794	1
4	4	10	4	2	0.999151	0.000849	1
5	8	5	10	10	0.999601	0.000399	1
6	9	1	3	5	0.999639	0.000361	1
7	5	3	2	7	0.999534	0.000466	1
8	5	8	3	4	0.999025	0.000975	1
9	9	4	5	5	0.999839	0.000161	1

different neural networks separately and compare the accuracy of the training results.

3.2.1. Benchmark Models

(1) General BP Neural Network. The principle of general BP neural network is shown in Section 2.2 The inputs and outputs are directly used to network training without any processing in the general BP neural network. To make the presentation clearer, the structure of the general BP neural network is described as follows. The prediction of probability of unsafe event in control department is essentially data fitting, by finding out inherent and opaque connections between the inputs and outputs through historical data. There is a consensus that the three-layer neural networks can fit most of the problems, so this model uses three-layer neural networks, which contain the input, hidden, and output layers:

(1) The input layer

Any safety-related influences can be used as inputs to the neural network, but these influences must be able to be quantified, meaning that these input data can be collected in practice. For a specific ATC department, as detailed in Section 2.3.3, the inputs of neural network can be found from the perspective of equipment, environment, personnel, and management according to SHEL model. At the same time, considering the collectability of the data, in this case, the following four indicators are used as inputs to the neural network, which are the number of equipment failures in the ATC department, number of equipment failures in the ATC department, number of problems related to management in the ATC department, and number of unsafe acts of human in the ATC department. It needs to be stressed again that, for the purpose of comparison, the input and output data are used directly to network training without any preprocessing.

(2) The hidden layer

The hidden layer needs to solve two problems: one is to determine the activation function and the other is to determine the number of nodes in the hidden layer. Considering that the domain of input in output layer may contain negative number, if the activation function of the hidden layer chooses the asymmetric sigmoid function, its output also used as the input of the output layer will not cover its domain. Therefore, the symmetric sigmoid function should be a better choice for the hidden layer as follows, whose range is in interval (−1, 1):

$$f_1(x) = \frac{(1-e^{-x})}{(1+e^{-x})}. \tag{46}$$

There is no method that everyone agrees on for figuring out the number of hidden layer nodes. Some experts have introduced an empirical formula as follows [54]:

$$K = \sqrt{M+N} + \alpha, \tag{47}$$

where K stands for the number in the hidden layer, M stands for the number in the input layer, and N stands for the number in the output layer, $\alpha \in [0, 10]$.

(3) The output layer

For the output layer, two problems need to be solved: one is to determine the output indicator and the other is the need to determine the activation function. There are some limitations on the output. First, the range of each output is in interval [0, 1]. Second, the outputs have to be the partition of the probability space. In order to meet the previously mentioned conditions, and taking into account the actual context of this case, there are two outputs, which are the probability of unsafe event and safe event. Since it is impossible to know the probability of unsafe event in advance, the occurrence rate of historical event can be used as the probability of ATC event for network training. The output layer chooses the asymmetric sigmoid function as activation function in the following, whose range is also in interval (0, 1), which is also the interval of the probability:

$$f_2(x) = \frac{1}{(1+e^{-x})}. \tag{48}$$

(2) Normalized Neural Network. The inputs, outputs, and number of nodes in the hidden layer of the normalized neural network are the same as those of the general neural network. In other words, the structure of the two networks is the same; the difference is that the normalized neural network needs to preprocess the input and output data before training.

The normalized neural network uses the following to normalize the inputs and outputs to the interval [−1, +1] based on the general BP neural network:

$$y = \frac{2(x - x_{\min})}{(x_{\max} - x_{\min})} - 1, \tag{49}$$

where y stands for the data used for training after normalization, $x_{\max}$ stands for the maximum value of an input or a output vector, and $x_{\min}$ stands for the minimum value of an input or a output vector. The normalized input and desired output data are shown in Table 2.

Because the outputs are normalized to the interval [−1, +1], the activation function of the output layer for the normalized neural network cannot use the sigmoid function whose range is in interval (0, 1). So, the linear function is used for activation function of the output layer as follows:

$$f_2(\cdot) = x. \tag{50}$$

In the normalized neural network model, the data used for training are normalized, and reverse normalization is required when making predictions or testing training accuracy. The reverse normalization formula is shown as follows:

$$x = \frac{(y+1) \times (x_{\max} - x_{\min})}{2} + x_{\min}. \tag{51}$$

The parameters in (51) can be referred to (49).

3.2.2. Improved BP Neural Network. The principle of improved BP neural network is shown in Section 2.4.3. In order to make the use of the improved neural network more clearly, the features of the improved neural network are summarized as follows:

(1) Defining the network structure

The purpose of defining the network structure is mainly to determine the number of inputs, outputs, and hidden layers of the network. For this case, the network structure of the three models is defined to be the same to make the comparison results more fairly. Details of the network structure can be found in Section 3.2.1.

(2) Output data preprocessing

First, let $u_2 = 0$. According to (38)–(40), u_1 can be calculated. See the third column data in Table 3. The network is trained with u_2 and u_1 as the target outputs of the neural network. Of course, to improve the speed of network training, we can also normalize the input and output of the network again for improved BP neural network.

(3) Network training

Network training involves the adjustment of weights and biases. The adjustment of weights and bias in the improved neural network are shown in (42) to (45).

(4) Probability of obtaining output

In the training process of the network, the original output data is not used. After the network training is completed, either to make predictions or calculate the accuracy of the training results, the network output needs to be converted to probability, and the conversion formula is shown in (29).

Table 2: Normalized input and desired output data.

Liveware	Software	Hardware	Environment	$t'(A_1)$	$t'(A_2)$
−0.75	0.556	0.5	0.5	−0.828	0.828
−0.75	−1	0.25	1	−0.256	0.256
−1	0.111	0.25	1	−0.555	0.555
−0.25	1	−0.5	−1	−0.69	0.69
0.75	−0.111	1	1	0.415	−0.415
1	−1	−0.75	−0.25	0.509	−0.509
0	−0.556	−1	0.25	0.251	−0.251
0	0.556	−0.75	−0.5	−1	1
1	−0.333	−0.25	−0.25	1	−1

3.2.3. Model Calculation Process. The raw data can be divided into training set, validation set, and test set in the training of neural network. The training set is used for network training, the validation set is used for checking if the training process is overfitting, and the test set is used to compare. In this paper, because the samples are not many, all the samples are used for training. At the same time, the training set also is used for comparing which model is better.

There is the question of why not collect more samples. The reason is that the quantitative data on the factors affecting unsafe event are confidential to the public for air traffic control department. For example, no one will make public the number of unsafe acts caused by ATC controllers in their department. The reason is simple things like that is not honorable. So, it is very difficult to get many operation data. Taking the actual situation mentioned previously into account, the data used in this numerical example is not many. Therefore, all samples are put in the training set.

Another question is how to validate the network and compare the network, if there is no validation set and test set? Test set is used to compare the accuracy of different neural networks, after the network is trained. In the absence of a test set, the training set can be used to calculate the accuracy of the network, which may have some impact in actual use, but the purpose in this paper is to compare the accuracy of different networks and determine which neural network model is more accurate. We only need to care about the order of the different network accuracies, not too much about what the exact accuracy of the network is, so doing this will not have much impact. The validation set is mainly used to avoid overfitting; when the overfitting is detected, the network will stop training. In addition to overfitting, the conditions for stopping training the network can be the maximum number of epochs to train, performance goal, minimum gradient, maximum time to train, and so on. So, the network can train without validation set. Of course, overfitting cannot be ignored. To avoid the effect of overfitting on model comparison, this paper makes a detailed explanation in Sections 3.3 and 3.4.

Table 3: Analysis results of the improved BP neural network.

$t(A_1)$	$t(A_2)$	u_1	$p(A_1)$	$p(A_2)$	$e(A_1)\times 10^{-5}$	$e(A_2)\times 10^{-5}$	$\mathrm{Re}(A_1)\times 10^{-5}$	$\mathrm{Re}(A_2)\times 10^{-2}$	$p(A)$
0.999095	0.000905	7.00667	0.99913018	0.00086982	3.52	3.52	3.52	3.89	1
0.999328	0.000672	7.30458	0.99932105	0.00067895	0.69	0.69	0.69	1.03	1
0.999206	0.000794	7.137632	0.99917990	0.00082010	2.61	2.61	2.61	3.29	1
0.999151	0.000849	7.070602	0.99914621	0.00085379	0.48	0.48	0.48	0.56	1
0.999601	0.000399	7.82615	0.99960591	0.00039409	0.49	0.49	0.49	1.23	1
0.999639	0.000361	7.926272	0.99962773	0.00037227	1.13	1.13	1.13	3.12	1
0.999534	0.000466	7.670859	0.99955517	0.00044483	2.12	2.12	2.12	4.54	1
0.999025	0.000975	6.932098	0.99901470	0.00098530	1.03	1.03	1.03	1.06	1
0.999839	0.000161	8.733945	0.99983823	0.00016177	0.08	0.08	0.08	0.48	1

The whole process is classified into four stages:

Step 1. The training set is brought into the different models as the inputs and desired outputs for network training.

Step 2. After the training is completed, all inputs are brought into the trained network to calculate the network outputs. For the normalized neural network, use the normalized input data as inputs.

Step 3. The network outputs are the actual outputs for the general BP neural network, because the inputs and outputs are not transformed in any way in this neural network. The actual outputs for the normalized neural network are obtained, after the network outputs are processed by the reverse normalization. The actual outputs for the improved BP neural network are obtained by bringing the network outputs into (29).

Step 4. At last, the absolute error and the relative error between the actual outputs and the desired outputs is calculated. The advantages and disadvantages can be derived by comparing the errors of different kinds of BP neural network. For the normalized neural network, use the normalized input data as inputs.

For the fairness of comparison, the computing parameters of different models are set to be the same. That is, the maximum number of iterations is 1000, the learning rate is 0.01, and the number of nodes in hidden layer is $K=10$ according to (47), considering $M=4$, $N=2$, and $\alpha=7$.

3.3. Results and Analysis

3.3.1. Detailed Analysis through One Training Result. Tables 3–5 show the results of different BP neural network, where $p(\cdot)$ is the probability of the different event, which also is the actual outputs of neural network. It is obtained by feeding the inputs into the trained network and is then transformed by reverse normalization in improved BP neural network and normalized BP neural network. $e(\cdot)$ represents the absolute error between the actual outputs and desired outputs, and $\mathrm{Re}(\cdot)$ represents the relative error between actual outputs and desired outputs. $p(A)$ is the sum of the probability of different event, which is used to check whether the normalization of probability is satisfied. The calculation formula of each parameter in the tables is as follows:

$$e(A_n) = \left|p(A_n) - t(A_n)\right|,$$
$$\mathrm{Re}(A_n) = \frac{e(A_n)}{t(A_n)}, \tag{52}$$
$$p(A) = p(A_1) + p(A_2),$$

where A_1 stands for safe event, and A_2 stands for unsafe event.

The analysis result of the general BP neural network is shown in Table 4. The analysis result of the normalized BP neural network is shown in Table 5. The analysis result of the improved BP neural network is shown in Table 3:

(1) From Table 3, it is easy to see that the sum of the actual outputs also used as the probability of ATC event is equal to one in the improved BP neural network. From Tables 4 and 5, it can be seen that whether outputs or inputs are normalized or not, general BP neural network and normalized BP neural network cannot guarantee that the sum of actual outputs is equal to one.

(2) By comparing the error of the three models, it is easy to see that the general BP neural network model has the worst training precision, especially that the precision of unsafe event is very poor, and there are some relative errors reaching dozens or hundreds of times. Obviously, such model cannot be applied to application. It is easy to see that the improved model has the best precision after comparing the errors of different models.

(3) In order to compare the accuracy of different models quantitatively on the whole, the mean square error is used to calculate the absolute total error AE and the relative total error RE of different models which is calculated as follows (the calculation results are shown in Table 6):

$$\mathrm{AE} = \sqrt{\frac{\sum_{i=1}^{9}\sum_{n=1}^{2}\left[e^i(A_n)\right]^2}{18}}, \tag{53}$$

$$\mathrm{RE} = \sqrt{\frac{\sum_{i=1}^{9}\sum_{n=1}^{2}\left[\mathrm{Re}^i(A_n)\right]^2}{18}}. \tag{54}$$

Table 4: Analysis results of the general BP neural network.

$t(A_1)$	$t(A_2)$	$p(A_1)$	$p(A_2)$	$e(A_1)\times 10^{-2}$	$e(A_2)\times 10^{-2}$	$\mathrm{Re}(A_1)\times 10^{-2}$	$\mathrm{Re}(A_2)\times 10^{0}$	$p(A)$
0.999095	0.000905	0.97353244	0.024643473	−2.56	2.37	−0.03	26.23	0.99818
0.999328	0.000672	0.931128293	0.008308042	−6.82	0.76	−0.07	11.36	0.93944
0.999206	0.000794	0.963675363	0.017205835	−3.55	1.64	−0.04	20.67	0.98088
0.999151	0.000849	0.886911194	0.12358584	−11.22	12.27	−0.11	144.57	1.01050
0.999601	0.000399	0.968466684	0.015835696	−3.11	1.54	−0.03	38.69	0.98430
0.999639	0.000361	0.981705286	0.116324163	−1.79	11.60	−0.02	321.23	1.09803
0.999534	0.000466	0.936218516	0.0111588	−6.33	1.07	−0.06	22.95	0.94738
0.999025	0.000975	0.933914479	0.031134188	−6.51	3.02	−0.07	30.93	0.96505
0.999839	0.000161	0.940056061	0.009269256	−5.98	0.91	−0.06	56.57	0.94933

Table 5: Analysis results of the normalized BP neural network.

$t(A_1)$	$t(A_2)$	$p(A_1)$	$p(A_2)$	$e(A_1)\times 10^{-5}$	$e(A_2)\times 10^{-5}$	$\mathrm{Re}(A_1)\times 10^{-5}$	$\mathrm{Re}(A_2)\times 10^{-2}$	$p(A)$
0.999095	0.000905	0.99900973	0.00096991	8.53	6.49	8.53	7.17	0.999980
0.999328	0.000672	0.99931329	0.00065971	1.47	1.23	1.47	1.83	0.999973
0.999206	0.000794	0.99930812	0.00073200	10.21	6.20	10.22	7.81	1.000040
0.999151	0.000849	0.99908764	0.00085421	6.34	0.52	6.34	0.61	0.999942
0.999601	0.000399	0.99965091	0.00034770	4.99	5.13	4.99	12.86	0.999999
0.999639	0.000361	0.99976458	0.00024216	12.56	11.88	12.56	32.92	1.000007
0.999534	0.000466	0.99938241	0.00059731	15.16	13.13	15.17	28.18	0.999980
0.999025	0.000975	0.99926498	0.00081474	24.00	16.03	24.02	16.44	1.000080
0.999839	0.000161	0.99962508	0.00036466	21.39	20.37	21.40	126.50	0.999990

It is not difficult to see from Table 6 that the improved neural network model has the highest precision, because both the absolute total error and the relative total error of this model are minimal.

3.3.2. Comprehensive Analysis through 100 Training Sessions. The previously mentioned analysis is based on the training results of each neural network at one time, and we can visualize the difference in the training accuracy of different neural networks from a numerical perspective. It is well known that the training process of neural networks is an optimal optimization process, in which the output error is minimized as the objective function and the network weights and bias are the decision variables. To prevent the neural network from falling into local optimum, when initializing the weights and bias, random initialization is used and multiple training will be performed to take the best one for the actual application. Therefore, the one-time training results cannot fully demonstrate the advantages of the improved model proposed in this paper in terms of training accuracy. To address this issue, we made 100 training sessions for each network and calculated their average error from 1 to 100 times, as shown in Figure 2. The black curve is the change of the average error of the improved neural network with the training sessions. The red curve is the change of the average error of the normalized neural network with the training sessions. The blue curve is the change of the average error of the general neural network with the training sessions. It can be easily seen from the figure that the average error of the improved neural network is the best at any time. It is enough to prove that the higher training accuracy of the improved neural network is not accidental.

Table 6: Precision analysis of different models.

General BP	Absolute total error (AE)	4.234648×10^{-2}
	Relative total error (RE)	8.547633×10^{-0}
Normalized BP	Absolute total error (AE)	1.238086×10^{-4}
	Relative total error (RE)	3.199931×10^{-1}
Improved BP	Absolute total error (AE)	1.730846×10^{-5}
	Relative total error (RE)	1.834107×10^{-2}

3.3.3. Excluding the Effect of Overfitting on Accuracy. Overfitting is a potential pitfall in neural network training. Since the samples collected in this paper are not many, all samples are used for training. Inevitably, a question arises whether the improved neural network in this paper is overfit to make the accuracy higher than the accuracy of other benchmark models. To illustrate this question, first, we are clear that overfitting may be caused by an increase in the number of training epochs. Based on this consensus, we compare the accuracy of the three models under different number of training epochs one by one. At the early stage of training, the number of training epochs is low, and the possibility of overfitting is extremely low, at which time we compare the training accuracy, and the higher accuracy of the improved neural network due to overfitting can be excluded. To improve the fairness of comparison, the training parameters of the three different neural network models are set to be the same, the maximum epochs of training is 1000, the learning rate is 0.01, and the same gradient descent algorithm is used. At the same time, to avoid the influence of falling to the local optimum on the training results, all three models are initialized by randomly assigning weights and bias to the network. Considering the randomness of the single training results, the average error is

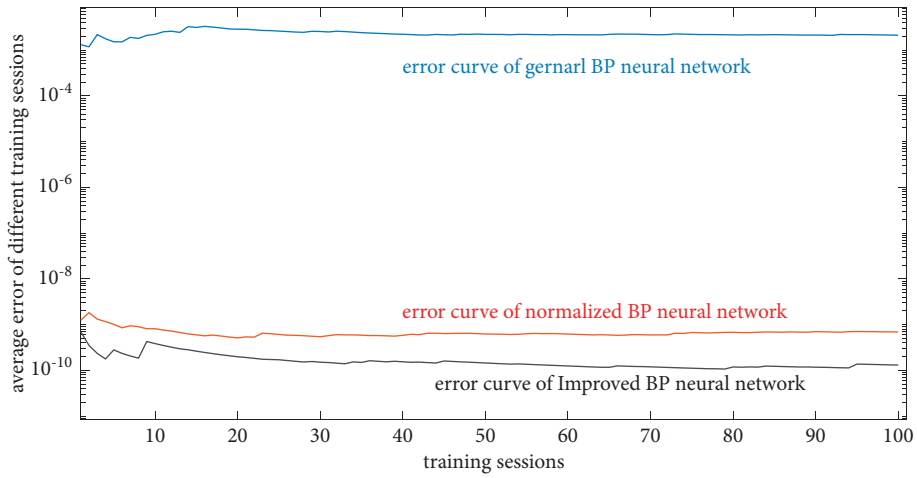

Figure 2: Average error of different networks with different training times.

taken for comparison after 100 independent training sessions. The training results are shown in Figure 3. The horizontal axis represents the 1000 training epochs, and the vertical axis represents the average error of 100 training sessions at each training epochs. The black curve is the change of the average error of the improved neural network after 100 training sessions with the number of training epochs. The red curve is the change of the average error of the normalized neural network after 100 training sessions with the training epochs. The blue curve is the change of the average error of the general neural network after 100 training sessions with the training epochs. It is not difficult to see from the figure that, at every training epoch, the accuracy of the improved neural network proposed in this paper is higher than that of the benchmark model, which excludes the possibility that the improved neural network has high accuracy due to overfitting.

3.4. Application of the Model. The trained BP neural network can be used for prediction of unsafe event in ATC department, by feeding new inputs to the network. For example, the safety managers in an air traffic control department have formulated the safety management objective in the next year, which requires that the number of unsafe acts of the controllers should not exceed five, the number of equipment failures should not exceed four, the number of management problems that cannot be solved in time should not exceed six, and the number of environmental problems should not exceed four. The question is what is the probability of an unsafe event, given that the above objectives can be achieved? The question can be answered using the model proposed in this paper. The solution process is described as follows.

In this paper, the entire samples are used for network training because of the limited samples, which is feasible for comparing the accuracy of different networks. However, when using the network for practical application, this approach may result in overfitting and lead to reduction in the generalization ability of the model. For addressing this problem, the early stopping method can be used to avoid overfitting. The general practice is to first divide the data into three subsets. The first subset is the training set, which is used for computing the gradient and updating the network weights and biases. The second subset is the validation set. The error on the validation set is monitored during the training process. The validation error normally decreases during the initial phase of training, as does the training set error. However, when the network begins to overfit the data, the error on the validation set typically begins to rise. The training stops when the error of the validation set is found to grow continuously in the training. The network weights and biases are saved at the minimum of the validation set error. The test set error is not used during training, but it is used to compare different model. Of course, the prerequisite is that there is enough data to ensure that there are enough samples in the different sets.

To illustrate the use of the network, the samples in Table 1 are divided into three sets, the training set, the validation set, and the test set. The training set contains five samples, whose number is 2, 6, 7, 8, and 9 in Table 1. The validation set contains two samples, whose number is 4 and 5 in Table 1. The test set contains two samples, whose number is 1 and 3 in Table 1. There are two points to clarify: one is that how the samples in the set are assigned is random, and the samples in the previously mentioned set is the outcome after the authors have divided samples to different set and trained the network many times to achieve the best result. The other is that this process is only to demonstrate the use of the model, since the samples are not many. The training results may not be very good. This is the reason why all the samples are input to training without dividing the sample into different set, when the network comparison was made in Section 3.3.

The training parameters are as follows: the learning rate is 0.01, the maximum number of epochs to train is 1000, the performance goal of training set is zero, and the maximum validation failures of validation set is six. After performing many training sessions, a network with better results was selected for illustration. The performance curves for different sets of improved BP neural network are shown in Figure 4.

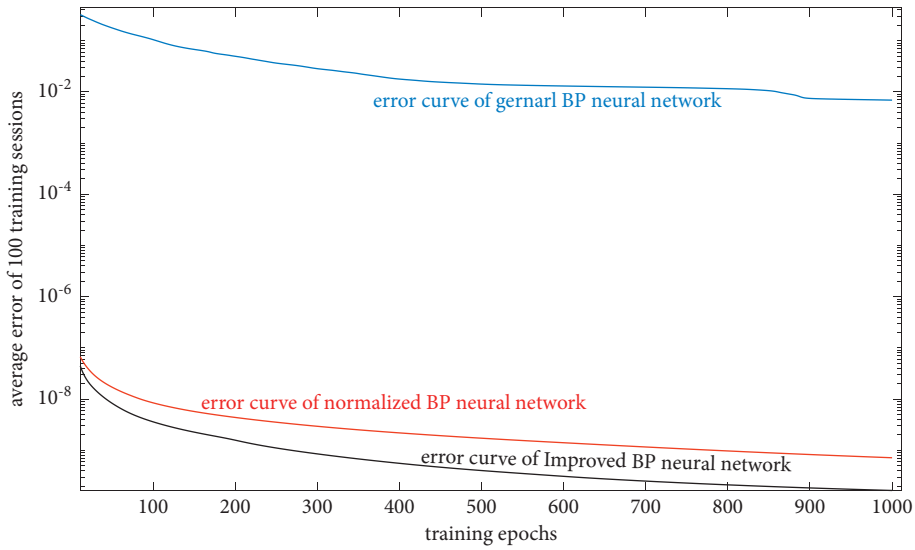

Figure 3: Average error of 100 training sessions of different neural network regarding training epochs.

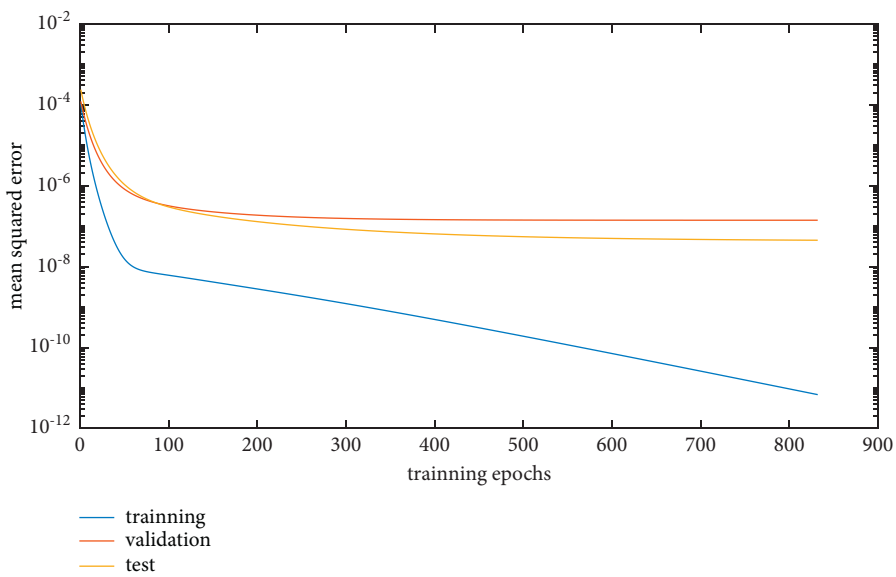

Figure 4: Performance curves for different sets of improved BP neural network.

In this training process, with the increase of training epochs, the errors of different sets are decreasing, and the decrease rate is smaller and smaller, which is fully consistent with the properties of gradient descent method. When the training epoch reaches 831, the error in the validation set was increasing for six consecutive times (the increase is small and the curve in Figure 4 is not clear) and reaches the maximum validation failure set by user. At this time, if the training continues, overfitting will occur, so the network stopped training. Obviously, the optimal network is obtained at 825 training epoch, so the network at this time can be used for practical applications.

Once the network has been trained, the question proposed in the first paragraph in this section on how to apply the trained network and known conditions to predict the probability of an unsafe event should be the focus. In fact, when the network has been trained, the problem becomes very simple. The probability can be predicted by feeding this set of data [5, 4, 6, 4] into the network. The predicted result is that the probability of unsafe event is 0.0006093, and the probability of safe event is 0.9993907.

3.5. Summary

(1) With its powerful ability of function fitting, BP neural network can be used to effectively predict the probability of unsafe event in air traffic control department, after reasonably designing the network structure and collecting historical data for training the neural network.

(2) The general BP neural network cannot guarantee the accuracy of output, if it is directly applied to predict the probability of unsafe event in ATC department, and it cannot ensure normalization of probability. However, after normalization of inputs and outputs before training the network with the help of normalized BP neural network, the prediction accuracy is improved, but the normalization of probability for actual outputs is still difficult to satisfy.

(3) The improved BP neural network proposed in this paper has high accuracy for the training of small probability event and can guarantee that the sum of the probability of all events is equal to one.

4. Conclusions

As an important means to ensure the safety of civil aviation, air traffic control plays a pivotal role in the protection of passengers' lives and property. To improve the level of safety management of the department which performs air traffic control work, the authors introduce artificial neural network to predict the probability of unsafe event for the air traffic control department. A three-layer neural network containing an input layer, hidden layer, and output layer is designed to solve the problem. The influence that affects ATC safety but can be quantified and collected is used as inputs according to SHEL model. The probability of unsafe event is used as the outputs of the network. The general BP neural network cannot be used for the network training of small probability event, which is proved theoretically in this paper, because the general BP neural network does not ensure that the sum of probability of all the outputs is equal to one and the error between the actual outputs and desired outputs is very large after the training of neural network. To address this issue, a new mapping method is put forward from the probabilistic viewpoint in this paper. It is theoretically proved that the mapping method proposed in this paper can not only improve the training accuracy, but also ensure that the sum of probability is equal to one. Finally, a case study demonstrates that the improved BP neural network model in this paper has a higher accuracy in predicting the probability of unsafe event in the air traffic control department.

However, one should note that this study also has two limitations, which should be improved in future research endeavors. The first limitation is that our current analysis is based on Chinese civil aviation. In particular, the outputs of the neural network are built on the air traffic management rules of civil aviation in China. So, if the model is used outside of China, the outputs of the network need to be modified according to the actual situation in other countries. The second limitation is that, like other artificial neural networks, the number of the nodes in the hidden layer has a great influence on the accuracy of the network, which is the common fault of artificial neural network models. In the actual application, the number of the nodes in the hidden layer needs to be adjusted several times to achieve good results.

BP neural network needs data for training. If a few data in the dataset are wrong, these wrong data will have side effects on network training. When a large amount of data is collected, the data should be preprocessed to remove the unreasonable data, which is very helpful to improve the accuracy of the network. This paper does not study the method of filtering data, and how to filter the data to remove some unreasonable data is the direction of future research.

Data Availability

Data used to support this study are available from the corresponding author upon request.

Conflicts of Interest

The authors declare that there are no conflicts of interest regarding the publication of the paper.

Acknowledgments

This research was supported by the General Project of Science and Technology Department of Sichuan Province (no. 2020YJ0500), General Project of Civil Aviation Flight University of China (nos. J2015-53, J2016-22, and J2019-105), Special Fund Project of Education and Teaching Reform of China (no. E2020028-5), and Open Fund of Key Laboratory of Flight Techniques and Flight Safety (grant no. FZ2020KF08).

References

[1] P. Zhao, D. Lu, H. Hu et al., "Population-development oriented comprehensive modern transport system in China," *Acta Geographica Sinica*, vol. 75, no. 12, pp. 2699–2715, 2020.

[2] C. Fu, "Evaluation on integrated transportation capacity and coordination in the urban agglomeration," *Journal of Transportation Systems Engineering and Information Technology*, vol. 17, no. 2, pp. 21–27, 2017.

[3] M. Shang and L. Zhang, "Study on the optimization of comprehensive transportation system in China under the perspective of total factor efficiency," in *Proceedings of the 2nd International Conference on Advances in Energy Resources and Environment Engineering*, Sapporo, Japan, August 2017.

[4] J. Jia and Y. Fang, "Underground space development in comprehensive transport hubs in China," in *Proceedings of the 15th International Scientific Conference Underground Urbanisation as a Prerequisite for Sustainable Development*, St. Petersburg, Russia, September 2016.

[5] N. Wang and W. Li, "Thoughts on China's comprehensive transportation system under financial crisis," in *Proceedings of the 5th Advanced Forum on Transportation of China*, Beijing, China, October 2009.

[6] Carnoc, "The work of China's civil aviation in 2019," 2020, http://news.carnoc.com/list/518/518087.html.

[7] S. A. Gómez, A. Goron, A. Groza, and I. A. Letia, "Assuring safety in air traffic control systems with argumentation and model checking," *Expert Systems with Applications*, vol. 44, pp. 367–385, 2016.

[8] J. Tang and B. Dong, "Safety risk evaluation of air traffic management system based on combination weights method

and matter element model," *Advances in Aeronautical Science and Engineering*, vol. 12, no. 1, pp. 30–38, 2021.

[9] H. H. De Jong, S. H. Stroeve, and H. A. P. Blom, "The roles of air traffic controllers and pilots in safety risk analysis," in *Proceedings of the European Safety and Reliability Conference 2006*, Estoril, Portugal, September 2006.

[10] J. Guo, C. Pan, and Y. Liao, "A method for unsafe event prediction of air traffic management (ATM) based on GBO-Markov model," *Journal of Safety and Environment*, vol. 16, no. 4, pp. 48–51, 2016.

[11] Z. Zhang and W. Li, "Study on risk control network model of approach control system," *China Safety Science Journal*, vol. 29, no. 2, pp. 32–37, 2019.

[12] Y. Zhao and J. Wan, "On the operational risk assessment of the air traffic control based on the set pair analysis method," *Journal of Safety and Environment*, vol. 18, no. 3, pp. 871–875, 2018.

[13] Y. Zhao and J. Wan, "An operational risk assessment model for air traffic control based on the set pair extension coupling method," *Journal of Safety and Environment*, vol. 18, no. 6, pp. 2059–2063, 2018.

[14] Y. Zhang, X. Wang, M. Wu et al., "Evaluation of the unconventional operational risks for the air traffic control based on the fuzzy hierarchical analysis process and the cloud model," *Journal of Safety and Environment*, vol. 16, no. 4, pp. 42–47, 2016.

[15] F. Chen, Q. Chen, and B. Xu, "Analysis on operation risk topics of air traffic control (ATC) based on text mining," *Journal of Safety Science and Technology*, vol. 16, no. 11, pp. 47–52, 2020.

[16] Y. Sikirda, T. Shmelova, and D. Tkachenko, "Automated system for evaluation of the organizational risk factors influence on flight safety in air traffic control," in *Proceedings of the 2018 IEEE 5th International Conference on Methods and Systems of Navigation and Motion Control*, Kiev, Ukraine, October 2018.

[17] K. Zhang, R. Sun, W. Feng et al., "Discussion on construction of safety integrity system in air traffic control," in *Proceedings of the 6th International Symposium on Project Management*, Chongqing, China, July 2018.

[18] J. A. Adam, "Air traffic control: satellites and artificial intelligence promise improved safety and efficiency," *IEEE Spectrum*, vol. 28, no. 2, pp. 27–32, 1991.

[19] V. D. Hopkin, "Safety and human error in automated air traffic control," *IEEE Conference Publication*, vol. 463, pp. 113–118, 1999.

[20] J. Zhang, W. Wang, Y. Liu et al., "Establishment of the safety culture in civil aviation air traffic control," in *Proceedings of the 12th COTA International Conference of Transportation Professionals*, Beijing, China, August 2012.

[21] Z. Bingxiang and L. Jimin, "Research on safety level assessment of air traffic control," in *Proceedings of the 2010 International Conference on Computer and Communication Technologies in Agriculture Engineering*, Chengdu, China, June 2010.

[22] Z. Guoliang and Y. Shaohua, "Evolution of safety management in China's air traffic control safety risk information management," in *Proceedings of the IFA 34th International Conference, and IATA-Sharing Knowledge to Improve Safety*, Shanghai, China, August 2004.

[23] Q. Wang and D. Yao, "A new method for evaluating air traffic control safety," in *Proceedings of the 2017 6th International Conference on Network, Communication and Computing*, Kunming, China, December 2017.

[24] J. Wan and M. Zhang, "Evaluation of air traffic control risk situation based on game theory and set pair analysis," *China Safety Science Journal*, vol. 28, no. 11, pp. 142–148, 2018.

[25] D. Yuan, Y. Lei, and N. Yang, "Approach to the aviation and air traffic and transportation safety evaluation based on the Dempster's combination rule," *Journal of Safety and Environment*, vol. 18, no. 3, pp. 1014–1019, 2018.

[26] D. Yao, Q. Wang, and X. Gan, "Safety risk assessment on the air traffic control via the improved fuzzy petri net," *Journal of Safety and Environment*, vol. 18, no. 2, pp. 413–417, 2018.

[27] J. Wang and X. Sun, "Research on safety analysis of air traffic control system based on STPA," *Journal of Wuhan University of Technology*, vol. 39, no. 12, pp. 49–55, 2017.

[28] Y. Liao, J. Guo, and C. Yang, "Probability assessment of ATC safety based on Bayes analysis," *China Sciencepaper*, vol. 10, no. 19, pp. 2271–2275, 2015.

[29] Y. Lin, L. Li, H. Jing, B. Ran, and D. Sun, "Automated traffic incident detection with a smaller dataset based on generative adversarial networks," *Accident Analysis & Prevention*, vol. 144, Article ID 105628, 2020.

[30] L. Li, Y. Lin, B. Du, F. Yang, and B. Ran, "Real-time traffic incident detection based on a hybrid deep learning model," *Transportmetrica A: Transportation Science*, vol. 16, no. 4, pp. 1–21, 2020.

[31] P. Mercader and J. Haddad, "Automatic incident detection on freeways based on Bluetooth traffic monitoring," *Accident Analysis & Prevention*, vol. 146, Article ID 105703, 2020.

[32] J. D. G. Paule, Y. Sun, and Y. Moshfeghi, "On fine-grained geolocalisation of tweets and real-time traffic incident detection," *Information Processing & Management*, vol. 56, no. 3, pp. 1119–1132, 2019.

[33] J. Lu, S. Chen, W. Wang, and B. Ran, "Automatic traffic incident detection based on nFOIL," *Expert Systems with Applications*, vol. 39, no. 7, pp. 6547–6556, 2012.

[34] X. Zhou, T. Chen, and T. Qiu, "BP neural network forecast of flight "estimated final arrival time" based on Levenberg-Marquardt algorithm optimization," in *Proceedings of the 2020 5th International Conference on Electromechanical Control Technology and Transportation*, Nanchang, China, May 2020.

[35] W. S. Mcculloch, "A heterarchy of values determined by the topology of nervous nets," *Bulletin of Mathematical Biophysics*, vol. 7, no. 2, pp. 89–93, 1945.

[36] Z. Wu, S. Tian, and L. Ma, "A 4D trajectory prediction model based on the BP neural network," *Journal of Intelligent Systems*, vol. 29, no. 1, pp. 1545–1557, 2020.

[37] Y. Yang, L. Chen, Y. Xiong, S. Li, and X. Meng, "Global sensitivity analysis based on bp neural network for thermal design parameters," *Journal of Thermophysics and Heat Transfer*, vol. 35, no. 1, pp. 187–199, 2021.

[38] I. J. Goodfellow, D. Erhan, P. Luc Carrier et al., "Challenges in representation learning: a report on three machine learning contests," *Neural Networks*, vol. 64, pp. 59–63, 2015.

[39] L. Xu, T. Quan, J. Wang et al., "GR and BP neural network-based performance prediction of dual-antenna mobile communication networks," *Computer Networks*, vol. 172, Article ID 107172, 2020.

[40] L. Wang and X. Bi, "Risk assessment of knowledge fusion in an innovation ecosystem based on a GA-BP neural network," *Cognitive Systems Research*, vol. 66, pp. 201–210, 2021.

[41] Y. Guo, "Credit risk assessment of P2P lending platform towards big data based on BP neural network," *Journal of Visual Communication and Image Representation*, vol. 71, Article ID 102730, 2020.

[42] M. Zou, L. Xue, H. Gai et al., "Identification of the shear parameters for lunar regolith based on a GA-BP neural network," *Journal of Terramechanics*, vol. 89, pp. 21–29, 2020.
[43] J. Hao, Y. Lin, G. Ren et al., "Comprehensive benefit evaluation of conservation tillage based on BP neural network in the Loess Plateau," *Soil and Tillage Research*, vol. 205, Article ID 104784, 2021.
[44] Y. Zhou and S. Li, "BP neural network modeling with sensitivity analysis on monotonicity based spearman coefficient," *Chemometrics and Intelligent Laboratory Systems*, vol. 200, Article ID 103977, 2020.
[45] M. Mirsadeghi, M. Shalchian, S. R. Kheradpisheh et al., "STiDi-BP: spike time displacement based error backpropagation in multilayer spiking neural networks," *Neurocomputing*, vol. 427, pp. 131–140, 2021.
[46] Z. Yu, L. Qin, Y. Chen et al., "Stock price forecasting based on LLE-BP neural network model," *Physica A: Statistical Mechanics and Its Applications*, vol. 553, Article ID 124197, 2020.
[47] A. Oztekin, *Development of a Safety Assessment Tool for Air Traffic Control System*SAE International, Warrendale, PA, USA, 2015.
[48] M. Pęski, "Large roommate problem with non-transferable random utility," *Journal of Economic Theory*, vol. 168, pp. 432–471, 2017.
[49] J. L. Lusk, J. M. Crespi, B. R. Mcfadden et al., "Neural antecedents of a random utility model," *Journal of Economic Behavior & Organization*, vol. 132, pp. 93–103, 2016.
[50] M. S. Hasnine, A. Graovac, F. Camargo et al., "A random utility maximization (RUM) based measure of accessibility to transit: accurate capturing of the first-mile issue in urban transit," *Journal of Transport Geography*, vol. 74, pp. 313–320, 2019.
[51] A. Papola, F. Tinessa, and V. Marzano, "Application of the combination of random utility models (CoRUM) to route choice," *Transportation Research Part B: Methodological*, vol. 111, pp. 304–326, 2018.
[52] D. Hojo, K. Murono, H. Nozawa et al., "Utility of a three-dimensional printed pelvic model for lateral pelvic lymph node dissection education: a randomized controlled trial," *Journal of the American College of Surgeons*, vol. 229, no. 6, pp. 552–559, 2019.
[53] K. J. Ray, P. Lalitha, N. V. Prajna et al., "The utility of repeat culture in fungal corneal ulcer management: a secondary analysis of the MUTT-I randomized clinical trial," *American Journal of Ophthalmology*, vol. 178, pp. 157–162, 2017.
[54] C. Song, S. Xie, J. Wang et al., "Research on tower crane safety based on grey relation and BP neural network," *Computer Simulation*, vol. 36, no. 10, pp. 472–476, 2019.

Hindawi
Mathematical Problems in Engineering
Volume 2021, Article ID 2232696, 8 pages
https://doi.org/10.1155/2021/2232696

Research Article

Study on Single-Machine Group Scheduling with Due-Window Assignment and Position-Dependent Weights

Weiguo Liu, Xuyin Wang, Xiaoxiao Wang, and Peizhen Zhao

Business School, Northwest Normal University, Lanzhou 730070, China

Correspondence should be addressed to Weiguo Liu; lwgwinterplum@163.com

Received 24 May 2021; Revised 3 August 2021; Accepted 11 August 2021; Published 26 August 2021

Academic Editor: Samuel Yousefi

This article considers a single-machine group scheduling problem with due-window assignment, where the jobs are classified into groups and the jobs in the same group must be processed in succession. The goal is to minimize the weighted sum of lateness and due-window assignment cost, where the weights depend on the position in which a job is scheduled (i.e., position-dependent weights). For the common, slack, and different due-window assignment methods, we prove that the problem can be solved polynomially, i.e., in $O(N\log N)$ time, where N is the number of jobs.

1. Introduction

Group scheduling (GS) is an approach, which schedules jobs with similar characteristics close together and reduces tooling changeovers and in-process inventories to improve efficiency in high-volume production (Neufeld et al. [1], Lu et al. [2], Yin et al. [3], and Wang and Liu [4]). Wang and Wang [5] studied the single-machine group scheduling problem with ready times and time-dependent processing times. Under the case of the group setup times and job processing times are proportional linear deterioration functions, they proved that the makespan minimization problem can be solved in polynomial time. He and Sun [6] considered the single-machine group scheduling problem with general deteriorating jobs and learning effects. They proved that the makespan and the sum of completion times minimizations remain solvable in polynomial time. Lu et al. [7] considered the single-machine group scheduling with learning effects and resource allocation. For the makespan minimization subject to limited resource availability, they proved that the problem can be solved in polynomial time under some special cases. For the general case, they proposed heuristic and branch-and-bound algorithms. Zhang et al. [8] studied the single-machine group scheduling with position-dependent processing times. For the makespan and the total completion time minimizations, they proved that the problem can be solved in polynomial time. Liu et al. [9] considered the single-machine group scheduling with the proportional deterioration effect. For the makespan minimization with release times, they proposed heuristic and branch-and-bound algorithms. Huang [10] studied the single-machine group problem with proportional deterioration effects, where the total weighted completion time minimization is the primary criterion and the maximum cost minimization is the secondary criterion. They proved that the problem remains solvable in polynomial time. Wang and Liang [11] and Liang et al. [12] considered the single-machine group scheduling problem with deteriorating jobs and resource allocation. Qin et al. [13] considered the flowshop group scheduling problem with learning effects. For some regular objectives (including the makespan, total completion time, total weighted completion time, and maximum lateness), they proposed heuristics and metaheuristics.

On the other hand, due to the increasing interest in the just-in-time (JIT) system, the problem of the due-date assignment has been closely focused on by scholars (Yin et al. [14], Wang et al. [15], and Shabtay [16]). However, under the group technology, there are relatively few studies on the problem of the assignment of jobs. Li et al. [17] studied the single-machine group scheduling with due-date assignment. For the common (CON), slack (SLK), and different (DIF) due-date assignment methods, they proved

that the nonregular objective minimization can be solved in polynomial time. Sun et al. [18], Lv et al. [19], and Wang et al. [20] considered single-machine group scheduling problems with resource allocation and learning effect. Under slack due-date assignment and the linear and convex resource consumption functions, Sun et al. [18] gave some results. Lv et al. [19] showed by two counter examples that the results of Sun et al. [18] were incorrect. Under the convex resource allocation, for some special cases, Wang et al. [20] proved that the problem can be solved in polynomial time. For the general case of the problem, Wang et al. [20] proposed the heuristic, tabu search, and branch-and-bound algorithms.

Recently, Wang et al. [21] considered the single-machine group scheduling problem with due-date assignment and positional-dependent weights. For the CON, SLK, and DIF due-date assignments, they proved that the problem can be solved in polynomial time. The importance of due-window assignment scheduling is widely recognized for the production company [22–27]. Ji et al. [28] investigated the single-machine group scheduling with slack due-window assignment. They proved that the nonregular objective minimization (including the earliness, tardiness, due-window starting time, and due-window size) can be solved in polynomial time. Li and Zhao [29] studied the single-machine group scheduling problem with multiple due-windows assignment. The objective is to determine an optimal sequence for both groups and jobs, and optimal due-windows such that the total cost of earliness, tardiness, and due-windows assignment is minimized. They showed that the problem can be solved in polynomial time. "The application of problems with positional-dependent weights can be found in many practical settings, such as the busyness of production services often changes with time. The weight of the processing queue can be increased when the production efficiency of a certain period of time needs to be improved. For example, in the Didi taxi dispatching (a similar mode to Uber), orders placed in the morning offer a higher bonus to the driver, which can effectively improve customer satisfaction in these locations by better meeting the needs of customers going to work in the morning [30]." In this article, the results of Wang et al. [21] are extended to the case of the due-window assignment with position-dependent weights (Wang et al. [24], Wang et al. [25], and Wang et al. [31]). In other words, this article studies the group scheduling with the due-window assignment and position-dependent weights, i.e., our model is more general and covers the results of Wang et al. [21], Wang et al. [24], and Wang et al. [25].

The rest of the study is organized as follows: in Section 2, the model and problem is formulated. In Section 3, we present several results of the optimal solution. In Section 4, some examples are given. In Section 5, the conclusions are summarized.

2. Problem Formulation

The notations used throughout this article are tabulated in Table 1.

Table 1: List of notations.

Notations	Definitions
N	Number of jobs
m	Number of groups
$T_l\,(l=1,2,\ldots,n)$	Index of job
$\widetilde{G}_h\,(h=1,2,\ldots,m)$	Index of group
n_h	Number of group $\widetilde{G}_h$
$T_{h,l}$	Job T_l of group $\widetilde{G}_h$
s_h	Setup time of group $\widetilde{G}_h$
$p_{h,l}$	Processing time of job $T_{h,l}$
$\langle d'_{h,l}, d''_{h,l}\rangle$	Due-window of job $T_{h,l}$
$d'_{h,l}$	Due-window starting time of job $T_{h,l}$
$d''_{h,l}$	Due-window finishing time of job $T_{h,l}$
$D_{h,l}=d''_{h,l}-d'_{h,l}$	Due-window size of job $T_{h,l}$
$C_{h,l}$	Completion time of job $T_{h,l}$
$d'_h(d''_h)$	Starting (finishing) time of common due-window in group $\widetilde{G}_h$
$q'_h(q''_h)$	Common flow allowance of slack due-window in group $\widetilde{G}_h$
ξ	An optimal schedule of jobs
$L_{h,l}$	Lateness penalty of job $T_{h,l}$
$\vartheta_{h,l}\,(l=1,2,\ldots,n_h)$	Weight of the lth position in group $\widetilde{G}_h$
$\vartheta_{h,0}$	Unit cost of $d'_{h,l}$
ϑ_{h,n_h+1}	Unit cost of $D_{h,l}$
CONDW	Common due-window assignment
SLKDW	Slack due-window assignment
DIFDW	Different due-window assignment
$[l]$	Job scheduled in the lth position
$\Phi_{h,l}$	Weight cost of lth position in group $\widetilde{G}_h$
Ω_h	Weight factor of group $\widetilde{G}_h$

There are N jobs ready to be processed on a single machine, and all the jobs are divided (grouped) into m groups $\{\widetilde{G}_1,\widetilde{G}_2,\ldots,\widetilde{G}_m\}$ in advance. All the jobs are available at time 0 and job preemption is not allowed. Each group $\widetilde{G}_h$ has n_h jobs, i.e., $\{T_{h,1},T_{h,2},\ldots,T_{h,n_h}\}$, where $T_{h,l}$ denotes the job T_l of group $\widetilde{G}_h$ and $n_1+n_2+\cdots+n_m=N$ $(h=1,2,\ldots,m, l=1,2,\ldots,n_h)$. The jobs in the same group must be processed in succession and do not need setup times, and each group $\widetilde{G}_h$ requires an independent setup time s_h. Each job $T_{h,l}$ has a processing time $p_{h,l}$ and a due-window $\langle d'_{h,l}, d''_{h,l}\rangle$, where $d'_{h,l}\le d''_{h,l}$, $d'_{h,l}(d''_{h,l})$ is the due-window starting (finishing) time of job $T_{h,l}$ in group $\widetilde{G}_h$, $D_{h,l}=d''_{h,l}-d'_{h,l}$ is due-window size, and both $d'_{h,l}$ and $d''_{h,l}$ are decision variables. The due-window is assignable according to the following three methods:

(1) The common due-window (CONDW) assignment: all jobs in group $\widetilde{G}_h$ are assigned the same due-window, i.e., $d'_{h,l}=d'_h$ and $d''_{h,l}=d''_h$ $(h=1,2,\ldots,m, l=1,2,\ldots,n_h)$

(2) The slack due-window (SLKDW) assignment: $d'_{h,l}=p_{h,l}+q'_h$ and $d''_{h,l}=p_{h,l}+q''_h$ $(h=1,2,\ldots,m, l=1,2,\ldots,n_h)$

(3) The different due-window (DIFDW) assignment: the due-window $\langle d'_{h,l}, d''_{h,l}\rangle$ for all jobs of group $\widetilde{G}_h$ is assigned with no restrictions $(h=1,2,\ldots,m, l=1,2,\ldots,n_h)$

Let $C_{h,l}$ be the completion time of job $T_{h,l}$. The objective of the study is to determine $d'_{h,l}$ and $d''_{h,l}$ (i.e., for CONDW, determine d'_h and d''_h; for SLKDW, determine q'_h and q''_h; and for DIFDW, determine $d'_{h,l}$, $d''_{h,l}$ of all jobs) and an optimal schedule ξ to minimize a cost function that comprises lateness (earliness-tardiness) penalties, due-window starting time, and due-window size costs, i.e.,

$$F\left(\xi, d'_{h,l}, d''_{h,l}\right) = \sum_{h=1}^{m}\sum_{l=1}^{n_h}\left(\vartheta_{h,l}L_{\xi(h,[l])} + \vartheta_{h,0}d_{\xi(h,[l])}{}' + \vartheta_{h,n_h+1}D_{\xi(h,[l])}\right), \tag{1}$$

where $\vartheta_{h,l}$ is the weight of the lth position in group $\widetilde{G}_h$ (i.e., position-dependent weights, Wang et al. [24], Wang et al. [25], and Wang et al. [31]), $\xi(h,[l])$ is the job scheduled in the lth position in group $\widetilde{G}_h$, $\vartheta_{h,0}$ denotes the unit cost of $d'_{h,l}$, and ϑ_{h,n_h+1} denotes the unit cost of $D_{h,l}$, and the lateness (earliness-tardiness) of job $T_{\xi(h,[l])}$ is

$$L_{\xi(h,[l])} = \begin{cases} d_{\xi(h,[l])}{}' - C_{\xi(h,[l])}, & \text{for } d_{\xi(h,[l])}{}' > C_{\xi(h,[l])}, \\ 0, & \text{for } d_{\xi(h,[l])}{}' \le C_{\xi(h,[l])} \le d_{\xi(h,[l])}{}'', \\ C_{\xi(h,[l])} - d_{\xi(h,[l])}{}'', & \text{for } C_{\xi(h,[l])} > d_{\xi(h,[l])}{}''. \end{cases} \tag{2}$$

By using the three-field notation (Graham etv al. [32]), the problem can be denoted by

$$1|\text{GS}, A|\sum_{h=1}^{m}\sum_{l=1}^{n_h}\left(\vartheta_{h,l}L_{\xi(h,[l])} + \vartheta_{h,0}d_{\xi(h,[l])}{}' + \vartheta_{h,n_h+1}D_{\xi(h,[l])}\right), \tag{3}$$

where $A \in \{\text{CONDW}, \text{SLKDW}, \text{DIFDW}\}$.

Procurement sharing of sustainable and regular products: self-competition and sharing incentives.

3. Preliminary Results

It is clear that there exists an optimal schedule that starts at time 0 and contains 0 machine idle times.

3.1. CONDW Method

Lemma 1. *For a given schedule ξ, the optimal values d'_h and d''_h coincide with the job completion times of group $\widetilde{G}_h$ $(h = 1, 2, \ldots, m)$.*

Proof. For the given schedule ξ, under group $\widetilde{G}_h$, we assume that

$$\begin{aligned} d'_h &= C_{\xi(h,[g_h])} = S_h + s_h + \sum_{l=1}^{g_h} p_{h,[l]}, \\ d''_h &= C_{\xi(h,[k_h])} = S_h + s_h + \sum_{l=1}^{k_h} p_{h,[l]}, \end{aligned} \tag{4}$$

where S_h denotes the starting time of group $\widetilde{G}_h$, g_h and k_h mean the $g_h{}^{\text{th}}$ and $k_h{}^{\text{th}}$ positions of group $\widetilde{G}_h$, respectively $(g_h \le k_h)$. Consider that there exists an optimal schedule without the stated property, i.e., $d'_h = S_h + s_h + \sum_{\theta=1}^{g_h} p_{h,[\theta]} + x$ and $d''_h = S_h + s_h + \sum_{\theta=1}^{k_h} p_{h,[\theta]} + y$, where $0 \le x \le p_{h,[g_h+1]}$ and $0 \le y \le p_{h,[k_h+1]}$.

For group $\widetilde{G}_h$, the total cost is

$$\begin{aligned} F_h(x,y) &= \sum_{l=1}^{n_h}\left(\vartheta_{h,l}L_{\xi(h,[l])} + \vartheta_{h,0}d_{\xi(h,[l])'} + \vartheta_{h,n_h+1}D_{\xi(h,[l])}\right) \\ &= \sum_{l=1}^{g_h}\vartheta_{h,l}\left(d_{h'} - C_{\xi(h,[l])}\right) + \sum_{l=k_h+1}^{n_h}\vartheta_{h,l}\left(C_{\xi(h,[l])} - d_{h''}\right) + n_h\vartheta_{h,0}d_{h'} + n_h\vartheta_{h,n_h+1}\left(d_{h''} - d_{h'}\right) \\ &= \sum_{l=1}^{g_h}\vartheta_{h,l}\left(\sum_{\theta=1}^{g_h}p_{h,[\theta]} + x - \sum_{\theta=1}^{l}p_{h,[\theta]}\right) \\ &\quad + \sum_{l=k_h+1}^{n_h}\vartheta_{h,l}\left(\sum_{\theta=1}^{l}p_{h,[\theta]} - \sum_{\theta=1}^{k_h}p_{h,[\theta]} - y\right) + n_h\vartheta_{h,0}\left(S_h + s_h + \sum_{\theta=1}^{g_h}p_{h,[\theta]} + x\right) + n_h\vartheta_{h,n_h+1}\left(\sum_{\theta=1}^{k_h}p_{h,[\theta]} + y - \sum_{\theta=1}^{g_h}p_{h,[\theta]} - x\right) \\ &= \sum_{l=1}^{g_h}\vartheta_{h,l}\left(\sum_{\theta=l+1}^{g_h}p_{h,[\theta]} + x\right) \\ &\quad + \sum_{l=k_h+1}^{n_h}\vartheta_{h,l}\left(\sum_{\theta=k_h+1}^{l}p_{h,[\theta]} - y\right) + n_h\vartheta_{h,0}\left(S_h + s_h + \sum_{\theta=1}^{g_h}p_{h,[\theta]} + x\right) + n_h\vartheta_{h,n_h+1}\left(\sum_{\theta=g_h+1}^{k_h}p_{h,[\theta]} + y - x\right) \\ &= \sum_{l=1}^{g_h}\vartheta_{h,l}\left(\sum_{\theta=l+1}^{g_h}p_{h,[\theta]}\right) + \sum_{l=k_h+1}^{n_h}\vartheta_{h,l}\left(\sum_{\theta=k_h+1}^{l}p_{h,[\theta]}\right) + n_h\vartheta_{h,0}\left(S_h + s_h + \sum_{\theta=1}^{g_h}p_{h,[\theta]}\right) + n_h\vartheta_{h,n_h+1}\left(\sum_{\theta=g_h+1}^{k_h}p_{h,[\theta]}\right) \\ &\quad + \left(\sum_{l=1}^{g_h}\vartheta_{h,l} + n_h\vartheta_{h,0} - n_h\vartheta_{h,n_h+1}\right)x + \left(n_h\vartheta_{h,n_h+1} - \sum_{l=k_h+1}^{n_h}\vartheta_{h,l}\right)y. \end{aligned} \tag{5}$$

From (5), we see that the term $F_h(x, y)$ is a linear function of x and y; hence, we can either decrease x and y to 0 or increase them to $p_{h,[g_h+1]}$ and $p_{h,[k_h+1]}$, respectively, to obtain a lower cost. This completes the proof.

Lemma 2. *For a given schedule ξ, the optimal values $d_h' = S_h + s_h + \sum_{l=1}^{g_h} p_{h,[l]}$ (where $\sum_{l=0}^{g_h-1} \vartheta_{h,l} \le \vartheta_{h,n_h+1} \le \sum_{l=0}^{g_h} \vartheta_{h,l}$) and $d_h'' = S_h + s_h + \sum_{l=1}^{k_h} p_{h,[l]}$ (where $\sum_{l=k_h+1}^{n_h} \vartheta_{h,l} \le \vartheta_{h,n_h+1} \le \sum_{l=k_h}^{n_h} \vartheta_{h,l}$).*

Proof. By the technique of small perturbations, the result can be easily obtained.

For a given schedule ξ, the total cost of all the jobs within $\widetilde{G}_h\,(h = 1, \ldots, m)$ is

$$\begin{aligned} F_h(\xi, d_h', d_h'') &= \sum_{l=1}^{g_h} \vartheta_{h,l} \left(\sum_{\theta=l+1}^{g_h} p_{h,[\theta]} \right) \\ &\quad + \sum_{l=k_h+1}^{n_h} \vartheta_{h,l} \left(\sum_{\theta=k_h+1}^{l} p_{h,[\theta]} \right) \\ &\quad + n_h \vartheta_{h,0} \left(S_h + s_h + \sum_{\theta=1}^{g_h} p_{h,[\theta]} \right) \\ &\quad + n_h \vartheta_{h,n_h+1} \left(\sum_{\theta=g_h+1}^{k_h} p_{h,[\theta]} \right) \\ &= \sum_{l=1}^{n_h} \Phi_{h,l} p_{h,[l]} + n_h \vartheta_{h,0} (S_h + s_h), \end{aligned} \tag{6}$$

where

$$\Phi_{h,l} = \begin{cases} n_h \vartheta_{h,0} + \sum_{\theta=1}^{l-1} \vartheta_{h,\theta}, & l = 1, 2, \ldots, g_h, \\ n_h \vartheta_{h,n_h+1}, & l = g_h + 1, g_h + 2, \ldots, k_h, \\ \sum_{\theta=l}^{n_h} \vartheta_{h,\theta}, & l = k_h + 1, k_h + 2, \ldots, n_h. \end{cases} \tag{7}$$

From (6) and HLP rule (Hardy et al. [33], i.e., the sum of products $\sum_{j=1}^{n} x_j y_j$ is minimized if the sequence $x_1, x_2, \ldots, x_n$ is ordered nondecreasingly and the sequence $y_1, y_2, \ldots, y_n$ is ordered nonincreasingly, or vice versa, and it is maximized if the sequences are ordered in the same way), minimizing $\sum_{l=1}^{n_h} \Phi_{h,l} p_{h,[l]}$ can be obtained by arranging the elements of the $\Phi_{h,l}$ and $p_{h,l}$ vectors in opposite orders. The term $n_h \vartheta_{h,0} (S_h + s_h)$ is only dependent on the starting time of the group $\widetilde{G}_h\,(h = 1, \ldots, m)$.

Lemma 3. *For the problem $1|GS, CONDW| \sum_{h=1}^{m} \sum_{l=1}^{n_h} (\vartheta_{h,l} L_{\xi(h,[l])} + \vartheta_{h,0} d'_{\xi(h,[l])} + \vartheta_{h,n_h+1} D_{\xi(h,[l])})$, the optimal group sequence can be obtained by arranging the groups in a nondecreasing order of $\Omega_h (s_h + \sum_{l=1}^{n_h} p_{h,[l]}) / (n_h \vartheta_{h,0})$, $h = 1, 2, \ldots, m$.*

Proof. By contradiction, let $\xi = [\pi, \widetilde{G}_f, \widetilde{G}_h, \rho]$ be an optimal schedule, such that

$$\frac{s_f + \sum_{l=1}^{n_f} p_{f,[l]}}{n_f \vartheta_{f,0}} > \frac{s_h + \sum_{l=1}^{n_h} p_{h,[l]}}{n_h \vartheta_{h,0}}, \tag{8}$$

where π and ρ are the partial sequences. We now perform an adjacent pairwise interchange of $\widetilde{G}_f$ and $\widetilde{G}_h$, leaving all other groups in their original positions, to derive a new schedule $\xi' = [\pi, G_h, G_f, \rho]$. Let B denote the completion time of the last job in π, and it follows that

$$\begin{aligned} S_h(\xi) &= B + s_f + \sum_{l=1}^{n_f} p_{f,[l]}, \\ S_f(\xi') &= B + s_h + \sum_{l=1}^{n_h} p_{h,[l]}, \\ &\quad F(\xi) - F(\xi') \\ &= n_f \vartheta_{f,0} (B + s_f) + n_h \vartheta_{h,0} \left(B + s_f + \sum_{l=1}^{n_f} p_{f,[l]} + s_h \right) \\ &\quad - n_h \vartheta_{h,0} (B + s_h) - n_f \vartheta_{f,0} \left(B + s_h + \sum_{l=1}^{n_h} p_{h,[l]} + s_f \right) \\ &= n_h \vartheta_{h,0} \left(s_f + \sum_{l=1}^{n_f} p_{f,[l]} \right) - n_f \vartheta_{f,0} \left(s_h + \sum_{l=1}^{n_h} p_{h,[l]} \right) \\ &\quad > 0. \end{aligned} \tag{9}$$

This contradicts the optimality of ξ and proves that groups are arranged in a nondecreasing order of $\Omega_h = (s_h + \sum_{l=1}^{n_h} p_{h,[l]}) / (n_h \vartheta_{h,0})$.

Based on the above analysis, the following algorithm can be proposed to solve the problem $1|GS, CONDW| \sum_{h=1}^{m} \sum_{l=1}^{n_h} (\vartheta_{h,l} L_{\xi(h,[l])} + \vartheta_{h,0} d_{\xi(h,[l])}' + \vartheta_{h,n_h+1} D_{\xi(h,[l])})$.

Theorem 1. *The problem $1|GS, CONDW| \sum_{h=1}^{m} \sum_{l=1}^{n_h} (\vartheta_{h,l} L_{\xi(h,[l])} + \vartheta_{h,0} d_{\xi(h,[l])}' + \vartheta_{h,n_h+1} D_{\xi(h,[l])})$ can be solved by Algorithm 1 in $O(N \log N)$ time.*

Proof. The correctness of Algorithm 1 follows Lemmas 1–3 and the above analysis. Steps 1 and 4 need $O(m)$ time. Step 2 needs $O(\sum_{h=1}^{m} (n_h \log n_h)) \le O(N \log N)$ time. Step 3 needs $O(m \log m) \le O(N \log N)$ time $(m < N)$. Thus, the total time of Algorithm 1 is $O(N \log N)$.

3.2. SLKDW Method. Similar to Subsection 3.1, we have the following.

Lemma 4. *For a given schedule ξ, the optimal values q_h' and q_h'' coincide with the job completion times of group $\widetilde{G}_h\,(h = 1, 2, \ldots, m)$.*

Lemma 5. *For a given schedule ξ, the optimal values $q_h' = S_h + s_h + \sum_{l=1}^{g_h-1} p_{h,[l]}$ (where $\sum_{l=0}^{g_h-1} \vartheta_{h,l} \le \vartheta_{h,n_h+1} \le \sum_{l=0}^{g_h} \vartheta_{h,l}$) and $q_h'' = S_h + s_h + \sum_{l=1}^{k_h-1} p_{h,[l]}$ (where $\sum_{l=k_h+1}^{n_h} \vartheta_{h,l} \le \vartheta_{h,n_h+1} \le \sum_{l=k_h}^{n_h} \vartheta_{h,l}$).*

Step 1: calculate g_h and k_h by Lemma 2, $h = 1, 2, \ldots, m$
Step 2: arrange the jobs of each group by the HLP rule (vectors $\Phi_{h,l}$ (7) and $p_{h,l}$)
Step 3: by Lemma 3, arrange the groups in a nondecreasing order of $\Omega_h = (s_h + \sum_{l=1}^{n_h} p_{h,[l]})/(n_h \vartheta_{h,0})\,(h = 1, 2, \ldots, m)$
Step 4: according to Lemma 2, calculate d_h' and $d_h''\,(h = 1, 2, \ldots, m)$

Algorithm 1

For a given schedule ξ, the total cost of all the jobs within $\widetilde{G}_h\,(h = 1, \ldots, m)$ is

$$\begin{aligned}
F_h(\xi, q_{h'}, q_{h''}) &= \sum_{l=1}^{n_h}\left(\vartheta_{h,l} L_{\xi(h,[l])} + \vartheta_{h,0} d_{\xi(h,[l])'} + \vartheta_{h,n_h+1} D_{\xi(h,[l])}\right) \\
&= \sum_{l=1}^{g_h} \vartheta_{h,l}\left(d_{\xi(h,[l])'} - C_{\xi(h,[l])}\right) + \sum_{l=k_h+1}^{n_h} \vartheta_{h,l}\left(C_{\xi(h,[l])} - d_{\xi(h,[l])''}\right) \\
&\quad + \vartheta_{h,0} \sum_{l=1}^{n_h} d_{\xi(h,[l])'} + \vartheta_{h,n_h+1} \sum_{l=1}^{n_h}\left(d_{\xi(h,[l])''} - d_{\xi(h,[l])'}\right) \\
&= \sum_{l=1}^{g_h} \vartheta_{h,l}\left(p_{h,[l]} + q_{h'} - C_{\xi(h,[l])}\right) + \sum_{l=k_h+1}^{n_h} \vartheta_{h,l}\left(C_{\xi(h,[l])} - p_{(h,[l])} - q_{h''}\right) \\
&\quad + \vartheta_{h,0} \sum_{l=1}^{n_h}\left(p_{h,[l]} + q_{h'}\right) + n_h \vartheta_{h,n_h+1}\left(q_{h''} - q_{h'}\right) \\
&= \sum_{l=1}^{g_h} \vartheta_{h,l}\left(\sum_{\theta=1}^{g_h-1} p_{h,[\theta]} - \sum_{\theta=1}^{l-1} p_{h,[\theta]}\right) + \sum_{l=k_h+1}^{n_h} \vartheta_{h,l}\left(\sum_{\theta=1}^{l-1} p_{h,[\theta]} - \sum_{\theta=1}^{k_h-1} p_{h,[\theta]}\right) \\
&\quad + \vartheta_{h,0} \sum_{l=1}^{n_h} p_{h,[l]} + n_h \vartheta_{h,0}\left(S_h + s_h + \sum_{\theta=1}^{g_h-1} p_{h,[\theta]}\right) + n_h \vartheta_{h,n_h+1}\left(\sum_{\theta=1}^{k_h-1} p_{h,[\theta]} - \sum_{\theta=1}^{g_h-1} p_{h,[\theta]}\right) \\
&= \sum_{l=1}^{g_h} \vartheta_{h,l}\left(\sum_{\theta=l}^{g_h-1} p_{h,[\theta]}\right) + \sum_{l=k_h+1}^{n_h} \vartheta_{h,l}\left(\sum_{\theta=k_h}^{l-1} p_{h,[\theta]}\right) \\
&\quad + \vartheta_{h,0} \sum_{l=1}^{n_h} p_{h,[l]} + n_h \vartheta_{h,0}\left(S_h + s_h + \sum_{\theta=1}^{g_h-1} p_{h,[\theta]}\right) + n_h \vartheta_{h,n_h+1}\left(\sum_{\theta=g_h}^{k_h-1} p_{h,[\theta]}\right) \\
&= \sum_{l=1}^{n_h} \Phi_{h,l} p_{h,[l]} + n_h \vartheta_{h,0}(S_h + s_h),
\end{aligned} \tag{10}$$

where

$$\Phi_{h,l} = \begin{cases} (n_h + 1)\vartheta_{h,0} + \sum_{\theta=1}^{l} \vartheta_{h,\theta}, & l = 1, 2, \ldots, g_h - 1, \\ \vartheta_{h,0} + n_h \vartheta_{h,n_h+1}, & l = g_h, g_h + 1, \ldots, k_h - 1, \\ \vartheta_{h,0} + \sum_{\theta=l+1}^{n_h} \vartheta_{h,\theta}, & l = k_h, k_h + 1, \ldots, n_h - 1 \\ \vartheta_{h,0}, & l = n_h. \end{cases} \tag{11}$$

From (10) and Subsection 3.1, the optimal schedule of each group can be obtained by the HLP rule.

Lemma 6. *For the problem $1|GS, SLKDW|\sum_{h=1}^{m}\sum_{l=1}^{n_h}(\vartheta_{h,l} L_{\xi(h,[l])} + \vartheta_{h,0} d_{\xi(h,[l])}' + \vartheta_{h,n_h+1} D_{\xi(h,[l])})$, the optimal group sequence can be obtained by arranging the groups in a nondecreasing order of $\Omega_h = (s_h + \sum_{l=1}^{n_h} p_{h,[l]})/(n_h \vartheta_{h,0}), h = 1, 2, \ldots, m$.*

Based on the above analysis, the following algorithm can be proposed to solve the problem $1|GS, SLKDW|\sum_{h=1}^{m}\sum_{l=1}^{n_h}(\vartheta_{h,l} L_{\xi(h,[l])} + \vartheta_{h,0} d_{\xi(h,[l])}' + \vartheta_{h,n_h+1} D_{\xi(h,[l])})$.

Theorem 2. *The problem $1|GS, SLKDW|\sum_{h=1}^{m}\sum_{l=1}^{n_h}(\vartheta_{h,l} L_{\xi(h,[l])} + \vartheta_{h,0} d_{\xi(h,[l])}' + \vartheta_{h,n_h+1} D_{\xi(h,[l])})$ can be solved by Algorithm 2 in $O(N\log N)$ time.*

Step 1: calculate g_h and k_h by Lemma 5, $h = 1, 2, \ldots, m$
Step 2: arrange the jobs of each group by the HLP rule (vectors $\Phi_{h,l}$ (11) and $p_{h,l}$)
Step 3: by Lemma 6, arrange the groups in a nondecreasing order of $\Omega_h = (s_h + \sum_{l=1}^{n_h} p_{h,[l]})/(n_h \vartheta_{h,0})$, $(h = 1, 2, \ldots, m)$
Step 4: according to Lemma 5, calculate q_h' and q_h'' $(h = 1, 2, \ldots, m)$

Algorithm 2

3.3. DIFDW Method

Lemma 7. *For the DIFDW method, there exists an optimal sequence, such that $d_{h,l}' \le d_{h,l}' \le C_{h,l}$.*

Proof. Similar to the proof of Wang et al. [24].

Lemma 8. *For the DIFDW method, let ξ be a given sequence, and the optimal $d_{\xi(h,[j])}'$ and $d_{\xi(h,[j])}''$ of job $J_{\xi(h,[j])}$ can be given as follows:*

(1) If $\min\{\vartheta_{h,0}, \vartheta_{h,l}, \vartheta_{h,n_h+1}\} = \vartheta_{h,0}$, then $d_{\xi(h,[j])}' = d_{\xi(h,[j])}'' = C_{\xi(h,[j])}$

(2) If $\min\{\vartheta_{h,0}, \vartheta_{h,l}, \vartheta_{h,n_h+1}\} = \vartheta_{h,l}$, then $d_{\xi(h,[j])}' = d_{\xi(h,[j])}'' = 0$

(3) If $\min\{\vartheta_{h,0}, \vartheta_{h,l}, \vartheta_{h,n_h+1}\} = \vartheta_{h,n_h+1}$, then $d_{\xi(h,[j])}' = 0, d_{\xi(h,[j])}'' = C_{\xi(h,[j])}$

Proof. Similar to the proof of Wang et al. [24].

From Lemma 8, the cost for job $J_{\xi(h,[l])}$ is

$$F_{\xi(h,[l])} = \psi_{h,l} C_{\xi(h,[l])}, \tag{12}$$

where $\psi_{h,l} = \min\{\vartheta_{h,0}, \vartheta_{h,l}, \vartheta_{h,n_h+1}\}$. The total cost of all the jobs within $\widetilde{G}_h$ is

$$\begin{aligned} F_h\left(\xi, d_{\xi(h,[j])}', d_{\xi(h,[j])}''\right) &= \sum_{la=1}^{n_h} \psi_{h,l} C_{\xi(h,[l])} \\ &= \sum_{l=1}^{n_h} \Phi_{h,l} p_{h,[l]} + (S_h + s_h) \sum_{l=1}^{n_h} \psi_{h,l}, \end{aligned} \tag{13}$$

where

$$\Phi_{h,l} = (n_h - l + 1)\psi_{h,l}. \tag{14}$$

From (13) and Subsection 3.1, the optimal schedule of each group can be obtained by the HLP rule.

Lemma 9. *For the problem $1|GS, DIFDW|\sum_{h=1}^{m}\sum_{l=1}^{n_h}(\vartheta_{h,l}L_{\xi(h,[l])} + \vartheta_{h,0}d_{\xi(h,[l])}' + \vartheta_{h,n_h+1}D_{\xi(h,[l])})$, the optimal group sequence can be obtained by arranging the groups in a nondecreasing order of $\Omega_h = (s_h + \sum_{l=1}^{n_h} p_{h,[l]})/(\sum_{l=1}^{n_h}\psi_{h,l})$, $h = 1, 2, \ldots, m$.*

Based on the above analysis, the following algorithm can be proposed to solve the problem $1|GS, SLKDW|\sum_{h=1}^{m}\sum_{l=1}^{n_h}(\vartheta_{h,l}L_{\xi(h,[l])} + \vartheta_{h,0}d_{\xi(h,[l])}' + \vartheta_{h,n_h+1}D_{\xi(h,[l])})$.

Theorem 3. *The problem $1|GS, DIFDW|\sum_{h=1}^{m}\sum_{l=1}^{n_h}(\vartheta_{h,l}L_{\xi(h,[l])} + \vartheta_{h,0}d_{\xi(h,[l])}' + \vartheta_{h,n_h+1}D_{\xi(h,[l])})$ can be solved by Algorithm 3 in $O(N\log N)$ time.*

4. Number Examples

Example 1. For the problem $1|\mathrm{GS}, \mathrm{CONDW}|\sum_{h=1}^{m}\sum_{l=1}^{n_h}(\vartheta_{h,l}L_{\xi(h,[l])} + \vartheta_{h,0}d_{\xi(h,[l])}' + \vartheta_{h,n_h+1}D_{\xi(h,[l])})$, consider $n = 13, m = 3, n_1 = 4, n_2 = 4, n_3 = 5$, $\widetilde{G}_1$: $s_1 = 5$, $p_{1,1} = 4$, $p_{1,2} = 3$, $p_{1,3} = 6$, $p_{1,4} = 2$, $\vartheta_{1,0} = 2$, $\vartheta_{1,1} = 3$, $\vartheta_{1,2} = 5$, $\vartheta_{1,3} = 4$, $\vartheta_{1,4} = 6$, $\vartheta_{1,5} = 7$; $\widetilde{G}_2$: $s_2 = 3$, $p_{2,1} = 8$, $p_{2,2} = 2$, $p_{2,3} = 7$, $p_{2,4} = 5$, $\vartheta_{2,0} = 6$, $\vartheta_{2,1} = 7$, $\vartheta_{2,2} = 4$, $\vartheta_{2,3} = 5$, $\vartheta_{2,4} = 2$, $\vartheta_{2,5} = 8$; $\widetilde{G}_3$: $s_3 = 6$, $p_{3,1} = 14$, $p_{3,2} = 7$, $p_{3,3} = 5$, $p_{3,4} = 10$, $p_{3,5} = 9$, $\vartheta_{3,0} = 3$, $\vartheta_{3,1} = 6$, $\vartheta_{3,2} = 7$, $\vartheta_{3,3} = 5$, $\vartheta_{3,4} = 8$, $\vartheta_{3,5} = 2$, and $\vartheta_{3,6} = 12$.

From Algorithm 1, we have the following.

Step 1: $g_1 = 2, k_1 = 3, g_2 = 1, k_2 = 2, g_3 = 2$, and $k_3 = 3$

Step 2: $\Phi_{1,1} = 8$, $\Phi_{1,2} = 11$, $\Phi_{1,3} = 28$, $\Phi_{1,4} = 6$; $\Phi_{2,1} = 24$, $\Phi_{2,2} = 32$, $\Phi_{2,3} = 7$, $\Phi_{2,4} = 2$; $\Phi_{3,1} = 15$, $\Phi_{3,2} = 21$, $\Phi_{3,3} = 60$, $\Phi_{3,4} = 10$, and $\Phi_{3,5} = 2$. The optimal sequence of jobs within each group is $\widetilde{G}_1$: $T_{1,l} \longrightarrow T_{1,2} \longrightarrow T_{1,4} \longrightarrow T_{1,3}$; $\widetilde{G}_2$: $T_{2,4} \longrightarrow T_{2,2} \longrightarrow T_{2,3} \longrightarrow T_{2,1}$; and $\widetilde{G}_3$: $T_{3,5} \longrightarrow T_{3,2} \longrightarrow T_{3,3} \longrightarrow T_{3,4} \longrightarrow T_{3,1}$.

Step 3: $\Omega_1 = 5/2$, $\Omega_2 = 25/24$, and $\Omega_3 = 51/15$; the optimal group sequence is $\widetilde{G}_2 \longrightarrow \widetilde{G}_1 \longrightarrow \widetilde{G}_3$.

Step 4: $d_2' = 8$, $d_2'' = 10$; $d_1' = 37$, $d_1'' = 39$; $d_3' = 67$, and $d_3'' = 72$

Example 2. For the problem $1|\mathrm{GS}, \mathrm{SLKDW}|\sum_{h=1}^{m}\sum_{l=1}^{n_h}(\vartheta_{h,l}L_{\xi(h,[l])} + \vartheta_{h,0}d_{\xi(h,[l])}' + \vartheta_{h,n_h+1}D_{\xi(h,[l])})$, the data are the same as in Example 1.

From Algorithm 2, we have the following.

Step 1: $g_1 = 2, k_1 = 3, g_2 = 1, k_2 = 2, g_3 = 2$, and $k_3 = 3$

Step 2: $\Phi_{1,1} = 13$, $\Phi_{1,2} = 30$, $\Phi_{1,3} = 8$, $\Phi_{1,4} = 2$; $\Phi_{2,1} = 38$, $\Phi_{2,2} = 13$, $\Phi_{2,3} = 8$, $\Phi_{2,4} = 6$; $\Phi_{3,1} = 24$, $\Phi_{3,2} = 63$, $\Phi_{3,3} = 13$, $\Phi_{3,4} = 5$, and $\Phi_{3,5} = 3$. The optimal sequence of jobs within each group is $\widetilde{G}_1$: $T_{1,2} \longrightarrow T_{1,4} \longrightarrow T_{1,1} \longrightarrow T_{1,3}$; $\widetilde{G}_2$: $T_{2,2} \longrightarrow T_{2,4} \longrightarrow T_{2,3} \longrightarrow T_{2,1}$; and $\widetilde{G}_3$: $T_{3,2} \longrightarrow T_{3,3} \longrightarrow T_{3,5} \longrightarrow T_{3,4} \longrightarrow T_{3,1}$.

Step 3: $\Omega_1 = 5/2$, $\Omega_2 = 25/24$, and $\Omega_3 = 51/15$; the optimal group sequence is $\widetilde{G}_2 \longrightarrow \widetilde{G}_1 \longrightarrow \widetilde{G}_3$.

Step 4: $q_2' = 3$, $q_2'' = 5$; $q_1' = 33$, $q_1'' = 35$; $q_3' = 58$, and $q_3'' = 63$

Step 1: arrange the jobs of each group by the HLP rule (vectors $\Phi_{h,l}$ (14) and $p_{h,l}$)
Step 2: arrange the groups in a nondecreasing order of $\Omega_h = (s_h + \sum_{l=1}^{n_h} p_{h,[l]})/(\sum_{l=1}^{n_h} \psi_{h,l})$, $(h = 1, 2, \ldots, m)$
Step 3: according to Lemma 8, calculate $d_{\xi(h,[j])}{}'$, $d_{\xi(h,[j])}{}''$, $h = 1, 2, \ldots, m$, and $j = 1, 2, \ldots, n_h$

Algorithm 3

Example 3. For the problem $1|\mathrm{GS}, \mathrm{DIFDW}|\sum_{h=1}^{m}\sum_{l=1}^{n_h}(\vartheta_{h,l}L_{\xi(h,[l])} + \vartheta_{h,0}d_{\xi(h,[l])}{}' + \vartheta_{h,n_h+1}D_{\xi(h,[l])})$, the data are the same as in Example 1.

From Algorithm 3, we have the following.

Step 1: $\Phi_{1,1} = 8$, $\Phi_{1,2} = 6$, $\Phi_{1,3} = 4$, $\Phi_{1,4} = 2$; $\Phi_{2,1} = 24$, $\Phi_{2,2} = 12$, $\Phi_{2,3} = 10$, $\Phi_{2,4} = 2$; $\Phi_{3,1} = 15$, $\Phi_{3,2} = 12$, $\Phi_{3,3} = 9$, $\Phi_{3,4} = 6$, and $\Phi_{3,5} = 2$. The optimal sequence of jobs within each group is $\widetilde{G}_1$: $T_{1,4} \longrightarrow T_{1,2} \longrightarrow T_{1,1} \longrightarrow T_{1,3}$; $\widetilde{G}_2$: $T_{2,2} \longrightarrow T_{2,4} \longrightarrow T_{2,3} \longrightarrow T_{2,1}$; and $\widetilde{G}_3$: $T_{3,3} \longrightarrow T_{3,2} \longrightarrow T_{3,5} \longrightarrow T_{3,4} \longrightarrow T_{3,1}$.

Step 2: $\Omega_1 = 5/2$, $\Omega_2 = 25/17$, and $\Omega_3 = 51/14$; the optimal group sequence is $\widetilde{G}_2 \longrightarrow \widetilde{G}_1 \longrightarrow \widetilde{G}_3$.

Step 3: $d_{2,2}{}' = d_{2,2}{}'' = 7$, $d_{2,4}{}' = d_{2,4}{}'' = 0$, $d_{2,3}{}' = d_{2,3}{}'' = 0$, $d_{2,1}{}' = d_{2,1}{}'' = 0$; $d_{1,4}{}' = d_{1,4}{}'' = 32$, $d_{1,2}{}' = d_{1,2}{}'' = 35$, $d_{1,1}{}' = d_{1,1}{}'' = 39$, $d_{1,3}{}' = d_{1,3}{}'' = 45$; $d_{3,3}{}' = d_{3,3}{}'' = 56$, $d_{3,2}{}' = d_{3,2}{}'' = 63$, $d_{3,5}{}' = d_{3,5}{}'' = 72$, $d_{3,4}{}' = d_{3,4}{}'' = 82$, and $d_{3,1}{}' = d_{3,1}{}'' = 0$

5. Conclusions

We extended the classical single-machine scheduling with the due-window assignment and position-dependent weights to the group technology assumption. For the CONDW, SLKDW, and DIFDW assignment methods, our objective is to minimize a cost function including lateness (earliness-tardiness), starting times, and sizes of due-window. Some properties of the above three assignment methods were given, and three algorithms can be proposed in the $O(N\log N)$ time algorithm. A future extension is to the group scheduling in the flowshop, parallel machines setting, or two-stage assembly flowshop. Other future research may study extending the group scheduling to scenario-dependent processing times (Wu et al. [34–36]) or variable processing times (Wang et al. [37, 38]).

Data Availability

No data were used to support this study.

Conflicts of Interest

The authors declare that they have no conflicts of interest.

Acknowledgments

This research was supported by the National Natural Science Regional Foundation of China (71861031 and 72061029).

References

[1] J. S. Neufeld, J. N. D. Gupta, and U. Buscher, "A comprehensive review of flowshop group scheduling literature," *Computers & Operations Research*, vol. 70, pp. 56–74, 2016.

[2] Y.-Y. Lu, J.-J. Wang, and J.-B. Wang, "Single machine group scheduling with decreasing time-dependent processing times subject to release dates," *Applied Mathematics and Computation*, vol. 234, pp. 286–292, 2014.

[3] N. Yin, L. Kang, and X.-Y. Wang, "Single-machine group scheduling with processing times dependent on position, starting time and allotted resource," *Applied Mathematical Modelling*, vol. 38, no. 19-20, pp. 4602–4613, 2014.

[4] J.-J. Wang and Y.-J. Liu, "Single-machine bicriterion group scheduling with deteriorating setup times and job processing times," *Applied Mathematics and Computation*, vol. 242, pp. 309–314, 2014.

[5] J.-B. Wang and J.-J. Wang, "Single machine group scheduling with time dependent processing times and ready times," *Information Sciences*, vol. 275, pp. 226–231, 2014.

[6] Y. He and L. Sun, "One-machine scheduling problems with deteriorating jobs and position-dependent learning effects under group technology considerations," *International Journal of Systems Science*, vol. 46, no. 7, pp. 1319–1326, 2015.

[7] Y.-Y. Lu, J.-B. Wang, P. Ji, and H. He, "A note on resource allocation scheduling with group technology and learning effects on a single machine," *Engineering Optimization*, vol. 49, no. 9, pp. 1621–1632, 2017.

[8] X. Zhang, L. Liao, W. Zhang, T. C. E. Cheng, Y. Tan, and M. Ji, "Single-machine group scheduling with new models of position-dependent processing times," *Computers & Industrial Engineering*, vol. 117, pp. 1–5, 2018.

[9] F. Liu, J. Yang, and Y.-Y. Lu, "Solution algorithms for single-machine group scheduling with ready times and deteriorating jobs," *Engineering Optimization*, vol. 51, no. 5, pp. 862–874, 2019.

[10] X. Huang, "Bicriterion scheduling with group technology and deterioration effect," *Journal of Applied Mathematics and Computing*, vol. 60, no. 1-2, pp. 455–464, 2019.

[11] J.-B. Wang and X.-X. Liang, "Group scheduling with deteriorating jobs and allotted resource under limited resource availability constraint," *Engineering Optimization*, vol. 51, no. 2, pp. 231–246, 2019.

[12] X.-X. Liang, M. Liu, Y.-B. Feng, J.-B. Wang, and L.-S. Wen, "Solution algorithms for single-machine resource allocation scheduling with deteriorating jobs and group technology," *Engineering Optimization*, vol. 52, no. 7, pp. 1184–1197, 2020.

[13] H. Qin, Z.-H. Zhang, and D. Bai, "Permutation flowshop group scheduling with position-based learning effect," *Computers & Industrial Engineering*, vol. 92, pp. 1–15, 2016.

[14] Y. Yin, M. Liu, T. C. E. Cheng, C.-C. Wu, and S.-R. Cheng, "Four single-machine scheduling problems involving due date determination decisions," *Information Sciences*, vol. 251, pp. 164–181, 2013.

[15] D.-J. Wang, Y. Yin, J. Xu, W.-H. Wu, S.-R. Cheng, and C.-C. Wu, "Some due date determination scheduling problems with two agents on a single machine," *International Journal of Production Economics*, vol. 168, pp. 81–90, 2015.

[16] D. Shabtay, "Optimal restricted due date assignment in scheduling," *European Journal of Operational Research*, vol. 252, no. 1, pp. 79–89, 2016.

[17] S. Li, C. T. Ng, and J. Yuan, "Group scheduling and due date assignment on a single machine," *International Journal of Production Economics*, vol. 130, no. 2, pp. 230–235, 2011.

[18] L. Sun, A. J. Yu, and B. Wu, "Single machine common flow allowance group scheduling with learning effect and resource allocation," *Computers & Industrial Engineering*, vol. 139, Article ID 106126, 2020.

[19] D.-Y. Lv, S.-W. Luo, J. Xue, J.-X. Xu, and J.-B. Wang, "A note on single machine common flow allowance group scheduling with learning effect and resource allocation," *Computers & Industrial Engineering*, vol. 151, Article ID 106941, 2021.

[20] W. Wang, J.-J. Wang, and J.-B. Wang, "Solution algorithms for single-machine group scheduling with learning effect and convex resource allocation," *Complexity*, vol. 2021, Article ID 6615824, 13 pages, 2021.

[21] L.-Y. Wang, M. Liu, J.-B. Wang, Y.-Y. Lu, and W.-W. Liu, "Optimization for due-date assignment single-machine scheduling under group technology," *Complexity*, vol. 2021, Article ID 6656261, 9 pages, 2021.

[22] A. Janiak, W. A. Janiak, T. Krysiak, and T. Kwiatkowski, "A survey on scheduling problems with due windows," *European Journal of Operational Research*, vol. 242, no. 2, pp. 347–357, 2015.

[23] G. A. Rolim and M. S. Nagano, "Structural properties and algorithms for earliness and tardiness scheduling against common due dates and windows: a review," *Computers & Industrial Engineering*, vol. 149, Article ID 106803, 2020.

[24] J.-B. Wang, B. Zhang, L. Li, D. Bai, and Y.-B. Feng, "Due-window assignment scheduling problems with position-dependent weights on a single machine," *Engineering Optimization*, vol. 52, no. 2, pp. 185–193, 2020.

[25] L.-Y. Wang, M. Liu, J.-B. Wang, Y.-Y. Lu, and W.-W. Liu, "Optimization for due-window assignment scheduling with position-dependent weights," *Discrete Dynamics in Nature and Society*, vol. 2020, Article ID 9746538, 7 pages, 2020.

[26] J.-B. Wang, Y. Hu, and B. Zhang, "Common due-window assignment for single-machine scheduling with generalized earliness/tardiness penalties and a rate-modifying activity," *Engineering Optimization*, vol. 53, no. 3, pp. 496–512, 2021.

[27] D.-Y. Lv and J.-B. Wang, "Study on resource-dependent no-wait flow shop scheduling with different due-window assignment and learning effects," *Asia Pacific Journal of Operational Research*, vol. 16, Article ID 2150008, 2021.

[28] M. Ji, K. Chen, J. Ge, and T. C. E. Cheng, "Group scheduling and job-dependent due window assignment based on a common flow allowance," *Computers & Industrial Engineering*, vol. 68, pp. 35–41, 2014.

[29] W.-X. Li and C.-L. Zhao, "Single machine scheduling problem with multiple due windows assignment in a group technology," *Journal of Applied Mathematics and Computing*, vol. 48, no. 1-2, pp. 477–494, 2015.

[30] X. Sun, X.-N. Geng, and T. Liu, "Due-window assignment scheduling in the proportionate flow shop setting," *Annals of Operations Research*, vol. 292, no. 1, pp. 113–131, 2020.

[31] J.-B. Wang, B. Cui, P. Ji, and W.-W. Liu, "Research on single-machine scheduling with position-dependent weights and past-sequence-dependent delivery times," *Journal of Combinatorial Optimization*, vol. 41, no. 2, pp. 290–303, 2021.

[32] R. L. Graham, E. L. Lawler, J. K. Lenstra, and A. H. G. R. Kan, "Optimization and approximation in deterministic sequencing and scheduling: a survey," *Annals of Discrete Mathematics*, vol. 5, pp. 287–326, 1979.

[33] G. H. Hardy, J. E. Littlewood, and G. Polya, *Inequalities*, Cambridge University Press, Cambridge, UK, 2nd ed edition, 1967.

[34] C.-C. Wu, D. Bai, X. Zhang et al., "A robust customer order scheduling problem along with scenario-dependent component processing times and due dates," *Journal of Manufacturing Systems*, vol. 58, pp. 291–305, 2021.

[35] C.-C. Wu, D. Bai, J.-H. Chen et al., "Several variants of simulated annealing hyper-heuristic for a single-machine scheduling with two-scenario-based dependent processing times," *Swarm and Evolutionary Computation*, vol. 60, Article ID 100765, 2021.

[36] C.-C. Wu, J. N. D. Gupta, S.-R. Cheng, B. M. T. Lin, S.-H. Yip, and W.-C. Lin, "Robust scheduling for a two-stage assembly shop with scenario-dependent processing times," *International Journal of Production Research*, vol. 8, pp. 1–16, 2020.

[37] J. B. Wang, D. Y. Lv, J. Xu, P. Ji, and F. Li, "Bicriterion scheduling with truncated learning effects and convex controllable processing times," *International Transactions in Operational Research*, vol. 28, no. 3, pp. 1573–1593, 2021.

[38] J.-B. Wang, B. Zhang, and H. He, "A unified analysis for scheduling problems with variable processing times," *Journal of Industrial and Management Optimization*, vol. 20, 2021.

Hindawi
Mathematical Problems in Engineering
Volume 2021, Article ID 1351426, 20 pages
https://doi.org/10.1155/2021/1351426

Research Article

Motion Reliability Analysis of Unlocking Trigger Device Based on CPSO-BR-BP Neural Network with Uncertain Parameters

Yun Tian, Hongtao Fan, Yuliang Zhang, Licheng Liu, and Kang Gong

Beijing Spacecrafts, Beijing 100083, China

Correspondence should be addressed to Yuliang Zhang; 1317906366@qq.com

Received 8 July 2021; Accepted 13 August 2021; Published 21 August 2021

Academic Editor: Mohammad Yazdi

Aiming at overcoming the problem that the mechanism function of the unlocking trigger device is difficult to obtain and the corresponding reliability analysis cannot be performed, a motion reliability analysis method based on the CPSO-BR-BP neural network proxy model is proposed. Firstly, the particle swarm algorithm is optimized through the chaotic sequence, and the back-propagation (BP) neural network is optimized using Chaos Particle Swarm Optimization (CPSO) and Bayesian Regularization (BR) algorithm. The CPSO-BR-BP neural network proxy model is established, and the reliability of shape memory alloys (SMA) wire unlocking based on the structural function is calculated. Moreover, according to the structural function of the separation process, the motion reliability based on the proxy model and the improved membership function is calculated. Finally, a series reliability model is established based on the unlocking process and the separation process to calculate the reliability of the whole machine. The reliability of the unlocking trigger device is analyzed by the proposed method. Results show that the proposed method is computationally efficient with the calculated reliability of 0.9987.

1. Introduction

The connection and separation device in the spacecraft is designed to realize the connection between spacecraft sections as well as that between the body and components in the launch section. At the same time, it achieves reliable unlocking and separation on the orbit according to the established requirements. The reliability can not only quantify the motion performance of the device under the condition of parameter uncertainty but also provide the necessary theoretical basis for its further optimization [1–5]. Future space station construction and manned missions to the moon make higher demands on the reliability, safety, and separation impact of the connection and separation device, and also more urgent needs for the connection and separation module with large load capacity and low impact are put forward [6, 7].

To reduce the separation impact of the device, ensure the safety of connection and separation, and avoid space pollution, researchers have applied shape memory alloys (SMA) to achieve the unlocking function [8–13]. Zhang et al. [8] designed a separation release device using SMA wire. The device has a simple structure, but it lacks further tests on impact performance and load-bearing capacity. Hu et al. [9] proposed an unlocking mechanism based on memory alloy drive with non-self-locking transmission characteristics and multistage force-increasing structure. The key parameters affecting the drive performance of memory alloy and the design of non-self-locking trapezoidal thread pairs were determined through simulation, but the impact of parameter uncertainty on device performance was not considered. Han et al. [10] proposed a low-impact, light-weight, interlocking connection and separation device based on the shape memory alloy tube unlocking. The key parameters were determined through theoretical analysis and simulation, and the unlocking impact and unlocking time of this prototype were tested. However, the reliability analysis of the device was not performed. Most of the above-mentioned studies were carried out on deterministic experiments or simulations to determine the structural parameters of the device, without considering the influences of parameter uncertainties on its motion reliability. Reliability analysis is the focus of the design process, which can be used to conduct quantitative analysis of sports

performance under deterministic conditions. Due to the complex structure of the unlocking trigger device, it is difficult to directly obtain its structure function. The proxy model is introduced to establish the mapping relationships between the uncertainty parameters and the responses.

Currently, the most widely used proxy models are polynomial response surface proxy model [11], Kriging proxy model [12–14], radial basis function proxy model [15, 16], and BP neural network proxy model [17–19]. Among them, the BP neural network proxy model significantly improves the robustness of the overall design of the mechanical structure with low calculation cost and high noise processing capability. However, the gradient descent method used by BP neural network models often converges to a local optimal solution, which affects the accuracy and efficiency of proxy models. For this reason, researchers have optimized the BP neural network models [20–23]. Tang et al. [20] proposed an analytic method for the reliability and sensitivity of motion mechanisms based on BP neural networks, which can effectively improve the reliability and robustness of machine tool motion mechanisms. Dai et al. [21] proposed an explorer optimization algorithm based on heuristic search, which trains the neural network through evolutionary methods to adjust the structure and parameters of the neural network. Gong et al. [22] improved the particle swarm optimization (PSO) by evolutionary strategy to optimize a BP neural network for storage reliability prediction and combined the global search capability of PSO with the local search capability of the BP network to improve the convergence speed and prediction accuracy of the algorithm. Yan et al. [23] proposed an artificial neural network model based on genetic algorithm optimization to analyze the reliability of aviation bearing fatigue and overcomed the problem of artificial neural network local optimization and premature convergence problems. The above studies mostly optimize the characteristics of BP neural network models and do not analyze the accuracy and efficiency of proxy models. Moreover, they are difficult to solve the reliability issues of actual engineering cases.

To this end, considering working principle of unlocking trigger device and uncertain parameters during movement, a new reliability analysis method based on CPSO-BR-BP neural network (Chaos Particle Swarm Optimization-Bayesian Regularization-BP neural network) is proposed, and the unlocking trigger device is used as the research object. The influence of each uncertainty parameter on the device performance is clarified, and the motion reliability of the SMA wire unlocking and separation process is analyzed under different coefficients to verify its motion reliability under uncertain parameters. The research method provides a reliable theoretical reference for further improving the structural performance of the unlocking trigger device.

2. Configuration and Working Principle of Unlocking Trigger Device

The overall configuration of unlocking trigger device is shown in Figure 1. The device is mainly composed of three parts: the SMA wire trigger component, the unlocking and transmission component, and the connection and separation component. Among them, the SMA wire trigger component plays a reliable limit and lock function when locked, and it provides trigger driving force for releasing the limit and lock when unlocked. The connection and separation component can realize the loading of the pretightening force to keep overall connection strength and rigidity when locked. Besides, it can quickly realize the separation of the connecting parts while unlocking. The unlocking and transmission components can complete the load amplification and reduce the impact while unlocking [6].

The unlocking trigger device is a new type of non-pyrotechnic unlocking device. It is to make the nut of the non-self-locking thread pair into a flywheel. When the connection is locked, the flywheel nut is restricted by the triggering mechanism to rotate in the circumferential direction. Besides, it is combined with the non-self-locking thread to realize the connection of the spacecraft and its accessories. To ensure the tightness of the connection, the lower end of the screw is pretightened by the loading nut to provide the unlocking driving force. At this time, the flywheel nut is in the unlocked state under the action of non-self-locking force. When it is released, the SMA wire is heated by electricity to shrink it to release the restriction of the locking mechanism on the nut. The flywheel nut is unlocked by inertial reversal under the action of the non-self-locking force of the threaded connection. The device can not only complete the heavy-duty connection through the thread pair connection but also complete the separation of the screw and the nut by releasing the non-self-locking thread after the nut limit to achieve the goal of low-impact separation. The working principle is shown in Figure 2.

3. Reliability Analysis Method Based on CPSO-BR-BP Neural Network Proxy Model

The premise of the reliability analysis of the unlocking trigger device is to construct the functional function of the mechanism. Since it is difficult to obtain the physical equation of the device uncertainty parameter and its response, the key is to obtain the relationship between the uncertainty parameter and its response, that is, the proxy model. Currently, the most widely used proxy models are polynomial response surface proxy model [11], Kriging proxy model [12–14], radial basis function proxy model [15, 16], and BP neural network proxy model [17–19]. Among them, the BP neural network proxy model significantly improved the robustness of the overall design of the mechanical structure with its low calculation cost and high noise processing capability [17]. To improve the accuracy and efficiency of the reliability calculation, the motion reliability analysis of the SMA wire unlocking process and the separation process is carried out based on the BP neural network proxy model.

3.1. BP Neural Network Proxy Model. BP neural network is an intelligent algorithm with error back-propagation. Its topological structure is mainly composed of three parts:

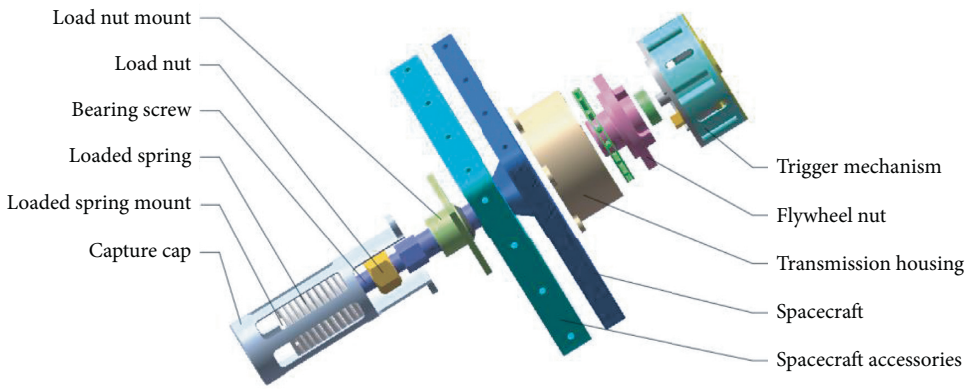

Figure 1: The overall configuration diagram of the unlocking trigger device.

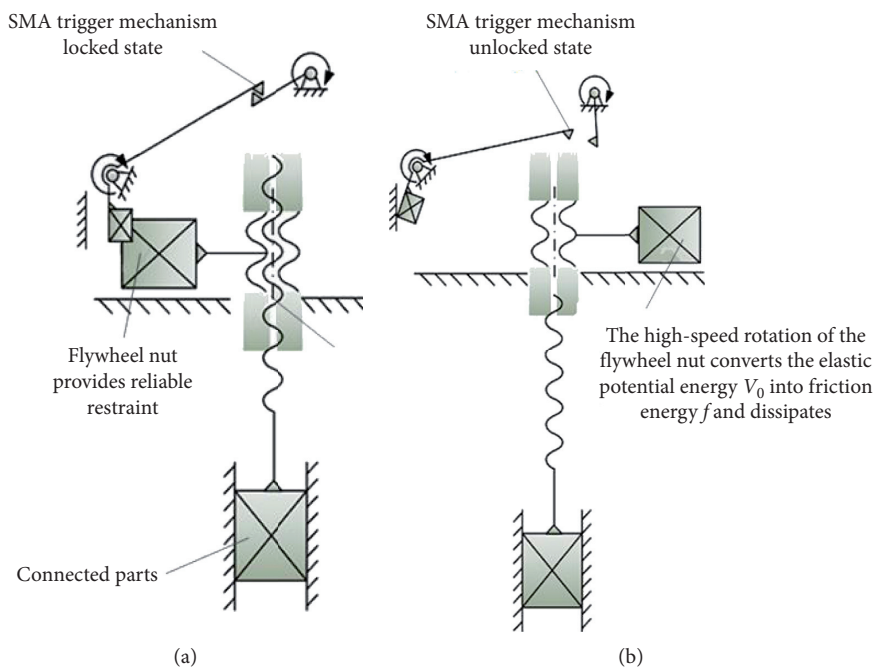

Figure 2: Working principle diagram of the separation device: (a) the connection status and (b) the separation status.

input layer, hidden layer, and output layer. Each layer is connected by neurons. Assuming that the nodes of the input layer, hidden layer, and output layer in the three-layer structure are m, n, and r, respectively, the function transmitted by the neuron can be expressed by

$$h_k = f_1\left(\sum_{i=1}^{m} W_{ik}x_i + b_k\right), \quad (j = 1, 2, \ldots, r), (i = 1, 2, \ldots, m), (k = 1, 2, \ldots, n), \tag{1}$$

$$y_k = f_2\left(\sum_{k=1}^{n} W_{kj}h_k + b_j\right), \quad (j = 1, 2, \ldots, r), (i = 1, 2, \ldots, m), (k = 1, 2, \ldots, n), \tag{2}$$

where h_k is the output of the hidden layer; y_k represents the output of the output layer; $f_1(x)$ and $f_2(x)$ are the activation functions; x_i denotes the input variable; b_k is the threshold of the hidden layer; b_j is the threshold of the output layer; W_{ik} reflects the weight between the hidden layer and the input layer; and W_{kj} is the weight between the output layer and the hidden layer.

According to equations (1) and (2), the mapping relationship between the network input variable x_i and the output response y can be expressed as

$$y = f_2\left(\sum_{k=1}^{n} W_{jk} f_1\left(\sum_{i=1}^{m} W_{ik} x_i + b_k\right) + b_j\right). \quad (3)$$

The BP neural network uses the gradient descent method as the training algorithm and the training error of the network as the performance function. The weights and thresholds in equation (3) can be iterated to make the fitting accuracy of the BP neural network proxy model reach the allowable error range. The performance function characterized by the gradient descent method can be expressed as

$$E_D = \sum_{i=1}^{s} (T_i - y_i)^2, \quad (4)$$

where s is the total number of weights; T_i is the actual output; and y_i is the network prediction output.

However, the gradient descent method often converges to the local optimal solution in which the initial values of weights and thresholds are randomly generated in the training process. This makes the network not fully trained, which will affect the fitting accuracy and computational efficiency of the agent model. Therefore, the Chaos Particle Swarm Optimization (CPSO) and Bayesian Regularization (BR) algorithm are used to optimize the BP neural network to improve the calculation efficiency as well as ensuring the calculation accuracy of the proxy model.

3.2. Chaos Particle Swarm Optimization. The particle swarm algorithm is an optimization algorithm developed based on the actual biological group activities. The significant features of the algorithm are fast convergence, high robustness, and strong global optimization ability. The particle swarm algorithm is prone to random oscillations and falls into local optimal values. To solve this problem, chaos algorithm is introduced into the particle swarm algorithm. In addition, the chaotic sequence is used to iterate the optimal particles in the particle swarm to improve the ability of the algorithm to jump out of the local optimal solution. The specific steps are given as follows:

(1) Initialize the population. Then, determine the population number N, dimension D, the maximum number of iterations $K_{\max}$, and other parameters.

(2) Calculate the fitness of each particle and update the local optimal position P_{best} and the global optimal position g_{best} of each particle.

(3) Normalize the optimal position of each particle $P_{\text{best}} = (P_{g1}, P_{g2}, \ldots, P_{g\,D})$ to obtain $(y_{k1}, P_{k2}, \ldots, y_{k\,D})$.

(4) Use the logistic equation to iterate on y_{k1} and denormalize the obtained results.

(5) Use the obtained new solution to calculate the fitness. If the new solution is better than the old solution, output the new one.

(6) Judge whether the maximum number of chaotic iterations is reached; if not, return to step (2).

3.3. CPSO-BR-BP Neural Network Proxy Model. According to the advantages of CPSO and BR algorithms in correcting weights and thresholds, the traditional BP neural network is optimized and a new CPSO-BR-BP neural network proxy model is proposed. The basic idea is as follows. Firstly, set the basic parameters of the chaotic particle swarm, determine the number of random variables and responses, randomly generate the initial position and initial velocity of the particle, update the particle velocity and position, and get the individual extreme value and global extreme value of the particle by using the mean square error of the BP neural network as the fitness function. Secondly, the global extreme value of the particle is optimized chaotically by the logistic equation. The best individual is output and used as the optimal initial weight and threshold. Finally, the BP neural network that obtains the optimal initial value is used for training by BR, and the correction function is introduced based on equation (4) to optimize the performance function. The revised performance function expression is as follows:

$$E = \alpha E_D + \beta E_W, \quad (5)$$

$$E_w = \frac{1}{s} \sum_{i=1}^{s} \omega_i^2, \quad (6)$$

where E is the modified performance function; α and β are the regularization coefficients; E_w is the weight attenuation term; and ω_i is the weight of the neural network connection.

The BR algorithm that takes equation (5) as a performance function adaptively adjusts the size of α and β during the training process. Under the condition of ensuring that the training error converges to the target error, the final weight and threshold are output, and CPSO-BR-BP neural network proxy model is established based on this.

The main process of the reliability analysis of the unlocking trigger device based on the CPSO-BR-BP neural network under the parameter uncertainty is shown in Figure 3.

3.4. Reliability Calculation Method Based on Improved Membership

3.4.1. Reliability Calculation Method of SMA Wire Unlocking Process. The successful completion of the unlocking process of the device within the specified time is the basis for ensuring its reliability. The mapping relationship between the uncertain parameters and the response is constructed, which is based on the BP neural network, and the key performance indicator is the recovery displacement. The probability distribution characteristics of the recovery displacement of the SMA wire under the condition of parameter uncertainty are obtained by the mapping relationship. The unlocking reliability of the shape memory alloy wire is obtained based on the allowable displacement. The function expression of

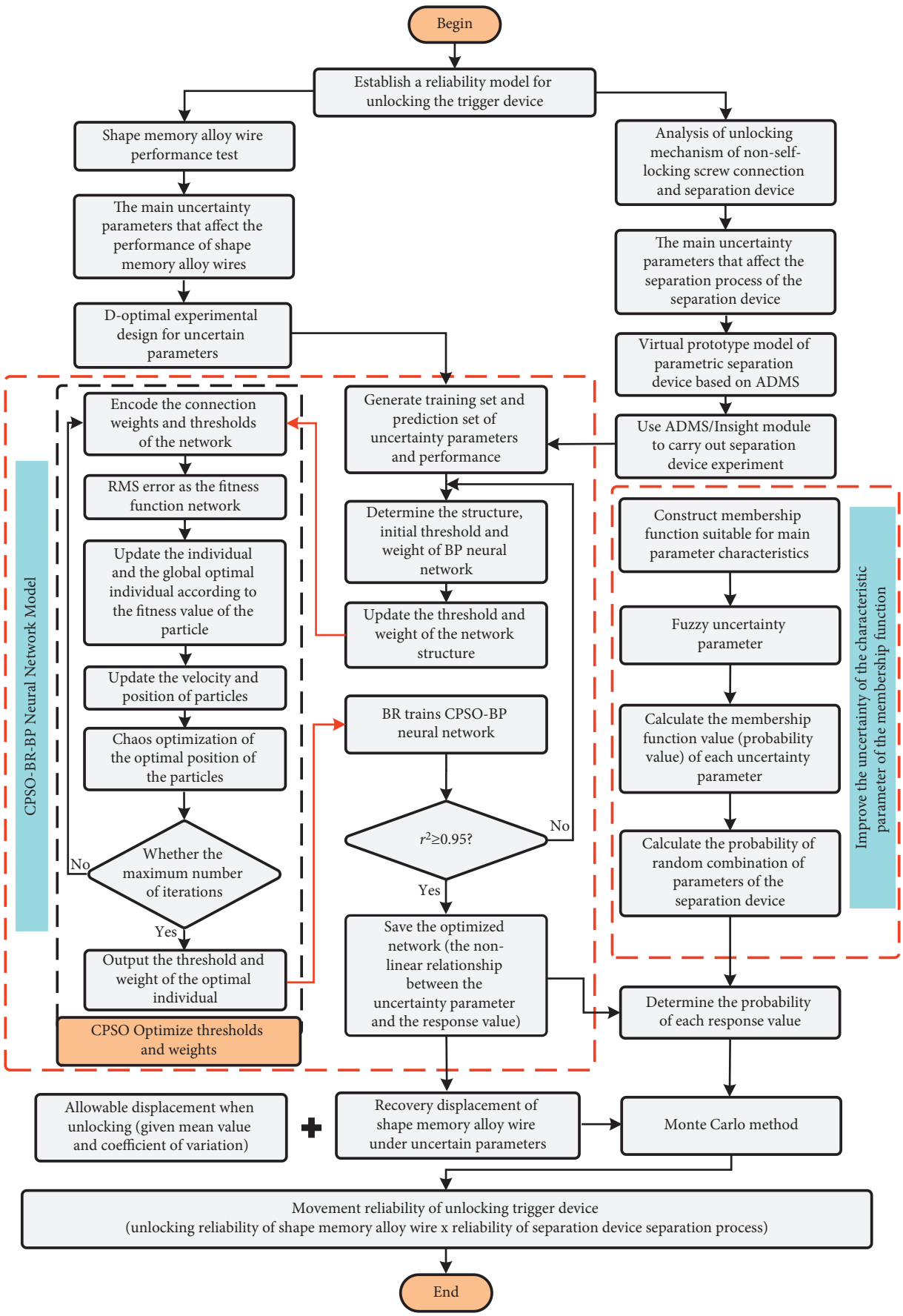

Figure 3: Main processes of reliability analysis of separation mechanism.

the SMA wire unlocking reliability analysis function can be represented as

$$X = L(x) - L = \begin{cases} > 0, & \text{displacement is greater than allowable displacement,} \\ = 0, & \text{displacement is equal to allowable displacement,} \\ < 0, & \text{displacement is less than allowable displacement,} \end{cases} \tag{7}$$

where $L(x)$ is the return displacement of the SMA wire; L is the allowable displacement when the SMA wire is unlocked.

According to equation (7), the reliability can be defined as

$$R(t) = \frac{n}{N}. \tag{8}$$

3.4.2. Reliability Calculation Method of the Separation Process. In the process of calculating motion reliability, a reasonable membership function is a prerequisite for the quantification of parameter uncertainty. The traditional distributions are in the neighborhood centered on the fuzzy median. It is necessary to artificially determine the value interval of the uncertainty parameter. Besides, it is difficult to reflect the actual value of the parameter. Considering the actual mechanical structure, the uncertainty parameters are mostly in the 6σ neighborhood centered on its mean value, and the reliability of mechanical parts based on this range can meet the actual engineering requirement [24]. The membership function based on the 6σ principle is improved to reduce the deviation between the uncertainty parameter and the actual manufacturing, and it also can improve the accuracy of the motion reliability analysis of the separation process.

The improved membership function can be represented as

$$A(x_i) = \begin{cases} 0, & x_i \le \mu_i - 6\sigma_i, \\ \sqrt[d]{\dfrac{x_i - \mu_i + 6\sigma_i}{6\sigma_i}}, & \mu_i - 6\sigma_i < x_i \le \mu_i, \\ \sqrt[d]{\dfrac{-x_i + \mu_i + 6\sigma_i}{6\sigma_i}}, & \mu_i < x_i \le \mu_i + 6\sigma_i, \\ 0, & \mu_i + 6\sigma_i \le x_i, \end{cases} \tag{9}$$

where x_i is the value of a random variable; $A(x_i)$ is the degree of membership corresponding to the random variable x_i; μ_i is the mean value of the random variable x_i; σ_i is the standard deviation of the random variable x_i; d is the undetermined coefficient.

The smooth completion of the separation process of the device within the specified time is the basis and prerequisite to ensure its movement reliability. For this reason, the fuzzy reliability model of the separation device is established, and the key performance index is the separation time of the device. Therefore, the separation process of the separation device can be calculated. According to the overall separation time index of the unlocking trigger device, the threshold of the response time of the separation process is determined, and the movement reliability function is constructed. The function can be represented as

$$G(x_i) = 0.0804 - t_2(x_i) = \begin{cases} > 0, & \text{reliable separation process,} \\ = 0, & \text{limit state separation process,} \\ < 0, & \text{failure of the separation process,} \end{cases} \tag{10}$$

where $t_2(x_i)$ is the response value under each uncertainty parameter combination, s; x_i is a set of uncertainty design parameters selected at random.

According to equation (10), the probability of each uncertainty parameter combination can be calculated, and its expression is as follows:

$$p\left(G\left(x_j\right)\right) = \prod_{i=1}^{n} A(x_i), \tag{11}$$

where i is the number of uncertain parameters considered, $i = 1, 2, \ldots, n$; j is the number of Monte Carlo simulations, $j = 1, 2, \ldots, m$.

According to equation (11), the calculation formula of the movement reliability of the separation process can be expressed as

$$R(G(x)) = \frac{\sum_{j=1}^{m} P\left(G\left(x_j\right)\right)}{m}, \tag{12}$$

$$P\left(G\left(x_j\right)\right) = \begin{cases} p\left(G\left(x_j\right)\right), & 0 \le G\left(x_j\right), \\ 1 - p\left(G\left(x_j\right)\right), & 0 > G\left(x_j\right). \end{cases} \tag{13}$$

3.4.3. Reliability Calculation Method of Unlocking Trigger Device. The unlocking trigger device consists of the SMA wire unlocking process and the separation device separation process according to the working principle, and the movement process conforms to the characteristics of the series reliability model. This means that any part of the failure will cause the entire system to fail during the movement of the unlocking trigger device. Its reliability block diagram is shown in Figure 4.

The reliability of the series system is equal to the product of the reliability of each subsystem, and its expression can be described as follows:

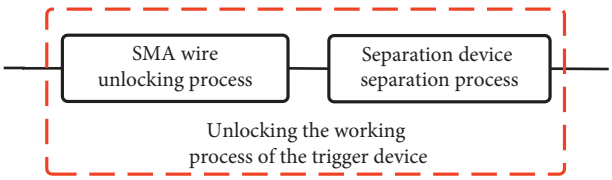

Figure 4: Series reliability model of the separation mechanism.

$$R(t) = \prod_{i=1}^{n} R_i(t), \tag{14}$$

where $R(t)$ is the reliability of the system, that is, the reliability of the whole machine for unlocking the trigger device; $R_i(t)$ is the reliability of each unit, that is, the reliability of the SMA wire unlocking or the separation device separation process.

4. Reliability Analysis of the Unlocking Trigger Device

The unlocking trigger device is effectively and reliably locked during the launch phase. After reaching the predetermined orbit, the unlocking action needs to be completed through the SMA wire, and the separation of the carrier and the payload is accomplished. In the process of analyzing the movement reliability of the whole machine, firstly, the movement reliability of the SMA wire in unlocking is analyzed. Then the movement reliability of the mechanical separation process is verified to obtain the reliability of the separation time under the fluctuation of the uncertainty parameter. Finally, the reliability of the whole machine is analyzed.

4.1. Analysis of Motion Reliability of SMA Wire in Unlocking

4.1.1. Reliability Calculation Method of Unlocking Trigger Device. Through the performance test of the SMA wire under different parameter conditions, the current, the time, the load, the wire diameter, and the temperature have significant impacts on the performance of the SMA wire, and there is large uncertainty in the working process. Therefore, the parameters are the main parameters that affect the reliability of its motion. The traditional performance analysis is carried out by changing a single parameter without efficient experimental design plans. For this reason, the D-optimal experimental design is used for the experimental design [25], and the CPSO-BR-BP neural network proxy model is used to obtain the relationship between inputs and outputs. Then the continuous characterization of the uncertainty parameter and the performance of the SMA wire can be set up, and the influences of parameter uncertainty on the performance of the SMA wire can be shown. According to the main parameters of traditional SMA wire performance analysis and the field test environment, the statistical values of each parameter are shown in Table 1, and the experimental design scheme and response values are shown in Table 2.

To observe the effects of different random parameters on the recovery time and recovery displacement of SMA wire more clearly, according to the test data and results in Table 2, the sample space of recovery time and recovery displacement under the action of any two uncertain parameters are shown in Figure 5.

It can be seen from Figure 5 that the recovery time and the recovery displacement of the SMA wire are evenly distributed in the sample space under the action of different random parameters with a large dispersion. This indicates that the sample value obtained through the D-optimal experimental design can reflect the variation range of the response value of random parameters. The proxy model established based on this set of data can more accurately characterize the mapping relationship between inputs and outputs.

25 sets of data from the sample data in Table 2 are randomly extracted for normalization, which are used as the prediction data of the neural network agent model. Besides, the remaining 6 sets of data are used as test data to test the prediction accuracy of the neural network proxy model. The proxy model of the uncertainty parameters on the response time of the SMA wire is obtained by predicting. The proxy model can be shown as

$$\begin{aligned} t_1 = {} & \frac{0.6497}{A_1} - \frac{2.2306}{A_2} + \frac{0.7450}{A_3} + \frac{0.0059}{A_4} + \frac{0.4022}{A_5} \\ & + \frac{0.3936}{A_6} + \frac{0.3936}{A_7} - 0.2406, \end{aligned} \tag{15}$$

where

$$\begin{aligned} A_1 &= 1 + \exp(0.2852I + 0.1185t' + 0.0054\ d \\ &\quad + 0.3902F - 0.5300T + 0.8283), \\ A_2 &= 1 + \exp(0.5403I - 0.0716t' - 1.6457\ d \\ &\quad - 0.0925F + 1.5852T + 2.7776), \\ A_3 &= 1 + \exp(0.3202I + 0.2112t' - 0.0746\ d \\ &\quad + 0.5373F - 0.5014T + 0.9512), \\ A_4 &= 1 + \exp(-0.2345I - 0.2453t' + 0.0687\ d \\ &\quad - 0.2266F + 0.0678T + 0.1210), \\ A_5 &= 1 + \exp(-0.4772I - 0.2026t' + 0.1036\ d \\ &\quad - 0.5309F + 0.0928T + 0.3704), \\ A_6 &= 1 + \exp(-0.4741I - 0.2099t' + 0.1063\ d \\ &\quad - 0.5222F + 0.0962T + 0.3668), \\ A_7 &= 1 + \exp(-0.4417I - 0.2242t' + 0.1008\ d \\ &\quad - 0.4833F + 0.0914T + 0.3371). \end{aligned} \tag{16}$$

The proxy model of uncertainty parameters on the recovery displacement of SMA wire is shown as

$$\begin{aligned} l = {} & \frac{2.6947}{B_1} - \frac{0.3673}{B_2} - \frac{1.0795}{B_3} - \frac{0.5471}{B_4} \\ & - \frac{0.6164}{B_5} + \frac{0.2473}{B_6} - \frac{0.4259}{B_7} + 0.1161, \end{aligned} \tag{17}$$

Table 1: Statistical values of uncertain parameters.

Uncertainty parameter	Symbol	Unit	Lower bound	Mean	Upper bound
Heating current	I	A	4.50	5.00	5.50
Heating time	$t\prime$	ms	90.00	100.00	110.00
Wire diameter	d	mm	0.25	0.30	0.35
Load	F	N	7.00	8.00	9.00
Temperature	T	°C	−70.00	0	70.00

Table 2: D-optimal experimental design and response values.

No.	Heating current	Heating time	Wire diameter	Load	Temperature	Response time	Response displacement
1	5.50	90.0	0.25	7.00	70.0	4.393	11.172
2	5.07	110.0	0.25	9.00	70.0	6.058	11.628
3	4.50	110.0	0.35	7.00	−70.0	140.306	11.989
...	...	...	...	...	...	...	...
29	5.50	110.0	0.35	7.00	70.0	11.932	7.695
30	5.07	110.0	0.25	9.00	70.0	6.058	11.628
31	5.50	101.6	0.25	8.15	70.0	4.826	11.609

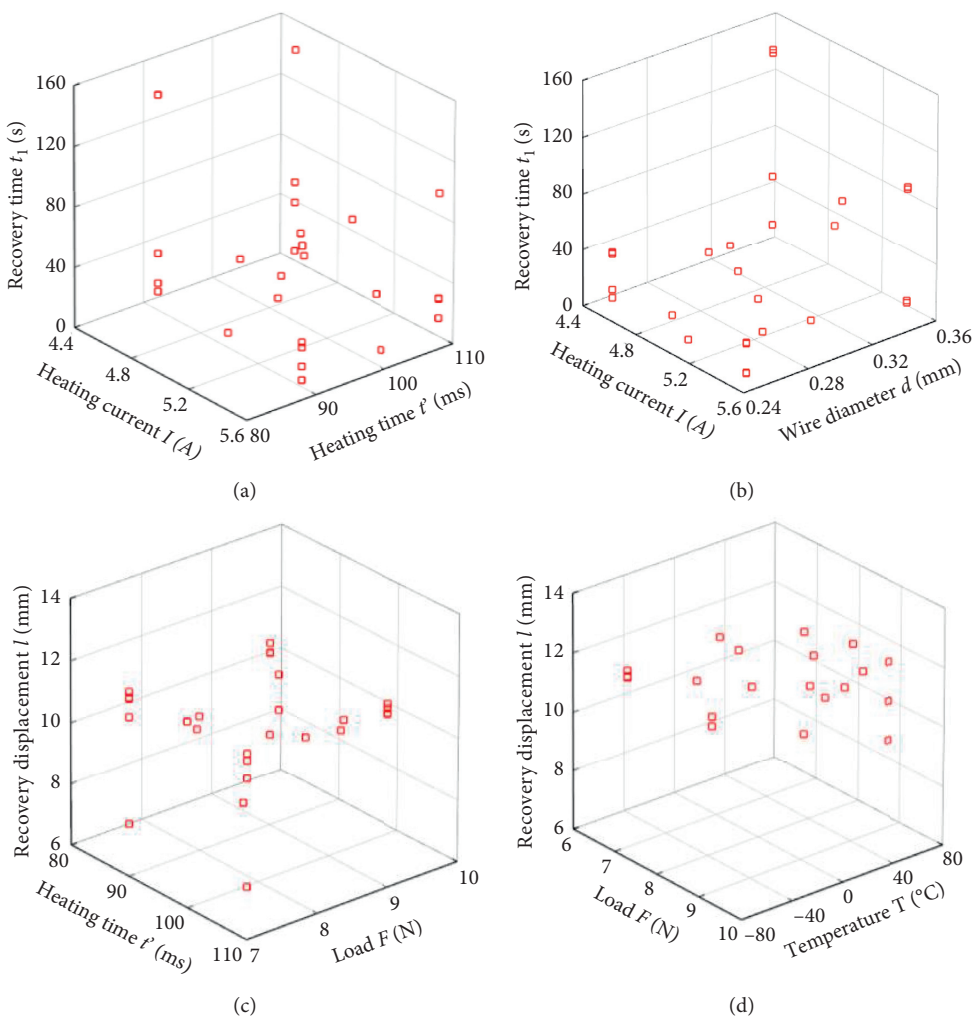

Figure 5: Sample space of uncertain parameters for heating current and heating time (a), heating current and wire diameter (b), heating time and load (c), and load and temperature (d).

where

$$\begin{aligned}
B_1 &= 1 + \exp\left(0.5639I + 0.8471t' - 1.4172\ d \right. \\
&\quad \left. + 0.7140F - 4.1718T + 4.1867\right), \\
B_2 &= 1 + \exp\left(-0.1706 - 0.0847t' + 0.0924\ d \right. \\
&\quad \left. + 0.2513F + 0.3391T + 0.5180\right), \\
B_3 &= 1 + \exp\left(0.4742I + 0.2539t' - 0.7967\ d \right. \\
&\quad \left. + 0.4270F - 2.0559T + 0.9893\right), \\
B_4 &= 1 + \exp\left(-0.3780I + 0.1858t' - 0.1279\ d \right. \\
&\quad \left. + 0.2607F + 0.55330T + 0.2446\right), \\
B_5 &= 1 + \exp\left(-0.4602I - 0.2625t' - 0.3707\ d \right. \\
&\quad \left. - 0.8604F - 0.4454T + 0.6977\right), \\
B_6 &= 1 + \exp\left(0.0307I - 0.0019t' - 0.1778\ d \right. \\
&\quad \left. - 0.0256F - 0.0648T + 0.1118\right), \\
B_7 &= 1 + \exp\left(-0.1985I - 0.0520t' + 0.0631\ d \right. \\
&\quad \left. + 0.2778F + 0.3952T + 0.2028\right).
\end{aligned} \tag{18}$$

The measurement coefficient is used to evaluate the accuracy of the CPSO-BR-BP proxy model so that the established proxy model has high accuracy to predict the response of the actual SMA wire under uncertainty parameters. The response time and the response displacement are tested on the accuracy of the proxy model, respectively. The results are shown in Table 3.

It can be seen from Table 3 that the determination coefficient values of the CPSO-BR-BP proxy model for the response time and the response displacement are both close to 1. This indicates that the predicted data obtained from the proxy model is relatively close to the actual values. Besides, the established proxy model can reflect the changing trend and specific values of the response value of the SMA wire with high accuracy. To show the fitting accuracy of the proxy model more intuitively, the actual values of the test data are compared with the predicted values obtained from the CPSO-BR-BP proxy model. The corresponding change trends and prediction errors are shown in Figures 6 and 7 .

It can be seen from Figure 6 that the predicted response time and recovery displacement using the CPSO-BR-BP neural network proxy model are consistent with the actual value change trend, while the changing trend obtained from the traditional BP neural network is quite different. This indicates that the model can more accurately characterize the mapping relationship between the uncertainty parameters on the recovery time and the recovery displacement. In addition, to further verify the fitting accuracy of the proxy model, the error between the predicted values and the actual values concerning the two proxy models is compared. Results show that the error of the CPSO-BR-BP neural network proxy model presents a relatively stable fluctuation and all distributes around 0, while the traditional BP neural network error is relatively larger with poorly stable fluctuations. This explains that the fitting accuracy of the improved proxy model is high, and it can accurately predict the recovery performance of the SMA wire under the condition of parameter uncertainty.

Table 3: Accuracy verification results of the surrogate model.

Proxy model	Decisive factor r^2
Response time t_1	0.9915
Response displacement l	0.9998

4.1.2. Analysis of Motion Reliability of SMA Wire in Unlocking. According to the working principle of SMA wire and its role in the separation device, its reliability is defined as the ability to release the limit stably under the specified time and conditions. It is more important to achieve the limit release of the mechanism under specified conditions for SMA wire. Therefore, the limit state equation of SMA wire in unlocking is constructed based on the recovery displacement value and the design recovery displacement index of the SMA wire under the uncertainty parameters. The Monte Carlo method is used to analyze the motion reliability of SMA wire in unlocking, and its reliability value with a certain probability distribution is obtained. The uncertainty parameters and their response values obtained by Monte Carlo simulation are shown in Table 4. The probability distribution characteristics of the uncertainty parameters are shown in Figures 8(a) to 8(e). The recovery displacement distribution of the SMA wire under the influence of the uncertainty parameters features is shown in Figure 8(f).

It can be seen from Figure 8(f) that the recovery displacement of the SMA wire shows a certain degree of fluctuation under the action of various uncertain parameters, and its value is mainly concentrated at about 12 mm. In addition, the probability distribution characteristics approximately obey the normal distribution. Through the analysis of its truncated data, the recovery displacement of the SMA wire is lower than the design recovery displacement due to the influence of uncertainty parameters. This indicates that the uncertain parameters have effects on the SMA, such as heating current and heating time, which will reduce the reliability of unlocking. Compared with the deterministic SMA wire unlocking analysis in the traditional sense, the uncertainty analysis can better evaluate the reliability of the SMA wire unlocking under the action of uncertain parameters. Based on the reliability theory and Figure 8(f), the cumulative probability of the limit state function of the SMA wire is obtained, as shown in Figure 9.

It can be seen from Figure 9 that when the limit state function is smaller than 0 (i.e., the recovery displacement of the SMA wire fails to reach the specified value), the Monte Carlo method is used to obtain the failure probability of the SMA wire unlocking motion; that is, the reliability of the recovery displacement is 0.9996. From the results of the reliability calculation, the uncertainty parameters have obvious influences on the recovery performance of the SMA wire, which can lead to low recovery performance. In addition, the recovery performance cannot fully meet the design index requirements. To further study the influence of parameter uncertainty on the motion reliability of the SMA wire in unlocking, 10,000 sets of sample data with the coefficient of variation within the range are analyzed based on the CPSO-BR-BP neural network proxy model, and the response value under each parameter combination is

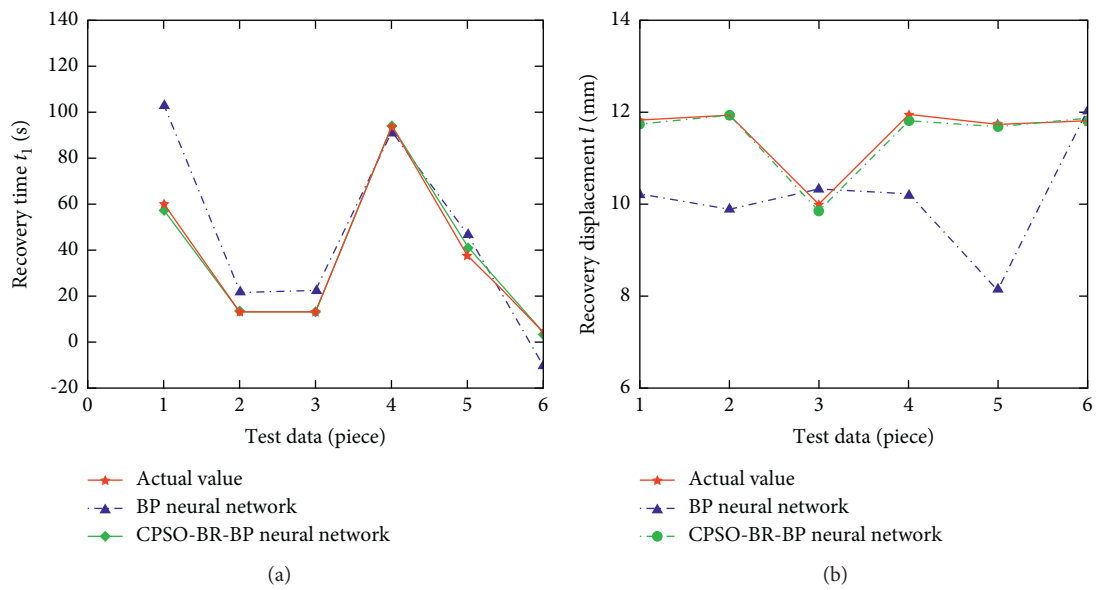

Figure 6: Comparison between predicted values and real values of surrogate model: (a) response time prediction and (b) recovery displacement prediction.

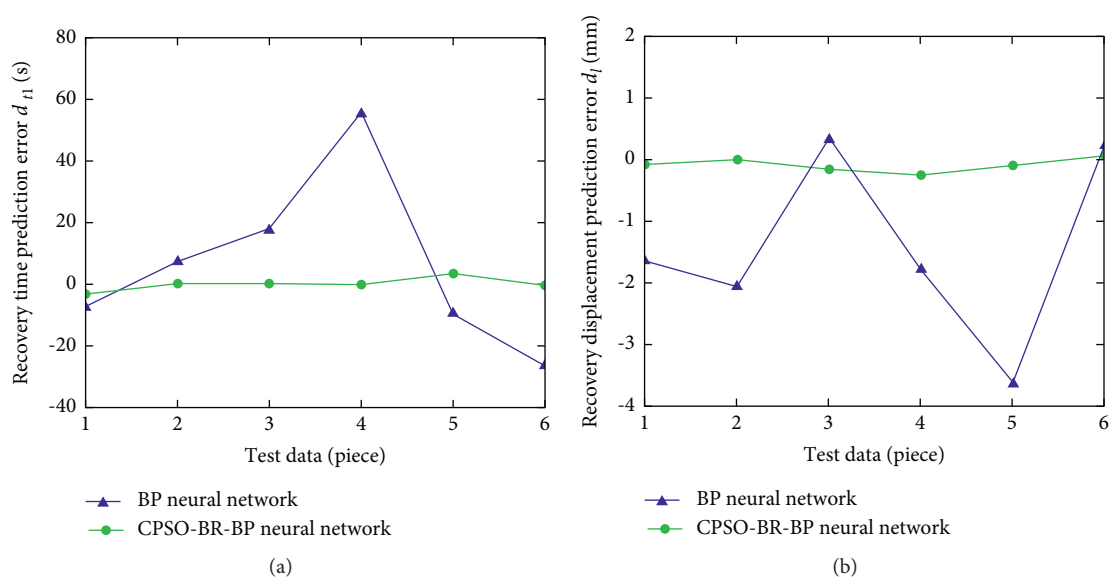

Figure 7: Prediction error of surrogate model: (a) recovery time and (b) recovery displacement.

Table 4: Prediction data of SMA wire under uncertainty parameter fluctuation.

No.	Heating current	Heating time	Wire diameter	Load	Temperature	Response time	Response displacement
1	6.07	92.11	0.20	6.51	6.06	27.87	12.02
2	5.21	105.89	0.30	8.49	−34.89	30.43	11.79
3	4.88	101.61	0.35	4.45	35.58	61.56	7.47
...	...	...	...	...	...	...	...
9998	4.15	116.92	0.30	11.05	−56.16	29.38	12.14
9999	3.61	95.80	0.31	7.78	10.71	25.85	11.62
10000	5.82	64.67	0.24	12.38	−9.48	23.51	12.13

predicted. The mean value and standard deviation of the recovery displacement of SMA wires with different coefficients of variation are calculated as shown in Figure 10.

It can be seen from Figure 10 that as the coefficient of variation increases, the standard deviation of the recovery displacement gradually increases, indicating that the

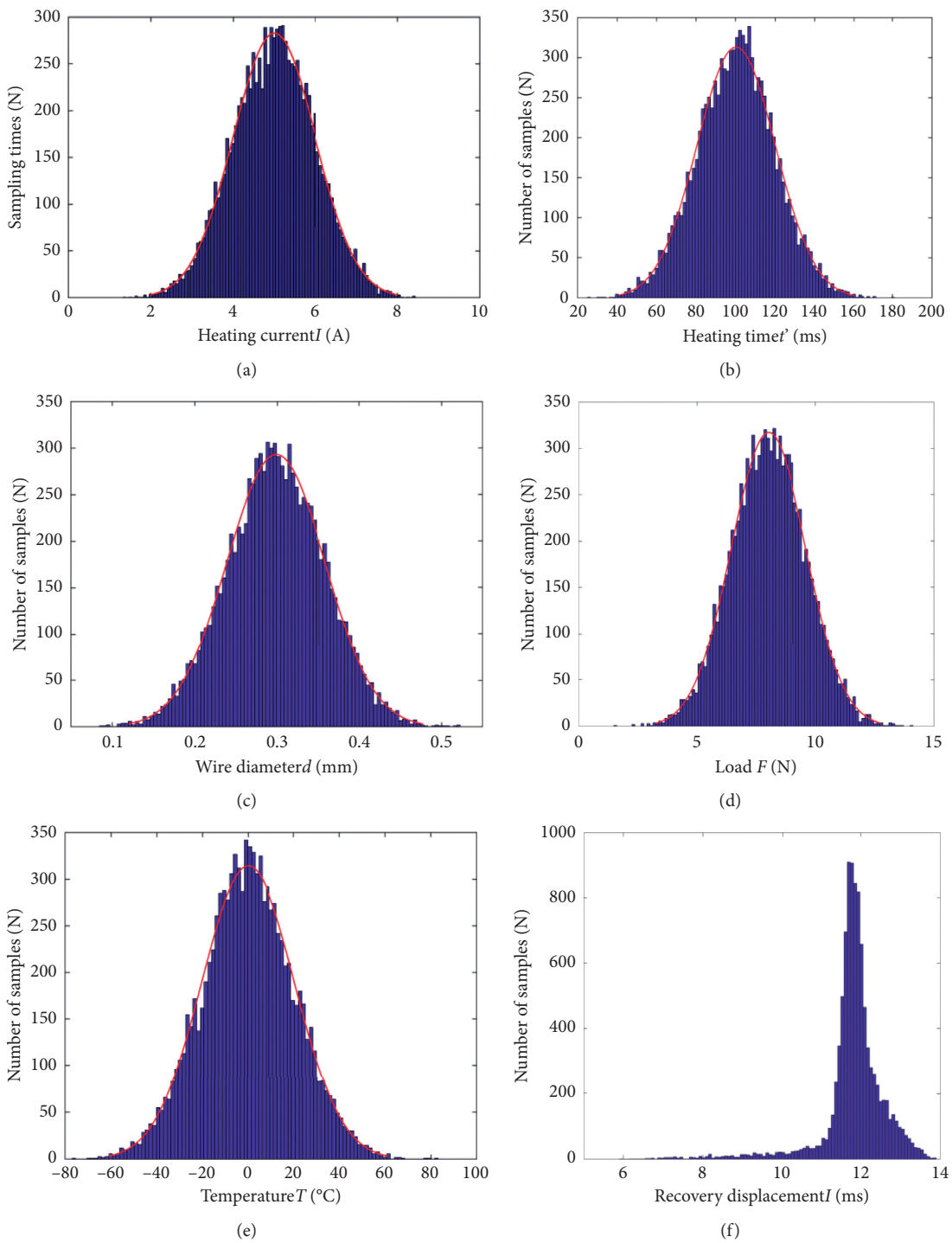

Figure 8: Probability distribution of heating current (a) (N (5, 0.252)), heating time (b) (N (100, 52)), wire diameter (c) (N (0.3, 0.0152)), load (d) (N (8, 0.42)), temperature (e) (N (0, 0.42)), and response displacement (f).

increase in the coefficient of variation makes the dispersion of the uncertainty parameter values increase. The dispersion of the recovery displacement of the SMA wire becomes larger, which increases the possibility that the recovery displacement is smaller than the prescribed threshold. Secondly, the mean value of the return displacement of the SMA wire continues to decrease, indicating that the increase of the coefficient of variation makes the coupling effects of the uncertain parameters lead to the reduction of the recovery performance of the SMA wire. To further quantify the relationship between parameter uncertainty and SMA wire movement reliability, the movement reliability of the SMA wire in unlocking under different coefficients of variation is calculated, as shown in Figure 11.

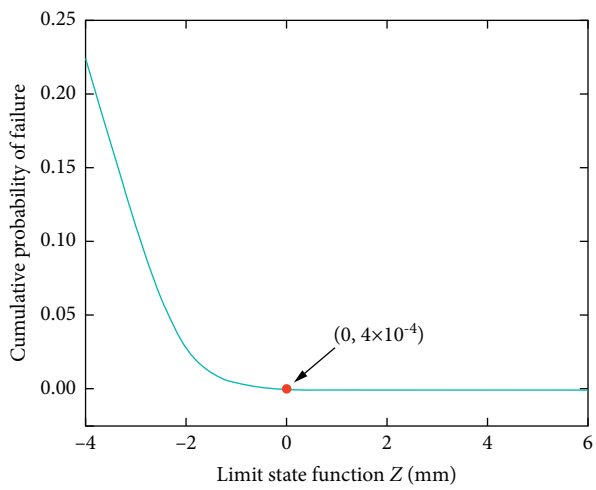

Figure 9: Cumulative failure probability of limit state function.

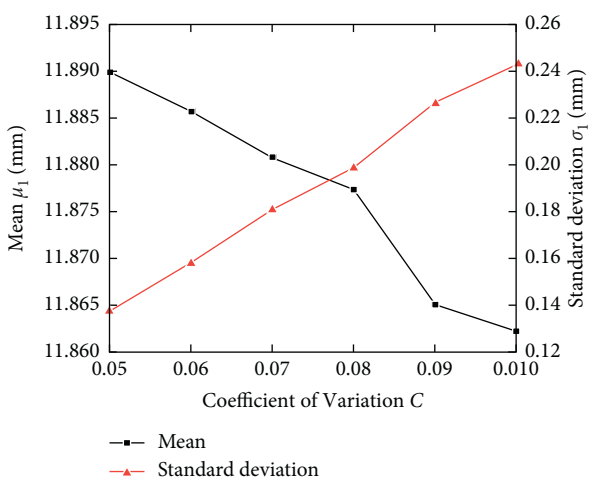

Figure 10: Mean and standard deviation of recovery displacement of SMA wires with different coefficients of variation.

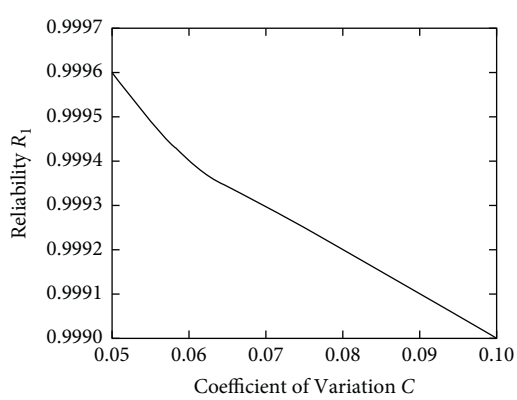

Figure 11: Kinematic reliability of SMA wire under different coefficients of variation.

It can be seen from Figure 11 that the movement reliability of the SMA wire in unlocking is continuously reduced with the increase of the uncertainty parameter variation coefficient. When the coefficient of variation is 0.05, the highest working reliability of the device is 0.9996. When the coefficient of variation is 0.10, the lowest working reliability of the device is 0.999, indicating that the parameter uncertainty has a significant impact on the movement reliability of the SMA wire. In work, the fluctuation range of various parameters should be strictly controlled to ensure the motion reliability of the SMA wire.

4.2. Motion Reliability Analysis of Separation Process

4.2.1. Deterministic Dynamic Simulation of the Separation Process. To consider the accuracy and efficiency of the motion reliability analysis of the separation process, ADAMS is used to simulate and analyze the motion process of the separation process. The deterministic analysis of the separation process is the basis and prerequisite to ensure the parameterization of the mechanism. For this reason, according to the simplified separation device, the virtual prototype model is established by ADAMS, as shown in Figure 12.

To accurately simulate the actual working conditions of the separation device, a measurement function of the distance between the top of the bearing screw and the bottom of the flywheel nut needs to be established. The simulation time is set to 0.1 s and the step length is 1000 steps. When the distance between the two is 0, it means that the bearing screw completely withdraws from the thread pair; that is, the device separation ends, and the simulation stops. The calculation result is shown in Figure 13.

It can be seen from Figure 13 that the constraints of the separation device at all levels are released at 0 s (initial state), and the flywheel nut starts to release the stored pretightening force and drive the bearing screw to rotate at high speed. At this time, there is a gap between the thread pair, the flywheel nut, and the thrust roller bearing, so that the normal pressure between the contact surfaces is small. In addition, the friction resistance torque of the bearing screw is smaller, and the resultant torque is relatively stable, so the acceleration of the bearing screw remains unchanged from 0 to 0.0049 s. As the separation process continues, the remaining pretightening force of the flywheel nut gradually decreases, and contact between the contact surfaces gradually occurs. At the same time, the normal pressure increases, and the friction resistance torque acting on the device continues to increase. In addition, the resultant torque continues to decrease, and the acceleration of the bearing screw gradually decreases within 0.0049–0.0184 s. During the entire movement, the speed of the bearing screw keeps increasing. When the separation process reaches 0.0184 s, the remaining pretightening force of the flywheel nut is relatively balanced with the frictional resistance torque received by the device, and the total torque received by the bearing screw is 0. In addition, the acceleration becomes 0, and the bearing screw moves at a constant speed until 0.0604 s and completely exits the thread pair, completing the device separation process.

4.2.2. Analysis of the Influence of Parameter Uncertainty on Separation Time. According to the unlocking mechanism of the separation device and the ADAMS simulation results, it

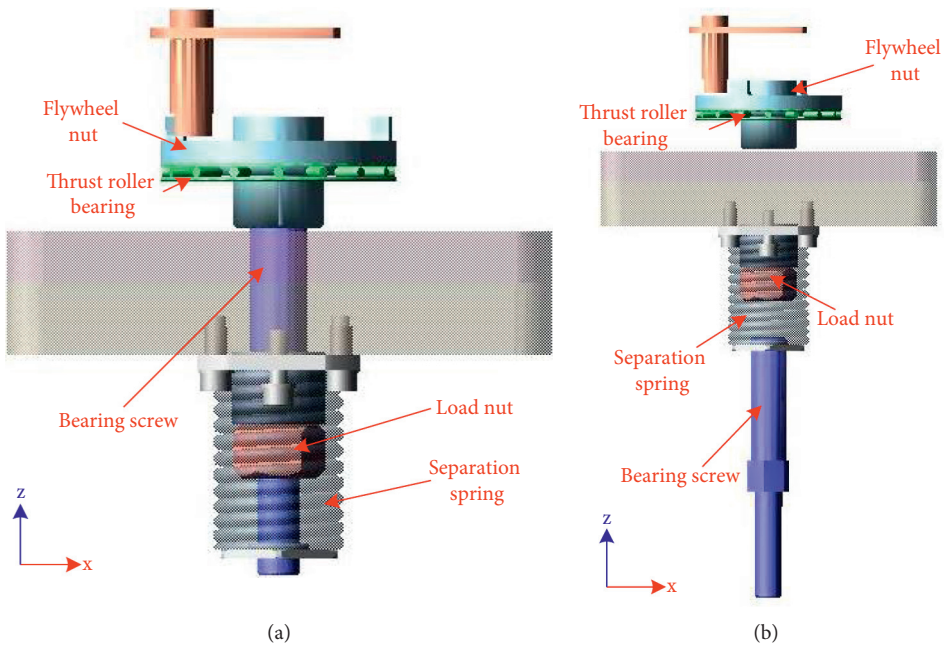

Figure 12: Virtual prototype model of separation device: (a) locking state and (b) unlocking state.

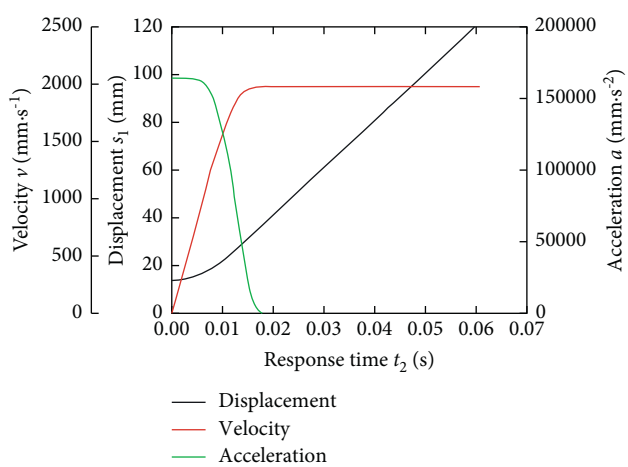

Figure 13: Simulation results of the separation process.

can be seen that the driving torque acting on the flywheel nut and the frictional resistance torque provided by the thrust roller bearing and the thread pair are the key factors affecting its kinematic parameters. Affected by various uncertain factors such as manufacturing, installation, and working environment, the force exerted on the separation device has certain randomness, which makes deviations from the theoretical value. Besides, this affects the separation time of the device and its working reliability. Therefore, three equal moments of driving torque, frictional resistance torque of thrust roller bearings, and frictional resistance torque of non-self-locking thread pairs are used as the uncertainty parameters that affect the reliability of the separation process. It is assumed that each parameter obeys the normal distribution with a coefficient of variation of 0.05 [24], and the characteristic values of its probability distribution are shown in Table 5.

The parametric virtual prototype model of the separation device is established based on the data provided in Table 5. 200 sets of samples are randomly selected by ADAMS for the three uncertainty parameters, and the motion simulation of the separation process is performed to obtain the uncertainty parameter combination under random sampling and its response value, as shown in Table 6. The random value process of the uncertainty parameter and the changing trend of the separation time under different parameter combinations are shown in Figure 14.

It can be seen from Figure 14(a) that the sample values of the 200 sets of uncertainty parameters obtained by ADAMS simulation have good randomness and can more accurately characterize the changes of parameters caused by the uncertainty factors, such as driving torque, frictional resistance torque of thrust roller bearings, and frictional resistance

Table 5: Probability distribution characteristics of uncertain parameters.

Uncertainty parameter	Symbol	Unit	Mean	Coefficient of variation	Distribution type
Driving torque	T_D	N·mm	786	0.05	Normal distribution
Friction torque of thrust roller bearings	T_{mtb}	N·mm	229	0.05	Normal distribution
Friction torque of thread pairs	T_{mf}	N·mm	245	0.05	Normal distribution

Table 6: Uncertain parameters and response values.

No.	Driving torque	Friction torque of thrust roller bearings	Friction torque of thread pairs	Separation time
1	731.434	246.719	268.045	0.0725
2	739.074	226.417	238.174	0.0644
3	808.139	234.354	244.573	0.0588
...	...	...	...	...
198	835.707	223.411	229.945	0.0545
199	807.476	220.945	270.760	0.0600
200	884.286	218.235	271.858	0.0537

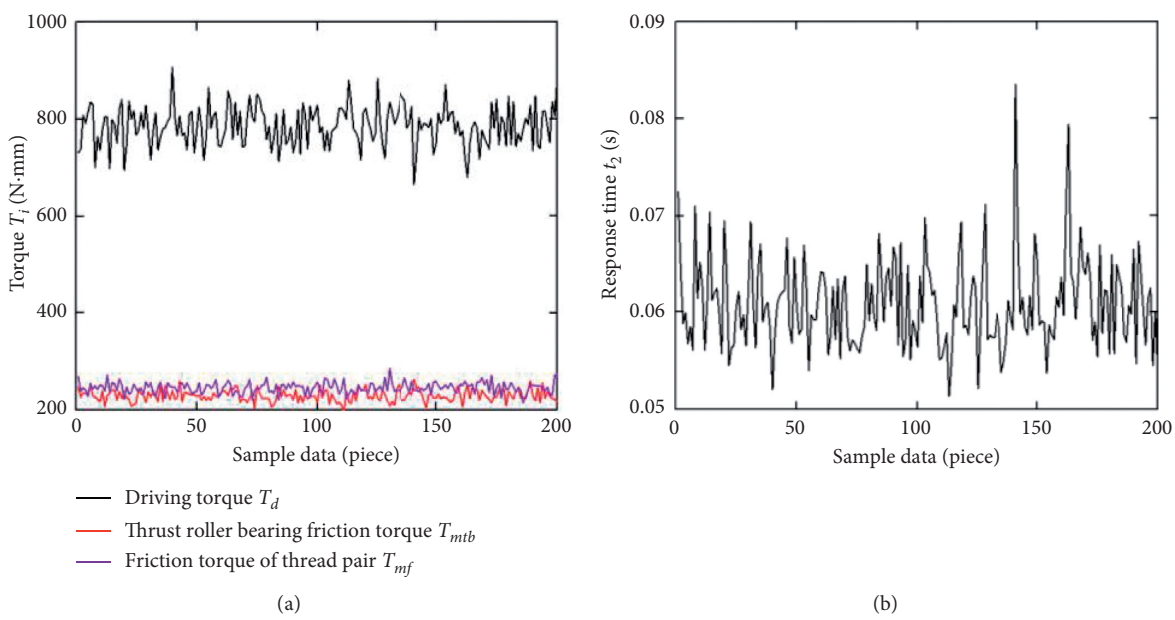

Figure 14: Sample value distribution of random variables (a) and response time (b).

torque of non-self-locking thread pairs. Figure 14(b) shows that, under the random fluctuation of parameters, the combination of parameters has a great impact on the separation time, and there are a few cases where the separation time exceeds the specified threshold. This indicates that the uncertainty of the parameters affects the movement reliability of the device's separation process. To more intuitively express the influence of the uncertainty parameters on the separation time, any two moments are selected as X-axis and Y-axis, and the sample space of different moments with respect to the separation time is drawn, as shown in Figure 15.

It can be seen from Figure 15 that the separation time of the device under the actions of any two moments shows a certain degree of dispersion, which is consistent with the random value of the parameter, and the phenomenon of clustering occurs in the sample space. This indicates that the random value range of the uncertainty parameter is relatively small, in line with the parameter fluctuation caused by uncertain factors under the conditions of continuously improving the processing and manufacturing level and the robust design. Secondly, most of the separation time is concentrated between 0.06 and 0.07 s, and a small part exceeds the specified threshold, which shows that the uncertainty of the moment leads to the reduction of the reliability of the separation process.

The motion reliability analysis of the separation process should be performed based on a large number of samples. However, more accurately reliable results cannot be obtained based on the sample points provided in Table 6. In addition, the efficiency to determine the sample data using

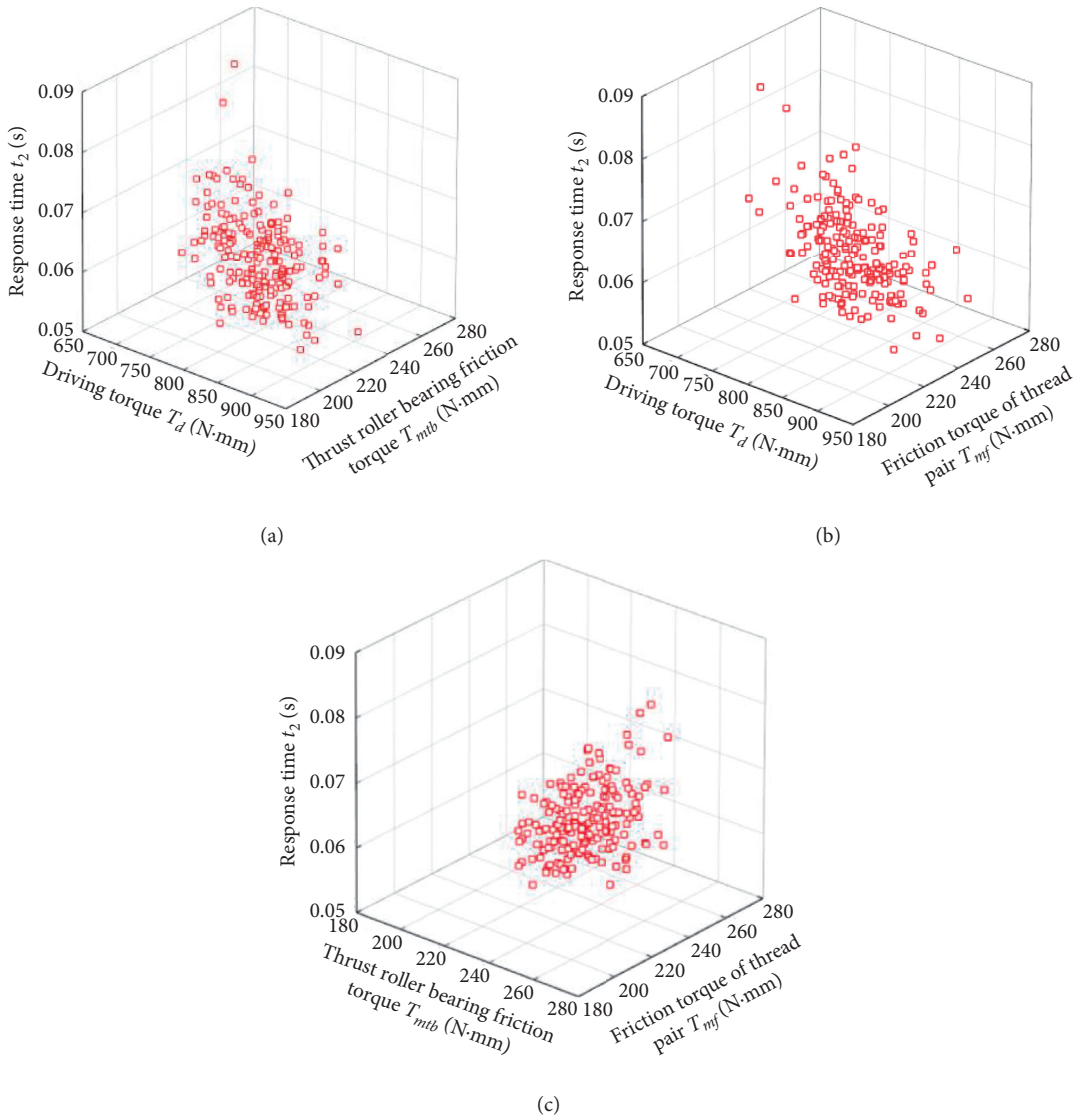

Figure 15: Sample space of uncertain parameters about separation time: (a) driving torque and friction torque of thrust roller bearings, (b) driving torque and friction torque of thread pairs, and (c) friction torque of thrust roller bearings and friction torque of thread pairs.

ADAMS simulation is low. For this reason, the proposed CPSO-BR-BP neural network proxy model is used to characterize the mapping relationship between the three moments and the separation time to improve the efficiency of motion reliability analysis.

170 sets of training samples are selected randomly as listed in Table 6 and normalized. According to the proposed method, the proxy model of three moments for separation time is established, and the expression is

$$t_2 = -\frac{0.3220}{C_1} + \frac{0.6547}{C_2} + \frac{0.6537}{C_3} + \frac{0.6744}{C_4} + \frac{1.1736}{C_5} - \frac{2.4037}{C_6} + \frac{0.9187}{C_7} + 0.4896, \tag{19}$$

where

$$\begin{aligned}
C_1 &= 1 + \exp\left(0.3005T_D - 0.2550T_{mtb} + 0.4176T_{mf} - 0.0161\right),\\
C_2 &= 1 + \exp\left(-0.3511T_D + 0.0938T_{mtb} + 0.1603T_{mf} + 0.0533\right),\\
C_3 &= 1 + \exp\left(-0.3548T_D + 0.0944T_{mtb} + 0.1475T_{mf} + 0.0524\right),\\
C_4 &= 1 + \exp\left(-0.3277T_D + 0.0934T_{mtb} + 0.2552T_{mf} + 0.0769\right),\\
C_5 &= 1 + \exp\left(-0.9894T_D + 0.1032T_{mtb} + 0.2814T_{mf} - 1.3137\right),\\
C_6 &= 1 + \exp\left(2.3090T_D - 0.7647T_{mtb} - 0.6694T_{mf} + 3.8676\right),\\
C_7 &= 1 + \exp\left(-1.1269T_D + 0.3873T_{mtb} + 0.3199T_{mf} - 0.5233\right).
\end{aligned} \tag{20}$$

The remaining 30 sets of sample data in Table 6 are used as test samples to test the accuracy of model fitting. The sample data is brought into the proxy model to compare and analyze the actual value and predicted value, and the

coefficient of determination is 0.99994. The comparative analysis result is shown in Figure 16.

It can be seen from Figure 16 that the predicted value based on the CPSO-BR-BP neural network proxy model is consistent with the actual value change trend, which shows that the model can more accurately represent the mapping relationship. To further characterize the fitting accuracy of the surrogate model, the error distribution is shown in Figure 17. It can be seen from Figure 17 that although the prediction errors of the 30 sets of data fluctuate to varying degrees, their magnitudes are 10^{-5}, indicating that the established proxy model has high accuracy and can accurately predict the separation time of the device under different moment values.

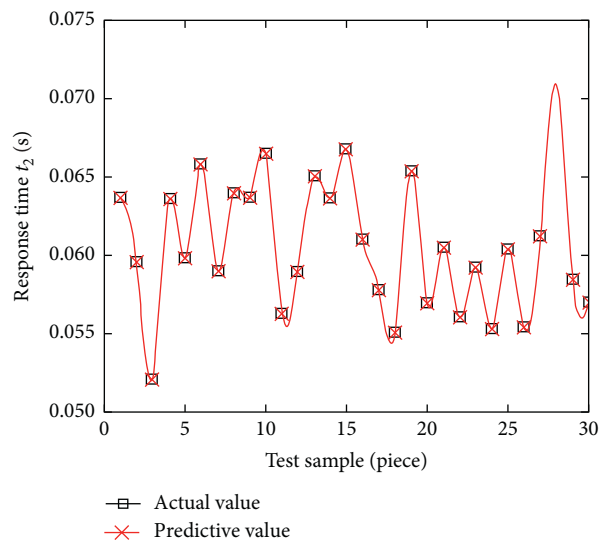

Figure 16: Comparison of predicted and actual values.

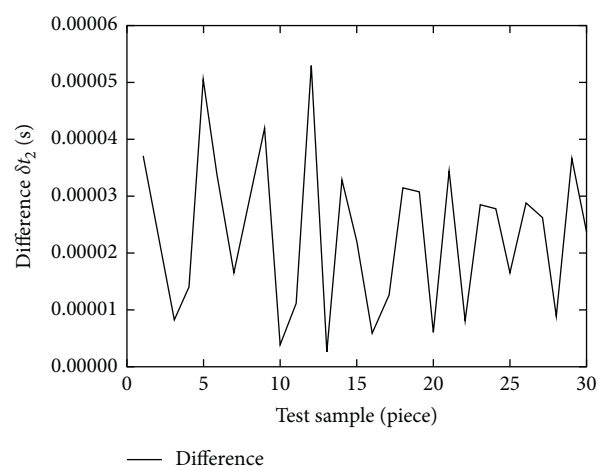

Figure 17: Data prediction error of 30 groups.

4.2.3. Motion Reliability Analysis of Separation Process. Based on the high-precision CPSO-BR-BP neural network proxy model, 10,000 Monte Carlo simulations are performed on the uncertain parameters, and the separation time of the device under each set of parameter combinations is predicted, as shown in Table 7. The random value of each parameter and the probability distribution characteristics of the corresponding separation time are shown in Figure 18.

It can be seen from Figures 18(a)–18(c) that the random distribution of each uncertainty parameter follows the normal distribution, which is basically consistent with the fluctuation form of the real situation, and the separation time of the device can also be predicted. The time for the device to complete the separation process under the uncertainty of parameter fluctuations is shown in Figure 18(d). Overall, the graph is affected by the parameter fluctuations, which make the separation time discrete, and it approximately obeys the probability characteristics of the normal distribution. However, there are a few cases where the response value exceeds the specified threshold at the censoring point, indicating that the uncertainty of the parameters affects the reliability of the separation process to a certain extent.

Incorporating the predicted separation time into equations (9)–(12), the motion reliability of the device separation process under the improved membership function is obtained. The undetermined coefficient d directly affects the profile of the membership function. As the value of d increases, the improved membership function gradually tends to the traditional rectangular membership function. To verify the advantages of the improved membership function, it is compared with the traditional rectangular membership function and the Monte Carlo simulation analysis results, as shown in Figure 19.

It can be seen from Figure 19 that the motion reliability obtained based on the improved membership function gradually tends to the Monte Carlo result as the number of iterations of the undetermined coefficient d increases. When the number of iterations of d reaches 25 times, the improved membership function is 0.9991, and the motion reliability calculated by the Monte Carlo method is 0.9998. The error between them is 0.07%. However, the motion reliability of the separation process based on the traditional rectangular membership function is not affected by the undetermined coefficient d, and the result is always maintained at 0.9763, the error of which is 2.35% compared with the Monte Carlo method. The comparative analysis shows that the use of the improved membership function to process the uncertainty parameters can better reflect the actual motion reliability of the device. The reliability calculation method based on the improved membership function is also certified to be of high accuracy.

To further study the influence of the uncertainty of the torque on the motion reliability of the separation process, the CPSO-BR-BP neural network proxy model is used to generate 10,000 sets of sample data with a coefficient of variation of 0.05–0.10 and to predict the response value of each parameter combination. The mean and standard deviation of the separation time under different coefficients of variation are obtained, as shown in Figure 20.

It can be seen from Figure 20 that both the mean and the standard deviation of separation time are positively correlated with the moment variation coefficient. This indicates

Table 7: Forecast data when the coefficient of variation is 0.05.

No.	Driving torque	Friction torque of thrust roller bearings	Friction torque of thread pairs	Separation time
1	801.4149	230.8262	249.5258	0.059537
2	830.3701	243.9656	236.3860	0.056992
3	709.8324	228.5464	222.1646	0.066253
...	...	...	...	...
9998	772.9308	242.3348	245.1185	0.063150
9999	798.3322	205.5270	239.0925	0.056708
10000	827.3862	227.1700	248.8006	0.056889

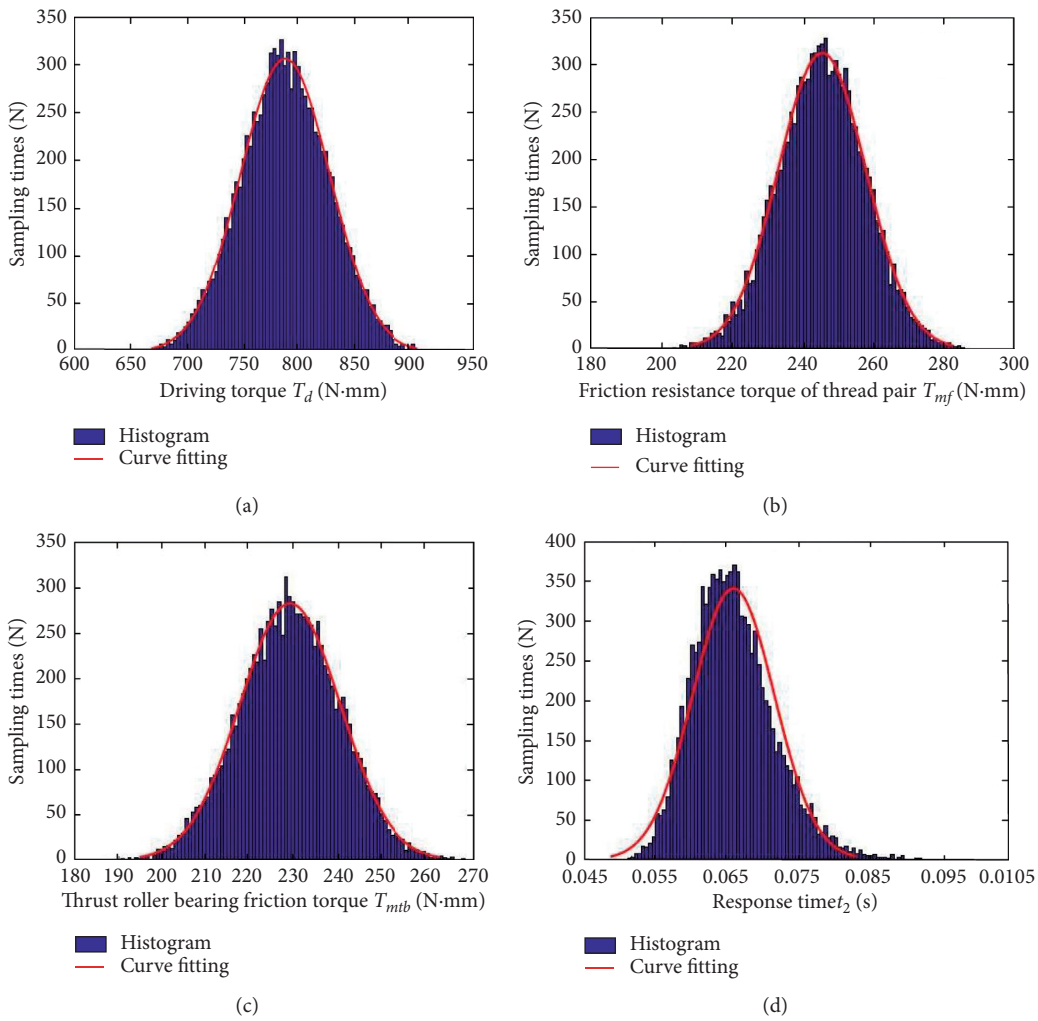

Figure 18: Probability distribution characteristics of driving torque (a) (N (786, 39.32)), friction torque of thrust roller bearings (b) (N (229, 11.452)), friction torque of thread pairs (c) (N (245, 12.252)), and response time (d) (N (0.0607, 0.00432)).

that as the moment variation coefficient increases, the uncertainty of the resultant moment acting on the load-bearing screw gradually increases, which expands the separation time fluctuation range. As a result, the standard deviation of the separation time continues to increase, and the possibility of exceeding the threshold becomes great, which affects the reliability of the separation process of the device to a certain extent. To quantify the relationship between the moment uncertainty and the movement reliability of the device separation process, the separation time obtained in Figure 20 is substituted into equations (9)–(12) to obtain the movement reliability of the device separation process under different coefficients of variation, as shown in Figure 21.

It can be seen from Figure 21 that the motion reliability of the separation process is negatively correlated with the moment variation coefficient, and the changing trend of the motion reliability obtained based on the improved membership function is consistent with the Monte Carlo method. The value of the result is smaller than that of the Monte Carlo method because of the fuzzy treatment of uncertainty of

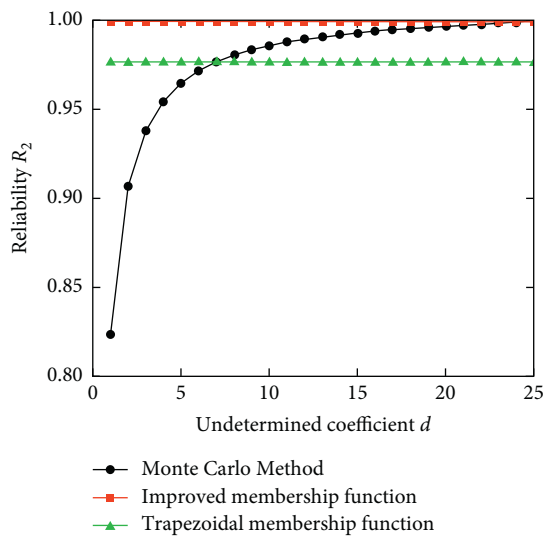

Figure 19: The iterative process of motion reliability for the separation process.

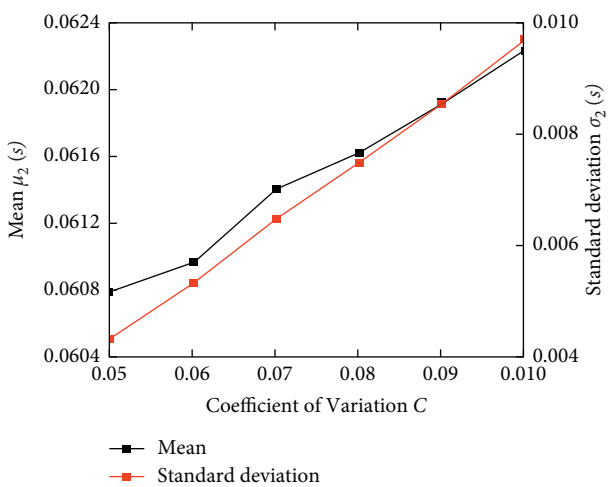

Figure 20: Mean and standard deviation of separation time under different coefficients of variation.

moment in the reliability calculation process. When the traditional rectangular membership function is used for calculation, the variation range of uncertainty parameters is large. Such variation range cannot reflect the manufacturing requirements of the actual device, resulting in a large error in the calculation compared with the Monte Carlo method.

The comparative analysis shows that the movement reliability of the device separation process under different coefficients of variation can be accurately obtained based on the improved membership function. When the coefficient of variation is 0.05, the maximum reliability of the separation process is 0.9991, and when the coefficient of variation is 0.10, the minimum movement reliability of the separation process is 0.9429, indicating that the moment uncertainty has a great influence on the movement reliability of the separation process. To ensure the working reliability of the separation device, the size of each moment should be strictly controlled, and the dispersion degree of each moment

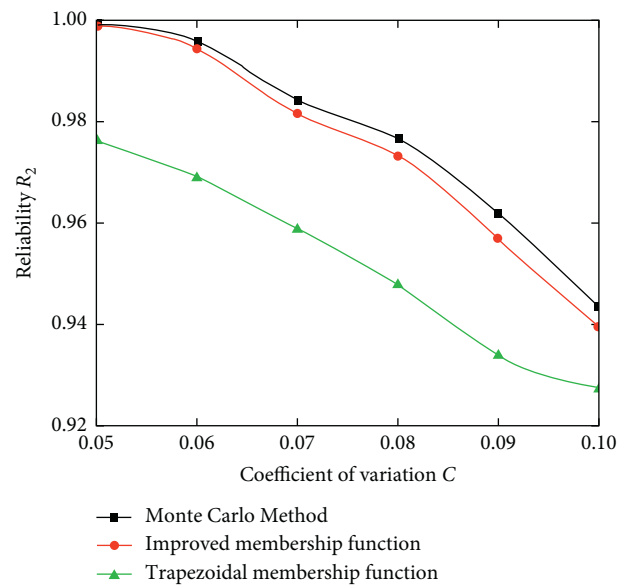

Figure 21: Motion reliability of separation process under different coefficients of variation.

should be reduced in the actual application of unlocking the trigger device.

4.3. Motion Reliability Analysis of Unlocking Trigger Device. According to the working principle of the unlocking trigger device, the reliability of the whole machine is composed of two parts of the reliabilities of the SMA wire unlocking and the separation process. To accurately characterize the influence of parameter uncertainty on the reliability of the whole machine, the reliability of the whole machine is calculated based on the established device reliability model, and the expression is

$$R_t = R_1 \times R_2 = 0.9996 \times 0.9991 = 0.9987, \tag{21}$$

where R_1 is the motion reliability of the SMA wire in unlocking and R_2 is the motion reliability of the separation process.

It can be seen from equation (21) that the reliability of the unlocking trigger device is 0.9987, which is lower than the reliability requirement of the design index 0.9999. The reason is that the influence of parameter uncertainty on the reliability of each part is considered in the analysis process. The reliability of the whole machine is lower than the reliability of each part under the separate action, indicating that the reliability of each part of the device has a great impact on the reliability of the whole machine. In the design process, it is necessary to strictly control the reliability of the SMA wire unlocking movement and the separation process to improve the reliability of the whole machine. To further explore the relationship between the parameter uncertainty and the overall reliability of the device, the series reliability model is used to calculate the reliability of the device under different coefficients of variation. The analysis result is shown in Figure 22.

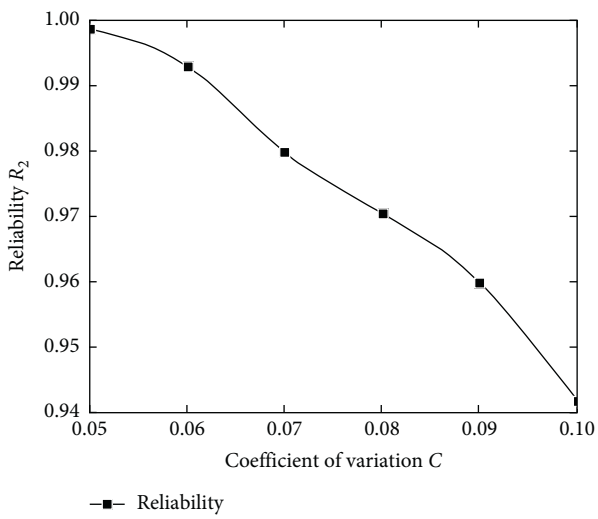

Figure 22: Reliability of the whole machine under different coefficients of variation.

It can be seen from Figure 22 that as the coefficient of variation of the uncertainty parameter increases, the reliability of the whole machine gradually decreases. When the coefficient of variation is 0.05, the reliability of the device is 0.9987; when the coefficient of variation is 0.10, the reliability of the device is 0.9419. The greater the uncertainty of the parameters is, the less the probability that the overall performance of the device meets the design index, which reduces the reliability of the device. To ensure that the device can work with high reliability, the influence of uncertain factors should be reduced as much as possible.

5. Conclusions

(1) Considering the influence of parameter uncertainty on the motion reliability of the unlocking trigger device, the BP neural network is optimized by combining CPSO and BR. Based on the construction of the unlocking trigger device reliability model, the CPSO-BR-BP neural network agent is established. Compared with the traditional neural network proxy model, the proposed proxy model has higher fitting accuracy. It can better characterize the mapping relationship between inputs and outputs and improve the efficiency of reliability calculation. Furthermore, it can save calculation costs.

(2) Based on the CPSO-BR-BP neural network proxy model, it is calculated that the motion reliability of the SMA wire in unlocking is 0.9996, the movement reliability of the separation process is 0.9991, and the movement reliability of the whole machine is 0.9987, which are under the condition of parameter uncertainty. The uncertainty of the parameters in the process of SMA wire in the unlocking and separation process makes the reliability of the whole machine lower than the reliability design index, but it is larger in line with the real reliability of the unlocking trigger device.

(3) The influences of different coefficients of variation on the motion reliability of SMA wire unlocking, the separation process, and the whole machine are compared and analyzed. The motion reliabilities of the three cases all show different degrees of reduction with the increase of the coefficient of variation, indicating that the degree of dispersion of parameters has a great impact on the dispersion of the response. Ultimately, it can result in the reduction of the motion reliability of the whole machine. Therefore, to ensure the stability of the device unlocking and separation process, the influences of uncertain factors should be minimized.

Data Availability

No data were used to support this study.

Conflicts of Interest

The authors declare that they have no conflicts of interest.

References

[1] M. Yazdi, S. Daneshvar, and H. Setareh, "An extension to fuzzy developed failure mode and effects analysis (FDFMEA) application for aircraft landing system," *Safety Science*, vol. 98, pp. 113–123, 2017.

[2] C.-G. Huang, H.-Z. Huang, and Y.-F. Li, "A bidirectional LSTM prognostics method under multiple operational conditions," *IEEE Transactions on Industrial Electronics*, vol. 66, no. 11, pp. 8792–8802, 2019.

[3] M. Yazdi and E. Zarei, "Uncertainty handling in the safety risk analysis: an integrated approach based on fuzzy fault tree analysis," *Journal of Failure Analysis and Prevention*, vol. 18, no. 2, pp. 392–404, 2018.

[4] W. Peng, Z.-S. Ye, and N. Chen, "Bayesian deep-learning-based health prognostics toward prognostics uncertainty," *IEEE Transactions on Industrial Electronics*, vol. 67, no. 3, pp. 2283–2293, 2020.

[5] M. Yazdi, S. Kabir, and M. Walker, "Uncertainty handling in fault tree based risk assessment: state of the art and future perspectives," *Process Safety and Environmental Protection*, vol. 131, pp. 89–104, 2019.

[6] Z. Zhong, H. Zhang, J. Zhou et al., "Research review of spacecraft non-pyrotechnic connection and separation technology," *Manned Spaceflight*, vol. 25, no. 1, pp. 128–142, 2019.

[7] J. Zhou, "The overall concept of my country's space station project," *Manned Spaceflight*, vol. 19, no. 2, pp. 1–10, 2013.

[8] X. Zhang, X. Yan, and Q. Yang, "Design and experimental validation of compact, quick-response shape memory alloy separation device," *Journal of Mechanical Design*, vol. 136, pp. 1–9, 2014.

[9] X. Hu, J. Wu, J. Peng et al., "Design and experimental study of large-load low-impact unlocking mechanism based on memory alloy," *Science Technology and Engineering*, vol. 16, no. 30, pp. 319–323, 2016.

[10] M. Han, D. Wang, Y. Tian et al., "Design and analysis of micro-nano satellite linkage connection and separation device," *Mechanical Science and Technology*, vol. 39, no. 9, pp. 1463–1470, 2020.

[11] L. Hong, H. Li, K. Peng et al., "Improved response surface method for reliability analysis based on efficient search method," *Journal of Beijing University of Aeronautics and Astronautics*, vol. 46, no. 1, pp. 95–102, 2020.

[12] P. Zhang, Z. Zhang, and H. Guo, "Optimal design of tapered hydrostatic bearing based on Kriging model," *Modular Machine Tool and Automatic Manufacturing Technology*, no. 2, pp. 62–65+68, 2021.

[13] Z.-H. Han, Y. Zhang, C.-X. Song, and K.-S. Zhang, "Weighted gradient-enhanced Kriging for high-dimensional surrogate modeling and design optimization," *AIAA Journal*, vol. 55, no. 12, pp. 4330–4346, 2017.

[14] Z. Wen, H. Pei, H. Liu, and Z. Yue, "A sequential Kriging reliability analysis method with characteristics of adaptive sampling regions and parallelizability," *Reliability Engineering & System Safety*, vol. 153, pp. 170–179, 2016.

[15] J. Zhao, Q. C. Jian, and L. Xu, "RBF-GA: an adaptive radial basis function metamodeling with genetic algorithm for structural reliability analysis," *Reliability Engineering & System Safety*, vol. 189, pp. 42–57, 2019.

[16] L. Shi, B. Sun, and D. S. Ibrahim, "An active learning reliability method with multiple kernel functions based on radial basis function," *Structural and Multidisciplinary Optimization*, vol. 60, no. 1, pp. 211–229, 2019.

[17] S. Chen and D. Wang, "Monte Carlo reliability analysis method based on neural network," *Journal of Shanghai Jiaotong University*, vol. 52, no. 6, pp. 687–692, 2018.

[18] A. Hraiba, A. Touil, and A. Mousrij, "Artificial neural network based hybrid metaheuristics for reliability analysis," *IFAC-PapersOnline*, vol. 53, no. 1, pp. 654–660, 2020.

[19] J. Izquierdo, A. Crespo Márquez, and J. Uribetxebarria, "Dynamic artificial neural network-based reliability considering operational context of assets," *Reliability Engineering & System Safety*, vol. 188, pp. 483–493, 2019.

[20] C. Tang, J. Zhang, W. Hou et al., "Reliability sensitivity analysis of motion mechanism based on artificial neural network," *Forging Technology*, vol. 44, no. 8, pp. 182–188, 2019.

[21] C. Dai, W. Chen, and Y. Zhu, "Seeker optimization algorithm for tuning the structure and parameters of neural networks," *Neurocomputing*, vol. 74, no. 6, 2010.

[22] H. Gong, Z. Li, H. Liu et al., "Storage reliability prediction based on improved PSO-BP neural network," *Operations Research and Management*, vol. 29, no. 8, pp. 105–111, 2020.

[23] Y. Jin, S. Liu, and J. Zhang, "Fatigue reliability of high-speed rolling bearings under artificial neural network optimized by genetic algorithm," *Journal of Aeronautics and Dynamics*, vol. 33, no. 11, pp. 2748–2755, 2018.

[24] K. Sun, J. Zhou, and L. Xie, "Reliability optimization design of CNC machine tool ball screw," *Mechanical Science and Technology*, vol. 29, no. 11, pp. 1530–1533, 2010.

[25] P. Zhi, Y. Li, and B. Chen, "Structural strength analysis of bogie frame considering parameter uncertainty," *China Mechanical Engineering*, vol. 30, no. 1, pp. 22–29, 2019.

Hindawi
Mathematical Problems in Engineering
Volume 2021, Article ID 1306742, 10 pages
https://doi.org/10.1155/2021/1306742

Research Article

An Integrated Simulation and Virtual Cellular Manufacturing System Concept Approach for Maintenance Policy Selection

Jamileh Hayati and Sohrab Abdollahzadeh

Department of Industrial Engineering, Urmia University of Technology, Urmia, Iran

Correspondence should be addressed to Sohrab Abdollahzadeh; s.abdollahzadeh@uut.ac.ir

Received 30 May 2021; Accepted 2 August 2021; Published 13 August 2021

Academic Editor: Noorbakhsh Amiri Golilarz

The main purpose of this study is to present a new hybrid approach to select the appropriate maintenance policy (NET) of machines utilizing analytic network process (ANP), computer simulation, and the concept of virtual cellular manufacturing system (VCMS). Since conventional methods select only one NET policy for all machines or production lines, the performance of machines that do not conform to the selected policy is reduced. In the proposed method, the information of the functional parameters of the machines is extracted by means of computer simulation and there is no need for expert opinion. Next, the appropriate net policy for each machine is selected using the ANP method. To reduce the diversity and complexity of NET applications, machines are grouped using the concept of virtual cellular manufacturing system based on the similarity of NET policies. A NET program is prepared for each group of machines. The proposed approach is used in a production unit with three widely used NET policies, and its efficiency was proved by comparing the results with conventional methods.

1. Introduction

One of the ways to achieve high productivity in production units is to have the right preventive and maintenance (PM) policy [1]. It is crucial to have a high productivity line to reduce costs [2]. One of the major obstacles to achieving the goals of manufacturing companies is the sudden breakdown of devices that have a direct impact on production [3]. Preventive and maintenance cost varies from 15 to 70 percent of total production cost [4].

PM is a set of activities that are clearly planned and performed to prevent the sudden breakdown of machinery, equipment, and facilities [5]. The main purpose of PM in a system is to extend the life of devices with minimum cost and maximum efficiency during the operation period [6].

However, proper preventive and maintenance policies directly affect the profitability of the organization; the lack of proper PM planning reduces the life of the equipment [7]. Different policies have been stated for the PM; each of them has advantages and disadvantages depending on the type of machine [8]. Taking advantage of the appropriate PM policy reduces the costs of a manufacturing organization [9]. According to [10], in many cases, preventive PM improves the performance of machinery due to more imposing defects, and repairing is only useful to items that have a certain pattern of damage.

Many studies have been done on the evaluation of the efficiency and effectiveness of each PM policy and the selection of the best one [11, 12]. Selecting the right PM policy does not depend on a single criterion and is considered a multicriteria decision-making issue [13]. The share of research on the use of multicriteria and multiobjective decision-making tools has been high [14, 15]. There are three main steps in the process of preparation for multicriteria decision-making [16]. First, determining the relevant criteria and options. Then, determining the relative importance of the criteria and performance of the options on the criteria. Finally, rank each option and select the best choice [17]. In multicriteria decision-making methods, criteria such as safety, cost, added value, and feasibility are selected to choose the best policy or a combination of different types of PM policies [18, 19]. The weight and values of the criteria

should be derived from the actual performance of the devices and production lines. However, due to the high cost or lack of required time, it is estimated by experts [20]. Due to the low number and high cost of experts, some research has used low-cost methods such as computer simulation to determine the criteria values [21, 22].

In a multiproduct manufacturing unit, the performance of the equipment on different production lines is different and requires separate PM policies so that a specific policy may be appropriate only for a set of equipment and may not be effective for another set. While in most conventional methods, a PM policy is chosen for the whole company or production lines [23]. If there is a need for several different policies in a manufacturing company, similar policies should fall into one category. Also, the concept of cellular manufacturing has been used to group different network policies [24].

Most NET policy selection methods use multicriteria decision-making tools that require the selection of appropriate criteria. These methods can be classified into two general categories. In the first method, only one NET policy is selected for the entire production machinery. But in the second method, for each production line, a separate NET policy is selected.

Studies have shown that in conventional methods, a number of machines are not compatible with the NET selection policy for all machines or production lines. Therefore, these methods have limited efficiency due to insufficient attention to the specific characteristics of machines in selecting the appropriate NET policy. As a result, new high-performance methods are essential for selecting the appropriate NET policy.

It should be noted that the new methods will require a lot of functional information from the machines as well as a variety of NET policies. In this regard, the capabilities of computer simulation softwares can be used to reduce the problem of selecting experts and the impact of their personal opinion. Clustering can reduce complexity [25]. It also reduced the diversity and complexity of NET programs by clustering similar machines in terms of NET policies.

In the present study, a new approach has been proposed by using computer simulation, ANP method, and the concept of the virtual cell to select the appropriate PM policy for the machine. The procedure is that the widely used PM policies and their evaluation criteria are extracted and selected from written sources. In the following, the required matrices of the ANP method, including policy-criterion and criterion-criterion, preparation, and appropriate PM policy of each machine, are selected. Then machines are grouped based on the similarity of the PM policy. If the number of machines belongs to each policy is large, there is a possibility of creating a variety of PM programs. In order to reduce the variety of PM programs, all machines of that policy are formed in a similar virtual cell. In fact, the machines are not physically moved, but the machines that belong to each cell are subjected to the same PM program. Important research innovations include the following:

(1) Choosing a suitable PM policy for each machine using simulation and without the use of expert opinion.

(2) Grouping machines based on similar PM policies regardless of location.

(3) Applying the concept of virtual cellular manufacturing system (VCMS) in order to result in cell formation of policy machines with a relatively large number of machines. This act reduces the variety of PM programs and performs operations on similar cells without altering the physical location of the machines.

The structure of the current research is as follows and will be described in the new methodology and proposed model in Section 2. In Section 3, the results of the proposed approach to data mining are presented. Finally, the discussion, conclusion, limitation, and future research proposals are represented in Section 4.

2. Research Methodology

The main goal of the current study is to provide an approach to selecting the most appropriate PM policy for each machine in a multiproduct manufacturing system. This action uses three tools of managerial, analytical decision-making: ANP, computer simulation, and the concept of VCMS. The conceptual scheme of the proposed approach is shown in Figure 1.

The research steps are explained in the following. Finally, the efficiency of the proposed approach is compared with conventional methods (Types A and B) [26].

2.1. Initial Steps and Basic Information. At this step, the evaluation criteria and the most used PM policies are selected. Also, the main activities of the PM are determined in each PM policy. However, the selection of experts is specific to common methods and does not include the proposed approach, but it is necessary to compare the results of the proposed model with conventional methods.

2.1.1. Selecting PM Criteria. Selection criteria can be defined as the characteristics, skills, and abilities of a policy that can effectively perform a given task. They are used to identify the right strategy [27]. Different categories of PM criteria are provided [11, 28, 29]. The authors of [30] have classified NET criteria into four main groups: cost, value-adding, safety, and availability. Each criterion, in turn, has subcriteria [31]. In the proposed approach, 12 subcriteria from the 4 main groups of criteria that can be calculated by computer simulation are selected as given in Table 1.

2.1.2. Selecting PM Policies. The types of PM policies are condition-based maintenance (CBM), predictive maintenance (PDM), total productive maintenance (TPM), corrective maintenance (CM), and reliability-based maintenance (RBM). Corrective, preventive, and predictive

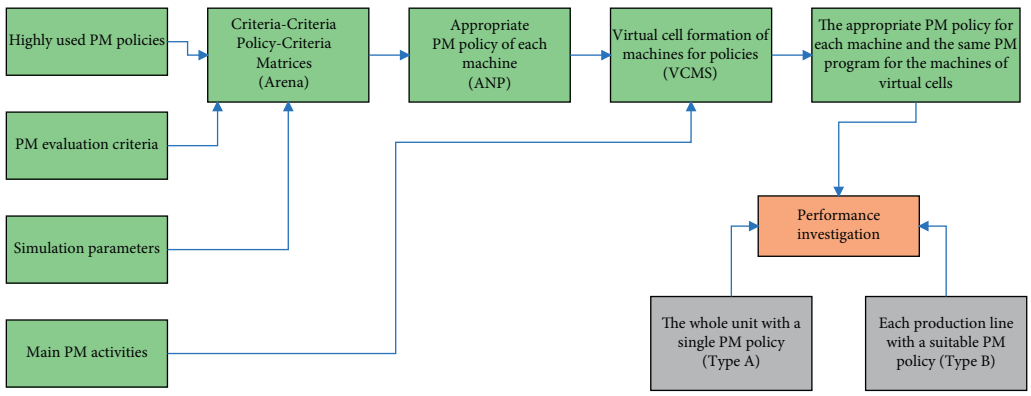

Figure 1: The conceptual framework of the hybrid approach.

Table 1: Criteria and subcriteria of selecting PM policies.

Cost		Value adding		Safety		Availability	
C_1:	Capital cost	C_4:	Reliability	C_7:	Operator skills	C_{10}:	Facility utilization
C_2:	Running cost	C_5:	Capability	C_8:	Flexibility	C_{11}:	Resource availability
C_3:	Maintenance downtime	C_6:	Repair load	C_9:	Efficiency		

PM policies are the most common policies in an effective PM management [31], which have also been used in current research.

2.1.3. Selecting Experts. This step is specific to conventional methods (Types A and B), and a sufficient number of PM experts are selected to perform pairwise comparisons between criteria and policies.

2.2. Selection of the Appropriate PM Policies

2.2.1. ANP. Although both the ANP and the hierarchical analysis process take precedence over pairwise comparisons, there are differences between them [32]. Multiobjective models are used to select appropriate PM policies [33]. A network analysis method has been used to select the appropriate PM policy. This method uses the super-matrix approach. At this step, the pairwise comparison criteria of the policy-criterion and the criterion-criterion must be completed. In conventional methods, these tables are completed by experts. In this method, there is a problem with supplying a large number of experts and also applying the possible manner of experts [34]. Computer simulation tools are used to solve the problem of the effect of experts' judgment on determining the values of criteria, pair comparison, their weight, and also the relationship between criteria in the ANP technique.

2.2.2. Computer Simulation. In the proposed model of the current research, regardless of the physical location and how the machines are installed in the production lines, the appropriate policy for each machine is selected separately. Therefore, considering the number of policies, there is the simulation for each machine, and the values of the policy-criteria and the criteria-criteria are calculated.

The authors of [35] have studied the optimization of PM systems based on simulation. By examining about 59 articles published between 2000 and 2013, they found results in using simulation techniques in optimizing PM systems, which is summarized in Table 2.

(1) Computer Simulation Model Assumptions

(1) The model consists of several continuous production lines, and each line consists of several machines
(2) Each production line is a single product that requires a specific sequence to build
(3) Production operations are continuous and in production line form
(4) The cost and time of the production operation are stochastic
(5) The production capacity of each of the lines and the whole factory in each period is constant, known, and limited
(6) Primary input materials to the system are assumed to be unlimited
(7) Start-up time is not considered for the system
(8) The study period or simulation time is 180 days
(9) Conveyors act as transmitters and have no role in PM programming

Hypotheses 1, 2, 3, and 5 are derived from conventional methods. But hypotheses 5 to 7 are new and relevant to current research. Hypotheses 7 and 9 are intended to simplify the model. The eighth assumption also determines the planning period.

(2) Simulation Model Parameters. In order to determine the policy-criterion as well as the policy-policy entry of the matrix directly, it is necessary to determine the simulation parameters in each of the production lines. These parameters

Table 2: Simulation application in optimizing PM systems.

PM	PDM	CM	PM
PM policy in simulation	Asset	PM resources	Dynamic production
Simulation techniques	Discrete event	Discrete event and other techniques	Other techniques
Optimization models	Advanced models	Classic models	Manual models
Advanced models	Integrated models	SA	GA
Optimization	Minimum cost	Maximum availability	Maximum output
Single objective or multiobjective	Multiobjective	Single objective	

are extracted through machine-building documentation. For example, the parameters of the Nugget production line, as described in Table 3, include failure time, repair time, repair cost, process time, production cost, and waste cost.

Using the Arena version 13.5 software, a computer simulation model is developed. The construction, validation, entry of information, and reporting of models in the current research is in accordance with the method of [36]. In order to test the structural error of the model, the results of simulation with real data are examined to confirm the accuracy of the prediction results of the model. For this purpose, all the studied parameters in the simulation are considered definitively and reviewed and controlled in Excel software. If the results obtained from the simulation are similar to the results of the statistical calculations, the accuracy of the model results is confirmed. At the end of this step, the machines are grouped regardless of their location and only based on the same PM policy.

2.3. Virtual Cell Formation. Cellular production is an industrial application of group technology concepts and is a production philosophy in which similar parts are produced, designed, identified, and grouped in order to take advantage of their similarity. This concept was first proposed by [37].

Sometimes moving machines may not be physically possible or cost-effective. In order to overcome this problem, there are approaches in which one of them is VCMS. Unlike static and classic cellular production, in a virtual cell system, machines, parts, and workers are temporarily grouped for a period of time. The grouped machines are not necessarily the same. If the demand pattern changes from one period to another, the machines in each cell may be transferred virtually to another part [38].

There is a PM program because of the number of machines in each PM policy, and this matter increases the complexity of the proposed model in practice; as a result, PM programs must be reduced by using techniques. To this end, in policies where the number of machines are so many, the machines are formed as cell according to the same PM program and with the help of the concept of virtual cellular production.

In the current research proposal, if the number of machines in each policy is more than 5, the machines will organize as cell layouts in virtual cells that have a similar PM program. If needed, the number of machines can be changed, and the number of cells can be controlled. With this act, the machines are subjected to a similar program to the PM with no need for physical movement. By changing demand or other production conditions in the next periods, the position of machines in virtual cells may change. In order to cell layout machines in any PM policy, it is necessary to select the PM activities related to that policy. For example, these activities for preventive PM are described in Table 4 [39].

Based on the documents submitted by the manufacturing factory, the requirements of each machine will be determined by the selected PM policy activities. The result will be a matrix, including the numbers 0 and 1. This matrix for machines that belong to the Preventive PM Policy is shown in Table 4. With the help of the mathematical model, machines are formed as cell layout based on the similarity of activities. This model is described as follows:

Indices:

i: index for activities $(i = 1, 2, \ldots, P)$
j: index for machines $(j = 1, 2, \ldots, M)$
k: index for clusters $(k = 1, 2, \ldots, C)$

Parameters:

rij: 1 if machine j requires activity i; 0, otherwise
e: minimum number of machines should be assigned to a formed cluster
A: large positive number

Decision variables:

Xik: 1 if activity i is assigned to cluster k; 0, otherwise
Yjk: 1 if machine j is assigned to cluster k; 0, otherwise
Zk: 1 if cluster k is to be formed; 0, otherwise

Objective function:

$$\begin{aligned} \text{Min } Z = & \sum_{k=1}^{C}\left(\sum_{i=1}^{P}\sum_{j=1}^{M} X_{ik}Y_{jk} - \sum_{i=1}^{P}\sum_{j=1}^{M} r_{ij}X_{ik}Y_{jk}\right) \\ & + \sum_{k=1}^{C}\sum_{i=1}^{P}\sum_{j=1}^{M} r_{ij}X_{ik}\left(1 - Y_{jk}\right). \end{aligned} \tag{1}$$

Constraints:

$$\sum_{k=1}^{C} X_{ik} = 1, \quad \forall i, \tag{2}$$

$$\sum_{i=1}^{M} X_{ik} \le A \times Z_k, \quad \forall k, \tag{3}$$

$$\sum_{k=1}^{C} Y_{jk} = 1, \quad \forall j, \tag{4}$$

Table 3: Nugget production line machines simulation parameters.

Machine	Process	Production line parameters					
		Failure time	Repair time	Repair cost	Process time	Production costs	Waste costs
M_{11}	Material preparation	TRIA (115,150,200)	EXPO (1.5)	6500	50	10	10
M_{12}	Material injection	TRIA (90,100,120)	EXPO (2.5)	3000	25	3	3
M_{13}	Spraying powder	TRIA (40,115,150)	EXPO (1.5)	2000	30	5	5
M_{14}	Cooking and freezing	TRIA (120,180,240)	EXPO (1.5)	2800	50	3	3
M_{15}	Packaging	TRIA (25,45,60)	EXPO (0.5)	2000	45	7	7

Table 4: PM activities for preventive PM policy.

O_1:	Inspection	O_7:	Take reading
O_2:	Predictive maintenance	O_8:	Lubrication
O_3:	Cleaning	O_9:	Schedule replacement
O_4:	Tightening	O_{10}:	Interview operator
O_5:	Operating	O_{11}:	Analysis
O_6:	Adjustment		

$$\sum_{j=1}^{M} Y_{jk} \le A \times Z_k, \quad \forall k, \tag{5}$$

$$\sum_{j=1}^{M} Y_{jk} \ge e \times Z_k, \quad \forall k, \tag{6}$$

$$X_{ik}, Y_{jk}, Z_k \in \{0, 1\}, \quad \forall i, j, k. \tag{7}$$

Linearization:

The objective function of the model is a nonlinear equation due to the multiplication of the variables X_{ik} and Y_{jk}. Let us define the following new variable.

$$W_{ijk} = X_{ik} Y_{jk}. \tag{8}$$

Hence, the following constraints should be added to the original mathematical model [40]:

$$W_{ijk} - X_{ik} - Y_{jk} + 1.5 \ge 0, \quad \forall i, j, k, \tag{9}$$

$$1.5 \times W_{ijk} - X_{ik} - Y_{jk} \le 0, \quad \forall i, j, k. \tag{10}$$

Now, we have linear programming as follows:

$$\begin{aligned} \text{Min } Z = & \sum_{k=1}^{C} \left(\sum_{i=1}^{P} \sum_{j=1}^{M} W_{ijk} - \sum_{i=1}^{P} \sum_{j=1}^{M} r_{ij} W_{ijk} \right) \\ & + \sum_{k=1}^{C} \sum_{i=1}^{P} \sum_{j=1}^{M} r_{ij} \left(X_{ik} - W_{ijk} \right). \end{aligned} \tag{11}$$

Constraints include equations (2)–(7), (9), and (10).

With the implementation of the linear model with the help of Lingo software, the machines of each policy are assigned to the cells. For example, the result of the cell formation of 9 machines to receive preventive PM policy activities is shown in Figure 2.

2.4. Calculation and Comparison of the Efficiency of the Methods (Types A and B). At this step, the efficiency of the production lines is calculated with the policies and the selected PM program and also compared with the performance results of the two conventional methods (Types A and B).

3. Case Mining

The proposed approach in current research has been validated by using case mining. The steps of case mining are exactly in line with the proposed model. In the following, a description of the steps of case mining will be explained.

3.1. Initial Steps and Basic Information. This study was performed on a production unit of Iranian meat and protein products, including three production lines: Nugget, Burger, and Sausage. The number of products is 3, the number of production lines is 3, and the number of machines is 15. The other assumptions of the proposed approach are precisely the same. According to previous explanations, PM policies are corrective, preventive, and predictive. The criteria and subcriteria for selecting the appropriate policy for PM include 12 criteria, as described in Table 1. Since conventional approaches require the opinion of experts for pairwise comparisons, 5 persons were selected, including 3 experts in the field of PM and 2 experts in the field of food industry machines.

3.2. Selecting the Appropriate PM Policies. In the new proposed method, it is necessary to determine the simulation parameters of the production lines. By conducting field studies on production line documentation, the parameters of all three production lines, including failure time, repair time, repair cost, process time, production costs, and waste costs, were extracted. As an example, these parameters for the Nugget line, which has 5 machines, are described in Table 3.

In the proposed model of the current research, computer simulation models are made according to the parameters of the machines. PM computer simulation model has been developed in the study company considering all the parameters of machines and the number of PM policies. For example, the developed model for the study company is related to preventive PM policy, as shown in Figure 3.

In order to check the accuracy of the simulation models and ensure their correct performance, the expected results of the model solution according to the input data were created in Excel software and compared with the output of the models. The results were very close, and, as a conclusion, the validity of the models was confirmed.

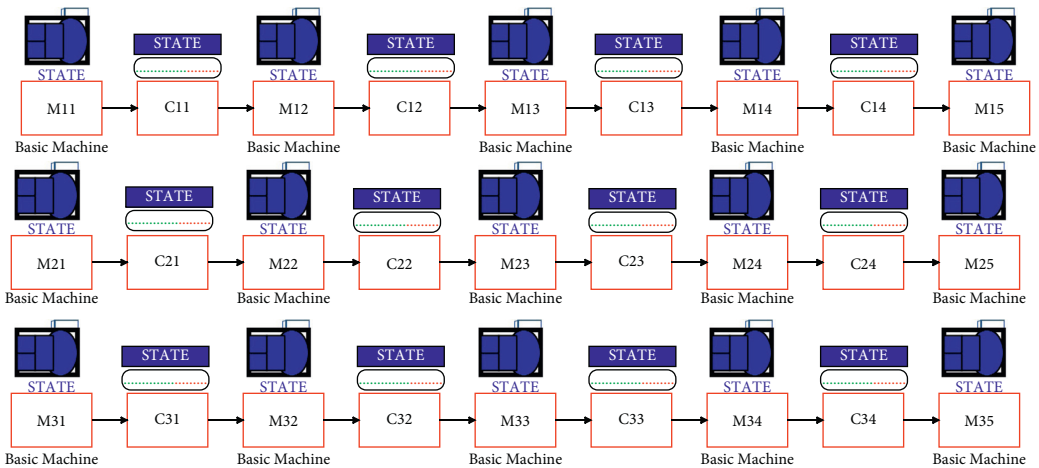

Figure 2: Clustering of machines for preventive PM policy.

	O_4	O_6	O_{10}	O_5	O_9	O_1	O_2	O_3	O_7	O_8	O_{11}
M_3	1	1	1	0	0	1	0	0	0	0	1
M_4	1	1	1	0	1	0	0	0	0	0	0
M_9	1	1	1	0	0	1	0	0	0	1	0
M_5	1	0	1	1	1	0	0	0	0	0	0
M_7	0	0	1	1	0	1	0	0	0	0	0
M_1	0	0	0	1	0	1	0	1	1	1	1
M_2	0	1	0	0	1	1	1	1	1	1	1
M_6	0	0	0	0	0	1	1	1	1	1	1
M_8	0	0	0	1	0	1	1	1	1	1	0

Figure 3: Production line simulation model for preventive PM policy.

In order to select the appropriate PM policies, an ANP approach is used. The ANP method used in this research consists of 5 steps [41].

For this purpose, it is first necessary to complete the criteria-policy matrix. The results of the implementation of simulation models were obtained for each of the three policies. For example, the values obtained for the criteria-policy matrix for the first machine of the Nugget production line are as described in Table 5.

Arena software has a tool called a process analyzer that allows you to extract the best possible performance for changing variables and sensitivity analysis. The techniques used in this tool are based on theories presented by Hong and Nelson [42]. By using this tool, the relationships between the PM criteria for the first machine of the Nugget production line are calculated and are shown in Table 6.

The criteria-policy matrix is normalized, and the relationships between the matrix of criteria and the weight of the criteria are obtained. For example, the result of the weights for the first machine of the Nugget production line is given in Table 7.

Finally, the preventive PM policy was chosen for the first machine of the Nugget production line. Similarly, calculations were repeated for other machines, and appropriate policies were obtained. These results are shown in Table 8. In order to compare the efficiency of the proposed model in current research with conventional methods (Types A and B), the most appropriate PM policy was obtained based on the opinion of experts for the entire production unit as well as each of the production lines. The most appropriate policy for all production line machines is preventive policy. The most appropriate policy of PM for the Nugget line was preventive and for the next two lines was predictive.

According to the results of the proposed model, the largest number of machines belongs to the policy of preventive PM (9 devices); the next one was the policy of predictive PM (4 devices) and the policy of corrective PM (2 devices). Therefore, in the next step, preventive PM policy machines will be formed as cell layouts.

According to the results of the proposed model, the largest number of machines belongs to the policy of preventive PM (9 devices); the next one was the policy of predictive PM (4 devices) and the policy of corrective PM (2 devices). Therefore, in the next step, preventive PM policy machines will be formed as cell layouts.

3.3. Forming a Virtual Cell. The machine-activity matrix, which determines the activities required for each machine with a preventive PM policy, is shown in Table 9.

The maximum number of cells is 4, and the minimum number of machines for each cell is 2 if it is formed. The linear clustering model for preventive PM policy has been solved with the help of "Lingo" and "GAMS" software, the results of which are shown in Figure 2. Due to the linearity of models, the obtained results are optimal global values.

This has two significant achievements. First, the diversity of PM programs has been reduced by approximately 65%, and the application of the model in practice is remarkably facilitated. Second, the cell for each operation team was determined. In this example, operations 4, 6, and 10 are deployed in the first cell, operations 5 and 9 in the second cell, and operations 1, 2, 3, 7, 8, and 11 in the third cell. Obviously, 12 operational services are provided outside the cells, which is the best possible situation.

3.4. Calculation and Comparison of the Efficiency of the Methods (Types A and B). This step is only to compare the efficiency of the proposed model of the current research with conventional methods (Types A and B), and in the running

Table 5: Results of the Nugget line criteria-policy matrix with simulation.

Policy	C_1	C_2	C_3	C_4	C_5	C_6	C_7	C_8	C_9	C_{10}	C_{11}
CM	152	147	147	155	141	140	127	126	119	114	122
PM	122	118	116	115	113	111	110	104	100	97	94
PDM	160	148	153	145	148	137	132	125	124	120	121

Table 6: Results of the criteria-criteria relationship with simulation.

	C_1	C_2	C_3	C_4	C_5	C_6	C_7	C_8	C_9	C_{10}	C_{11}
C_1	1	2	4	4.5	6	4	8	5	7	4	4
C_2	0.5	1	5	4	6	4	5	5	6	4	4
C_3	0.3	0.2	1	2	2	0.2	2	0.3	0.3	0.3	0.3
C_4	0.2	0.3	0.5	1	5	2	4	2	0.3	2	0.3
C_5	0.2	0.2	0.5	0.2	1	0.2	2	0.3	2	2	2
C_6	0.3	0.3	5	0.5	5	1	5	0.3	0.5	0.3	0.3
C_7	0.1	0.2	0.5	0.3	0.5	0.2	1	0.3	2	0.5	0.5
C_8	0.2	0.2	3.3	0.5	3.3	3.3	3.3	1	4	0.3	0.3
C_9	0.1	0.2	3.3	3.3	0.5	2	0.5	0.3	1	4	4
C_{10}	0.3	0.3	3.3	0.5	0.5	3.3	2	3.3	0.3	1	2
C_{11}	0.3	0.3	3.3	3.3	0.5	3.3	2	3.3	0.3	0.5	1

Table 7: Criteria of weight values by simulation for the Nugget line.

Criterion weight	C_1 0.071	C_2 0.085	C_3 0.063	C_4 0.067	C_5 0.080	C_6 0.041	C_7 0.069	C_8 0.031	C_9 0.063	C_{10} 0.066	C_{11} 0.182
CM	92	81	76	78	76	74	73	62	59	54	47
PM	154	152	150	146	141	134	131	120	112	113	105
PDM	157	145	163	139	147	150	148	146	142	139	134

Table 8: Appropriate PM policies.

Model	Nugget					Burger					Sausage				
	M_{11}	M_{12}	M_{13}	M_{14}	M_{15}	M_{21}	M_{22}	M_{23}	M_{24}	M_{25}	M_{31}	M_{32}	M_{33}	M_{34}	M_{35}
Proposed model	PM	PM	PM	PDM	CM	PM	PM	PDM	CM	PDM	PM	PM	PM	PM	PDM
A policy for each line (Type B)	PM					PDM					PDM				
A policy for all lines (Type A)	PM														

Table 9: Matrix of machine-activity for preventive PM policy.

	O_1	O_2	O_3	O_4	O_5	O_6	O_7	O_8	O_9	O_{10}	O_{11}
M_1	1	0	1	0	1	0	1	1	0	0	1
M_2	1	1	1	0	0	1	1	1	1	0	1
M_3	1	0	0	1	1	1	0	0	0	1	1
M_4	0	0	0	1	0	1	0	0	1	1	0
M_5	0	0	0	1	1	0	0	0	1	1	0
M_6	1	1	1	0	0	0	1	1	0	0	1
M_7	1	0	0	0	1	0	0	0	0	1	0
M_8	1	1	1	0	1	0	1	0	0	0	1
M_9	1	0	0	1	0	1	0	1	0	1	0

model, this step is not required. In order to compare them and prove the efficiency of the proposed method, the utilization of the whole system has been used. First, according to the appropriate policy of the PM, by using simulation, the parameters of the NET are calculated. The values of the total utilization of this current research approach and conventional methods (Types A and B) are in accordance with Table 10.

Table 10: Comparison of the effectiveness of appropriate policies for methods.

	Type A	Type B			Proposed model				
					Group 1 (PM)				
	All lines (PM)	Nugget (PM)	Burger (PDM)	Sausage (PDM)	Cell 1	Cell 2	Cell 3	Group 2 (PDM)	Group 3 (CM)
Number of machines	15	5	5	5	3	2	4	4	2
System efficiency	0.6484		0.7023				0.8748		

3.5. Sensitivity Analysis. The policy and schedule selected for each machine can change under the influence of key factors. In the following, various situations are discussed; those key factors affect the choice of policy and NET program of each machine. These sensitivity analyses can be performed in scenario-based research and the results can be compared with the results of the current research.

3.5.1. Change in the NET Policy Selection Criteria. According to Table 1, in the current study, 11 criteria have been used to select the appropriate NET policy. The type and number of these criteria can be changed according to the type of machines of each manufacturing company. However, the policy of choice for each machine may change.

3.5.2. Change in NET Policies. In the current study, three policies CM, PM, and PDM were used. Depending on the needs of manufacturing organizations and the type of machines, the type and number of NET policies can be changed. In this case, the results obtained for machine policy and application may change.

3.5.3. Change in Production Line Parameters

(Case 1) Change in the number of parameters: in the current research, according to Table 3, six performance parameters are considered for each machine. As the number of these parameters increases, the accuracy of the model increases, and the policies chosen for the machines may change.

(Case 2) Change in the type of parameters: according to Table 3, in the current study, out of six functional parameters, four are definite parameters, and the other two parameters are random. Changes in the type of these parameters may change the type of policy selected for the machine.

3.5.4. Change in Cell Formation Type. In the current study, the number of cells that indicate the type of NET program is determined by the model. In practice, as the number of machines in each policy increases, the number of cells may be limited by the model. This decision will change the type of car NET program.

4. Discussion

In various studies, different methods have been proposed to select the best NET policy. Most of these methods use multicriteria decision-making tools by selecting criteria. These common methods of choosing the optimal NET policy can be categorized into two general categories. In the first method (A), only one NET policy is selected for all production machines. In the second common method (B), a separate policy is selected for each production line. The results of the study on several articles showed that due to the choice of NET policy for a large number of machines and insufficient attention to the specific characteristics of each machine, the common methods have limited efficiency. As a result, new methods of high-performance NET policy selection need to be introduced, focusing on the specific characteristics of each machine. In this regard, the capabilities of simulation software can be used and the impact of personal opinion of experts can be reduced. Also, by clustering machines according to similar NET policies, it reduces the variety and complexity of NET programs.

5. Conclusion

The main focus of the present study is on selecting the appropriate NET policy for a group of similar machines in terms of NET policy. For this purpose, first, with the help of computer simulation, the values of the functional parameters of the machines are extracted. This information is for completing the ANP matrices. In the usual way, this information was given by experts and led to applying personal taste in choosing the NET policy. Next, the appropriate policy for each machine is selected using the ANP method. In this approach, the number of NET executable programs increases and makes the operation more complex. In order to reduce the number of NET applications, similar machines are grouped in virtual cells without physical displacement. For each cell, a NET program is prepared and executed. The results of a case study in a food industry show that the optimal NET policies of some machines located on a production line are different from each other. Also, the results obtained from the executive method were compared with two conventional methods. According to the results, the efficiency of the proposed research method is higher than both conventional methods. Given the limitations of the current research, it is suggested that the sensitivity analyses presented in the current research should be performed in a scenario-based research and the results should be compared with the current research. Increase the accuracy of results and analyses by using decision-making methods with multiple criteria in an uncertainty environment such as FANP.

Data Availability

The data used to support the findings of this study are available from the corresponding author upon request.

Conflicts of Interest

The authors declare that they have no conflicts of interest.

References

[1] X. Zhang, X. Ming, L. Zhiwen, D. Yin, and Z. Chen, "A reference system of smart manufacturing talent education (SMTE) in China," *The International Journal of Advanced Manufacturing Technology*, vol. 100, no. 9, pp. 2701–2714, 2019.

[2] H. W.-C. Yeung and N. Coe, "Toward a dynamic theory of global production networks," *Economic Geography*, vol. 91, no. 1, pp. 29–58, 2015.

[3] A. Van Horenbeek and L. Pintelon, "Development of a maintenance performance measurement framework-using the analytic network process (ANP) for maintenance performance indicator selection," *Omega*, vol. 42, no. 1, pp. 33–46, 2014.

[4] M. Ilangkumaran and S. Kumanan, "Selection of maintenance policy for textile industry using hybrid multi-criteria decision making approach," *Journal of Manufacturing Technology Management*, vol. 20, no. 7, pp. 1009–1022, 2009.

[5] M. Zandieh, A. R. Khatami, and S. H. A. Rahmati, "Flexible job shop scheduling under condition-based maintenance: improved version of imperialist competitive algorithm," *Applied Soft Computing*, vol. 58, pp. 449–464, 2017.

[6] S. H. Khajavi, J. Partanen, and J. Holmström, "Additive manufacturing in the spare parts supply chain," *Computers in Industry*, vol. 65, no. 1, pp. 50–63, 2014.

[7] S. Khan, P. Phillips, I. Jennions, and C. Hockley, "No fault found events in maintenance engineering part 1: current trends, implications and organizational practices," *Reliability Engineering & System Safety*, vol. 123, pp. 183–195, 2014.

[8] R. Palmarini, J. A. Erkoyuncu, R. Roy, and H. Torabmostaedi, "A systematic review of augmented reality applications in maintenance," *Robotics and Computer-Integrated Manufacturing*, vol. 49, pp. 215–228, 2018.

[9] M.-C. Fitouhi and M. Nourelfath, "Integrating noncyclical preventive maintenance scheduling and production planning for multi-state systems," *Reliability Engineering & System Safety*, vol. 121, pp. 175–186, 2014.

[10] M. A. Levin and T. T. Kalal, *Improving Product Reliability*, John Wiley & Sons, Chichester, UK, 2003.

[11] R. Barlow and L. Hunter, "Optimum preventive maintenance policies," *Operations Research*, vol. 8, no. 1, pp. 90–100, 1960.

[12] M. M. A. Malakoutian and M. Khaksar, "SBM model based productivity evaluation," *Eng Transactions*, vol. 1, no. 1, 2020.

[13] J. Guo, H. Zheng, B. Li, and G.-Z. Fu, "Bayesian hierarchical model-based information fusion for degradation analysis considering non-competing relationship," *IEEE Access*, vol. 7, pp. 175222–175227, 2019.

[14] M. Shafiee, "Maintenance strategy selection problem: an MCDM overview," *Journal of Quality in Maintenance Engineering*, vol. 21, no. 4, 2015.

[15] M. Taleghani and A. Taleghani, "Identification and ranking of factors affecting the implementation of knowledge management based on TOPSIS technique," *ENG Transactions*, vol. 1, pp. 1–10, 2013.

[16] J. Guo, H. Zheng, B. Li, and G.-Z. Fu, "A bayesian approach for degradation analysis with individual differences," *IEEE Access*, vol. 7, pp. 175033–175040, 2019a.

[17] S.-H. Ding and S. Kamaruddin, "Maintenance policy optimization—literature review and directions," *The International Journal of Advanced Manufacturing Technology*, vol. 76, no. 5–8, pp. 1263–1283, 2015.

[18] A. S. Eruguz, T. Tan, and G.-J. van Houtum, "A survey of maintenance and service logistics management: classification and research agenda from a maritime sector perspective," *Computers & Operations Research*, vol. 85, pp. 184–205, 2017.

[19] E. C. Özcan, S. Ünlüsoy, and T. Eren, "A combined goal programming—AHP approach supported with TOPSIS for maintenance strategy selection in hydroelectric power plants," *Renewable and Sustainable Energy Reviews*, vol. 78, pp. 1410–1423, 2017.

[20] M. Madhikermi, S. Kubler, J. Robert, A. Buda, and K. Främling, "Data quality assessment of maintenance reporting procedures," *Expert Systems with Applications*, vol. 63, pp. 145–164, 2016.

[21] A. Azadeh, M. Sheikhalishahi, and F. Monshi, "Selecting optimum maintenance activity plans by a unique simulation-multivariate approach," *International Journal of Computer Integrated Manufacturing*, vol. 29, no. 2, pp. 1–15, 2015.

[22] A. Azadeh and S. Abdolhossein Zadeh, "An integrated fuzzy analytic hierarchy process and fuzzy multiple-criteria decision-making simulation approach for maintenance policy selection," *Simulation*, vol. 92, no. 1, pp. 3–18, 2016.

[23] N. C. Caballé, I. T. Castro, C. J. Pérez, and J. M. Lanza-Gutiérrez, "A condition-based maintenance of a dependent degradation-threshold-shock model in a system with multiple degradation processes," *Reliability Engineering & System Safety*, vol. 134, pp. 98–109, 2015.

[24] N. Aghajani-Delavar, E. Mehdizadeh, R. Tavakkoli-Moghaddam, and H. Haleh, "A multi-objective vibration damping optimization algorithm for solving a cellular manufacturing system with manpower and tool allocation," *Scientia Iranica*, 2020, In press.

[25] F. J. Golrokh and A. Hasan, "A comparison of machine learning clustering algorithms based on the DEA optimization approach for pharmaceutical companies in developing countries," *Eng Transactions*, vol. 1, no. 1, 2020.

[26] D. Klein and E. Hannan, "An algorithm for the multiple objective integer linear programming problem," *European Journal of Operational Research*, vol. 9, no. 4, pp. 378–385, 1982.

[27] F. T. S. Chan and A. Prakash, "Maintenance policy selection in manufacturing firms using the fuzzy MCDM approach," *International Journal of Production Research*, vol. 50, no. 23, pp. 7044–7056, 2012.

[28] H. Wang, "A survey of maintenance policies of deteriorating systems," *European Journal of Operational Research*, vol. 139, no. 3, pp. 469–489, 2002.

[29] L. Wang, J. Chu, and J. Wu, "Selection of optimum maintenance strategies based on a fuzzy analytic hierarchy process," *International Journal of Production Economics*, vol. 107, no. 1, pp. 151–163, 2007.

[30] E. Triantaphyllou, B. Kovalerchuk, L. Mann, and G. M. Knapp, "Determining the most important criteria in maintenance decision making," *Journal of Quality in Maintenance Engineering*, vol. 3, no. 1, pp. 16–28, 1997.

[31] S. Zaim, A. Turkyilmaz, M. F. Acar, U. M. Al-Turki, and F. Demirel, "Maintenance strategy selection using AHP and ANP algorithms: a case study," *Journal of Quality in Maintenance Engineering*, vol. 18, no. 1, pp. 16–29, 2012.

[32] T. L. Saaty, "The modern science of multicriteria decision making and its practical applications: the AHP/ANP approach," *Operations Research*, vol. 61, no. 5, pp. 1101–1118, 2013.

[33] A. T. de Almeida, C. A. V. Cavalcante, M. H. Alencar, R. J. P. Ferreira, A. T. de Almeida-Filho, and T. V. Garcez, *Multicriteria And Multiobjective Models For Risk, Reliability And Maintenance Decision Analysis*, Springer International Publishing, Cham, Germany, 2015.

[34] F. Dweiri, S. Kumar, S. A. Khan, and V. Jain, "Designing an integrated AHP based decision support system for supplier selection in automotive industry," *Expert Systems with Applications*, vol. 62, pp. 273–283, 2016.

[35] A. Alrabghi and A. Tiwari, "State of the art in simulation-based optimisation for maintenance systems," *Computers & Industrial Engineering*, vol. 82, pp. 167–182, 2015.

[36] T. Altiok and B. Melamed, *Simulation Modeling and Analysis with ARENA*, Elsevier, Amsterdam, Netherlands, 2007.

[37] N. C. Suresh and J. Slomp, "Performance comparison of virtual cellular manufacturing with functional and cellular layouts in DRC settings," *International Journal of Production Research*, vol. 43, no. 5, pp. 945–979, 2005.

[38] M. M. Paydar and M. Saidi-Mehrabad, "A hybrid genetic algorithm for dynamic virtual cellular manufacturing with supplier selection," *The International Journal of Advanced Manufacturing Technology*, vol. 92, no. 5, pp. 3001–3017, 2017.

[39] A. Hameed, F. Khan, and S. Ahmed, "A risk-based shutdown inspection and maintenance interval estimation considering human error," *Process Safety and Environmental Protection*, vol. 100, pp. 9–21, 2016.

[40] M. M. Paydar and M. Saidi-Mehrabad, "A hybrid genetic-variable neighborhood search algorithm for the cell formation problem based on grouping efficacy," *Computers & Operations Research*, vol. 40, no. 4, pp. 980–990, 2013.

[41] E. B. Tirkolaee, A. Mardani, Z. Dashtian, M. Soltani, and G.-W. Weber, "A novel hybrid method using fuzzy decision making and multi-objective programming for sustainable-reliable supplier selection in two-echelon supply chain design," *Journal of Cleaner Production*, vol. 250, Article ID 119517, 2020.

[42] L. J. Hong and B. L. Nelson, "A brief introduction to optimization via simulation," in *Proceedings of the 2009 Winter Simulation Conference (WSC)*, pp. 75–85, IEEE, Austin, TX, USA, December 2009.

Hindawi
Mathematical Problems in Engineering
Volume 2021, Article ID 8770725, 10 pages
https://doi.org/10.1155/2021/8770725

Research Article

ECLP: Friend Recommendation Using Ensemble Approach for Detecting Communities Performing Link Prediction

Hasan Saeidinezhad,[1] Elham Parvinnia,[1] and Reza Boostani[2]

[1]*Department of Computer Engineering, Shiraz Branch, Islamic Azad University, Shiraz, Iran*
[2]*CSE and IT Department, Electrical and Computer Engineering Faculty, Shiraz University, Shiraz, Iran*

Correspondence should be addressed to Elham Parvinnia; parvinnia@iaushiraz.ac.ir

Received 21 April 2021; Revised 8 May 2021; Accepted 22 May 2021; Published 9 August 2021

Academic Editor: Mohammad Yazdi

Social networks provide a variety of online services that play an important role in new connections among members to share their favorite media, document, and opinions. For each member, these networks should precisely recommend (predict) the link of members with the highest common interests. Because of the huge volume of users with different types of information, these networks encounter challenges such as dispersion and accuracy of link prediction. Moreover, networks with numerous users have the problem of computational and time complexity. These problems are caused because all the network nodes contribute to calculations of link prediction and friend suggestions. In order to overcome these drawbacks, this paper presents a new link prediction scheme containing three phases to combine local and global network information. In the proposed manner, dense communities with overlap are first detected based on the ensemble node perception method which leads to more relevant nodes and contributes to the link prediction and speeds up the algorithm. Then, these communities are optimized by applying the binary particle swarm optimization method for merging the close clusters. It maximizes the average clustering coefficient (ACC) of the whole network which results in an accurate and precise prediction. In the last phase, relative links are predicted by Adamic/Adar similarity index for each node. The proposed method is applied to Astro-ph, Blogs, CiteSeer, Cora, and WebKB datasets, and its performance is compared to state-of-the-art schemes in terms of several criteria. The results imply that the proposed scheme has a significant accuracy improvement on these datasets.

1. Introduction

Studies in computer science have rapidly developed in recent decades, and many aspects of computer science are currently being studied [1–7]. These studies include many areas such as image processing and the advanced relevant techniques, machine learning and pattern recognition, data mining, and relative discussions [8–13]. On the other hand, there are many studies dealing with issues such as developing Statistical Process Control (SPC) techniques to take advantage of the advanced measurement technologies and sensors or even assessing the capability of these measurements such as 3D laser scanner that provides high-density data [14–19]. Researchers have also studied social networks and related issues [20–26].

Social networks play an important role in people's daily lives [27–30]. Social media creates a substrate for users to share their information, in terms of media, documents, and opinions [31–34]. These networks provide online services imitating and simulating real-life interactions and relationships. Social networks also enable making connections among members, in a way that each user can select and add new friends from a long list of candidates, suggested by the recommender system module. Research findings show that users usually connect with their friends/colleagues (who they know and see in real life) as well as new friends who are introduced by the link prediction service of social networks [35, 36].

With the daily growth of information in social networks, the process of introducing proper friends by the link prediction service has been a very challenging task and requires high precision [37]. Recommender systems, which predict the link for users, have been used for more than ten years to

offer products and services to users based on their interests, preferences, and online behavior [38–45]. Another challenge in the LP problem is precise link prediction among members in the large size network [46, 47]. Also in the link suggestion systems, in which actual communities are very scattered, the prediction will be challenging. In other words, the nodes in these communities are associated with only a small fraction of all network nodes. For example, in the case of Facebook, a user typically only connects to about 100 (out of 500 million) nodes. Therefore, this method gives acceptable accuracy of prediction in a way that out of 500 million possible predictions, only 100 errors can occur. One of the most important problems that recommender (link prediction) systems are faced with is the problem of cold start that means there is not enough and sufficient information (ratings) in the system to provide a recommendation [48–52].

In general, link prediction methods are divided into two categories: supervised (with observer) such as decision tree, Bayes, and K-nearest neighbor (KNN) [14] and unsupervised (without observer) which are based on the network's topology information. These methods are divided into three categories: local, global, and semilocal [53].

Local criteria are based on neighborhood topological information. These methods are based on the idea that if there are some similarities between the nodes m_1 and m_2, they will be more likely to be connected in the near future. The most important local criteria are common neighbors (CN) [48, 54], Jaccard's coefficient [55, 56], and Adamic/Adar index (AA) [57]. These criteria successfully reduce the computational cost; however, they do not have relatively high accuracy in forecasting [58]. Semilocal criteria need more information about the network topology rather than the local criteria but do not require the information of all the network connections. This criterion has been created with the aim of balancing the local and global criteria and does not have the challenges of global criteria such as being time-consuming and difficulties to find the complete network structure. It is also a good trade-off between the complexity and performance, such as local path index (LPI) methods and local random walk (LRW). Global criteria, similar to methods based on all paths in the network [10], need complete information about network topology. In this approach, based on all the paths between the two nodes in the network and all the information extracted from the entire network topology, the similarity of the two nodes is measured. Well-known global criteria are Katz [59], random walk, collision time (Hitting Time), and Sim-Tank, all of which suffer from high computational complexity [60, 61].

Some of the link prediction methods are designed based on data mining methods such as clustering that can categorize each group of members with mutual interests into one cluster. This technique can highly limit the search space and suggests a list of candidate members who are selected from the corresponding cluster for each member in a cluster. This process can be used to improve the matching process and provide suggestions on social networks and also predict future events. Previous researchers clustered the nodes of a social network for their link prediction algorithm and deduced that there was a significant relation between communities related to the network structure and the precision of their algorithm. Moreover, using the similarity-based link prediction algorithm, which used the clustering information, improved the accuracy of link prediction [62]. A gravity-based link prediction method was proposed which included community information of networks. The researchers used the Louvain algorithm for community detection as well as parallelism in the community processing to speed up the prediction globally [59].

None of the previous work considered overlapping between the recognized clusters; also, they did not check merging clusters to find an optimum combination of clusters for this particular problem. Therefore, a three-phase method is proposed in this paper which considers all the prediscussed subjects. In the first phase of the algorithm (community detection), ensemble of clustering is applied. In this phase, dense communities are searched by deploying node perception algorithm, which, despite the previous works, is a clustering method that considers overlapping between the detected clusters by using three hyperparameters. To find proper values for the parameters, a greedy search is applied. In the second phase, the clustering process is continued by applying binary particle swarm optimization (BPSO) algorithm to optimize clusters by merging near-enough neighbor clusters. The fitness function of BPSO is defined to maximize average clustering coefficient (ACC) of the network. Then, those communities are merged where their merge enhances the fitness value. Executing this phase leads to more suitable communities because they improve network ACC. Eventually, in the third phase of our work, a similarity-based link prediction algorithm (Adamic/Adar) is applied with the hope of achieving high performance in link prediction in social networks.

The rest of this paper is organized as follows. Section 2 presents previous related works. Our proposed algorithm is described in Section 3 in detail. Section 4 describes the dataset and evaluation criteria. The results and analysis of our work are reported in Section 5, and the last section concludes our paper.

2. Related Work

Due to the importance of friend suggestions in social networks, this issue has been investigated in several studies. Bastami et al. [59] introduced a new similarity measure called Triadic, which used some units called Motifs. They defined Motifs as the different forms of a Triadic network including three nodes. Their main proposed method consisted of two phases; in the first phase, a data table was created including the information of each node in the graph. Then, in the second phase, they used a classifier to be trained on the data table entries to predict the links. They applied their work on directed datasets to identify the Motifs, which means that the undirected networks cannot be analyzed by their algorithm. They also did not consider the problem of an imbalance dataset in their model. Datasets in link prediction are very imbalanced because the positive class (existing links) is in minority compared with nonexisting links.

Rafiee et al. [60] proposed link prediction based on common neighbors degree penalization (CNDP) and used quasilocal techniques instead of using local or global techniques, by considering neighbors of neighbors instead of only direct neighbors. They defined a new similarity score which is determined according to the topological structure of the network including common neighbors of each two nodes and the average clustering coefficient of the network. They performed their experiments on BUP, CEG, SMG, and HMT datasets and showed that their proposed method was superior to other methods such as adaptive degree penalization (ADP), the node-coupling clustering coefficient of node (NCCCN), and Triadic measure. They showed that contributing the common neighbors of three Triadic nodes including x, y, and z as the two desired nodes for calculating their similarity (x, y) and common neighbor (z) can affect the prediction performance. They also calculated the degree penalization scores in terms of area under the curve (AUC) and precision metrics using regression over different datasets which improved their work compared with the ADP algorithm that used a fixed value for degree penalization.

Most of the studies consider a static network to assess their method while this is a rough approximation because all social networks are updated over time. In this regard, Yao et al. [61] introduced a hybrid method based on link prediction that is assessed over dynamic networks with three metrics: the time-varied weight (revealing topological structure changes over time), the degree of common neighbors, and the intimacy between common neighbors. The last metric checks whether two common neighbor nodes have mutual relationships and checks the probability of a link appearing between the increases. They redefined the common neighbors by considering the nodes within two hops to achieve better performance. In their proposed method, they only focused on the topological features of common neighbors that can change over time, but the other metrics related to other features such as the node's attributes or graph topology on a larger scale (communities) or the change of path between two nodes were ignored. Moreover, one of their metrics, which check if intimacy between the common neighbors exists or not, is independent of time and can be used in static networks. They performed their experiments on DBLP datasets and used the Jaccard similarity criterion. They also used TPR and execution time to evaluate the performance of their method.

Bao et al. [61] proposed an incremental dynamic link prediction method that predicts relative links in dynamic social networks. Their algorithm called DLP-IRA is based on the resource allocation (RA) algorithm which is an algorithm based on the nodes' degree and considers the fact that the smaller the degree two nodes have, the higher the chance of establishing a link. Therefore, they defined a weight on each nonexisting link which is inverse of the maximum degree of source and destination nodes. They also stated that common neighbors of two nodes have a huge impact on link appearance, so they contributed the common neighbors' degree in their calculation. To adapt their algorithm with the dynamic network, they update the changing node set S with all the nodes with changed connected links. When no new node was added, subgraphs including the nodes in S and their neighbors are considered as the input of their improved resource allocation algorithm. They claimed that their algorithm can avoid recomputing when the graph structure changes and also speeds up the process. The basis of their algorithm is nodes' degree, and no other extra information of the network had contributed. Even though the statement of the reverse correlation between the nodes' degree and their chance of link creation is generally true, in many situations, it is totally reverse, like when a TV star becomes famous, and as his popularity increases, more fans follow him, or when a person is extrovert, he tries to connect with more and more people. Furthermore, they did not consider the graph change evolution over time and just relied on the last change.

3. Proposed Method

In this research, a combined method based on three phases has been proposed for link prediction (suggesting friends) in social networks. In this regard, one can easily combine local, global, and community information in very large spaces with millions of users and billions of links, where it can increase the prediction accuracy and cover all possible modes that solve the problem of data scattering. It also improves the problem of the cold start of users and the accuracy of the offer. The three stages of the proposed method are (i) community detection, which detects dense communities with the node perception algorithm, (ii) optimization task with binary particle swarm optimization (BPSO) algorithm, and (iii) applying link prediction algorithm to the output of the former phase. The roadmap of the proposed method is illustrated in Figure 1 and Tables 1 and 2.

Since the simulations and algorithms are applied to the graph, we shortly discuss the role of graphs in link prediction systems.

3.1. Graph Theory. Interactions on social networks and their structure can be simulated and implemented on a graph. A graph $G = (V, E)$ consists of a set of nodes V and a set of edges E, where the edges connect the nodes. V demonstrates the role of users in the social network and E is the relationship between users. Adjacent matrix A of graph G is a two-dimensional matrix; if two users are connected, the corresponding edge is set to 1; otherwise, it sets to zero as shown in Figure 2.

3.2. Community Detection. As shown in Figure 1, the first phase is community detection. To detect the communities, nodes should be clustered, and each cluster can be considered as a community. For each node, we determined the clustering coefficient (CC) as follows:

$$C_x = \frac{\Sigma_{y,z} \in \Gamma x \text{ and } E_{y,z} \in EE_{y,z}}{|\Gamma x|\,(|\Gamma x| \times -1)}, \tag{1}$$

where Γ_x demonstrates the neighbors of node x and $|\Gamma_x|$ is the degree of node x. $E_{y,z}$ represents the edge that exists between two nodes y and z. Therefore, to calculate the clustering coefficient of node x, all the edges between the

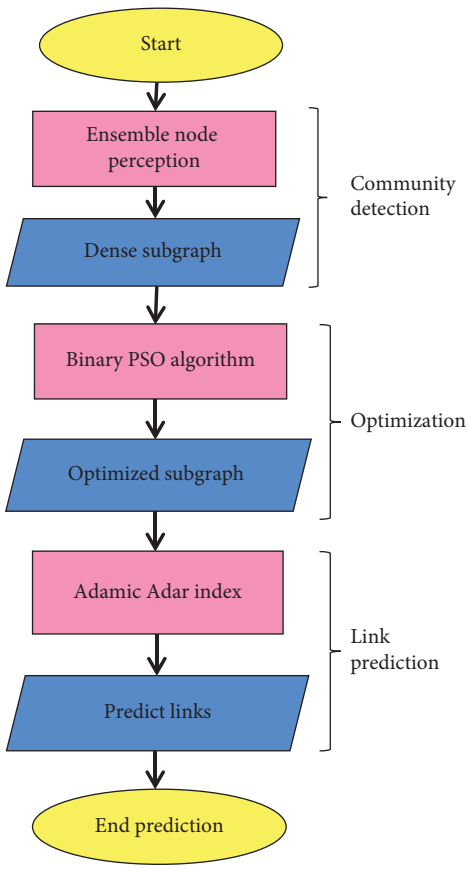

Figure 1: Diagram of the proposed method.

Table 1: Nomenclature table.

Symbol	Meaning
$\|V\|$	Number of nodes
Γ_x	Neighbors of node x
$\|\Gamma_x\|$	Degree of node x
$E_{y,z}$	Edge between two nodes y and z
C_x	Clustering coefficient of node x
CC	Clustering coefficient
ACC	Average clustering coefficient
t	Time snapshot
Xij	A binary array for indicating the communities i and j are merged together or not
Vij	Velocity function as a probability threshold value that determines whether the position vector is zero or one
$s(z)$	Sigmoid function that takes the velocity function of next time as input

Table 2: The statistical information of experimental datasets [51, 52, 63–65].

Dataset	NN	NE	NC	MO	DA	AD	ACC	NT
Astro-ph	18771	198050	321	0.619	014	21.09	0.677	1351441
Blogs	1224	19025	010	0.426	008	31.38	0.213	101043
CiteSeer	3312	4732	467	0.887	008	1.421	0.080	1223
Cora	2708	5429	098	0.805	015	3.891	0.293	1630
WebKB	0877	1608	043	0.757	010	3.372	0.332	389

neighbors of node x are counted and divided into the total number of possible mutual relationships between the neighbors of node x. In other words, we determine how many people (nodes) are neighbors of our desired node, and among whom, how many of the nodes are friends with each other. More friendships between the neighbors of the desired node lead to its higher CC value. After determining the CC value of all nodes in each community, we determined the value average clustering coefficient (ACC) as the aggregation of that community according to the following equation:

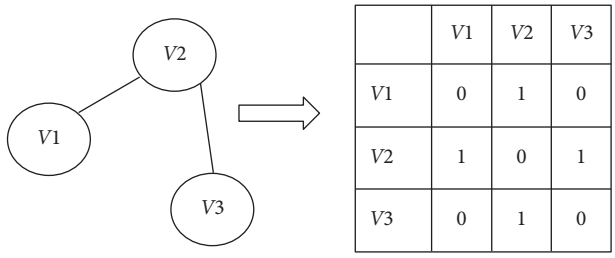

Figure 2: As shown above, a graph consists of three users, and their interaction is expressed in the corresponding matrix.

$$\mathrm{ACC} = \frac{\sum_{x \in v} C_x}{|V|}, \tag{2}$$

where C_x represents the clustering coefficient of node x and |V| is the number of nodes in the graph. After determining the ACC of each community, all of them are summed together, and the result is divided into the number of the communities. To detect each community by the node perception algorithm, first, we identify small communities [23]. This algorithm has an acceptable performance even when encountering millions of users and billions of links. This method has some properties compared to other competitive methods in which one user can be assigned to more than one cluster. This algorithm uses three hyperparameters to perform clustering. To properly set the parameters, the ensemble of clustering is used, which performs a greedy search on parameters in the search space. This algorithm consists of two phases that run alternately. Suppose that we are dealing with a network with n vertices. First, we take each vertex equal to a community. Hence, first, we have several communities equal to the number of vertices; then for each vertex i, we find the neighboring community j in a way that for removing i from its community and joining it to community j, modularity is maximized, and then, we add vertex i to community j. This is done only if the modularity is increased; otherwise, vertex i remains in its community. This is repeated frequently for all vertices until no change happens. At this stage, the first phase is finished. It should be noted that in the first phase, a vertex may be moved several times between different communities. The first phase stops at a locally optimal point. Then, in the second phase, clustering continues by merging small groups that have the ability to form larger groups. We continue this process until we reach the desired number of communities or exceed a certain threshold. This process should satisfy some constraints. The size of each community should be lower than a threshold. We have an overlap threshold that controls the overlap tolerance of communities. A threshold is determined for the tolerance required to merge communities. The threshold parameter is set between 0.1 and 1, and we change the value of this parameter by increasing step 0.1. We set the smallest community size that can be detected. To properly set the parameters, we used an ensemble of clustering. The ensemble is a set of parameters set in node preservation with different values, which is considered to increase the value of aggregation indicating the ACC. To obtain the ACC value in a community, we must first calculate the value of the clustering coefficient for all nodes in the community based on equation (1). Then, based on equation (2), we determine the ACC of each community, and exceeding this value from a threshold implies that it is a valid community.

3.3. Clusters' Optimization by BPSO. Particle swarm optimization (PSO) is one of the known evolutionary algorithms introduced by Kennedy and Supermart (1995). Similar to other metaheuristic algorithms, PSO starts with a population of particles, each having the potential to be a solution to the problem. These particles are first randomly initialized all over the search space. After determining the fitness value of all particles, one of them has the highest fitness score, and it attracts all particles toward itself. After the second iteration, particles are moved according to two directions: the direction to the position of the best particle (gbest) and the direction to the position of best fitness that the corresponding particle has experienced (pbest). Unlike other evolutionary computational techniques, each particle (particle) in PSO depends on the position, velocity, and acceleration. The particles continuously move in the search space at an acceleration that is dynamically calculated according to their previous behaviors. Meanwhile, through the movement of particles, two random parameters try to insert a degree of randomness to enhance the exploration of this algorithm while PSO preserves a good exploitation property. If through the movement of particles, the fitness of one particle exceeds gbest, this particle is considered as the new gbest [24, 25].

Due to the discrete nature of our problem, the continuous operators of PSO should be discretized. In binary PSO (BPSO), introduced by Kennedy and Eberhart [24, 25], velocity is used as a probability threshold value that determines whether the position vector is zero or one. Suppose that X_{ij} is the value of the jth bit of the binary vector which represents the position of the ith particle. In this case, the following equation describes how the binary PSO algorithm works:

$$X_{ij}(t+1) = \left\{ \begin{array}{l} 0 \ \text{ if rand}(.) \geq S\left(v_{ij}(t+1)\right) \\ 1 \ \text{ if rand}(.) < S\left(v_{ij}(t+1)\right) \end{array} \right\},$$
$$S_x = \frac{1}{1+e^{-x}},$$
$$v_{ij}(t-1) = m * v_{ij}(t) + c_1 r_{ij}(t)\left[y_{ij}(t) - z_{ij}(t)\right] + c_2 r_{2j}(t)\left[y_j(t) - z_{ij}(t)\right], \tag{3}$$

where X_{ij} is an array with 1 and 0 elements, which, respectively, indicate if the corresponding community should merge to other communities or not. t indicates the iteration, v_{ij} is a velocity function, $s(z)$ is a sigmoid function that takes the velocity function of the next time as an input, and then, if the output of the sigmoid function is greater than a random number, the value of 1 is placed in X_{ij} array for the corresponding community; otherwise, 0 is placed.

In binary PSO, the particle velocity is changed similar to the standard PSO algorithm. In addition to introduced parameters, the number of particles (initial population), which can increase the exploration, and the maximum number of iterations are important parameters of the algorithm. BPSO optimizes the communities that were detected in the first stage to achieve greater ACC. The fitness function of each particle (network) is the summation of ACC of its corresponding elements (community). We come to an array for each particle whose size is equal to the number of the communities. Then, we specify the position of each community, which can be zero and one. It should be noted that for multiple communities, integrated by BPSO, ACC plays the main role in merging communities. A high value indicates that the integration has been done properly; otherwise, we ignore merging.

For example, if we have a network with 5 communities, we consider a $5 * 1$ array whose elements are 0 or 1, which is initialized at random. For example, if the array elements are [0, 0, 0, 1, 1], this particle means that the first and fourth communities should be merged. Then, for all the resulting community nodes, we calculate the clustering coefficient and consequently calculate the ACC as the fitness of the integrated community. These operations are repeated until all possible particles of integration are checked. This is where the work of the second step ends, and the best possible communities were selected.

3.4. Link Prediction. In the first phase, we had an initial graph, and we came to divide this network into smaller communities that had more density. Then, in the second phase, we optimized the communities of the first part by BPSO. We created subgraphs that merged with each other to give better fitness results, leading to the production of more valuable communities. In this regard, we considered each of these subgraphs as input and using the Adamic/Adar index method (AA) to find the suggested link according to equation (4). Then, for each edge of the graph based on the obtained score in equation (4), a high value indicated that the edge can appear.

$$\text{Score}(x, y) = \sum_{Z \in \Gamma(x) \cap \Gamma(y)} \frac{1}{\log|\Gamma z|}, \tag{4}$$

where x and y are two nodes, which we tend to calculate their similarity and z is the set of their common neighbors. Γ_z demonstrates the neighbors of node z and $|\Gamma_z|$ is the degree of node z. In this regard, we find common neighbors for two nodes (x, y), then for each common neighbor obtained, we divide 1 by the log (logarithm) of the desired number of nodes, and finally, the values obtained from the common nodes are added together, which results in a score for each edge connected to the two nodes. This score indicates the amount of similarity between the two nodes x and y, creating a link between them. Assuming that if x and y are nodes that have a large number of common neighbors, then according to the AA index, a higher score is determined. In other words, it can be said that there is a high probability that a connection is established between x and y in the future (link). At this stage, a threshold is considered, and based on it, if the value of that edge exceeds this threshold, it means that there is a very high probability that there will be a link between them; otherwise, no link is suggested. For example, in Figure 3, to calculate AA (2, 5), we have

$$\text{AA}(2, 5) = \sum_{z \in \Gamma 2 \cap \Gamma 5} \frac{1}{\log|\Gamma(z)|}. \tag{5}$$

4. Datasets and Evaluation Criteria

To evaluate the proposed method, we divided the edges in the graph into two categories: E_train and E_test. E-train are the edges that are used for calculating the similarity score between each pair of nodes in the graph and E_test are the edges that are used to validate the proposed method. Based on this, we use the following data to show the effectiveness of the proposed method. The employed datasets are Astro-ph [26], Blogs [27], CiteSeer [28], Cora [26], and WebKB [28], and the features that make up the dataset can be expressed as the number of nodes (NN), number of edges (NE), number of communities (NC), modularity (MO), diameter (DA), average degree (AD), average clustering coefficient (ACC), and number of triangles (NT).

The criteria used to assess the proposed method, compared to the counterparts, are expressed as follows. The confusion matrix includes true positive (TP), true negative (TN), false positive (FP), and false negative (FN). Based on these four parameters, it is possible to determine sensitivity, specificity, precision, recall, TP rate (TPR), FP rate (FPR), receiver operative curve (ROC), and (AUC). Precision means the number of correctly identified links divided by the total number of links classified as positive, and accuracy means the number of correctly identified links divided by the total number of links. Recall means the number of classified positive links divided by the total number of real positive links. ROC curve sketches TPR versus FPR, and AUC is the area under ROC. Important indicators that have shown their performance in link prediction are Adamic/Adar (AA) index, common neighbor (CN), Jaccard index (JC), and KI.

5. Experimental Results

The purpose of the experiments was to evaluate the proposed method (ECLP) versus state-of-the-art methods over the introduced datasets in terms of the described criteria. The tests were performed on a system with Intel Core i7 GHz CPU specifications and 16 GB RAM. The test results of the proposed method (ECLP) were tested and compared with

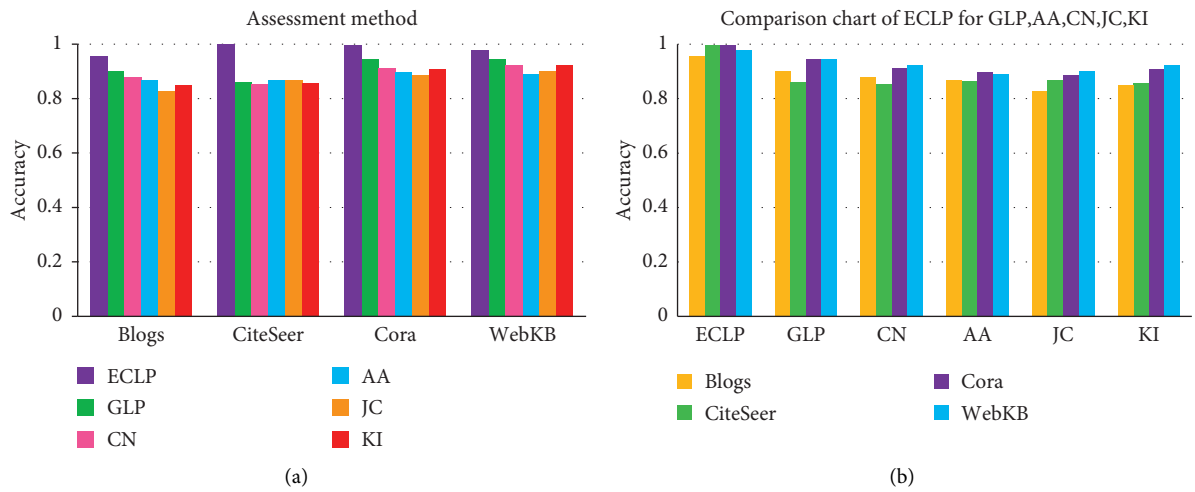

Figure 3: Comparison of the algorithms for different datasets in terms of AUC. (a) Comparison of the algorithms together for each dataset separately. (b) The accuracies obtained for different datasets for each algorithm.

KI, CN, JC, AA, and GLP methods. It should be noted that in the deployed graphs, the edges are considered weightless.

In order to evaluate our new method, we use fivefold cross-validation which divides the data into five folds; each time picks a fold as test data and keeps the rest as train data. Then, based on the proposed method, the similarity scores are calculated for the nodes in four folds of train data, and these scores are evaluated on the test fold and thus accuracy is determined. This process is repeated for all five folds. Finally, AUC is calculated based on the five accuracy values obtained in fivefold cross-validation and this average accuracy is recorded in Table 3.

As shown in Table 3, the proposed method works well in real-world datasets. Evaluation of experimental results is expressed in terms of the AUC metric. Table 3 indicates that our method is significantly improved compared to state-of-the-art methods. A comparison of columns two and three in Table 3 shows that ECLP outperforms the GLP algorithm in all datasets except one of them, and by comparing ECLP to the methods of columns four to seven, it is obvious that ECLP significantly improved (more than 4%) the prediction accuracy in terms of AUC.

Figure 3 visualizes the quantitative results of Table 3, to better understand the difference between the aforementioned algorithm results. Figure 3(a) represents the accuracy (AUC) values for a unique dataset when different algorithms are applied. As shown in Figure 3, ECLP outperforms other algorithms for the four datasets (Blogs, CiteSeer, Cora, and WebKB). It is noteworthy to say that ECLP performs better than even GLP for these four datasets, especially for the CiteSeer dataset, where there was a big difference between ECLP and GLP accuracy. Figure 4 shows the results in a different way, facilitating comparison among the algorithms' performance. It is so obvious that ECLP performs better than state-of-the-art algorithms such GLP, AA, CN, JC, and KI in terms of AUC criterion. Moreover, it can be interpreted that ECLP performs better on two datasets (Cora and CiteSeer) compared with the other two.

Table 3: Accuracy of the proposed and compared methods (in terms of AUC).

Dataset	Accuracy					
	ECLP	GLP	CN	AA	JC	KI
Astro-ph	0.9340	0.9313	0.8912	0.8653	0.8732	0.8695
Blogs	0.9559	0.9014	0.8786	0.8679	0.8274	0.8483
CiteSeer	0.9985	0.8612	0.8534	0.8658	0.8677	0.8565
Cora	0.9972	0.9455	0.9123	0.8975	0.8865	0.9078
WebKB	0.9768	0.9468	0.9233	0.8897	0.9011	0.9236
Average (%)	97.2	91.7	89.1	87.7	87.1	88.1

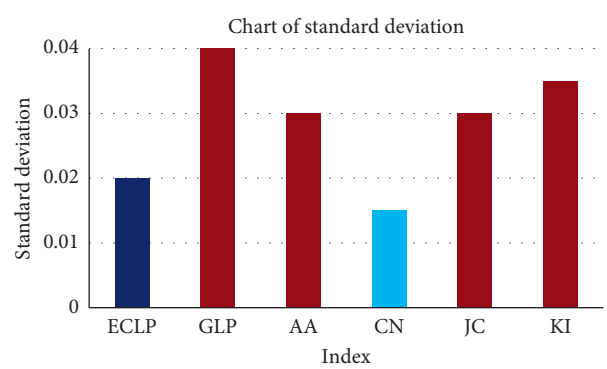

Figure 4: Comparison of the algorithms in terms of standard deviation.

As shown in Figure 4, our proposed method had a lower standard deviation compared to the other algorithms except CN. This indicates that our proposed method is more robust.

6. Conclusion

This paper proposes a three-stage scheme by optimizing the community detection to improve link prediction precision in social networks. In the first stage of the proposed method, we are faced with an initial graph, which should be divided into smaller dense subgraphs (communities). This is performed by applying node ensemble perception, which

incorporates global information. Then, in the second phase, we applied BPSO to optimize the communities of the former phase and, therefore, merge those communities that alleviate the fitness function. The second phase preserves semilocal information of the network. The third phase computes the similarity between each pair of nodes by applying Adamic/Adar similarity-based algorithm and then the edges with a high similarity score considered as the predicted edges of the algorithm. This phase enables ECLP to capture local information of the network. Moreover, our method considers the overlap between communities which means a node may belong to multiple communities while GLP uses the Louvain algorithm for community detection that does not consider the overlapping between communities. Our proposed algorithm was evaluated and analyzed by applying it to different datasets, and the results indicated that it performs better than all rival algorithms.

Data Availability

The data used to support the findings of this study are available from the first author, Hasan Saeidinezhad, upon request.

Conflicts of Interest

The authors declare that they have no conflicts of interest.

References

[1] J. Zhao, J. Liu, J. Jiang, and F. Gao, "Efficient deployment with geometric analysis for mmWave UAV communications," *IEEE Wireless Communications Letters*, vol. 9, 2020.

[2] Z. Xiong, N. Xiao, F. Xu et al., "An equivalent exchange based data forwarding incentive scheme for socially aware networks," *Journal of Signal Processing Systems*, vol. 93, 2021.

[3] K. Shi, Y. Tang, X. Liu, and S. Zhong, "Secondary delay-partition approach on robust performance analysis for uncertain time-varying Lurie nonlinear control system," *Optimal Control Applications & Methods*, vol. 38, 2017.

[4] M. Mortazavi, F. T. Hocanın, and A. Davarpanah, "Application of quantitative computer-based analysis for student's learning tendency on the efficient utilization of mobile phones during lecture hours," *Sustainability*, 2020.

[5] B. Daryayehsalameh, M. Nabavi, and B. Vaferi, "Modeling of CO_2 capture ability of [Bmim][BF_4] ionic liquid using connectionist smart paradigms," *Environmental Technology & Innovation*, vol. 22, 2021.

[6] A. Davarpanah, R. Shirmohammadi, B. Mirshekari, and A. Aslani, "Analysis of hydraulic fracturing techniques: hybrid fuzzy approaches," *Arabian Journal of Geosciences*, vol. 12, 2019.

[7] X. Ma, K. Zhang, L. Zhang et al., "Data-driven niching differential evolution with adaptive parameters control for history matching and uncertainty quantification," *SPE Journal*, vol. 26, 2021.

[8] R. Dastoorian and L. Wells, "Gauge capability studies for high-density data: SPC phase 0," *Procedia Manufacturing*, vol. 48, 2020.

[9] M. Abasi, A. Saffarian, M. Joorabian, and S. G. Seifossadat, "Fault location in double-circuit transmission lines compensated by generalized unified power flow controller (GUPFC) based on synchronous current and voltage phasors," *IEEE Systems Journal*, 2020.

[10] M. Abasi, A. Saffarian, M. Joorabian, and S. Ghodratollah Seifossadat, "Fault classification and fault area detection in GUPFC-compensated double-circuit transmission lines based on the analysis of active and reactive powers measured by PMUs," *Journal of the International Measurement Confederation*, vol. 169, 2021.

[11] S. Qu, W. Xu, J. Zhao, and H. Zhang, "Design and implementation of a fast sliding-mode speed controller with disturbance compensation for SPMSM syste," *IEEE Transactions on Transportation Electrification*, 2021.

[12] X. Xue, K. Zhang, K. C. Tan et al., "Affine transformation-enhanced multifactorial optimization for heterogeneous problems," *IEEE Transactions on Cybernetics*, vol. 8, 2020.

[13] A. Davarpanah, "Parametric study of polymer-nanoparticles-assisted injectivity performance for axisymmetric two-phase flow in EOR processes," *Nanomaterials*, vol. 10, 2020.

[14] Q. Jiang, F. Shao, W. Lin, K. Gu, G. Jiang, and H. Sun, "Optimizing multistage discriminative dictionaries for blind image quality assessment," *IEEE Trans Multimed*, vol. 20, 2018.

[15] Q. Jiang, F. Shao, W. Gao, Z. Chen, G. Jiang, and Y. S. Ho, "Unified No-reference quality assessment of singly and multiply distorted stereoscopic images," *IEEE Transactions on Image Processing*, vol. 28, 2019.

[16] S. He, F. Guo, Q. Zou, and H. Ding, "MRMD2.0: a Python tool for machine learning with feature ranking and reduction," *Current Bioinformatics*, vol. 15, 2020.

[17] S. Lv and Y. Liu, "PLVA: privacy-preserving and lightweight V2I authentication protocol," *IEEE Transactions on Intelligent Transportation Systems*, vol. 21, 2021.

[18] B. H. Li, Y. Liu, A. M. Zhang, W. H. Wang, and S. Wan, "A survey on blocking technology of entity resolution," *Journal of Computer Science and Technology*, vol. 25, 2020.

[19] B. Li, R. Liang, W. Zhou, H. Yin, H. Gao, and K. Cai, "LBS meets blockchain:an efficient method with security preserving trust in SAGIN," *IEEE Internet of Things Journal*, vol. 1, 2021.

[20] L. J. Wells, R. Dastoorian, and J. A. Camelio, "A novel NURBS surface approach to statistically monitor manufacturing processes with point cloud data," *Journal of Intelligent Manufacturing*, vol. 32, 2021.

[21] C. Zuo, Q. Chen, L. Tian, L. Waller, and A. Asundi, "Transport of intensity phase retrieval and computational imaging for partially coherent fields: the phase space perspective," *Optics and Lasers in Engineering*, vol. 71, 2015.

[22] C. Zuo, J. Sun, J. Li, J. Zhang, A. Asundi, and Q. Chen, "High-resolution transport-of-intensity quantitative phase microscopy with annular illumination," *Scientific Reports*, vol. 7654, 2017.

[23] Y. Zhou, L. Tian, C. Zhu, X. Jin, and Y. Sun, "Video coding optimization for virtual reality 360-degree source," *IEEE Journal of Selected Topics in Signal Processing*, vol. 14, 2020.

[24] H. Sheng, S. Wang, Y. Zhang et al., "Near-online tracking with Co-occurrence constraints in blockchain-based edge computing," *IEEE Internet of Things Journal*, vol. 8, 2021.

[25] K. Zhang, J. Zhang, X. Ma et al., "History matching of naturally fractured reservoirs using a deep sparse autoencoder," *SPE Journal*, 2021.

[26] A. Armin Razmjoo, A. Sumper, and A. Davarpanah, "Energy sustainability analysis based on SDGs for developing

countries," *Energy Sources, Part A: Recovery, Utilization, and Environmental Effects*, vol. 42, 2019.

[27] H. Safari-Katesari, S. Y. Samadi, and S. Zaroudi, "Modelling count data via copulas," *Statistics*, vol. 54, 2020.

[28] H. Safari Katesari and B. Fathi Vajargah, "Testing adverse selection using frank copula approach in Iran insurance markets," *Journal of Mathematical and Computational Science*, vol. 15, 2015.

[29] S. S. Kalantari and A. A. Taleizadeh, "Mathematical modelling for determining the replenishment policy for deteriorating items in an EPQ model with multiple shipments," *Journal of Systems Science: Operations & Logistics*, vol. 7, 2020.

[30] A. Roghani, S. H. Nyarko, and C. Sparks, "The first family formation among young Americans: the role of family process," *SN Social Science*, vol. 50, 2021.

[31] A. Chapnevis, I. Güvenç, and E. Bulut, "Traffic shifting based resource optimization in aggregated IoT communication," in *Proceedings of the 45th IEEE Conference on Local Computer Networks (LCN)*, Sydney, Australia, October 2020.

[32] M. Masoumnezhad, M. Rajabi, A. Chapnevis et al., "An approach for the global stability of mathematical model of an infectious disease," *Symmetry (Basel)*, vol. 12, 2020.

[33] S. Arasteh, M. Mahdavi, P. N. Bideh, S. Hosseini, and A. Chapnevis, "Security analysis of two key based watermarking schemes based on QR decomposition," in *26th Iranian Conference on Electrical Engineering (ICEE)*, Mashhad, Iran, May 2018.

[34] A. Chapnevis and B. Sadeghiyan, "A secure two-party computation protocol for intersection detection between two convex hulls," 2020, https://arxiv.org/abs/2011.00319v3.

[35] D. M. Boyd and N. B. Ellison, "Social network sites: definition, history, and scholarship," *Journal of Computer-Mediated Communication*, vol. 13, 2007.

[36] A. Azma, E. Narreie, A. Shojaaddini et al., "Statistical modeling for spatial groundwater potential map based on gis technique," *Sustainability*, vol. 13, 2021.

[37] F. Li, J. He, G. Huang, Y. Zhang, Y. Shi, and R. Zhou, "Node-coupling clustering approaches for link prediction," *Knowledge-Based System*, vol. 38, 2015.

[38] D. M. Boyd and N. B. Ellison, "Social network sites: definition, history, and scholarship," *IEEE Engineering Management Review*, vol. 38, 2010.

[39] M. Jalali Sarvestani and P. Charehjou, "Fullerene (C20) as a potential adsorbent and sensor for the removal and detection of picric acid contaminant: DFT Studies," *Central Asian Journal of Environmental Science and Technology Innovation*, vol. 2, no. 1, 2021.

[40] Y. Maina, B. Kyari, and M. Jimme, "Impact of household fuel expenditure on the environment: the quest for sustainable energy in Nigeria," *Central Asian Journal of Environmental Science and Technology Innovation*, vol. 1, no. 2, pp. 109–118, 2020.

[41] M. Mohammadi, "An in-depth study of specific pathway linked to abnormal reproductive system: a meta-analysis in a specific Caucasian ethnicity," *Central Asian Journal of Medical and Pharmaceutical Sciences Innovation*, vol. 1, no. 1, pp. 1–7, 2021.

[42] M. Sabernezhad, "Quantitative analysis of the p53 substitution mutation and breast cancer: an informative study in Iranian population," *Central Asian Journal of Medical and Pharmaceutical Sciences Innovation*, vol. 1, no. 1, pp. 8–14, 2021.

[43] R. Asgari, "The role of ESR1 PvuII T/C variant in the female reproductive process: a review," *Central Asian Journal of Medical and Pharmaceutical Sciences Innovation*, vol. 1, no. 1, pp. 22–27, 2021.

[44] S. Qayyum, I. Khan, K. Meng, Y. Zhao, and C. Peng, "A review on remediation technologies for heavy metals contaminated soil," *Central Asian Journal of Environmental Science and Technology Innovation*, vol. 1, no. 1, pp. 21–29, 2020.

[45] A. Rivera-Diaz, C. Patricia Ortiz, and D. Ricardo Delgado, "The crucial role of estrogen/androgen hormones and their receptors in male infertility risk," *Central Asian Journal of Medical and Pharmaceutical Sciences Innovation*, vol. 1, no. 1, pp. 35–43, 2021.

[46] T. Keim, "Extending the applicability of recommender systems: a multilayer framework for matching human resources," in *Proceedings of the 40th Annual Hawaii International Conference on System Sciences*, Big Island, Hawaii, January 2007.

[47] L. Jin, J. B. D. Joshi, and M. Anwar, "Mutual-friend based attacks in social network systems," *Computers and Security*, vol. 37, 2013.

[48] Y. Chen, V. M. Patel, P. J. Phillips et al., "An optimizing and differentially private clustering algorithm for mixed data in SDN-based smart grid," *IEEE Access*, vol. 7, 2018.

[49] X. Chen, D. Y. Wang, J. B. Tang, W. C. Ma, and Y. Liu, "Geotechnical stability analysis considering strain softening using micro-polar continuum finite element method," *Journal of Central South University*, vol. 28, no. 1, pp. 297–310, 2021.

[50] M. Abasi, M. Razaz, G. Seifossadat, and S. Moosapour, "Presenting a new formulation to analyze and determine unbalance voltage produced at the place of load resulting from network and loads unbalance and asymmetry of transmission lines in radial power systems," *Majlesi Journal of Energy Management*, vol. 6, no. 3, p. 4, 2015.

[51] J. Leskovec, "Astro physics collaboration network," https://snap.stanford.edu/data/ca-AstroPh.html.

[52] Lise's INQuisitive Students, "Link based classification," http://www.cs.umd.edu/projects/linqs/projects/lbc.

[53] L. L. Linyuan and T. Zhou, "Link prediction in complex networks: a survey," *Physica A: Statistical Mechanics and its Applications*, vol. 39, 2011.

[54] D. Liben-Nowell and J. Kleinberg, "The link-prediction problem for social networks," *Journal of the American Society for Information Science and Technology*, vol. 58, 2007.

[55] R. H. Li, J. X. Yu, and J. Liu, "Link prediction: the power of maximal entropy random walk," in *Proceedings of the 20th ACM international conference on Information and knowledge management*, Glasgow, Scotland, October 2011.

[56] C. A. Bliss, M. R. Frank, C. M. Danforth, and P. S. Dodds, "An evolutionary algorithm approach to link prediction in dynamic social networks," *Journal of Computational Science*, vol. 5, 2014.

[57] A. Papadimitriou, P. Symeonidis, and Y. Manolopoulos, "Fast and accurate link prediction in social networking systems," *Journal of Systems and Software*, vol. 85, 2012.

[58] L. Adamic and E. Adar, "How to search a social network," *Social Networks*, vol. 27, 2005.

[59] E. Bastami, A. Mahabadi, and E. Taghizadeh, "A gravitation-based link prediction approach in social networks," *Swarm and Evolutionary Computation*, vol. 44, 2019.

[60] S. Rafiee, C. Salavati, and A. Abdollahpouri, "CNDP: link prediction based on common neighbors degree penalization,"

Physica A: Statistical Mechanics and its Applications, vol. 539, 2020.
[61] L. Yao, L. Wang, L. Pan, and K. Yao, "Link prediction based on common-neighbors for dynamic social network," *Procedia Computer Science*, vol. 83, 2016.
[62] Z. Liu, Q. M. Zhang, L. Lü, and T. Zhou, "Link prediction in complex networks: a local naïve Bayes model," *EPL*, vol. 96, 2011.
[63] https://paperswithcode.com/dataset/citeseer.
[64] https://paperswithcode.com/dataset/cora.
[65] https://paperswithcode.com/dataset/webkb.

Hindawi
Mathematical Problems in Engineering
Volume 2021, Article ID 3017607, 9 pages
https://doi.org/10.1155/2021/3017607

Research Article

Dynamic Path Optimization with Real-Time Information for Emergency Evacuation

Huajun Zhang, Qin Zhao, Zihui Cheng, Linfan Liu, and Yixin Su

School of Automation, Wuhan University of Technology, Wuhan, China

Correspondence should be addressed to Qin Zhao; zhaoqin@whut.edu.cn

Received 12 April 2021; Revised 14 July 2021; Accepted 28 July 2021; Published 3 August 2021

Academic Editor: Mohammad Yazdi

In order to find the optimal path for emergency evacuation, this paper proposes a dynamic path optimization algorithm based on real-time information to search the optimal path and it takes fire accident as an example to introduce the algorithm principle. Before the accidents, it uses the Dijkstra algorithm to get the prior evacuation network which includes evacuation paths from each node to the exit port. When the accidents occur, the evacuees are unable to pass through the passage where the accident point and the blocking point are located, then the proposed method uses the breadth-first search strategy to solve the path optimization problem based on the prior evacuation network, and it dynamically updates the evacuation path according to the real-time information. Because the prior evacuation network includes global optimal evacuation paths from each node to the exit port, the breadth-first search algorithm only searches local optimal paths to avoid the blockage node or dangerous area. Because the online optimization solves a local pathfinding problem and the entire topology optimization is an offline calculation, the proposed method can find the optimal path in a short time when the accident situation changes. The simulation tests the performances of the proposed algorithm with different situations based on the topology of a building, and the results show that the proposed algorithm is effective to get the optimal path in a short time when it faces changes caused by the factors such as evacuee size, people distribution, blockage location, and accident points.

1. Introduction

The most important thing for emergency evacuation is to guide people to move from dangerous areas to safe areas in the shortest time. Facing emergencies such as hurricanes, tsunamis, fires, and poisonous gas leakage [1], some methods were proposed to find the optimal path according to the prior information [2, 3], and the methods are not suitable for the emergency evacuation when the situations are significantly different from the prior information. Studies have shown that fire is the most frequent accident among the above emergencies [4–6], and it gets more attention from researchers since fire accidents frequently cause huge losses to mankind; then, this paper takes fire accident as an example to introduce the proposed algorithm principle. The evacuation environment includes route topology, exit location, evacuee size, and people distribution, and changes of each element bring different evacuation paths. Fire accidents often happen suddenly and unpredictably, and the static path planning algorithms have limited application in practice since the prior environment information is different from the real-time environment information during emergencies. According to the studies of some fire event cases [7–9], chaotic and untimely evacuation is the important reason for the high casualty rate. In crowded buildings such as shopping malls, supermarkets, and large cruise, people always move without any regular pattern, and it is necessary to search evacuation paths according to exit locations, real-time evacuee locations, and evacuee size [10, 11]. It is dangerous for evacuees to pass a passageway that is full of smoke, and the smoke spreading changes the route topology during the evacuation. The old path is not fit for the new situation when some passageways change, and it is a time-consuming process to find a new optimal path. In order to find the evacuation path in a short time, some methods [12] simplified the route topology to reduce the

computation time, and the incomplete dynamic route topology made the new path different from the shortest one. With the development of stochastic optimization, some intelligent algorithms such as ant colony algorithm [13–15], particle swarm algorithm [16–18], bee colony algorithm [19–21], and genetic algorithm [22] or greedy algorithm [23] were used to find the dynamic path. When route topography and constraints changed, intelligent algorithms took the old path as a feasible solution for dynamic path searching. Although intelligent algorithms are able to search for optimal solutions globally, they converge slowly when facing dynamic evacuation problems.

Recently, the dynamic evacuation problem has become a hot research topic, and many scholars try to get the shortest path according to dynamic situations. The authors in references [24–27] built the intelligent integrated fire rescue system which updated optimal paths by using the wireless sensor or vision camera to detect people locations. However, the wireless sensors and vision cameras are difficult to get accurate dynamic information about the people, and the online computation is also complex and time consuming. In order to get the shortest paths in a short time, basic and improved Dijkstra algorithms are the most popular methods used to search the optimal paths [28–30]. Beside the path length, safety is also important for people during the evacuation, and the authors references [31–33] took the safest and shortest paths as the cost function to search the optimal paths. Facing the dynamic situation, the authors in references [34–37] used dynamic planning to search for the optimal paths and informed everyone on the ship how to move toward the exit. Neural networks are good at learning the hidden knowledge from sample data, and the authors in [38–41] used neural networks to decide which paths are available for people to evacuate dynamically. Because the smog keeps spreading during the fire accident, feasible evacuation paths should consider the future changes of dangerous areas. The authors in [42–44] tried to predict the dangerous area and searched the optimal paths step by step, and the prediction performances influenced the effectiveness of the evacuation significantly.

Effective emergency evacuation paths are important for the safety of personal in accidents, and the basic requirement is that the commander gets the optimal paths to fit the dynamic changes in a short time. This paper proposes a dynamic path optimization method which includes offline search and online search. The offline optimization gets the prior evacuation network which includes evacuation paths from each node to the exit port, and the online optimization searches the local optimal paths based on the prior evacuation network when the accidents happen. The changes from accident locations, dangerous areas, and blocking paths call the online optimization algorithm to search the dynamic optimal paths. Online optimization quickly plans the evacuation paths to adapt the real-time situations.

This paper is organized as follows: Section 2 introduces the method of establishing the network topology of the building. Section 3 details the proposed dynamic optimization algorithm that uses offline optimization and online optimization to search the optimal evacuation paths. The simulation results and analysis are in Section 4. Section 5 summaries the conclusions.

2. Evacuation Environment Model

The emergency evacuation model mainly includes microscopic model and macroscopic model [45]. The microscopic model focuses on the study of individual behavior characteristics, and the path optimization algorithm simulates human individual behavior and mental activities to select evacuation paths. Typical microscopic models include the social force model, cellular automata model, and lattice gas model [46]. Because the microscopic model uses less overall information about the environment, it always gets local feasible paths and ignores the global optimal paths. The local feasible paths are able to guide people to move toward the exit, but it is different from the optimal solution that considers the evacuation time and personal safety during the evacuation process. In addition, the optimization algorithms based on the microscopic model converge slowly, and the online pathfinding requires fast convergence algorithms [47]. The macroscopic model pays attention to the people flow of each evacuation path at different moments based on global information. People move at different speeds when the density of people changes, and the move speeds are macroviews of individual behavior. The relationship between move speed and people density is summarized by the characteristics of individual movement and saved as a piecewise function. Since the optimization outputs based on the macroscopic model are global optimal solutions, the paths are more effective for emergency evacuation.

In the macroscopic model, paths and intersections of the building are regarded as the edges and nodes of a graph. The macroscopic model is a weighted graph as follows:

$$G = (V, E, W), \tag{1}$$

where V is the set of nodes, $V = \{v_i \mid i \in [1, n]\}$, in which n is the total number of the network nodes. E is the set of graph edges, $V = \{e_{ij} \mid i, j \in V\}$. W is the set of weights of each edge. Usually, corridors or stairways in a building are set as edges, and the endpoints of corridors are set as nodes, and the weight of each edge is the actual distance between the connected nodes. In the large-scale macroscopic model, optimization also requires complex computation due to a large number of nodes and edges.

This paper uses macroscopic modeling principles to establish the model of an underground shopping mall and related passage spaces. This shopping mall is the middle floor of a three-floor structure, the bottom floor is the subway station, and the top floor has several urban traffic roads. The macroscopic model represents the fire evacuation environment of the surrounding area, and its graph is shown in Figure 1. The model is a multioutlet network, where V is a set of ordinary nodes and $V = \{N_1, N_2, \ldots, N_{22}\}$ and O is a set of safe exit nodes and $O = \{O_1, O_2, O_3, O_4\}$. Each weight is the actual distance between adjacent nodes, and the weight values are shown in Table 1.

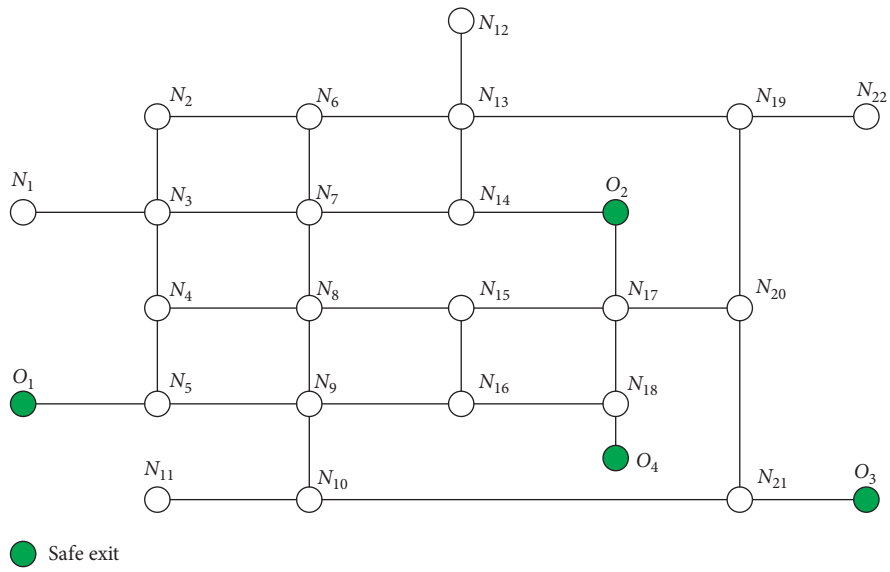

Figure 1: Network model of the underground shopping mall.

Table 1: The weight values between adjacent nodes.

Node number	Weight value (m)
1	$w_{1,3} = 32$
2	$w_{2,3} = 7$, $w_{2,6} = 11$
3	$w_{3,1} = 32$, $w_{3,2} = 7$, $w_{3,4} = 21$, $w_{3,7} = 5$
4	$w_{4,3} = 21$, $w_{4,5} = 13$, $w_{4,8} = 8$
5	$w_{5,4} = 13$, $w_{5,9} = 14$, $w_{5,O1} = 6$
6	$w_{6,2} = 11$, $w_{6,7} = 43$, $w_{6,13} = 64$
7	$w_{7,3} = 5$, $w_{7,6} = 43$, $w_{7,8} = 17$, $w_{7,14} = 11$
8	$w_{8,4} = 8$, $w_{8,7} = 17$, $w_{8,9} = 4$, $w_{8,15} = 11$
9	$w_{9,5} = 14$, $w_{9,8} = 4$, $w_{9,10} = 44$, $w_{9,16} = 5$
10	$w_{10,9} = 44$, $w_{10,11} = 8$, $w_{10,21} = 92$
11	$w_{11,10} = 8$
12	$w_{12,13} = 8$
13	$w_{13,6} = 64$, $w_{13,12} = 8$, $w_{13,14} = 51$, $w_{13,19} = 13$
14	$w_{14,7} = 11$, $w_{14,13} = 51$, $w_{14,O2} = 3$
15	$w_{15,8} = 11$, $w_{15,16} = 13$, $w_{15,17} = 41$
16	$w_{16,9} = 5$, $w_{16,15} = 13$, $w_{16,18} = 37$
17	$w_{17,15} = 41$, $w_{17,18} = 26$, $w_{17,20} = 81$, $w_{17,O2} = 14$
18	$w_{18,16} = 37$, $w_{18,17} = 26$, $w_{18,O4} = 99$
19	$w_{19,13} = 13$, $w_{19,20} = 52$, $w_{19,22} = 14$
20	$w_{20,17} = 81$, $w_{20,19} = 52$, $w_{20,21} = 34$
21	$w_{21,10} = 92$, $w_{21,20} = 34$, $w_{21,O3} = 12$
22	$w_{22,19} = 14$

3. Dynamic Path Optimization

The proposed dynamic path optimization includes offline optimization and online optimization. With prior information of the evacuation model shown in Figure 1, the offline optimization is used to search for the optimal paths that contain evacuation routes from each node to exit nodes. The online optimization dynamically searches the optimal paths when real-time information is different from the prior information. The online optimization searches the local areas and converges fast, and it gets new optimal paths that fit the real-time requirement in a short time.

3.1. Offline Prior Evacuation Path Network. Before the fire accident, it is necessary to get the shortest evacuation path from each node to each exit for the building. This search is an offline process that uses the Dijkstra algorithm to get the prior evacuation path network that stores the node number of each evacuation path. The Dijkstra algorithm is a typical algorithm for searching the shortest path between nodes in a graph, and it has been widely used to search for the shortest evacuation paths in fire incidents. The flow of the standard Dijkstra algorithm is shown as Algorithm 1. The operation $u \leftarrow vertex\ in\ Q\ with\ min\ dist\ [u]$ means the algorithm searches for the vertex u in the vertex set Q that has the least distance. Operation length(u, v) returns the length of the edge connecting two adjacent nodes u and v.

The variable *expand* is the length of the path from the source node to the node v via u. The principle used to determine whether the node v satisfies the slack condition is as follows:

$$d_{(u,v)} > d_{(u,q)} + d_{(q,v)}, \tag{2}$$

where $d_{(u,v)}$ is the distance between node u and node v. Equation (2) shows that the distance from node u to node v via node q is shorter than the old distance between node u and node v, and then the path $p(u, v)$ is updated as follows:

$$p(u, v) = \{u, q, v\}. \tag{3}$$

According to the Dijkstra algorithm, we get the evacuation path network of the building shown in Figure 1. The network includes the shortest path from each node to each exit. Since the network is too large to display, Table 2 describes the nodes from node 3 to the four exits and the paths are shown in different colors in Figure 2. If people are at node N_3, they will use the information shown in Table 2 to quickly escape to the safety exit, so this network is the prior information for the people to escape. When the fire environment is the same as the offline optimized hypothetical

```
create vertex set Q
for each vertex v in Graph:
   dist [v] ⟵ Infinity
   path [v] ⟵ Undefined
   add v to Q
dist [source] ⟵ 0
while Q is not empty:
   u ⟵ vertex in Q with min dist [u]
   remove u from Q
   for each neighbor v of u:
      expand ⟵ dist [u] + length (u, v)
      if expand < dist [v]:
         dist [v] ⟵ expand
         path [v] ⟵ u
return dist [], path []
```

Algorithm 1: Offline evacuation path optimization.

Table 2: Evacuation paths from node 3 to the exits.

Start node and exit node	Shortest path	Distance (m)
N_3-O_1	$\{N_3, N_4, N_5, O_1\}$	40
N_3-O_2	$\{N_3, N_7, N_{14}, O_2\}$	19
N_3-O_3	$\{N_3, N_7, N_{14}, O_2, N_{17}, N_{20}, N_{21}, O_3\}$	160
N_3-O_4	$\{N_3, N_7, N_{14}, O_2, N_{17}, N_{18}, O_4\}$	158

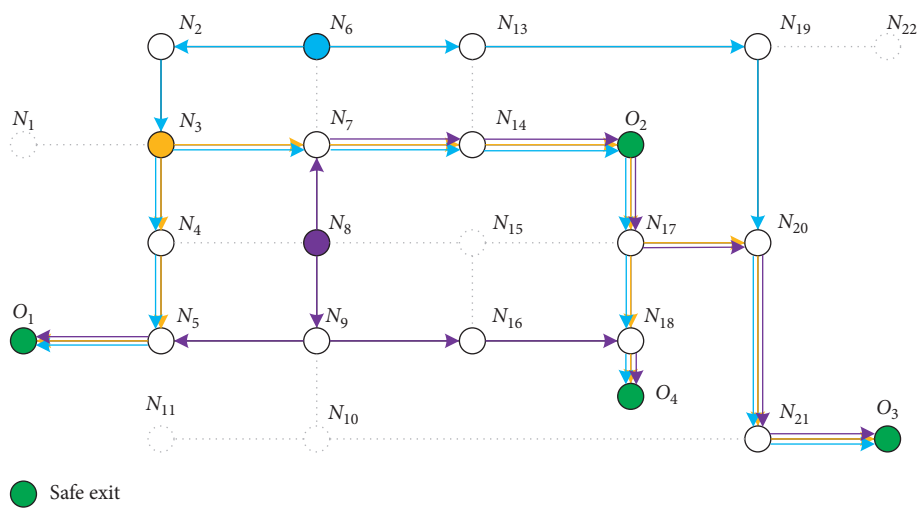

Figure 2: The paths from node 3 and node 8 to different exits in the prior evacuation network.

environment, people can move according to the prior evacuation network.

3.2. Online Local Path Optimization. The location and time of the fire are unpredictable; the distribution of people inside the building is also changing. The prior evacuation network needs to be modified when some edges are blocked or in a dangerous area. This modification only adjusts the nodes of the paths that are affected by the fire, and it is a local path optimization based on the prior evacuation network. Because the fire is changing during the evacuation, then the online local path optimization keeps searching for the new solutions. In the network graph model $G = (V, E, W)$, the evacuation path $p(i, j)$ from the start node i to the end node j is as follows:

$$p(i, j) = \{N_i, N_r, \ldots, N_s, N_j\}, \tag{4}$$

where N_i, N_r, N_s, and N_j are the node number. The total distance $\text{dist}\{p(i, j)\}$ of the evacuation path $p(i, j)$ is

$$\text{dist}\{p(i, j)\} = \sum_{t=i}^{j} w_{(t,t+1)}, \tag{5}$$

where $w_{(t,t+1)}$ is the actual distance between node t and node $t + 1$. The cost function of the dynamic optimization is to search for the paths that do not include the impassable

nodes. Suppose the real-time impassable nodes set is IV, then the online optimization problem is as follows:

$$\min \sum_{t=i}^{j} w_{(t,t+1)}, \quad t \in V,\ t \notin IV. \tag{6}$$

Equation (6) is a constraint optimization problem; the optimization result $p(i, j)$ only includes the safe and passable nodes. Suppose PNet is the prior evacuation path network, NBNode is the neighbor nodes of the impassable nodes in IV. The online optimization starts to search for the optimal paths when the PNet is not fit for the real-time situation, and the online optimization algorithm flow is shown as Algorithm 2.

This paper uses the online dynamic optimization algorithm to search for the real-time optimal paths for the graph in Figure 1. Suppose N_7 is in the fire area and the impassable node set $IV = \{N_7\}$. According to the dynamic optimization algorithm in Algorithm 2, the *S*Node stores the starting nodes of the prior paths that contains N_7, and the nodes of *S*Node are as follows:

$$\begin{aligned}
&S\text{Node}(1) = \{N_{12}, N_{13}, N_{14}, N_{17}, N_{19}, N_{20}, N_{22}\},\\
&S\text{Node}(2) = \{N_1, N_2, N_3, N_4, N_5, N_6, N_8, N_9, N_{10}, N_{11}, N_{15}, N_{16}\},\\
&S\text{Node}(3) = \{N_1, N_2, N_3, N_4, N_5, N_8, N_9, N_{10}, N_{11}\},\\
&S\text{Node}(4) = \{N_1, N_2, N_3, N_6\},
\end{aligned} \tag{7}$$

where *S*Node(i) contains the starting nodes of the prior paths that are from each node to O_i via N_7. Because the paths from the nodes in *S*Node to exits are impassable, then these paths are adjusted dynamically. N_3, N_6, N_8, and N_{14} are neighbor nodes of N_7; then, the nodes of NBNode are as follows:

$$\begin{aligned}
&\text{NBNode}(1) = \{N_{14}\},\\
&\text{NBNode}(2) = \{N_3, N_6, N_8\},\\
&\text{NBNode}(3) = \{N_3, N_8\},\\
&\text{NBNode}(4) = \{N_6\},
\end{aligned} \tag{8}$$

where NBNode(i) contains the neighbor nodes of N_7 in *S*Node$\{i\}$. Because the nodes of NBNode are around node N_7, the paths from these nodes to the exits help the people to avoid the impassable node N_7. We use the breadth-first search (BFS) algorithm to search for the optimal paths from the nodes of SNode to the exits. Since the paths from each node to the exits are stored in the prior evacuation network, the BFS gets the shortest path from a node when it visits the node. This prior evacuation path network reduces the search time significantly, and it only needs a little lookup time to get the path information when it visits a node. The BFS visits nodes of NBNode and checks whether the shortest paths contain impassable node. If path from node N_k to exit O_h does not contain the impassable node, then the new path from node N_i to exit O_h is updated as follows:

$$p(N_i, O_h) = p(N_i, N_k) + p(N_k, O_h), \tag{9}$$

where node $N_i \in$ *S*Node, $N_k \in$ NBNode, and O_h is the exit node. The paths from nodes of SNode to the exit nodes are updated according to equation (9) step by step. Although the new paths avoid impassable node, some paths are not the shortest, and it is necessary to fine-tune the suboptimal paths. Suppose DPNode is the set of the new dynamic paths, and one of the new paths is

$$p(N_i, O_h) = \{N_i, N_r, \ldots, N_k, N_t, \ldots, N_n, O_h\}, \tag{10}$$

where N_i, N_r, …, $N_n \notin IV$. Nodes around the node of $p(N_i, O_h)$ are used to check whether there is a much shorter path; if a node N_α around N_k satisfies the inequality as follows:

$$w(N_k, N_\alpha) + \text{dist}(N_\alpha, O_h) < w(N_k, N_t) + \text{dist}(N_t, O_h), \tag{11}$$

then the new shorter path is as follows:

$$p\prime(N_i, O_h) = p(N_i, N_\alpha) + p(N_\alpha, O_h). \tag{12}$$

The real-time information triggers the online dynamic optimization to search for the new shortest paths according to the above algorithm principle. In Figure 1, suppose node N_7 is in the fire area, there are 35 paths that contain N_7. Different paths are shown in Figure 3. Path_1 is the prior shortest evacuation path from node N_6 to exit O_2, Path_2 is a feasible path that avoids node N_7, and Path_3 is the final shortest path obtained by global search. It takes 11 ms to update the shortest paths from nodes in *S*Node to the exits.

4. Simulation Results and Analysis

The more nodes in the network model, the more time it takes to search for evacuation paths in real-time. This paper establishes a network model with 2000 nodes to compare the performances of the proposed dynamic optimization and the traditional Dijkstra algorithm. Suppose the set of safe exit nodes is $O = \{N_7, N_{77}, N_{777}\}$ and each node has two edges connecting to other nodes, the weight of each edge is randomly assigned a positive value between 0 and 100.

Let node N_{18} be in the fire area; both the proposed dynamic algorithm and the Dijkstra algorithm are used to search for the shortest paths from node N_{1225} to exit N_7 and N_{777}. The path optimization results are shown in Table 3. The M1 is the method that uses the Dijkstra algorithm to search for the shortest path offline. M2 and M3 are the methods that use the proposed dynamic algorithm and the Dijkstra algorithm to search for the shortest path according to the real-time information as node N_{18} is in the fire area. M2 and M3 are online searching that avoid passing through node N_{18}. The results show that the evacuation paths of the online searching algorithms are longer than those of the offline algorithm; this difference is due to the fact that the online search algorithms need to avoid node N_{18}. M2 gets the same path as M3 in online path searching, and it shows that the proposed dynamic algorithm has the ability to get the shortest path.

The node from N_1 to N_{200} is set as a fire point step by step, and the curve of the number of nodes in *S*Node is shown in Figure 4. Different nodes cause different sizes of *S*Node, and the online searching time is also shown in

```
for p in PNet
  for d in IV
    if path p contains node d
      SNode ⟵ the first node of path p
for N_i in NBNode
  p(N_i, O_h) is updated by the breadth-first search algorithm
for N_k in SNode
  update the path of DPNode as p(N_k, O_h) = p(N_k, N_i) + p(N_i, O_h)
for p in DPNode
  for N_r in path p
    p ⟵ check the nodes around N_r whether p is the shortest
return DPNode
```

Algorithm 2: Online dynamic path optimization.

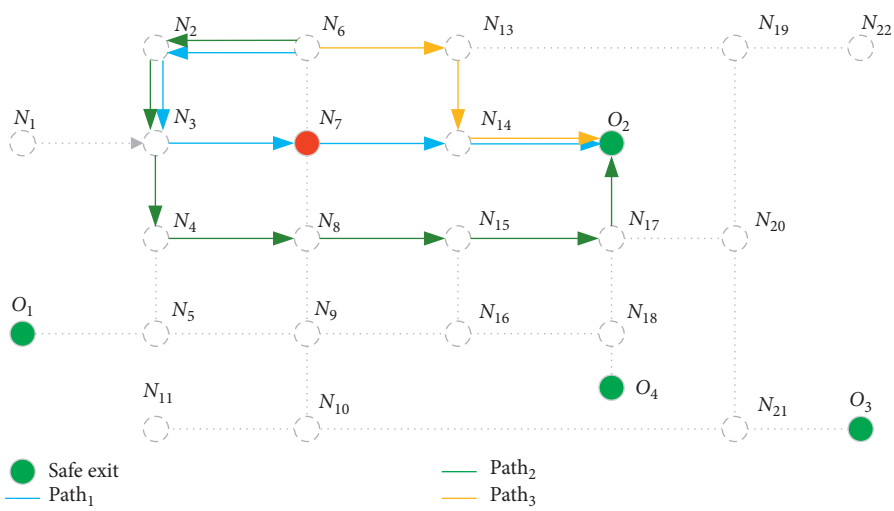

Figure 3: The paths from node N_6 to exit O_2 updated by the proposed dynamic algorithm.

Table 3: Evacuation paths of different algorithms.

Start-end	Method	Evacuation path	Distance
N_{1225}–N_7	M1	$\{N_{1225}, N_{564}, \mathbf{N}_{18}, N_{1587}, N_{113}, N_{1210}, N_{653}, N_{1030}, N_{334}, N_{1503}, N_{51}, N_{1289}, N_{1201}, N_7\}$	291
	M2	$\{N_{1225}, N_{1631}, N_{801}, N_{979}, N_{1668}, N_{1580}, N_{432}, N_{1218}, N_7\}\ N_{1218}, N_7\}$	324
	M3	$\{N_{1225}, N_{1631}, N_{801}, N_{979}, N_{1668}, N_{1580}, N_{432}, N_{1218}, N_7\}\ N_{1218}, N_7\}$	324
N_{1225}–N_{777}	M1	$\{N_{1225}, N_{564}, \mathbf{N}_{18}, N_{474}, N_{761}, N_{558}, N_{777}\}$	234
	M2	$\{N_{1225}, N_{564}, N_{1372}, N_{607}, N_{895}, N_{1938}, N_{197}, N_{777}\}$	279
	M3	$\{N_{1225}, N_{564}, N_{1372}, N_{607}, N_{895}, N_{1938}, N_{197}, N_{777}\}$	279

Figure 4. The curves in Figure 4 show that the online searching time is positively correlated with the size of SNode.

With the same nodes in SNode, this paper compares the online searching time of the proposed dynamic algorithm with that of the Dijkstra algorithm, and the results are shown in Figure 5. The comparison result shows that the proposed dynamic algorithm searches much faster than the Dijkstra algorithm all the time. The Dijkstra algorithm executes a global optimization when facing a new order to search for a path from the node in SNode to the exit; it takes a long time to find out the shortest path. The proposed dynamic algorithm takes advantage of the prior evacuation path and only visits the nodes around the fire area to get the local shortest paths. Because the proposed dynamic algorithm does not search each node of the model, it is more effective than the Dijkstra algorithm. Let t_p denote the online searching time of the proposed dynamic algorithm and t_d denote the online searching time of the Dijkstra algorithm; the ration of t_p to t_d is also shown in Figure 5. The maximum ratio is 0.92, and the minimum ratio is 0.02, and there are some ratios that have a

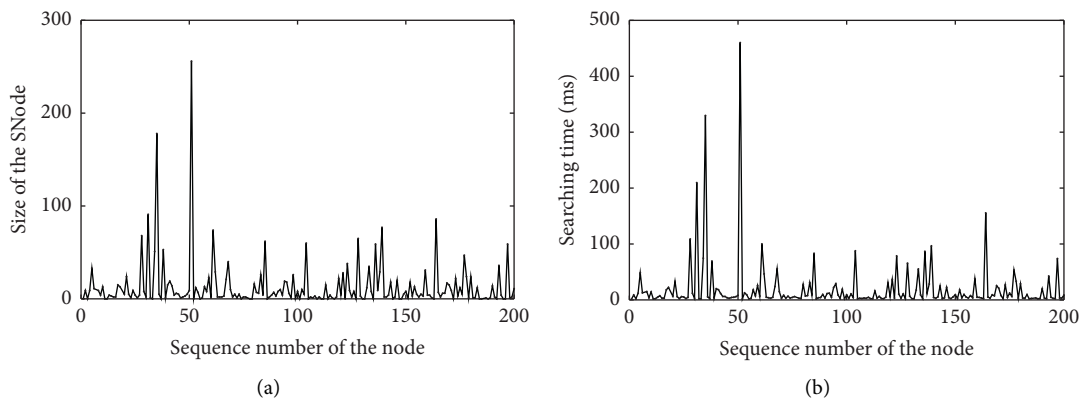

Figure 4: The performance of the proposed dynamic algorithm: (a) relationship between the size of SNode and node number; (b) relationship between the searching time and the node number.

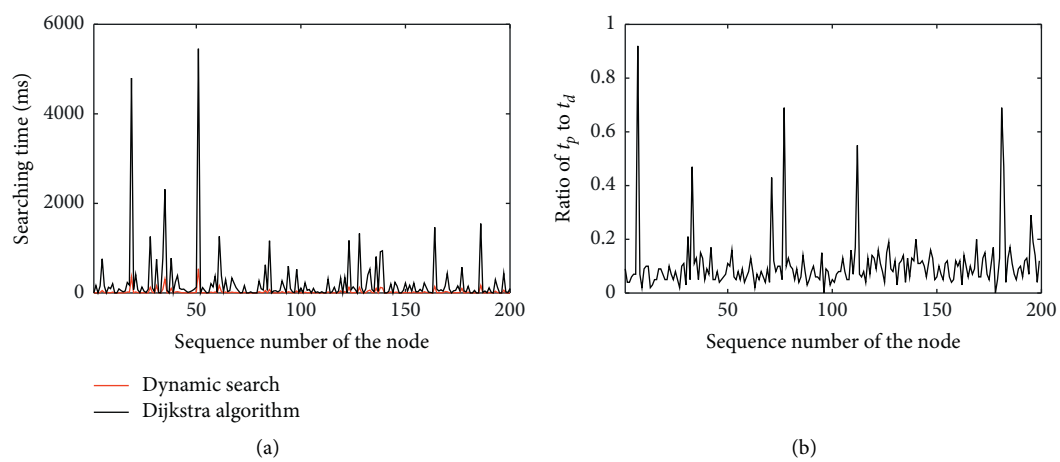

Figure 5: The performance comparison between the proposed dynamic algorithm and the Dijkstra algorithm: (a) comparison of the searching time; (b) ratio of t_p to t_d.

value of 0 since they have no node pass through the fire area. At node N_{51}, there are 256 paths that need to be modified and the ratio is 0.1. At node N_{35}, there are 178 paths that need to be modified and the ratio is 0.05. It is efficacious to use the proposed dynamic algorithm as there are many nodes in the *S*Node.

5. Conclusions

The prior evacuation paths are inefficient when the situations are different from the prospective environments. It takes a long time to search for the shortest paths from each node to the exits, and it is unsuitable for online searching. The proposed dynamic algorithm adjusts the prior paths that pass through the fire areas according to the situations. Because the proposed method takes advantages of the prior evacuation path network, it visits the nodes around the fire area to get the path information instead of searching each node of the model. It modifies the paths that pass through the fire areas in a short time, and each path is the shortest one from itself to the exit. The proposed dynamic algorithm is suitable for the online evacuation path optimization because of its fast convergence and global searching.

Data Availability

The data used to support the findings of this study are included within the article.

Conflicts of Interest

The authors declare that they have no conflicts of interest.

References

[1] S. Aalami and L. Kattan, "Fairness and efficiency in pedestrian emergency evacuation: modeling and simulation," *Safety Science*, vol. 121, pp. 373–384, 2020.

[2] T. Yamada, "A network flow approach to a city emergency evacuation planning," *International Journal of Systems Science*, vol. 27, no. 10, pp. 931–936, 1996.

[3] R. E. Meouche, M. Abunemeh, I. Hijaze, A. Mebarki, and I. Shahrour, "Developing optimal paths for evacuating risky

construction sites," *Journal of Construction Engineering and Management*, vol. 144, no. 2, Article ID 04017099, 2018.

[4] J. M. Czerniak, H. Zarzycki, Ł. Apiecionek, W. Palczewski, and P. Kardasz, "A cellular automata-based simulation tool for real fire accident prevention," *Mathematical Problems in Engineering*, vol. 2018, Article ID 3058241, 12 pages, 2018.

[5] H. Mi, Y. Liu, W. Wang, and G. Xiao, "An integrated method for fire risk assessment in residential buildings," *Mathematical Problems in Engineering*, vol. 2020, Article ID 9392467, 14 pages, 2020.

[6] I. Bakas, K. Georgiadis-Filikas, and K. J. Kontoleon, "Treasures gutted by fire. Fire safety design awareness as a consequence of historic building accidents and disasters," *IOP Conference Series. Earth and Environmental Science*, vol. 410, no. 1, Article ID 12113, 2020.

[7] Z. Dou, A. Mebarki, Y. Cheng et al., "Review on the emergency evacuation in chemicals-concentrated areas," *Journal of Loss Prevention in the Process Industries*, vol. 60, pp. 35–45, 2019.

[8] R. R. M. Gershon, "The world trade center evacuation study: factors associated with initiation and length of time for evacuation,," *Fire and Materials*, vol. 36, no. 5-6, pp. 481–500, 2012.

[9] C. Minji, "Effect of dynamic emergency cues on fire evacuation performance in public buildings," *Journal of Infrastructure Systems*, vol. 24, no. 4, 2018.

[10] P. Chen and F. Feng, "A fast flow control algorithm for real-time emergency evacuation in large indoor areas," *Fire Safety Journal*, vol. 44, no. 5, pp. 732–740, 2019.

[11] F. Mirahadi and B. Y. McCabe, "EvacuSafe: a real-time model for building evacuation based on Dijkstra's algorithm,," *Journal of Building Engineering*, vol. 34, Article ID 101687, 2020.

[12] W. Y. Lin and P. H. Lin, "Intelligent generation of indoor topology (i-GIT) for human indoor pathfinding based on IFC models and 3D GIS technology," *Automation in Construction*, vol. 94, pp. 340–359, 2018.

[13] M. Goodwin, O.-C. Granmo, and J. Radianti, "Escape planning in realistic fire scenarios with ant colony optimisation," *Applied Intelligence*, vol. 42, no. 1, pp. 24–35, 2015.

[14] Y. Zhao, H. Liu, and K. Gao, "An evacuation simulation method based on an improved artificial bee colony algorithm and a social force model," *Applied Intelligence*, vol. 51, no. 1, pp. 100–123, 2021.

[15] L. Liu, H. Zhang, J. Xie, and Q. Zhao, "Dynamic evacuation planning on cruise ships based on an improved ant colony system (IACS)," *Journal of Marine Science and Engineering*, vol. 9, no. 2, p. 220, 2021.

[16] F. Li, "Modelling multi-exit large-venue pedestrian evacuation with dual-strategy adaptive particle swarm optimization," *IEEE Access*, vol. 8, pp. 114554–114569, 2021.

[17] Y. Zhang, D. Zhang, and J. Jin, "Evacuation path optimization algorithm for inland river passenger ship in emergency situation," *Journal of Coastal Research*, vol. 83, p. 256, 2018.

[18] Y.-J. Zheng, H.-F. Ling, J.-Y. Xue, and S.-Y. Chen, "Population classification in fire evacuation: a multiobjective particle swarm optimization approach," *IEEE Transactions on Evolutionary Computation*, vol. 18, no. 1, pp. 70–81, 2014.

[19] N. Khamis, H. Selamat, F. S. Ismail, O. F. Lutfy, M. F. Haniff, and I. N. A. M. Nordin, "Optimized exit door locations for a safer emergency evacuation using crowd evacuation model and artificial bee colony optimization," *Chaos, Solitons & Fractals*, vol. 131, Article ID 109505, 2020.

[20] H. Liu, B. Xu, D. Lu, and G. Zhang, "A path planning approach for crowd evacuation in buildings based on improved artificial bee colony algorithm," *Applied Soft Computing*, vol. 68, pp. 360–376, 2018.

[21] C. Wang, L. C. Wood, H. Li, Z. Aw, and A. Keshavarzsaleh, "Applied artificial bee colony optimization algorithm in fire evacuation routing system," *Journal of Applied Mathematics*, vol. 2018, Article ID 7962952, 17 pages, 2018.

[22] L. Yapeng, C. Wei, and A. K. Austin, "Design of level of service on facilities for crowd evacuation using genetic algorithm optimization," *Safety Science*, vol. 120, pp. 237–247, 2019.

[23] Z. Yu, D. Li, S. Zhu, W. Luo, Y. Hu, and L. Yuan, "Multisource multisink optimal evacuation routing with dynamic network changes: a geometric algebra approach," *Mathematical Methods in the Applied Sciences*, vol. 41, no. 11, pp. 4179–4194, 2018.

[24] Y. Amirgaliyev, R. Yunussov, and O. Mamyrbayev, "Optimization of people evacuation plans on the basis of wireless sensor networks," *Open Engineering*, vol. 6, no. 1, pp. 206–213, 2016.

[25] R. Löhner, E. Haug, C. Zinggerling, and E. Oñate, "Real-time micro-modelling of city evacuations," *Computational Particle Mechanics*, vol. 5, no. 1, pp. 71–86, 2018.

[26] J.-S. Chou, M.-Y. Cheng, Y.-M. Hsieh, I.-T. Yang, and H.-T. Hsu, "Optimal path planning in real time for dynamic building fire rescue operations using wireless sensors and visual guidance," *Automation in Construction*, vol. 99, pp. 1–17, 2019.

[27] V. Karthik and S. Suja, "Optimized multiple existence for pedestrian evacuation using geographic map-based path discovery," *Cluster Computing*, vol. 22, no. S5, pp. 11227–11236, 2019.

[28] Sunita and D. Garg, "A retroactive approach for dynamic shortest path problem," *National Academy Science Letters*, vol. 42, no. 1, pp. 25–32, 2019.

[29] A. Sedeño-noda and M. Colebrook, "A biobjective Dijkstra algorithm," *European Journal of Operational Research*, vol. 276, no. 1, pp. 106–118, 2019.

[30] Sunita and D. Garg, "Dynamizing Dijkstra: a solution to dynamic shortest path problem through retroactive priority queue," *Journal of King Saud University—Computer and Information Sciences*, vol. 33, no. 3, pp. 364–373, 2021.

[31] M. Choi and S. Chi, "Optimal route selection model for fire evacuations based on hazard prediction data," *Simulation Modelling Practice and Theory*, vol. 94, pp. 321–333, 2019.

[32] A. Veeraswamy, E. R. Galea, L. Filippidis et al., "The simulation of urban-scale evacuation scenarios with application to the Swinley forest fire," *Safety Science*, vol. 102, pp. 178–193, 2018.

[33] Y. Kazuhiro, S. Yuusuke, and N. Shinnosuke, "Simulation of tunnel fire for evacuation safety assessment," *Safety*, vol. 4, no. 2, p. 12, 2018.

[34] X. Zhao, R. Lovreglio, and D. Nilsson, "Modelling and interpreting pre-evacuation decision-making using machine learning," *Automation in Construction*, vol. 113, Article ID 103140, 2020.

[35] Y. Ma, K. Liu, M. Chen et al., "ANT: deadline-aware adaptive emergency navigation strategy for dynamic hazardous ship evacuation with wireless sensor networks," *IEEE Access*, vol. 8, pp. 135758–135769, 2020.

[36] A. Darvishan and G. J. Lim, "Dynamic network flow optimization for real-time evacuation reroute planning under multiple road disruptions," *Reliability Engineering & System Safety*, vol. 214, Article ID 107644, 2021.

[37] D. Hartama, H. Mawengkang, M. Zarlis et al., "Evacuation planning for disaster management by using the relaxation based algorithm and route choice model," *IFIP Advances in Information and Communication Technology*, vol. 516, pp. 136–144, 2019.

[38] I. A. Ndiaye, E. Neron, and A. Jouglet, "Macroscopic evacuation plans for natural disasters," *OR Spectrum*, vol. 39, no. 1, pp. 231–272, 2017.

[39] Y. Peng, S.-W. Li, and Z.-Z. Hu, "A self-learning dynamic path planning method for evacuation in large public buildings based on neural networks," *Neurocomputing*, vol. 365, pp. 71–85, 2019.

[40] K. Tkachuk, X. Song, and I. Maltseva, "Application of artificial neural networks for agent-based simulation of emergency evacuation from buildings for various purpose," *IOP Conference Series, Materials Science and Engineering*, vol. 365, no. 4, Article ID 42064, 2018.

[41] S. M. Lo, M. Liu, P. H. Zhang, and R. K. K. Yuen, "An artificial neural-network based predictive model for pre-evacuation human response in domestic building fire," *Fire Technology*, vol. 45, no. 4, pp. 431–449, 2009.

[42] W. Liu, "A dynamic evacuation algorithm based on CCRP under fire conditions," *China Work Safety Science and Technology*, vol. 16, no. 5, pp. 32–37, 2020.

[43] J. Radianti, O.-C. Granmo, P. Sarshar, M. Goodwin, J. Dugdale, and J. J. Gonzalez, "A spatio-temporal probabilistic model of hazard- and crowd dynamics for evacuation planning in disasters," *Applied Intelligence*, vol. 42, no. 1, pp. 3–23, 2015.

[44] M. Saeed Osman and B. Ram, "Distributed scheduling approach for dynamic evacuation networks," *Mathematical and Computer Modelling of Dynamical Systems*, vol. 23, no. 6, pp. 554–569, 2017.

[45] T. N. Dhamala, U. Pyakurel, and S. Dempe, "A critical survey on the network optimization algorithms for evacuation planning problems," *International Journal of Operations Research*, vol. 15, no. 3, pp. 101–133, 2018.

[46] J. Qin, C. Liu, and Q. Huang, "Simulation on fire emergency evacuation in special subway station based on Pathfinder," *Case Studies in Thermal Engineering*, vol. 21, Article ID 100677, 2020.

[47] D. Yin, S. Wang, and Y. Ouyang, "ViCTS: a novel network partition algorithm for scalable agent-based modeling of mass evacuation," *Computers, Environment and Urban Systems*, vol. 80, Article ID 101452, 2020.

Hindawi
Mathematical Problems in Engineering
Volume 2021, Article ID 2882930, 11 pages
https://doi.org/10.1155/2021/2882930

Research Article

Reconstruction Rating Model of Sovereign Debt by Logical Analysis of Data

Elnaz Gholipour,[1] **Béla Vizvári**,[1] **and Zoltán Lakner**[2]

[1]*Department of Industrial Engineering, Eastern Mediterranean University, Famagusta, North Cyprus, Mersin 10, Turkey*
[2]*Department of Food Economics, Hungarian University of Agriculture and Life Sciences, Gödöllő, Hungary*

Correspondence should be addressed to Elnaz Gholipour; elnaz.gholipour@emu.edu.tr

Received 1 July 2021; Revised 16 July 2021; Accepted 24 July 2021; Published 2 August 2021

Academic Editor: Mohammad Yazdi

Sovereign debt ratings provided by rating agencies measure the solvency of a country, as gauged by a lender or an investor. It is an indication of the risk involved in investment and should be determined correctly and in a well-timed manner. The current system is lacking transparency of rating criteria and mechanism. The present study reconstructs sovereign debt ratings through logical analysis of data (LAD), which is based on the theory of Boolean functions. It organizes groups of countries according to 20 World Bank-defined variables for the period 2012–2015. The Fitch Rating Agency, one of the three big global rating agencies, is used as a case study. An approximate algorithm was crucial in exploring the rating method, in correcting the agency's errors, and in determining the estimated rating of otherwise unrated countries. The outcome was a decision tree for each year. Each country was assigned a rating. On average, the algorithm reached almost 98% matched ratings in the training set and was verified by 84% in the test set.

1. Introduction

The aim of the research reported in this paper was to understand sovereign debt rating procedure as rating affects the economies of countries and to develop a simple tool for determining the rating of the debts of sovereign countries. If a country is rated, then its rating can be obtained from the Internet. However, even in this case, it is possible that it is underrated or overrated. There are countries that are not rated at all. These countries need debts as well. An investor might be interested to the risk of borrowing money to such a country. In that case, a tool determining an approximate rating of the country can help in the decision. It is obvious that a tool that can be used by all investors cannot be complicated. For example, the journal *World Bank Research Observer* claims from the authors that "*No equations, or if they have to be used, they should be comprehensible at about the seventh-grade level*" [1]. The tool which has been developed is a simple decision tree, which satisfies this requirement. The method that is used to obtain the decision tree is logical analysis of data (LAD).

1.1. Sovereign Credit Ratings (SCRs). Sovereign credit ratings (SCRs) refer to a country's capability to repay the money that it has borrowed. Therefore, sovereign debt rating can be a metric to help potential investors, financial organizations, banks, and even other governments when making investment or making lending decisions regarding a particular country. Sovereign debt rating reflects the risk involved in doing so. Generally, governments look for credit ranking to simplify their access to international capital markets, where investors desire to pick rating securities over unrated ones even with the same credit risk [2]. With an SCR, the government is less reliant on the banks' monetary policy, and it can join international markets. Moreover, SCR can lead to financial improvement by drawing in foreign investors [3].

SCRs play an important role in the credit rating industry [4]. They can decrease the asymmetric information between investors and borrowers to increase the borrower's willingness to access funds and lessen the credit risk from the lender`s point of view [5]. The rating class of Fitch Agency, as one of the CRAs, has been shown in Table 1.

Table 1: Fitch ranking system and descriptions (source: [6]).

#	Description	Fitch rating scale
1	(Highest rank): the safest, least risky investments	AAA
2	(Above average): safer and less risky	AAP
3		AA
4		AAM
5	(Average): average risk and safety	AP
6		A
7		AM
8	(Slightly below average): slightly risky and less safe	BBBP
9		BBB
10		BBBM
11	(Well below average): riskier and less safe	BBP
12		BB
13		BBM
14	(Lowest): the riskiest and least safe	BP
15		B
16		BM

This process is carried out by credit rating agencies (CRAs) to reduce the information gap between lenders and borrowers. An SCR is supposed to reflect a country's financial, economic, and political position [7]. In particular, since economic and political factors are taken into account by SCRs, it is not easy to measure qualitative variables in the rating procedure in terms of predicting sovereign ratings. Because governments may renege on their obligations or become less financially solvent due to a political decision, the inclusion of qualitative measures in the rating process is difficult. This is why CRAs give their opinions on the creditworthiness of the country and not an investment advice or assessments for obligation [8]. This fact was proved by Ferri et al. [9], who noted that CRAs were not able to foresee the East Asia crisis of 1999, and this influenced them to become sufficiently conservative to downgrade high-risk countries. Fund [10] explained the importance of political and economic factors in SCRs. From a different point of view, "conflicts of interest" has been used to justify the failures of CRAs [11]. Arguments among experts are abound in concerning the effectiveness of these variables on SCRs.

1.2. Credit Rating Agencies and Significant Factors. Documented proof is available of how credit rating agencies' shortcomings contributed to the 2008 financial crisis—when they overrated and underrated some countries—and how they can take down governments and blow up capital markets [12]. At the time in question, they appeared to publish their SCRs in the manner of a black box, while hiding important issues from investors [4]. In the present study, the Fitch agency's rating system has been chosen for analysis. There are a number of financial, political, and social variables that could have been studied when exploring its rating model. Research on the significant variables of CRAs is used as input, along with the corresponding data from the World Bank, so that the Fitch rating method—otherwise concealed—can be illuminated. Cantor and Packer [2] were the first researchers in SCR to observe that items such as GDP per capita, GDP growth, inflation, external debt, and default history are important variables. Many other papers have used the same variables while adding new ones. A number of variables being taken into account by different investigators time after time are unemployment, government debt, foreign reserves, fiscal balance, economic development, political stability, mobile phones, real interest rate, total debt, real exchange rate, and unit labor costs [8, 13, 14]. Spilioti and Vamvoukas [15] prove that there is a positive correlation on government debt and economic growth. Alexe et al. [16] proposed a model for the Standard and Poor agency's rating system by selecting certain economic-financial and political parameters and by using multiple regression. In another study, fiscal uncertainty as a single determinant was used to explain the reason for changes in sovereign ratings during the financial crisis [17]. The application of the results of previous research requires expertise in statistics and is therefore not easy for noneconomists.

Gültekin-Karakaş et al. [4] claimed that high-income countries tend to receive higher ratings than low-income ones. GDP per capita was an essential variable for the high-income countries' rating evaluation. Unlikely, regression analysis has been applied in some previous investigations [4, 8, 13]. Routinely, the regression models that were employed involved different significant indicators that needed to have coefficients as a certain weight of the related variable to give a country's rating. Therefore, the users of these methods would most probably have had a certain expertise. The present study introduces a different way by the application of LAD for the approximation of the credit rating of countries, which is understandable and applicable for every user, and it makes our technique distinctive and untried.

The SCR process is still not understood completely. There are several recent papers connecting SCR with other factors. Bouri et al. [18] investigate the oil production of BRICS countries (Brazil, Russia, India, China, and South Africa) to their ratings. Bouri et al. [19] also connect oil production and sovereign ratings in general. They also logically analyze the relation of ratings with financial factors. Amstad et al. [20] analyze the effect of the exchange rates. Agiakloglou and Deligiannakis [21] investigate the effect of credit default swaps in eight important countries of European Union. Volz et al. [22] even connect the rating of sovereign debts and climate change.

1.3. Logical Analysis of Data. Logical analysis of data (LAD) is a way of studying datasets consisting of two classes. Generally, LAD classifies the outputs into two categories as true-false, positive-negative, yes-no, or 1-0 to explore the hidden classification processes. LAD consists of several main steps. First, a set of patterns is generated, and each pattern covers a subset of the desired observations. Mainly, the number of patterns is substantial. As a second main step, a small subset of the patterns is selected such that the target subset of the observations is covered in an accurate way. This

subset of the selected patterns gives a disjunctive normal form in the sense of mathematical logic. There are different methods for the way of selection; thus, LAD has many approaches [23]. Besides, Hammer and Bonates[24] analyzed the application of LAD to medical problems, including the evolution of diagnostic and prognostic systems in cancer investigation. Mirzaei [25] applied the LAD approach to a one-year series of Moody's ratings. Hammer et al. [26] and Hammer et al. [27] also analyzed sovereign debt rating by LAD with quite different approaches. There are also cases in natural sciences such that more than two classes must be distinguished [28]. LAD has been applied in several areas recently. Many engineering and medical applications are surveyed in [29]. Das et al. [30] detect cyber-attacks against large system such as power grid and water treatment plant. Another application in fault detection is discussed in Ragab et al. [31]. Jocelyna et al. [32] use LAD for the prevention of accidents caused by belt conveyors. LAD also has applications in computer science [33, 34]. Leujune et al. [29] and Ouyang & Chou [35] also report recent developments in the theory of LAD.

To sum up, previous studies have revealed drawbacks and advantages in the application of this methodology to CRA policies. The most valuable contribution of the present study is that it offers instructions to all users who wish to rank countries, without them having to possess any special mathematical, financial, or political knowledge. The user must compare only the values of some significant variables of a country to some fixed values determined *a priori* by LAD to learn if the country in question has a certain rating. The rating classes are organized into a binary *decision tree* according to their strength as it is shown in Figure 1. This type of decision tree has no stochastic component.

A decision tree is a rooted directed graph in which every nonleaf vertex has two outgoing arcs and the leaf vertices are assigned to either 0 or 1. This well-known structure is applied for instance in [29]. In the case of the current study, each leaf represents a different credit rating class of the countries. The decision procedure by using the decision tree is as follows: starting from the root, a top-down approach is made in the tree. The procedure arrives in a leaf, i.e., the rating class of the country is identified as the rating class represented by the leaf, if the attributes of the country satisfy the constraints determined by LAD for that rating class (Figure 1).

Incidentally, decision trees can be successful and competitive with other classifications models [36].

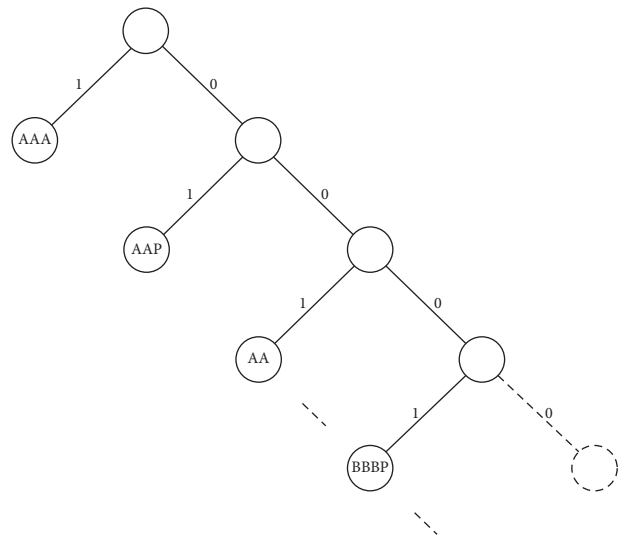

Figure 1: The decision tree of the ratings.

2. Material and Methods

The present study examined the Fitch agency rating system to reconstruct a rating model of sovereign debt with LAD, a classifying methodology based on optimization and Boolean logic. It uses binary data (i.e., 0 and 1) [37].

2.1. Logical Analysis of Data (LAD). LAD was initiated by Peter L. Hammer. He demonstrated that the LAD classification system produces accurate, transparent, and generalizable results [38]. There is a set of objects that are similar to each other and are described by the same set of attributes. The objects can be very different according to the area of application, for example, patients in a hospital, customers who obtain a loan from a bank, or drilling locations in the oil industry. However, the nature of the objects is the same in an application. The objects are divided into two parts, for instance, patients who have a particular disease and those who do not. LAD is a method that creates a description for each of the two parts. It is a machine learning method with supervisor as the objects in the database are classified *a priori*. The descriptions of the two classes generated by LAD can be applied to new objects. It is supposed that all attributes of the objects are Boolean variables, that is, the value of each attribute is either true or false. If the values must be expressed numerically, then 1stands for true and 0 stands for false. It is also assumed that there is no contradiction in the database, i.e., there is no pair of objects such that the two objects have the same values in all attributes but belong to the two aforementioned different subsets of objects. The number of different objects is at most 2^n, where n is the number of the binary attributes. However, even in the case when n has a moderate value such as 15 to 20, it is unlikely that all possible observations will have occurred. LAD aims to forecast which new (i.e., until now nonoccurring) observation belongs to which subset.

The database can be considered as the description of an incomplete Boolean function of n Boolean variables. The function is incomplete because its value is not known for all possible values of the attributes (variables), just for the observed values. What LAD must do is to find a complete Boolean function such that its value is the same as the value of the incomplete Boolean function. The database of the training set must contain a complete classification, that is, each object must be classified as either 1 or 0. LAD can describe any of the two subsets. The synonyms of class 1 and 0 are positive and negative, respectively. Numerical data can be approximated by Boolean attributes as it is illustrated in the example of the BBBM or better ratings as it is discussed later.

The countries are described by economic data that are numeric and not Boolean. These data are transformed in the example to Boolean ones. For example, let us consider that GDP per capita is at least $5,436, and this divides countries into two classes. For some, the GDP per capita is $5,436 and above, and it is less in case of other countries. A Boolean variable is then introduced. If the condition is satisfied, that is, GDP per capita is at least $5,436, then it is *true*—otherwise *false* value is obtained. It is possible to divide the countries into two groups by using the same economic variable in a different way. GDP per capita is used a second time in the example below, where it is at least $14,189. Again, if the condition is satisfied, then it is *true*—otherwise *false* value is obtained. The transformation of numerical data to Boolean variables is discussed in Section 2.3.

If a country had a BBBM rating or higher in 2012, then it could be checked in three different ways. If any of the three groups gave a positive result, then the country belonged to that category. If none of the three options were satisfied, then its rating was BBP or worse.

First group: the GDP per capita of the country is at least $5,436 AND the export of goods and services is at least 38.185 percentage of GDP AND the PPP conversion factor is at most 6.075%.

Second group: the net cash surplus/deficit is at least -5.88 percentage of GDP, that is, the deficit is not too high, AND the total reserves are at least $17,824,012,000 AND the inflation rate of consumer prices is at most 9.165%.

Third group: the expenses are not greater than $53.195 AND the male unemployment rate is at least 8.5% (where the proportion of male labor force is modelled on ILO estimates) AND the GDP per capita is at least $14,189.

To have a rating BBBM or better, a country must satisfy *all* conditions for at least one of the three groups. It is not enough that it satisfies some conditions for every group. Assume, for example, that the GDP of a country called *Nowhere* is $8,000. The GDP per capita occurs twice, that is, in the 1st and 3rd groups. Nowhere satisfies the GDP constraint of the 1st group, but violates the similar constraints of the 3rd group, that is, overall. Therefore, if its exports are great enough and its PPP conversion factor is low enough, it still can be a BBBM country because it satisfies the criteria of the first group.

2.2. The Original Concept of LAD. The original concept of LAD is based on mathematical logic and Boolean variables. One basic theorem of mathematical logic is that every Boolean function can be obtained as a disjunctive normal form (DNF). The three groups of Section 2.1 cover all the countries that have the BBBM or better ratings. This is an example of a DNF. The three ways consist of conjunctions of Boolean variables. Each of these conjunctions of (perhaps several) Boolean variables is called *patterns* in the context of LAD. The general form of the DNF is that there are several subsets of statements. The Boolean function (DNF) is true if and only if all statements of at least one subset are true. One statement or its opposite can be a part of several subsets. The subsets of statements may have a different number of elements. It is just by chance that each group in the example has three statements.

2.3. Transformation of Numerical Values to Boolean Attributes. Most real-life problems have numerical attributes, not Boolean ones. LAD is applicable only if the numerical data are "translated" into Boolean attributes. The example of the BBBM or better rating shows how this can be done. Each statement in the example has a numerical value that separates the countries. These numerical values are always between a BBBM or a better country and a country with a lower rating for instance, the two countries are closest with a GDP of $5,436 per capita; Azerbaijan belonged to the BBBM class in 2012, with a GDP per capita of $7,189. Meanwhile, Guatemala had a lower GDP per capita ($3,166) and was in the BBP class. The statement that the country *Nowhere* has a GDP greater than $5,436 has a Boolean value, i.e., it is either *true* or *false*. The name of any country can be substituted for *Nowhere* in this statement because every country has a Boolean value in this respect. LAD constructs the DNF from these Boolean attributes. The separating values are called cut-points. Thus, $5,436 is a cut-point in the example above.

Mathematically, binarization can be achieved by introducing cut-points for each of the numerical variables in such a way that the resulting partitioning of the space should consist only of "pure intervals," that is, intervals that do not contain both positive and negative points (see the different color points in Figure 2). Minimizing sets of cut-points with corresponding variables was the optimization element of the present study. We explored and described the rating categories of the Fitch rating system by the minimum number of patterns for each year. Figure 2 visualizes the iterative procedure of generating decision trees by logical analysis of data. The countries of the rating category of the iteration and the countries of the better rating classes are assigned to LAD class 1. Any other country is assigned to LAD class 0 like in Figure 2(a). The LAD classes of the countries of the next rating category are changed from 0 to 1 in the next iteration. To go through all predefined rating categories, the countries are moved to LAD class 1 gradually except for rating category BM (Figures 2(b) and 2(c)). At the end, there may be regions such that countries in the region are not classified by LAD (Figure 2(d)). The iterative procedure starts with rating category AAA by Fitch rating agency. These countries are always in LAD class 1. In the first step of the algorithm, these AAA countries are separated from the other countries. Separation means the determination of groups like in the example of Section 2.1, which exactly cover the AAA countries. If a country is classified as AAA country in the first step, then this classification is never modified. In the second step, AAA and AAP countries are separated from the countries, which have rating AA or worse. The logic of the description of AAP countries is as follows: if a country is separated, and it is not an AAA country, then it is classified as an AAP country. AAA, AAP, and AA countries are separated from other countries in the third step, etc. The steps of the algorithm are represented in Figures 3 and 4.

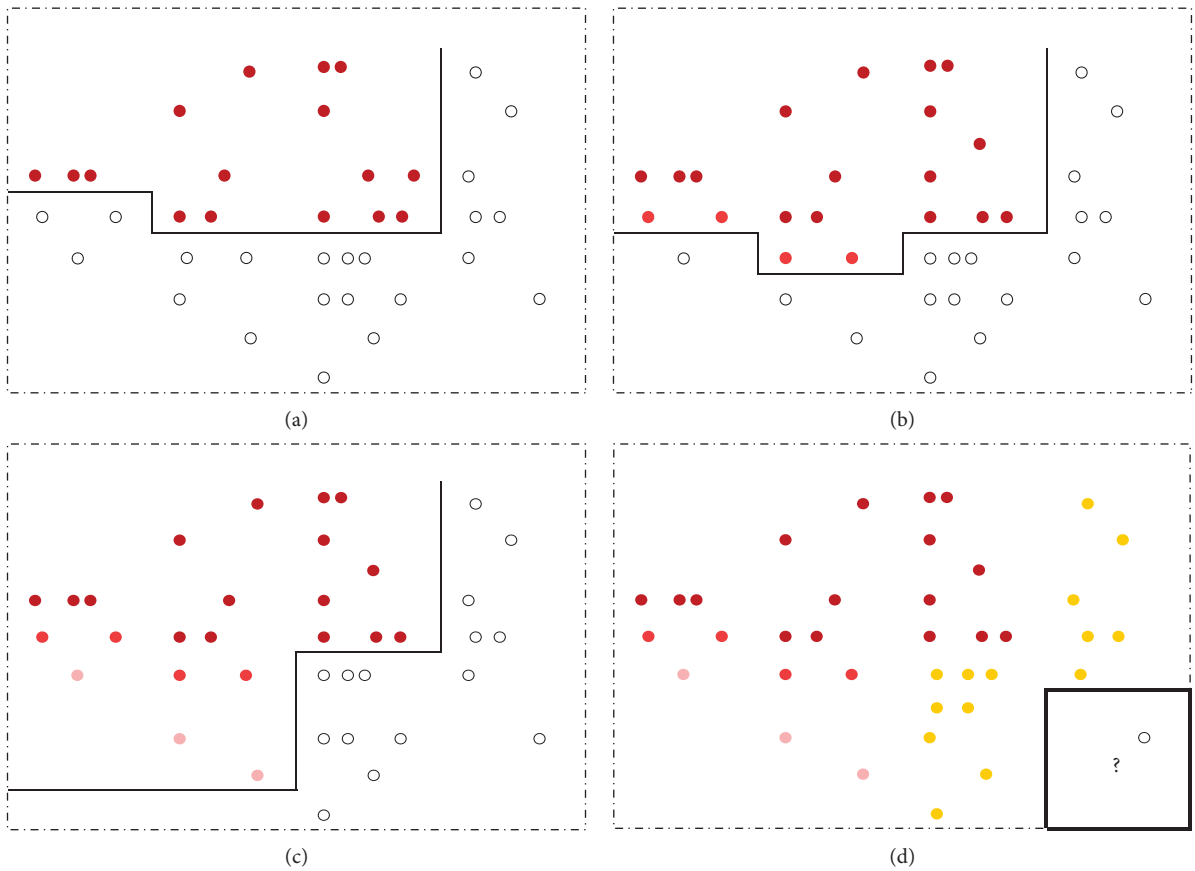

Figure 2: Selected cases as an output of LAD for each rating class.

```
For r: = AAA to BM do
  Begin Create Positive class P: = {c ϵ Countries, Rank c ≥ r}
        Create Negative class N: = {c ϵ Countries, Rank c < r}
        Apply LAD to (P, N)
        Add theory of P to the decision tree
  End
```

Figure 3: The algorithm of rating.

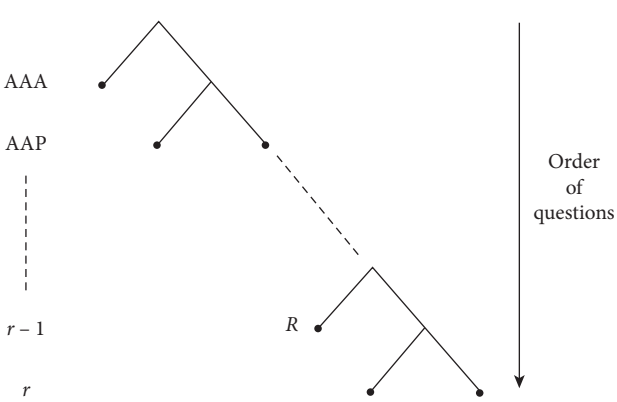

Figure 4: Order of the questions.

R is the position of theory of rating class r in the decision tree.

3. Results

3.1. How to Apply LAD to Sovereign Credit Rating? LAD was designed to separate two classes from one another. Sovereign rating has many classes. These classes are ordered according to the risk represented by the countries of the classes. Thus, it is possible to decompose the multiclass rating into a sequence of binary classifications. Countries representing a certain level of risk consist of one class and all other countries with a higher risk are in the other. For example, countries with a rating from AAA to AAM are in the first class and countries having AP or lower are in the second. Every such separation creates a problem for LAD. The DNFs provided by LAD form a decision tree. If a country satisfies the DNF separating AAA countries from other countries, then it is an AAA country. Otherwise, if it satisfies the DNF separating AAA and AAP countries from the others, then it is an AAP country.

3.2. Parameters Used in LAD Calculation. To apply LAD, we made a number of assumptions. The extent of a pattern is the number of Boolean variables in a conjunction. The

prevalence of a positive (negative) pattern is the ratio of positive (negative) observations covered by the pattern to the number of all positive (negative) observations in the dataset. The homogeneity of a positive (negative) pattern is the percentage of the positive (negative) observations covered by the pattern to the number of all observations covered by it. Every database may require a different value for the LAD parameters. The highest permitted degree for a pattern was 3. It means that a pattern may have three conditions only and not more. The prevalence was at least 70%. The homogeneity was claimed to be 100%. The decision trees for four years from 2012 to 2015 are shown in Tables 2–5. The abbreviations of the selected variables that are used in the tables are listed in Table 6.

The dataset of 116 countries contains populations of more than half a million in the form of two sets, namely, training and test: 68 ± 2 and 48 ± 2 countries, respectively. These are gathered from World Bank data covering the period 2012–2015. Countries with very small populations were excluded, as they have a special risk. This fact has been proven by Iceland, which experienced an extreme financial crisis in 2008. The Fitch ratings are listed in Table 1. There are further scales for risky countries. However, the occurrence of these scales is so rare that they are omitted from the calculation.

The following decision trees indicate the prediction of the rating for each country in the set.

3.3. Decision Trees. The decision trees obtained from the multiple applications of LAD are summarized in Table 2–5. These tables contain the basic logical rules in Boolean form.

The use of decision tree is simple. Only the values of the attributes of the country in question must be available. The user must only compare these values with the values of the cut-points given in the table.

3.4. Key Variables of the Decision Trees. The four decision trees share certain properties. The most important attributes are listed in Table 7.

The GDP per capita was an essential factor in all rating classes except the lowest. For ratings from AAA to AAM, there was no pattern without it. GDP occurs from AP to AM in more than 50% of the patterns. In addition to GDP, total reserves, gross savings, and inflation are the dominant variables in the classification of countries with BBB and BB rating levels. In the lowest rating class, that is, B, *male unemployment rate* and *industry value added* are the major variables.

4. Discussion

It can be seen from Tables 2–5 that LAD gives simple formulas for the classification that can be interpreted easily. The decision trees make it possible to predict an approximate rate to rank countries that are not rated by Fitch; then any user can do this prediction.

4.1. Fitch Rating Predictions. The dataset of the study was divided into two subsets, namely, training and test sets. These included 67 and 45 countries, respectively. The decision trees are estimated for the whole years as well as separately for the two subsets. In our result, the explored patterns in the form of the decision trees could predict the same credit ratings of the countries by high percentage as Fitch has reported. We obtained 93%, 89%, 91.5%, and 90.5% identical ratings with Fitch agency's country ratings for each of the four years. The high accuracy confirms the value of prognosis and robustness of the LAD rating system. On average, we matched the Fitch rating results in the training set by 98% and in the test set by 84%. The mismatched ratings according to country and the corresponding ratings are shown in Tables 8–11.

The year 2012 showed a ratio of matched consequences of 100% for the training set and 85.7% for the test set.

The year 2013 showed a ratio of matched consequences of 98.5% for the training set and 78% for the test set. The different output of the two sets is shown in Table 9.

For the year 2014, the ratio of matched outcomes for training and test sets is 98.5% and 85%. The different output of the two sets is shown in Table 10.

For the year 2015, the ratio of the matched result of training and test sets is 94% and 87%. The differences in rating of the two sets are shown in Tables 10 and 11.

First, the high proportions of matched ratings with the Fitch rating system show that our LAD methodology was successful. Second, in the majority of the misclassified cases through the years, Fitch has showed a bias towards downgrading rather than upgrading the countries, as it has already been proven by previous studies on CRAs. The incentive for being conservative is that it may deflect criticism, especially in periods of economic and financial crisis. Using our methodology, downgrading outnumbered upgrading considerably −75.8%, compared with 24.2% in mismatched cases. Fitch had misrated several countries twice or more than twice in the four years (Table 12).

As can be seen, seven countries were misrated at least twice. The Democratic Republic of Congo, which is rich in minerals, is the main producer of cobalt in the world. There were several military conflicts in the area, and thus, the situation was uncertain. Cyprus became a divided country after the events of 1974. No solution has been found yet. The country was also affected by the Greek financial crisis. Iceland was the first victim of the 2008–2009 economic crisis. Its population is less than 400,000. Therefore, its currency has also a small total value, which was considered by investors to be a source of instability. The Namibian economy is tied to the strong economy of South Africa. Fitch considers Namibia stronger than is merited by its attributes. Portugal is a European Union country in the Mediterranean region. As with other similar countries, it suffered a great deal after the 2008–2009 crisis and accumulated high debts. Rwanda is a neighbor of the Democratic Republic of Congo. Genocide was committed to the country's Tutsi minority in 1994, and the region as a whole remains unstable. Ukraine was another of the countries that were hit by the financial crisis in 2008–2009. It is also unstable politically. It has

Table 2: Decision tree of the year 2012.

Rating class	Year 2012 Decision tree
AAA	(U ≥ 73.715, G ≥ 52456.10), OR (U ≤ 90.02, C ≥ −9.54, G ≥ 40460.80)
AAP	(UN ≤ 3.60, GS ≥ 26.17.5, G ≥ 34424.90), OR (C ≥ −9.54, U ≤ 90.02, G ≥ 40460.80)
AA	(G ≥ 34424.90, CG ≤ 107.355)
AAM	(G ≥ 34424.90, CG ≤ 107.355), OR (GS ≥ 25.435, U ≥ 73.715, G ≥ 22801.90)
AP	(GS ≥ 23.5438, U ≥ 65.98, G ≥ 22293.20), OR (GS ≥ 12.64, U ≥ 73.03, G ≥ 34424.90), OR (GG ≥ 1.285, PA ≤ 16.985, G ≥ 16463.90), OR (SD ≤ 26.6415, PA ≥ 15.88, PA ≤ 18.755)
A	(GS ≥ 12.83, U ≥ 84.915, G ≥ 22293.20), OR (CG ≤ 99.96, I ≥ −0.32, G ≥ 16463.90), OR (PG ≥ 0.35, GS ≥ 22.085, PA ≤ 19.7.5)
AM	(GG ≥ −1.37, CG ≤ 109.17, G ≥ 16463.90), OR (CG ≤ 99.96, E ≥ 29.4973, U ≥ 73.03), OR (CG ≥ 42.545, UN ≤ 0.91, PA ≤ 17.785)
BBBP	GS ≥ 12.83, GG ≥ −1.37, G ≥ 15008.10), OR (I ≤ 5.60, R ≥ 26351500000, PPP ≤ 6.075), OR (GS ≥ 21.18, G ≥ 25449.20, U ≥ 74.11)
BBB	(EX ≥ 39.785, CG ≤ 54.94, G ≥ 8405), OR (GG ≤ 7.92, GS ≥ 12.83, G ≥ 15008.10), OR (GS ≥ 14.58, E ≥ 16.33, R ≥ 49114000000), OR (M ≥ 91.745, PPP6≤116.135, R ≥ 48396000000)
BBBM	(G ≥ 5435.98, EX ≥ 38.185, PPP ≤ 6.075), OR (C ≥ −5.88, R ≥ 17824000000, I ≤ 9.165), OR (E ≤ 53.195, UN ≤ 8.5, G ≥ 14189.30)
BBP	(R ≥ 47951500000, G ≥ 1357.30), OR (EX ≥ 30.42, GG ≤ 4.36, SD ≥ 8.625), OR (IV ≥ 19.845, R ≥ 3462500000, I ≤ 6.45), OR (PA ≤ 30.175, I ≤ 6.68, GS ≥ 14.04), OR (IV ≥ 21, M ≥ 106.835, G ≥ 13587.10)
BB	C ≥ −5.75, R ≥ 3462500000, I ≤ 9.165), OR (GS ≥ 14.715, M ≥ 96, G ≥ 13587.10), OR (GS ≥ 16.51, IV ≤ 31.075, M ≥ 96), OR (I ≤ 6.68, IV ≥ 19.555, PA ≤ 30.175)
BBM	(SD ≤ 23.1219, C ≥ 37.075), OR (GS ≥ 16.925, GG ≤ 4.125, GS ≤ 30.36), OR (IV ≥ 21.655, GG ≤ 5.035, IM ≥ 26.645), OR (I ≤ 9.165, IV ≥ 21.095, R ≥ 3462500000), OR (IV ≥ 21.655, PG ≤ 1.03, PA ≥ 14.14), OR (PA ≤ 30.175, I ≤ 7.905, GS ≥ 13.505)
BP	(EX ≥ 31.19, PG ≥ 0.175, RE ≥ 26.4706), OR (GG ≤ 5.675, GS ≥ 9.27, SD ≥ 10.075), OR (EX ≥ 23.73, GS ≥ 15.78, UN ≥ 0.325), OR (IV ≥ 21.655, PA ≤ 30.175, M ≤ 121.28))
B	(E ≤ 53.195, SD ≤ 23.1219), OR (GS ≥ 9.27, PPP ≥ 0.705), OR (GS ≥ 9.27, UN ≥ 0.325)
BM	(E ≤ 53.195)

Table 3: Decision tree of the year 2013.

Rating Class	Year 2013 Decision tree
AAA	(G ≥ 47058.30, PA ≤ 19.40), OR (G ≥ 42861.50, EX ≤ 68.985, GS ≥ 24.62)
AAP	(G ≥ 35760.90, CG ≤ 102.88, GG ≤ 1.515), OR (U ≥ 78.615, M ≥ 122.63, R ≥ 1443740000000)
AA	(CG ≤ 118.525, PPP ≤ 10.545, G ≥ 35760.90), OR (G ≥ 45717.70, U ≤ 90.575, CG ≤ 118.52)
AAM	(PA ≤ 20.81, CG ≤ 118.52, G ≥ 23758.60), OR (G ≥ 23029.80, CG ≤ 63.955, PA≥14.835)
AP	(G ≥ 15203.90, GG ≥ −0.96, PA ≤ 19.40), OR (IV ≥ 32.155, I ≥ 2.805, G ≥ 15172.90), OR (G ≥ 15172.90, PPP ≥ 0.81, R ≥ 3240000000), OR (UN ≥ 3.05, PA ≤ 21.59, IV ≥ 35.055)
A	(U ≥ 78.615, PPP ≥ 0.505, G ≥ 15203.90), OR (PA ≤ 19.40, GG ≥ −0.96, G ≥ 15203.90)
AM	(U ≥ 72.18, G ≥ 15203.90, PPP ≥ 0/685), OR (PA ≤ 19.40, GG ≥ 0.305, CG ≥ 51.565), OR (CG ≤ 58.835, IV ≥ 31.855, EX ≥ 54.065), OR (UN ≤ 13.55, I ≤ 4.02, EX ≥ 74.515), OR (SD ≤ 57.89, IV ≥ 31.85.5, PA ≤ 19.68)
BBBP	(I ≤ 4.24235, R ≥ 43160000000, G ≥ 5808.70), OR (CG ≤ 50.22, I ≤ 3.13, G ≥ 9139.48), OR (I ≤ 2.685, C ≥ −3.66, E ≥ 28.825)
BBB	(G ≥ 10738.50, I ≤ 5.125, UN ≤ 15.95), OR (IV ≤ 23.88, TD ≥ 11.425, CG ≤ 116.03), OR (IM ≤ 31.14, GG ≤ 1.46, EX ≤ 41.555)
BBBM	(PA ≤ 34.91, CG ≤ 67.12.71, SD ≤ 68.87), OR (PPP ≤ 6.405, EX ≥ 38.815, G ≥ 5669.61), OR (GS ≥ 21.57, GS ≤ 23.945, U ≤ 94.895)
BBP	(TD ≥ 6.66, GS ≥ 18.72, IV ≤ 32.025), OR (G ≥ 5669.61, IV ≤ 39.53, IV ≥ 20.625), OR (GS ≥ 17.485, PA ≤ 29.015, I ≤ 6.735), OR (GG ≤ 1.46, R ≥ 4830000000, C ≥ −3.37)
BB	No case
BBM	(IV ≥ 22.675, EX ≥ 26.235, GG ≤ 3.91), OR (IV ≥ 25.265, I ≤ 9.835, TD ≥ 10.365), OR (SD ≥ 7.53, I ≤ 5.09, PG ≥ −0.53), OR (PPP ≤ 266.50, PG ≤ 1.425, IV ≥ 25.265)
BP	(UN ≥ 4.35, GS ≥ 13.82, C ≤ 3.65), OR (R ≥ 2505000000, M ≥ 60.91, C ≥ −8.36)
B	(G ≥ 5808.70, GS ≥ 12.985), OR (IV ≤ 39.53, C ≥ −8.905)
BM	No case

Table 4: Decision tree of the year 2014.

Rating Class	Year 2014 Decision tree
AAA	(CG ≤ 97.51, G ≥ 44264.40)
AAP	(CG ≤ 97.14, G ≥ 44264.40), OR (IM ≥ 31.69, R ≥ 76865000000, G ≥ 37322.70)
AA	(GG ≤ 3.325, CG ≤ 102.37, G ≥ 37322.70), OR (G ≥ 23895.10, UN≤7.20, CG ≤ 76.265)
AAM	(PA ≤ 20.59, CG ≤ 117.265, G ≥ 24571)
AP	(C ≤ 0.365, G ≥ 15730.30, E ≤ 30.185), OR (C ≥ −4.20, CG ≤ 102.37, G ≥ 24512.50), OR (E ≤ 42.62, PG ≥ 0.465, PA ≤ 19.10)

Table 4: Continued.

Rating Class	Year 2014 Decision tree
A	(GG ≥ −0.725, G ≥ 15730.30, PA ≤ 18.245), OR (GS ≥ 22.90, U ≥ 66.17, GG ≤ 1.985), OR (M ≤ 138.415, I ≤ 2.72, R ≥ 65565000000)
AM	(GG ≥ −0.225, GG ≤ 1.545, I ≤ 3.66), OR (M ≤ 152.09, R ≥ 6285000000, G ≥ 13680.90), OR (GG ≥ −0.99, PA ≤ 19.29, G ≥ 15618.90), OR (GG ≤ 3.295, GS ≥ 22.90, U ≥ 72.715), OR (M ≤ 138.415, R ≥ 54060000000, I ≤ 2.805)
BBBP	(I ≤ 2.91, I ≥ 0.315, G ≥ 13680.90), OR (R ≥ 60320000000, UN ≤ 7.82, PPP ≤ 14.815), OR (M ≥ 83.455, U ≥ 77.645, GG ≤ 2.285)
BBB	R ≥ 565000000, G ≥ 13680.90, GS ≥ 17.065), OR (PG ≥ −0.365, R≥93800000000, I ≤ 5.525), OR (UN ≤ 9.90, U ≥ 66.505, I ≤ 2.91)
BBBM	(R≥565000000, G ≥ 13680.90, UN ≤ 15.10), OR (PG ≥ 0.15, R ≥ 32595000000, SD ≥ 9.635), OR (U ≥ 54.17, M ≥ 121.215, PA ≤ 27.475), OR (UN ≤ 7.82, PA ≤ 22.905, M ≥ 103.16)
BBP	(GG ≤ 3.265, TD ≥ 13.52, GS ≥ 20.40), OR (TD ≥ 7.595, GG ≥ 0.195, R ≥ 16430000000), OR (I ≤ 4.345, GG ≥ −0.03, R ≥ 6935000000), OR (G ≥ 22493.40, I ≤ 2.76, M ≥ 83.455)
BB	(TD ≤ 32.585, IM ≤ 81.065, R ≥ 12170000000, SD ≥ 18.68), OR (I ≥ 0.93, M ≤ 146.655, M ≥ 105.905, I5≤5.66)
BBM	(PG≤1.26, GS ≥ 13.755, GS ≤ 3.63), OR (SD ≥ 32.355, IV ≥ 23.23, GG ≤ 4.30), OR (IM ≤ 53.395, R ≥ 6285000000, UN ≤ 7.67), OR (IM ≤ 48.27, U ≥ 54.29, EX ≥ 30.805)
BP	(SD ≥ 32.355, IV ≥ 16.485, SD ≤ 59.535), OR (G ≥ 1873.54, SD ≥ 32.355, IV ≥ 21.35), OR (IM ≥ 31.85, IV ≥ 28.755, U ≥ 41.26), OR (GG ≤ 2.93, I ≤ 5.455, UN ≤ 16.45), OR (PG ≤ 1.485, GS ≥ 15.50, PG ≥ −0.325)
B	(CG ≤ 141.95, E ≥ 31.395), OR (IV ≥ 11.60, SD ≥ 0.16, TD ≤ 24.205)
BM	(R ≤ 455530000000, G ≤ 11380.10), OR (SD ≥ 0.16, TD ≤ 35.125)

Table 5: Decision tree of the year 2015.

Rating Class	Year 2015 Decision tree
AAA	(PA ≤ 19.675, E ≤ 42.43, G ≥ 47533.40)
AAP	(C ≤ −1.3747, G ≥ 45329.50, M ≥ 116.68), OR (UN ≤ 8.35, PPP ≤ 10.825, G ≥ 45329.50)
AA	(GS ≥ 24.55, PG ≥ 0.42, G ≥ 24204.20), OR (GG ≤ 4.24, PPP ≤ 10.825, G ≥ 38710.90)
AAM	(U ≤ 87.21, UN ≤ 6.55, G ≥ 24204.20), OR (GG ≤ 4.24, PPP ≤ 10.825, G ≥ 38710.90)
AP	(U ≤ 87.585, G ≥ 17495.60, C ≤ −1.479), OR (U ≥ 53.66, GS ≥ 25.535, R ≥ 52161000000), OR (PPP ≤ 10.825, U ≥ 65.38, G ≥ 38710.90), OR (GG ≤ 1.655, GG ≥ 0.74, U ≥ 79.13)
A	(PPP ≤ 117.435, U ≥ 65.38, G ≥ 35666.20), OR (C ≤ 0.305, UN ≤ 6.20, PA ≤ 20.835), OR (M ≥ 117.495, GS ≥ 23.705, G ≥ 14451.70), OR (M ≤ 131.47, M ≥ 114.29, G ≥ 15065)
AM	(GS ≥ 20.755, G ≥ 14179.60, C ≤ −1.63), OR (UN ≤ 10.90, R ≥ 22763500000, G ≥ 14179.60), OR (I ≤ 2.055, M5≥111.635, U ≥ 73.88)
BBBP	(EX ≥ 23.73, C ≤ −1.245, R ≥ 82865000000), OR (GS≥16.94, R ≥ 8469500000, G ≥ 14179.60), OR (UN≤5.15, R ≥ 16708000000, G ≥ 10561.40), OR (M ≤ 147.075, RE ≤ 29.38, SD ≥ 42.33)
BBB	(GS ≥ 19.735, PPP ≤ 14.99, G ≥ 10327.40), OR (R ≥ 11365000000, UN ≤ 5.25, G ≥ 10383.10), OR (I ≤ 6.34, PG ≤ 1.345, R ≥ 44997500000), OR (M ≤ 134.165, U ≥ 73.325, M ≥ 111.15))
BBBM	(PPP ≤ 1.77, I ≤ 299, GS ≥ 14.77), OR (GS ≥ 23.47, G ≥ 14179.60, PA ≤ 28.295), OR (IM ≤ 33.47, M ≥ 103.755, PA ≤ 29.275), OR (PA ≤ 37.02, PPP ≤ 117.435, R ≥ 19915000000), OR (U ≥ 72.05, PG ≤ 1.06, GS ≥ 14.77)
BBP	(GG ≥ 0.09, TD ≥ 10.915, R ≥ 8469500000), OR (TD ≥ 5.145, R ≥ 15619500000, SD ≥ 11.155), OR (G ≥ 9845.96, PG ≤ 1.63, M ≥ 111.15), OR (PA ≤ 22.905, GS ≥ 20.74, M ≥ 90.31)
BB	(GS≥20.575, M ≥ 104.745, G ≥ 11039.60), OR (M ≥ 111.15, PG ≤ 1.52, G ≥ 10593.80), OR (R ≥ 66.115, IM ≤ 47.05, U ≥ 48.055), OR (PPP ≤ 5808.54, PG ≤ 2.295, R ≥ 15028000000), OR (PA ≤ 22.905, GS ≥ 20.575, M ≥ 104.745)
BBM	(I ≤ 6.80, SD ≥ 20.235, GG ≥ 1.335), OR (IV ≥ 28.14, SD ≥ 27.36, M ≥ 105.065), OR (PG ≤ 1.35, IV ≥ 28.14, PA ≥ 16.725), OR (PPP ≤ 134.13, UN ≤ 7.61, PPP ≥ 1.095), OR (PA ≤ 28.07.5, PPP ≤ 134.135, GS ≥ 14.77)
BP	(IM ≤ 47.345, G ≥ 1889.15, PPP ≥ 2.585), OR (SD ≥ 18.905, I ≤ 7.545, U ≤ 65.38), OR (PPP ≤ 45.59, UN ≤ 19.60, IV ≤ 27.45), OR (IV ≥ 17.98, C ≤ 1.005, PG ≤ 1.35), OR (TD ≥ 4.865, I ≤ 9.515, M ≥ 111.15)
B	(GG ≥ −4.645, PG ≥ 1.12), OR (I ≤ 8.175, R ≤ 4104500000), OR (C ≤ 1.005, I ≤ 38.83, RE ≤ 44.995)
BM	(RE ≤ 44.995, I ≤ 38.83, C ≤ 1.005), OR (PG ≥ −0.62, IV ≤ 28.125), IV ≥ 29.46)

Table 6: Applied variables for exploring the hidden pattern of the Fitch rating system.

Notation	Attribute
C	Cash surplus/deficit (% age of GDP)
EX	Exports of goods and services (% of GDP)
G	GDP per capita (current US$)
IM	Imports of goods and services (% age of GDP)
RE	Revenue, excluding grants (% age of GDP)
SD	Short-term debt (% age of total reserves)
TD	Total debt service (% age of exports of goods, services, and primary income)

Table 6: Continued.

Notation	Attribute
CG	Central government debt, total (% age of GDP)
E	Expense (% age of GDP)
GG	GDP per capita growth (annual % age)
GS	Gross savings (% age of GDP)
IV	Industry, value added (% age of GDP)
I	Inflation, consumer prices (annual % age)
PPP	PPP conversion factor, GDP (LCU per international $)
R	Total reserves (includes gold, current US$)
U	Urban population (% age of total)
PG	Population growth (annual % age)
PA	Population ages 0–14 (% age of total)
UN	Unemployment, male (% age of male labor force) (modelled ILO estimate)
M	Mobile cellular subscriptions (per 100 people)

Table 7: The most common properties of the classified ranking classes.

Rating class	Common variables in all trees
AAA	G
AAP-AA-AAM	G
AP-A-AM	G-PA-I
BBBP-BBB-BBBM	R-GS-G-UN-PPP-I–U
BBP-BB-BBM	R-G-GG-SD-IV-I-GS-PG
BP-B-BM	UN-IV

Table 8: Mismatched cases of the test set for 2012.

Country	Rating by LAD	Fitch rating
Ukraine	BBBM	B
Suriname	BBBM	BBM
Rwanda	BP	B
Ghana	BB	BP
Dominican Republic	BB	B

Table 9: The mismatched cases and mismatched result of the test set for 2013.

	Country	Rating by LAD	Fitch rating
Mismatched cases	Malta	AP	A
	Vietnam	BBM	BP
	Ukraine	BBM	B
	Kazakhstan	BBB	BBBP
	Zambia	BP	B
	Congo, Dem Republic	BBM	BP
	Paraguay	BBP	BBM
	Portugal	BBB	BBP
	Iceland	AAM	BBB
	Spain	AAM	BBB
	Cyprus	BBB	B
Mismatched result	Israel	AAM	A

Table 10: The mismatched cases and mismatched result of the test set for 2014.

	Country	Rating by LAD	Fitch rating
Mismatched cases	South Africa	BBBM	BBB
	Portugal	A	BBP
	Panama	B	BBB
	Iceland	AAM	BBB
	Cyprus	AP	BM
	Costa Rica	BBBM	BBP
Mismatched result	Namibia	BBP	BBBM

Table 11: Mismatched ratings of the test set and training set for 2015.

	Country	Rating by LAD	Fitch rating
Test set	Congo, Dem Republic	B	BP
	Rwanda	B	BP
	Latvia	A	AM
	Iceland	BBM	BBB
	Armenia	BBM	BP
Training set	Ireland	BBB	AM
	Malaysia	AP	AM
	Peru	BBB	BBBP
	Namibia	BBM	BBBM

Table 12: Significant misclassified countries by Fitch between 2012 and 2015.

	No. of misclassification	
Country	Twice	More than twice
Ukraine	√	
Rwanda	√	
Portugal	√	
Namibia	√	
Iceland		√
Cyprus	√	
Congo, Dem Republic	√	

recently gone through a civil war, and it has been in serious conflict with Russia. The misratings by the LAD model can have different reasons including both technical and political ones.

5. Conclusion

Sovereign debt rating plays an important role in the world economy. The method of the most important rating companies is not public. This can be explained by two facts: the algorithms are considered as individual properties of these enterprises, and the rating is based on some tacit knowledge of experts, built of their experiences, personal interviews, gray literature, open-source intelligence, etc. That is why a perfect reproduction of the classifications of these agencies does not seems possible. It would be important for both countries and investors to know the method or a good approximation of the method to all countries.

The present study reconstructed the Fitch rating of sovereign debts in years 2012 to 2015 by applying the method of LAD. The analysis is based on 20 important attributes of countries. The data were obtained from the database of World Bank. The outcomes of the calculation are summarized in the form of decision trees. An approximate rating of an unrated country can be obtained by using the decision tree. This application does not need any expertise or professional understanding of rating methods. Previous papers were not providing such tool for investors. The sovereign debt rating given by the decision trees is largely the same as Fitch's rating. The discrepancies may be due in part to the fact that an unknown function was approximated by regression. Another important reason is that for some countries the rating is biased from what is expected in some direction. A deeper analysis of the discrepancies is one of the research topics of the future.

The LAD technology was originally developed to separate only two classes. The paper also showed that LAD may be able to distinguish several classes simultaneously in the case of a systematic application. In the future, it is worth exploring the conditions for such applications and creating additional applications accordingly.

Data Availability

All data were collected from World Bank website, https://data.worldbank.org/country.

Disclosure

This paper has been presented as preprint in arXiv [39].

Conflicts of Interest

The authors declare no conflicts of interest.

References

[1] Anon1 https://academic.oup.com/wbro/pages/General_Instructions (last accessed: 15.07.2021).

[2] R. Cantor and F. Packer, "Determinants and impact of sovereign credit ratings," *The Journal of Fixed Income*, vol. 6, no. 3, pp. 76–91, 1996.

[3] P. Luitel and R. Vanpée, "How do sovereign credit ratings help to financially develop low-developed countries?," 2018, https://ideas.repec.org/p/eps/ecmiwp/13956.html ECMI Papers.

[4] A. D. Gültekin-Karakaş, M. Hisarcıklılar, and H. Öztürk, "Sovereign risk Ratings : biased toward developed countries?" *Challenges and Opportunities in Emerging Markets*, vol. 47, pp. 69–87, 2011.

[5] O. Canuto, P. F. P. Dos Santos, and P. C. De SÁ Porto, "Macroeconomics and sovereign risk ratings," *Journal of International Commerce, Economics and Policy*, vol. 3, no. 2, Article ID 1250011, 2012.

[6] Anon2 https://www.fitchratings.com/products/rating-definitions#about-rating-definitions (last accessed: 15.07.2021).

[7] M. Kunczik, "Globalisation: news media, images of nations and the flow of international capital with special reference to the role of rating agencies," *The Journal of International Communication*, vol. 8, no. 1, pp. 39–79, 2002.

[8] V. Bozic and C. Magazzino, "Credit rating agencies: the importance of fundamentals in the assessment of sovereign ratings," *Economic Analysis and Policy*, vol. 43, no. 2, pp. 157–176, 2013.

[9] G. Ferri, L.-G. Liu, and J. E. Stiglitz, "The procyclical role of rating agencies: evidence from the East asian crisis," *Economic Notes*, vol. 28, no. 3, pp. 335–355, 1999.

[10] I. M. Fund, "The relative importance of political and economic variables in creditworthiness ratings," 1998. IMF Working Papers.

[11] O. Bernal, A. Girard, and J.-Y. Gnabo, "The importance of conflicts of interest in attributing sovereign credit ratings," *International Review of Law and Economics*, vol. 47, pp. 48–66, 2016.

[12] G. Mattarocci, *The Independence of Credit Rating Agencies: How Business Models and Regulators Interact*, Academic Press, Cambridge, MA, USA, 2013.

[13] A. Afonso, P. Gomes, and P. Rother, "What "hides" behind sovereign debt ratings?" 2007, https://ideas.repec.org/p/ecb/ecbwps/2007711.html Working Paper Series.

[14] E. Bissoondoyal-Bheenick, R. Brooks, and A. Y. N. Yip, "Determinants of sovereign ratings: a comparison of case-based reasoning and ordered probit approaches," *Global Finance Journal*, vol. 17, no. 1, pp. 136–154, 2006.

[15] S. Spilioti and G. Vamvoukas, "The impact of government debt on economic growth: an empirical investigation of the Greek market," *Journal of Economic Asymmetries*, vol. 12, no. 1, pp. 34–40, 2015.

[16] S. Alexe, P. Hammer, A. Kogan, and M. Lejeune, *A Non-Rrecursive Regression Model for Country Risk Rating*, Rutgers University, New Brunswick, NJ, USA, 2003.

[17] A. Hantzsche, "Sovereign credit ratings under fiscal uncertainty," *SSRN Electronic Journal*, vol. 32, 2018.

[18] E. Bouri, S. J. H. Shahzad, N. Raza, and D. Roubaud, "Oil volatility and sovereign risk of BRICS," *Energy Economics*, vol. 70, pp. 258–269, 2018.

[19] E. Bouri and I. Kachacha, D. Roubaud, Oil market conditions and sovereign risk in MENA oil exporters and importers," *Energy Policy*, vol. 137, Article ID 111073, 2019.

[20] M. Amstad, F. Packer, and J. Shek, "Does sovereign risk in local and foreign currency differ?" *Journal of International Money and Finance*, vol. 101, Article ID 102099, 2020.

[21] C. Agiakloglou and E. Deligiannakis, "Sovereign risk evaluation for European Union countries," *Journal of International Money and Finance*, vol. 103, Article ID 102117, 2020.

[22] U. Volz, J. Beirne, N. Ambrosio Preudhomme et al., *Climate Change and Sovereign Risk*, SOAS University of London, Asian Development Bank Institute, World Wide Fund for Nature Singapore, Four Twenty Seven, London, UK, 2020.

[23] G. Alexe, S. Alexe, P. L. Hammer, and A. Kogan, "Comprehensive vs. comprehensible classifiers in logical analysis of data," *Discrete Applied Mathematics*, vol. 156, no. 6, pp. 870–882, 2008.

[24] P. L. Hammer and T. O. Bonates, "Logical analysis of data-An overview: from combinatorial optimization to medical applications," in *Annals of Operations Research*vol. 148, no. 1, , pp. 203–225, Springer, 2006.

[25] N. Mirzaei, "Reconstruction of World Bank's classification of countries," *African Journal of Business Management*, vol. 5, no. 32, 2011.

[26] P. L. Hammer, A. Kogan, and M. A. Lejeune, "Modeling country risk ratings using partial orders," *European Journal of Operational Research*, vol. 175, no. 2, pp. 836–859, 2006.

[27] P. L. Hammer, A. Kogan, and M. A. Lejeune, "Reverse-engineering country risk ratings: a combinatorial non-recursive model," *Annals of Operations Research*, vol. 188, no. 1, pp. 185–213, 2011.

[28] J. F. Avila-Herrera and M. M. Subasi, "Logical analysis of multi-class data," in *Proceedings of 2015 41st Latin American Computing Conference, CLEI 2015*, Arequipa, Peru, October 2015.

[29] M. Lejeune, V. Lozin, I. Lozina, A. Ragab, and S. Yacout, "Recent advances in the theory and practice of logical analysis of data," *European Journal of Operational Research*, vol. 275, no. 1, pp. 1–15, 2019.

[30] T. O. Das, S. Adepu, and J. Zhou, "Anomaly detection in industrial control systems using logical analysis of data," *Computers & Security*, vol. 96, Article ID 101935, 2020.

[31] A. Ragaba, M. El-Koujok, B. Poulinb, M. Amazouz, and S. Yacout, "Fault diagnosis in industrial chemical processes using interpretable patterns based on logical analysis of data," *Journal of Expert Systems with Applications*, vol. 95, pp. 368–383, 2018.

[32] S. Jocelyna, Y. Chinniah, M.-S. Ouali, and S. Yacout, "Application of logical analysis of data to machinery-related accident prevention based on scarce data," *Reliability Engineering & System Safety*, vol. 159, pp. 223–236, 2017.

[33] R. Bruni, G. Bianchi, C. Dolente, and C. Leporelli, "Logical analysis of data as a tool for the analysis of probabilistic discrete choice behavior," *Computers and Operations Research*, vol. 106, pp. 191–201, 2019.

[34] R. Janostik, J. Konecny, and P. Krajca, "Interface between logical analysis of data and formal concept analysis," *European Journal of Operational Research*, vol. 284, pp. 792–800, 2020.

[35] R. Ouyang and Ch-A. Chou, "Integrated optimization model and algorithm for pattern generation and selection in logical analysis of data," *Computers & Operations Research*, vol. 124, Article ID 105049, 2020.

[36] P. Addo, D. Guegan, and B. Hassani, "Credit risk analysis using machine and deep learning models," *Risks*, vol. 6, no. 2, p. 38, 2018.

[37] G. Alexe and P. L. Hammer, "Spanned patterns for the logical analysis of data," *Discrete Applied Mathematics*, vol. 154, no. 7, pp. 1039–1049, 2006.

[38] E. Boros, P. L. Hammer, T. Ibaraki, and A. Kogan, "Logical analysis of numerical data," *Mathematical Programming*, vol. 79, no. 1–3, pp. 163–190, 1997.

[39] E. Gholipour, B. Vizvári, and Z. Lakner, "Reconstruction rating model of sovereign debt by logical analysis of data," 2020, http://arxiv.org/abs/2011.14112.

Hindawi
Mathematical Problems in Engineering
Volume 2021, Article ID 5543542, 12 pages
https://doi.org/10.1155/2021/5543542

Research Article

Multiteam Competitive Optimization Algorithm and Its Application in Bearing Fault Diagnosis

Bo Zheng,[1] **Huiying Gao**,[1] **Xin Ma**,[2] **and Xiaoqiang Zhang**[1]

[1]*Aviation Engineering Institute, Civil Aviation Flight University of China, Guanghan 618307, China*
[2]*Air Traffic Management College, Civil Aviation Flight University of China, Guanghan 618307, China*

Correspondence should be addressed to Xiaoqiang Zhang; xqzhanguestc@163.com

Received 1 March 2021; Accepted 25 June 2021; Published 8 July 2021

Academic Editor: Mohammad Yazdi

A novel multiteam competitive optimization (MTCO) algorithm has been proposed to diagnose the fault patterns of bearings. This algorithm is inspired by competitive behaviors of multiple teams. It is a three-level organization structure; thus, more potential optimal areas can be searched. By imitating human thinking, such as the betrayal and replacement behavior along with the introduction of an acceptable vector, new strategies within the MTCO are designed to increase the diversity and guide jumping out of location suboptimal areas. In addition to this, a kernel function has been introduced to reduce the recognition errors caused by data which are nonlinearly distributed in original space. The obtained experimental results demonstrate that the proposed MTCO is globally stable and optimal decision performance. After that the MTCO is applied for the fault diagnosis of bearings, and it has also been compared with other commonly used methods. The comparison indicates that the proposed algorithm has higher recognition accuracy.

1. Introduction

Fault diagnosis, which has been formed as an independent interdisciplinary during the 1960s, plays a significant role in modern industrial processes. It is the key to prevent serious accidents, ensure safety and obtain maximum economic benefits [1, 2]. With the development of industrial equipment, new data-driven methods including intelligence algorithms, data fusion, multivariate statistical analysis, signal processing and machine learning are paid much attention and get rapid development [3, 4]. A large number of researches on data-driven methods have been proposed to promote the development of fault diagnosis technology [5].

In recent decade, the researches on fault diagnosis mainly focus on data-driven methods. Yuan and Chu [6] investigated the discrete particle swarm optimization (PSO) algorithm to select the best fault features and optimize the performance of the support vector machine (SVM) classifier. There the experimental results proved that the developed method shows better performance than the SVM based on principal component analysis (PCA), or SVM based on genetic algorithm (GA) in the application of fault diagnosis of the turbo pump rotor. Zheng and Ma [7] introduced a method using the dual-mutation PSO to determine the optimal parameters for SVM. The experiments for damage type recognition of civil aeroengine indicated that the method could achieve higher diagnostic accuracy than that of the single or multiple kernels SVM where parameters were set randomly. Korürek and Doğan [8] introduced the data-driven method into the field of life sciences, and the classifier radial basis function (RBF) neural network whose structure was evolved by PSO, the optimized RBF network could classify electrocardiogram beats with a smaller size of network without making any concessions on the classification performance. Based on the above studies and other works presented by Lu et al. and Shang et al. [9, 10], a conclusion can be made that an appropriate classifier is essential for detection and identification of unknown fault patterns. Inspired by the heuristic random search process of swarm, this paper proposes a swarm intelligence algorithm called multiteam competitive optimization (MTCO) algorithm. This proposed algorithm is a data-driven method and mainly

used to recognize unknown fault patterns. The essence of this algorithm is to search an optimal single-class center for each unknown fault pattern. Lots of researchers have focused on studying human decision methods by imitating human behaviors. Among them, some improved methods have achieved remarkable calculation effect, such as the work presented by Zheng [11]. Research on human learning behaviors had shown that the best planners adjusted their decisions considering the current state and their perception of the best experiences from others. Based on this idea, Tanweer et al. [12] designed two learning strategies for PSO incorporating the best human learning strategies for finding the optimum solution. Cheng and Jin [13] developed a social learning PSO (SL-PSO), which allowed the individuals to learn behaviors from other better particles in the current swarm. There the comparative results showed the SL-PSO performed well on low-dimensional problems and was promising for solving large-scale problems as well. Li et al. [14] proposed an information sharing mechanism (ISM) to make each particle share its best search information, through which all the particle could take advantage of the shared information. In this way, a competitive and cooperative operator inspired by human behaviors was designed to control the shared information being utilized in a proper and efficient way. The competitive and cooperative PSO with ISM (CCPSO-ISM) can prevent the premature convergence when solving global optimization problems. In addition, aging had been explored by biologists to be an important mechanism for maintaining diversity. In a human social, aging made the old leader of the colony become weak, which provides opportunities for the other individuals to challenge the leadership position. Inspired by this natural phenomenon, Zheng et al. [15] incorporated this mutation mechanism into PSO and PSO with a trying mutation strategy, to overcome the problem of premature convergence without significantly impairing the fast-converging feature of PSO.

In this paper, based on the traditional PSO, we constructed a new organization structure for the particles, in which the competition of multiple teams is introduced to recognize unknown fault patterns and then find the optimal decision. The particles are redefined as members and classified into three groups, that is, staff belonging to the majority, leaders belonging to the minority, and the only boss. The organization structure of the proposed algorithm is shown in Figure 1. These staff follow different leaders and the leaders are accountable towards the boss. Finally, the boss adjusts the decision again based on the optimal decision made by staff and leaders. So the method is termed as MTCO algorithm.

Aiming to search more potential optimal areas, the MTCO algorithm is conducive to get rid of the premature convergence effectively and overcome the influence of randomness on the optimal decision solution. Thus, the global optimal decision solution can be obtained with a higher probability. Therefore, the proposed algorithm can obviously improve the accuracy of unknown fault patterns via looking for the optimal class centers of different fault patterns.

The rest of the paper is organized as follows. In Section 2, MTCO algorithm has been proposed. Section 3 introduces the recognition process of the MTCO algorithm. After that the application problem that is the fault diagnosis of bearing has been discussed in Section 4. Finally, in the last section, conclusion has been drawn.

2. The MTCO Algorithm

2.1. The Optimization Principle. The MTCO algorithm is constructed on the basis of the traditional PSO. But the meanings of particles, updating strategy, and organization structure have been redesigned. The traditional PSO has to suffer from the premature convergence due to trap into local optimal areas, or the lack of diversity [16, 17]. Also, the traditional PSO is not very efficient when coping with complex multimodal functions because the whole particles only follow the single global extremum and cannot efficiently exchange search information. Inspired by the competition of multiple teams, this paper designs a new organization structure and corresponding updating strategy to solve the exiting problems mentioned above.

The fitness function $\mathrm{fit}(\cdot)$ existing in the traditional PSO is redefined as the decision function $\mathrm{dec}(\cdot)$ for the competition behaviors of multiple teams. And the fitness value is also redefined as the decision value. Assume that it is a maximization problem. As shown in Figure 1, the global extremum $\mathbf{m}_{g\ d}$ is redefined as the only boss, and the ordinary individuals are redesigned as leaders $\mathbf{m}_l$ and staff $\mathbf{m}_s$, respectively. The number of leaders is n_l, and the number of staff is n_s. Leaders and staff have their own individual extremum $\mathbf{m}_{l\_i\ d}$ and $\mathbf{m}_{s\_i\ d}$, respectively. Each team only has one leader. The staff in one team make decisions under the guidance of their team leaders. So the leaders belong to the minority with higher decision values, and the staff belong to the majority with relatively low decision values, usually, $n_l < 10\% \cdot n_s$.

Based on this structure, the procedure of the MTCO is described as follows.

Step 1. Initialize each individual's initial velocity and position randomly using a certain method. Each position is a potential optimal decision solution.

Step 2. Calculate individual's decision value and sort these values in an ascending order according to their decision values. The individual with the highest decision value is the boss $\mathbf{m}_{g\ d}$.

Step 3. Choose n_l individuals as leaders from the top of ranking. The rest of n_s individuals are the staff. Then the staff will be randomly assigned to different teams, and each team may have different number of staff according to their decision values. The higher the decision value is, the more staff the team has. The number $N(\mathbf{m}_{l(j)})$ of staff belonging to $\mathbf{m}_{l(j)}$ is calculated by

$$N\left(\mathbf{m}_{l(j)}\right) = \frac{n_s \cdot j}{\mathrm{sum}\left(n_l\right)}, \tag{1}$$

where $j = 1, \ldots, n_l$ denotes the leaders' ordinal in an ascending order. $\mathrm{sum}(n_l) = 1 + \cdots j \cdots + n_l$.

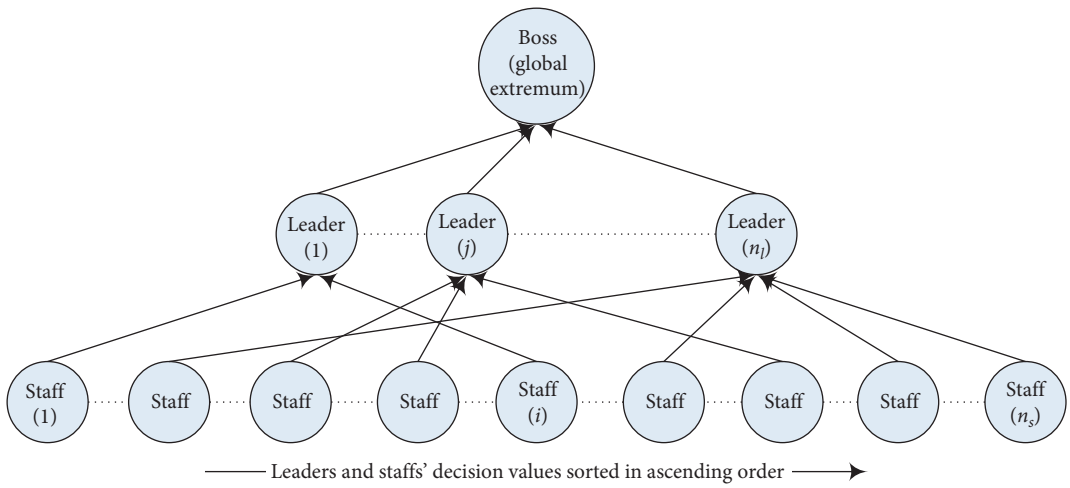

Figure 1: The organization structure chart of MTCO algorithm.

Step 4. Update these staff's velocities and positions using equations (2) and (3), respectively.

$$\mathbf{v}_{s(i)}^{t+1} = \omega_{s(i)}^{t}\mathbf{v}_{s(i)}^{t} + c_1 r_1 \mathbf{a}_1\left(\mathbf{m}_{s\_i\ d(i)}^{t} - \mathbf{m}_{s(i)}^{t}\right) + c_2 r_2 \mathbf{a}_2\left(\mathbf{m}_{l\_i\ d(i\in j)}^{t} - \mathbf{m}_{s(i)}^{t}\right), \tag{2}$$

$$\mathbf{m}_{s(i)}^{t+1} = \mathbf{m}_{s(i)}^{t} + \mathbf{v}_{s(i)}^{t+1}, \tag{3}$$

and $\omega_{s(i)}^{t}$ can be calculated by

$$\omega_{s(i)}^{t+1} = \omega_{s(i)}^{t}\frac{-(\omega_{\max} - \omega_{\min})}{t_{\max}}, \tag{4}$$

where $i = 1, \ldots, n_s$ denotes the staff's ordinal in an ascending order. t denotes the current iteration number, $t_{\max}$ is the maximum iteration number. c_1 and c_2 are constants, usually, $c_1 = 1.5$, and $c_2 = 1.7$. r_1 and r_2 are random control parameter sets in interval [0, 1]. $\mathbf{m}_{l\_i\ d(i\in j)}^{t}$ represents the individual extremum of the jth leader which is the leader of the ith staff. $\mathbf{a}_1$ and $\mathbf{a}_2$ are newly designed as acceptable vector which is a binary. $\omega_{s(i)}^{t}$ is the inertia weight, $\omega_{\max}$ is the maximum value, and $\omega_{\min}$ is the minimum value. The initial value of $\omega_{s(i)}^{t}$ is $\omega_{\max}$. $\omega_{s(i)}^{t}$ is a linear decreasing inertia weight adopted by these staff. It is because that these staff should gradually converge to their leaders to search for better decision values. So the linear decreasing inertia weight adopted here is reasonable.

In this study, $\omega_{s(i)}^{t}\mathbf{v}_{s(i)}^{t}$ is denoted as the cumulative experience which represents the gradual process from indistinct to clarity for cognizing the decision problem. $\mathbf{m}_{s\_i\ d(i)}^{t} - \mathbf{m}_{s(i)}^{t}$ is explained as the independent-amendment ability. It means that the staff amend their decisions depending on their own recognition. And in a team, the leader's opinion usually affects the staff's judgment. So $\mathbf{m}_{l\_i\ d(i\in j)}^{t} - \mathbf{m}_{s(i)}^{t}$ is described as the dependent-amendment ability which is affected by the leader. In practical engineering, some uncertainty or random events around the staff may affect the decision-making. It will lead to a better or worse decision. So after amending a decision, the staff may accept some amending suggestions or reject it. The acceptable vector just imitates this process. Moreover, another function of acceptable vector is used to increase the diversity of staff and avoid the aggregation of staff. The acceptable vector is a binary vector as the same dimensions as staff, which can be calculated by

$$\mathbf{a}_i = \operatorname{bin}\left(\operatorname{unifrnd}(0, 1, D) - r_N\right), \tag{5}$$

where $\mathbf{a}_i = [a_{i1}, a_{i2}, \ldots, a_{i\ D}]$, a_{ij} is an element of $\mathbf{a}_i$. $\operatorname{bin}(\cdot)$ is a function for the purpose that if $a_{ij} \le 0$, $a_{ij} = 0$; otherwise $a_{ij} = 1$. r_N is a random threshold in interval [0, 1]. $\operatorname{unifrnd}(\cdot)$ is a function used for generating a uniform distribution real vector with D dimensions in interval [0, 1]. So if $a_{ij} = 1$, the amendment for the jth dimension will be accepted. Otherwise, the amendment will be rejected.

Actually, the updating process of staff is consistent with the process of human decision-making. Meanwhile, the values of r_1 and r_2 can control the personality of the staff who tend to depend on their own amendment or leader's guidance, or a compromise.

In this step, the betrayal mechanism is introduced to guide the staff leaving the current team leader when they cannot change their individual extremum. We design a two-dimensional betrayal vector $\mathbf{b} = [b_L, b_U]$ called betrayal vector. b_L and b_U are lower and upper limit values, respectively, initialized randomly. When $\operatorname{dec}(\mathbf{m}_{s(i)}^{t+1})$ is lower than $\operatorname{dec}(\mathbf{m}_{s\_i\ d(i)}^{t})$, $b_L = b_L + 1$. It means that if the staff cannot achieve a better decision solution, it will create discontent for leader, like human, the increasing of discontent is gradually cumulative. When $b_L = b_U$, the staff may leave the current leader and enter another team with a certain probability, the probability of $\mathbf{m}_{s(i)} \in \mathbf{m}_{l(j)}$ which denotes the ith staff belongs to the jth leader is as follows:

$$P\left(\mathbf{m}_{s(i)} \in \mathbf{m}_{l(j)}\right) = \frac{j}{\operatorname{sum}(n_l)}. \tag{6}$$

Due to $j = 1, \ldots, n_l$, the staff which intends to betray its current leader may go to other teams, or may still follow its current leader. After reselecting the new leader, then initialize the betrayal vector $\mathbf{b}$ again.

If $\mathrm{dec}(\mathbf{m}_{s(i)}^{t+1})$ is higher than $\mathrm{dec}(\mathbf{m}_{s\_i\ d(i)}^{t})$, $\mathbf{m}_{s\_i\ d(i)}^{t+1} = \mathbf{m}_{s(i)}^{t+1}$; if $\mathrm{dec}(\mathbf{m}_{s(i)}^{t+1})$ is higher than $\mathrm{dec}(\mathbf{m}_{l\_i\ d(i\longrightarrow j)}^{t})$, $\mathbf{m}_{l\_i\ d(i\longrightarrow j)}^{t} = \mathbf{m}_{s(i)}^{t+1}$, and if $\mathrm{dec}(\mathbf{m}_{s(i)}^{t+1})$ is higher than $\mathrm{dec}(\mathbf{m}_{g\ d}^{t})$, $\mathbf{m}_{g\ d}^{t+1} = \mathbf{m}_{s(i)}^{t+1}$. Using this updating strategy, the staff can make better decisions. Meanwhile, the communication with leaders and boss can be completed, which will provide better references for leaders and boss.

Step 5. Update these leaders' velocities and positions using equations (7) and (8), respectively.

$$\begin{aligned}\mathbf{v}_{l(j)}^{t+1} &= \omega_{l(j)}^{t}\mathbf{v}_{l(j)}^{t} + c_1 r_1 \mathbf{a}_1\left(\mathbf{m}_{l\_i\ d(j)}^{t} - \mathbf{m}_{l(j)}^{t}\right)\\ &\quad + c_2 r_2 \mathbf{a}_2\left(\mathbf{m}_{g\ d}^{t} - \mathbf{m}_{l(j)}^{t}\right),\end{aligned} \tag{7}$$

$$\mathbf{m}_{l(j)}^{t+1} = \mathbf{m}_{l(j)}^{t} + \mathbf{v}_{l(j)}^{t+1}. \tag{8}$$

Similarly, $\omega_{l(j)}^{t}$ can be calculated by

$$\omega_{l(j)}^{t+1} = \omega_{l(j)}^{t} + \frac{(\omega_{\max} - \omega_{\min})}{t_{\max}}. \tag{9}$$

For these leaders, the dependent-amendment ability in equation (7) is influenced by the boss $\mathbf{m}_{g\ d}$ compared with staff's velocities updating formula. The meanings of other terms in equation (7) are described as same as equation (2). The function of acceptable vector in equation (7) is to reduce the over dependency on the boss and avoid trapping into local suboptimal decision areas. But $\omega_{l(j)}^{t}$ is a linear increasing inertia weight. The reason is that these leaders can obtain higher decisions. They have a duty to explore more solution space for searching for the global optimal decision value. So $\omega_{s(i)}^{t}$ and $\omega_{l(j)}^{t}$ can balance the exploitation and exploration ability between staff and leaders, which increases the probability of obtaining the global optimal decision solution.

A leader cannot be a leader for ever. Its leader status depends on its decision-making ability. So a replacement mechanism is necessary for these leaders when they have relative lower decision values than some staff. At the iteration t, if some leaders drop outside the top n_l in the ranking, they will be relegated to staff, and given a new leader and new betrayal vector randomly, the staff with higher decision solutions will replace the leaders. Meanwhile, these staff belonging to the relegated leaders will reselect a new leader with the probability calculated by equation (6). The replacement mechanism can ensure the whole staff follow the excellent leaders all the time, which is conducive to make the global optimal decision solution.

If $\mathrm{dec}(\mathbf{m}_{l(j)}^{t+1})$ is higher than $\mathrm{dec}(\mathbf{m}_{l\_i\ d(j)}^{t})$, $\mathbf{m}_{l\_i\ d(j)}^{t+1} = \mathbf{m}_{l(j)}^{t+1}$, and if $\mathrm{dec}(\mathbf{m}_{l(j)}^{t+1})$ is higher than $\mathrm{dec}(\mathbf{m}_{g\ d}^{t})$, $\mathbf{m}_{g\ d}^{t+1} = \mathbf{m}_{l(j)}^{t+1}$.

Step 6. Update the boss's position using

$$\mathbf{m}_{g\ d}^{t+1} = \mathbf{m}_{g\ d}^{t} + \mathbf{a}\cdot \mathrm{unifrnd}\left(-\omega^{t}{}_{r}, \omega^{t}{}_{r}, D\right), \tag{10}$$

and ω_r^t can be calculated using

$$\omega_r^t = \omega_{rs} - \frac{t\cdot(\omega_{rs} - \omega_{re})}{t_{\max}}, \tag{11}$$

ω_r^t is also a linear decreasing inertia weight, where ω_{rs} is initial value of ω_r, and ω_{re} is the final value of ω_r, usually $\omega_{rs} > \omega_{re}$. In the prophase of iteration, a larger ω_r is conducive to explore the lager solution space roughly. In the later stage of iteration, a smaller ω_r is conducive to exploit the more precise solution.

On the basis of global optimal decision solution made by all subordinates, the boss will amend the current global decision value with random free updating strategy. The decision-making for the future is still an uncertain process. Uncertainty factors also influence the amendment of boss, which leads to a higher or lower decision solution. So acceptable vector still works on equation (10). The elite strategy is used to update the boss's position. The description for elite strategy is like that if $\mathrm{dec}(\mathbf{m}_{g\ d}^{t+1})$ is higher than $\mathrm{dec}(\mathbf{m}_{g\ d}^{t})$, retain $\mathbf{m}_{g\ d}^{t+1}$; otherwise, retain $\mathbf{m}_{g\ d}^{t}$.

Step 7. Stop the iteration if the terminal condition $t = t_{\max}$ is satisfied; otherwise, go to Step 2.

Finally, the flow chart of the MTCO algorithm is illustrated in Figure 2.

The MTCO algorithm can increase the diversity of staff and make the leaders get rid of the over dependency on the global optimal decision solution effectively. The layered organization structure can make the staff follow more potential optimal decision solutions. Meanwhile, the boss of each iteration also takes part in making decision, which increases the exploitation ability for obtaining optimal decision solution. So in the following section, the MTCO algorithm would be verified for its global optimal decision ability.

2.2. Optimization Experiment and Comparison. Some well-known test functions are used for comparing the performances of different optimization algorithms. The commonly used test functions include the Schaffer function f_{Sch}, the Griewank function f_{Gri}, and the Rosenbrock function f_{Ros}, which are given as follows:

$$\begin{aligned} f_{\mathrm{Sch}} &= 0.5 + \frac{\left(\sin\sqrt{x_1^2 + x_2^2}\right)^2 - 0.5}{1 + 0.001\left(x_1^2 + x_2^2\right)},\\ f_{\mathrm{Gri}} &= \sum_{i=1}^{n}\frac{x_i^2}{4000} - \prod_{i=1}^{n}\cos\left(\frac{x_i}{\sqrt{i}}\right) + 1,\\ f_{\mathrm{Ros}} &= \sum_{i=1}^{n-1}\left[100\left(x_i^2 - x_{i+1}\right)^2 + \left(x_i - 1\right)^2\right]. \end{aligned} \tag{12}$$

The graphics of these functions in the three-dimensional coordinate are shown in Figure 3. f_{Sch} is a complex two-dimension function having countless local extremum. This can acquire the global extremum at the location of $(x_1, x_2) = (0, 0)$, so it is difficult to search the global extremum. f_{Gri} has lots of local extremum point. The global

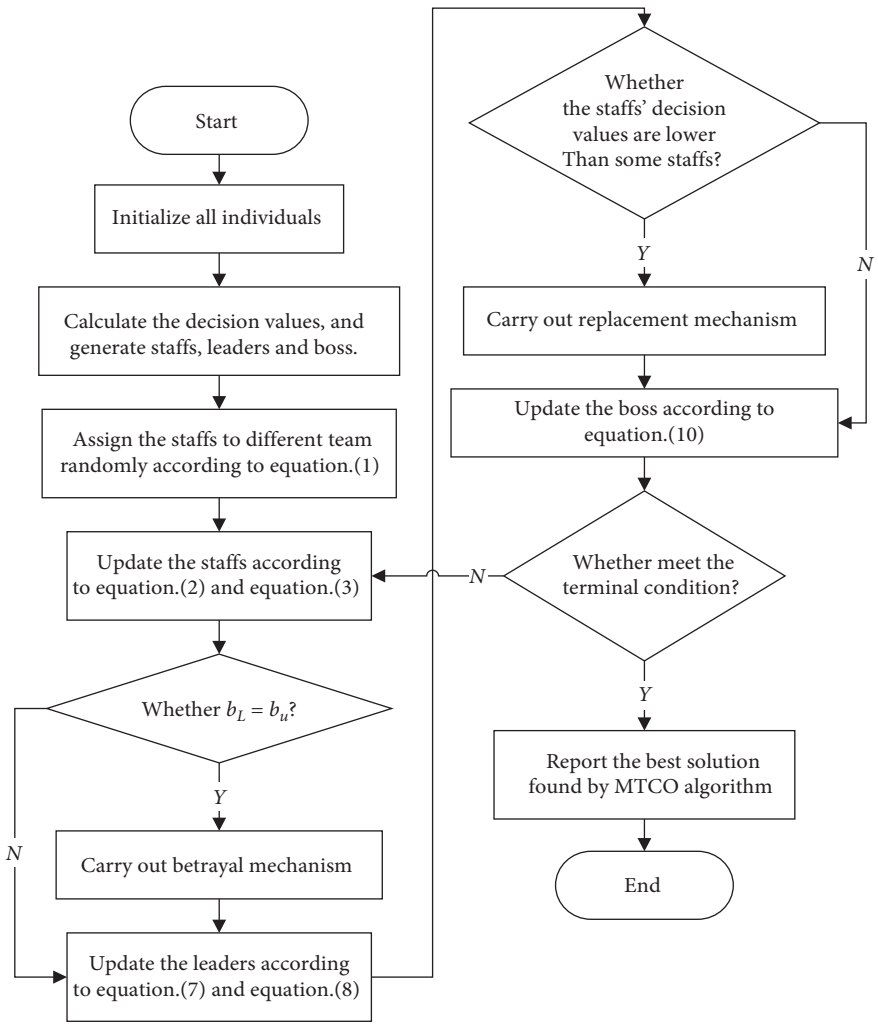

Figure 2: The flow chart of MTCO algorithm.

extremum is 0, which can be searched at the location of $(x_1, x_2, \ldots, x_n) = (0, 0, \ldots, 0)$. The Griewank function is a typical nonlinear multimode function, which is always regarded as a more complex optimization problem. As for f_{Ros}, its global extremum is located in a smooth and narrow area similar to valley formed by parabolas, and thus the information provided by f_{Ros} is limited that many optimization algorithms have a problem on the identification of searching direction.

The self-regulating PSO (SR-PSO) proposed by Tanweer et al. [12], the seeker optimization algorithm (SOA) proposed by Dai [18], and the ALC-PSO proposed by Singh et al. [19] were used to obtain relative better optimization results by imitating some human decision-making behaviors. Therefore, the MTCO algorithm will compare with them, besides Standard PSO (SPSO). The population size for all algorithms is 60, and the total iteration number is set as 600. As for the MTCO algorithm, the number of leaders is set as 3, $\omega_{\max}$ is set as 0.9, $\omega_{\min}$ is set as 0.2, ω_{rs} is set as 0.5, ω_{re} is set as $5e{-}5$, the b_L is set randomly in interval [80, 90], and the b_U is set randomly in interval [95, 100], b_L and b_U are both integers. How to set the parameters for other algorithms mentioned have been described in previous studies [12, 18, 19], and the terminal conditions is $t = t_{\max}$. At the same time, random settings are applied on initializing the parameters including velocities and positions. To compare the global optimal decision ability, the algorithms are calculated one hundred times repeatedly, which can verify the influence of randomness. Min, Mean, Max, and STD (Standard Deviation) of fitness values can be used for performance verification. Table 1 shows the comparison results for Schaffer, Griewank, and Rosenbrock functions, respectively.

These comparisons demonstrate that the proposed MTCO algorithm has much stronger decision-making ability than other algorithms. Its stable and reliable performance ensures that the global optimal decision solution can be obtained with higher probability. Accordingly, the MTCO can be applied on recognizing unknown fault patterns for the fault diagnosis of critical equipment.

3. Recognition Process of the MTCO Algorithm

3.1. The Recognition Principle. The recognition principle for recognizing the unknown fault patterns is shown in Figure 4.

As shown in Figure 4, there are two categories of data with two dimensions representing different patterns. Firstly,

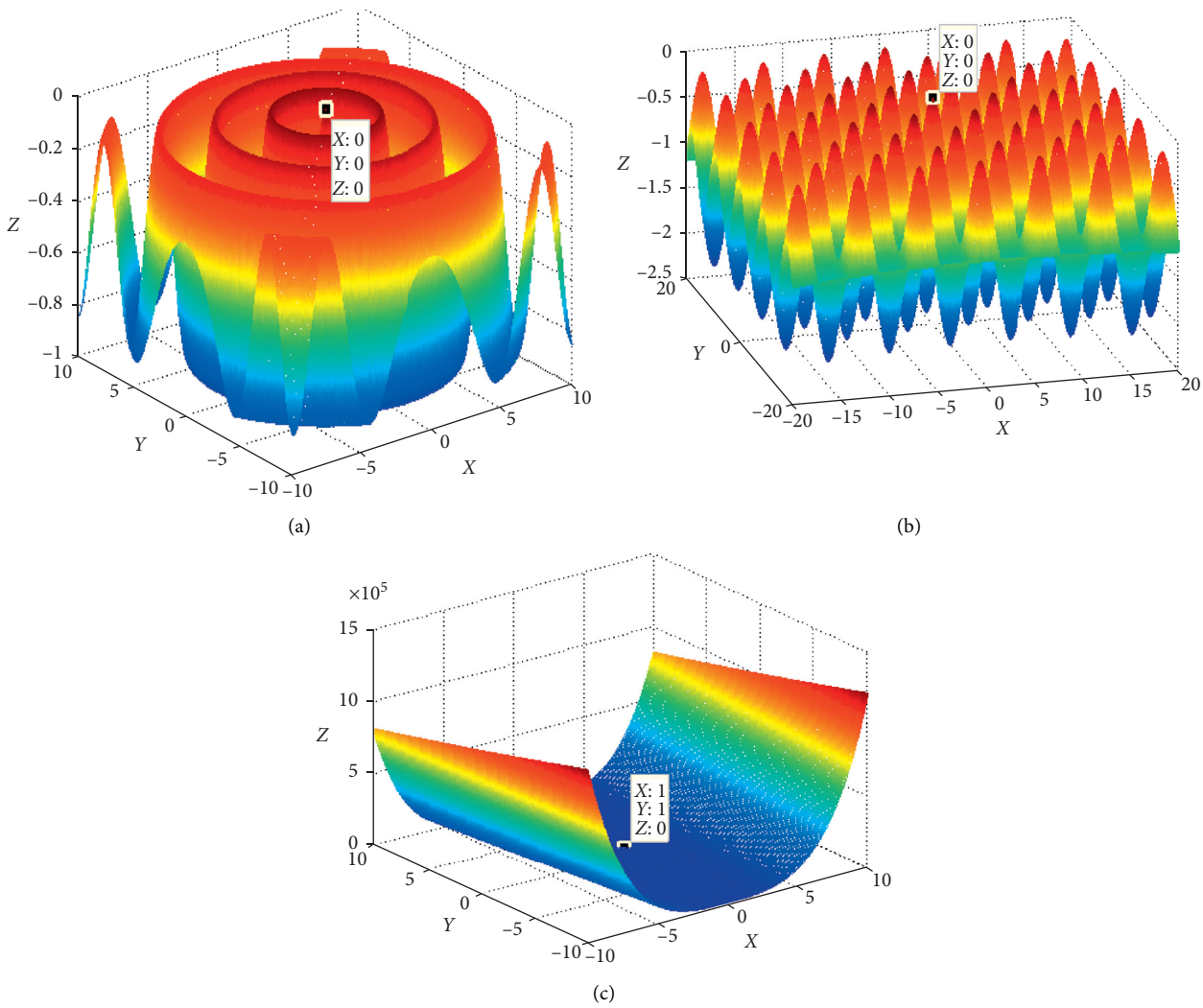

Figure 3: Graphics of three commonly used functions. (a) The graphic of the Schaffer function. (b) The graphic of the Griewank function. (c) The graphic of the Rosenbrock function.

Table 1: Comparison of MTCO and other algorithms when using the test functions.

Test function		Algorithm	Min	Mean	Max	STD
Schaffer	Search ranged: [−50, 50], dimension: 50	MTCO	0.0097	0.0185	0.0372	0.0130
		SRPSO	0.2277	0.3194	0.3961	0.0331
		ALCPSO	0.2727	0.3389	0.3961	0.0303
		SOA	0.0782	0.1060	0.1728	0.0262
		SPSO	0.2277	0.2990	0.3733	0.0333
Griewank	Search ranged: [−50, 50], dimension: 50	MTCO	$1.1171e{-}06$	0.0038	0.0296	0.0071
		SRPSO	$9.4550e{-}06$	0.0050	0.0392	0.0089
		ALCPSO	0.0139	0.0536	0.0984	0.0191
		SOA	0.0042	0.0177	0.0556	0.0123
		SPSO	0.0196	0.0406	0.0741	0.0125
Rosenbrock	Search ranged: [−50, 50], dimension: 50	MTCO	41.4554	57.3950	184.7532	27.5666
		SRPSO	41.6435	82.1011	458.1885	56.6290
		ALCPSO	131.7000	373.2552	$1.1812e+03$	188.4061
		SOA	54.2086	223.3483	$1.0162e+03$	214.7484
		SPSO	77.9133	379.2736	$1.2122e+03$	216.9144

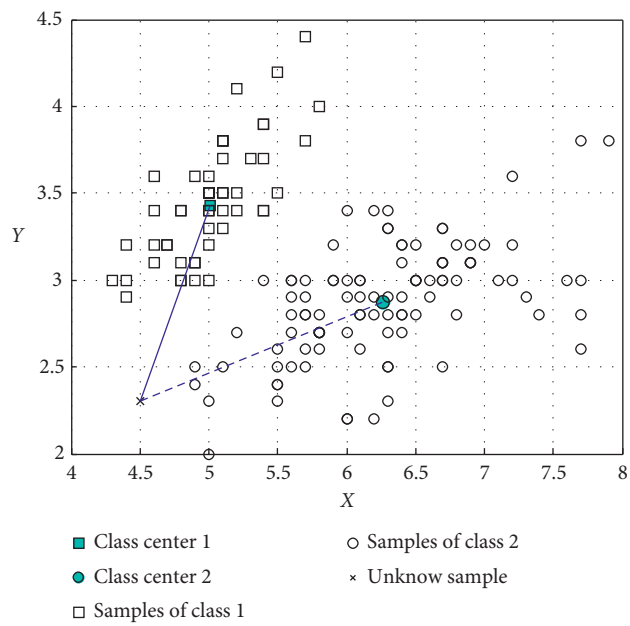

Figure 4: Example of recognition of an unknown sample.

a decision function is selected to determine an optimal class center for each category of data, and the class center need to meet three optimization conditions, that is, shorter intraclass distance, longer interclass distance, and higher recognition accuracy. Virtually, the intraclass distance is defined as the sum of distances from all known samples having the same class label to their class center. The interclass distance is defined as the sum of distances between all the class centers. And higher recognition accuracy means the proportion of the known samples classified into right categories. For an unknown sample, its recognition criterion still depends on the distance. That is to say, if the distance from an unknown sample to the center of Class 1 is the shortest, this unknown sample should be classified into this class. In this study, the Euclidean distance (ED) is used to express the distance between two samples, which can be calculated by

$$\begin{aligned}\mathrm{ED}_{ij} &= \left\|\mathbf{x}_i - \mathbf{x}_j\right\| = \sqrt{\left\|\mathbf{x}_i - \mathbf{x}_j\right\|^2} = \sqrt{\langle \mathbf{x}_i - \mathbf{x}_j, \mathbf{x}_i - \mathbf{x}_j \rangle} \\ &= \sqrt{\sum_{d=1}^{D}\left(x_{i\,d} - x_{j\,d}\right)^2},\end{aligned} \tag{13}$$

and the criterion can be expressed as follows:

$$\left(y_j\right)_{\text{catgory}} = \langle i | \mathrm{ED}_{ji} = \min\left(\mathrm{ED}_{j1} \ldots \mathrm{ED}_{ji} \ldots \mathrm{ED}_{jn_c}\right)\rangle, \tag{14}$$

where $\mathbf{y}_j$ is a unknown sample, n_c is the total number of classes, $\|\cdot\|$ is the 2-norm, $x_{i\,d}$ is the dth element of sample $\mathbf{x}_i$ and $x_{j\,d}$ is the dth element of sample $\mathbf{x}_j$.

As previously mentioned, the decision function should meet three conditions, and thus the proposed decision function is defined as

$$\mathrm{dec}(\mathbf{m}) = \frac{N_r}{N} + \frac{\sum_{i=1}^{n_c}\sum_{j=i}^{n_c}\left\|\mathbf{c}_i - \mathbf{c}_j\right\|}{\sum_{i=1}^{n_{c(j)}}\sum_{j=1}^{n_c}\left\|\mathbf{x}_i - \mathbf{c}_j\right\|}, \tag{15}$$

where $\mathbf{m}$ is a member, N is the total number of train samples, N_r is the number of train samples classified into the correct classes, $n_{c(j)}$ is the number of the train samples belonging to the jth class, and $\mathbf{c}_j$ is the jth class center vector. This is a maximization decision problem, and a larger value of decision function means the MTCO algorithm has stronger recognition ability for unknown samples.

3.2. Kernel Function in the MTCO Algorithm. A kernel function is paid more attention with the development of SVM. The kernel function must meet the Mercer condition and can combine the nonlinear mapping and inner-product of two vectors in feature space so that the nonlinear mapping is carried out implicitly. So the kernel function makes the mapping from the original space with nonlinear distribution to the high-dimension feature space with linear distribution, the latter of which can be realized easily and simply. RBF kernel and polynomial kernel are the most commonly used kernel functions [20], which are given as follows:

$$\begin{aligned}&\text{Polynomial kernel}: \cdot\, k\left(\mathbf{x}_i, \mathbf{x}_j\right) = \left(\mathbf{x}_i^T \mathbf{x}_j + 1\right)^{\gamma}, \\ &\text{RBF Kernel}: \cdot\, k\left(\mathbf{x}_i, \mathbf{x}_j\right) = \exp\left(-\frac{\left\|\mathbf{x}_i - \mathbf{x}_j\right\|^2}{2\sigma^2}\right).\end{aligned} \tag{16}$$

According to the Mercer condition, $k(\mathbf{x}_i, \mathbf{x}_j) = \langle \Phi(\mathbf{x}_i) \cdot \Phi(\mathbf{x}_j)\rangle$, where $\Phi(\cdot)$ is the mapping function [21], the ED of two samples can also calculated in feature space via mapped by $\Phi(\cdot)$, which can remove the influence of nonlinear distribution of data on the recognizing unknown samples, the ED in feature space can be calculated by

$$\begin{aligned}\mathrm{ED}_{ij} &= \left\|\Phi(\mathbf{x}_i) - \Phi\left(\mathbf{x}_j\right)\right\| = \sqrt{\left\|\Phi(\mathbf{x}_i) - \Phi\left(\mathbf{x}_j\right)\right\|^2} \\ &= \sqrt{\langle \Phi(\mathbf{x}_i) - \Phi\left(\mathbf{x}_j\right), \Phi(\mathbf{x}_i) - \Phi\left(\mathbf{x}_j\right)\rangle} \\ &= \sqrt{\langle \Phi(\mathbf{x}_i), \Phi(\mathbf{x}_i)\rangle - 2\langle \Phi(\mathbf{x}_i), \Phi\left(\mathbf{x}_j\right)\rangle + \langle \Phi(\mathbf{x}_i), \Phi(\mathbf{x}_i)\rangle} \\ &= \sqrt{k(\mathbf{x}_i, \mathbf{x}_i) - 2k\left(\mathbf{x}_i, \mathbf{x}_j\right) + k\left(\mathbf{x}_j, \mathbf{x}_j\right)}.\end{aligned} \tag{17}$$

Using equation (17), the decision function can be recalculated in feature space. After applying the kernel function, the data with linear distribution in feature space can be obviously conducive to recognition.

It is critical for mapping and decision-making, that how to choose an appropriate kernel function and determine corresponding kernel parameters. With the help of powerful optimization ability of the MTCO algorithm, it is easy to determine appropriate parameters for the kernel function. Kernel functions are generally categorized into two groups, including global kernel and local kernel. The former is more suitable for classification. The polynomial kernel is a typical

local kernel, and the RBF kernel is a typical global kernel. Due to $\|\mathbf{x}_i - \mathbf{x}_i\| = 0$, the RBF kernel is chosen for the MTCO algorithm. Equation (17) is then rewritten as follows:

$$\mathrm{ED}_{ij} = \sqrt{2 - 2k\left(\mathbf{x}_i, \mathbf{x}_j\right)}, \tag{18}$$

on the basis of equation (18), the decision function is rewritten as follows:

$$\mathrm{dec}\left(\mathbf{m}\right) = \frac{N_r}{N} + \frac{\sum_{i=1}^{n_c} \sum_{j=i}^{n_c} \sqrt{2 - 2k\left(c_i, c_j\right)}}{\sum_{i=1}^{n_{c(j)}} \sum_{j=1}^{n_c} \sqrt{2 - 2k\left(x_i, c_j\right)}}. \tag{19}$$

After calculating the optimal decision value in the high-dimension feature space, the Standard MTCO (S-MTCO) algorithm is transformed into Kernel MTCO (K-MTCO) algorithm.

3.3. Recognition Experiment and Comparison. To verify the recognition performance of the K-MTCO algorithm, several classic and typical data sets are used, whose relative information is listed in Table 2. All data sets are collected from University of California Irvine (UCI) machine-learning repository, whereas the train number and test number are selected randomly. In this study, some most widely used fault diagnosis classifiers such as SVM [22], back propagation (BP) network [23], and learning vector quantization (LVQ) network [24] besides S-MTCO algorithm are used to compare with the K-MTCO algorithm. From this, one may have the necessity of kernel function.

The setting for K-MTCO and S-MTCO is similar as such the population size is 80; the total iteration number is 800; the number of leaders is 6; $\omega_{\max}$ is 0.9; $\omega_{\min}$ is 0.2; ω_{rs} is 0.2; ω_{re} is 0.001; the b_L is set randomly in the interval [85, 90]; and the b_U is set randomly in interval [95, 100], the number of parameters optimized by the S-MTCO is $n_c \cdot D$, and optimized by K-MTCO is $n_c \cdot D + 1$, where '1' denotes the kernel parameter σ. The k-NN is sensitive to the parameter k, so we will verify the influence of difference values of k on the recognition. Besides $k = 1$ will be listed in the tables, we will also list the value of k that makes the recognition accuracy highest and lowest. As for the settings of the parameters and network structures of SVM, BP, and LVQ network, please refer to the references mentioned above. Especially, the error goals for BP and LVQ network are set as 0.001, and the iteration numbers for them are 2,000 and 500, respectively. All 4 data sets should be scaled to be in interval [0, 1], which can reduce the searching range and improve the algorithm's efficiency.

Tables 3 to 6 show the comparison results using different algorithms. Similarly, random settings also exist in the BP network, the LVQ network, and SVM, and the calculation is repeated 3 times for verifying the influence of the randomness on the recognition accuracy.

Tables 3 to 6 list the ratio between the samples recognized correctly and the total samples of each class. For example, in the second line of the row of the K-MTCO in Table 3, the notation '(31/33)' means that the second class has 33 samples, but only 31 samples are recognized correctly.

These results indicate that the MTCO algorithm is effectual and its accuracy is usually higher than other algorithms. The K-MTCO algorithm has the highest recognition performance. In the following section, the MTCO algorithm will be applied for the fault diagnosis of the bearing.

4. Application in Bearing Fault Diagnosis

Rolling element bearings may lead to fatal breakdowns and even unacceptably long-time maintenance stops if the faults occur [25] as the key components located between the stationary and rotating part of the motors. Therefore, it is significant to recognize unknown fault patterns accurately occurred in the bearings. In this section, some features are firstly extracted from vibration signals of bearing and then the MTCO algorithm is applied for the fault diagnosis of bearing.

4.1. Collection of Bearing Vibration Signals. The vibration signals are obtained from Case Western Reserve University (CWRU) bearing data center. As shown in Figure 5, the test stand consists of a 2 hp (horse power) motor, a torque transducer, and a dynamometer. The test bearings manufactured by Svenska Kullager Fabriken (SKF) support the motor shaft. Single-point faults were introduced to the test bearings using electro-discharge machining (EDM) with fault diameters of 0.007 inches and 0.021 inches. Vibration data are collected by accelerometers for normal bearings, single-point drive-end bearings defects which include outer race fault with defect size of 0.007 inches and 0.021 inches, inner race fault with defect size of 0.007 inches and 0.021 inches, and ball fault with defect size of 0.007 inches and 0.021 inches. Data are collected at 12,000 samples per second for drive-end bearing experiments. In this study, there are 7 original vibration signals covering the 7 drive end bearing conditions including 1 normal condition and 6 types' faults. Each original signal is divided into 100 subsignals with 12,000 data points.

4.2. Feature Extraction. Four time-domain features such as mean, root mean square (RMS), clearance factor and kurtosis factor are chosen here. In fact, mean describes the static character of the signal; RMS reflects the signal amplitude characteristic, and it is not sensitive to the early faults but with a good stability; clearance and kurtosis factor are dimensionless statistical parameters, which are sensitive to the early faults, but have worse stability. Based on the above consideration, these four features in time domain is chosen. Their expressions are shown in the following equations:

Table 2: Information on data sets.

Name	Dimensions	Categories	Train samples	Test samples	Area	Year
Wine	13	3	98 (34 + 38 + 26)	80 (25 + 33 + 22)	Physical	1991
Haberman's survival	3	2	121 (80 + 41)	105 (65 + 40)	Life	1999
Seeds	7	3	120 (40 + 40 + 40)	90 (30 + 30 + 30)	Life	2012
Indian liver patients	10	2	213 (106 + 107)	120 (60 + 60)	Life	2012

Table 3: The comparison of test samples recognition accuracy for wine.

Algorithm	Recognition accuracy 1	Recognition accuracy 2	Recognition accuracy 3
K-MTCO	97.5% (78/80) (25/25) (31/33) (22/22)	97.5% (78/80) (25/25) (31/33) (22/22)	97.5% (78/80) (25/25) (31/33) (22/22)
S-MTCO	97.5% (78/80) (25/25) (32/33) (21/22)	97.5% (78/80) (25/25) (32/33) (21/22)	96.25% (77/80) (25/25) (31/33) (21/22)
SVM	96.25% (77/80) (24/25) (32/33) (21/22)	97.5% (78/80) (25/25) (32/33) (21/22)	96.25% (77/80) (24/25) (32/33) (21/22)
BP	95% (76/80) (25/25) (29/33) (22/22)	95% (76/80) (25/25) (30/33) (21/22)	92.50% (74/80) (25/25) (29/33) (20/22)
LVQ	92.50% (74/80) (25/25) (27/33) (22/22)	92.50% (74/80) (25/25) (27/33) (22/22)	93.75% (75/80) (25/25) (28/33) (22/22)
k-NN	$k = 1$: 91.25% (73/80) (25/25) (27/33) (21/22)	$k = 15$: 96.25% (77/80) (25/25) (30/33) (22/22)	$k = 15$: 96.25% (77/80) (0/25) (33/33) (0/22)

Table 4: The comparison of test samples recognition accuracy for Haberman's survival.

Algorithm	Recognition accuracy 1	Recognition accuracy 2	Recognition accuracy 3
K-MTCO	69.52% (73/105) (60/65) (13/40)	69.52% (73/105) (61/65) (12/40)	69.52% (73/105) (60/65) (13/40)
S-MTCO	68.57% (72/105) (61/65) (11/40)	68.57% (72/105) (59/65) (13/40)	68.57% (72/105) (61/65) (11/40)
SVM	44.76% (47/105) (19/65) (28/40)	44.76% (47/105) (19/65) (28/40)	44.76% (47/105) (20/65) (27/40)
BP	67.62% (71/105) (62/65) (9/40)	60% (63/105) (48/65) (15/40)	58.10% (61/105) (50/65) (11/40)
LVQ	53.33% (56/105) (45/65) (11/40)	61.90% (65/105) (55/65) (10/40)	64.76% (68/105) (58/65) (10/40)
k-NN	$k = 1$: 53.33% (56/105) (33/65) (23/40)	$k = 10$: 67.62% (71/105) (58/65) (13/40)	$k = 3$: 49.52% (52/105) (31/65) (21/40)

Table 5: The comparison of test samples recognition accuracy for seeds.

Algorithm	Recognition accuracy 1	Recognition accuracy 2	Recognition accuracy 3
K-MTCO	97.78% (88/90) (29/30) (30/30) (29/30)	97.78% (88/90) (29/30) (30/30) (29/30)	97.78% (88/90) (28/30) (30/30) (30/30)
S-MTCO	95.56% (86/90) (27/30) (30/30) (29/30)	95.56% (86/90) (27/30) (30/30) (29/30)	95.56% (86/90) (27/30) (30/30) (29/30)
SVM	95.56% (86/90) (27/30) (30/30) (29/30)	95.56% (86/90) (27/30) (30/30) (29/30)	95.56% (86/90) (27/30) (30/30) (29/30)
BP	94.44% (85/90) (25/30) (30/30) (30/30)	95.56% (86/90) (26/30) (30/30) (30/30)	96.67% (87/90) (27/30) (30/30) (30/30)
LVQ	95.56% (86/90) (27/30) (29/30) (30/30)	94.44% (85/90) (27/30) (29/30) (29/30)	94.44% (85/90) (27/30) (29/30) (29/30)
k-NN	$k = 1$: 95.56% (86/90) (26/30) (30/30) (30/30)	$k = 4$: 97.78% (88/90) (28/30) (30/30) (30/30)	$k = 87$: 92.22% (83/90) (24/30) (30/30) (29/30)

Table 6: The comparison of test sample recognition accuracy for Indian liver patients.

Algorithm	Recognition accuracy 1	Recognition accuracy 2	Recognition accuracy 3
K-MTCO	73.33% (88/120) (30/60) (58/60)	74.17% (89/120) (30/60) (59/60)	73.33% (88/120) (35/60) (53/60)
S-MTCO	71.67% (86/120) (35/60) (51/60)	72.50% (87/120) (35/60) (52/60)	72.50% (87/120) (35/60) (52/60)
SVM	43.33% (52/120) (33/60) (19/60)	44.17% (53/120) (34/60) (19/60)	44.17% (53/120) (34/60) (19/60)
BP	50.83% (61/120) (28/60) (33/60)	43.33% (52/120) (28/60) (24/60)	55.83% (67/120) (33/60) (34/60)
LVQ	67.50% (81/120) (43/60) (39/60)	69.17% (83/120) (30/60) (53/60)	59.17% (71/120) (36/60) (35/60)
k-NN	$k = 1$: 52.50% (63/120) (29/60) (34/60)	$k = 34$: 67.50% (81/120) (21/60) (60/60)	$k = 3$: 47.50% (57/120) (24/60) (33/60)

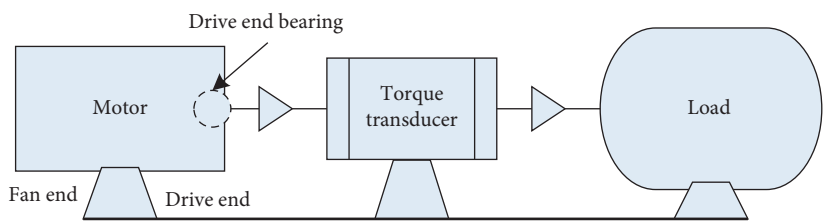

Figure 5: Schematic diagram of the experimental apparatus.

$$\mathbf{s}_{t\,(\mathrm{mean})} = \frac{1}{n_t}\sum_{i=1}^{n_t} s_i,$$
$$\mathbf{s}_{t\,(\mathrm{rms})} = \sqrt{\frac{1}{n_t}\sum_{i=1}^{n_t} s_i},$$
$$\mathrm{CL}_f\left(\mathbf{s}_t\right) = \frac{\max\left(\mathbf{s}_t\right)}{\left(\left(1/n_t\right)\sum_{i=1}^{n_t}\left|s_i\right|\right)^2},$$
$$K_f\left(\mathbf{s}_t\right) = \frac{\left(1/n_t\right)\sum_{i=1}^{n_t} s_i^4}{\left(s_{t\,(\mathrm{rms})}\right)^4}, \tag{20}$$

where n_t is the total number of data points, $\mathbf{s}_t$ is a time-domain signal, s_i is the ith data point of signal $\mathbf{s}_t$, and $\max(\mathbf{s}_t)$ is a function for calculating the maximum data point.

After applying the fast Fourier transform (FFT) to the signal $\mathbf{s}$, three features in frequency domain are calculated by the following equations:

$$F_1 = \frac{1}{n_f}\sum_{i=1}^{n_f} s_i,$$
$$F_2 = \frac{1}{n_f}\sum_{i=1}^{n_f}\left(s_i - F_1\right)^2, \tag{21}$$
$$F_3 = \frac{1}{n_f\cdot\sqrt{F_2^3}}\sum_{i=1}^{n_f}\left(s_i - F_1\right)^3,$$

where n_f is the total number of spectrum lines, $\mathbf{s}_f$ is a frequency-domain signal, and s_i is the ith data point of signal $\mathbf{s}_f$. F_1 describes the size of vibration energy in frequency domain, F_2 is deviation that reflect the dispersion or concentration of the spectrum, and F_3 also reflect the dispersion or concentration of the spectrum.

Table 7 shows the distribution of 7 different classes data. Each class data are divided in a proportion of 60% for training and 40% for testing randomly. Using the last six attributes, two three-dimensional data distribution of bearing conditions is shown in Figure 6. This indicates that the condition data have relatively better separability. Furthermore, Figure 6 also indicates that the feature extraction is helpful for recognizing these fault patterns. Before the recognition, an optimal single-class center is determined for each working condition.

4.3. Fault Diagnosis. Now, the MTCO algorithm is applied to recognize the bearing patterns. Substantially, the proposed algorithm can recognize multiclass fault patterns easily, whereas SVM is designed for recognizing the double-class problems [26]. So the MTCO algorithm can work well when coping with the multiclass fault patterns of bearing. In the subsection, the SVM [27], BP network [23], LVQ network [24], S-MTCO algorithm, and the swarm intelligence based on supervised PSO (S-PSO) classification algorithm [22] are compared with the K-MTCO algorithm, and the calculation is also repeated 3 times for the same purpose. The parameters for SVM are set according to ICDF (intercluster distance in the feature space) proposed by Zhang et al. [27], and the parameters for S-PSO classification algorithm are set according to the method proposed by Zheng and Gao [22].

Table 7: Description for bearing data.

The number of samples	For training	For testing	Defect size (inches)	Operation condition	Label
100	60	40		Normal	1
100	60	40	0.007	Outer race	2
100	60	40	0.021	Outer race	3
100	60	40	0.007	Inner race	4
100	60	40	0.021	Inner race	5
100	60	40	0.007	Ball	6
100	60	40	0.021	Ball	7

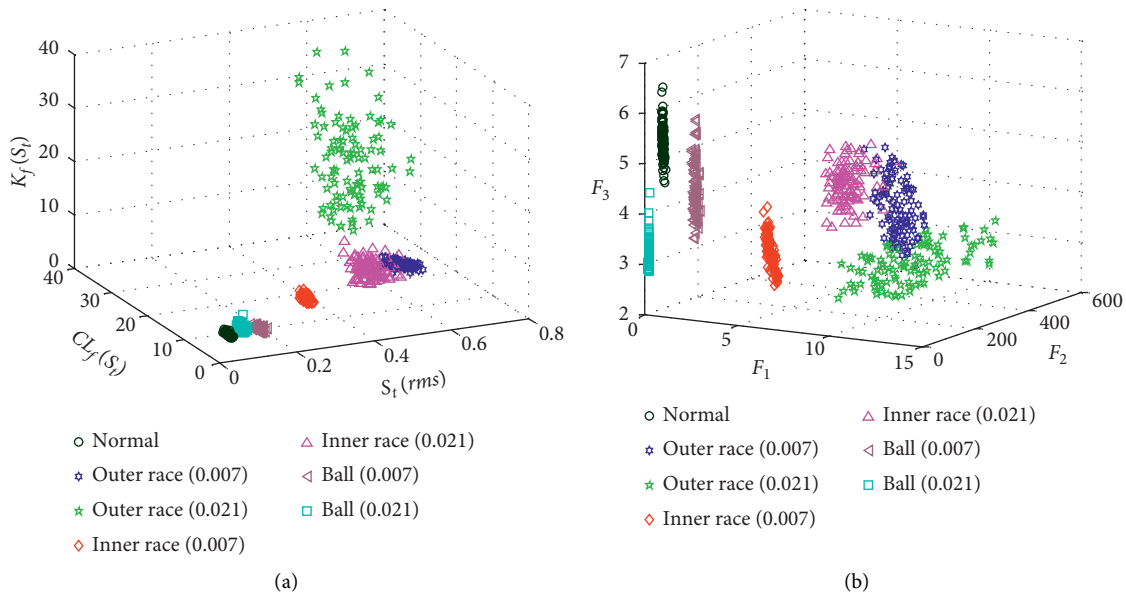

Figure 6: Data distribution of bearing faults: (a) time-domain feature distribution and (b) frequency-domain feature distribution.

Table 8: The comparison of test sample recognition accuracy for bearing data.

Algorithm	Recognition accuracy 1	Recognition accuracy 2	Recognition accuracy 3
K-MTCO	99.64% (279/280)	99.64% (279/280)	99.64% (279/280)
S-MTCO	99.29% (278/280)	99.29% (278/280)	99.29% (278/280)
SVM	98.93% (277/280)	98.93% (277/280)	98.93% (277/280)
BP	99.29% (278/280)	98.57% (276/280)	98.93% (277/280)
LVQ	84.64% (237/280)	85.71% (240/280)	85.00% (238/280)
S-PSO	98.93% (277/280)	98.21% (275/280)	98.21% (275/280)

The parameters for other algorithms are as same as that in Section 3.3.

The comparison results shown in Table 8 demonstrate that the MTCO algorithm, especially the K-MTCO algorithm, consistently has higher recognition accuracy than other algorithms. And the results calculated by the K-MTCO algorithm are quite a remarkable achievement from an engineering point of view. So this stable and reliable global optimal decision ability completely makes the proposed algorithm powerful for bearing fault diagnosis.

5. Conclusion

In this paper, a novel MTCO algorithm has been proposed. The optimization and recognition performance of the MTCO algorithm is evaluated using different typical characteristic test functions and data sets. The comparisons have been made with various commonly used intelligence algorithms based on human behaviors and pattern recognition. From the results, it can be seen that the MTCO algorithm performs consistently better than other human behavior-based algorithms, such as SRPSO, ALCPSO, SOA, SPSO. Moreover, it can also be concluded that the proposed algorithm has a stable and reliable global optimal decision-making ability. Finally, the MTCO algorithm is applied to identify multiple bearing faults. The recognition results indicate that the recognition accuracy calculated by the MTCO algorithm is better and higher than other commonly used algorithms including SVM, BP, and LVQ especially when the kernel function is introduced to the proposed algorithm.

Data Availability

The data used to support the findings of this study are included within the article.

Disclosure

The funders had no role in the design of the study; in the collection, analyses, or interpretation of data; in the writing of the manuscript; or in the decision to publish the results.

Conflicts of Interest

The authors declare no conflict of interest.

Acknowledgments

This research was supported by Sichuan Science and Technology Program, grant numbers 2019YJ0395 and 2021YJ0519, China Civil Aviation Administration Development Foundation Educational Talents Program (14002600100018J034), General Foundation of Civil Aviation Flight University of China (2019-053), Youth Foundation of Civil Aviation Flight University of China (Q2018-139).

References

[1] K. Li, P. Chen, and S. Wang, "An intelligent diagnosis method for rotating machinery using least squares mapping and a fuzzy neural network," *Sensors*, vol. 12, no. 5, pp. 5919–5939, 2012.

[2] Y. F. Li, H. Z. Huang, N. Liu, and H. Xiao, "A new fault tree analysis method: fuzzy dynamic fault tree analysis," *Eksploatacja I Niezawodnosc-Maintenance and Reliability*, vol. 14, no. 3, pp. 208–214, 2012.

[3] H.-Z. Huang, Y. Liu, Y. Li, L. Xue, and Z. Wang, "New evaluation methods for conceptual design selection using computational intelligence techniques," *Journal of Mechanical Science and Technology*, vol. 27, no. 3, pp. 733–746, 2013.

[4] H.-Z. Huang, H.-K. Wang, Y.-F. Li, L. Zhang, and Z. Liu, "Support vector machine based estimation of remaining useful life: current research status and future trends," *Journal of Mechanical Science and Technology*, vol. 29, no. 1, pp. 151–163, 2015.

[5] B. Zheng, H. Gao, X. Ma, and X. Zhang, "Graph partition based on dimensionless similarity and its application to fault diagnosis," *IEEE Access*, vol. 9, pp. 35573–35583, 2021.

[6] S.-F. Yuan and F.-L. Chu, "Fault diagnostics based on particle swarm optimisation and support vector machines," *Mechanical Systems and Signal Processing*, vol. 21, no. 4, pp. 1787–1798, 2007.

[7] B. Zheng and X. Ma, "Application on damage types recognition in civil aeroengine based on SVM optimized by DMPSO," *Computer Science*, vol. 47, no. 11A, pp. 132–138, 2020.

[8] M. Korürek and B. Doğan, "ECG beat classification using particle swarm optimization and radial basis function neural network," *Expert Systems with Applications*, vol. 37, no. 12, pp. 7563–7569, 2010.

[9] L. Lu, J. Yan, and C. W. de Silva, "Dominant feature selection for the fault diagnosis of rotary machines using modified genetic algorithm and empirical mode decomposition," *Journal of Sound and Vibration*, vol. 344, pp. 464–483, 2015.

[10] W. Shang, X. Zhou, and J. Yuan, "An intelligent fault diagnosis system for newly assembled transmission," *Expert Systems with Applications*, vol. 41, no. 9, pp. 4060–4072, 2014.

[11] B. Zheng, *Research on Aeroengine Fault Diagnosis and Performance Parameters Prediction Based on Particle Swarm Optimization*, University of Electronic Science and technology, Chengdu, China, 2018.

[12] M. R. Tanweer, S. Suresh, and N. Sundararajan, "Self regulating particle swarm optimization algorithm," *Information Sciences*, vol. 294, pp. 182–202, 2015.

[13] R. Cheng and Y. Jin, "A social learning particle swarm optimization algorithm for scalable optimization," *Information Sciences*, vol. 291, pp. 43–60, 2015.

[14] Y. Li, Z.-H. Zhan, S. Lin, J. Zhang, and X. Luo, "Competitive and cooperative particle swarm optimization with information sharing mechanism for global optimization problems," *Information Sciences*, vol. 293, pp. 370–382, 2015.

[15] B. Zheng, X. Ma, H. Y. Gao, and X. Q. Zhang, "Direct position updating-based trying-mutation particle swarm optimization algorithm and its application on reliability optimization," *Mechanical Science and Technology for Aerospace Engineering*, vol. 40, no. 1, pp. 155–164, 2021.

[16] F.-Q. Lu, M. Huang, W.-K. Ching, and T. K. Siu, "Credit portfolio management using two-level particle swarm optimization," *Information Sciences*, vol. 237, pp. 162–175, 2013.

[17] H. Wang, H. Sun, C. Li, S. Rahnamayan, and J.-s. Pan, "Diversity enhanced particle swarm optimization with neighborhood search," *Information Sciences*, vol. 223, pp. 119–135, 2013.

[18] C. H. Dai, *Seeker Optimization Algorithm and Its Application*, Southwest Jiaotong University, Chengdu, China, 2009.

[19] R. P. Singh, V. Mukherjee, and S. P. Ghoshal, "Optimal reactive power dispatch by particle swarm optimization with an aging leader and challengers," *Applied Soft Computing*, vol. 29, pp. 398–309, 2015.

[20] G. Mehmet and A. Ethem, "Cost-conscious multiple kernel learning," *Pattern Recognition Letters*, vol. 31, pp. 959–965, 2010.

[21] V. N. Vapnik, "An overview of statistical learning theory," *IEEE Transactions on Neural Networks*, vol. 10, no. 5, pp. 988–999, 1999.

[22] B. Zheng and F. Gao, "Fault diagnosis method based on S-PSO classification algorithm," *Acta Aeronautica et Astronautica Sinica*, vol. 36, no. 11, pp. 3640–3651, 2015.

[23] J. Ben Ali, N. Fnaiech, L. Saidi, B. Chebel-Morello, and F. Fnaiech, "Application of empirical mode decomposition and artificial neural network for automatic bearing fault diagnosis based on vibration signals," *Applied Acoustics*, vol. 89, pp. 16–27, 2015.

[24] B. Biswal, M. Biswal, S. Hasan, and P. K. Dash, "Nonstationary power signal time series data classification using LVQ classifier," *Applied Soft Computing*, vol. 18, pp. 158–166, 2014.

[25] C. Shen, D. Wang, F. Kong, and P. W. Tse, "Fault diagnosis of rotating machinery based on the statistical parameters of wavelet packet paving and a generic support vector regressive classifier," *Measurement*, vol. 46, no. 4, pp. 1551–1564, 2013.

[26] K. Zhu, X. Song, and D. Xue, "A roller bearing fault diagnosis method based on hierarchical entropy and support vector machine with particle swarm optimization algorithm," *Measurement*, vol. 47, pp. 669–675, 2014.

[27] X. Zhang, D. Qiu, and F. Chen, "Support vector machine with parameter optimization by a novel hybrid method and its application to fault diagnosis," *Neurocomputing*, vol. 149, pp. 641–651, 2015.

Hindawi
Mathematical Problems in Engineering
Volume 2021, Article ID 7919264, 8 pages
https://doi.org/10.1155/2021/7919264

Research Article

Integrated Technical and Economical Methodology for Assessment of Undeveloped Shale Gas Prospects: Applying in the Lurestan Shale Gas, Iran

Reza Abdollahi,[1] **Seyed Mahdia Motahhari**,[1] **and Hamid Esfandyari**[2]

[1]*EOR Research Department, Research Institute of Petroleum Industry, Tehran, Iran*
[2]*Abadan Faculty of Petroleum Engineering, Petroleum University of Technology, Abadan, Iran*

Correspondence should be addressed to Hamid Esfandyari; esfandyari_shirazu@yahoo.com

Received 22 May 2021; Revised 27 June 2021; Accepted 29 June 2021; Published 8 July 2021

Academic Editor: Mohammad Yazdi

Shale gas resources can supply the substantial growing demand for clean energy. In comparison with conventional reservoirs, shale gas reservoirs have lower production potential, and selecting the most favorable areas from the broad region of shale gas prospect is very crucial in commercial development. These areas are screened regarding some key evaluation indicators that affect the ultimate recovery of shale gas reservoirs. Many attempts have been made to screen sweet spots by applying the different evaluation indicators. These studies mainly focus on geological sweet spot identification without considering the economic indicators that may influence the order of geological sweet spots for development. The current study introduces a methodology for selecting the best techno-economic spots in undeveloped shale gas regions by integrating the technical and economic criteria. The techno-economic areas are defined as the geological sweet spots with the highest rate of return under the currently employed technology. The economic objective functions for selecting these areas are net present value, internal rate of return, and payback time. To estimate the unknown features for integrating the technical and economic criteria in undeveloped areas, an analogy study is applied. Due to the large number of unknowns and uncertainties in shale gas evaluation and low confidence of deterministic results, a probabilistic approach is used. As the first attempt in shale gas assessment in Iran, the Lurestan shale gas region is evaluated by applying this approach. The results indicate that no selected geological sweet spots in this region are commercial regarding the current cost rates and the available technology in Iran, and it can be considered as a future affordable source of energy.

1. Introduction

Conventional reservoirs dwindle in parallel with rising energy demands. Many techniques and approaches (reservoir-based and well-based) have been applied to enhance the ultimate recovery of available conventional reservoirs [1–7]. One of the main substitutes for conventional reservoirs are unconventional resources, especially shale gas resources [8]. In recent years, with the development of horizontal drilling and hydraulic fracturing, shale gas reservoirs have an essential share in the energy portfolio [9, 10].

Shale gas reservoirs are more complicated with respect to conventional reservoirs because they have more complex nature and the broader prospect region. Hence, quantification and production of these resources encounter a higher risk [11]. To reduce the risk in shale gas production, favorable areas with better geological and reservoir properties are selected for exploration of drillings and development. These areas are known as sweet spots [11–16].

Total organic carbon (TOC), effective shale thickness, depositional depth, gas content, thermal maturity (Ro), mineral contents, and mechanical properties are the most common criteria usually applied to screen the broad shale gas region for selecting the sweet spots [11–16]. Many attempts have been conducted by various means to identify sweet spots in shale gas regions [16–24].

Successful exploration and development of shale gas reservoirs have started in North America. Other countries

lag far behind the U.S. in developing shale gas with early exploration stages or production on small scales and regard it as a future energy source [10]. Shale gas regions with different exploration degrees need different assessment approaches for greater exploration and appraisal activity. The analogy study is suggested for areas with limited data and low exploration degree [25]. Usually, undeveloped shale gas regions are compared with developed shale plates in U.S. and Canada. The analogy study can be categorized as qualitative, semiquantitative, and quantitative [26–30].

All these researches tie some set of favorable properties to locating shale gas sweet spots without conducting the economic assessment. The geological sweet spots are not necessarily commercial, and geologic evaluation should be tied for economic evaluation. These disciplines traditionally have not been integrated in techno-economic shale gas evaluation, especially in undeveloped regions with many unknowns.

The current study introduces an approach for locating the best techno-economic shale gas regions in undeveloped regions. The geological sweet spots were screened regarding the key geological indicators in shale gas evaluation. The analogy study was used to estimate unknown necessary parameters for integrating the geologic and economic criteria to locate the best techno-economic area and estimating the value of economically recoverable reserve (ERR). The geological sweet spots were economically assessed by evaluating net present value (NPV), IRR, and payback time through a probabilistic approach ($P10$, $P50$, and $P90$). As a case study, the Lurestan shale gas region was assessed by applying the aforementioned approach. The economic analysis was conducted regarding the unit cost rates in Iran.

2. Methodology

The approach presented here is designed to locate the best techno-economic shale gas areas in undeveloped regions. Figure 1 represents the workflow of the presented approach. This approach includes six phases as follows:

(i) Identification of geological sweet spots
(ii) Analogy study
(iii) Estimation of drainage area and required well number
(iv) Estimation of the technically recoverable reserve (TRR), and estimated ultimate recover per well (EUR/well)
(v) Production profile estimation
(vi) Economic analysis

2.1. Identification of Geologic Sweet Spots. The geological sweet spots are regions thicker than 30 m with TOC content above 2 wt.%, gas content above 2.5 m^3/tone, and Ro greater than 1.2 wt.%. These cutoff values are used regularly in shale gas evaluation [11, 20].

2.2. Analogy Study. Since there is no production data in undeveloped shale gas regions, the analogous shale plate with high exploration level and abundant data can provide the necessary data (average production profile of a well, recovery factor (RF), and average horizontal leg section length) for techno-economic evaluation of undeveloped shale gas regions. The criteria usually utilized for analogy study are brittle mineral percentage, clay content, free to adsorbed gas ratio, pressure gradient, effective reservoir thickness, and fracture intensity.

2.3. Estimation Drainage Area and Required Well Number. For economic evaluation of selected geological sweet spots, estimating the drainage area of each well and consequently calculating the required number of wells in each spot is necessary. In shale gas reservoirs, the drainage area is typically constrained around the fracture network area due to extremely low matrix permeability.

Dong et al., by analyzing many shale gas wells and plays in the United States, established a typical width for the drainage area of the shale gas reservoir to be 1000 ft, and for both ends, the margin from the end of the horizontal well to the boundary of the drainage area was established to be 400 ft (Figure 2). [31]. Regarding the Dong assumption, the drainage area (D_w) of the well with the horizontal leg section length of HL can be calculated by equation (1). Thus, the well spacing depends on the lateral length of the shale well:

$$D_w = 1000 * (\mathrm{HL}(\mathrm{ft.}) + 800). \tag{1}$$

The drainage area determines the required number of wells (W_n) in each geological sweet spot. Equation (2) shows how W_n is calculated. In this equation, A_{gs} is the area of each geological sweet spot.

$$W_n = \frac{A_{gs}}{D_w}. \tag{2}$$

2.4. Estimation of the TRR and EUR/Well. TRR is the amount of technically recoverable gas and is estimated by multiplying the original gas in place (OGIP) by RF (equation (3)). The RF is extracted from an analogous shale plate because there is not any choice to estimated RF in undeveloped shale gas region:

$$\mathrm{TRR} = \mathrm{OGIP} * \mathrm{RF}. \tag{3}$$

Regarding the values of W_n and TRR, the value of EUR/Well is calculated by the following equation:

$$\frac{\mathrm{EUR}}{\mathrm{Well}} = \frac{\mathrm{TRR}}{W_n}. \tag{4}$$

2.5. Production Profile Estimation. The production profile in each geological sweet spot can be estimated from its analogous shale plate. Regarding the general shape of the analogous shale plate and the estimated EUR/well in each spot, the production profile is adjusted so that the area under

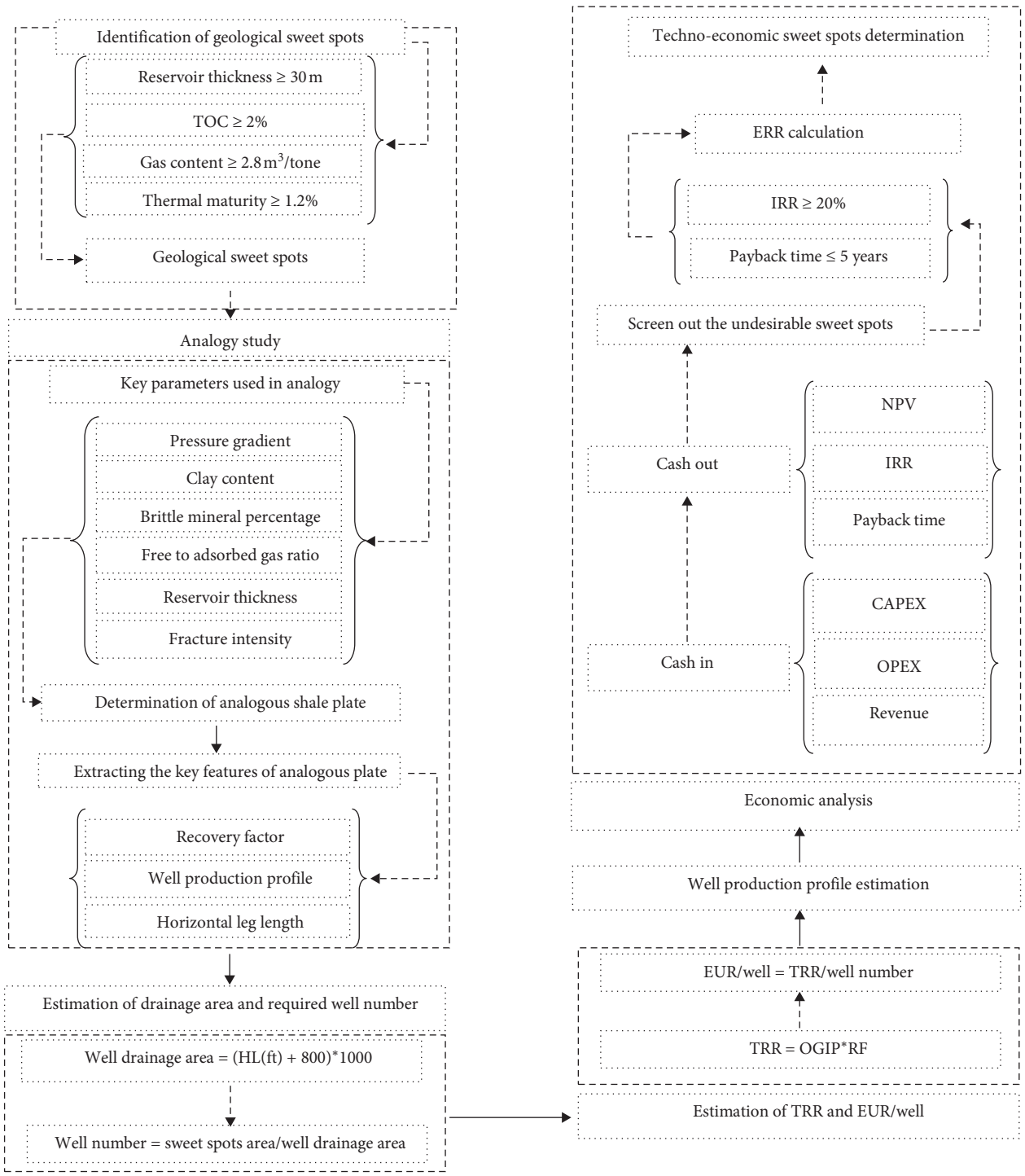

Figure 1: The methodology of techno-economic sweet spot identification.

the production profile matches the estimated EUR/well through 25 years (Figure 3). The area under the production profile curve is equal to the estimated EUR/well.

2.5.1. Economic Analysis. Economic analysis is the last step in selecting the best techno-economic areas in undeveloped shale gas regions. Objective functions in the economic assessment are NPV, IRR, and payout time. Regarding the Madani and Holditch (2011) approach, each geological sweet spot with IRR greater than 20% and a maximum 5-year payout is economical. ERR is the amount of economically recoverable gas in the techno-economic spot. The economic evaluation is conducted applying a probabilistic approach, which regards the uncertainty of input data, including gas price, capital expenditure (CAPEX), operational expenditure (OPEX), RF, and discount rate (DR). CAPEX in shale gas mainly includes costs related to rig, casing/cementing,

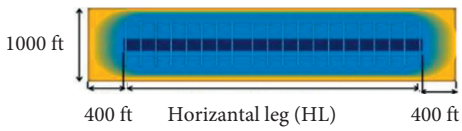

Figure 2: Well drainage in shale gas well [31].

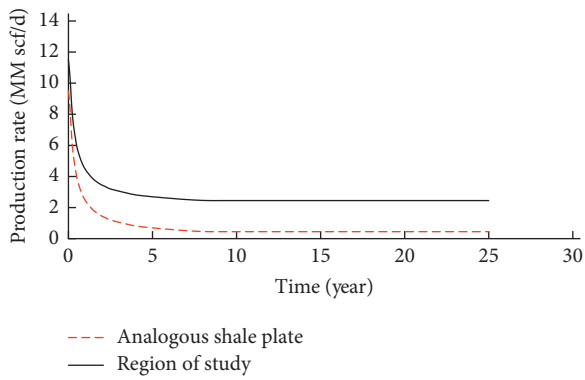

Figure 3: Adjusting the production profile of well based on the analogous shale plate and its EUR/well.

fracking, and completion fluid/proppant. OPEX is related to water disposal, labors, pumping/compression energy costs, gathering, transport, and processing costs.

3. Case Study

3.1. Geological Setting. In comparison with North America, a few research studies have been conducted on shale gas resources in the Middle East [32]. Recent investigations of shale gas reservoirs in Iran led to the recognition of two main organic-rich shale formations ($S1$ and $S2$) within the Lurestan area [32–37]. This prospect is a part of the Zagros fold-thrust belt and is confined with Zagros reverse fault and Dezful embayment [34, 38, 39]. This prospect is widely extended, and since there is no production test, a reliable strategy for assessing the prospect and selecting the best techno-economic regions with the usual development costs in Iran is needed.

4. Results and Discussion

The defined cutoff for reservoir thickness, thermal maturity, TOC, and gas content were applied in the Lurestan region to screen the desirable geological areas for further assessment. These cutoffs were applied in the existing static model of the Lurestan region to screen out the unfavorable areas. Shale gas production requires a significant amount of water for fracturing, and the availability of water has a direct effect on the economics of shale gas production. In this study, the assumption is that the required water is supplied from adjacent rivers and water wells. Figure 4 shows the locations of 21 selected geological sweet spots with respect to the protected areas, gas trunk lines, rivers, and water wells. Green areas represent desirable areas, and unfavorable cells are shown in gray color.

To extract the necessary data for further economic analysis, the $S1$ and $S2$ formations in the prospect region were compared by some devolved shale plates, including Fayettville, Marcellus, Haynesville, Utica, Muskwa, Eagle Ford, Barnett, Bossier, and Montney. Many comparison criteria can be select for analogy study. The selection of criteria depends on the objective functions. The main objective functions for finding the analogous shale plate are to extract two key features (production profile and RF). Since these features mainly relate to production potential of shale plates, the parameters, which have the direct effect on production potential, are selected. Figure 5 depicts the normalized value of the comparative criteria including, clay content (C), brittle mineral percentage (BI), adsorbed gas ratio (A), effective reservoir thickness (H), pressure gradient (PG), and fracture intensity (FI) in $S1$ and $S2$ formations and the aforementioned plates.

Applying equation (5) for commutative criteria shows that the Eagle Ford shale plate has the least difference with $S1$ and $S2$ formations, and this shale plate was considered as the analog in further assessment of the Lurestan shale gas region (Table 1).

$$\text{analogous plate} = \text{Min}\left(\left(C_{\text{Plate}} - C_S\right)^2 + \left(BI_{\text{Plate}} - BI_S\right)^2 + \left(A_{\text{Plate}} - A_S\right)^2 + \left(H_{\text{Plate}} - H_S\right)^2 + \left(PG_{\text{Plate}} - PG_S\right)^2 + \left(FI_{\text{Plate}} - FI_S\right)^2\right)^{0.5}. \quad (5)$$

The average RF in the Eagle Ford shale plate is 31% (probability distribution of RF is Pearson 5), and the average length of the horizontal leg in the Eagle Ford shale wells is about 6655 ft. [40]. Regarding these values and by applying equations (1) to (4), the values of D_w, W_n, TRR, and EUR/well in each geological sweet spot was calculated. Table 2 represents the exact value of W_n and P10–P50–P90 values of TRR and EUR/well for all geological sweet spots.

The last phase in the techno-economic evaluation of shale gas is the economic analysis and, subsequently, estimating the ERR. The required well number per year depends to production strategy. The production strategy in this study is to have a maximum allowable plateau for 25 years in each geological spot. Hence, the required wells (Table 2) in each spot were planned regarding this strategy. Considering this assumption, the plateau rate and the required well number per year in all geological sweet spots were estimated. Figure 6 shows the plateau rate in selected geological sweet spots.

Table 3 summarizes the selected economic input (considering the unit costs in Iran) in the cash flow model. The drilling cost for each well is estimated regarding a single wellbore, which completed in two $S1$ and $S2$ formations.

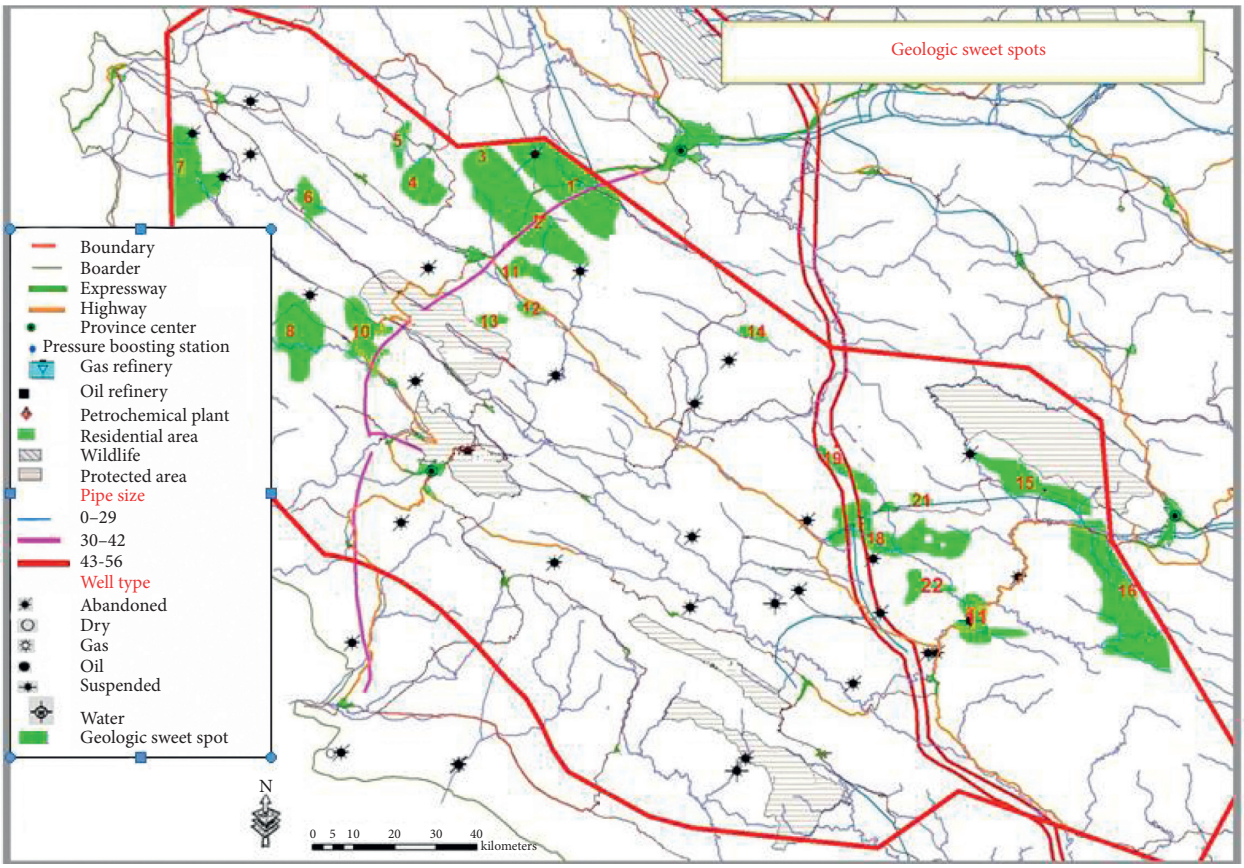

Figure 4: Locations of geological sweet spots.

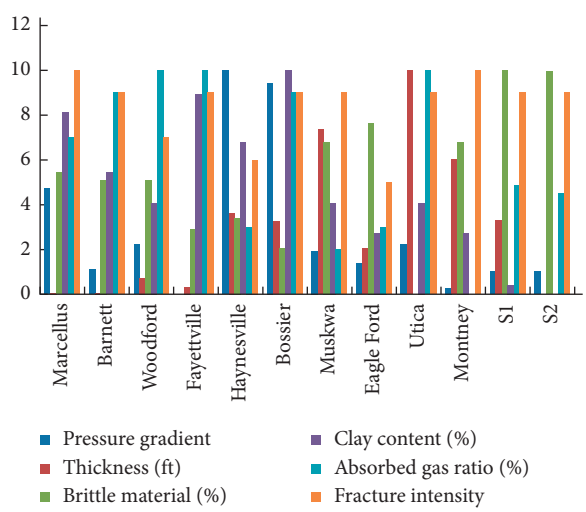

Figure 5: The normalized value of critical characteristics used for analogy study.

Table 1: Comparison of $S1$ and $S2$ formations with developed shale plates in the USA and Canada.

Shale plate	Marcellus	Barnett	Woodford	Fayettville	Haynesville	Bossier	Muskwa	Eagle Ford	Utica	Montney
$S1$	10.42	8.74	8.46	12.6	12.96	15.58	7.01	4.01	13.64	4.27
$S2$	10.3	8.56	8.51	12.68	13.59	16.25	9.36	4.4	15.73	8.63

Table 2: W_n and P10–P50–P90 values of TRR and EUR/well in geological sweet spots.

Spot no.	W_n	TRR (TCF)			EUR (BCF/well)		
		P_{90}	P_{50}	P_{10}	P_{90}	P_{50}	P_{10}
1	458	3.01	3.74	4.82	6.58	8.16	10.53
2	247	1.33	1.65	2.13	5.38	6.68	8.62
3	257	1.23	1.52	1.97	4.78	5.93	7.65
4	130	0.85	1.05	1.36	6.53	8.10	10.45
5	45	0.24	0.30	0.39	5.36	6.65	8.58
6	69	0.48	0.60	0.78	7.02	8.71	11.23
7	241	1.06	1.31	1.69	4.39	5.44	7.02
8	263	1.42	1.76	2.28	5.41	6.71	8.65
9	61	0.25	0.31	0.40	4.13	5.12	6.60
10	175	0.94	1.17	1.51	5.39	6.68	8.62
11	61	0.38	0.47	0.61	6.23	7.73	9.97
12	36	0.17	0.21	0.27	4.66	5.77	7.45
13	32	0.26	0.32	0.41	8.05	9.99	12.89
14	33	0.17	0.21	0.27	5.12	6.35	8.20
15	215	0.83	1.03	1.32	3.85	4.77	6.16
16	520	2.09	2.59	3.34	4.02	4.98	6.43
17	147	0.49	0.61	0.79	3.37	4.17	5.39
18	352	1.45	1.80	2.33	4.13	5.12	6.61
19	81	0.41	0.51	0.65	5.04	6.25	8.06
20	68	0.21	0.26	0.33	3.05	3.78	4.88
21	26	0.10	0.13	0.16	3.93	4.87	6.29

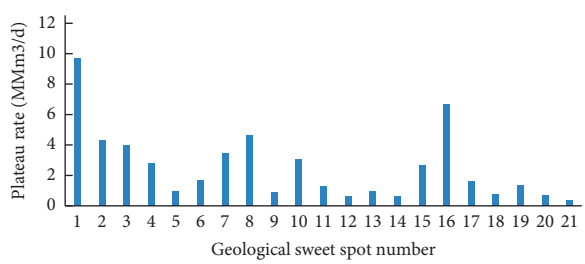

Figure 6: Plateau rate in selected geological sweet spots.

Table 3: $P10$–$P50$–$P90$ values of economic parameters and RF.

Name	Function	Mean	P_{10}	P_{50}	P_{90}
Completion unit cost (MM$/stage)	Normal	0.22	0.25	0.22	0.22
Drilling unit cost ($/ft)	Normal	610	692	610	527
Horizontal/vertical drilling price	Normal	1.11	1.22	1.11	1.1
OPEX ($/Mscf)	Normal	1.38	1.54	1.38	1.38
Gas price ($/Mscf)	Triangle	4.22	3	3.5	5.66
DR (%)	Normal	15	18	15	12
RF (%)	Pearson 5	32.16	25	31	40

Since unit costs and economic parameters may vary depending on many conditions, the probability distribution of these parameters was used in the economic analysis. The completion costs should be regarded based on the real expected costs in the case study. However, there is not any experience in Iran about the hydraulic fracturing and related completion costs; the best decision is to select these costs regarding the analogous shale plates, which was applied in this study. The $P10$, $P50$, and $P90$ values for the gas price were selected regarding the total gas price delivered to Iranian petrochemical, international energy hub, and the real price of exported gas from Iran to neighboring countries. Drilling and completion costs were determined by multiplying specific well design factors (measured depth and number of the fracking stage) by their specific rates (drilling ($/ft) and completion ($/Stage)). Other well-cost components have a minor contribution to the capital costs as they usually amount to less than half a million dollars. They comprise equipment to push the products to gathering lines, roads, pumps, compressors, and flow lines. These costs were estimated based on their contributions in Eagle Ford shale plate development. The total well cost was obtained by the sum of all of these subordinate costs. Regarding the contribution of major components of OPEX in the Eagle Ford shale plate and by adjusting these components, a range of 1.3 to 1.55 with an average of 1.38 $/Mscf was considered for operating cost in the economic evaluation of geological sweet spots in the current study.

Table 4: NPV values in developing geological sweet spots.

Spot no.	NPV (MMM$)		
	P_{10}	P_{50}	P_{90}
1	−3.32	−2.18	−0.66
2	−1.85	−1.34	−0.66
3	−1.95	−1.45	−0.83
4	−0.97	−0.66	−0.22
5	−0.34	−0.24	−0.11
6	−0.51	−0.33	−0.06
7	−1.88	−1.43	−0.9
8	−1.82	−1.29	−0.57
9	−0.44	−0.33	−0.2
10	−1.28	−0.92	−0.43
11	−0.46	−0.32	−0.12
12	−0.32	−0.24	−0.15
13	−0.22	−0.12	−0.03
14	−0.23	−0.18	−0.08
15	−1.78	−1.39	−0.97
16	−4.88	−3.87	−2.78
17	−1.28	−1.03	−0.76
18	−3.07	−2.4	−1.66
19	−0.63	−0.46	−0.25
20	−0.62	−0.51	−0.39
21	−0.18	−0.14	−0.82

Discounted cash flow models for these sweet spots were developed based on the production profile, gas wellhead price, discount rate, and development expenditures. As shown in Table 3, a range of 12 to 18% with an average of 15% was considered for DR in the current study.

Regarding the Madani and Holditch approach, each shale plate with IRR greater than 20 percent and payout time less than 5 years considered economic and most prone for development [41].

Table 4 represents the $P10$–$P50$–$P90$ values of estimated NPV for developing the geological sweet spots. The results show that regarding the current economic cost rates, the NPV for all spots in all conditions is negative; thus, they are not profitable at this condition.

5. Conclusion

The outcomes of the proposed approach for detecting the best techno-economic regions in undeveloped shale gas regions and its implementation in the Lurestan shale gas assessment lead to the following conclusion:

(i) The geological sweet spots are not necessarily commercial and geologic evaluation should be tied by economic evaluation to locate the best techno-economic areas.

(ii) The necessary unknown features of undeveloped areas can be estimated from analogous developed shale plates through quantitative analogy study.

(iii) The evaluation of shale gas in the Lurestan region (the case study) is the first attempt in shale gas evaluation in Iran.

(iv) The analogy study identified the Eagle Ford shale plate as the analog in the Lurestan region.

(v) Regarding the current cost rates in Iran, at any conditions ($P10$-$P50$-$P90$), none of the selected geological sweet spots in the Lurestan region is not economical. Due to the lack of infrastructure, experience and expertise in comparison to US, shale gas extraction in Iran is much more expensive than in U.S., and it is considered as future affordable energy in Iran.

Data Availability

The data used to support the findings of this study are included within the article.

Conflicts of Interest

The authors declare that they have no conflicts of interest.

References

[1] R. Abdollahi, M. Nadri, H. Gholghanddashti, M. Safari, and M. Zare Reisabadi, "A stepwise approach for identification of water production mechanisms in gas reservoirs," *Energy Sources, Part A: Recovery, Utilization and Environmental Effects*, 2021.

[2] R. Abdollahi, H. Esfandyari, M. Nadri Pari, and A. Davarpanah, "Conventional diverting techniques and novel fibr-assisted self-diverting system in carbonate reservoir acidizing with successful case studies," *Petroleum Research*, 2021.

[3] R. Abdollahi and S. R. Shadizadeh, "The effect of spent acid on carbonate rock wettability during a matrix acidizing treatment," *Petroleum Science and Technology*, vol. 32, 2014.

[4] R. Abdollahi and S. R. Shadizadeh, "Effect of acid additives on anticorrosive property of henna in regular mud acid," *Statistical Centre of Iran*, vol. 19, 2012.

[5] R. Abdollahi, S. R. Shadizadeh, and G. Zargar, "Experimental investigation of acid-induced sludge precipitation: using acid additives in Iran," *Energy Sources, Part A: Recovery, Utilization and Environmental Effects*, vol. 36, 2014.

[6] H. Esfandyari, S. R. Shadizadeh, F. Esmaeilzadeh, and A. Davarpanah, "Implications of anionic and natural surfactants to measure wettability alteration in EOR processes," *Fuel*, vol. 278, 2020.

[7] H. Esfandyari, A. Haghighat Hoseini, S. R. Shadizadeh, and A. Davarpanah, "Simultaneous evaluation of capillary pressure and wettability alteration based on the USBM and imbibition tests on carbonate minerals," *Journal of Petroleum Science and Engineering*, vol. 200, 2020.

[8] X. J. Li, S. Y. Hu, and K. M. Cheng, "Suggestions from the development of fractured shale gas in North America," *Shiyou Kantan Yu Kaifa/Petroleum Exploration and Development*, vol. 34, 2007.

[9] M. Mistré, M. Crénes, and M. Hafner, "Shale gas production costs: historical developments and outlook," *Energy Strategy Reviews*, vol. 20, 2018.

[10] M. Ahmed and S. Rezaei-Gomari, "Economic feasibility analysis of shale gas extraction from UK's carboniferous bowland-hodder shale unit," *Resources*, vol. 8, 2019.

[11] R. Rezaee, *Fundamentals of Gas Shale Reservoirs*, John Wiley and Sons, Inc., New York, NY, USA, 2015.

[12] J. B. Curtis, "Fractured shale-gas systems," *AAPG Bulletin*, vol. 86, 2002.

[13] D. M. Jarvie, R. J. Hill, T. E. Ruble, and R. M. Pollastro, "Unconventional shale-gas systems: the Mississippian Barnett Shale of north-central Texas as one model for thermogenic shale-gas assessment," *AAPG Bulletin*, vol. 91, 2007.

[14] M. Burnaman, W. Xia, and J. Shelton, "Shale Gas Play Screening and Evaluation Criteria," *China Petroleum Exploration*, vol. 14, 2009.

[15] A. Ghazwani, R. Littke, G. Gaus, and C. Hartkopf-Fröder, "Assessment of unconventional shale gas potential of organic-rich Mississippian and Lower Pennsylvanian sediments in western Germany," *International Journal of Coal Geology*, vol. 198, 2018.

[16] Y. Ma, X. Cai, and P. Zhao, "China's shale gas exploration and development: understanding and practice," *Petroleum Exploration and Development*, vol. 45, 2018.

[17] T. Jing, J. Zhang, S. Xu, Z. Liu, and S. Han, "Critical geological characteristics and gas-bearing controlling factors in Longmaxi shales in southeastern Chongqing, China," *Energy Exploration and Exploitation*, vol. 34, 2016.

[18] Z. Li, J. Zhang, X. Tang et al., "Approaches for the evaluation of favorable shale gas areas and applications: implications for China's exploration strategy," *Energy Science and Engineering*, vol. 8, 2020.

[19] J. B. Aldrich and J. P. Seidle, ""Sweet Spot" identification and optimization in unconventional reservoirs," in *Proceedings of the AAPG 2018 AAPG Annual Convention and Exhibition*, Salt Lake City, UT, USA, May 2018.

[20] X. Li, J. Zhang, Y. Wang, M. Guo, Z. Wang, and F. Wang, "Accumulation condition and favorable area evaluation of shale gas from the Niutitang Formation in northern Guizhou, South China," *Journal of Natural Gas Geoscience*, vol. 3, 2018.

[21] A. C. Gringarten, M. Bozorgzadeh, S. Daungkaew, and A. Hashemi, "Well test analysis in lean gas condensate reservoirs: theory and practice," in *SPE Russian Oil and Gas Technical Conference and Exhibition*, Moscow, Russia, October 2006.

[22] M. Ver Hoeve, C. Meyer, J. Preusser, and A. Makowitz, *Basinwide Delineation of Gas-Shale "Sweet Spots" Using Density and Neutron Logs: Implications for Qualitative and Quantitative Assessment of Gas-Shale Resources*, American Association of Petroleum Geologists, Tulsa, OK, USA, 2013.

[23] P. Tahmasebi, F. Javadpour, and M. Sahimi, "Data mining and machine learning for identifying sweet spots in shale reservoirs," *Expert Systems with Applications*, vol. 88, 2017.

[24] M. Kormaksson, M. R. Vieira, and B. Zadrozny, "A data driven method for sweet spot identification in shale plays using well log data," in *Proceedings of the SPE Digital Energy Conference and Exhibition 2015*, Woodlands, TX, USA, March 2015.

[25] X. Chen, S. Bao, D. Hou, and X. Mao, "Methods and key parameters for shale gas resource evaluation," *Petroleum Exploration and Development*, vol. 39, 2012.

[26] X. Zhang, C. Liu, Y. Zhu, S. Chen, Y. Wang, and C. Fu, "The characterization of a marine shale gas reservoir in the lower Silurian Longmaxi Formation of the northeastern Yunnan Province, China," *Journal of Natural Gas Science and Engineering*, vol. 27, 2015.

[27] X. Ma and J. Xie, "The progress and prospects of shale gas exploration and exploitation in southern Sichuan Basin, SW China," *Shiyou Kantan Yu Kaifa/Petroleum Exploration and Development*, vol. 45, 2018.

[28] Y. Chen, J. Xu, and P. Wang, "Shale gas potential in China: a production forecast of the Wufeng-Longmaxi Formation and implications for future development," *Energy Policy*, vol. 147, 2020.

[29] EIA, *Technically Recoverable Shale Oil and Shale Gas Resources*, EIA, Argentina, 2015.

[30] S. F. Wang, D. Z. Dong, Y. M. Wang, X. J. Li, J. L. Huang, and Q. Z. Guan, "A comparative study of the geological feature of marine shale gas between China and the United States," *Journal of Natural Gas Geoscience*, vol. 26, 2015.

[31] Z. Dong, S. A. Holditch, and D. A. McVay, "Resource evaluation for shale gas reservoirs," *SPE Economics and Management*, vol. 5, 2013.

[32] M. R. Kamali and M. R. Rezaee, "Identification and evaluation of unconventional hydrocarbon reserves: examples from Zagros and Central Iran basins," *Journal of Petroleum Science and Technology*, vol. 2, 2012.

[33] M. Alavi, "Regional stratigraphy of the Zagros fold-thrust belt of Iran and its proforeland evolution," *American Journal of Science*, vol. 304, 2004.

[34] A. Vafaie, B. Habibnia, and S. A. Moallemi, "Experimental investigation of the pore structure characteristics of the Garau gas shale formation in the Lurestan Basin, Iran," *Journal of Natural Gas Science and Engineering*, vol. 27, 2015.

[35] A. Negahdari, M. Ziaii, and J. Ghiasi-Freez, "Application of discriminant analysis for studying the source rock potential of probable formations in the Lurestan Basin, Iran," *International Journal of Mining and Geo-Engineering*, vol. 48, 2014.

[36] M. L. Bordenave and R. Burwood, "Source rock distribution and maturation in the zagros orogenic belt: provenance of the asmari and bangestan reservoir oil accumulations," *Organic Geochemistry*, vol. 16, 1990.

[37] I. Rahimzadeh Kivi, M. Zare-Reisabadi, M. Saemi, and Z. Zamani, "An intelligent approach to brittleness index estimation in gas shale reservoirs: a case study from a western Iranian basin," *Journal of Natural Gas Science and Engineering*, vol. 44, 2017.

[38] Y. Ezampanah, A. Sadeghi, A. M. Jamali, and M. H. Adabi, "Biostratigraphy of the garau formation (Berriasian?-lower cenomanian) in central part of lurestan zone, northwest of zagros, Iran," *Cretaceous Research*, vol. 46, 2013.

[39] A. Farzipour-saein, A. Yassaghi, S. Sherkati, and H. Koyi, "Basin evolution of the Lurestan region in the zagros fold-and-thrust belt, Iran," *Journal of Petroleum Geology*, vol. 32, 2009.

[40] EIA, *Trends in U.S. Oil and Gas Upstream Costs*, U.S. Energy Information Administration (EIA), Washington, D.C., USA, 2016.

[41] H. A. D. S. Madani and S. Holditch, "A methodology to determine both the technically recoverable resource and the economically recoverable resource in an unconventional gas play," in *Proceedings of the SPE Middle East Oil and Gas Show and Conference*, Manama, Bahrain, September 2011.

Hindawi
Mathematical Problems in Engineering
Volume 2021, Article ID 5944828, 22 pages
https://doi.org/10.1155/2021/5944828

Research Article

Efficient Crisis Management by Selection and Analysis of Relief Centers in Disaster Integrating GIS and Multicriteria Decision Methods: A Case Study of Tehran

Hassan Ahmadi Choukolaei,[1] Mustafa Jahangoshai Rezaee,[1] Peiman Ghasemi,[2] and Morteza Saberi[3]

[1]*Faculty of Industrial Engineering, Urmia University of Technology, Urmia, Iran*
[2]*Department of Industrial Engineering, South Tehran Branch, Islamic Azad University, Tehran, Iran*
[3]*School of Information, Systems and Modelling, University of Technology Sydney, Sydney, NSW, Australia*

Correspondence should be addressed to Mustafa Jahangoshai Rezaee; m.jahangoshai@uut.ac.ir

Received 28 April 2021; Revised 21 May 2021; Accepted 17 June 2021; Published 2 July 2021

Academic Editor: Mohammad Yazdi

In Iran, location is usually done by temporary relief organizations without considering the necessary standards or conditions. The inappropriate and unscientific location may have led to another catastrophe, even far greater than the initial tragedy. In this study, the proposed locations of crisis management in the region and the optimal points proposed by the Geographic Information System (GIS), taking into account the opinions of experts and without the opinion of experts, were evaluated according to 18 criteria. First, the optimal areas have been evaluated according to standard criteria extracted by GIS and the intended locations of the region for accommodation in times of crisis. Then, the position of each place is calculated concerning each criterion. The resulting matrix of optimal options was qualitatively entered into the Preference Ranking Organization Method for Evaluation (PROMETHEE) for analysis. The triangular fuzzy aggregation method for weighting and standard classification of criteria for extracting optimal areas using GIS and integrating entropy and the Multiobjective Optimization Based on Ratio Analysis (MOORA) method for prioritizing places in the region are considered in this research. Finally, by applying constraints and using net input and output flows, optimal and efficient options are identified by PROMETHEE V. Among the research options, only four options were optimal and efficient. A case study of the Tehran metropolis is provided to show the ability of the proposed approach for selecting the points in three modes, with/without applying weights and applying crisis management.

1. Introduction

Natural disasters, especially earthquakes, have long been considered the most destructive factors that harm humans, society, and habitat. Data show that natural disasters such as earthquakes have increased in recent years. Therefore, the need for proper planning for equipment before the disaster is more important than ever [1–3]. During a crisis, homes are often damaged or unsafe for use, and at this time, creating suitable temporary shelters for families is very important. Temporary shelter is transferring people from emergency shelters to their permanent housing, which is provided to homeless families for several months to several years. Transforming urban spaces into temporary shelters is an effective way to support and improve the aftermath of natural disasters [4]. The process of selecting a temporary location for use in future critical situations must be done in a principled manner. Because the main need of the injured people is to have shelter and provide relief services in the fastest possible time, it is not possible to provide suitable places for earthquake victims immediately after the earthquake. In such crises, the right places (urban access, security, avoidance of risk-prone areas, and so on) should be provided to earthquake victims [5]. Because the injured person

without shelter is exposed to serious physical, mental, and psychological injuries. For this reason, selecting an appropriate and safe location is very important in urban planning. Improper location of relief centers will lead to a crisis far worse than the initial crisis. For example, not observing the distance between relief centers and fault lines will lead to the destruction of these places during aftershocks, which will injure or kill many people due to the role of relief centers in crises. Due to the active faults in the region and the importance of locating relief centers in times of crisis, in this study, relief centers considered by Tehran Crisis Management with optimal centers extracted by the Geographic Information System (GIS) in terms of efficiency, performance, and optimization have been evaluated. Also, in this study, by comparing the desired methods and locations in the area and the proposed locations of GIS, it has been tried to introduce the most optimal locations or areas for temporary accommodation of people in critical situations by evaluating potential locations and areas. Comparison and review of points considered by the Regional Crisis Management Organization and points introduced by GIS are other topics studied in this research. Many researchers have focused specifically on planning and policy-making. Researchers and crisis management managers are willing to act in decisions that can improve system performance as much as possible. Hosseini and Machyani [6] identified and ranked places prone to food storage and facilities in times of crisis. They used the GIS method and the AHP method. Esmaelian et al. [7] proposed a multicriteria spatial decision that integrates a GIS support system and a multicriteria decision method to identify evacuation shelters and emergency service locations. Marcelin et al. [8] have adopted a p-median modeling framework with GIS. Their goal was to discover the locations of relief distribution facilities after a possible storm in the city of Leon, Florida. Chen et al. [9] designed a system theory-based planning framework and GIS in China for urban emergency shelters in critical situations. In this study, the opinions of local experts and citizens were used to build temporary settlements in Guangzhou. The results showed that this framework is a good tool for planning urban emergency shelters. Saeidian et al. [10] have used (GIS), TOPSIS method, a simple clustering method, and two metaheuristic algorithms (particle swarm optimization (PSO) and ant colony optimization (ACO)) to locate relief centers. The results of the evaluations showed that PSO responds better than ACO and has higher adaptability. Nappi et al. [11] have proposed a new multicriteria decision model that focuses on humanitarian to select temporary collective shelters. The results quantify the importance of criteria and allow the development of a SHELTERPRO software decision tool that can be used for support. The results also showed that facility safety, cultural adequacy, and access to space were the most valuable criteria. Baharmand et al. [12] have developed a spatial allocation model and applied their approach to a real data set of Nepal 2015 earthquake response. The analysis showed that with a relative coverage of 0.4, the balance between procurement costs and response time affects the number and location. Borhani et al. [13] identified the shelters and multipurpose spaces by analyzing the collected data and the opinions of 26 experts using the GIS and SAW model. Su et al. [14] developed a two-stage floating catchment (2SFCA) method with variable service radius, and evacuation radius has been developed to describe emergency shelter access in the main Lanzhou area and compare it with traditional 2SFCA. Yao et al. [15] used a multicriteria TOPSIS evaluation model and, through a combined process, service area, and POI analysis, developed a model that provided an overall assessment at the district level. The results showed that the distribution of open spaces did not match the dynamics of population distribution. Considering the existing challenges in the literature of the subject as well as the analysis of studies, the research gap can be expressed as follows:

(i) Lack of attention to location constraints
(ii) Lack of attention to the efficiency of the optimal locations
(iii) Lack of attention to the feasibility of the output of the GIS

Given the research gap mentioned, the research contributions are listed as follows:

(i) Using PROMETHEE V to consider constraints to suggest optimal locations
(ii) Determining the efficiency of the final optimal options according to the net input and output currents
(iii) Determining the feasibility of the extracted places

The rest of the paper is organized as follows. In the second section, the criteria for measuring criteria and ranking options will be explained. In Section 3, the proposed approach and problem statement will be expressed. In Section 4, we will introduce a case study. In the fifth and sixth sections, the data, output analysis, and related results will be described, respectively. Finally, the conclusion will be stated in the last section.

2. Methodology

The methodology of this research consists of four parts. These methods were used to weigh the criteria and prioritize the options. Research weighting methods include the triangular fuzzy method and entropy. MOORA and PROMETHEE methods have also been used to prioritize options. The entropy-MOORA combination method was used in the second phase of the research to rank the relief sites in the area, and the PROMETHEE method was used to prioritize the options. The PROMETHEE V method has been used to determine the final optimal options and compare the performance of the methods.

2.1. Weighting Method. The use of fuzzy sets is more compatible with linguistic and sometimes ambiguous human explanations. Therefore, it is better to use long-term predictions and real-world decisions using fuzzy numbers. Each triangular fuzzy number consists of three parameters

$F = (l{\cdot}m{\cdot}u)$. The upper bound (u) is the maximum value that a fuzzy number F can take. The lower bound (l) is the minimum value that a fuzzy number can take, and m is the most probable value of a fuzzy number.

$$\mu_F(x) = \begin{cases} \dfrac{x-l}{m-l}, & l < x < m, \\ \dfrac{u-x}{u-m}, & m < x < u, \\ 0, & \text{otherwise.} \end{cases} \tag{1}$$

In this weighting step, the sum of triangular fuzzy numbers is obtained according to the following formula:

$$\begin{aligned} F_1 &= (l_1 \cdot m_1 \cdot u_1), \\ F_1 + F_2 &= (l_1 + l_2 \cdot m_1 + m_2 \cdot u_1 + u_2), \\ F_2 &= (l_2 \cdot m_2 \cdot u_2). \end{aligned} \tag{2}$$

After collecting the criteria and evaluating them, the experts evaluated the criteria fuzzy (VH, H, M, L, VL). Then, the obtained fuzzy numbers were defuzzified, and the weights of the indicators were calculated and normalized.

2.2. Entropy Method. In this research, the entropy method has been used to determine the weight of the criteria. Entropy is used for calculating the weight of criteria. This method requires a criterion-option matrix. This method was proposed in 1974 by Shannon and Weaver [16]. Entropy represents the amount of uncertainty in a continuous probability distribution. The basic idea of this method is that the higher the scatter in the values of a criterion, the more important that criterion. First, the values of each cell of the matrix by the sum of the column values (simple normalization) are divided.

$$n_{ij} = \frac{x_{ij}}{\sum_{i=1}^{m} x_{ij}}. \tag{3}$$

The entropy value of characteristic j is calculated as follows:

$$E_j = -K \sum_{i=1}^{m} n_{ij} \ln(n_{ij}), \quad k = \frac{1}{\ln m}, \tag{4}$$

where M is the number of options.

Using (E_j), the values of d_j for each characteristic are calculated:

$$d_j = 1 - E_j. \tag{5}$$

By normalizing the values ofd_j, the characteristic weight is obtained:

$$W_j = \frac{d_j}{\sum_{j=1}^{n} d_j}. \tag{6}$$

After weighing the criteria, problem options (crisis management candidate locations in the region) are prioritized using the MOORA method.

2.3. MOORA Method. MOORA is a multiobjective decision-making method introduced by Brauers and Zavadskas in 2006 [17]. In 2010, Azar and Rajabzadeh improved the method and added the complete multiplication form to it [18]. The steps for applying this method in the problems are as follows:

Step 1. The first step in the MOORA method is to construct a decision matrix for the problem. The criteria (goals) and options are listed in the column and row of the decision matrix, respectively. The decision matrix shows the performance of different options according to different criteria.

$$\begin{bmatrix} x_{11} & x_{12} & \cdots & x_{1n} \\ x_{21} & x_{22} & \cdots & x_{2n} \\ \vdots & \vdots & \cdots & \vdots \\ x_{m1} & x_{m2} & \cdots & x_{mn} \end{bmatrix}. \tag{7}$$

Step 2. Normalizing each column as follows:

$$n_{ij} = \frac{x_{ij}}{\sum_{i=1}^{m} x_{ij}^2}, \quad \forall j. \tag{8}$$

Step 3. Creating a harmonic decision matrix like the TOPSIS method, the weight of each criterion is multiplied by the normal decision matrix, and then a balanced normal decision matrix is formed.

Step 4. Selecting the optimal option from the following formula:

$$y_i = \sum_{j=1}^{g} w_j x_{ij}^* - \sum_{j=g+1}^{n} w_j x_{ij}^*, \quad (j = 1, 2, \ldots, n). \tag{9}$$

2.4. PROMETHEE Method. The PROMETHEE 1 method performs a partial ranking, and the PROMETHEE 2 method performs a complete ranking. It was first developed by Brans in 1982 and was widely used in the early years [19]. A few years later, two new versions of PROMETHEE, PROMETHEE 3 (ranking by time intervals), and PROMETHEE 4 (continuous case) were developed [20]. One of the important advantages of the PROMETHEE method is the simplicity, clarity, and reliability of results. This method can perform the evaluation process on a limited set of alternatives as a partial or complete ranking. Suppose A is a set of options from which to choose. Assume there is an effective K criterion in the decision, $A \in a$; for each option, $F_j(a)$ represents the value of the criterion j in option a. Ranking is done in three steps as follows:

Step 1. P_j the preference function is assigned to each of the jth criteria. The value of $Pj(a, b)$ is calculated for each option pair. If the relation $\mathsf{F}_j(a) = \mathsf{F}_j(b)$ is established, the value of $P_j(a \cdot b)$ becomes zero, and with increasing $\mathsf{F}_j(a) = \mathsf{F}_j(b)$, this value increases, and when the difference is equal to 1, if it increases enough, the value of $P_j(a \cdot b)$ also reaches one. Different shapes can be assumed for the $P_j$function, depending on how

the jth criterion is modeled. The PROMETHEE method proposes six generalized criteria for the preference function to the decision-maker.

Step 2. The total preference $\pi(a.b)$ for each action is calculated on action (b). Although $\pi(a.b)$ is higher, action (a) is more preferable. $\pi(a.b)$ is calculated as follows [21]:

$$\pi(a.b) = \sum_{j=1}^{K} wjpj(a.b).\left(\sum_{j=1}^{K} wj = 1\right). \quad (10)$$

Step 3. $\pi(a.b)$ indicates the degree of preference of action (a) over action (b) [21, 22]. $\varnothing^{+}$ is a positive current obtained from (11) and examines the degree of preference of (a) over $n-1$ of the other action. This is the amount of power of action (a). The positive preference flow or output current is as follows:

$$\varnothing^{+}(a) = \frac{1}{n-1}\sum_{x\epsilon A}\pi(x.a). \quad (11)$$

This flow indicates the priority of option (a) over other options. The preference of other options over option (a) is called input flow. The negative preference flow or input flow is as follows:

$$\varnothing^{-}(a) = \frac{1}{n-1}\sum_{x\epsilon A}\pi(x\cdot a). \quad (12)$$

This quantifies how a given action (a) is being globally preferred by all the other actions. The smallest negative flow $\varnothing^{-}(a)$ represents the best action [23]. For the complete ranking of options, the net flow of ranking options is considered [23]:

$$\varnothing(a) = \varnothing^{+}(a) - \varnothing^{-}(a). \quad (13)$$

The net flow score $(\varnothing(a))$ is computed as a difference between the positive flow and negative flow.

3. Proposed Approach and Problem Statement

In this research, a set of standard criteria for optimal location of relief centers as evaluation intervals and information layers in ArcGIS have been prepared. The weighting of criteria in the first phase was done by experts using the triangular fuzzy aggregation method. Then, the information layers are combined once by applying the weight of criteria and once without applying weight, and the optimal points are extracted. The Raster Calculator tool is used to merge layers so that all the layers were first gathered together and the final weightless map was produced. In the next step, we have multiplied each of the produced raster maps by their weight and combined them. Each point (weighted and nonweighted) is evaluated and scored against the criteria by GIS. After locating the proposed areas by GIS and observing unusable places in crisis (military centers and residential areas), in the next phase, 30 points of places were designated by the regional crisis management as post-crisis relief centers and identified by the GIS, and the problem was evaluated according to standard criteria. Then, the criteria were weighted by the entropy method, and the options were ranked by the MOORA method. Finally, due to the net input and output flows and the addition of constraints, optimal and efficient options were introduced. The performance of each of the options (options extracted by the GIS and selected options in the region) was evaluated according to their performance score. Due to incompatibilities between some research options, it may not be logical and possible to select some options at the same time. For this reason, there are 9 constraints for choosing the final optimal options. In this research, 2 constraints for the minimum and maximum options for selecting relief places and 7 other constraints for observing the standard distance set by experts have been considered. Figure 1 shows the general structure of the research.

In this study, after determining and evaluating the criteria, their weighting was done by the fuzzy aggregation method (by experts) and entropy method (point output information matrix) to determine the effect of each method on the results. Candidate points of the region extracted by the MOORA rank method were compared with the top points extracted from the GIS by the PROMETHEE method. This comparison was performed to evaluate and analyze the performance of each method to select relief centers in crises.

4. Case Study

The city of Tehran, located in the foothills of the Alborz Mountains range, has a high seismic risk and many active faults. Region 1 is located in the north and northeast of Tehran. This area is about 60 square kilometers. Relief centers are being set up to house the victims and people who lost their homes during the crisis. One of these crises is earthquakes. One of the secondary effects of earthquakes is liquefaction [24]. Liquidation causes severe damage to many structures, especially buildings [25]. The Japan International Cooperation Agency (JICA) has researched the Tehran earthquake. They have identified four-fault models that cause a lot of damage and loss, including the Ray fault model, Mosha fault model, North Tehran fault model, and floating model. One of the most important faults in the region is a North Tehran fault (more than 90 km). North Tehran fault, the northern part of the city, is facing many seismic hazards and damages because the fault is located on the northern outskirts of the city. According to research by JICA, in North Tehran fault, in the worst case, 130,000 people or about 2% of Tehran's population will be killed. The loss ratio in the northern part of the city will be high in areas 1 to 5. Also, the number of damages to buildings in this area is estimated at more than 60,000 buildings according to four fault models [26]. Therefore, in this research, we try to identify and evaluate the optimal places and areas for housing in crises. Table 1 shows the number and percentage of damage to buildings in area 1 based on each of the models [26].

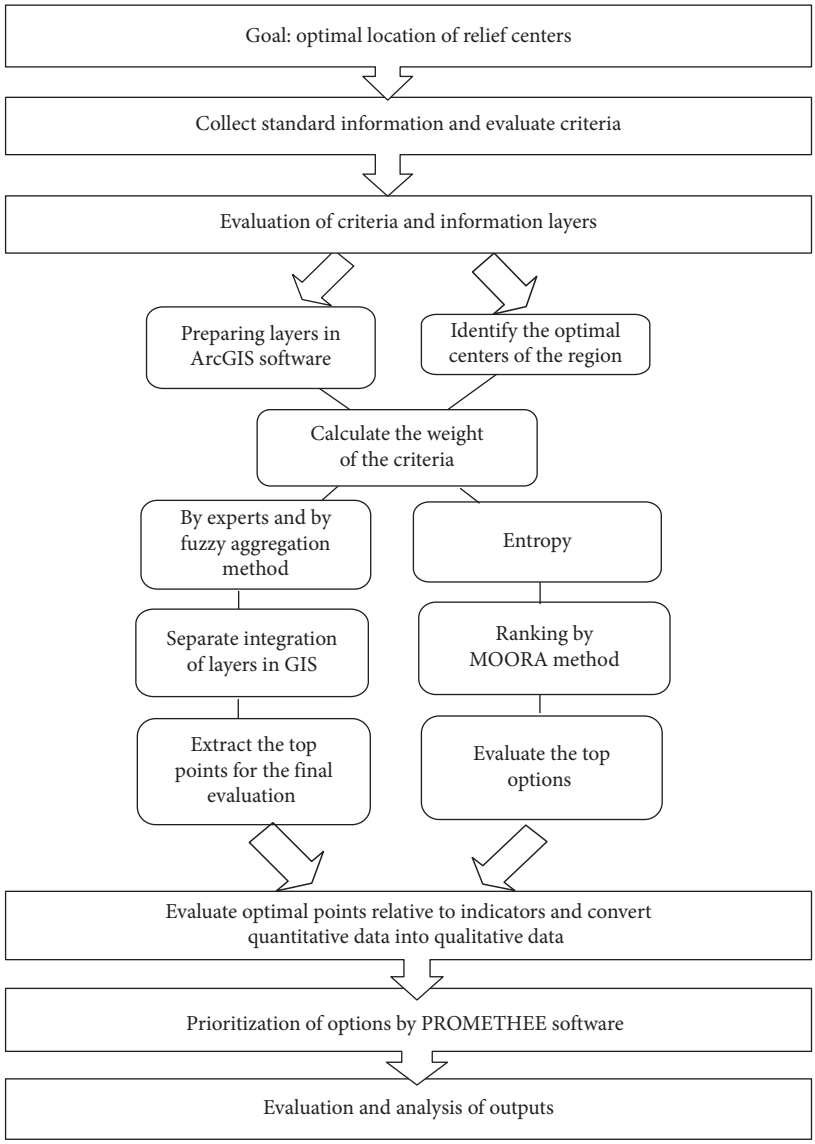

Figure 1: A schema of the proposed framework.

Table 1: Number and percentage of damages to buildings in Region 1.

Region	Floating model		Mosha fault model		North Tehran fault model		Ray fault model		Total number of damaged buildings
	Percentage	Number of buildings	Percentage	Number of buildings	Percentage	Number of buildings	Percentage	Number of buildings	
1	51.9	19.905	17.9	6.869	61.6	23.633	30.4	11.665	62.072

5. Data and Results

Criteria based on previous studies and classification of these criteria have been considered in collaboration with crisis management experts. The research criteria are shown in Table 1, which are defined in two parts (compatible access and incompatible access). The evaluation criteria are as follows:

(1) Standard mode of each criterion in the range (Good)

(2) Better than the standard mode in the range (Very good)

(3) A little away from the standard mode in the range (Average)

(4) Slightly longer than standard in (Bad) range

(5) If it is too far from the standard range, it is in the (Very bad) range

Table 2 shows the classification and evaluation of criteria.

Table 2: Classification and evaluation of criteria for locating relief centers in crises.

	C	A				
		Very good	Good	Average	Bad	Very bad
Compatible access	Area	3000	2000–3000	2000	1000–2000	0–1000
	Worn texture	0–100	100–200	200–300	300–400	400
	Main ways	0–100	100–200	200–300	300–400	400
	Security	0–200	200–400	400–600	600–800	800
	Slope percent	1–4	4–6	6–10	10–12	+12
	Hospital	0–500	500–1000	1000–1500	1500–2000	2000
	Fire station	0–500	500–1000	1000–1500	1500–2000	2000
	Population	120	90–120	60–90	30–60	0–30
	Health centers	0–200	200–500	500–700	700–1000	1000
	Educational centers	0–150	150–300	300–500	500–700	700
	Parks and gardens	0–200	200–400	400–600	600–1000	1000
Incompatible access	City gas station	400	200–400	100–200	50–100	0–50
	CNG and fuel station	400	200–400	100–200	50–100	0–50
	Wells and aqueducts	300	200–300	100–200	50–100	0–50
	Electric post	100	80–100	60–80	30–60	0–30
	Subway	300	200–300	100–200	50–100	0–50
	Fault	400	200–400	200	100–200	0–100
	Rivers	700	500–700	200–500	100–200	0–100

Table 3 shows the corresponding triangular fuzzy scale, and Table 4 presents the fuzzy opinions of experts, respectively. Also, the calculated weight of the criteria is given in Table 5, where the highest weight is related to the indicators of proximity to hospitals, medical centers, and worn tissue (1.0) and the lowest weight is related to the indicators of proximity to educational centers and surface area (0.7).

Table 3: Linguistics variables of fuzzy for the weight of each criterion.

VH	0.75	1	1
H	0.5	0.75	1
M	0.25	0.5	0.75
L	0	0.25	0.5
VL	0	0	0.25

5.1. Layer Valuation and GIS Output Evaluation. A Geographic Information System (GIS) is a coherent system of hardware, software, and data that allows data entered into a computer to be stored, analyzed, transferred, evaluated, and retrieved as a map, tabular, and zoned information geographies to be published. With the help of GIS, all kinds of processing and analysis can be done with cost and time savings [27]. GIS, with its capabilities in collecting, storing, retrieving, controlling, processing, analyzing, modeling, and displaying geographic data, can be a powerful tool in the hands of managers and planners for optimal use of resources [28]. In this study, the information layer was stored using the capabilities of the GIS. For uniformity and impact, the layers are evaluated as numerical intervals based on the buffer created in ArcGIS software. The following maps including a map of distance to the river (Figure 2), map of slope percentage (Figure 3), map of population density (Figure 4), map of distance to the gas station (Figure 5), map of distance to parks (Figure 6), and map of distance to the fire station (Figure 7) are an example of the criteria layers related to this research.

Figure 8 shows the favorable and unfavorable areas of the region for the establishment of relief centers. The blue area indicates favorable areas, and the red area indicates unfavorable areas.

After weighing the criteria, using GIS, and preparing information layers, first, the layers are matched without applying the weight of the indicators, and in the next step by

Table 4: Evaluated matrix of research criteria by experts.

	TM1			TM2			TM3		
Area	0.25	0.5	0.75	0	0.25	0.5	0	0.25	0.5
Main ways	0.5	0.75	1	0.25	0.5	0.75	0.5	0.75	1
Security	0.5	0.75	1	0.75	1	1	0.5	0.75	1
City gas station	0.25	0.5	0.75	0.25	0.5	0.75	0.5	0.75	1
CNG station	0.25	0.5	0.75	0.25	0.5	0.75	0.5	0.75	1
Percent slope	0	0.25	0.5	0.25	0.5	0.75	0.5	0.75	1
Hospital	0.5	0.75	1	0.75	1	1	0.75	1	1
Fire station	0.25	0.5	0.75	0.25	0.5	0.75	0.25	0.5	0.75
Electricity post	0.25	0.5	0.75	0.25	0.5	0.75	0.75	1	1
Population	0.25	0.5	0.75	0	0.25	0.5	0.25	0.5	0.75
Subway	0.25	0.5	0.75	0.25	0.5	0.75	0.5	0.75	1
Fault	0.75	1	1	0.5	0.75	1	0.5	0.75	1
Health centers	0.5	0.75	1	0.75	1	1	0.75	1	1
Rivers	0.5	0.75	1	0.5	0.75	1	0.25	0.5	0.75
Educational centers	0	0.25	0.5	0	0.25	0.5	0.25	0.5	0.75
Parks and gardens	0.25	0.5	0.75	0.25	0.5	0.75	0.25	0.5	0.75
Wells and aqueducts	0	0.25	0.5	0.25	0.5	0.75	0.25	0.5	0.75
Worn texture	0.5	0.75	1	0.75	1	1	0.75	1	1

Table 5: Weight of criteria obtained by experts.

Criteria	Weight	Final normal weight
Area	0.33	0.4
Main ways	0.67	0.8
Security	0.78	0.9
City gas station	0.58	0.7
CNG station	0.58	0.7
Percent slope	0.50	0.6
Hospital	0.83	1.0
Fire station	0.50	0.6
Electricity post	0.58	0.7
Population	0.42	0.5
Subway	0.58	0.7
Fault	0.78	0.9
Health centers	0.83	1.0
Rivers	0.67	0.8
Educational centers	0.33	0.4
Parks and gardens	0.50	0.6
Wells and aqueducts	0.42	0.5
Worn texture	0.83	1.0

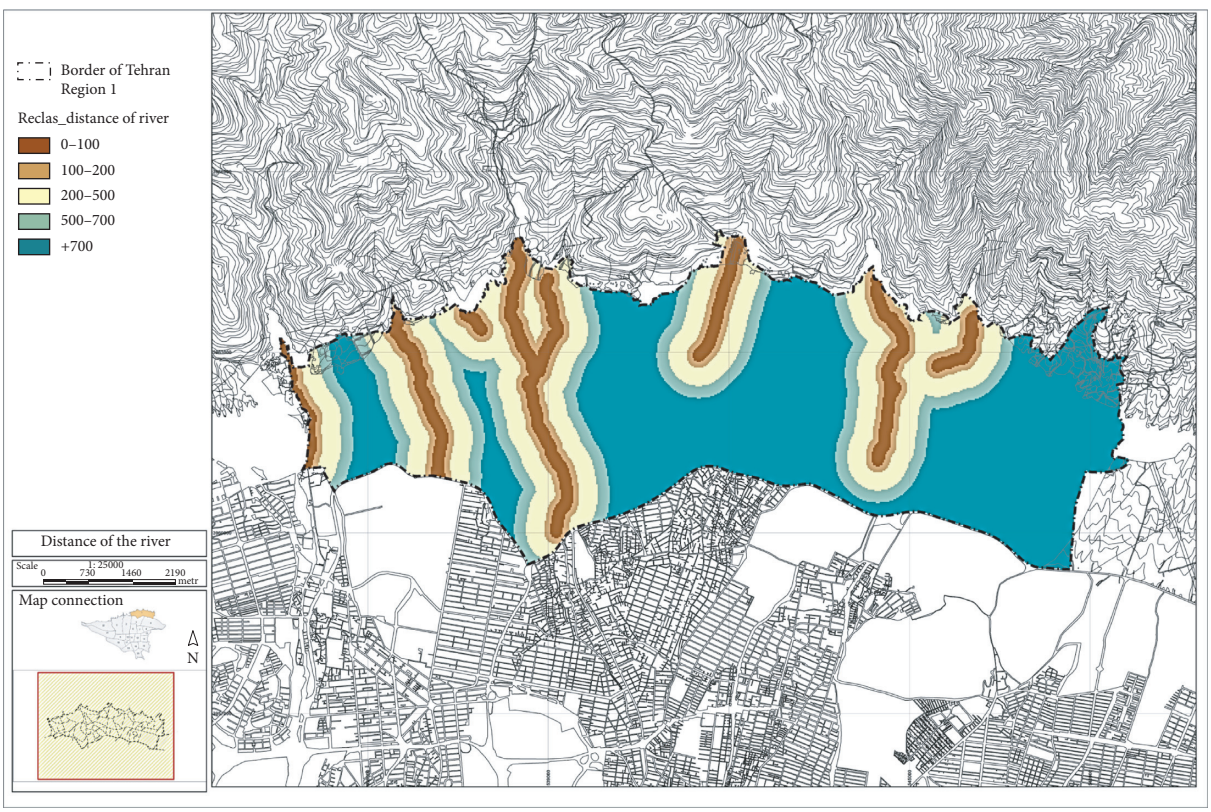

Figure 2: Distance to the river.

applying the weight of the indicators in ArcGIS software, the proposed optimal points among the optimal areas are extracted in the area. Figures 9 and 10 show the proposed points extracted for the construction of relief bases in both cases (by applying the weight of the criteria and without applying the weight of the criteria).

5.2. Evaluation and Feasibility of the Proposed Optimal Points. After combining the information layers and determining the proposed optimal points by the GIS, the proposed points are evaluated in terms of the location of each extracted optimal area relative to the indicators evaluated in Table 1. As shown in Figures 9 and 10, the proposed optimal points of the GIS

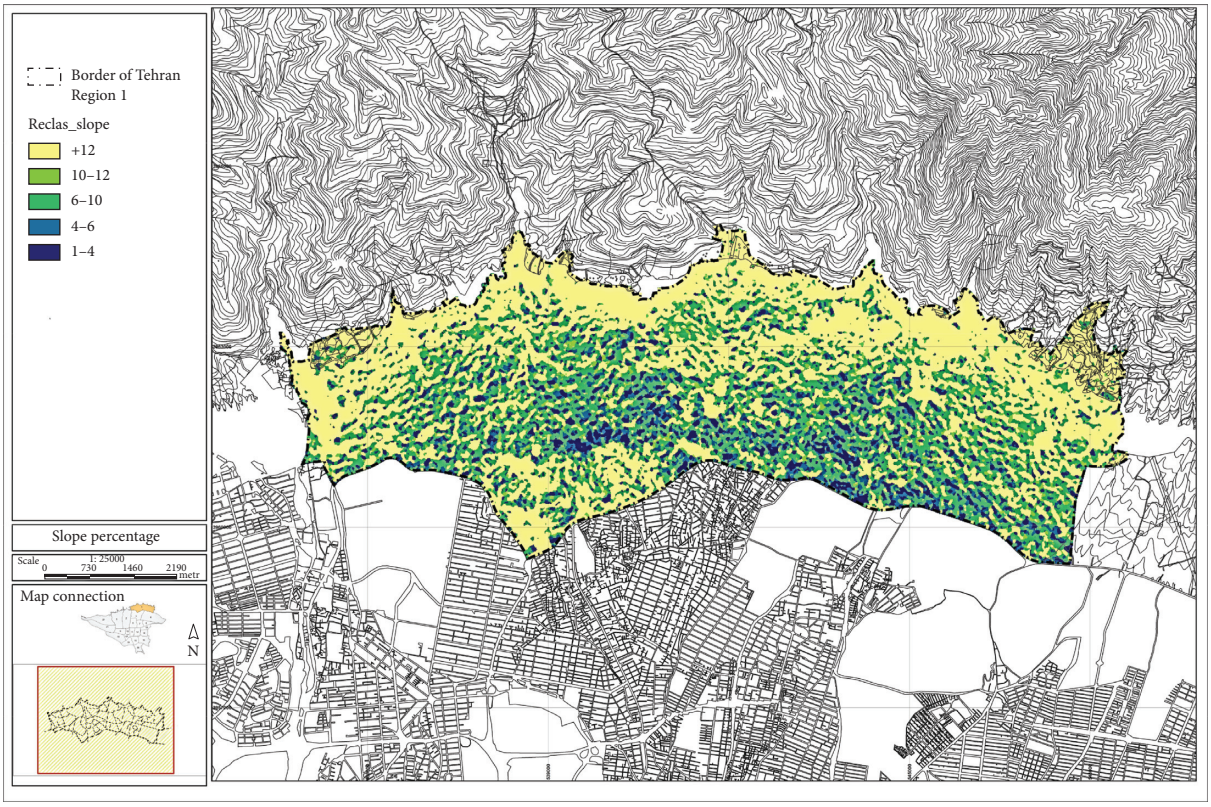

Figure 3: Slope percentage.

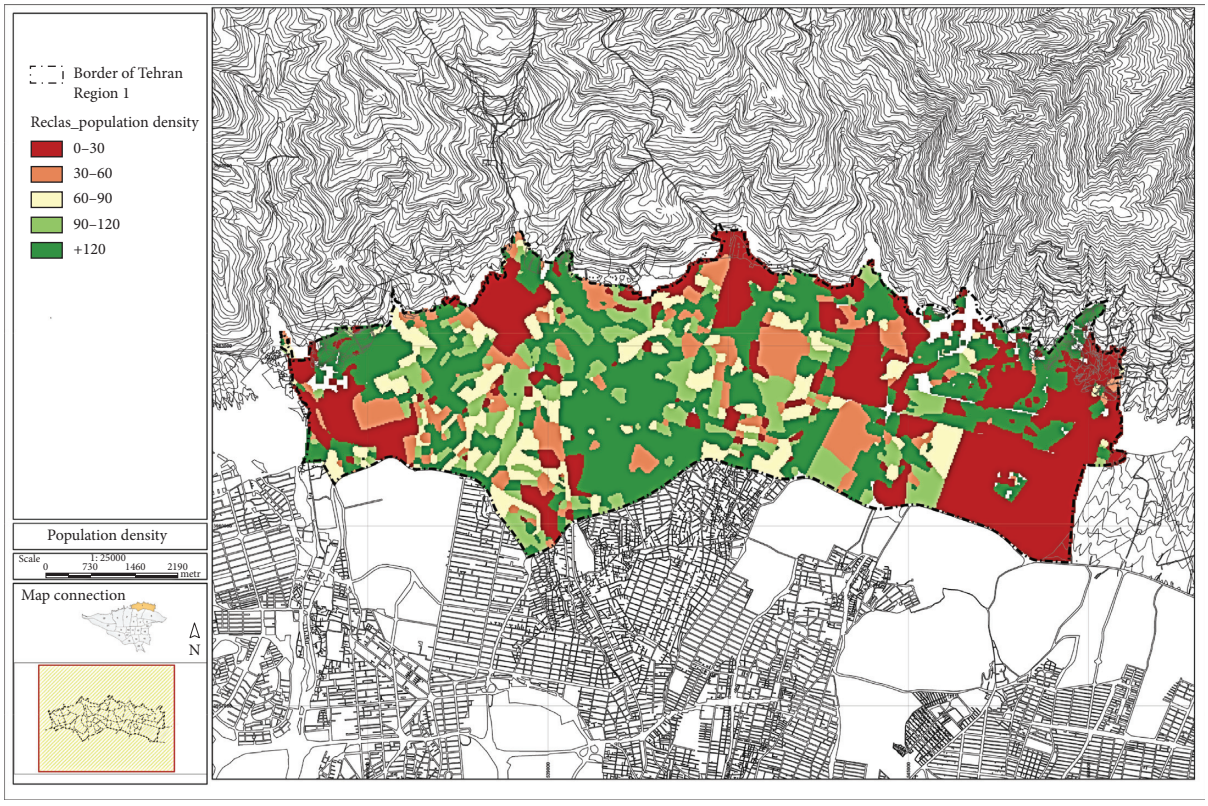

Figure 4: Population density.

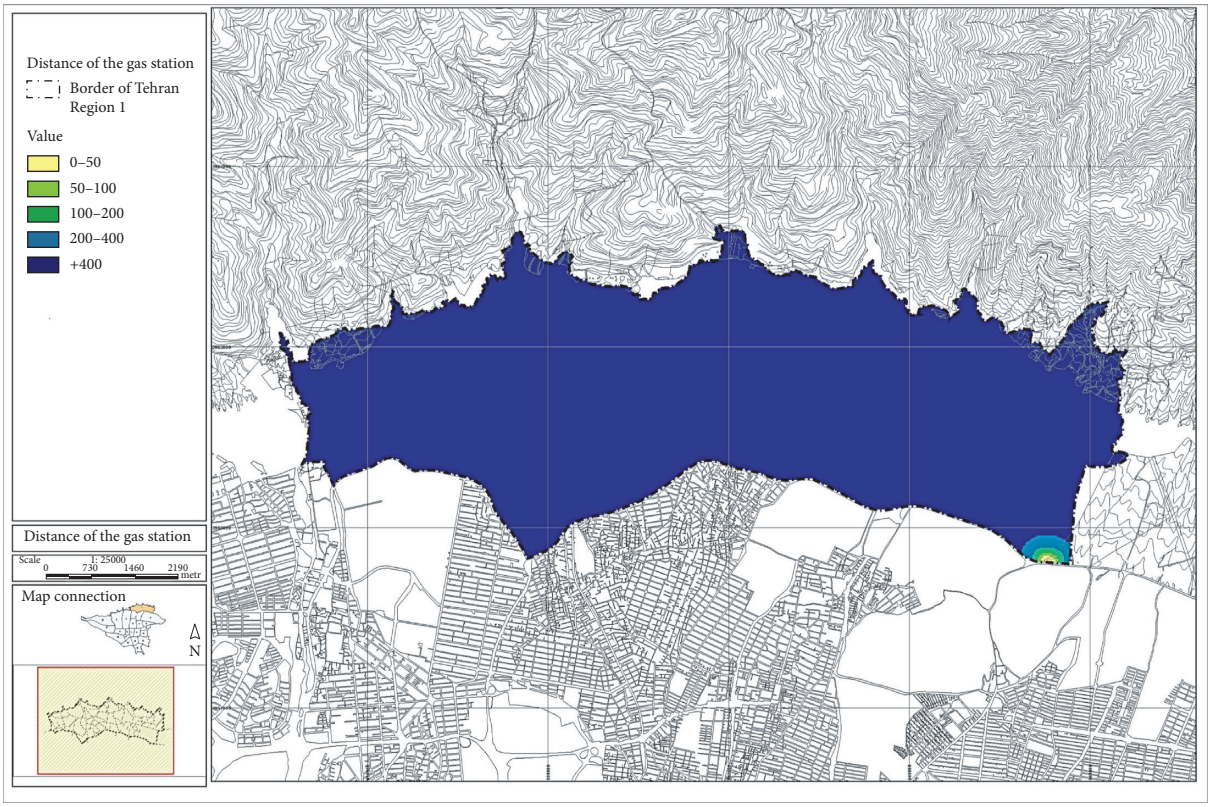

Figure 5: Distance to the gas station.

Figure 6: Distance to parks.

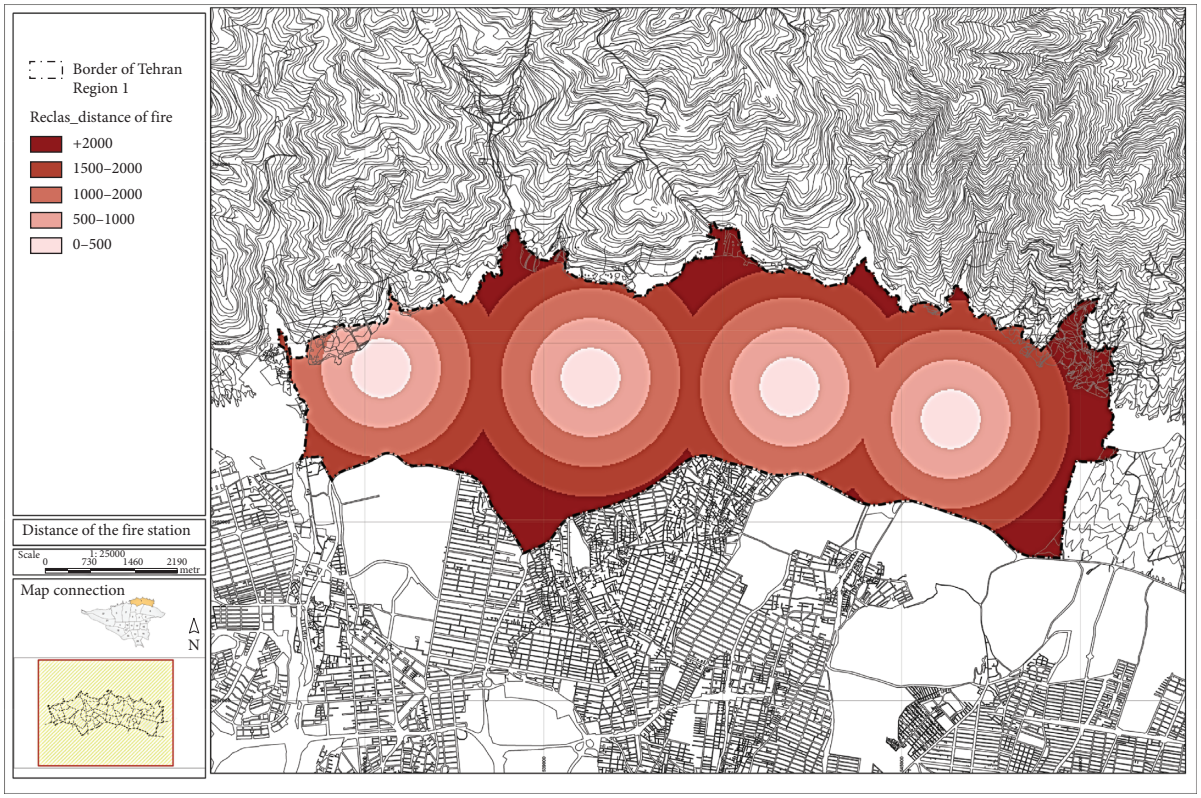

Figure 7: Distance to the fire station.

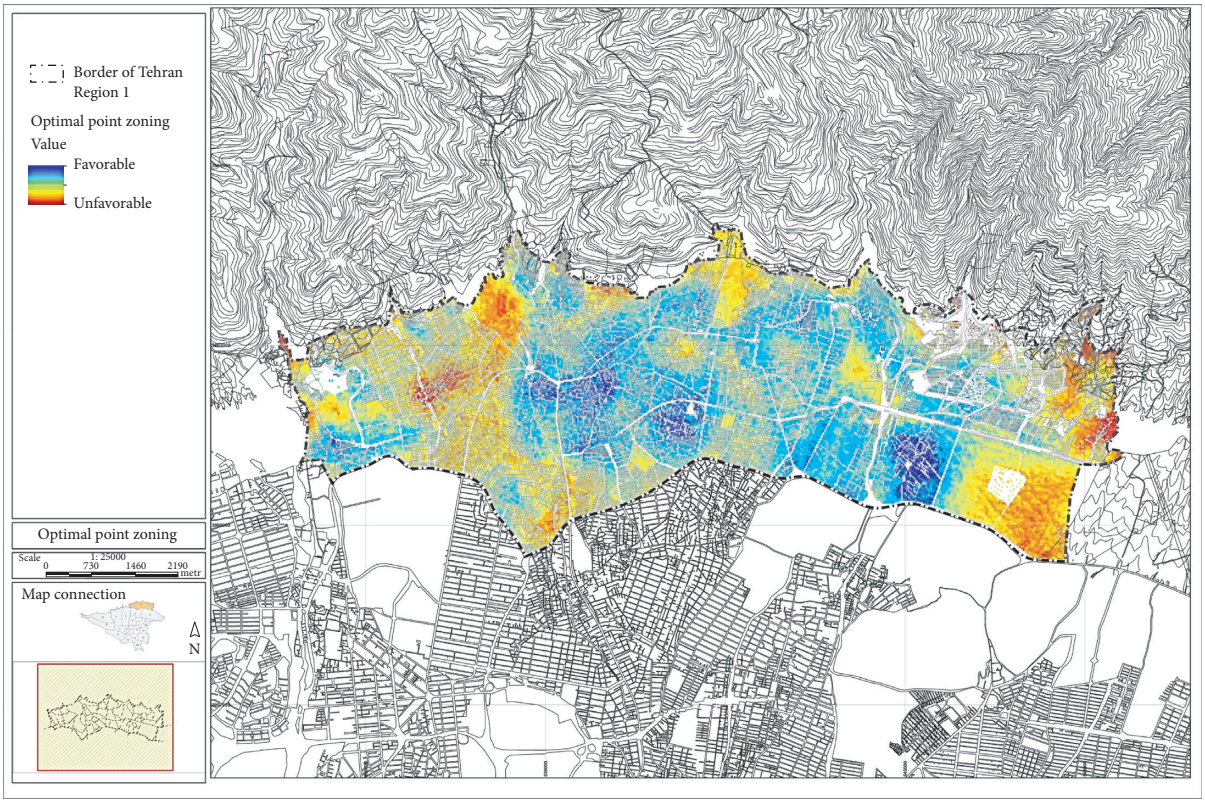

Figure 8: Favorable and unfavorable areas for the construction of relief centers.

Figure 9: Optimal areas extracted by GIS without applying weight.

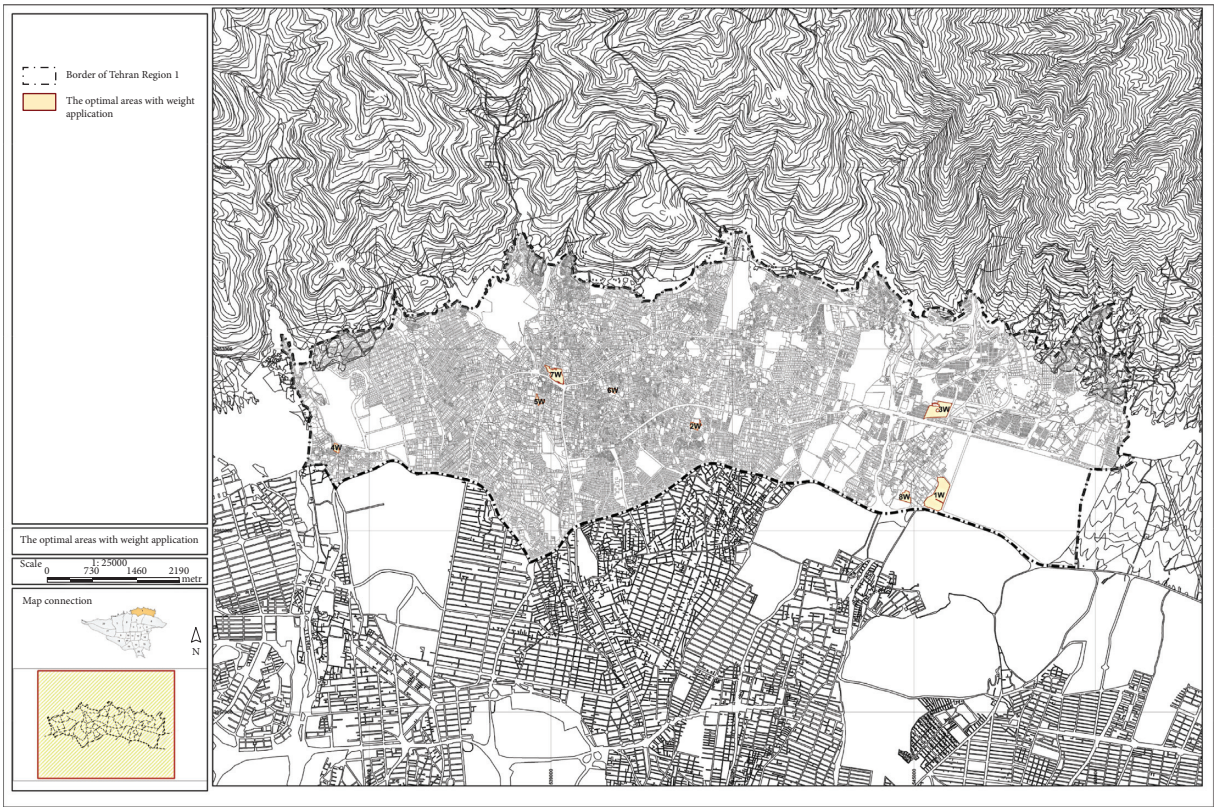

Figure 10: Optimal areas extracted by GIS by applying weight.

with the application of criteria weights (PW1, PW2, PW3, PW4, PW5, PW6, PW7, and PW8) and without the application of criteria weights (P1, P2, P3, P4, P5, P6, P7, and P8) are different. Table 6 shows the results of the evaluation of points without assigned weight (eight optimal regions obtained in Figure 9), and Table 7 shows the results of the evaluation of points with assigned weight (eight optimal regions obtained in Figure 10). For example, the results of evaluating the optimal points extracted without applying weights (see Figure 9) to the distance criteria from the fault were as follows: points p1, p2, p3, p4, p7, and p8 in the range above 400 m, and point p6 and p5 in the range of 400–200 were placed. Also, the results of evaluating the optimal points introduced by applying the weight of the indicators (see Figure 9) were as follows: PW1, PW2, PW3, PW4, and PW8 in the range above 400 meters, and PW5 and PW6 in the range of 400–200 and PW9 in the range of 0–100 were placed. The evaluation results of other optimal points extracted are shown in Tables 6 and 7.

Afterward, the criteria have been qualitatively evaluated (Very bad; Good; Average; Bad; Very good). Very good has the highest score and Very bad has the lowest score. Each of these points (points with the weight of experts and points without the weight of experts) is placed in one of the scoring points after evaluation by the GIS. For example, point PW1, after evaluation by the Geographic Information System (GIS), is in the range of 0–200 in terms of security criteria, which according to the classification considered in Table 2 is qualitatively in the range of Very good. Also, if we examine point P1 with the same criteria, it is shown in Table 6 that this point is in the range of 200–400, which according to the classification considered in Table 1 will be in the range of Good.

5.3. Feasibility Study of the Proposed Areas of the GIS and Relief Centers in the Case Study. Using Google Earth, the output of the optimal areas proposed for the establishment of relief centers in times of crisis has been examined (see Figure 11). As can be seen in Figures 12 and 13, some of the selected areas of the GIS (optimal proposed areas of Figures 9 and 10) have been military or residential. It will not be possible to use these places as postcrisis relief centers.

Usually, after an earthquake, to create safe conditions for residents and citizens and get them out of dangerous conditions, safe evacuation operations are carried out. Safe evacuation centers include all safe evacuation sites and spaces where people can be accommodated if needed. They use basic facilities to meet their needs (for 72 hours). The Tehran Crisis Management Organization has identified suitable locations in all 22 districts of Tehran to use these shelters in times of crisis. Figure 14 shows the location of these places, which are mostly stadiums and parks in the area.

6. Evaluation of Calculation Results

Then, 30 locations determined by Tehran Crisis Management in the study area were identified and evaluated by the GIS according to the standard criteria of this study (Table 2). Most of these places are stadiums, universities, and parks that cover almost all parts of the region. The results of the evaluation of these places by the GIS are shown in Table 8.

After evaluating 30 relief sites considered by the regional crisis management and forming a pairwise comparison matrix, the criteria were weighted and then prioritized. Table 9 shows the weight of the criteria calculated by the entropy method. As can be seen in Table 9, the criterion of distance from the river and distance from the main roads has the highest weight (0.0589, 0.0576) and the criteria of worn texture and land slope have the lowest weight (0.0470, 0.0514).

Problem options are prioritized according to the MOORA method (see Table 10). As can be seen, the performance score (Yi) of Morvarid Park, Gol Mohammadi Park, and Negin Park is higher than that of other options, so these options ranked first to third.

After ranking the proposed locations in the area for temporary accommodation, the top eight locations were selected and quantitative values were converted to qualitative (according to the information in Table 2) to compare and evaluate these options with the proposed optimal points of GIS. After evaluating the proposed areas by GIS in both modes (with the weight of experts and without the weight of experts) and the places determined by the Crisis Management of Region 1, the final optimal options with the PROMETHEE method were compared and evaluated. In the options evaluation step, the obtained qualitative values are considered a pairwise comparison matrix for options and criteria. Table 11 shows the result of flow evaluation, which shows the values of positive $\varnothing^{+}$, negative $\varnothing^{-}$, and net $\varnothing$ Flows. As can be seen in Table 11, P5 with a net flow of 0.1232, P6 with a net flow of 0.1208, and PW8 with a net flow of 0.1159 were ranked first to third in the PROMETHEE rankings. Also, Morvarid Park with a net flow of −0.1860, Shadi Park with a net flow of −0.1715, and Aseman Park with a net flow of −0.1570 had the worst performance. Table 11 shows the PROMETHEE ranking results of options.

In Figure 15, GAIA diagram shows the options. The length of an axis also indicates the relative strength of that criterion. A longer axis indicates a more important criterion. On the other hand, the direction of an axis indicates where the best possible options for this criterion are located. In the GAIA form, options that are similar to each other are closer to each other, and options that conflict with each other are farther apart. Criteria that have similar preferences are in the same direction, and criteria that have conflicting preferences are in different directions. For example, the PW1 option is in line with the percentage of slope and distance from worn texture, which shows good performance compared with these indicators. This option has performed very poorly in terms of the criteria of main roads, distance from the subway, and distance from parks (due to being in the opposite direction of these criteria). As can be seen, the proposed locations in the region are scattered and far from the axes of the criteria, and this poor performance has led to a lower ranking than other options.

Table 6: Evaluation of optimal points according to criteria (without applying normalized weight).

Optimal points	Criteria							
	P_1	P_2	P_3	P_4	P_5	P_6	P_7	P_8
Area	More than 3000	More than 3000	More than 3000	More than 3000	More than 3000	More than 3000	More than 3000	More than 3000
Worn texture	More than 400	More than 400	200_300	0–100	100_200	100_200	100_200	More than 400
Main ways	0–100	200–300	200–300	0–100	0–100	100–200	100–200	100–200
Security	200–400	400–600	200–400	More than 800	200–400	0–200	200–400	0–200
Gas station	200–400	More than 400	More than 400	More than 400	More than 400	More than 400	More than 400	More than 400
CNG station	More than 400	More than 400	More than 400	More than 400	More than 400	More than 400	More than 400	More than 400
Percent slope	6–10	6–10	6–10	More than 12	More than 12	1–4	1–4	More than 12
Wells and aqueducts	200_300	More than 300	More than 300	More than 300	More than 300	More than 300	200_300	More than 300
Hospital	500_1000	500_1000	1000_1500	500_1000	500_1000	500_1000	1000_1500	500_1000
Fire station	1000_1500	0_500	1000_1500	1000_1500	0_500	0_500	1500_2000	500_1000
Electricity post	More than 100	More than 100	More than 100	More than 100	More than 100	More than 100	More than 100	More than 100
Population	More than 120	90–120	90_120	More than 120	More than 120	30_60	0_30	30_60
Subway	More than 300	50–100	More than 300	More than 300	More than 300	More than 300	More than 300	More than 300
Fault	More than 400	More than 400	More than 400	More than 400	200–400	200–400	More than 400	More than 400
Health centers	More than 1000	700–1000	0–200	200–500	700–1000	700–1000	0–200	More than 1000
Rivers	More than 700	500_700	More than 700	200_500	More than 700	More than 700	More than 700	More than 700
Educational centers	0_150	0_150	150_300	150_300	300_500	300_500	0_150	500_700
Parks and gardens	0_200	0_200	0_200	0_200	0_200	0_200	0_200	0_200

Among the research criteria, incompatible access criteria (criteria in Table 2) must observe the standard distance set by crisis management experts. For example, relief centers must be 400 meters away from the city gas station; otherwise, they will not be eligible for use as relief centers (even if they perform well in other criteria). PROMETHEE V selects the optimal options based on a 0-1 linear program in which the objective function maximizes the sum of the net flow points (Phi). For each constraint, it is possible to enter the coefficients and specify the type of constraint (≤, = or ≥). Table 12 sets the limits and shows the optimal options offered by PROMETHEE V. The "Optimal" column displays the optimal solution. The "Total" rows show the value of the objective function (i.e., the sum of the net flow scores of the selected actions) for both selections. PROMETHEE V offers P1, P2, P3, P5, P6, PW1, PW2, PW3, PW4, PW6, PW8, and Niavaran Park as optimal options for the overall flow of 0.8671.

Figure 16 shows the efficiency of research options. This figure is a two-dimensional representation of the input and output flows. An efficiency frontier is drawn in red. Efficient options with different functions are on the line. Higher net flows of an action's outputs and lower net flows of its inputs are better. For instance, option PW7 has a high input flow and higher output flow. The other actions lag behind the efficient frontier. Finally, considering the amount of net flow (∅) and the performance score obtained for each of the options, the overall performance of the options in each optimal location extraction method is evaluated and shown in Figure 17. As can be seen, the performance of points without applying weights is 37% and with applying weights is 36% and the performance of places designated by crisis management is 27%. The reason for the poor performance of the places in the region can be considered their poor performance in some standard criteria such as distance to main roads, distance to the river, and safety, which have been among the important criteria of the issue. The difference between optimal options and efficient options is in their evaluation process. The basis of the PROMETHEE V rating is the full rating (PROMETHEE II), which, by adding additional constraints to the multicriteria net flow rating f (Phi), provides a global assessment of the measures taking into account all criteria. Efficient options are the result of comparing the input and output streams of the criteria classification. This is similar to the input/output model used in data envelopment analysis (DEA). When measuring the

Table 7: Evaluation of optimal points according to the criteria (by applying normalized weight).

Optimal points	Criteria							
	P_{W1}	P_{W2}	P_{W3}	P_{W4}	P_{W5}	P_{W6}	P_{W7}	P_{W8}
Area	More than 3000	More than 3000	More than 3000	More than 3000	More than 3000	More than 3000	More than 3000	More than 3000
Worn texture	More than 400	100–200	0–100	0–100	100–200	0_100	0_100	More than 400
Main ways	200_300	100–200	200_300	0–100	200_300	100_200	100_200	100_200
Security	0–200	200–400	600–800	More than 800	400–600	200–400	0–200	0–200
Gas station	More than 400	More than 400	More than 400	More than 400	More than 400	More than 400	More than 400	More than 400
CNG station	More than 400	More than 400	More than 400	More than 400	More than 400	More than 400	More than 400	More than 400
Percent slope	6_10	1_4	6_10	More than 12	6_10	1_4	6_10	1_4
Wells and aqueducts	More than 300	200–300	More than 300	More than 300	More than 300	More than 300	More than 300	More than 300
Hospital	1000_1500	1000_15000	500_1000	500_1000	0_ 500	500_1000	0_ 500	500_1000
Fire station	1000_1500	1500–2000	1000–1500	1000_1500	1000_1500	0_500	500_1000	1000_1500
Electricity post	more than 100	more than 100	more than 100	more than 100	more than 100	more than 100	0_30	more than 100
Population	90_120	0–30	90_120	More than 120	60_90	30_60	0_30	0_30
Subway	More than 300	More than 300	More than 300	More than 300	More than 300	More than 300	0_50	More than 300
Fault	More than 400	More than 400	More than 400	More than 400	400–200	400–200	0_100	More than 400
Health centers	0_200	0–200	700–1000	200_500	200_500	700_1000	200_500	200_500
Rivers	More than 700	More than 700	500–700	200_500	0_100	More than 700	0_100	More than 700
Educational centers	150_300	0_150	0_150	150_300	150_300	300_500	150_300	150_300
Parks and gardens	200–400	0_200	0_200	0_200	0_200	0_200	0_200	200_400

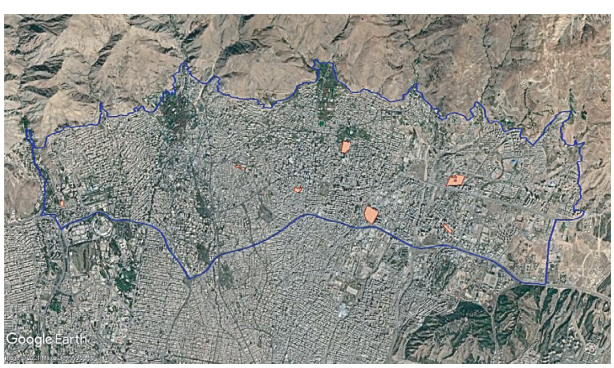

Figure 11: Optimal areas extracted by GIS in the zone.

efficiency of operational units (or DMUs—decision-making units—in the DEA), it is common to compare input criteria (different resources allocated to the units) to output criteria (results generated by the activity of the units) and to look for some kind of "best" output/input ratio [29, 30]. Suppose we have n DMUs, where DMUj ($j = 1, \ldots, n$) uses m inputs x_{ij}

Figure 12: Military area (one of the optimal output areas of GIS).

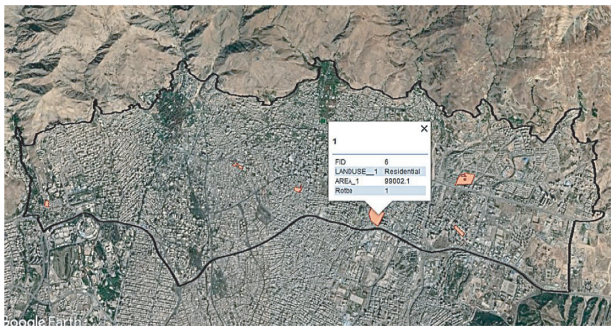

Figure 13: Residential area (one of the optimal output areas of GIS).

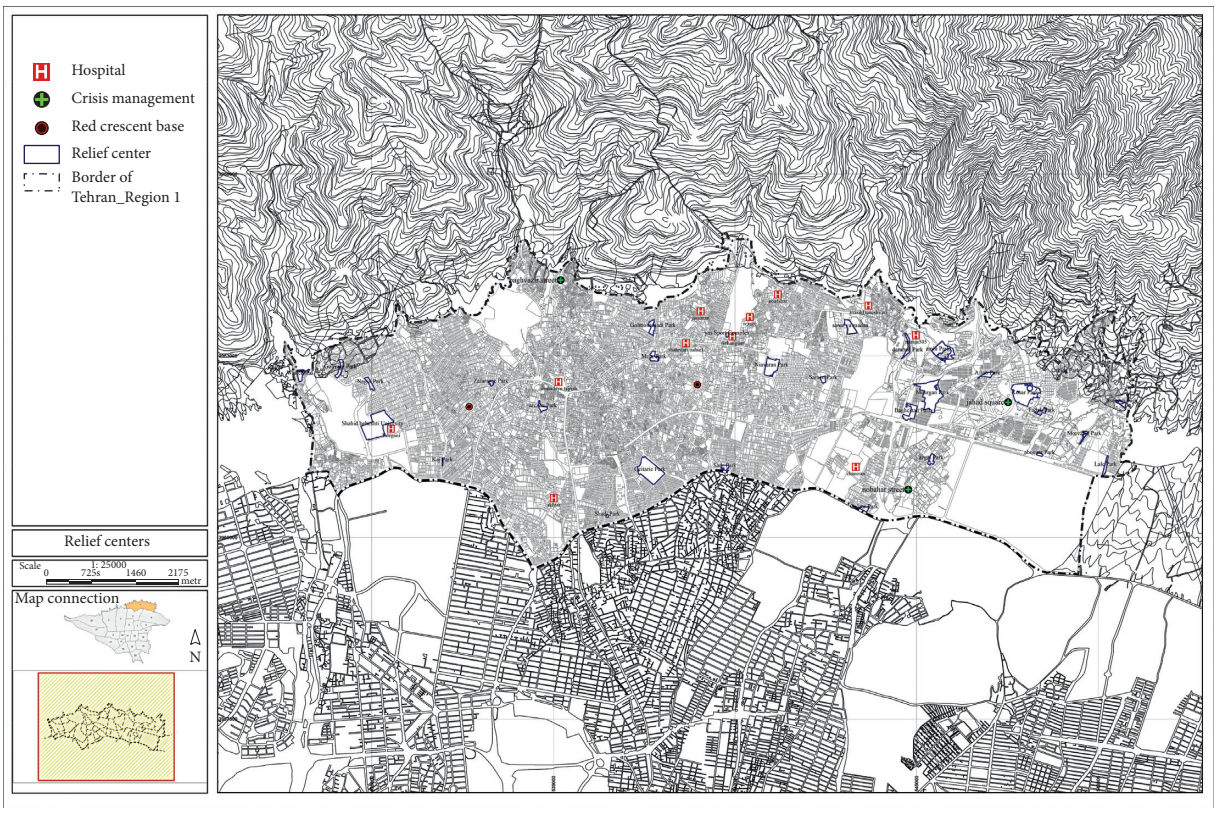

Figure 14: Relief centers for crisis accommodation in area 1.

Table 8: Evaluation results of places in the region.

Optimal points	Criteria																	
	Area	Worn texture	Main ways	Security	City gas station	CNG station	Slope percent	Wells and aqueducts	Hospital	Fire station	Electricity post	Population	Subway	Fault	Health centers	Rivers	Educational centers	Parks and gardens
Laleh Park	VG	VB	VG	G	VG	VG	A	G	VB	VB	VG	VB	VG	VG	VB	VG	VB	VG
Aseman Park	VG	VG	VG	VB	VG	VG	VB	VG	VB	VB	VG	VB	VG	VG	VB	VG	VB	VG
Morvarid Park	VG	VB	VG	A	VG	VG	VB	VG	VB	VB	VG	VB	VG	VG	VB	VG	B	VG
Aboozar Park	VG	VB	VG	VG	VG	VG	B	VG	VB	A	VG	VB	VG	VG	VB	VG	VG	VG
Fadak Park	VG	VB	G	A	VG	VG	VB	VG	VB	A	VG	VB	VG	VG	VB	VG	VG	VG
Orchid Garden	B	VB	VG	VB	VG	VG	VB	VG	VB	VB	VG	VG	VG	VG	VB	VG	VG	VG
Kowsar Park	VG	VB	VG	G	VG	VG	VB	VG	B	A	VG	VB	VG	VG	VB	VG	VG	VG
Golzar Park	VG	VB	VG	VG	VG	VG	VG	VG	A	VB	VG	VG	G	VG	B	VG	VG	VG
Ozgol Park	VG	VG	VG	VG	VG	VG	A	VG	A	G	VG	A	VG	VG	A	G	B	VG
Mehregan Park	VG	VB	VG	VG	VG	VG	VB	VG	VG	G	VG	A	VG	VG	VB	A	VG	VG
Aftab Park	VG	VB	VG	VG	VG	VG	VB	VG	A	G	VG	VB	VG	VG	VB	A	G	VG
Amin Park	VG	VB	A	B	VG	VG	VB	VG	VG	A	VG	VG	VG	VG	VB	A	A	VG
Baghestan Park	VG	VB	G	G	VG	VG	VG	VG	G	G	B	VB	A	VG	B	B	G	VG
Darabad Coastal Park	VG	VG	G	G	VG	VG	VB	VG	VG	VB	VG	B	VG	VG	VB	VB	VB	VG
Samen Park	VG	VB	G	G	VG	VG	A	VG	A	VG	VG	VG	VG	VG	VB	VG	VB	VG
Industry Sports Complex	VG	B	VG	G	VG	VG	VB	VG	VG	A	VG	VB	VG	VG	VB	G	VB	VG
Niavaran Park	VG	VB	VG	VG	VG	VG	VB	VG	G	G	VG	B	VG	VG	VB	VG	B	VG
Yas Sport Complex	VB	VB	G	G	VG	VG	VB	A	VG	VB	VG	VB	VG	VG	VB	B	VG	VG
Gol Mohammadi Park	VG	VB	VG	G	VG	VG	VB	VG	G	A	VG	G	VG	VG	VB	VG	VB	VG
Mehr Park	VG	VB	VG	A	VG	VG	VB	VG	G	A	VG	VB	VG	VG	VB	VG	G	VG
Sadr Park	VG	VB	VG	VB	VG	VG	VB	VG	B	VB	VG	A	VG	VG	B	VG	B	VG
Qeytarieh Park	VG	B	VG	VB	VG	VG	VB	VG	A	A	VG	B	VG	VG	B	VG	A	VG
Shadi Park	B	VB	G	VB	VG	VG	VB	VG	G	VB	VG	VG	VG	VG	VB	G	G	VG
Arezoo Park	VG	G	G	A	VG	VG	A	VG	VG	G	VG	A	VG	VG	G	VB	VG	VG
Zaferaniyeh Park	VG	VB	VG	B	VG	VG	VB	VG	G	VB	VG	A	VG	VB	VB	G	B	VG
Kaj Park	G	VB	VG	A	VG	VG	VB	VG	G	VB	VG	VG	VG	VG	VB	VB	VB	VG

Table 8: Continued.

Optimal points	Criteria																	
	Area	Worn texture	Main ways	Security	City gas station	CNG station	Slope percent	Wells and aqueducts	Hospital	Fire station	Electricity post	Population	Subway	Fault	Health centers	Rivers	Educational centers	Parks and gardens
Beheshti University	VG	VB	VG	A	VG	VG	VB	VG	VG	G	VG	B	VG	VB	A	VG	A	VG
Golrizan Park	VG	VB	VG	B	VG	VG	VB	VG	A	G	VG	VG	VG	B	B	VG	G	VG
Negin Park	VG	VB	VG	VB	VG	VG	VB	VG	G	VG	VG	VG	VG	B	B	VG	VG	VG
Wasteland	VG	VB	G	VG	VG	VG	VB	VG	B	A	VG	VB	VG	VG	B	VB	VB	VG

Table 9: Weight of criteria calculated by the entropy method.

Criteria	W_j
Area	0.0559
Worn texture	0.047
Main ways	0.0576
Security	0.0556
City gas station	0.0575
CNG station	0.0575
Percent slope	0.0514
Wells and aqueducts	0.0573
Hospital	0.0561
Fire station	0.0542
Electricity post	0.0573
Population	0.0556
Subway	0.0573
Fault	0.0562
Health centers	0.0515
Rivers	0.0589
Educational centers	0.0556
Parks and gardens	0.0575

Table 10: MOORA method ranking results.

Rank	Options	Y_i
1	Morvarid Park	0.10128
2	Gol Mohammadi Park	0.10109
3	Negin Park	0.09347
4	Maher Park	0.09332
5	Kaj Park	0.0909
6	Orchid Garden	0.0891
7	Aboozar Park	0.0864
8	Sadr Park	0.08616
9	Kowsar Park	0.08504
10	Fadak Park	0.08453
11	Industry Sports Complex	0.0834
12	Golzar Park	0.08311
13	Aftab Park	0.08255
14	Zaferaniyeh Park	0.08222
15	Amin Park	0.08204
16	Shadi Park	0.08204
17	Ozgol Park	0.08167
18	Yas Sport Complex	0.08153
19	Arezoo Park	0.08134
20	Wasteland	0.07764
21	Samen Park	0.07725
22	Mehregan Park	0.07646
23	Darabad Coastal Park	0.07604
24	Aseman Park	0.06842
25	Baghestan Park	0.06321
26	Niavaran Park	0.06189
27	Shahid Beheshti University	0.06068
28	Golrizan Park	0.05907
29	Laleh Park	0.05538
30	Qeytarieh Park	0.03015

Table 11: The values of the flows calculated by the PROMETHEE method.

Actions	∅	∅+	∅
P5	0.1232	0.2947	0.1715
P6	0.1208	0.3068	0.1860
PW8	0.1159	0.2633	0.1473
P4	0.0942	0.2633	0.1691
PW1	0.0870	0.2633	0.1763
P3	0.0821	0.2705	0.1884
PW6	0.0580	0.2947	0.2367
PW2	0.0531	0.2826	0.2295
P1	0.0386	0.2633	0.2246
PW4	0.0362	0.2609	0.2246
Niavaran Park	0.0362	0.2246	0.1884
PW3	0.0169	0.2657	0.2488
P2	0.0048	0.2609	0.2560
P7	−0.0048	0.2778	0.2826
PW5	−0.0072	0.2657	0.2729
P8	−0.0072	0.2029	0.2101
Mohammadi Park	−0.0145	0.1884	0.2029
PW7	−0.0290	0.2995	0.3285
Amin Park	−0.0894	0.1836	0.2729
Darabad Park	−0.0918	0.1860	0.2778
Qeytarieh Park	−0.1087	0.1812	0.2899
Aseman Park	−0.1570	0.1425	0.2995
Shadi Park	−0.1715	0.1498	0.3213
Morvarid Park	−0.1860	0.1256	0.3116

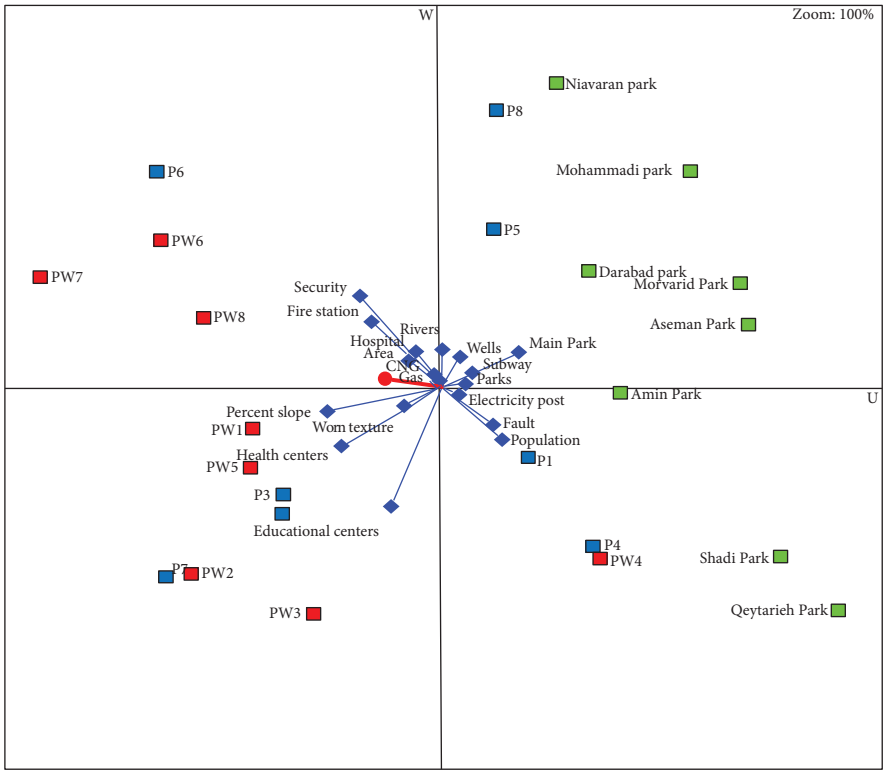

Figure 15: GAYA PROMETHEE diagram for analyzing criteria and options.

Table 12: Limitations and optimal options offered by PROMETHEE V.

Actions	Net flow TOTAL	Optimal 0.8671	Compare 0.8671
P1	0.0386	Yes	Yes
P2	0.0048	Yes	Yes
P3	0.0821	Yes	Yes
P4	0.0942	Yes	Yes
P5	0.1232	Yes	Yes
P6	0.1208	Yes	Yes
P7	−0.0048	No	No
P8	−0.0072	No	No
PW1	0.0870	Yes	Yes
PW2	0.0531	Yes	Yes
PW3	0.0169	Yes	Yes
PW4	0.0362	Yes	Yes
PW5	−0.0072	No	No
PW6	0.0580	Yes	Yes
PW7	−0.0290	No	No
PW8	0.1159	Yes	Yes
Aseman Park	−0.1570	No	No
Morvarid Park	−0.1860	No	No
Mohammadi Park	−0.0145	No	No
Darabad Park	−0.0918	No	No
Amin Park	−0.0894	No	No
Qeytarieh Park	−0.1087	No	No
Shadi Park	−0.1715	No	No
Niavaran Park	0.0362	Yes	Yes

Constraints	Optimal			Compare		
	LHS		RHS	LHS		RHS
Minimum	13.00	≥	1	13.00	≥	1
Maximum	13.00	≤	24	13.00	≤	24
Gas	18205	≥	400	18205	≥	400
CNG	147900	≥	400	147900	≥	400
Wells	10190	≥	50	10190	≥	50
Electricity post	22281	≥	30	22281	≥	30
Subway	16345	≥	50	16345	≥	50
Fault	9110	≥	100	9110	≥	100
Rivers	12680	≥	100	12680	≥	100

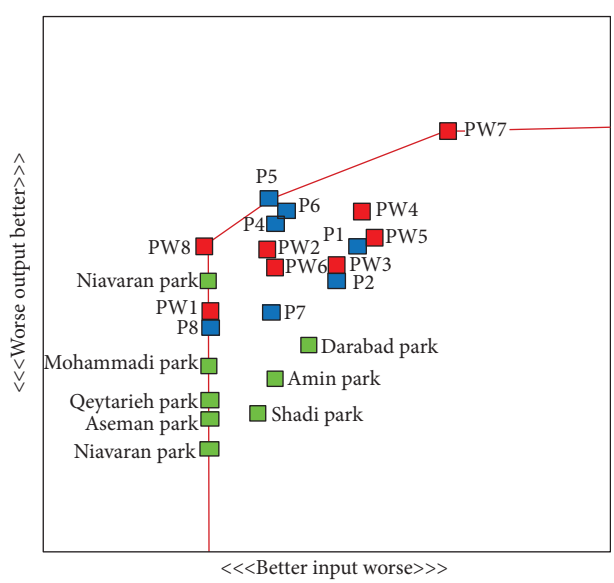

Figure 16: Performance of efficient options and inefficient options of research.

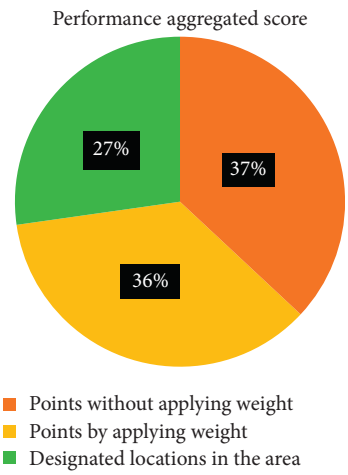

Figure 17: Comparing the overall performance of the options.

$(i = 1, \ldots, m)$ to produce s outputs y_{rj} $(r = 1, \ldots, s)$. DEA uses the following model for evaluating kth DMU's efficiency (denoted byθ):

$$\begin{aligned} &\min \theta \\ &\text{s.t: } \sum_j \lambda_j x_{ij} \leq \theta x_{io}, \quad \forall i \sum_j \lambda_j y_{rj} \geq y_{ro}, \quad \forall r \lambda_j, \quad \theta \geq 0 \forall i, j, r. \end{aligned} \tag{14}$$

7. Conclusion

In this study, the proposed locations of the Regional Crisis Management Organization and the proposed optimal points of the GIS according to 18 standardized criteria were evaluated. Also, by examining the feasibility of the optimal areas extracted by the GIS, the applicability or nonapplicability of the optimal areas introduced in crises has been addressed. The information layers were overlapped once by applying the criteria weight and once without applying the weight, and the optimal points were extracted. Each point (weighted and without weight) was evaluated and scored by GIS according to the indicators. In the next step, the designated crisis management locations in the study area are evaluated concerning the problem indicators and ranked by the MOORA method. By entering the qualitative information of the optimal location and points in the PROMETHEE method, each of the suggested points was evaluated. Finally, considering the amount of net flow (φ) and the performance score of each of the options and by applying constraints, the optimal and efficient options were determined. Limitations include the minimum and maximum options for selecting relief sites ranging from 1 to 24 options and restrictions that must meet the standard distance set by crisis management experts. The results showed good performance of areas without weight application (37%) and optimal areas with weight application (36%) compared with the proposed locations of the Regional Crisis Management Organization (27%) so that the results of the net flow performance analysis and the score of each of the options (see Figure 3) indicate the superiority of points without applying weights.

The reason for the closeness of the results of the GIS can be considered the reasonable opinion of experts. The noteworthy point of this research is the performance of the considered places in the region, which have not been very satisfactory. The difference in the performance of 10% of GIS output with the locations in the region can be considered the poor performance of these locations in some indicators. The performance of the places means the top eight places in the region (the top eight places in the MOORA ranking), but if we examine other places concerning these optimal places and standard criteria, we will see more worrying results. Also, by applying research limitations, it was found that only 13 out of 24 research options were optimal. According to the net input and output flows, the 14 options do not have the necessary performance for crises [31, 32].

Due to the high importance of location, especially the location of relief centers, and due to the high sensitivity of these centers, the use of more accurate and reliable methods should be a priority. It is recommended that managers and staff of the Regional Crisis Management Organization consider these places in terms of cost and economic criteria.

Data Availability

The data are available upon request.

Conflicts of Interest

The authors declare that they have no conflicts of interest.

References

[1] F. Sabouhi, Z. S. Tavakoli, A. Bozorgi-Amiri, and J. B. Sheu, "A robust possibilistic programming multi-objective model for locating transfer points and shelters in disaster relief," *Transportmetrica A: Transport Science*, vol. 15, no. 2, pp. 326–353, 2019.

[2] D. Guha-Sapir, F. Vos, R. Below, and S. Ponserre, *Annual Disaster Statistical Review 2011: The Numbers and Trends*, Centre for Research on the Epidemiology of Disasters (CRED), Brussels, Belgium, 2012.

[3] J. A. Vega and C. A. Hidalgo, "Quantitative risk assessment of landslides triggered by earthquakes and rainfall based on direct costs of urban buildings," *Geomorphology*, vol. 273, pp. 217–235, 2016.

[4] M. GhafouriAshtiani, *Seismic Risk Reduction in Tehran*, National Committee to Reduce the Effects of Natural Disasters, Tehran, Iran, in Persian, 2001.

[5] S. Yasuda and T. Hashimoto, "New project to prevent liquefaction-induced damage in a wide existing residential area by lowering the ground water table," *Soil Dynamics and Earthquake Engineering*, vol. 91, pp. 246–259, 2016.

[6] S. A. Hosseini and H. H. Machyani, "Locating sites for temporary accommodation and food storage silos in the event of a crisis in rasht city-Iran," *J. Mater. Environ. Sci*, vol. 6, no. 10, pp. 2825–2835, 2015.

[7] M. Esmaelian, M. Tavana, F. J. S. Arteaga, and S. Mohammadi, "A multicriteria spatial decision support system for solving emergency service station location problems," *International JournalOf Geographical Information Science*, vol. 29, no. 7, pp. 1187–1213, 2015.

[8] J. M. Marcelin, M. W. Horner, and E. E. Ozguven, "How does accessibility to post disaster relief compare between the aging and the generalpopulation? A spatial network optimization analysis of hurricane relief facility locations," *International Journal of Disaster Risk Reduction*, vol. 15, pp. 61–72, 2016.

[9] W. Chen, G. Zhai, C. Fan, W. Jin, and Y. Xie, "A planning framework based on system theory and GIS for urban emergency shelter system: a case of Guangzhou, China," *Human and Ecological Risk Assessment: An International Journal*, vol. 23, no. 3, pp. 441–456, 2017.

[10] B. Saeidian, M. S. Mesgari, B. Pradhan, and M. Ghodousi, "Optimized location-allocation of earthquake relief centers using PSO and ACO, complemented by GIS, clustering, and TOPSIS," *ISPRS International Journal of Geo-Information*, vol. 7, no. 8, p. 292, 2018.

[11] M. M. L. Nappi, V. Nappi, and J. C. Souza, "Multi-criteria decision model for the selection and location of temporary shelters in disaster management," *Journal of International Humanitarian Action*, vol. 4, no. 1, p. 16, 2019.

[12] H. Baharmand, T. Comes, and M. Lauras, "Supporting group decision makers to locate temporary relief distribution centres after sudden-onset disasters: a case study of the 2015 Nepal earthquake," *International Journal of Disaster Risk Reduction*, vol. 45, Article ID 101455, 2020.

[13] K. Borhani, A. AzimzadehIrany, and A. Elhami, "Spatial analysis of urban multi-functional land uses integrating MCDM and GIS methods Case study: emergency shelter in Saravan City," *Scientific-Research Quarterly of Geographical Data (SEPEHR)*, vol. 29, no. 116, pp. 103–118, 2021.

[14] H. Su, W. Chen, and M. Cheng, "Using the variable two-step floating catchment area method to measure the potential spatial accessibility of urban emergency shelters," *GeoJournal*, pp. 1–15, 2021.

[15] Y. Yao, Y. Zhang, T. Yao, K. Wong, J. Y. Tsou, and Y. Zhang, "A GIS-based system for spatial-temporal availability evaluation of the open spaces used as emergency shelters: the case of Victoria, British Columbia, Canada," *ISPRS International Journal of Geo-Information*, vol. 10, no. 2, p. 63, 2021.

[16] R. M. Gray, *Entropy and Information Theory*, Springer Science & Business Media, Berlin, Germany, 2011.

[17] W. K. Brauers and E. K. Zavadskas, "The MOORA method and its application to privatization in a transition economy," *Control and Cybernetics*, vol. 35, pp. 445–469, 2006.

[18] A. Azar and A. Rajabzadeh, "Applied decision making of MADM approach, tehran," 2010.

[19] P. Ghasemi and E. TalebiBrijani, "An integrated FAHP-PROMETHEE approach for selecting the best Flexible manufacturing system," *European Online Journal of Natural and Social Sciences*, vol. 3, no. 4, p. 1137, 2014.

[20] S. Mamalis, I. Kamenidou, S. Pavlidis, and A. Xatziaggelou, "Perceptions of hospital quality: a case study from Greece," in *Strategic Innovative Marketing and Tourism*, pp. 403–410, Springer, Cham, Switzerland, 2020.

[21] M. Behzadian, R. B. Kazemzadeh, A. Albadvi, and M. Aghdasi, "PROMETHEE: a comprehensive literature review on methodologies and applications," *European Journal of Operational Research*, vol. 200, no. 1, pp. 198–215, 2010.

[22] S. Greco, J. Figueira, and M. Ehrgott, *Multiple Criteria Decision Analysis*, Springer, New York, NY, USA, 2016.

[23] X. Qi, X. Yu, L. Wang, X. Liao, and S. Zhang, "PROMETHEE for prioritized criteria," in *Soft Computing*vol. 23, no. 22, pp. 11419–11432, 2019.

[24] P. Verma, "Promethee: a tool for multi-criteria decision analysis," in *Multi-Criteria Decision Analysis in Management*, pp. 282–309, IGI Global, Hershey, PA, USA, 2020.

[25] Habibi, M. Seyed, and M. Sedigheh, *Per Capita Urban Land Use*, National Land and Housing Organization Publications, Tehran, Iran, 1999.

[26] L. Zhao, H. Li, Y. Sun et al., "Planning emergency shelters forUrban disaster resilience: an integrated location-allocation modeling approach," *Sustainability*, vol. 9, no. 11, p. 2098, 2017.

[27] C. Jica, "The study on seismic microzoning of the Greater Tehran Area in the Islamic Republic of Iran," Pacific Consultants International Report, OYO Cooperation, Tokyo, Japan, 2000.

[28] A. Baležentis, T. Baležentis, and W. Brauers, "MULTIMOORA-FG: a multi-objective decision making method for linguistic reasoning with an application to personnel selection," *Informatica*, vol. 23, no. 2, pp. 173–190, 2012.

[29] T. Balezentis and A. Balezentis, "A survey on development and applications of the multicriteria decision making MethodMULTIMOORA," *Journal of Multi-Criteria Decision Analysis*, vol. 21, pp. 209–222, 2014.

[30] F. Jolai, M. J. Rezaee, and A. Vazifeh, "Multi-criteria decision making for assembly line balancing," *Journal of Intelligent Manufacturing*, vol. 20, no. 1, pp. 113–121, 2009.

[31] M. J. Rezaee and S. Yousefi, "An intelligent decision making approach for identifying and analyzing airport risks," *Journal of Air Transport Management*, vol. 68, pp. 14–27, 2018.

Hindawi
Mathematical Problems in Engineering
Volume 2021, Article ID 5583125, 13 pages
https://doi.org/10.1155/2021/5583125

Research Article

A New Multiobjective Time-Cost Trade-Off for Scheduling Maintenance Problem in a Series-Parallel System

Leyla Sadat Tavassoli,[1] Reza Massah,[2] Arsalan Montazeri,[3] Mirpouya Mirmozaffari,[4] Guang-Jun Jiang,[5,6] and Hong-Xia Chen[5,6]

[1]*Department of Industrial Manufacturing and Systems Engineering, University of Texas at Arlington, Arlington, TX, USA*
[2]*Department of Civil Engineering, University of Texas at Arlington, Arlington, TX, USA*
[3]*Department of Chemical Engineering, The University of Isfahan, Isfahan, Iran*
[4]*Department of Industrial Manufacturing and Systems Engineering, University of Texas at Arlington, Arlington, TX, USA*
[5]*School of Mechanical Engineering, Inner Mongolia University of Technology, Hohhot, Inner Mongolia 010051, China*
[6]*Inner Mongolia Key Laboratory of Advanced Manufacturing Technology, Hohhot 010051, Inner Mongolia, China*

Correspondence should be addressed to Guang-Jun Jiang; jianggj_2003@163.com

Received 2 March 2021; Revised 25 March 2021; Accepted 21 June 2021; Published 1 July 2021

Academic Editor: Wenyu Zhang

In this paper, a modified model of Nondominated Sorting Genetic Algorithm 2 (NSGA-II), which is one of the Multiobjective Evolutionary Algorithms, is proposed. This algorithm is a new model designed to make a trade-off between minimizing the cost of preventive maintenance (PM) and minimizing the time taken to perform this maintenance for a series-parallel system. In this model, the limitations of labor and equipment of the maintenance team and the effects of maintenance issues on manufacturing problems are also considered. In the mathematical model, finding the appropriate objective functions for the maintenance scheduling problem requires all maintenance costs and failure rates to be integrated. Additionally, the effects of production interruption during preventive maintenance are added to objective functions. Furthermore, to make a better performance compared with a regular NSGA-II algorithm, we proposed a modified algorithm with a repository to keep more unacceptable solutions. These solutions can be modified and changed with the proposed mutation algorithm to acceptable solutions. In this algorithm, modified operators, such as simulated binary crossover and polynomial mutation, will improve the algorithm to generate convergence and uniformly distributed solutions with more diverse solutions. Finally, by comparing the experimental solutions with the solutions of two Strength Pareto Evolutionary Algorithm 2 (SPEA2) and regular NSGA-II, MNSGA-II generates more efficient and uniform solutions than the other two algorithms.

1. Introduction

In today's industrial world, it is crucial for manufacturing companies to keep the production rates of machines constant. Since cost reduction and profit increase are the main goals of all manufacturing companies, the breakdown of production machines can cause a decrease in production or stop production in some cases, which will reduce the profits of companies eventually. In this situation, the need for a preventive maintenance (PM) system to keep the machines running is essential [1, 2].

Calculating the optimal time for PM actions will prevent not only the unexpected breakdown of machines but also save cost as too many maintenance operations could potentially increase the cost of production [3]. It is more complex when two preventive maintenance programs coincide. For example, labor shortage or lack of equipment for PM maintenance makes it difficult to perform the PM process on different machines simultaneously [4]. Since the maintenance team is unable to perform more than one maintenance at a time, the maintenance schedule should be changed so that no more than one maintenance is scheduled at a time [5].

Therefore, in cases where the machines' maintenance schedules overlap, we need to change the optimal time of the parts replacement by modifying the schedule. Hence, our goal is to create a trade-off between the optimal time for preventive maintenance and the limitations of labor and equipment in order to create an executable schedule at the lowest cost.

Preventive maintenance (PM) is an old well-known problem in the manufacturing world with a proven effect on production scheduling and output [6, 7]. It had been studied from the last century, starting from the policy development of replacement which was based on the limit for the repair cost to more complex methods such as the joint optimization of predictive maintenance planning and production scheduling [8].

There are a few approaches to how PM problems can be solved. The first one is to create policies/PM schedules by maximizing system availability. It has been done by using the different methods in [9–13]. Most of the existing research on PM overlooks the interrelationship between maintenance planning and equipment work schedules. As a result, maintenance planning is often done without considering the interactions between these two activities [14, 15]. The most recent research focuses on combining production scheduling with PM scheduling. Thus, the second approach to solve a PM problem is to create a PM scheduling model that considers the production schedule of the machines as the constraints [16, 17]. Another approach is to build the production scheduling model with the PM constraints, such as in [18]. Furthermore, the joint optimization of preventive maintenance and production scheduling planning gained a lot of interest. The goal is to minimize all the costs (maintenance and production-related) and satisfy the demand while creating the optimal production and preventive maintenance schedule [19–21]. Tardiness cost can also have an impact on the production and PM planning and was added to the objective function by [22, 23]. Additionally, the problem can be extended by considering the effect of maintenance on the quality of the products or simultaneously making the quality decision together with the production and maintenance.

Any scheduling problem is known as a complex problem that includes multiple objectives that have to be minimized or maximized at the same time. However, multiple scheduling criteria are rarely considered simultaneously in the literature [24] but, in recent years, it has gained more interest through a trade-off between conflicting objectives such as in [25, 26]. Multiple objectives are typically being used in such problems as the assignment-allocation problem [27] or supply chain network design problems [28]. In production scheduling models, it is very important to find the balance between the time and the total production cost [29, 80]. To buttress this point, [81] uses the multiobjective evolutionary algorithm to minimize the total flow time of jobs and the number of tardy jobs. PM scheduling and rescheduling are also done by minimizing total operational cost (job's total completion times, maintenance cost, and compression cost) and total completion time deviation simultaneously [30].

PM problem is categorized as an NP-hard problem as any scheduling model with a lot of constraints and large datasets. Metaheuristic is a to-go method for many scheduling/assignment problems that provides very good results in a short period of time that is a critical concern in the industry. Metaheuristic methods are a wide class of algorithms that can conduct searching phases based on their stochastic cores [31–41]. They have found their place among viral methods to be utilized for intelligent systems [42–46] and hybrid pattern recognition works [47–55]. These methods can be basic or enhanced methods with other evolutionary bases, and some examples include evolutionary algorithms, ant colony optimization (ACO) [36, 47], memetic and hybrid algorithms [56–60], tabu search, simulated annealing, etc. [47, 61]. Evolutionary algorithms have been found to be very successful in solving multiobjective optimization problems. They also have the potential to be integrated with the hybrid and new machine learning models in the future [62–67]. In the past decade, the nondominated sorting genetic algorithm (NSGA-II) has been one of the most popular and practical evolutionary multiobjective optimization (EMO) algorithms [32, 68–70].

There are many modified versions of heuristics algorithms that solve the scheduling and assignment problems, such as [35, 52, 55]. For example, in many studies, modified versions of NSGA-II were utilized in order to create algorithms to find more accurate solutions because the regular NSGA-II algorithms were not able to find it [71–74]. The other modified algorithms, such as SPEA-II and MOPSO, were generated in order to find solutions for particular problems which could not be solved by regular algorithms [36, 39, 75, 76].

In this study, we first review scheduling maintenance and cost optimization problems and integrate these two problems with other related problems in a series-parallel system. We convert these problems to a mathematical model and propose a modified-NSGA-II algorithm to get optimal solutions. Since many of the generated solutions are not acceptable due to having overlap with other solutions, this algorithm has a repository to keep these unacceptable solutions, which are changed from unacceptable to acceptable solutions by a mutation operator. Therefore, the performance of solution generation in the algorithm is increased. This mutation operator includes a complicated procedure to change the start times of preventive maintenance in solutions in order to convert unacceptable solutions to acceptable solutions in the repository.

In this modified NSGA-II algorithm, we propose to add a repository with a new mutation operator algorithm. Then we analyze the comparison of the results obtained from this algorithm with two regular algorithms.

2. Problems

2.1. Maintenance Scheduling Problem. Let us consider a factory in which several machines are working. Each piece of equipment has parts that wear out (depreciate) over time and need to be repaired or replaced. Obviously, the replacement time of these parts is different. In addition, the

time that the maintenance team spends to replace each of these parts varies. Therefore, considering the number of machines in operation and the several parts that must be repaired or replaced, the possibility of scheduling two different maintenance at the same time is very high. Due to the limited labor and equipment of the maintenance team, it is necessary to change the preventive replacement schedule when two or more maintenance coincides with each other. Potentially, it can help to prevent the accumulation of preventive maintenance over a period of time.

If we assume the total number of PM actions in a period of time is m so that the maintenance is arranged in order of its start time from 1 to m, then assuming that n is a number between 0 and m, the connection of the end time of the maintenance n with the start time of maintenance $n+1$ can have 3 modes.

In the first case, as soon as the maintenance n is completed, the maintenance $n+1$ begins. Since no time is wasted by the maintenance team between the two maintenance, it is an ideal situation.

The second case is when the period of time between PM actions n and $n+1$ overlaps. Indeed, the maintenance, $n+1$, begins before the completion of the maintenance, n. Due to the accumulation of the PM program and the limited capacity of the maintenance team, if the volume of maintenance work in a period of time is more than the capacity of the maintenance team, it becomes impossible to perform and the schedule would have to be modified. To solve this problem, we need to shift the maintenance n slightly backward or the maintenance $n+1$ slightly forward so that the overlap is eliminated and the maintenance planning becomes feasible.

In the last case, we have a gap or time interval between the end time of the maintenance n and the start time of the maintenance $n+1$, which means the maintenance team has to be idle during this period. This case is acceptable for the maintenance team, but it is not ideal due to the gap. Since our goal is to perform all periodic maintenance within a defined time frame, the presence of different gaps can waste time and cost. Hence, to create the optimal schedule, we can eliminate or reduce the gap or time interval between the two PM actions to get closer to the ideal state.

2.2. Cost Optimization and Failure Rate. A machine that works in a factory has parts that wear out over time. These parts need to be replaced periodically. Since for most of the parts, the possibility of failure increases over time with aging, the late replacement of each part escalates the probability of failure of that part. Failures may result in damage to other parts and components of the machine, which causes additional costs and inactivity of the machine for a period. On the other hand, the early replacement of defective parts can impose additional costs such as increased utilization of spare parts, the maintenance team's wages, and inactivity of the machine during the replacement period on the factory. Therefore, finding the exact time to replace defective parts is very important in reducing costs.

2.3. Production Problem in a Series-Parallel System. As mentioned earlier, keeping the production rate of machines constant is the main goal of the maintenance team. In a series-parallel system shown in Figure 1, stopping a machine due to a failure or stopping a manufacturing process due to PM activities will reduce production. This reduction rate or R_S is determined as follows:

$$R_s = \frac{R_i}{R_T}, \tag{1}$$

where R_i is the amount of reduction in production and R_T is the total production rate of machines in one of subsystems 1 to N while all the machines in that subsystem are working and it can be formulated as follows:

$$R_T = \sum_{i=1}^{n} R_n. \tag{2}$$

Therefore, R_S is a number between 0 and 1.

2.4. Trade-Off between Problems. As discussed in Section 2.2, early and late replacement of parts can increase costs. The exact time of replacement of each part can be calculated. The problem occurs when the maintenance team has limited working time. Therefore, it will be difficult to execute the schedule accurately. On the other hand, as mentioned in Section 2.3, keeping the production rate constant is also one of the goals of the maintenance unit.

Therefore, a trade-off between a production rate and PM costs is needed considering the limitations of labor and equipment of the maintenance team. In order to obtain this trade-off, a mathematical model is required.

3. Mathematical Model

In this paper, to create a mathematical model, we begin with identifying the problem assumptions and stating the constraints. Then the probability of failure of parts in the machine is calculated and the objective function by specifying the decision variables and the parameters are defined.

The assumptions of the problem are based on the following:

(i) The maintenance team is not able to perform a PM action on two machines at the same time

(ii) The daily and hourly efficiency of the maintenance team is constant

(iii) The maintenance team is available to perform PM action during all working hours of the company

(iv) The spare parts are available, and there are no restrictions on access to the required spare parts

(v) All required PM actions are performed within a specified time frame

where $T_{i,j,k}$ is the time allocated for PM action in the kth turn, to repair the part j^{th} of the machine i^{th}.

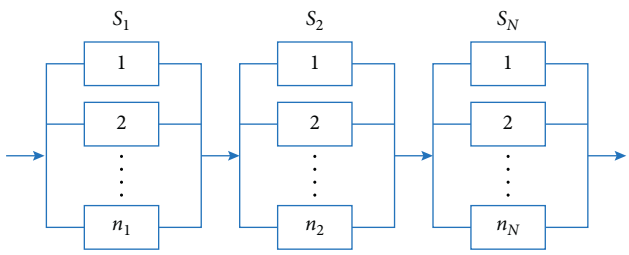

Figure 1: Series-parallel systems.

3.1. Identification of Failure Rate. We need an exponential function to calculate the failure time of parts in machines. The Weibull function [77] is used to check the failure time in the depreciation state. The Weibull function is a function with continuous values. The values of this function are nonnegative real numbers, so this distribution can be used in cases where the random variable is related to longevity. Therefore, to find the failure probability density function, the cumulative distribution function (CDF) would be a good option, which can be computed as follows:

$$r_{(y)} = 1 - e^{-(y/\lambda)^k}. \tag{3}$$

The part's age plays a decisive role in calculating the probability of part failure. If $r(y)$ is a function of the failure rate of the part, the probability of failure after time L is obtained from the following equation:

$$F(y) = \int_0^L r(y)\mathrm{d}x, \tag{4}$$

where L is the age of the part at time t, and the age of the part at the beginning of the period is equal to 0 due to PM action.

3.2. Identification of Decision Variables and Objective Functions. The decision variable in this problem is $L_{i,j,k}$, which is a matrix with i rows, j columns, and k dimension. In this matrix, i is the number of machines in operation, j is the number of parts of a machine that need preventive maintenance, and k is the number of times parts that need to be repaired. The number shown in each cell of this matrix is assigned to the start time of the PM action.

The duration of PM process for each part of the machine is a fixed number and it is indicated by $T_{i,j}$. The cost of the repair team for each hour of work on the ith machine and j^{th} part is specified as $P_{i,j}$, the cost of PM for the part j^{th} of the machine i^{th} is obtained from the following equation:

$$\mathrm{CPM}_{i,j} = \left(\left(T_{i,j} \times \left(P_{i,j} + M_{i,j}\right)\right) + S_{i,j}\right), \tag{5}$$

where $S_{i,j}$ is the price of spare part j^{th} of the machine i^{th} and $M_{i,j}$ is the cost of one hour of inactivity of the machine i^{th}.

Then the cost objective function is formulated as follows:

$$\text{minimize } Z = \sum_{i=1}^{I}\sum_{j=1}^{J}\sum_{k=1}^{K}\left(\mathrm{CPM}_{i,j} + \left(\left(\int_0^{L_{i,j,k}} r_{i,j}(y)dy\right) \times C_{i,j}\right)\right), \tag{6}$$

where $C_{i,j}$ is the cost of part j's breakdown of the machine i^{th}.

Since inactivity of the production line due to failure or PM process leads to decrease in the volume of the production, time objective function that can be formulated as follows:

$$\text{minimize } Z = \sum_{i=1}^{I}\sum_{j=1}^{J}\sum_{k=1}^{K}\left(\left(\left(\int_0^{L_{i,j,k}} r_{i,j}(y)\mathrm{d}y\right) \times R_i^s \times T_{i,j}'\right) + \left(Q_{i,j} \times T_{i,j} \times R_i^s\right)\right), \tag{7}$$

where R_i^s is the cost of inactivity for the machine, which has $T_{i,j}'$ hour inactivity for the machine i and the part j and $Q_{i,j}$ is the number of maintenance actions performed on the machine i and the part j.

s.t.

$$\sum_{i=1}^{I}\sum_{j=1}^{J}\sum_{k=1}^{K} T_{i,j,k} \le T_{\text{total}}, \quad i, j \in N, \tag{8}$$

$$\sum_{i=1}^{I} T_i' \le F_i, \quad i \in N, \tag{9}$$

$$A_t \in \{0\} \cup N, \quad \forall t \in T_{\text{total}}. \tag{10}$$

The total number of hours that the maintenance team is available to perform a PM action in the company is defined by T_{total}. Then we determine how many preventive maintenance activities should be done for each part of a single machine per year. It should be noted that each maintenance team has a certain capacity in terms of labor and equipment. Hence, the total time spent in a certain period should not exceed the capacity of the maintenance team. This period is usually considered to be annual—this constraint model as equation (8).

The constraint modeled by equation (9) allocates to the inactivity time of machine i in the time interval 0 to T_{total} which cannot be longer than the specified value F_i. The last constraint specifies the number of assignments assigned to the maintenance team at time t, denoted by A_t.

4. Methodology

On a production line, we often use a significant number of machines in the process, which affects the time and cost decisions of PM actions. In order to mitigate the computational difficulties of solving the resulting large-scale problem because of the nonlinear objective functions, we apply a modified NSGA-II heuristic algorithm. The modifications in the mutation and crossover operators are applied, which generate convergence and uniformly distributed solutions.

4.1. Initialization. Before creating the crossover and mutation operators, maintaining a diverse population of candidate solutions is required. This could subsequently be incorporated into a chromosome matrix. To solve the objective functions, the solutions created for this algorithm are in the form of a three-dimensional matrix. We assign a row that corresponds to each machine i in operation, a column that represents each part j of a machine in need of PM action, and a dimension that stands for time k that parts need to be repaired. The number shown in each element indicates the start time of the PM action for the machine i, the part j in the time k.

4.2. Simulated Binary Crossover (SBX). The simulated binary crossover operator produces children in the vicinity of the parents [78]. In this operator, the parents are generated using the roulette wheel selection. Moreover, the two corresponding elements from both matrices are randomly selected and then for u, a random value between 0 and 1 is generated. Then, the value of β is calculated as follows:

$$\beta = \begin{cases} (2u)^{1/\eta+1}, & \text{if } u \le 0.5, \\ \left(\dfrac{1}{2(1-u)}\right)^{1/\eta+1}, & \text{otherwise}, \end{cases} \tag{11}$$

where η is the distribution index, which is a real number.

Two new children are produced using the following formula. We use the following equations to create new solution candidates:

$$\begin{aligned} x_1 &= 0.5\left[(1+\beta)x_i + (1-\beta)x_j\right], \\ x_2 &= 0.5\left[(1-\beta)x_i + (1+\beta)x_j\right], \end{aligned} \tag{12}$$

where x_1 and x_2 are the children produced and x_i and x_j are the parents which are 2 elements of the decision variable matrix.

4.3. Polynomial Mutation. In polynomial mutation, it is possible to find a new solution at any distance from the parent, but it is more likely to be found around the parent than elsewhere [79]. To find the solution, first, the parameter δ is computed as follows:

$$\delta = \begin{cases} (2r)^{1/\eta-1} - 1, & \text{if } r < 0.5, \\ 1 - [2(1-r)]^{1/\eta+1}, & \text{if } r \ge 0.5, \end{cases} \tag{13}$$

where r is a random number between 0 and 1, and η is a positive real number that can directly control the probability distribution as an external parameter.

The mutated child is obtained from equation (14), in which x_U and x_L are the upper and lower bonds, to extract a new solution from the mutation operator.

$$x_2 = x_1 + (x_U - x_L)\delta. \tag{14}$$

4.4. Developed Mutation Algorithm (Mutation Type 2). This mutation operator is designed to convert unacceptable solutions to acceptable ones. Unacceptable solutions are solutions that overlap at least once with the other solutions. To solve this problem, we define a mutation operator (Figure 2). The mutation operator type 2 is designed by picking the first cell of the first row from the first column of the first aisle of the solutions matrix. If there is an overlap, the time interval of PM action for the cell increases or decreases to avoid any overlap with the other cells. Likewise, all cells in a row are reviewed to prevent overlapping between the cells. After reviewing one row, we will review the next row, and after reviewing all the rows of one aisle, we will review the other aisles until the last cell of the matrix is reviewed. After reviewing the last cell, the solution changes from an unacceptable solution to an acceptable solution.

4.5. Nondominated Sorting. To sort the solutions, we use the convexity crowding distance method. For every chromosome, we have the following:

$$\sum_{i=1}^{I} \frac{f_i(x) - F}{f_i^{\max} - f_i^{\min}}, \tag{15}$$

where $f_i(x)$ is the ith objective function and $f_i^{\max}$ and $f_i^{\min}$ are the highest and lowest values of the ith objective function value, respectively. F is the closest value generated to the considered objective value. Solutions with higher distance crowding are better solutions.

4.6. Repository. Since the number of acceptable solutions generated per iteration is very small, if we use standard algorithms to solve this problem, many solutions will be unacceptable due to overlap. If these solutions are eliminated, the speed of the algorithm is greatly reduced, and it takes a long time for the algorithm to find the optimal solutions for the problem. So, to solve this problem, we are looking for a new method to convert unacceptable solutions to acceptable ones.

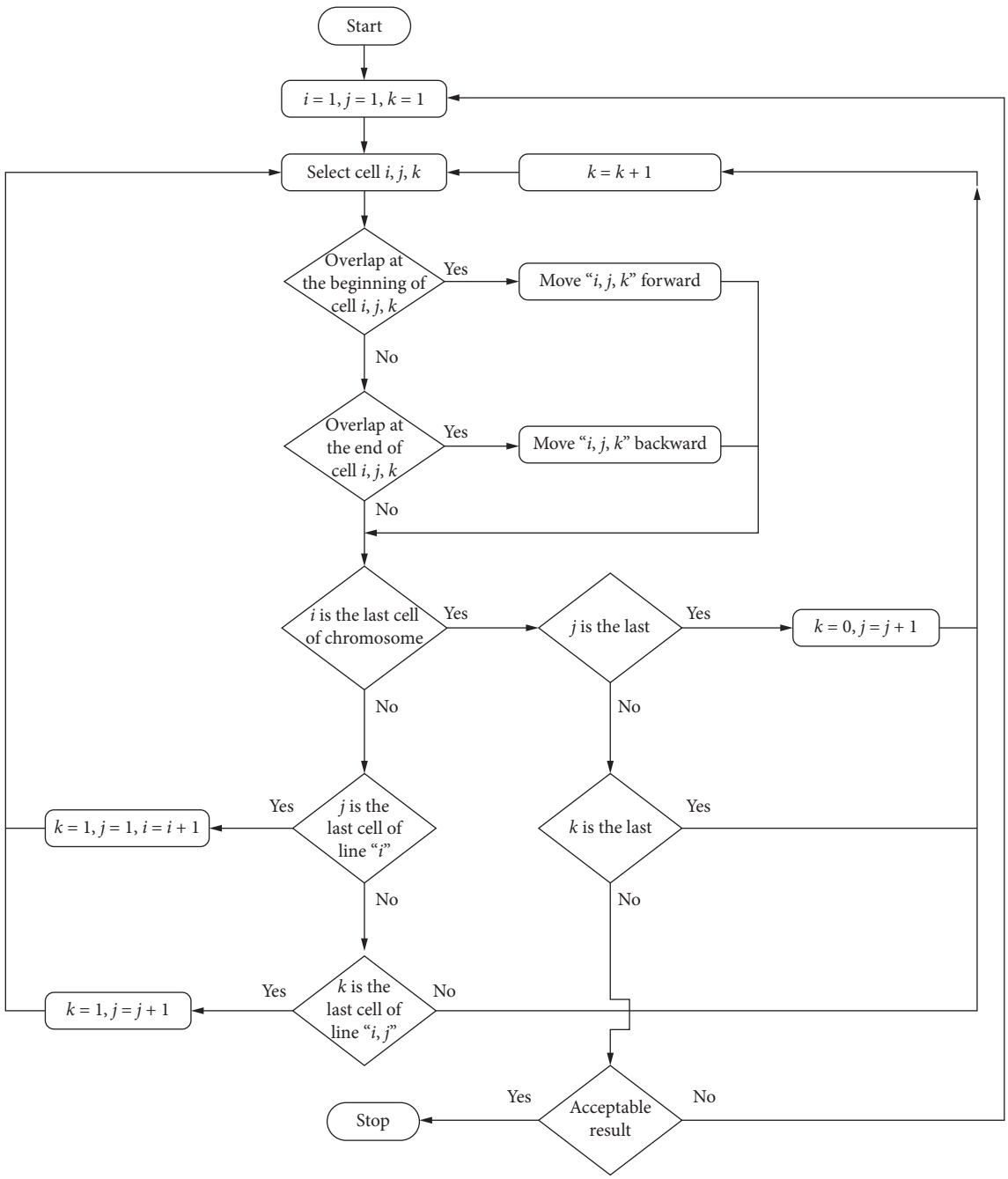

Figure 2: Developed mutation algorithm.

The proposed method is to use a repository to store unacceptable solutions generated by mutation type 1 and crossover operators. Since there is a high probability that some of the solutions generated by mutation and crossover operators are unacceptable solutions because of the time overlap among solution matrix cells, these unacceptable generated solutions are stored in the repository and then after performing mutation operator type 2, they are converted to acceptable solutions. Because the time consumption of mutation operator type 2 is significant, not all solutions are sent to this operator. Therefore, after ranking solutions in the repository, a certain number of the best solutions are sent to mutation operator type 2 and then they are converted into acceptable solutions.

The cycle of entering solutions into the repository and leaving solutions from the repository is shown in Figure 3. The only repository input is the unacceptable solutions generated by crossover and mutation type 1 operators. Since the capacity of the repository is limited and it is not possible to store all unacceptable solutions generated in the repository, in each iteration, a number of lower-ranked solutions in the repository are removed so that the repository has enough space to store the solutions generated in the next iteration. The number of removed solutions in each iteration

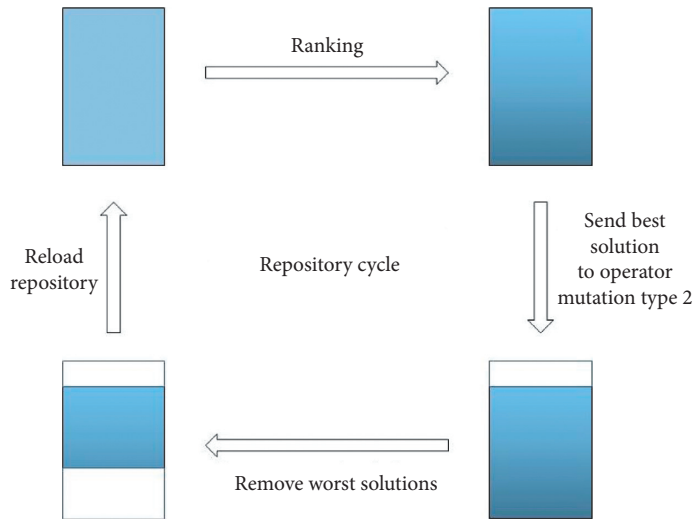

Figure 3: Repository cycle in MNSGA2 algorithm.

depends on the number of solutions entered into the repository and the number of solutions removed from the repository so that the number of solutions stored in the repository does not exceed the capacity of the repository.

The use of a repository in the NSGA2 algorithm also has disadvantages. The first drawback is to increase the computation time for each iteration of the algorithm. Although the presence of a repository in the algorithm causes more optimal solutions to be generated by the algorithm in each iteration, more significant time per iteration in the MNSGA2 algorithm is spent compared to the regular NSGA2 algorithm. It is because of the time required to perform operations in the type 2 mutation operator. A comparison between the time of each iteration between the algorithms is performed in the numerical example and result section. Another disadvantage of using this method is that many of the solutions generated by the type 2 mutation operator may no longer be the optimal solutions. The type 2 mutation operator converts unacceptable solutions into acceptable ones by changing the values of each solution matrix cell that overlaps with other cells in the same solution matrix, but these changes may result in to change the ranking of solutions.

4.7. Modified NSGA-II Algorithm. The idea behind the proposed algorithm is to increase the speed of generating optimal solutions. By adding a repository and a developed mutation algorithm (mutation type 2) to the regular NSGA-II algorithm, the modified NSGA-II algorithm is created, which has an extra loop compared to the regular NSGA-II algorithm. In the new algorithm, unacceptable optimal solutions that are in danger of being deleted because of having overlap between one cell in matrix solution and another cell in the same matrix solution are stored in the repository. These solutions are converted to acceptable solutions with the help of the mutation type 2 operator and then added to the candidate solutions. We conduct a modified NSGA-II algorithm that is illustrated in Figure 4.

5. Numerical Example and Result

We used the real data collected from a company that produced car spare parts for the computational experiments. In this company, there are 40 machines that are producing metal parts in a production line. This production line has 10 stations where there are 4 machines in each station. All machines are milling or turning machine tools that are under preventive maintenance scheduling.

These machines have some moving parts such as spindle, tool change, turret, pallet change, and moving table, all of which are depreciated due to their mobility. In addition to the mobility of these parts, machining vibration, corrosion of parts due to use of cooling fluid, and damage of machine parts because of metal chips increase the depreciation of machine parts. Typically, ball bearings, spindles, various parts of the cooling system, tool change, and pallet change are subject to preventive maintenance.

5.1. Results for Modified-NSGA-II, NSGA-II, and SPEA-II. We initialized the algorithm by randomly generating a population of 100 solutions. The number of the initial population and the solutions provided by mutation and crossover operators, repository capacity, and the maximum number of unacceptable solutions sent from repository to operator mutation type 2 would be different based on their importance on the problem. For this problem, values of algorithm and repository specifications are demonstrated in Table 1.

To assess the performance of our Modified-NSGA-II algorithm and compare it with the two algorithms NSGA-II and SPEA-II, we defined a reference set based on 100 best candidate solutions obtained by the Modified-NSGA-II, NSGA-II, and SPEA-II. Each was replicated 1000 times after every 100 iterations. Table 2 illustrates the number of nondominated solutions (NNS) by reference in all three algorithms, and as shown in Table 2, the Modified-NSGA-II algorithm has more nondominated solutions than the other

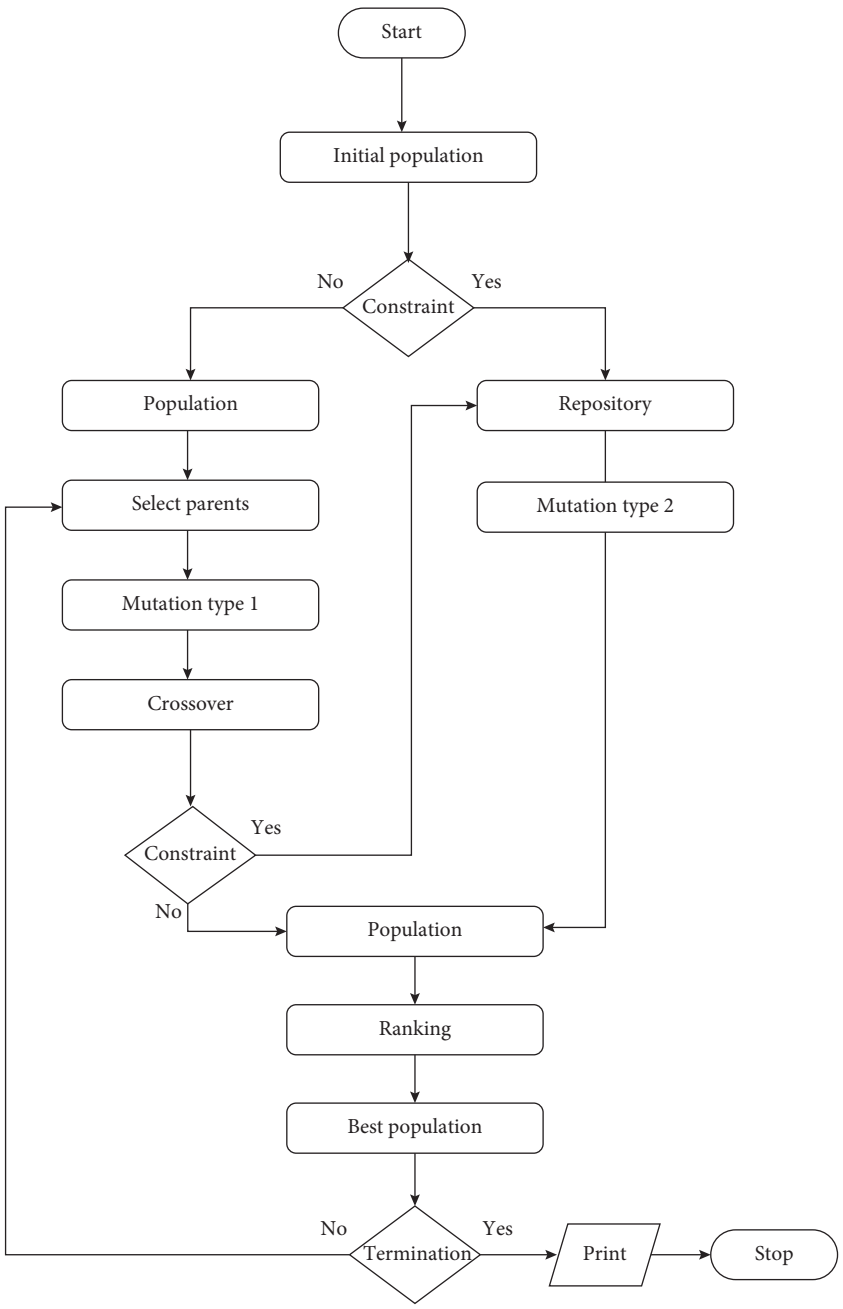

Figure 4: Modified-NSGA-II algorithm.

Table 1: Algorithm and repository specifications.

Algorithm specification	Number of produced populations
Initial population	100
Mutation (type 1)	30
Crossover	30
Repository capacity	500
Maximum number of unacceptable solutions sent from repository to operator mutation type 2 in each iteration	20

Table 2: The number of NNS for MNSGA-II, NSGA-II, and SPEA-II.

Generation	MNSGA-II	NSGA-II	SPEA2
100	88	2	4
200	87	0	1
300	80	0	0
400	76	0	0
500	77	0	0
600	72	0	0
700	72	0	0
800	72	0	0
900	73	0	0
1000	73	0	0

two algorithms. We conducted the experiment using the MATLAB platform on a Windows-based server with 16 GB RAM, i7 CPU, and 1.8GHs.

For further assessment, we compared the performance of the Modified-NSGA-II algorithm with the regular NSGA-II and SPEA-II algorithms using three methods: inverted generated distance, distribution metric, and spacing metric. The results of the comparison among the MNSGA-II, the NSGA-II, and the SPEA-II can be seen in Table 3.

5.2. Inverted Generated Distance. This approach is designed to assess diversity and convergence and can be calculated as follows:

$$\mathrm{IGD} = \frac{\sum_{v \in P^*} d(v, P)}{|P^*|}, \tag{16}$$

where P^* is equal to uniformly distributed points in a true Pareto front, P is a nondominated solution obtained by a selected algorithm, v is a solution that belongs to P^*, and 0 (v, P) is equal to the minimum Euclidean distance between v and the point in P. The results shown in Table 3 illustrate that, in general, the modified-NSGA-II algorithm has lower IGD values than the other two algorithms.

5.3. Delta Index. In the delta approach, the distribution of the solutions in the Pareto front is examined considering the following equation:

$$\Delta(s) = \sum_{i=1}^{|s|-1} \frac{|d_i - \overline{d}|}{|s| - 1}, \tag{17}$$

where d_i is the Euclidean distance between two consecutive solutions of Pareto front with s optimal solutions and $\overline{d}$ is the average d_i. The lower the value of delta is, the more uniformly the Pareto front is distributed. According to the values specified in Table 3, with a slight difference after the SPEA-II algorithm, the modified-NSGA-II algorithm has the lowest value.

5.4. Spacing Metrics. The uniformity of the distance between the Pareto front and the reference set is analyzed in the Spacing Metric method. A lower space parameter (SP) value

Table 3: Comparison of three algorithms.

Algorithm	IGD	Delta	Spacing
MNSGA-II	244900	7684	6
NSGA-II	2324000	15393	408
SPEA2	7814000	6398	6110

indicates a more uniform distance between the Pareto front and the reference. The SP value is calculated as follows:

$$\mathrm{SP}(s) = \sqrt{\frac{1}{|S| - 1} \sum_{i=1}^{|s|} \left(\overline{d} - d_i\right)^2}. \tag{18}$$

In this case, d_i is the minimum distance of solution i from the reference point. $\overline{d}$ is the average of d_i for s optimal solution set. According to the values specified in Table 3, with a significant difference compared to the other two algorithms, the SPEA2 algorithm has a uniform distance between the reference and Pareto front.

5.5. Operation Time. As mentioned in Section 4.6, although the MNSGA2 algorithm generates better solutions per iteration compared to the SPEA2 and NSGA2 algorithms due to the existence of a repository, it requires more time to perform the calculations. The more complexity the type 2 mutation operator has, the more time is required to perform calculations. Also, the more machines and parts that need preventive maintenance, the more cells the solution matrix has. In this case, the probability of overlap's existence is higher, and the probability of unacceptable solutions' existence increases as well. Also, more calculations in the type 2 mutation operator are required to make changes in the solution matrix and produce an acceptable solution. The increase in the computational volume in the type 2 mutation operator increases the whole operation time of the algorithm for each iteration. Figure 5 represents the computation time for this problem between MNSGA2, NSGA2, and SPEA2 algorithms. In Figure 5, the average operation time of NSGA2, MNSGA2, and SPEA2 algorithms is shown for 10 operations so that each one has 1000 iterations.

5.6. Fitness of Generated Solutions. Another problem that the MNSGA2 algorithm has in comparison with the two NSGA2 and SPEA2 algorithms is the change in the fitness or rank of the solutions after converting the unacceptable solutions into the acceptable ones in the type 2 mutation operator. As mentioned earlier, the type 2 mutation operator converts unacceptable solutions into acceptable ones by changing the values of the solution matrix cells that have overlapped with other cells, but after examining the fitness of the solutions, it becomes clear that the values obtained may no longer be our optimal solutions and may be dominated by other solutions obtained in the Pareto front. These solutions are removed after ranking and do not help speed up the algorithm to find optimal solutions. In this case, 73.6% of the total solutions generated by the mutation type 1 and crossover operators

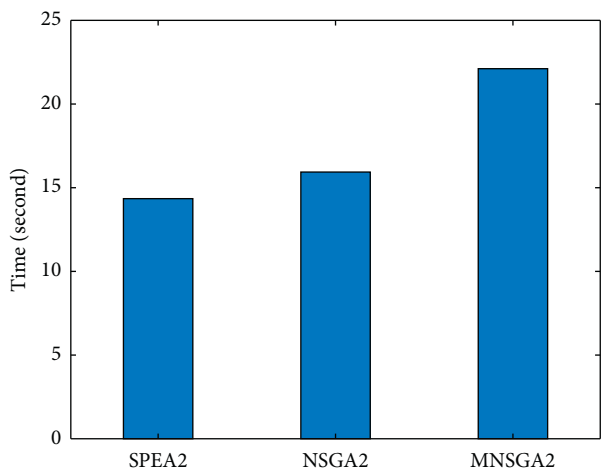

Figure 5: Operation time of algorithms.

were unacceptable, and 68.7% of the solutions generated by the type 2 mutation operator were dominated by other Pareto front solutions. These results are obtained from the average 10 times operation of the MNSGA2 algorithm, which has 1000 iterations each operation.

6. Conclusion

In this study, we developed a model to solve the scheduling problem in preventive maintenance for series-parallel systems. In this model, we addressed the problems in PM process scheduling in series-parallel systems and then turned this integrated model into a mathematical model. In this mathematical model, we considered a matrix as a decision variable where each cell represents the time scheduling of the PM process for a specific part of a single machine. In the future, the scale of the mathematical model can be changed by adding more decision variables to obtain more results. Then, we defined the objective functions in order to find the optimal solutions. Moreover, we proposed a modified genetic algorithm with customized mutation and crossover operators that allowed us to find a better solution compared to the existing algorithms. We implemented our experiments on a case study drawn from the real data then analyzed and compared the solutions.

Our results confirm the better performance of the MNSGA-II algorithm, which proposes that evolutionary algorithms alone do not necessarily provide more viable optimal solutions and need customized operators for better computational efficiency. In our future works, we will consider more objective functions like the scheduling of special equipment's use in the PM process, the spare parts supply, and the employment of specially trained personnel by utilizing the modified NSGA-II that presented in this study. Analysis of the scheduling time of PM action provides manufacturing companies with valuable information to determine meticulous scheduling decisions and planning, prevent production interruptions, and increase the amount of production.

Abbreviations

Parameters of mathematical model

R_i: Amount of reduction in production
R_T: Total production rate of machines
R_S: Reduction rate
T_{total}: Total number of maintenance team working hours
$T_{i,j,k}$: Time allocated for PM action in the kth turn, to repair the part j^{th} of the machine i^{th}
$S_{i,j}$: Price of spare part j^{th} of the machine i^{th}
$CPM_{i,j}$: Cost of PM for the part j^{th} of the machine i^{th}
$P_{i,j}$: Hours of work on the ith machine and j^{th} part
$C_{i,j}$: Cost of part j's breakdown of the machine i^{th}
$T'_{i,j}$: Hours of inactivity for the machine i and the part j
$Q_{i,j}$: Number of maintenance actions performed on the machine i and the part j
R_i^s: Cost of inactivity for machine i.

Data Availability

No data were used to support this study.

Conflicts of Interest

The authors declare that they have no conflicts of interest.

Acknowledgments

This work was partially supported by the National Natural Science Foundation of China under the contract number 71761030 and the Natural Science Foundation of Inner Mongolia under the contract number 2019LH07003.

References

[1] F. Fallahi, M. Yildirim, J. Lin, and C. Wang, "Predictive multi-microgrid generation maintenance: formulation and impact on operations & resilience," *IEEE Transactions on Power Systems*, vol. 36, p. 1, 2021.

[2] M. Mirmozaffari, R. Yazdani, E. Shadkam, L. S. Tavassoli, and R. Massah, "VCS and CVS: new combined parametric and non-parametric operation research models," *Sustainable Operations and Computers*, vol. 2, pp. 36–56, 2021.

[3] M. Yazdi, "Acquiring and sharing tacit knowledge in failure diagnosis analysis using intuitionistic and Pythagorean assessments," *Journal of Failure Analysis and Prevention*, vol. 19, no. 2, pp. 369–386, 2019.

[4] N. Wang, S. Ren, Y. Liu, M. Yang, J. Wang, and D. Huisingh, "An active preventive maintenance approach of complex equipment based on a novel product-service system operation mode," *Journal of Cleaner Production*, vol. 277, Article ID 123365, 2020.

[5] M. Yazdi, N. A. Golilarz, A. Nedjati, and K. A. Adesina, "An improved lasso regression model for evaluating the efficiency of intervention actions in a system reliability analysis," *Neural Computing and Applications*, vol. 33, pp. 1–16.

[6] L. S. Tavassoli, N. Sakhavand, and S. S. Fazeli, "Integrated preventive maintenance scheduling model with redundancy for cutting tools on a single machine," *Engineering, Technology & Applied Science Research*, vol. 10, no. 6, pp. 6542–6548, 2020.

[7] M. Tavana, K. Khalili-Damghani, D. Di Caprio, and Z. Oveisi, "An evolutionary computation approach to solving repairable multi-state multiobjective redundancy allocation problems," *Neural Computing and Applications*, vol. 30, no. 1, pp. 127–139, 2018.

[8] Q. Liu, M. Dong, and F. F. Chen, "Single-machine-based joint optimization of predictive maintenance planning and production scheduling," *Robotics and Computer-Integrated Manufacturing*, vol. 51, pp. 238–247, 2018.

[9] J. Pulido, "Using accelerated life testing techniques for preventive maintenance scheduling," in *Proceedings of the 2014 Reliability and Maintainability Symposium*, pp. 1–6, IEEE, Colorado Springs, CO, USA, January 2014.

[10] Y. Gao, Y. Feng, Z. Zhang, and J. Tan, "An optimal dynamic interval preventive maintenance scheduling for series systems," *Reliability Engineering & System Safety*, vol. 142, pp. 19–30, 2015.

[11] A. Abdelhadi, "Preventive maintenance operations scheduling based on Eigenvalue and clustering methods," in *Proceedings of the 2019 IEEE 6th International Conference on Industrial Engineering and Applications (ICIEA)*, pp. 183–186, IEEE, Tokyo, Japan, January 2019.

[12] M. Hamedi, S. Sharafi, and M. T. Delshad, "Optimization of preventive maintenance scheduling based on Monte Carlo simulation in processing plants," in *Proceedings of the 2019 15th Iran International Industrial Engineering Conference (IIIEC)*, pp. 293–296, IEEE, Yazd, Iran, January 2019.

[13] X. Wang, H. Zhou, A. K. Parlikad, and M. Xie, "Imperfect preventive maintenance policies with unpunctual execution," *IEEE Transactions on Reliability*, vol. 69, no. 4, pp. 1480–1492, 2020.

[14] Z. Zhu, Y. Xiang, M. Li, W. Zhu, and K. Schneider, "Preventive maintenance subject to equipment unavailability," *IEEE Transactions on Reliability*, vol. 68, no. 3, pp. 1009–1020, 2019.

[15] J. Huang, Q. Chang, and J. Arinez, "Deep reinforcement learning based preventive maintenance policy for serial production lines," *Expert Systems with Applications*, vol. 160, Article ID 113701, 2020.

[16] S. N. Mirabedini and H. Iranmanesh, "A scheduling model for serial jobs on parallel machines with different preventive maintenance (PM)," *The International Journal of Advanced Manufacturing Technology*, vol. 70, no. 9–12, pp. 1579–1589, 2014.

[17] Q. Wang, D. Li, and X. Zhang, "A new model of preventive maintenance scheduling for parallel production line," in *Proceedings of the 2016 Prognostics and System Health Management Conference (PHM-Chengdu)*, pp. 1–4, IEEE, Chengdu, China, October 2016.

[18] S. Chen and L. Wang, "ACO-based parallel machine scheduling considering both setup time and run-based preventive maintenance with reliability constraints," in *Proceedings of the 2018 IEEE International Conference on Industrial Engineering and Engineering Management (IEEM)*, pp. 227–231, IEEE, Bangkok, Thailand, December 2018.

[19] S. Wang, "Integrated model of production planning and imperfect preventive maintenance policy for single machine system," *International Journal of Operational Research*, vol. 18, no. 2, pp. 140–156, 2013.

[20] M.-C. Fitouhi and M. Nourelfath, "Integrating noncyclical preventive maintenance scheduling and production planning for multi-state systems," *Reliability Engineering & System Safety*, vol. 121, pp. 175–186, 2014.

[21] A. Wolter and S. Helber, "Simultaneous production and maintenance planning for a single capacitated resource facing both a dynamic demand and intensive wear and tear," *Central European Journal of Operations Research*, vol. 24, no. 3, pp. 489–513, 2016.

[22] J. Ye and H. Ma, "Multiobjective joint optimization of production scheduling and maintenance planning in the flexible job-shop problem," *Mathematical Problems in Engineering*, vol. 2015, Article ID 725460, 9 pages, 2015.

[23] L. Xiao, S. Song, X. Chen, and D. W. Coit, "Joint optimization of production scheduling and machine group preventive maintenance," *Reliability Engineering & System Safety*, vol. 146, pp. 68–78, 2016.

[24] S. S. Fazeli, *Stochastic Programming Models for Electric Vehicles' Operation: Network Design and Routing Strategies*, Wayne State University, Detroit, MI, USA, 2020.

[25] M. Tavana, A.-R. Abtahi, and K. Khalili-Damghani, "A new multiobjective multi-mode model for solving preemptive time-cost-quality trade-off project scheduling problems," *Expert Systems with Applications*, vol. 41, no. 4, pp. 1830–1846, 2014.

[26] S. S. Fazeli, S. Venkatachalam, and J. M. Smereka, "Efficient algorithms for autonomous electric vehicles' min-max routing problem," 2020, https://arxiv.org/pdf/2008.03333.pdf.

[27] H. Jiang, J. Yi, S. Chen, and X. Zhu, "A multiobjective algorithm for task scheduling and resource allocation in cloud-based disassembly," *Journal of Manufacturing Systems*, vol. 41, pp. 239–255, 2016.

[28] S.-H. Liao, C.-L. Hsieh, and W.-C. Ho, "Multiobjective evolutionary approach for supply chain network design problem within online customer consideration," *RAIRO-Operations Research*, vol. 51, no. 1, pp. 135–155, 2017.

[29] Z.-H. Jia, M.-L. Pei, and J. Y.-T. Leung, "Multiobjective ACO algorithms to minimise the makespan and the total rejection cost on BPMs with arbitrary job weights," *International Journal of Systems Science*, vol. 48, no. 16, pp. 3542–3557, 2017.

[30] D.-J. Wang, F. Liu, J.-J. Wang, and Y.-Z. Wang, "Integrated rescheduling and preventive maintenance for arrival of new jobs through evolutionary multiobjective optimization," *Soft Computing*, vol. 20, no. 4, pp. 1635–1652, 2016.

[31] H. Yu, W. Li, C. Cheng et al., "Dynamic Gaussian bare-bones fruit fly optimizers with abandonment mechanism: method and analysis," *Engineering with Computers*, vol. 36, pp. 1–29, 2020.

[32] J. Hu, H. Chen, A. A. Heidari et al., "Orthogonal learning covariance matrix for defects of grey wolf optimizer: insights, balance, diversity, and feature selection," *Knowledge-Based Systems*, vol. 213, Article ID 106684, 2021.

[33] C. Yu, M. Chen, K. Cheng et al., "SGOA: annealing-behaved grasshopper optimizer for global tasks," *Engineering with Computers*, vol. 37, pp. 1–28, 2021.

[34] W. Shan, Z. Qiao, A. A. Heidari, H. Chen, H. Turabieh, and Y. Teng, "Double adaptive weights for stabilization of moth flame optimizer: balance analysis, engineering cases, and medical diagnosis," *Knowledge-Based Systems*, vol. 214, Article ID 106728, 2020.

[35] J. Tu, H. Chen, J. Liu et al., "Evolutionary biogeography-based whale optimization methods with communication structure: towards measuring the balance," *Knowledge-Based Systems*, vol. 212, Article ID 106642, 2021.

[36] D. Zhao, L. Liu, F. Yu et al., "Chaotic random spare ant colony optimization for multi-threshold image segmentation of 2D Kapur entropy," *Knowledge-Based Systems*, vol. 216, Article ID 106510, 2020.

[37] H. Chen, A. A. Heidari, H. Chen, M. Wang, Z. Pan, and A. H. Gandomi, "Multi-population differential evolution-assisted Harris hawks optimization: framework and case studies," *Future Generation Computer Systems*, vol. 111, pp. 175–198, 2020.

[38] X. Zhao, X. Zhang, Z. Cai et al., "Chaos enhanced grey wolf optimization wrapped ELM for diagnosis of paraquat-poisoned patients," *Computational Biology and Chemistry*, vol. 78, pp. 481–490, 2019.

[39] Y. Xu, H. Chen, J. Luo, Q. Zhang, S. Jiao, and X. Zhang, "Enhanced Moth-flame optimizer with mutation strategy for global optimization," *Information Sciences*, vol. 492, pp. 181–203, 2019.

[40] M. Wang and H. Chen, "Chaotic multi-swarm whale optimizer boosted support vector machine for medical diagnosis," *Applied Soft Computing Journal*, vol. 88, Article ID 105946, 2020.

[41] M. Wang, H. Chen, B. Yang et al., "Toward an optimal kernel extreme learning machine using a chaotic moth-flame optimization strategy with applications in medical diagnoses," *Neurocomputing*, vol. 267, pp. 69–84, 2017.

[42] W. Zhu, C. Ma, X. Zhao et al., "Evaluation of sino foreign cooperative education project using orthogonal sine cosine optimized kernel extreme learning machine," *IEEE Access*, vol. 8, pp. 61107–61123, 2020.

[43] G. Liu, W. Jia, M. Wang et al., "Predicting cervical hyperextension injury: a covariance guided sine cosine support vector machine," *IEEE Access*, vol. 8, pp. 46895–46908, 2020.

[44] Y. Wei, H. Lv, M. Chen et al., "Predicting entrepreneurial intention of students: an extreme learning machine with Gaussian Barebone Harris Hawks optimizer," *IEEE Access*, vol. 8, pp. 76841–76855, 2020.

[45] H. Tang, Y. Xu, A. Lin et al., "Predicting green consumption behaviors of students using efficient firefly grey wolf-assisted K-nearest neighbor classifiers," *IEEE Access*, vol. 8, pp. 35546–35562, 2020.

[46] A. Lin, Q. Wu, A. A. Heidari et al., "Predicting intentions of students for master programs using a chaos-induced sine cosine-based fuzzy K-Nearest neighbor classifier," *Ieee Access*, vol. 7, pp. 67235–67248, 2019.

[47] X. Zhao, D. Li, B. Yang, C. Ma, Y. Zhu, and H. Chen, "Feature selection based on improved ant colony optimization for online detection of foreign fiber in cotton," *Applied Soft Computing*, vol. 24, pp. 585–596, 2014.

[48] Y. Zhang, R. Liu, A. A. Heidar et al., "Towards augmented kernel extreme learning models for bankruptcy prediction: algorithmic behavior and comprehensive analysis," *Neurocomputing*, vol. 430, pp. 185–212, 2020.

[49] Y. Zhang, R. Liu, X. Wang, H. Chen, and C. Li, "Boosted binary Harris hawks optimizer and feature selection," *Engineering with Computers*, vol. 36, pp. 1–30, 2020.

[50] H.-L. Chen, G. Wang, C. Ma, Z.-N. Cai, W.-B. Liu, and S.-J. Wang, "An efficient hybrid kernel extreme learning machine approach for early diagnosis of Parkinson's disease," *Neurocomputing*, vol. 184, pp. 131–144, 2016.

[51] L. Hu, G. Hong, J. Ma, X. Wang, and H. Chen, "An efficient machine learning approach for diagnosis of paraquat-poisoned patients," *Computers in Biology and Medicine*, vol. 59, pp. 116–124, 2015.

[52] L. Shen, H. Chen, Z. Yu et al., "Evolving support vector machines using fruit fly optimization for medical data classification," *Knowledge-Based Systems*, vol. 96, pp. 61–75, 2016.

[53] J. Xia, H. Chen, Q. Li et al., "Ultrasound-based differentiation of malignant and benign thyroid Nodules: an extreme learning machine approach," *Computer Methods and Programs in Biomedicine*, vol. 147, pp. 37–49, 2017.

[54] C. Li, L. Hou, B. Y. Sharma et al., "Developing a new intelligent system for the diagnosis of tuberculous pleural effusion," *Computer Methods and Programs in Biomedicine*, vol. 153, pp. 211–225, 2018.

[55] X. Xu and H.-L. Chen, "Adaptive computational chemotaxis based on field in bacterial foraging optimization," *Soft Computing*, vol. 18, no. 4, pp. 797–807, 2014.

[56] Y. Fan, P. Wang, A. A. Heidari et al., "Rationalized fruit fly optimization with sine cosine algorithm: a comprehensive analysis," *Expert Systems with Applications*, vol. 157, Article ID 113486, 2020.

[57] E. Rodríguez-Esparza, L. A. Zanella-Calzada, D. Oliva et al., "An efficient Harris hawks-inspired image segmentation method," *Expert Systems with Applications*, vol. 155, Article ID 113428, 2020.

[58] S. Jiao, G. Chong, C. Huang et al., "Orthogonally adapted Harris hawks optimization for parameter estimation of photovoltaic models," *Energy*, vol. 203, Article ID 117804, 2020.

[59] Z. Xu, Z. Hu, A. A. Heidari et al., "Orthogonally-designed adapted grasshopper optimization: a comprehensive analysis," *Expert Systems with Applications*, vol. 150, Article ID 113282, 2020.

[60] M. Mahjoob, S. S. Fazeli, S. Milanlouei, and L. S. Tavassoli, "A modified adaptive genetic algorithm for multi-productmulti-period inventory routing problem," 2021, https://arxiv.org/abs/2104.09031.

[61] Z. Mujkic, A. Qorri, and A. Kraslawski, "Sustainability and optimization of supply chains: a literature review," *Operations and Supply Chain Management: An International Journal*, vol. 11, no. 4, pp. 186–199, 2018.

[62] X. Zhang, J. Wang, T. Wang, R. Jiang, J. Xu, and L. Zhao, "Robust feature learning for adversarial defense via hierarchical feature alignment," *Information Sciences*, vol. 560, pp. 256–270, 2020.

[63] X. Zhang, T. Wang, W. Luo, and P. Huang, "Multi-level fusion and attention-guided CNN for image dehazing," *IEEE Transactions on Circuits and Systems for Video Technology*, vol. 30, p. 1, 2020.

[64] X. Zhang, M. Fan, D. Wang, P. Zhou, and D. Tao, "Top-k feature selection framework using robust 0-1 integer programming," *IEEE Transactions on Neural Networks and Learning Systems*, vol. 31, pp. 1–15, 2020.

[65] X. Zhang, D. Wang, Z. Zhou, and Y. Ma, "Robust low-rank tensor recovery with rectification and alignment," *IEEE Transactions on Pattern Analysis and Machine Intelligence*, vol. 43, no. 1, pp. 238–255, 2019.

[66] X. Zhang, R. Jiang, T. Wang, and J. Wang, "Recursive neural network for video deblurring," *IEEE Transactions on Circuits and Systems for Video Technology*, vol. 30, p. 1, 2020.

[67] X. Zhang, T. Wang, J. Wang, G. Tang, and L. Zhao, "Pyramid channel-based feature attention network for image dehazing," *Computer Vision and Image Understanding*, vol. 197-198, Article ID 103003, 2020.

[68] F. Zhao, L. Huan, Y. Zhang, W. Ma, and C. Zhang, "A novel multiobjective optimization algorithm based on differential evolution and NSGA-II," in *Proceedings of the 2018 IEEE 22nd International Conference on Computer Supported Cooperative Work in Design ((CSCWD))*, pp. 570–575, IEEE, Nanjing, China, May 2018.

[69] N. A. Golilarz, A. Addeh, H. Gao et al., "A new automatic method for control chart patterns recognition based on

ConvNet and harris hawks meta heuristic optimization algorithm," *IEEE Access*, vol. 7, pp. 149398–149405, 2019.

[70] N. Amiri Golilarz, H. Gao, and H. Demirel, "Satellite image de-noising with Harris hawks meta heuristic optimization algorithm and improved adaptive generalized Gaussian distribution threshold function," *IEEE Access*, vol. 7, pp. 57459–57468, 2019.

[71] S. Bandyopadhyay and R. Bhattacharya, "Solving multi-objective parallel machine scheduling problem by a modified NSGA-II," *Applied Mathematical Modelling*, vol. 37, no. 10-11, pp. 6718–6729, 2013.

[72] F. T. S. Chan, A. Jha, and M. K. Tiwari, "Bi-objective optimization of three echelon supply chain involving truck selection and loading using NSGA-II with heuristics algorithm," *Applied Soft Computing*, vol. 38, pp. 978–987, 2016.

[73] S. H. R. Pasandideh, S. T. A. Niaki, and K. Asadi, "Bi-objective optimization of a multi-product multi-period three-echelon supply chain problem under uncertain environments: NSGA-II and NRGA," *Information Sciences*, vol. 292, pp. 57–74, 2015.

[74] S. Bandyopadhyay and R. Bhattacharya, "Applying modified NSGA-II for bi-objective supply chain problem," *Journal of Intelligent Manufacturing*, vol. 24, no. 4, pp. 707–716, 2013.

[75] A. K. Paul and P. C. Shill, "New automatic fuzzy relational clustering algorithms using multiobjective NSGA-II," *Information Sciences*, vol. 448-449, pp. 112–133, 2018.

[76] M. Wang and H. Chen, "Chaotic multi-swarm whale optimizer boosted support vector machine for medical diagnosis," *Applied Soft Computing*, vol. 88, Article ID 105946, 2020.

[77] D. P. Murthy, M. Xie, and R. Jiang, *Weibull Models*, John Wiley & Sons, Hoboken, NJ, USA, 2004.

[78] S. Ramesh, S. Kannan, and S. Baskar, "Application of modified NSGA-II algorithm to multiobjective reactive power planning," *Applied Soft Computing*, vol. 12, no. 2, pp. 741–753, 2012.

[79] K. Deb, "Multiobjective optimisation using evolutionary algorithms: an introduction," in *Multiobjective Evolutionary Optimisation for Product Design and Manufacturing*, pp. 3–34, Springer, London, UK, 2011.

[80] M. Mahjoob, S. S. Fazeli, S. Milanlouei, A. K. Mohammadzadeh, and L. S. Tavassoli, "Green supply chain network design with emphasis on inventory decisions," *Sustainable Operations and Computers*, vol. 2, 2021.

[81] M. Mahjoob, S. S. Fazeli, L. S. Tavassoli, M. Mirmozaffari, and S. Milanlouei, "A green multi-period inventory routing problem with pickup and split delivery: a case study in flour industry," *Sustainable Operations and Computers*, vol. 2, 2021.

Hindawi
Mathematical Problems in Engineering
Volume 2021, Article ID 5579218, 9 pages
https://doi.org/10.1155/2021/5579218

Research Article

Reliability Analysis of Special Vehicle Critical System Using Discrete-Time Bayesian Network

Zong-Yuan Li,[1] **Guang-Jun Jiang**,[1,2] **Hong-Xia Chen**,[1,2] **Hai-Bin Li**,[1] **and Hong-Hua Sun**[1,2]

[1]*School of Mechanical Engineering, Inner Mongolia University of Technology, Hohhot 010051, Inner Mongolia, China*
[2]*Inner Mongolia Key Laboratory of Advanced Manufacturing Technology, Hohhot 010051, Inner Mongolia, China*

Correspondence should be addressed to Guang-Jun Jiang; jiang2003@imut.edu.cn

Received 19 January 2021; Accepted 17 June 2021; Published 23 June 2021

Academic Editor: Mohammad Yazdi

The reliability assessment of special vehicles has become very important. However, due to the special structure of special vehicles, it is difficult to collect a large amount of experimental data. The use of traditional fault tree analysis cannot accurately assess product reliability. In this paper, dynamic fault trees are used to model the critical systems of special vehicles, and discrete Bayesian networks are used to evaluate the reliability of critical systems of special vehicles, which solved the problems of difficulty in accurately describing complex systems in the process of system reliability analysis and difficulty in obtaining accurate data in the process of analysis. Finally, through the combination of expert experience and the evaluation of the calculation results, the rationality of the method used in this paper in the reliability evaluation of special vehicles is verified.

1. Introduction

In recent years, the dynamic characteristics of the heavy Ammonium Nitrate/Fuel Oil (ANFO) vehicle are more obvious with the increase of parts or subsystems with dynamic characteristics. The conventional reliability analysis methods such as static fault tree are applied to calculate the reliability of ANFO. These methods usually do not consider dynamic correlation of parts in the system, such as sequence enforcing relationship, functional dependency, and spare relationship. It is widely used in various engineering fields, and the analysis accuracy can meet the engineering requirements as discussed by Mi et al. [1]. However, modern equipment such as the heavy ANFO vehicle has complex systems and cannot use the conventional fault tree to describe dynamic correlation [2]. Therefore, the reliability analysis of the subsystem with dynamic characteristics is the emphasis and difficulty of reliability analysis for the heavy ANFO vehicle.

Fault tree analysis is a risk assessment method to improve the traditional fault tree analysis, mainly for the study of uncertainty in qualitative and quantitative risk assessment procedures [3, 4]. The reliability analysis of the dynamic fault tree can be carried out by Markov chain, cut sequence, extended cut sequence, module method, and Bayesian network as discussed by Fang et al. [2, 5]. In the initial stage of dynamic fault tree research, the minimum cut sequence is solved by the mixed integral formula, and then, the dynamic fault tree can be analyzed. Many scholars have extended the dynamic fault tree analysis method. Tremyasov and Tremyasov [6] established the dynamic fault tree model of the wind turbine generator and used Markov to calculate their operational reliability. Because the state explosion problem of Markov chain limits its application, Boudali and Dugan [3] proposed using the Bayesian network to solve dynamic fault tree, and a method of transforming dynamic fault tree logic gates into the Bayesian network was developed. Li et al. [2, 7] estimated the reliability of floating offshore wind turbines and their crucial systems by Bayesian networks. Li et al. [4] abandoned the global state modeling method and used the continuous time Bayesian network to analyze the dynamic fault tree. Meanwhile, the fuzzy number was applied to describe the parameter uncertainty caused by insufficient failure data. In the initial study of the dynamic fault tree, the distribution of spare parts' nodes can only be

exponential distribution. Li et al. [8] solved this limitation through an in-depth study. Ge et al. [9, 10] developed Sequential Binary Decision Diagrams (SBDDs) based on the BDD method and used the improved ITE (if-then-else) algorithm to avoid generating invalid nodes when building SBDDS. Some scholars divided the dynamic fault tree model into the parental Markov condition and other condition using the modular method. The former was analyzed by establishing the Markov model, while the latter was reasoned by building the Bayesian network model as discussed by Yuge et al. [11]. Although many scholars had studied SBDDs to optimize its state space explosion, computational efficiency, and application scope, there were still some limitations compared with the Bayesian network method as discussed by Mi et al. [1], Zhang et al. [12], and Zhang et al. [13]. Because of the disadvantages of the discrete-time Bayesian network, many scholars had further improved it. The accuracy and efficiency of the Bayesian network was greatly improved by the error compensation. The failure probability can be accurately calculated even in a short time interval as discussed by Lan et al. [14]. The collection of reliability data, as in [15–18], improved the accuracy of evaluation using multisource information fusion. Due to the complex state of nodes, the dynamic fault tree cannot be solved and reasoned manually and software was needed. Dugan [19] proposed Galileo, which is a prototype software tool for dynamic fault tree reliability analysis. It is mainly used to construct and analyze the dynamic fault tree containing the sequential failure mode. Firstly, it divides the dynamic fault tree into several subsystems. Then, a subsystem is transformed into a submodel based on BDD and Markov chain. Finally, the reliability of these submodels is analyzed as discussed by Dugan et al. [19, 20]. In recent years, RAATSS and Matlab tools are widely used in the reliability analysis of dynamic fault tree models because of their high accuracy and simple modeling. The dynamic fault tree analysis method had been used in the reliability analysis for different systems in various fields. It had obtained fruitful research results and had great significance for improving the reliability of the system. The advantage of the discrete-time Bayesian network is more obvious with the development. Therefore, this paper will apply it to analyze the reliability of the heavy ANFO vehicle.

2. Dynamic Fault Tree

The static fault tree is a graphical expression, which is widely used in reliability analysis of complex engineering. The static fault tree model can intuitively describe the combined failure form of parts that cause system failure. However, complex engineering equipment is not only affected by the external environment but also the relationship between internal parts. The reliability modeling of the system is facing great difficulties because of the correlation between parts. To solve such problems, Dugan et al. [20] proposed some dynamic logic gates to describe the relevance of parts. The method can well describe the temporary characteristic and dynamic failure behavior of the system (see [21]). In addition to using the logic gates of the static fault tree, this method added four dynamic logic gates: priority-AND (PAND) gate, function dependency (FDEP) gate, sequence enforcing (SQE) gate, and spare gate.

2.1. Priority-AND. The input events of PAND are base events or the output event of the logical gate. The failure mechanism of PAND is that the output event occurs if the input events occur in the order from left to right. Assuming that a PAND has three input events, its graphical symbols are shown in Figure 1. When B fails before A, C fails before A or B and C fail before A at the same time; the output event of the PAND fails.

2.2. Function Dependency. The input events of FDEP contain a trigger event and one or more related events. Basic events or other logic gates can be used as trigger events. Input events of other logic gates can be used as output events. Assuming that an FDEP has two related events A and B and a trigger event Tr, the dynamic logic gates are shown in Figure 1. When A or B fails or Tr fails to cause A and B failures, the output event fails.

2.3. Sequence Enforcing. Although both SQE and PAND describe the temporary characteristic of the system, they differ from each other in input event and failure mechanisms. There are multiple basic events in the input event of SEQ. The failure mechanism of SEQ is that all the base events occur in a certain order. Assuming that SQE has n basic event inputs, its graphical symbol is shown in Figure 1. The output event will fail only if input events fail in the order of 1 to n.

2.4. Spare. The spare gate consists of a set of spare parts and a main part. When the main part fails, the transfer switch starts to make the spare part run. The condition for the failure of the spare parts' door is that all spare parts fail. In the spare gate, there is a dormancy factor. According to the size of the dormancy factor, the spare gate has the following states: cold spare (CSP), warm spare (WSP), and hot spare (HSP). The graphical symbols are shown in Figure 2. The dormancy factor of the three logic gates is $\alpha = 0, 0 < \alpha < 1$, and $\alpha = 1$, respectively.

In CSP gate, the base event enters the working state when the system begins to work, while the spare parts are in a nonworking state. After the failure of the base event, the spare event begins to work until all spare events fail.

The input of WSP is same as CSP. CSP do not fail before they are used. But WSP may have failed before they are used. It has two kinds of failure processes. The first is that the spare parts do not fail and can continue to work after the failure of the main part. The second is that the warm parts have failed before the failure of the main part.

The inputs of the warm spare part are same as WSP. The base event and spare parts of HSP operate at the same time. If a base event fails, the spare part becomes a base event. If all spare parts fail, the system fails.

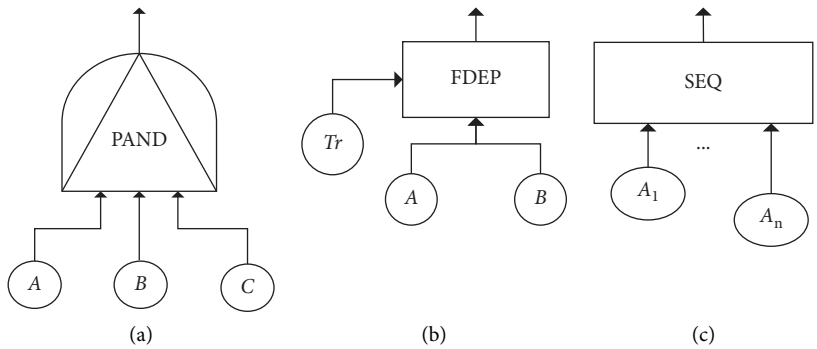

Figure 1: Dynamic logic gates. (a) Priority-AND. (b) Functional dependency. (c) Sequence enforcing.

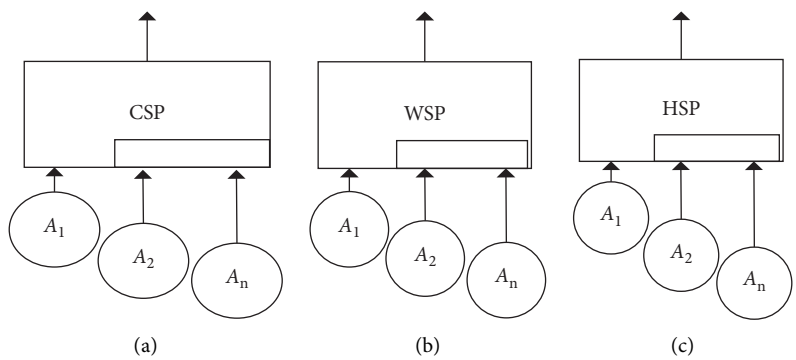

Figure 2: Spare gate.

3. Bayesian Network

3.1. The Principle of Bayesian Network. The direction of the directed line of the Bayesian network can be regarded as the causality of random variables. For a two-state system with n components, variables are defined as $Y_i, i = 1, 2, \ldots, n$. The Bayesian network aggregates multiple random variables, which can represent the logical relationship between random variables. The direction of the directed line can be regarded as the causality of random variables, when there are n components in the system. Assuming that all variables are not independent, variables are defined as $Y_i, i = 1, 2, \ldots, n$. The chain rule can be used to describe the joint probability distribution, as shown in

$$P(Y_1, Y_2, \ldots, Y_n) = P(Y_1)P(Y_2|Y_1)\ldots P(Y_n|Y_1, Y_2, \ldots, Y_{n-1}) = \prod_{i=1}^{n} P(Y_i|Y_1, Y_2, \ldots, Y_{i-1}). \quad (1)$$

When the Bayesian network is established, the relationship between nodes is determined first. In addition to input nodes and output node, the node is conditionally independent from other remaining nodes. If $pa(Y_i) \subseteq \{Y_1, Y_2, \ldots, Y_{i-1}\}$, Y_i is independent in $\{Y_1, Y_2, \ldots, Y_{i-1}\}$. Its joint probability distribution is shown in

$$P(Y_1, Y_2, \ldots, Y_n) = \prod_{i=1}^{n} P(Y_i|\delta pa(Y_i)), \quad (2)$$

where $pa(Y_i)$ is the set of input nodes for nodeY_i.

3.2. Discrete-Time Bayesian Network. The discrete-time Bayesian network is a modeling and evaluation method for nonrepairable systems, and it is an event-based Bayesian network. In discrete-time Bayesian networks, it is assumed that each event in the system can only occur once in the timeline.

The discrete Bayesian network divides the assumed task time interval $[0, t]$ into n equal parts. The length of each interval is defined as $\Delta = t/n$. Finally, it contains nondiscrete intervals $[t, +\infty]$, which are divided into n+1 subintervals. Time interval is defined as when a node fails in time interval $[(i-1)\Delta, i\Delta]$. If $i \leq n$, it indicates that the node failed during the task time. When a node fails in time interval $[n\Delta, +\infty]$, the state of the node is marked as n+1. Therefore, the time intervals corresponding to the state space of all nodes are defined as $[0, \Delta], [\Delta, 2\Delta], \ldots, [(n-1)\Delta, n\Delta], [n\Delta, +\infty]$. The state is marked as $\{1, 2, \ldots, n, n+1\}$. The unreliability of the

system at task time t is the sum of the probabilities of the first n states. The reliability of the system at time t is the probability of state n+1. Each state represents the behavior of the node in the corresponding time interval. If the node indicates a system failure, the division of the node indicates that the default system fails in the node. If the node indicates the gate, then the node is in this state, which means the gate output in the corresponding time interval.

3.3. Transform of Dynamic Fault Tree and Bayesian Network. The transformation between the dynamic fault tree and Bayesian network includes two parts: one is the transformation of the structure between the dynamic fault tree and Bayesian network; the other is the establishment of the conditional probability table for nonroot nodes as discussed by Jiang and Gao [8].

3.3.1. Static Logic Gate. Static logic gates contain AND gate and OR gate. If $A = [A_1, A_2, \ldots, A_m]$, where m is the number of input events for static logic gates, $A_i, i = 1, 2, \ldots, m$, are input events. Assuming that B is the state variable of the output variable for the static logic gate and its state space is $\{1, 2, \ldots, n+1\}$. If it is AND gate, then $j = \max(A_1, A_2, \ldots, A_m)$. If it is OR gate, then $j = \min(A_1, A_2, \ldots, A_m)$. The probability distribution of output event B is shown in

$$P(B = k|A) = \begin{cases} 1, & k = j, \\ 0, & k \neq j. \end{cases} \tag{3}$$

The AND/OR gate of the Bayesian network transformation is shown in Figure 3.

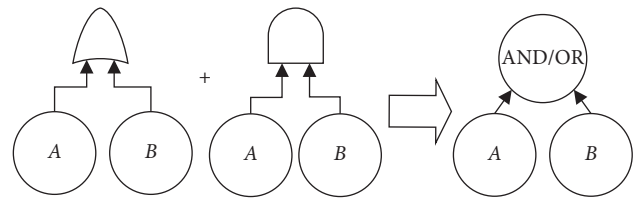

Figure 3: Bayesian network model of AND gate and OR gate.

3.3.2. Function Dependency. An FDEP of Bayesian network transformation is shown in Figure 4. An FDEP contains a trigger event Tr and two input events A and B. The conditional probability t is shown as

$$P\{A = j|\mathrm{Tr} = i\} = \begin{cases} F(j\Delta) - F((j-1)\Delta), & 0 < j < i, \\ 1 - F((i-1)\Delta), & j = i, \\ 0, & \text{other}. \end{cases} \tag{4}$$

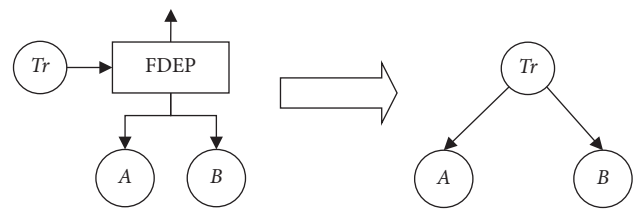

Figure 4: Bayesian network model of FDEP.

3.3.3. Spare. WSP and HSP have the same way for building the Bayesian network, but their conditional probability tables are different (see Figure 5); A represents the main part; B represents the spare part. Assuming that the distribution function of the main component is $F(t)$. The distribution function of the spare part in the reserve period is $F\alpha(t)$. After the warm spare parts are converted from the warm reserve state to the working state, the previous working process is ignored. In other words, after entering the working state, the failure probability of the component at time t is $F(t - t_0)$, where t_0 is the time when the reserve component starts to work normally.

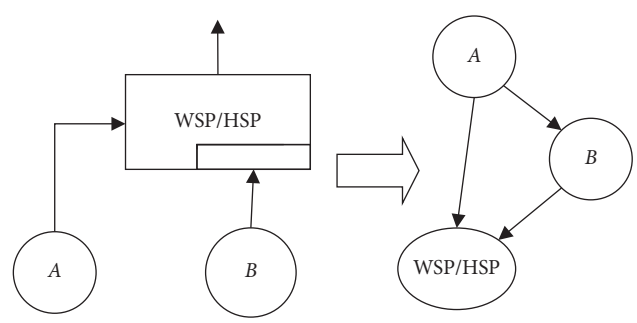

Figure 5: Bayesian network model of WSP and HSP.

Assume that t_0 when the reserve component starts to work is exactly an integer multiple of Δ. Since the component failure distribution can satisfy the human failure form, the conditional probability of failure of the reserve component in a certain time interval cannot be given analytically. When A fails in time interval i and B fails in time interval $j\,(i < j \leq n)$, the failure probability is shown in

$$\Pr\{B = j|A = i\} = F((j-i)\Delta) - F((j-i-1)\Delta). \tag{5}$$

The conditional probability table of node B is shown in

$$\Pr\{B = j|A = i\} = \begin{cases} F_\alpha(j\Delta) - F_\alpha((j-1)\Delta), & 0 < j \leq i, \\ F((j-i)\Delta) - F((j-i-1)\Delta), & i < j \leq n, \\ 1 - \sum_{p=1}^{n} \Pr\{B = p|A = i\}, & h = n+1. \end{cases} \tag{6}$$

For CSP, the main part cannot directly cause output event failure, so there is no direct relationship between the main part and output event. Its Bayesian network takes on a chain shape. Its conditional probability table only needs dormancy factor $\alpha = 0$ in WSP.

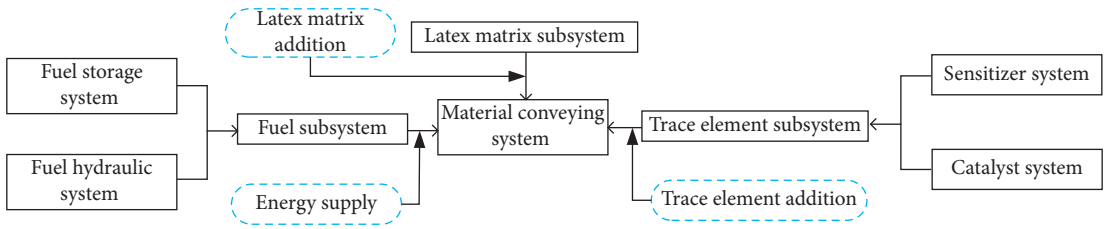

Figure 6: Material conveying system schematic.

Table 1: The table of event coding.

Event	Encoding
Material conveying system failure	T
Fuel filter failure	Tr1
Sensitizer filter failure	Tr2
Catalyst filter failure	Tr3
Fuel subsystem failure	$A1$
Latex matrix subsystem failure	$A2$
Trace element subsystem failure	$A3$
Fuel pipeline failure	$B1$
Hydraulic subsystem failure	$B2$
Fuel storage subsystem failure	$B3$
Latex matrix storage subsystem failure	$B4$
Latex matrix pump subsystem failure	$B5$
Latex matrix pipeline failure	$B6$
Sensitizer system failure	$B7$
Catalyst system failure	$B8$
Hydraulic joint failure	$C1$
Hydraulic control valve I failure	$C2$
Hydraulic control valve II failure	$C3$
Storage subsystem I failure	$C4$
Storage subsystem II failure	$C5$
Sensitizer hydraulic subsystem failure	$C6$
Sensitizer storage subsystem failure	$C7$
Sensitizer pipeline failure	$C8$
Catalyst hydraulic subsystem failure	$C10$
Catalyst storage subsystem failure	$C11$
Catalyst pipeline failure	$C12$
Catalyst pump subsystem failure	$C13$
Washer of float flowmeter failure	$X1$
Fuel pump failure	$X2$
Fuel pipe sealing ring failure	$X3$
Fuel pipe joint failure	$X4$
Fuel pipe failure	$X5$
Fuel inlet joint failure	$X6$
Hydraulic joint of fuel pipe failure	$X7$
Washer of fuel return pipe failure	$X8$
Fuel throttle valve failure	$X9$
Two-position four-way electro-hydraulic valve failure	$X10$
Fuel pipe of liquid level meter failure	$X11$
Fuel liquid level meter failure	$X12$

Table 1: Continued.

Event	Encoding
Fuel tank failure	$X13$
Latex matrix tank failure	$X14$
Latex matrix tank thermometer failure	$X15$
Latex matrix pump failure	$X16$
Flange sealing washer failure	$X17$
Rubber washer failure	$X18$
Latex matrix pump joint failure	$X19$
Latex matrix pump hose failure	$X20$
Sealing washer failure	$X21$
Butterfly valve failure	$X22$
Latex matrix pump rubber pipe failure	$X23$
Joint failure	$X24$
Clip failure	$X25$
Hose reel failure	$X26$
Two-position four-way solenoid valve failure	$X27$
Sensitizer pipe failure	$X28$
Sensitizer tank failure	$X29$
Liquid level display tube failure	$X30$
Sensitizer tank screw failure	$X31$
Sensitizer flowmeter failure	$X32$
Sensitizer hose failure	$X33$
Sensitizer hose joint failure	$X34$
Sensitizer hose jaw failure	$X35$
Sensitizer pump failure	$X36$
Sensitizer pump hose failure	$X37$
Fuel throttle valve failure	$X38$
Two-position four-way electro-hydraulic valve failure	$X39$
Latex matrix tank failure	$X40$
Latex matrix tank thermometer failure	$X41$
Catalyst flowmeter failure	$X42$
Two-position four-way solenoid valve failure	$X43$
Catalyst pipe failure	$X44$
Catalyst tank failure	$X45$
Liquid level display tube failure	$X46$
Catalyst box screw failure	$X47$
Catalyst rubber tube failure	$X48$
Catalyst hose joint failure	$X49$
Catalyst pump failure	$X51$
Catalyst pump rubber tube failure	$X52$

4. Reliability Modeling and Analysis of Material Conveying System

4.1. Dynamic Fault Tree. In order to ensure the accuracy of the establishment of the model, it is necessary to fully understand the main subcomponents contained in the research object system and the logical relationship between the various components before modeling. FMEA technology can sort out the logical relationships between the components in the system as well as failure modes [22, 23]. The ANFO vehicle material conveying system consists of three main systems. They are a fuel subsystem composed of a fuel storage system and a fuel hydraulic control system and a trace element subsystem composed of a sensitizer subsystem and a catalyst subsystem. The third is the latex matrix subsystem, which works, as shown in Figure 6.

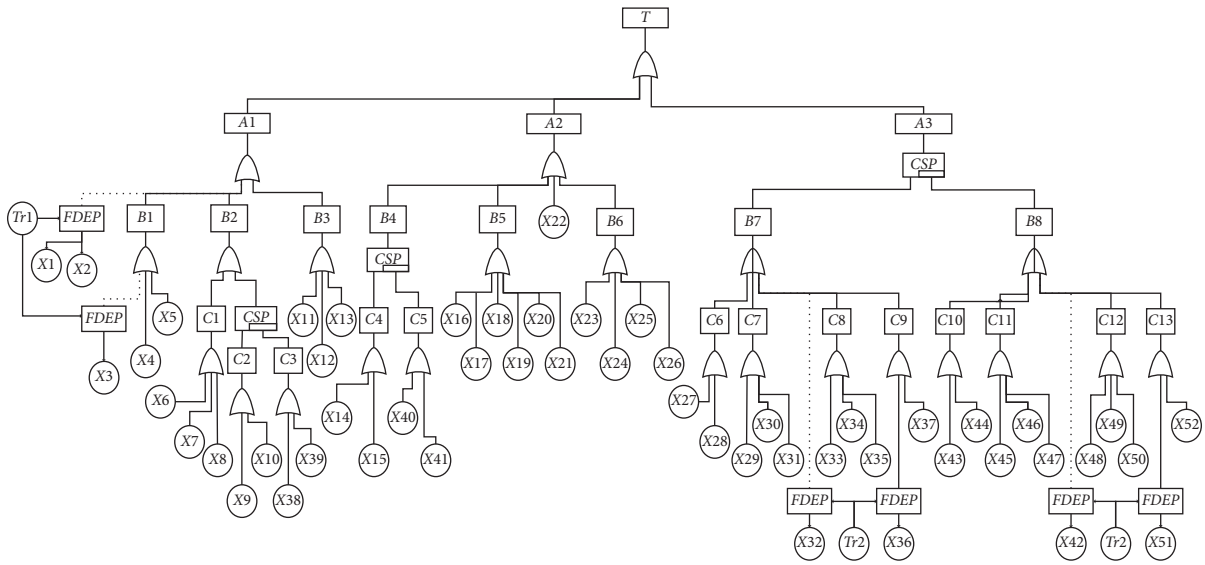

Figure 7: The diagram of the dynamic fault tree of the material conveying system.

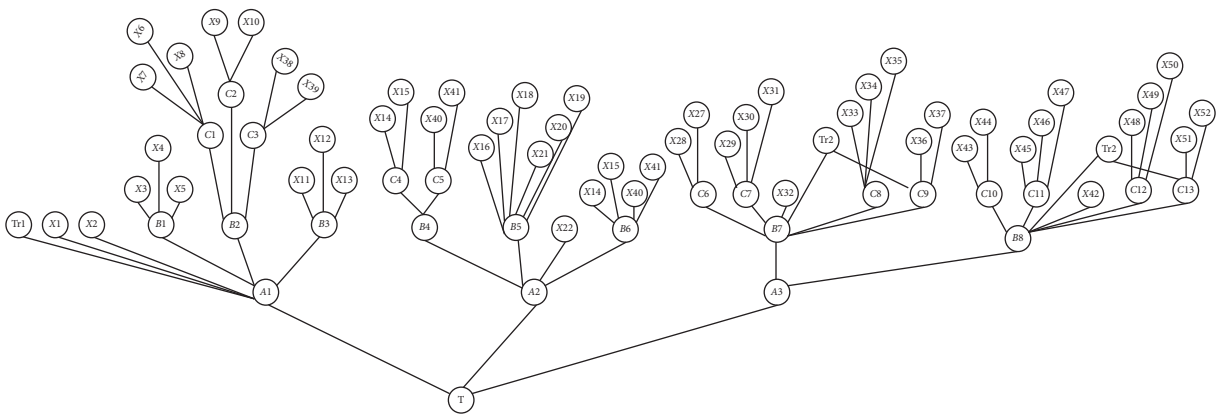

Figure 8: Bayesian network of the material conveying subsystem.

The material conveying system is the most important subsystem of the ANFO vehicle. The system is divided into the fuel conveying subsystem, latex matrix conveying subsystem, and trace element conveying subsystem through an in-depth study on the structure and principle of the system. The fuel conveying subsystem consists of two FDEP dynamic logic gates and one CSP dynamic logic gate. The latex matrix conveying subsystem contains one CSP dynamic logic gate. The trace element subsystem includes the sensitizer subsystem and catalyst subsystem. And, each of them contains one CSP dynamic logic gate. The events in the dynamic fault tree are shown in Table 1.

Except for dynamic components, the failure relationships of other components are independent of each other. Combined with the failure cause analysis of all modules, the dynamic fault tree model of the material conveying system is shown in Figure 7.

4.2. Bayesian Network Model. The Bayesian network model of dynamic fault tree conversion is shown in Figure 7. The probability distribution of the spare part is the same as the main part. Therefore, the spare parts of $C2$, $C4$, and $B7$ are no longer displayed. $\mathrm{Tr}1, \mathrm{Tr}2, X1, \ldots, X37$ are basic events of the dynamic fault tree corresponding to the root nodes of the Bayesian network.$C1, C2, \ldots, C9, B1, B2, \ldots, B8$ are intermediate events of the dynamic fault tree corresponding to intermediate nodes of the Bayesian network. T is the top event of the dynamic fault tree corresponding to the leaf node of the Bayesian network. The Bayesian network model is shown in Figure 8.

Because of the difficulty of collecting the operation data for this system, we will analyze the operation data of ten equipment for 2.5 years. The data source mainly comes from the maintenance records of the material transfer system of the ANFO vehicle. It is determined that all basic events obey exponential distribution, and their parameters are shown in Table 2.

All relevant subsystems involving dynamic logic gates can be defined in conditional probability according to their special meaning, which is not shown in the Bayesian network diagram.

Table 2: Summary table of failure probabilities for base events ($10^{-4}h^{-1}$).

Event	Parameter
Tr1	0.59
Tr2	0.71
$X1$	0.51
$X2$	0.89
$X3$	0.25
$X4$	0.11
$X5$	0.28
$X6$	0.38
$X7$	0.51
$X8$	0.13
$X9$	0.63
$X10$	0.76
$X11$	0.76
$X12$	0.76
$X13$	0.11
$X14$	0.25
$X15$	0.13
$X16$	0.51
$X17$	0.38
$X18$	0.13
$X19$	0.24
$X20$	0.34
$X21$	0.13
$X22$	0.76
$X23$	0.42
$X24$	0.18
$X25$	0.13
$X26$	0.15
$X27$	0.17
$X28$	0.13
$X29$	0.51
$X30$	0.25
$X31$	0.13
$X32$	0.38
$X33$	0.19
$X34$	0.25
$X35$	0.13
$X36$	0.63
$X37$	0.38
$X25$	0.13
$X26$	0.15
$X27$	0.17
$X28$	0.13
$X29$	0.51

The following data sources are from the maintenance records of the BZ15 heavy-duty oil ammonia explosive vehicle and related experimental data in the factory.

4.3. Reliability Analysis Based on Discrete Bayesian Network. Assuming that the task time is 240 h, when the discrete number n is 4, 5, and 6, the calculation time intervals are 48 h, 40 h, and 34.3 h. The reliability of the material conveying system is shown in Figure 9. The reliability under different discrete numbers was analyzed. At each time node, the maximum deviation of reliability under adjacent discrete numbers was calculated. The maximum deviation of reliability was 0.16% when the discrete numbers were 4 and 5.

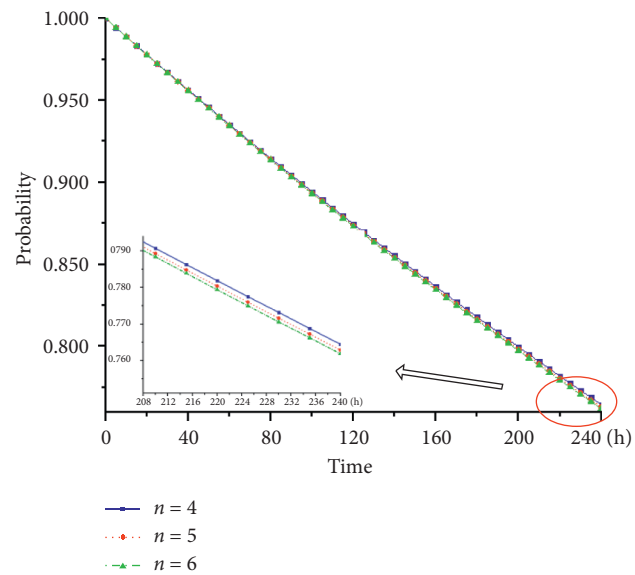

Figure 9: Reliability curves under different discrete numbers.

Table 3: The probability distribution table of the top event.

$T=i$	1	2	3	4	5	6	7
$P(T=i)$	0.0382	0.0386	0.0391	0.0399	0.0407	0.0416	0.7619

The maximum deviation of reliability was 0.1% when the discrete numbers were 5 and 6. The results of reliability calculation for discrete numbers 4, 5, and 6 had little deviation. Considering other uncertain factors, when the discrete number was 6, it can fully meet the accuracy requirements of the system evaluation. When the task time is 240 h and the discrete number is 6, the probability distribution of the top event in seven intervals is shown in Table 3.

Therefore, the failure probability of the material conveying system during the task time is $P = \sum_{i=1}^{6} P(T = i) = 0.2381$, and the reliability is $R = P(T = 7) = 0.7619$. When the state value of leaf nodes is 6, the joint tree reasoning algorithm can be used to calculate the failure probability of each basic event. The results are listed in Table 4. It can be seen that the failure probability of the fuel inlet joint and hydraulic joint of the fuel pipe is very small. They are reliable parts of the material conveying system. Sensitizer filter, sensitizer pump, sensitizer flowmeter, latex matrix tank, two-position four-way electro-hydraulic valve, fuel throttle valve, latex matrix tank thermometer, latex matrix pump rubber pipe, and sensitizer pump hose have high failure probability, which have a great impact on system reliability. Through the two-way reasoning algorithm, if the state value of each root node is 6 in turn, the failure probability of the leaf node is shown in Table 5.

From above Table 4, it can be seen that when the system fails, the sensitizer filter, sensitizer flowmeter, and sensitizer pump are more likely to fail. Therefore, this group of components can be considered as the weak link in the system. Improving its reliability may improve the overall reliability of the system and will have a significant impact.

Table 4: The failure probability of the top event when the basic event fails.

Event	Probability
Tr1	0.0461
Tr2	0.8680
$X1$	0.0460
$X2$	0.0460
$X3$	0.0461
$X4$	0.0085
$X5$	0.0216
$X6$	0.0004
$X7$	0.0006
$X8$	0.0001
$X9$	0.4574
$X10$	0.5509
$X11$	0.0586
$X12$	0.0586
$X13$	0.0085
$X14$	0.6589
$X15$	0.3431
$X16$	0.0393
$X17$	0.0293
$X18$	0.0100
$X19$	0.0185
$X20$	0.0262
$X21$	0.0100
$X22$	0.0586
$X23$	0.3209
$X24$	0.0100
$X25$	0.0100
$X26$	0.0116
$X27$	0.0031
$X28$	0.0024
$X29$	0.0094
$X30$	0.0046
$X31$	0.0024
$X32$	0.8676
$X33$	0.0035
$X34$	0.0046
$X35$	0.0024
$X36$	0.8680
$X37$	0.1388

Table 5: The failure probability of basic events when the top event fails.

Event	Probability
Tr1	1.0000
Tr2	0.2223
$X1$	1.0000
$X2$	1.0000
$X3$	1.0000
$X4$	1.0000
$X5$	1.0000
$X6$	0.8081
$X7$	0.8081
$X8$	0.8082
$X9$	0.2274
$X10$	0.2274
$X11$	1.0000
$X12$	1.0000
$X13$	1.0000
$X14$	0.2352
$X15$	0.2352
$X16$	0.5100
$X17$	1.0000
$X18$	1.0000
$X19$	1.0000
$X20$	1.0000
$X21$	1.0000
$X22$	1.0000
$X23$	1.0000
$X24$	1.0000
$X25$	1.0000
$X26$	1.0000
$X27$	0.2391
$X28$	0.2391
$X29$	0.2391
$X30$	0.2391
$X31$	0.2391
$X32$	0.2223
$X33$	0.2391
$X34$	0.2391
$X35$	0.2391
$X36$	0.2223
$X37$	0.2231

5. Discussion

Due to the obvious dynamic characteristics of the material conveying system, the traditional static fault tree analysis method cannot evaluate the system very well. In this paper, the dynamic fault tree is analyzed using the discrete Bayesian network. The results have shown that the reliability of the equipment was only 0.7619 in 240 h. The accuracy can meet the evaluation requirements of the equipment, when the discrete number was 6. Sensitizer filter, sensitizer pump, sensitizer flowmeter, and other parts are the weak links of the system. It is shown that the reliability of the system needs to be improved urgently. The improvement of sensitizer filter, sensitizer pump, sensitizer flowmeter, and other parts is an effective way to enhance the reliability of the system. In this article, the empirical method and statistical method were used to determine the failure distribution of parts. It is difficult to determine the exact failure distribution of parts because the acquisition period of equipment operation data is very long. In the future, fuzzy theory and multidata synthesis method may be used to study data uncertainty.

6. Conclusion

The traditional static fault tree cannot accurately analyze the reliability of the system, where the dynamic characteristics of the system are ignored. In this paper, the method of combining dynamic fault tree analysis and Bayesian network is used to analyze the reliability of the material conveying system. The discrete Bayesian network was applied to improve the accuracy of reliability analysis results.

The discrete-time Bayesian network calculates the possible time periods of the research object on the basis of the original Bayesian network. When the specific aging time of the product cannot be determined, it provides more calculation results, so as to realize the reliability of the product.

More comprehensive analysis can be performed through the above information obtained. The continual improvement of the system can be carried out according to the results.

Data Availability

The data used to support the findings of the study are available from the corresponding author upon request.

Conflicts of Interest

The authors declare that there are no conflicts of interest.

Acknowledgments

This work was partially supported by the National Natural Science Foundation of China under the Grant nos. 71761030 and 51965051, Natural Science Foundation of Inner Mongolia under the Grant nos. 2019LH07003 and 2019LH05029, and Scientific Research Project of High Educational Institution of Inner Mongolia under the Grant no. NJZY19085.

References

[1] J. Mi, Y. F. Li, W. Peng, and H. Z. Huang, "Reliability analysis of complex multi-state system with common cause failure based on evidential networks," *Reliability Engineering & System Safety*, vol. 174, pp. 71–81, 2018.

[2] H. Li, C. Guedes Soares, and H. Z. Huang, "Reliability analysis of a floating offshore wind turbine using Bayesian Networks," *Ocean Engineering*, vol. 217, Article ID 107827, 2020.

[3] H. Boudali and J. B. Dugan, "A new Bayesian network approach to solve dynamic fault trees," in *Proceedings of the Annual Reliability and Maintainability Symposium*, pp. 451–456, Alexandria, VA, USA, January 2005.

[4] Y. F. Li, J. Mi, Y. Liu, Y. J. Yang, and H. Z. Huang, "Dynamic fault tree analysis based on continuous-time Bayesian networks under fuzzy numbers," *Journal of Risk and Reliability*, vol. 229, pp. 530–541, 2015.

[5] B. W. Fang, Z. Q. Huang, Y. Li, and Y. Wang, "Quantitative analysis method of dynamic fault tree of complex system using Bayesian network," *Acta Electronica Sinica*, vol. 44, pp. 1234–1239, 2016.

[6] V. A. Tremyasov and T. V. Tremyasov, "Reliability evaluation method of the wind-diesel installation with application of dynamic fault tree," *Journal of Siberian Federal University. Engineering and Technologies*, vol. 10, pp. 414–425, 2017.

[7] H. Li and C. Guedes Soares, "Reliability analysis of floating offshore wind turbines support structure using hierarchical Bayesian network,," in *Proceedings of the 29th European Safety and Reliability Conference*, pp. 2489–2495, Research Publishing Services, Hannover, Germany, September 2019.

[8] X. Y. Li, H. Z. Huang, and Y. F. Li, "Reliability analysis of phased mission system with non-exponential and partially repairable components," *Reliability Engineering & System Safety*, vol. 175, pp. 119–127, 2018.

[9] D. C. Ge, M. Lin, Y. H. Yang, R. Zhang, and Q. Chou, "Quantitative analysis of dynamic fault trees using improved sequential binary decision diagrams," *Reliability Engineering and System Safety*, vol. 142, pp. 289–299, 2015.

[10] D. C. Ge, D. Li, Q. Chou, R. Zhang, and Y. Yang, "Quantification of highly coupled dynamic fault tree using IRVPM and SBDD," *Quality and Reliability Engineering International*, vol. 32, pp. 139–151, 2016.

[11] T. Yuge and S. Yanagi, "Dynamic fault tree analysis using Bayesian networks and sequence probabilities," *IEICE Transactions on Fundamentals of Electronics Communications and Computer Science*, vol. E96A, pp. 953–962, 2013.

[12] X. Zhang, H. Gao, H. Z. Huang, Y. F. Li, and J. Li, "Dynamic reliability modeling for system analysis under complex load," *Reliability Engineering & System Safety*, vol. 180, pp. 345–351, 2018.

[13] X. C. Zhang, X. F. Yan, and Y. Zhou, "Method of SBDD based on dynamic fault tree," *Computer Science*, vol. 44, pp. 195–199, 2017.

[14] J. Lan, H. J. Yuan, and J. Xia, "Improved method for dynamic fault tree analysis based on discrete-time Bayesian network," *Systems Engineering and Electronics*, vol. 40, pp. 948–953, 2018.

[15] J. Mi, Y. F. Li, Y. J. Yang, W. Peng, and H. Z. Huang, "Reliability assessment of complex electromechanical systems under epistemic uncertainty," *Reliability Engineering & System Safety*, vol. 152, pp. 1–15, 2016.

[16] H. Li, H. Z. Huang, Y. F. Li, J. Zhou, and J. Mi, "Physics of failure-based reliability prediction of turbine blades using multi-source information fusion," *Applied Soft Computing*, vol. 72, pp. 624–635, 2018.

[17] H. Li, A. P. Teixeira, and C. Guedes Soares, "A two-stage Failure Mode and Effect Analysis of offshore wind turbines," *Renewable Energy*, vol. 162, pp. 1438–1461, 2020.

[18] H. Li, H. Diaz, and C. Guedes Soares, "A developed failure mode and effect analysis for floating offshore wind turbine support structures," *Renewable Energy*, vol. 164, pp. 133–145, 2021.

[19] J. B. Dugan, "Galileo: a tool for dynamic fault tree analysis," *Computer Performance Evaluation.Modelling Techniques and Tools*, vol. 1786, pp. 328–331, 2000.

[20] J. B. Dugan, K. J. Sullivan, and D. Sullivan, "Developing a low-cost high-quality software tool for dynamic fault tree analysis," *IEEE Transactions on Reliability*, vol. 49, pp. 49–59, 2000.

[21] Z. Q. Li, T. X. Xu, J. Y. Gu, H. Wang, and J. Zhao, "Reliability modeling of redundant systems considering CCF based on DBN," *Arabian Journal for Science and Engineering*, vol. 44, pp. 2567–2577, 2019.

[22] H. Li, H. Diaz, and C. Guedes Soares, "A failure analysis of floating offshore wind turbines using AHP-FMEA methodology," *Ocean Engineering*, vol. 234, p. 109261, 2021.

[23] H. C. Liu, L. E. Wang, Z. Li, and Y. P. Hu, "Improving risk evaluation in FMEA with cloud model and hierarchical TOPSIS method," *IEEE Transactions on Fuzzy Systems*, vol. 27, no. 1, pp. 84–95, 2018.

Hindawi
Mathematical Problems in Engineering
Volume 2021, Article ID 9997740, 14 pages
https://doi.org/10.1155/2021/9997740

Research Article

Consistent Conjectural Variations Equilibrium in the Semi-Mixed Oligopoly

Gabriela Renata Huarachi-Benavídez,[1] **José Guadalupe Flores-Muñiz**,[1] **Nataliya Kalashnykova**,[1] **and Viacheslav Kalashnikov**[2]

[1]*Universidad Autónoma de Nuevo León (UANL), Av. Universidad S/N, Ciudad Universitaria, San Nicolás de los Garza, Nuevo León 66455, Mexico*
[2]*Instituto Tecnológico y de Estudios Superiores de Monterrey (ITESM), Campus Monterrey, Ave. Eugenio Garza Sada 2501 Sur, Monterrey, Nuevo León 64849, Mexico*

Correspondence should be addressed to José Guadalupe Flores-Muñiz; jfloresm@uanl.edu.mx

Received 15 March 2021; Revised 8 April 2021; Accepted 13 April 2021; Published 18 June 2021

Academic Editor: Mohammad Yazdi

We study a variant of the mixed oligopoly model with conjectural variations equilibrium, in which one of the producers maximizes not his net profit but the convex combination of the latter with the domestic social surplus. The coefficient of this convex combination is named socialization level. The producers' conjectures concern the price variations depending upon their production output variations. In this work, we extend the models studied before, considering the case of the producers' cost functions being convex but not necessarily quadratic. The notion of exterior and interior equilibrium is introduced (similarly to previous works), developing a consistency criterion for the conjectures. Existence and uniqueness theorems are formulated and proven. Results concerning the comparison between conjectural variations, perfect competition, and Cournot equilibriums are provided. Based on these results, we formulate an optimality criterion for the election of the socialization level. The existence of the optimal socialization level is proven under the condition that the public company cannot be too weak as compared to the private firms.

1. Introduction

During the last 20 years, models of mixed oligopolies have become a very popular theme in the literature. The high interest in mixed oligopolies is due to their importance for the economies of Europe (Germany, England, and others), Canada, and Japan (see [1]). There are examples of mixed oligopolies in the United States such as the overnight delivery industries. Mixed oligopolies are also common in Eastern Europe and the former Soviet Union, where competition between public and private companies has existed and still exists in many industries such as banking, mortgage loans, life insurance, airlines, telecommunications, natural gas, electric power, railway, automotive, steel, education, hospitality, healthcare, broadcasting, and delivery services.

In contrast to the classical oligopoly, the mixed oligopoly usually boasts at least one special producer, apart from private producers maximizing his net profit. The special company usually deals with an objective function distinct from the net profit. Plenty of such models include a producer who maximizes domestic social surplus (see [1–4] and [5], to mention but a few). An income-per-worker function replaces the standard net profit objective function in some other papers (cf. [6–9]). Researchers [10, 11] examine the third kind of mixed oligopoly with an exclusive participant aiming to enhance a convex combination of his net profit and domestic social surplus.

In many of the abovementioned works, the authors study the mixed oligopoly models in the frameworks of Cournot, Hotelling, or Stackelberg. Notwithstanding, nowadays, a concept of conjectural variations equilibrium (CVE)

introduced in [12, 13] as another possible solution form in static games is used ever wider. This concept puts that the producers behave as follows: each producer chooses his most favorable strategy having supposed that every adversary's action is a conjectural variation function of his own move.

In [14], a scheme different from [12, 13] is proposed for the concept of equilibrium with conjectural variations. In [14], it was assumed that every model's agent contemplates the variations of the total production volume as a response to his own output variations and thus evaluates his influence. The selection of the total output as the contemplated parameter is explained by the fact that the classical Cournot model was selected as the basic point. In more detail, instead of the classical Cournot hypothesis, it was supposed that every producer uses conjectural variations of the total market's volume in the function of the variation of its own production volume as follows:

$$G_i(\eta) = G + (\eta - q_i)\omega_i(G, q_i), \tag{1}$$

where

(i) G is the total market production volume

(ii) q_i is the quantity of the current production by producer i

(iii) η is the expected production quantity by producer i

(iv) $G_i(\eta)$ is the total production volume conjectured by producer i after his production volume changes from q_i to η

The conjecture function $\omega_i(G, q_i)$ in formula (1) represents the influence coefficient of producer i. In the classical Cournot model, this coefficient is equal to 1, and in the perfect competition model, it is equal to zero. For the given conjectures, under general enough assumptions, it was proved the existence and uniqueness of the abovementioned equilibrium. However, the following important question was not answered: Which conjectures can be considered as optimal ones?

To answer this important question, Bulavsky in [15] brought up a truly new approach. The first important variation proposed was in the structure of the demand. In the classical oligopoly models, the total volume of transactions drops when the price rises. However, there exists a dual postulate that the price increases as the demand grows. To eliminate this seeming contradiction, it is necessary to distinguish between two types of demand: the passive one and the active one. The standard demand function in the classical oligopoly models is used to describe the passive demand: the consumers wait, when a product is selling at a certain price, they decide whether to buy it or not. However, the active demand does not depend on the price and forms an additional component of the total demand. This component may reflect a rush demand, as well as a kind of demand related to some needs outside the model (for example, related to military actions).

The second important variation was the proposed procedure of verification for the consistency of the influence coefficients. Rather than assuming the equivalence (symmetry) of the producers in the oligopoly, it is supposed that every producer makes conjectures regarding, not the (optimal) response functions of each of the other producers, but only about the variations of the market clearing price depending upon (infinitesimal) variations in the same producer's output volume. Knowing the adversaries' conjectures (called influence coefficients), every producer smears on a verification procedure and reveals if his influence coefficient is consistent with those of the rest of the producers.

In the works [16–20], the results of [15] were extended to the mixed duopoly and oligopoly cases, respectively. In [18–20], partially mixed duopoly and oligopoly models were studied, i.e., where the semi-public company, the same as in [12, 13], maximizes the convex combination of the functions of social surplus and the participant's net utility function with a parameter $\beta \in (0, 1]$, considering quadratic market cost functions of the market's producers. Furthermore, in the works mentioned above, it is shown that the consistent conjectural variations equilibrium (CCVE) and the classical Cournot–Nash equilibrium do not coincide, and in many applications, the CCVE models provide more efficient and attractive results than the classical models. In particular, when the CCVE concept is applied to the electricity market in [16], the consistent conjectural variations equilibrium led to better results for producers and consumers.

In Sections 2, 3, and 4 of the present study, we extend the results from [18, 19] to the case of convex (but not necessarily quadratic) cost functions. Based upon the established existence and uniqueness results for the conjectural variations equilibrium (called the exterior equilibrium) for any set of feasible conjectures, the notion of interior equilibrium is introduced by developing a consistency criterion for the conjectures (referred to as influence coefficients), and the existence theorem for the interior equilibrium (understood as the CVE with consistent conjectures) is proven.

When studying oligopolies in addition to the problems of existence and calculation of the equilibrium states, much importance and interest is attracted by the comparative analysis of the different equilibria. Such a comparative analysis for the semi-mixed duopoly has been realized in [21]. Based on this analysis, in [21], we formulated the optimality criterion for the socialization level β and proved the existence of the optimal socialization level $\beta^{\text{opt}} \in (0, 1)$. In Section 5 of the present study, this analysis is extended to the oligopoly case, where all private firms have the same cost function, the optimality criterion for the election of the optimal socialization level has been formulated, and its existence is demonstrated.

In Section 6, we describe the methodology and algorithms used to find the equilibriums and the optimal value of β. In Section 7, some numerical experiments, together with the analysis of the results, are provided. Concluding remarks (Section 8), funding bodies, and the list of references complete the paper. The proofs of the lemmas and theorems can be found in the Supplementary Materials.

2. The Model's Specification

Let us consider an oligopoly market of one homogeneous product with $n+1$ producers, $n \geq 1$. Each producer $i \in \{0, 1, \ldots, n\}$ has its cost function $f_i(q_i)$, where q_i is the production volume for every producer i.

In the classical oligopoly models, the total volume of products in the market usually decreases as the price rises. The latter agrees with the postulate that the price falls when the supply increases.

However, there is a second postulate: the price rises with an increase in demand. To deal with this apparent contradiction, we need to distinguish between 2 types of demand: passive and active.

The passive demand in the oligopoly models is a function that describes the behavior of the consumers who take into account the price of a product to decide whether to buy it or not.

On the other hand, the active demand reflects the behavior of the consumers who buy the product regardless of the price. Thus, in theory, an increment in the active demand should raise the price in the market. This component can be represented by an urgent demand or the demand associated with some needs outside the model, for example, related to military operations, the development of defense industries, or something else. The possible dependence of the active demand upon the price in the market is outside the studied model.

Therefore, we consider here both types of demand. The passive demand depends on the price and is determined by the function $G(p)$, where p is the market price proposed by all producers. The active demand D is nonnegative and does not depend on the market price.

The equilibrium between the offer and the demand, for the price value p, is defined by the following balance equation:

$$\sum_{i=0}^{n} q_i = G(p) + D. \tag{2}$$

The behavior of the passive demand described above is represented in the following assumption:

A1. The demand function $G(p)$ is defined for price values $p \in (0, +\infty)$, is nonnegative, continuously differentiable, and $G'(p) < 0$.

Moreover, since we consider total cost functions, we assume that these functions are strictly increasing and strictly convex. This is described by the following assumption:

A2. For each producer $i \in \{0, 1, \ldots, n\}$, its cost function, $f_i(q_i)$, is defined for each $q_i \geq 0$ and is twice continuously differentiable with $f_i'(0) > 0$ and $f_i''(q_i) > 0$. In addition,

$$f_0'(0) \leq \max_{i \in \{1, \ldots, n\}} \{f_i'(0)\}. \tag{3}$$

The producers $i \in \{1, \ldots, n\}$ are called private producers and they select their production volume q_i in order to maximize its net profit function:

$$\pi_i(p, q_i) = pq_i - f_i(q_i). \tag{4}$$

On the other hand, producer $i = 0$ is a semi-public company and it selects its production volume q_0 such that it maximizes the convex combination of the functions of the social surplus and the net utility function:

$$\begin{aligned} S(\beta, p, q_0, q_1, \ldots, q_n) = {} & \beta\left(\int_0^{\sum_{i=0}^{n} q_i} p(x)\mathrm{d}x - p\sum_{i=1}^{n} q_i - f_0(q_0)\right) \\ & + (1-\beta)(pq_0 - f_0(q_0)), \end{aligned} \tag{5}$$

where, like in [10, 11], $\beta \in (0, 1]$ is a parameter. From now on, we will call this parameter, β, *socialization level.*

Assume that all the producers (both semi-public and private) accept that the election of their production volumes will affect the market price value p. In this way, the first-order optimality conditions describing the market equilibrium will have the following form:

For private producers $(i \in \{1, \ldots, n\})$,

$$\frac{\partial \pi_i}{\partial q_i} = p + q_i \frac{\partial p}{\partial q_i} - f_i'(q_i) \begin{cases} = 0, & \text{if } q_i > 0, \\ \leq 0, & \text{if } q_i = 0. \end{cases} \tag{6}$$

And for the semi-public producer $(i = 0)$,

$$\frac{\partial S}{\partial q_0} = p + \left[(1-\beta)q_0 - \beta\sum_{i=1}^{n} q_i\right]\frac{\partial p}{\partial q_0} - f_0'(q_0) \begin{cases} = 0, & \text{if } q_0 > 0, \\ \leq 0, & \text{if } q_0 = 0. \end{cases} \tag{7}$$

As we can see, in order to describe the behavior of the producers, the most important is to know, not the function p, but rather its derivatives:

$$\frac{\partial p}{\partial q_i} = -\nu_i. \tag{8}$$

Here, we introduce the negative sign in (8) in order to work with nonnegative values of ν_i.

In addition, we must guarantee that the derivatives of p with respect to its production volume $i \in \{0, 1, \ldots, n\}$ provide the concavity of the function. Otherwise, we cannot guarantee that the necessary conditions are also sufficient.

For private producers $i \in \{1, \ldots, n\}$ in order for conditions (6) to be sufficient, one has to guarantee that the function $\pi_i(q_i)$ is concave. As we suppose that the cost functions are strictly convex, it lacks only the concavity of the product pq_i, with respect to q_i, to guarantee that. But for the latter, it is sufficient to suppose that the coefficient ν_i (which we call *influence coefficient* of producer i) is nonnegative and constant. In the latter case, the function of the conjectured local dependence for the net utility of the private producer i with respect to the variation of his production volume η_i has the form

$$\widehat{\pi}_i(\eta_i) = [p - \nu_i(\eta_i - q_i)]\eta_i - f_i(\eta_i), \tag{9}$$

which is a quadratic and concave function.

Therefore, the first-order necessary (and now sufficient) conditions for the equilibrium's production volume, $\eta_i = q_i$, to be optimal are given as follows:

$$\begin{cases} p = \nu_i q_i + f_i'(q_i), & \text{if } q_i > 0, \\ p \le f_i'(0), & \text{if } q_i = 0, \end{cases} \quad i \in \{1, \ldots, n\}. \tag{10}$$

In a similar manner, the semi-public producer's conjectured local dependence of its objective function has the form

$$\widehat{S}(\eta_0) = \beta\left(\int_0^{\eta_0 + \sum_{i=1}^n q_i} p(x)\mathrm{d}x - [p - \nu_0(\eta_0 - q_0)]\sum_{i=1}^n q_i - f_0(\eta_0)\right) + (1-\beta)([p - \nu_0(\eta_0 - q_0)]\eta_0 - f_0(\eta_0)), \tag{11}$$

which is also a concave function and allows one to obtain the necessary and sufficient conditions for the equilibrium production volume, $\eta_0 = q_0$, to be optimal, which are as follows:

$$\begin{cases} p = \left[(1-\beta)q_0 - \beta\sum_{i=1}^n q_i\right]\nu_0 + f_0'(q_0), & \text{if } q_0 > 0, \\ p \le -\beta\left(\sum_{i=1}^n q_i\right)\nu_0 + f_0'(0), & \text{if } q_0 = 0. \end{cases} \tag{12}$$

If the producers' conjectures are given exogenously, then its production volumes are determined uniquely as a function of the model's parameters and also of the other producers' volumes. This equilibrium is called *exterior* and is described by the vector $(p, q_0, q_1, \ldots, q_n)$.

However, in this work, we study the second concept of equilibrium, called *interior* (consistent), in which the influence coefficients ν_i are not given beforehand but are found from the models' data by solving a special system of equations.

3. Exterior Equilibrium

Definition 1. The vector $(p, q_0, q_1, \ldots, q_n)$ is called the exterior equilibrium for the influence coefficients $(\nu_0, \nu_1, \ldots, \nu_n)$, $\nu_i \ge 0$, $i \in \{0, 1, \ldots, n\}$, whenever the balance equation (2) is valid, and for all the producers, the optimality conditions (10) and (12) are valid.

From now on, we assume that the number of participants in the model is always the same regardless of the influence coefficients. In order to guarantee that, we introduce the value p_0 and prove Lemma 1 presented below:

$$p_0 = \max_{i \in \{1, \ldots, n\}} \{f_i'(0)\} \ge f_0'(0). \tag{13}$$

Lemma 1. *Let assumptions A1 and A2 be true. If the vector $(p, q_0, q_1, \ldots, q_n)$ is the exterior equilibrium for the given influence coefficients $(\nu_0, \nu_1, \ldots, \nu_n)$, then the relation $p > p_0$ is equivalent to the fact that all production volumes are positive, i.e., $q_i > 0$, $\forall i \in \{0, 1, \ldots, n\}$.*

Now, we introduce the following assumption:

A3. For the price p_0 and for any $\nu_i \ge 0$, $i \in \{0, 1, \ldots, n\}$, there exists the production volume $q_i^0 \ge 0$ (unique by A2), such that

$$p_0 = f_i'(q_i^0), \tag{14}$$

and in addition,

$$\sum_{i=0}^n q_i^0 < G(p_0). \tag{15}$$

Assumption A3, together with A1 and A2, guarantees the existence and uniqueness of the exterior equilibrium for any nonnegative values of $\nu_i \ge 0$, $i \in \{1, \ldots, n\}$, and $\nu_0 \in [0, \overline{\nu}_0)$, where

$$\overline{\nu}_0 = \begin{cases} \dfrac{f_0'\left(G(p_0) - \sum_{i=1}^n q_i^0\right) - p_0}{\sum_{i=1}^n q_i^0}, & \text{if } \beta = 1, \displaystyle\sum_{i=1}^n q_i^0 > 0, \\ \dfrac{f_0'\left(G(p_0) - \sum_{i=1}^n q_i^0\right) - p_0}{\sum_{i=1}^n q_i^0 - (1-\beta)G(p_0)}, & \text{if } \beta \in (0,1), \displaystyle\sum_{i=1}^n q_i^0 > \max\left\{(1-\beta)G(p_0), \frac{1-\beta}{\beta} q_0^0\right\}, \\ +\infty, & \text{otherwise.} \end{cases} \tag{16}$$

This fact is formulated and established in the following theorem.

Theorem 1. *Under assumptions A1, A2, and A3, for any $\beta \in (0,1]$, $D \geq 0$, $\nu_i \geq 0$, $i \in \{1,\ldots,n\}$, and $\nu_0 \in [0, \overline{\nu}_0)$, there exists uniquely the exterior equilibrium $(p, q_0, q_1, \ldots, q_n)$, which is continuously differentiable with respect to the parameters β, D, and ν_i, $i \in \{0,1,\ldots,n\}$. Moreover, $p > p_0$ and*

$$\frac{\partial p}{\partial D} = \frac{1}{\left(1/\left((1-\beta)\nu_0 + f_0''(q_0)\right)\right) + \left((\nu_0 + f_0''(q_0))/\left((1-\beta)\nu_0 + f_0''(q_0)\right)\right) \sum_{i=1}^n \left(1/\left(\nu_i + f_i''(q_i)\right)\right) - G'(p)}. \tag{17}$$

4. Interior Equilibrium

Before defining the key concept of interior equilibrium, we recall the procedure of verification of the equilibrium introduced in [22]. Suppose that, for some parameters $(\nu_0, \nu_1, \ldots, \nu_n)$ and D, the exterior equilibrium $(p, q_0, q_1, \ldots, q_n)$ has been found. Now assume that one of the producers, for example, producer k, temporarily changes his behavior and stops maximizing his expected net profit and starts making small variations around his optimal production volume q_k. The latter is equivalent to considering that only the producers belonging to the set $I_{-k} = \{0,1,\ldots,n\} \backslash \{k\}$ continue to operate in the model, subtracting the production volume q_k from the active demand D. In this case, the variations of the production volume q_k (from producer k) are equivalent to the variations (in the opposite direction) of the active demand $D_k = D - q_k$. Considering the variations of q_k as infinitesimal, we can suppose that, by observing the variations in the equilibrium price p corresponding to the variations of the active demand D_k, producer k can obtain the variations in p with respect to his production volume q_k, given in the form

$$\frac{\partial p}{\partial D_k} = \frac{\partial p}{\partial (D - q_k)} = -\frac{\partial p}{\partial q_k} = \nu_k, \tag{18}$$

which is his influence coefficient.

In the proposed model, if producer $k \in \{1,\ldots,n\}$ leaves the market, in order to calculate the corresponding derivative $\partial p / \partial D_k$ we apply formula (17) from Theorem 1, remembering that producer k is absent, so the terms corresponding to the index $i = k$ must be excluded from the formula. On the other hand, if the semi-public producer $i = 0$ is the one who leaves the market, then only private producers will remain in the model; thus, we have to apply the theorem and the formula obtained in [15] for the classical oligopoly model. With this in mind, we obtain the following criterion.

Definition 2 (consistency criterion). We say that the influence coefficients $(\nu_0, \nu_1, \ldots, \nu_n)$ are consistent if they, together with their corresponding exterior equilibrium $(p, q_0, q_1, \ldots, q_n)$, satisfy the following equalities:

$$\nu_0 = \frac{1}{\sum_{i=1}^n \left(1/\left(\nu_i + f_i''(q_i)\right)\right) - G'(p)}, \tag{19}$$

and for all $i \in \{1,\ldots,n\}$,

$$\nu_i = \frac{1}{\left(1/\left((1-\beta)\nu_0 + f_0''(q_0)\right)\right) + \left((\nu_0 + f_0''(q_0))/\left((1-\beta)\nu_0 + f_0''(q_0)\right)\right) \sum_{\substack{j=1 \\ j \neq i}}^n \left(1/\left(\nu_j + f_j''(q_j)\right)\right) - G'(p)}. \tag{20}$$

Now we can define the concept of interior equilibrium.

Definition 3. The collection $(p, q_0, q_1, \ldots, q_n, \nu_0, \nu_1, \ldots, \nu_n)$ where $\nu_i \geq 0$, $i \in \{0,1,\ldots,n\}$, is called the interior equilibrium if, for the given influence coefficients $(\nu_0, \nu_1, \ldots, \nu_n)$, the vector $(p, q_0, q_1, \ldots, q_n)$ is the exterior equilibrium, and the consistency criterion (Definition 2) is valid, i.e., equations (19) and (20) are satisfied for all $i \in \{0,1,\ldots,n\}$.

The existence of the interior equilibrium has been formulated and proven in the following theorem.

Theorem 2. *Under assumptions A1, A2, and A3, there exists the interior equilibrium.*

5. A Particular Case: Affine Demand Function, Identical Private Producers, and Quadratic Cost Functions

When studying an oligopoly in the framework proposed in this study, apart from the questions of the existence of the consistent equilibrium and how to calculate it, special attention is paid to the comparison of the latter with the ones appearing in the Cournot model and the perfect competition model.

Let us consider a particular case in which the active demand is zero, the passive demand is a piecewise linear function, all the producers have a quadratic cost function, and this cost function is the same for every private producer.

For this particular case, we reformulate the main model's assumptions, A1 and A2, as follows:

A4. The passive demand is given by the piecewise function

$$G(p) = \begin{cases} -Kp + T, & \text{if } 0 < p < \dfrac{T}{K}, \\ 0, & \text{if } p \geq \dfrac{T}{K}, \end{cases} \tag{21}$$

where $K > 0$ and $T > 0$.

A5. The cost functions are quadratic, i.e.,

$$f_0(q_0) = \frac{1}{2}a_0 q_0^2 + b_0 q_0, \quad a_0 > 0,\ b_0 > 0, \tag{22}$$

and for all $i \in \{1, \ldots, n\}$

$$f_i(q_i) \equiv f(q) = \frac{1}{2}aq^2 + bq, \quad a > 0,\ b \geq b_0. \tag{23}$$

In this particular case, since the demand function $G(p)$ is piecewise linear, it is nondifferentiable at the point $p = T/K$, so assumption A1 does not hold. However, from the proof of Theorem 1, it follows that the price p of the exterior equilibrium $(p, q_0, q_1, \ldots, q_n)$ is given by the intersection of the total volume function $Q(p) = \sum_{i=0}^{n} q_i(p)$ and the demand function $G(p)$; moreover, this intersection lies within the open interval $(p_0, T/K)$ where the demand function defined in assumption A4 is given by $G(p) = -Kp + T > 0$, thus satisfying the conditions of assumption A1. Thus, the results presented in the previous section hold true for this particular case.

Assumption A3 is reformulated in the following form:

A6. For the price $p_0 = b$, it holds that

$$\frac{p_0 - b_0}{a_0} < -Kp_0 + T. \tag{24}$$

The balance equality takes the form

$$q_0 + nq = -Kp + T. \tag{25}$$

The net utility function for private producers is reduced to

$$\pi(p, q) = pq - \left(\frac{1}{2}aq^2 + bq\right). \tag{26}$$

However, the objective function for the semi-public producer transforms into

$$S(\beta, p, q_0, q) = \beta\left[\int_0^{q_0+nq} p(x)\mathrm{d}x - npq - \left(\frac{1}{2}a_0 q_0^2 + b_0 q_0\right)\right] + (1-\beta)\left[pq_0 - \left(\frac{1}{2}a_0 q_0^2 + b_0 q_0\right)\right]. \tag{27}$$

The first-order necessary (and sufficient) optimality conditions are as follows.

For the private producers,

$$\begin{cases} p = \nu q + aq + b, & \text{if } q > 0, \\ p \leq b, & \text{if } q = 0. \end{cases} \tag{28}$$

And for the semi-public producer,

$$\begin{cases} p = [(1-\beta)q_0 - n\beta q]\nu_0 + aq_0 + b_0, & \text{if } q_0 > 0, \\ p \leq -n\beta q \nu_0 + b_0, & \text{if } q_0 = 0. \end{cases} \tag{29}$$

5.1. Analysis of the Consistent Equilibrium. Taking into account that in the considered particular case, all private producers have the same influence coefficient, i.e., $\nu_i \equiv \nu$, $\forall i \in \{1, \ldots, n\}$, we obtain the following consistency criterion.

Definition 4 (consistency criterion for the particular case). The influence coefficients (ν_0, ν) are consistent for the corresponding exterior equilibrium (p, q_0, q), if the following equalities are valid:

$$\nu_0 = \frac{1}{(n/(\nu + a)) + K}, \tag{30}$$

$$\nu = \frac{1}{(1/((1-\beta)\nu_0 + a_0)) + ((\nu_0 + a_0)/((1-\beta)\nu_0 + a_0))((n-1)/(\nu + a)) + K}. \tag{31}$$

Theorem 3. *Under assumptions A4, A5, and A6, for every $\beta \in (0, 1]$, there exists uniquely the interior equilibrium $(p^*, q_0^*, q^*, \nu_0^*, \nu^*)$.*

By Theorem 3, for each $\beta \in (0, 1]$, there exists uniquely the consistent (interior) equilibrium $(p^*(\beta), q_0^*(\beta), q^*(\beta), \nu_0^*(\beta), \nu^*(\beta))$, and we denote the profit of private producers calculated for this equilibrium by $\pi^*(\beta) = \pi(p^*(\beta), q^*(\beta))$.

Theorem 4. *The interior equilibrium* $(p^*(\beta), q_0^*(\beta), q^*(\beta), \nu_0^*(\beta), \nu^*(\beta))$ *and the function* $\pi^*(\beta)$ *are continuously differentiable with respect to* $\beta \in (0,1]$. *Moreover, the functions* $p^*(\beta)$, $\nu_0^*(\beta)$, *and* $\nu^*(\beta)$ *are strictly decreasing for all* $\beta \in (0,1]$.

5.2. Analysis of the Cournot Equilibrium. The Cournot conjecture for oligopoly models is described by the following identity:

$$\omega_i = \frac{\partial G}{\partial q_i} = 1, \quad \forall i \in \{0, 1, \ldots, n\}. \tag{32}$$

The previous identity (32), in our model, corresponds to the following equality for the influence coefficients:

$$\nu_i = -\frac{\partial p}{\partial q_i} = -\frac{\omega_i}{G'(p)} = -\frac{1}{G'(p)}, \quad \forall i \in \{0, 1, \ldots, n\}. \tag{33}$$

Therefore, for our particular case, the Cournot conjecture is given by

$$\nu_0 = \nu = \frac{1}{K}. \tag{34}$$

By Theorem 1, for every $\beta \in (0,1]$, there exists uniquely the exterior equilibrium $(p^c(\beta), q_0^c(\beta), q^c(\beta))$, corresponding to the Cournot conjecture, which we denote for our particular case by $\nu_0^c = \nu^c = 1/K$.

It is easy to see that the Cournot equilibrium does not coincide with the interior (consistent) equilibrium in our model because the consistency criterion is not satisfied. Indeed,

$$\begin{gathered}\frac{1}{(n/(\nu^c + a)) + K} < \frac{1}{K} = \nu_0^c, \\ \frac{1}{(1/((1-\beta)\nu_0^c + a_0)) + ((\nu_0^c + a_0)/((1-\beta)\nu_0^c + a_0))((n-1)/(\nu^c + a)) + K} < \frac{1}{K} = \nu^c.\end{gathered} \tag{35}$$

For each $\beta \in (0,1]$, we denote the net profit of private producers for the Cournot equilibrium by $\pi^c(\beta) = \pi(p^c(\beta), q^c(\beta))$.

Theorem 5. *Under assumptions A4, A5, and A6, the exterior equilibrium* $(p^c(\beta), q_0^c(\beta), q^c(\beta))$ *and the function* $\pi^c(\beta)$ *are continuously differentiable with respect to* $\beta \in (0,1]$. *Moreover, the function* $p^c(\beta)$ *is strictly decreasing for all* $\beta \in (0,1]$.

5.3. Analysis of the Perfect Competition Equilibrium. The perfect competition conjecture for oligopoly models is represented by the following identities:

$$\omega_i = \frac{\partial G}{\partial q_i} = 0, \quad \forall i \in \{0, 1, \ldots, n\}, \tag{36}$$

which in our model corresponds to the following influence coefficients:

$$\nu_i = -\frac{\partial p}{\partial q_i} = -\frac{\omega_i}{G'(p)} = 0, \quad \forall i \in \{0, 1, \ldots, n\}. \tag{37}$$

The latter, for our particular case, is reduced to

$$\nu_0 = \nu = 0. \tag{38}$$

By Theorem 1, for each $\beta \in (0,1]$, there exists uniquely the exterior equilibrium $(p^t(\beta), q_0^t(\beta), q^t(\beta))$, corresponding to the perfect competition conjecture, which is denoted in our particular case by $\nu_0^t = \nu^t = 0$.

It is easy to check that the perfect competition equilibrium does not match with the consistent equilibrium in our model since the consistency criterion is not met. Indeed,

$$\begin{gathered}\frac{1}{\left(n/\left(\nu^t + a\right)\right) + K} > 0 = \nu_0^t, \\ \frac{1}{\left(1/\left((1-\beta)\nu_0^t + a_0\right)\right) + \left(\left(\nu_0^t + a_0\right)/\left((1-\beta)\nu_0^t + a_0\right)\right)\left(\left(n-1\right)/\left(\nu^t + a\right)\right) + K} > 0 = \nu^t.\end{gathered} \tag{39}$$

For each $\beta \in (0,1]$, we denote the net profit of private producers for the perfect competition equilibrium by $\pi^t(\beta) = \pi(p^t(\beta), q^t(\beta))$.

Theorem 6. *Under assumptions A4, A5, and A6, the exterior equilibrium* $(p^t(\beta), q_0^t(\beta), q^t(\beta))$ *and the function* $\pi^t(\beta)$ *are constant with respect to* $\beta \in (0,1]$.

5.4. Comparative Analysis. It is of great interest the comparison among the three types of equilibrium: the consistent (interior) equilibrium, the Cournot equilibrium, and the perfect competition equilibrium. For the case of duopoly, i.e., when $n = 1$, the analysis of these three equilibria can be found in [21]. Because of that, in this study, we consider only the case of oligopoly, i.e., when $n \geq 2$.

Theorem 7. *Under assumptions A4, A5, and A6, the following inequalities hold:*

$$\lim_{\beta \downarrow 0} p^c(\beta) > \lim_{\beta \downarrow 0} p^*(\beta) > p^t. \tag{40}$$

For the case of duopoly, it was shown in [21] that for any $\beta \in (0,1]$, the inequality $p^c(\beta) > p^*(\beta)$ holds. However, for the case of oligopoly in our model, inequality (40) between the prices when $\beta \uparrow 1$ may or may not hold, depending on the model's parameters. Examples of both situations can be found in the numerical experiments of Section 7.

Theorem 8. *Under assumptions A4, A5, and A6, for any $\beta \in (0,1]$, if $\pi^c(\beta) \geq \pi^*(\beta)$, then it is satisfied that $p^*(\beta) < p^c(\beta)$.*

Theorem 9. *Suppose that assumptions A4, A5, and A6 are true. If the relationship*

$$\frac{(n-1)a}{n+aK} \geq a_0, \tag{41}$$

is valid, then there exists the value $\widehat{\beta} \in (0,1)$ such that $\pi^c(\widehat{\beta}) = \pi^*(\widehat{\beta})$ and $p^*(\widehat{\beta}) < p^c(\widehat{\beta})$.

In other words, if relationship (41) holds, we may consider this value $\widehat{\beta}$ (from Theorem 9) as the optimal socialization level. Indeed, for this value $\widehat{\beta}$, the net profits for the private producers are the same in both, the Cournot equilibrium and the consistent equilibrium; hence, the semi-public company can convince the private firms to change their Cournot strategies for the consistent strategies, guaranteeing that the market price will be lower than the one appearing in the Cournot model. Thereby, the semi-public company is not only fulfilling its social responsibility, but also will keep safe its own budget since it does not need to pay any subsidies to the private firms nor the consumers.

The existence of this optimal socialization level was shown in [21] for the case of a partially mixed duopoly without the need of relation (41), but in the oligopoly case, this optimal socialization level may not exist (indeed, it might be that $\pi^*(\beta) < \pi^c(\beta)$ for all $\beta \in (0,1]$); the latter can happen when the semi-public company is much weaker than the private firms. For such cases, we plan (in future works) to make use of the politics of subsidies in order to define a different optimality criterion for the socialization level.

6. Solution Methodology

In this section, we describe the methodology and algorithms used to find the exterior equilibrium, the interior equilibrium, and the optimal socialization level for the particular case introduced in Section 5.

To find the exterior equilibrium (p^*, q_0^*, q^*) for a fixed set of values $\beta \in (0,1]$ and $\nu_0, \nu \geq 0$, we first isolate the variables q and q_0 from the first-order necessary conditions (28) and (29), assuming that $q_0, q > 0$. Thus, we define the continuous functions $q(p,\nu)$ and $q_0(p,\beta,\nu_0,\nu)$, given by the equations (E.25) and (E.26), respectively, in Supplementary Materials, respectively, within the proof of Theorem 4.

Now, by assumption A6, for the price $p_0 = b$, we have that

$$q_0(p_0,\beta,\nu_0,\nu) + q(p_0,\nu) < G(p_0), \tag{42}$$

and from Theorem 3, we know that there exists uniquely the exterior equilibrium, and thus, we can find a value $p_1 > p_0$ large enough (since the functions q_0 and q are strictly increasing with respect to p, and G is strictly decreasing with respect to p) such that

$$q_0(p_1,\beta,\nu_0,\nu) + q(p_1,\nu) > G(p_1). \tag{43}$$

After finding the value p_1, the exterior equilibrium's price p^* is given by the intersection of the functions

$$\begin{aligned} &q_0(p,\beta,\nu_0,\nu) + q(p,\nu), \\ &\qquad G(p), \end{aligned} \tag{44}$$

in the variable p within the interval (p_0, p_1), which we can easily find using a bisection algorithm.

Finally, the exterior equilibrium's volume outputs are given by the values $q_0^* = q_0(p^*,\beta,\nu_0,\nu)$ and $q^* = q(p^*,\nu)$.

To find the interior equilibrium $(p^*, q_0^*, q^*, \nu_0^*, \nu^*)$ for a fixed value $\beta \in (0,1]$, we first define a map with the right-hand sides of the consistency criterion's equations (30) and (31). The defined map $H(\nu_0,\nu) = (F_0(\nu_0,\nu), F(\nu_0,\nu))$ is given by the functions (D.3) and (D.4) in Supplementary Materials within the proof of Theorem 3.

From the proof of Theorem 3, we also know that the map $H(\nu_0,\nu)$ is a contraction and has a unique fixed point in the region $\nu_0, \nu \geq 0$. This fixed point is the vector of consistent conjectures (ν_0^*, ν^*), which we can find by applying the iterated function sequence

$$\left(\nu_0^{k+1}, \nu^{k+1}\right) = H\left(\nu_0^k, \nu^k\right), \tag{45}$$

starting with the point $(\nu_0^0, \nu^0) = (0,0)$, until the distance between (ν_0^k, ν^k) and $H(\nu_0^k, \nu^k)$ is small enough.

Finally, the values of (p^*, q_0^*, q^*) are given by the exterior equilibrium corresponding to (ν_0^*, ν^*).

To find the optimal socialization level $\widehat{\beta}$, we first define the private firms' profit functions $\pi^*(\beta) = \pi(p^*(\beta), q^*(\beta))$ and $\pi^c(\beta) = \pi(p^c(\beta), q^c(\beta))$, for the consistent and Cournot equilibriums, respectively, in the variable $\beta \in (0,1]$, where $\pi(p,q)$ is the net profit for the private firms given by (26), the vector $(p^*(\beta), q_0^*(\beta), q^*(\beta), \nu_0^*(\beta), \nu^*(\beta))$ is the interior equilibrium for the value β, and the vector $(p^c(\beta), q_0^c(\beta), q^c(\beta))$ is the exterior equilibrium for the value β and the influence coefficients $(\nu_0^c, \nu^c) = (1/K, 1/K)$.

From the proof of Theorem 9, we know that

$$\lim_{\beta\downarrow 0} \pi^* (\beta) < \lim_{\beta\downarrow 0} \pi^c (\beta), \tag{46}$$

so we can find a small enough $\beta_0 \in (0,1)$ such that $\pi^* (\beta_0) < \pi^c (\beta_0)$. Also from the proof of Theorem 9, we have that $\pi^* (1) > \pi^c (1)$.

Thus, after finding the value β_0, the optimal socialization level $\widehat{\beta}$ is given by the intersection of the functions

$$\begin{aligned} &\pi^* (\beta), \\ &\pi^c (\beta), \end{aligned} \tag{47}$$

within the interval $(\beta_0, 1)$, which, again, we can easily find using a bisection algorithm.

7. Numerical Experiments and Discussion

In the classic oligopoly models, the Cournot conjecture, $\partial G/\partial q_i = 1$, and the perfect competition conjecture, $\partial G/\partial q_i = 0$, are known to be the extreme cases of the more general conjectural variations conjecture, $(\partial G/\partial q_i) = \omega_i \in [0,1]$ (see [14]). In the Cournot equilibrium, the market price is always higher than the market price appearing in the conjectural variations' equilibrium, and compared with the latter, the market price in the perfect competition equilibrium is always lower. Thus, the common perception that the Cournot model is more profitable for the private producers, while the perfect competition model benefits consumers. However, as it was proven in Section 5, this is not always the case when dealing with mixed (or semi-mixed) oligopolies.

Here, in this section, we provide some numerical experiments to illustrate the different situations (formulated in Theorems 4 to 9) that may arise in the semi-mixed oligopoly and lead to the optimality criterion for the socialization level. The examples are based on the numerical experiments presented in [23] where the electricity energy market was considered.

The active demand is $D = 0$ and the inverse demand function is accepted as the following one:

$$p(G) = 50 - 0.002G, \tag{48}$$

which means that the demand is given by the following affine function:

$$G(p) = -50p + 2500. \tag{49}$$

The cost function for the semi-public company is given by the quadratic function

$$f_0(q_0) = 0.01q_0^2 + 2q_0. \tag{50}$$

We assume that the number of the private firms is $n = 5$ and that all of them have the same quadratic cost function given by the following formula:

$$f_i(q_i) \equiv f(q) = \kappa q^2 + 3.25q, \quad \forall i \in \{1, \ldots, 5\}, \tag{51}$$

where the value of κ is given by $\kappa = 0.0075$ for Experiment 1, $\kappa = 0.025$ for Experiment 2, and $\kappa = 0.0025$ for Experiment 3.

In the cost function (51) for the private firms, the parameter κ can be interpreted as the strength of the private firms when the production in the market is high (indeed, if the output volume q is large enough, the linear term of the quadratic cost functions is negligible), and thus, for Experiment 1 we consider the private firms to be stronger than the semi-public company, and even more strong for Experiment 3, and for Experiment 2, we consider the private firms to be weaker than the semi-public company.

In all 3 experiments, we compare the equilibriums of consistent conjectural variations (CCVE), Cournot, and perfect competition (P-C). Also, in order not to lose the more intuitive notion of the influence coefficients, we are going to use the following relationships:

$$\omega_i \equiv \frac{\partial G}{\partial q_i} = \frac{\partial G}{\partial p}\frac{\partial p}{\partial q_i} = -K\frac{\partial p}{\partial q_i} = K\nu_i, \quad \forall i \in \{0, 1, \ldots, 5\}, \tag{52}$$

to work with the influence coefficients ω_i. With this notation, the Cournot conjecture is represented by $\omega_i^c = 1$ for all $i \in \{0, 1, \ldots, 5\}$, whereas the perfect competition conjecture is given by $\omega_i^t = 0$ for all $i \in \{0, 1, \ldots, 5\}$.

In all the figures, the limit values when $\beta\downarrow 0$ correspond to the classic oligopoly model since the semi-public company focuses solely on profit maximization, and on the other hand, the values corresponding to $\beta = 1$ correspond to the mixed oligopoly model where the semi-public company only maximizes social welfare.

Experiment 1. In Figures 1 to 5, we present the graphs of the 3 equilibriums as functions of the socialization level β.

In the graphs of Figure 1, we see that the consistent influence coefficients lie within the open interval $(0,1)$. This is always true (as one can see from equations (19) and (20), of the consistency criterion, and the relationship (52)), so we can consider the CCVE model as somewhat intermediate between Cournot and perfect competition.

We also can see how the influence coefficients decrease with respect to β; however, the influence coefficient of the private firms decreases considerably faster compared to the semi-public company, which reflects that, in a mixed oligopoly market, the public firm (even when it is the weakest) has the greatest influence in the market given that it selects its output volume to maximize social welfare, regardless of the production cost.

In Figures 2 and 3, we can see that the semi-public company's production increases in the CCVE and Cournot equilibriums as it leans towards social welfare, which is a consequence of trying to decrease the market price (by increasing the total volume) to maximize social welfare.

As mentioned above, the Cournot conjecture favors the private firms, which is why the increment in the semi-public company's production shown in Figure 2 is considerably larger in the Cournot equilibrium compared with the CCVE equilibrium; thus, maximizing social welfare is especially harder under Cournot competition.

On the other hand, we can see that the private firms' production decreases to compensate for the overproduction

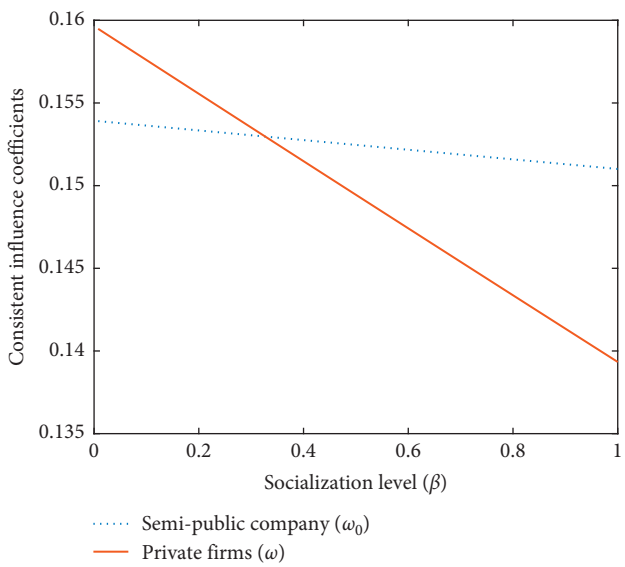

Figure 1: Consistent influence coefficients for the semi-public company and private producers in Experiment 1.

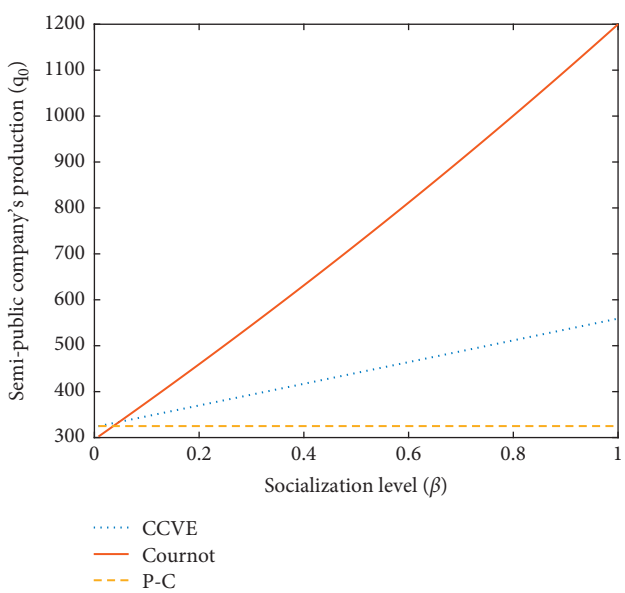

Figure 2: Semi-public company's production for the 3 types of equilibrium in Experiment 1.

of the semi-public company. Meanwhile, for the perfect competition equilibrium, the production output for any producer is always the same regardless of the socialization level β chosen by the semi-public company, which reflects the nature of perfect competition (i.e., no producer has influence over the market).

Here, we can see the consequence of a public firm entering a classic oligopoly market; as the public firm seeks to maximize social welfare, the influence of the producers' decreases, approaching perfect competition, thus benefiting the customers; however, in the process, the public firms have to increase its production, forgetting about its profit, which may result in expenses higher than what the public company

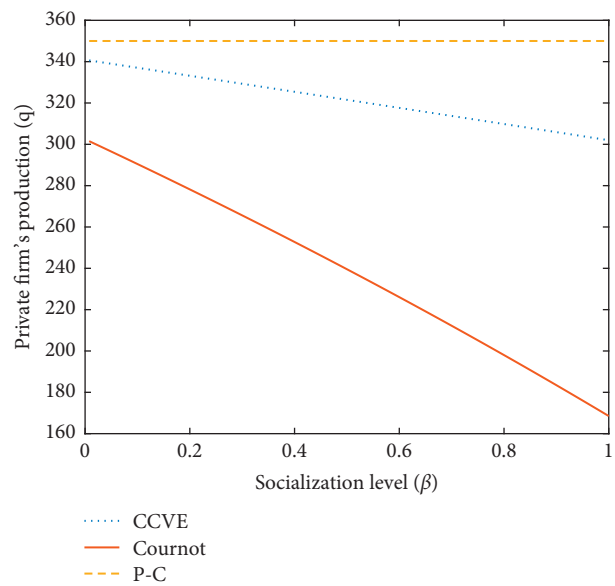

Figure 3: Private firms' production for the 3 types of equilibrium in Experiment 1.

can afford. Here is where the importance of the semi-mixed oligopoly framework arises, by maximizing the convex combination of social welfare and net profit, the semi-public company does not only watch over costumers but its own budget too.

In Figure 4, we can see that, in the CCVE and Cournot equilibriums, the market price decreases as the socialization level β increases (i.e., as the semi-public company prioritizes social welfare over its net profit), having a greater decrease in the Cournot equilibrium since the market price in the classic oligopoly (i.e., when $\beta \downarrow 0$) is considerably higher in the Cournot equilibrium compared to the CCVE equilibrium. Meanwhile, in the perfect competition equilibrium, the market price is constant since the total output volume does not change with respect to β.

Even so, we can see the intuitive behavior of the market price, the latter being the lowest in the perfect competition equilibrium, the highest in the Cournot equilibrium, and something intermediate in the CCVE equilibrium.

In Figure 5, we can see that, in the classic oligopoly (i.e., when $\beta \downarrow 0$), the market follows the intuitive behavior mentioned above, so the Cournot equilibrium shows the highest net profit for the private firms and the perfect competition equilibrium shows the lowest (which again is constant). However, in the mixed oligopoly (i.e., when $\beta = 1$), the latter is no longer the case as the CCVE equilibrium becomes the most profitable for the private firms whereas the Cournot equilibrium is now the least profitable.

Hence, there exists the socialization level within the open interval $(0, 1)$ such that the net profit for the private firms is the same in both, the CCVE and Cournot equilibriums. Thus, by choosing this (optimal) socialization level, the semi-public company can convince the private firms to change its Cournot behavior to that of the CCVE, since their net profit will remain the same; however, the market price will still be lower in the CCVE equilibrium (compared with

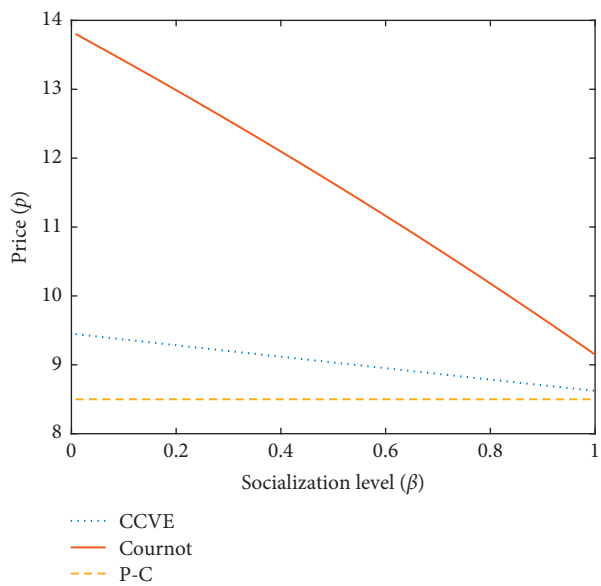

Figure 4: Market clearing price for the 3 types of equilibrium in Experiment 1.

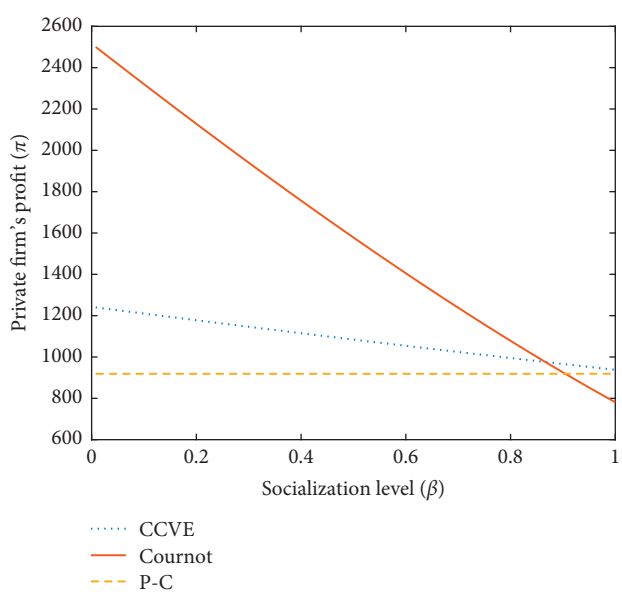

Figure 5: Private firms' profit for the 3 types of equilibrium in Experiment 1.

the Cournot equilibrium) so the semi-public company is fulfilling its social responsibility while also taking care of its budget (since the optimal socialization level is less than 1).

For this experiment, the optimal socialization level is $\widehat{\beta} \approx 0.8664$, the corresponding interior equilibrium is

$$(p^*, q_0^*, q^*, v_0^*, v^*) \approx (8.73, 527.37, 307.22, 0.003028, 0.002841), \tag{53}$$

and the corresponding Cournot (exterior) equilibrium is

$$(p^c, q_0^c, q^c) \approx (9.84, 1065.9, 188.39), \tag{54}$$

having in both equilibriums the private firms' profit of $\pi^* = \pi^c \approx 975.96$.

Experiment 2. In Figures 6 and 7, we present the market price and private firms' profit functions for the 3 types of equilibrium.

In Figure 6, we can see that the decrease (as β increases) in the market price for both, Cournot and CCVE equilibriums, is more notable now that the private firms are weaker, compared to Experiment 1, falling even below the market price in the perfect competition equilibrium. Moreover, in the case of mixed oligopoly (when $\beta = 1$), the market price of the Cournot equilibrium is now the lowest, which is completely counterintuitive.

In Figure 7, we can see that (as a consequence of the faster decrease in the price) the private firms' net profit in the CCVE and Cournot equilibriums intersects in a smaller socialization level β, compared to Experiment 1; thus, the semi-public company can convince the private firms to change to the CCVE conjectures, while taking a little more into account its net profit.

Moreover, even though the market price in the Cournot equilibrium becomes the lowest when $\beta = 1$, the latter occurs only after the private firms' profit in the CCVE and Cournot equilibriums intersects; therefore, the value of β in which this intersection occurs is, again, the optimal socialization level.

For this experiment, the optimal socialization level is $\widehat{\beta} \approx 0.7067$, the corresponding interior equilibrium is

$$(p^*, q_0^*, q^*, v_0^*, v^*) \approx (14.32, 785.52, 199.69, 0.00713, 0.005438), \tag{55}$$

and the Cournot (exterior) equilibrium is

$$(p^c, q_0^c, q^c) \approx (14.75, 941.52, 164.23), \tag{56}$$

providing in both equilibriums an individual profit for the private firms of $\pi^* = \pi^c \approx 1213.8$.

Experiment 3. In Figures 8 and 9, we present the market price and private firms' profit functions for the 3 types of equilibrium.

In Figures 8, we see that now (since the private firms are again stronger than the semi-public company) the market price behaves intuitively just like in Experiment 1. However, since the private firms are now even stronger, the decrease of the market price in the CCVE and Cournot equilibriums is now less notable compared to the decrease in Experiment 1.

In Figure 9, we see that (as a consequence of the market price not decreasing enough) the private firms' net profit in the Cournot equilibrium does not fall below their net profit in the CCVE (nor the perfect competition) equilibrium; thus, the semi-public company (regardless of the socialization level) cannot convince the private firms to change to the CCVE conjectures without paying them any kind of compensation for the losses in their profit. Because of this, there is no optimal socialization level in the sense defined in Section 5.

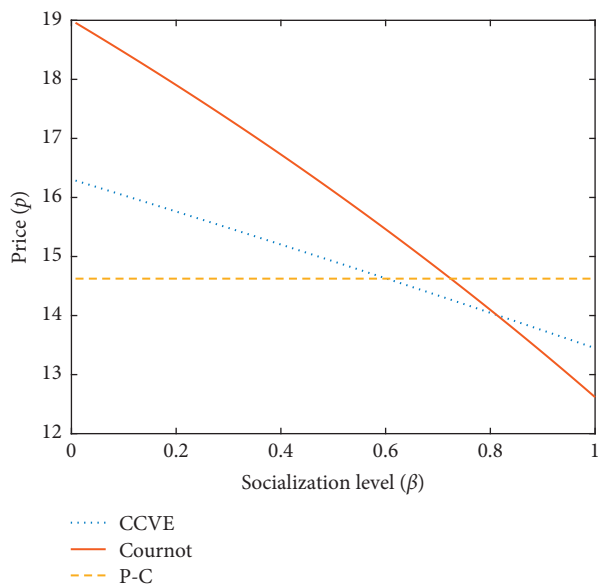

Figure 6: Market clearing price for the 3 types of equilibrium in Experiment 2.

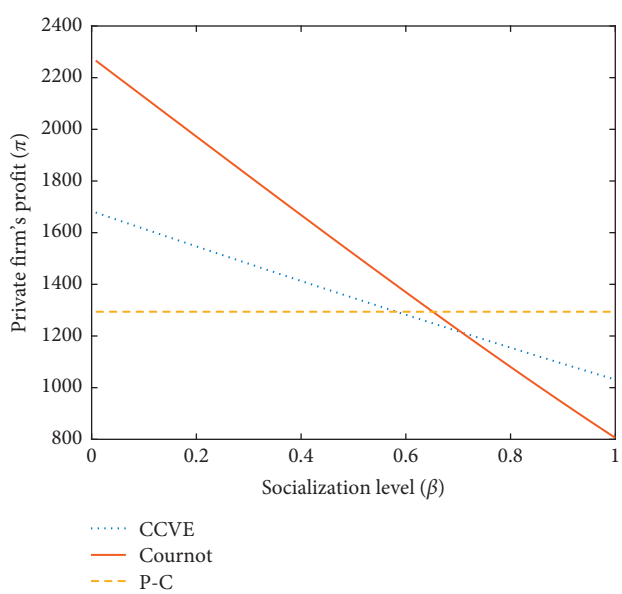

Figure 7: Private firms' profit for the 3 types of equilibrium in Experiment 2.

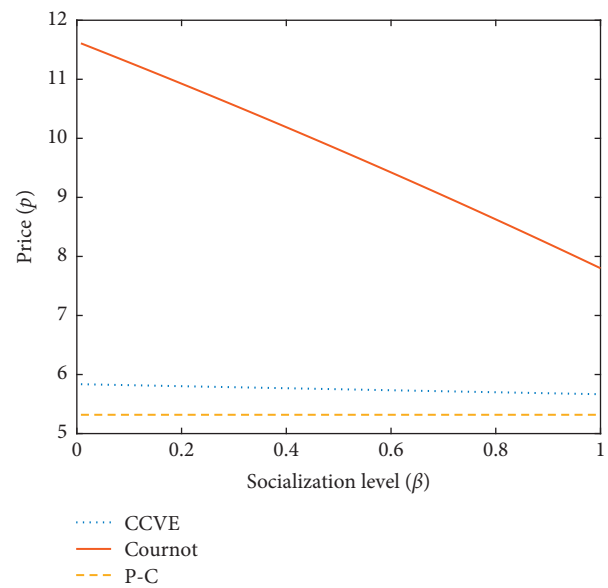

Figure 8: Market clearing price for the 3 types of equilibrium in Experiment 3.

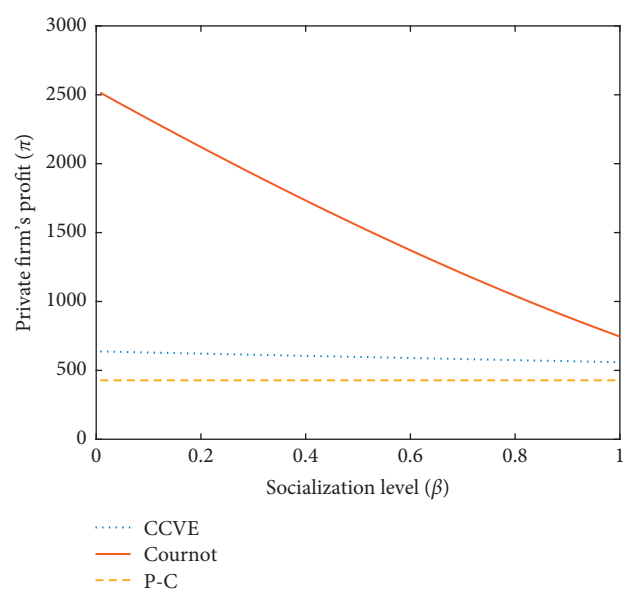

Figure 9: Private firms' profit for the 3 types of equilibrium in Experiment 3.

In [21], the existence of this optimal socialization level was shown for the case of a partially mixed duopoly without the need for relation (41); however, as shown in Experiment 3, for the case of oligopoly (when the number of producers is at least 3), this optimal socialization level may not exist; in fact, from Theorem 9, we can see that condition (41) is decreasing with respect to both, a and n, and thus, we can conclude that the stronger the private firms are (i.e., the smaller the coefficient a is), the larger the number n of private firms should be to guarantee the existence of the optimal socialization level.

However, even if the optimal socialization level (as defined in Section 5) does not exist, the semi-public company can still convince the private firms to use the CCVE model instead of the Cournot one by paying them a subsidium equal (at the least) to the difference between their expected profits in both models (to make up for their losses).

In our future works, we plan to use this politics of subsidiums to define the optimal socialization level as such that minimizes the total costs of the semi-public company, given as the sum of its production cost and the subsidium that it would be paying to all the private firms.

8. Conclusion

In this paper, we extended the previously studied mixed oligopoly models with conjectural variations equilibrium to the case of the agents' cost functions being convex but not necessarily quadratic. We established the existence and uniqueness results for the conjectural variations equilibrium (called exterior equilibrium) for any set of feasible conjectures. To introduce the notion of interior equilibrium (understood as the CVE with consistent conjectures, or CCVE), we developed a consistency criterion for the conjectures (referred to as influence coefficients) and proved the existence theorem.

Then, we analyzed the behavior of the CCVE, Cournot, and perfect competition equilibriums, and conducted a comparative analysis for the semi-mixed oligopoly with the affine demand function, the firms' cost functions being quadratic, and all private firms having the same cost function. Based on this analysis, we formulated the criterion for the optimal value of the semi-public company's socialization level and proved its existence (under the additional condition that the domestic company cannot be too weak as compared to the private firms). These results were illustrated with numerical experiments for a small electrical power market, showing the different situations that can arise from a public company entering a classic oligopoly market.

In our forthcoming papers, we are going to examine the qualitative behavior of prices and production outputs when the demand function is not necessarily differentiable, and the cost functions are not quadratic.

Data Availability

No data were used to support this study.

Conflicts of Interest

The authors declare that they have no conflicts of interest.

Acknowledgments

This research was financially supported in Mexico by the Secretaría de Educación Pública and the Consejo Nacional de Ciencia y Tecnología (grant number FC-2016-01–1938).

Supplementary Materials

The PDF file contains the proofs of the lemmas and theorems presented in this work. (*Supplementary Materials*)

References

[1] N. Matsushima and T. Matsumura, "Mixed oligopoly and spatial agglomeration," *Canadian Journal of Economics*, vol. 36, no. 1, pp. 62–87, 2004.

[2] R. C. Cornes and M. Sepahvand, *Cournot vs Stackelberg Equilibria with a Public Enterprise and International Competition*, University of Nottingham, Nottingham, England, 2003.

[3] C. Fershtman, "The interdependence between ownership status and market structure: the case of privatization," *Economica*, vol. 57, no. 22, pp. 319–328, 1990.

[4] T. Matsumura, "Stackelberg mixed duopoly with a foreign competitor," *Bulletin of Economic Research*, vol. 55, no. 3, pp. 275–287, 2003.

[5] T. Matsumura and O. Kanda, "Mixed oligopoly at free entry markets," *Journal of Economics*, vol. 84, no. 1, pp. 27–48, 2005.

[6] N. J. Ireland and P. J. Law, *The Economics of Labour-Managed Enterprises*, Croom Helm, London, UK, 1982.

[7] J. P. Bonin and L. G. Putterman, *Economics of Cooperation and the Labor-Managed Economy*, Harwood Academic Publishers, Geneva, Switzerland, 1987.

[8] F. H. Stephen, *The Performance of Labour-Managed Firms*, Palgrave Macmillan, London, UK, 1982.

[9] L. Putterman, "Labour-managed firms," in *The New Palgrave Dictionary of Economics*, S. N. Durlauf and L. E. Blume, Eds., pp. 791–795, Palgrave Macmillan, London, UK, 2008.

[10] B. Saha and R. Sensarma, "State ownership, credit risk and bank competition: a mixed oligopoly approach," *Macroeconomics and Finance in Emerging Market Economies*, vol. 6, no. 1, pp. 1–13, 2013.

[11] A. Mumcu, S. Oğur, and U. Zenginobuz, *Competition between Regulated and Non-regulated Generators on Electric Power Networks*, Bogazici University, Istanbul, Turkey, 2001.

[12] A. L. Bowley, "The mathematical groundwork of economics," *Social Forces*, vol. 3, no. 1, p. 185, 1924.

[13] R. Frisch, "Monopoly, polypoly: the concept of force in the economy," *International Economics Papers*, vol. 1, pp. 23–36, 1951.

[14] G. Isac, V. A. Bulavsky, and V. V. Kalashnikov, *Complementarity, Equilibrium, Efficiency and Economics*, Kluwer Academic Publishers, Dordrecht, Netherlands, 2002.

[15] V. A. Bulavsky, "Structure of demand and equilibrium in a model of oligopoly," *Economics and Mathematical Methods (Ekonomika I Matematicheskie Metody)*, vol. 33, pp. 112–134, 1997, in Russian.

[16] V. V. Kalashnikov, V. A. Bulavsky, N. I. Kalashnykova, and F. J. Castillo, "Mixed oligopoly with consistent conjectures," *European Journal of Operational Research*, vol. 210, no. 3, pp. 729–735, 2011.

[17] N. I. Kalashnykova, V. A. Bulavsky, V. A. Bulavsky, and V. V. Kalashnikov, "Consistent conjectural variations equilibrium in a mixed duopoly," *Journal of Advanced Computational Intelligence and Intelligent Informatics*, vol. 15, no. 4, pp. 425–432, 2011.

[18] V. V. Pérez, V. A. Bulavsky, V. A. Bulavsky, N. I. Kalashnykova, and J. Watada, "Analysis of consistent equilibria in a mixed duopoly," *Journal of Advanced Computational Intelligence and Intelligent Informatics*, vol. 18, no. 6, pp. 962–970, 2014.

[19] V. V. Hernández-Rodríguez, V. A. Bulavsky, V. A. Bulavsky, N. I. Kalashnykova, and J. Watada, "Mixed oligopoly: analysis of consistent equilibria," *Journal of Advanced Computational Intelligence and Intelligent Informatics*, vol. 18, no. 6, pp. 971–984, 2014.

[20] J. G. Flores Muñiz, N. Kalashnykova, V. V. Kalashnikov, and V. Kreinovich, "Public interest and private enterprize: new developments," in *Lecture Notes in Networks and Systems*, Springer International Publishing, Berlin, Germany, 2021.

[21] V. V. Kalashnikov- Jr., J. G. Flores-Muñiz, V. V. Kalashnikov, and N. I. Kalashnykova, "Consistent conjectural variations equilibrium in a semi-mixed duopoly," *Journal of Advanced*

Computational Intelligence and Intelligent Informatics, vol. 21, no. 7, pp. 1125–1134, 2017.

[22] V. A. Bulavsky, "An imagined experiment in the framework of the generalized Cournot model," *Economics and Mathematical Methods (Ekonomika I Matematicheskie Metody)*, vol. 32, pp. 128–137, 1996, in Russian.

[23] Y. Liu, Y. X. Ni, F. F. Wu, and B. Cai, "Existence and uniqueness of consistent conjectural variation equilibrium in electricity markets," *International Journal of Electrical Power & Energy Systems*, vol. 29, no. 6, pp. 455–461, 2007.

Hindawi
Mathematical Problems in Engineering
Volume 2021, Article ID 3839071, 16 pages
https://doi.org/10.1155/2021/3839071

Research Article

Type-2 Fuzzy Expert System Approach for Decision-Making of Financial Assets and Investing under Different Uncertainty

Zuzana Janková and Petr Dostál

Institute of Informatics, Faculty of Business and Management, Brno University of Technology, Brno 612 00, Czech Republic

Correspondence should be addressed to Zuzana Janková; zuzana.jankova@vutbr.cz

Received 19 April 2021; Revised 10 May 2021; Accepted 26 May 2021; Published 18 June 2021

Academic Editor: Mohammad Yazdi

Extensive research results of stock market time series using classical fuzzy sets (type-1) are available in the literature. However, type-1 fuzzy sets cannot fully capture the uncertainty associated with stock market developments due to their limited descriptiveness. This paper fills a scientific gap and focuses on type-2 fuzzy logic applied to stock markets. Type-2 fuzzy sets may include additional uncertainty resulting from unclear, uncertain, or inaccurate financial data through which model inputs are calculated. Here we propose four methods based on type-2 fuzzy logic, which differ in the level of uncertainty contained in fuzzy sets and compared with the type-1 fuzzy model. The case study aims to create a model to support investment decisions in Exchange-Traded Funds (ETFs) listed on international equity markets. The created models of type-2 fuzzy logic are compared with the classic type-1 fuzzy logic model. Based on the results of the comparison, it can be said that type-2 fuzzy logic with dual fuzzy sets is able to better describe data from financial time series and provides more accurate outputs. The results reflect the capability and effectiveness of the approach proposed in this document. However, the performance of type-2 fuzzy logic models decreases with the inclusion of increasing uncertainty in fuzzy sets. For further research, it would be appropriate to examine the different levels of uncertainty in the input parameters themselves and monitor the performance of such a modified model.

1. Introduction

The stock market occupies a key position in the economic system of each country. Predicting the future development of the stock market is a key task and an important area of research in the financial field, and thus in the economy as a whole. Stock markets are characterized by nonlinear behavior, including its chaotic nature; therefore the data collected generally show some uncertainty and may be incomplete or even incorrect. Uncertainty is therefore a major challenge in real-world applications, and there is a need for easy access to deal with such vague information, as Shukla et al. [1]. In this paper, attention is focused on the integration of the approach facilitating decisions on the future direction of the stock market through fuzzy logic. Fuzzy set theory was first introduced by Lotfi Zadeh in the 1960s as a way to capture uncertainty and ambiguity. Fuzzy logic can be considered as a generalization of classical set theory. Over time, research has revealed improvements in fuzzy logic that better reflect its true meaning, i.e., the linguistic expression of input variables, including uncertainty stemming from unclear or ambiguous information. This idea has sprung three main representations of fuzzy logic: type-1 fuzzy sets (T1FS), interval type-2 fuzzy sets (IT2FS), and general type-2 fuzzy sets (GT2FS). The first approach is the simplest form of fuzzy logic and also the most widespread and applicable. A more complex approach is represented by IT2FS, where the concept of uncertainty in the form of intervals is introduced. Although computationally complex compared to T1FS, they derive an improvement in the general fuzzy model by being more resistant to external noise, as reported by Castro et al. [2]; Puška et al. [3]; Eren [4]; Tavossi et al. [5].

Fuzzy logic is widely used in many areas not only because it can handle incomplete or uncertain data, but also because its tools have been simplified using parameterized FS. Building fuzzy rules and building the right membership

function (MF) have been challenging for decades now. The fuzzy membership feature is a key concept in designing fuzzy systems. Correct and accurate use of the membership function is essential for the reliability of the results obtained. The construction of the member function and the determination of its parameters are therefore still a current problem, as stated by Yankova et al. [6]. The choice of the shape and parameters of the membership functions plays an important role in the fuzzy model, as it can affect the performance of the whole system as a state of Wijayasekara and Manic [7]. Although the user can choose from a large number of shapes of membership functions, the choice of parameters is individual depending on the specific application. This will require expertise or sophisticated methods to fine-tune membership features. In addition, membership functions are, as reported by Kayacan et al. [8], a subjective matter of perceiving vague concepts entering the model. Sadollah [9] further adds that there is still no clear criterion for assessing the appropriateness of choosing the membership function. The MFs can take any shape and form as long as they map the data with the required degree of membership. As for the choice of MF, it is up to us to decide. This is where the fuzzy system offers individual degrees of freedom. With experience, you will learn which MF shape is suitable for the intended application.

In this work, we use type-2 fuzzy sets to overcome this uncertainty and develop a fuzzy system to support stock market investment decisions. This type-2 fuzzy system takes the delayed value of the stock index as inputs, fuzzifies it is using a type-2 fuzzy member function, and implies fuzzy rules in the fuzzy system. The output of the fuzzy system, which is in the form of a type-2 fuzzy membership function, reduced to a type-1 fuzzy membership function, decrypts it to a sharp value and creates decision support for the future development of the monitored stock index. The aim of the paper is to create models based on type-2 fuzzy logic with different levels of uncertainty contained in type-2 fuzzy sets with application to stock markets with subsequent comparison with classical type-1 fuzzy logic. The model will serve as decision support for investors. The purpose is to determine whether IT2FLS provides more accurate results compared to classical T1FLS.

The main contributions of the research can be considered: (1) creation of models that combine different locations of upper and lower functions of type-2 fuzzy logic membership focused on the financial and economic area of interest which has so far been insufficiently researched in terms of the applicability of type-2 fuzzy logic. (3) The model is intended directly to support decision-making regarding investments in Exchange-Traded Funds. We believe that focusing on a specific investment instrument is more suitable for the general investor public and makes it easier to invest your funds in the entire portfolio of assets through a single share than focusing on the stock index. (4) The authors provide an alternative approach to investment evaluation for investment funds compared to classical statistical methods. Our study is organized as follows: Section 1 focuses on a review of the literature applying fuzzy logic in stock markets. Section 2 explains the type-2 fuzzy logic technique, including metrics for evaluating the overall performance and error rate of the model. Section 3 describes the examined data set, including the creation of the IT2FLS model, and Section 4 deals with the subsequent validation and comparison of the created models.

2. Review of the Scientific Literature

Fuzzy logic is used in a wide range of decision-making problems such as risk management, finance, economics, and management, but also in weather forecasting, physics, and many other areas. The usability of fuzzy logic is huge, mainly due to the fact that they allow you to work on the principle of human thinking, unlike neural networks or genetic algorithms. Since the introduction of fuzzy logic prediction models, this method is increasingly used in a number of studies to solve problems related to stock market forecasts or as a support to decision-making tool for investors, analysts, or the general investor public.

An example is the short-term technical business strategy discussed in Chourmouziadis and Chatzoglou [10] using fuzzy logic. The authors focused on the methodology of buying and selling securities without the support of portfolio managers. Ijegwa et al. [11] developed a fuzzy model that, based on technical indicators, provides a signal to buy, sell, or hold an investment. Model outputs provide satisfactory results. Khayamim et al.'s [12] results showed that the proposed fuzzy method responds appropriately to the psychological component of the market. In addition, for all investor profiles, the recommended strategy completely outperforms the market and the remaining strategies. The conditional fuzzy inference approach is used in the study by Hassanniakalager et al. [13]. This approach is used for forecasting under constraint file conditions. Through conditional selection of rules, the model is able to achieve higher performance and interpretability. To predict the Chinese stock index, Sun et al. [14] use fuzzy sets and combine the traditional fuzzy model with the rough set method. This approach, according to the authors, provides better prediction results. Mansour et al. [15] formulated a multiobjective financial portfolio selection approach involving fuzzy parameters, where the distribution options are given by fuzzy numbers from the information provided by the decision environment. Tsai et al. [16], in contrast to traditional methods, use more variables included in the fuzzy model to predict and better reflect the issue of stock volatility. The results suggest that the authors' model with multiple periods is better and provides sufficient decision support for investors. Hasan and Fong [17] introduced some components for improving decision-making through sentiment analysis and simple fuzzy decision-making. The best model was chosen as the basis for a fuzzy decision-making mechanism provided to investors.

Other researchers have focused on hybrid strategies such as the integration of fuzzy logic and neural networks. Examples are the studies of Su and Cheng [18] and Vella and Ng [19]. These authors used adaptive neurofuzzy inference systems (ANFIS), modifying this model to type-2 fuzzy logic instead of classical type-1 fuzzy logic. Vlasenko et al. [20]

modify the classical ANFIS model, where in the fourth layer they use multidimensional Gaussian functions instead of polynomials. The experimental results showed clear advantages of the described model and its learning. Dutta [21] states that the nature of stock/capital market data makes it more complex and challenging to predict stock price movements. The study combined both fuzzy c-means and neural network technique for stock price prediction. Research will find the optimal solution for predicting the future share price. A comparison of the complexity of time and space has shown that the proposed method is better than existing methods. Rajab and Sharma [22] focused on the Bombay Stock Exchange, CNX Nifty, and S&P 500 and proposed an effective neurofuzzy model for their prediction. The authors point out that the hybrid model strikes a better balance between accuracy and interpretability. In her study, Janková [23] discusses the design of a neurofuzzy model to support decision-making when investing in investment instruments listed on the stock exchange in the Czech Republic. Empirical results show that the neurofuzzy model behaves more naturally than other statistical tools that simulate the decision-making process in stock trading without increasing the risk in the form of the investor's subjective judgment. Similarly, García et al. [24] demonstrate the suitability of the implementation of technical indicators and their predictive ability on the German stock index DAX-30 using a hybrid neurofuzzy model. In addition to the accuracy of the model, the authors also highlight the creation of less risky strategies, which are more profitable than using other methods.

The above study demonstrated exclusively the use of type-1 fuzzy logic, which is represented by membership functions or fuzzy sets ranging from zero to one. Such membership functions represent a precise point or exact degree of membership. However, this leads to problems with the inclusion of additional uncertainty and unclear information that enters the model according to Jiang et al. [25]. Therefore, type-2 fuzzy sets have been introduced that allow the uncertainty of the associated degrees of membership to solve the uncertainty problems of Liu et al. [26]. The proposed models based on the type-2 fuzzy system are used in finding solutions to some known problems reported in the literature, as described by Sumati et al. [27]. An example of using type-2 fuzzy logic is given in the following paragraph.

Jiang et al. [25] propose an interval type-2 fuzzy system for stock index prediction based on fuzzy time series and fuzzy logical relationship map (FLRM). The authors applied this methodology to data from the Taiwan Stock Exchange Capitalization Weighted Stock Index, the Dow Jones Industrial Average, and the National Association of Securities Dealers Automated Quotation. The outputs of the authors point out that the chosen method of solution exceeds classical statistical methods. Huarng and Yu [28] study their extension of type-1 fuzzy time series models to type-2 models. They designed a type-2 model for TAIEX index prediction. In this model, additional observations were made to refine the FLRs obtained from the type-1 model, resulting in better predictive performance. The authors' empirical evidence points to a lower error rate measured by RMSE type-2 than in the case of type-1 fuzzy logic. Similar results are presented by Bajestani and Zare [29], adding that this new type of fuzzy logic is more efficient than previous methods. Liu et al. [26] modified the classical hybrid neurofuzzy model and integrated a type-2 fuzzy set into it, which they used to predict the TAIEX index. The obtained knowledge points to a higher accuracy of the prognosis of this hybrid model than to the individual approaches alone. Zarandi et al. [30] developed an expert system based on type-2 fuzzy rules in their article for stock price analysis. They used a type-2 fuzzy model to predict the company's stock prices in Asia. The results of the forecast of price deviations are very encouraging. The genetic system of type-2 fuzzy logic was introduced in Bernardo et al. [31]. The authors used this hybrid model for prediction and modeling in the field of finance. This model overcame the white box problem and provided comparable performance to black box models. Janková and Dostál [32] apply IT2FL on the Czech stock market and they are used when deciding on investing in shares of the PX index. The proposed type-2 fuzzy model uses the return and risk of investment instruments as input variables. The created system is able to generate aggregated models from a number of language rules, which allows the investor to understand the created financial model. The use of T2FLS can lead to more realistic and accurate results than T1FLS. Another hybrid approach to IT2FLS was provided by Hasan et al. [33]. Their results correspond to similar outputs of other authors. Thus, it can be stated that type-2 fuzzy logic is able to improve the performance of existing models.

3. Type-2 Fuzzy Logic System

Quantification of sustainability data is very difficult; therefore, the evaluation of this data requires a personal point of view, namely, the evaluation by experienced experts in the field who provide a relevant opinion. In addition, sustainability data are often imperfect or inaccessible. This problem can be solved by fuzzy logic, the main advantage of which is that it allows language evaluation of each indicator. In order to implement the required assessment technique, methodologies should provide flexibility regarding the set of indicators applied, recognize data uncertainty, and mimic the human cognitive ability to assign scores to evaluated scores. This is essential for the holistic sustainability of evaluation and the associated large-scale impacts, as stated [34].

Fuzzy logic is based on the ability to deal with highly uncertain, inaccurate, or chaotic data files. Zadeh [34] has developed acceptable techniques for characterizing this uncertainty through fuzzy sets instead of complex mathematical formulations. The obvious advantage of fuzzy models is the ability to present data through linguistic qualitative concepts rather than quantitative data [35]. Fuzzy logic consists of three basic mechanisms, which are fuzzification, inference engine, and defuzzification. The relationship of these components is schematically illustrated in Figure 1, including fuzzy logic operators, member functions, and fuzzy rules. Member functions allow you to demonstrate a fuzzy set. In addition, fuzzy "if-then" rules represent the views and opinions of experts in their field that can be easily calculated.

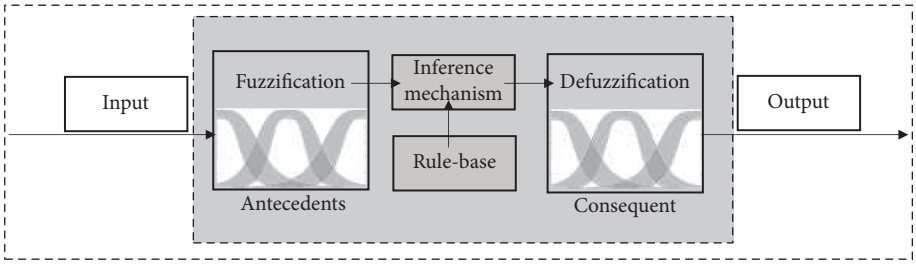

Figure 1: The mechanism of type-2 fuzzy logic.

The method of fuzzy logic allows the system to take advantage of modeling an environment that mimics human cognitive behavior and to enable language input in recognizing record uncertainty. The goal of FLS is therefore to provide a person with a descriptive understanding of problem solving. Without losing the generality, it is a fuzzy set of elements that allow their members different degrees of membership in the range [0, 1]. The degree of similarity of each input variable in such a fuzzy set is thus given by the membership function [36, 37]. A type-1 fuzzy membership function is defined by accurate and sharp values in the range [0, 1], while type-2 fuzzy membership function can be designed for each input variable in domain x. Furthermore, it can be stated that the T2FLS membership function can handle a higher level of uncertainty compared to the T2FLS membership function [38]. This is achieved by incorporating different degrees of footprint of uncertainty (FOU) combined with the three-dimensional nature of type-2 fuzzy sets. The secondary membership function is linked to the degree of membership. When this secondary member function takes the maximum uncertainty 1 in a certain interval [a, b], a fuzzy set of a type-2 interval is formed. The key elements of the interval type-2 fuzzy sets are footprint of uncertainty (FOU), upper membership function (UMF), and lower membership function (LMF). Note that the maximum uncertainty expressed in the secondary membership function is equal to 1, so a fuzzy set of type-2 intervals can be simplified. Fuzzy sets are associated with linguistic terms that form part of fuzzy rules that are conditioned by statements [39].

The T2FLS structure is very similar to the T1FLS structure. The measured real variables are first transformed in a fuzzification block into linguistic variables, with the linguistic variables based on the basic linguistic variables. Janková et al. [40] state that three to seven attributes of this basic variable are usually used. The degree of attribute of a given variable in a set is represented by a mathematical function. Three types of fuzzification are available in T2FLS. If the measured data is perfect, modeled as a sharp set, data with noise and data with stationary noise are modeled as type-1 fuzzy sets, with nonstationary noise modeled as type-2 fuzzy sets. The latter type of fuzzification cannot be performed in T1FLS.

Type-2 fuzzy logic systems are represented by the possibility of a distribution function that can be written, according to Sang et al. [41] and Mendel et al. [42], such as

$$\widetilde{A} = \int_{x\epsilon X}\int_{u\epsilon J_x} \frac{\mu_{\widetilde{A}}(x,\mu)}{x,u} = \int_{x\epsilon X}\int_{u\epsilon J_x} \frac{\mu_{\widetilde{A}}(x,\mu)/(x,u)}{x}, \quad (1)$$

where x is the first variable, $J_x \epsilon [0,1]$ is the first fuzzy possibility of x, u is the second variable, and $\int_{u\epsilon J_x}\mu_{\widetilde{A}}(x,\mu)/(x,u)$ is secondary fuzzy possibility distribution at x.

Mendel [43] defines the IT2FLS method, in which they use a generalized interval fuzzy set interval. The requirement for secondary possibility distribution is a condition of normality, which means that the X elements are fully distributed for x, which are defined as follows: IT2FLS is

$$\widetilde{A} = \int_{x\epsilon X}\int_{u\epsilon J_x} \frac{1}{(x,u)} = \int_{x\epsilon X}\int_{u\epsilon J_x} \frac{1/(x,u)}{x}, \quad (2)$$

where x is the first variable, $J_x \epsilon [0,1]$ is the first possibility distribution of x, u is the second variable, and $\int_{u\epsilon J_x} 1/(x,u)$ is secondary possibility distribution at x.

For IT2FLS X are upper possibility distribution $\overline{\mu}(x)$ and lower possibility distribution $\underline{\mu}(x)$, type-1 possibility distribution, the footprint uncertainty of $\widetilde{X}(FOU(\widetilde{X}))$ is defined as [42]

$$FOU(\widetilde{X}) = \bigcup_{x\epsilon X} J_s = \left\{(x,y)\colon J_X = \left[\overline{\mu}(x), \underline{\mu}(x)\right]\right\}. \quad (3)$$

IT2FLS $\widetilde{X} = [\overline{\mu}(x), \underline{\mu}(x)] = ((a,b,d;h^U), (e,b,f;h^L))$, where $\overline{\mu}(x)$ and $\underline{\mu}(x)$ are fuzzy sets of type-1, a,b,d,e,f are reference points of the IT2FLS, h^U indicates the possible value of the element a,b,d in the upper possibility function, h^L indicates the possibility value of the element e,b,f in lower possibility function, $h^U \epsilon [0,1]$, and $h^L \epsilon [0,1]$. And the lower possibility distribution and the upper possibility distribution can be denoted as

$$\overline{\mu}^U(x) = \begin{cases} \dfrac{\mu^U(x-a)}{b-a}, & a \le x \le b, \\ \dfrac{\mu^U(d-x)}{d-b}, & b \le x \le d, \\ 0, & \text{otherwise.} \end{cases} \quad (4)$$

$$\underline{\mu}^L(x) = \begin{cases} \dfrac{\mu^L(x-e)}{b-e}, & e \le x \le b, \\ \dfrac{\mu^L(f-x)}{f-b}, & b \le x \le f, \\ 0, & \text{otherwise.} \end{cases} \quad (5)$$

The comparison method for IT2FLS is described below, which is based on the assumption of an uncertain average and variation coefficient. For all $\widetilde{X} = ((a, b, d; h^U), (e, b, f; h^L))$, whose possibility uncertainty mean value is defined, according to Sang and Liu [44],

$$M(\widetilde{X}) = \frac{\widetilde{MX^U + MX^L}}{2}, \tag{6}$$

where possibility uncertainty mean of the upper membership function $M(\widetilde{X^U})$ and lower membership function $M(\widetilde{X^L})$ are, respectively, written as

$$M\left(\widetilde{X^U}\right) = \frac{1}{2}\int_0^{h^U}\left(\underline{X^U}(\alpha) + \overline{X^U}(\alpha) + 2b\right)f(\alpha)\mathrm{d}\alpha, \tag{7}$$

$$M\left(\widetilde{X^L}\right) = \frac{1}{2}\int_0^{h^L}\left(\underline{X^L}(\alpha) + \overline{X^L}(\alpha) + 2b\right)f(\alpha)\mathrm{d}\alpha. \tag{8}$$

$f(r)$ is an increasing function satisfying $f(0) = 0$, $f(1) = 1$, and $\int_0^{h^U} f(\alpha)d\alpha = (1/2)$.

For all IT2FLS, as further reported by Sang and Liu [44], the coefficient of variation of possibility uncertainty is defined as

$$VC(\widetilde{X}) = \begin{cases} \dfrac{D(\widetilde{X})}{M(\widetilde{X})}, & \text{if } M(\widetilde{X}) \neq 0, \\[2ex] \dfrac{D(\widetilde{X})}{\epsilon}, & \text{if } M(\widetilde{X}) = 0, \end{cases} \tag{9}$$

where ϵ is an extremely small value to present the approximate $M(\widetilde{X}), D(\widetilde{X})$ is the variation values. This expression $D(\widetilde{X})$ is defined as

$$\begin{aligned} DX &= \sqrt{\widetilde{D\widetilde{X^U}D\widetilde{X^L}}}, \\ D\widetilde{X^U} &= \frac{1}{4}\int_0^{h^U} \overline{X^U}\alpha - \underline{X^U}\alpha^2 f\alpha d\alpha, \\ D\widetilde{X^L} &= \frac{1}{4}\int_0^{h^U} \overline{X^U}\alpha - \underline{X^L}\alpha^2 f\alpha d\alpha, \end{aligned} \tag{10}$$

where $f(\alpha)$ is an increasing function satisfying $f(0) = 0$, $f(1) = 1$, and $\int_0^{h^U} f(\alpha)\mathrm{d}\alpha = 1/2$.

Let $\widetilde{X}$ and $\widetilde{Y}$ be two IT2FLS, whose comparison criteria are defined according to Sang and Liu [44] as follows:

$$\begin{aligned} &\text{If } M(\widetilde{X}) < M(\widetilde{Y}), \quad \text{then } \widetilde{X} \prec \widetilde{Y}, \\ &\text{If } M(\widetilde{X}) > M(\widetilde{Y}), \quad \text{then } \widetilde{X} \succ \widetilde{Y}, \\ &\text{If } M(\widetilde{X}) = M(\widetilde{Y}), \quad \text{then,} \\ &\text{if } VC(\widetilde{X}) < VC(\widetilde{Y}), \quad \text{then } \widetilde{X} \prec \widetilde{Y}, \\ &\text{if } VC(\widetilde{X}) > VC(\widetilde{Y}), \quad \text{then } \widetilde{X} \succ \widetilde{Y}, \\ &\qquad \text{else } \widetilde{X} \sim \widetilde{Y}. \end{aligned} \tag{11}$$

It is denoted that > means "larger than" in the sense of order, < means "less than" in the sense of order, and ~ means "same order".

3.1. Evaluation of the Accuracy of the Model. The model can be used in practice if the verification shows that the model provides accurate results. The following metrics are used to verify and evaluate the accuracy or error rate of individual MFs. For this reason, the RMSE indicator is used, which is focused on comparing the original data y_t with the data generated by the model $\dot{y}_t$. The Mean Absolute Percentage Error (MAPE), Mean Absolute Error (MAE), Relative Root Mean Squared Error (RMSE), and Mean Squared Error (MSE) indicators are also used. These metrics are used to evaluate which type of MF and which level of uncertainty provide the best results for analyzing a stock market that exhibits a specific feature, as described by Soto et al. [45] and Bas et al. [46].

The formulas of these evaluations are shown below:

$$\text{RMSE} = \sqrt{\frac{1}{n}\sum_{t=1}^{n}(y_t - \dot{y}_t)^2}, \tag{12}$$

$$\text{MAPE} = \frac{1}{n}\sum_{t=1}^{n}\frac{|y_t - \dot{y}_t|}{y_t}x100, \tag{13}$$

$$\text{MAE} = \frac{1}{n}\sum_{t=1}^{n}|y_t - \dot{y}_t|. \tag{14}$$

4. Data and Methodology

It is well known that the stock market is a dynamic system exhibiting chaotic behavior, which makes it very difficult to predict its future development. In particular, nonlinear and complex laws limit quick decisions on the right investments. For this reason, many researchers are focusing on developing an intelligent system that is able to reduce the amount of risk in the market that results from its nonlinear nature. For this reason, alternative techniques are increasingly used in stock market modeling and analysis, including fuzzy logic, which is able to include the uncertainty, nonlinearity, and noise that occur in financial time series. The study focuses on the application of interval type-2 fuzzy logic as a sophisticated tool that is able to intuitively model human judgment through linguistic values in combination with quantitative data, as reported by Ulubeyli and Kazaz [47]. Fuzzy logic allows you to better express preferences and subjective opinions when making decisions. In other words, if objective facts cannot be accurately identified, at least its scope of membership can be defined. The fuzzy logic interval operates with approximate numerical data used for decision-making, as stated by Liu [48].

4.1. Description and Processing of the Dataset. For testing interval type-2 fuzzy logic system, which in this paper serves to create a model to support decision-making in investment

instruments, a data set of 40 Exchange-Traded Funds (ETFs) from four continents over the last 5 years, i.e., from 2015 to 2019, is selected. Monthly data is used. Specifically, the 10 most powerful ETFs are selected from each continent of Europe, USA, and Asia-Pacific and Emerging markets. ETFs are basically index funds, which represent an alternative way of investing for institutional and retail investors. The most important characteristic of Exchange-Traded Funds is, as the name suggests, the fact that they are traded similarly to shares on the stock exchange. They are valued and traded on an ongoing basis throughout the trading day, allowing investors to buy or sell without delay. Exchange-Traded Funds invest in a defined index, or baskets of assets, thus allowing investors to invest in the entire portfolio using a single share. Originally, they were established as passive funds with the aim of replicating the underlying benchmark as faithfully as possible; however, in recent years, ETFs with active management have also expanded to outperform the underlying index or basket of assets.

Figure 2 shows a PMFG graph from a pairwise correlation matrix based on the monthly data of all 40 examined ETFs. This graph is the first extension of the Minimum Spanning Tree (MST) and the full name is Planar Maximally Filtered Graph. PMFG is a comprehensive network that was first introduced in Tumminello et al. [49] and Aste et al. [50]. In this case, the degree of similarity of the ETFs is given by the Person correlation coefficient. Individual ETFs are marked according to ticker. A lighter color indicates a stronger correlation between the funds. Conversely, a darker color indicates independence or even a negative correlation between individual ETFs. The largest correlation is between European, American, and Asia-Pacific funds. ETFs from Europe and Asia-Pacific correlate more positively. On the contrary, the positive correlation between the USA and Europe or Asia-Pacific is not so dominant. Conversely, some Emerging markets ETFs even have a negative correlation with all other funds.

Table 1 shows the basic characteristics of ETFs by continents. The table shows that ETFs from the USA have the highest return with an average return of 65.59%, followed by funds from the Asia-Pacific continent with an average return of 23.46%. The lowest average return was achieved by ETFs from Emerging markets with a value of 7.88%. In terms of fluctuations in returns or riskiness of the fund represented by the standard deviation, ETFs from Asia-Pacific are calculated to be the riskiest. Paradoxically, although US funds have the highest returns, they also have the lowest risks. In terms of total cost ratio, measured by the total expansion ratio (TER), ETFs from the US show the lowest cost on average, followed by ETFs from Europe. On the contrary, similar costs above 0.5% are achieved by ETFs from the Asia-Pacific and Emerging markets. Despite these values, all analyzed ETFs show a low overall cost compared to mutual funds, which is one of the main advantages of these Exchange-Traded Funds. Selected ETFs are then compared with their underlying indices. All analyzed funds are equity, so to determine the coefficient of determination and subsequent indicators, the underlying index specified in the fund's articles of association is chosen, or the best alternative is chosen according to the availability of data. Funds from the USA with a value of the coefficient of determination of 0.94 best replicate their benchmarks. From this point of view, it can be assumed that the deviation from the underlying index is very small. Both underlying assets and ETFs from Emerging markets replicate relatively well. ETFs from Europe and the Asia-Pacific continent show the same value of the coefficient of determination with a value of 0.76. The last of the analyzed indicators in Table 1 is the beta coefficient. A beta coefficient value higher than 1 means that the fund is able to outperform the market and these are cyclical funds, while a value below 1 indicates anticyclical funds that do not achieve comparable or higher performance in a bull market, respectively. They are unable to outperform the market. On the contrary, these funds are suitable at a time of a bear market, when they limit losses compared to the market as a whole. It can be noted that values above 1 are achieved by ETFs from Asia-Pacific and Emerging market, respectively, and basically the USA. On the contrary, funds from Europe with a beta coefficient of 0.95 lag behind the market, which can be attributed to the not very good replication of benchmarks.

4.2. Calculation of Input Variables. The indicators are then selected as input variables into the interval type-2 fuzzy model, which are explained in Table 2 and scored in Table 3. Based on the analyzed ETFs, indicators of return, risk, and performance are calculated. Subsequently, the results are summarized according to the individual continents and the average score is determined for each indicator separately. The higher the point rating is, the higher the ETF achieves higher returns, higher risk, or higher performance.

From Table 3 it is clear that the highest annual return is achieved by ETFs from the USA, which has already resulted from Table 1. It is also evident that ETFs from the USA also show the highest return above risk-free rate and also have the highest telling value in the form of information ratio. On the contrary, ETFs from Europe show the highest return above benchmark. In terms of overall profitability indicators, ETFs from Emerging markets are the worst off. In terms of risk, they clearly dominate with the lowest score, and thus the lowest risk, through standard deviation, specific and systematic risk, and ETFs from the US. A similarly low risk can be seen with ETFs from Europe. Therefore, it can be concluded that especially American and European ETFs have an almost perfectly diversified portfolio. ETFs from Emerging markets show the greatest systematic risk, while the greatest specific risk and standard deviation can be seen in ETFs from Asia-Pacific. The specific risk can be diversified with a suitable composition of investment instruments. Therefore, the reason may be the inadequate number of constituents included in the portfolio, but also the poor management of the asset manager of the ETF from the Asia-Pacific continent. The tracking error indicator is derived from the return above the benchmark, which expresses the volatility of the differences in the performance of the fund and the benchmark by means of a standard deviation. It is desirable that the value of this indicator for passively

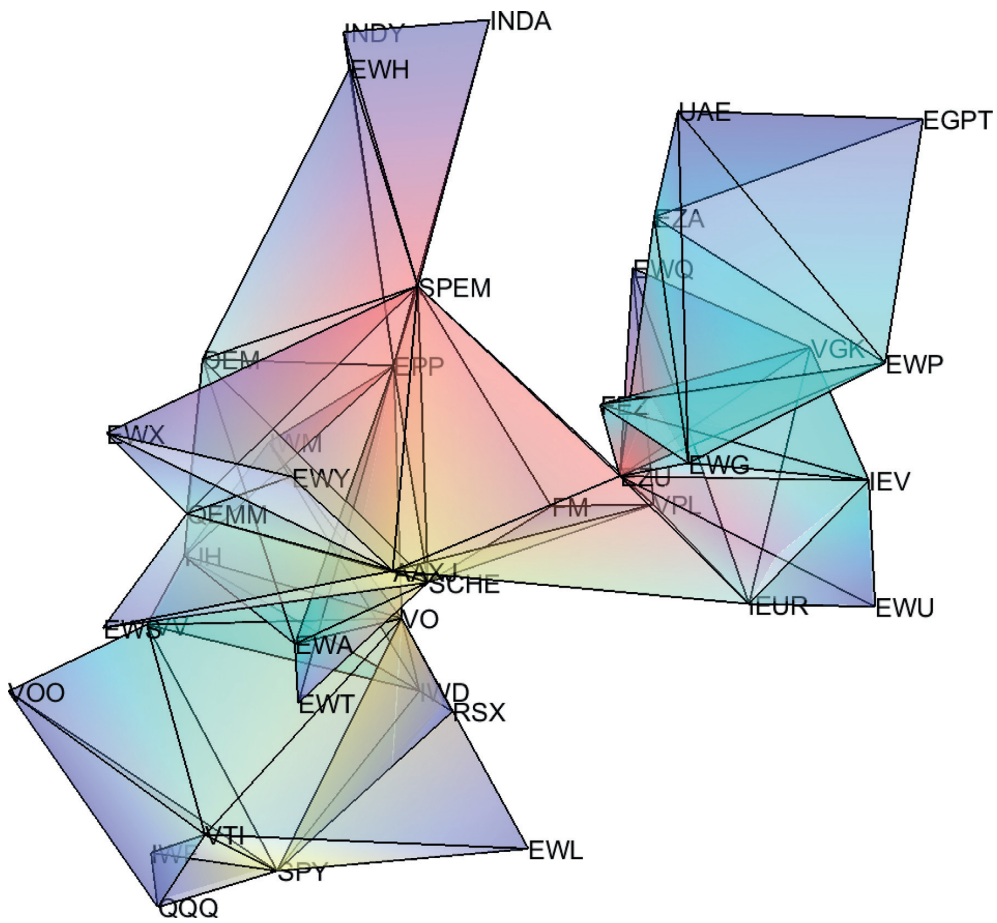

Figure 2: PMFG graph from a matrix of Pearson's correlation.

Table 1: Summary of ETFs statistics by continents.

Continent	Europe	USA	Asia-Pacific	Emerging markets
Return	16.91%	65.59%	23.46%	7.88%
Std. deviation	14.53%	13.08%	19.89%	18.36%
TER	0.40%	0.11%	0.56%	0.54%
R^2	0.76	0.94	0.76	0.82
Beta	0.95	0.99	1.11	1.01

managed ETFs be as small as possible. The absolute best results were achieved by ETFs from the USA, which perfectly replicate the underlying benchmarks. On the contrary, funds from the Asia-Pacific continent are worse off. The chart also shows the ratios that represent the fund's performance. The Treynor ratio expresses the reward for volatility. Therefore, a higher score is desirable, which means higher performance of the fund. All analyzed continents show very similar points. However, the US is the worst off, which may be surprising given the claims made so far. The reason can be seen in the fact that the shortcoming of the Treynor ratio is that it completely ignores the unique risk, as it presupposes a perfect diversification of the portfolio. Jensen's alpha expresses the added value of the fund manager to achieve a higher return than the market return, taking into account the sensitivity of the fund to the movement of the entire market represented by the beta coefficient. If alpha shows positive values, it indicates the ability of the fund manager to beat the market and better deal with systematic risk; with a negative alpha, active portfolio management fails. All analyzed funds managed to outperform the market represented by the reference index. ETFs from the Asia-Pacific market achieved the highest score. The last indicator is the Appraisal ratio. This indicator evaluates the quality selection of equities for the fund's portfolio by the manager and focuses on the nondiversified part of the portfolio.

5. Creating the IT2FLS Model

In particular, the stock market works with vague concepts, so it is appropriate to use fuzzy logic, which is able to contain this data, as a decision support. The MATLAB software toolbox is used to create a type-2 fuzzy model. The fuzzy model for examining equity ETFs consists of three input

Table 2: Summary of variables used as inputs.

Variable		Description
Return	Annual return	Standardized rate of return for one year.
	Return above benchmark	Return achieved over the return achieved by the underlying index or basket of assets.
	Return above risk-free rate	A risk premium required by an investor when investing in an asset with a higher risk than government bonds.
Risk	Standard deviation	Indicates the quadratic average of the deviations of the fund's portfolio returns from the arithmetic average, i.e., the square root of the variance.
	Systematic risk	It results from the overall economic situation and individual macroeconomic variables, so it is undiversified and affects all economic entities.
	Specific risk	It is a unique risk for each asset and can be eliminated by appropriate portfolio diversification.
	Tracking error	Measures variations in fund portfolio and benchmark performance.
Performance	Information ratio	It compares the fund's performance with the market's performance taking into account risk.
	Treynor ratio	It represents a reward for volatility and assumes that the fund eliminates unique risk by appropriate portfolio diversification and only counts on systematic risk.
	Jensen alpha	It measures the ability of the fund manager to generate a fund return above the return given by the benchmark and the ability to deal with systematic market risk.
	Appraisal ratio	It expresses the additional return, adjusted for the systematic risk per unit of individual risk taken.

Table 3: Point scores of input variables by continent.

Continent	Europe	USA	Asia-Pacific	Emerging markets
Return above benchmark	37	18	18	16
Return above risk-free rate	24	66	24	10
Standard deviation	28	25	38	35
Systematic risk	54	54	64	69
Specific risk	14	5	22	15
Tracking error	14	5	22	15
Information ratio	22	46	10	11
Treynor ratio	41	36	46	48
Jensen alpha	10	6	20	8
Appraisal ratio	13	7	21	9

variables (return, risk, and performance), one block of rules, and one output variable to determine whether or not it is appropriate to invest in the ETFs. This model is shown in Figure 3, with the figure showing that each of the three input indicators consists of other indicators, which were described in Section 3. The aim is to create a suitable, clear, and accurate model based on IT2FLS, which will serve as a support for investors to decide whether or not to invest in ETFs according to input parameters.

A fuzzy inference system of the Mamdani type is chosen for the creation of the model, because it is able to work better and more intuitively with unstructured or poorly structured data inputs than the Sugeno type. In addition, it is able to imitate human thinking and comprehensively describe the system using natural language. This type of output is sufficient to interpret stock ETF analysis. Each input variable is represented by a Gaussian membership function (MF), which consists of fuzzy sets containing a total of five linguistic fuzzy values or attributes: VL: very low, *L*: low, *M*: medium, H: high, and VH: very high. Input 1 represents the overall return of the ETF, input 2 represents the overall riskiness of the ETF, and finally input 3 indicates the overall performance of the ETF examined on three continents, namely, Europe, the USA, Asia-Pacific, and Emerging markets. The output variable is also represented through the five attributes of the member function based on the point rating, namely, S: sell (0 points), RS: rather sell, H: hold, RB: rather buy, and B: buy (100 points). Member functions are in the range [0; 1] and are used to create fuzzy models with different degrees of uncertainty. Table 4 shows examples of input variables and output variables by means of numerical values as well as linguistic expressions corresponding to the attributes of MF.

As an example, the first ETF can be described, which in terms of input 1 achieves a score of 35.85 points, or the total return for this ETF is medium. Input 2 expresses the overall riskiness of a particular ETF with a score of 24.35, which is a fuzzy set with low risk. Input 3 evaluates the overall performance with the total point score of the given ETF 33.11 or according to the fuzzy notation it is a high score. The recommendation for the ETF is a score of 80, which means rather buy. A similar procedure can be used for all other analyzed ETFs.

6. Results and Evaluations

This study focuses on IT2FL, which consists of dual membership functions containing upper and lower MFs,

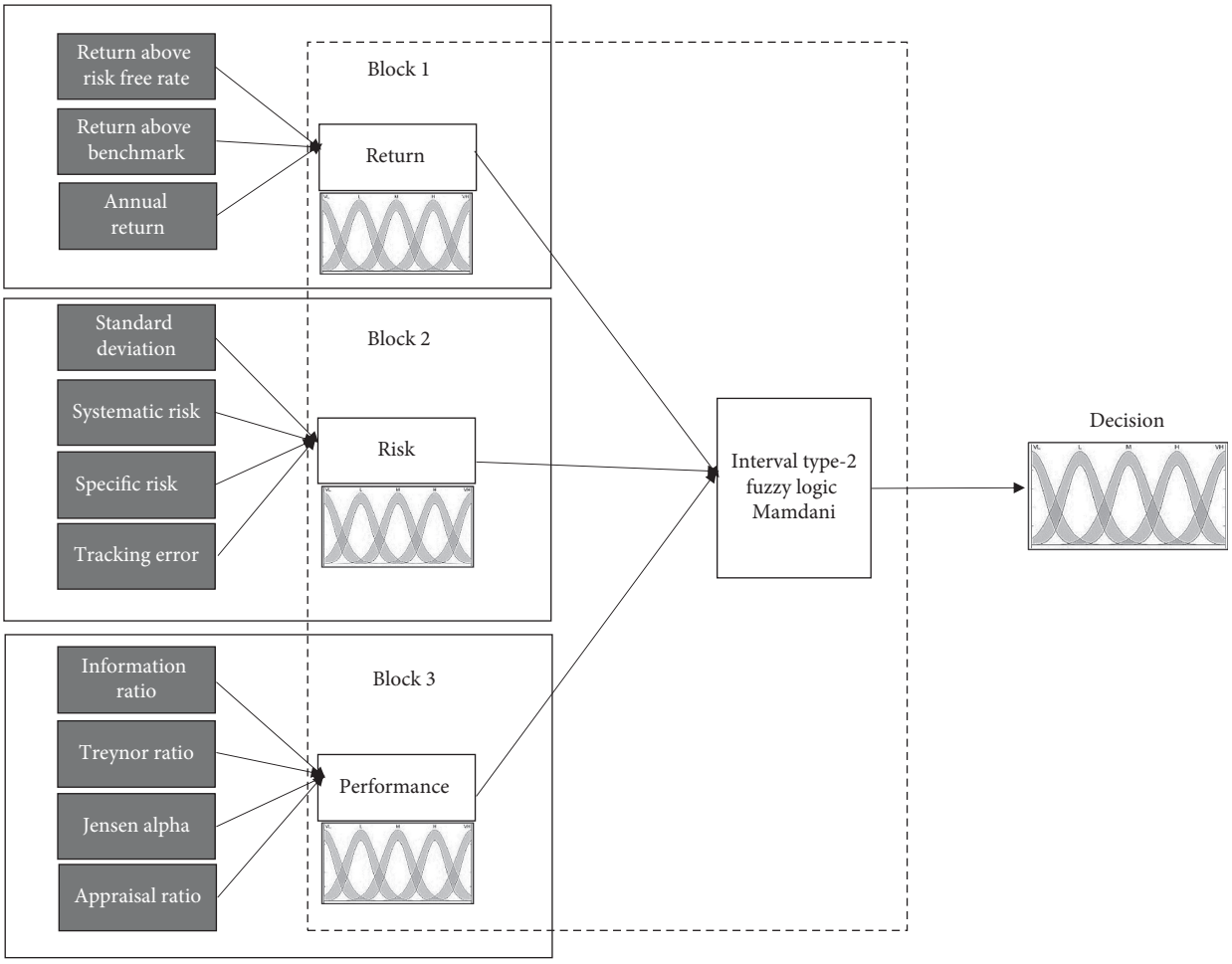

Figure 3: IT2 FS architecture of ETFs.

Table 4: Example of input numerical and linguistic values and output variables.

Input 1		Input 2		Input 3		Results	
Numeric value	Linguistic value	Numeric value	Linguistic value	Numeric value	Linguistic value	Numeric value	Linguistic value
35.85	Medium	24.35	Low	33.11	High	80	Rather BUY
26.78	Low	29.12	Medium	21.99	Low	50	HOLD
36.34	Medium	23.63	Low	17.52	Low	80	Rather BUY
25.77	Low	25.82	Low	19.99	Low	65	HOLD
35.28	Medium	27.77	Medium	19.96	Low	75	Rather BUY
54.88	High	20.81	Very low	27.14	Medium	100	BUY
55.51	High	20.69	Very low	28.26	Medium	100	BUY
55.72	High	20.50	Very low	29.03	High	100	BUY
57.09	High	20.59	Very low	32.53	High	100	BUY
72.25	Very high	23.99	Low	31.10	High	100	BUY
62.99	Very high	20.66	Very low	28.88	Medium	100	BUY

with the space between these MFs being filled with additional FOU uncertainty. According to the literature mentioned in Section 1, the use of IT2FL should bring more accurate results, especially for use in a stock market that contains a high degree of uncertainty. Several representative models were selected to evaluate the accuracy of the generated IT2FLs. In total, 5 models are created and tested, which differ in the level and degree of uncertainty contained in the type-2 fuzzy sets. The functions of membership depend on the scope and depth of knowledge of the problem being solved, as well as on the context in which the problem is solved.

(i) Model 1: T1FLS or IT2FLS with 0% uncertainty in MF,

(ii) Model 2: IT2FLS with 10% uncertainty in MF,

(iii) Model 3: IT2FLS with 20% uncertainty in MF,

(iv) Model 4: IT2FLS with 30% uncertainty in MF,

(v) Model 5: IT2FLS with 40% uncertainty in MF.

Other models with higher uncertainty were not considered relevant by the authors of the paper. Subsequently, to evaluate the created models, it is necessary to determine the knowledge base or block of rules. The knowledge base representing rules in the form "if - then" expresses expert knowledge about the relationship between input variables and output variables. A total of 125 rules are created, based on which the created models are evaluated. The block of rules is determined by experts and authors of the article. The rules represent a knowledge base that describes the behavior of the entire fuzzy system. For this reason, it is necessary to describe the whole issue using a sufficient number of rules. These rules were generated by experts in the field. The result is the assignment of a verbal description to the output variables based on the knowledge base. In other words, the input data is converted to output data using these rules. The defuzzification part of the model sets out the final assessment, which serves as a decision support for investors whether to invest in the ETF or not. The specific defuzzification value from all 5 models is given in Table 4; the values given correspond to the input values, which are given in Table 3. In particular, an ETF with a total return of 35.85 points, a total risk of 24.35 points, and a total performance of 33.11 points should have a score of 80 points with a rather buy recommendation. Model 1, i.e., the classic T1FLS, sets the total value of the result at 70 points. Models 2 and 3, i.e., IT2FLS with 10% and 20% uncertainty, contained in the MF give a result of 75 points. Models 4 and 5, based on the knowledge base and the uncertainty contained in the MF, give a final score of 74 points. Thus, specifically for this fund, the recommendation for all models is rather buy, while the most accurate results were achieved by models with 10% and 20% uncertainty. Similarly, other examples of ETFs entering the models can be analyzed.

From Table 5 it can be further noted that the differences in the point evaluation of the results are not very different for all examined models. Especially for IT2FLS models, the results differ by 1 to 3 points, which is not a big difference. To evaluate the performance of the analyzed models, the selected metrics are listed in Section 2.3. The results of evaluation and comparison of models are given in Tables 6–10. The tables also show MFs with different levels of uncertainty. The figure also shows how the distance between the individual functions gradually increases with the addition of uncertainty.

Table 6 shows an evaluation of the error rate and performance of the T1FLS model. The RMSE indicator is used to compare the quality of models. Equation (12) is used to calculate it. A lower RMSE value indicates a better model. Model 1 shows the value of this indicator is 15.43. Compared to other models, T1FLS shows the worst result or other IT2FLS models containing uncertainty in membership functions provide better results than the classic fuzzy model. Indicator value for model 1, the MAE value calculated based on equation (14), is set to 12.1. In terms of this indicator, model 1 achieves the highest error rate and deviates the most from reality compared to all other models. The last indicator used to compare the created models is the MAPE indicator calculated on the basis of equation (13). The value of the MAPE indicator is a dimensionless characteristic by which different models can be compared. Even with this indicator, the T1FLS model achieves the worst results with a value of 13.95 compared to other models.

Table 7 evaluates the indicators described above for the IT2FLS model with a degree of uncertainty of 10%. The figures captured in this table already show the difference between the upper and lower membership function. This space is filled with additional uncertainty resulting from uncertain data coming from the stock market. It is clear that model 2 shows the lowest values of all examined indicators. Specifically, the RMSE indicator indicates the value for this model is 12.15, i.e., the best model when compared to other IT2FLS models. The MAE and MAPE error indicators are also the lowest, so the model with 10% uncertainty shows the smallest deviation from the original result and is best able to serve as a decision support for investors regarding investments in ETFs.

Table 8 evaluates the performance of model 3 with 20% uncertainty included in the MF. Although this model is worse than model 2, it still provides much better results than T1FLS, as well as other models with a higher degree of uncertainty in MF. In addition, it can be stated that the difference in performance between the best model (model 2) and model 3 is very small to negligible in our case. Because RMSE is 12.32, MAE is 9.29, and MAPE is 10.88, looking back at Table 6, there is a minimal difference in performance and in any case, using this model would not significantly distort the final assessment of whether or not to invest in ETFs.

The evaluation of the penultimate model is given in Table 9, which evaluates a model containing 30% uncertainty in MF. A higher degree of uncertainty is also evident from the MFs shown in the figure, which are more distant from each other than in the other models described earlier. Also, in this model, as in model 3, there is a deterioration in performance according to the error indicators MAE (9.47) and MAPE (9.47) and the performance indicator RMSE (11.02).

The last model examined is model 5 containing the highest degree of uncertainty or the most distant fuzzy MF. It is also the model with the worst performance compared to other IT2FLS models. However, even this model still achieves much better results than the classic T1FLS model. Type-2 fuzzy logic features three-dimensional shapes of membership functions. These duplicate membership functions are able to include additional uncertainty resulting from insufficient information. They are used especially when it is difficult to determine the exact shape and location of membership functions. Using these functions, type-2 fuzzy logic is severely limited mainly due to the increasing computational complexity associated with their implementation.

Table 5: Evaluation of the output through the created models.

Model 1		Model 2		Model 3		Model 4		Model 5	
Numeric value	Linguistic value	Numeric value	Linguistic value	Numeric value	Linguistic value	Numeric value	Linguistic value	Numeric value	Linguistic value
70	Rather BUY	75	Rather BUY	75	Rather BUY	74	Rather BUY	74	Rather BUY
69	HOLD	68	HOLD	67	HOLD	66	HOLD	65	HOLD
66	HOLD	72	Rather BUY	72	Rather BUY	71	Rather BUY	69	HOLD
71	Rather BUY	68	HOLD	69	HOLD	68	HOLD	67	HOLD
67	HOLD	72	Rather BUY	72	Rather BUY	71	Rather BUY	70	Rather BUY
76	Rather BUY	79	Rather BUY	78	Rather BUY	78	Rather BUY	78	Rather BUY
76	Rather BUY	80	Rather BUY	79	Rather BUY	79	Rather BUY	78	Rather BUY
77	Rather BUY	80	Rather BUY	80	Rather BUY	79	Rather BUY	78	Rather BUY
78	Rather BUY	81	BUY	81	BUY	81	BUY	80	Rather BUY
79	Rather BUY	88	BUY	88	BUY	88	BUY	87	BUY
78	Rather BUY	86	BUY	87	BUY	86	BUY	85	BUY

Table 6: Evaluation of the model 1.

Model 1	Input 1	Input 2	Input 3
T1FLS	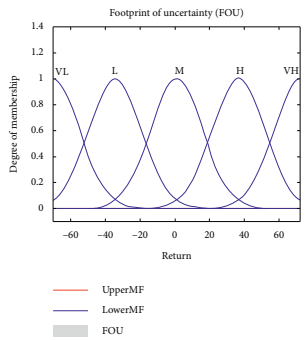	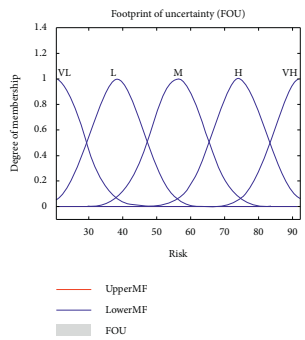	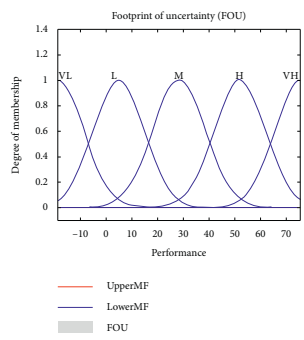
Evaluation	RMSE 15.43	MAE 12.01	MAPE 13.95

Table 7: Evaluation of model 2.

Model 2	Input 1	Input 2	Input 3
10% uncertainty	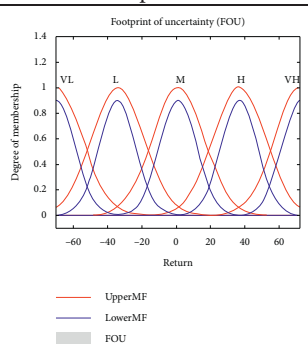	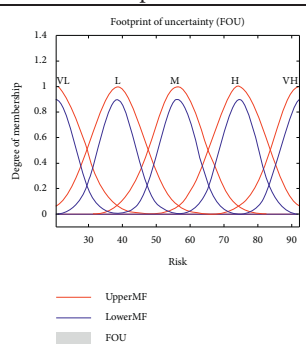	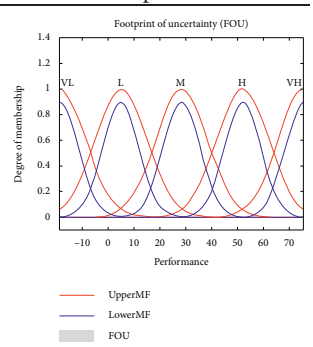
Evaluation	RMSE 12.15	MAE 9.15	MAPE 10.73

Figure 4 captures the surface of the three input variables: overall return, overall risk, and overall performance of the analyzed ETFs in relation to the overall model outcome. It is clear from the figure that the higher the fund's performance score and the lower the fund's risk score (Figure 4(a)), the more recommended it is to invest in ETFs. On the contrary, the higher the risk rating and the lower the performance score (Figure 4(b)), the more recommended it is, according to the results of IT2FLS, not to invest in ETFs or sell ETF shares. The last combination concerns performance and

Table 8: Evaluation of model 3.

Model 3	Input 1	Input 2	Input 3
20% uncertainty	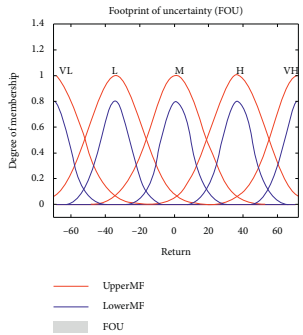	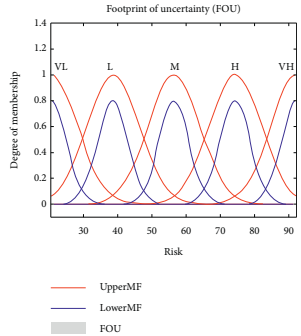	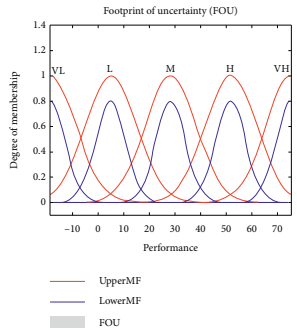
Evaluation	RMSE 12.32	MAE 9.29	MAPE 10.88

Table 9: Evaluation of the model 4.

Model 4	Input 1	Input 2	Input 3
30% uncertainty	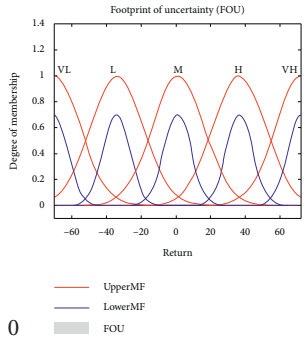	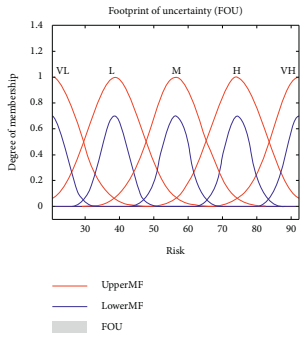	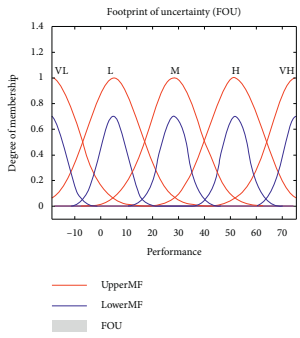
Evaluation	RMSE 12.51	MAE 9.47	MAPE 11.02

Table 10: Evaluation of model 5.

Model 5	Input 1	Input 2	Input 3
40% uncertainty	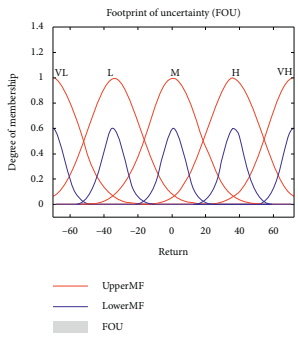	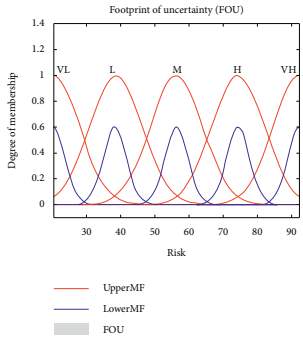	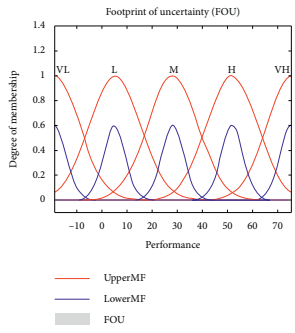
Evaluation	RMSE 12.51	MAE 9.47	MAPE 11.02

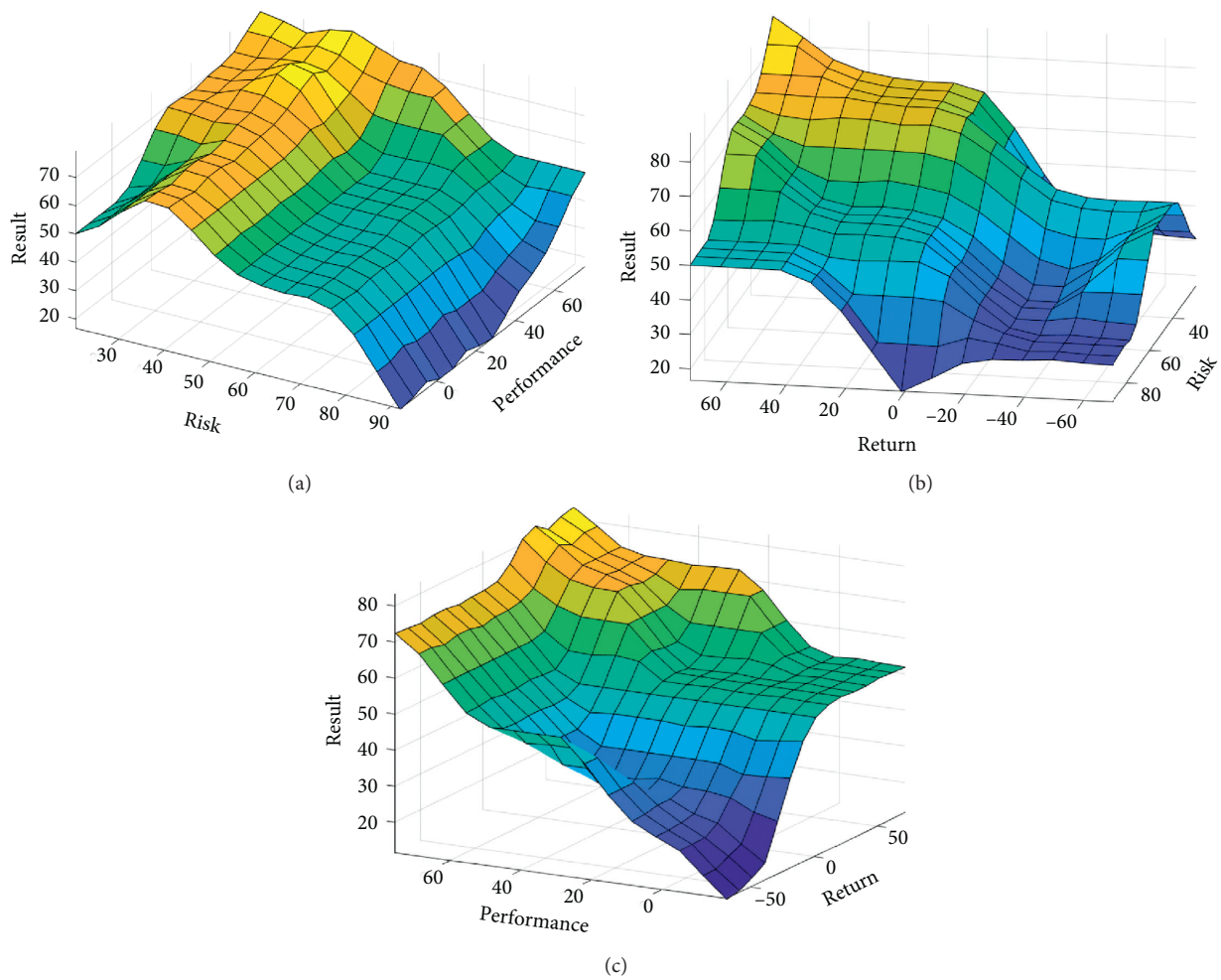

Figure 4: IT2 FS surface of three inputs. (a) Performance and risk, (b) return and risk, and (c) performance and return.

return (Figure 4(c)). In the case of the mean values of these variables, the investor is advised to hold ETF shares or refrain from any action, whether in terms of sale or purchase.

7. Conclusion and Future Search

The presented paper tried to apply a sophisticated method that is rarely used in the financial field and points out to the general investor public the possibility of using it to successfully analyze the stock market based on intuitive behavior. We present specific advanced methods of fuzzy logic for decision-making areas for successful investing. Conventional methods for decision support in various fields require accurate and unambiguous numerical evaluation. However, an accurate numerical assessment may not fully reflect the real preferences of decision-makers. People are often sensitive to intuitive judgments based on an individual's experience and knowledge. It offers a suitable alternative to use the method of evaluation, which is able to evaluate verbal descriptions and expressions. This achieves a subjective expression of the decision-maker on the basis of their own judgments. A fuzzy logic tool is suitable for this purpose.

In this research, a new fuzzy time series model is used to predict stock market prices. The proposed model is based on the type-2 fuzzy logic approach. The proposed model is verified using experimental data sets originating from stock markets from different continents. Specifically, this study focuses on Exchange-Traded Funds (ETF) shares. These investment instruments provide investors with better performance due to their nature compared to traditional mutual funds. In addition, the authors believe that the use of ETFs will provide more realistic results for investors. Because the majority of the contributions examined focus exclusively on the stock index, in which it is not easy to invest, an alternative to investing in stock indices is ETFs, which try to replicate the underlying benchmarks as faithfully as possible.

The aim of the papers was to create a model based on type-2 fuzzy logic, which has not yet been sufficiently researched in the literature. Moreover, in the context of the ETF, such a model was not created at all according to the authors' findings. Based on the time series examined by the ETFs over a five-year period, indicators were compiled, which are summarized into three input variables entering the model: indicators of overall return, overall risk, and overall performance. Based on expert judgment, a

knowledge base or a set of rules was determined, on the basis of which the overall model is compiled. The result of the model is a recommendation for potential investors whether or not to invest in ETF shares based on set parameters.

The created models of type-2 fuzzy logic are compared with the classic type-1 fuzzy logic model. Based on the evaluation and comparison of different degrees of uncertainty in fuzzy sets, it can be stated that the analysis of the stock market represented by the ETF is best suited to the MF with 10% uncertainty. Based on the results of the comparison, it can be said that type-2 fuzzy logic with dual membership functions is able to better describe data from financial time series. However, the performance of type-2 fuzzy logic models decreases with the inclusion of increasing uncertainty in fuzzy sets, as evidenced by a comparison of MAPE, MSE, and RMSE performance indicators, where in other 20%, 30%, and 40% models levels of uncertainty continue to increase. However, the increase in these indicators is not significant and in no way will affect the overall decision for investors whether to invest in ETFs or not. Based on the results of the comparison, it can be said that type-2 fuzzy logic with dual fuzzy sets is able to better describe data from financial time series and provides more accurate outputs. The results reflect the capability and effectiveness of the approach proposed in this document. However, the performance of type-2 fuzzy logic models decreases with the inclusion of increasing uncertainty in fuzzy sets.

However, it is necessary to point out the weaknesses and limitations of our research. As described in previous research, when applying fuzzy methods, fuzzy rules are established and defined through human judgment and may involve a degree of subjectivity. However, this process of setting fuzzy rules and defining membership functions can be time consuming. For this reason, some other techniques and methods are being promoted that will facilitate the process of setting fuzzy rules. For example, machine learning techniques (e.g., decision tree) or combinations of fuzzy logic and neural networks (e.g., ANFIS) are used in the literature for this purpose, which are able to generate a set of fuzzy rules automatically. Model with a larger number of variables, the number of fuzzy rules that need to be defined logically, increases, thus increasing computational complexity and increasing the time required for computation. Inherent limitations in the selection of a database concerns in particular the input data. Another limitation concerns especially the fuzzy logic itself, as it is an approach that is not able to learn and has no memory. In addition, the results of the fuzzy model can be skewed due to the choice of multiple shapes and numbers of member functions.

For further research, it would be appropriate to examine the different levels of uncertainty in the input parameters themselves and monitor the performance of such a modified model. It would be appropriate to examine different types of fuzzy sets, not just the Gaussian function of membership, which is demonstrated in this study, and to monitor the validity and accuracy of different types of fuzzy sets that can improve the model. Furthermore, it would be appropriate to focus the paper on a larger dataset using, for example, stocks or stocks of continental companies, as most studies still concern Anglo-Saxon companies. Last but not least, it would be appropriate to revise the further developed model and integrate it, for example, with neural networks.

Data Availability

The authors provide relevant data of calculation used to support the findings of this study in the Supplementary Information files.

Conflicts of Interest

The authors declare that there are no conflicts of interest regarding the publication of this paper.

Acknowledgments

This paper was supported by project No. FP-S-20-6376 'Modeling and optimization of business processes in conditions of digital transformation' from the Internal Grant Agency at Brno University of Technology.

Supplementary Materials

The manuscript is accompanied by Supplementary Materials containing a raw data set, which is used for financial analysis, processed, and used as inputs to the model. (*Supplementary Materials*)

References

[1] A. K. Shukla, S. K. Banshal, T. Seth, A. Basu, R. John, and P. K. Muhuri, "A bibliometric overview of the field of type-2 fuzzy sets and systems [discussion forum]," *IEEE Computational Intelligence Magazine*, vol. 15, no. 1, pp. 89–98, 2020.

[2] J. R. Castro, M. A. Sanchez, C. I. Gonzalez, P. Melin, and O. Castillo, "A new method for parameterization of general type-2 fuzzy sets," *Fuzzy Information and Engineering*, vol. 10, no. 1, pp. 31–57, 2018.

[3] A. Puška, S. Kozarevic, Ž. Stevic, and J. Stovrag, "A new way of applying interval fuzzy logic in group decision making for supplier selection," *Economic Computation and Economic Cybernetics Studies and Research*, vol. 52, pp. 217–234, 2018.

[4] M. Eren, "Forecasting of the fuzzy univariate time series by the optimal lagged regression structure determined based on the genetic algorithm," *Economic Computation and Economic Cybernetics Studies and Research*, vol. 52, pp. 201–215, 2018.

[5] J. Tavoosi, A. Mohammadzadeh, and K. Jermsittiparsert, "A review on type-2 fuzzy neural networks for system identification," *Soft Computing*, vol. 25, no. 10, pp. 7197–7212, 2021.

[6] T. Yankova, G. Ilieva, and S. Klisarova, "The bezier curve as a fuzzy membership function shape," *Mathematics and Its Applications: Annals of the Academy of Romanian Scientists*, vol. 10, no. 2, pp. 245–265, 2018, http://aos.ro/wp-content/anale/MVol10Nr2Art.4.pdf.

[7] D. Wijayasekara and M. Manic, "Data driven fuzzy membership function generation for increased understandability," in *Proceedings of the IEEE International Conference on Fuzzy Systems*, IEEE, Beijing, China, pp. 133–140, 2014.

[8] E. Kayacan, A. Sarabakha, S. Coupland, R. John, and M. A. Khanesar, "Type-2 fuzzy elliptic membership functions

for modeling uncertainty," *Engineering Applications of Artificial Intelligence*, vol. 70, pp. 170–183, 2018.

[9] A. Sadollah, "Introductory chapter: which membership function is appropriate in fuzzy system?," in *Fuzzy Logic Based in Optimization Methods and Control Systems and its Applications*, A. Sadollah, Ed., IntechOpen, London, UK, 2018.

[10] K. Chourmouziadis and P. D. Chatzoglou, "An intelligent short term stock trading fuzzy system for assisting investors in portfolio management," *Expert Systems with Applications*, vol. 43, pp. 298–311, 2016.

[11] A. D. Ijegwa, V. O. Rebecca, F. Olusegun, and O. O. Isaac, "A predictive stock market technical analysis using fuzzy logic," *Computer and Information Science*, vol. 7, no. 3, pp. 1–17, 2014.

[12] A. Khayamim, A. Mirzazadeh, and B. Naderi, "Portfolio rebalancing with respect to market psychology in a fuzzy environment: a case study in Tehran Stock Exchange," *Applied Soft Computing*, vol. 64, pp. 244–259, 2018.

[13] A. Hassanniakalager, G. Sermpinis, C. Stasinakis, and T. Verousis, "A conditional fuzzy inference approach in forecasting," *European Journal of Operational Research*, vol. 283, no. 1, pp. 196–216, 2020.

[14] B. Sun, H. Guo, H. Reza Karimi, Y. Ge, and S. Xiong, "Prediction of stock index futures prices based on fuzzy sets and multivariate fuzzy time series," *Neurocomputing*, vol. 151, no. 3, pp. 1528–1536, 2015.

[15] N. Mansour, M. S. Cherif, and W. Abdelfattah, "Multi-objective imprecise programming for financial portfolio selection with fuzzy returns," *Expert Systems with Applications*, vol. 138, 2019.

[16] M. C. Tsai, C. H. Cheng, and M. I. Tsai, "A multifactor fuzzy time-series fitting model for forecasting the stock index," *Symmetry*, vol. 11, no. 12, 2019.

[17] A. A. Hasan and A. C. Fong, "Sentiment analysis based fuzzy decision platform for the Saudi stock market," in *Proceedings of the 2018 IEEE International Conference on Electro/Information Technology (EIT)*, pp. 0023–0029, IEEE, Rochester, MI, USA, 2018.

[18] C.-H. Su and C.-H. Cheng, "A hybrid fuzzy time series model based on ANFIS and integrated nonlinear feature selection method for forecasting stock," *Neurocomputing*, vol. 205, pp. 264–273, 2016.

[19] V. Vella and W. Lon Ng, "Improving risk-adjusted performance in high frequency trading using interval type-2 fuzzy logic," *Expert Systems with Applications*, vol. 55, pp. 70–86, 2016.

[20] A. Vlasenko, O. Vynokurova, N. Vlasenko, and M. Peleshko, "A hybrid neuro-fuzzy model for stock market time-series prediction," in *Proceedings of the 2018 IEEE Second International Conference on Data Stream Mining & Processing (DSMP)*, pp. 352–355, IEEE, Lviv, Ukraine, 2018.

[21] K. A. Dutta, "A fuzzy based soft computing technique to predict the movement of the price of a stock," *International Journal of Advanced Computer Science and Applications*, vol. 9, no. 2, 2018.

[22] S. Rajab and V. Sharma, "An interpretable neuro-fuzzy approach to stock price forecasting," *Soft Computing*, vol. 23, pp. 921–936, 2019.

[23] Z. Janková, "Application of artificial neural networks and fuzzy logic in stock trading," in *Proceedings of the 33rd International Business Information Management Association Conference (IBIMA)*, pp. 2610–2619, IBIMA, Granada, Spain, 2019, https://ibima.org/accepted-paper/application-of-artificial-neural-networks-and-fuzzy-logic-in-stock-trading/.

[24] F. García, F. Guijarro, J. Oliver, and R. Tamošiūnienė, "Hybrid fuzzy neural network to predict price direction in the German DAX-30 index," *Technological and Economic Development of Economy*, vol. 24, no. 6, pp. 2161–2178, 2018.

[25] J.-A. Jiang, C.-H. Syue, C.-H. Wang, J.-C. Wang, and J.-S. Shieh, "An interval type-2 fuzzy logic system for stock index forecasting based on fuzzy time series and a fuzzy logical relationship map," *IEEE Access*, vol. 6, pp. 69107–69119, 2018.

[26] C.-F. Liu, C.-Y. Yeh, and S.-J. Lee, "Application of type-2 neuro-fuzzy modeling in stock price prediction," *Applied Soft Computing*, vol. 12, no. 4, pp. 1348–1358, 2012.

[27] V. Sumati, P. Chellapilla, S. Paul, and L. Singh, "Parallel interval type-2 subsethood neural fuzzy inference system," *Expert Systems with Applications*, vol. 60, pp. 156–168, 2016.

[28] K. Huarng and H.-K. Yu, "A Type 2 fuzzy time series model for stock index forecasting," *Physica A: Statistical Mechanics and Its Applications*, vol. 353, pp. 445–462, 2005.

[29] N. S. Bajestani and A. Zare, "Forecasting TAIEX using improved type 2 fuzzy time series," *Expert Systems with Applications*, vol. 38, no. 5, pp. 5816–5821, 2011.

[30] M. H. Zarandi, B. Rezaee, I. B. Turksen, and E. Neshat, "A type-2 fuzzy rule-based expert system model for stock price analysis," *Expert Systems with Applications*, vol. 36, no. 1, pp. 139–154, 2009.

[31] D. Bernardo, H. Hagras, and E. Tsang, "A genetic type-2 fuzzy logic based system for the generation of summarised linguistic predictive models for financial applications," *Soft Computing*, vol. 17, no. 12, pp. 2185–2201, 2013.

[32] Z. Janková and P. Dostál, "Expertní systém type-2 fuzzy logika pro investiční analýzu," *Scientific Papers of the University of Pardubice*, vol. 47, no. 27, pp. 79–90, 2019.

[33] S. Hassan, A. Khosravi, J. Jaafar, and M. A. Khanesar, "Hybrid model for the training of interval type-2 fuzzy logic system," *Neural Information Processing*, vol. 9489, pp. 644–653, 2015.

[34] L. A. Zadeh, "Probability measures of fuzzy events," *Journal of Mathematical Analysis and Applications*, vol. 23, no. 2, pp. 421–427, 1968.

[35] R. Rustum, *Modelling Activated Sludge Wastewater Treatment Plants Using Artificial Intelligence Techniques (Fuzzy Logic and Neural Networks)*, Heriot-Watt University, Edinburgh, UK, 2009.

[36] J. Mendel, *Uncertain Rule-Based Fuzzy Logic Systems*, Vol. 68, Springer, Berlin, Germany, 2017.

[37] S. P. Wan, Z. H. Chen, and J. Y. Dong, "An integrated interval type-2 fuzzy technique for democratic–autocratic multi-criteria decision making," *Knowledge-based Systems*, vol. 214, p. 214, 2021.

[38] S. H. Khairuddin, M. H. Hasan, M. A. Hashmani, and M. H. Azam, "Generating clustering-based interval fuzzy type-2 triangular and trapezoidal membership functions: a structured literature review," *Symmetry*, vol. 13, no. 2, 2021.

[39] E. Ferreyra, H. Hagras, M. Kern, and G. Owusu, "Enabling field force operational sustainability: a big bang-big crunch type-2 fuzzy logic system for goal-driven simulation," in *Proceedings of the 2018 IEEE Symposium Series on Computational Intelligence (SSCI)*, pp. 2223–2230, Bangalore, India, 2018.

[40] Z. Janková, D. K. Jana, and P. Dostál, "Investment decision support based on interval type-2 fuzzy expert system," *Engineering Economics*, vol. 32, no. 2, pp. 118–129, 2021.

[41] X. Sang, Y. Zhou, and X. Yu, "An uncertain possibility-probability information fusion method under interval type-2 fuzzy environment and its application in stock selection," *Information Sciences*, vol. 504, pp. 546–560, 2019.

[42] J. M. Mendel, R. I. John, and F. Liu, "Interval type-2 fuzzy logic systems made simple," *IEEE Transactions on Fuzzy Systems*, vol. 14, no. 6, pp. 808–821, 2006.

[43] J. M. Mendel, *Uncertain Rule-Based Fuzzy Logic*, Prentice-Hall, Systems, CA, Los Angeles, 2001.

[44] X. Sang and X. Liu, "Possibility mean and variation coefficient based ranking methods for type-1 fuzzy numbers and interval type-2 fuzzy numbers," *Journal of Intelligent and. Fuzzy System*, vol. 30, no. 4, pp. 2155–2168, 2016.

[45] J. Soto, P. Melin, and O. Castillo, "A new approach for time series prediction using ensembles of IT2FNN models with optimization of fuzzy integrators," *International Journal of Fuzzy Systems*, vol. 20, no. 3, pp. 701–728, 2018.

[46] E. Bas, U. Yolcu, and E. Egrioglu, "Picture fuzzy regression functions approach for financial time series based on ridge regression and genetic algorithm," *Journal of Computational and Applied Mathematics*, vol. 370, p. 370, 2020.

[47] S. Ulubeyli and A. Kazaz, "Fuzzy multi-criteria decision making model for subcontractor selection in international construction projects," *Technological and Economic Development of Economy*, vol. 22, no. 2, pp. 210–234, 2016.

[48] P. Liu, "Special issue "intuitionistic fuzzy theory and its application in economy, Technology and management,"" *Technological and Economic Development of Economy*, vol. 22, no. 3, pp. 327–335, 2016.

[49] M. Tumminello, T. Aste, T. Di Matteo, and R. N. Mantegna, "A tool for filtering information in complex systems," *Proceedings of the National Academy of Sciences*, vol. 102, no. 30, pp. 10421–10426, 2005.

[50] T. Aste, T. Di Matteo, and S. T. Hyde, "Complex networks on hyperbolic surfaces," *Physica A: Statistical Mechanics and Its Applications*, vol. 346, no. 1-2, pp. 20–26, 2005.

Hindawi
Mathematical Problems in Engineering
Volume 2021, Article ID 7332885, 12 pages
https://doi.org/10.1155/2021/7332885

Research Article

Do Intellectual Capital Elements Spur Firm Performance? Evidence from the Textile and Apparel Industry in China

Liang Zhang, Qi Yu, Zhenji Jin, and Jian Xu

School of Management, Qingdao Agricultural University, Qingdao 266109, China

Correspondence should be addressed to Zhenji Jin; zhenji12@aliyun.com and Jian Xu; xujiansword@163.com

Received 30 April 2021; Revised 18 May 2021; Accepted 20 May 2021; Published 27 May 2021

Academic Editor: Mohammad Yazdi

This paper examines how investment in intellectual capital (IC) elements by textile and apparel companies improves firm performance measured in terms of profitability, market value, and productivity. The modified value-added intellectual coefficient (MVAIC) model is applied to measure IC. Using a panel of 35 Chinese textile and apparel companies for a six-year period (2013–2018), the results show that physical and human capitals are the strong factors that contribute to firm performance. In addition, relational capital negatively influences profitability and market value, and structural capital and innovation capital have a negative impact on employee productivity. We also find that the MVAIC model performs better in measuring IC than the original value-added intellectual coefficient (VAIC) model. This paper can provide some insights for corporate managers to enhance firm performance and gain competitive advantage by proper utilization of IC in traditional industries.

1. Introduction

The resource-based theory emphasizes the heterogeneity of firms' resources and the existence of capabilities. Nowadays, managing and upgrading knowledge resources determine the success of any organization [1–3]. In the knowledge economy, intellectual capital (IC) as an intangible resource can help a firm to generate economic returns and build competitive advantage along with tangibles [4–8].

The textile and apparel industry is traditionally labor-intensive, and this old manufacturing industry has become a sunset industry with low added-value products because of low level of technological innovation [9]. It requires large input of water and energy in fabric production, which could bring serious damage to ecological environment by various pollutants. This industry is also one of the most important customer merchandise industries with a long supply chain from the distribution of fibers to end users or consumers [10]. Textile and apparel companies generally have tight connections with suppliers, manufacturers, intermediaries, and customers in the whole product life cycle [11]. In recent years, this industry is exposed to the increase in the price of raw materials such as cotton, which lowers the profits of manufacturers. In order to overcome some barriers, firms started to search a new way with production of high-tech and technically demanding textiles.

China's textile and apparel industry as the pillar of national economy accounts for about one-fifth of total production in the world [12]. Its comparative advantage in the global market is not obvious [13], and it is still at the low end of the global value chain [14]. In the face of fierce market competition, textile and apparel companies are forced to cut prices, which leads to lower profitability. In addition, there is an increasingly great demand for clothing and footwear products in China's domestic market, but there are not many internationally influential brands of domestic companies. Due to the outbreak of the novel coronavirus (COVID-19), the production and export of this industry experienced a great decrease from January to April in 2020 compared with the previous year [15]. The rising costs of domestic production, insufficient domestic and foreign demand, trade barriers, and other factors have led to the continuous decrease in industrial competitiveness [16–18]. Therefore, it is urgently important that this industry transform industrial structure from the energy-consuming pattern to the eco-

environment-oriented pattern. Intangibles will play a significant role in this transformation, especially IC.

The objective of this paper is to explore empirically the impact of IC elements on firm performance, using China's textile and apparel companies as our selected sample. Following Ge and Xu [19], Xu and Liu [20], and Liu et al. [21], we use the modified value-added intellectual coefficient (MVAIC) model as a measure of IC in comparison with pulic's [22] original value-added intellectual coefficient (VAIC) model.

There are few studies that are conducted in the context of China, and the IC's impact in textile and apparel industry is not fully understood. In addition, empirical analysis in the current IC literature is still based on the original VAIC model by ignoring the role of relational capital (RC) and innovation capital (INC) in value creation. Therefore, this study contributes to the theoretical perspective by employing the MVAIC model with the inclusion of them. Finally, it might help managers of China's textile and apparel industry to enhance firm performance and gain their competitiveness through effective IC utilization.

In the remaining parts of the paper, a literature review is provided in Section 2. Section 3 develops the relevant hypotheses, followed by Section 4 detailing the methodology. Section 5 shows the empirical results, and Section 6 discusses these results. Finally, Section 7 is the conclusion.

2. Literature Review

2.1. IC Definition, Classification, and Measurement. There are many definitions of IC explained in the current IC literature. At the initial stage, Stewart [23] described IC as the tools of intangibles in creating wealth. It was defined as the set of all knowledge possessed by the employees and the company [24]. Additionally, Edvinsson and Malone [25] defined the difference between a firm's market value and book value as IC.

It is generally believed that there are three key areas, namely, human capital (HC), structural capital (SC), and RC constitute IC [26–36]. HC includes employees and their attributes such as knowledge, experience, and skills [37]. SC includes firm's strategies, databases, information management, intellectual property, corporate culture, and the like [24]. RC deals with internal and external relationships with various stakeholders [38].

Several methods have been proposed to measure IC. Among them, the VAIC model explains the efficiency of value creation in any organization depending on capital employed efficiency (CEE), human capital efficiency (HCE), and structural capital efficiency (SCE). Its simplicity and data availability lead to the wide use of this method in measuring IC. However, it also suffers from several weaknesses. First, this model only measures past IC based on the historical data from financial reports. Second, the synergy effects between different forms of tangible and intangible assets are not taken into account in this model [39]. Third, it neglects the existence of RC and INC that is considered as the measures of the efficiency of IC [40]. Therefore, we will employ the MVAIC model to systematically measure IC in this paper.

Figure 1 demonstrates the classification of a company's assets.

2.2. IC and Firm Performance. Although much research has been devoted to developed countries, emerging markets have drawn the attention of scholars in the current IC research [6, 8, 19–21, 29–33, 35, 36, 39–42]. In addition, most studies use a three-dimensional framework to analyze IC performance based on the original VAIC model. Table 1 shows an overview of the relationship between IC and firm performance, but the results are not consistent.

3. Hypotheses Development

CEE refers to all necessary financial funds and physical capital in the pulic's [22] VAIC model. Researchers such as Chen et al. [40], Tandon et al. [55], Dzenopoljac et al. [56], and Poh et al. [57] documented a positive impact of CEE on organizational performance. Taking agricultural enterprises as the sample, Xu and Wang [49] found a positive relationship between CEE and firms' profitability and productivity. A study on commercial banks by Oppong and Pattanayak [58] found CEE to be positive and significant with ATO and employee productivity (EP). In the light of these arguments, the study hypothesizes the following.

Hypothesis 1 (H1). Physical capital can enhance firm performance in China's textile and apparel industry.

Concerning HC, Nimtrakoon [27] found that HC contributes most to financial performance (margin ratio and ROA). Similarly, Xu and Wang [5], Xu et al. [32], and Xu and Li [33, 35] confirmed this positive relationship. Using the VAIC model, Smriti and Das [59] in their study observed that HC positively affects firm productivity while its impact on profitability is not significant in Indian listed companies. Also, a study in an emerging economy (Ghana) by Oppong et al. [6] showed that HCE positively affects firm productivity. Conversely, Kasoga [52] documented this negative relationship using ROA, ATO, sales growth, and Tobin's Q as performance indicators. Therefore, the current study hypothesizes the following.

Hypothesis 2 (H2). HC can enhance firm performance in China's textile and apparel industry.

The findings of Kasoga [52] revealed a significant and positive relationship between SCE and financial performance. In the context of Russia, Andreeva and Garanina [60] pointed out that SC contributes to the performance of manufacturing companies. Likewise, Alipour [61], Soriya and Narwal [62], and Onyekwelu et al. [63] found that SCE does drive the firms' performance. Examining the association between IC and productivity, Oppong and Pattanayak [58] found that SC component plays a role in improving the productivity of public and private banks. Liu et al. [21] argued that SC has the strongest impact on financial competitiveness in China's renewable energy sector. Therefore, the third hypothesis is as follows.

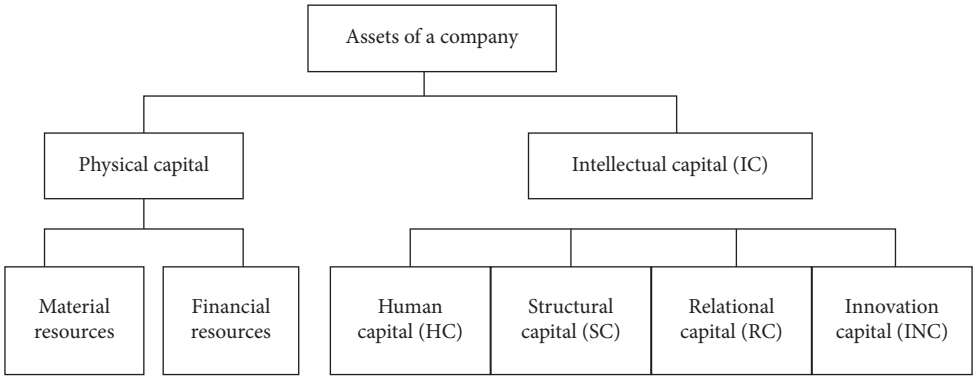

Figure 1: Company assets and IC classification of this paper.

Table 1: Representative studies on IC and firm performance.

Author	IC measurement	Dependent variable	Sample	Data source	Main findings
Kweh et al. [41]	Ratios	Operating performance	Life insurance firms in Taiwan and China	Financial reports	HC is positively linked to operating performance, while SC is negatively related.
Bhatia and Aggarwal [42]	VAIC	Return on assets (ROA) and return on net worth	Software companies in India	PROWESS	All IC components are positively related with financial performance.
Nimtrakoon [27]	MVAIC	Market-to-book ratio (MB), margin ratio, and ROA	Technology firms in the ASEAN	Five stock exchanges	Physical capital and HC are the most influential factors, while SC and RC have less impact.
Dženopoljac et al. [43]	VAIC	ROA, return on equity (ROE), return on invested capital, profitability, and asset turnover ratio (ATO)	Information communication technology companies in Serbia	Serbian Agency for Business Registers	Only physical capital has a significant impact on financial performance.
Meles et al. [44]	VAIC	ROA and ROE	Commercial banks in US	Bankscope Bureau Van Dijk	HC has a positive impact on financial performance.
Ozkan et al. [45]	VAIC	ROA	Banks in Turkey	Financial reports	Physical capital and HC positively affect financial performance.
Smriti and Das [46]	VAIC	ROA, MB, and ATO	Pharmaceutical and drug companies in India	CMIE	Physical capital and SC determine business performance.
Xu et al. [47]	VAIC	ROA and ROE	Environmental protection companies in China	Financial reports	HC and SC exert a positive impact, while INC does not have an impact.
Chowdhury et al. [48]	VAIC	ATO, ROA, and ROE	Textile firms in Bangladesh	Financial reports	Tangible capital and SC have a positive impact, whereas the impact of HC is not significant.
Tiwari and Vidyarthi [29]	MVAIC	ROA and ROE	Banks in India	PROWESS	HC and SC show a positive linkage with banks' performance.
Xu and Wang [49]	VAIC	Earnings before interest and taxes (EBIT), ROA, ROE, and ATO	Agricultural companies in China	CSMAR	Physical and human capitals impact firm performance.
Xu et al. [32]	MVAIC	ROA and ROE	Manufacturing companies in China	RESSET	HC and SC positively affect firm performance, while RC exerts a negative impact.
Yao et al. [50]	VAIC and MVAIC	ROA, net operating margin, and ATO	Financial institutions in Pakistan	Financial reports	HC can increase firm performance significantly.

Table 1: Continued.

Author	IC measurement	Dependent variable	Sample	Data source	Main findings
Bansal and Singh [51]	VAIC	ROA and ATO	Software companies in India	PROWESS	Intangible capital has the greatest impact.
Costa et al. [34]	MVAIC	ROA	Hospitality and tourism industry in Portuguese	SABI	CEE and HCE have a positive impact, while SCE presents a negative impact.
Kasoga [52]	VAIC	ROA, ATO, sales growth (SG), and Tobin's Q	Service and manufacturing firms in Tanzania	Financial reports	A positive impact of SC and a negative impact of physical and human capitals are observed.
Gupta and Raman [53]	MVAIC	ROA	Information technology (IT) and pharmaceutical firms in India	Financial reports and S&P Global Capital IQ	Physical capital, HC, RC, and process capital have an impact on ROA.
Neves and Proença [54]	VAIC	ROA, ROE, and net interest margin	Banks in Portugal	Financial reports	All IC components influence banks' performance.
Xu and Liu [8]	IC index	Earnings before interest, taxes, depreciation and amortization (EBITDA), net profit margin, gross profit margin, return on investment, ROA, and ROE	Manufacturing companies in China	CSMAR and RESSET	IC is positively related to all performance indicators except EBITDA.

Hypothesis 3 (H3). SC can enhance firm performance in China's textile and apparel industry.

With regard to RC, Barkat et al. [64] conducted a survey in large textile companies in Pakistan and reported that three dimensions of IC including HC, RC, and INC have a direct effect on organizational performance. Xu and Wang [5] found it to be the most influential factor to financial performance and sustainable growth. The empirical evidence from Indian pharmaceutical companies by Gupta et al. [65] confirmed a correlation between RC and firm profitability. A study on manufacturing firms by Xu and Li [35] similarly recorded a strong association between RC and profitability and productivity for a five-year period (2012–2016). Xu et al. [66] also documented a positive relationship between RC and corporate sustainable growth. Therefore, we propose the following hypothesis.

Hypothesis 4 (H4). RC can enhance firm performance in China's textile and apparel industry.

INC refers to the skills and capabilities that a company needs to create new products and services and to place them promptly on the market [67]. It can drive wealth generation, economic development, and human well-being [68, 69]. Chen et al. [40] claimed that INC has a positive effect in the MB, ROA, and SG models. The findings of Lu et al. [70] found that INC positively enhances firm performance of Chinese firms that accepted Venture-Capital Syndication funding. Bayraktaroglu et al. [71] declared that INC directly leads to the increase in firms' productivity. As Ni et al. [72] revealed, INC might be beneficial for firms to improve firm value because firms need to search for new ideas to achieve innovation. Therefore, we propose the following hypothesis.

Hypothesis 5 (H5). INC can enhance firm performance in China's textile and apparel industry.

4. Methodology

4.1. Data Source. This paper is based on the secondary data that are obtained from the China Stock Market and Accounting Research (CSMAR) database. The sample includes textile and apparel companies listed on the Shanghai and Shenzhen stock exchanges from 2013 to 2018. After screening and removing companies with missing information, companies with debt ratio great than 1, and special treatment (ST) companies, an unbalanced panel of 35 companies with 165 observations has been left for estimation.

4.2. Variables

(1) *Dependent Variables.* Firm performance (PER) is measured in three aspects: profitability, market value, and productivity. ROA (measured by the ratio of net income to average total assets) and ROE (measured by the ratio of net income to average shareholders' equity) measure the profitability of the companies. MB is used to measure market value of the companies. EP is calculated as the ratio of pretax income (unit: 10,000 yuan) to the number of employees. It is included as a measure of productivity in the IC literature [40, 58, 73–76].

(2) *Independent Variables.* This study measures the efficiency of IC components by using the MVAIC model. The MVAIC model is a sum of five components: CEE, HCE, SCE, relational capital efficiency

(RCE), and innovation capital efficiency (INCE). They are calculated as follows:

VA = total revenues − total expenses + employee expenditures
CEE = VA/book value of net assets
HCE = VA/all employee expenditures
SCE = (VA − all employee expenditures)/VA
RCE = marketing, selling, and advertising expenses/VA
INCE = R&D expenses/VA

(3) *Control Variables*. Firm size (SIZE) is the natural log of total assets. Debt ratio (LEV) is defined as total liabilities divided by total assets. Firm age (AGE) is the natural log of the number of years since the setup of the company. The growth rate of gross domestic product (GDP) is used to control external influences. Additionally, a year dummy (YEAR) is also included in the models.

Table 2: Descriptive statistics.

Variable	Mean	Median	Max	Min	SD
ROA	0.0427	0.0461	0.2178	−0.5645	0.0753
ROE	0.0650	0.0654	0.5104	−0.8789	0.1267
MB	2.3734	1.7364	33.3767	0.3406	2.8990
EP	7.8857	5.0915	76.8660	−121.3850	19.8886
CEE	0.2448	0.2609	0.6603	−1.2371	0.1894
HCE	1.8697	1.6861	6.3110	−5.1907	1.3439
SCE	0.4236	0.4208	7.7953	−4.0805	0.7785
RCE	1.6619	1.7038	14.8287	−112.7872	9.2253
INCE	0.0715	0.0687	0.8335	−1.5822	0.1637
SIZE	22.0108	21.8336	25.0489	19.0976	1.0942
LEV	0.3512	0.3225	0.7598	0.0796	0.1638
AGE	2.7079	2.7081	3.2189	1.9459	0.2871
GDP	0.0696	0.068	0.078	0.066	0.0040

4.3. Models. The panel models are estimated to examine the effect of different IC elements on firm performance. Model (1) is based on the original VAIC method, and Model (2) is on the basis of the MVAIC method including RC and INC. The panel model specifications are as follows:

$$\begin{aligned}\mathrm{PER}_{i,t} &= \beta_0 + \beta_1\mathrm{CEE}_{i,t} + \beta_2\mathrm{HCE}_{i,t} + \beta_3\mathrm{SCE}_{i,t} + \beta_4\mathrm{SIZE}_{i,t} \\ &\quad + \beta_5\mathrm{LEV}_{i,t} + \beta_6\mathrm{AGE}_{i,t} + \beta_7\mathrm{GDP}_{i,t} + \sum \mathrm{YEAR} + \varepsilon_{i,t},\end{aligned} \tag{1}$$

$$\begin{aligned}\mathrm{PER}_{i,t} &= \beta_0 + \beta_1\mathrm{CEE}_{i,t} + \beta_2\mathrm{HCE}_{i,t} + \beta_3\mathrm{SCE}_{i,t} + \beta_4\mathrm{RCE}_{i,t} \\ &\quad + \beta_5\mathrm{INCE}_{i,t} + \beta_6\mathrm{SIZE}_{i,t} + \beta_7\mathrm{LEV}_{i,t} + \beta_8\mathrm{AGE}_{i,t} + \beta_9\mathrm{GDP}_{i,t} + \sum \mathrm{YEAR} + \varepsilon_{i,t},\end{aligned} \tag{2}$$

where i stands for the individual firm; t stands for the year; β is the presumed parameter; and ε is the measurement error term.

5. Results

5.1. Descriptive Statistics. Descriptive statistics are depicted in Table 2. In the observed period (2013–2018), it can be noticed that profitability, measured by ROA and ROE, has a mean score of 0.0427 and 0.0650, respectively. The high value of MB implies that on average, market value of textile and apparel companies is higher than their book value. EP has a mean of 7.8857 with a maximum of 76.8660 and a minimum of −121.3850. An increase in EP means that employees make more contribution to the firm. The average CEE in our sample is 0.2448. As for IC elements, IC performance of companies in textile and apparel sector mainly depends on HC and RC. It is worth noticing that the standard deviations of HCE and RCE are higher. INC seems to create the smallest amount of value over the study period. Companies with low level of R&D expense are more likely to restrict their innovative ability of new product development and patent application, which will lead to low competitiveness and intangible assets. Also, the average ratio of total leverage is about 35%. The mean value of SIZE and AGE is 22.0108 and 2.7079, respectively.

5.2. Correlation Analysis. Table 3 shows the results of correlation analysis. The results show that ROA and ROE are significantly positively correlated with CEE, HCE, and RCE. MB is negatively correlated with CEE, HCE, and RCE. EP proxy used for productivity is positively correlated with CEE, HCE, and RCE. In addition, the variance inflation factor (VIF) values are less than 10, indicating that multicollinearity is not a major issue.

5.3. Regression Results. Regression results are shown in Table 4. The Hausman tests indicate that the fixed effects model is appropriate in estimating the results of ROA, ROE, and MB, and the random effects model is suitable when EP is the dependent variable. It is noticeable that the MVAIC model has higher adjusted R^2 values with ROA, ROE, and MB being dependent variables. However, for EP, the adjusted R^2 value slightly decreases in the MVAIC model. On the whole, the MVAIC model is more applicable to measure IC than the original VAIC model.

When ROA and ROE are the dependent variables, CEE and HCE play an important role in increasing the profits of textile and apparel companies. SCE exerts a positive impact on only the ROE indicator. However, RCE is found to negatively affect the profitability in this traditional industry. INC has no significant impact on profitability indicators. LEV is negatively associated with ROA and ROE.

Table 3: Correlation matrix.

Variable	ROA	ROE	MB	EP	CEE	HCE	SCE	RCE	INCE	SIZE	LEV	AGE	GDP
ROA	1												
ROE	0.957***	1											
MB	−0.237***	−0.258***	1										
EP	0.782***	0.755***	−0.376***	1									
CEE	0.782***	0.792***	−0.348***	0.574***	1								
HCE	0.745***	0.803***	−0.378***	0.818***	0.527***	1							
SCE	0.052	0.127*	0.084	0.032	−0.119	0.075	1						
RCE	0.382***	0.378***	−0.780***	0.481***	0.390***	0.459***	−0.073	1					
INCE	0.040	−0.039	−0.030	0.053	0.031	0.046	−0.873***	0.037	1				
SIZE	0.193**	0.318***	−0.459***	0.372***	0.234***	0.518***	0.063	0.200**	−0.067	1			
LEV	−0.255***	−0.069	−0.092	−0.120	0.102	0.087	−0.138**	−0.117	0.041	0.492***	1		
AGE	−0.138*	−0.048	0.056	−0.086	−0.053	−0.007	0.057	0.010	−0.068	−0.107	0.258***	1	
GDP	0.127*	0.112	−0.057	0.098	0.046	0.052	−0.014	0.028	0.045	−0.058	−0.032	−0.315***	1

* $p < 0.10$; ** $p < 0.05$; *** $p < 0.01$.

Table 4: Regression results.

Variable	ROA		ROE		MB		EP	
	Model (1)	Model (2)	Model (1)	Model (2)	Model (1)	Model (2)	Model (1)	Model (2)
Constant	0.203 (0.74)	−0.117 (−0.45)	−0.165 (−0.34)	−0.746 (−1.65)	114.880 (4.46)	54.286** (3.96)	−87.174** (−2.02)	−53.612 (−1.22)
CEE	0.313*** (14.58)	0.320*** (15.92)	0.531*** (14.03)	0.546*** (15.57)	2.520 (1.25)	3.047*** (2.86)	34.825*** (6.32)	30.731*** (5.72)
HCE	0.020*** (6.88)	0.021*** (7.55)	0.033*** (6.66)	0.036*** (7.20)	−0.185 (−0.69)	0.315** (2.10)	9.164*** (11.81)	9.821*** (12.32)
SCE	0.0002 (0.11)	0.004 (0.72)	0.015*** (3.87)	0.027** (2.62)	0.361* (1.79)	0.137 (0.44)	−1.417** (−2.17)	−7.968*** (−4.53)
RCE		−0.001*** (−4.53)		−0.002*** (−4.47)		−0.203*** (−17.61)		0.087 (1.38)
INCE		0.026 (0.95)		0.073 (1.52)		0.138 (0.10)		−32.967*** (−4.05)
SIZE	−0.013** (−2.21)	−0.0004 (−0.07)	0.002 (0.23)	0.025** (2.36)	−4.923*** (−8.85)	−2.427*** (−7.63)	1.917 (1.46)	0.631 (0.47)
LEV	−0.094*** (−4.73)	−0.132*** (−6.67)	−0.091** (−2.59)	−0.160*** (−4.62)	6.747*** (3.59)	−0.212 (−0.20)	−22.949*** (−4.08)	−16.506*** (−2.97)
AGE	−0.005 (−0.09)	0.003 (0.07)	−0.023 (−0.26)	−0.006 (−0.08)	−0.139 (−0.03)	0.831 (0.33)	6.077 (1.10)	4.829 (0.85)
GDP	0.830 (0.55)	1.215 (0.87)	0.968 (0.36)	1.685 (0.69)	−105.948 (−0.74)	−36.508** (−0.49)	266.262 (1.28)	274.549 (1.34)
YEAR	Included	Included	Included	Included	Included	Included	Included	Included
R^2	0.9067	0.9231	0.8993	0.9183	0.5736	0.8885	0.7281	0.6976
F	105.11***	108.03***	96.62***	101.20***	14.55***	71.72***	730.01***	870.54***
N	165	165	165	165	165	165	165	165
Hausman test	Prob > χ^2 = 0.0000	Prob > χ^2 = 0.0039	Prob > χ^2 = 0.0047	Prob > χ^2 = 0.0276	Prob > χ^2 = 0.0000	Prob > χ^2 = 0.0000	Prob > χ^2 = 0.4004	Prob > χ^2 = 0.1027

* $p < 0.10$; ** $p < 0.05$; *** $p < 0.01$; t values are in parentheses.

Table 5: Summary of regression results.

IC components	VAIC model				MVAIC model			
	ROA	ROE	MB	EP	ROA	ROE	MB	EP
Physical capital	+	+	Insignificant	+	+	+	+	+
HC	+	+	Insignificant	+	+	+	+	+
SC	Insignificant	+	+	—	Insignificant	+	Insignificant	—
RC	N/A	N/A	N/A	N/A	—	—	—	Insignificant
INC	N/A	N/A	N/A	N/A	Insignificant	Insignificant	Insignificant	—

Regarding the variable MB, physical and human capitals positively influence MB in the MVAIC model. The impact of two IC elements (i.e., SC and INC) is not significant while RC has a negative and significant impact, which indicates that investors do not consider the values of IC in their decision. Pal and Soriya [77] found that IC does not help Indian textile companies to be more competitive in the increasingly dynamic environment.

In case of productivity measured by EP, physical and human capitals have a positive impact while structural and innovation capitals have a negative impact in the selected companies. The results are inconsistent with Oppong and Pattanayak [58] who stated that CEE is the only component that has a positive impact on EP and Phusavat et al. [73] and Bontis et al. [76] who concluded that human resources positively affect EP.

6. Discussion

Table 5 shows the summary of regression analysis in our study. From the results, it can be concluded that physical assets and HC are the most influential factors in improving the performance of Chinese textile and apparel companies.

Physical capital has the greatest influence on all performance indicators. Textile and apparel companies belong to manufacturing industry and traditionally depend on machinery and equipments. The findings are in line with Ge and Xu [19], Xu and Liu [20], Xu and Wang [31], and Xu and Li [33, 35]. However, in the Industry 4.0 era, such companies are required to achieve their industrial transformation. It is necessary for Chinese textile and apparel companies to increase investment in fixed assets and speed up the pace of upgrading equipment in order to gain international competitiveness under complex environment [17].

Table 5 shows that the better the HC of a firm is, the better its performance is. Although textile and apparel industry creates huge amount of jobs, most companies are still difficult to attract and retain high-quality employees. It should be pointed out that globally about 80% of workers are women in this industry [78]. The lack of training and education is a primary challenge the textile and apparel companies face in sustainable development [10].

As for SC, a survey conducted by Malinowska-Olszowy [67] showed that textile and apparel industry does not pay attention to the special role of intellectual property, especially patents. These may become a source of success for innovative textile and apparel manufacturers. In addition, the use of IT can improve corporate responsiveness and increase operational flexibility. Andersen and Segars [79] concluded that investment in IT has an indirect impact on performance enhancement in the US textile and apparel industry. Innovation in information and communications technology (ICT) and logistics technology is also needed in this sector that focuses on a mass production [80]. In China's economic transformation, such companies have begun to realize the salient importance of corporate culture, routines, processes, and technology.

RC seems to become a detrimental factor to firm performance improvement. However, the increasing interdependency of supply chain in this sector emphasizes stronger partnership-based alliances, thus reducing production costs [81]. In an emerging market (Vietnam), the best selection of suitable suppliers in this sector has been the concern of many practitioners that is affected by many unpredictable and uncertain issues [82]. Textile and apparel companies should determine the best supplier selection based on sourcing country, organization features (i.e., relationship, capability, and company's image) and performance metrics (i.e., quality, costs, delivery, and service) [83].

INC is not observed to stimulate firm performance in China's textile and apparel industry. In China, brand counterfeiting and imitation are serious, and most companies' revenue depends mainly on processing without automation or robots [16]. Malinowska-Olszowy [84] found that the poor performance of textile and apparel companies in Poland is caused by lack of introducing innovations. In Vietnam, undeveloped technology is a huge barrier to productivity improvement of this sector [85]. However, technology innovation ability in this industry has been improving since 2005 [9]. Furthermore, production time and reaction to trends are greatly shortened in this industry [86], which requires brand designers to have more innovative and novel ideas.

7. Conclusions

The study measures the impact of IC elements on firm performance on a sample of 35 textile and apparel companies listed over a period of 6 years (2013–2018). The MVAIC method is applied to measure the efficiency of IC, and firm performance is measured through ROA, ROE, MB, and EP. The results show that the MVAIC model is more appropriate in IC measurement than the conventional VAIC model of Pulic [22]. Regarding IC elements, HC exerts a positive impact on firm performance whereas SC and INC have a negative impact on only employee productivity. RC is

found to negatively influence profitability and market valuation. In addition, physical capital is the most influencing contributor to firm performance improvement.

This study has several valuable implications. Firstly, management should incorporate IC strategies into their business strategies, effectively manage the level of IC, and make reasonable investments in each IC elements. Secondly, employees should get sufficient training to grasp the latest innovative technology and procedures applied in their production. Thirdly, corporate managers should also pay attention to SC, RC, and INC because they are also which drive firm performance in China's economic transformation. More importantly, they should develop new design concept and conduct more international cooperation and exchanges, thus improving firm profitability. In addition, these companies need to adopt green technology and develop new ecological protection products. They should also implement enterprise resource plan (ERP) system and computer integrated manufacture system (CIMS) to realize great-leap-forward development and upgrade industrial structure. Finally, the government should create a more favorable external environment, establish the industry management system, and provide more policy supports for R&D activities.

The current study has some limitations that should be addressed for future research. First, the research is restricted to textile and apparel companies, and future studies may be extended to other business industries. Second, more countries should be included in the future. Besides that, future studies may consider more variables in assessing IC toward firm performance.

Data Availability

The data used to support the findings of this study are available from the corresponding author upon request.

Conflicts of Interest

The authors declare that they have no conflicts of interest.

Acknowledgments

The authors would like to thank Prof. Mohammad Yazdi (Lead Editor) for his useful comments on earlier drafts. This research was supported by the Social Science Planning Research Program of Shandong Province (grant no. 18CKJJ01), the Scientific Research Project of Qingdao Agricultural University (grant nos. 6611114Q016 and 6611118703), the Scientific Research Foundation for High-Level Talents of Qingdao Agricultural University (grant no. 6631120701), and the Postgraduate Innovation Program of Qingdao Agricultural University (grant no. NYCX20011).

References

[1] L. Namdarian, A. Sajedinejad, and S. Bahanesteh, "The impact of knowledge management on organizational performance: a structural equation modeling study," *AD-minister*, vol. 37, no. 37, pp. 85–108, 2020.

[2] M. Chopra and V. Gupta, "Linking knowledge management practices to organizational performance using the balanced scorecard approach," *Kybernetes*, vol. 49, no. 1, pp. 88–115, 2020.

[3] M. S. Khan, P. Saengon, S. Charoenpoom, H. Soonthornpipit, and D. Chongcharoen, "The impact of organizational learning culture, workforce diversity and knowledge management on innovation and organization performance: a structural equation modeling approach," *Human Systems Management*, vol. 40, no. 1, pp. 103–115, 2021.

[4] C. M. Jardon, "The use of intellectual capital to obtain competitive advantages in regional small and medium enterprises," *Knowledge Management Research & Practice*, vol. 13, no. 4, pp. 486–496, 2015.

[5] J. Xu and B. Wang, "Intellectual capital, financial performance and companies' sustainable growth: evidence from the Korean manufacturing industry," *Sustainability*, vol. 10, no. 12, p. 4651, 2018.

[6] G. K. Oppong, J. K. Pattanayak, and M. Irfan, "Impact of intellectual capital on productivity of insurance companies in Ghana," *Journal of Intellectual Capital*, vol. 20, no. 6, pp. 763–783, 2019.

[7] M. A. I. Cisneros, F. H. Perlines, and M. R. García, "Intellectual capital, organisational performance and competitive advantage," *European Journal of International Management*, vol. 14, no. 6, pp. 976–998, 2020.

[8] J. Xu and F. Liu, "Nexus between intellectual capital and financial performance: an investigation of Chinese manufacturing industry," *Journal of Business Economics and Management*, vol. 22, no. 1, pp. 217–235, 2021.

[9] H. F. Zhu, M. L. Huang, and Z. Zheng, "Research on the technology innovation ability of textile and apparel industry," *Advanced Materials Research*, vol. 627, pp. 609–612, 2013.

[10] F. Jia, S. Y. Yin, L. J. Chen, and X. W. Chen, "The circular economy in the textile and apparel industry: a systematic literature review," *Journal of Cleaner Production*, vol. 259, Article ID 120728, 2020.

[11] W. C. A. Chu, M. H. E. Chan, J. Cheung, and H.-O. Nguyen, "Looking back to look forward: setting future research agenda for international business in textiles and clothing industry," *Journal of International Logistics and Trade*, vol. 17, no. 1, pp. 21–32, 2019.

[12] C.-K. Lau, K.-M. To, Z. Zhang, and J. Chen, "Determinants of competitiveness: observations in China's textile and apparel industries," *China & World Economy*, vol. 17, no. 2, pp. 45–64, 2009.

[13] H. S. Karaalp and N. D. Yilmaz, "Comparative advantage of textiles and clothing: evidence for Bangladesh, China, Germany and Turkey," *Fibres & Textiles in Eastern Europe*, vol. 21, no. 1, pp. 14–17, 2013.

[14] M.-Y. Huang and X.-H. Deng, "Empirical analysis on the driving factors of China's textile and garment industry transformation and upgrading-based on quarterly panel data analysis of listed companies," *Journal of Technical Economics & Management*, vol. 39, no. 9, pp. 118–123, 2018, in Chinese.

[15] S. Chakraborty and M. C. Biswas, "Impact of COVID-19 on the textile, apparel and fashion manufacturing industry supply chain: case study on a ready-made garment manufacturing industry," *Journal of Supply Chain Management, Logistics and Procurement*, vol. 3, no. 2, pp. 181–199, 2020.

[16] R. Y. Wang, "Analysis and research on innovation motivation and ability of listed companies in textile and garment

industry," *Shandong Textile Economy*, vol. 37, no. 6, pp. 5–7, 2020, in Chinese.

[17] Z. Guan, Y. Xu, H. Jiang, and G. Jiang, "International competitiveness of Chinese textile and clothing industry—a diamond model approach," *Journal of Chinese Economic and Foreign Trade Studies*, vol. 12, no. 1, pp. 2–19, 2019.

[18] W. Chen, "Thoughts on the upgrading and development of China's textile and garment industry-based on the development of textile industry for reform and opening-up in the past 40 years," *Review of Economic Research*, vol. 40, no. 61, pp. 75–80, 2018, in Chinese.

[19] F. L. Ge and J. Xu, "Does intellectual capital investment enhance firm performance? Evidence from pharmaceutical sector in China," *Technology Analysis & Strategic Management*, vol. 33, pp. 1–16, 2020.

[20] J. Xu and F. Liu, "The impact of intellectual capital on firm performance: a modified and extended VAIC model," *Journal of Competitiveness*, vol. 12, no. 1, pp. 161–176, 2020.

[21] S. Liu, Q. Yu, L. Zhang, J. Xu, and Z. J. Jin, "Does intellectual capital investment improve financial competitiveness and green innovation performance? Evidence from renewable energy companies in China," *Mathematical Problems in Engineering*, vol. 2021, Article ID 9929202, 13 pages, 2021.

[22] A. Pulic, "VAIC™-an accounting tool for IC management," *International Journal of Technology Management*, vol. 20, no. 5–8, pp. 702–714, 2000.

[23] T. A. Stewart, *Intellectual Capital. The New Wealth of Organizations*, Doubleday, New York, NY, USA, 1997.

[24] N. Bontis, "Assessing knowledge assets: a review of the models used to measure intellectual capital," *International Journal of Management Reviews*, vol. 3, no. 1, pp. 41–60, 2001.

[25] L. Edvinsson and M. S. Malone, *Intellectual Capital: Realizing Your Company's True Value by Finding its Hidden Brainpower*, Harper Business, New York, NY, USA, 1997.

[26] K. E. Sveiby, *The New Organizational Wealth: Managing and Measuring Knowledge-Based Assets*, Berrett-Koehle, San Francisco, CA, USA, 1997.

[27] S. Nimtrakoon, "The relationship between intellectual capital, firms' market value and financial performance," *Journal of Intellectual Capital*, vol. 16, no. 3, pp. 587–618, 2015.

[28] F. Sardo, Z. Serrasqueiro, and H. Alves, "On the relationship between intellectual capital and financial performance: a panel data analysis on SME hotels," *International Journal of Hospitality Management*, vol. 75, pp. 67–74, 2018.

[29] R. Tiwari and H. Vidyarthi, "Intellectual capital and corporate performance: a case of Indian banks," *Journal of Accounting in Emerging Economies*, vol. 8, no. 1, pp. 84–105, 2018.

[30] H. Vidyarthi and R. Tiwari, "Cost, revenue, and profit efficiency characteristics, and intellectual capital in Indian Banks," *Journal of Intellectual Capital*, vol. 21, no. 1, pp. 1–22, 2019.

[31] J. Xu and B. Wang, "Intellectual capital performance of the textile industry in emerging markets: a comparison with China and South Korea," *Sustainability*, vol. 11, no. 8, p. 2354, 2019.

[32] J. Xu, Y. Shang, W. Z. Yu, and F. Liu, "Intellectual capital, technological innovation and firm performance: evidence from China's manufacturing sector," *Sustainability*, vol. 11, no. 19, p. 5328, 2019.

[33] J. Xu and J. Li, "The impact of intellectual capital on SMEs' performance in China," *Journal of Intellectual Capital*, vol. 20, no. 4, pp. 488–509, 2019.

[34] V. Costa, L. Silva, and L. Paula, "Intellectual capital and its impact on business performance: an empirical study of Portuguese hospitality and tourism sector," *Intangible Capital*, vol. 16, no. 2, pp. 78–89, 2020.

[35] J. Xu and J. S. Li, "The interrelationship between intellectual capital and firm performance: evidence from China's manufacturing sector," *Journal of Intellectual Capital*, vol. 22, 2020.

[36] Y. Q. Lu, G. W. Li, Z. Luo, M. Anwar, and Y. J. Zhang, "Does intellectual capital spur sustainable competitive advantage and sustainable growth?: a study of Chinese and Pakistani firms," *Sage Open*, vol. 11, no. 1, Article ID 2158244021996702, 2020.

[37] N. Bontis, "Intellectual capital: an exploratory study that develops measures and models," *Management Decision*, vol. 36, no. 2, pp. 63–76, 1998.

[38] G. Roos and J. Roos, "Measuring your company's intellectual performance," *Long Range Planning*, vol. 30, no. 3, pp. 413–426, 1997.

[39] S. K. W. Chiu, K. H. Chan, and W. W. Y. Wu, "Charting intellectual capital performance of the gateway to China," *Journal of Intellectual Capital*, vol. 12, no. 2, pp. 249–276, 2011.

[40] M. C. Chen, S. J. Cheng, and Y. Hwang, "An empirical investigation of the relationship between intellectual capital and firms' market value and financial performance," *Journal of Intellectual Capital*, vol. 6, no. 2, pp. 159–176, 2005.

[41] Q. L. Kweh, W.-M. Lu, W.-K. Wang, and M.-H. Su, "Life insurance companies' performance and intellectual capital: a long-term perspective," *International Journal of Information Technology & Decision Making*, vol. 13, no. 4, pp. 755–777, 2014.

[42] A. Bhatia and K. Aggarwal, "Intellectual capital and financial performance of Indian software industry: a panel data analysis," *Pacific Business Review International*, vol. 7, no. 8, pp. 33–43, 2015.

[43] V. Dženopoljac, S. Janoševic, and N. Bontis, "Intellectual capital and financial performance in the Serbian ICT industry," *Journal of Intellectual Capital*, vol. 17, no. 2, pp. 373–396, 2016.

[44] A. Meles, C. Porzio, G. Sampagnaro, and V. Verdoliva, "The impact of the intellectual capital efficiency on commercial banks performance: evidence from the US," *Journal of Multinational Financial Management*, vol. 36, pp. 64–74, 2016.

[45] N. Ozkan, S. Cakan, and M. Kayacan, "Intellectual capital and financial performance: a study of the Turkish Banking Sector," *Borsa Istanbul Review*, vol. 17, no. 3, pp. 190–198, 2017.

[46] N. Smriti and N. Das, "Impact of intellectual capital on business performance: evidence from Indian pharmaceutical sector," *Polish Journal of Management Studies*, vol. 15, no. 1, pp. 232–243, 2017.

[47] X.-L. Xu, X.-N. Yang, L. Zhan, C. K. Liu, N.-D. Zhou, and M. Hu, "Examining the relationship between intellectual capital and performance of listed environmental protection companies," *Environmental Progress & Sustainable Energy*, vol. 36, no. 4, pp. 1056–1066, 2017.

[48] L. A. M. Chowdhury, T. Rana, M. Akter, and M. Hoque, "Impact of intellectual capital on financial performance: evidence from the Bangladeshi textile sector," *Journal of Accounting & Organizational Change*, vol. 14, no. 4, pp. 429–454, 2018.

[49] J. Xu and B. H. Wang, "Intellectual capital and financial performance of Chinese agricultural listed companies," *Custos e Agronegocio On Line*, vol. 15, no. 1, pp. 273–290, 2019.

[50] H. Yao, M. Haris, G. Tariq, H. M. Javaid, and M. A. S. Khan, "Intellectual capital, profitability, and productivity: evidence from Pakistani financial institutions," *Sustainability*, vol. 11, no. 14, p. 3842, 2019.

[51] D. Bansal and S. Singh, "Impact of intellectual capital on financial performance of the Indian software sector," *Asia-Pacific Management Accounting Journal*, vol. 15, no. 1, pp. 67–95, 2020.

[52] P. S. Kasoga, "Does investing in intellectual capital improve financial performance? Panel evidence from firms listed in Tanzania DSE," *Cogent Economics & Finance*, vol. 8, no. 1, Article ID 1802815, 2020.

[53] K. Gupta and T. V. Raman, "Influence of intellectual capital on performance," *International Journal of Human Capital and Information Technology Professionals*, vol. 12, no. 2, pp. 53–71, 2021.

[54] E. Neves and C. Proença, "Intellectual capital and financial performance: evidence from Portuguese banks," *International Journal of Learning and Intellectual Capital*, vol. 18, no. 1, pp. 93–108, 2021.

[55] K. Tandon, H. Purohit, and D. Tandon, "Measuring intellectual capital and its impact on financial performance: empirical evidence from CNX nifty companies," *Global Business Review*, vol. 17, no. 4, pp. 980–997, 2016.

[56] V. Dzenopoljac, C. Yaacoub, N. Elkanj, and N. Bontis, "Impact of intellectual capital on corporate performance: evidence from the Arab region," *Journal of Intellectual Capital*, vol. 18, no. 4, pp. 884–903, 2017.

[57] L. T. Poh, A. Kilicman, and S. N. I. Ibrahim, "On intellectual capital and financial performances of banks in Malaysia," *Cogent Economics & Finance*, vol. 6, no. 1, Article ID 1453574, 2018.

[58] G. K. Oppong and J. K. Pattanayak, "Does investing in intellectual capital improve productivity? Panel evidence from commercial banks in India," *Borsa Istanbul Review*, vol. 19, no. 3, pp. 219–227, 2019.

[59] N. Smriti and N. Das, "The impact of intellectual capital on firm performance: a study of Indian firms listed in COSPI," *Journal of Intellectual Capital*, vol. 19, no. 5, pp. 935–964, 2018.

[60] T. Andreeva and T. Garanina, "Do all elements of intellectual capital matter for organizational performance? Evidence from Russian context," *Journal of Intellectual Capital*, vol. 17, no. 2, pp. 397–412, 2016.

[61] M. Alipour, "The effect of intellectual capital on firm performance: an investigation of Iran insurance companies," *Measuring Business Excellence*, vol. 16, no. 1, pp. 53–66, 2012.

[62] S. Soriya and K. P. Narwal, "Intellectual capital performance in Indian banks: a panel data analysis," *International Journal of Learning and Intellectual Capital*, vol. 12, no. 2, pp. 103–121, 2015.

[63] U. L. Onyekwelu, J. I. Okoh, and F. C. Iyidiobi, "Effect of intellectual capital on financial performance of Banks in Nigeria," *European Journal of Accounting, Auditing and Finance Research*, vol. 5, no. 2, pp. 28–57, 2017.

[64] W. Barkat, L.-S. Beh, A. Ahmed, and R. Ahmed, "Impact of intellectual capital on innovation capability and organizational performance: an empirical investigation," *Serbian Journal of Management*, vol. 13, no. 2, pp. 365–379, 2018.

[65] K. Gupta, S. Goel, and P. Bhatia, "Intellectual capital and profitability: evidence from Indian pharmaceutical sector," *Vision: The Journal of Business Perspective*, vol. 24, no. 2, pp. 204–216, 2020.

[66] X. L. Xu, J. Li, D. Wu, and X. Zhang, "The intellectual capital efficiency and corporate sustainable growth nexus: comparison from agriculture, tourism and renewable energy sector," *Environment, Development and Sustainability*, vol. 24, 2021.

[67] M. Malinowska-Olszowy, "Importance of intellectual capital in enterprise growth, with special emphasis on the textile and clothing industry in Poland," *Fibres & Textiles in Eastern Europe*, vol. 20, no. 5, pp. 10–15, 2012.

[68] J. Woiceshyn and P. Eriksson, "How innovation systems in Finland and Alberta work: lessons for policy and practice," *Innovation*, vol. 16, no. 1, pp. 19–31, 2014.

[69] F. Liu, K. Park, and U. Whang, "Organizational capabilities, export growth and job creation: an investigation of Korean SMEs," *Sustainability*, vol. 11, no. 14, p. 3986, 2019.

[70] Y. Z. Lu, Z. R. Tian, G. A. Buitrago, S. W. Gao, Y. J. Zhao, and S. Zhang, "Intellectual capital and firm performance in the context of venture-capital syndication background in China," *Complexity*, vol. 2021, Article ID 3425725, 17 pages, 2021.

[71] A. E. Bayraktaroglu, F. Calisir, and M. Baskak, "Intellectual capital and firm performance: an extended VAIC model," *Journal of Intellectual Capital*, vol. 20, no. 3, pp. 406–425, 2019.

[72] Y. S. Ni, Y.-R. Cheng, and P. Y. Huang, "Do intellectual capitals matter to firm value enhancement? Evidences from Taiwan," *Journal of Intellectual Capital*, vol. 22, no. 4, pp. 725–743, 2021.

[73] K. Phusavat, N. Comepa, A. Sitko-Lutek, and K. B. Ooi, "Interrelationships between intellectual capital and performance empirical examination," *Industrial Management & Data Systems*, vol. 111, no. 5-6, pp. 810–829, 2011.

[74] R. G. Ahangar, "The relationship between intellectual capital and financial performance: an empirical investigation in an Iranian company," *African Journal of Business Management*, vol. 5, no. 1, pp. 88–95, 2011.

[75] S. Janosevic and V. Dzenopoljac, "Impact of intellectual capital on financial performance of Serbian companies," *Actual Problems of Economics*, vol. 133, pp. 554–564, 2012.

[76] N. Bontis, S. Janošević, and V. Dženopoljac, "Intellectual capital in Serbia's hotel industry," *International Journal of Contemporary Hospitality Management*, vol. 27, no. 6, pp. 1365–1384, 2015.

[77] K. Pal and S. Soriya, "IC performance of Indian pharmaceutical and textile industry," *Journal of Intellectual Capital*, vol. 13, no. 1, pp. 120–137, 2012.

[78] V. Slvalogathasan and X. B. Wu, "Impact of organization motivation on intellectual capital and innovation capability of the textile and apparel industry in Sri Lanka," *International Journal of Innovation Science*, vol. 7, no. 2, pp. 153–165, 2015.

[79] T. J. Andersen and A. H. Segars, "The impact of IT on decision structure and firm performance: evidence from the textile and apparel industry," *Information & Management*, vol. 39, no. 2, pp. 85–100, 2011.

[80] Y. Ogai, Y. Matsumura, Y. Hoshino, T. Yasuda, and K. Ohkura, "Centralized business-to-business networks in the Japanese textile and apparel industry: using network analysis and an agent-based model," *Journal of Robotics and Mechatronics*, vol. 31, no. 4, pp. 546–557, 2019.

[81] J. Su and V. B. Gargeya, "Supplier selection in small- and medium-sized firms," *American Journal of Business*, vol. 31, no. 4, pp. 166–186, 2016.

[82] H. L. Lee, "Aligning supply chain strategies with product uncertainties," *California Management Review*, vol. 44, no. 3, pp. 105–119, 2002.

[83] N.-M. T. Nong, P. T. Ho, and P. T. Ho, "Criteria for supplier selection in textile and apparel industry: a case study in vietnam," *The Journal of Asian Finance, Economics and Business*, vol. 6, no. 2, pp. 213–221, 2019.

[84] M. Malinowska-Olszowy, "The choice of appropriate tools for measuring intellectual capital as a determinant of success with special emphasis on the textile and clothing market," *Autex Research Journal*, vol. 13, no. 4, pp. 122–127, 2013.

[85] T.-N. Le and C.-N. Wang, "The integrated approach for sustainable performance evaluation in value chain of Vietnam textile and apparel industry," *Sustainability*, vol. 9, no. 3, p. 477, 2017.

[86] A. Gavranovic, "How to deal with new challenges? Economic, technological and social aspects of the textile and clothing industry," *Textile & Leather Review*, vol. 1, no. 1, pp. 29–33, 2018.

Hindawi
Mathematical Problems in Engineering
Volume 2021, Article ID 5569701, 18 pages
https://doi.org/10.1155/2021/5569701

Research Article

Optimal Operation of the Campus Microgrid considering the Resource Uncertainty and Demand Response Schemes

Hafiz Abd ul Muqeet,[1] Hafiz Mudassir Munir,[2] Aftab Ahmad,[1] Intisar Ali Sajjad,[1] Guang-Jun Jiang,[3,4] and Hong-Xia Chen[3,4]

[1]*Department of Electrical Engineering, University of Engineering and Technology, Taxila 47050, Pakistan*
[2]*Department of Electrical Engineering, Sukkur IBA University, Sukkur 65200, Pakistan*
[3]*School of Mechanical Engineering, Inner Mongolia University of Technology, Hohhot, Inner Mongolia 010051, China*
[4]*Inner Mongolia Key Laboratory of Advanced Manufacturing Technology, Hohhot 010051, Inner Mongolia, China*

Correspondence should be addressed to Guang-Jun Jiang; jianggj_2003@163.com

Received 5 January 2021; Accepted 23 April 2021; Published 27 May 2021

Academic Editor: Samuel Yousefi

Present power systems face problems such as rising energy charges and greenhouse gas (GHG) releases. These problems may be assuaged by participating distributed generators (DGs) and demand response (DR) policies in the distribution system (DS). The main focus of this paper is to propose an energy management system (EMS) approach for campus microgrid (μG). For this purpose, a Pakistani university has been investigated and an optimal solution has been proposed. Conventionally, it contains electricity from the national grid only as a supply to fulfil the energy demand. Under the proposed setup, it contains campus owned nondispatchable DGs such as solar photovoltaic (PV) panels and microturbines (MTs) as dispatchable sources. To overcome the random nature of solar irradiance, station battery has been integrated as energy storage. The subsequent nonlinear mathematical problem has been scheduled by mixed-integer nonlinear programming (MINLP) in MATLAB for saving energy cost and battery aging cost. The framework has been validated under deterministic and stochastic environments. Among random parameters, solar irradiance and load have been taken into consideration. Case studies have been carried out considering the demand response strategies to analyze the proposed model. The obtained results show that optimal management and scheduling of storage in the presence of DGs mutually benefit by minimizing consumption cost (customer) and grid load (utility) which show the efficacy of the proposed model. The results obtained are compared to the existing literature and a significant cost reduction is found.

1. Introduction

Energy systems have been facing problems such as inflating consumption cost [1] and greenhouse gas (GHG) emission [2–4], as well as network overloading [2, 5–11]. The conventional grid may not resolve these problems; however, a smart distribution system (DS) equipped with DGs and demand response (DR) has the potential to overcome these issues. A microgrid may be defined as a combination of DGs, well-defined load, and storage system. DR policies and energy storages are used to help reduce energy cost and network overloading, etc [12, 13]. Microgrids with heavy load have a more pronounced impact on the stated problems. Among different types of high load μGs, institutional buildings falling under the class of commercial customers, need an optimal energy management strategy for consumption cost reduction. Microgrid facilitates bidirectional energy exchange with national power pool or may operate independently in islanded mode possessing enough on-site generation [14], while various energy management systems are given in [15]. For this purpose, researchers have already researched the following.

The smart microgrid energy management system is implemented in various countries in the world due to its

multibenefits [16]. In a conventional system, one way of energy flow was in practice and consumer act was a passive entity of the power system [17–20]. While, in microgrid, having some distributed energy resources and storages can operate in grid-connected and islanded mode [21, 22]. In microgrid, prosumer which is a consumer can participate in the electricity market through the selling of surplus energy to the national grid or nearby customers [23]. Different types and levels of prosumers can operate in microgrid operation [24]. The commercial prosumers have high energy demand along with large-scale distributed resources. Prosumer stores surplus energy from various sources such as solar PV, wind, and biomass during off-peak hours and sells in peak hours [25]. Energy forms RERs, which are intermittent because they depend on weather and temperature [26]. So, the energy storage system [27] requires continual operation with multibenefits such as price arbitrage, frequency regulation, RE integration, and backup power [28]. Different types of storage systems are used in microgrid operation such as electrical, electromagnetic, electrochemical, mechanical, thermal, and chemical. Electrochemical energy storage can convert chemical energy to electrical energy, i.e., batteries [29]. Different types of batteries are used in microgrid operation for smooth function. As compared to other types of batteries the initial cost of lithium-ion batteries is high but more reliable with a competitive number of life cycles [30]. The degradation of battery energy storage system (BESS) depends on many factors, such as external temperature, internal resistance, depth of discharge (DOD), and a number of cycles [31]. The optimal scheduling of distributed energy resources in a microgrid is the proposed model considering system constraints.

Some other contribution of our work can be summarized as follows:

(i) Campus microgrid nonlinear model is devised considering the battery degradation cost and demand response strategies

(ii) Randomness in solar irradiance and load are modelled for day-ahead scheduling operation

(iii) Grid support and grid outage-based modes are also considered for emergency operations to analyze the effects on the operational cost supply continuity

The remaining paper is comprised of the following sections. Section 2 presents the literature review. In Section 3, the proposed system model is presented, while in Sections 4 and 5, problem formulation of day-ahead scheduling and proposed solution are presented. Results and discussion are given in Section 6. Section 7 concludes the findings of this paper.

2. Literature Review

Several kinds of literature have been working in resource management in a microgrid. Like other developing countries, Pakistan is also facing energy shortage and issues due to some regulatory and managerial reasons. Scheduled grid outage is in practice from 4 to 6 h per day [32]. Hassan et al. [33] proposed the model of a microgrid in Pakistani environment, considering the stability, power quality, and load tracking. Historical and real-time data of Islamabad was used to design an energy management system strategy for said goals. The proposed model is solved using power algorithm in MATLAB, which is popular software in optimization [34–44] and machine learning [45–50] literature as well. Waqar et al. [51] presented a microgrid model for Pakistani environment. A combined heat and power- (CHP-) based multitasking analysis of six cities was analyzed on HOMER and the most suitable city for CHP integration was found. Rehman et al. [52] devised the PV integrated microgrid model considering grid reliability. The feasibility analysis was carried out to find the optimal condition of available resources. Furthermore, greenhouse gas (GHG) emission was also investigated for on HOMER software. Zia and Shaikh [53] analyzed the economic and environmental impact of a microgrid in Baluchistan. The proposed model investigated on HOMER and the total amount for the initial investment was found. The system comprised of solar PV, wind, and diesel generators, and its net present cost (NPC) was found.

Energy systems and their related research are very popular and widespread among engineers [54–56]. Different types of microgrid models are introduced in the existing literature to improve the resilience and reduce the operational cost. A general proposed model of the microgrid system is given in Figure 1 which elaborates the microgrid energy and information flow system. Uncertainty of renewable energy resources, loads, and grid intermittency was incorporated in some microgrid models such as Gao et al. [57], who presented the model for microgrid cost reduction considering penalty factors and uncertainty of renewable energy resources (RERs). Rehman et al. [52, 58] presented the PV energy storage system considering grid intermittency. Nasir et al. [59] presented the grid load reduction model considering the grid availability using linear programming in MATLAB. Low-cost hardware PV-storage solution was proposed in the Pakistani environment considering the various loads' shedding hours through online optimization technique. Li et al. [60] presented a probabilistic spinning reserve solution for isolated microgrid using chance constraint programming. The proposed problem was converted into MILP-based model and solved in GAMS by using the CPLEX solver. The proposed system reduced the cost and computation time and presented a trade-off strategy for cost and reliability. Similarly, in [61], the authors devised the scheduling of campus microgrid using the MIP however and ignored the uncertainties of DGs. Ahmad et al. [62] investigated the university campus in India. The HOMER-based analysis revealed that the optimal siting and sizing of DGs attract the investors for microgrid establishment. Soleja et al. [63] analyzed the economical analysis of the PV grid system. The payback period with other financial parameters was also calculated for South Asian Countries. However, the energy storage system was ignored, that is, the most important part of the energy management system. Liu et al. [64] explored the prosumer-based energy management system. The proposed model found that the scheduling of peer-to-peer prosumer enhanced the energy trading potential of

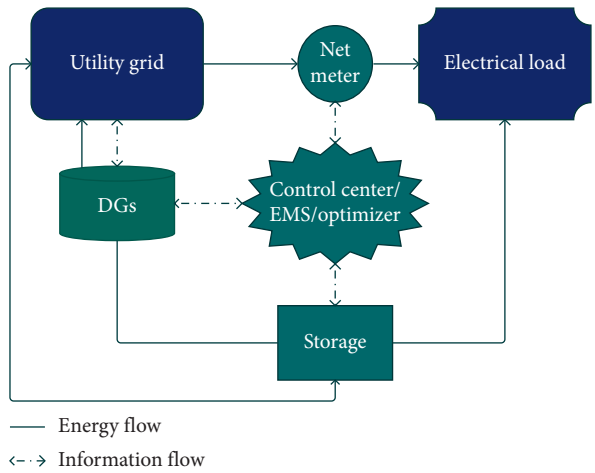

Figure 1: General microgrid architecture.

customers. In [65], the authors investigated the Korean campus to find the viability of microgrid implementation especially investors. The payback period revealed that the initial cost will cover within a few years and shifted the conventional system into a smart [66–68] power system. In [69], the authors analyzed a large number of customers in the US region. The base system is investigated that the specific values of both PV and energy storage system (ESS) might attract the consumers to install the PV-storage system. The analysis discovered that the retail electricity price should be above \$0.4/kWh and feed-in tariff below \$0.05/kWh. Rodríguez-Gallegos et al. [70] devised the optimal scheduling, considering the economic benefits. The results revealed the importance of ESS in the microgrid operation system. Liu and Wang [71] investigated energy trading with national grid considering the operational cost.

Literature survey shows that placing the ESS in microgrids makes it robust, cost-effective [72], and capable to integrate large-scale RERs. The energy storage system which has microgrid energy management has many issues such as energy consumption cost reduction and maximizes the profit of utility grid. So, the resilient smart microgrid is the potential solution for developing countries [59]. In South Asia, Pakistan has great potential for solar PV and other renewable energy resources (RERs) [73], as discussed earlier.

Net metering was launched in 2016 which promoted the passive consumer to active prosumer. In this work, an institutional microgrid has been devised for optimal energy exchanges between a university campus building and the national grid. The existing literature addressed the microgrid considering uncertainties but ignored the battery life which is a very important factor. Optimal energy management system considered the mixed price-based/incentive-based demand response, and ESS life is incorporated in our proposed system.

3. Proposed System Architecture

The transition of the legacy power system into a smart power system is at the initial stage after the net metering installation. The net metering has started in 2016 from the Government of Pakistan but needs regulatory system improvement. Given this step, we proposed UET Taxila as a campus microgrid to get the economic and environmental benefits. The Taxila city location has latitude and longitude as 33.70 and 72.840, respectively, and aerial view is shown in Figure 2. In the day time, the energy demand is high as compared to evening although evening classes are also offered on campus. To control the whole resources and storage scheduling, a scheduler is designed for optimal operation. In the control room, the signals are received from each entity through the Internet of Things (IoT). In critical situations, such as grid outages and other emergency events, the controller curtails the noncritical loads.

The database has historical weather and load data for the last ten years and does the forecasting.

The day-ahead scheduling considering the uncertainties of RERs is modelled in Section 4. In the proposed model, ESS stores surplus energy during the off-peak hours and sells the stored energy to the nearby consumer of the national grid in peak hours, as shown in Figure 3. Feed-in-tariff (FIT) is an important factor of energy-sharing willingness. Here, we assumed that the selling and purchasing energy prices are the same, which motivate the prosumers to sells its surplus energy to the national grid. The detailed layered structure of the proposed scheduler is resented in Figure 4 with its functions.

4. Problem Formulation

In this study, various types of distributed generation are integrated. Rooftop solar PV is taken in large scale with energy storage (ES). The proposed model comprised of the national grid, diesel generator, solar PV, and ESS. The ESS has many advantages over the single solar PV grid system such as backup storage, grid stability, and frequency regulation. The rooftop capacity of the campus is 4 MW, but we take only 2 MW. A mathematical model of day-ahead scheduling is presented in the next section following the network constraints. Initially, the deterministic model is analyzed for a proposed system. While in the second part, the real-time stochastic-based system is analyzed using historical data.

4.1. Objective Function. To optimize the proposed model, a nonlinear objective function is modelled. As the real-time model of ESS is nonlinear,

$$\min \sum_{t=1}^{24} \left\{ \left(P^{g}(t) K_{b}(t) - P^{g}(t) Q_{s}(t) \right) + J. \left(\mathrm{SOE}(t) - \mathrm{SOE}(t-1) \right)^{2} \right\}, \quad \forall t. \tag{1}$$

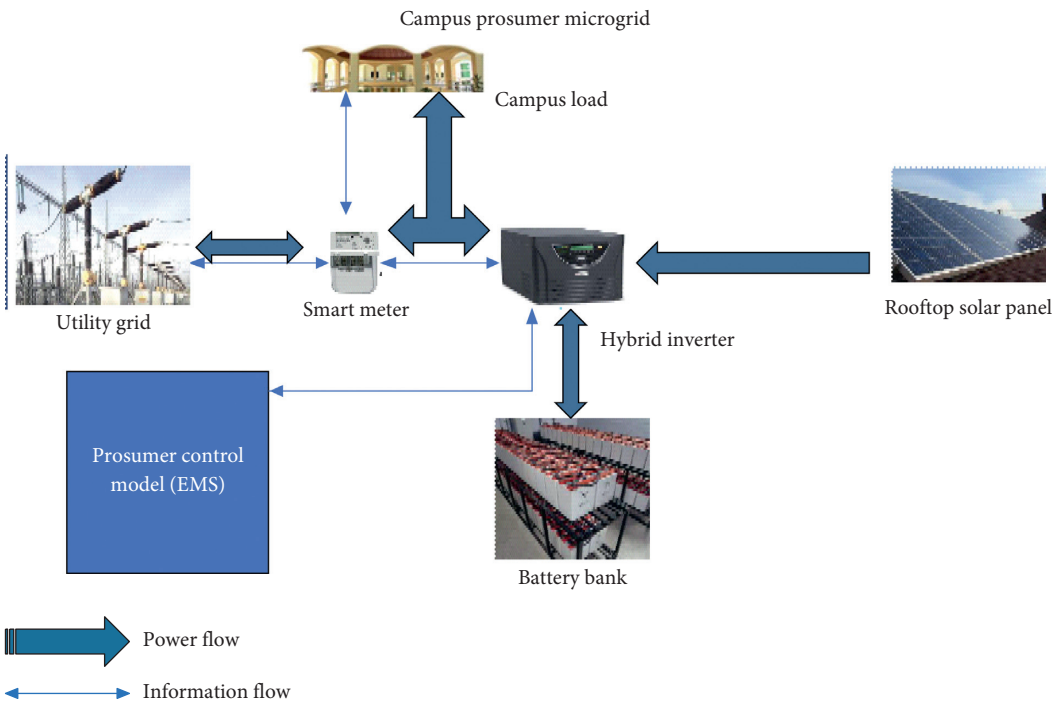

Figure 2: Aerial view of campus.

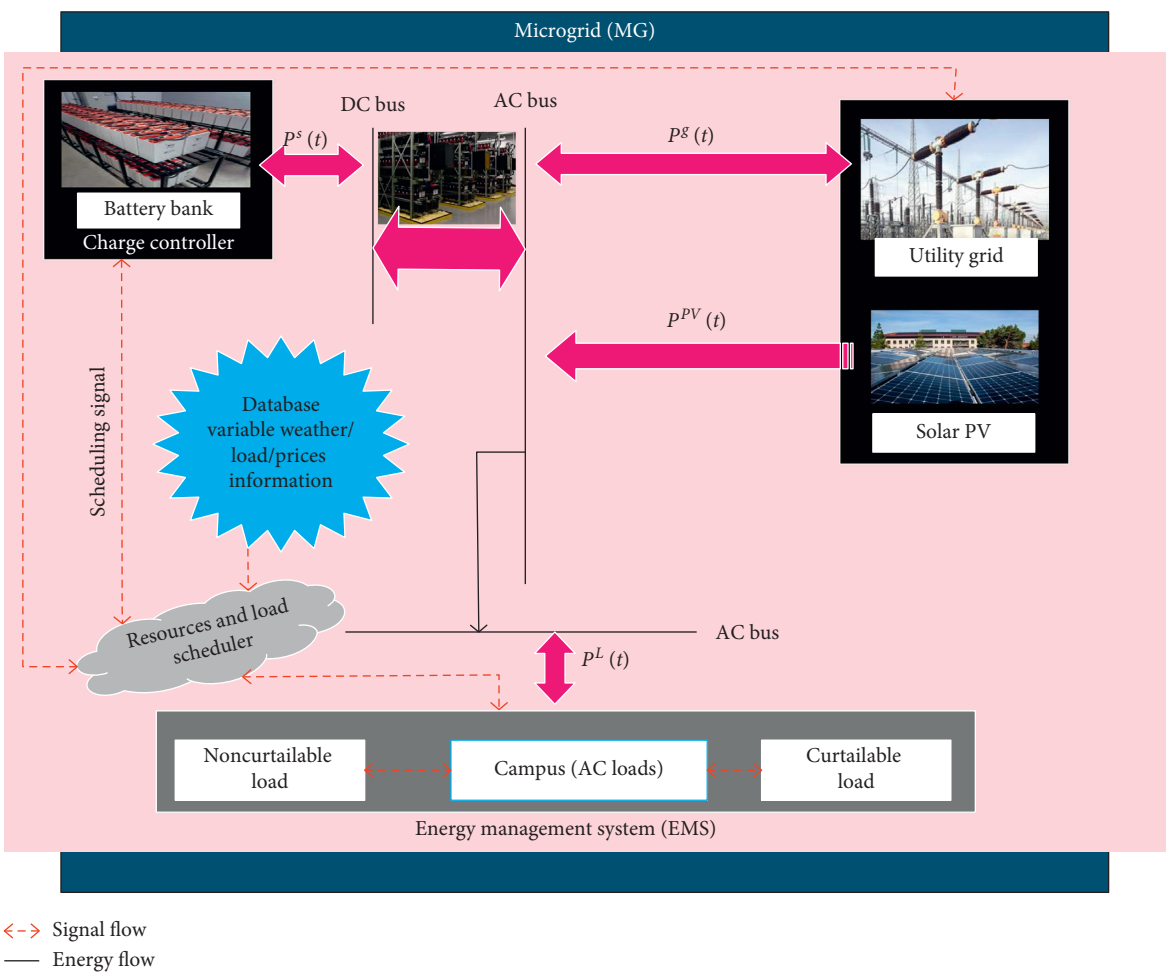

Figure 3: Proposed system architecture.

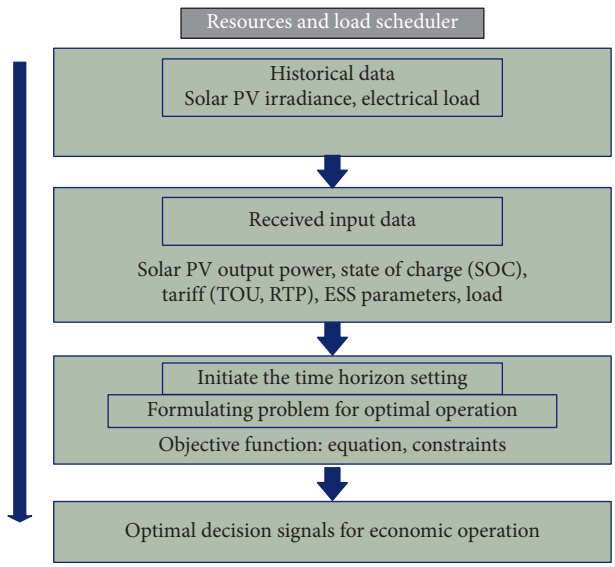

Figure 4: Proposed scheduler for optimal operation.

The goal of this study is to investigate the resource scheduling considering the system constraints. The exchange energy with the grid is beneficial for both utility and customers. In equation (1), the first part is energy exchange with the grid, while the second part calculates the battery aging cost. The battery aging depends on some specific factors, i.e., the number of cycles, internal resistance, and depth of discharge (DoD). Exchange power with the grid is expressed as $P^g(t)$, while the unit prices' buying and selling rates $K_b(t)$ and $Q_s(t)$ are expressed, respectively. The state of energy (SOE) shows the battery energy state in percentage concerning its total capacity, with J as a weighting factor for the whole operation which is taken as 0.5 here. It is analyzed for 24 hours with one hour time interval. The undetermined variables are grid exchange power, state of charge, and storage output power.

4.2. Power Balance Equation. To reduce the supply and demand gap, a power balance constraint is expressed as

$$P^g(t) + P^s(t) = P^L(t) + P^C(t) - P^{PV}(t). \tag{2}$$

The output power of storage $P^s(t)$ and the grid should be equal to the sum of all powers in the right-hand side, as prosumer load, contracted power $P^L(t)$ and $P^C(t)$, and the output power of solar PV $P^{PV}(t)$, respectively. The positive and negative storage output powers have expressed the discharge and charging of the battery system, respectively.

4.3. Energy Trading. Prosumer can sell its surplus energy to the utility grid, especially in contracted hours. In emergency cases, the grid support mode is also carried out for peak shaving:

$$\mathrm{Net}_e = \sum_{t=1}^{t=24} P^g(t) \times t. \tag{3}$$

Total selling and buying power are presented by the following equations, considering system limitations. In the prosumer market, the large commercial customer also exchanges energy with the utility grid which is allowed about 1 MW:

$$\begin{aligned} \mathrm{Net}_{e,\exp} &= \sum_{t=1}^{t=24} P^g(t) \times t, \quad \forall P^g(t) \pm P^s(t) > 0, \\ \mathrm{Net}_{e,\mathrm{imp}} &= \sum_{t=1}^{t=24} P^g(t) \times t, \quad \forall P_t^{\mathrm{grid}} \pm P^s(t) < 0, \\ & P^g_{\min}(t) \le P^g(t) \le P^g_{\max}(t). \end{aligned} \tag{4}$$

The export energy mainly depends on the distributed generation utilization scheduling. As the solar PV irradiance gets in a normal pattern, extra energy is stored in the batteries. The lithium-ion batteries are utilized due to its competitive features. As the length of complete transmission lines is short, so considering only active power and neglected the line losses.

4.4. Constraints of Battery Storage. Energy storage has some upper and lower bounds for smooth operation. As the life of the battery depends on many factors as discussed earlier, its output power also is controlled by the following constraints (6) and (7):

$$\frac{\mathrm{SOE}(t-1) - \mathrm{SOE}_{\max}}{100}\mathrm{Cap}^s \le P^s(t), \tag{5}$$

$$P^s(t) \le \frac{\mathrm{SOE}(t-1) - \mathrm{SOE}_{\min}}{100}\mathrm{Cap}^s. \tag{6}$$

The capacity of storage system $\mathrm{Cap}^s$is given by the manufacturer. Three modes of batteries are usually observed: charging state, discharging state, and standby position:

$$\mathrm{SOE}(t) = \mathrm{SOE}(t-1) - \frac{100.P_t^s}{\mathrm{Cap}^s}, \tag{7}$$

$$\mathrm{SOC}_{24} = \mathrm{SOC}_0. \tag{8}$$

The current state of energy is determined by equation (7), while the starting and ending of operation are controlled using equation (8) for next-day energy participation:

$$\Delta P^{\mathrm{Bat}}(t) \le \left(P_t^{\mathrm{Bat}} - P_{t+1}^{\mathrm{Bat}}\right) \le \Delta P^{\mathrm{Bat}}(t). \tag{9}$$

In a one-time step, a specific amount of power can deliver and emit in the form of energy for the storage, which is expressed in equation (9) as a gradient of power:

$$P_{\min}^s \le P^s(t) \le P_{\max}^s, \tag{10}$$

$$\mathrm{SOE}_{\min} \le \mathrm{SOE}(t) \le \mathrm{SOE}_{\max}, \tag{11}$$

$$P_{\min}^s \le P^s(t) \le P_{\max}^s. \tag{12}$$

The national grid has some specific values for energy exchange given in (10). The storage upper and lower bound is represented in equation (11). To model the uncertainty of solar PV and loads, the following sections present the probability distribution functions.

4.5. Probabilistic Load and Solar PV Modelling. The load of the campus is varying variable and change with time. In order to model the uncertainty of load, the normal distribution is used:

$$f_l\left(P^L\right) = \frac{1}{\sqrt{2\pi}\sigma_L}\exp\left(-\frac{\left(P^L - \mu_L\right)^2}{2\sigma_L^2}\right), \tag{13}$$

where P^L is the active power and μ_L and σ are mean and standard deviation concerning P^L [23]:

$$f_l(I) = \frac{1}{\sqrt{2\pi}\sigma_I}\exp\left(-\frac{\left(I - \mu_I\right)^2}{2\sigma_I^2}\right). \tag{14}$$

Distributed generation such as solar PV is highly intermittent. Aside from its numerous advantages, the distribution function is used to model the uncertainty in solar irradiance. The beta distribution, as presented in equation (16), is the function of solar irradiance uncertainty. To generate the scenarios based on historical data, Latin hypercube sampling technique [74] is used. The generated samples are 545 which are reduced to about ten by fast forward reduction method [75], where α and β are parameters for the beta distribution function. These parameters are determined by the following expressions (17) and (19). The mean and standard deviation are μ and σ, respectively, which are used to calculate parameters of the beta distribution function of the random variable irradiance "I."

The output power of solar PV is calculated using the following expression [76]:

$$P_{pv,j}(t) = \eta_{pv,j}\beta_{pv}I, \tag{15}$$

where $\eta_{pv,j}$ is the efficiency of installed solar PV panels, β_{pv} is the covered rooftop area (m^2) of solar PV panels, and I is the irradiance of solar ($\mathrm{kW/m}^2$), respectively.

4.6. Demand Response Constraints. Demand response is the branch of energy management which optimally reduces the peak load demand by involving the customers in the electricity market. For the system reliability, it is necessary to operate the system.

4.7. Real-Time Pricing. In real-time pricing, the retail prices of electricity vary during the day and effect on the customer consumption cost. In our study, 0%, 10%, and 20% DR are analyzed using the optimal load curtailment, considering the following constraint:

$$\Delta\mathrm{DR}(t) = \sum_{t=1}^{24}\mathrm{DR}(t), \tag{16}$$

$$\Delta\mathrm{DR}^{\min} \le \Delta\mathrm{DR} \le \Delta\mathrm{DR}^{\max}. \tag{17}$$

4.8. Time of Use Pricing. The time of use model is expressed in (18)–(21):

$$\Delta\, dr^{\min} \le \Delta\, dr(t) \le \Delta\, dr^{\max}, \tag{18}$$

$$dr(t) = dr^0(t) + \Delta\, dr(t), \tag{19}$$

$$\lambda^{\mathrm{off},p} = \lambda^0 + \Delta\lambda^{\mathrm{off},p}, \tag{20}$$

$$\lambda^p = \lambda^0 + \Delta\lambda^p, \tag{21}$$

where $dr(t)$ and λ^p are the energy demand and the pricing, respectively, in the peak and off-peak time.

5. Methodology

The proposed system is a single nonlinear objective, with linear constraints. As the mathematical differential technique, it generates an exact solution with some other features, so quadratic programming is used to solve the model. The general expression of QP is given in the following equation:

$$\begin{aligned} &\text{Minimize} \quad f(x) = C^T x + \frac{1}{2} * x^T D x, \\ &\text{subject to} \quad Ax \le B, x \ge 0. \end{aligned} \tag{22}$$

Solver interior-point convex technique is used in MATLAB to solve the proposed system. In Section 6, the obtained results are presented.

The interior-point convex algorithm of linear programming is used in MATLAB R2018a environment on Dell Latitude System with i5 4670 processor @3.4 GHz and 4 GB RAM.

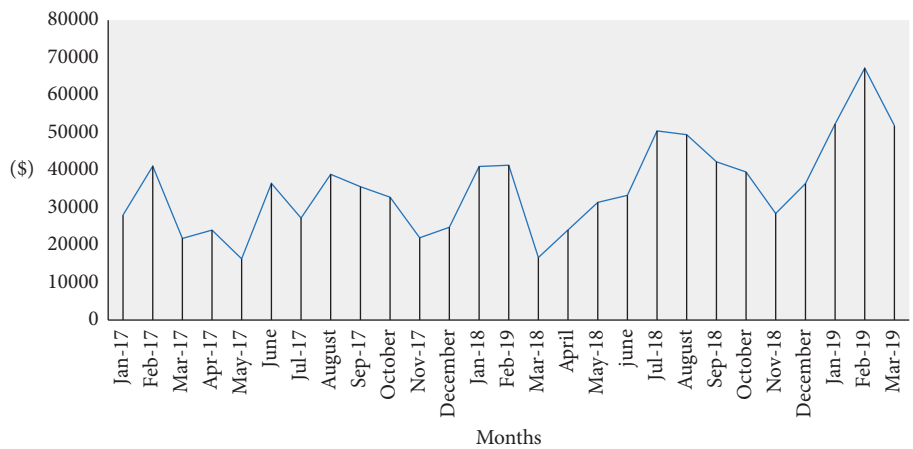

Figure 5: Monthly energy consumption cost (bill) of the existing campus.

6. Results

Optimal scheduling of reserves is analyzed to utilize the dispatchable and nondispatchable energy resources. A load of the campus is taken from nearby grid station and a model is proposed as presented above.

Demand response programs such as incentive and price based are analyzed. The exponential increasing energy consumption cost of the existing campus is shown in Figure 5. The case study has been carried out to separately investigate the time of use (TOU) and real-time pricing (RTP). The exchange energy with the grid is based on the following flowchart steps.

6.1. Case Studies. As described earlier, the grid outage is also the problem of developing countries such as Pakistan. So, it is also considered here with a grid support case. Here, we suppose the energy exchange with the grid at the same unit prices. The basic parameters of the proposed model are given in Table 1.

Two types of pricing are analyzed, as shown in Figure 6: time of use (TOU) and real-time pricing [77]. AC loads are attached and are composed of air conditions, lighting, fans, and PCs, as shown in Figure 7, whereas solar PV output power is expressed in Figure 8. Furthermore, loads are divided into critical and noncritical loads. The critical loads cannot curtail and must run loads [78].

Figure 9 shows the flowchart of the proposed strategy.

6.1.1. Case 01 A (Real-Time Pricing Analysis/with 0% DR). Case 1(a) (grid available mode (existing system)): in this case, the campus has only one energy source to supply the energy and operate all its loads. The total operational cost of this case is $2422.2 which will be considered as the base case.

Case 1(b) (operational cost without scheduling): In this case, DG solar PV and ESS are utilized without any schedule. The result obtained is $1349.9. The installation and replacement cost is not included in this case.

Case 1(c) (cost after grid outage for two hours): in this case, the scheduled outage of the grid is analyzed as shown in Figure 10. The operational one-day cost is $1354.3. The predefined outage is compensated through BESS and solar PV, as a time of outage is 10 to 11 AM. The solar PV is available and can run the whole system smoothly at critical peak pricing [79].

Case 1(d) (grid support in emergency case): in this case, the consumer received a signal from the grid to support the grid. So, the consumer acts as energy importer to the grid through an aggregator. The operational cost, in this case, is $1332.4.

Case 1(e) (proposed scheduling mode): in this case, available resources are utilized optimally through price-based scheduling. The contracted neighbour of prosumer power is also supplied at 15:00 to 16:00 PM for two hours, as shown in Figure 11. The total cost reduced about 65.3% compared to the base case is expressed in Table 2.

6.1.2. Case 1. B: With Load Curtailment (10% DR). Case 1(f) grid available mode (existing system): in this case, the campus has only one energy source to supply the energy and operate all its loads. The total operational cost of this case is $2422.2 which will be considered as the base case.

Case 1(g) (operational cost without scheduling): in this case, DG solar PV and ESS are utilized without any schedule. The result obtained is $1349.9. The installation and replacement cost is not included in this case.

Case 1(h) (cost after grid outage for two hours): in this case, the scheduled outage of the grid is analyzed, as shown in Figure 12. The operational one-day cost is $1354.3. The predefined outage is compensated trough BESS and solar PV, as a time of outage is 10 to 11 AM. The solar PV is available and can run the whole system smoothly.

Case 1(i) (grid support in emergency case): in this case, the consumer received a signal from the grid to support the grid. So, the consumer acts as the energy importer to the grid through an aggregator. The operational cost, in this case, is $1332.4, as shown in Figure 13.

Table 1: Techno-economic parameters of the proposed model.

Parameters	Value	Parameters	Value
P^{pv} rated	2000 kW	Cap^{s}	2000 kWh
$P^{g}_{\max}$	4000 kW	$P^{\mathrm{grid}}_{t,\min}$	−4000 kW
$P^{\mathrm{bat}}_{t,\max}$	800 kW	$P^{\mathrm{bat}}_{t,\min}$	−800 kW
$\mathrm{SOC}_{\max}$	90%	$\mathrm{SOC}_{\min}$	10%
SOC_{0}	50%	1$	159 PKR

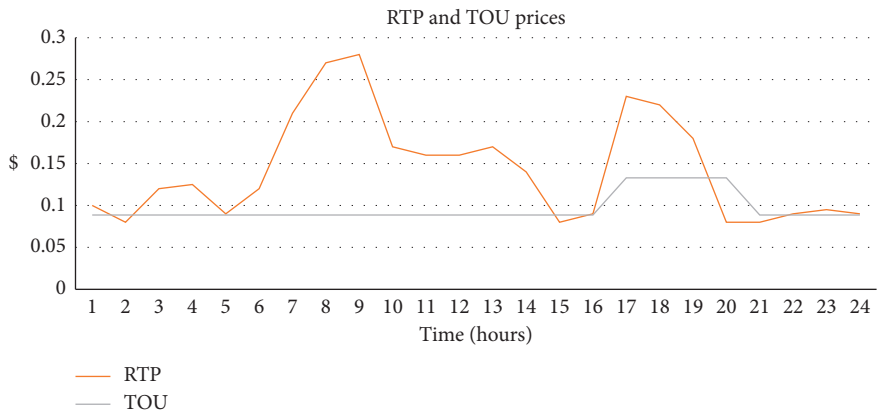

Figure 6: Monthly unit price.

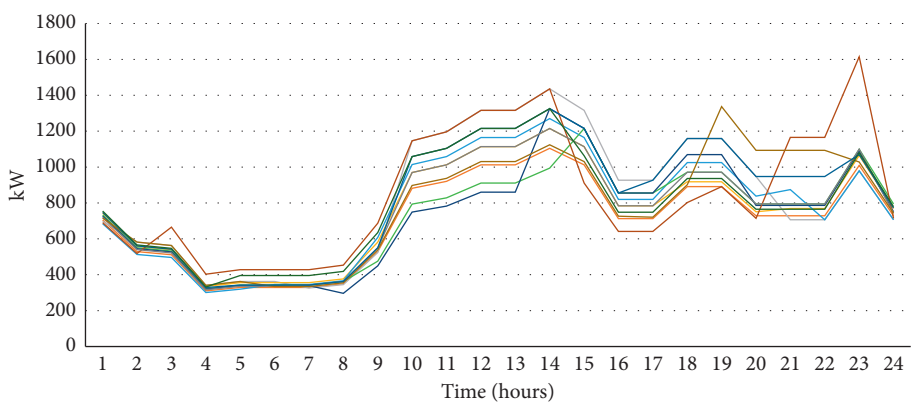

Figure 7: Campus load pattern.

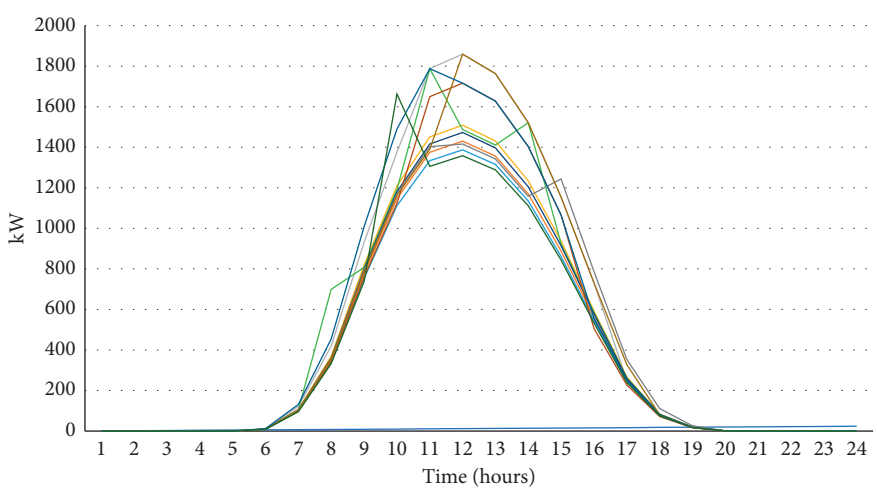

Figure 8: Solar output power pattern.

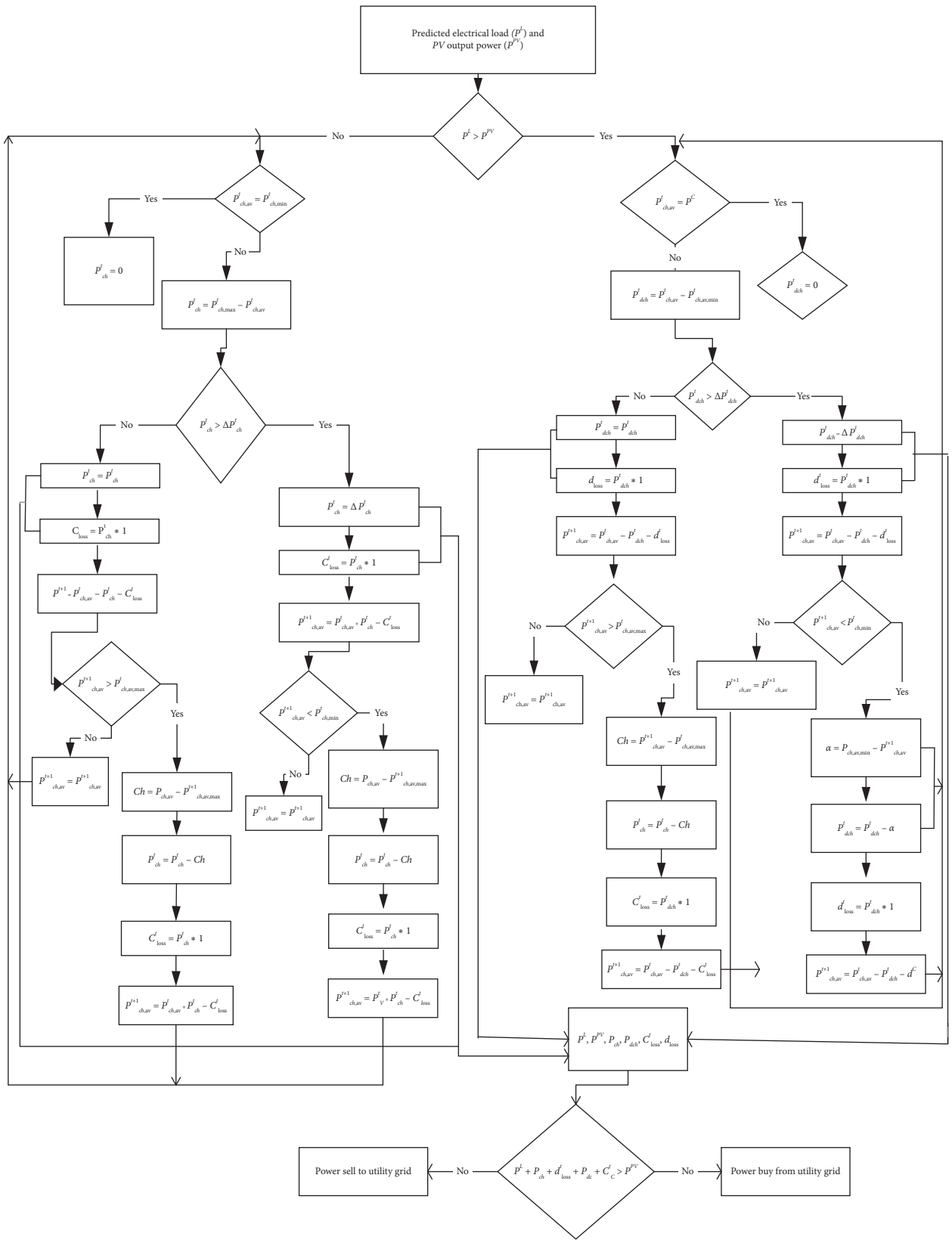

Figure 9: Flowchart for proposed energy storage scheduling, where the parameters P^t_{ch} is the ESS charging power, P^t_{dch} is the ESS discharging power, $P^t_{ch,\max}$ is the maximum charging power of ESS, $\pm\Delta P_{ch}$ is the threshold ESS output power in one hour, $P_{ch,av}/P_{dch,av}$ is charging and discharging available at time t, and $D_{\text{loss}}/C_{\text{loss}}$ is losses during charging and discharging.

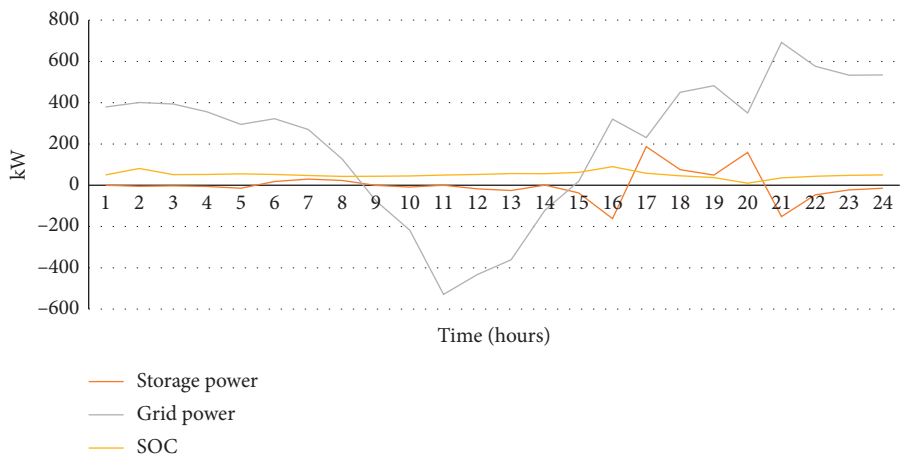

Figure 10: Case 1(c): grid outage for two hours.

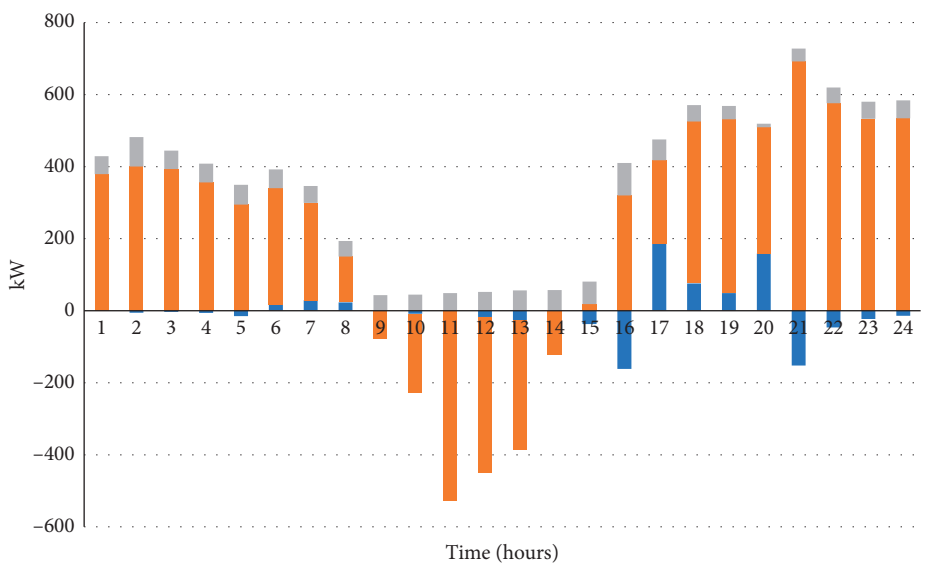

Figure 11: Case 1(e): proposed scheduling case.

Table 2: Real-time pricing analysis.

Cases 01	Utility grid mode (base case) ($)	Total cost without scheduling	Cost after a grid outage	Grid support case ($)	Proposed scheduling	Saving recorded ($)	Percentage benefits (%)
With 0% DR	2422.6	1349.9	1354.3	1332.4	840.34	1582.26	65.3
With 10% DR	2312.5	1288.7	1210.7	1100.36	830.5	1482	64
With 20% DR	2290.5	1217.8	1137.5	809.2	809.29	1481.21	64.7

Case 1(j) (proposed scheduling mode): in this case, available resources are utilized optimally through price-based scheduling. The contracted neighbour of prosumer power is also supplied at 15:00 to 16:00 PM for two hours, as shown in Figure 14. The total cost reduced about 65.3% as compared to the base case as expressed in Table 2.

6.1.3. Case 1. C: With Load Curtailment (20% DR). Case 1(k) (grid only mode with DR): this case is the combination of incentive and price-based demand response, with 20% load curtailment during the high-cost hours.

In the base case, the only grid is available as an energy source and witnessed a result of $2290.5. The difference

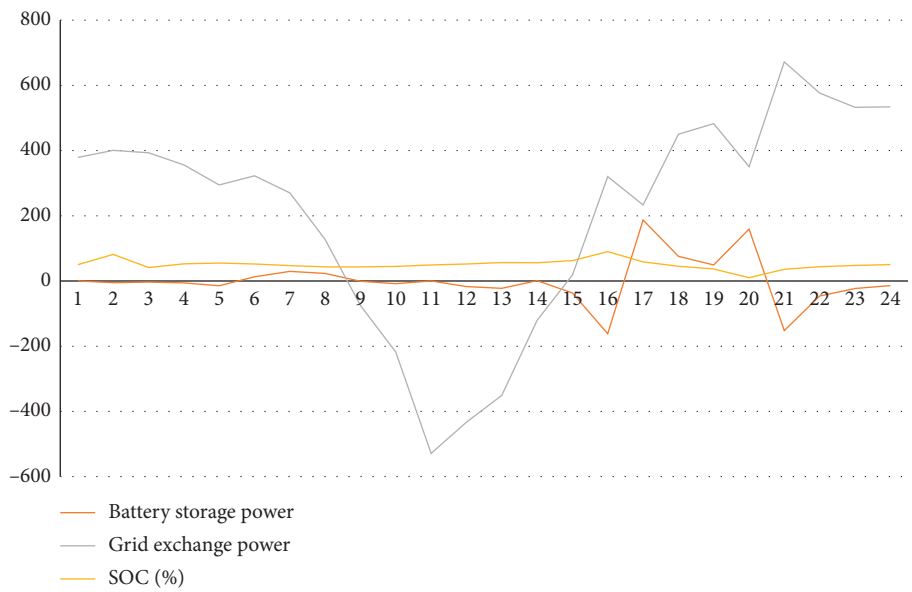

Figure 12: Case 1(h): grid outage for two hours.

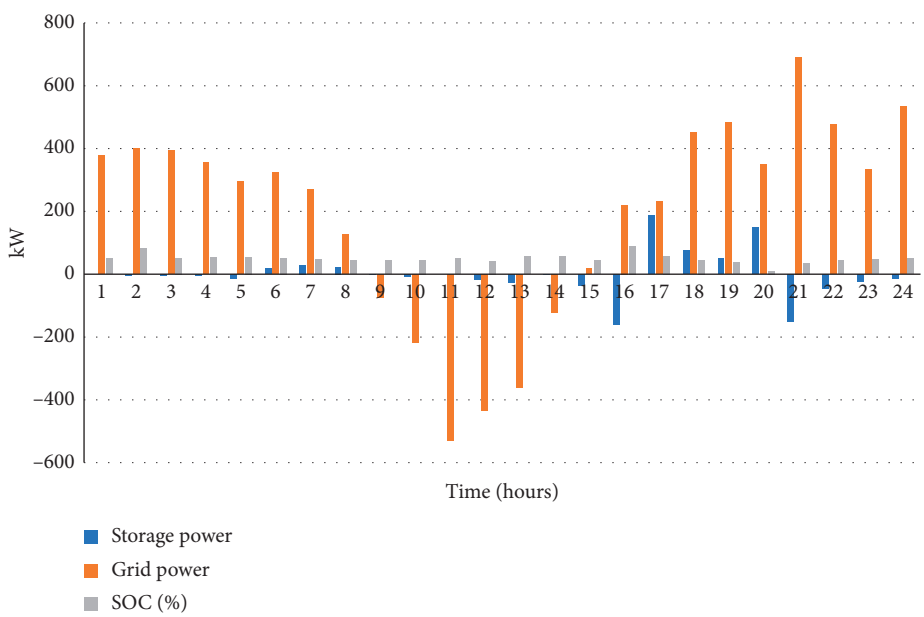

Figure 13: Case 1(i): grid support case with (10% DR).

between the above Case 1(a) is significant and reduced from 2442.6 to 2290.5 which is 6%.

Case 1(l) (total cost without scheduling with DR): in this case, the total operational cost is reduced to 1217.8 as solar PV and ESS are incorporated. The output power of solar PV and ESS utilized randomly without considering any constraints' schedule.

Case 1(m and n) (grid outage and grid support with DR): both cases have similar situations, as described in Case 1(c and d), besides its reduced cost. In grid support mode, cost is reduced from \$1332 to \$809.2. In this case, the storage output power supports the grid from 10:00 to 11:00 for two hours. The state of energy shifts in the discharging mode until the request is complete. In grid outage, that is, due to the energy shortfall, scheduled grid outage occurs at the same time any day from 10:00 to 11:00, as shown in Figure 15. The cost is reduced from \$1354.3 to \$1137.5, due to load curtailment during these hours.

Case 1(o) (proposed scheduling with DR): in this case, the scheduler considered the available resources and loads and generated a controlled signal for optimal operation. In this case, significant cost is reduced from \$2290.5 to \$809.29, which is about 64% as compared to the base case. Similarly, the whole process with defined parameters is presented in Table 2.

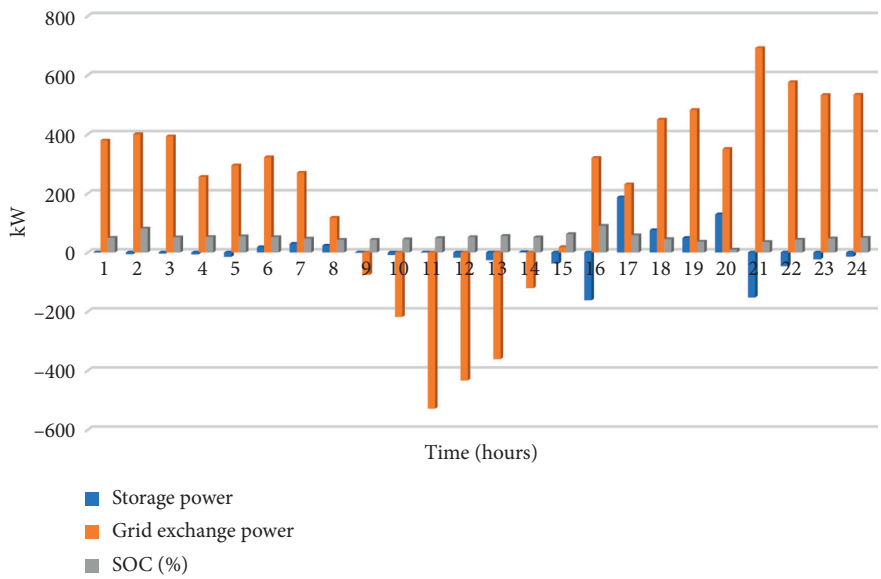

Figure 14: Case 1(j): proposed scheduling case (10% DR).

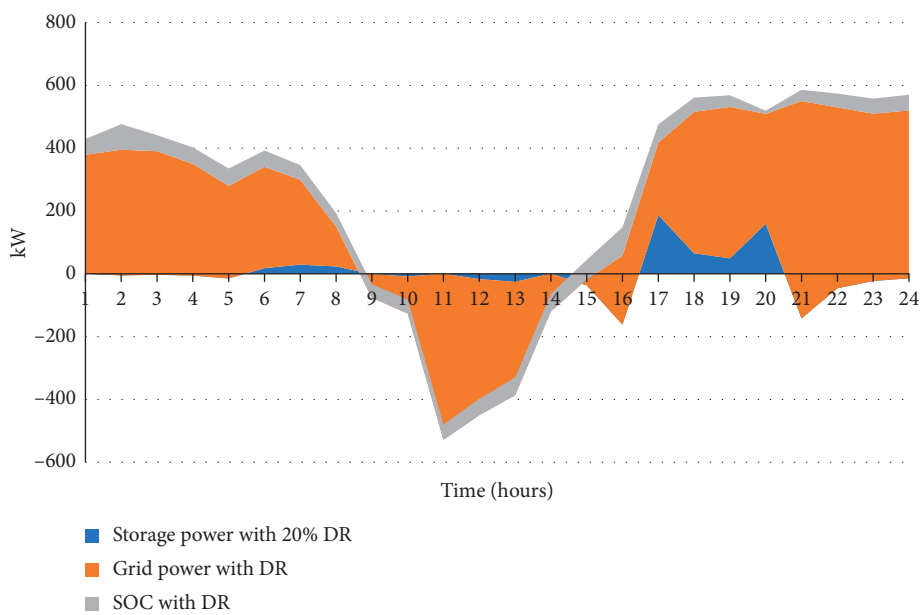

Figure 15: Case 1(m): grid outage for two hours.

6.1.4. Case 02: Time of Use- (TOU-) Based Analysis without Demand Response. Case 2(a) (grid only (base case)): in this case, as discussed earlier in Case 1, the grid is an available source of energy. So, operational cost is calculated \$1648.9, which is an existing system.

Case 2(b) (without scheduling): in this case, solar PV and storage are available for backup. The solar PV output power is utilized for self-consumption that reduced the energy consumption cost from \$1648.9 to \$1325.7. The charging-discharging of energy storage is randomly utilized and free from any bound. So, it is economical but needs proper usage for optimal operation, while Figure 16 shows the real-time pricing.

Case 2(c) (grid outage without DR): the scheduled grid outage hours are from 10:00 to 11:00 for two hours and PV-storage compensates the loss of grid. So, the cost is reduced as compared to the above two subcases and is found to be \$1301.9.

Case 2(d) (grid support case): in this case, prosumer receives emergency signals from the grid for support due to peak hours, contract, or some incident. The cost is calculated after the fulfilment of grid requirement is about \$1180.5, as shown in Figure 17.

Case 2(e) (proposed scheduling): in this case, cost reduced from \$1325.7 to \$990.6 which is about 39%, as shown in Figure 18. All parameters are representing in the graph

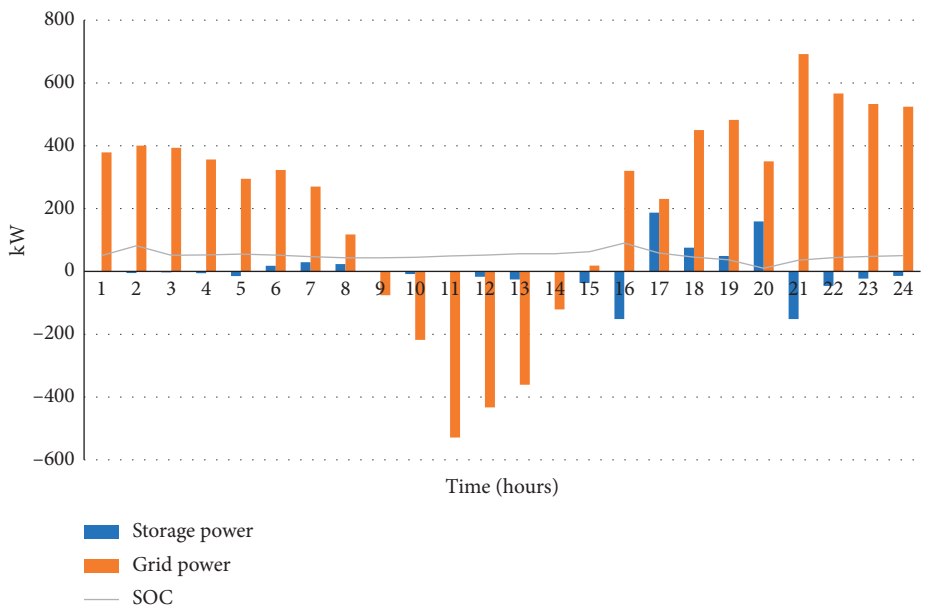

Figure 16: Case 2(h): grid outage for two hours.

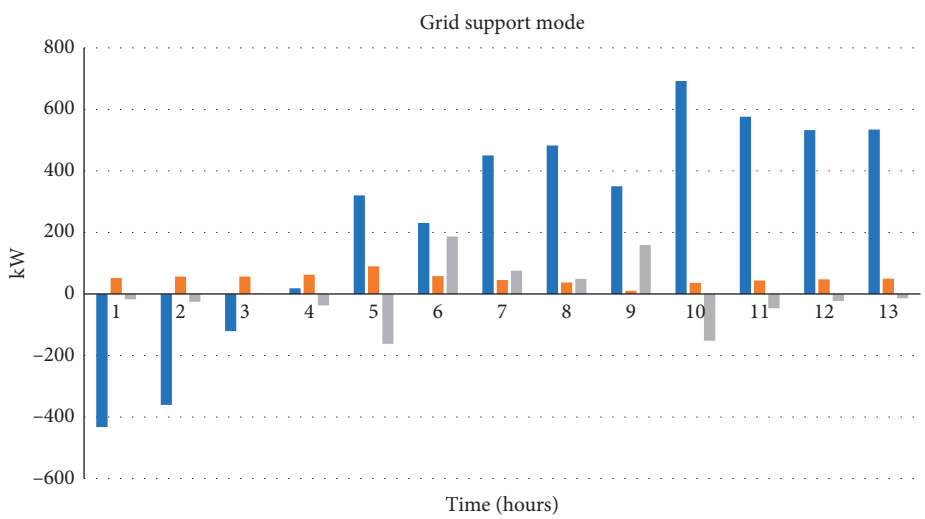

Figure 17: Case 2(d): grid support case.

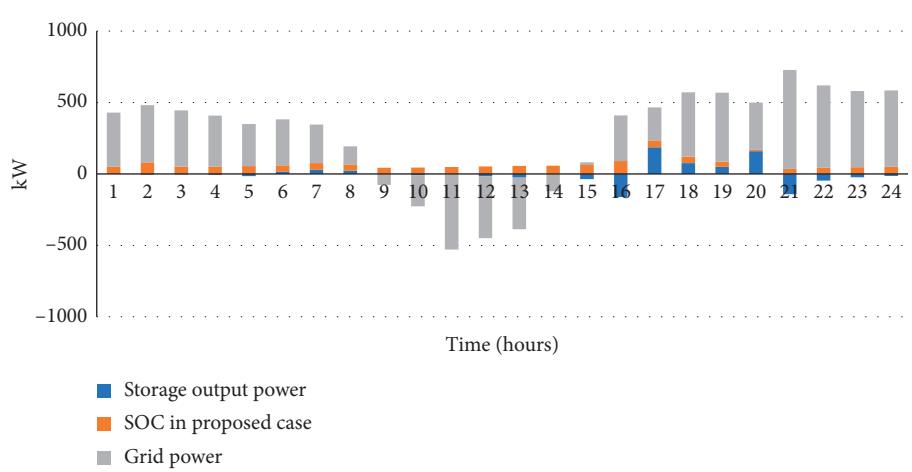

Figure 18: Case 2(e): proposed scheduling results.

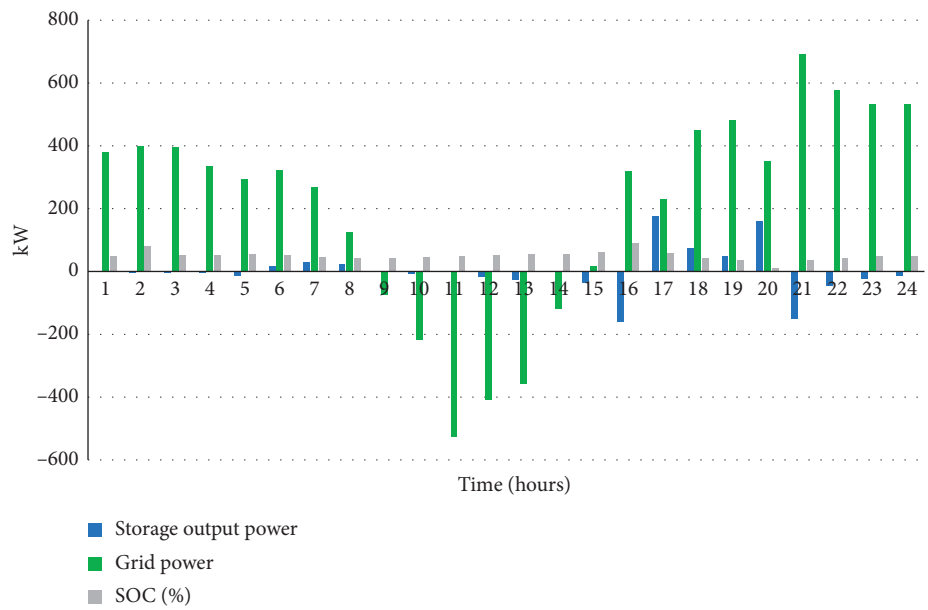

Figure 19: Case 2(i): grid support in emergency.

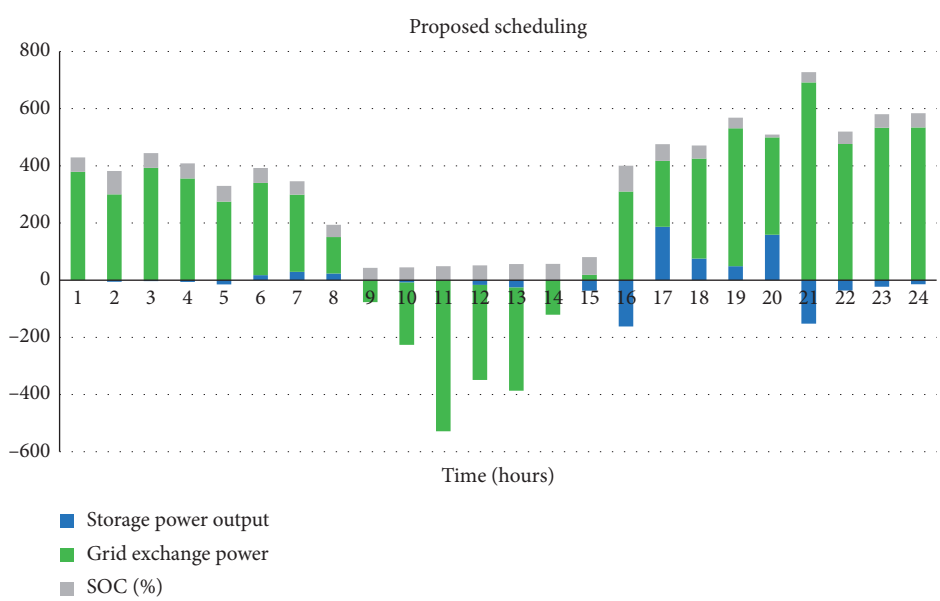

Figure 20: Time of use price-based scheduling.

Table 3: TOU price-based analysis.

Cases 01	Utility grid mode (base case) ($)	Total cost without scheduling	Cost after a grid outage	Grid support case ($)	Proposed scheduling	Saving recorded ($)	Percentage benefits (%)
Without 0% DR	1648.9	1325.7	1301.9	1180.5	990.6	658.3	39.9
Without 10% DR	1630.7	1304.3	1170.2	1044.5	952.1	678.6	41.7
With 20% DR	1620.2	1297	1070	961.59	944.9	675.35	41.68

using different colours. As the load changes, PV-storage operates accordingly considering the time of use prices and contracted power.

Case 2(f) (grid only (base case)): in this case, load curtails according to the peak hours and the load is shifted into off-peak hours. The cost is reduced from $1648.9 to $1620.2.

Case 2(g) (energy reserve utilization without scheduling): in this case, PV-storage is utilized with scheduling with the grid-connected mode. The cost is calculated as $1297, as

compared to without load curtail in previous case 2(b) which was high about 2%. This shows the benefits of load curtailment for economical operation.

Case 2(h) (grid outage with DR): a scheduled grid outage is considered in this case and the result after analyzing the system is found. The grid outage in our case is from 11:00 to 12:00 for two hours. The obtained result is $1070 considering the 20% load curtailment scenarios, as shown in Figure 16.

Case 2(i) (grid support mode): in this case, the whole scenario will be like case 2(d), but, considering the load curtailment, the total cost is found to be about $961.59 which is 18% less than the case of 0% incentive-based demand response (IBDR). The detailed features of this case are presented in Figure 19.

Case 2(j) (proposed scheduling): in this case, all parameters are scheduled through a microgrid-proposed scheduler that optimally utilizes the energy reserves. The contracted power shows from 15:00 to 16:00 for two hours.

The state of charge and storage output power is expressed in black and hollow square symbols. When the prices are high, the storage power retains itself to more charging. Figure 20 shows the optimal scheduling of all parameters in time of use demand response environment. Table 3 presents all the results of TOU price-based demand response.

7. Discussion

Form the above analysis, it is deduced that both price-based and incentive-based demand response strategies are beneficial for the customer in the electricity market. The analysis is carried out for the Pakistani environment, which is a developing country. The renewable integration with the existing grid by optimal scheduling of the available resources is analyzed and a significant reduction in scheduled utilization is found. So, a microgrid scheduler is necessary for smooth and economical operation. Furthermore, the obtained results show that the RTP reduction is more as compared to TOU strategy.

8. Conclusion

Optimal scheduling of DGs and ESS are addressed in the literature; however, the storage degradation cost and some system constraints are missed. In this paper, we investigated the campus microgrid energy management system with real-time local problems such as grid outage, grid support, and demand response strategies. As the storage system is highly nonlinear in nature, a nonlinear model is solved using quadratic programming. Two price-based cases, TOU and RTP, are analyzed in incentive-/nonincentive-based environment which were not addressed earlier. The prosumer-based market model is presented and contracted with the utility and neighbour customer. Results reveal that operation cost and peak load reduced to serve both customer and utility.

Nomenclature

$P^g(t)$: Grid power at time t
$P^s(t)$: Storage power at time t
$P^L(t)$: Energy demand of the prosumer
$P^C(t)$: Contracted power
$P^{PV}(t)$: Output power of solar PV
$\mathrm{SOE}(t)$: State of charge at time t
Cap^s: Battery energy capacity
CHP: Combined heat and power
MT: Microturbine
RERs: Renewable energy resources
DG: Distributed generation
ESS: Energy storage system
MILP: Mixed integer linear programming
DR: Demand response
DS: Distribution system
EMS: Energy management system
DSM: Demand-side management.

Data Availability

The load grid data used to support the findings of this study are available from the corresponding author upon request.

Conflicts of Interest

The authors declare that they have no conflicts of interest.

Acknowledgments

The authors are grateful to Aamir Raza Naqvi for his valuable suggestions and revision to complete this work. The authors are also grateful to U.E.T., Taxila, Pakistan, for providing a conducive environment for the completion of this research work. The authors are also thankful to the management of Taxila substation for data providing. This work was partially supported by the National Natural Science Foundation of China under contract no. 71761030 and Natural Science Foundation of Inner Mongolia under contract no. 2019LH07003.

References

[1] B. Wang, Z. Song, and L. Sun, "A review: comparison of multi-air-pollutant removal by advanced oxidation processes—industrial implementation for catalytic oxidation processes," *Chemical Engineering Journal*, vol. 409, Article ID 128136, 2020.

[2] Y. Chen, L. He, Y. Guan, H. Lu, and J. Li, "Life cycle assessment of greenhouse gas emissions and water-energy optimization for shale gas supply chain planning based on multi-level approach: case study in Barnett, Marcellus, Fayetteville, and Haynesville shales," *Energy Conversion and Management*, vol. 134, pp. 382–398, 2017.

[3] Y. Chen, L. He, J. Li, and S. Zhang, "Multi-criteria design of shale-gas-water supply chains and production systems towards optimal life cycle economics and greenhouse gas emissions under uncertainty," *Computers & Chemical Engineering*, vol. 109, pp. 216–235, 2018.

[4] J. Arshad, "Intelligent greenhouse monitoring and control scheme: an arrangement of sensors, raspberry pi based embedded system and IoT platform," *Indian Journal of Science and Technology*, vol. 13, no. 27, pp. 2811–2822, 2020.

[5] X. Zhao, Y. Ye, J. Ma, P. Shi, and H. Chen, "Construction of electric vehicle driving cycle for studying electric vehicle energy consumption and equivalent emissions," *Environmental Science and Pollution Research*, vol. 27, no. 30, pp. 37395–37409, 2020.

[6] B. Wang, L. Zhang, H. Ma, H. Wang, and S. Wan, "Parallel LSTM-based regional integrated energy system multienergy source-load information interactive energy prediction," *Complexity*, vol. 2019, Article ID 7414318, 13 pages, 2019.

[7] D. Yu, Y. Mao, B. Gu, S. Nojavan, K. Jermsittiparsert, and M. Nasseri, "A new LQG optimal control strategy applied on a hybrid wind turbine/solid oxide fuel cell/in the presence of the interval uncertainties," *Sustainable Energy, Grids and Networks*, vol. 21, Article ID 100296, 2020.

[8] C. Yang, F. Gao, and M. Dong, "Energy efficiency modeling of integrated energy system in coastal areas," *Journal of Coastal Research*, vol. 103, no. 1, pp. 995–1001, 2020.

[9] Y. Cao, Q. Wang, W. Cheng, S. Nojavan, and K. Jermsittiparsert, "Risk-constrained optimal operation of fuel cell/photovoltaic/battery/grid hybrid energy system using downside risk constraints method," *International Journal of Hydrogen Energy*, vol. 45, no. 27, pp. 14108–14118, 2020.

[10] Y. Cao, Y. Li, G. Zhang, K. Jermsittiparsert, and M. Nasseri, "An efficient terminal voltage control for PEMFC based on an improved version of whale optimization algorithm," *Energy Reports*, vol. 6, pp. 530–542, 2020.

[11] L. He, Y. Chen, H. Zhao, P. Tian, Y. Xue, and L. Chen, "Game-based analysis of energy-water nexus for identifying environmental impacts during Shale gas operations under stochastic input," *Science of the Total Environment*, vol. 627, pp. 1585–1601, 2018.

[12] H. Shayeghi, E. Shahryari, M. Moradzadeh, and P. Siano, "A survey on microgrid energy management considering flexible energy sources," *Energies*, vol. 12, no. 11, p. 2156, 2019.

[13] H. M. Munir, J. Zou, C. Xie, K. Li, T. Younas, and J. M. Guerrero, "Direct harmonic voltage control strategy of shunt active power filters suitable for microgrid applications," *Journal of Power Electronics*, vol. 19, no. 1, pp. 265–277, 2019.

[14] H. M. Munir, R. Ghannam, H. Li et al., "Control of distributed generators and direct harmonic voltage controlled active power filters for accurate current sharing and power quality improvement in islanded microgrids," *Inventions*, vol. 427 pages, 2019.

[15] C. A. Macana and H. R. Pota, "Optimal energy management system for strategic prosumer microgrids: an average bidding algorithm for prosumer aggregators," in *Proceedings of the 2017 11th Asian Control Conference (ASCC)*, pp. 705–710, IEEE, Gold Coast, Australia, December 2017.

[16] A. Yousaf, B. A. Khan, U. Bashir, and F. Ahmad, "Overview of implementing microgrid, its policies, incentives and challenges in Pakistan," in *Proceedings of the 2019 6th International Conference on Electrical and Electronics Engineering (ICEEE)*, pp. 6–11, IEEE, Istanbul, Turkey, April 2019.

[17] H. Abd ul Muqeet and A. Ahmad, "An optimal operation of prosumer microgrid considering demand response strategies and battery life," *Technical Journal*, vol. 25, no. 2, pp. 41–51, 2020.

[18] Y. Liu, "Development of 340-GHz transceiver front end based on GaAs monolithic integration technology for THz active imaging array," *Applied Sciences*, vol. 10, no. 21, p. 7924, 2020.

[19] Z. Niu, B. Zhang, J. Wang et al., "The research on 220 GHz multicarrier high-speed communication system," *China Communications*, vol. 17, no. 3, pp. 131–139, 2020.

[20] B. Zhang, D. Ji, D. Fang, S. Liang, Y. Fan, and X. Chen, "A novel 220-GHz GaN diode on-chip tripler with high driven power," *IEEE Electron Device Letters*, vol. 40, no. 5, pp. 780–783, 2019.

[21] H. A. Khan, H. F. Ahmad, M. Nasir, M. F. Nadeem, and N. A. Zaffar, "Decentralised electric power delivery for rural electrification in Pakistan," *Energy Policy*, vol. 120, pp. 312–323, 2018.

[22] H. M. Munir, J. Zou, C. Xie, and J. M. Guerrero, "Cooperation of voltage controlled active power filter with grid-connected DGs in microgrid," *Sustainability*, vol. 11, no. 1, p. 154, 2019.

[23] L. Park, S. Jeong, J. Kim, and S. Cho, "Joint geometric unsupervised learning and truthful auction for local energy market," *IEEE Transactions on Industrial Electronics*, vol. 66, no. 2, pp. 1499–1508, 2018.

[24] F. Nadeem, S. S. Hussain, P. K. Tiwari, A. K. Goswami, and T. S. Ustun, "Comparative review of energy storage systems, their roles, and impacts on future power systems," *IEEE Access*, vol. 7, pp. 4555–4585, 2018.

[25] R. Zafar, A. Mahmood, S. Razzaq, W. Ali, U. Naeem, and K. Shehzad, "Prosumer based energy management and sharing in smart grid," *Renewable and Sustainable Energy Reviews*, vol. 82, pp. 1675–1684, 2018.

[26] M. Di Somma, G. Graditi, E. Heydarian-Forushani, M. Shafiekhah, and P. Siano, "Stochastic optimal scheduling of distributed energy resources with renewables considering economic and environmental aspects," *Renewable Energy*, vol. 116, pp. 272–287, 2018.

[27] X. Hu, P. Ma, B. Gao, and M. Zhang, "An integrated step-up inverter without transformer and leakage current for grid-connected photovoltaic system," *IEEE Transactions on Power Electronics*, vol. 34, no. 10, pp. 9814–9827, 2019.

[28] X. Li, B. Anvari, A. Palazzolo, Z. Wang, and H. Toliyat, "A utility-scale flywheel energy storage system with a shaftless, hubless, high-strength steel rotor," *IEEE Transactions on Industrial Electronics*, vol. 65, no. 8, pp. 6667–6675, 2017.

[29] C. Zhang, Y.-L. Wei, P.-F. Cao, and M.-C. Lin, "Energy storage system: current studies on batteries and power condition system," *Renewable and Sustainable Energy Reviews*, vol. 82, pp. 3091–3106, 2018.

[30] H. A. U. Muqeet and A. Ahmad, "Optimal scheduling for campus prosumer microgrid considering price based demand response," *IEEE Access*, vol. 8, pp. 71378–71394, 2020.

[31] M. Kim, K. Kim, H. Choi, S. Lee, and H. Kim, "Practical operation strategies for energy storage system under uncertainty," *Energies*, vol. 12, no. 6, p. 1098, 2019.

[32] M. Nasir, M. Anees, H. A. Khan, and J. M. Guerrero, "Dual-loop control strategy applied to the cluster of multiple nanogrids for rural electrification applications," *IET Smart Grid*, vol. 2, no. 3, pp. 327–335, 2019.

[33] S. Z. Hassan, H. Li, T. Kamal, I. Hussain, F. Mehmood, and A. Kabir, "Performance study of microgrid system for a small community at Islamabad, Pakistan," in *Proceedings of the 2016 19th International Multi-Topic Conference (INMIC)*, pp. 1–6, IEEE, Islamabad, Pakistan, December 2016.

[34] M. M. A. Malakoutian and M. Khaksar, "SBM model based productivity evaluation," *ENG Transactions*, vol. 1, no. 1, 2020.

[35] F. Jafari Golrokh and A. Hasan, "A comparison of machine learning clustering algorithms based on the DEA optimization approach for pharmaceutical companies in developing countries," *ENG Transactions*, vol. 1, no. 1, 2020.

[36] C. Yu, M. Chen, K. Cheng et al., "SGOA: annealing-behaved grasshopper optimizer for global tasks," *Engineering with Computers*, pp. 1–28, 2021.

[37] F. Jafari Golrokh, G. Azeem, and A. Hasan, "Eco-efficiency evaluation in cement industries: DEA malmquist productivity index using optimization models," *ENG Transactions*, vol. 1, no. 1, 2020.

[38] J. Tu, H. Chena, J. Liu et al., "Evolutionary biogeography-based whale optimization methods with communication structure: towards measuring the balance," *Knowledge-Based Systems*, vol. 212, Article ID 106642, 2021.

[39] M. Taleghani and A. Taleghani, "Identification and ranking of factors affecting the implementation of knowledge management engineering based on TOPSIS technique," *ENG Transactions*, vol. 1, no. 1, 2020.

[40] H. Chen, A. A. Heidari, H. Chen, M. Wang, Z. Pan, and A. H. Gandomi, "Multi-population differential evolution-assisted Harris hawks optimization: framework and case studies," *Future Generation Computer Systems*, vol. 111, pp. 175–198, 2020.

[41] M. Khaksar and M. M. A. Malakoutian, "Productivity evaluation for banking system in developing countries: DEA malmquist productivity index based on CCR, BCC, CCR-BCC (a case study)," *ENG Transactions*, vol. 1, no. 1, 2020.

[42] Y. Xu, H. Chen, J. Luo, Q. Zhang, S. Jiao, and X. Zhang, "Enhanced Moth-flame optimizer with mutation strategy for global optimization," *Information Sciences*, vol. 492, pp. 181–203, 2019.

[43] M. Wang and H. Chen, "Chaotic multi-swarm whale optimizer boosted support vector machine for medical diagnosis," *Applied Soft Computing Journal*, vol. 88, Article ID 105946, 2020.

[44] S. M. Hosseinian and V. Najafi Moghaddam Gilani, "Analysis of factors affecting urban road accidents in rasht metropolis," *ENG Transactions*, vol. 1, no. 1, pp. 1–4, 2020.

[45] N. Amiri Golilarz, H. Gao, R. Kumar, L. Ali, Y. Fu, and C. Li, "Adaptive wavelet based MRI brain image de-noising," *Frontiers in Neuroscience*, vol. 14, p. 728, 2020.

[46] A. Addeh and M. Iri, "Brain tumor type classification using deep features of MRI images and optimized RBFNN," *ENG Transactions*, vol. 2, no. 1, 2021.

[47] R. U. Khan, X. Zhang, R. Kumar et al., "An adaptive multilayer botnet detection technique using machine learning classifiers," *Applied Sciences*, vol. 9, no. 11, p. 2375, 2019.

[48] A. Addeh, A. Khormali, and N. A. Golilarz, "Control chart pattern recognition using RBF neural network with new training algorithm and practical features," *ISA Transactions*, vol. 79, pp. 202–216, 2018.

[49] N. A. Golilarz, A. Addeh, H. Gao et al., "A new automatic method for control chart patterns recognition based on ConvNet and Harris Hawks meta heuristic optimization algorithm," *IEEE Access*, vol. 7, pp. 149398–149405, 2019.

[50] N. A. Golilarz, H. Gao, and H. Demirel, "Satellite image denoising with Harris Hawks meta heuristic optimization algorithm and improved adaptive generalized Gaussian distribution threshold function," *IEEE Access*, vol. 7, pp. 57459–57468, 2019.

[51] A. Waqar, M. Shahbaz Tanveer, J. Ahmad, M. Aamir, M. Yaqoob, and F. Anwar, "Multi-objective analysis of a CHP plant integrated microgrid in Pakistan," *Energies*, vol. 10, no. 10, p. 1625, 2017.

[52] S. U. Rehman, S. Rehman, M. Shoaib, and I. A. Siddiqui, "Feasibility study of a grid-tied photovoltaic system for household in Pakistan: considering an unreliable electric grid," *Environmental Progress & Sustainable Energy*, vol. 38, no. 3, Article ID e13031, 2019.

[53] Z. Zia and F. A. Shaikh, "Economics and environmental impact assessment of microgrid for rural areas of Pakistan," *Proceedings of SEEP*, pp. 27–30, 2017.

[54] J. Liu, Y. Liu, and X. Wang, "An environmental assessment model of construction and demolition waste based on system dynamics: a case study in Guangzhou," *Environmental Science and Pollution Research*, vol. 27, no. 30, pp. 37237–37259, 2020.

[55] H. Lu, "LiFSI as a functional additive of the fluorinated electrolyte for rechargeable Li-S batteries," *Journal of Materials Science: Materials in Electronics*, vol. 32, no. 5, p. 5907, 2021.

[56] P. Wang, T. Yao, Z Li et al., "A superhydrophobic/electrothermal synergistically anti-icing strategy based on graphene composite," *Composites Science and Technology*, vol. 198, Article ID 108307, 2020.

[57] H.-C. Gao, J.-H. Choi, S.-Y. Yun, H.-J. Lee, and S.-J. Ahn, "Optimal scheduling and real-time control schemes of battery energy storage system for microgrids considering contract demand and forecast uncertainty," *Energies*, vol. 11, no. 6, p. 1371, 2018.

[58] S. Rehman, "Hybrid power systems–Sizes, efficiencies, and economics," *Energy Exploration & Exploitation*, vol. 39, no. 1, pp. 3–43, Article ID 0144598720965022, 2020.

[59] M. Nasir, H. A. Khan, I. Khan et al., "Grid load reduction through optimized PV power utilization in intermittent grids using a low-cost hardware platform," *Energies*, vol. 12, no. 9, p. 1764, 2019.

[60] Y. Li, Z. Yang, G. Li, D. Zhao, and W. Tian, "Optimal scheduling of an isolated microgrid with battery storage considering load and renewable generation uncertainties," *IEEE Transactions on Industrial Electronics*, vol. 66, no. 2, pp. 1565–1575, 2018.

[61] B.-C. Jeong, D.-H. Shin, J.-B. Im, J.-Y. Park, and Y.-J. Kim, "Implementation of optimal two-stage scheduling of energy storage system based on big-data-driven forecasting—an actual case study in a campus microgrid," *Energies*, vol. 12, no. 6, p. 1124, 2019.

[62] F. Ahmad and M. S. Alam, "Optimal sizing and analysis of solar PV, wind, and energy storage hybrid system for campus microgrid," *Smart Science*, vol. 6, no. 2, pp. 150–157, 2018.

[63] T. J. Soleja, M. F. Siddiqui, M. Kashan, and A. Waseem, "Economic feasibility analysis of on-grid PV system without battery storage for a commercial building in Karachi, Pakistan," in *Proceedings of the 2018 5th International Symposium on Environment-Friendly Energies and Applications (EFEA)*, pp. 1–4, IEEE, Rome, Italy, September 2018.

[64] N. Liu, M. Cheng, X. Yu, J. Zhong, and J. Lei, "Energy-sharing provider for PV prosumer clusters: a hybrid approach using stochastic programming and Stackelberg game," *IEEE Transactions on Industrial Electronics*, vol. 65, no. 8, pp. 6740–6750, 2018.

[65] M. Husein and I.-Y. Chung, "Optimal design and financial feasibility of a university campus microgrid considering renewable energy incentives," *Applied Energy*, vol. 225, pp. 273–289, 2018.

[66] X. Wang, Y. Liu, and K. R. Choo, "Fault tolerant multi-subset aggregation scheme for smart grid," *IEEE Transactions on Industrial Informatics*, p. 1, 2020.

[67] H. Chen, A. Chen, L. Xu et al., "A deep learning CNN architecture applied in smart near-infrared analysis of water pollution for agricultural irrigation resources," *Agricultural Water Management*, vol. 240, Article ID 106303, 2020.

[68] J. Song, Q. Zhong, W. Wang, C. Su, Z. Tan, and Y. Liu, "FPDP: flexible privacy-preserving data publishing scheme for smart agriculture," *IEEE Sensors Journal*, 2020.

[69] E. Barbour and M. C. González, "Projecting battery adoption in the prosumer era," *Applied Energy*, vol. 215, pp. 356–370, 2018.

[70] C. D. Rodríguez-Gallegos, O. Gandhi, D. Yang et al., "A siting and sizing optimization approach for PV–battery–diesel hybrid systems," *IEEE Transactions on Industry Applications*, vol. 54, no. 3, pp. 2637–2645, 2017.

[71] N. Liu and J. Wang, "Energy sharing for interconnected microgrids with a battery storage system and renewable energy sources based on the alternating direction method of multipliers," *Applied Sciences*, vol. 8, no. 4, p. 590, 2018.

[72] H. A. Muqeet, I. A. Sajjad, A. Ahmad, M. M. Iqbal, S. Ali, and J. M. Guerrero, "Optimal operation of energy storage system for a prosumer microgrid considering economical and environmental effects,"vol. 4, pp. 1–6, in *Proceedings of the 2019 International Symposium on Recent Advances in Electrical Engineering (RAEE)*, vol. 4, pp. 1–6, IEEE, Islamabad, Pakistan, August 2019.

[73] A. K. Shukla, K. Sudhakar, and P. Baredar, "Renewable energy resources in South Asian countries: challenges, policy and recommendations," *Resource-Efficient Technologies*, vol. 3, no. 3, pp. 342–346, 2017.

[74] G. Sun, C. Li, and L. Deng, "An adaptive regeneration framework based on search space adjustment for differential evolution," *Neural Computing and Applications*, pp. 1–17, 2021.

[75] W. Zhu, C. Ma, X. Zhao et al., "Evaluation of sino foreign cooperative education project using orthogonal sine cosine optimized kernel extreme learning machine," *IEEE Access*, vol. 8, pp. 61107–61123, 2020.

[76] G. Liu, W. Jia, M. Wang et al., "Predicting cervical hyperextension injury: a covariance guided sine cosine support vector machine," *IEEE Access*, vol. 8, pp. 46895–46908, 2020.

[77] G. Hafeez, N. Javaid, S. Iqbal, and F. A. Khan, "Optimal residential load scheduling under utility and rooftop photovoltaic units," *Energies*, vol. 11, no. 3, p. 611, 2018.

[78] A. Paudel, K. Chaudhari, C. Long, and H. B. Gooi, "Peer-to-peer energy trading in a prosumer-based community microgrid: a game-theoretic model," *IEEE Transactions on Industrial Electronics*, vol. 66, no. 8, pp. 6087–6097, 2018.

[79] M. Naz, Q. Z. Iqbal, N. Javaid et al., "Efficient power scheduling in smart homes using hybrid grey Wolf differential evolution optimization technique with real time and critical peak pricing schemes," *Energies*, vol. 11, no. 2, pp. 1–25, 2018.

Hindawi
Mathematical Problems in Engineering
Volume 2021, Article ID 5587392, 16 pages
https://doi.org/10.1155/2021/5587392

Research Article

Five-Echelon Multiobjective Health Services Supply Chain Modeling under Disruption

Farnaz Javadi Gargari,[1] Mahjoube Sayad,[1] Seyed Ali Posht Mashhadi,[2] Abdolhossein Sadrnia,[3] Arman Nedjati,[3] and Tahereh Yousefi Golafshani[4]

[1]*Department of Industrial Engineering, Alzahra University, Tehran, Iran*
[2]*Department of Industrial Engineering, Islamic Azad University, South Tehran Branch, Iran*
[3]*Assistant Professor of Department of Industrial Engineering, Quchan University of Technology, P.O. Box: 94771-67335, Quchan, Iran*
[4]*Almahdi Aluminum Co, Hormozgan Province, Bandar Abbas, Iran*

Correspondence should be addressed to Abdolhossein Sadrnia; a.sadrnia@qiet.ac.ir

Received 18 March 2021; Revised 19 April 2021; Accepted 25 April 2021; Published 19 May 2021

Academic Editor: Mohammad Yazdi

Medicine unreliability problem is taken into consideration as one of the most important issues in health supply chain management. This research is associated with the development of a multiobjective optimization problem for the selection of suppliers and distributors. To achieve the purposes, the optimal quota allocation is determined with respect to disruption of suppliers in a five-echelon supply chain network and consideration of the distributor centers as a hub location-allocation mode. The objective of the optimization model is involved in simultaneous minimization of transactions costs dealing with suppliers, expected purchasing costs from suppliers, expected percentages of delayed and returned products in each distributor, as well as transportation cost in each echelon and fixed cost for distributor centers, and finally maximization of the expected scores for suppliers and high priority of product customers. The optimization problem is formulated as a mixed-integer nonlinear programming model. The proposed optimization model is utilized to investigate a numerical case study for asthma-specific medicines. The analyzing procedure is conducted based on the collected real data from Cobel Darou pharmaceutical company in 2019. Furthermore, a fuzzy multichoice goal programming model is considered to solve the proposed optimization model by *R* optimization solver. The numerical results confirmed the authenticity of the model.

1. Introduction

Nowadays, engineering and science advances have contributed to the significant reduction of incurable disease and infant mortality in human societies. It occurred due to the classification of the issue of health and treatment as one of the most important multidisciplinary topics in human societies. However, healthcare costs have had a rising trend, and thus, controlling and mitigating of costs of health systems make considerable concerns in this domain [1]. Therefore, scholars and researchers and also governments attempt to reduce the rate of healthcare costs by monitoring these kinds of costs. The health organizations demand reduction of the treatment costs, increment of the quality of health systems, patient safety, as well as improvement and enhancement of the effectiveness, and efficiency through a methodology, which is called the health supply chain.

Many researchers believe that the application of principles of management in the health supply chain, in addition to the decrement of the cost of care and treatment, leads to the improvement of the quality of services [2, 3]. Nevertheless, potential disturbances have raised risks against supply chains [4]. Healthcare area has suffered continuous challenges over decades [5]. To deal with this, researchers and practitioners have focused on devise and implementation of various practices [6]. The major challenges for

the pharmaceutical supply chain include lack of coordination, inventory management, human resource dependency, absent demand information, order management, shortage avoidance, warehouse management, expiration, shipment visibility, and temperature control [7]. One of the challenges of this field is the disorder of medicine distribution that leads to medicine deficiencies. Inadequate distribution and medicine and equipment deficiencies disrupt suppliers so that they cannot supply the demand for distribution centers and hospitals in time. Thereby, the overall efficiency of the system and responsibility reduces significantly. The origin of such disorders may be either in transportation systems or in supplier centers themselves, which includes price fluctuations, demand fluctuations, equipment failure, and quality failure [8]. Moreover, natural disasters, equipment failures, terrorist attacks, labor strikes, and change in property could be the reason for such disorders [9]. In reality, the cases that include such disorders are summarized as follows: (1) the tragic earthquake in Bam caused severe damage to the infrastructure, underground, and transport systems [10], (2) Hurricane Katrina (2005), which caused the destruction of manufacturing and transportation equipment in the coast of the Persian Gulf [11], (3) the earthquake in Japan (2011) that halted production in a wide range of industries due to the power outage and the blockage of transportation routes [12], and (4) the outbreak of coronavirus in the Wuhan city in the winter of 2020, which caused more than 213 countries (based on https://www.worldometers.info/coronavirus/countries-where-coronavirus-has-spread/%20live%20data%20in%20the%20first%20of%20June%202020) to implement the quarantine, more than policy and disruption to transport systems. Coronavirus outbreak affected more than 6,235,658 cases and taken the lives of about 373,176 up to the end of May 2020. It should be noted that these statistics relate to the end of March 2020; significantly, infected population numbers and death rates change daily [13]. The earthquake in China (2008), the tornados of the Philippines in 2013, and the Indian Ocean tsunami are also among the natural disasters. Apart from natural disasters, human disasters have also disrupted related organizations. Disasters like the Mumbai attacks in 2011 and the September 11 terrorist attack in the United States are among the human disasters. [14] This shows the importance of logistics network design with high reliability in unfavorable conditions.

The supply chain disruption makes vital impacts on patient level, especially in the shortage of medicines [15, 16]. The world has witnessed a 300% increase in new medicine shortages since 2006. Recently, multiple countries and domains have been involved in this problem [15]. The problem posed by the supply chain disruptions puts the pharmaceutical companies under tangible pressure and may also compromise human health by medicine shortages. Inappropriate situations for distribution of medicines, hospital equipment, and their shortage can cause irreparable damage to countries and health systems. However, desirable implementation of the health supply chain management can considerably contribute to the reduction of the total costs in the healthcare sector [17]. Besides, the evolution of the logistics system can lead to the improvement of the distribution of medicines and equipment in this sector. To date, studies have been done on supply chain network design under disruptions in different areas, such as supplier selection and order allocation [18] and blood supply chain [19] by using different quantitative approaches. Accordingly, some of the studies have affected the impact of epidemic outbreaks on supply chains [20, 21]. Due to two unique features, the disasters caused by disease outbreaks vary from other disasters: their long-term damage and their growing spread. Failure to control such disasters will result in severe disruptions in supply chains and communities and will result in irreparable losses. Coronavirus 2019 (COVID-19) is one of those disasters that has caused severe disease [22]. Also, careful pharmacy management has a strong effect on the capacity of a country to tackle public health issues. Pharmaceutical supply management is one of the most operational problems in the healthcare industries [23].

However, as the relevant literature demonstrates, few studies have been carried out in the field of hierarchical localization, which considers disruption in supply centers within the health services networks. According to the mentioned cases, this paper presents a five-objective hierarchical location for designing health services networks that distribution centers are considered as a hub location-allocation method. In the proposed model, unlike the previous research, we consider several key issues, which help to manage and design health services networks, such as the hierarchical organization of the networks, purchasing a group of medicine, disrupting the tasks of the suppliers, and its effects, which undoubtedly lead to a lack of inventory. Since the model is formulated as a multiobjective function, a fuzzy multiobjective goal programming model is considered to solve the proposed optimization model using the *R* optimization solver. A practical case study is also presented according to the actual information of Cobel Darou pharmaceutical company to show the application of the proposed model and effectiveness of the designed method.

The rest of this paper is structured as follows. Section 2 comprises a review of the health supply chain literature. In Section 3, the proposed methodology and assumptions are characterized for the problem. Section 4 presents a case study for validation of the represented model. Section 5 is dealt with the development of sensitivity analysis for the model, and the results are displayed by a diagram. Finally, the whole results of this paper are provided in Section 6. The obtained conclusion proves the application of the proposed model in the real world.

2. Literature Review

In this section, we examine the relevant literature in two separate but complementary parts in the field of health services networks: hierarchical location-allocation for health networks and facility location problems under disruptions.

2.1. Hierarchical Location-Allocation for Supply Chains of Health Networks. Location-allocation of facilities is the location of a set of facilities to minimize the cost of the

response to demands. In other words, hierarchical location-allocation models deal with the location of new facilities in specific regions and the assignment of demand nodes to established facilities. Depending on the nature of the system, these models can include single-level or hierarchical networks. Several studies have been carried out in this field. The purpose of the present study is not to investigate all the impacts related to the location-allocation model, but a selection of research studies is presented to review this field comprehensively. The studies carried out for single-level systems include the location-allocation model in the field of health care services with geographical considerations to assess different options for providing services [24], assessing the location of blood banks of the American red cross in the middle region of the Atlantic Ocean [25], the multistage location-allocation model for organ transplant centers [26], and the evaluation of the location models of emergency services using a simulation method [27]. Khodaparasti et al. [28] presented a multiperiod location-allocation model for the home for the aged network to improve access to services. In cases where there is a relationship between facilities at different levels of communication, the system is considered hierarchical. The majority of health care systems have a hierarchical organization, some of which are as follows: due to the weak geographical access in developing countries, Rahman and Smith [29] proposed a hierarchical location-allocation model for scheduling the health services. Hodgson and Jacobsen [30] proposed the concept of "expected distance under referral" for primary health care centers using the P-median hierarchical location-allocation model. Fahimnia et al. [14] investigated a two-objective location of mobile blood donation facilities in a blood supply network, which includes different levels including blood donors, mobile blood donation facilities (blood donation vehicles), local and regional blood donation centers, and hospitals (demand points). In the same year, Mestre et al. [31] presented two hierarchical location-allocation models with a demand under uncertainty to enhance the geographic access while minimizing the costs in the hospital network. Also, Hovav and Tsadikovich [32] proposed a facility location inventory problem to reduce the cost of the influenza vaccination program. Elalouf et al. [33] to reduce operating costs by repairing and maintaining blood sample collection chain have developed a model for facility location problem solving and proposed the dynamic programming (DP) algorithm and fully polynomial time approximation scheme (FPTAS) algorithm to solve it. Chaiwuttisak et al. [34] proposed a binary integer programming model for location-allocation problem in two-level based on goals of improving blood supply while reducing transport costs. Safaei et al. [35] proposed a location-allocation model for pharmacies in Chalus city according to the Group Purchase Organization (GPO) which is the proposed multiobjective model that was optimized using goal programming. Wang et al. [36] proposed a hierarchical location-allocation model to describe trade between social, economic, and environmental factors in health networks from the supply and demand perspective. Then, they solved the model by a bilevel multiobjective particle swarm optimization algorithm. Finally, Barzinpour et al. [37] proposed a hierarchical location-allocation model for health network design considering the referral system.

2.2. Facility Location Problems under Disruptions. In this section, primarily, we report a brief history of disruption in the systems and supply chain. Afterward, we review the studies that have been carried out in the field of health care. In the last decade, the problems under the disruption have been considered by many researchers. Drezner [38] conducted the first study of *Two Location Problems with Unreliable Facilities* and defined the P-Median and (p, q) problems by assuming that the facilities may be inactive. On the other hand, supply chain disruption orientation (SCDO) concept is considered as the first systematic empirical investigation for organizational responses to the disruptions of the supply chain, which was introduced by [39]. It is essential to carry out some research studies about various aspects of supply chain disruption such as strategic management [40, 41], strategic (resilience) management [42, 43], and risk management [44, 45]. The supply chain is highly affected by information flow, as well as goods and financial resource flows, and thus it is necessary to integrate these items to decline the vulnerabilities [46]. Another research by Cui et al. [47] and Shen et al. [48], which considered the stochastic scenario-based formulations, also has investigated the supply chain disruption. Furthermore, Peng et al. [12] decreased the risk of disruption for a logistics network under facility failure using p-robust. To solve the problem, a hybrid metaheuristic algorithm was employed based on genetic algorithms, local improvement, and the shortest pathway. Shishebori and Yousefi Babadi [49] addressed the designing problem of a robust and reliable medical service (MS) center location network by considering the disruption in the system and constraint on investment budget and p-robust constraints. At this time, An et al. [50] have designed an article to address potential risks and disruptions in emergency service planning that including the facility disruption risks, congestion in road traffic, and queuing delays in facilities. A scenario-based stochastic mixed-integer nonlinear program (MINLP) used the Lagrangian relaxation approach to solve. Zarrinpoor et al. [51] designed the reliable hierarchical location-allocation model for medical service networks in which they considered disruption in the facilities. To ensure the quality of services and demand, they added the queuing systems to their model. Finally, the model is formulated based on the two-stage optimization approach, and decision making is defined in two stages. To minimize the cost and time of emergency delivery of products to customers after a disaster, a biobjective robust optimization model has been designed with considering possible disruptions in facilities and routes and a Lagrangian relaxation and ε-constraint to solving the approach have been proposed [52]. To reduce greenhouse gas emissions in the biofuel supply chain network, Fattahi and Govindan [53] proposed a cost-effective multistep random program to show the impact of disruption risk dimensions and sustainability dimensions on biofuels. To reduce potential risks and disruptions in supply chain design, Sabouhi et al. [9] have provided an integrated

approach based on data envelopment analysis (DEA) and mathematical planning methods. First, the efficiency of potential suppliers is determined by fuzzy DEA, and then a two-stage possibilistic-stochastic programming model is created to select a supplier, and the results are examined in a pharmaceutical company for the application of the presented model. In the health supply chain section, Haghjoo et al. [54] proposed a dynamic robust location-allocation model to solve the disruption in the blood supply to hospitals and designed a scenario-based robust approach for the inherent uncertainty of the problem. Besides, to solve the large-scale problems, they proposed two metaheuristic algorithms, namely, the self-adaptive imperialist competitive and invasive weed optimization. In this regard, Hamdan and Diabat [19] designed a biobjective robust optimization model for the medical blood supply chain with considering disruption in the facilities. A Lagrangian relaxation-based algorithm is developed for solving large-scale instances. Table 1 shows how the proposed model covers all of these. The coding of columns of the problem type in Table 1 is also defined in Table 2.

According to Table 1, most of the research papers presented in the health supply chain section consider the model as a single level, and also, no research in the literature uses different aspects of capacity constraint, multiperiod, and hub simultaneously.

3. Problem Description

This paper is focused on a five-echelon multiobjective optimization program for the selection of suppliers and distributors. In this regard, the optimal quota allocation is determined with respect to disruption of suppliers and consideration of the distributor centers as a hub location-allocation mode. The relationships between the five echelons in the model are shown in Figure 1.

In this study, the proposed objective functions are characterized as follows: minimization of transactions costs with suppliers, minimization of expected purchasing costs from suppliers, minimization of expected percentages of delayed goods and returned goods in each distributor, as well as transportation cost in each echelon and fixed cost for distributor centers, and finally maximization of the expected scores for suppliers and total priority of product for customers.

The number of two suppliers is generally selected for each hub-center distributor. The second supplier is designated as the backup supplier for the first selected center. If the demand is not supplied by the first center because of disruption, the backup supplier will be allocated 100 percent of the quota.

Assumptions of the problem are denoted as follows:

Suppliers may be nonaccessible because of disruption

Delay in providing each quota is allowed

It is allowed to return the product to distributors by customers or other distributors

The problem is investigated in multiple periods

Each quota can be allocated to the second supplier for supporting the nonprovided demands, which cannot be supplied by the first supplier

Only one center is selected in each level of the distribution

3.1. Mathematical Model. This section is developed to address the proposed mathematical model for the problem. To do this, the mathematical model is given in equations (1)–(40). Table 3 represents the required notations for the models.

The objective functions are as follows:

$$\begin{aligned} Min\, z1:\ & \sum_k \sum_j \sum_p \sum_t \left(Q_{kjpt} C_{kjpt} Y_{kjt} \left(1 - R_k\right) + R_k Q_{kjpt} + \sum_{\substack{k \\ k \neq k}} \sum_j \sum_p \sum_t C_{kjpt} Y_{kjt} \right) \\ & + \sum_j F_j X_j + \sum_h F_h X_h + \sum_n F_n X_n + \sum_k \sum_j \sum_p \sum_t TS_{kjpt}\left(L_{kj}\right) Y_{kjt}\left(Q_{kjpt}\right)\left(1 - R_k\right) + R_k Q_{kjpt} \\ & \sum_{\substack{k \\ k \neq k}} \sum_j \sum_p \sum_t TS_{kjpt}\left(L_{kj}\right) Y_{kjt} + \\ & \sum_j \sum_h \sum_p \sum_t TS_{jhpt}\left(L_{jh}\right) \beta Y_{kjt} Q_{jhpt} + \sum_h \sum_n \sum_p \sum_t TS_{hnpt}\left(L_{hn}\right) Y_{jht} Q_{hnpt} + \sum_n \sum_i \sum_p \sum_t TS_{nipt}\left(L_{ni}\right) Y_{nit} Q_{nipt}, \end{aligned} \tag{1}$$

$$\text{Min } Z_2:\ \sum_k \sum_j \sum_p \sum_t \alpha_{kpt} CC_{kjpt} Y_{kjt}, \tag{2}$$

$$\text{Min } Z_3:\ \sum_j \sum_h \sum_p \sum_t h_{jpt} Q_{jhpt} Y_{jht} + \sum_h \sum_n \sum_p \sum_t h_{hpt} Q_{hnpt} Y_{hnt} + \sum_n \sum_i \sum_p \sum_t h_{npt} Q_{nipt} Y_{nit}, \tag{3}$$

Table 1: Classification of the related papers.

Articles	Problem Type	Health supply chain	System disruption	Network structure			Model features		Solution method	Case study
				Single level	Hierarchical	Hub	Multiperiod	Capacity		
Jacobs et al. [25]	FLP	✓		✓					Scenario base	✓
Zahiri et al. [26]	FLAP	✓		✓			✓		Robust possibilistic programming and GAMS	✓
Ünlüyurt and Tunçer. [27]	MCLP	✓		✓					CPLEX	✓
Khodaparasti et al. [28]	LAP	✓		✓			✓	✓	Outer approximation algorithm (AOA)	✓
Hodgson and Jacobsen. [30]	MHLAP	✓			✓				CPLEX	
Fahimnia et al. [14]	FLP	✓			✓		✓	✓	ε-constraint and Lagrangian relaxation and GAMS	
Mestre et al. [31]	MHLAP	✓			✓		✓	✓	ε-constraint and CPLEX	✓
Hovav and Tsadikovic [32]	FLIP	✓			✓		✓	✓	Heuristic algorithm	✓
Elalouf et al. [33]	FLP	✓			✓				DP algorithm and FPTAS algorithm	✓
Chaiwuttisak et al. [34]	FLAP	✓			✓			✓	CPLEX	✓
Safaei et al. [35]	HGPP	✓			✓				Weighted goal programming (WGP) and Lingo	✓
Li et al. (2018)	HFLAP	✓			✓				(BLMOPSO) algorithm	✓
Barzinpour et al. [37]	HLAP	✓			✓			✓	ε-constraint	
Drezner [38]	PQCP		✓	✓					Heuristic algorithm	
Cui et al. [47]	UFLP		✓	✓					Lagrangian relaxation	
Shen et al. [48]	UFLP		✓	✓					Approximation algorithm	✓
Peng et al. [12]	LNDP		✓	✓				✓	Genetic algorithm	
Shishebori and Yousefi Babadi [49]	FL/NDP	✓	✓	✓				✓	CPLEX	✓
An et al. [50]	FLP		✓	✓					Lagrangian relaxation	✓
Zarrinpoor et al. [51]	MHLAP	✓	✓		✓			✓	Benders decomposition (BD)	✓
Diabat et al. [52]	HFLAP		✓		✓		✓	✓	Lagrangian relaxation and ε-constraint	✓
Fattahia and Govindan [53]	FLP		✓		✓		✓	✓	Rolling horizon procedure	✓
Sabouhi et al. [9]	LIP	✓	✓		✓			✓	Fuzzy DEA	✓
Haghjoo et al. [54]	DRLAP	✓	✓	✓			✓	✓	Robust optimization and two metaheuristic	✓
Hamdan and Diabat. [19]	HFLAP	✓	✓		✓		✓	✓	Lagrangian relaxation	✓
Current study	HHLAP	✓	✓		✓	✓	✓	✓	Fuzzy multichoice goal programming model and *R* solver	✓

Table 2: Coding of problem type in Table 1.

Problem type	
Facility location problem	FLP
Facility location inventory problem	FLIP
Maximal coverage location problem	MCLP
Hierarchical group purchasing problem	HGPP
Hierarchical location-allocation problem	HLAP
Logistic network design problem	LNDP
Median hierarchical location-allocation problem	MHLAP
Hierarchical hub location-allocation problem	HHLAP
Location-allocation problem	LAP
Location inventory problem	LIP
Facility location-allocation problem	FLAP
Hierarchical facility location-allocation problem	HFLAP
(p, q)-center problem	PQCP
Facility location/network design problem	FL/NDP
Dynamic robust location-allocation problem	DRLAP

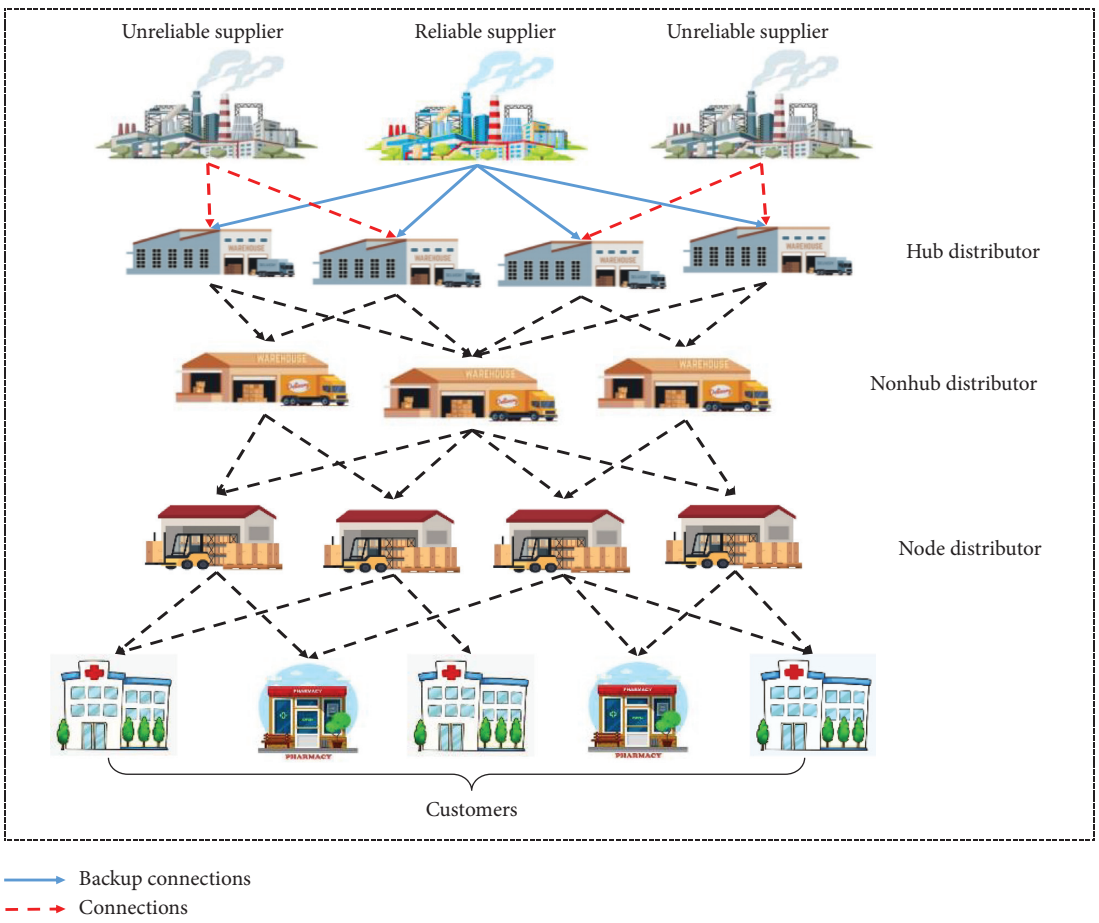

Figure 1: General view of the problem.

$$\text{Min } Z_4: \sum_j \sum_h \sum_p \sum_t s_{jpt} Q_{jhpt} Y_{jht} + \sum_h \sum_n \sum_p \sum_t s_{hpt} Q_{hnpt} Y_{hnt} + \sum_n \sum_i \sum_p \sum_t s_{npt} Q_{nipt} Y_{nit}, \tag{4}$$

$$\text{Max } Z_5: \sum_k \sum_j \sum_t q_k Y_{kjt}, \tag{5}$$

Table 3: Notations.

$\mathbf{C_{kjpt}}$: unit purchasing price of product p given by supplier k to hub distributor j at period t
$\mathbf{CC_{kjpt}}$: transaction costs of providing product p via supplier k to hub distributor j at period t
$\mathbf{TS_{kjpt}}$: unit transportation price of product p from supplier k to hub distributor j at period t
$\mathbf{TS_{jhpt}}$: unit transportation price of product p from hub distributor j to nonhub distributor h at period t
$\mathbf{TS_{hnpt}}$: unit transportation price of product p from nonhub distributer h to node distributor n at period t
β: rate of discount for the transference of products from hub distributors to nonhub distributors
$\alpha_{\mathbf{kpt}}$: binary parameter (equal to one if product p can be supplied by supplier k at period t; otherwise, zero)
h_{jpt} : percentage of returned product p to hub distributor j at period t
h_{hpt} : percentage of returned product p to nonhub distributor h at period t
h_{npt} : percentage of returned product p to node distributor n at period t
s_{jpt} : percentage of late delivered product p by hub distributor j at period t
s_{hpt} : percentage of late delivered product p by nonhub distributor h at period t
s_{npt} : percentage of late delivered product p by node distributor n at period t
L_{jh}: distance from hub distributor j to nonhub distributor h
L_{hn}: distance from nonhub distributor h to node distributor n
$\mathbf{Y_{kjt}}$: binary parameter (equal to one if the trade from supplier k to hub distributor j at period t is set; otherwise, zero)
$\mathbf{Y_{jht}}$: binary parameter (equal to one if the trade from hub distributor j to nonhub distributor h at period t is set; otherwise, zero)
$\mathbf{Y_{hnt}}$: binary parameter (equal to one if the trade from nonhub distributor h to node distributor n at period t is set; otherwise, zero)
$\mathbf{Y_{nit}}$: binary parameter (equal to one if the trade from node distributor n to customer i at period t is set; otherwise, zero)
$\mathbf{X_j}$: binary parameter (equal to one if the hub distributor j is established; otherwise, zero)
Q_{kjpt}: optimal order of product p from supplier k to hub distributor j at period t
Q_{jhpt}: optimal order of product p from hub distributor j to nonhub distributor h at period t
Q_{hnpt}: optimal order of product p from nonhub distributor h to node distributor n at period t
Q_{nipt}: optimal order of product p from node distributor n to customer i at period t
X_h: binary parameter (equal to one if the nonhub distributor h is established; otherwise, zero)

$$\text{Max } Z_6\text{: } \sum_n \sum_i \sum_p \sum_t \lambda_{npt} Q_{nipt} Y_{nit}. \tag{6}$$

Equation (1) gives the first objective function, which is developed to minimize the total purchase cost from suppliers considering disruption of them, also the total fixed cost of distributors, and total transportation cost. Equation (2) characterizes the second objective function. It minimizes the total transaction cost of products between suppliers and hub distributors. The transaction cost is comprised of those fixed costs for the establishment of relations and cooperation with suppliers such as supplier selection, negotiations for contracting, an inspection of goods, and quality control. Equation (3) denotes the third objective function. This function is aimed to minimize the expected total percentages of the returned products. This type of cost will occur if each distributor has not the ability to supply the next level of distributor or customer demand with the expected quality. Equation (4) represents the fourth objective function. It minimizes the expected total percentage of the late delivered products. The fifth objective function is developed in equation (5). This objective function maximizes the expected scores for the selected suppliers based on a conducted periodical evaluation. Equation (6) describes the sixth objective function. This function leads to maximize the priority of the supplied products for customers.

The constraints are formulated for the optimization model as the following equations:

$$\sum_k \sum_p \left(Q_{kjpt} Y_{kjt} (1 - R_k) + Q_{kjpt} (R_k) \sum_{\substack{k \\ k \neq k}} Y_{kjt} \right) \leq W_j \quad \forall j, t, \tag{7}$$

$$\sum_j \sum_p Q_{jhpt} Y_{jht} \leq W_h \quad \forall h, t, \tag{8}$$

$$\sum_h \sum_p Q_{hnpt} Y_{hnt} \leq W_n \quad \forall n, t, \tag{9}$$

$$\sum_n Q_{nipt} Y_{nit} \leq D_{ipt} \quad \forall i, p, t, \tag{10}$$

$$\sum_h Q_{jhpt} Y_{jht} \leq \sum_k Q_{kjpt} Y_{kjt} \quad \forall j, p, t, \tag{11}$$

$$\sum_n Q_{hnpt} Y_{hnt} \leq \sum_j Q_{jhpt} Y_{jht}, \quad \forall h, p, t, \tag{12}$$

$$\sum_i Q_{nipt} Y_{nit} \leq \sum_h Q_{hnpt} Y_{hnt}, \quad \forall n, p, t, \tag{13}$$

$$\sum_h \sum_t h_{jpt} Q_{jhpt} Y_{jht} \leq H_{jp} \quad \forall j, p, \tag{14}$$

$$\sum_{n}\sum_{t} h_{hpt}\cdot Q_{hnpt}\cdot Y_{hnt} \le H_{hp}, \quad \forall h, p, \tag{15}$$

$$\sum_{i}\sum_{t} h_{npt}\cdot Q_{nipt}\cdot Y_{nit} \le H_{np}, \quad \forall n, p, \tag{16}$$

$$\sum_{h}\sum_{t} s_{jpt}\cdot Q_{jhpt}\cdot Y_{jht} \le S_{jp}, \quad \forall j, p, \tag{17}$$

$$\sum_{n}\sum_{t} s_{hpt}\cdot Q_{hnpt}\cdot Y_{hnt} \le S_{hp}, \quad \forall h, p, \tag{18}$$

$$\sum_{n}\sum_{t} s_{hpt}\cdot Q_{hnpt}\cdot Y_{hnt} \le S_{hp}, \quad \forall n, p, \tag{19}$$

$$\sum_{k} Y_{kjt} \le 2, \quad \forall j, t, \tag{20}$$

$$\sum_{j} Y_{jht} \le 1, \quad \forall h, t, \tag{21}$$

$$\sum_{h} Y_{hnt} \le 1, \quad \forall n, t, \tag{22}$$

$$\sum_{n} Y_{nit} \le 1, \quad \forall i, t, \tag{23}$$

$$Y_{kjt} \le \alpha_{kpt}, \quad \forall j, p, t, \tag{24}$$

$$Y_{kjt} \le X_{j}, \quad \forall k, j, t, \tag{25}$$

$$Y_{jht} \le X_{j}, \quad \forall j, h, t, \tag{26}$$

$$Y_{jht} \le X_{h}, \quad \forall j, h, t, \tag{27}$$

$$Y_{hnt} \le X_{h}, \quad \forall h, n, t, \tag{28}$$

$$Y_{hnt} \le X_{n}, \quad \forall h, n, t, \tag{29}$$

$$Q_{kjpt}, Q_{jhpt}, Q_{hnpt}, Q_{nipt} \ge 0, \quad \forall k, j, h, n, i, p, t, \tag{30}$$

$$Y_{kjt}, Y_{jht}, Y_{hnt}, Y_{nit}, X_{j}, X_{h}, X_{n} \in \{0, 1\}, \quad \forall k, j, h, n, i, t. \tag{31}$$

Constraints (7)–(9) ensure that the total products which are supplied by each distributor do not exceed their initial planned capacities. They ensure that the orders do not violate the capacity of hub distributors j, h, and n. Constraint (10) refers to satisfaction of the buyer's demand for each product at each time period by the last echelon of distributors. Constraints (11)–(13) control the feasibility of supply of goods in every echelon of supply chain. Constraint (11) says for each distributor at each time period if there is a trade from a supplier, then an order less than or equal to the supplier trade could be set to a nonhub distributor. Constraints (14)–(16) guarantee that the total percentages of the returned product for each product at all periods of time do not exceed the maximum acceptable percentage of each product for each distributor. Constraints (17)–(19) guarantee that the total percentages of late delivered product for each product at all periods of time do not exceed the maximum acceptable percentage of each product for each distributor. Constraint (20) controls the number of the selected trade between each hub distributor and suppliers which must be less than or equal 2 in our problem. Indeed, both suppliers require to supply products, whereas the second supplier is considered as a backup for the first supplier in the disruption condition. Constraints (21)–(23) reveal that only one trade must occur between distributors, as well as node distributors and customers. Constraints (24)–(29) control that each supplier to be selected before to be allocated a quota. It ensures that if the hub or node distributor is not selected, the right hand side is zero, and thus the trades in the left hand side could not be set. Constraints (30) and (31) indicate the given values for the decision variables in the model.

3.2. Solution Method. In this paper, a fuzzy multichoice goal programming model is utilized to solve the proposed model. In this approach, three goals (choices) are considered for each objective function. The model chooses a goal among the three choices for each function, and somehow the answer of all objective functions is close to their optimal answer. Due to the ease and accuracy in solving the model, a linearized model is proposed for this method [55]. Table 4 and constraints (20)–(28) are represented to introduce new symbols for the model and linearized model of the fuzzy three-choice goal programming method, respectively. Additionally, constraints (6)–(19) are repeated for this model.

$$\max zt = f_1\mu_1 + f_2\mu_2 + f_3\mu_3 + f_4\mu_4 + f_5\mu_5 + f_6\mu_6, \tag{32}$$

$$\mu_1 \le 1 - \frac{z_1 - \widetilde{g}_1}{d_1^-}u_1 + \frac{z_1 - \widetilde{g}_2}{d_2^-}(v_1 - u_1) + \frac{z_1 - \widetilde{g}_3}{d_3^-}(v_2 - u_1), \tag{33}$$

$$\mu_2 \le 1 - \frac{z_2 - \widetilde{g}_4}{d_4^-}u_2 + \frac{z_2 - \widetilde{g}_5}{d_5^-}(v_3 - u_2) + \frac{z_2 - \widetilde{g}_6}{d_6^-}(v_4 - u_2), \tag{34}$$

$$\mu_3 \le 1 - \frac{z_3 - \widetilde{g}_7}{d_7^-}u_3 + \frac{z_3 - \widetilde{g}_8}{d_7^-}(v_5 - u_3) + \frac{z_3 - \widetilde{g}_9}{d_9^-}(v_6 - u_3), \tag{35}$$

$$\mu_4 \le 1 - \frac{z_4 - \widetilde{g_{10}}}{d_{10}^-}u_4 + \frac{z_4 - \widetilde{g_{11}}}{d_{11}^-}(v_7 - u_4) + \frac{z_4 - \widetilde{g_{12}}}{d_{12}^-}(v_8 - u_4) \tag{36}$$

$$\mu_5 \le 1 - \frac{\widetilde{g_{13}} - z_5}{d_{13}^+}u_5 + \frac{\widetilde{g_{14}} - z_5}{d_{14}^+}(v_9 - u_5) + \frac{\widetilde{g_{15}} - z_5}{d_{15}^+}(v_{10} - u_5), \tag{37}$$

Table 4: The fuzzy three-choice goal programming model. Formula (32) refers to maximization of the membership function for each single objective function.

Parameters
$\widetilde{\mathbf{g}_1} \dots \widetilde{\mathbf{g}_{18}}$:considered fuzzy goals for functions
$\mathbf{f}_1 \dots \mathbf{f}_6$: the weight of the objective functions of (1) to (6) in the general objective function
$d_1^- \dots d_{12}^-$: maximum negative permissible deviation of each aspiration choice of the relevant objective function value
$d_{13}^+ \dots d_{18}^+$: maximum positive permissible deviation of each aspiration choice of the relevant objective function value
Variables
$\mathbf{v}_1 \dots \mathbf{v}_{12}$: binary variable aspiration choice
$\mu_1 \dots \mu_6$: the membership function of z_1 to z_6

$$\mu_6 \le 1 - \frac{\widetilde{g_{16}} - z_6}{d_{16}^+} u_6 + \frac{\widetilde{g_{17}} - z_5}{d_{17}^+} (v_{11} - u_6) + \frac{\widetilde{g_{18}} - z_6}{d_{18}^+} (v_{12} - u_6), \tag{38}$$

$$\begin{aligned} u_1 &\le \begin{cases} v_1 \\ v_2 \end{cases}, \\ u_2 &\le \begin{cases} v_3 \\ v_4 \end{cases}, \\ u_3 &\le \begin{cases} v_5 \\ v_6 \end{cases}, \\ u_4 &\le \begin{cases} v_7 \\ v_8 \end{cases}, \\ u_5 &\le \begin{cases} v_9 \\ v_{10} \end{cases}, \\ u_6 &\le \begin{cases} v_{11}, \\ v_{12}, \end{cases} \end{aligned} \tag{39}$$

$$\begin{aligned} u_1 &\ge v_1 + v_2 - 1, \\ u_2 &\ge v_3 + v_4 - 1, \\ u_3 &\ge v_5 + v_6 - 1, \\ u_4 &\ge v_7 + v_8 - 1, \\ u_5 &\ge v_9 + v_{10} - 1, \\ u_6 &\ge v_{11} + v_{12} - 1, \end{aligned} \tag{40}$$

$$u_1 \cdot u_{10} \ge 0, \tag{41}$$

$$v_1 \cdot v_{12} \in \{0, 1\}, \tag{42}$$

$$\mu_1 \cdot \mu_6 \ge 0. \tag{43}$$

Constraints (33)–(38) are utilized to control the membership functions of Z_1 to Z_6. They are used for minimization of Z_1 to Z_6; the maximum value of the negative permissible deviation for the objective function of any aspiration value is considered in the fraction denominator of these functions. Besides, because Z_5 and Z_6 are maximum, the maximum value of the positive deviation for the objective function of any aspiration value is applied in the denominator of the fraction. Constraint (39) is dealt with the limitation of choosing the aspiration, which demonstrates that the model can select an aspiration in each function. Constraint (40) is concerned with the linearization of the model. Constraints (41)–(43) represent the type and range of the variables.

In Section 4, a real numerical case study is considered for this model.

4. Numerical Results

In this section, a numerical case study is surveyed for asthma-specific medicines. Accordingly, the real data of Cobel Darou pharmaceutical company were collected in 2019. Also, it is noted that the R optimization solver is utilized to solve this real example. The value of parameters is specified as follows. The exact values are represented for the demand and probability of supplier disruption in Table 5 and Table 6, respectively. It would be valuable to denote that the buyer of pharmacies is located in 4 cities of Iran comprising Tehran, Esfahan, Ahvaz, and Mashhad which is demonstrated in Figure 2. The demands for the investigated centers are considered as 5 of the highest level of applicants in each city, which are indicated to be expressed for cities with the indexes 1 to 20, respectively. The value of other parameters is declared on the base of the interval in Table 7 due to improving expression in the paper. The whole exact value of parameters is in the introduced intervals, and generally, the value has been obtained for the parameters of q and λ using the well-known AHP methods [56].

It is obvious that there are 2 suppliers for the selected pharmacies, with the names of AstraZeneca and GSK, which are introduced by the indexes $k = 1$ and $k = 2$ in the model, respectively. In addition, indexes $p = 1$ to $p = 5$ are devoted to the pharmacies with the names of Pulmicort, Symbicort, Flixotide, Seretide, and Rhinocort, respectively.

Furthermore, the values of the first choice are considered for aspirations as the optimal value of the single function, and consequently, the second and third choices are considered for aspirations with 10 and 20% variations, respectively. It is done in comparison with the optimal value (increase for minimization and decrease for maximization functions). The maximum negative and positive deviations for each choice and the weight of the objective functions are also determined by experts.

The presented model has been solved based on these parameters. Table 8 gives the results of the objective functions for the numerical example.

The obtained values are considered for objective function as rational results. These values are proportionate to the expectation level with the emphasis on actual parameters. In

Table 5: The values of demands.

D_{ipt}		$p=1$	$p=2$	$p=3$	$p=4$	$p=5$
$i=1$	$t=1$	570	640	120	346	90
	$t=2$	1001	720	456	221	54
	$t=3$	375	370	0	408	60
	$t=4$	367	10	15	25	5
$i=2$	$t=1$	484	60	123	423	110
	$t=2$	1965	60	310	1046	68
	$t=3$	1687	115	10	890	0
	$t=4$	236	130	80	75	50
$i=3$	$t=1$	352	128	651	780	15
	$t=2$	2005	1328	450	654	87
	$t=3$	426	147	12	38	26
	$t=4$	190	0	30	580	0
$i=4$	$t=1$	269	56	98	69	52
	$t=2$	706	244	53	471	22
	$t=3$	54	10	0	30	10
	$t=4$	10	168	0	54	1
$i=5$	$t=1$	189	120	94	39	0
	$t=2$	1007	23	152	430	0
	$t=3$	52	0	26	15	164
	$t=4$	67	0	11	25	52
$i=6$	$t=1$	406	357	83	124	351
	$t=2$	0	401	112	131	25
	$t=3$	18	1314	12	1807	173
	$t=4$	8	0	4	110	0
$i=7$	$t=1$	127	11	87	250	56
	$t=2$	21	29	2	469	32
	$t=3$	1	79	23	16	5
	$t=4$	36	163	0	123	1
$i=8$	$t=1$	298	0	36	14	169
	$t=2$	47	101	149	0	42
	$t=3$	17	22	11	0	0
	$t=4$	136	0	170	0	0
$i=9$	$t=1$	230	36	1113	14	75
	$t=2$	126	0	26	159	41
	$t=3$	1008	85	0	21	7
	$t=4$	13	13	0	5	6
$i=10$	$t=1$	552	11	0	39	63
	$t=2$	123	25	0	137	1
	$t=3$	63	140	0	11	1
	$t=4$	20	63	102	1	0
$i=11$	$t=1$	363	160	498	260	1109
	$t=2$	106	350	52	11	114
	$t=3$	106	113	110	0	15
	$t=4$	98	39	110	231	18
$i=12$	$t=1$	630	1100	98	469	0
	$t=2$	117	1100	174	47	112
	$t=3$	12	0	24	58	0
	$t=4$	69	1100	16	132	112
$i=13$	$t=1$	392	99	613	26	95
	$t=2$	20	36	59	2	41
	$t=3$	3	48	7	26	0
	$t=4$	11	5	7	2	59
$i=14$	$t=1$	123	56	635	98	1115
	$t=2$	4	169	15	135	52
	$t=3$	46	110	12	135	0
	$t=4$	26	0	19	0	569

Table 5: Continued.

$\mathbf{D}_{ipt}$		$p=1$	$p=2$	$p=3$	$p=4$	$p=5$
$i=15$	$t=1$	1405	690	120	75	0
	$t=2$	55	2	20	25	101
	$t=3$	236	3	2	0	141
	$t=4$	10	95	46	12	10
$i=16$	$t=1$	460	15	300	169	75
	$t=2$	145	10	100	115	115
	$t=3$	84	52	250	50	77
	$t=4$	41	63	22	59	55
$i=17$	$t=1$	290	504	605	130	20
	$t=2$	1296	575	123	102	109
	$t=3$	232	325	457	25	64
	$t=4$	85	240	110	90	74
$i=18$	$t=1$	40	500	20	134	23
	$t=2$	818	250	17	79	125
	$t=3$	196	215	68	230	513
	$t=4$	70	100	105	300	420
$i=19$	$t=1$	142	235	500	151	495
	$t=2$	210	320	120	100	858
	$t=3$	520	300	407	72	21
	$t=4$	400	326	98	510	600
$i=20$	$t=1$	190	440	105	410	480
	$t=2$	440	4	120	100	80
	$t=3$	193	80	220	25	110
	$t=4$	770	80	540	312	100

Table 6: The values of disruption of suppliers.

$\mathbf{R}_1$	5.87%
$\mathbf{R}_2$	3.61%

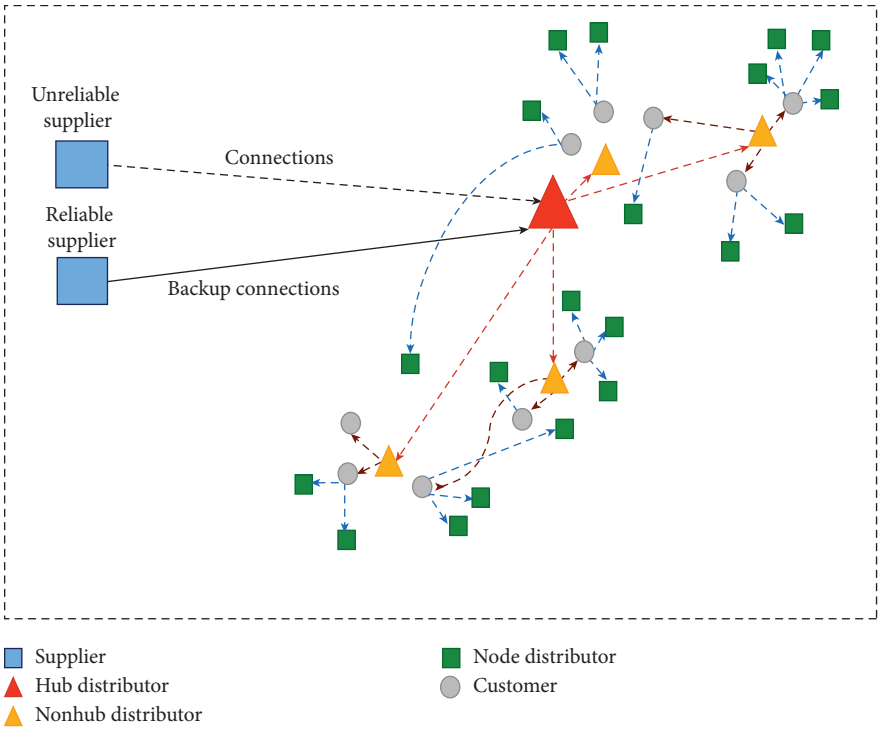

Figure 2: The case study's network topology.

Table 7: The intervals of parameters.

TS	[50,150]
W	[5000,10000]
C	[200,850]
CC	[20,50]
h	[0, 0.1]
s	[0.01, 0.25]
H	[0.1,0.2]
S	[0.1,0.4]
F	[4000,10000]
q	[3,8]
L	$[5 \times 10^4,\ 9 \times 10^5\ ]$
λ	[2,9]
β	35%
α	$\in\{0, 1\}$

Table 8: The membership functions of a numerical example.

μ_1	0.91
μ_2	0.89
μ_3	0.72
μ_4	0.67
μ_5	0.80
μ_6	0.81

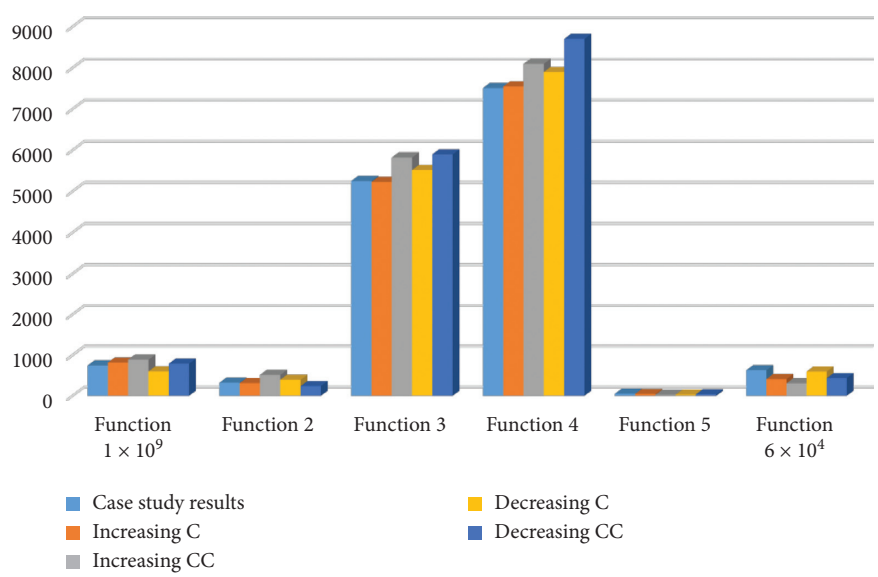

Figure 3: The results of function with alteration values of C and CC in four examples.

the next section, the sensitivity analysis is investigated for the case study by changing the value of some parameters.

5. Sensitivity Analysis

In this section, an attempt has been performed to prove the authority of the presented model. Therefore, it is essential to analyze the model by changing the values of some parameters. The alternations are addressed in the following paragraphs, and their results are depicted by the diagram. To develop a sensitivity analysis, the first step has been associated with changing the interval of values of C and CC. The attained consequences are shown in Figure 3. The next step is focused on changing the range of h and q. The outcomes are demonstrated in Figure 4. In the last step, the values of q and R are changed and their results are indicated in Figure 5.

In these examples, it is obvious that the value of functions proportionally alters with the fluctuation of parameters. Indeed, all of them correctly respond to any alterations. Increment and decrement of the values of C and CC have virtually effect on all function. According to the formulas of the objective functions, increasing or decreasing the values of C and CC directly affects the first and second objective functions, respectively, and indirectly affects other

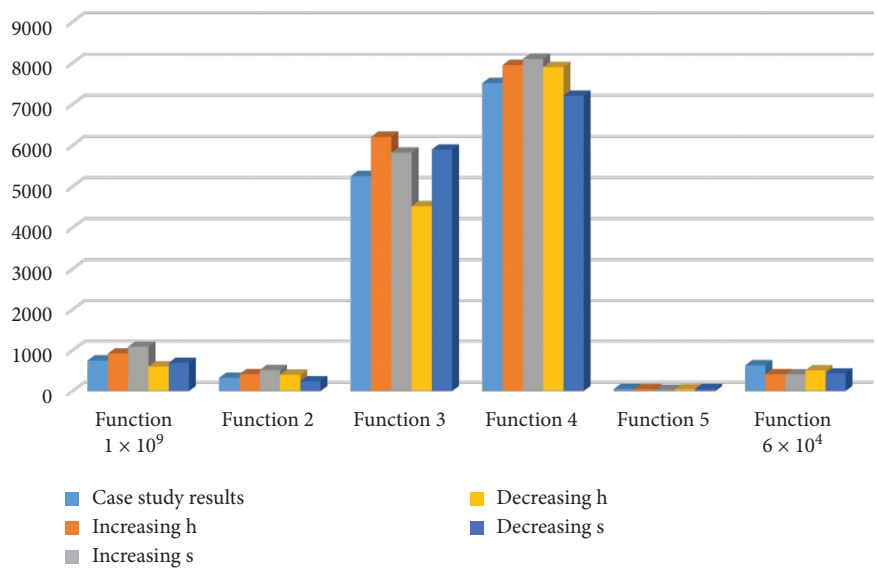

Figure 4: The results of function with alteration values of h and s in four examples.

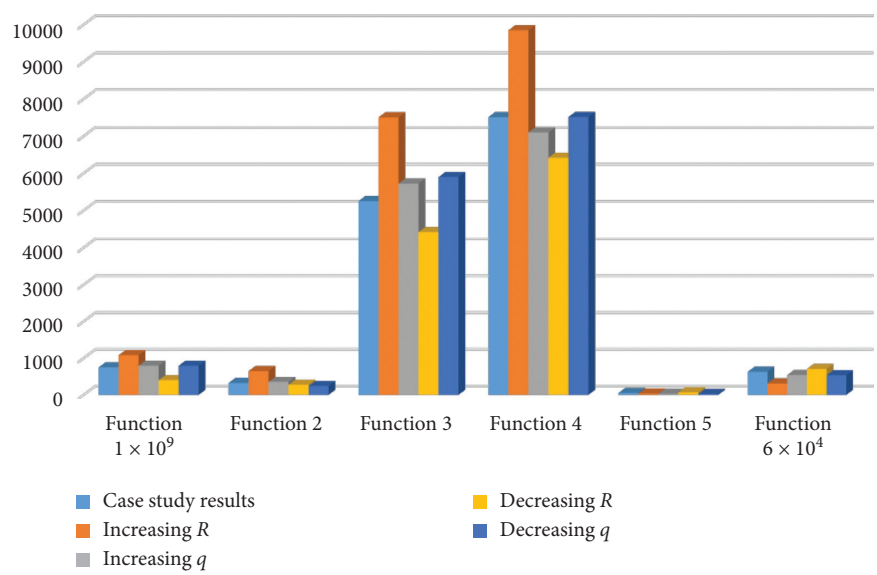

Figure 5: The results of function with alteration values of R and q in four examples.

functions. Increasing or decreasing the value of C has not had such an effect on the objective functions, while increasing or decreasing the value of CC has a more significant effect on the objective functions than C. However, this effect is not to improve the performance of the functions, Because objective functions 1 to 4 are of type Min and objective functions 5 and 6 are of type Max and by increasing the value of CC, the values of objective functions 1 to 4 increased and the values of objective functions 5 and 6 decreased, and by decreasing the value of CC, only the objective function 2 improved slightly in terms of performance. Furthermore, variations in the values of h and s have expected reactions, and according to the above analysis, we can conclude that the values of the objective functions improved collectively only through decreasing the value of h. Finally, increasing and decreasing the value of q have not had such an effect on the objective functions. However, the most important repercussion is reached by variation in R. The functionality of all functions improves by reducing the value of R, and by increasing the values of R, all functions become more undesirable than the optimal results. These results demonstrate the magnitude of surveying the disruptive conditions in supply chain management. The dynamic and inaccurate nature of the quantity and quality of manufactured products has created a high degree of uncertainty and risk in supply chains. Therefore, it is necessary to identify and formulate these kinds of risks. Additionally, the uncertain mode of supplier disruption probability brings the model closer to the real-world model. Eventually, it is vivid that the validity of the modeling process is proved through this analysis.

6. Conclusions and Further Research Ideas

In this paper, the hub location-allocation problem was studied to optimize six objective functions such as minimization of transaction costs, delayed goods, returned goods, and total fixed cost. Medicine unreliability problem is one of the most important issues in health supply chain management. This study tries to help the decision makers in health management institutions to optimize the distribution activities. It is worth noting that the parameters of supplier disruption probabilities were considered as uncertain parameters. An authentic case study was exerted for health supply chain management, and then it was investigated via the fuzzy multichoice goal programming method in *R* optimization solver. According to these results, it is certified that the introduced model is proper and adaptable for problems in real-world situations. Also, sensitivity analyses were considered with respect to variations in parameters, and the importance of the *R* parameter is clearly shown in a way that if the risks and disruptions in the supply chain are properly identified and addressed for reducing it, all the expected goals in the supply chain management can be achieved, which generally includes cost reduction, minimization of expected percentages of delayed and returned goods, and increase customer satisfaction. This evaluation procedure confirms the significance and validity of the recommended model.

Some limitations of the study are the traffic situation consideration during the distribution time which affect of the delayed products. The truck load layout design could be considered for the last echelon. The vehicle types and capacities could improve the problem design.

As further research studies in this area, it is possible to use multiobjective metaheuristic algorithms and multicriteria decision-making methods for the selection of suppliers and distributors. In addition, various types of supply risks can also be considered for analyzing the process. Other extensions can expand the model and represent other benefits of a supply chain for the achievement of a win-win position.

Data Availability

The data used to support the study are available from the corresponding author upon request.

Conflicts of Interest

The authors declare that they have no conflicts of interest.

References

[1] N. Rego, J. Claro, and J. Pinho de Sousa, "A hybrid approach for integrated healthcare cooperative purchasing and supply chain configuration," *Health Care Management Science*, vol. 17, no. 4, pp. 303–320, 2014.

[2] N. Habidin, N. A. Shazali, M. Ithnin, Z. Zainol, N. Salleh Hudin, and W. S. W. Mustaffa, "A review of supply chain innovation and healthcare performance in healthcare industry," *Performance in Supply Chain Management (SCM)*, vol. 35, pp. 195–200, 2015.

[3] R. Uthayakumar and S. Priyan, "Pharmaceutical supply chain and inventory management strategies: optimization for a pharmaceutical company and a hospital," *Operations Research for Health Care*, vol. 2, no. 3, pp. 52–64, 2013.

[4] C. W. Craighead, J. Blackhurst, M. J. Rungtusanatham, and R. B. Handfield, "The severity of supply chain disruptions: design characteristics and mitigation capabilities," *Decision Sciences*, vol. 38, no. 1, pp. 131–156, 2007.

[5] M. Taghi, A. Nedjati, and R. Kazemi, "Solving health care facility location problems with new heuristic algorithm method," *International Journal Of Modeling and Optimization*, vol. 3, pp. 12–14, 2013.

[6] N. Agami, M. Saleh, and M. Rasmy, "Supply chain performance measurement approaches: review and classification," *Journal of Organizational Management Studies*, vol. 2012, Article ID 872753, 20 pages, 2012.

[7] N. Privett and D. Gonsalvez, "The top ten global health supply chain issues: perspectives from the field," *Operations Research for Health Care*, vol. 3, no. 4, pp. 226–230, 2014.

[8] J.-M. Lawrence, N. U. Ibne Hossain, R. Jaradat, and M. Hamilton, "Leveraging a Bayesian network approach to model and analyze supplier vulnerability to severe weather risk: a case study of the U.S. pharmaceutical supply chain following Hurricane Maria," *International Journal of Disaster Risk Reduction*, vol. 49, Article ID 101607, 2020.

[9] F. Sabouhi, M. S. Pishvaee, and M. S. Jabalameli, "Resilient supply chain design under operational and disruption risks considering quantity discount: a case study of pharmaceutical supply chain," *Computers & Industrial Engineering*, vol. 126, pp. 657–672, 2018.

[10] H. Abolghasemi, M. H. Radfar, M. Tabatabaee, N. S. Hosseini-Divkolayee, and F. M. Burkle, "Revisiting blood transfusion preparedness: experience from the Bam earthquake response," *Prehospital and Disaster Medicine*, vol. 23, no. 5, pp. 391–394, 2008.

[11] N. Aydin and A. Murat, "A swarm intelligence based sample average approximation algorithm for the capacitated reliable facility location problem," *International Journal of Production Economics*, vol. 145, no. 1, pp. 173–183, 2013.

[12] P. Peng, L. V. Snyder, A. Lim, and Z. Liu, "Reliable logistics networks design with facility disruptions," *Transportation Research Part B: Methodological*, vol. 45, no. 8, pp. 1190–1211, 2011.

[13] WHO, *Corona Virus Disease (COVID-19) Outbreak Situation. 1 June 2020*, WHO, Geneva, Switzerland, 2020, https://www.who.int/emergencies/diseases/novel-coronavirus-2019.

[14] B. Fahimnia, A. Jabbarzadeh, A. Ghavamifar, and M. Bell, "Supply chain design for efficient and effective blood supply in disasters," *International Journal of Production Economics*, vol. 183, pp. 700–709, 2017.

[15] P. Bogaert, T. Bochenek, A. Prokop, and A. Pilc, "A qualitative approach to a better understanding of the problems underlying drug shortages, as viewed from Belgian, French and the European union's perspectives," *PLoS One*, vol. 10, no. 5, Article ID e0125691, 2015.

[16] K. Pauwels, S. Simoens, M. Casteels, and I. Huys, "Insights into European drug shortages: a survey of hospital pharmacists," *PLoS One*, vol. 10, no. 3, Article ID e0119322, 2015.

[17] J. De Vries and R. Huijsman, "Supply chain management in health services: an overview," *Supply Chain Management: An International Journal*, vol. 16, no. 3, pp. 159–165, 2011.

[18] S. PrasannaVenkatesan and M. Goh, "Multi-objective supplier selection and order allocation under disruption risk," *Transportation Research Part E: Logistics and Transportation Review*, vol. 95, pp. 124–142, 2016.

[19] B. Hamdan and A. Diabat, "Robust design of blood supply chains under risk of disruptions using Lagrangian relaxation," *Transportation Research Part E: Logistics and Transportation Review*, vol. 134, Article ID 101764, 2020.

[20] T.-M. Choi, "Innovative "bring-service-near-your-home" operations under corona-virus (COVID-19/SARS-CoV-2) outbreak: can logistics become the messiah?" in *Transportation Research Part E: Logistics and Transportation Review*Elsevier, Amsterdam, Netherlands, 2020.

[21] D. Ivanov, "Predicting the impacts of epidemic outbreaks on global supply chains: a simulation-based analysis on the coronavirus outbreak (COVID-19/SARS-CoV-2) case," *Transportation Research Part E: Logistics and Transportation Review*, vol. 136, Article ID 101922, 2020.

[22] K. Govindan, H. Mina, and B. Alavi, "A decision support system for demand management in healthcare supply chains considering the epidemic outbreaks: a case study of coronavirus disease 2019 (COVID-19)," *Transportation Research Part E: Logistics and Transportation Review*, vol. 138, Article ID 101967, 2020.

[23] O. Aptel and H. Pourjalali, "Improving activities and decreasing costs of logistics in hospitals: a comparison of U.S. and French hospitals," *The International Journal of Accounting*, vol. 36, no. 1, pp. 65–90, 2001.

[24] P. Harper, A. K. Shahani, J. E. Gallagher, and C. Bowie, "Planning health services with explicit geographical considerations: a stochastic location–allocation approach," *Omega*, vol. 33, no. 2, pp. 141–152, 2005.

[25] D. A. Jacobs, M. N. Silan, and B. A. Clemson, "An analysis of alternative locations and service areas of American red cross blood facilities," *Interfaces*, vol. 26, no. 3, pp. 40–50, 1996.

[26] B. Zahiri, R. Tavakkoli-Moghaddam, and M. S. Pishvaee, "A robust possibilistic programming approach to multi-period location-allocation of organ transplant centers under uncertainty," *Computers & Industrial Engineering*, vol. 74, pp. 139–148, 2014.

[27] T. Ünlüyurt and Y. Tunçer, "Estimating the performance of emergency medical service location models via discrete event simulation," *Computers & Industrial Engineering*, vol. 102, pp. 467–475, 2016.

[28] S. Khodaparasti, M. E. Bruni, P. Beraldi, H. R. Maleki, and S. Jahedi, "A multi-period location-allocation model for nursing home network planning under uncertainty," *Operations Research for Health Care*, vol. 18, pp. 4–15, 2018.

[29] S.-U. Rahman and D. K. Smith, "Use of location-allocation models in health service development planning in developing nations," *European Journal of Operational Research*, vol. 123, no. 3, pp. 437–452, 2000.

[30] M. J. Hodgson and S. K. Jacobsen, "A hierarchical location-allocation model with travel based on expected referral distances," *Annals of Operations Research*, vol. 167, no. 1, pp. 271–286, 2008.

[31] A. M. Mestre, M. D. Oliveira, and A. P. Barbosa-Póvoa, "Location-allocation approaches for hospital network planning under uncertainty," *European Journal of Operational Research*, vol. 240, no. 3, pp. 791–806, 2015.

[32] S. Hovav and D. Tsadikovich, "A network flow model for inventory management and distribution of influenza vaccines through a healthcare supply chain," *Operations Research for Health Care*, vol. 5, pp. 49–62, 2015.

[33] A. Elalouf, S. Hovav, D. Tsadikovich, and L. Yedidsion, "Minimizing operational costs by restructuring the blood sample collection chain," *Operations Research for Health Care*, vol. 7, pp. 81–93, 2015.

[34] P. Chaiwuttisak, H. Smith, Y. Wu, C. Potts, T. Sakuldamrongpanich, and S. Pathomsiri, "Location of low-cost blood collection and distribution centres in Thailand," *Operations Research for Health Care*, vol. 9, pp. 7–15, 2016.

[35] A. S. Safaei, F. Heidarpoor, and M. M. Paydar, "A novel mathematical model for group purchasing in healthcare," *Operations Research for Health Care*, vol. 15, pp. 82–90, 2017.

[36] L. Wang, H. Shi, and L. Gan, "Healthcare facility location-allocation optimization for China's developing cities utilizing a multi-objective decision support approach," *Sustainability*, vol. 10, no. 12, 2018.

[37] F. Barzinpour, M. Maleki Rastaghi, and M. S. Pishvaee, "A multi-objective hierarchical location-allocation model for the healthcare network design considering a referral system," *International Journal of Engineering*, vol. 31, no. 2, pp. 365–373, 2018, http://www.ije.ir/article_73129_7191547c1a8311e212712e9f8632ddb9.pdf.

[38] Z. Drezner, "Heuristic solution methods for two location problems with unreliable facilities," *Journal of the Operational Research Society*, vol. 38, no. 6, pp. 509–514, 1987.

[39] C. Bode, S. M. Wagner, K. J. Petersen, and L. M. Ellram, "Understanding responses to supply chain disruptions: insights from information processing and resource dependence perspectives," *Academy of Management Journal*, vol. 54, no. 4, pp. 833–856, 2011.

[40] Y. Sheffi and J. B. Rice, "A supply chain view of the resilient enterprise," *MIT Sloan Management Review*, vol. 47, no. 1, p. 41, 2005.

[41] C. S. Tang, "Robust strategies for mitigating supply chain disruptions," *International Journal of Logistics Research and Applications*, vol. 9, no. 1, pp. 33–45, 2006.

[42] U. Jüttner and S. Maklan, "Supply chain resilience in the global financial crisis: an empirical study," *Supply Chain Management: An International Journal*, vol. 16, no. 4, pp. 246–259, 2011.

[43] S. Y. Teoh and H. S. Zadeh, "Strategic resilience management model: complex enterprise systems upgrade implementation," *Pacific Asia Journal of the Association for Information Systemss*, vol. 103, 2013.

[44] H.-C. Pfohl, H. Köhler, and D. Thomas, "State of the art in supply chain risk management research: empirical and conceptual findings and a roadmap for the implementation in practice," *Logistics Research*, vol. 2, no. 1, pp. 33–44, 2010.

[45] D. Vlachos, E. Iakovou, K. Papapanagiotou, and D. Partsch, "Building robust supply chains by reducing vulnerability and improving resilience," *International Journal of Agile Systems and Management*, vol. 5, no. 1, pp. 59–81, 2012.

[46] H. Peck, "Reconciling supply chain vulnerability, risk and supply chain management," *International Journal of Logistics Research and Applications*, vol. 9, no. 2, pp. 127–142, 2006.

[47] T. Cui, Y. Ouyang, and Z.-J. M. Shen, "Reliable facility location design under the risk of disruptions," *Operations Research*, vol. 58, no. 4, pp. 998–1011, 2010.

[48] Z.-J. M. Shen, R. L. Zhan, and J. Zhang, "The reliable facility location problem: formulations, heuristics, and approximation algorithms," *INFORMS Journal on Computing*, vol. 23, no. 3, pp. 470–482, 2011, https://EconPapers.repec.org/RePEc:inm:orijoc:v:23:y:2011:i:3.

[49] D. Shishebori and A. Yousefi Babadi, "Robust and reliable medical services network design under uncertain

environment and system disruptions," *Transportation Research Part E: Logistics and Transportation Review*, vol. 77, pp. 268–288, 2015.

[50] S. An, N. Cui, Y. Bai, W. Xie, M. Chen, and Y. Ouyang, "Reliable emergency service facility location under facility disruption, en-route congestion and in-facility queuing," *Transportation Research Part E: Logistics and Transportation Review*, vol. 82, pp. 199–216, 2015.

[51] N. Zarrinpoor, M. S. Fallahnezhad, and M. S. Pishvaee, "Design of a reliable hierarchical location-allocation model under disruptions for health service networks: a two-stage robust approach," *Computers & Industrial Engineering*, vol. 109, pp. 130–150, 2017.

[52] A. Diabat, A. Jabbarzadeh, and A. Khosrojerdi, "A perishable product supply chain network design problem with reliability and disruption considerations," *International Journal of Production Economics*, vol. 212, pp. 125–138, 2019.

[53] M. Fattahi and K. Govindan, "A multi-stage stochastic program for the sustainable design of biofuel supply chain networks under biomass supply uncertainty and disruption risk: a real-life case study," *Transportation Research Part E: Logistics and Transportation Review*, vol. 118, pp. 534–567, 2018.

[54] N. Haghjoo, R. Tavakkoli-Moghaddam, H. Shahmoradi-Moghadam, and Y. Rahimi, "Reliable blood supply chain network design with facility disruption: a real-world application," *Engineering Applications of Artificial Intelligence*, vol. 90, Article ID 103493, 2020.

[55] B. Bankian-Tabrizi, K. Shahanaghi, and M. Saeed Jabalameli, "Fuzzy multi-choice goal programming," *Applied Mathematical Modelling*, vol. 36, no. 4, pp. 1415–1420, 2012.

[56] C. Kubat and B. Yuce, "hybrid intelligent approach for supply chain management system," *Journal of Intelligent Manufacturing*, vol. 23, no. 4, pp. 1237–1244, 2012.

Hindawi
Mathematical Problems in Engineering
Volume 2021, Article ID 5545307, 13 pages
https://doi.org/10.1155/2021/5545307

Research Article

Process-Based Improvement of Urban Metabolism in Optimizing the Development Cycle of the Small City Using MIA Method

Farzad Delivandani, Azita Rajabi, and Ali Nouri Kermani

Department of Geography, Central Tehran Branch, Islamic Azad University, Tehran, Iran

Correspondence should be addressed to Azita Rajabi; azitarajabi@yahoo.com

Received 23 February 2021; Revised 26 March 2021; Accepted 18 April 2021; Published 19 May 2021

Academic Editor: Noorbakhsh Amiri Golilarz

In order to maintain the health and stability of the urban ecosystem, humans must undermine the negative effects of improper land use in cities by planning to reduce entropy and regulate urban metabolism, material, and energy cycles, and considering resource capacity when providing the needs of the urban ecosystem population. Subsequently, the general purpose of this study is to explain the process-based pattern of healthy urban metabolism in the development cycle of a small city. The purpose of studying the urban metabolism, which is an integral part of the government from the environment, is to prepare reports and take measures indicating city sustainability. Indeed, the urban metabolism incorporates the relevant information on energy saving, material cycle, and management of waste and infrastructure in the urban systems. The present study employs a descriptive-analytical method. Accordingly, the metabolic impact assessment (MIA) method was utilized to analyze the data and achieve the study results. According to the assessment results in the input part of the urban metabolism process, the water and energy criteria are closer to the ideal status with 64% and 40%, respectively. In total, the performance of the input process is equal to 52%, and after that, the air quality, materials, and output sectors have a performance equal to 35, 31, and 33%, respectively. Moreover, land cover and transport have a performance of 14% and 65%, respectively, revealing that they are in a desirable condition. The above results based on mathematical optimization illustrate that there is no balance between the input and output of the urban metabolism model in the study area, and the main problems are evident in the output sectors and particularly in the recycling of materials and water.

1. Introduction

Metabolism in each city on different aspects includes urban body, urban spatial system, economic, social, and cultural dimensions, and in general, identifying urban issues and sustainable development. There should be some limitations in executive function for every city in the outer and the inner dimension. If the outer dimension, which is the same as the city's privacy, is located on the margins of metropolises and plays the role of attractive and capitalist margins, it will definitely be problematic in marginal practice, and it is logical that measures will be taken by balancing and controlling the losses outside the limits and controlling the attractiveness of keeping urban capital and its orientation towards the center. Urban planners recognize a small town's performance in determining the status of urban metabolism by mathematical calculations, which is considered an effective step in the optimal realization of urban capital and the study of the entry and exit of renewable and irreversible resources. Today, the most important challenge of urban planning is how to consume energy and resources and how to recycle them; in the first view, the metabolism of restoring urban waste to the reuse cycle is considered, but in a deep view, the reduction of the volume of irreversible capitals, which is the view of prosperity in the path of sustainable development and the creation of the balance in the urban entrance and exit in the metropolis dimension, as well as in the dimension of marginal and small cities, ensures that, unlike the past, metabolism deals with resources and in this regard, metabolism will affect the structure of the city with

the growth of technology and economic, social, and cultural dimensions.

Today, the metropolises have turned into decision-making centers due to the concentration of capital, facilities, and talents that can shape the course of future developments. On the one hand, this issue leads to the rapid growth and development of these metropolises and their suburbs, and on the other hand, poses risks to them in terms of the development mechanism. The area of environmental hazards is naturally the first to be impacted [1, 2], and this is especially evident in the metropolises of the developing countries [3]. In these countries, due to the weak economic structure and the pressure of population needs resulting from widespread migration from other parts of the country in metropolitan areas, irreparable damage is induced to the environment. While this trend is intensifying with the concentration of industries [4], cars, and other environmental pollutants, Iran is not either far from the above trends [5–7]. The city has a life in which the course of changes and development can be evaluated every day, whose complexity should not prevent the consideration of details and proper planning; in fact, managers and experts aim to achieve sustainable development in all dimensions and emphasize reducing urban capital flight on survival and continuation of development.

Sustainable development considers the greatest humanitarian challenge in today's world and has become an essential concept for all people living on the planet [3, 8–16]. In this respect, sustainability includes (a) environmental sustainability that incorporates best practices in the management of the energy, transportation, waste, and pollution, (b) social sustainability related to green business and service activities and promoting the responsibilities of individuals in the community, (c) economic sustainability that includes self-reliance and equality [17, 18]. According to the United Nations' forecast, by 2050, 70% of the world's population is expected to be living in the cities. Accordingly, the high population concentration in the urban areas poses threats to economic, social, and environmental well-being and puts pressure on these systems [19–22].

The urban metabolism considers the city as a living thing and provides a broad framework for analyzing the relationship of input and output sources to the urban system and with the surroundings [23]. The urban metabolism is a model to facilitate the description and analysis of material and energy flows in the cities. Urban metabolism allows researchers to study the interaction of natural and human systems in urban areas with a metaphorical framework. Urban metabolism is studied at different scales, including global, regional, national, urban, and even domestic. By studying it, valuable information about the flow of resources in the urban system is obtained [24–27].

The urban metabolism examines the inputs, outputs, and storage of energy, water, pollutants, food, waste, and raw materials. Moreover, it accounts for the socioeconomic and environmental changes that affect or result from the metabolic balance. Therefore, the urban metabolism contains an integrated review of the sustainability principles that are considered in creating an accurate plan. Precise assessment of energy and material exchanges depends on diverse physical infrastructure and types of construction. Materials and tools, such as solid waste, air, water pollutants, and water and energy flows, can provide significant insight and help identify sustainable urban structures. It can be argued that understanding the processes of urban metabolism provides the possibility of more sustainable development and management of cities by optimizing the use of available resources and increasing environmental protection [28–35].

The great social challenge of small cities with easy access to large cities, including the capital, population, and the abundance of ethnicity and different cultures, the lack of coherence of which forces urban management to take multiple actions, and the lack of the integrated urban management, have made the urban planning intermittent, and its instability has turned into a problem. The environmental situation in a small town, if it is stratum, is formed by clayey soil (impermeable). The urban effluent causes full-scale pollution of livestock and agriculture in the region, which spreads to a wider area of the region. The problem of municipal waste and lack of proper recycling (mostly by garbage collectors) and the manner of transfer to the landfill in urban management is caused by fluctuations in cleaning the environment and the place of loading, etc., and has disrupted the urban management.

In this study, using the AHP method, the city's input and output criteria, including water, energy, air, materials, ground cover, and weighted transportation, are compared with the ideal situation by MIA metabolic outcomes assessment method. The input and output equilibrium percentage is obtained, and the metabolic status of the city is determined by determining the equilibrium percentage. Finally, the total input process performance is 52%, and the output part has a yield of 33%.

2. Problem Definition

Qarchak city is the result of formation in a periodical process of several decades, which was initially a rural point and suddenly became a population center near the metropolis of Tehran. Environmental studies show that one of the main environmental problems of this city is the existence of many polluting jobs in the city such as tanning workshops, smelting metals (lead), brick factories, directing sewage to the unsuitable environment, recycling workshops, air pollution, lack of municipal wastewater collection and treatment plant, active mines, industrial pollution from fossil fuels (petroleum pollution), and industrial wastes such as wastes containing zinc oxides and aluminum due to the operation of cast iron and aluminum foundry units and production of slag by them, leading to adverse effects on the health of citizens. As a result, this city has a high volume of waste and sewage production. On the other hand, this city's population is growing increasingly, and this issue causes the maximum utilization of the environmental capacities of the city and environmental issues. Thus, the investigation into this small city to improve the process-based pattern of urban metabolism in the development cycle is in line with the research topic. Based on the mentioned problems, this study

seeks to answer this hypothesis. The status of this small city is not considered favorable based on the mathematical operations and assessment of the urban metabolism using the MIA.

3. Definitions, Concepts, and History of Metabolism

Metabolism is derived from the Greek word (Metabol) and has been used in a variety of contexts, including medicine, sports, psychology, politics, society, and architecture. However, its literal meaning in all areas is life-sustaining developments. Since cities could be evaluated as living and dynamic organs with specific inputs-outputs, the term metabolism in the sense of the metabolism of a living organism from biological sciences entered into the urban studies. In the postmetropolitan era, which is still moving towards the globalization of the city and the urbanization of the world, due to the concentration of population in cities and the unbridled use of various mechanical and chemical products and uncontrolled exploitation of natural resources, and due to the phenomenon such as housing crisis, transportation, economy, the coexistence and meaningful interaction between man and his ecosystem is severely threatened, peace and ecological balance are taken away from the ecosystem of the city, and the new city, unlike the stable cities of the past, has indicated an increasing metabolism (energy and resources) on the output (pollutants) and input (energy and resources).

Biologically, the city acts as a living organism using vital resources such as air, water, and food in urban metabolism. The larger the city, the more it demands from its surroundings, thus increasing the risk of environmental degradation. The factors such as urban structure, shape, climate, quality, and age of buildings, urban plant life, and transportation technology affect the rate of metabolism in the city.

Metabolic analysis of the city itself is considered as an indicator to assess the development of urban sustainability because, in the general sense, sustainability can be considered the use of materials and energy, given the ecological tolerance capacity.

In assessing urban sustainability, the three parameters of urban quality, urban flows, and urban patterns must be taken into account. In order to analyze the interactions between urban systems and the environment, the focus could be placed on the trends related to the quality of the environment in cities or their impact on the natural environment. Still, to understand these interactions, it would be necessary to examine the cities' functionality and their spatial structure, urban organization, and the impact of their lifestyles and practices. Urban metabolism is a concept that has taken a special place in urban and environmental studies in recent decades, but unfortunately, it does not have a good position in Iran. The uncontrolled expansion of the urban population and the growth of urbanization in the small cities have increased the consumption of resources and pollution caused by them. On the other hand, the linear pattern of resource consumption in the city, without quantitative and qualitative feedback to the urban system, is indicative of a linear and low-interest succession. This urban growth has used natural resources to its advantage and has disrupted the environmental system, and consequently, environmental instability has manifested itself in it. Metabolism consists of two main stages. In the first stage, the cells and tissues absorb nutrients and convert them into synthetic chemicals and store them as a part of their protoplasm structure. This stage, in which the combined, analytical, and structural actions occur, is called anabolism, where the living organism's potential energy increases. In the second stage, called catabolism, cells and tissues break down and burn their protoplasmic material and excrete the resulting waste into the environment.

At this stage, some of the reserve force of the living organism becomes a kinetic force, and the reserve force of the living organism is reduced. Historically, the term metabolism was developed in the early 19th century to describe chemical changes within living cells and was widely used in the next 50 years in biology and biochemistry to describe the organ fusion processes within living organisms (at the cellular scale) and between living organisms and their environment. Since then, metabolism in the natural sciences has been dual; it has been used in processes related to the effects of body changes and their reproduction and in more comprehensive concepts in ecosystem connections and relationships [36, 37].

The urban metabolism considers the city as a living thing and provides a broad framework for analyzing the relationship of input and output sources to the urban system and with the surroundings [8]. The urban metabolism is a model to facilitate the description and analysis of material and energy flows in the cities. Urban metabolism allows researchers to study the interaction of natural and human systems in urban areas with a metaphorical framework. Urban metabolism is studied at different scales, including global, regional, national, urban, and even at the domestic level, and by studying it, valuable information about the flow of resources in the urban system is obtained.

The urban metabolism examines the inputs, outputs, and storage of energy, water, pollutants, and food, waste, and raw materials. Moreover, it accounts for the socioeconomic and environmental changes that affect or result from the metabolic balance. Therefore, the urban metabolism contains an integrated review of sustainability principles considered in creating an accurate plan. Precise assessment of energy and material exchanges depends on diverse physical infrastructure and types of construction. Materials and tools, such as solid waste, air and water pollutants, and water and energy flows, can provide significant insight and help to identify sustainable urban structures. It can be argued that understanding the processes of urban metabolism provides the possibility of more sustainable development and management of cities by optimizing the use of available resources and increasing environmental protection [28, 38].

4. Urban Metabolism-related Views

4.1. Theory of Urban Metabolism and Extended Urban Metabolism Model. The concept of urban metabolism that is currently deemed as the main driver of urban environmental

instability was first introduced in the United States in 1965 by Wellman to evaluate the energy, water, materials, and waste cycles in an imaginary city with one million population, which turned into the basis for the sustainable development of cities and communities and was further developed by Newman [39, 40].

Basically, these people consider the city as a biological system and believe that the city as a human system takes resources, processes them, and ultimately removes the waste of this process from the system. The ecosystem metabolism is recognized by ecologists as the production and consumption of organic matter. This concept is typically related to the discussion of energy. A closer look at the similarities between urban metabolism and human biological metabolism leads us to conclude that the processes that take place in the city can have two different outcomes: The first is a positive output when the components of the system play their role well and cause the city liveability. The second deals with the negative output when system components do not play their role properly and lead to the city vulnerability.

In the general view of the city and the city theory as a complex system, it is possible to provide a broad framework for it based on the mathematics, analysis of the relationship of input and output sources to the urban system and their relationship with the biophysical environment around the city. This view is referred to as urban metabolism. This model has features such as goal orientation (increasing viability and reducing waste), empowerment to use statistics and criteria (standards and indicators), represents the basic parts of a habitat (health, transportation, and housing) and has a kind of systematic thinking mechanism.

This model considers the cities and suburbs as the systems that require input from the key sources. These inputs are used in the domestic, industrial, urban, and governmental processes to produce two categories of outputs. The first category of outputs is liveability, the purpose of which is to improve them over time. The second category of outputs is wastes that are desirable to be reduced and eliminated over time.

Liveability in this model means humans need to provide social facilities, health, and welfare in the range of man-made and natural environments. Various consumption sources (data) are entered into the urban system. As a result of the operation of this system (outputs) of the same waste, the information that is often used to indicate the size of the city are population, number of households, size, and distribution of employment; this general information does not provide any indication of the city's impact on the environment. In this regard, Wellman examines only the three major factors of urban metabolism that are problematic in most cities of the world based on population: water, waste, air pollution, etc. In the existing urban systems, data and outputs are minimally related to each other, whereas, in metabolism with a natural cycle, each output is simultaneously considered data for the other part, which gives life and stability to life in nature. Urban spaces can be well represented using the concept of landscape.

The city is represented by the physical infrastructure such as roads, streets, and waterways, and energy and water routes, on the one hand, and on the other hand by infrastructure such as health, educational, and recreational facilities.

These infrastructures facilitate socioeconomic activities in the process of production, consumption, and connection between the city and the surrounding areas. The urban areas with good infrastructure but a high level of civic participation might have good liveability. On the other hand, the urban areas with old infrastructure might present many problems at the national level. These vulnerable areas are depicted in Figure 1 indicating an urban metabolism. This model has been developed over the past three decades. Figure 1 shows an overview of the ecosystem of cities, which shows the efficiency of the closed sources and loops in which all outputs and inputs are potential, thus having a stronger perspective on achieving sustainability.

As shown in Figure 1, the configuration of the urban metabolism flow is majorly linear. Cities need their interior areas for most matters (ecosystem, water, building materials, and energy). Waste from the consumption of these matters is excreted in solid, liquid, or gaseous forms. Hence, cities are vulnerable due to resource dependence in their current linear metabolism, which puts pressure on the local resources and has a negative impact on the natural environment when extracting resources and disposing of the waste.

An ecosystem metaphor of the cities represents the efficiency of the closed sources and loops in which all outputs and inputs are potential, thus providing a stronger perspective for achieving urban sustainability. Circular metabolism is similar to a natural ecosystem with efficient consumption, recycling, and reuse of resource streams. This issue reduces dependence on the inland areas and other cities. Cities typically design their infrastructure under a linear metabolism. In light of the limitations of planetary resources, the long-term liveability and sustainability of cities rely on a shift from a linear function to a circular metabolism.

In recent years, the idea that urban areas should follow ecosystems has been aligned with the main theories of sustainable urban planning and development. Natural systems are inherently cyclical and efficient in their consumption of matter and energy, while urban systems are seen more as linear, consuming resources and producing waste.

Most studies of matter and urban energy flows encourage the use of urban metabolism as the basis of urban policy and usually conclude with a list of proposed policies. Many researchers also argue that urban metabolism studies can be a tool to identify environmental issues and design more effective urban planning policies in their Toronto-wide neighborhood metabolism studies.

4.2. Research Methodology. This research is applied-developmental in terms of purpose, descriptive-exploratory in terms of method, and in terms of how to collect the required information and data, it is considered as a field and survey research. A questionnaire is also used to collect data, which is distributed among urban specialists (experts). The main research tool is observation and a questionnaire.

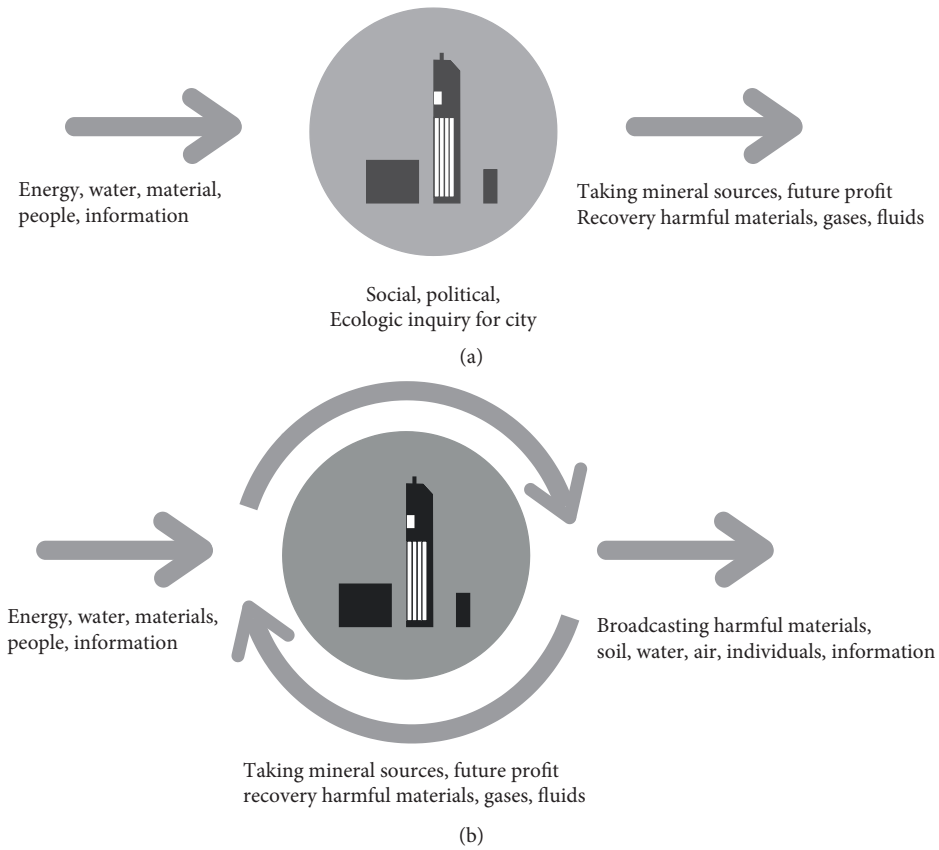

Figure 1: Urban Metabolism for Resources [41]. (a) Linear metabolism, instability, deficient, live landscape. (b) Circular metabolism, efficient stability, ecosystem landscape.

The Metabolic Impact Assessment (MIA) method is used to analyze information and achieve research results. In such a way, the data required for analysis and evaluation will be formed based on the indicators obtained from the study of theoretical principles related to the field of urban metabolism and urban patterns and the case study of small cities in relation to these data. In this way, the metabolic analysis of this city will be accomplished to evaluate the sustainability and urban management in relation to urban patterns.

After examining the factors and perspectives affecting the urban metabolism in this study, the criteria selected in Table 1 have been taken to evaluate the metabolism of Qarchak city.

4.3. Research Findings. First, based on the information of various valid sources, the desired status of the indicators is determined for evaluation. It should be noted that indicators without reliable and codified information about their optimal status from reliable sources are removed in the evaluation, which is few in number.

Then, based on the information of the indicators in the current state and the desired situation, the performance of the small city in all indicators and metabolism criteria is assessed. Assessment of the metabolic consequences of Qarchak city is made as follows:

(i) Analysis of the current and desired states of each indicator

(ii) Analysis of current and desired states of each criterion based on its indicators and assessment of the impact of each indicator on the criterion's functionality

(iii) Analysis and assessment of the effectiveness degree of the criteria on the performance of the current state, compared to the desired status

(iv) Assessment of performance of all criteria of the current state compared to the desired status

In the next step, the indicators are determined using the MIA method.

At this stage, the indicators of different criteria in terms of scale and their unit type become the same, and in fact, scaling operations are applied. The method used in this step is linear scaling so that the indicators can be compared with each other. The following formula has been used to scale the indicators:

$$n_{ij} = \frac{a_{ij}}{\max_i a_{ij}}. \tag{1}$$

According to the information collected from the indicators in the current and desired states, 25 indicators from different criteria are presented for evaluation (Table 2).

Table 1: Research criteria.

Criterion	Subcriterion	Indicator	Unit
Land cover	Barren areas	Area of lands in which no buildings or facilities are constructed	Hectare
	Urban reconstructed areas	Area of reconstructed areas	Hectare
	Land use	Green space per capita	Hectare
Visual pollution	Unfavorable view of buildings	#	#
	Inobservance of sanitary principles	#	#
	Crowds and congestion	#	#
	Undesirable design of urban furniture	#	#
Wastewater management	Water consumption	Water consumption per capita	Water consumption per capita
	Wastewater production	Wastewater production per capita	%
Waste management	Wastes	Per capita solid waste collected per year	Ton/person/year
		Per capita waste production per year	Kg/person/year
		Construction waste materials amount	Ton
		Per capita construction waste materials	Ton/person/year
	Recycling	Share of recycled waste	%
	Landfills	Share of buried solid waste	%
		Number of waste disposal sites and their capacity	%
Air pollution	CO_2 emission	Annual direct emission of CO_2, per capita road transport	Per capita ton of CO_2 emissions per year
		Direct annual CO_2 emissions from the per capita residential sector	Per capita ton of CO_2 emissions per year
	Air pollutants	Per capita total amount of air pollutants	Kg/person/year
		Average annual air pollution indicators	To be determined based on each pollutant

Based on the nonscaled values, it can be said that all indicators are less than their desired state. In the scaled data, a lower value means a more unfavorable situation, and since the indicators are measured relative to the unit, the average value of the indicators can be compared as a percentage. According to the information obtained, the average of the unscaled indicator in the current state is equal to 0.420, and based on this, it has 10 indicators above the average and 15 ones below the average. Indicators of construction waste and renewable energy sources have the worst situation compared to the other indicators, and indicators of public transportation use and per capita water consumption have the best performance compared to the other indicators in the desired state.

Second step: Normalizing the indicators in each criterion and analysis of each criterion based on its indicators.

At this step, the indicators of each criterion are assessed based on the average of the indicators and are also normalized. Performance analysis of a criterion states that its indicators based on the normalized relationship allow the relative evaluation of indicators with each other.

$$d_j = \frac{x_j}{\sum_{j=1}^{n} x_j} \times 100. \tag{2}$$

Third step: weighted scoring of the criteria, metabolic analysis, and assessment of the area based on the criterion. At this step, based on the values obtained from the total values of the indicators of each criterion, assessment is made between the criteria, and finally, all the criteria of the current and desired states are evaluated to determine the overall metabolic status of the study area compared to its optimal status. In order to more accurately assess the current state of the urban metabolism, the coefficient of significance (weight) is determined for each criterion, and then the weight of the criteria is affected by the values obtained from them. The importance of the criteria has been determined based on studies of theoretical principles. One future direction in this aspect can be the application of machine learning models [42–48], decision-making approaches [8, 49, 50], enhanced deep learning models [51–55], machine learning-based tools [56, 57], deep learning methods [58], optimized prediction tasks [59–63], optimization algorithms [64–68], and intelligent systems and hybrid feature selection methods [69–90] for weighting the importance of the criteria.

To score weights for the criteria, they are compared two by two. The comparison results are given in Table 3. For equal importance, score 1; for a little more importance, score 3; for more importance, score 5; 7 points for much more importance; and for absolute importance, a score of 9 is given. Scores 6, 4, 2, 8 are also compared for intermediate values. A 5×5 matric is used for the two-by-two comparisons. To calculate the importance factor of the criteria, first, the geometric mean of the rows of the matrix is derived, and then the results are normalized.

After determining the importance factor of the criteria, the sum of the values obtained from the indicators of each criterion obtained in the previous step is considered as the value of each criterion, and these values are normalized to their desired state in each criterion. Then, the weight of the

Table 2: Value of indicators in the current and desired state and linear unscaling operation on the indicators.

Criterion	Subcriterion	Indicator	Unit	Value of indicator based on the main unit		Value of unitless unscaled indicator	
				Current state	Desired state	Current state	Desired state
Land cover	Urban area	Total value of the constructed area	Hectare	11925597	1232547	0.10	1
	Reconstructed urban areas	Area of constructed lands	Hectare	15	100	0.15	1
	Land use	Green space per capita	Hectare	2	11	0.19	1
Water	Water consumption	Water consumption per capita	Liter/number/day	190	187	0.98	1
		Water consumption per capita by residential sector	Liter/number/day	160	113	0.70	1
		Water consumption share by residential sector	Liter/number/day	80	50	0.62	1
	Wastewater production	Wastewater production per capita	%	150	120	0.80	1
		Population connected to the domestic sewage network	%	10	100	0.10	1
Materials	Waste materials	Per capita of solid waste collected per year	M^3/person/year	1	1	0.62	1
		Per capita of waste production per year	Kg/person/year	850	150	0.17	1
		Volume of construction waste materials	ton	670	55	0.08	1
	Recycling	Share of recycled waste materials	%	4	28	0.14	1
		Share of buried solid wastes	%	78	45	0.57	1
Air quality	Annual average of air pollutants	Suspended particles less than 10 microns	Micrograms	114	20	0.17	1
		Suspended particles less than 2.5 microns	Micrograms	36	10	0.28	1
		SO_2	ppb	13	7	0.54	1
		NiO_2	ppb	50	21	0.42	1
Energy		Energy consumption per capita	KWh	17055	5840	0.34	1
		Energy consumption per constructed area	KWh	450	85	0.18	1
		Ratio of renewable energy sources, to total energy consumption	%	1	16	0.06	1
		Use of public transport	%	70	75	0.93	1
		Access to the public transport	%	60	100	0.60	1
		Share of passenger transport modes- bus	%	10	25	0.39	1
		Number of parking lots	Number of parking lots per each 1000 citizens	2	5	0.44	1
		Share of passenger transport modes- private car	%	11	25	0.44	1
		Number of taxis	Number of cars per each 1000 citizens	91	426	0.21	1

criteria is multiplied by their normalized value, and the final score of each criterion is obtained in the current and desired state. Finally, the total score of the criteria shows the result of the metabolic status of Qarchak city. In addition, by normalizing the final score of the criteria, it is possible to evaluate each criterion and the extent of its impact on the metabolic performance of the range. In Table 4, the related values are presented, and in Figure 2, metabolic assessment factors are shown.

According to the calculations performed and the results obtained from the evaluation criteria, it can be said that the final score of the study area in the current state is 29.61. In contrast, the final score of the desired state is equal to 60.64. In fact, the current state of the area has gained about 45% scores compared to the desired situation, indicating that the study area's metabolic performance has gained on a score basis and indicates that based on the information obtained, the metabolic status of the study area is poor. In general, if

Table 3: Comparison matrix of the criteria and determination of their significance coefficient.

Criterion	Land cover	Water	Materials	Air quality	Energy	Importance factor	Normalization factor
Land cover	1	4	1	4	2	2.10	0.1924
Water	4	1	5	3	4	2.92	0.2711
Materials	1	5	1	1.2	1.4	1.53	0.1223
Air quality	4	3	1.2	1	3	2.12	0.2220
Energy	2	4	1.4	3	1	2.10	0.1922

Table 4: Metabolic assessment of the area based on the criteria.

Criterion	Value of criterion		Weight of criterion	Normalized criterion		Final scope of the criterion		Relative comparison
	Current state	Desired state		Current state	Desired state	Current state	Desired state	
Land cover	0.44	3	0.1924	15.18	41.42	2.92	7.96	13.20
Water	3.20	5	0.2711	40.50	59.25	10.97	16.06	33.33
Materials	1.58	5	0.1223	22.34	70.34	2.73	8.60	8.60
Air quality	1.41	4	0.2220	19.26	72.23	4.72	16.03	31.57
Energy	3.59	9	0.1922	45.4	62.41	8.72	11.99	14.04
Sum	10.23	26	1.0000	139.68	306.15	29.61	60.64	100
Total performance	* * * *	* * * *	* * * *	* * * *	* * * *	45.125	100	100

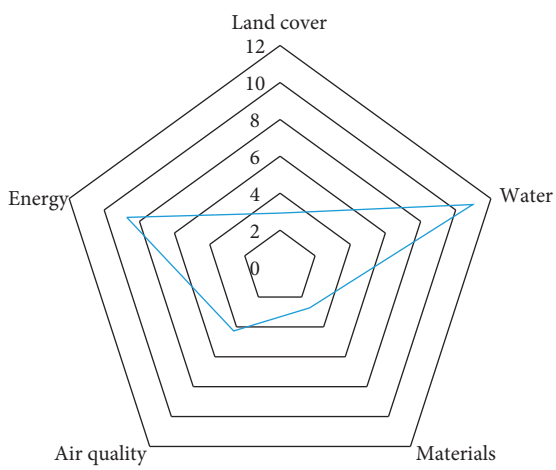

Figure 2: Metabolic assessment factors.

any criterion or optimal condition is compared, it can be concluded that the water criterion of 64% and the energy criterion of the transportation sector are 40% closest to the ideal conditions. After these two, air quality, materials, and land cover stand, respectively. The result of the assessment circular urban metabolism around the study is shown in Figure 3. Moreover, the comparison of the ideal and current situation is illustrated in Figure 4.

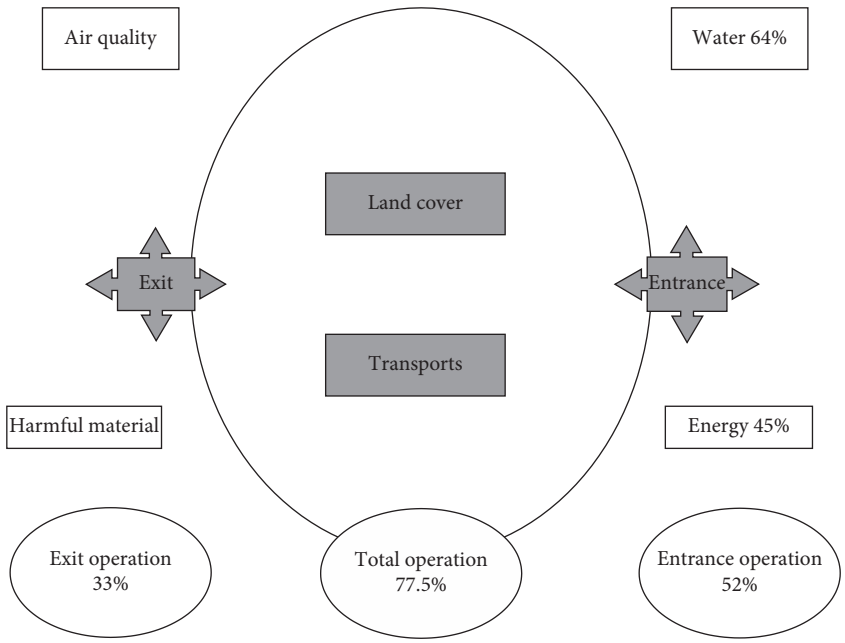

Figure 3: Result of assessment circular.

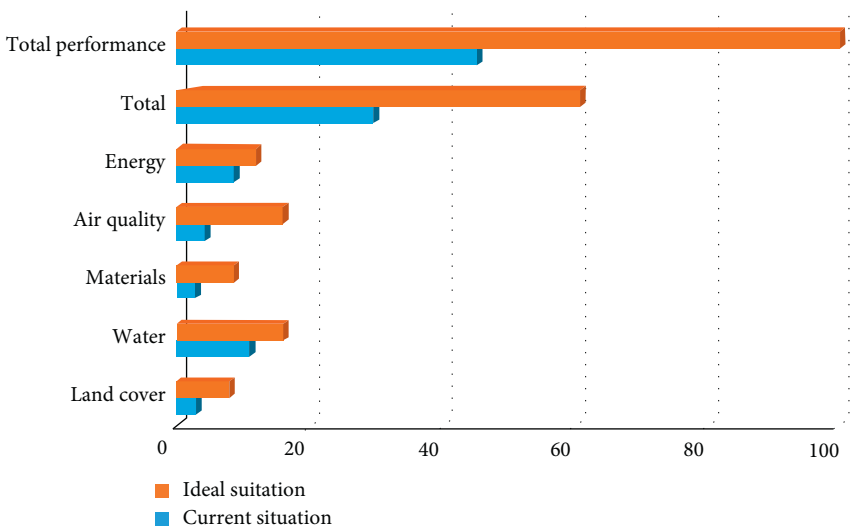

Figure 4: Comparison of the ideal and current situation.

5. Conclusion and Future Directions

Qarchak city is one of the metropolises of Iran that has had great physical growth in the last two decades due to its innumerable immigration, and this uneven growth and population density and special geographical location have caused environmental challenges in this city.

The environmental issues of Qarchak city, which are caused by internal and external factors, have a wide impact on health, mental health, economic, social, and urban environmental health, and if they are not controlled in a strategic urban development plan, the consequences and effects will remain not only for the present generation but also for future generations.

As previously stated in the study of theoretical principles, the cycle of urban metabolism has inputs and outputs whose interactions occur in the urban system, which herein is limited to urban structures, patterns, and forms. In order to achieve greater stability, it is necessary that linear metabolism, which includes the input of resources, their consumption, and the output of waste materials, be converted into the cyclic metabolism, and in fact, the processes of material recycling and its conversion into reusable materials and energy production. According to the assessment results in the input sector of the urban metabolism process, the water criterion of 64% and the energy criterion of the transportation sector have 40% of the closest distance to the ideal conditions. In total, the performance of the input

process is 52%, and after that, air quality, materials, and output sectors have a performance of 35, 31, and 33%, respectively. In addition, land cover and transport have the performance of 14 and 65%, compared to the desired state.

The above results reveal that there is no balance between input and output of the urban metabolism model in the study area, and the main problems are evident in the output sectors, especially in the material and water recycling sector. This issue affects the sustainability of the study area because, in the broad model of the urban metabolism, the goal of urban sustainability is to reduce the use of natural resources and decrease waste production to improve its livability and not only the consumption of natural materials in the area in terms of energy, water, and food, but also the amount of waste and not returning it to the reuse cycle is very problematic and critical.

Sustainability is created if urban development is such that the rate of resource utilization is not more than the rate of their rehabilitation; if based on the results expressed in the study area, the opposite has happened. In order to achieve stability in the cycle of urban metabolism, it is necessary to establish a balance between its input and output, and also, it is required to achieve this balance by paying attention to the proper functioning of the urban systems.

Finally, the general measures that can be taken to improve the metabolism of Qarchak city could be expressed. These measures are as follows:

(i) Optimizing energy consumption, maximizing energy efficiency, maximizing the share of renewable energy sources, and using clean energy in the public transportation

(ii) Development of green spaces and paying attention to their extent and distribution in the area, renovation of old structures, and nondestruction of buildings until they are completely out of service

(iii) Changing the industrial uses to green uses and mixed residential-commercial areas

(iv) Minimizing water consumption, minimizing damage to the natural water cycle, optimizing water recycling, and reuse

(v) Minimizing waste production, optimizing material recycling, proper use of recycled materials for consumption and energy production, and minimizing landfilling

Data Availability

Request for data, 4 months after publication of this article, will be considered by the corresponding author.

Conflicts of Interest

The authors declare no conflicts of interest.

References

[1] J. Liu, Y. Liu, and X. Wang, "An environmental assessment model of construction and demolition waste based on system dynamics: a case study in Guangzhou," *Environmental Science and Pollution Research*, vol. 27, no. 30, pp. 37237–37259, 2020.

[2] L. Cao, "Changing port governance model: port spatial structure and trade efficiency," *Journal of Coastal Research*, vol. 95, no. sp1, pp. 963–968, 2020.

[3] X. Zhao, Y. Ye, J. Ma, P. Shi, and H. Chen, "Construction of electric vehicle driving cycle for studying electric vehicle energy consumption and equivalent emissions," *Environmental Science and Pollution Research*, vol. 27, no. 30, pp. 37395–37409, 2020.

[4] Z. Niu, B. Zhang, J. Wang et al., "The research on 220GHz multicarrier high-speed communication system," *China Communications*, vol. 17, no. 3, pp. 131–139, 2020.

[5] M. Javanbakht, A. Darvishi Boloorani, M. Kiavarz, N. Neisany Samany, L. Zebardast, and M. Zangiabadi, "Spatial-temporal analysis of urban environmental quality of Tehran, Iran," *Ecological Indicators*, vol. 120, Article ID 106901, 2021.

[6] A. Najmeddin, F. Moore, B. Keshavarzi, and Z. Sadegh, "Pollution, source apportionment and health risk of potentially toxic elements (PTEs) and polycyclic aromatic hydrocarbons (PAHs) in urban street dust of Mashhad, the second largest city of Iran," *Journal of Geochemical Exploration*, vol. 190, pp. 154–169, 2018.

[7] R. Shad, M. Khorrami, and M. Ghaemi, "Developing an Iranian green building assessment tool using decision making methods and geographical information system: case study in Mashhad city," *Renewable and Sustainable Energy Reviews*, vol. 67, pp. 324–340, 2017.

[8] S. Liu, F. T. S. Chan, and W. Ran, "Decision making for the selection of cloud vendor: an improved approach under group decision-making with integrated weights and objective/subjective attributes," *Expert Systems with Applications*, vol. 55, pp. 37–47, 2016.

[9] C. Yang, F. Gao, and M. Dong, "Energy efficiency modeling of integrated energy system in coastal areas," *Journal of Coastal Research*, vol. 103, no. sp1, pp. 995–1001, 2020.

[10] B. Wang, Z. Song, and L. Sun, "A review: comparison of multi-air-pollutant removal by advanced oxidation processes--Industrial implementation for catalytic oxidation processes," *Chemical Engineering Journal*, Article ID 128136, 2020.

[11] X. Han, D. Zhang, J. Yan, S. Zhao, and J. Liu, "Process development of flue gas desulphurization wastewater treatment in coal-fired power plants towards zero liquid discharge: energetic, economic and environmental analyses," *Journal of Cleaner Production*, vol. 261, Article ID 121144, 2020.

[12] H. Lu, P. Tian, and L. He, "Evaluating the global potential of aquifer thermal energy storage and determining the potential worldwide hotspots driven by socioeconomic, geo-hydrologic and climatic conditions," *Renewable and Sustainable Energy Reviews*, vol. 112, pp. 788–796, 2019.

[13] Y. Chen, J. Li, H. Lu, and P. Yan, "Coupling system dynamics analysis and risk aversion programming for optimizing the mixed noise-driven shale gas-water supply chains," *Journal of Cleaner Production*, vol. 278, Article ID 123209, 2021.

[14] Y. Chen, L. He, Y. Guan, H. Lu, and J. Li, "Life cycle assessment of greenhouse gas emissions and water-energy optimization for shale gas supply chain planning based on multi-level approach: case study in Barnett, Marcellus, Fayetteville, and Haynesville shales," *Energy Conversion and Management*, vol. 134, pp. 382–398, 2017.

[15] Y. Chen, L. He, J. Li, and S. Zhang, "Multi-criteria design of shale-gas-water supply chains and production systems towards optimal life cycle economics and greenhouse gas

emissions under uncertainty," *Computers & Chemical Engineering*, vol. 109, pp. 216–235, 2018.

[16] X. Cheng, L. He, H. Lu, Y. Chen, and L. Ren, "Optimal water resources management and system benefit for the Marcellus shale-gas reservoir in Pennsylvania and West Virginia," *Journal of Hydrology*, vol. 540, pp. 412–422, 2016.

[17] M. Taleghani and A. Taleghani, "Identification and ranking of factors affecting the implementation of knowledge management engineering based on TOPSIS technique," *Eng Transactions*, vol. 1, no. 1, 2020.

[18] R. F. Young and K. Lieberknecht, "From smart cities to wise cities: ecological wisdom as a basis for sustainable urban development," *Journal of Environmental Planning and Management*, vol. 62, no. 10, pp. 1675–1692, 2019.

[19] A. Boretti and L. Rosa, "Reassessing the projections of the world water development report," *NPJ Clean Water*, vol. 2, no. 1, pp. 1–6, 2019.

[20] F. Liu and W. Sun, "Impact of active organic decentralization population policy on future urban built-up areas: beijing case study," *Habitat International*, vol. 105, Article ID 102262, 2020.

[21] N. A. Golilarz, N. Robert, J. Addeh, and A. Salehpour, "Translation invariant wavelet based noise reduction using a new smooth nonlinear improved thresholding function," *Computational Research Progress in Applied Science & Engineering*, vol. 3, pp. 104–108, 2017.

[22] N. A. Golilarz and H. Demirel, "Image de-noising using undecimated wavelet transform (UWT) with soft thresholding technique," in *Proceedings of the 2017 9th International Conference on Computational Intelligence and Communication Networks (CICN)*, pp. 16–19, IEEE, Cyprus, Turkey, September 2017.

[23] G. W. McDonald and M. G. Patterson, "Bridging the divide in urban sustainability: from human exemptionalism to the new ecological paradigm," *Urban Ecosystems*, vol. 10, no. 2, pp. 169–192, 2007.

[24] S. M. Hosseinian and V. Najafi Moghaddam Gilani, "Analysis of factors affecting urban road accidents in rasht metropolis," *Eng Transactions*, vol. 1, no. 1, pp. 1–4, 2020.

[25] J. R. Carréon and E. Worrell, "Urban energy systems within the transition to sustainable development. A research agenda for urban metabolism," *Resources, Conservation and Recycling*, vol. 132, pp. 258–266, 2018.

[26] D. Beloin-Saint-Pierre, B. Rugani, S. Lasvaux et al., "A review of urban metabolism studies to identify key methodological choices for future harmonization and implementation," *Journal of Cleaner Production*, vol. 163, pp. S223–S240, 2017.

[27] G. Thomson and P. Newman, "Urban fabrics and urban metabolism - from sustainable to regenerative cities," *Resources, Conservation and Recycling*, vol. 132, pp. 218–229, 2018.

[28] M. M. A. Malakoutian and M. Khaksar, "SBM model based productivity evaluation," *Eng Transactions*, vol. 1, no. 1, 2020.

[29] A. Addeh, A. Khormali, and N. A. Golilarz, "Control chart pattern recognition using RBF neural network with new training algorithm and practical features," *ISA Transactions*, vol. 79, pp. 202–216, 2018.

[30] H. M. Munir, R. Ghannam, H. Li et al., "Control of distributed generators and direct harmonic voltage controlled active power filters for accurate current sharing and power quality improvement in islanded microgrids," *Inventions*, vol. 4, no. 2, p. 27, 2019.

[31] A. Sadeghpour and G. Ozay, "Evaluation of reinforced concrete frames designed based on previous Iranian seismic codes," *Arabian Journal for Science and Engineering*, vol. 45, no. 10, pp. 8069–8085, 2020.

[32] A. Yang, X. Chen, G. Huang, S. Zhao, X. Lin, and E. Mcbean, "Coordinative urban-rural solid waste management: a fractional dual-objective programming model for the regional munifcipality of xiamen," *Mathematical Problems in Engineering*, vol. 2019, Article ID 1360454, 13 pages, 2019.

[33] Z. Ma, D. Huang, C. Li, and J. Guo, "Travel time reliability-based signal timing optimization for urban road traffic network control," *Mathematical Problems in Engineering*, vol. 2020, Article ID 8898062, 11 pages, 2020.

[34] F. Jafari Golrokh and A. Hasan, "A comparison of machine learning clustering algorithms based on the DEA optimization approach for pharmaceutical companies in developing countries," *Eng Transactions*, vol. 1, no. 1, 2020.

[35] M. Feizbahr, C. Kok Keong, F. Rostami, and M. Shahrokhi, "Wave energy dissipation using perforated and non perforated piles," *International Journal of Engineering*, vol. 31, no. 2, pp. 212–219, 2018.

[36] M. Dinarès, "Urban metabolism: a review of recent literature on the subject," *Documents D'anàlisi Geogràfica*, vol. 60, no. 3, pp. 551–571, 2014.

[37] G. Lyons, P. Mokhtarian, M. Dijst, and L. Böcker, "The dynamics of urban metabolism in the face of digitalization and changing lifestyles: understanding and influencing our cities," *Resources, Conservation and Recycling*, vol. 132, pp. 246–257, 2018.

[38] L. Liu, G. Huang, B. Baetz, C. Z. Huang, and K. Zhang, "A factorial ecologically-extended input-output model for analyzing urban GHG emissions metabolism system," *Journal of Cleaner Production*, vol. 200, pp. 922–933, 2018.

[39] R. J. Kennedy and L. Buys, "Dimensions of liveability: a tool for sustainable cities," in *Proceedings of the SB10mad Sustainable Building Conference*, Madrid, Spain, April 2010.

[40] P. W. G. Newman, "Sustainability and cities: extending the metabolism model," *Landscape and Urban Planning*, vol. 44, no. 4, pp. 219–226, 1999.

[41] K. Musango, P. Currie, and B. Robinson, "Urban metabolism for resource-efficient cities: from theory to implementation," in *Book of Abstracts*p. 12, UNESCO, Paris, France, 2017.

[42] X. Zhang, J. Wang, T. Wang, R. Jiang, J. Xu, and L. Zhao, "Robust feature learning for adversarial defense via hierarchical feature alignment," *Information Sciences*, vol. 560, pp. 256–270, 2020.

[43] X. Zhang, T. Wang, W. Luo, and P. Huang, "Multi-level fusion and attention-guided CNN for image dehazing," *IEEE Transactions on Circuits and Systems for Video Technology*, p. 1, 2020.

[44] X. Zhang, M. Fan, D. Wang, P. Zhou, and D. Tao, "Top-k feature selection framework using robust 0-1 integer programming," *IEEE Transactions on Neural Networks and Learning Systems*, pp. 1–15, 2020.

[45] X. Zhang, D. Wang, Z. Zhou, and Y. Ma, "Robust low-rank tensor recovery with rectification and alignment," *IEEE Transactions on Pattern Analysis and Machine Intelligence*, vol. 43, no. 1, pp. 238–255, 2019.

[46] X. Zhang, R. Jiang, T. Wang, and J. Wang, "Recursive neural network for video deblurring," *IEEE Transactions on Circuits and Systems for Video Technology*, p. 1, 2020.

[47] X. Zhang, T. Wang, J. Wang, G. Tang, and L. Zhao, "Pyramid channel-based feature attention network for image dehazing," *Computer Vision and Image Understanding*, vol. 197-198, Article ID 103003.

[48] L. Ding, L. Huang, S. Li et al., "Definition and application of variable resistance coefficient for wheeled mobile robots on

deformable terrain," *IEEE Transactions on Robotics*, vol. 36, no. 3, pp. 894–909, 2020.

[49] C. Wu, P. Wu, J. Wang, R. Jiang, M. Chen, and X. Wang, "Critical review of data-driven decision-making in bridge operation and maintenance," *Structure and Infrastructure Engineering*, pp. 1–24, 2020.

[50] S. Liu, W. Yu, F. T. S. Chan, and B. Niu, "A variable weight-based hybrid approach for multi-attribute group decision making under interval-valued intuitionistic fuzzy sets," *International Journal of Intelligent Systems*, vol. 36, no. 2, pp. 1015–1052, 2021.

[51] T. Qiu, X. Shi, J. Wang et al., "Deep learning: a rapid and efficient route to automatic metasurface design," *Advanced Science*, vol. 6, no. 12, Article ID 1900128, 2019.

[52] T. Li, M. Xu, C. Zhu, R. Yang, Z. Wang, and Z. Guan, "A deep learning approach for multi-frame in-loop filter of HEVC," *IEEE Transactions on Image Processing*, vol. 28, no. 11, pp. 5663–5678, 2019.

[53] H. Chen, A. Chen, L. Xu et al., "A deep learning CNN architecture applied in smart near-infrared analysis of water pollution for agricultural irrigation resources," *Agricultural Water Management*, vol. 240, Article ID 106303, 2020.

[54] J. Qian, S. Feng, Y. Li et al., "Single-shot absolute 3D shape measurement with deep-learning-based color fringe projection profilometry," *Optics Letters*, vol. 45, no. 7, pp. 1842–1845, 2020.

[55] J. Qian et al., "Deep-learning-enabled geometric constraints and phase unwrapping for single-shot absolute 3d shape measurement," *APL Photonics*, vol. 5, no. 4, Article ID 046105, 2020.

[56] R. U. Khan, X. Zhang, R. Kumar, A. Sharif, N. A. Golilarz, and M. Alazab, "An adaptive multi-layer botnet detection technique using machine learning classifiers," *Applied Sciences*, vol. 9, no. 11, p. 2375, 2019.

[57] S. Yang, "Scalable digital neuromorphic architecture for large-scale biophysically meaningful neural network with multi-compartment neurons," *IEEE Transactions on Neural Networks and Learning Systems*, vol. 31, no. 1, pp. 148–162, 2019.

[58] B. Wang, L. Zhang, H. Ma, H. Wang, and S. Wan, "Parallel LSTM-based regional integrated energy system multienergy source-load information interactive energy prediction," *Complexity*, vol. 2019, Article ID 7414318, 13 pages, 2019.

[59] W. Zhu, C. Ma, X. Zhao et al., "Evaluation of sino foreign cooperative education project using orthogonal sine cosine optimized kernel extreme learning machine," *IEEE Access*, vol. 8, pp. 61107–61123, 2020.

[60] G. Liu, W. Jia, M. Wang et al., "Predicting cervical hyperextension injury: a covariance guided sine cosine support vector machine," *IEEE Access*, vol. 8, pp. 46895–46908, 2020.

[61] Y. Wei, H. Lv, M. Chen et al., "Predicting entrepreneurial intention of students: an extreme learning machine with Gaussian barebone harris hawks optimizer," *IEEE Access*, vol. 8, pp. 76841–76855, 2020.

[62] H. Tang, Y. Xu, A. Lin et al., "Predicting green consumption behaviors of students using efficient firefly grey wolf-assisted K-nearest neighbor classifiers," *IEEE Access*, vol. 8, pp. 35546–35562, 2020.

[63] A. Lin, Q. Wu, A. A. Heidari et al., "Predicting intentions of students for master programs using a chaos-induced sine cosine-based fuzzy K-Nearest neighbor classifier," *IEEE Access*, vol. 7, pp. 67235–67248, 2019.

[64] Y. Fan, P. Wang, A. A. Heidari et al., "Rationalized fruit fly optimization with sine cosine algorithm: a comprehensive analysis," *Expert Systems with Applications*, vol. 157, Article ID 113486, 2020.

[65] E. Rodríguez-Esparza, L. A. Zanella-Calzada, D. Oliva et al., "An efficient Harris hawks-inspired image segmentation method," *Expert Systems with Applications*, vol. 155, Article ID 113428, 2020.

[66] S. Jiao, G. Chong, C. Huang et al., "Orthogonally adapted Harris hawks optimization for parameter estimation of photovoltaic models," *Energy*, vol. 203, Article ID 117804, 2020.

[67] Z. Xu, Z. Hu, A. A. Heidari et al., "Orthogonally-designed adapted grasshopper optimization: a comprehensive analysis," *Expert Systems with Applications*, vol. 150, Article ID 113282, 2020.

[68] A. Abbassi, R. Abbassi, A. A. Heidari et al., "Parameters identification of photovoltaic cell models using enhanced exploratory salp chains-based approach," *Energy*, vol. 198, Article ID 117333, 2020/05.

[69] H. Yu, W. Li, C. Cheng, and J. Liang, "Dynamic Gaussian bare-bones fruit fly optimizers with abandonment mechanism: method and analysis," *Engineering with Computers*, pp. 1–29, 2020.

[70] X. Zhao, D. Li, B. Yang, C. Ma, Y. Zhu, and H. Chen, "Feature selection based on improved ant colony optimization for online detection of foreign fiber in cotton," *Applied Soft Computing*, vol. 24, pp. 585–596, 2014.

[71] J. Hu, H. Chen, A. A. Heidari et al., "Orthogonal learning covariance matrix for defects of grey wolf optimizer: insights, balance, diversity, and feature selection," *Knowledge-Based Systems*, vol. 213, p. 106684, 2021.

[72] C. Yu et al., "SGOA: annealing-behaved grasshopper optimizer for global tasks," *Engineering with Computers*, pp. 1–28, 2021.

[73] W. Shan, Z. Qiao, A. A. Heidari, H. Chen, H. Turabieh, and Y. Teng, "Double adaptive weights for stabilization of moth flame optimizer: balance analysis, engineering cases, and medical diagnosis," *Knowledge-Based Systems*, p. 106728, 2020.

[74] J. Tu, H. Chen, J. Liu et al., "Evolutionary biogeography-based whale optimization methods with communication structure: towards measuring the balance," *Knowledge-Based Systems*, vol. 212, p. 106642, 2021.

[75] D. Zhao, "Chaotic random spare ant colony optimization for multi-threshold image segmentation of 2D Kapur entropy," *Knowledge-Based Systems*, p. 106510, 2020.

[76] Y. Zhang, "Towards augmented kernel extreme learning models for bankruptcy prediction: algorithmic behavior and comprehensive analysis," *Neurocomputing*, 2020.

[77] Y. Zhang, R. Liu, X. Wang, H. Chen, and C. Li, "Boosted binary Harris hawks optimizer and feature selection," *Engineering with Computers*, pp. 1–30, 2020.

[78] H.-L. Chen, G. Wang, C. Ma, Z.-N. Cai, W.-B. Liu, and S.-J. Wang, "An efficient hybrid kernel extreme learning machine approach for early diagnosis of Parkinson′s disease," *Neurocomputing*, vol. 184, pp. 131–144, 2016.

[79] H. Chen, A. A. Heidari, H. Chen, M. Wang, Z. Pan, and A. H. Gandomi, "Multi-population differential evolution-assisted Harris hawks optimization: framework and case studies," *Future Generation Computer Systems*, vol. 111, pp. 175–198, 2020.

[80] L. Hu, G. Hong, J. Ma, X. Wang, and H. Chen, "An efficient machine learning approach for diagnosis of paraquat-poisoned patients," *Computers in Biology and Medicine*, vol. 59, pp. 116–124, 2015.

[81] L. Shen, H. Chen, Z. Yu et al., "Evolving support vector machines using fruit fly optimization for medical data classification," *Knowledge-Based Systems*, vol. 96, pp. 61–75, 2016.

[82] J. Xia, H. Chen, Q. Li et al., "Ultrasound-based differentiation of malignant and benign thyroid Nodules: an extreme learning machine approach," *Computer Methods and Programs in Biomedicine*, vol. 147, pp. 37–49, 2017.

[83] C. Li, L. Hou, B. Y. Sharma et al., "Developing a new intelligent system for the diagnosis of tuberculous pleural effusion," *Computer Methods and Programs in Biomedicine*, vol. 153, pp. 211–225, 2018.

[84] X. Zhao, X. Zhang, Z. Cai et al., "Chaos enhanced grey wolf optimization wrapped ELM for diagnosis of paraquat-poisoned patients," *Computational Biology and Chemistry*, vol. 78, pp. 481–490, 2019.

[85] Y. Xu, H. Chen, J. Luo, Q. Zhang, S. Jiao, and X. Zhang, "Enhanced Moth-flame optimizer with mutation strategy for global optimization," *Information Sciences*, vol. 492, pp. 181–203, 2019.

[86] M. Wang and H. Chen, "Chaotic multi-swarm whale optimizer boosted support vector machine for medical diagnosis," *Applied Soft Computing Journal*, vol. 88, Article ID 105946, 2020.

[87] X. Xu and H.-L. Chen, "Adaptive computational chemotaxis based on field in bacterial foraging optimization," *Soft Computing*, vol. 18, no. 4, pp. 797–807, 2014.

[88] M. Wang, H. Chen, B. Yang et al., "Toward an optimal kernel extreme learning machine using a chaotic moth-flame optimization strategy with applications in medical diagnoses," *Neurocomputing*, vol. 267, pp. 69–84, 2017.

[89] A. Sadeghpour and G. Ozay, "Evaluation of seismic design parah progmeters for reinforced concrete frames retrofitted using eccentric steel bracings," *Computational Researcress in Applied Science & Engineering: CRPASE: Transactions of Civil and Environmental Engineering*, vol. 6, pp. 173–178, 2020.

[90] M. R. A. Taleshmekaiil, S. M. R. Khatibi, M. Mohemsaz, M. H. Azimi, and A. Sadeghpour, "Investigating the effective factors of renewable energy development in tehran metropolis," *Mathematical Problems in Engineering*, vol. 2021, Article ID 6636955, 13 pages, 2021.

Hindawi
Mathematical Problems in Engineering
Volume 2021, Article ID 5557320, 11 pages
https://doi.org/10.1155/2021/5557320

Research Article

Influence of the Inherent Safety Principles on Quantitative Risk in Process Industry: Application of Genetic Algorithm Process Optimization (GAPO)

Mehdi Jahangiri,[1] Abolfazl Moghadasi,[2] Mojtaba Kamalinia,[3] Farid Sadeghianjahromi,[4] and Sean Banaee[5]

[1]*Department of Occupational Health Engineering, School of Health, Shiraz University of Medical Sciences Occupational Health, Shiraz, Iran*
[2]*Student Research Committee, School of Health, Shiraz University of Medical Sciences, Shiraz, Iran*
[3]*School of Health, Department of Occupational Health, Shiraz University of Medical Sciences, Shiraz, Iran*
[4]*Department of Chemical Engineering, University of Isfahan, Isfahan, Iran*
[5]*College of Health Sciences, Old Dominion University, Norfolk, VA, USA*

Correspondence should be addressed to Abolfazl Moghadasi; a_moghadasi@sums.ac.ir

Received 20 February 2021; Revised 21 April 2021; Accepted 27 April 2021; Published 8 May 2021

Academic Editor: Mohammad Yazdi

Inherent safety (IS) refers to a set of measures that enhance the safety level of processes and equipment, rendering additional equipment and/or add-ons. The early design phase of processes is suited best for implementation of IS strategies as some of such strategies either are impossible to be implemented at the operation phase or substantially increase costs. The purpose of this study is to present a new approach called genetic algorithm process optimization (GAPO), by which processes can be made inherently safer even at the operation phase. This study simulates the IS principle, assessing its impact on quantitative risk and the possible consequences of process incidents identified by Hazard and Operation Study (HAZOP). The principle of intensification was simulated through GAPO, and feasibility of implementation was approved by HYSYS. Moreover, the integrated inherent safety index (I2SI) was used to evaluate and quantify the level of IS following implementation of GAPO compared to the initial design. Our result shows that GAPO substantially reduced the risk of consequences and quantitative risks and concomitantly improved the I2SI. The proposed GAPO can be applied to process operation as an approach to enhance IS at no cost and without decrease in production.

1. Introduction

Engineers and safety activists have always tried to optimize and increase the level of safety in industry through utilizing knowledge and advanced technologies to reduce the probability and severity of human and financial consequences [1–3]. Meanwhile, given the inherent nature of processes, reactions, raw materials, and products, process industries contribute a special role in the occurrence of incidents [4–6]. In process industries including petrochemical facilities, raw materials are converted into intermediate or final products using a physical and/or chemical chain of circumstances. In such industries, production, storage, transportation, use, and disposal of chemicals are inherently dangerous, and the potential for catastrophic accidents is a significant concern. Since simple negligence in these industries may lead to loss of life, damage to equipment, economic losses, and environmental pollution, great efforts have been made to minimize the chance for occurrence of such incidents.

In a general classification, approaches towards achieving higher levels of safety can be divided into two groups: conventional and inherent [7–10]. Conventional approaches

include control of hazards by safety add-ons such as active or passive engineering strategies, procedural corrective actions, and preventive laws and regulations [3]. In passive safety systems, hazards are controlled through process or equipment design features without additional active functioning of any device. Active safety systems include process controls, safety instrumented systems (SIS), and mitigation systems. Such preventative measures mitigate hazards through controls and systems designed to monitor and maintain specific conditions, which may be triggered by an event. Procedural safety systems use personnel education and management, including standard operating procedures (SOPs), safety rules and procedures, training, emergency response plans, and management systems to control the hazards [10].

Many safety activists applied the inherent safety principles to reduce or eliminate risks and make processes or plants safer without knowing or categorizing the techniques as inherent safety [3, 11, 12]. In 1970, Klets came up with the idea that "What you do not have, cannot leak, or burn" [11]. Ten years after the explosion of Flixborough, and just a few weeks before the Bhopal tragedy, Klets introduced the four basic principles for inherent safety including intensification, substitution, attenuation, and limitation of the effects of failures. During the following years, these principles were reviewed and modified by various researchers [11]. For example, the I2SI described the inherent safety principles (ISPs) in five elements as limitation of effects, minimization, substitution, attenuation, and simplification [3].

Inherent safety refers to a set of measures that enhance the processes and equipment safety level without the need for further equipment and/or add-ons and prevents or reduces the severity of possible incidents [13]. Inherent safety seeks to eliminate the risk with different approaches rather than ignoring or controlling them [14, 15]. Inherent safety design strategies eliminate or reduce hazards to avoid or mitigate the consequences of incidents through principles such as substitution, moderation, and simplification of conventional safety approach. Although implementation of ISPs seems logical, simple, and obvious at first glance, it is challenging because of the required modification in process design, tools, and layouts. Moreover, enforcement of ISPs in a simple process is more difficult due to limited options for achieving inherent safety. For instance, chemicals may not be toxic, and processes are not complicated. These challenges are greater when the process is at the operation stage of the lifecycle, because any modification in the process must be logically feasible, justifiable, and cost-effective [16]. Many studies have emphasized that implementation of ISPs in the early stages of the system lifecycle is more economical and practical due to the lack of need to change the equipment and process layout [17–19].

In the 1970s, quantitative risk assessment (QRA) was initially introduced to the nuclear industry and then integrated into the process industry as legal criteria. During the last four decades, substantial emphasis has been placed on QRA [20]. QRA can be used to numerically quantify the existing risks, determine the unacceptable risks according to a numerical criterion, and prioritize the risk control measures [21]. QRA is based on identifying the incident scenarios and evaluating the risk by defining the probability of failure, the prospect of various consequences, and the potential impact of those consequences. The QRA risk is defined as a function of probability, frequency, and consequence of a particular incident scenario. The QRA is commonly presented as individual and societal risk. The individual risk expresses the likelihood of experiencing fatal effects at a given location and is not affected by the distribution of population in the area. In other words, the term "individual risk" is used to calculate the risk of fatality for someone at a specific location, assuming an employee is always present at the location [22, 23]. The societal risk is a measure of the risk that the incidents pose to the population and takes into account population distribution in the area. The societal risk is expressed in terms of the likelihood of incident outcomes that affects a given number of people in a single incident. Societal risk is expressed using an F-N curve, which indicates that the expected frequency (F) of incident scenarios resulted in the number of N or more fatalities. The x-axis of the F-N curve represents the number of fatalities (N), which is depicted on a logarithmic axis with a minimum value of 1. The y-axis of the F-N curve represents the cumulative frequency of events with the number of fatalities equal to N or more [6, 9, 20]. PHAST software package is a tool that helps in calculating QRA. In 2020, Wu et al. used PHAST to study quantitative analysis of ground flare [24]. Also, Wang and Ma (2021) applied PHAST to calculate quantitative risk for hydrogen refueling station [25]. In 2019, Shuang et al. used QRA to conduct fire and explosion risk assessment in urban natural gas pipeline [26]. In 2016, Tong et al. studied long-distance oil and gas pipelines [23]. However, PHAST software can be used to develop consequence modeling and draw out valid data on QRA.

Genetic Algorithm is an approach, in which the machine can simulate the natural selection mechanism. This is done by searching the problem space to find the better answer, not necessarily the optimal one [27–30]. GA is widely used in studies, in which the stochastic search algorithms are applied to find the optimal or the most immediate answer. In such algorithms, optimization strategies are defined by mixed continuous discrete variables and discontinuous and/or nonconvex system spaces [30]. As with early random generations, initial responses produced randomized generations of children by modifying and combining initial parent answers [31, 32]. This cycle will continue until the full recognition of specified process conditions. Approaching the optimal solution is a necessary condition for the process completion [30]. In optimization problems with various processes, variables, and conditions, GA can be used to find the best/optimum operating conditions for equipment and process to enhance inherent safety without reducing the production of final product (s) at industries.

Numerous studies have been conducted into the assessment of ISPs in reducing both the frequency (more influenced by the vessels construction material) and severity (mostly affected by nature and volume of chemical and process condition) [2–5, 7–10]. Most of these studies reach the conclusion that the best chance to make process

inherently safer is at the design phase of process life cycle. Implementation of these approaches in operation phase would be costly or, in the best situation, need to change the design layout that is not practically applicable in all processes. For instance, Chen (2011) cited the purpose of the Explosion-Proof Technology in Oil Storage and Transportation Devices [5]; Palaniappan et al. (2004) suggested that layout design is playing a key role on making process inherently safer [15]; Rathnayaka et al. (2014), Tugnoli et al. (2008), and Kossoy et al. (2012) suggested the same point of view as Palaniappan [7, 8, 18]. Also, Syaza et al. (2016) purposed a graphical approach to make process inherently safer through research and development phase of process design. Although the earlier phase of process design is the greater opportunity to make the process inherently safer, there is a chance to implement the inherent safety in other phases of process life cycle. The present study aims to simulate the genetic algorithm process optimization (GAPO) and evaluate its effects on quantitative risk and inherent safety status at the operation phase of a methane recovery unit.

2. Methodology

The present study was carried out at the methane recovery unit of a petrochemical plant in the south of Iran to simulate the GAPO and evaluate its effects on quantitative risk. In GAPO, the level of produced methane was kept constant compared to the existing state, providing a higher level of safety without reducing methane separation or any add-on. The study was carried out in the following steps (Figure 1).

Figure 2 represents the process flow diagram of the studied methane recovery unit. The process consists of two drums for the refrigeration cycle, a feeding drum, a demethanizer tower, and two heat exchangers. First, the solid particles and the natural gas moisture are removed by filters and dryers. The feed gas (with the composition listed in Table 1) is then cooled to −94°C by the propane refrigeration (blue in Figure 2) and pumped into different parts of the demethanizer unit. The demethanizer tower is heated with a reboiler, which is embedded at the bottom (first tray) of the tower. Eventually, methane is separated from natural gas based on its bubble point and is exhausted from the top of the tower. The liquid gas, which is known as C2+, is exhausted from the bottom of the tower.

In this study, GAPO was used to optimize propane refrigerant consumption. For this purpose, the initial process was optimized using the GA Module in MATLAB. The implementation feasibility was investigated in terms of compatibility of the stability and energy equilibrium equations with fluids and thermodynamics rules using Aspen HYSYS (Figure 3) process simulator. The statistical population in GA was 10, and calculations are completed for 10 generations.

The role of 8 variables in reducing propane refrigerant consumption was investigated in this study. The initial value and the range of their changes are presented in Table 2.

The intended range of variables for optimization of propane consumption was determined according to the sensitivity analysis performed in the PHAST-Risk software for

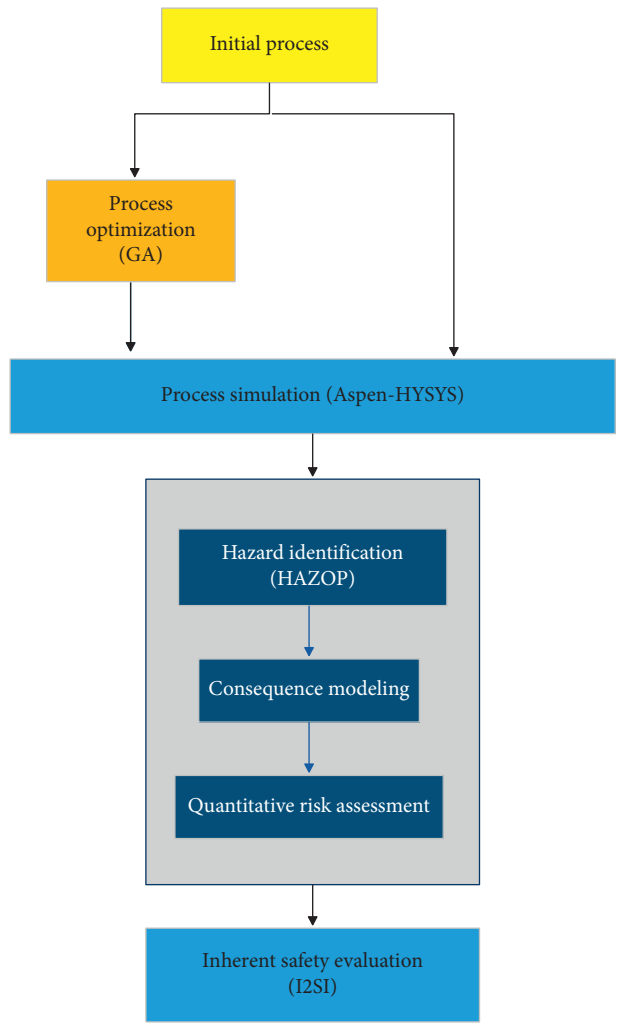

Figure 1: Overview of the procedure used in this study.

quantitative risk reduction, as well as variables changes versus the objective function. The objective function of the study was to reduce the propane refrigerant consumption and modify operational conditions to reduce the quantitative risk. Therefore, the optimal answer with minimum quantitative risk has been achieved. In addition, during the initial demethanizer process, the temperature of lines 22–26 (Figure 1), which plays the role of a reboiler in the system, was changed so that the LP steam consumption is approaching zero. The constraints of the problem are shown in Table 3; the objective function has been defined as the ratio of final to initial propane mass flow (kg/hr).

Next, the feasibility of GAPO was confirmed by Aspen HYSYS simulation to check whether the initial process was simulated for Aspen-HYSYS validation. The equation of the state of mixture fluid was PRSV.

The HAZOP method was used to identify the process hazards in the studied process unit. To this end, the process and equipment were divided into separate sections and nodes according to the nature of operation, including process lines, process vessels, process equipment, offsite systems, emergency shutdown systems, isolation at battery limits, and interface with other facilities. Members of the

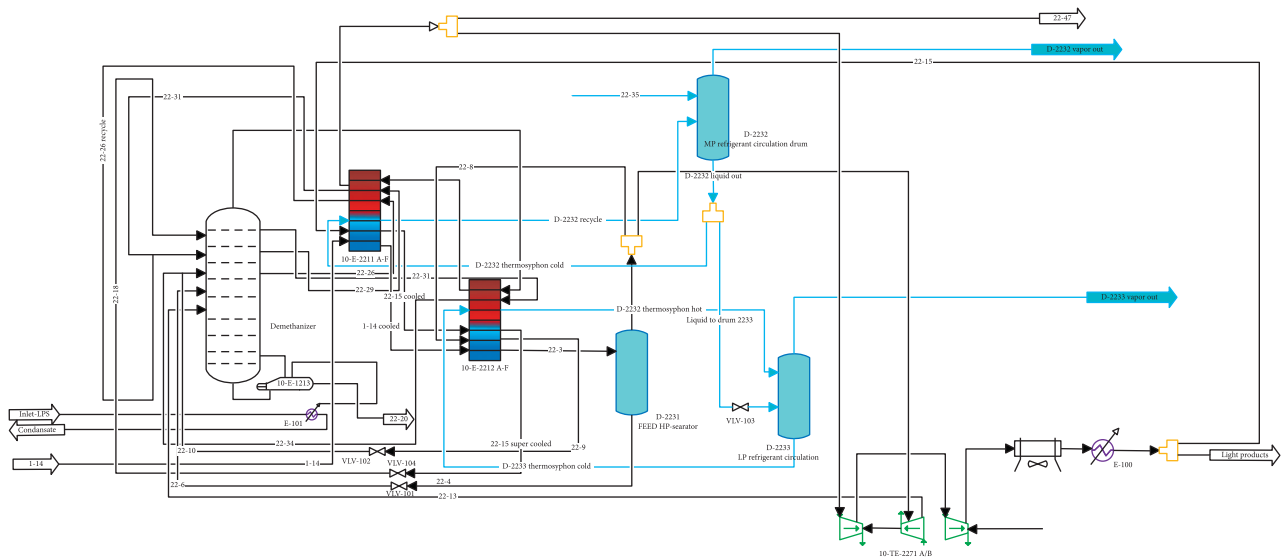

Figure 2: Process flow diagram for initial process of studied methane recovery.

Table 1: Feed composition in a studied methane recovery unit.

Composition	Mole fraction
Nitrogen	0.0356
CO_2	0.0102
Methane	0.8677
Ethane	0.0553
Propane	0.0209
i-Butane	0.0038
n-Butane	0.0055
i-Pentane	0.0004
n-Pentane	0.0003
n-Hexane	0.0001
n-Heptane	0.0001
n-Octane	0.0001

Table 2: Designed parameters applied for process optimization with genetic algorithm.

Input variable	Value
X1: temperature of stream 22-3 (°C)	−59.94
X2: molar flow of stream 22-8 (Kgmol/h)*	293306
X3: molar flow of stream 22-15 (Kgmol/h)**	129306
X4: temperature of stream 22–31 (°C)	−17.22
X5: temperature of stream 22–34 (°C)	−49.75
X6: boil up ratio	0.8012
X7: outlet pressure of expender	32.01
X8: pressure of top stage of column	31.51

*Expander is assumed to work in the range of 95%~105% of its normal capacity. **Reflux Ratio is considered to be in the range of 65%~110% of its normal flow rate.

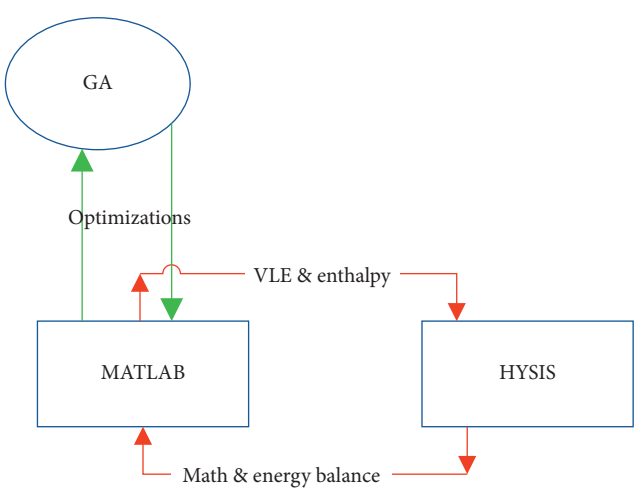

Figure 3: Implemented architecture links between Genetic algorithm, MATLAB, and HYSYS (GA: Algorithm Genetic–VLE: Vapor-liquid equilibrium).

Table 3: Constraints of genetic algorithm.

Constrains	Base case
C1 recovery % (from demethanizer (T-2211)) > 80	82
Minimum approach temperature of 10-E-2211 A-F > 4.1°C	4.3
Minimum approach temperature of 10-E-2212 A-F > 0.54°C	0.54

HAZOP team, consisting of 17 process, safety, and mechanical engineers, identified the hazards and possible incident scenarios for each node (Table 4).

The consequences of possible scenarios in the studied process unit were modeled using the PHAST software package. The information needed for consequence modeling was derived from the HAZOP study and the operational conditions contained in the P and IDs and PFDs (Table 5). Leakage size and their frequencies were selected based on the

Table 4: Identified scenarios for consequence modeling extracted from HAZOP study in the studied methane recovery unit.

Scenario	Composition	Description	Leak size (mm)	Frequency (occurrence/year)	Phase to release	Outcome consequence
Sc01-T01-S	Composition from Table 1	Small leak of demethanizer tower	25	$1.38E-0.03$	Gas	Jet fire flash fire vapor cloud
Sc02-T01-M	Composition from Table 1	Medium leak of demethanizer tower	100	$5.4E-5$	Gas	Jet fire flash fire vapor cloud
Sc03-T01-CR	Composition from Table 1	Large leak of demethanizer tower	609	$4.8E-5$	Gas	Jet fire flash fire vapor cloud
Sc04-D32-S	C_3H_8 (propane)	Small leak of MP REFR circulation drum	25	$1.38E-0.03$	Liquid	Jet fire flash fire vapor cloud
Sc05-D32-M	C_3H_8 (propane)	Medium leak of MP REFR circulation drum	100	$5.4E-5$	Liquid	Jet fire flash fire pool fire vapor cloud
Sc06-D32-CR	C_3H_8 (propane)	Large leak of MP REFR circulation drum	609	$4.8E-5$	Liquid	Fireball flash fire vapor cloud jet fire pool fire
Sc07-D31-S	Composition from Table 1	Small leak of feed HP separator	25	$1.38E-0.03$	2 phase	Jet fire flash fire vapor cloud
Sc08-D31-M	Composition from Table 1	Medium leak of feed HP separator	100	$5.4E-5$	2 phase	Jet fire flash fire vapor cloud
Sc09-D31-CR	Composition from Table 1	Large leak of feed HP separator	609	$4.8E-5$	2 phase	Jet fire fireball flash fire vapor cloud
Sc010-D33-S	C_3H_8 (propane)	Small leak of LP REFR. Circulation drum	25	$1.38E-0.03$	Liquid	Jet fire flash fire pool fire vapor cloud
Sc011-D33-M	C_3H_8 (propane)	Medium leak of LP REFR. Circulation drum	100	$5.4E-5$	Liquid	Jet fire flash fire pool fire vapor cloud
Sc012-D33-CR	C_3H_8 (propane)	Large leak of LP REFR. Circulation drum	609	$4.8E-5$	Liquid	Jet fire flash fire pool fire vapor cloud

Table 5: Process information for the initial process design of the studied methane recovery unit.

Equipment	Capacity (m^3)	Tem. (°C)	Pressure (bar)	Inventory (kg)
Demethanizer	1137	−94.6	33.5	84250
MP REFR circulation drum	49.1	−13.5	3.8	26840
LP REFR circulation drum	54.4	−43.8	1.2	31800
Feed HP separator	82.6	−60	55.6	8119

guidelines of OGP (Risk Assessment Data Directory, Release Failure Frequency, 2010) and DNV. The required climatic information was obtained from the hourly records during the last five consecutive years by the Meteorological Organization (Table 6). Due to weather difference, consequence modeling was carried out in two climatic conditions of spring/summer (Weather 1) and fall/winter (Weather 2).

In this stage, quantitative risks (societal and individual) were calculated using PHAST-Risk software for the initial process design (IPD) and proposed GAPO. The quantitative

Table 6: Meteorological data used for quantitative risk assessment.

Period	Average temperature (°C)	Relative humidity (%)	Wind velocity (m/s)	Prevailing wind direction	Stability class
Weather 1	31.75	46.83	2.71	WNW	A
Weather 2	21.13	52.25	2.69	WNW	B

risk was assessed based on process information derived from simulated processes (Aspen-HYSYS), consequence modeling, and population dispersion. The aim was to assess the effectiveness of GAPO in reducing the risks.

This study implemented I2SI, presented by Faisal Khan et al. (2004), to assess the process inherent safety status in GAPO compared to IPD. I2SI is calculated by dividing the inherent safety potential index (ISPI) to the hazard index (HI) for each subset or equipment (equation 1)), and finally, for the entire system (equation (2)). An increase in the score of I2SI reflects the improvement of the inherent safety status [33].

$$\mathrm{I2SI} = \frac{\mathrm{ISPI}}{\mathrm{HI}}, \tag{1}$$

$$\mathrm{I2SI}_{\mathrm{system}} = \left(\prod_{i=1}^{B} \mathrm{I2SI}_i\right)^{0.5}. \tag{2}$$

In this study, after determining the scenario and identifying the high-risk equipment in the process, I2SI was calculated for optimized process with GA compared to the IPD. Inherent safety status of process and equipment was calculated through I2SI approach according to the field expert's opinion and information from consequences modeling (for each equipment and for the whole system).

3. Results and Discussion

3.1. GAPO and Aspen-HYSYS. Figure 4 shows mean GA fitness generation for 10 populations in each module compared to the best fitness. Best fitness refers to the fitness of the best individual in the population compare to the goal and condition of study. Each generation provides a new average population fitness that is called mean fitness. In this study, as can be seen, after 10 generations, the mean fitness approached the best fitness. Meanwhile, not only the difference between the mean fitness and best fitness is as low as acceptable (about 0.017934), but also the mean fitness after seven generations has been stabilized, showing that the obtained final objective function is optimum.

The optimized values of the parameters selected as genetic algorithm generations are shown in Table 7. As indicated, by increasing the temperature of stream 22–31 (variable X4) from −17.22°C to −5.25°C, the required propane refrigerant mass flow rate increased due to refrigeration reduction in 10-E-2211 cold box. Finally, the refrigerant mass flow rate was decreased by increasing propane temperature in stream 22–26. As the temperature of stream 22–3 (inlet stream to 10-D-2231) (variable X1) increased from −59.94°C to −56°C, propane refrigeration decreased due to

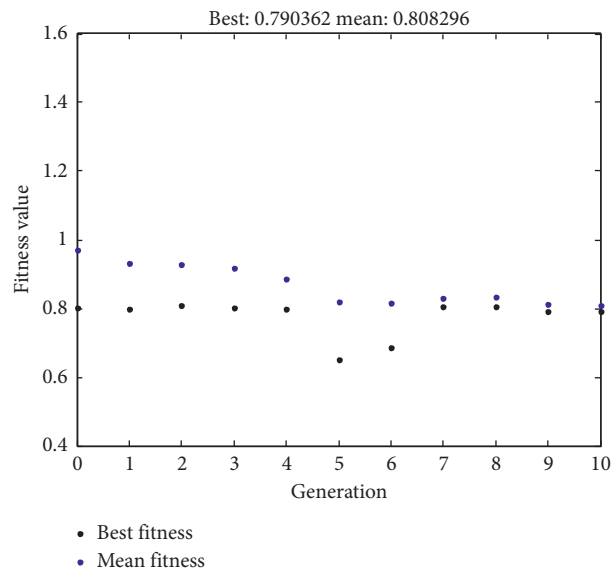

Figure 4: Fitness of generation versus best fitness.

increasing conversion of liquid to gas. The increase in gas was caused partly by the stream entering into the 10-TE-2271 expander. Since the pressure drop in the expander caused a cool down, the streams also reduced propane refrigeration flow rate. The pressure drops at the tower from 31.51 barg to 29 barg caused a reduction in the propane refrigeration flow rate. By reducing both the tower pressure (variable X8) and boil-up ratio (variable X6), the temperature of the outlet methane stream decreased, and consequently, the required cooling reduction was achieved. As the boil-up ratio dropped from 0.8012 to 0.7900, the gas flow in the tower also declined, which resulted in a flow rate reduction at tower side streams. The decrease in the rate at side streams eventually reduced the amount of propane refrigeration.

Table 8 shows the process information of methane recovery unit after simulation with genetic algorithm. As can be seen, after implementing the GAPO model, vessels have been changed to the lowest volume and safest status. The drop-in values of all parameters shown in Table 7 indicate a reduction in energy consumption. In other words, while the percentage of methane separation (production of methane and C2+) remained constant, the amount of propane consumption was reduced by 20%, which reduces the volume of vessel, thereby reducing quantitative risk and increasing inherent safety of the process. Therefore, a feasible approach to improve inherent safety at no cost and without decrease in production would be the application of the proposed genetic algorithm process optimization.

Table 7: Main properties and results of genetic algorithm optimization applied in this study.

Properties	Amount
Population size	10
Selection method	Stochastic uniform
Probability of crossover	0.8
Number of generations	10
Input variable	Optimized values
X1: temperature of stream 22-3 (°C)	−56 ↑
X2: molar flow of stream 22-8 (Kgmol/h) *	260000 ↓
X3: molar flow of stream 22-15 (Kgmol/h) **	85000 ↓
X4: temperature of stream 22–31 (°C)	−15.25 ↑
X5: temperature of stream 22–34 (°C)	−48 ↑
X6: boil-up ratio	0.79 ↓
X7: outlet pressure of expender	29.3 ↓
X8: pressure of top stage of column	29.00 ↓
Objective function	0.8 ↓

*Increase ↑ decrease ↓ (changing from main amount).

Table 8: Process information of methane recovery unit after simulation with genetic algorithm.

Involved equipment	Capacity (m^3)	Tem. (°C)	Pressure (bar)	Inventory (kg)
Demethanizer 1	1043	−96.37	29	29220
MP REFR circulation drum	42.1	−13.5	3.8	23020
LP REFR. Circulation drum	27.85	−43.8	1.2	16280
Feed HP separator	70.81	−56	55.6	6352

3.2. Hazard Identification and Consequence Modeling. Table 4 presents the identified scenarios for consequence modeling extracted from HAZOP study. This table reveals a total of 12 scenarios and details about the 4 most hazardous equipment devices including demethanizer, MP REFR circulation drum, Feed HP separator, and LP REFR. The circulation drum was extracted from HAZAOP study.

Table 9 represents the various consequences of scenarios in the process optimized with GA and the IPD. As can be seen, the vapor cloud radius decreased in all scenarios related to the demethanizer tower (scenarios 1 to 3). The highest reduction was observed in scenario 1, where the vapor cloud radius dropped to 44% at 23780 ppm in GAPO. This reduction is related to the 23% and 20% related to scenarios 2 and 3, respectively. But in scenarios 4 and 5, due to constant temperature and pressure in the drum, there is no decrease in the vapor cloud. However, in the worst-case scenario for this drum (Scenario 6), there is a 22% reduction in the vapor cloud radius. The radius of the vapor cloud in the feed drum is not significantly different due to a similar reason. In LP drum, due to reduction in the temperature and

Table 9: Results of consequence modeling for GAPO compared to IPD for average annual weather conditions.

Scenario	Consequence	IPD	GAPO
Sc01-T01-S	Vapor cloud-23780 ppm (m^2)	55	31
	Jet fire-lethality of 100% (m)	23	21
	Flash fire radius (m)	12–32	10–26
Sc02-T01-M	Vapor cloud-23780 ppm (m^2)	4093	3141
	Jet fire-lethality of 100% (m)	82	75
	Flash fire radius (m)	125–186	110–168
Sc03-T01-CR	Vapor cloud-23780 ppm (m^2)	160756	129135
	Jet fire-lethality of 100% (m)	410	373
	Flash fire radius (m)	668–850	625–784
Sc04-D32-S	Vapor cloud-10000 ppm (m^2)	179	174
	Jet fire-lethality of 100% (m)	31	31
	Flash fire radius (m)	21–37	20–36
Sc05-D32-M	Vapor cloud-10000 ppm (m^2)	5028	5049
	Jet fire-lethality of 100% (m)	106	106
	Flash fire radius (m)	99–138	99–138
	Pool fire zone-lethality of 100% (m^2)	5028	5028
Sc06-D32-CR	Vapor cloud-10000 ppm (m^2)	80759	62686
	Jet fire-lethality of 100% (m)	478	426
	Flash fire radius (m)	353–480	313–426
	Pool fire zone-lethality of 100% (m^2)	20601	15386
	Fireball zone-lethality of 100% (m^2)	13677	11304
Sc07-D31-S	Vapor cloud-22370 ppm (m^2)	118	106
	Jet fire-lethality of 100%(m)	28	27
	Flash fire radius (m)	17–44	16–42
Sc08-D31-M	Vapor cloud-22370 ppm (m^2)	6161	5863
	Jet fire-lethality of 100% (m)	96	94
	Flash fire radius (m)	152–220	148–218
Sc09-D31-CR	Vapor cloud-22370 ppm (m^2)	43481	37566
	Jet fire-lethality of 100% (m)	480	468
	Flash fire radius (m)	406–496	390–467
	Fireball zone-lethality of 100% (m^2)	40049	34618
Sc010-D33-S	Vapor cloud-10000 ppm (m^2)	75	52
	Jet fire-lethality of 100% (m)	20	16
	Flash fire radius (m)	11–20	9–17
	Pool fire zone-lethality of 100% (m^2)	452	254
Sc011-D33-M	Vapor cloud-10000 ppm (m^2)	1195	939
	Jet fire-lethality of 100% (m)	40	33
	Flash fire radius (m)	28–46	25–42
	Pool fire zone-lethality of 100% (m^2)	3215	1962
Sc012-D33-CR	Vapor cloud-10000 ppm (m^2)	6800	4961
	Jet fire-lethality of 100% (m)	141	133
	Flash fire radius (m)	76–117	68–104
	Pool fire zone-lethality of 100% (m^2)	5805	3419

Figure 5: Individual risks contours (1pmpy) for GAPO compared to IPD (IPD: Initial Process Design; GAPO: Genetic Algorithm Process Optimization).

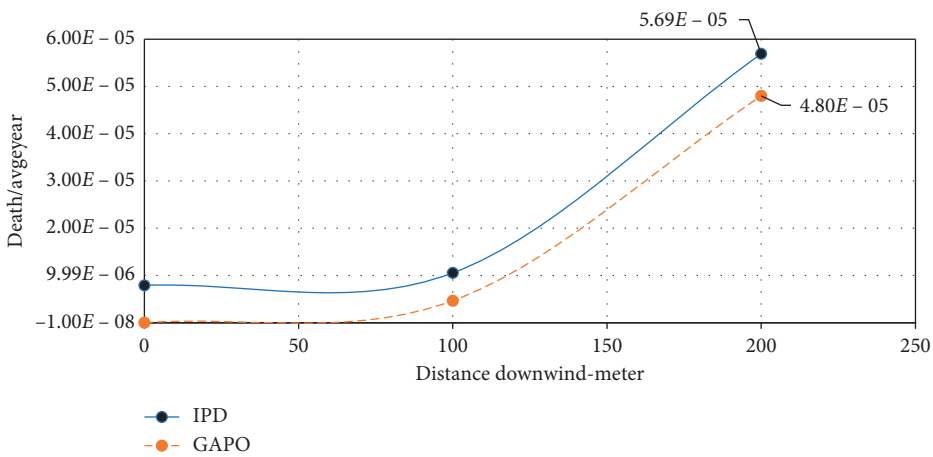

Figure 6: Calculated individual risk for GAPO compared to IPD (IPD: Initial Process Design; GAPO: Genetic Algorithm Process Optimization).

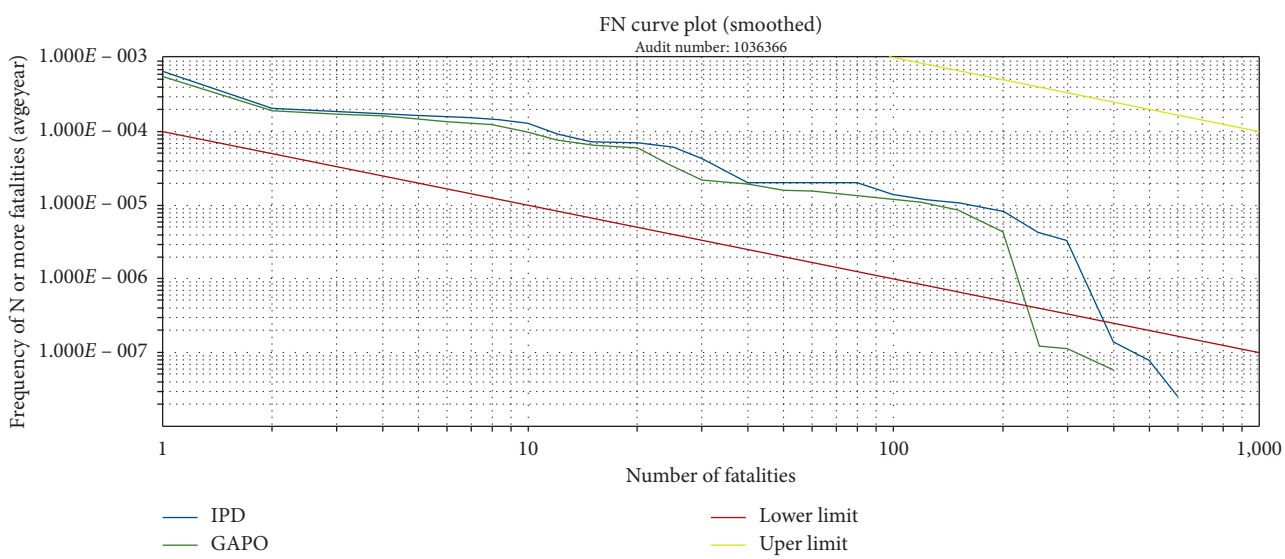

Figure 7: Calculated social risk (F-N Curve) for GAPO compared to IPD (IPD: Initial Process Design; GAPO: Genetic Algorithm Process Optimization).

Table 10: Result of I2SI for initial Process Design (IPD) compared to Genetic Algorithm Process Optimization (GAPO).

Equipment	Hazard index (HI)		Inherent safety potential index (ISPI)		Integrated inherent safety index (I2SI)		Total I2SI of process	
	IPD	GAPO	IPD	GAPO	IPD	GAPO	IPD	GAPO
Demethanizer tower	3.13	2.00	1.20	2.26	0.38	1.13	0.23	0.79
MP REFR circulation drum	1.47	1.75	0.53	1.18	0.32	0.68		
Feed HP separator	2.00	2.40	0.49	1.45	0.25	0.60		
LP REFR. circulation drum	1.32	1.85	2.39	2.50	1.81	1.35		

inventory, the vapor cloud radius decreased from 21% to 31% (Scenarios 10 to 12) in GAPO approach compared to the initial process.

After optimization of the studied methane process, the operating process of equipment was not significantly changed, and therefore, intensity of jet fire was not highly different. For example, in all three scenarios related to the demethanizer tower in GAPO, the jet fire was reduced by 9%. In scenarios for MR drum and feed drum, the amount of jet fire was almost identical. But in the LP drum scenarios, the jet fire dropped from 6% to 20% due to the reduction of temperature and inventory in GAPO. For the other fire scenarios, the intensity of incidents has decreased; for instance, intensity of pool fire decreased by 44% for LP drum (Scenario 11). Finally, implementing GAPO, it can reduce both the hazardous materials in the process and the capacity of the vessels while keeping production constant.

3.3. Cumulative Quantitative Risk Assessment. The individual risk contour of 1 pmpy, for GAPO compared to the IPD, is shown in Figure 5. As illustrated, implementation of GAPO was associated with reduction in 1 pmpy individual risk from 726473.54 m^2 in IPD to 596901.44 m^2 in GAPO. This decrease was more tangible in the downwind, due to the vapor cloud tending to spread in the wind direction; therefore, the individual risk was higher in the downwind incidents.

Figure 6 shows the individual risk transect for GAPO compared to the IPD in 200 m from the incident location, where the workers are resting. As can be seen, the individual risk at the employee's resting place reduced from $69.5E-05$/Avgeyear in IPD to $03.5E-05$/Avgeyear in GAPO.

In Figure 7, the results of societal risks are presented in GAPO and supported by Aspen HYSYS, compared to the IPD, which exists in the operation phase. As shown, the frequency of deaths is not significantly different in GAPO from the existing process. This uniformity is because the present study focused on the severity of incident consequences. As indicated, in the IPD, the number of deaths is 200 in almost frequency of 105/Avgeyear, which is reduced to 107/Avgeyear in GAPO. The number of deaths in integrated consequences of 12 scenarios in the IPD reduced from 600 to 400 in GAPO, which shows a 33% decrease.

3.4. Inherent Safety Assessment. Results of assessing process for inherent safety by I2SI for IPD and GAPO are present in Table 10. As the tables show, reducing hazard index for demethanizer tower has great impact on total inherent safety of initial process. Since the demethanizer tower is the most hazardous equipment on the process, implementing inherent safety into the process will improve the safety of the whole operation. This table also shows that the total I2SI of process increased significantly in the optimized process without a need to add safety equipment or use conventional safety methods and procedures.

4. Conclusion

The aim of this study was to investigate the effect of genetic algorithm process optimization on inherent safety enhancement and reduction of quantitative risks in operation phase of process. The results showed that, after optimizing the process with the genetic algorithm, the number of deaths decreased by one-third without reducing the amount of methane production. In addition, process optimization led to reduced energy consumption and improved efficiency. In conclusion, genetic algorithms can be implemented at no extra cost in all phases of the process life cycle to optimize processes and equipment, especially during the operation phase.

Abbreviations

GAPO: Genetic algorithm process optimization
HYSYS: Hyprotech system
PFD: Process flow diagram
NG: Natural gas
PHAST: Process hazard analysis software tools
I2SI: Integrated inherent safety index
IS: Inherent safety
HI: Hazard index
ISPI: Inherent safety potential index
IPD: Initial process design
ISP: Inherent safety principle
P and ID: Piping and instrumentation diagram
GA: Genetic algorithm
RCY: Recycle operator
TEE: Flow splitter
FB: Fire ball
MC: Maximum concentration
QRA: Quantitative risk assessment
HAZOP: Hazard and operability study
ESDV: Emergency shut down valve
NRV: None return valve
VLE: Vapor-liquid equilibrium

ISDS: Inherently safer design strategy
D-2232: MP refrigerant circulation drum
D-2231: FEED HP-separator
D-2233: LP refrigerant circulation
Pmpy: Part million per year
VLE: Vapor-liquid equilibrium
PRSV: Peng–Robinson-Stryjek-Vera equations of state
SIS: Safety instrument system
SOP: Standard operation procedure
DNV: Det Norske veritas
OGP: Oil and gas producers
P and ID: Piping and instrumentation diagram.

Data Availability

The data used to support the findings of this study are included within the article.

Conflicts of Interest

The authors declare that they have no conflicts of interest.

Acknowledgments

This article was extracted from the thesis written by Abolfaz Moghadasi, M.Sc. student of Occupational Health Engineering, and was financially supported by Shiraz University of Medical Sciences, Shiraz, Iran (Grant No. 95-01-04–13890).

References

[1] H. M. Hassim and H. N. Hanafi, "Current status and future direction of inherently healthier design in Malaysia," *Energy Procedia*, vol. 14, pp. 1939–1944, 2012.

[2] P. R. Amyotte, F. I. Khan, and T. A. Kletz, "Inherently safer design activities over the past decade," in *Proceedings of the IChemE Symposium Series*, Manchester, UK, November 2009.

[3] F. I. Khan and P. R. Amyotte, "I2SI: a comprehensive quantitative tool for inherent safety and cost evaluation," *Journal of Loss Prevention in the Process Industries*, vol. 18, no. 4–6, pp. 310–326, 2005.

[4] F. I. Khan and P. R. Amyotte, "How to make inherent safety practice a reality," *The Canadian Journal of Chemical Engineering*, vol. 81, no. 1, pp. 2–16, 2003.

[5] C. Sining, "Application of inherent safety explosion-proof technology in oil storage & transportation device," *Procedia Engineering*, vol. 15, pp. 4814–4818, 2011.

[6] H. Pasman and G. Reniers, "Past, present and future of quantitative risk assessment (QRA) and the incentive it obtained from land-use planning (LUP)," *Journal of Loss Prevention in the Process Industries*, vol. 28, pp. 2–9, 2014.

[7] A. Tugnoli, F. Khan, P. Amyotte, and V. Cozzani, "Safety assessment in plant layout design using indexing approach: implementing inherent safety perspective," *Journal of Hazardous Materials*, vol. 160, no. 1, pp. 100–109, 2008.

[8] S. Rathnayaka, F. Khan, and P. Amyotte, "Risk-based process plant design considering inherent safety," *Safety Science*, vol. 70, pp. 438–464, 2014.

[9] A. R. Carpenter, R. A. Ogle, S. J. Dee, and B. Cox, "Inherently safer design: lessons learned about the principle of simplification," in *Proceedings of the 2014 AIChE Spring National Meeting*, New Orleans, LA, USA, March 2014.

[10] E. J. Bernechea and J. Arnaldos, "Optimizing the design of storage facilities through the application of ISD and QRA," *Process Safety and Environmental Protection*, vol. 92, no. 6, pp. 598–615, 2014.

[11] T. A. Kletz, "Inherently safer design: the growth of an idea," *Process Safety Progress*, vol. 15, no. 1, pp. 5–8, 1996.

[12] A. M. Shariff and C. T. Leong, "Inherent risk assessment-a new concept to evaluate risk in preliminary design stage," *Process Safety and Environmental Protection*, vol. 87, no. 6, pp. 371–376, 2009.

[13] M. Gentile, W. J. Rogers, and M. S. Mannan, "Development of a fuzzy logic-based inherent safety index," *Process Safety and Environmental Protection*, vol. 81, no. 6, pp. 444–456, 2003.

[14] X. Lin, B. Chen, B. Yingli, and B. Zhu, "Study on effect of product liability to inherent safety," *Procedia Engineering*, vol. 45, pp. 271–275, 2012.

[15] C. Palaniappan, R. Srinivasan, and R. Tan, "Selection of inherently safer process routes: a case study," *Chemical Engineering and Processing: Process Intensification*, vol. 43, no. 5, pp. 641–647, 2004.

[16] P. R. Amyotte, A. U. Goraya, D. C. Hendershot, and F. I. Khan, "Incorporation of inherent safety principles in process safety management," *Process Safety Progress*, vol. 26, no. 4, pp. 333–346, 2007.

[17] R. Rusli and A. Mohd Shariff, "Qualitative assessment for inherently safer design (QAISD) at preliminary design stage," *Journal of Loss Prevention in the Process Industries*, vol. 23, no. 1, pp. 157–165, 2010.

[18] A. A. Kossoy, Y. G. Akhmetshin, and A. I. Benin, "Applying mathematical simulation for design of inherently safe chemical processes: I. providing inherent safety," *Russian Journal of Applied Chemistry*, vol. 85, no. 9, pp. 1466–1474, 2012.

[19] S. Shah, U. Fischer, and K. Hungerbühler, "Assessment of chemical process hazards in early design stages," *Journal of Loss Prevention in the Process Industries*, vol. 18, no. 4–6, pp. 335–352, 2005.

[20] J. Di Domenico, C. A. Vaz, and M. B. De Souza, "Quantitative risk assessment integrated with process simulator for a new technology of methanol production plant using recycled CO_2," *Journal of Hazardous Materials*, vol. 274, pp. 164–172, 2014.

[21] M. F. Milazzo, C. Vianello, and G. Maschio, "Uncertainties in QRA: analysis of losses of containment from piping and implications on risk prevention and mitigation," *Journal of Loss Prevention in the Process Industries*, vol. 36, pp. 98–107, 2015.

[22] L. Ma, L. Cheng, and M. Li, "Quantitative risk analysis of urban natural gas pipeline networks using geographical information systems," *Journal of Loss Prevention in the Process Industries*, vol. 26, no. 6, pp. 1183–1192, 2013.

[23] S.-J. Tong, Z.-Z. Wu, R.-J. Wang, and H. Wu, "Fire risk study of long-distance oil and gas pipeline based on QRA," *Procedia Engineering*, vol. 135, pp. 369–375, 2016.

[24] T. Wu, Q. Kong, X. Wei, X. Gao, and X. Xiong, "Quantitative analysis of enclosed ground flare based on PHAST analysis," *Heat Transfer*, vol. 49, no. 5, pp. 2746–2769, 2020.

[25] X. Wang and X. Ma, "Risk control analysis of safety accident in hydrogen refueling station based on PHAST software," *IOP Conference Series: Earth and Environmental Science*, vol. 680, no. 1, p. 012119, 2021.

[26] S. Li, C. Cheng, G. Pu, and B. Chen, "QRA-grid: quantitative risk analysis and grid-based pre-warning model for urban natural gas pipeline," *ISPRS International Journal of Geo-Information*, vol. 8, no. 3, p. 122, 2019.

[27] P. Baybutt, "A critique of the hazard and operability (HAZOP) study," *Journal of Loss Prevention in the Process Industries*, vol. 33, pp. 52–58, 2015.

[28] M. G. Jacobsen and S. Skogestad, "Active constraint regions for optimal operation of chemical processes," *Industrial & Engineering Chemistry Research*, vol. 50, no. 19, pp. 11226–11236, 2011.

[29] M. V. Pathan, S. Patsias, and V. L. Tagarielli, "A real-coded genetic algorithm for optimizing the damping response of composite laminates," *Computers & Structures*, vol. 198, pp. 51–60, 2018.

[30] R. Wang, Y. Wu, Y. Wang, and X. Feng, "An industrial area layout design methodology considering piping and safety using genetic algorithm," *Journal of Cleaner Production*, vol. 167, pp. 23–31, 2017.

[31] A. Velásco-Mejía, V. Vallejo-Becerra, A. U. Chávez-Ramírez, J. Torres-González, Y. Reyes-Vidal, and F. Castañeda-Zaldivar, "Modeling and optimization of a pharmaceutical crystallization process by using neural networks and genetic algorithms," *Powder Technology*, vol. 292, pp. 122–128, 2016.

[32] A. C. Caputo, P. M. Pelagagge, M. Palumbo, and P. Salini, "Safety-based process plant layout using genetic algorithm," *Journal of Loss Prevention in the Process Industries*, vol. 34, pp. 139–150, 2015.

[33] F. I. Khan and P. R. Amyotte, "Integrated inherent safety index (I2SI): a tool for inherent safety evaluation," *Process Safety Progress*, vol. 23, no. 2, pp. 136–148, 2004.

Hindawi
Mathematical Problems in Engineering
Volume 2021, Article ID 9916914, 10 pages
https://doi.org/10.1155/2021/9916914

Research Article

Numerical Well Test Analysis of Condensate Dropout Effects in Dual-Permeability Model of Naturally Fractured Gas Condensate Reservoirs: Case Studies in the South of Iran

Mohsen Safari-Beidokhti,[1] **Abdolnabi Hashemi**,[2] **Reza Abdollahi**,[1] **Hamed Hematpur**,[1] **and Hamid Esfandyari**[3]

[1]*EOR Research Department, Research Institute of Petroleum Industry, Tehran, Iran*
[2]*Department of Petroleum Engineering, Petroleum University of Technology, Ahvaz, Iran*
[3]*Abadan Faculty of Petroleum Engineering, Petroleum University of Technology, Abadan, Iran*

Correspondence should be addressed to Hamid Esfandyari; esfandyari_shirazu@yahoo.com

Received 1 April 2021; Revised 19 April 2021; Accepted 27 April 2021; Published 7 May 2021

Academic Editor: Mohammad Yazdi

Naturally fractured reservoirs (NFR) represent an important percentage of worldwide hydrocarbon reserves and production. The performance of naturally fractured gas condensate reservoirs would be more complicated regarding both rock and fluid effects. In contrast to the dual-porosity model, dual-porosity/dual-permeability (dual-permeability) model is considered as a modified model, in which flow to the wellbore occurs through both matrix and fracture systems. Fluid flow in gas condensate reservoirs usually demonstrates intricate flow behavior when the flowing bottom-hole pressure falls below the dew point. Accordingly, different regions with different characteristics are formed within the reservoir. These regions can be recognized by pressure transient analysis. Consequently, distinguishing between reservoir effects and fluid effects is challenging in these specific reservoirs and needs numerical simulation. The main objective of this paper is to examine the effect of condensate banking on the pressure behavior of lean and rich gas condensate NFRs through a simulation approach. Subsequently, evaluation of early-time characteristics of the pressure transient data is provided through a single well compositional simulation model. Then, drawdown, buildup, and multirate tests are conducted to establish the condition in which the flowing bottom-hole pressure drops below the dew point causing retrograde condensation. The simulation results are confirmed through well test analysis in both Iranian naturally fractured rich and lean gas condensate fields. Interpretations of simulation analysis revealed that the richer gas is more prone to condensation. When the pressure drops below the dew point, the pressure derivative curves in the rich gas system encounter a more shift to the right, and the trough becomes more pronounced as compared to the lean one.

1. Introduction

1.1. Naturally Fractured Reservoirs. A substantial amount of worldwide oil and gas was produced by Naturally Fractured Reservoirs (NFR) [1–8]. The recovery factor in NFR varies widely (10 to over 60%). On the one hand, fractures could play the role of the main path of fluid flow, especially in tight formations, and consequently improve the ultimate reservoir recovery [9]. On the other hand, fractures may have the adverse effect on reservoir productivity and cause earlier unwanted water production, erratic sweep patterns, and consequently low recovery factor [9–11]. This issue is more critical in naturally fracture water drive gas reservoirs. This water expansion in naturally fractured reservoirs, particularly with low matrix permeability, fills up the fractures, and the free gas will stop flowing. Thus, water would be the only fluid passing through the fractures, and early breakthrough happens [12]. Beaver River Field of Canada [13], Dengying gas reservoir in Weiyuan gas Field in China [14], and Aguarague Field in Argentina [15] with the gas recovery of 12, 37, and 34 percent, respectively, are

examples of these kinds of reservoirs. Thus, the effect of fracture on ultimate reservoir recovery could be either positive or negative.

Well test data can offer crucial information about the reservoir properties. The existence of fractures introduces a layer of difficulty in interpreting the pressure response. By now, several idealizations have been suggested to analyze the NFR pressure behavior. The most common idealization is the dual-porosity model proposed by Barenblatt et al. (1960). This model was firstly applied in reservoir engineering by Warren and Root (1963) by introducing two additional parameters as follows [16].

Storativity ratio (ω):

$$\omega = \frac{(\varphi c_t)_{\text{fracture}}}{(\varphi c_t)_{\text{fracture}} + (\varphi c_t)_{\text{matrix}}}. \quad (1)$$

Interporosity flow coefficient (λ):

$$\lambda = \frac{\alpha k_{\text{matrix}} r_w^2}{k_{\text{fracture}}}, \quad (2)$$

in which α is defined as

$$\alpha = \frac{4n(n+2)}{L_{\text{matrix}}^2}. \quad (3)$$

Figure 1 depicts different matrix system elements, $n = 1$, 2, 3 for slab, cylinder, and cubic matrix blocks, respectively [17]. The dual-porosity model assumes the existence of the two media with large bulk porosity/relatively low permeability (matrix) and very low bulk porosity/relatively high permeability (fracture). In this model, fluid flow from the matrix to the fracture system, and subsequently, through the fracture to the wellbore, leads to hydrocarbon production. The fluid regime between the matrix and interconnected fracture is pseudosteady state flow [18–21].

The incorporation of the dual-porosity idealization and numerical modeling for large-scale fluid flow application was firstly introduced by Kazemi et al. (1976) [19]. It has been recognized as the standard for NFR modeling and well test interpretation [5, 9, 18–29].

Figure 2 depicts the pressure transient behavior in the dual-porosity model. Figure 3 represents the different flow behaviors of such reservoirs on log-log pressure derivative response schematically [16, 21].

The dual-porosity dual-permeability is another idealization introduced to improve the previous dual-porosity model. This idealization was first suggested by Blaskovich et al. (1983) and Hill and Thomas (1985). Matrix blocks are connected in this model and participate in the overall fluid flow. In comparison to the dual-porosity model, which is suitable only for intensely fractured reservoirs, the dual-porosity/permeability model can be applied for many reservoirs with different fracture degrees [31–36].

Figures 4 and 5 show a schematic of fluid flow in these two aforementioned models [37].

Overall, dual-porosity/dual-permeability reservoir includes two homogeneous layers. The cross flow between layers exists, and both can flow into the well. The pressure difference between layers determined the amount of interlayer cross flow. The parameters resulting from well test analysis define the mathematic model to describe this reservoir [38]:

Mobility ratio (κ):

$$\kappa = \frac{k_1 h_1}{k_1 h_1 + k_2 h_2} = \frac{k_1 h_1}{k h_{\text{TOTAL}}}. \quad (4)$$

Storativity ratio (ω):

$$\omega = \frac{(\varphi C_t h)_1}{(\varphi C_t h)_1 + (\varphi C_t h)_2} = \frac{(\varphi C_t h)_1}{(\varphi C_t h)_{\text{Total}}}. \quad (5)$$

Interlayer cross flow coefficient (λ):

$$\lambda = \frac{r_w{}^2}{k_1 h_1 + k_2 h_2} \cdot \frac{2}{h_1/k_{z1} + h_2/k_{z2}}. \quad (6)$$

At the early time, cross-flow does not occur, and the layers are produced independently. When the interlayer cross flow starts, a transition period is detected by an inflection in the pressure response and a valley in the derivative. After the transition, the reservoir acts as a homogeneous medium, with total kh and storativity. When the mobility ratio is equal to one, the response of the dual-porosity and dual-porosity/permeability is the same. In addition, the response tends to a homogeneous reservoir when the mobility ratio decreases, as shown in Figure 6.

The different flow behavior, which can be observed in the log-log pressure derivative, is the same as that in Figure 3. The only difference is that, in all cases, the matrix can also produce into the well [21]. Many researches have been conducted on naturally fractured reservoirs applying the dual-porosity and dual-permeability model [36, 38–51].

1.2. Gas Condensate Reservoirs and Pressure Transient Analysis. A gas condensate is a naturally occurring hydrocarbon mixture found between the cricondentherm and critical reservoir temperature [52–55]. It can be categorized into rich and lean gas condensate reservoirs. Below the dew point, rich and lean gas condensate generates 100 and more than 150 STB/MMSCF of liquid, respectively [56]. Due to the complex phase and fluid flow behavior of these reservoirs, their evaluation becomes a challenging issue. With condensate accumulation around the well, the effective permeability is reduced substantially [38, 57–68].

The first investigation on condensate blockage was directed by Muskat (1949) [69]. O'Dell and Miller (1967) suggested a pseudopressure equation to analyze this phenomenon. This equation is limited to reservoirs over the dew point pressure and when the radius of condensate banking is not significant. In 1973, Fussel developed the compositional model, which was applicable to analysis gas condensate reservoirs behavior below the dew point pressure [70]. Later, Jones, and Raghavan (1988) used buildup and drawdown pressure tests to study the gas condensate reservoirs [71]. The concept three-flow region in gas condensate reservoirs was proposed by Fevang and Whitson (1996) and Penuela

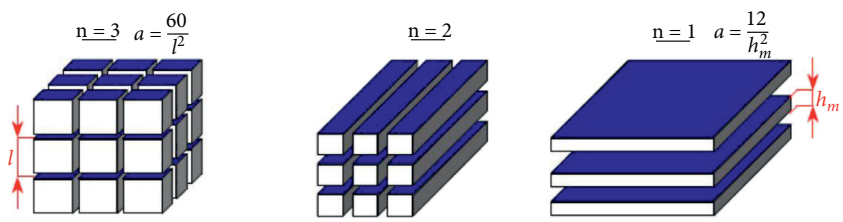

Figure 1: Three different matrix block geometries in the dual-porosity model [17].

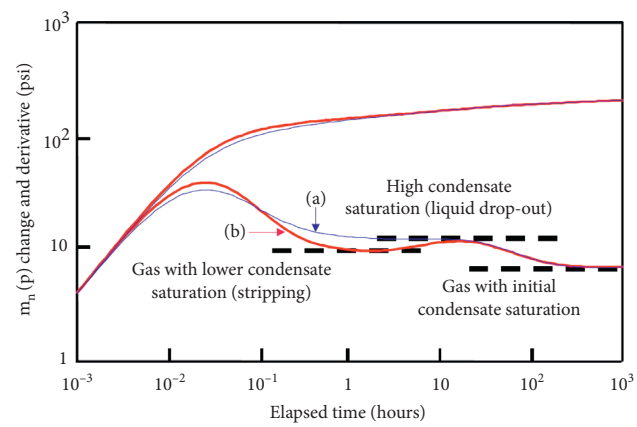

Figure 2: Schematic of pressure and derivative of composite behaviors: (a) two- and (b) three-region composite

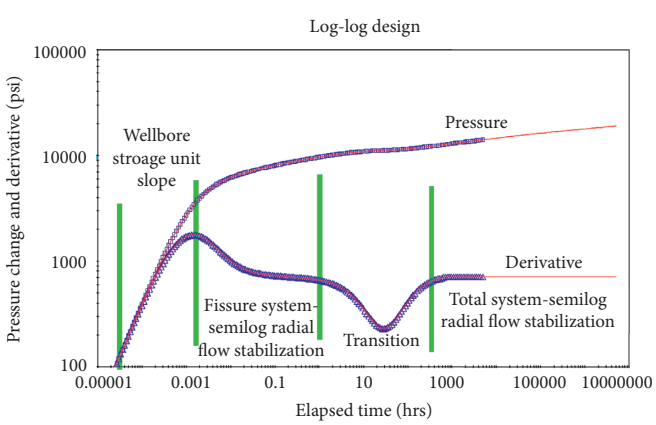

Figure 3: Pressure and derivative log-log curve in dual-porosity reservoirs.

and Civan (2000) [59, 72]. Properties of these regions can be summarized as follows:

Region (1): this is the farthest region around the well with pressure over the dew point. The system contains a single gas-phase including the initial liquid saturation.

Region (2): this region is near the first region toward the well. It is generated with pressure reduction below the dew point, and where the liquid saturation increases rapidly. It should be noted that, in this region, the liquid phase is immobile (SL < SLC).

Region (3): this region is the nearest region around the well. The liquid saturation is higher than the critical saturation of condensate, so, gas and oil phases are mobile.

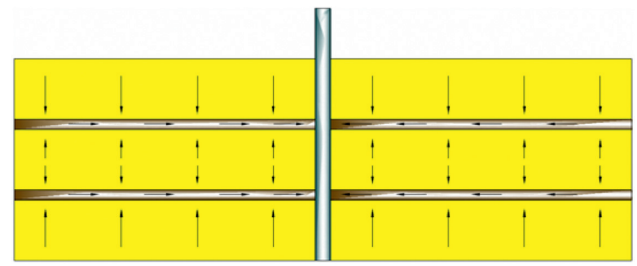

Figure 4: Dual-porosity idealization of naturally fractured reservoirs [36].

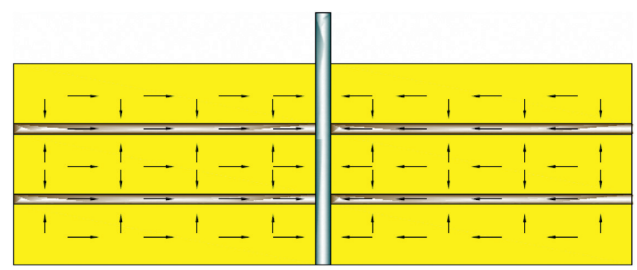

Figure 5: Dual-porosity/dual-permeability idealization of naturally fractured reservoirs [36].

In some references, the existence of another region in the vicinity of wells was reported. This fourth region was firstly reported by Gringarten et al. (2000) [30].

Three-region composite is the most frequently used model in the gas condensate reservoir evaluation [42, 52, 56, 58–63].

One of the approved methods in investigating the gas condensate reservoir behavior is well-test analysis (pressure transient tests). Figure 7 shows the regions around the wellbore by applying a single-phase pseudopressure function for gas condensate reservoir.

Due to the high conductivity of fractures, condensate flow in fractures is simpler, and consequently, condensate saturation near the wellbore can be higher with respect to other regions in reservoirs. In opposition, the residual condensate saturation in the matrix is relatively large; hence, it could remain immobile for quite sometimes.

In gas condensate NFRs, these regions are usually formed in the fracture system because of the high fracture mobility and minor change in matrix gas saturation. Figure 8 illustrates the profile of gas saturation in naturally fracture reservoirs [37].

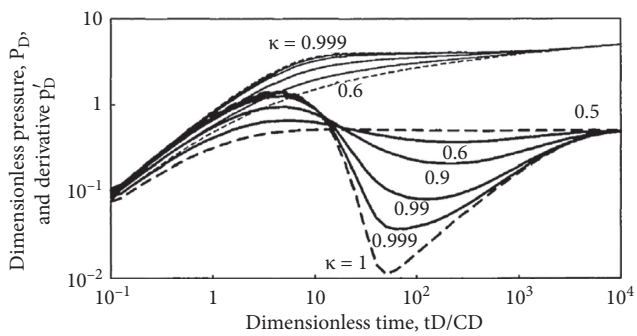

Figure 6: Pressure and derivative log-log curve in dual-porosity/dual-permeability reservoir. The two dashed curves correspond to the homogeneous reservoir responses (κ=0.5) and dual-porosity response (κ=1) [21].

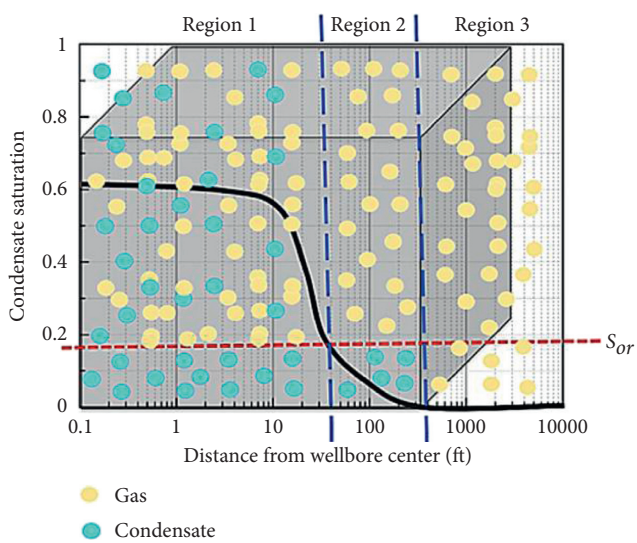

Figure 7: Different regions of condensate dropout.

Interaction of competing viscous, capillary, and inertial forces as the pressure change during reservoir life can affect the well deliverability of gas condensate reservoirs. The physical processes that reduce productivity are condensate banking, and inertial effect, which leads to the reduction of k_{rg} as the velocity increases. Conversely, positive coupling or velocity stripping effect (capillary number effect) results in the increase of gas relative permeability and to some extent that of liquid, as velocity increases and/or IFT decreases. The overall balance of these forces specifies the well deliverability [30].

2. Approach

Since there is not any analytical composite model for gas condensate NFRs, a numerical compositional model is a suitable choice to assess the pressure behavior in these types of reservoirs.

In the current study, the effect of condensate banking on the pressure behavior of lean and rich gas condensate NFRs is investigated through a simulation approach. The necessary simulation data (fluid and rock properties) was acquired from a real gas condensate field. Multirate tests (drawdown and buildup) were conducted to create a condition in which the flowing bottomhole pressure went below the dew point, and consequently, the condensate was formed. In the next step, the results of the numerical model were analyzed by standard well tests analysis to derive the results.

2.1. Simulation Studies. The characteristics of the proposed model for dual-porosity/dual permeability reservoirs will be discussed. Two types of gases (lean and rich) were used for validating the presented model.

2.1.1. Model Setup. The compositional simulator (Elipse-300) was utilized to set up a single vertical model in radial coordinates. The thickness of the synthetic multilayer model proposed for the dual-porosity/dual-permeability reservoir is 100 ft. For attaining a better resolution near the wellbore to detect condensate behavior, the gird blocks were adjusted, so that their numbers increased logarithmically toward the well. The reservoir simulation input, initial reservoir saturations, rock properties, and rate schedules are presented in Tables 1–4, respectively.

2.1.2. PVT Modeling. The reservoir fluid behavior is an essential part of reservoir simulation. The PVTi package is utilized to simulate the reservoir fluid properties. The results of all PVT experiments are matched simultaneously to determine a representative equation of state (EOS) for the reservoir fluid. 3-parameter Peng–Robinson (PR3) with lumped 8 and 13 components is selected as EOS input into the simulator in lean and rich gas, respectively. Tables 5 and 6 show the composition of lean and rich gas, and Table 7 summarizes detailed results of PVT matching.

2.1.3. Relative Permeability. The feed relative permeability data in the simulator were taken from laboratory core analysis. Since the relative permeability curve in gas condensate reservoirs depends mainly on velocity and IFT, Eclipse-300 interpolates the objective curve between a base and a miscible curve. The base curve is measured when IFT is at the highest level, and velocity is at the lowest possible level. The miscible curve accounts for inertial effects. The interpolation is weighted by capillary number dependent functions.

2.2. Model Validation. The output of the well test model was used to validate the accuracy of the proposed numerical model. To compare the results of real field (input data of simulator) and simulations, the buildup test was conducted. Tables 8 and 9 represent the comparison results above the dew point pressure.

2.2.1. Simulation Results. The proposed models (lean and rich gas condensate) are representative of dual-porosity/dual-permeability NFR, and the main objective is the

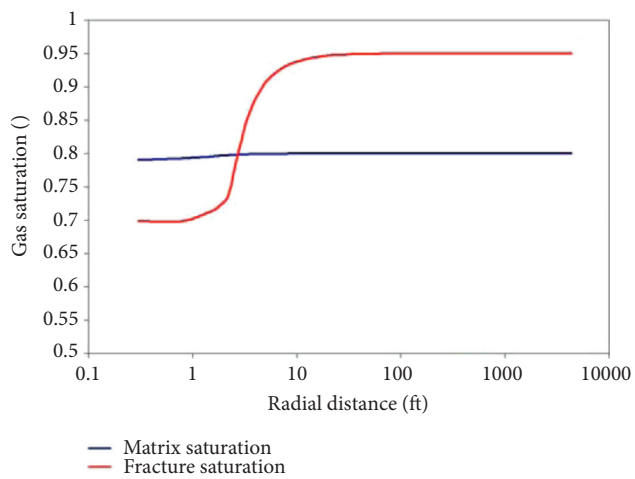

Figure 8: Gas saturation profile for idealizations of dual-porosity/dual-permeability gas-condensate reservoirs [21].

Table 1: Reservoir simulation input data for the reservoir model.

Grid information	
Number of cells in r-direction, $I_{\max}$	52
Number of cells (layers) in z-direction, $K_{\max}$	15
Reservoir radius (r_e), (ft)	6000
Well information	
Wellbore radius (r_w), (ft)	0.25
Wellbore storage coefficient (C_w) [RB/psi]	0
Roughness	0
Perforated nodes	1-15

Table 2: Initial saturation for the reservoir model.

Initial saturation			
Matrix		Fracture	
S_{wi}	0.36	S_{wi}	0.00
S_{oi}	0.00	S_{oi}	0.00
S_{gi}	0.63	S_{gi}	1.00

Table 3: Rock properties for the reservoir model.

Rock properties			
Matrix		Fracture	
$k^{[m\ d]}$	1.2	$k^{[m\ d]}$	9000
φ	0.11	φ	1
$C_f{}^{[psi-1]}$	4.25E-06	$C_f{}^{[psi-1]}$	1E-4

Table 4: Rate schedule for the modified isochronal test.

Elapse time (hr)	Gas rate (Mscf/day)
600	8000
9.6	0
1200	10000
9.6	0
2400	12000
12	0

investigation of condensate blockage. Simulation scenarios and their characteristics are presented in Table 10.

In addition, the log-log plot of buildup data for lean and rich gas reservoir model at pressures above and below dew point is shown in Figures 9 and 10.

3. Discussion

As can be seen in both Figures 9 and 10, the effect of condensate accumulation is superimposed on dual-porosity/dual-permeability flow behavior. The observed fluid flow behavior can be categorized into early transition and late time zones.

3.1. Early Time Behavior. Derivative curves indicate that, below the dew point, reduced mobility region is formed near the wellbore. This behavior occurs after an upward shift in the early time derivative stabilization. Although more liquid saturation is formed in the case of the rich gas condensate system compared to the lean one, there is no sharp difference in the upward shift between these two different gas systems. This phenomenon is observed because condensate is mainly developed in the high mobility of the fracture systems.

3.2. Transition Behavior. Fluid flow between the matrix and fractures in the reservoir starts at the transition zone. Any phenomenon that restricted this communication results in the expansion of this period. Interpretations of log-log curves reveal that the surface of matrix blocks can be damaged by condensate formation. This damage is interpolated by an additional interporosity skin factor. This particular skin factor causes a delay in fluid flow from the matrix blocks to the fractures. Since the rich gas is more prone to condensation with respect to the lean gas, the skin factor is higher in the rich gas system. Consequently, the reduction in the value of interlayer cross-flow coefficientλ is more. This fact is illustrated in Figures 9 and 10, in which the derivative curve is shifted to the right in the transition period.

3.3. Late Time Behavior. As the bottom-hole pressure decreases, more condensate is formed and accumulated. If the entire reservoir pressure drops below the dew point, the

Table 5: Composition of lean gas/condensate fluid.

Number	Components	Mole fraction (%)
1	PC1 (C_1, N_2)	86.065
2	C_2	5.23
3	PC2 (C_3, H_2S)	2.18
4	CO_2	1.93
5	PC3 (iC_4, NC_4, C_5, iC_5, NC_5)	1.75
6	PC4 (C_6, BEN, C_7, TOL, C_8, C_9, C_{10}, C_{11}, C_{12})	2.34
7	PC5 (C_{13} to C_{19})	0.42
8	PC6 (C_{20} to C_{35} and C_{36+})	0.085

Table 6: Composition of rich gas/condensate fluid.

Number	Components	Mole fraction (%)
1	N_2	3.48
2	CO_2	1.60
3	C_1	75.43
4	C_2	8.05
5	C_3	3.61
6	iC_4	0.62
7	NC_4	1.08
8	iC_5	0.31
9	NC_5	0.41
10	C_6	0.47
11	PC1 (C_7 to C_{12})	3.07
12	PC2 (C_{13} to C_{22})	1.02
13	PC3 (C_{23+})	.85

Table 7: Comparison between observed and calculated PVT data.

	Observed dew point pressure (psia)	Calculated dew point pressure (psia)	Maximum liquid dropout in the CVD experiment (%) Observed and calculated)
Lean gas	4898	4891.37	4
Rich gas	3250	3235	1.9

Table 8: Buildup test analysis for the lean gas reservoir model above the dew point pressure.

	Input data	Log-log analysis
$P_i[Psia]$	6000	5984
$kh[m\ d-ft]$	480	452
$k_{reff}[m\ d]$	4.61	4.34

Table 9: Buildup test analysis for the rich gas reservoir model above the dew point pressure.

	Input data	Log-log analysis
$P_i[Psia]$	4000	3994
$kh[m\ d-ft]$	480	463
$k_{reff}[m\ d]$	4.61	4.45

Table 10: Summary of simulation models run in this work.

	Above dew point	Below dew point
Lean gas	$P_i = 6000$	$P_i = 4500$
Rich gas	$P_i = 4000$	$P_i = 3300$

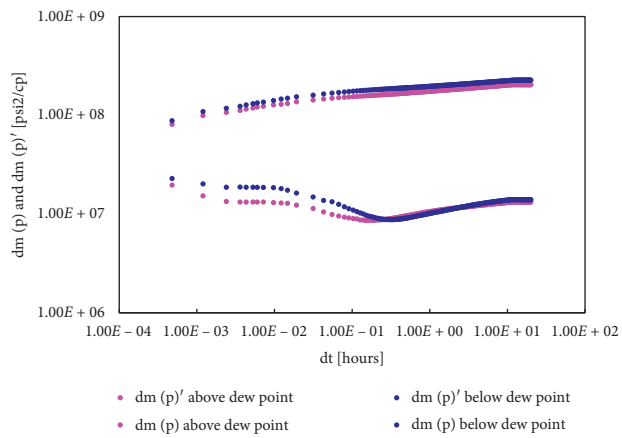

Figure 9: Log-log plot of buildup test results for the lean gas reservoir model.

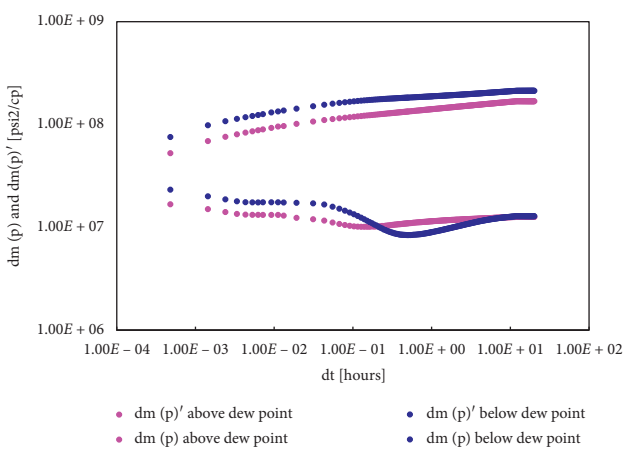

Figure 10: Log-log plot of buildup test results for the rich gas reservoir model.

composite behavior can appear at the late times. This situation happens more in the lean gas system, in which condensate can be formed in the entire reservoir. On the contrary, in the rich gas system, the falling of reservoir pressure below the dew point is less probable; thus, the probability of condensate formation in the entire reservoir, especially in far regions from the wellbore, is less. In this situation, late time stabilization is the same for both below and above dew point cases (Figure 10). Similar to the early times periods, liquid condensation causes a reduction ink_{rg}, which is characterized with an upward shift in the late time derivative stabilization (Figure 9).

4. Conclusion

The outcomes of the proposed simulator for detecting the condensate formation in lean and rich gas reservoirs lead to the following conclusion:

(1) During the well test analysis of gas condensate naturally fractured reservoirs, condensate creation adds more complexity to the analysis.

(2) Since external edges of the matrix blocks will be the first to host condensate in the system, condensation deposition creates an impediment layer at surface of the matrix blocks, which results in delaying matrix feeding to fractures. This phenomenon shifts pressure derivative curve to the right and causes deeper transition period.

(3) The richer gas is more prone to condensation. When the pressure drops below the dew point, the pressure derivative curves in rich gas system encounter a more shift to the right, and the trough becomes more prominent as compared to the lean one.

(4) Applying conventional analytical techniques for analyzing the pressure behavior in gas condensate NFRs suffered condensate banking issue, leading to unreliable results. In order to address this issue, the numerical simulation for more accurate results should be used.

Nomenclatures

c_t: Total compressibility (psi^{-1})
c_t: Total compressibility (psi^{-1})
h_1, h_2: Thickness of the layer (ft)
k_1, k_2: Permeability of the layer (mD)
k_{z1}, k_{z2}: Vertical permeability of the layer (mD)
k_m: Matrix permeability (mD)
k_f: Fracture permeability (mD)
k_{rg}: Gas relative permeability
m: Characteristic fracture spacing, ft
L
n: Number of orthogonal sets of parallel fractures (1, 2 or 3)
φ: Porosity
P: Pressure (psi)
P_i: Initial pressure (psi)
r_w: Wellbore radius (ft).

Subscripts
f: Fracture
i: Initial
m: Matrix.

Data Availability

The data used to support the findings of this study are included within the article.

Conflicts of Interest

The authors declare that they have no conflicts of interest.

References

[1] M. Presho, S. Wo, and V. Ginting, "Calibrated dual porosity, dual permeability modeling of fractured reservoirs," *Journal of Petroleum Science and Engineering*, vol. 77, 2011.

[2] P. Ø. Andersen, "A simplified modelling approach for petroleum recovery by spontaneous imbibition in naturally fractured reservoirs," *Journal of Natural Gas Science and Engineering*, vol. 63, 2019.

[3] G. H. Spence, G. D. Couples, T. G. Bevan et al., "Advances in the study of naturally fractured hydrocarbon reservoirs: a broad integrated interdisciplinary applied topic," *Geological Society Special Publication*, vol. 374, 2014.

[4] P. Lemonnier and B. Bourbiaux, "Simulation of naturally fractured reservoirs. State of the art: Part 2 - matrix-fracture transfers and typical features of numerical studies," *Oil & Gas Science and Technology - Revue d'IFP Energies nouvelles*, vol. 65, 2010.

[5] P. Lemonnier and B. Bourbiaue, "Simulation of naturally fractured reservoirs. State of the Art: Part 1 - physical mechanisms and simulator formulation," *Oil & Gas Science and Technology*, vol. 65, 2010.

[6] H. Esfandyari, A. Moghani Rahimi, F. Esmaeilzadeh et al., "Amphoteric and cationic surfactants for enhancing oil recovery from carbonate oil reservoirs," *Journal of Molecular Liquids*, vol. 322, 2020.

[7] M. Yazdi, "Ignorance-aware safety and reliability analysis: a heuristic approach," *Quality and Reliability Engineering International*, vol. 36, 2020.

[8] S. Kabir, T. K. Geok, M. Kumar, M. Yazdi, and F. Hossain, "A method for temporal fault tree analysis using intuitionistic fuzzy set and expert elicitation," *IEEE Access*, vol. 8, pp. 980–996, 2020.

[9] A. Firoozabadi, "Recovery mechanisms in fractured reservoirs and field performance," *Journal of Petroleum Technology and Alternative Fuels*, vol. 39, 2000.

[10] J. M. Babadimas, "Modelling trapped gas expansion in water-drive reservoirs," in *Proceedings of the SPE/IATMI Asia Pacific Oil & Gas Conference and Exhibition*, Jakarta, Indonesia, October 2017.

[11] J. R. Gilman and H. Kazemi, "Improvements IN simulation OF naturally fractured reservoirs," *Society of Petroleum Engineers Journal*, vol. 23, 1983.

[12] J. Yang, C. Li, S. Geng, S. He, and K. Li, "Microscopic flow mechanism of water invasion in ideal fracture models," *Energy Sources, Part A Recover*, vol. 28, 2020.

[13] D. A. Davidson and D. M. Snowdon, "Beaver river middle devonian carbonate: performance review OF a high-relief, fractured gas reservoir with water influx," *Journal of Petroleum Technology*, vol. 30, 1978.

[14] G. Wei, G. Chen, S. Du, L. Zhang, and W. Yang, "Petroleum systems of the oldest gas field in China: neoproterozoic gas pools in the Weiyuan gas field, Sichuan Basin," *Marine and Petroleum Geology*, vol. 25, 2008.

[15] R. Aguilera, J. J. Conti, and E. A. Lagrenade, "Reducing gas-production decline through dewatering: a case history from the naturally fractured Aguarague field, Salta Argentina," *SPE Reservoir Evaluation & Engineering*, vol. 6, 2003.

[16] J. E. Warren and P. J. Root, "The behavior of naturally fractured reservoirs," *Society of Petroleum Engineers Journal*, vol. 3, 1963.

[17] E. W. Moore, C. W. Crowe, and A. R. Hendrickson, "Formation, effect and prevention of asphaltene sludges during stimulation treatments," *Journal of Petroleum Technology*, vol. 17, 1965.

[18] G. I. Barenblatt, I. P. Zheltov, and I. N. Kochina, "Basic concepts in the theory of seepage of homogeneous liquids in fissured rocks [strata]," *Journal of Applied Mathematics and Mechanics*, vol. 24, 1960.

[19] E. Hamid, A. Moghani, F. Esmaeilzadeh, and A. Davarpanah, "A laboratory approach to measure carbonate rocks' adsorption density by surfactant and polymer," *Hindawi Mathematical Problems in Engineering*, vol. 2021, Article ID 5539245, 7 pages, 2021.

[20] M. Abbasi, M. Madani, M. Sharifi, and A. Kazemi, "Fluid flow in fractured reservoirs: exact analytical solution for transient dual porosity model with variable rock matrix block size," *Journal of Petroleum Science and Engineering*, vol. 164, 2018.

[21] D. Bourdet, Well Test Analysis: The Use of Advanced Interpretation Models, 2002.

[22] F. Kuchuk and D. Biryukov, "Pressure-transient behavior of continuously and discretely fractured reservoirs," *SPE Reservoir Evaluation & Engineering*, vol. 17, 2014.

[23] Z. X. Chen, "Transient flow of slightly compressible fluids through double porosity double permeability systems a state of the art review," *Transport in Porous Media*, vol. 4, no. 2, pp. 147–184, 1989.

[24] M. Yazdi, "Introducing a heuristic approach to enhance the reliability of system safety assessment," *Quality and Reliability Engineering International*, vol. 35, 2019.

[25] M. Yazdi, "Footprint of knowledge acquisition improvement in failure diagnosis analysis," *Quality and Reliability Engineering International*, vol. 35, 2019.

[26] D. O. Egya, S. Geiger, P. W. M. Corbett et al., "Analysing the limitations of the dual-porosity response during well tests in naturally fractured reservoirs," *Petroleum Geoscience*, vol. 25, 2019.

[27] Y. Wan, Y. Liu, W. Ouyang, G. Han, and W. Liu, "Numerical investigation of dual-porosity model with transient transfer function based on discrete-fracture model," *Applied Mathematics and Mechanics (English Edition)*, vol. 37, 2016.

[28] A. Taymourtash and B. S. Sola, "Investigation of applicability of dual-porosity model for polymer flooding simulation," *Journal of Porous Media*, vol. 21, 2018.

[29] K. L. Morton, F. J. Kuchuk, and A. J. Fitzpatrick, "Active and interference well pressure transient data interpretation in naturally fractured reservoirs," in *Proceedings of the 77th EAGE Conference and Exhibition 2015*, Madrid, Spain, June 2015.

[30] A. C. Gringarten, A. Al-Lamki, S. Daungkaew, R. Mott, and T. M. Whittle, "Well test analysis in gas-condensate reservoirs," in *Proceedings of the SPE Annual Technical Conference and Exhibition*, Dallas, Texas, U.S.A, October 2000.

[31] A. Afanasyev, "Fluid displacement in a dual-permeability medium with local capillary equilibrium," *Transport in Porous Media*, vol. 135, 2020.

[32] J. Lu, J. Qu, and M. M. Rahman, "A new dual-permeability model for naturally fractured reservoirs," *Special Topics & Reviews in Porous Media*, vol. 10, 2020.

[33] J. P. Aguilar-López, T. Bogaard, and H. H. Gerke, "Dual-permeability model improvements for representation of preferential flow in fractured clays," *Water Resources Research*, vol. 56, 2020.

[34] A. C. Hill and G. W. Thomas, New approach for simulating complex fractured reservoirs, 1985.

[35] F. T. Blaskovich, G. M. Cain, S. Fernand, D. Waldren, and S. J. Webb, "Multicomponent isothermal system for efficient reservoir simulation," 1983.

[36] C.A. Pereira Tavares, H. Kazemi, and E. Ozkan, "Combined effect of non-Darcy flow and formation damage on gas-well performance of dual-porosity and dual-permeability reservoirs," *Procedia Manufacturing*, vol. 48, 2006.

[37] R. Dastoorian and L. Wells, Gauge capability studies for high-density data: SPC Phase 0, 2020.

[38] M. Safari-Beidokhti and A. Hashemi, "Condensate blockage effects in well test analysis of dual-porosity/dual-permeability,

naturally fractured gas condensate reservoirs: a simulation approach," *Journal of Petroleum Exploration and Production Technology*, vol. 6, 2016.

[39] A. Al-Muftah, Well test simulation for dual porosity-dual permeability using orthogonal collocation, 2017.

[40] A. A. Alramadhan, R. J. Guerrero, A. M. Alzahrani, and B. A. Al Awami, "Numerical approach in analyzing pressure transient responses in dual-porosity dual-permeability DPDP reservoirs," in *Proceedings of the SPE Middle East Oil and Gas Show and Conference*, Abu Dhabi, UAE, March 2019.

[41] V. de Souza Rios, D. J. Schiozer, L. O. S. Dos Santos, and A. Skauge, "Improving coarse-scale simulation models with a dual-porosity dual-permeability upscaling technique and a near-well approach," *Journal of Petroleum Science and Engineering*, vol. 198, 2021.

[42] K. Uleberg and J. Kleppe, "Dual Porosity, Dual Permeability Formulation for Fractured Reservoir Simulation," *Norwegian University of Science and Technology (NTNU), Stavanger, Norway*, 1996.

[43] N. A. Golilarz, H. Gao, S. Pirasteh, M. Yazdi, J. Zhou, and Y. Fu, "Satellite multispectral and hyperspectral image denoising with enhanced adaptive generalized Gaussian distribution threshold in the wavelet domain," *Remote Sensing*, vol. 13, 2021.

[44] M. R. Maleki, F. Rashidi, H. Mahani, and E. Khamehchi, "A simulation study of the enhancement of condensate recovery from one of the Iranian naturally fractured condensate reservoirs," *Journal of Petroleum Science and Engineering*, vol. 92, pp. 158–166, 2012.

[45] H. M. Uba, Y. Chiffoleau, T. Pham, V. Divry, A. Kaabi, and J. Thuwaini, "Application of a hybrid dual-porosity/dual-permeability representation of large-scale fractures to the simulation of a giant carbonate reservoir," in *Proceedings of the SPE Middle East Oil and Gas Show and Conference*, Manama, Bahrain, March 2007.

[46] H. Uematsu, G. Auxiette, S. Bellah, V. Virlan, and T. Stojic, "New approach using dual porosity dual permeability and dissolved pore network to simulation modeling for fractured carbonate reservoir in Abu Dhabi," in *Proceedings of the Abu Dhabi International Petroleum Exhibition & Conference*, Abu Dhabi, UAE, November 2017.

[47] K. Sepehrnoori, Y. Xu, and W. Yu, "Numerical approaches for modeling complex fractures," *Developments in Petroleum Science*, pp. 31–42, 2020.

[48] F. Torres, M. Xavier, J. Ailin et al., Comparison of Dual Porosity Dual Permeability with Embedded Discrete Fracture Model for Simulation Fluid Flow in Naturally Fractured Reservoirs, 2020.

[49] L. J. Wells, R. Dastoorian, and J. A. Camelio, "A novel NURBS surface approach to statistically monitor manufacturing processes with point cloud data," *Journal of Intelligent Manufacturing*, vol. 32, no. 2, pp. 329–345, 2021.

[50] S. Granet, P. Fabrie, P. Lemonnier, and M. Quintard, "A two-phase flow simulation of a fractured reservoir using a new fissure element method," *Journal of Petroleum Science and Engineering*, vol. 32, 2001.

[51] S. Kumar, A. Rey, G. Dufour, and B. Ogunyomi, "Understanding fluid flow behavior in fractured reservoir using dual porosity dual permeability and discretized fracture model," in *Proceedings of the SPE Annual Technical Conference and Exhibition*, Calgary, Canada, October 2019.

[52] E. M. Mansour and M. El Aily, "Hydrocarbon simulation behavior of wet natural gas reservoirs, Egypt," *Journal of Chemistry*, vol. 64, 2021.

[53] R. Jadidi, B. Sedaee, S. Gerami, and A. Nakhaee, "Development of production data analysis models for multi-well gas condensate reservoirs," *Journal of Petroleum Science and Engineering*, vol. 202, 2021.

[54] Y. Yang, H. Wang, Z. Lun, and W. Hu, "A new method to calculate the in-situ compositions of gas condensate reservoirs," *Energy Sources, Part A Recover*, 2020.

[55] S. H. Yousefi, A. Eslamian, and F. Rashidi, "Investigation of well test behavior in gas condensate reservoir using single-phase pseudo-pressure function," *Korean Journal of Chemical Engineering*, vol. 31, 2014.

[56] L. Fan, B. W. Harris, A. Jamaluddin et al., "Understanding gas-condensate reservoirs," *Corrosion in the Oil Industry*, vol. 17, 2005.

[57] M. Bozorgzadeh and A. C. Gringarten, "Condensate-bank characterization from well-test data and fluid PVT properties," *SPE Reservoir Evaluation & Engineering*, vol. 9, 2006.

[58] B. Onoabhagbe, P. Russell, J. Ugwu, and S. Rezaei Gomari, "Application of phase change tracking approach in predicting condensate blockage in tight, low, and high permeability reservoirs," *Energies*, vol. 13, 2020.

[59] Ø. Fevang and C. H. Whitson, "Modeling gas-condensate well deliverability," *SPE Reservoir Evaluation & Engineering*, vol. 11, 1996.

[60] M. Yazdi, F. Khan, and R. Abbassi, "A dynamic model for microbiologically influenced corrosion (MIC) integrity management of subsea pipelines," *Journal of Hazardous Materials*, vol. 127, 2021.

[61] R. J. Wheaton and H. R. Zhang, "Condensate banking dynamics in gas condensate fields: compositional changes and condensate accumulation around production wells," in *Proceedings of the SPE Annual Technical Conference and Exhibition*, Dallas, TX, U.S.A, October 2000.

[62] R. Mott, "Engineering calculations of gas-condensate-well productivity," *SPE Reservoir Evaluation & Engineering*, vol. 6, 2003.

[63] S. Bapat and N. Akhter, Mathematical Model for Predicting the Reservoir Performance of Gas Condensate in Multiphase Flow Systems, 2020.

[64] K. Davani, S. Kord, O. Mohammadzadeh, and J. Moghadasi, "Numerical simulation and three-phase pressure transient analysis considering capillary number effect - case study of a gas condensate reservoir," *International Journal of Oil, Gas and Coal Technology*, vol. 25, 2020.

[65] D. H. Pham, S. K. Hoang, V. X. Trinh, and T. V. Tran, Condensate Banking Characterization and Quantification of Improvement from Different Mitigations Using Pressure Transient Analysis: A Case Study in Hai Thach Field Offshore Vietnam, 2020.

[66] M. P. P. C. Santos and M. S. Carvalho, "Pore network model for retrograde gas flow in porous media," *Journal of Petroleum Science and Engineering*, vol. 185, 2020.

[67] N. Salmani, R. Fatehi, and R. Azin, "On the liquid condensate vertical migration near the production wells of gas-condensate reservoirs," *Engineering Science and Technology an International Journal*, vol. 23, 2020.

[68] A. Rahimzadeh, M. Bazargan, R. Darvishi, and A. H. Mohammadi, "Condensate blockage study in gas condensate reservoir," *Journal of Natural Gas Science and Engineering*, vol. 33, 2016.

[69] M. Muskat, "Physical principles of oil production," *The Journal of Geology*, vol. 59, no. 5, pp. 513–515, 1949.

[70] D. D. Fussell, "Single-well performance predictions for gas condensate reservoirs," *Journal of Petroleum Technology*, vol. 25, 1973.
[71] J. R. Jones and R. Raghavan, "Interpretation of flowing well response in gas-condensate wells," *SPE (Society of Petroleum Engineers) Format Evaluation*, vol. 3, 1988.
[72] G. Penuela and F. Civan, Gas-Condensate Well Test Analysis with and without Relative Permeability Curves, 2000.

Hindawi
Mathematical Problems in Engineering
Volume 2021, Article ID 5534643, 10 pages
https://doi.org/10.1155/2021/5534643

Research Article

A Novel Probabilistic Fatigue Life Prediction Method for Welded Structures Based on gPC

Huiying Gao, Xiaoqiang Zhang, Xiaoqiang Yang, and Bo Zheng

Aviation Engineering Institute, Civil Aviation Flight University of China, Guanghan 618307, China

Correspondence should be addressed to Xiaoqiang Zhang; xqzhanguestc@163.com

Received 20 February 2021; Revised 4 April 2021; Accepted 20 April 2021; Published 26 April 2021

Academic Editor: Samuel Yousefi

The traditional fatigue life prediction methods based on the S-N curve all believe that the parameters in the model are deterministic constants and can be categorized to the deterministic life prediction. However, in practice, it is difficult to carry out a large number of experiments due to the limitation of time or the possible shortage of funds. In addition, the specimens used in the experiments are not exactly the same, and the test operations and data reading depend on the accuracy of the test equipment as well as the subjective judgment of the testers, which result to the uncertainty of the S-N curve. Therefore, the uncertainty should be considered in order to improve the accuracy of the fatigue life prediction. In this paper, the uncertain factors affecting the fatigue life of welded joints are summarized, and the generalized polynomial chaos (gPC) is introduced into fatigue life prediction. A novel probabilistic fatigue life prediction method combined with the nonlinear cumulative damage model considering the uncertainty of the S-N curve is constructed. An illustrative example is presented to demonstrate the advantages of the proposed approach.

1. Introduction

The S-N curve is mainly obtained through a large number of fatigue tests and fitting analysis. Many fatigue life prediction methods based on the S-N curve believe that the parameters in the life prediction models are deterministic, that is, in a given loading environment, each parameter is a constant. Since this kind of methods considers the parameters in the models as constants, it is known as deterministic life prediction methods. In practice, these assumptions are not always true. Due to the influence of uncertain factors such as test samples, conditions, operations, and data reading, the fatigue life under constant amplitude load is often dispersed in different degrees, which leads to the uncertainty of the S-N curve. For welded joints, the S-N curve is affected not only by external uncertainties such as load and environment but also by internal factors such as the welding process, joint form, residual stress, and welding defects. The internal factors, such as welding defects, are the important causes of stress concentration. Under a cyclic loading, stress concentration usually becomes the birthplace of fatigue cracks, and it will affect the fatigue life of the welded structure. Generally, the shape, size, and stress distribution of the welded structure are uncertain, resulting in the uncertainty and dispersion of fatigue life. Even for the same type of welded joints and the same welding materials, different S-N curves will be obtained while different welding methods are used. Xu and Zhang [1] studied the fatigue properties of a TC4 thin plate of T-welded joint and found that the weld toe or weld surface was the most frequent location of fracture initiation and different welding processes had different characteristics. As a result, the welded joints with the same welding materials and joints have different S-N curves. Jonsson et al. [2] studied the fatigue performance of the welded bogie joint under different welding process parameters, that is, by changing the current and voltage, it was found that the static load strength and the shape of the joint were not sensitive to the change of welding parameters, but the fatigue limit decreased with the increase of current. There are many kinds of welded joints used in complex mechanical structures including butt joint, lap joint, and cross joint. The notch forms for each type of welded joints are different, and the degree of nonuniformity of stress distribution is usually different. For example, the stress

distribution of the butt joint is relatively uniform while it is nonuniform for the cross joint because of the sharp transition from the weld to the base metal. For lap joints, the nonuniformity of stress distribution is reflected not only in the weld but also in the lap plate [3]. The nonuniform stress distribution will lead to stress concentration, and the stress concentration factors are quite different for each form of welded joints.

Up to now, scholars have proposed many probabilistic fatigue life prediction models for various uncertainties. The main theoretical bases of these models include probability and statistics, entropy theory, Bayes theory, fuzzy theory, and rough set theory.

The method of fatigue life prediction based on probability and statistics randomizes the relevant parameters in the models, including load, material parameters [4, 5], and structural size [6], and describes the objective uncertainty as a variable that obeys a random distribution. There are two ways to deal with this kind of methods. One is to randomize the fatigue life or damage under constant amplitude load. Rao et al. [7] considered the uncertainty of stress range and material properties and adopted the probabilistic S-N curve and a fatigue cumulative damage model to obtain the distribution of fatigue life. Shen et al. [8] considered the uncertainty of the loading process and the fatigue strength of the material, randomized the damage caused by a single cycle, and found the relationship between the distribution function and the stress amplitude. Liu and Mahadevan [9] regarded the fatigue life under different constant amplitude loads as random processes, and Karhunen–Loeve expansion was used to describe the variability of the corresponding random processes. Ni and Mahadevan [10] combined the probabilistic Miner rule and random stress-strain curve family to propose an energy-based probabilistic fatigue life prediction method under multiaxial variable amplitude loading. The other way is to randomize the parameters such as load, material properties and structural dimensions in the life prediction model. Based on the Kitagawa–Takahashi diagram, Liu and Mahadevan [11] proposed that the equivalent initial flaw size (EIFS) was only related to the fatigue limit and the threshold value of stress intensity factor. Maljaars et al. [12] predicted probabilistic fatigue crack growth of welded joints in civil engineering structures by randomizing the parameters in the model and considering the relative importance of random variables. Luo et al. [13] considered the effects of crack nucleation life and crack growth resistance variability and proposed a framework for fatigue life prediction based on crack nucleation and surface defects.

Entropy theory is widely used in medicine, environment, management, statistics, physics, and so on. The main applications for entropy in probabilistic fatigue life prediction are maximum entropy and thermodynamic entropy. Yi et al. [14] proposed a method to determine the type of probability distribution of fatigue life and describe the dispersion of fatigue life. Guan et al. [15] proposed the overall framework of probabilistic fatigue damage prediction based on the maximum correlation entropy method and found that this method can give satisfactory prediction results. In addition, the maximum correlation entropy theory and Bayes theory are combined to provide support for health management decision making [16]. Thermodynamic entropy theory is also used to predict fatigue life. Zhu et al. [17] proposed a probabilistic fatigue life prediction model combining with thermodynamic entropy theory and Bayes theory. Naderi and Khonsari [18] used the theory of thermodynamic entropy to realize the real-time monitoring of fatigue life. Temfack and Basaran [19], Wang and Yao [20], and Kim et al. [21] also applied entropy theory to life prediction.

The probabilistic fatigue life prediction method based on Bayes theory is another common method to deal with uncertainties. Guan et al. [22] adopted Bayes update to reduce the uncertainty in fatigue damage prediction and then used MCMC (Markov Chain Monte Carlo) simulation to select and update models and predict fatigue damage with mean probability. An et al. [23] introduced field failure data into prior information and adopted Bayes theory combined with MCMC simulation to obtain the parameters of fatigue life distribution. Chookah et al. [24] proposed a probabilistic failure physical model considering pitting fatigue degradation mechanism. The probability density function was used to represent the uncertainty of the parameters of the proposed model, and the Bayes theory combined with experimental data was used to evaluate the model. Zárate et al. [25] proposed a theoretical framework for updating and predicting crack length based on Bayes theory. The theoretical framework includes two main contents: the model update part, which is used to identify the probability density function of fracture mechanics parameters, and the prediction part, which is used to predict the crack length of the specimen and regards it as a function related to the number of cycles. Huang et al. [26], Mustafa et al. [27], Zhu et al. [28], and so on have been working on fatigue life prediction based on Bayes theory and have achieved many results.

The probabilistic fatigue life prediction method based on fuzzy theory introduces fuzzy sets and membership functions to deal with the uncertain phenomena in fatigue life prediction. Since it was put forward, many models and methods have emerged. Muc [29] established the uncertainty model of fatigue life by using the fuzzy set method combined with preselection of material parameters. Nopiah et al. [30] identified low fatigue damage by using typical statistical characteristics based on fuzzy theory. Bhalla et al. [31] established a fuzzy probabilistic damage model to predict the residual life of bolted joints. Zhu et al. [32] proposed a fatigue life prediction model by the fuzzy set method.

In addition to the abovementioned theories, there are other theories and methods that can be applied to probabilistic fatigue life prediction, such as rough set theory [33, 34] and grey theory [35].

Among the abovementioned methods, the fatigue life prediction method based on probability and statistics is obtained on the basis of a large number of experiments and has high credibility. The life prediction method based on entropy theory, rough set theory, and grey theory has a short history and needs to be further discussed. Compared with the abovementioned methods, the development course of

fatigue life prediction based on Bayes theory and fuzzy mathematics is longer while the maturity of them is not enough, and further research is needed.

Although a lot of research works have been carried out, some theories and methods which have strong ability to deal with uncertain problems, such as polynomial chaos theory [36], evidence theory [37], and concept lattice theory [38], are rarely reported in the field of fatigue life prediction. In this paper, a novel probabilistic fatigue life prediction method combined with the nonlinear cumulative damage model based on gPC is proposed.

The remainder of this paper is organized as follows. Section 2 introduces the generalized polynomial chaos. Section 3 discusses the uncertainties and proposes a novel probabilistic fatigue life prediction method. Section 4 presents an illustrative example. Conclusions are finally summarized in Section 5.

2. The Generalized Polynomial Chaos (gPC)

The main idea of polynomial chaos theory is to approximately represent a random process by the sum of orthogonal polynomials corresponding to a specific distribution type. It was first proposed by Wiener [39] to establish a turbulence model. The polynomial chaos method belongs to the non-statistical method. Compared with the traditional statistical method, the polynomial chaos method has the advantages of small amount of calculation and high accuracy. Because of these advantages, scholars applied this method to various engineering fields, such as finite deformation problems, transient heat transfer problems, and stochastic difference equations. At present, the polynomial chaos theory mainly includes generalized polynomial chaos (gPC), multielement generalized polynomial chaos (ME-gPC), and arbitrary polynomial chaos (aPC). Compared with gPC, ME-gPC can deal with the discontinuity of random space, and aPC can carry out polynomial chaos expansion while the uncertain parameters are distributed arbitrarily, but gPC has a longer development time and is more widely used and more mature.

We suppose a model

$$Y = \kappa(z). \tag{1}$$

Assuming that Y cannot be expressed analytically by z, but the probability space of z is smooth sufficiently, and the response Y corresponding to z can be obtained by numerical simulation, the relevant statistical properties of Y can be obtained by the surrogate model. For a system, if the input is affected by random parameters represented by the set $\{\xi_i\}_{i=1}^n$, then, since the uncertainty of the output is only determined by the input, the output of the system can also be represented by the set $\{\xi_i\}_{i=1}^n$. For the random field of Gaussian distribution, the series of Wiener–Askey polynomial chaos converges exponentially, so Wiener polynomial chaos can well deal with the problem of Gaussian distribution random field. For the random field with non-Gaussian distribution, Ghanem [40] proved that the series of Wiener polynomials chaos also converges, but the speed is relatively slow. In order to solve this problem, Xiu [41] and Sepahvand [42] extended Hermite polynomials and finally obtained a family of polynomial chaos for random variables with different distribution types. The polynomial chaos families corresponding to common distribution types are shown in Table 1.

Assuming that the input random variables of the system follow a Gaussian distribution, the polynomial chaos corresponding to the Gaussian distribution can be expanded as

$$\begin{aligned} Y = {} & \alpha_0\Gamma_0 + \sum_{i_1}^{\infty} \alpha_{i_1}\Gamma_1\left(\xi_{i_1}\right) \\ & + \sum_{i_1=1}^{\infty}\sum_{i_2=1}^{i_1} \alpha_{i_1 i_2}\Gamma_2\left(\xi_{i_1}, \xi_{i_2}\right) \\ & + \sum_{i_1=1}^{\infty}\sum_{i_2=1}^{i_1}\sum_{i_3=1}^{i_2} \alpha_{i_1 i_2 i_3}\Gamma_3\left(\xi_{i_1}, \xi_{i_2}, \xi_{i_3}\right) + \cdots, \end{aligned} \tag{2}$$

where $\alpha_i\,(i = 1, 2, 3, \ldots)$ are the undetermined constant coefficients, $\xi_j\,(j = 1, 2, 3, \ldots)$ are independent variables and obey the standard normal distribution, and $\Gamma_k(\xi_{i_1}, \xi_{i_2}, \ldots, \xi_{i_k})$ is the kth multidimensional Hermite polynomial.

For simplicity, equation (2) can be written in a compact form:

$$Y = \sum_{j=0}^{\infty} \beta_j \Pi_j(\boldsymbol{\xi}), \tag{3}$$

where β_j is the coefficient of polynomial, $\Pi_j(\xi)$ is the Wiener–Askey polynomial chaos, and $\xi = (\xi_1, \xi_2, \ldots, \xi_n)$ is the random variable vector.

Assuming that ξ is a two-dimensional random variable vector, equation (2) can be rewritten as

$$\begin{aligned} Y = {} & \alpha_0\Gamma_0 + \alpha_1\Gamma_1(\xi_1) + \alpha_2\Gamma_1(\xi_2) \\ & + \alpha_{11}\Gamma_2(\xi_1, \xi_1) + \alpha_{12}\Gamma_2(\xi_1, \xi_2) \\ & + \alpha_{22}\Gamma_2(\xi_2, \xi_2) + \alpha_{111}\Gamma_3(\xi_1, \xi_1, \xi_1) + \alpha_{112}\Gamma_3(\xi_1, \xi_1, \xi_2) \\ & + \alpha_{122}\Gamma_3(\xi_1, \xi_2, \xi_2) + \alpha_{222}\Gamma_3(\xi_2, \xi_2, \xi_2) + \cdots. \end{aligned} \tag{4}$$

Comparing equations (4) with (3), it can be seen that the function is changed only by the subscript. Therefore, equation (4) is equivalent to

$$\begin{aligned} Y = {} & \beta_0\Pi_0 + \beta_1\Pi_1 + \beta_2\Pi_2 + \beta_3\Pi_3 + \beta_4\Pi_4 + \beta_5\Pi_5 + \beta_6\Pi_6 \\ & + \beta_7\Pi_7 + \beta_8\Pi_8 + \beta_9\Pi_9 + \cdots. \end{aligned} \tag{5}$$

The expression of the n-order Hermite polynomial is

$$\Gamma_n\left(\xi_{i_1}, \xi_{i_2}, \xi_{i_3}, \ldots, \xi_{i_n}\right) = e^{(1/2)\xi^T\xi}(-1)^n \frac{\partial^n}{\partial\xi_{i_1}, \partial\xi_{i_2}, \ldots, \partial\xi_{i_n}} e^{-(1/2)\xi^T\xi}. \tag{6}$$

According to equation (6), it is easy to obtain a one-dimensional Hermite polynomial.

Table 1: The polynomial chaos corresponding to random variables of different distribution types.

Distribution type	Polynomial chaos type
Gaussian	Hermite chaos
Uniform	Legendre chaos
Gamma	Laguerre chaos
Beta	Jacobi chaos
Poisson	Charlier chaos
Binomial	Krawtchouk chaos
Hypergeometric	Hahn chaos
Nonnegative binomial	Meixner chaos

$$\begin{aligned}&\Gamma_0(\xi) = 1,\\&\Gamma_1(\xi) = \xi,\\&\Gamma_2(\xi) = \xi^2 - 1,\\&\Gamma_3(\xi) = \xi^3 - 3\xi, \ldots, \Gamma_n(\xi) = \xi\,\Gamma_{n-1}(\xi) - (n-1)\Gamma_{n-2}(\xi).\end{aligned} \tag{7}$$

Tables 2 and 3 show the one-dimensional and two-dimensional Hermite polynomial of each order, respectively.

If the random variables in Hermite polynomials follow the standard normal distribution and are independent from each other, then the polynomials are orthogonal, that is,

$$\langle \Pi_m, \Pi_n \rangle = 0, \quad m \neq n. \tag{8}$$

Then, the Hermite polynomials form a set of complete orthogonal bases in 2-dimensional space, and it has

$$\begin{aligned}\langle \Pi_m, \Pi_n \rangle &= \langle \Pi_m^2 \rangle \delta_{mn},\\ \langle p(\xi), q(\xi) \rangle &= \int p(\xi) q(\xi) \theta(\xi) \mathrm{d}\xi,\end{aligned} \tag{9}$$

where $\langle \cdot, \cdot \rangle$ is the inner product, δ_{mn} is the Kronecker function, $\theta(\xi)$ is the weight function of the Hermite polynomial, and it satisfies

$$\theta(\xi) = \frac{1}{\sqrt{2\pi}} e^{-(1/2)\xi^T \xi}. \tag{10}$$

The coefficient of Hermite polynomial β_j in equation (3) can be obtained by Galerkin projection method, that is,

$$\beta_j = \frac{\langle Y, \Pi_i \rangle}{\langle \Pi_i^2 \rangle} = \frac{1}{\langle \Pi_i^2 \rangle} \int Y \Pi_i \theta(\xi) \mathrm{d}\xi. \tag{11}$$

This Galerkin projection method has some limitations; it requires that Y must have a clear analytical solution. Therefore, the random response surface method will be adopted in this paper.

3. The Proposed Probabilistic Fatigue Life Prediction Method

3.1. The Uncertainty Analysis and Probabilistic Fatigue Life Prediction of the S-N Curve. For the life prediction method based on the S-N curve and fatigue cumulative damage theory, the S-N curve is crucial, which affects the prediction accuracy. In the case of a given stress ratio, the S-N curve is tested under different levels of constant amplitude load, and the corresponding fatigue life of all levels of load is recorded and then fitted in the later stage. In the deterministic fatigue life prediction method, the "N" in the S-N curve usually refers to the average fatigue life under all levels of stress, without considering its dispersion. However, for welded structures and parts in engineering, this treatment method often cannot achieve satisfactory results and may even lead to catastrophic accidents.

Table 2: The Hermite polynomial of each order for a one-dimensional random variable.

j	The order χ	The jth Hermite polynomial Π_j
0	$\chi = 0$	1
1	$\chi = 1$	ξ_1
2	$\chi = 2$	$\xi_1^2 - 1$
3	$\chi = 3$	$\xi_1^3 - 3\xi_1$
4	$\chi = 4$	$\xi_1^4 - 6\xi_1^2 + 3$

Table 3: The Hermite polynomial of each order for two-dimensional random variables.

j	The order χ	The jth Hermite polynomial Π_j
0	$\chi = 0$	1
1	$\chi = 1$	ξ_1
2		ξ_2
3	$\chi = 2$	$\xi_1^2 - 1$
4		$\xi_1\xi_2$
5		$\xi_2^2 - 1$
6	$\chi = 3$	$\xi_1^3 - 3\xi_1$
7		$\xi_1^2\xi_2 - \xi_2$
8		$\xi_1\xi_2^2 - \xi_1$
9		$\xi_2^3 - 3\xi_2$
10	$\chi = 4$	$\xi_1^4 - 6\xi_1^2 + 3$
11		$\xi_1^3\xi_2 - 3\xi_1\xi_2$
12		$\xi_1^2\xi_2^2 - \xi_1^2 - \xi_2^2 + 1$
13		$\xi_1\xi_2^3 - 3\xi_1\xi_2$
14		$\xi_2^4 - 6\xi_2^2 + 3$

The expression of the S-N curve is more commonly used in the form of power function, that is, the relationship between fatigue life and stress level is expressed by

$$N_f (\Delta\sigma)^m = C, \tag{12}$$

where N_f is the fatigue life cycle, $\Delta\sigma$ is the stress, and C and m are the material parameters.

Taking logarithms on both sides of the abovementioned equation, it can be transformed into

$$\ln N_f + m \ln(\Delta\sigma) = \ln C. \tag{13}$$

From equation (12), it is found that the fatigue life cycle N_f will be affected by material parameters C and m under the action of steel. The study shows that, for a given material, the parameters C and m are not fixed constants, and there is a certain degree of dispersion and uncertainty, which is due to the uncertainty of inclusions, pores, and microcracks in the specimen. For welded joints, the internal welding defects are inevitable, including more pores, inclusions, and

microcracks, than nonwelded structures, and the distribution is more complex than that of nonwelded structures. Therefore, when the method based on the S-N curve and fatigue cumulative damage theory is used to predict the life of welded joints, it is necessary to consider the uncertainty of the S-N curve which originates from the uncertainty of material parameters C and m. In this paper, the gPC is proposed to consider the uncertainty of the S-N curve and combine with the improved Manson–Halford model and the improved Corten–Dolan model to predict the probabilistic fatigue life.

The fatigue life under constant amplitude load is obtained on the basis of the S-N curve. Generally speaking, it is considered that the fatigue life $N(\mathbf{x})$ follows a lognormal distribution or a Weibull distribution. $\mathbf{x} = x_1, x_2, \ldots, x_n$ is the uncertain parameter vector of the fatigue life. For example, $N(\mathbf{x})$ follows a lognormal distribution, while $\ln(N(\mathbf{x}))$ follows a normal distribution. In order to establish the polynomial chaos expansion model of fatigue life, it is assumed that the uncertain parameters $x_1, x_2, \ldots, x_n$ are independent of each other. Therefore, the fatigue life corresponding to all levels of stress can be approximately calculated by

$$\ln(N(\mathbf{x})) = \sum_{j=0}^{\infty} \beta_j \prod_j (\mathbf{x}), \quad \mathbf{x} = \{x_1, x_2, \ldots, x_n\}. \tag{14}$$

According to the properties of the polynomial chaos expansion, the finite term can be used to approximately estimate the fatigue life. Assuming that the number of terms is s, the fatigue life prediction model can be simplified as

$$\ln(N(\mathbf{x})) = \sum_{j=0}^{s-1} \beta_j \prod_j (\mathbf{x}), \quad \mathbf{x} = \{x_1, x_2, \ldots, x_n\}, \tag{15}$$

where $s = ((n+\chi)!/(n!\chi!))$ and χ is the order of expansion for polynomial chaos.

In order to improve the speed of calculation, $x_1, x_2, \ldots, x_n$ can be normalized into random variables $\zeta_1, \zeta_2, \ldots, \zeta_n$.

$$\zeta_i = \frac{x_i - E(x_i)}{\sqrt{\mathrm{Var}(x_i)}}, \tag{16}$$

where $E(x_i)$ and $\mathrm{Var}(x_i)$ denote the expectation and variance of the random variable x_i, respectively. Since the random variables are independent from each other, after standardization, the random variables in $\zeta = (\zeta_1, \zeta_2, \ldots, \zeta_n)$ are independent from each other. The multidimensional orthogonal polynomial $\prod_j(\zeta)$ can be derived as

$$\prod_j (\boldsymbol{\zeta}) = \prod_{i=1}^{n} \varphi_i^{l_i}(\zeta_i), \tag{17}$$

where $j = 0, 1, 2, \ldots, s-1$, $l_i = 0, 1, 2, \ldots, \chi$, $\sum_{i=1}^{n} l_i \le \chi$. $\varphi_i^{l_i}(\zeta_i)$ is the l_i-order orthogonal polynomial, whose parameters are random variables $\zeta_i\,(i = 1, 2, \cdots, n)$. According to the distribution type of ζ_i, the corresponding relations in Table 1, the base of one-dimensional orthogonal polynomial $\varphi_i^{l_i}(\zeta_i)$ can be determined.

It is assumed that the fatigue life of the material under constant amplitude load $\Delta\sigma$ is expressed by $N(\mathbf{x})$. It is known that the material parameters C and m are random variables and $\mathbf{x} = (\ln(C), m)$. Then, the polynomial chaos of fatigue life under constant amplitude load can be obtained by substituting $\mathbf{x} = (\ln(C), m)$ into the abovementioned model and solving the coefficients of the polynomial chaos. The probabilistic fatigue life prediction model based on gPC is finally obtained. The whole calculation process is shown in Figure 1.

From Figure 1, it is known that the key point for the uncertainty analysis of the S-N curve and probabilistic fatigue life prediction based on gPC is solving the coefficients of the polynomial chaos. In this paper, the stochastic response surface method is used.

3.2. gPC-Based Stochastic Response Surface Method. As mentioned above, how to calculate the coefficients of the polynomial chaos β_j is the fundamental and critical procedure. In the space expanded by the base vector of $\{\xi_i\}_{i=1}^{n}$, each set of determined sample value corresponds to a point named sampling point. For the model with multidimensional random variables, the common prescription is to accomplish polynomial chaos expansion and calculate the coefficients via choosing appropriate sampling points; then, the polynomial chaos of the model is obtained. The key of the stochastic response surface method is how to choose the appropriate sampling points. Taking the random field of Gaussian distribution as an example, it can be expanded into an approximate expression based on Hermite polynomials according to the Wiener polynomial chaos theory. It is assumed that the highest order in the expansion is χ, and then, the roots of the $\chi + 1$ order Hermite primary function can be taken as the collocation points.

Let $n = 2, \chi = 2$, that is, the model containing two-dimensional random variables is expanded to a second-order Hermite polynomial, then $s = (((\chi + n)!)/(\chi!n!)) = ((2+2)!/(2!2!)) = 6$, and the combinatorial number of the corresponding roots is $(\chi+1)^n = (2+1)^2 = 9$. The partial Hermite primary functions corresponding to the Gaussian distribution random field are shown in Table 4.

From Table 4, the root of the third-order Hermite primary function can be obtained, that is, $0, \sqrt{3}, -\sqrt{3}$; thus, the corresponding sampling points include $(0,0)$, $(0,\sqrt{3})$, $(0,-\sqrt{3})$, $(\sqrt{3},0)$, $(\sqrt{3},\sqrt{3})$, $(\sqrt{3},-\sqrt{3})$, $(-\sqrt{3},0)$, $(-\sqrt{3},\sqrt{3})$, and $(-\sqrt{3},-\sqrt{3})$. The selection of the sampling points should follow some principles, including that the sampling points should be chosen as close as possible to the origin and it should be tried to make them symmetrical about the origin. For the random field of Gaussian distribution, the collocation point should include the origin, and the number of sampling points is generally twice as the expansion terms of the polynomial chaos. Then, the unknown coefficients are obtained by the collocation approximation method, and the specific formula satisfies

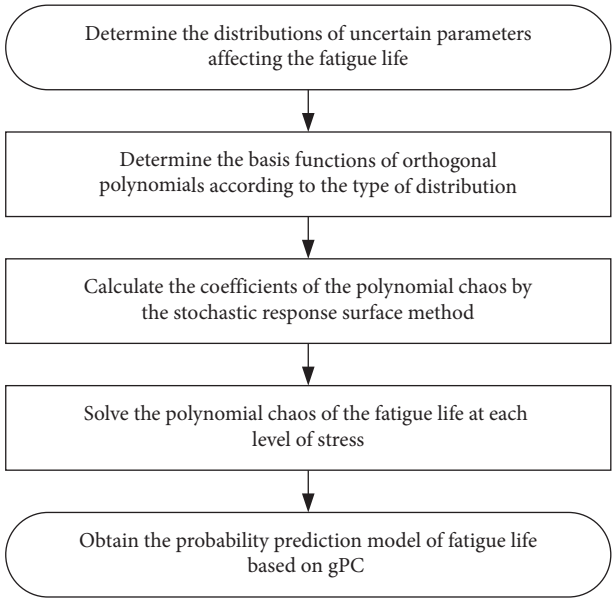

Figure 1: The flow chart of probabilistic fatigue life prediction based on gPC.

Table 4: The Hermite primary functions.

$\Gamma_0(x) = 1$
$\Gamma_1(x) = x$
$\Gamma_2(x) = (1/\sqrt{2})(x^2 - 1)$
$\Gamma_3(x) = (1/\sqrt{6})(x^3 - 3x)$
$\Gamma_4(x) = (1/2\sqrt{6})(x^4 - 6x^2 + 3)$
$\Gamma_5(x) = (1/2\sqrt{30})(x^5 - 10x^3 + 15x)$
$\Gamma_6(x) = (1/12\sqrt{5})(x^6 - 15x^4 + 45x^2 - 15)$

$$\begin{pmatrix} \Pi_0(\eta_0) & \Pi_1(\eta_0) & \dots & \Pi_{s-1}(\eta_0) \\ \Pi_0(\eta_1) & \Pi_1(\eta_1) & \dots & \Pi_{s-1}(\eta_1) \\ \vdots & \vdots & \vdots & \vdots \\ \Pi_0(\eta_N) & \Pi_1(\eta_N) & \dots & \Pi_{s-1}(\eta_N) \end{pmatrix} \begin{pmatrix} \beta_0 \\ \beta_1 \\ \vdots \\ \beta_{s-1} \end{pmatrix} = \begin{pmatrix} Y(\eta_0) \\ Y(\eta_1) \\ \vdots \\ Y(\eta_N) \end{pmatrix}, \tag{18}$$

where $\eta_0, \eta_1, \dots, \eta_N$ are the sampling points and N is the number of the sampling points.

The whole process of solving the expansion coefficients of polynomials by the random response surface method can be represented by the flow chart shown in Figure 2.

4. An Illustrative Example

To verify the feasibility of the proposed probabilistic fatigue life prediction method, two different nonlinear fatigue cumulative damage models including the improved Manson–Halford model [43] and the improved Corten–Dolan model [44] are used to predict the probabilistic fatigue life, respectively. The prediction results are compared with those of the Monte Carlo method. The probabilistic fatigue life prediction of aluminum alloy welded joints is carried out considering the uncertainty of the S-N curve. Constant amplitude loading or two-stage loading mode is usually an ideal load-bearing state, but in engineering practice, the load

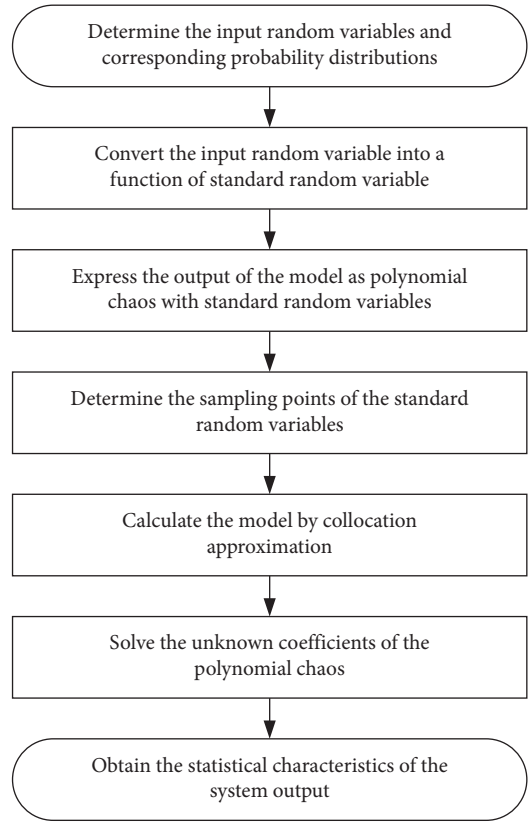

Figure 2: The implementation process of the stochastic response surface method.

of welded joints is more complex and changeable. Therefore, this section will predict the probabilistic fatigue life of welded joints under multistage variable amplitude loading on the basis of gPC, the improved Manson–Halford model, and the improved Corten–Dolan model. The data in this section are from the fatigue tests of 45 # steel welded joints under constant amplitude and program block loads. A total of five groups of 10 specimens were tested under constant amplitude loading, and the test fatigue life under applied stress amplitude and all levels of load is shown in Table 5. The program block load is loaded by multistage variable amplitude load, and the amplitude and cycle times of all levels of stress are shown in Figure 3. A total of 6 specimens are used to carry out the program block load test, and the fatigue life obtained is shown in Table 6.

First of all, the statistical characteristics of the parameters C and m which affect the fatigue life are analyzed according to Table 5. There are 5 groups of fatigue tests carried out in reference [45]. Taking one from the 10 test data under each stress amplitude, a group of C and m can be obtained by fitting. There are 50 experimental data here, and there are a total of $(C_{10}^1)^5 = 10^5$ groups. It is not realistic to combine and fit all the forms. Therefore, 200 combinations are randomly selected for statistical analysis of C and m. The statistical results are shown in Figures 4 and 5, where $\ln(C)$ and m follow normal distributions. Therefore, the influence of the uncertainty of the S-N curve on the fatigue life can be analyzed by the Hermite polynomial chaos expansion, as shown in Figures 6 and 7.

Table 5: The fatigue life test data of a 45 # steel welded joint under constant amplitude load.

Group ID	Experiment life ($N_f/105$) (105 cycles)				
	$\Delta\sigma = 750$ MPa	$\Delta\sigma = 650$ MPa	$\Delta\sigma = 630$ MPa	$\Delta\sigma = 590$ MPa	$\Delta\sigma = 520$ MPa
1	0.2080	0.4940	0.7089	1.3219	1.9670
2	0.2215	0.8175	0.9041	1.4129	2.0951
3	0.2430	0.8590	0.9281	1.5269	3.2367
4	0.2550	0.9629	0.9430	1.5678	4.5625
5	0.2700	1.0200	0.9616	1.6421	4.6132
6	0.2900	1.0869	1.0030	1.7002	4.7381
7	0.3470	1.1269	1.1981	1.7848	5.2336
8	0.3780	1.1830	1.2020	1.9280	5.4815
9	0.4610	1.1929	1.5321	2.4638	6.5569
10	0.6100	1.6850	1.8919	2.6272	12.9211

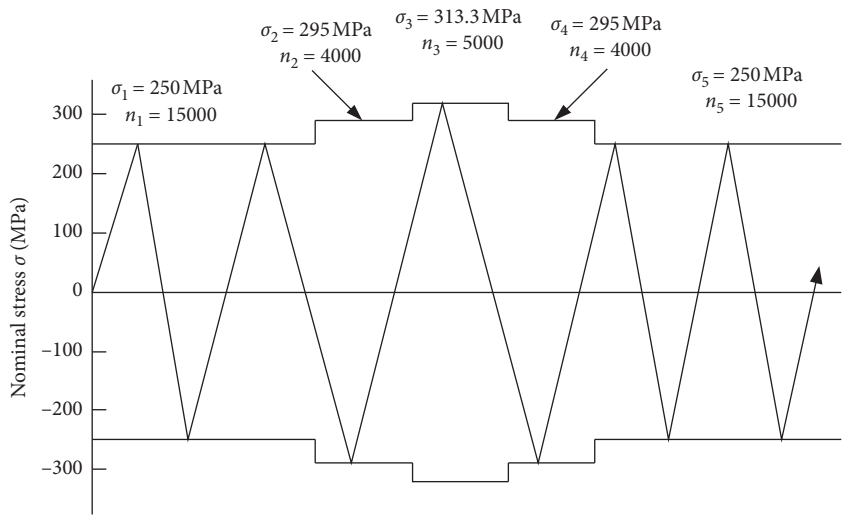

Figure 3: The schematic diagram of multistage variable amplitude loading for a 45 # steel welded joint.

Table 6: The fatigue life test data of a 45 # steel welded butt joint under multistage variable amplitude load.

Group ID	Experimental value of fatigue life (load block)	Predicted value of fatigue life (load block)	
		Modified Manson–Halford model	Modified Corten–Dolan model
1	3.717	9.3918	13.8566
2	5.189		
3	6.729		
4	7.452		
5	7.943		
6	12.151		

The probability of each predicted value can be judged from Figures 6 and 7, that is, when the uncertainty of the S-N curve is considered, the fatigue life predicted by the improved Manson–Halford model and the improved Corten–Dolan model has a certain uncertainty, but not a definite value. This can provide a more reasonable explanation for the abovementioned phenomenon, that is, the welded joint designed according to the model with high prediction accuracy may still have fatigue failure during its safety period.

The gPC method uses the addition and subtraction algorithm to express the dispersion and randomness of fatigue life caused by the uncertainty of material parameters C and m under constant amplitude load, so as to conside the uncertainty of the S-N curve. Compared with the power function form, the calculation is faster. However, compared with the Monte Carlo method, the polynomial chaos theory has a limitation, that is, the calculation process of the polynomial chaos expansion method is more complex and tedious when there are more parameters, and the calculation efficiency is higher when the parameters are less. Therefore, in the fatigue life prediction of welded joints, if there are more uncertain parameters input, the polynomial chaos theory still needs to be studied more deeply in order to simplify the calculation process and save time and cost. In the analysis of this chapter, the uncertainty of the S-N curve is due to the dispersion and randomness of the two material

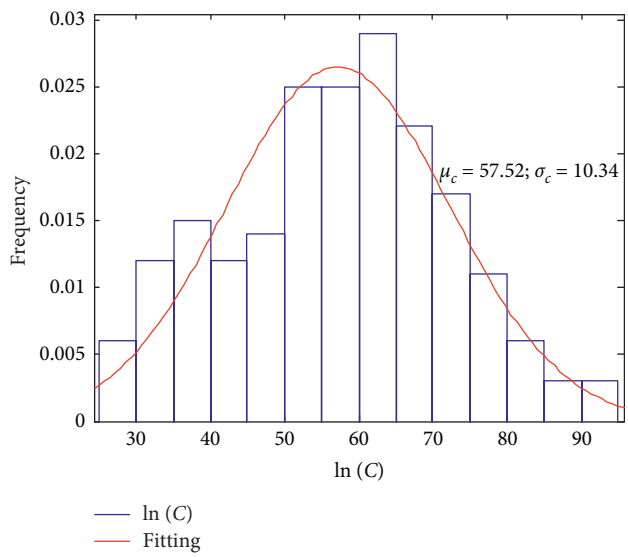

Figure 4: The statistical distribution results for C of the S-N curve (45 # steel welded butt joint).

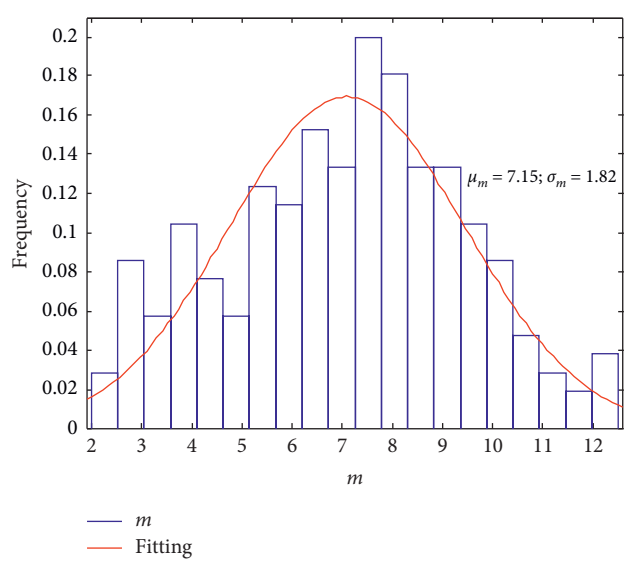

Figure 5: The statistical distribution results for m of the S-N curve (45 # steel welded butt joint).

parameters. In the process of calculation, it is found that the fatigue life prediction under second-order and multistage loading by the gPC method is more efficient than that by the Monte Carlo method, and the prediction results are close. Therefore, the fatigue life prediction method based on gPC expansion and considering the uncertainty of the S-N curve proposed in this chapter can obtain satisfactory probabilistic life prediction results through a simple and efficient calculation process.

By comparing the probabilistic fatigue life of a 45 steel welded butt joint obtained by the gPC expansion method and Monte Carlo simulation method under multistage variable amplitude block load, a conclusion similar to that of second-order loading mode can be obtained, that is, the probabilistic fatigue life prediction result of polynomial

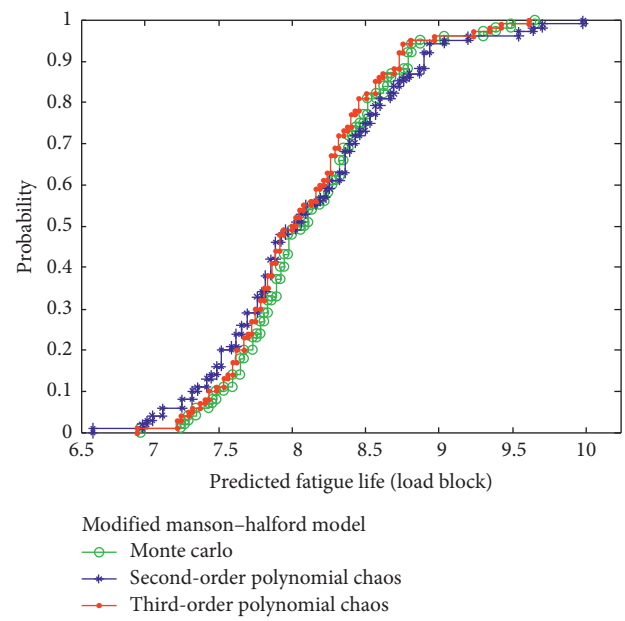

Figure 6: The probabilistic fatigue life prediction results under the modified Manson–Halford model (45 # steel welded butt joints).

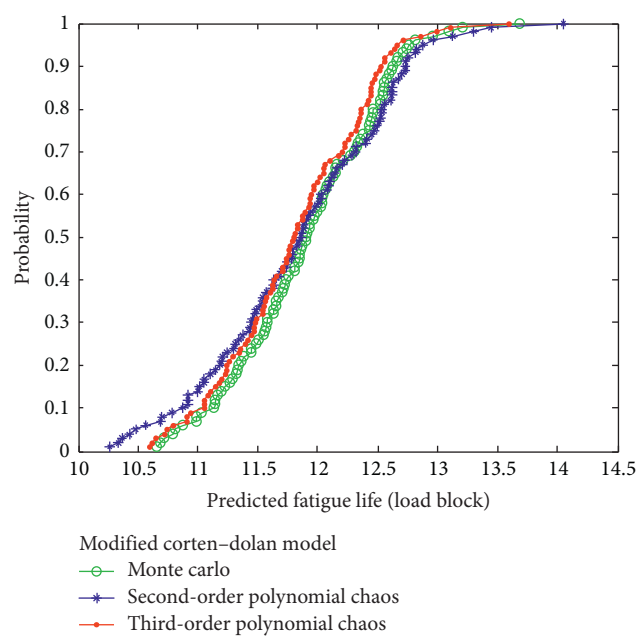

Figure 7: The probabilistic fatigue life prediction results under the modified Corten–Dolan model (45 # steel welded butt joints).

chaos expansion is quite close to that of the Monte Carlo method. This shows that the polynomial chaos theory is applicable in the field of fatigue life prediction and is an effective method to reflect and characterize the uncertainty of the S-N curve.

5. Summary and Conclusions

Based on the gPC, the uncertain parameters that affect the fatigue life under constant amplitude load are regarded as

random variables to consider the uncertainty of the S-N curve of welded joints. Combined with the improved Manson–Halford model and the improved Corten–Dolan model, the probabilistic fatigue life of welded joints is predicted. By comparing the results of probabilistic fatigue life prediction under secondary and multistage load, it is found that the probabilistic fatigue life prediction method based on gPC is close to the Monte Carlo method when it reaches the second or third order. Therefore, this method can be applied to fatigue life prediction under secondary or more complex loading conditions. The polynomial chaotic expansion method expresses the fatigue life as the polynomial of the addition and subtraction rule, and the calculation efficiency is higher than that of the Monte Carlo method, which verifies the feasibility of gPC expansion in fatigue life prediction, broadens the engineering application field of polynomial chaos theory, and provides a more practical way to deal with the uncertainty in the process of life prediction.

Data Availability

The data used to support the findings of this study are included within the article.

Conflicts of Interest

The authors declare no conflicts of interest.

Authors' Contributions

H. G. and X. Z. conceptualized the work; H. G. formulated the methodology, conducted formal analysis and investigation, collected resources, prepared the original draft, reviewed and edited the manuscript, was involved in project administration, and acquired funding; X. Z. was responsible for the software, curated data, and performed visualization; H. G., X. Z., X. Y., and B. Z. performed validation; and X. Y. and B. Z. supervised the work. All authors have read and agreed to the published version of the manuscript.

Acknowledgments

This research was supported by the Sichuan Science and Technology Program, grant nos. 2019YJ0395 and 2021YJ0519, and General Aviation Special Research Project of Civil Aviation Flight University of China, grant no. THZX2018-09. The funders had no role in the design of the study; in the collection, analyses, or interpretation of data; in the writing of the manuscript; or in the decision to publish the results.

References

[1] W.-f. Xu and Z.-l. Zhang, "Microstructure and mechanical properties of laser beam welded TC4/TA15 dissimilar joints," *Transactions of Nonferrous Metals Society of China*, vol. 26, no. 12, pp. 3135–3146, 2016.

[2] B. Jonsson, Z. Barsoum, and J.-O. Sperle, "Weight optimization and fatigue design of a welded bogie beam structure in a construction equipment," *Engineering Failure Analysis*, vol. 19, pp. 63–76, 2012.

[3] S. A. Oosterhof and R. G. Driver, "Effects of connection geometry on block shear failure of welded lap plate connections," *Journal of Constructional Steel Research*, vol. 67, no. 3, pp. 525–532, 2011.

[4] J.-C. He, S.-P. Zhu, D. Liao, and X.-P. Niu, "Probabilistic fatigue assessment of notched components under size effect using critical distance theory," *Engineering Fracture Mechanics*, vol. 235, Article ID 107150, 2020.

[5] Y. Ai, S. P. Zhu, D. Liao et al., "Probabilistic modeling of fatigue life distribution and size effect of components with random defects," *International Journal of Fatigue*, vol. 126, pp. 165–173, 2019.

[6] X.-P. Niu, R.-Z. Wang, D. Liao, S.-P. Zhu, X.-C. Zhang, and B. Keshtegar, "Probabilistic modeling of uncertainties in fatigue reliability analysis of turbine bladed disks," *International Journal of Fatigue*, vol. 142, Article ID 105912, 2021.

[7] K. B. Rao, M. Anoop, G. Raghava, M. Prakash, and A. Rajadurai, "Probabilistic fatigue life analysis of welded steel plate railway bridge girders using S-N curve approach," *Proceedings of the Institution of Mechanical Engineers, Part O: Journal of Risk and Reliability*, vol. 227, no. 4, pp. 385–404, 2013.

[8] H. Shen, J. Lin, and E. Mu, "Probabilistic model on stochastic fatigue damage," *International Journal of Fatigue*, vol. 22, no. 7, pp. 569–572, 2000.

[9] Y. Liu and S. Mahadevan, "Stochastic fatigue damage modeling under variable amplitude loading," *International Journal of Fatigue*, vol. 29, no. 6, pp. 1149–1161, 2007.

[10] K. Ni and S. Mahadevan, "Strain-based probabilistic fatigue life prediction of spot-welded joints," *International Journal of Fatigue*, vol. 26, no. 7, pp. 763–772, 2004.

[11] Y. Liu and S. Mahadevan, "Probabilistic fatigue life prediction using an equivalent initial flaw size distribution," *International Journal of Fatigue*, vol. 31, no. 3, pp. 476–487, 2009.

[12] J. Maljaars, H. M. G. M. Steenbergen, and A. C. W. M. Vrouwenvelder, "Probabilistic model for fatigue crack growth and fracture of welded joints in civil engineering structures," *International Journal of Fatigue*, vol. 38, pp. 108–117, 2012.

[13] J. Luo and P. Bowen, "A probabilistic methodology for fatigue life prediction," *Acta Materialia*, vol. 51, no. 12, pp. 3537–3550, 2003.

[14] G. Yi and M. P. Norton, "Materials fatigue life distribution: a maximum entropy approach," *Journal of Testing and Evaluation*, vol. 26, no. 1, pp. 53–63, 1998.

[15] X. Guan, R. Jha, and Y. Liu, "Probabilistic fatigue damage prognosis using maximum entropy approach," *Journal of Intelligent Manufacturing*, vol. 23, no. 2, pp. 163–171, 2012.

[16] X. Guan, Y. Liu, R. Jha, A. Saxena, J. Celaya, and K. Geobel, "Comparison of two probabilistic fatigue damage assessment approaches using prognostic performance metrics," *International Journal of Prognostics and Health Management*, vol. 5, no. 1, 2011.

[17] S.-P. Zhu, H.-Z. Huang, V. Ontiveros, L.-P. He, and M. Modarres, "Probabilistic low cycle fatigue life prediction using an energy-based damage parameter and accounting for model uncertainty," *International Journal of Damage Mechanics*, vol. 21, no. 8, pp. 1128–1153, 2012.

[18] M. Naderi and M. Khonsari, "Real-time fatigue life monitoring based on thermodynamic entropy," *Structural Health Monitoring*, vol. 10, no. 2, pp. 189–197, 2011.

[19] T. Temfack and C. Basaran, "Experimental verification of thermodynamic fatigue life prediction model using entropy as

damage metric," *Materials Science and Technology*, vol. 31, no. 13, pp. 1627–1632, 2015.

[20] J. Wang and Y. Yao, "An entropy-based failure prediction model for the creep and fatigue of metallic materials," *Entropy*, vol. 21, no. 11, p. 1104, 2019.

[21] J. Kim, J. Yi, J. Kim, G. Zi, and J. S. Kong, "Fatigue life prediction methodology using entropy index of stress interaction and crack severity index of effective stress," *International Journal of Damage Mechanics*, vol. 22, no. 3, pp. 375–392, 2013.

[22] X. Guan, R. Jha, and Y. Liu, "Model selection, updating, and averaging for probabilistic fatigue damage prognosis," *Structural Safety*, vol. 33, no. 3, pp. 242–249, 2011.

[23] D. An, J.-H. Choi, N. H. Kim, and S. Pattabhiraman, "Fatigue life prediction based on Bayesian approach to incorporate field data into probability model," *Structural Engineering and Mechanics*, vol. 37, no. 4, pp. 427–442, 2011.

[24] M. Chookah, M. Nuhi, and M. Modarres, "A probabilistic physics-of-failure model for prognostic health management of structures subject to pitting and corrosion-fatigue," *Reliability Engineering & System Safety*, vol. 96, no. 12, pp. 1601–1610, 2011.

[25] B. A. Zárate, J. M. Caicedo, J. Yu, and P. Ziehl, "Bayesian model updating and prognosis of fatigue crack growth," *Engineering Structures*, vol. 45, pp. 53–61, 2012.

[26] H.-Z. Huang, M. J. Zuo, and Z.-Q. Sun, "Bayesian reliability analysis for fuzzy lifetime data," *Fuzzy Sets and Systems*, vol. 157, no. 12, pp. 1674–1686, 2006.

[27] G. Mustafa, C. Crawford, and A. Suleman, "Fatigue life prediction of laminated composites using a multi-scale M-LaF and Bayesian inference," *Composite Structures*, vol. 151, pp. 149–161, 2016.

[28] S.-P. Zhu, H.-Z. Huang, R. Smith, V. Ontiveros, L.-P. He, and M. Modarres, "Bayesian framework for probabilistic low cycle fatigue life prediction and uncertainty modeling of aircraft turbine disk alloys," *Probabilistic Engineering Mechanics*, vol. 34, pp. 114–122, 2013.

[29] A. Muc, "Fuzzy approach in modeling static and fatigue strength of composite materials and structures," *Neurocomputing*, vol. 393, pp. 156–164, 2020.

[30] Z. M. Nopiah, M. H. Osman, S. Abdullah, and M. N. Baharin, "The identification of low fatigue damage using Fuzzy double clustering framework," in *Proceedings of the 2011 IEEE 7th International Colloquium on Signal Processing and its Applications (CSPA)*, pp. 181–186, Penang, Malaysia, March 2011.

[31] S. Bhalla, P. A. Vittal, and M. Veljkovic, "Piezo-impedance transducers for residual fatigue life assessment of bolted steel joints," *Structural Health Monitoring: An International Journal*, vol. 11, no. 6, pp. 733–750, 2012.

[32] S.-P. Zhu, H.-Z. Huang, and Z.-L. Wang, "Fatigue life estimation considering damaging and strengthening of low amplitude loads under different load sequences using fuzzy sets approach," *International Journal of Damage Mechanics*, vol. 20, no. 6, pp. 876–899, 2011.

[33] S.-P. Zhu, H.-Z. Huang, W. Peng, H.-K. Wang, and S. Mahadevan, "Probabilistic physics of failure-based framework for fatigue life prediction of aircraft gas turbine discs under uncertainty," *Reliability Engineering & System Safety*, vol. 146, pp. 1–12, 2016.

[34] Y. Ren, D. Gao, and L. Xu, "Prediction of service life of large centrifugal compressor remanufactured impeller based on clustering rough set and fuzzy Bandelet neural network," *Applied Soft Computing*, vol. 78, pp. 132–140, 2019.

[35] D. Zhao, C. Gao, Z. Zhou, S. Liu, B. Chen, and J. Gao, "Fatigue life prediction of the wire rope based on grey theory under small sample condition," *Engineering Failure Analysis*, vol. 107, Article ID 104237, 2020.

[36] Y. Xu, L. Mili, A. Sandu, M. R. von Spakovsky, and J. Zhao, "Propagating uncertainty in power system dynamic simulations using polynomial chaos," *IEEE Transactions on Power Systems*, vol. 34, no. 1, pp. 338–348, 2018.

[37] S. Yin, D. Yu, H. Yin, and B. Xia, "A new evidence-theory-based method for response analysis of acoustic system with epistemic uncertainty by using Jacobi expansion," *Computer Methods in Applied Mechanics and Engineering*, vol. 322, pp. 419–440, 2017.

[38] P. K. Singh, "Complex neutrosophic concept lattice and its applications to air quality analysis," *Chaos, Solitons & Fractals*, vol. 109, pp. 206–213, 2018.

[39] N. Wiener, "The homogeneous chaos," *American Journal of Mathematics*, vol. 60, no. 4, pp. 897–936, 1938.

[40] R. Ghanem, "Stochastic finite elements with multiple random non-Gaussian properties," *Journal of Engineering Mechanics*, vol. 125, no. 1, pp. 26–40, 1999.

[41] D. Xiu, *Generalized (Wiener-Askey) Polynomial Chaos*, Brown University, Providence, RI, USA, 2004.

[42] K. Sepahvand, S. Marburg, and H.-J. Hardtke, "Uncertainty quantification in stochastic systems using polynomial chaos expansion," *International Journal of Applied Mechanics*, vol. 2, no. 2, pp. 305–353, 2010.

[43] H. Gao, H. Z. Huang, S. P. Zhu, Y. F. Li, and R. Yuan, "A modified nonlinear damage accumulation model for fatigue life prediction considering load interaction effects," *The Scientific World Journal*, vol. 2014, Article ID 164378, 2014.

[44] H. Gao, H.-Z. Huang, Z. Lv, F.-J. Zuo, and H.-K. Wang, "An improved Corten-Dolan's model based on damage and stress state effects," *Journal of Mechanical Science and Technology*, vol. 29, no. 8, pp. 3215–3223, 2015.

[45] J. Yan, X. L. Zheng, and K. Zhao, "Prediction of fatigue life and its probability distribution of notched friction welded joints under variable-amplitude loading," *International Journal of Fatigue*, vol. 22, no. 6, pp. 481–494, 2000.

Hindawi
Mathematical Problems in Engineering
Volume 2021, Article ID 9929202, 13 pages
https://doi.org/10.1155/2021/9929202

Research Article

Does Intellectual Capital Investment Improve Financial Competitiveness and Green Innovation Performance? Evidence from Renewable Energy Companies in China

Shuang Liu, Qi Yu, Liang Zhang, Jian Xu, and Zhenji Jin

School of Management, Qingdao Agricultural University, Qingdao 266109, China

Correspondence should be addressed to Jian Xu; xujiansword@163.com and Zhenji Jin; zhenji12@aliyun.com

Received 2 April 2021; Revised 20 April 2021; Accepted 20 April 2021; Published 26 April 2021

Academic Editor: Mohammad Yazdi

This paper aims to investigate the impact of intellectual capital (IC) and its components on financial competitiveness and green innovation performance. The data are collected from renewable energy companies listed on the Shanghai and Shenzhen stock exchanges during 2013–2018. The modified Value Added Intellectual Coefficient (MVAIC) model is applied as a proxy for IC efficiency, an index system is constructed to systematically measure financial competitiveness, and green innovation performance is measured by the total number of green patents, the number of green invention patents, and the number of green noninvention patents. The empirical results show that IC has an inverted U-shaped relationship with financial competitiveness and no impact on green innovation performance. Regarding IC components, human capital (HC), structural capital, and relational capital positively affect financial competitiveness. HC has a negative impact on green patents, while innovation capital has a positive impact on green invention patents. Physical capital is the main driving force of green innovation performance. This study will help managers to reasonably manage their IC resources to strengthen financial competitiveness and achieve green development.

1. Introduction

In the knowledge era, intellectual capital (IC) is reckoned as the primary source of competitive advantage and financial sustainability, which has drawn the attention of many researchers [1–5]. It is the sum of intangible resources possessed by an organization to generate value [6]. However, traditional accounting fails to reflect the value created by intangibles in companies.

Financial competitiveness is strategic oriented to achieve sustainable competitive advantage and integrate the existing financial elements of companies [7, 8]. In order to survive in today's globalized economic environment, firms are required to improve their competitiveness. The current research on financial competitiveness is still scarce.

In recent years, the supply of traditional energy has greatly declined. China, a global leader in the renewable energy sector, is continuously increasing the utilization ratio of renewable energy with the support of a series of policies [9]. In line with the goal of building a beautiful China, renewable energy has become the mainstay of national energy strategy. Compared with developed countries, China's renewable energy industry is still in the initial stage of development. Renewable energy is a knowledge- and technology-intensive industry, and the effective utilization of IC is particularly important. Green innovation requires enterprises to carry out technological innovation activities under strict environmental constraints. Additionally, green innovation in the renewable energy sector can reduce greenhouse gas emissions and the cost of renewable energy, achieve economic development, and create a sustainable society [10–12].

Most of the existing studies on IC have been restricted to a certain knowledge-intensive sector such as manufacturing, pharmaceuticals, and banking, and little has been done in the renewable energy sector. The primary objective of this

paper is to explore the impact of IC and its components on financial competitiveness and green innovation performance. We choose renewable energy companies listed on the Shanghai and Shenzhen stock exchanges from 2013 to 2018 as the research sample. The modified Value Added Intellectual Coefficient (MVAIC) model is used as the measurement of IC, and an index system is set up for analyzing financial competitiveness. Green innovation performance is measured in three aspects: green patents, green invention patents, and green noninvention patents.

This paper contributes to the existing literature in four aspects. First, it expands the current IC literature by examining its impact in the renewable energy sector that attracts relatively little attention. Second, it is the first study to investigate the relationship between IC and financial competitiveness. As financial competitiveness is influenced by many variables, defining it is still a research problem. This paper attempts to construct a financial competitiveness index that can measure a company's competitive position. Third, little has been done on the impact of IC on green innovation performance, and this paper attempts to fill this gap. Finally, the results of this paper would help managers to improve the competitive performance of the firms via effective utilization of their IC resources.

The paper is structured as follows: Section 2 provides the literature review and develops the testable hypotheses, followed by Section 3 describing the research methodology. Section 4 presents and discusses the empirical results. Finally, conclusions are made in Section 5.

2. Literature Review and Hypotheses Development

2.1. IC Definition and Measurement. IC, an important intangible asset and strategic resource, is utilized by the organization to create value by transforming it into intellectual property. IC was initially defined as the set of knowledge possessed by the employees as well as the companies [13]. The difference between the market and book value of a firm is also considered as IC [14].

Various typologies of IC have been proposed in the extant research. It is generally believed that IC can be divided into human, structural, and relational capitals [4, 15–27]. Human capital (HC), the most important element of IC, consists of the knowledge, experience, commitment, and motivation of an organization's employees [28]. Structural capital (SC) relates to organizational infrastructure, production processes, operating system, production techniques, organizational culture, and intellectual property [29]. SC can provide a guarantee for HC practices [14]. Relational capital (RC) includes a formal and informal relationship with customers, competitors, and suppliers [30]. In addition, some scholars [2, 31–35] argued that innovation capital (INC) is also an important element of IC that drives wealth creation and superior performance.

There are various methods developed to measure IC, such as the Skandia Navigator, the Intangible Assets Monitor, the balanced scorecard approach, market capitalization methods, and the Value Added Intellectual Coefficient (VAIC). Among them, the VAIC model proposed by Pulic [36] is universally accepted and utilized in the current IC research. It provides a standardized and consistent basis of measure that allows comparison across organizations, industries, and countries [37]. Another merit is that the easy and simple calculation of VAIC is based on audited financial statements that are reliable and verifiable [36]. Conversely, this method has also received some criticism. First, the model depends on historical data from annual financial reports and thus might not be an appropriate tool for evaluating firms' future value-creating potential. Second, the measure for SC might not be complete by ignoring the important role of RC and INC. Chen et al. [31] argued that RC and INC can build brand value and improve the technological progress of a company.

2.2. Financial Competitiveness. Financial competitiveness is an extension of the theory of corporate core competitiveness from a financial point of view [7]. It refers to a kind of competitiveness that is based on knowledge and innovation and integrates the ability of financial capability to obtain sustainable competitive advantage [38]. Buckley et al. [39] pointed out that competitiveness is related to a firm's long-term financial performance to compensate employees and generate attractive returns for shareholders. Porter [40] defined competitiveness as the firm's ability to successfully compete in a given business environment. Based on factor analysis and fuzzy comprehensive evaluation method, He et al. [41] focused on profitability, solvency, assets management capability, growth ability, and cash support capability to evaluate financial competitiveness of top 20 telecom enterprises chosen from Fortune 500 companies. Ran and Zhang [42] developed an integrated index competitiveness evaluation system that covers three different aspects-profitability capability, debt paying capability, and operation capability. Crowder and Reganold [43] evaluated the financial competitiveness of organic agriculture in terms of costs, gross returns, benefit/cost ratios, net present values, and premiums. Luo [44] used factor analysis with 14 indicators to assess the financial competitiveness of China's agricultural listed companies in three areas of financial viability, financial development, and financial potential. Vijayakumar [45] applied factor analysis to examine the financial competitiveness of 20 Indian automobile companies from 10 aspects: profitability, asset utilization, cost-effectiveness, liquidity, working capital efficiency, solvency, market value, foreign trade, productivity, and value added performance. Based on factor analysis, Zhu et al. [38] measured financial competitiveness with 13 indicators such as solvency, development capability, operational capability, profitability, and cash flow ability.

2.3. IC and Financial Performance. A large body of literature has proved a positive relationship between IC and firms' financial performance, and little has been done on the IC-financial competitiveness relationship. For example, Sardo and Serrasqueiro [46] argued that IC efficiency of the current

period positively affects the financial performance of listed firms in 14 Western European countries. Xu and Wang [47], using the VAIC model, concluded that the aggregate IC improves the financial performance of publicly traded agribusinesses in China with a lagged effect. Taking manufacturing and service firms listed in Tanzania as the sample, Kasoga [48] discovered that IC is significantly positively related to financial performance measured by return on assets (ROA), asset turnover ratio (ATO), sales growth, and market value.

In terms of IC components, an early study conducted by Ahangar [49] revealed that HC is more efficient than SC and physical capital in financial performance improvement. Based on the model of VAIC, Chowdhury et al. [50] found that SC has an effect on ROA and ATO while HC has an insignificant impact in the Bangladeshi textile sector. Using the same model, Poh et al. [51] pointed out that physical assets have a significant relationship with ROA while HC and SC have a significant relationship with return on equity (ROE). Mohammad and Bujang [52] documented a positive relationship between HC and SC and financial performance in the finance sector while documenting a negative relationship between them in the construction and plantain sector. Xu and Li [24] found that HC and SC are the main drivers for increasing the performance of China's small- and medium-sized enterprises (SMEs) while RC does not play an important role. Bansal and Singh [53] analyzed the IC performance of software companies in India and found that an increase in SC will lead to the generation of more profit than HC and physical capital. The findings of Zhu et al. [38] showed that R&D investment is positively related to the financial competitiveness of China's new energy listed firms. Hence, we formulate the following set of hypotheses:

Hypothesis 1 (H1): there is a positive relationship between IC and financial competitiveness

Hypothesis 1a (H1a): there is a positive relationship between HC and financial competitiveness

Hypothesis 1b (H1b): there is a positive relationship between SC and financial competitiveness

Hypothesis 1c (H1c): there is a positive relationship between RC and financial competitiveness

Hypothesis 1d (H1d): there is a positive relationship between INC and financial competitiveness

2.4. IC and Green Innovation Performance. The research on IC and green innovation performance is very scarce. Januškaitė and Užienė [54] found that IC is of great importance for sustainable regional economic, environmental, and social sustainability. Green innovation and green production can alleviate the pressure of resources in developing countries, which is the cornerstone of enterprise growth. In terms of HC, Bassi and Buren [55] believed that HC has a positive impact on the competitive advantage of enterprises. Employees' awareness and knowledge of environmental protection might lead to corporate green production [56]. With regard to environmental issues, enterprises abide by environmental rules, establish a green management system, green corporate culture, and green database, and integrate green concepts into each management system, which can enable them to apply for more green patents and bring differentiated competitive advantages [57]. Garcés-Ayerbe et al. [58] found that enterprises are facing more and more environmental pressure from the perspective of stakeholders. Under such circumstances, enterprises hope to establish long-term cooperation with suppliers that provide green raw materials and intermediate products, which in turn improve green innovation performance by providing customers with green products and services. Fu et al. [59] pointed out that regional innovation capability can promote the improvement of green technology manufacturing efficiency in China. Based on the data from Chinese listed firms, Xu et al. [60] found that R&D investment has a positive impact on green innovation performance. Hence, we formulate the following set of hypotheses:

Hypothesis 2 (H2): there is a positive relationship between IC and green innovation performance

Hypothesis 2a (H2a): there is a positive relationship between HC and green innovation performance

Hypothesis 2b (H2b): there is a positive relationship between SC and green innovation performance

Hypothesis 2c (H2c): there is a positive relationship between RC and green innovation performance

Hypothesis 2d (H2d): there is a positive relationship between INC and green innovation performance

3. Method

3.1. Sample Selection. The sample consists of renewable energy companies listed on the Shanghai and Shenzhen stocks exchange over a six-year period (2013–2018). Companies with missing information, companies with a debt ratio greater than 1, and special treatment (ST) companies are excluded from the original sample. Finally, we obtain 176 companies with 934 observations. Financial data are retrieved from the China Stock Market & Accounting Research (CSMAR) database, and green patent information is sourced from China's State Intellectual Property Office.

3.2. Variables

(1) Dependent variables: the financial competitiveness index of renewable energy companies is constructed on the basis of five aspects, namely, solvency, development capability, operating capability, profitability, and cash flow ability. Thirteen ratios used in factor analysis are presented in Table 1.

Referring to Xu et al. [60] and Liao [61], green innovation performance (GPATENT) is measured by the total number of green patents (GP) including green invention and noninvention patents, the number of green invention patents (GIP), and the number of green noninvention patents (GNIP).

Table 1: Financial competitiveness evaluation index system.

Variable	Symbol	Description
Solvency	Current ratio (Y1)	Current assets/current liabilities
	Quick ratio (Y2)	(Current assets – inventory)/current liabilities
	Cash ratio (Y3)	Cash and cash equivalents/current liabilities
Development capability	Growth rate of return on equity (Y4)	(Current year's return on equity – last year's return on equity) – 1
	Net profit growth rate (Y5)	(Current year's net profit – last year's net profit) – 1
Operating capability	Total assets turnover (Y6)	Net sales/total assets
	Current assets turnover (Y7)	Net sales/current assets
Profitability	Asset profit ratio (Y8)	Net profit/total assets
	Ratio of profits to cost (Y9)	Total profits/(operating costs + total expenses)
	Return on assets (Y10)	(Total profits + financial expenses)/average total assets
	Earnings before interest and tax (Y11)	Earnings before interest and tax/total sales
Cash flow ability	Operating cash flows to current liabilities ratio (Y12)	Net cash flow from operating activities/current liabilities
	Operating cash flows to total liabilities ratio (Y13)	Net cash flow from operating activities/total liabilities

(2) Independent variables: guided by Tripathy et al. [32], Xu and Liu [34], and Singla [62], the MVAIC model with the introduction of RC and INC is applied to measure IC efficiency. It is based on value added (VA) generated by resources that a company possesses. VA is calculated as the difference between total sales and total expenses excluding employee expenditures. MVAIC is the summation of capital employed efficiency (CEE), human capital efficiency (HCE), structural capital efficiency (SCE), relational capital efficiency (RCE), and innovation capital efficiency (INCE). Their calculations are listed in Table 2.

(3) Control variables: guided by Xu et al. [3, 63], Xu and Liu [5, 34], Buallay et al. [20], Xu and Li [27], and Xu and Wang [47], firm size (SIZE), debt ratio (LEV), and gross domestic product growth rate (GDP) are chosen as control variables. In addition, a year dummy (YEAR) is also included in the regression model.

Table 2 presents the definition of all variables used in the current study.

3.3. Models. Models (1) and (2) are used to examine the impact of IC and its components on financial competitiveness:

$$\begin{aligned} \mathrm{FC}_{i,t} &= \beta_0 + \beta_1 \mathrm{MVAIC}_{i,t} + \beta_2 \mathrm{SIZE}_{i,t} \\ &\quad + \beta_3 \mathrm{LEV}_{i,t} + \beta_4 \mathrm{GDP}_{i,t} + \Sigma \mathrm{YEAR} + \varepsilon_{i,t}, \end{aligned} \tag{1}$$

$$\begin{aligned} \mathrm{FC}_{i,t} &= \beta_0 + \beta_1 \mathrm{CEE}_{i,t} + \beta_2 \mathrm{HCE}_{i,t} \\ &\quad + \beta_3 \mathrm{SCE}_{i,t} + \beta_4 \mathrm{RCE}_{i,t} + \beta_5 \mathrm{INCE}_{i,t} \\ &\quad + \beta_6 \mathrm{SIZE}_{i,t} + \beta_7 \mathrm{LEV}_{i,t} + \beta_8 \mathrm{GDP}_{i,t} + \Sigma \mathrm{YEAR} + \varepsilon_{i,t}. \end{aligned} \tag{2}$$

Models (3) and (4) are applied to examine the impact of IC and its components on the green innovation performance of the selected sample:

$$\begin{aligned} \mathrm{GPATENT}_{i,t} &= \beta_0 + \beta_1 \mathrm{MVAIC}_{i,t} + \beta_2 \mathrm{SIZE}_{i,t} + \beta_3 \mathrm{LEV}_{i,t} \\ &\quad + \beta_4 \mathrm{GDP}_{i,t} + \Sigma \mathrm{YEAR} + \varepsilon_{i,t}, \end{aligned} \tag{3}$$

$$\begin{aligned} \mathrm{GPATENT}_{i,t} &= \beta_0 + \beta_1 \mathrm{CEE}_{i,t} + \beta_2 \mathrm{HCE}_{i,t} + \beta_3 \mathrm{SCE}_{i,t} \\ &\quad + \beta_4 \mathrm{RCE}_{i,t} + \beta_5 \mathrm{INCE}_{i,t} + \beta_6 \mathrm{SIZE}_{i,t} \\ &\quad + \beta_7 \mathrm{LEV}_{i,t} + \beta_8 \mathrm{GDP}_{i,t} + \Sigma \mathrm{YEAR} + \varepsilon_{i,t}. \end{aligned} \tag{4}$$

where i and t represent the firm and year, respectively; β stands for the presumed parameters; and ε denotes the measurement error term.

4. Results and Discussion

4.1. Factor Analysis. Table 3 shows that the KMO value is 0.684, which is midiocre but still satisfactory. Bartlett's test is significant ($p < 0.05$), which suggests that all variables are uncorrelated.

Table 4 lists the eigenvalues associated with each factor before extraction, after extraction, and after rotation. The results before extraction are shown in the columns labeled initial eigenvalues. The second set of columns, labeled extraction sums of squared loadings, contains the factor solutions after extraction. The third set of columns, labeled rotation sums of squared loadings, display the factors after rotation. Five factors with an eigenvalue greater than 1 account for 84.881% of the overall variance.

In Table 5, we can see Y8, Y9, Y10, and Y11 load on Factor 1 (profitability); Y1, Y2, and Y3 on Factor 2 (solvency); Y12 and Y13 on Factor 3 (cash flow ability); Y4 and Y5 on Factor 4 (development capability); and the remaining variables on Factor 5 (operating capability). Based on these results, the composite score of firm's financial competitiveness can be expressed as follows:

Table 2: Variable definition.

Variable	Symbol	Description
Financial competitiveness	FC	Composite score
Green patent	GP	Total number of GIP and GNIP
Green invention patent	GIP	Number of green invention patents
Green noninvention patent	GNIP	Number of green utility model and industrial design
Modified Value Added Intellectual Coefficient	MVAIC	CEE + HCE + SCE + RCE + INCE
Capital employed efficiency	CEE	VA/book value of net assets
Human capital efficiency	HCE	VA/total employee expenditures
Structural capital efficiency	SCE	(VA− total employee expenditures)/VA
Relational capital efficiency	RCE	Marketing, selling, and advertising expenses/VA
Innovation capital efficiency	INCE	R&D expenses/VA
Firm size	SIZE	Natural logarithm of total assets
Debt ratio	LEV	Total liabilities/total assets
Gross domestic product growth rate	GDP	Growth rate of gross domestic product
Year dummy	YEAR	Dummy variable that takes 1 for the test year, 0 otherwise

Table 3: KMO and Bartlett tests.

KMO test value		0.684
Bartlett test	The approximate chi-square	13338.926
	df	78
	Sig.	0.000

Table 4: Total variance explained.

Component	Initial eigenvalue			Extraction sums of squared loadings			Rotation sums of squared loadings		
	Total	% of variance	Cumulative %	Total	% of variance	Cumulative %	Total	% of variance	Cumulative %
1	4.112	31.631	31.631	4.112	31.631	31.631	3.162	24.321	24.321
2	3.065	23.579	55.210	3.065	23.579	55.210	2.908	22.368	46.689
3	1.627	12.519	67.729	1.627	12.519	67.729	1.938	14.909	61.598
4	1.207	9.281	77.010	1.207	9.281	77.010	1.519	11.687	73.285
5	1.023	7.871	84.881	1.023	7.871	84.881	1.507	11.596	84.881
6	0.701	5.391	90.272	—	—	—	—	—	—
7	0.504	3.875	94.147	—	—	—	—	—	—
8	0.371	2.851	96.998	—	—	—	—	—	—
9	0.145	1.117	98.114	—	—	—	—	—	—
10	0.130	0.997	99.112	—	—	—	—	—	—
11	0.094	0.719	99.831	—	—	—	—	—	—
12	0.016	0.121	99.952	—	—	—	—	—	—
13	0.006	0.048	100.000	—	—	—	—	—	—

Table 5: Component matrix.

Variable	Component				
	1	2	3	4	5
Y1	0.026	0.971	0.133	0.018	−0.086
Y2	0.031	0.972	0.165	0.013	−0.069
Y3	0.010	0.926	0.148	−0.012	−0.028
Y4	0.428	0.030	−0.095	0.664	0.038
Y5	0.031	−0.014	0.075	0.827	−0.036
Y6	0.013	0.041	−0.107	0.046	0.908
Y7	0.094	−0.245	0.263	−0.052	0.778
Y8	0.832	0.079	0.133	0.430	0.142
Y9	0.918	0.052	0.174	0.136	−0.051
Y10	0.831	−0.019	0.192	0.388	0.181
Y11	0.834	−0.019	0.008	−0.182	−0.024
Y12	0.173	0.202	0.932	0.000	0.033
Y13	0.126	0.221	0.907	0.046	0.066

Table 6: Descriptive statistics.

Variable	N	Mean	Max	Min	SD
FC	934	0.3726	8.6772	−19.2801	1.2826
GP	934	2.28	90	0	6.8048
GIP	934	0.73	39	0	3.2064
GNIP	934	1.55	58	0	4.7281
MVAIC	934	5.2433	39.6007	−1.3193	2.5121
CEE	934	0.3279	2.2902	−0.0589	0.1929
HCE	934	4.0095	38.3861	−0.4114	2.4402
SCE	934	0.6916	3.4309	−1.7424	0.1917
RCE	934	0.1174	0.8966	−2.1526	0.1222
INCE	934	0.0969	0.6722	−1.1049	0.0888
SIZE	934	22.6301	27.2931	19.0072	1.3425
LEV	934	0.4824	0.9085	0.0398	0.1915
GDP	934	0.070	0.078	0.066	0.0040

$$\mathrm{FC} = \frac{(24.321 \times \mathrm{Factor1} + 22.368 \times \mathrm{Factor2} + 14.909 \times \mathrm{Factor3} + 11.687 \times \mathrm{Factor4} + 11.596 \times \mathrm{Factor5})}{84.881}. \quad (5)$$

4.2. Descriptive Statistics. Descriptive statistics of all variables are shown in Table 6. FC has a mean value of 0.3276, indicating that the financial competitiveness of China's renewable energy companies is relatively weak. The mean values of GP, GIP, and GNIP are 2.28, 0.073, and 1.55, respectively, which suggests that these companies do not pay enough attention to clean production and green development. MVAIC has a mean value of 5.2433, suggesting that renewable energy companies can generate an average value of 5.2433 for one monetary unit invested. Firms operating in the energy sector are found to have better IC performance [61]. HCE is a major component of MVAIC with a mean value of 4.0095, which indicates the cruciality of HC in value generation. This finding is in line with most previous studies [2, 3, 5, 16, 24–27, 32, 34, 47, 50, 64]. The sum of the mean value of HCE, SCE, RCE, and INCE (4.9154) is much higher than the mean value of CEE (0.3279), implying that intangibles are of greater importance than tangibles in firms' value creation. It is worth noticing that INCE has the lowest mean value of 0.0969, which indicates that R&D investment in renewable energy companies is not sufficient. In addition, the mean values of SIZE and LEV are 22.6301 and 0.4824, respectively.

4.3. Correlation Analysis. Table 7 shows the results of correlation analysis. FC is positively correlated with MVAIC, HCE, SCE, and INCE while it is negatively correlated with CEE. GP, GIP, and GNIP are all positively correlated with CEE, RCE, and INCE. All values of variance inflation factor (VIF) are calculated to be less than 5, suggesting that multicollinearity is not a major issue in this study.

4.4. Regression Results

4.4.1. IC and Financial Competitiveness. Table 8 shows the regression results of Models (1) and (2). Based on the Hausman specification test [65], the fixed effects (FE) model is used in Models (1) and (2). It is clearly shown in Model (1) that the coefficient of MVAIC is positive and significant ($\beta = 0.208$, $t = 7.55$), supporting H1. Xu and Liu [5] also concluded that IC is positively correlated with economic sustainable performance measured through ROA. In terms of IC components, HC, SC, and RC exert a significantly positive impact on financial competitiveness, which leads to the acceptance of H1a, H1b, and H1c. SC is the most influential contributor to the financial competitiveness of renewable energy companies. The coefficient of INCE is positive but not statistically significant at the 5% level ($\beta = 1.522$, $t = 1.47$). Therefore, H1d is not supported. Huo [66] and Zhang [67] found that the R&D input performance of China's renewable energy companies is still low. However, Zhu et al. [38] concluded that the current R&D investment has a significant positive impact on the financial competitiveness of China's new energy companies. It is noticeable that physical capital has no significant impact on financial competitiveness, which proved that the development pattern of companies has changed from the capital-driven to the knowledge-driven. Conversely, Xu and Liu [5] found that renewable energy companies rely mainly on physical and financial assets from 2010 to 2016. In addition, based on the survey of 50 energy enterprises, Zhang [68] found that HC management, proprietary knowledge base, RC, and technology capital have the most significant positive effect on enterprise value.

As for control variables, firm size (SIZE) has a positive impact on financial competitiveness while debt ratio (LEV) has a negative impact.

4.4.2. IC and Green Innovation Performance. Table 9 presents the regression results of Models (3) and (4). The probability values of the Hausman test are greater than 0.05, and the random effects (RE) model is more appropriate to be used in Model (3). In Model (4), the FE model is used with the GP and GNIP variables, while the RE model is used when GIP is the dependent variable. In Model (3), the coefficients of MVAIC are negative but not significant at the 5% level, rejecting our H2. In Model (4), CEE exerts a positive impact

Table 7: Correlation analysis.

Variable	1	2	3	4	5	6	7	8	9	10	11	12	13
1 FC	1												
2 GP	0.010	1											
3 GIP	0.013	0.784***	1										
4 GNIP	0.007	0.907***	0.451***	1									
5 MVAIC	0.152***	0.024	0.004	0.032	1								
6 CEE	−0.087***	0.160***	0.138***	0.137***	−0.011	1							
7 HCE	0.142***	−0.002	−0.019	0.009	0.994***	−0.092***	1						
8 SCE	0.222***	0.039	0.016	0.045	0.536***	−0.071**	0.506***	1					
9 RCE	0.018	0.121***	0.113***	0.098***	−0.051	0.162***	−0.109***	−0.328***	1				
10 INCE	0.064*	0.144***	0.139***	0.114***	−0.076**	−0.031	−0.115***	−0.291***	0.514***	1			
11 SIZE	−0.027	0.104***	0.058*	0.111***	0.086***	0.154***	0.091***	0.086***	−0.266***	−0.220***	1		
12 LEV	−0.302***	0.067**	−0.008	0.101***	0.059*	0.426***	0.043	−0.005	−0.158***	−0.226***	0.572***	1	
13 GDP	0.022	−0.106***	−0.084**	−0.095***	−0.020	0.066**	−0.027	0.049	−0.015	−0.053	−0.128***	−0.032	1

* $p < 0.10$, ** $p < 0.05$, and *** $p < 0.01$.

Table 8: Regression results of Models (1) and (2).

Variable	Model (1) FE	Model (2) FE
Constant	−11.287*** (−3.12)	−12.330*** (−3.06)
MVAIC	0.208*** (7.55)	—
CEE	—	0.255 (0.62)
HCE	—	0.127*** (3.92)
SCE	—	1.887*** (5.54)
RCE	—	1.345* (1.86)
INCE	—	1.522 (1.47)
SIZE	0.471*** (3.53)	0.477*** (3.15)
LEV	−4.011*** (−8.49)	−3.955*** (−6.87)
GDP	24.916* (1.86)	21.458 (1.57)
YEAR	Included	Included
R^2	0.1755	0.2038
F	19.58***	15.61***
N	934	934
Hausman test	Prob > chi2 = 0.0000	Prob > chi2 = 0.0000

*$p < 0.1$ and ***$p < 0.01$. t values are in parentheses.

Table 9: Regression results of Models (3) and (4).

Variable	Model (3)			Model (4)		
	GP RE	GIP RE	GNIP RE	GP FE	GIP RE	GNIP FE
Constant	−2.059 (−0.27)	0.131 (0.04)	0.038 (0.01)	−51.728*** (−3.00)	−3.136 (−0.86)	−40.916*** (−2.95)
MVAIC	−0.056 (−0.63)	−0.029 (−0.74)	−0.015 (−0.24)	—	—	—
CEE	—	—	—	4.042** (2.30)	1.371** (2.26)	2.850** (2.02)
HCE	—	—	—	−0.267* (−1.92)	−0.068 (−1.50)	−0.170 (−1.52)
SCE	—	—	—	−0.214 (−0.15)	0.640 (1.15)	−0.375 (−0.32)
RCE	—	—	—	−2.271 (−0.73)	0.259 (0.24)	−2.180 (−0.87)
INCE	—	—	—	5.090 (1.15)	2.609* (1.69)	3.778 (1.06)
SIZE	0.742*** (2.62)	0.205 (1.55)	0.441** (2.30)	2.643*** (4.07)	0.313** (2.31)	2.029*** (3.89)
LEV	0.081 (0.05)	−0.233 (−0.33)	0.656 (0.56)	−3.266 (-1.32)	−0.987 (−1.19)	−2.486 (−1.25)
GDP	−167.977*** (−3.65)	−54.021*** (−2.70)	−118.063*** (−3.26)	−59.966 (−1.02)	−52.036** (−2.58)	−28.702 (−0.61)
YEAR	Included	Included	Included	Included	Included	Included
R^2	0.0213	0.0119	0.0252	0.0731	0.0520	0.0562
F (wald)	46.41***	33.37***	34.83***	4.81***	44.38***	3.63***
N	934	934	934	934	934	934
Hausman test	Prob > chi2 = 0.4809	Prob > chi2 = 0.9449	Prob > chi2 = 0.3923	Prob > chi2 = 0.0063	Prob > chi2 = 0.2997	Prob > chi2 = 0.0041

*$p < 0.1$, **$p < 0.05$, and ***$p < 0.01$. t values are in parentheses.

Table 10: Regression results of nonlinear relationship.

Variable	Coefficient	t value
Constant	−9.860***	−2.78
MVAIC	0.522***	8.79
$MVAIC^2$	−0.018***	−5.93
SIZE	0.384***	2.92
LEV	−3.990***	−8.64
GDP	17.740	1.35
YEAR	Included	
R^2	0.2132	
F	22.12***	
N	934	
Hausman test	Prob > chi2 = 0.0000	

*** $p < 0.01$.

on green innovation performance. HC is significantly negatively related to only GP, which results in the rejection of H2a. This might be explained by the fact that the accumulation of HC in China's renewable energy companies is relatively weak, especially the lack of professional and technical personnel. Energy companies are losing their knowledge workers with the rising demand in the market [69]. It was reported that it takes a long time for less experienced employees to reach full productivity [69]. Cao et al. [70] argued that HC displays a significant and negative impact on the innovation performance of growth firms in the case of China.

SCE and RCE have no impact on green innovation performance, rejecting H2b and H2c. It might be because the database and institutionalized knowledge stored in enterprises are not beneficial to the knowledge transformation, which hinders green innovation performance. There is a significant and positive relationship between INC and GIP. Thus, H2d is partially accepted. Chen and Lin [10] found that R&D spending is conducive to the patent counts of renewable energy technologies in China.

In addition, for manufacturing listed companies, human, structural, and relational capitals promote enterprise innovation performance [71]. Regarding control variables, SIZE positively influences green innovation performance in China's renewable energy sector.

4.5. Robustness Check. We also use one-year lagged IC and its components and reestimate Models (1)–(4). The results are similar to the findings in Tables 8 and 9. Thus, it can be concluded that our results are robust.

4.6. Additional Analysis. We attempt to explore the nonlinear relationship between IC and financial competitiveness by adding the square of MVAIC in Model (1). The regression results are shown in Table 10, and the FE model is used. The coefficient of MVAIC is positive and statistically significant ($\beta = 0.522$, $t = 8.79$), and the coefficient of $MVAIC^2$ is negative and significant ($\beta = -0.018$, $t = -5.93$), which suggests an inverted U-shaped relationship between IC and financial competitiveness. This is in line with the findings of Yao et al. [26] and Haris et al. [72].

5. Conclusions

The present study analyzes the impact of IC and its components on financial competitiveness and green innovation performance within the Chinese industry of renewable energy. The MVAIC model is adopted for the measurement of IC. An index system is constructed to measure financial competitiveness, and green innovation performance is measured in three aspects: total number of green patents, the number of green invention patents, and the number of green noninvention patents. Correlation analysis and multiple regressions are used to find the relationship between the dependent variables and the independent variables. The main conclusions are summarized as follows:

(1) IC has a nonlinear relationship with financial competitiveness. Specifically, investment in IC resources can stimulate the financial competitiveness of renewable energy companies in China; up to a certain level, it becomes a restrictive determinant hindering financial competitiveness.

(2) Human, structural, and relational capitals exert a positive impact on financial competitiveness, while physical capital and INC have no impact.

(3) IC has no significant impact on green innovation performance. Physical assets enhance green innovation performance. INC has a positive impact on green invention patents, while HC has a negative impact on the application of green patents.

The theoretical contributions can be discussed in three aspects. First, this paper intends to contribute to the measurement of financial competitiveness by constructing an index system. Second, it is one of the few studies to examine the impact of IC on green innovation performance and extends prior research. Furthermore, it also helps management have a holistic understanding of the important role of IC in the competitive improvement and green development.

Based on the above analysis, this paper puts forward the following practical implications:

(1) Managers in the renewable energy sector should be aware of the importance of IC and strengthen the management of IC. Although physical assets are not beneficial to financial competitiveness, there is no doubt that they positively affect green innovation performance. Therefore, renewable energy companies should take full advantage of their physical capital.

(2) Renewable energy companies should put great emphasis on HC management, improve employees' quality by continuous training, and recruit high-level talents. Meanwhile, they need to construct a perfect employee incentive system and build an innovative work environment to enhance employees' ability of knowledge application.

(3) The insignificant impact of SC on green innovation performance indicates the lack of SC integration within the firm. Renewable energy companies should

enhance information transmission, construct a standardized production process, and establish an institutionalized management mode for innovation and cooperation. Meanwhile, they should also pay attention to the accumulation of proprietary knowledge base such as the patent right and information system.

(4) Renewable energy companies should not only pay attention to the demand of consumers but also keep close relationships with suppliers, distributors, government, partners, and competitors. They can carry out marketing activities through various social networks to earn more profits.

(5) Managers should foster technological innovation and make continuous investment in R&D activities to improve resource utilization efficiency and implement cleaner production in industrial transformation.

This paper has some limitations. First, it is based on a sample of Chinese renewable energy companies, and the results should be tested in different sectors. Second, some other factors (e.g., corporate governance) should be taken into consideration in future research.

Data Availability

The data used to support the findings of this study are available from the corresponding author upon request.

Conflicts of Interest

The authors declare that they have no conflicts of interest.

Acknowledgments

The research was funded by the Social Science Planning Research Program of Shandong Province (Grant no. 18CKJJ01), the Scientific Research Foundation for High-Level Talents of Qingdao Agricultural University (Grant no. 6631120701), and the Postgraduate Innovation Program of Qingdao Agricultural University (Grant no. QNYCX20013).

References

[1] S. Cabrilo, T. Savic-Sikoparija, D. Hristic, and J. Vemic-Djurkovic, "Defining indicators of organizational intellectual capital: the study of Serbian mining and energy sector," *Metalurgia International*, vol. 18, no. 3, pp. 174–180, 2013.

[2] J. Xu and B. Wang, "Intellectual capital, financial performance and companies' sustainable growth: evidence from the Korean manufacturing industry," *Sustainability*, vol. 10, no. 12, p. 4651, 2018.

[3] J. Xu, M. Haris, and H. X. Yao, "Should listed banks be concerned with intellectual capital in emerging Asian markets? a comparison between China and Pakistan," *Sustainability*, vol. 11, no. 23, p. 6582, 2019.

[4] J. Xu, Y. Shang, W. Z. Yu, and F. Liu, "Intellectual capital, technological innovation and firm performance: evidence from China's manufacturing sector," *Sustainability*, vol. 11, no. 19, p. 5328, 2019.

[5] X.-L. Xu and C. K. Liu, "How to keep renewable energy enterprises to reach economic sustainable performance: from the views of intellectual capital and lifecycle," *Energy Sustainability and Society*, vol. 9, no. 1, p. 7, 2019.

[6] A. Kianto, J. Sáenz, and N. Aramburu, "Knowledge-based human resource management practices, intellectual capital and innovation," *Journal of Business Research*, vol. 81, pp. 11–20, 2017.

[7] J. Tang and Y. Fu, "Analysis and research on financial competitiveness of listed companies in offshore engineering manufacturing," *Journal of Coastal Research*, vol. 106, pp. 45–48, 2020.

[8] W. Lv and Z. A. Salam, "Evaluation and research on financial competitiveness of innovation-driven enterprises based on interval data mining," *International Journal of Pattern Recognition and Artificial Intelligence*, vol. 34, no. 12, Article ID 2059040, 2020.

[9] K. Chang, Q. Wan, Q. Lou, Y. Chen, and W. Wang, "Green fiscal policy and firms' investment efficiency: new insights into firm-level panel data from the renewable energy industry in China," *Renewable Energy*, vol. 151, pp. 589–597, 2020.

[10] Y. Chen and B. Lin, "Decomposition analysis of patenting in renewable energy technologies: from an extended LMDI approach perspective based on three five-year plan periods in China," *Journal of Cleaner Production*, vol. 269, Article ID 122402, 2020.

[11] N. Shen, Y. Wang, H. Peng, and Z. Hou, "Renewable energy green innovation, fossil energy consumption, and air pollution-Spatial empirical analysis based on China," *Sustainability*, vol. 12, no. 16, p. 6397, 2020.

[12] W. Chen, X. F. Wang, N. Peng, X. Wei, and C. R. Lin, "Evaluation of the green innovation efficiency of Chinese industrial enterprises: research based on the three-stage chain network SBM model," *Mathematical Problems in Engineering*, vol. 2020, Article ID 3143651, 11 pages, 2020.

[13] N. Bontis, "Assessing knowledge assets: a review of the models used to measure intellectual capital," *International Journal of Management Reviews*, vol. 3, no. 1, pp. 41–60, 2001.

[14] L. Edvinsson and M. S. Malone, *Intellectual Capital: Realizing Your Company's True Value by Finding its Hidden Brainpower*, Harper Business, New York, NY, USA, 1997.

[15] M. H. F. Zarandi, N. Mohammadhasan, and S. Bastani, "A fuzzy rule-based expert system for evaluating intellectual capital," *Advances in Fuzzy Systems*, vol. 2012, Article ID 823052, 11 pages, 2012.

[16] S. Nimtrakoon, "The relationship between intellectual capital, firms' market value and financial performance: empirical evidence from the ASEAN," *Journal of Intellectual Capital*, vol. 16, no. 3, pp. 587–618, 2015.

[17] S. G. Yaseen, D. Dajani, and Y. Hasan, "The impact of intellectual capital on the competitive advantage: applied study in Jordanian telecommunication companies," *Computers in Human Behavior*, vol. 62, pp. 168–175, 2016.

[18] N. Smriti and N. Das, "Impact of intellectual capital on business performance: evidence from Indian pharmaceutical sector," *Polish Journal of Management Studies*, vol. 15, no. 1, pp. 232–243, 2017.

[19] F. Sardo, Z. Serrasqueiro, and H. Alves, "On the relationship between intellectual capital and financial performance: a panel data analysis on SME hotels," *International Journal of Hospitality Management*, vol. 75, pp. 67–74, 2018.

[20] A. Buallay, R. Cummings, and A. Hamdan, "Intellectual capital efficiency and bank's performance: A comparative

study after the global financial crisis," *Pacific Accounting Review*, vol. 31, no. 4, pp. 672–694, 2019.

[21] S. Muda and M. R. C. A. Rahman, "Sectoral effects of intellectual capital on Malaysian SME business performance," *Asia-Pacific Management Accounting Journal*, vol. 14, no. 3, pp. 151–175, 2019.

[22] S. Ulubeyli and D. Yorulmaz, "Intellectual capital based reputation for market internationalization: the case of engineering consultancy firm," *Journal of Intellectual Capital*, vol. 21, no. 1, pp. 40–61, 2019.

[23] H. Vidyarthi and R. Tiwari, "Cost, revenue, and profit efficiency characteristics, and intellectual capital in Indian banks," *Journal of Intellectual Capital*, vol. 21, no. 1, pp. 1–22, 2019.

[24] J. Xu and J. Li, "The impact of intellectual capital on SMEs' performance in China: Empirical evidence from non-high-tech vs. high-tech SMEs," *Journal of Intellectual Capital*, vol. 20, no. 4, pp. 488–509, 2019.

[25] J. Xu and B. Wang, "Intellectual capital performance of the textile industry in emerging markets: a comparison with China and South Korea," *Sustainability*, vol. 11, no. 8, p. 2354, 2019.

[26] H. Yao, M. Haris, G. Tariq, H. M. Javaid, and M. A. S. Khan, "Intellectual capital, profitability, and productivity: evidence from Pakistani financial institutions," *Sustainability*, vol. 11, no. 14, p. 3842, 2019.

[27] J. Xu and J. S. Li, "The interrelationship between intellectual capital and firm performance: evidence from China's manufacturing sector," *Journal of Intellectual Capital*, vol. 22, 2020.

[28] N. Bontis, "Intellectual capital: an exploratory study that develops measures and models," *Management Decision*, vol. 36, no. 2, pp. 63–76, 1998.

[29] W. H. A. Johnson, "An integrative taxonomy of intellectual capital: measuring the stock and flow of intellectual capital components in the firm," *International Journal of Technology Management*, vol. 18, pp. 562–575, 1999.

[30] G. Roos and J. Roos, "Measuring your company's intellectual performance," *Long Range Planning*, vol. 30, no. 3, pp. 413–426, 1997.

[31] M. C. Chen, S. J. Cheng, and Y. Hwang, "An empirical investigation of the relationship between intellectual capital and firms' market value and financial performance," *Journal of Intellectual Capital*, vol. 6, no. 2, pp. 159–176, 2005.

[32] T. Tripathy, L. A. G. Alana, and D. Sahoo, "The effect of intellectual capital on firms' financial performance: an empirical investigation in India," *International Journal of Learning and Intellectual Capital*, vol. 12, no. 4, pp. 342–371, 2015.

[33] A. E. Bayraktaroglu, F. Calisir, and M. Baskak, "Intellectual capital and firm performance: an extended VAIC model," *Journal of Intellectual Capital*, vol. 20, no. 3, pp. 406–425, 2019.

[34] J. Xu and F. Liu, "The impact of intellectual capital on firm performance: a modified and extended VAIC model," *Journal of Competitiveness*, vol. 12, no. 1, pp. 161–176, 2020.

[35] Y. Z. Lu, Z. R. Tian, G. A. Buitrago, S. W. Gao, Y. J. Zhao, and S. Zhang, "Intellectual capital and firm performance in the context of venture-capital syndication background in China," *Complexity*, vol. 2021, Article ID 3435725, 17 pages, 2021.

[36] A. Pulic, "VAIC^{TM}-an accounting tool for IC management," *International Journal of Technology Management*, vol. 20, no. 5–8, pp. 702–714, 2020.

[37] S. Firer and S. Mitchell Williams, "Intellectual capital and traditional measures of corporate performance," *Journal of Intellectual Capital*, vol. 4, no. 3, pp. 348–360, 2003.

[38] Z. Zhu, Z. Zhu, P. Xu, and D. Xue, "Exploring the impact of government subsidy and R&D investment on financial competitiveness of China's new energy listed companies: an empirical study," *Energy Reports*, vol. 5, pp. 919–925, 2019.

[39] P. J. Buckley, C. L. Pass, and K. Prescott, "Measures of international competitiveness: a critical survey," *Journal of Marketing Management*, vol. 4, no. 2, pp. 175–200, 1988.

[40] M. E. Porter, *The Competitive Advantage of Nations*, Free Press, New York, NY, USA, 1990.

[41] Y. He, J. Dong, and R. H. Bai, "The evaluation model of financial competitiveness in telecom enterprises," *Advances in Applied Economics, Business and Development*, vol. 209, 2011 https://link.springer.com/chapter/10.1007%2F978-3-642-23020-2_4.

[42] F. Ran and X. L. Zhang, "Financial competitiveness evaluation on sporting goods listed enterprises: a China study," *African Journal of Business Management*, vol. 5, no. 17, pp. 7404–7409, 2011.

[43] D. W. Crowder and J. P. Reganold, "Financial competitiveness of organic agriculture on a global scale," *Proceedings of the National Academy of Sciences*, vol. 112, no. 24, pp. 7611–7616, 2015.

[44] X.-T. Luo, "A study on the financial competitiveness of listed companies-taking agricultural listed companies as an example," 2017, http://download.atlantis-press.com/php/download_paper.php?id=25876866.

[45] A. Vijayakumar, "Financial competitiveness of firms: a study of the Indian automobile industry," *SMART Journal of Business Management Studies*, vol. 14, no. 1, pp. 91–103, 2018.

[46] F. Sardo and Z. Serrasqueiro, "Intellectual capital, growth opportunities, and financial performance in European firms: dynamic panel data analysis," *Journal of Intellectual Capital*, vol. 19, no. 4, pp. 747–767, 2018.

[47] J. Xu and B. H. Wang, "Intellectual capital and financial performance of Chinese agricultural listed companies," *Custos e Agronegocio On Line*, vol. 15, no. 1, pp. 273–290, 2019.

[48] P. S. Kasoga, "Does investing in intellectual capital improve financial performance? panel evidence from firms listed in Tanzania DSE," *Cogent Economics & Finance*, vol. 8, no. 1, Article ID 1802815, 2020.

[49] R. G. Ahangar, "The relationship between intellectual capital and financial performance: an empirical investigation in an Iranian company," *African Journal of Business Management*, vol. 5, no. 1, pp. 88–95, 2011.

[50] L. A. M. Chowdhury, T. Rana, M. Akter, and M. Hoque, "Impact of intellectual capital on financial performance: evidence from the Bangladeshi textile sector," *Journal of Accounting & Organizational Change*, vol. 14, no. 4, pp. 429–454, 2018.

[51] L. T. Poh, A. Kilicman, and S. N. I. Ibrahim, "On intellectual capital and financial performances of banks in Malaysia," *Cogent Economics & Finance*, vol. 6, no. 1, Article ID 1453574, 2018.

[52] H. S. Mohammad and I. Bujang, "Does intellectual capital influence firms' financial performance? a comparative analysis into three Malaysian industries," *International Journal of Business and Society*, vol. 20, no. 1, pp. 260–276, 2019.

[53] D. Bansal and S. Singh, "Impact of intellectual capital on financial performance of the Indian software sector," *Asia-Pacific Management Accounting Journal*, vol. 15, no. 1, pp. 67–95, 2020.

[54] V. Januškaitė and L. Užienė, "Intellectual capital as a factor of sustainable regional competitiveness," *Sustainability*, vol. 10, no. 12, p. 4848, 2018.
[55] L. J. Bassi and M. E. V. Buren, "Valuing investments in intellectual capital," *International Journal of Technology Management*, vol. 18, pp. 414–432, 1999.
[56] C. L. Pan and H. Tian, "How does green intellectual capital become firm competitive advantages in China's economic new normal stage?" *Journal of Shanghai University of Finance and Economics*, vol. 18, no. 2, pp. 77–90, 2016, (In Chinese).
[57] C.-L. Pan and H. Tian, "The study of the impact of the proactive environmental strategy on green innovation performance-The chain mediation effect of green intellectual capital and a absorptive capacity," *Collected Essays on Finance and Economics*, vol. 32, no. 7, pp. 85–93, 2016, (In Chinese).
[58] C. Garcés-Ayerbe, P. Rivera-Torres, and J. L. Murillo-Luna, "Stakeholder pressure and environmental proactivity: moderating effect of competitive advantage expectations," *Management Decision*, vol. 50, no. 1–2, pp. 189–206, 2012.
[59] Y. Fu, A. Supriyadi, T. Wang, L. Wang, and G. T. Cirella, "Effects of regional innovation capability on the green technology efficiency of China's manufacturing industry: evidence from listed companies," *Energies*, vol. 13, no. 20, p. 5467, 2020.
[60] J. Xu, F. Liu, and Y. Shang, "R&D investment, ESG performance and green innovation performance: evidence from China," *Kybernetes*, vol. 50, no. 3, pp. 737–756, 2020.
[61] Z. Liao, "Is environmental innovation conducive to corporate financing? The moderating role of advertising expenditures," *Business Strategy and the Environment*, vol. 29, no. 3, pp. 954–961, 2020.
[62] H. K. Singla, "Does VAIC affect the profitability and value of real estate and infrastructure firms in India? A panel data investigation," *Journal of Intellectual Capital*, vol. 21, no. 3, pp. 309–331, 2020.
[63] X.-L. Xu, X.-N. Yang, L. Zhan, C. K. Liu, N.-D. Zhou, and M. Hu, "Examining the relationship between intellectual capital and performance of listed environmental protection companies," *Environmental Progress & Sustainable Energy*, vol. 36, no. 4, pp. 1056–1066, 2017.
[64] K. Tandon, H. Purohit, and D. Tandon, "Measuring intellectual capital and its impact on financial performance: empirical evidence from CNX nifty companies," *Global Business Review*, vol. 17, no. 4, pp. 980–997, 2016.
[65] J. A. Hausman, "Specification tests in econometrics," *Econometrica*, vol. 46, no. 6, pp. 1251–1271, 1978.
[66] Z. F. Huo, "Research on the performance of new energy enterprise technology research and development project based on DEA model," Master's Dissertation, North China Electric Power University, Beijing, China, 2017.
[67] H. X. Zhang, "Research on evaluation of technology innovation efficiency of new energy enterpirses," Master's Dissertation, Xi'an University of Science and Technology, Xi'an, China, 2020.
[68] X. F. Zhang, "The value creation study of intellectual capital for energy science and technology enterprises," Master's Dissertation, Xi'an Shiyou University, Xi'an, China, 2014.
[69] D. A. Buczek, "Combating brain drain: retaining intellectual capital in the energy industry," *Journal of Petroleum Technology*, vol. 54, no. 1, pp. 26–30, 2002.
[70] Y. Cao, S. Y. Xiong, and H. L. Hu, "A study of the relationship between intellectual capital and innovation performance based on the life cycle of enterprises," *Science Research Management*, vol. 37, no. 10, pp. 69–78, 2016, (In Chinese).
[71] K. Y. Cui, "A study of the relationship between intellectual capital and enterprise innovation performance," Master's Dissertation, Shandong University, Jinan, China, 2016.
[72] M. Haris, H. Yao, G. Tariq, A. Malik, and H. Javaid, "Intellectual capital performance and profitability of banks: evidence from Pakistan," *Journal of Risk and Financial Management*, vol. 12, no. 2, p. 56, 2019.

Hindawi
Mathematical Problems in Engineering
Volume 2021, Article ID 5582034, 9 pages
https://doi.org/10.1155/2021/5582034

Research Article

On Chamfer Distances on the Square and Body-Centered Cubic Grids: An Operational Research Approach

Gergely Kovács,[1] **Benedek Nagy**,[2] **Gergely Stomfai**,[3] **Neşet Deniz Turgay**,[2] **and Béla Vizvári**[4]

[1]*Edutus University, Tatabánya, Hungary*
[2]*Faculty of Arts and Sciences, Department of Mathematics, Eastern Mediterranean University, Famagusta, North Cyprus, via Mersin 10, Turkey*
[3]*ELTE Apáczai Csere János High School, Budapest, Hungary*
[4]*Department of Industrial Engineering, Eastern Mediterranean University, Famagusta, North Cyprus, via Mersin 10, Turkey*

Correspondence should be addressed to Benedek Nagy; nbenedek.inf@gmail.com

Received 19 February 2021; Revised 30 March 2021; Accepted 3 April 2021; Published 22 April 2021

Academic Editor: Mohammad Yazdi

Linear programming is used to solve optimization problems. Thus, finding a shortest path in a grid is a good target to apply linear programming. In this paper, specific bipartite grids, the square and the body-centered cubic grids are studied. The former is represented as a "diagonal square grid" having points with pairs of either even or pairs of odd coordinates (highlighting the bipartite feature). Therefore, a straightforward generalization of the representation describes the body-centered cubic grid in 3D. We use chamfer paths and chamfer distances in these grids; therefore, weights for the steps between the closest neighbors and steps between the closest same type points are fixed, and depending on the weights, various paths could be the shortest one. The vectors of the various neighbors form a basis if they are independent, and their number is the same as the dimension of the space studied. Depending on the relation of the weights, various bases could give the optimal solution and various steps are used in the shortest paths. This operational research approach determines the optimal paths as basic feasible solutions of a linear programming problem. A directed graph is given containing the feasible bases as nodes and arcs with conditions on the used weights such that the simplex method may step from one feasible basis to another one. Thus, the optimal bases can be determined, and they are summarized in two theorems. If the optimal solution is not integer, then the Gomory cut is applied and the integer optimal solution is reached after only one Gomory iteration. Chamfer distances are frequently used in image processing and analysis as well as graphics-related subjects. The body-centered cubic grid, which is well-known in solid state physics, material science, and crystallography, has various applications in imaging and graphics since less samples are needed to represent the signal in the same quality than on the cubic grid. Moreover, the body-centered cubic grid has also a topological advantage over the cubic grid, namely, the neighbor Voronoi cells always share a full face.

1. Introduction

Grids have a significant role not only in crystallography, material science, and solid state physics but also in various engineering applications, e.g., in image processing and in digital geometry [1]. There is a large variety of ways to tessellate the plane and the three dimensional space. Regular grids in 2D are the square, the hexagonal, and the triangular grids, and the only regular grid in 3D is the cubic grid [2, 3]. The square and the cubic grids are most popular grids since their coordinate systems are the Cartesian coordinate systems. They are considered as the traditional grids. One of the earliest results on the square grid is the introduction of chessboard and cityblock motions which is given in [4]. The dual of the square grid is again a square grid, whereas the hexagonal and the triangular grids are duals of each other. The hexagonal grid has a useful symmetric coordinate frame, and every pixel, also called hexel [5], has six neighbors. The triangular grid is also described by the symmetric coordinate system. The useful

descriptions of these grids by three coordinates are given in [6–8]. These two regular grids are also studied from various points of view such as topological/combinatorial coordinate systems [9] and applied in discrete tomography [5, 10, 11].

Irregular grids are also applied in various places, e.g., triangulation in computer graphics. These grids are usually ad hoc and miss any type of structure. On the other hand, there are various well-structured grids. Two of the nontraditional grids in 3D are the body-centered Cubic (BCC) and the face-centered cubic (FCC) grids. They provide structures of various solid materials, and thus they play crucial importance in crystallography. They are alternative to the cubic grid in various engineering applications. These grids have many application areas, e.g., image processing [12], visualization [13], and topology preserving digitization [14]. It is worth noting that the FCC and BCC grids are point lattices. Further, BCC and FCC grids are generalizations of the hexagonal grid to 3D. Especially, in the hexagonal grid, there is only one usual neighborhood relation among the hexagon-shaped tiles/pixels, and two neighbor hexagons share a full side. The BCC grid generalizes this property to 3D, i.e., both of the used types of neighbor relations are among voxels such that either a full hexagon face or a square face is shared between the neighbor voxels. This topological advantage of the BCC grid can be used, e.g., by combinatorial coordinate systems in boundary tracking [15]. Moreover, the BCC grid is proven to have some better properties in applications than the cubic grid [16–18] highlighting the importance of our study. In electronic imaging, it is important what kind of mesh we scan the object according to. BCC grid is often used for this purpose [19]. Further, the BCC grid also plays an important role in the latest chapters of material science [20].

In 2D, one of the irregular grids is the Khalimsky grid. In this grid, the 4-neighbor and the 8-neighbor relations are used for the points of the grid, alternately, depending on their positions. Khalimsky's topology on the integers is introduced by Efim Khalimsky [21, 22]. This topology is a digital counterpart of the Euclidean topology on the real line and is useful in connection with digital geometry. Digital geometry of the 2D Khalimsky grid is studied, e.g., in [23].

In digital geometry, the distance between two points is defined by the number of steps in a shortest path connecting these points [1, 3, 4]. An algorithm which finds the shortest path and also their number between arbitrary two points in the square grid is given in [24]. Distance on the hexagonal grid is computed in [25]. Moreover, in [8], an algorithm, which produces the shortest path between two arbitrary points of the hexagonal grid is introduced. Weighted distances play also an important role in image processing, e.g., morphological filtering [26]. Weighted distances (chamfer distances) are also studied in various grids [23, 27, 28]. One may think about to finding a minimal path (and so, to determine the digital distance) as an optimization problem. We should note here that there are various shortest path algorithms in graph theory and in artificial intelligence [29], but those algorithms, e.g., Dijkstra algorithm (see, e.g., in [1]), are very general and do not take into account the very definite structures of the grids used in digital geometry. For this reason, both of their space and time complexities are much worse than the complexities of some more specific algorithms ([8]) and computations. Our aim here is to provide direct formulae for the distance computation.

Another important subject of our work is linear programming. Linear programming is an optimization problem. The objective function is linear, the constraints are linear equations, and the variables are nonnegative. The linear programming was discovered by George Dantzig in 1947. He published the simplex method in 1949 [30]. It is still one of the most effective methods of linear optimization. A great advantage of the simplex method is that its theory is a complete geometric description of the structure of the problem. In this paper, the results are based on the optimality criterion of the method. It is important to know that if optimal solution exists, then an optimal solution must exist among finitely many points. They are the so-called basic feasible solutions. Each such point belongs to a linear basis of the columns of the matrix of the equation system.

In the next section, as a preliminary part, we recall the simplex method and the Gomory cut [31] from operational research. In this paper, the 2D square grid and the 3D BCC grid are studied. Their formal description is given in Section 3. Both of these grids are bipartite grids (according to the new concept, we investigate in Subsection 3.1). Actually, we use an unusual description of the square grid which is somewhat related to the coordinate system we have invented for the Khalimsky grid (see, e.g., [23]). In this novel representation that we named as "diagonal square grid," the closest neighbor points are represented by coordinates with different parities (see the details in Subsection 3.2). Although the square grid is the most known, the new description gives us a new way of view that allows us to make an analogous study in nontraditional higher dimensional grids, as we do also in the 3D BCC grid. Section 4 shows our linear programming model for each grid in its subsections, respectively. Depending on the relation of the weights assigned to the two types of neighbors, various bases could give the optimal solution, i.e., various types (and directions) of steps could be used in the shortest paths. If the optimal solution is not integer (one case of both problems), then the so-called Gomory cut cuts the noninteger solutions, and the integer optimal solution is reached after only one Gomory iteration. Our theorems can easily be applied by knowing the fixed weights for the two types of neighbors; the distance of any two points can be computed directly, as we show it in examples. It is widely known that weighted distances were already studied both in the square and the BCC grids; however, our approach has not been applied yet, by giving a nice relation between digital geometry and linear programming. Moreover, our approach, up to our knowledge, is more general than the study, e.g., in [32, 33] since the case when closest neighbors get a larger weight than the second closest neighbors is not studied yet in detail for the BCC grid. In this way, our results also complement the previous knowledge on this field. Finally, the paper is closed by a concluding section.

2. Methods: On the Simplex Method and the Gomory Cuts

The simplex method of linear programming solves an optimization problem given in the form as follows:

$$\begin{aligned} &\max c^T x, \\ &Ax = b, \\ &x \geq 0, \end{aligned} \tag{1}$$

where A is an $m \times n$ matrix, b is an m-dimensional vector, c is an n-dimensional vector of constants, and x is the n-dimensional vector of variables.

The constraints determine a polyhedral set. What is called the corner point in the usual geometry is called extreme point here. A point is an extreme point of the polyhedral set if it is the only intersection point of the polyhedral set and a hyperplane. The extreme points of the polyhedral set of the linear programming problem are the so called basic feasible solutions. For the sake of simplicity, assume that the rank of matrix A is m. Let B be a subset of the columns of A such that the vectors of B form a basis. The matrix formed from the elements of B is an $m \times m$ matrix. It is also denoted by B. Assume that matrix A and vector x are partitioned accordingly, i.e., $A = (B, N)$ and $x^T = (x_B^T, x_N^T)$. The basic solution of basis B is obtained if x satisfies the equation system, and its x_N part is 0. It can be obtained as follows:

$$Ax = (B, N)\begin{pmatrix} x_B \\ x_N \end{pmatrix} = Bx_B + Nx_N = b. \tag{2}$$

Hence,

$$x_B = B^{-1}b - B^{-1}Nx_N. \tag{3}$$

Thus, the x_B part of the basic solution is $B^{-1}b$. The basic solution is feasible if $B^{-1}b \geq 0$.

An important consequence of the linearity, that if optimal solution exists, then at least one basic feasible solution is optimal.

Roughly speaking, the finite versions of the simplex method start from a basic feasible solution. It improves the solution by stepping to another basic feasible solution along an edge of the polyhedral set. It repeats this step until it recognizes that the current extreme point is optimal. This property also proves that the set of edges of a convex polyhedral set is a connected graph.

Gomory's method of integer programming is based on the observation that the basic variables are expressed by the other variables in the form of the equation system (3). Assume that one of this equation is

$$x_i = d_{i0} - \sum_{j \in K} d_{ij} x_j, \tag{4}$$

where K is the index set of the nonbasic variables. Assume further on, that d_{i0} is noninteger. It is the current value of the integer variable x_i. Let f_j be the fractional part of the coefficient, i.e., the fractional part of d_{tj}:

$$f_j = d_{ij} - \lfloor d_{ij} \rfloor, \quad j \in K \cup \{0\}. \tag{5}$$

Let us substitute these quantities into the equation. If the equation is rearranged such that all terms which are integer for sure are in the left-hand side, the new form of the equation is obtained as follows:

$$x_t - \lfloor d_{t0} \rfloor + \sum_{j \in K} \lfloor d_{tj} \rfloor x_j = f_0 - \sum_{j \in K} f_j x_j. \tag{6}$$

Hence,

$$f_0 \equiv \sum_{j \in K} f_j x_j \,(\mathrm{mod} 1). \tag{7}$$

All the coefficients of this relation are between 0 and 1. Thus, the two sides can be congruent only if the value of the right-hand side is in the set $\{f_0, f_0 + 1, f_0 + 2, \ldots\}$. Hence, the inequality

$$\sum_{j \in K} f_j x_j \geq f_0 \tag{8}$$

must be satisfied. This inequality is not satisfied by the current basic feasible solution as the values of the variables in the sum are all 0. This inequality is the Gomory cut.

3. Formal Descriptions of the Diagonal Square Grid and the BCC Grid

In this paper, we are focusing on two grids, the first is the 2D square grid but with a nontraditional description, while the second one is the body-centered cubic grid. We use a nontraditional view to represent the square grid in such a way that its description generalizes to 3D exactly in a way that produces a description of the BCC grid.

3.1. On Bipartite Grids. One may connect the closest neighbor point pairs of a grid by edges. Therefore, grids can be seen as infinite graphs with a kind of regular, periodic structure. Various grids could have various (graph-theoretic) properties. We call a graph and thus also a grid "bipartite" if there it does not contain any odd cycle. It is easy to see that the square grid is bipartite, and this well-known property is reflected, e.g., by the coloring of a chessboard: the two partitions of the points (i.e., pixels and fields in the usual square grid terminology) are colored by two different colors, e.g., black and white. The cubic and also the BCC grids are bipartite, as well as, the triangular and the diamond grids (moreover, these two latter grids are not point lattices, the relation of the two partitions—called also types or parities of the points in these cases—does not provide closure under translations). On the other hand, it is also easy to show grids which are not bipartite, e.g., the hexagonal or the FCC grids (in both of these grids, 3 cycles—i.e., triangles—exist among closest neighbor points). Now, for bipartite grids, it is interesting to see what is the grid structure of the partitions and what is the type of the subgrids. At the case of triangular grid, each of the partitions of the even and odd points forms a hexagonal subgrid. The even and odd points of the

diamond grid have the structure of two separate FCC subgrids. The two partitions of the BCC grid are cubic subgrids. Finally, each partition of the square grid is again a square grid. In the next subsection, by showing an unusual coordinate system for the square grid, we underline its bipartite property.

3.2. The Diagonal Square Grid: Reflecting the Bipartite Property of the Grid. We use a 45° rotation of the usual square grid, and we call this representation and description as the diagonal square grid (see Figure 1). The two coordinates are used in a similar manner, as we have described the so-called Khalimsky grid in [23, 34], but in this paper, we consider every point/pixel of the grid with the same connectedness, i.e., the same neighborhood. In this way, although the coordinate pairs of the represented points/pixels are similar to those that are used for the Khalimsky grid, our description fits to the square grid, which is in fact, a regular grid and it represents a point lattice at the same time. We note here that in the mentioned papers, integer coordinate pairs addressed half of the points of the grid, while coordinate pairs having value integer plus a half the other half of the points. In contrast to this, here, we prefer to use only integer coordinates (by multiplying each of the Khalimsky coordinates by 2); thus, we have two subgrids as follows. The even-subgrid is built up by the points (or squares, depending on the representation used) addressed by a pair of even coordinates. The odd-subgrid is built up by points addressed by odd coordinate pairs. Consequently, we call the points even or odd depending on the fact which subgrid they belong. It is worth noting that both the even and the odd subgrids are square grids themselves, and our grid which is the union of these two subgrids is also a square grid. The traditional 4-neighborhood relation consists of pairs of points that are different types and closest to each other (i.e., always an even and an odd point). They are depicted by vectors (±1, ±1). Additionally, the traditional 8-neighborhood contains also the pairs of the closest same type points (i.e., two even or two odd points). They are described by vectors (±2, 0) and (0, ±2). In Figure 2, part (a) shows also a part of this grid (in the dual representation, showing "grid points"—i.e., midpoints of the pixels—instead of pixels) with the assigned coordinate pairs of the points, and the neighbors of the point (0, 0) are also shown. Chamfer distances are defined first on the square grid [35, 36]. Based on the two classical neighborhoods, assigning weight a for steps between the closest neighbors (examples are shown by pink lines) and weight b for the steps between the second closest neighbors (examples are shown by black lines), the shortest weighted path between two points gives their chamfer (or weighted) distance. The paths we refer here are built in graph-theoretic sense by consecutive steps between (various type of) neighbor points of the grid.

3.3. A (Usual) Coordinate System for the BCC Grid. Now, as a straightforward generalization of the previous description, one can obtain the grid which is the union of the two 3D subgrids: the grid of even points (addressed by triplets of even numbers) and the grid of odd points (addressed by triplets of odd numbers). Here, both the even and the odd subgrids are cubic grids, and their union is actually the BCC grid [32, 33] (see also Figure 2, part (b)), where the "grid point" representation of the diagonal square grid can easily be generalized from two to three dimensions. For explanation, we recall that, e.g., the caesium chloride (CsCl) has such 3D structure: the caesium ions are represented by black balls and the chloride ions are represented by red-while balls. In the BCC grid, there are also two usual neighborhoods. The closest neighbor points are different type, and each point has 8 of them (as a chloride ion has 8 caesium ion neighbors). They are described by vectors (±1, ±1, ±1) (in Figure 2, part (b), the eight closest neighbors of the point (−1, 1, 1) are also highlighted, pink color is used to connect those neighbors, and their Euclidean distance is $\sqrt{3}/2$ times the length of the edge of the cubes of the unit cell, which is 2 here to ensure to use only integer coordinates to address the points of the grid). On the other hand, the second closest neighbors are actually the closest neighbors inside a given subgrid; that is, they are the closest same type points. Each point has 6 such neighbors, and they are described by vectors of the form (±2, 0, 0), (0, ±2, 0) and (0, 0, ±2) as, e.g., a chloride ion has 6 closest chloride ion neighbors. Actually, every point pair having their distance exactly the same as the length of the edge (shown by black lines on the figure) of a unit cell are representing two such neighbors. By our coordinate system, this length is exactly 2. Chamfer distances on the BCC grid can be defined analogously to the way they have been defined on the (diagonal) square grid: steps between two closest neighbor points (shown, e.g., by pink line in Figure 2) have weight a, while between the closest same type points (connected, e.g., by black line) weight b is used. Then, the weighted length of a corresponding shortest path connecting the points gives the chamfer distance of the points. We note here that in the mentioned literature, one may found also results about the weighted distances; however, in this paper, we use an approach coming from operational research. Moreover, we study also the case in which the steps to the second closest neighbors have a smaller weight than the steps to the closest neighbors, i.e., $b < a$. Therefore, we present not only a new approach but also some new results. We should also note here, that in 2D, the square grid and the diagonal square grid have the same structure, same number of neighbors, and so on. However, in 3D, the cubic and the BCC grids are two essentially different grids. The BCC grid is more compact than the cubic grid; both the number of closest neighbors and its packing density are larger than the corresponding values of the cubic grid.

4. Results and Discussion: The Linear Programming Model

Many problems of combinatorial optimization are actually linear programming problems. The shortest path problem in a finite graph has also its linear programming version. A grid can be represented by an infinite graph. Therefore, the linear programming model is different.

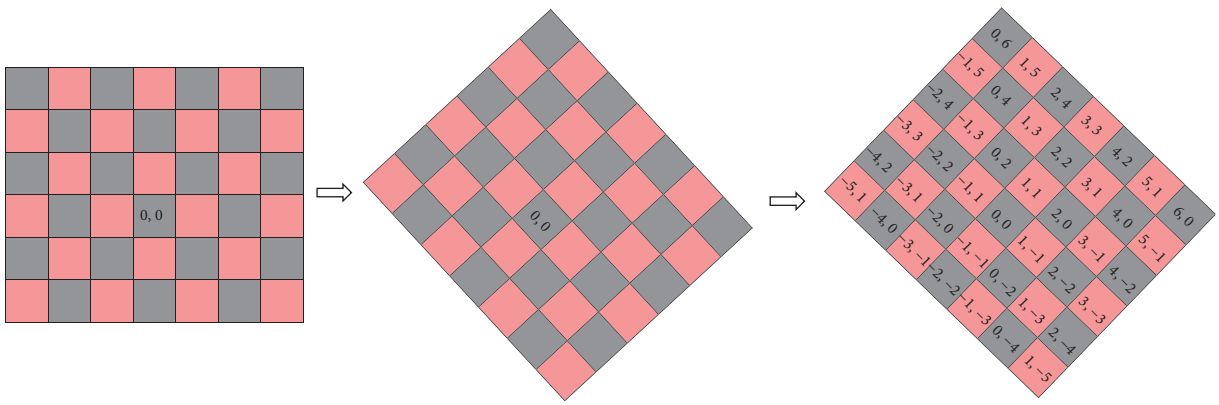

Figure 1: Turning the square grid by 45° obtaining the diagonal square grid (showing the origin (0, 0)), the two subgrids, and the assigned coordinate system.

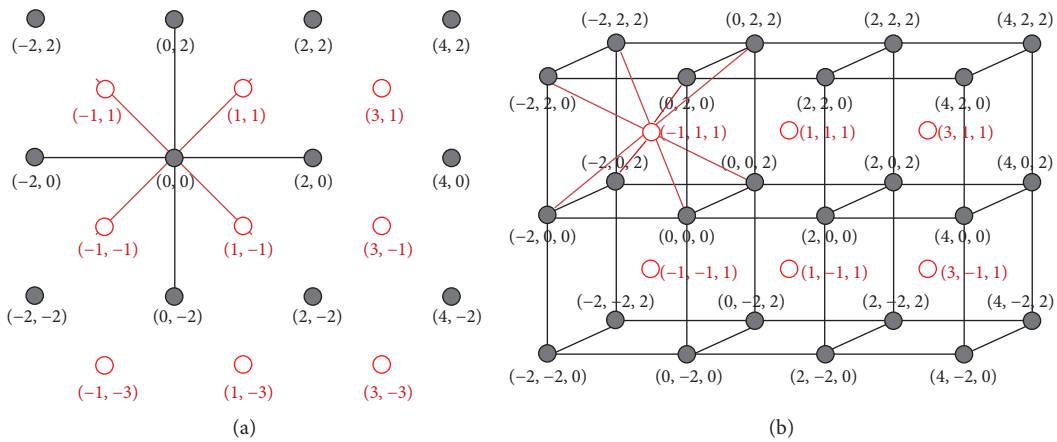

Figure 2: (a) The diagonal square grid with the neighbors of the origin (0, 0). (b) The BCC grid with some points of its two subgrids and their coordinates.

The matrices of the steps of the diagonal square grid and the 3-dimensional BCC grid are given in the matrices shown in formulae (9) and (10), respectively.

The matrix of the diagonal square grid is as follows:

$$\begin{pmatrix} 2 & 0 & -2 & 0 & 1 & 1 & -1 & -1 \\ 0 & 2 & 0 & -2 & 1 & -1 & 1 & -1 \end{pmatrix}. \tag{9}$$

The matrix of the BCC grid is as follows:

$$\begin{pmatrix} 2 & 0 & 0 & -2 & 0 & 0 & 1 & 1 & 1 & 1 & -1 & -1 & -1 & -1 \\ 0 & 2 & 0 & 0 & -2 & 0 & 1 & 1 & -1 & -1 & 1 & 1 & -1 & -1 \\ 0 & 0 & 2 & 0 & 0 & -2 & 1 & -1 & 1 & -1 & 1 & -1 & 1 & -1 \end{pmatrix}. \tag{10}$$

It can be seen immediately that the matrix of the BCC grid is the generalization of the matrix of diagonal square grid to 3-dimension.

It is supposed that the paths start at the origins and those go to the target points which are $(p, q)^T$ and $(p, q, r)^T$, respectively. As the grids are highly symmetric, it is enough to investigate just a segment of the plane. Therefore, it is supposed that $p > q > 0$ and $p > q > r > 0$, respectively. All the components of the target points must be either even numbers or odd numbers. The lengths of the steps are positive numbers. The lengths of the vertical and horizontal steps are equal and are denoted by b. The lengths of the cross steps are equal, too, and it is denoted by a.

4.1. The Diagonal Square Grid. The optimization model in the case of the diagonal square grid is as follows:

$$\min bx_1 + bx_2 + bx_3 + bx_4 + ax_5 + ax_6 + ax_7 + ax_8\,, \tag{11}$$

$$2x_1 + 0x_2 - 2x_3 + 0x_4 + x_5 + x_6 - x_7 - x_8 = p\,, \tag{12}$$

$$0x_1 + 2x_2 + 0x_3 - 2x_4 + x_5 - x_6 + x_7 - x_8 = q\,, \tag{13}$$

$$x_1, \ldots, x_8 \geq 0\,, \tag{14}$$

$$x_1, \ldots, x_8 \text{ is integer.} \tag{15}$$

Models (11)–(15) areinteger programming models as (15) claims the integrality of the variables. First, the linear programming problem (11)–(14) is solved based on the

theory of the simplex method. If the solution is not integer, then the Gomory method of integer programming is applied.

There are 28 pairs of the columns of matrix (9). However, there are only six out of the 28 which give a feasible, i.e., nonnegative, solution of the equation system. According to the theory of linear programming, an optimal solution must be among these solutions. The optimal solution depends on the right-hand sides. Table 1 summarizes the six solutions. Instead of the columns, the variables are given.

The only basis which may produce a fractional solution is basis 1. All other solutions are integer because the parities of p and q are the same. It is easy to see that the objective function value of the solution of basis 2 is smaller than the objective function values of the solutions of bases 3, 4, and 5. Thus, only bases 1, 2, and 6 can be linearly optimal. If either basis 2 or basis 6 is linearly optimal, then it is the optimal solution of the integer programming problem, i.e., the optimal linear solution provided with the steps of the optimal path.

The solution of basis 2 is better than the solution of basis 1 if and only if

$$\frac{(p+q)b}{2} > \frac{(p-q)b}{2} + qa. \tag{16}$$

It is equivalent to

$$b > a. \tag{17}$$

Similarly, the solution of basis 6 is better than the solution of basis 2 if and only if

$$\frac{(p-q)b}{2} + qa > pa. \tag{18}$$

It is equivalent to

$$b > 2a. \tag{19}$$

Another calculation shows that the solution of basis 6 is better than the solution of basis 1 if and only if

$$b > \frac{2p}{p+q}a. \tag{20}$$

The multiplier $2p/(p+q)$ is between 1 and 2. Thus, when the solution of basis 6 is better than the solution of basis 2, it is already better than the solution of basis 1. The results can be summarized as follows.

Theorem 1. *Assume that $p > q > 0$ are integers such that either both of them are even or both of them are odd.*

(i) If both p and q are even and $b < a$, then the minimal path from the polygon of the origin to the target polygon (p, q) consists of p horizontal and q vertical steps.

(ii) If $a < b < 2a$, then the minimal path from the polygon of the origin to the target polygon (p, q) consists of $(p-q)/2$ horizontal steps and q steps which go at 45° to right and up.

(iii) If $b > 2a$, then the minimal path from the polygon of the origin to the target polygon (p, q) consists of $(p+q)/2$ steps which go at 45° to right and up and $(p-q)/2$ steps which go at 45° to right and down.

The only case which is not discussed yet is when $b < a$ and both p and q are odd numbers. The starting point is the origin. Its coordinates are even numbers. Thus, at least one step must exists such that the parities of the coordinates change. It is equivalent to the inequality

$$x_5 + x_6 + x_7 + x_8 \geq 1. \tag{21}$$

The first method of integer programming such that it could solve problems with unbounded integer variables was the Gomory method. It is still the most general method. It is a cutting plane method. It starts from the linear programming relaxation. If the optimal linear programming solution is not integer, then a cut is generated. It is called Gomory cut. It cuts the last linear programming optimal solution which is not integer. However, it does not cut any integer feasible solution. A new linear programming problem is generated in this way. It is solved by the lexicographic simplex method. Interestingly, the first Gomory cut is (21).

The cut generation in this particular case is as follows. The simplex method works in a way such that the basic variables are expressed with the nonbasic variables. If x_1 and x_2 are the two basic variables, then the expression of x_1 is obvious.

$$x_1 = \frac{p}{2} - \frac{1}{2}x_5 - \frac{1}{2}x_6 + \frac{1}{2}x_7 + \frac{1}{2}x_8. \tag{22}$$

Collecting all terms which are integer to the left-hand side, the new form of the equation is

$$x_1 - \frac{p-1}{2} - x_7 - x_8 = \frac{1}{2} - \frac{1}{2}x_5 - \frac{1}{2}x_6 - \frac{1}{2}x_7 - \frac{1}{2}x_8. \tag{23}$$

The right-hand side must be integer. As every term with the exception of the constant are nonpositive on the right-hand side, the value of the right-hand side is a nonpositive integer implying that

$$\frac{1}{2} \leq \frac{1}{2}x_5 + \frac{1}{2}x_6 + \frac{1}{2}x_7 + \frac{1}{2}x_8. \tag{24}$$

It is equivalent to (21).

The lexicographic simplex method makes only one simplex iteration and immediately gets the integer optimal solution which is

$$x_1 = \frac{p-1}{2}, x_2 = \frac{q-1}{2}, \quad x_3 = x_4 = 0, \quad x_5 = 1, \quad x_6 = x_7 = x_8 = 0. \tag{25}$$

After describing our method in detail in this 2D case, we are ready to go to 3D and discuss and apply it on the BCC grid to obtain our main and most important results.

4.2. The BCC Grid. The matrix of (10) must be used in the linear programming model of the BCC grid. Thus, there are 14 variables. The lengths of the horizontal and vertical steps are again b, and the lengths of the other steps are a. There are 17 bases which can give basic feasible solutions. These bases are shown on Figure 3. Table 2 summarizes the solutions.

Table 1: The feasible bases of problem (11)–(14).

Number	Basic variables	Solution	The value of the objective function
1	x_1, x_2	$x_1 = p/2, x_2 = q/2$	$(p+q)b/2$
2	x_1, x_5	$x_1 = (p-q)/2, x_5 = q$	$(p-q)b/2 + qa$
3	x_1, x_7	$x_1 = (p+q)/2, x_7 = q$	$(p+q)b/2 + qa$
4	x_2, x_6	$x_2 = (p+q)/2, x_6 = p$	$(p+q)b/2 + pa$
5	x_4, x_5	$x_4 = (p-q)/2, x_5 = p$	$(p-q)b/2 + pa$
6	x_5, x_6	$x_5 = (p+q)/2, x_6 = (p-q)/2$	pa

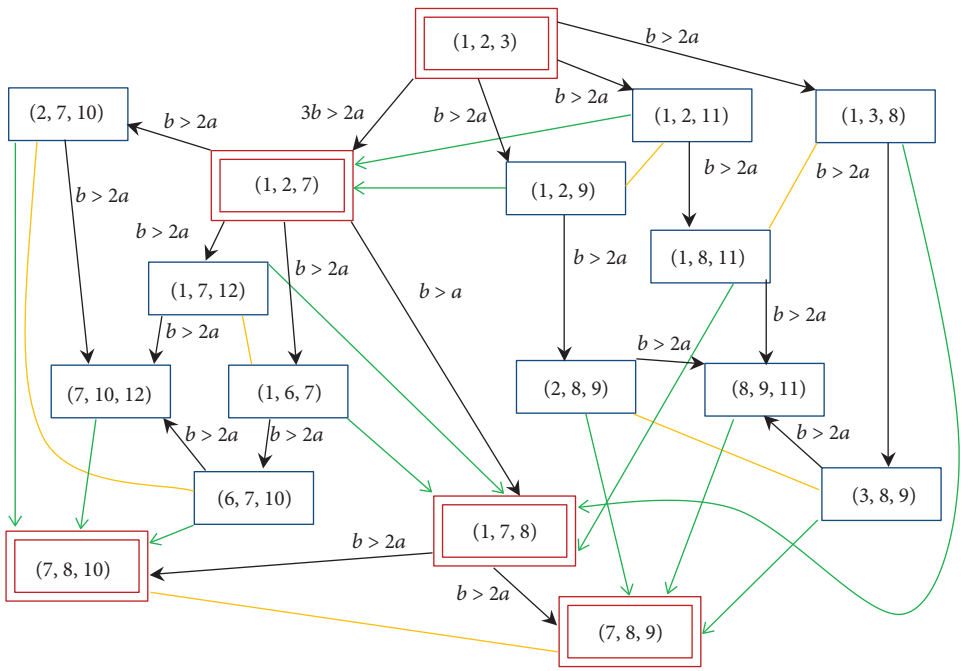

Figure 3: The feasible bases for BCC grid with their relation. Bases that can be optimal are marked with double frame. Black arrows show how one can shift from one basis to other by replacing a vector. Condition on the arrow shows when the change provides a better solution. Opposite condition implies that the change going opposite direction gives a better solution. For instance, from the basis (1, 2, 3), in case $3b > 2a$, one gets a better solution by changing vector 3 to 7 obtaining basis (1, 2, 7). However, in case $3b < 2a$, reverse direction changes, i.e., from basis (1, 2, 7) to (1, 2, 3) provides a better solution. Green arrows mean trivial conditions, e.g., $a > 0$; thus, these arrows can be used only in one direction and they always lead to a possible optimal basis. The orange lines show indifferent changes, i.e., the solutions of the related two basis are equivalent.

Table 2: The feasible bases of the linear programming problem of the BCC grid.

Number	Basic variables	Solution	The value of the objective function
1	x_1, x_2, x_3	$x_1 = p/2, x_2 = q/2, x_3 = r/2$	$(p+q+r)b/2$
2	x_1, x_2, x_7	$x_1 = (p-r)/2, x_2 = (q-r)/2, x_7 = r$	$(p+q-2r)b/2 + ra$
3	x_1, x_2, x_9	$x_1 = (p-r)/2, x_2 = (q+r)/2, x_9 = r$	$(p+q)b/2 + ra$
4	x_1, x_2, x_{11}	$x_1 = (p+r)/2, x_2 = (q-r)/2, x_{11} = r$	$(p+q)b/2 + ra$
5	x_1, x_3, x_8	$x_1 = (p-q)/2, x_3 = (q+r)/2, x_8 = q$	$(p+r)b/2 + qa$
6	x_1, x_6, x_7	$x_1 = (p-q)/2, x_6 = (q-r)/2, x_7 = q$	$(p-r)b/2 + qa$
7	x_1, x_7, x_8	$x_1 = (p-q)/2, x_7 = (q+r)/2, x_8 = (q-r)/2$	$(p-q)b/2 + qa$
8	x_1, x_7, x_{12}	$x_1 = (p-r)/2, x_7 = (q+r)/2, x_{12} = (q-r)/2$	$(p-r)b/2 + qa$
9	x_1, x_8, x_{11}	$x_1 = (p+r)/2, x_8 = (q-r)/2, x_{11} = (q+r)/2$	$(p+r)b/2 + qa$
10	x_2, x_7, x_{10}	$x_2 = (q+r)/2, x_7 = (p+r)/2, x_{10} = (p-r)/2$	$(q-r)b/2 + pa$
11	x_2, x_8, x_9	$x_2 = (q+r)/2, x_8 = (p-r)/2, x_9 = (p+r)/2$	$(q+r)b/2 + pa$
12	x_3, x_8, x_9	$x_3 = (q+r)/2, x_8 = (p+q)/2, x_9 = (p-q)/2$	$(q+r)b/2 + pa$
13	x_6, x_7, x_{10}	$x_6 = (q-r)/2, x_7 = (p+q)/2, x_{10} = (p-q)/2$	$(q-r)b/2 + pa$
14	x_7, x_8, x_9	$x_7 = (q+r)/2, x_8 = (p-r)/2, x_9 = (p-q)/2$	pa
15	x_7, x_8, x_{10}	$x_7 = (p+r)/2, x_8 = (q-r)/2, x_{10} = (p-q)/2$	pa
16	x_7, x_{10}, x_{12}	$x_7 = (p+q)/2, x_{10} = (p-r)/2, x_{12} = (q-r)/2$	$(p+q-r)a$
17	x_8, x_9, x_{11}	$x_8 = (p+q)/2, x_9 = (p+r)/2, x_{11} = (q+r)/2$	$(p+q+r)a$

If the optimal solution belonging to basis 1 is not integer, then the Gomory cut is

$$1 \leq \sum_{j=7}^{14} x_j. \tag{26}$$

The first lexicographic simplex iteration again finds the optimal solution which is

$$\begin{aligned} &x_1 = \frac{p-1}{2}, x_2 = \frac{q-1}{2}, x_3 = \frac{r-1}{2}, x_7 = 1, \\ &x_4 = x_5 = x_6 = x_8 = \cdots = x_{14} = 0. \end{aligned} \tag{27}$$

As it can be seen from Figure 3, only five bases can be optimal. They are in the rows 1, 2, 7, 14, and 15 of Table 2. The order of steps of the minimal paths can be interchanged.

Theorem 2. *If the steps are made according to the values of the variables, then the optimal paths of the BCC grid are as follows:*

(i) If $3b < 2a$ and p, q, and r are even numbers, then the path consists of $p/2$, $q/2$, and $r/2$ steps parallel to the three axis.

(ii) If $3b < 2a$ and p, q, and r are odd numbers, then the path consists of $(p-1)/2$, $(q-1)/2$, and $(r-1)/2$ steps parallel to the three axis and one step into the direction $(1, 1, 1)^T$.

(iii) If $3b > 2a$ and $b < a$, then the path makes r steps of type $(1, 1, 1)^T$ and get to the $(r, r, r)^T$ point. It continues parallel with the first two axis.

(iv) If $2a > b > a$, then the path goes first to the $(p-q, 0, 0)^T$ point with steps parallel to the first axis. Then, it continues by $(q+r)/2$ steps of type $(1, 1, 1)^T$. Finally, it completes by $(q-r)/2$ steps of type $(1, 1, -1)^T$.

(v) If $b > 2a$, then the path makes $(q+r)/2$ steps of type $(1, 1, 1)^T$. It continues with $(p+r)/2$ steps of type $(1, 1, -1)^T$. Finally, it completes by $(p-q)/2$ steps of type $(1, -1, 1)^T$. An alternative solution exists. The path makes $(p+r)/2$ steps of type $(1, 1, 1)^T$. It continues with $(q+r)/2$ steps of type $(1, 1, -1)^T$. Finally, it completes by $(p-q)/2$ steps of type $(1, -1, -1)^T$.

Example 1. Let $a = 4$, $b = 3$, and $(p, q, r) = (5, 3, 1)$. It is the third case of Theorem 2. Then, the optimal basis is basis (1, 2, 7). In this case, $x_1 = 2$, $x_2 = 1$, $x_7 = 1$, and the length of the minimal path is 13.

Example 2. Let $a = 1$, $b = 3$, and $(p, q, r) = (5, 3, 1)$. It is the fifth case of Theorem 2. Then, the optimal basis is basis (7, 8, 9) or basis (7, 8, 10). In the case of the basis (7, 8, 9), the solution is $x_7 = 2$, $x_8 = 2$, and $x_9 = 1$, and the length of the minimal path is 5. In the case of the basis (7, 8, 10), the solution is $x_7 = 3$, $x_8 = 1$, and $x_{10} = 1$, and the length of the minimal path is 5, too.

As we have proven, based on the respective ratio of the weight, the case can be easily determined, and direct formulae give the weighted distance. One may think that Dijkstra or other well-known shortest path algorithms from graph theory could be used, and it is true. However, their complexity is much worse, i.e., the time we need to get the result will be much longer. On the one hand, we cannot use the upper bound as the size of the graph since our grids are infinite. On the other hand, practically, of course only a finite segment of the grid could and will play role in shortest paths between two fixed points. However, the size of this segment is proportional to the third power of the largest coordinate difference of the points, which also implies a relatively large time complexity with respect to our approach. This means that the results presented in this paper give a more efficient way to determine weighted distances.

5. Conclusions

In this paper, it is shown that linear programming gives an efficient tool to find optimal solutions in some digital geometry problems. Chamfer distances on the square grid and on the BCC grid are studied. The BCC grid plays importance in solid state physics, crystallography, and material science since it describes the structure of the atoms/ions in various materials. This structure is more compact than the simple cubic structure and has various advantages also in engineering applications. The distances we have computed are based on weighted paths among the grid points. These distances are useful in various applications (e.g., 2D and 3D image processing) since they could provide relatively good approximations of the Euclidean distance, but since they are step-based, efficient incremental algorithms, e.g., distance transform [37] can easily be adapted. Feasible and optimal bases are found for various cases of the used weights. We have also studied the case when the second closest neighbors can be reached by a smaller weighted step than the closest neighbors (up to our knowledge this has not been done before on the BCC grid). The structure of all optimal paths is explicitly given. Moreover, one needs to check only the respective ratio of the weights and then can easily choose the case, thus, an optimal path and the chamfer distance.

We believe that our method can easily be applied for other similar grids, similarly as we also used in the second part of the paper, where n-dimensional generalizations of the BCC are considered [38].

Data Availability

No data were used to support this study.

Conflicts of Interest

The authors declare that they have no conflicts of interest regarding the publication of this article.

References

[1] S. Marchand-Maillet and Y. M. Sharaiha, *Binary Digital Image Processing: A Discrete Approach*, Elsevier Publishing Company, Amsterdam, Netherlands, 2000.

[2] C. O. Kiselman, *Elements of Digital Geometry, Mathematical Morphology, and Discrete Optimization*, World Scientific, Singapore, 2021.

[3] R. Klette and A. Rosenfeld, *Digital Geometry: Geometric Methods for Digital Picture Analysis*, Morgan Kaufmann Publishers Inc., San Francisco, CA, USA, 1 edition, 2004.

[4] A. Rosenfeld and J. L. Pfaltz, "Distance functions on digital pictures," *Pattern Recognition*, vol. 1, no. 1, pp. 33–61, 1968.

[5] S. Matej, A. Vardi, G. T. Herman, and E. Vardi, "Binary tomography using Gibbs priors," in *Discrete Tomography: Foundations, Algorithms and Applications*, G. T. Herman and A. Kuba, Eds., pp. 191–212, Birkhäuser, Basel, Switzerland, 1999.

[6] I. Her, "A symmetrical coordinate frame on the hexagonal grid for computer graphics and vision," *Journal of Mechanical Design*, vol. 115, no. 3, pp. 447–449, 1993.

[7] I. Her, "Geometric transformations on the hexagonal grid," *IEEE Transactions on Image Processing*, vol. 4, no. 9, pp. 1213–1222, 1995.

[8] B. Nagy, "Shortest paths in triangular grids with neighbourhood sequences," *Journal of Computing and Information Technology*, vol. 11, no. 2, pp. 111–122, 2003.

[9] B. Nagy, "Cellular topology and topological coordinate systems on the hexagonal and on the triangular grids," *Annals of Mathematics and Artificial Intelligence*, vol. 75, no. 1-2, pp. 117–134, 2015.

[10] S. Matej, G. T. Herman, and A. Vardi, "Binary tomography on the hexagonal grid using Gibbs priors," *International Journal of Imaging Systems and Technology*, vol. 9, no. 2-3, pp. 126–131, 1998.

[11] B. Nagy and T. Lukić, "Binary tomography on the isometric tessellation involving pixel shape orientation," *IET Image Processing*, vol. 14, no. 1, pp. 25–30, 2020.

[12] R. Strand and G. Borgefors, "Distance transforms for three-dimensional grids with non-cubic voxels," *Computer Vision and Image Understanding*, vol. 100, no. 3, pp. 294–311, 2005.

[13] R. Strand and P. Stelldinger, "Topology preserving marching cubes-like algorithms on the face-centered cubic grid," in *Proceedings of 14th International Conference on Image Analysis and Processing (ICIAP 2007)*, pp. 781–788, Modena, Italy, 2007.

[14] P. Stelldinger and R. Strand, "Topology preserving digitization with FCC and BCC grids," in *Lecture Notes in Computer Science, Combinatorial Image Analysis*, et al. Springer, Berlin, Germany, pp. 226–240, 2006.

[15] L. Comic and B. Nagy, "A combinatorial coordinate system for the body-centered cubic grid," *Graphical Models*, vol. 87, pp. 11–22, 2016.

[16] B. Csébfalvi, "An evaluation of prefiltered B-spline reconstruction for quasi-interpolation on the body-centered cubic lattice," *IEEE Transactions on Visualization and Computer Graphics*, vol. 16, no. 3, pp. 499–512, 2010.

[17] L. Ibáñez, C. Hamitouche, and C. Roux, "Ray-tracing and 3-D objects representation in the BCC and FCC grids," *Discrete Geometry for Computer Imagery*, Springer, Berlin, Germany, pp. 235–241, 1997.

[18] L. X. Mei, L. Jin, and Y. X. Xia, "3D visualization technology based on BCC-grid shear-warp algorithm," in *The Proceedings of the Multiconference on "Computational Engineering in Systems Applications*, pp. 1454–1459, Beijing, China, October 2006.

[19] F. Labelle, *Tetrahedral Mesh Generation with Good Dihedral Angles Using Point Lattices, PhD Dissertation*, University of California, Berkeley, CA, USA, 2007.

[20] E. Moreno, P. González, R. Emadi, J. B. Roldán, and E. A. Michael, "BCC-Grid versus SC-Grid in the modeling of a sheet of graphene as a surface boundary condition in the context of ADE-FDTD," *Mathematics and Computers in Simulation*, vol. 186, pp. 52–61, 2021.

[21] E. Khalimsky, "Topological structures in computer science," *Journal of Applied Mathematics and Simulation*, vol. 1, no. 1, pp. 25–40, 1987.

[22] E. Khalimsky, R. Kopperman, and P. Meyer, "Computer graphics and connected topologies on finite ordered sets," *Topology and Its Applications*, vol. 36, no. 1, pp. 1–17, 1990.

[23] G. Kovács, B. Nagy, and B. Vizvári, "Weighted distances and digital disks on the Khalimsky grid," *Journal of Mathematical Imaging and Vision*, vol. 59, no. 1, pp. 2–22, 2017.

[24] P. P. Das, "An algorithm for computing the number of minimal paths in digital images," *Pattern Recognition Letters*, vol. 9, no. 2, pp. 107–116, 1988.

[25] E. Luczak and A. Rosenfeld, "Distance on a hexagonal grid," *IEEE Transactions on Computers*, vol. 25, no. 5, pp. 532-533, 1976.

[26] M. A. Butt and P. Maragos, "Optimum design of chamfer distance transforms," *IEEE Transactions on Image Processing*, vol. 7, no. 10, pp. 1477–1484, 1998.

[27] B. Nagy, "Weighted distances on a triangular grid," in *Lecture Notes in Computer Science IWCIA 2014*, R. P. Barneva, V. E. Brimkov, and J. Slapal, Eds., Springer, Cham, Switzerland, pp. 37–50, 2014.

[28] R. Strand and B. Nagy, "Weighted neighbourhood sequences in non-standard three dimensional grids–metricity and algorithms," in *DGCI 2008. LNCS*, D. Coeurjolly, I. Sivignon, L. Tougne, and F. Dupont, Eds., pp. 201–212, Springer, Berlin, Germany, 2008.

[29] S. J. Russel and P. Norvig, *Artificial Intelligence: A Modern Approach*, Prentice-Hall, Hoboken, NJ, USA, 1995.

[30] G. B. Dantzig, "Programming in a linear structure," *Econometrica*, vol. 17, pp. 73-74, 1949.

[31] R. E. Gomory, "Outline of an algorithm for integer solutions to linear programs," *Bulletin of the American Mathematical Society*, vol. 64, no. 5, pp. 275–279, 1958.

[32] B. Nagy and R. Strand, "Approximating euclidean distance using distances based on neighbourhood sequences in non-standard three-dimensional grids," in *Lecture Notes in Computer Science IWCIA 2006*, R. Reulke, U. Eckardt, B. Flach, U. Knauer, and K. Polthier, Eds., Springer, Heidelberg, Germany, pp. 89–100, 2006.

[33] R. Strand and B. Nagy, "Distances based on neighbourhood sequences in non-standard three-dimensional grids," *Discrete Applied Mathematics*, vol. 155, no. 4, pp. 548–557, 2007.

[34] G. Kovács, B. Nagy, and B. Vizvári, "On weighted distances on the Khalimsky grid," in *Discrete Geometry for Computer Imagery*, N. Normand, J. Guédon, and F. Autrusseau, Eds., Springer, Cham, Switzerland, pp. 372–384, 2016.

[35] H. G. Barrow, J. M. Tenenbaum, R. C. Bolles, and H. C. Wolf, "Parametric correspondence and chamfer matching: two new techniques for image matching," in *Proceedings of the 5th international joint conference on Artificial intelligence*, pp. 659–663, Cambridge, MA, USA, 1977.

[36] G. Borgefors, "Distance transformations in arbitrary dimensions," *Computer Vision, Graphics, and Image Processing*, vol. 27, no. 3, pp. 321–345, 1984.

[37] R. Strand, B. Nagy, and G. Borgefors, "Digital distance functions on three-dimensional grids," *Theoretical Computer Science*, vol. 412, no. 15, pp. 1350–1363, 2011.

[38] G. Kovács, B. Nagy, G. Stomfai, N. D. Turgay, and B. Vizvári, "Discrete optimization: the case of generalized BCC lattice," *Mathematics*, vol. 9, no. 3, p. 208, 2021.

Hindawi
Mathematical Problems in Engineering
Volume 2021, Article ID 6615634, 10 pages
https://doi.org/10.1155/2021/6615634

Research Article

Integrated Quality-Based Production-Distribution Planning in Two-Echelon Supply Chains

Husein Pasha, Isa Nakhai Kamalabadi, and Alireza Eydi

Department of Industrial Engineering, University of Kurdistan (UOK), Sanandaj, Iran

Correspondence should be addressed to Isa Nakhai Kamalabadi; nakhai.isa@gmail.com

Received 13 December 2020; Revised 23 March 2021; Accepted 1 April 2021; Published 14 April 2021

Academic Editor: Mohammad Yazdi

The integrated production-distribution (P-D) planning has turned into one of the most essential areas in supply chain (SC) management in recent years, especially in the case of perishable products in which the quality of products can change over time. Nonetheless, so far, the suggested models have focused on the P-D stages of the chain while the delivery of high-quality products to customers is of paramount significance in the perishable SC. In the present paper, a multiobjective, mixed-integer, and nonlinear programming (MOMINLP) mathematical model was developed for integrated P-D deteriorating items in a two-echelon SC that emphasizes quality degradation. Quality is monitored and calculated as a function of temperature and time throughout the SC, and the main purpose of the model is to first increase the quality of products delivered to customers and, second, minimize the SC costs. To optimize the problem, the particle swarm optimization (PSO) approach was also incorporated into the model. The obtained model was applied to a case study in Protein Gostar Sina Company in Iran, which resulted in decreased P-D costs as well as increased customer satisfaction.

1. Introduction

Supply chain (SC) can be depicted as a chain attempting to establish effective communication between customers and suppliers by efficient management of the flow of material, information, and money [1]. SCs include procedures that create certain values offered to the final customer as products or services. SC is a complicated system requiring its members to share their information to increase the integration of chain members, better coordinate financial flows and materials, and reduce the undesirable consequences of the SC [2]. Two essential areas in SC are production planning and distribution planning, while integration has also been significantly emphasized in this respect over the past years [3]. Nowadays, in markets worldwide, products with short life cycles as well as customers with great expectations make companies pay special attention to SC. Nevertheless, SC members require proper arrangement as well as harmonization to make a supply chain management (SCM) effective [4]. This can have serious implications for perishability that can in turn influence all SC processes such as production process, inventory management, and distribution [5].

Recently, the integrated P-D planning models for deteriorating items have attracted considerable interest among researchers. This is especially the case for food SCs and real-world models that relate to product lifespans and efforts to deliver quality goods to customers. A range of topics is always discussed concerning the food SC. Food SCs are intricate and constantly changing. The effective network design for SC can significantly contribute to the flow of products, the reduction of the costs related to its transportation, and the increasing food safety [6]. Most studies in this area have attempted to model the issue of quality and decrease of product life in SC separately just using one of the models of production, distribution, or inventory. However, today the integration and presentation of models for simultaneous coverage of a broader segment of the SCs have found widespread popularity.

Considering the importance of an integrated model for simultaneous quality concern of products and P-D planning, the main purpose of the present paper is to provide a

multiobjective mathematical model for the integrated P-D problem of perishable goods which first maximizes the quality of products delivered to customers and second reduces the overall costs of the SC. To this end, in the current study, a multiobjective, mixed-integer, and nonlinear programming (MOMINLP) mathematical model was developed where the global criterion method (GCM) has been used for the allocation of weights to each objective function. In the proposed model, the perishability of goods in all stages of the SC (from production to delivery to the customer) is accurately measured based on the effective parameters of temperature and time where quality is defined as a function of temperature and time based on Arrhenius equation. Since by adding the Arrhenius equation, the mathematical model became nonlinear, and the Taylor series was used to linearize the model. Moreover, since one of the disadvantages of integrated models is the inefficiency of precise solution methods, the particle swarm optimization (PSO) metaheuristic solution method was applied to enhance the efficiency of the proposed model and solve problems on large scales.

In addition to the above, since mathematical models are generally far from the real world, two steps were taken to bring the model closer to the real world. First, products were qualitatively graded according to the realistic customer demands. Second, to measure the real-world performance of the model, it was implemented in the poultry industry in Protein Gostar Sina Company in Iran. The results indicated that integrated planning in P-D, taking into account the product groupings and quality loss throughout the SC, would result in higher chain responsiveness and thus reduce the overall SC costs in the long run.

The rest of the paper is organized as follows. In Section 2, the focus is on some relevant works on the integrated P-D and quality models in SC. In addition to illustrating the PSO-based solution used, Section 3 presents the problem statement or the proposed approach of the research and the mathematical modeling applied. In Section 4, the case study is presented, and the results are analyzed in Section 5. Finally, Section 6 is dedicated to the conclusion and suggestions for future research.

2. Literature Review

From an overall perspective, the integrated P-D focuses on two distinct stages. The first stage is the production phase which converts the inputs into the final products and reduces all production costs, including setup costs, regular working hours, and overtime. The second stage is related to the distribution network of the final goods from production places to the customers aiming to reduce the costs of transportation, warehousing, etc. [6].

Fahimnia et al. [3] presented a review paper on this subject, categorized these models into seven according to the complexity of the modeling, and discussed the solution approach. Abid et al. developed a novel model of integrated P-D in a stochastic intermodal SC focusing on two points: minimization of overall costs and maximization of the level of satisfaction of customers. They propose a biobjective stochastic model for handling uncertainty in demands as well as production capacities [7]. Ma et al., using bilevel programming for modeling the problem, proposed a model for a real case study [8]. Rafiei et al. presented a biobjective model that integrates suppliers, producers, distributors, and end users in four levels whose objective is minimizing the total cost of SC and maximizing the service level of the chain [9].

Also, managing deterioration is a remarkable topic in SC about which many studies have been conducted. Perishability is defined as the deterioration, decay, damage, spoilage, evaporation, obsolescence, waste, loss of utility, or loss of marginal value of a commodity that results in decreasing the usefulness of the original product [10]. According to this definition, all the products whose value is reduced over time are categorized under this class. The first study on perishability was carried out by Whitin [11]. Readers can find a comprehensive review of deterioration models in SC from previous research [5, 12–15]. Some problems arise in SCM due to the perishability of food products. According to Nematollahi and Tajbakhsh, a large proportion of reviewed studies focus on food quality and safety issues [16]. Also, the perishability and quality of food products are among the essential factors in managing the food SC from the stages of production to storage and finally to transportation [17]. Thus, both product flow and product quality affect SC performance. As a result, it is vital to adopt an integrative approach to control the food quality from producers to the final customers. In the integrated P-D model proposed by Jia et al., no deterioration occurs at the facilities, but different quality degradation processes are noticed in the transportation and sales stages. Moreover, shelf life is considered constant and definite [18]. Zhang et al. proposed an innovative idea for the integration of product quality. They assume three stages for the SC in their model where a function of time and temperature is adopted to represent the quality of food products for production, storage, and transportation [19].

The recent decade has witnessed a proliferation of new models for perishable items. The first model was introduced in [20], which included an integrated allocation and distribution design for deteriorating items supposed to be distributed in different locations with random demands. Later, the topic drew the attention of other scholars. The product quality was taken into account throughout the processes of P-D planning using the MIP model by [17] as well. He et al. [21] focus on the models of quantitative operations management associated with the management of food quality and classify the literature into four problem categories of storage, distribution, and pricing (for perishable food products), as well as operations management (for food traceability and safety). Yang and Tseng proposed a model considering deterioration for chilled food with an eye to the model of Gompertz, which illustrates the growth degree of microorganisms with time. Moreover, they take the rate of deterioration dependent on temperature and conduct a case study on pork sandwich [22]. The multiobjective framework was proposed at the operational level with an eye on two types of perishable goods fixed and loose

shelf life in the previous studies [23]. The researchers have also offered a new solution using the adaptive large neighborhood search framework to deal with the MILP model of integrated P-D planning for perishable products. In this study, the planning phase included lot sizing, scheduling, and line assessment decisions, whereas the distribution planning phase entailed the problem of vehicle routing with time windows [24]. With a focus on inventory planning, Priyan and Uthayakumar investigated the fuzzy deterioration in modeling integrated P-D. Furthermore, they viewed the setup cost as a function of capital expenditure that can reduce extra investment [25]. Rezaeian et al. suggested a new MINLP model for integrated P-D and inventory planning of fixed life products in a two-echelon SC. Also, the multivehicle and FIFO systems were considered in these models, and the combination of genetic algorithm and Taguchi method was employed for solving the problem [26].

The main target of deteriorating SCs is to keep the quality of products while improving their logistic performance and pay the highest attention to temperature as a delicate feature; therefore, an integrated production routing model was developed for perishable products. In this model, various factors, including the production, inventory, temperature of storage, and routing, as well as the temperature of the vehicle were considered [27]. A four-objective mixed-integer linear programming model was developed for an intelligent food logistics system. The goal was to first minimize total system expense, Co2 emission amount during transportation, and production, as well as total weighted delivery lead time and the second was to maximize the average quality of food. To solve the model, a modified multiobjective PSO algorithm with multiple social structures was developed [28].

As an overview of this section, it can be concluded that the models developed in this area can be divided into three categories. The first category is related to integrated P-D models that do not take into account the assumption of the perishability of goods. The second category includes models that focus on perishability but apply this assumption in either production or distribution models. The third category that includes only a few models and is more relevant to the present study, which includes integrated P-D models that consider the assumption of perishability, either as deterioration or as quality degradation. The main difference between the presented model and the above models is in the direct calculation of product quality (based on temperature and time) over a continuous period, the ability to be developed for multiple products, and adaptation to real-world problems.

3. The Problem Statement and Proposed Model

The modeling approach is based on a two-echelon SC that consists of manufacturing plants and customer centers shown in Figure 1.

According to Figure 1, the presented model is related to the two-echelon SC. At one echelon, there are manufacturing plants that meet all the assumptions associated with production such as working in regular time, overtime, outsourcing, setup costs, and capacity constraints. At the other echelon, some customers have a specific demand that depends on the quality of the products. The problem is modeled based on the MOMINLP mathematical model whose results are as follows: grouping products in factories and determining the amount of production in each unit, choosing the optimal production method, choosing the best route to send products from manufacturing plants to customers in a way that the quality of the products delivered to customers increases, and reducing waste.

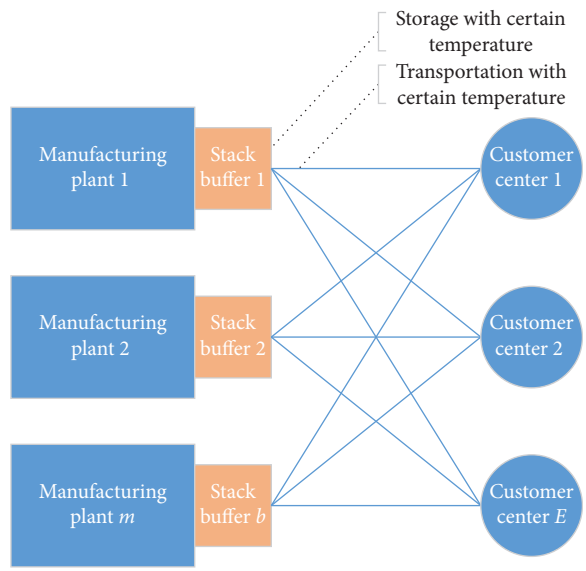

Figure 1: The scope of the proposed model.

The SC relates to food types that have a perishable nature and lose their quality over time. This quality is stated as a function consisting of the rate of deterioration and the reactions' order. The food quality (q) is stated as

$$\frac{\mathrm{d}q}{\mathrm{d}t} = kq^n, \tag{1}$$

where q shows product quality, t shows the elapsed time, and n as a power factor known as the reactions' order is 0 (reaction with zero-order) in the case of fresh fruits or vegetables or 1 (reactions with first-order) in the case of meats as well as dairy products. The quality of the products decays linearly if $n = 0$ and exponentially if $n = 1$ [29]. Also, k is the rate of degradation developed by the Swedish chemist Svante Arrhenius in 1899. He combined the concepts of activation energy and the Boltzmann distribution law into one of the most essential relations in physical chemistry as follows [30]:

$$k = k_0 \cdot e^{-E_a/\mathrm{RT}}, \tag{2}$$

where k_0 is a constant and called the pre-exponential factor independent from temperature, E_a the activation energy, R the gas constant which equals $8.314\,\mathrm{J\,mol^{-1}{\cdot}K^{-1}}$, and T the absolute temperature, where RT is the average kinetic energy.

The quality of a product can be estimated at a certain point in the P-D network, according to the initial quality (q_0), subsequent storage timespans $i = 1, \ldots, m$ with the time interval t_i, and degradation rate k_i (determined by the temperature T_i), which results in

$$q = q_0 \cdot \exp\left[-\sum_{i=1}^{T} k_0 t_i \cdot \exp\left[\frac{-E_a}{\mathrm{RT}_i}\right]\right]. \quad (3)$$

With this equation, the expected quality of food products can be assessed after being stored and transported at certain timespans and temperatures [17].

3.1. Mathematical Modeling. As regards the nature of the integrated P-D problems, which may result in reduced product quality, a mathematical model was developed with the following specifications.

Products of m factories lie within the g-class of quality. In each factory, production takes place in standard working hours or overtime while being partly outsourced whenever appropriate. Depending on the nature of the products manufactured, all products are dispatched to e customer centers immediately after production. As indicated by the Arrhenius equation, products can corrupt under the impact of any change in temperature and time.

To apply this relation to the model, the first and main objective function was formulated to increase the quality of the products delivered to the customer. Moreover, a condition was set for the constraints specifying that if the product quality was lower than the minimum defined, the product was considered as waste. In the meantime, some factors were considered in the transportation of products from factories to customer centers. The main one was transportation time, directly affecting the perishability, along with other parameters such as road tolls, traffic, and traffic congestion as secondary determinants which influence shipping costs. The model also entailed two objective functions: increased quality of products received by the customers and reduced P-D costs.

3.1.1. Assumptions. The following assumptions are adopted in the model:

(i) The capacity of all manufacturing plants is known and limited

(ii) The required level and minimum quality of each product grade for end users are known

(iii) Production is performed only once at the outset of the period, and then, the products are directly sent to the end users

(iv) The shortage is not allowed

(v) Besides time, the shipping cost is affected by the amount of toll, road quality, traffic congestion, etc.

(vi) At each stage of the chain, products lose their quality over time due to the activity of internal microorganisms

(vii) The temperature is assumed constant in all stages of SC and quality degradation is only affected by time spent or transportation based on the Arrhenius equation

(viii) The products have high quality just when produced in the manufacturing plants

(ix) Factories offer customers their products in several quality grades

3.1.2. Indices, Parameters, and Decision Variables. The indices, parameters, and decision variables used throughout the paper are given below.

Indices:

m Manufacturing plants ($m = 1, 2, \ldots, M$)

e End users ($e = 1, 2, \ldots, E$)

g Products' quality grades ($g = 1, 2, \ldots, G$)

Parameters:

RP_{mg}: unit's production cost in regular time for the product at manufacturing plant m having quality grade g

OP_{mg}: unit's overtime production cost for the product at manufacturing plant m having quality grade g

OS_{mg}: unit's production cost of outsourcing for the product at manufacturing plant m having quality grade g

R_{eg}: forecasted demand for the product with quality grade g at the end user e

O_m: fixed cost of opening and operating manufacturing plant m

TC_{meg}: transportation cost for the product at quality grade g from manufacturing plant m to end user e

T_{meg}: transportation time for the product at quality grade g from manufacturing plant m to end user e

λ_{mg}: capacity hours for production in regular time for the product having quality grade g at manufacturing plant m

λ_{mg}': capacity hours for overtime production for the product having quality grade g at manufacturing plant m

$Q_g^{\max}$: the quality level of the product with grade g just after the production

$Q_g^{\min}$: the quality level of product with grade g that end user accepts

WC_g: waste cost for the product with quality grade g in period t

M: a large positive number

Decision variables:

P_{mg}: product quantity when manufactured in regular time at manufacturing plant m having quality grade g

P_{mg}': product quantity when manufactured overtime at manufacturing plant m having quality grade g

P''_{mg}: product quantity when outsourced by manufacturing plant m having quality grade g

D_{meg}: quantity of product with quality grade g transported from manufacturing plant m to end user e

Y_{meg}: the binary variable which indicates the selection of path of manufacturing plant m to end user e

W_g: waste amount of product with quality grade g

Z_m: the binary variable of operating manufacturing plant m

3.1.3. Model Formulation.

$$\text{Max}\, Z_1 = \sum_m \sum_e \sum_g Y_{meg} \left(Q_g^{\max} \exp\left[-\sum_{i=1}^{T_{meg}} k_0 t_i \exp\left(\frac{-E_a}{\text{RT}} \right) \right] \right), \tag{4}$$

$$Min\, Z_2 = \sum_m O_m Z_m + \sum_m \sum_g \left(\text{RP}_{mg} P_{mg} + \text{OP}_{mg} P'_{mg} + \text{OS}_{mg} P''_{mg} \right) + \sum_m \sum_e \sum_g Y_{meg} D_{meg} \text{TC}_{meg} + \sum_g \text{WC}_g W_g, \tag{5}$$

which subject to

$$\sum_m \left(P_{mg} + P'_{mg} + P''_{mg} \right) \geq \sum_e R_{eg}, \quad \forall g \in G, \tag{6}$$

$$\sum_e D_{meg} = P_{mg} + P'_{mg} + P''_{mg}, \quad \forall m \in M, \forall g \in G, \tag{7}$$

$$\sum_m D_{meg} - W_g = R_{eg}, \quad \forall e \in E, \forall g \in G, \tag{8}$$

$$W_g = \sum_m \sum_e D_{meg} Y_{meg}\, \forall g \in G,\ T_{meg} \geq \gamma_g, \text{where}\ \gamma_g = \frac{-Ln\left(\exp\left(-\beta_g t_0 \right) - \beta_g Q_g^{min} \right)}{\beta_g} \& \beta_g = k_0 e^{\left[-E_a/\text{RT} \right]}, \tag{9}$$

$$P_{mg} \leq \lambda_{mg}, \quad \forall m \in M, g \in G, \tag{10}$$

$$P'_{mg} \leq \lambda'_{mg}, \quad \forall m \in M, g \in G, \tag{11}$$

$$\sum_g P_{mg} \leq M \cdot Z_m, \quad \forall m \in M, \tag{12}$$

$$\sum_g P_{mg} \geq Z_m, \quad \forall m \in M, \tag{13}$$

$$P'_{mg} \leq Pmg, \quad \forall m \in M, g \in G, \tag{14}$$

$$MY_{meg} \geq D_{meg}, \quad \forall m \in M, e \in E, g \in G, \tag{15}$$

$$M\left(Y_{meg} - 1 \right) < D_{meg}, \quad \forall m \in M, e \in E, g \in G, \tag{16}$$

$$\begin{gathered} P_{mg}, P'_{mg}, P''_{mg}, D_{meg}, W_g \geq 0, \\ \text{int}\, \forall m \in M, e \in E, g \in G, \end{gathered} \tag{17}$$

$$Z_m, Y_{meg} \in \{0, 1\}, \quad \forall m \in M, e \in E, g \in G. \tag{18}$$

The first objective function (equation (4)) in the above formulation aims to maximize the quality of the products made available to the customers. Equation (5) represents the second objective function consisting of fixed cost for operating facilities, regular time and overtime production cost, outsourcing expenses, and transportation, as well as waste disposal costs. Constraint (6) indicates that the demand of end users must be satisfied. Constraint (7) ensures that the shipping amount exactly equals the manufactured products.

Constraint (8) guarantees that the sum of goods shipped from factories to the final customers meets the customer demand following the waste deduction. Constraint (9) is used to determine the amount of waste in the chain extracted according to the Arrhenius equation [17, 30], such that, considering the minimum quality ($Q_{\min}$) available for each product, the maximum shelf life is estimated through (γ_g), and if the product time in the chain exceeds this value, it is considered a waste. Constraints (10) and (11) show the production capacity in the manufacturing plant, while constraints (12) and (13) ensure that factories are viewed as operating in case they are engaged in the production process. Constraint (14) ensures that overtime production is allowed if it is carried out at a regular time. Constraints (15) and (16) ensure that shipping occurs between factories and customers if the lane is selected. The remaining constraints, i.e., (17) and (18), are nonnegativity, binary, and integer constraints on the decision variables.

3.2. Simplification of the Model. Since this model assumes a constant temperature, the first objective function can be simplified as follows:

$$\xi_0 = k_0 \exp\left(\frac{-E_a}{\mathrm{RT}}\right) \text{ then } \operatorname{Max} Z_1 = \sum_m \sum_e \sum_g Y_{meg}\left[Q_g^{\max} \exp\left(-\sum_{i=1}^{T_{meg}} \xi_0 t_i\right)\right]. \tag{19}$$

As the above relation is nonlinear and exponential, it can be transformed into a quadratic function using the Taylor series as follows:

$$\exp\left(-\sum_{i=1}^{T_{meg}} \xi_0 t_i\right) = 1 - \sum_{i=1}^{T_{meg}} \xi_0 t_i + \frac{\left(\sum_{i=1}^{T_{meg}} \xi_0 t_i\right)^2}{2} - O\left(x^3\right). \tag{20}$$

According to the results of the low-dimensional model solution, the $O(x^3)$ value is minimal and negligible. Therefore, the following relation can be considered as an alternative for the original with good approximation:

$$\operatorname{Max} Z_1 = \sum_m \sum_e \sum_g Y_{meg}\left[Q_g^{\max} 1\left(-\sum_{i=1}^{T_{meg}} \xi_0 t_i + \frac{\left(\sum_{i=1}^{T_{meg}} \xi_0 t_i\right)^2}{2}\right)\right]. \tag{21}$$

As it is clear, the objective functions Z_1 and Z_2 go against each other. Namely, improvement in each function results in a departure from the optimal point by the other. Therefore, the simultaneous optimization of each of the given objective functions requires a specific method [31]. The GCM was employed in the current case to detect the minimization point for the totality of the relative deviations of the entire objective functions from the optimal values (Z_i^*). The ultimate objective function, calculated using the GCM, is given in relation (23):

$$\operatorname{Min} Z = w_1 \times \frac{Z_1^* - Z_1}{Z_1^*} + w_2 \times \frac{Z_2 - Z_2^*}{Z_2^*}, \tag{22}$$

$$\operatorname{Min} Z = w_1 \times \frac{Z_1^* - \left\{\sum_m \sum_e \sum_g Y_{meg}\left(Q_g^{\max} \exp\left[-\sum_{i=1}^{T_{meg}} k_0 t_i \exp\left(-E_a/\mathrm{RT}\right)\right]\right)\right\}}{Z_1^*} + w_2 \times \frac{\sum_m O_m Z_m + \sum_m \sum_g \left(\mathrm{RP}_{mg} P_{mg} + \mathrm{OP}_{mg} P_{mg}' + \mathrm{OS}_{mg} P_{mg}''\right) + \sum_m \sum_e \sum_g Y_{meg} D_{meg} \mathrm{TC}_{meg} + \sum_g \mathrm{WC}_g W_g - Z_2^*}{Z_2^*}. \tag{23}$$

According to this method, the objective functions can receive different weights to reveal the ideas of decision makers (DM). In this relation, w_i refers to the weight of the objective function determined by DM, while the sum of all weights equals 1. Based on this method, if a higher weight is assigned to a function by the DM, the solution will be closer to the optimal level of the given function. An independent calculation was performed for the optimal values of all functions (Z_i^*) in equation (23). In this stage, the objective functions which required maximization were normalized based on $(Z_i^* - Z_i)/Z_i$. Also, the normalization of the objective functions which needed minimization was conducted using $(Z_i - Z_i^*)/Z_i^*$.

3.3. Solution Procedure. This study developed a mixed-integer nonlinear formulation for the two-echelon SCs based on the integration of aggregate P-D plans and the concept of perishability. For solving this complex model, first, the GAMS optimization software was used and test runs were performed on a 2.33 GHz Core i5 with a 4 GB RAM system. The results were not applicable because the model was complex and the solution time was too long. Therefore, metaheuristic PSO was applied to solve the model within a more acceptable timespan.

To detect the optimal solution in the PSO algorithm, the initial population was generated at random. Given the constraints of the problem and its discrete nature, the probability for the random population generated to fall out of the limitations was very high. Therefore, the production of the initial population was performed such that the solution was kept within the range of the answer. To this end, several factories were randomly activated so that the minimum distance from one of the active factories to the customer was less than the product loss threshold. In this case, at least one factory was kept active to meet the needs of customers, so the limitation of satisfying customer needs was met.

After determining the active factories, customer demand was allocated to the factories. To this end, a percentage of customer demand was assigned to a randomly selected active manufacturing plant at any time, and this amount was deducted from the customer demand. This loop continued until all the demands were allocated to the factories. Next, the demands allocated to the factory were divided, due to the limitation of production capacity in regular hours, overtime, and during outsourcing. In this way, all the constraints of the problem were fulfilled, and the initial population was produced within the acceptable problem space.

In the PSO algorithm, the generation of subsequent solutions occurs through the movement of the initial population solutions. That is, the new birds' position (next-generation solution) is calculated based on the previous position, the distance to the best bird of the current generation, and the distance to the best bird among all generations. Structured matrices are used in the proposed algorithm to represent solutions, where each of the decision variables is a property of the matrix. In other words, a position is assumed for the bird for each of the decision variables. Similarly, a velocity vector is developed for each decision variable. Using the position and motion of the vector of the decision variables in the initial population, the birds move and these steps continue until the stopping condition is fulfilled.

There are some parameters of control that affect the PSO algorithm. They include the problem dimension, particle numbers in each generation, coefficients of acceleration, weight of inertia, size of the neighborhood, and iteration frequencies, as well as random values. Moreover, in the case of the adoption of velocity constriction, PSO performance is impacted by the maximum coefficient of velocity and constriction. The control parameters used in the problem under study are listed in Table 1:

4. The Illustrative Case Study

To study the performance of the model, a case study was conducted at Protein Gostar Sina Company in the poultry industry which is one of the largest companies in Iran producing meat and protein. In the sector dealing with the production of poultry products, the company has seven slaughterhouse units and 25 customer center units throughout Iran, which are increasingly growing and expanding. Based on the type and quality of input materials, as well as slaughter and packaging conditions in the slaughterhouses, hot poultry products of this company fall into three quality grades: A, B, and C. Grade A contains the best quality products, without any problems in the process of slaughter and packaging. Grade B includes products that are not cut correctly during the slaughter process and have so-called contusion and ecchymosis. Finally, grade C includes products that have undergone some problems in the process of slaughter and packaging and contain contusion, ecchymosis, blood, and remainders of poultry trachea, esophagus, and some viscera in the packaging.

Modeling the P-D process of the company was carried out at a single time. In practice, live chickens ready to be slaughtered were loaded and shipped to the slaughterhouse during the night before slaughter. The slaughter normally took place during the night and the packaging process ended by morning. After completing the packaging process, the product had to reach the final customers within a maximum of 72 hours, and the model was designed to reduce the time of product delivery to the customer. However, it must be kept in mind that meat products could become corrupt over time due to the activities of internal microorganisms. This factor was taken into account in this study by using the Arrhenius equation. The model examines the effect of the factors of time and temperature on the growth of these microorganisms and the product quality reduction. For meat products, these quality changes occur exponentially. Due to the use of refrigerated machines and storage in particular refrigerated areas, the temperature factor was assumed to be constant at 4°C. Thus, the only factor in product corruption and the quality decrease was time.

As for the importance of the final quality of the product delivered to the customers and according to industry experts, the minimum acceptable quality for the three quality grades of manufactured products equals 0.4, 0.3, and 0.2. Also, the objective function coefficients, including values w_1 and w_2 in this model, respectively, equal 0.65 and 0.35. The

Table 1: Control parameters in PSO.

Particle numbers	100
Iteration frequencies	100
Coefficients of acceleration	$c_1 = 2$, $c_2 = 2$
Weight of inertia	1
Size of neighborhood	Particles at a distance of 2 units from one another

Table 2: Values of the production parameters.

	Grade A			Grade B			Grade C				
Manufacturing plant	RP	OP	OS	RP	OP	OS	RP	OP	$O(*10^5)$	$\lambda(\lambda = 2\lambda')$	OS
m_1	457	554	750	408	522	720	362	495	690	25	30,000
m_2	423	541	735	390	510	720	343	485	660	23	30,000
m_3	415	530	700	380	505	670	320	485	650	20	40,000
m_4	423	545	750	390	510	730	343	500	700	25	20,000
m_5	400	520	720	370	500	700	340	480	690	25	30,000
m_6	480	580	800	465	580	780	450	580	760	35	50,000
m_7	510	600	800	490	600	780	470	600	760	30	40,000

Table 3: Values related to the customer demand.

R	e_1	e_2	e_3	e_4	e_5	e_6	e_7	e_8	e_9	e_{10}	e_{11}	e_{12}	e_{13}	e_{14}
GA	950	1420	950	1400	2800	1890	675	540	815	675	1100	500	1000	5000
GB	330	500	340	500	1000	675	243	193	286	243	900	750	1500	20,000
GC	700	100	700	100	200	260	490	390	430	490	400	1000	400	20,000
	e_{15}	e_{16}	e_{17}	e_{18}	e_{19}	e_{20}	e_{21}	e_{22}	e_{23}	e_{24}	e_{25}			
GA	8000	7500	9500	9000	7500	1150	4700	4000	7000	6500	12000			
GB	3000	2700	3400	3000	2700	400	1700	2000	2500	3000	9100			
GC	600	600	700	700	550	80	340	3500	1000	7000	10,000			

$*$ denotes GA = Grade A, GB = Grade B, and GC = Grade C.

values of the waste cost for the decayed items for each quality grade also equaled 6000, 5200, and 4700, respectively. Other dimensions of the problem include those of production such as factory setup costs, production at a regular time, overtime, or outsourcing, and quantitative limitations which are listed in Table 2:

The values for customer demand are also presented in Table 3.

Other model-related parameters are given in Supplementary Materials (available here).

5. Result Analysis

The following procedures were used to estimate the model performance. Initially, the model developed for the case study referred to in Section 4 was solved solely with the second objective function and only with the emphasis on cost reduction. The results indicated that the objective function value was equal to $8.9 * 10^7$ and the production units 2, 3, 4, and 5 started working (Figure 2). However, when the model was solved with two objective functions, while simultaneously minimizing costs and enhancing product quality, the value of the second objective function equaled $10.4 * 10^7$, and the production units 1, 2, 4, and 5 initiated production.

By carefully examining the production and allocated values in both cases, it became clear that, in the dual-purpose case, the total time spent on delivering the products to customers was less than the single-objective state. This indicates an increase in the quality of the products offered to the customers. Nowadays, the increasing importance of the use of healthy food products, high value of quality, and customer dissatisfaction have given a pivotal role to the quality and prevention of excessive reduction of the product quality in the SC.

Since the initial model was a MOMINLP and the solution time was not justified for large-scale problems, two steps were considered: first, the nonlinearity of the problem with part 3.2 transformation from exponential to the second-order problem, and second, the development of PSO algorithm to solve the larger samples. To investigate the performance of the developed solutions, random samples with different sizes were generated with varying factory and customer numbers and solved using all three methods (main model, quadratic function, and PSO). The results are summarized in Table 4. Items related to the 5th rows are justified if the sales policy is direct.

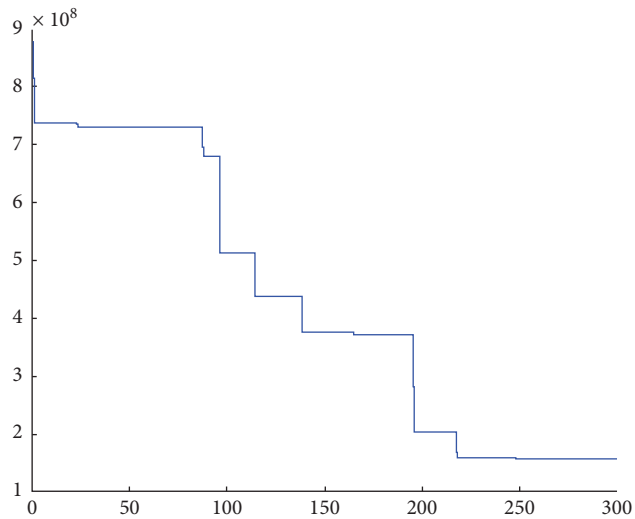

Figure 2: The result of PSO.

Table 4: The results of solving random samples with different methods.

No	Number of manufacturing plants	Number of customers	Time to solve (second)/ deviation from global solution (%)				
			Main	Quadratic		PSO	
1	10	30	60	45	0	70	0
2	10	50	110	87	0	75	0
3	20	100	320	183	0	92	2
4	20	200	1270	582	0	180	4
5	20	500	3850	1300	0	225	3.7
6	20	700	12,000	4300	0	310	5.2
7	20	1000	58,000	6400	0	390	4
8	20	5000	—	18,600	0	840	—
9	20	10,000	—	—	—	1200	—
10	20	50,000	—	—	—	3740	—

6. Conclusion

The development of integrated models in the food SC on the one hand and the increased demand for healthy food on the other have doubled the need to develop integrated models for enhancing the quality of products. In this study, a new integrated P-D model was developed with a focus on the quality of products in the SC of perishable materials. For validation, the model was implemented in the poultry industry. Model solutions were developed and applied to improve efficiency, which ultimately led to increased quality of products throughout the chain. The research findings can be summarized as follows:

(i) The integrated P-D models play an essential role in creating integrity in SC decisions if they are adapted and used in operational cases. These models can be used as a management decision support system (DSS) that helps managers in decisions at different time intervals. For example, if the current status is compared to the optimal one, an overall estimate of the reasons for customer dissatisfaction can be observed and, in coordination with the quality assurance unit, appropriate corrective actions can be taken. Moreover, by examining the costs in the optimal status of the model and matching them with the costs of the financial unit, a suitable budgeting plan can be devised.

(ii) Among the models developed to estimate the quality of products in the SC, the Arrhenius equation is most capable of adapting to real-world problems due to its simplicity and distinct categorization. It seems that the capabilities of the model can be used more extensively in complementary models in the future, which certainly will require a focus on solution methods.

(iii) Based on the Arrhenius equation, temperature and time are among the most influential parameters in the quality of products and materials. By adopting effective solutions, these two factors can be substantially controlled in the chain. Future studies can delve further into the nature of the relation between the given factors and the use of modern packaging methods, equipped transportation systems, and food warehouses.

Data Availability

The data used to support the findings of this study are included within the article.

Conflicts of Interest

The authors declare that there are no conflicts of interest regarding the publication of this paper.

Supplementary Materials

Supplementary Table 1: the table represents transportation time for products at quality grade g from manufacturing

plant m to end user e. g_1, g_2, and g_3 represent quality grades A, B, and C, respectively, in the case study. Supplementary Table 2: the table describes transportation cost for the products at quality grade g from manufacturing plant m to end user e. g_1, g_2, and g_3 represent quality grades A, B, and C, respectively, in the case study. (*Supplementary Materials*)

References

[1] A. Agrawal, R. Shankar, and M. K. Tiwari, "Modeling the metrics of lean, agile and leagile supply chain: an ANP-based approach," *European Journal of Operation Research*, vol. 173, no. 1, pp. 211–225, 2006.

[2] F. Zhang and Z. Gong, "Supply chain inventory collaborative management and information sharing mechanism based on cloud computing and 5G Internet of Things," *Mathematical Problems in Engineering*, vol. 2021, Article ID 6670718, 2021.

[3] B. Fahimnia, R. Marian, and L. Luong, "A review and critique on integrated production-distribution planning models and techniques," *Journal of Manufacturing Systems*, vol. 32, no. 1, pp. 1–19, 2013.

[4] S. Yousefi, M. Jahangoshai Rezaee, and M. Solimanpur, "Supplier selection and order allocation using two-stage hybrid supply chain model and game-based order price," *Operational Research*, vol. 21, pp. 553–588, 2019.

[5] P. Amorim, C. Almeder, and B. Almada-Lobo, "Managing perishability in production-distribution planning: a discussion and review," *Flexible Services and Manufacturing Journal*, vol. 25, no. 3, pp. 389–413, 2013.

[6] C. Meyr, Z. Goff, and R. Accorsi, "Chapter 10 - mathematical modeling of food and agriculture distribution," in *Sustainable Food Supply Chains*, R. Accorsi and R. Manzini, Eds., Academic Press, Cambridge, MA, USA, 2019.

[7] T. Ben Abid, O. Ayadi, and F. Masmoudi, "An integrated production-distribution planning problem under demand and production capacity uncertainties: new formulation and case study," *Mathematical Problems in Engineering*, vol. 2020, Article ID 1520764, 2020.

[8] Y. Ma, F. Yan, K. Kang, and X. Wei, "A novel integrated production-distribution planning model with conflict and coordination in a supply chain network," *Knowledge-Based Systems*, vol. 105, pp. 119–133, 2016.

[9] H. Yan, F. Safaei, and M. Rabbani, "Integrated production-distribution planning problem in a competition-based four-echelon supply chain," *Computers & Industrial Engineering*, vol. 119, pp. 85–99, 2018.

[10] M. Kärkkäinen, "Increasing efficiency in the supply chain for short shelf life goods using RFID tagging," *International Journal of Retail & Distribution Management*, vol. 31, no. 10, pp. 529–536, 2003.

[11] T. M. Whitin, *Theory of Inventory Management*, Princeton University Press, Princeton, NJ, USA, 1957.

[12] L. Janssen, T. Claus, and J. Sauer, "Literature review of deteriorating inventory models by key topics from 2012 to 2015," *International Journal of Production Economics*, vol. 182, pp. 86–112, 2016.

[13] J. Pahl and S. Voß, "Integrating deterioration and lifetime constraints in production and supply chain planning: a survey," *European Journal of Operational Research*, vol. 238, no. 3, pp. 654–674, 2014.

[14] M. Bakker, J. Riezebos, and R. H. Teunter, "Review of inventory systems with deterioration since 2001," *European Journal of Operational Research*, vol. 221, no. 2, pp. 275–284, 2012.

[15] N. Khanlarzade, B. Yousefi Yegane, I. Nakhai Kamalabadi, and H. Farughi, "Inventory control with deteriorating items: a state-of-the-art literature review," *International Journal of Industrial Engineering Computations*, vol. 5, no. 2, pp. 179–198, 2014.

[16] M. Yousefi Yegane and A. Tajbakhsh, "Past, present, and prospective themes of sustainable agricultural supply chains: a content analysis," *Journal of Cleaner Production*, vol. 271, Article ID 122201, 2020.

[17] A. Rong, R. Akkerman, and M. Grunow, "An optimization approach for managing fresh food quality throughout the supply chain," *International Journal of Production Economics*, vol. 131, no. 1, pp. 421–429, 2011.

[18] T. Jia, X. Li, N. Wang, and R. Li, "Integrated inventory routing problem with quality time windows and loading cost for deteriorating items under discrete time," *Mathematical Problems in Engineering*, vol. 2014, Article ID 537409, 2014.

[19] G. Zhang, W. Habenicht, and W. E. Ludwig Spieß, "Improving the structure of deep frozen and chilled food chain with tabu search procedure," *Journal of Food Engineering*, vol. 60, no. 1, pp. 67–79, 2003.

[20] A. Federgruen, G. Prastacos, and P. H. Zipkin, "An allocation and distribution model for perishable products," *Operations Research*, vol. 34, no. 1, pp. 75–82, 1986.

[21] Y. He et al., "Quality and operations management in food supply chains: a literature review," *Journal of Food Quality*, vol. 2018, Article ID 7279491, 14 pages, 2018.

[22] M.-F. Yang and W.-C. Tseng, "Deteriorating inventory model for chilled food," *Mathematical Problems in Engineering*, vol. 2015, Article ID 816876, 2015.

[23] P. Amorim, H.-O. Günther, and B. Almada-Lobo, "Multi-objective integrated production and distribution planning of perishable products," *International Journal of Production Economics*, vol. 138, no. 1, pp. 89–101, 2012.

[24] M. A. F. Belo-Filho, P. Amorim, and B. Almada-Lobo, "An adaptive large neighbourhood search for the operational integrated production and distribution problem of perishable products," *International Journal of Production Research*, vol. 53, no. 20, pp. 6040–6058, 2015.

[25] S. Priyan and R. Uthayakumar, "An integrated production-distribution inventory system for deteriorating products involving fuzzy deterioration and variable setup cost," *Journal of Industrial and Production Engineering*, vol. 31, no. 8, pp. 491–503, 2014.

[26] J. Rezaeian, S. Haghayegh, and I. Mahdavi, "Designing an integrated production/distribution and inventory planning model of fixed-life perishable products," *Journal of Optimization in Industrial Engineering*, vol. 9, no. 19, pp. 47–60, 2016.

[27] F. Manouchehri, A. S. Nookabadi, and M. Kadivar, "Production routing in perishable and quality degradable supply chains," *Heliyon*, vol. 6, no. 2, Article ID e03376, 2020.

[28] F. T. Chan et al., "Multi-objective particle swarm optimisation based integrated production inventory routing planning for efficient perishable food logistics operations," *International Journal of Production Research*, pp. 1–20, 2020.

[29] T. P. Labuza, *Shelf-Life Dating of Foods*, Food & Nutrition Press, Inc., Cambridge, MA, USA, 1982.

[30] S. R. Logan, "The origin and status of the Arrhenius equation," *Journal of Chemical Education*, vol. 59, no. 4, p. 279, 1982.

[31] S. Yousefi, H. Mahmoudzadeh, and M. Jahangoshai Rezaee, "Using supply chain visibility and cost for supplier selection: a mathematical model," *International Journal of Management Science and Engineering Management*, vol. 12, no. 3, pp. 196–205, 2017.

Hindawi
Mathematical Problems in Engineering
Volume 2021, Article ID 5598267, 10 pages
https://doi.org/10.1155/2021/5598267

Research Article

Short-Term Load Forecasting Using Neural Network and Particle Swarm Optimization (PSO) Algorithm

Zahra Shafiei Chafi and Hossein Afrakhte

Department of Electrical Engineering, University of Guilan, Rasht, Iran

Correspondence should be addressed to Zahra Shafiei Chafi; z_shafiei@phd.guilan.ac.ir

Received 29 January 2021; Revised 1 March 2021; Accepted 24 March 2021; Published 14 April 2021

Academic Editor: Noorbakhsh Amiri Golilarz

Electrical load forecasting plays a key role in power system planning and operation procedures. So far, a variety of techniques have been employed for electrical load forecasting. Meanwhile, neural-network-based methods led to fewer prediction errors due to their ability to adapt properly to the consuming load's hidden characteristic. Therefore, these methods were widely accepted by the researchers. As the parameters of the neural network have a significant impact on its performance, in this paper, a short-term electrical load forecasting method using neural network and particle swarm optimization (PSO) algorithm is proposed, in which some neural network parameters including learning rate and number of hidden layers are determined in order to forecast electrical load using the PSO algorithm precisely. Then, the neural network with these optimized parameters is used to predict the short-term electrical load. In this method, a three-layer feedforward neural network trained by backpropagation algorithm is used beside an improved gbest PSO algorithm. Also, the neural network prediction error is defined as the PSO algorithm cost function. The proposed approach has been tested on the Iranian power grid using MATLAB software. The average of three indices beside graphical results has been considered to evaluate the performance of the proposed method. The simulation results reflect the capabilities of the proposed method in accurately predicting the electrical load.

1. Introduction

Load forecasting is an effective and crucial process in the management and operation of power systems which can lead to significant cost savings when accurately calculated. Also, very important decisions are made based on the forecasted load, the economic consequences of which are notable [1].

Load forecasting can be divided into three categories: short-term, mid-term, and long-term forecasting [2]. Due to the vital role of short-term load forecasting in optimizing the unit commitment, turning the thermal units on and off, spinning reserve control, and buying and selling the electricity in interconnected systems, the efforts are majorly concentrated on short-term load forecasting [3]. Appropriate load prediction has always been one of the main challenges for researchers, so that if the predicted load is less than its actual value, the required load will not be supplied, and if it is estimated to be more than the actual amount, it will impose additional costs and cause energy waste.

Due to the great ability in nonlinear relationships modelling between inputs and outputs, artificial neural networks are increasingly used in load forecasting [4–7]. These networks are able to extract the implicit relations between input variables by learning through training data [8]. The first reports of the neural network application in load forecasting were published in the late 1980s and early 1990s and since then their number steadily increased [9].

Optimizing neural network architecture design, including determining the number of input variables, the number of input nodes, and the number of hidden neurons to enhance prediction performance, is an important issue in intelligent systems [10–13]. In recent years, many intelligent methods such as PSO have been proposed to improve artificial neural networks' training and architecture in short-

term electrical load forecasting [8, 14, 15]. The results reflect the capability of these methods compared to the past ones.

Reference [16] proposed a hybrid method that consists of deep neural network and empirical mode decomposition (EMD) technique. The EMD is used to decompose the load time series and deep neural network is used to perform short-term load forecasting. In [17], a new ensemble residual network model is presented. At first, a recurrent neural network similar structure is built and then a modified residual network is applied, where the final outputs are obtained. Reference [18] proposed a deep learning framework based on a combination of a convolutional neural network (CNN) [19] and long short-term memory (LSTM) [20]. The CNN layers are used for feature extraction [21] from the input data and LTSM layers are used for sequence learning. In [22], a multifactorial framework for short-term load forecasting is proposed. At first, the candidate feature set is chosen from the load data. Next, partial mutual information is used to omit the redundant and irrelevant features from the candidate set. Then artificial neural network optimized by genetic algorithm is applied to train this set. Finally, the optimized trained network is used to predict the shot-term load forecasting. Reference [23] investigates the way to apply sequence-to-sequence recurrent neural networks to short-term load forecast. Reference [24] proposes a full wavelet neural network method for short-term load forecasting. Decomposition of the load profile and various features is performed using the full wavelet packet transform model. The neural networks are then trained using these features and the outputs of these trained neural networks are known as the forecasted load. In [25], a data mining and artificial neural network optimized by multiobjective grasshopper and phase space reconstruction method is presented. In [26], a short-term load forecasting approach that can capture variations in building operation regardless of building type and location is proposed. Also, nine different hybrids of recurrent neural networks and clustering methods are explored. In [27], the applications and features of support vector machine method, the random forest regression method, and the LSTM neural network method are discussed and compared. Also, a fusion forecasting approach and a data preprocessing technique are proposed by integrating these methods' advantages. In [28], the past load data is considered as a feature and the time series characteristics of load data simultaneously. In order to forecast the load, an approach named multi-temporal-spatial-scale temporal convolutional network is adopted. Reference [29] presented six clustering techniques involving different combinations of Kalman filtering (KF), wavelet neural network (WNN), and artificial neural network (ANN) schemes. In [30], a hybrid method based on Elman neural network (ENN) and PSO is proposed. Reference [31] proposes a genetic-algorithm-based backpropagation neural network (GABPNN) considering data loss. Also, a particle swarm optimization-supporting vector regression (PSO-SVR) algorithm is further used to integrate the GABPNN results with better accuracy. In addition, a combined ultra-short-term load forecasting model for industrial power users is introduced. Furthermore, the proposed model combines the cubature Kalman filter (CKF) prediction model with good performance in nonlinear dynamic systems and the least square support vector machine (LS-SVM) prediction model with good performance in small-scale data prediction. The grey neural network is used to integrate the two algorithms, which further improves the accuracy of ultra-short-term load forecasting.

The rest of this paper is organized as follows: A brief overview of neural networks and PSO algorithms is presented in Sections 2 and 3. In Section 4, the proposed method is demonstrated and, in Section 5, the methodology applied to predict the load is explained. In Section 6, results are reflected and finally Section 7 is devoted to conclusion.

2. Neural Network

An artificial neural network is derived from the way of information process in human biological systems and consists of an interconnected group of elements called neurons [32–35]. Various architectures are used in neural networks [36–41]. Some of them include feedforward networks and recurrent networks. In the meantime, feedforward neural networks have become more popular. In this type of the network, the input signal from the input layer propagates to the output layers through the hidden layers, where the outputs of one layer will be the inputs of the next layer [32] as depicted in Figure 1. This figure shows a neural network with R input and s output. It has three layers named input layer, hidden layer, and output layer. The output of the input layer is the input of the hidden layer and the output of the hidden layer is the input of the output layer. In most of the presented papers, this architecture has been used in order to perform short-term electrical load forecasting [42].

An artificial neural network with an input layer, one or more hidden layers, and an output layer is called multilayer perceptron network. Each layer consists of several neurons, each of which is connected in a layer to its adjacent layers through some weights. Weight and bias are the two adjustable parameters in neural networks. Tuning the neural networks parameters is done in a process called training algorithm [43]. Neural networks training is accompanied by minimizing a cost function [44–46]. The most well-known training algorithm in neural networks is the backpropagation algorithm in which the mentioned mathematical cost function is the mean of the squared errors. In order to minimize the errors, in backpropagation technique, weights and biases are modified according to the errors returned to the system [32].

3. Particle Swarm Optimization (PSO) Algorithm

Swarm intelligence algorithms are classified to several old-style methods such as ant colony optimizer (ACO) [47, 48], PSO [49], differential evolution (DE) [50, 51], differential search (DS) [52], and some recent methods and their advanced versions such as Harris Hawks Optimizer (HHO) [53–55], slime mould algorithm (SMA) [56], fruit fly optimizer (FFO) [57, 58], moth-flame optimizer (MFO)

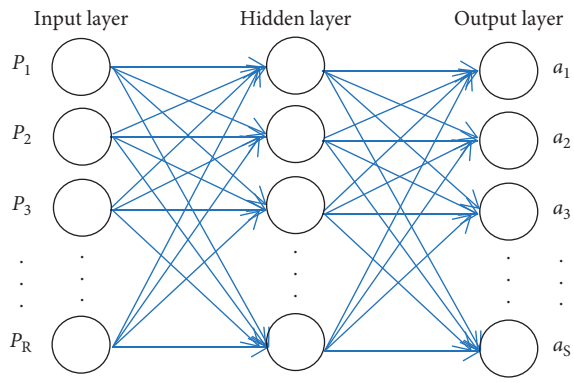

Figure 1: Feedforward neural network with a hidden layer.

[59–61], whale optimization algorithm (WOA) [62–64], grey wolf optimizer (GWO) [65, 66], bacterial foraging optimization (BFO) [67], and grasshopper optimization algorithm (GOA) [68]. The aim of optimization is to determine a suitable value for one or more parameters between all possible values for them in order to minimize or maximize a function and it can be applied to find feasible answer to many potential real-life applications such as deployment optimization [69], adaptive control concepts [35, 70–72], computer vision techniques [73], transportation networks [74], image and video processing [75–80], decision-making approaches [81–83], power allocation systems [84], sensor fusion approaches [85], monitoring systems [86–89], and deep learning models [19, 90–93]. The PSO algorithm as an optimization algorithm is a social interaction model between independent particles that use their social knowledge to find the minimum and maximum value of a function [15]. Kennedy and Eberhart first proposed this algorithm in 1994 [94, 95].

PSO algorithm is an iterative optimization method in which a population is produced for the search process at first called particles. Then these particles travel a multidimension space formed by each particle [96]. There are two parameters, position and velocity, in PSO algorithm, which are updated for each particle and in all considered dimensions [95]. Each particle alters its position according to best position it has ever achieved and the best position achieved by other particles up to now.

Benefits of PSO over other metaheuristic approaches are computational feasibility and effectiveness. PSO shows its uniqueness such as easy implementation and consistency in performance [97]. The main advantage of PSO in comparison to other optimization methods is its ability to accomplish fast convergence in many complicated optimization problems. In addition , PSO has several attractive advantages like simplicity with fewer mathematical equations and having fewer parameters in implementation [98]. PSO has many key features that attracted the attention of many researchers to use it in various applications in which traditional optimization algorithms might fail. We have the following examples:

-Only a fitness function to measure the "quality" of a solution instead of complex mathematical operations like gradient, Hessian, or matrix inversion is required. This reduces the computational complexity and relieves some of the restrictions that are usually imposed on the objective function like differentiability, continuity, or convexity.

(i) As it is a population-based algorithm, it is less sensitive to a good initial solution.

(ii) Easily incorporates with other optimization tools to form hybrid ones.

(iii) It has the ability to escape local minima, since it follows probabilistic transition rules.

More interesting PSO advantages can be emphasized when compared to other members of evolutionary methods like GA, HHO, GWO, and so forth as follows:

(i) Easily programmed and modified with basic mathematical and logic operations.

(ii) Inexpensive in terms of computation time and memory.

(iii) Less parameter tuning is required.

(iv) It works with direct real valued numbers, which omits the need to do binary conversion of classical canonical genetic algorithm [99].

Different PSO algorithms have been known up to now, among which gbest algorithm is more popular. In this approach, the whole population is considered as a unique neighborhood for that particle during the gaining experience process. In order to optimize the search procedure, the best particle shares its coordinates information with other particles [99].

In this algorithm, the ith particle velocity, v_i^{k+1}, is updated according to the following equatio (1) [95, 99]:

$$v_i^{k+1} = wv_i^k + c_1\beta_1\left(p\varphi_i - x_i^k\right) + c_2\beta_2\left(g\varphi_i - x_i^k\right), \tag{1}$$

where β_1 and β_2 are two random numbers between zero and one, x_i^k and v_i^k are the position and velocity of the ith particle in k^{th} iteration, respectively, $g\varphi_i$ is the best position experienced by the whole particles, and $p\varphi_i$ represents the best personal experience of the particle. Also, w is called the inertia constant, which actually considers a percentage of the previous particle velocity in the new velocity calculation. c_1 and c_2 are constants called personal learning factor and social learning factor, respectively.

Updating the particle position is done according to the following equation:

$$x_i^{k+1} = x_i^k + v_i^k, \tag{2}$$

where x_i^{k+1} is the new particle position, x_i^k is the previous particle position, and v_i^k is the new particle velocity obtained according to (1). The velocity and position of each particle are updated according to (1) and (2) until all particles move. Then the next iteration occurs and this procedure continues until finding the best solution [94].

The old types of PSO algorithm had some undesirable dynamic characteristics including velocity restrictions to control the particle path. In this paper, by applying the limitation on factors according to (3) and (4), the possibility of the dynamic characteristic control on the particle swarms

and making a balance between local search and global search is provided [100]. According to (3), the factors related to PSO algorithm are considered as in (4).

$$\rho = \rho_1 + \rho_2 > 4,$$
$$\theta = \frac{2\alpha}{\rho - 2 + \sqrt{\rho^2 - 4\rho}}, \tag{3}$$

$$\begin{aligned} w &= \theta, \\ c_1 &= \rho_1 \theta, \\ c_2 &= \rho_2 \theta, \end{aligned} \tag{4}$$

where ρ_1 and ρ_2 are positive random numbers gained from a unified distribution, where their sum, ρ, should be more than 4, and α has a value between zero and one. Also, θ is known as restriction factor.

4. Proposed Method

In this paper, in order to predict the short-term electrical load, a feedforward neural network trained by backpropagation algorithm has been chosen. This network consists of one hidden layer, and the number of neurons in this layer is considered as the optimization parameter. In designing the neural network architecture, the number of neurons in the hidden layer has an important effect on the network performance, making the precision in choosing them. If the number of these layers is chosen to be low, the network gets in trouble in the training step; and if the number of these layers is chosen to be high, the network will face overfitting. Also, the network learning rate between other parameters of the neural network is considered the other optimization parameter. Suitable values for the two optimization parameters are found, utilizing the improved PSO algorithm introduced in Section 3. This algorithm's parameters are selected in accordance with (3) and (4) to overcome the dynamic problems, involved in traditional PSO algorithm. The resulting error by the neural network for load forecasting is considered the cost function and, as declared before, two variables of the network, the learning rate and the number of hidden layer neurons, are considered the optimization variables for the PSO algorithm. Along with minimizing the neural network error, which leads to minimizing the load forecasting error, the PSO algorithm tries to find the best values for the learning rate and the hidden layer neurons. The neural network with these optimized parameters is then used to predict the load.

The flowchart of the proposed method is reflected in Figure 2. At the beginning, the preprocessed input data are fed into the three-layer backpropagation neural network, where its learning rate and the number of the hidden layer neurons are considered as the optimizing parameters for the PSO algorithm. PSO travels the search space to find the best values for the intended neural network. After simulation, these two parameters are obtained, while the neural network prediction error is minimal. Next, the trained, optimized neural network is used for electrical load forecasting. This network is used to predict load per day and, for each day, three indices that will be introduced in Section 6 are calculated. The total values of these indices for all days for which the load is predicted are obtained by averaging all indices.

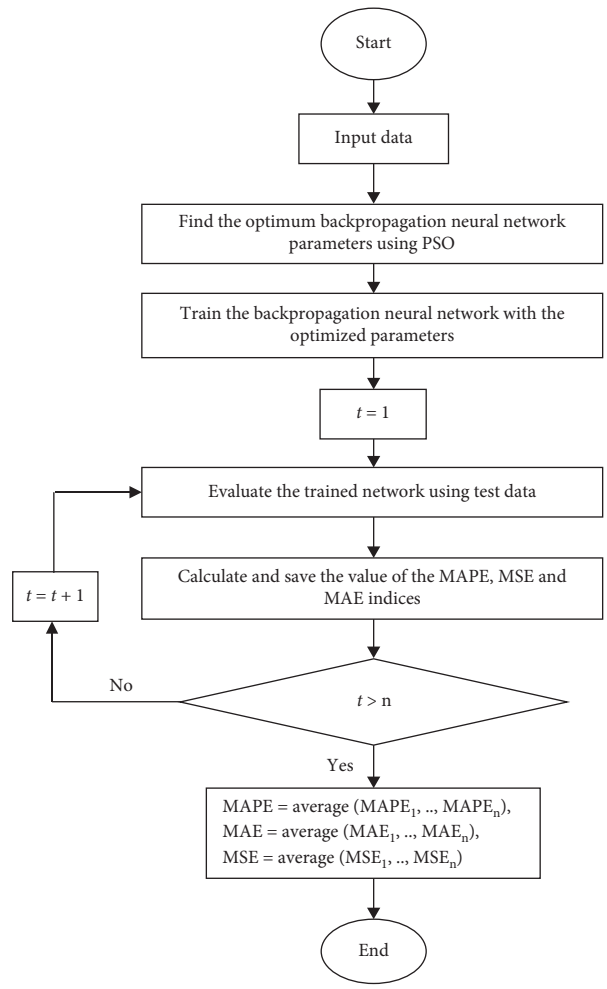

Figure 2: The flowchart of the proposed method (n is the total number of pieces of test data).

5. Methodology

This section provides more details about the proposed method that was presented in the previous section. As stated in Section 4, a neural network with one hidden layer is used to forecast the electrical load. At first, the information of the total hourly daily load consumption of Iran's power grid was extracted from [101] and the data related to its 1093 days (22 March 2010 to 18 March 2013) was selected for study. The simulations are performed in MATLAB software environment.

In order to improve the performance of the neural network and prevent the neurons saturations phenomena, all used data in neural network are normalized using the following formula:

$$\text{normalized data} = \frac{\text{actual amoumt of data}}{\text{Maximum amount of data}}. \quad (5)$$

The first 900 days of 1093 studying days are considered as training data and the remaining 193 are considered neural network test data. The number of neurons in the output layer is 24 and, due to crucial role of the number of the hidden layer neurons, its number is considered as an optimization parameter. The transition function for the output layer and hidden layer is considered tansig and the learning law is considered Levenberg-Marquardt [100, 102]. Also, the network learning rate between other parameters of the neural network is considered the other optimization parameter.

The resulting error by the neural network for load forecasting is considered the cost function and, as declared before, two variables of the network, the learning rate and the number of hidden layer neurons, are considered the optimization variables for the PSO algorithm. The improved type of PSO is considered, the parameters of which are as in (3) and (4). The optimized value of ρ is considered 4.2 and w is considered as 0.729843.

6. Results

This section demonstrates the effectiveness of the proposed method; it has been simulated in MATLAB software. The computing system is a core i5 system with 1.6 GHz CPU and 4 GB memory.

The chosen test data are adopted to evaluate this network's performance, where the results for some days are according to Figure 3 through Figure 4. They show the consumed load according to hour of the day. In each figure, the solid graph is related to the actual load and the dashed graph reflects the result of the prediction. It can be seen that Iran's load is a two-peak load, meaning that it has two peaks. One appears around noon at 3 p.m. and the other appears in the evening at 8 p.m. These Figures (Figures 3, 5, 6, and 7) follow nearly the same load pattern except for Figures 8 and 4, where their first peak appears at a lower level of the power. This pattern is impressed by the day of the week, the special religious ceremony, certain TV program, and so on. In all cases, the maximum prediction error is not more than 1000 MW.

The obtained results apparently show the appropriate performance of the introduced approach.

For more investigation, in order to evaluate the forecasting model, MSE, MAPE, and MAE indices are calculated according to Table 1, where the average results of these calculations for all test data are summarized in Table 2. In Table 1, N is the total number of pieces of the test data, $y_m(i)$ is the ith data actual load value, and $y_p(i)$ is the ith data predicted load value.

Although these results are acceptable and proper, in this paper, only the load historical data is used, whereas using other impressive factors on load behaviour can reduplicate the approach's performance.

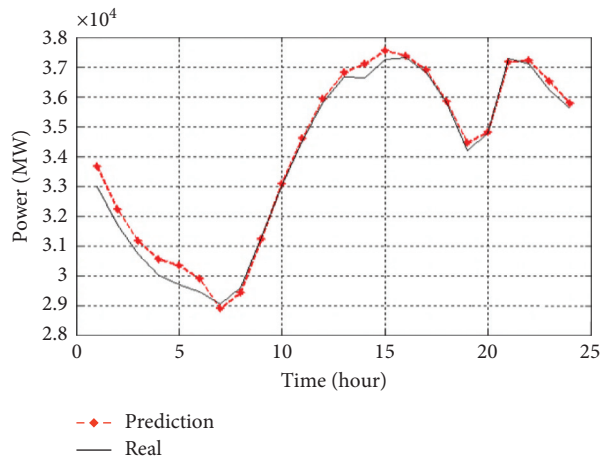

Figure 3: Load forecasting for 7 September 2012.

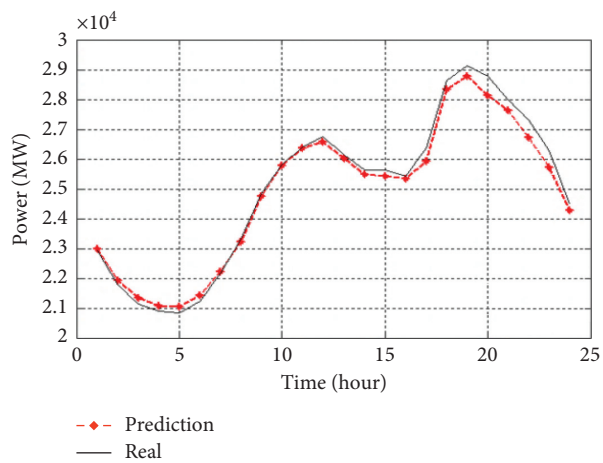

Figure 4: Load forecasting for 24 December 2012.

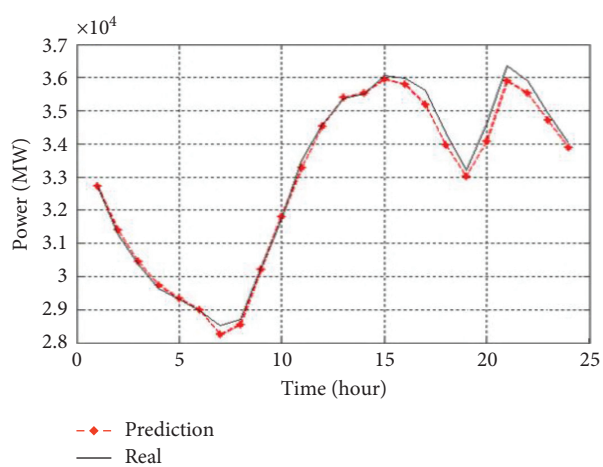

Figure 5: Load forecasting for 17 September 2012.

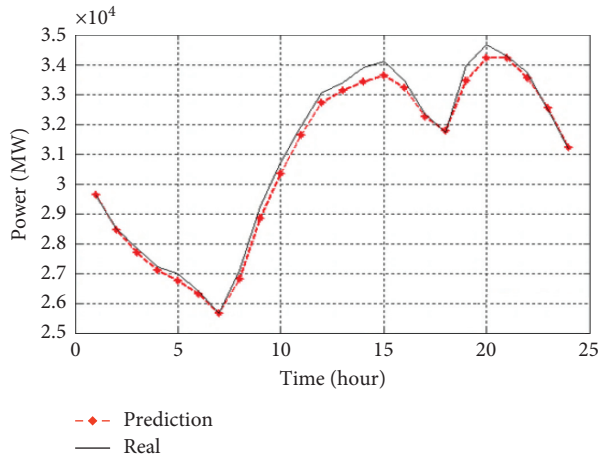

Figure 6: Load forecasting for 26 September 2012.

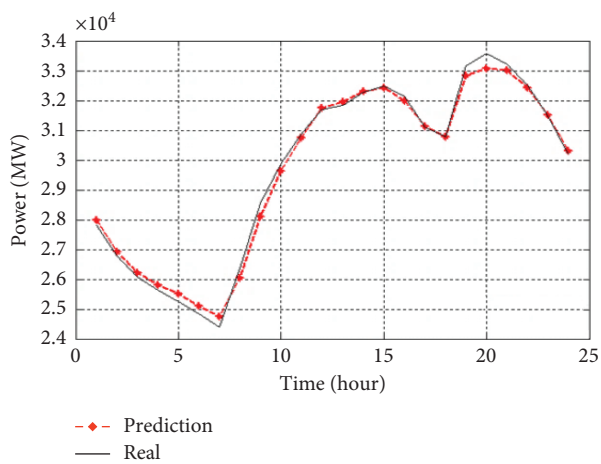

Figure 7: Load forecasting for 1 October 2012.

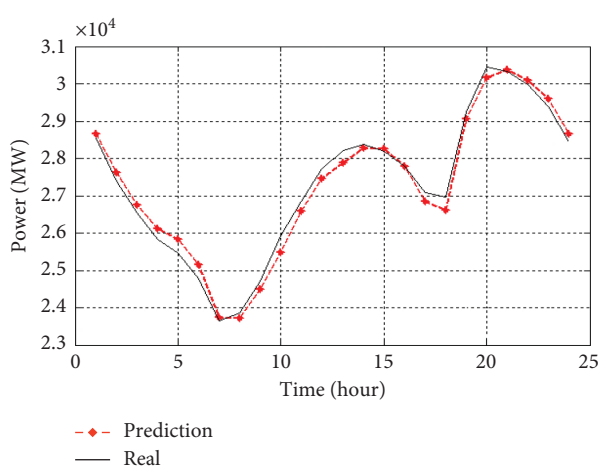

Figure 8: Load forecasting for 30 September 2012.

Table 1: Error indices.

MAPE	$\frac{1}{N}\sum_{i=1}^{N}\left\lvert\frac{y_{m(i)}-y_{p(i)}}{y_{m(i)}}\right\rvert$
MSE	$\frac{1}{N}\sum_{i=1}^{N}\lvert y_{m(i)}-y_{p(i)}\rvert^2$
MAE	$\frac{1}{N}\sum_{i=1}^{N}\lvert y_{m(i)}-y_{p(i)}\rvert$

Table 2: Error calculations results.

MAPE	MSE	MAE
0.03388	$1.26268e-003$	0.02191

7. Conclusions

Electrical load forecasting affected the power system operation and planning processes in a way where the correct operation of the power system depends on precision of this prediction. Also, the power system's behaviour, especially its generation units in small or large scale, is affected by this prediction and its deviation from the actual value can impose additional costs to the system. Numerous load forecasting methods have been proposed up to now, where neural-network-based methods are one of them. Due to the nonlinear relationship between load pattern changes and effective parameters on it and complex relations between load pattern changes and these parameters and neural networks' ability to discover them, researchers have accepted them more than other methods. Meanwhile, numerical to neural network parameters have an obvious effect on their performance. So, exploiting algorithms such as PSO algorithm can be helped. This paper proposes an approach for electrical load forecasting using PSO algorithm and neural network with backpropagation algorithm. At first, the PSO algorithm is used to tune some neural network parameters to access the optimized and appropriate model. Then, the neural network with obtained optimized parameters is used for short-term electrical load forecasting. The simulation results indicate the precision and power of the proposed method in short-term electrical load forecasting. For future directions, we will develop a model according to the deep learning techniques [103, 104] and fuzzy logic [105, 106]. Also, more parameters can be used for load forecasting beside the load information like the temperature, the humidity, and so forth in order to improve the prediction accuracy.

Data Availability

The data used to support the findings of this study are included within the article.

Conflicts of Interest

The authors declare that there are no conflicts of interest regarding the publication of this paper.

References

[1] J. Wang, S. Zhu, W. Zhang, and H. Lu, "Combined modeling for electric load forecasting with adaptive particle swarm optimization," *Energy*, vol. 35, no. 4, pp. 1671–1678, 2010.

[2] C.-N. Ko and C.-M. Lee, "Short-term load forecasting using SVR (support vector regression)-based radial basis function neural network with dual extended Kalman filter," *Energy*, vol. 49, pp. 413–422, 2013.

[3] N. Kandil, R. Wamkeue, M. Saad, and S. Georges, "An efficient approach for short term load forecasting using artificial neural networks," *International Journal of Electrical Power and Energy Systems*, vol. 28, no. 8, pp. 525–530, 2006.

[4] Q. Zhang, Y. Ma, G. Li, J. Ma, and J. Ding, "Short-term load forecasting based on frequency domain decomposition and deep learning," *Mathematical Problems in Engineering*, vol. 2020, Article ID 7240320, 9 pages, 2020.

[5] J. Huang, Y. Tang, and S. Chen, "Energy demand forecasting: combining cointegration analysis and artificial intelligence algorithm," *Mathematical Problems in Engineering*, vol. 2018, Article ID 5194810, 13 pages, 2018.

[6] S. Zheng, Q. Zhong, L. Peng, and X. Chai, "A simple method of residential electricity load forecasting by improved Bayesian neural networks," *Mathematical Problems in Engineering*, vol. 2018, Article ID 4276176, 16 pages, 2018.

[7] L. Wu, C. Kong, X. Hao, and W. Chen, "A short-term load forecasting method based on GRU-CNN hybrid neural network model," *Mathematical Problems in Engineering*, vol. 2020, Article ID 1428104, 9 pages, 2020.

[8] H. Shayeghi, H. Shayanfar, and G. Azimi, "A hybrid particle swarm optimization back propagation algorithm for short term load forecasting," *International Journal on, Technical and Physical Problems (IJTPE)*, vol. 4, no. 2, pp. 12–22, 2010.

[9] H. S. Hippert, C. E. Pedreira, and R. C. Souza, "Neural networks for short-term load forecasting: a review and evaluation," *IEEE Transactions on Power Systems*, vol. 16, no. 1, pp. 44–55, 2001.

[10] H.-L. Chen, G. Wang, C. Ma, Z.-N. Cai, W.-B. Liu, and S.-J. Wang, "An efficient hybrid kernel extreme learning machine approach for early diagnosis of Parkinson′s disease," *Neurocomputing*, vol. 184, pp. 131–144, 2016.

[11] L. Hu, G. Hong, J. Ma, X. Wang, and H. Chen, "An efficient machine learning approach for diagnosis of paraquat-poisoned patients," *Computers in Biology and Medicine*, vol. 59, pp. 116–124, 2015.

[12] J. Xia, H. Chen, Q. Li et al., "Ultrasound-based differentiation of malignant and benign thyroid Nodules: an extreme learning machine approach," *Computer Methods and Programs in Biomedicine*, vol. 147, pp. 37–49, 2017.

[13] C. Li, L. Hou, B. Y. Sharma et al., "Developing a new intelligent system for the diagnosis of tuberculous pleural effusion," *Computer Methods and Programs in Biomedicine*, vol. 153, pp. 211–225, 2018.

[14] X. Zheng, X. Ran, and M. Cai, "Short-term load forecasting of power system based on neural network intelligent algorithm," *IEEE Access,* 1 page, 2020.

[15] Y. K. Semero, J. Zhang, and D. Zheng, "EMD–PSO–ANFIS-based hybrid approach for short-term load forecasting in microgrids," *IET Generation, Transmission and Distribution*, vol. 14, no. 3, pp. 470–475, 2019.

[16] Z. Kong, C. Zhang, H. Lv, F. Xiong, and Z. Fu, "Multimodal feature extraction and fusion deep neural networks for short-term load forecasting," *IEEE Access*, vol. 8, pp. 185373–185383, 2020.

[17] Q. Xu, X. Yang, and X. Huang, "Ensemble residual networks for short-term load forecasting," *IEEE Access*, vol. 8, pp. 64750–64759, 2020.

[18] M. Alhussein, K. Aurangzeb, and S. I. Haider, "Hybrid CNN-LSTM model for short-term individual household load forecasting," *IEEE Access*, vol. 8, pp. 180544–180557, 2020.

[19] H. Chen, A. Chen, L. Xu et al., "A deep learning CNN architecture applied in smart near-infrared analysis of water pollution for agricultural irrigation resources," *Agricultural Water Management*, vol. 240, Article ID 106303, 2020.

[20] B. Wang, L. Zhang, H. Ma, H. Wang, and S. Wan, "Parallel LSTM-based regional integrated energy system multienergy source-load information interactive energy prediction," *Complexity*, vol. 2019, Article ID 7414318, 13 pages, 2019.

[21] J. Zhang and B. Liu, "A review on the recent developments of sequence-based protein feature extraction methods," *Current Bioinformatics*, vol. 14, no. 3, pp. 190–199, 2019.

[22] Y. Gao, Y. Fang, H. Dong, and Y. Kong, "A multifactorial framework for short-term load forecasting system as well as the jinan's case study," *IEEE Access*, vol. 8, pp. 203086–203096, 2020.

[23] E. Skomski, J.-Y. Lee, W. Kim, V. Chandan, S. Katipamula, and B. Hutchinson, "Sequence-to-sequence neural networks for short-term electrical load forecasting in commercial office buildings," *Energy and Buildings*, vol. 226, Article ID 110350, 2020.

[24] M. El-Hendawi and Z. Wang, "An ensemble method of full wavelet packet transform and neural network for short term electrical load forecasting," *Electric Power Systems Research*, vol. 182, Article ID 106265, 2020.

[25] C. Li, "Designing a short-term load forecasting model in the urban smart grid system," *Applied Energy*, vol. 266, Article ID 114850, 2020.

[26] G. Chitalia, M. Pipattanasomporn, V. Garg, and S. Rahman, "Robust short-term electrical load forecasting framework for commercial buildings using deep recurrent neural networks," *Applied Energy*, vol. 278, Article ID 115410, 2020.

[27] W. Guo, L. Che, M. Shahidehpour, and X. Wan, "Machine-Learning based methods in short-term load forecasting," *The Electricity Journal*, vol. 34, no. 1, Article ID 106884, 2021.

[28] L. Yin and J. Xie, "Multi-temporal-spatial-scale temporal convolution network for short-term load forecasting of power systems," *Applied Energy*, vol. 283, Article ID 116328, 2020.

[29] H. H. H. Aly, "A proposed intelligent short-term load forecasting hybrid models of ANN, WNN and KF based on clustering techniques for smart grid," *Electric Power Systems Research*, vol. 182, Article ID 106191, 2020.

[30] K. Xie, H. Yi, G. Hu, L. Li, and Z. Fan, "Short-term power load forecasting based on Elman neural network with particle swarm optimization," *Neurocomputing*, vol. 416, pp. 136–142, 2020.

[31] H. Jiang, A. Wu, B. Wang, P. Xu, and G. Yao, "Industrial ultra-short-term load forecasting with data completion," *IEEE Access*, vol. 8, pp. 158928–158940, 2020.

[32] E. Banda and K. A. Folly, "Short term load forecasting based on hybrid ANN and PSO," in *Proceedings of the International Conference in Swarm Intelligence*, pp. 98–106, Springer, Beijing, China, June 2015.

[33] L. Ding, S. Li, H. Gao, C. Chen, and Z. Deng, "Adaptive partial reinforcement learning neural network-based tracking control for wheeled mobile robotic systems," *IEEE Transactions on Systems, Man, and Cybernetics: Systems*, vol. 50, no. 7, pp. 2512–2523, 2018.

[34] S. Wang, Y. Zhao, J. Li et al., "Neurostructural correlates of hope: dispositional hope mediates the impact of the SMA gray matter volume on subjective well-being in late adolescence," *Social Cognitive and Affective Neuroscience*, vol. 15, no. 4, pp. 395–404, 2020.

[35] J. Wang, P. Zhu, B. He, G. Deng, C. Zhang, and X. Huang, "An adaptive neural sliding mode control with ESO for uncertain nonlinear systems," *International Journal of Control, Automation and Systems*, pp. 1–11, 2020.

[36] X. Zhang, J. Wang, T. Wang, R. Jiang, J. Xu, and L. Zhao, "Robust feature learning for adversarial defense via hierarchical feature alignment," *Information Sciences*, vol. 560, pp. 256–270, 2020.

[37] X. Zhang, T. Wang, W. Luo, and P. Huang, "Multi-level fusion and attention-guided CNN for image dehazing," *IEEE Transactions on Circuits and Systems for Video Technology*, p. 1, 2020.

[38] X. Zhang, M. Fan, D. Wang, P. Zhou, and D. Tao, "Top-k feature selection framework using robust 0-1 integer programming," *IEEE Transactions on Neural Networks and Learning Systems*, pp. 1–15, 2020.

[39] X. Zhang, D. Wang, Z. Zhou, and Y. Ma, "Robust low-rank tensor recovery with rectification and alignment," *IEEE Transactions on Pattern Analysis and Machine Intelligence*, vol. 43, no. 1, pp. 238–255, 2019.

[40] X. Zhang, R. Jiang, T. Wang, and J. Wang, "Recursive neural network for video deblurring," *IEEE Transactions on Circuits and Systems for Video Technology*, p. 1, 2020.

[41] X. Zhang, T. Wang, J. Wang, G. Tang, and L. Zhao, "Pyramid channel-based feature attention network for image dehazing," *Computer Vision and Image Understanding*, vol. 197-198, Article ID 103003.

[42] R. ZhiChao, Y. Qiang, W. Haiyan, C. Chao, and L. Yuan, "Power load forecasting in the spring festival based on feedforward neural network model," in *Proceedings of the 2017 3rd IEEE International Conference on Computer and Communications (ICCC)*, pp. 2855–2858, IEEE, Chengdu, China, December 2017.

[43] M. Hagan, H. Demuth, M. Beale, and O. De Jesús, *Neural Network Design*, Vol. 20, Pws Pub, Boston, MA, USA, 1996.

[44] A. Baliyan, K. Gaurav, and S. K. Mishra, "A review of short term load forecasting using artificial neural network models," *Procedia Computer Science*, vol. 48, pp. 121–125, 2015.

[45] X.-F. Wang, P. Gao, Y.-F. Liu, H.-F. Li, and F. Lu, "Predicting thermophilic proteins by machine learning," *Current Bioinformatics*, vol. 15, no. 5, pp. 493–502, 2020.

[46] L. Ding, S. Li, H. Gao, Y.-J. Liu, L. Huang, and Z. Deng, "Adaptive neural network-based finite-time online optimal tracking control of the nonlinear system with dead zone," *IEEE Transactions on Cybernetics*, vol. 51, no. 1, pp. 382–392, 2021.

[47] X. Zhao, D. Li, B. Yang, C. Ma, Y. Zhu, and H. Chen, "Feature selection based on improved ant colony optimization for online detection of foreign fiber in cotton," *Applied Soft Computing*, vol. 24, pp. 585–596, 2014.

[48] D. Zhao, "Chaotic random spare ant colony optimization for multi-threshold image segmentation of 2D Kapur entropy," *Knowledge-Based Systems*, Article ID 106510, 2020.

[49] B. Bai, Z. Guo, C. Zhou, W. Zhang, and J. Zhang, "Application of adaptive reliability importance sampling-based extended domain PSO on single mode failure in reliability engineering," *Information Sciences*, vol. 546, pp. 42–59, 2021.

[50] G. Sun, C. Li, and L. Deng, "An adaptive regeneration framework based on search space adjustment for differential evolution," *Neural Computing and Applications*, pp. 1–17, 2021.

[51] G. Sun, B. Yang, Z. Yang, and G. Xu, "An adaptive differential evolution with combined strategy for global numerical optimization," *Soft Computing*, pp. 1–20, 2019.
[52] J. Liu, C. Wu, G. Wu, and X. Wang, "A novel differential search algorithm and applications for structure design," *Applied Mathematics and Computation*, vol. 268, pp. 246–269, 2015.
[53] Y. Zhang, R. Liu, X. Wang, H. Chen, and C. Li, "Boosted binary Harris hawks optimizer and feature selection," *Engineering with Computers*, pp. 1–30, 2020.
[54] H. Chen, A. A. Heidari, H. Chen, M. Wang, Z. Pan, and A. H. Gandomi, "Multi-population differential evolution-assisted Harris hawks optimization: framework and case studies," *Future Generation Computer Systems*, vol. 111, pp. 175–198, 2020.
[55] N. A. Golilarz, H. Gao, and H. Demirel, "Satellite image denoising with Harris hawks meta heuristic optimization algorithm and improved adaptive generalized Gaussian distribution threshold function," *IEEE Access*, vol. 7, pp. 57459–57468, 2019.
[56] Y. Zhang, "Towards augmented kernel extreme learning models for bankruptcy prediction: algorithmic behavior and comprehensive analysis," *Neurocomputing*, vol. 430, pp. 185–212, 2020.
[57] H. Yu, "Dynamic Gaussian bare-bones fruit fly optimizers with abandonment mechanism: method and analysis," *Engineering with Computers*, pp. 1–29, 2020.
[58] L. Shen, H. Chen, Z. Yu et al., "Evolving support vector machines using fruit fly optimization for medical data classification," *Knowledge-Based Systems*, vol. 96, pp. 61–75, 2016.
[59] W. Shan, Z. Qiao, A. A. Heidari, H. Chen, H. Turabieh, and Y. Teng, "Double adaptive weights for stabilization of moth flame optimizer: balance analysis, engineering cases, and medical diagnosis," *Knowledge-Based Systems*, vol. 214, Article ID 106728, 2020.
[60] Y. Xu, H. Chen, J. Luo, Q. Zhang, S. Jiao, and X. Zhang, "Enhanced Moth-flame optimizer with mutation strategy for global optimization," *Information Sciences*, vol. 492, pp. 181–203, 2019.
[61] M. Wang, H. Chen, B. Yang et al., "Toward an optimal kernel extreme learning machine using a chaotic moth-flame optimization strategy with applications in medical diagnoses," *Neurocomputing*, vol. 267, pp. 69–84, 2017.
[62] J. Tu, H. Chen, J. Liu et al., "Evolutionary biogeography-based whale optimization methods with communication structure: towards measuring the balance," *Knowledge-Based Systems*, vol. 212, Article ID 106642, 2021.
[63] M. Wang and H. Chen, "Chaotic multi-swarm whale optimizer boosted support vector machine for medical diagnosis," *Applied Soft Computing Journal*, vol. 88, Article ID 105946, 2020.
[64] Y. Cao, Y. Li, G. Zhang, K. Jermsittiparsert, and M. Nasseri, "An efficient terminal voltage control for PEMFC based on an improved version of whale optimization algorithm," *Energy Reports*, vol. 6, pp. 530–542, 2020.
[65] J. Hu, H. Chen, A. A. Heidari et al., "Orthogonal learning covariance matrix for defects of grey wolf optimizer: insights, balance, diversity, and feature selection," *Knowledge-Based Systems*, vol. 213, Article ID 106684, 2021.
[66] X. Zhao, X. Zhang, Z. Cai et al., "Chaos enhanced grey wolf optimization wrapped ELM for diagnosis of paraquat-poisoned patients," *Computational Biology and Chemistry*, vol. 78, pp. 481–490, 2019.
[67] X. Xu and H.-L. Chen, "Adaptive computational chemotaxis based on field in bacterial foraging optimization," *Soft Computing*, vol. 18, no. 4, pp. 797–807, 2014.
[68] C. Yu, "SGOA: annealing-behaved grasshopper optimizer for global tasks," *Engineering with Computers*, pp. 1–28, 2021.
[69] B. Cao, J. Zhao, Y. Gu, S. Fan, and P. Yang, "Security-aware industrial wireless sensor network deployment optimization," *IEEE Transactions on Industrial Informatics*, vol. 16, no. 8, pp. 5309–5316, 2019.
[70] Z. Chen, J. Wang, K. Ma, X. Huang, and T. Wang, "Fuzzy adaptive two-bits-triggered control for nonlinear uncertain system with input saturation and output constraint," *International Journal of Adaptive Control and Signal Processing*, vol. 34, no. 4, pp. 543–559, 2020.
[71] J. Wang, Y. Huang, T. Wang, C. Zhang, and Y. h. Liu, "Fuzzy finite-time stable compensation control for a building structural vibration system with actuator failures," *Applied Soft Computing*, vol. 93, Article ID 106372, 2020.
[72] Y. Huang, J. Wang, F. Wang, and B. He, "Event-triggered adaptive finite-time tracking control for full state constraints nonlinear systems with parameter uncertainties and given transient performance," *ISA Transactions*, vol. 108, pp. 131–143, 2021.
[73] S. Xu, J. Wang, W. Shou, T. Ngo, A. Sadick, and X. Wang, "Computer vision techniques in construction: a critical review," *Archives of Computational Methods in Engineering*, 2020.
[74] C. Wu, P. Wu, J. Wang, R. Jiang, M. Chen, and X. Wang, "Ontological knowledge base for concrete bridge rehabilitation project management," *Automation in Construction*, vol. 121, Article ID 103428, 2021.
[75] Q. Zhu, "Research on road traffic situation awareness system based on image big data," *IEEE Intelligent Systems*, vol. 35, no. 1, pp. 18–26, 2019.
[76] Q. Jiang, F. Shao, W. Gao, Z. Chen, G. Jiang, and Y.-S. Ho, "Unified no-reference quality assessment of singly and multiply distorted stereoscopic images," *IEEE Transactions on Image Processing*, vol. 28, no. 4, pp. 1866–1881, 2018.
[77] M. Xu, C. Li, S. Zhang, and P. L. Callet, "State-of-the-Art in 360° video/image processing: perception, assessment and compression," *IEEE Journal of Selected Topics in Signal Processing*, vol. 14, no. 1, pp. 5–26, 2020.
[78] M. Yang and A. Sowmya, "An underwater color image quality evaluation metric," *IEEE Transactions on Image Processing*, vol. 24, no. 12, pp. 6062–6071, 2015.
[79] B. Wang, B. Zhang, and X. Liu, "An image encryption approach on the basis of a time delay chaotic system," *Optik*, vol. 225, Article ID 165737, 2020.
[80] S. Hinojosa, D. Oliva, E. Cuevas, G. Pajares, D. Zaldivar, and M. Pérez-Cisneros, "Reducing overlapped pixels: a multi-objective color thresholding approach," *Soft Computing*, vol. 24, no. 9, pp. 6787–6807, 2020.
[81] C. Wu, P. Wu, J. Wang, R. Jiang, M. Chen, and X. Wang, "Critical review of data-driven decision-making in bridge operation and maintenance," *Structure and Infrastructure Engineering*, pp. 1–24, 2020.
[82] S. Liu, W. Yu, F. T. S. Chan, and B. Niu, "A variable weight-based hybrid approach for multi-attribute group decision making under interval-valued intuitionistic fuzzy sets," *International Journal of Intelligent Systems*, vol. 36, pp. 1015–1052, 2021.
[83] S. Liu, F. T. S. Chan, and W. Ran, "Decision making for the selection of cloud vendor: an improved approach under group decision-making with integrated weights and

objective/subjective attributes," *Expert Systems with Applications*, vol. 55, pp. 37–47, 2016.

[84] J. Yan, W. Pu, S. Zhou, H. Liu, and Z. Bao, "Collaborative detection and power allocation framework for target tracking in multiple radar system," *Information Fusion*, vol. 55, pp. 173–183, 2020.

[85] J.-W. Hu, B.-Y. Zheng, C. Wang et al., "A survey on multi-sensor fusion based obstacle detection for intelligent ground vehicles in off-road environments," *Frontiers of Information Technology & Electronic Engineering*, vol. 21, no. 5, pp. 675–692, 2020.

[86] C. Li, L. Sun, Z. Xu, X. Wu, T. Liang, and W. Shi, "Experimental investigation and error analysis of high precision FBG displacement sensor for structural health monitoring," *International Journal of Structural Stability and Dynamics*, vol. 20, Article ID 2040011, 2020.

[87] L. Sun, C. Li, C. Zhang, T. Liang, and Z. Zhao, "The strain transfer mechanism of fiber bragg grating sensor for extra large strain monitoring," *Sensors*, vol. 19, no. 8, p. 1851, 2019.

[88] C. Zhang, Z. Alam, L. Sun, Z. Su, and B. Samali, "Fibre Bragg grating sensor-based damage response monitoring of an asymmetric reinforced concrete shear wall structure subjected to progressive seismic loads," *Structural Control and Health Monitoring*, vol. 26, no. 3, Article ID e2307, 2019.

[89] L. Sun, C. Li, C. Zhang, Z. Su, and C. Chen, "Early monitoring of rebar corrosion evolution based on FBG sensor," *International Journal of Structural Stability and Dynamics*, vol. 18, no. 8, Article ID 1840001, 2018.

[90] T. Qiu, X. Shi, J. Wang et al., "Deep learning: a rapid and efficient route to automatic metasurface design," *Advanced Science*, vol. 6, no. 12, Article ID 1900128, 2019.

[91] T. Li, M. Xu, C. Zhu, R. Yang, Z. Wang, and Z. Guan, "A deep learning approach for multi-frame in-loop filter of HEVC," *IEEE Transactions on Image Processing*, vol. 28, no. 11, pp. 5663–5678, 2019.

[92] J. Qian, S. Feng, Y. Li et al., "Single-shot absolute 3D shape measurement with deep-learning-based color fringe projection profilometry," *Optics Letters*, vol. 45, no. 7, pp. 1842–1845, 2020.

[93] J. Qian, "Deep-learning-enabled geometric constraints and phase unwrapping for single-shot absolute 3d shape measurement," *APL Photonics*, vol. 5, no. 4, Article ID 046105, 2020.

[94] R. Eberhart and J. Kennedy, "A new optimizer using particle swarm theory." in *Proceedings of the Sixth International Symposium on Micro Machine and Human Science MHS'95*, pp. 39–43, Nagoya, Japan, 1995.

[95] S. Mishra and S. K. Patra, "Short term load forecasting using neural network trained with genetic algorithm & particle swarm optimization," in *Proceedings of the 2008 First International Conference on Emerging Trends in Engineering and Technology*, pp. 606–611, IEEE, Nagpur, India, July 2008.

[96] S. Quaiyum, Y. I. Khan, S. Rahman, and P. Barman, "Artificial neural network based short term load forecasting of power system," *International Journal of Computer Applications*, vol. 30, no. 4, pp. 1–7, 2011.

[97] J. Joy, S. Rajeev, and V. Narayanan, "Particle swarm optimization for resource constrained-project scheduling problem with varying resource levels," *Procedia Technology*, vol. 25, pp. 948–954, 2016.

[98] W. Ali and S. Malebary, "Particle swarm optimization-based feature weighting for improving intelligent phishing website detection," *IEEE Access*, vol. 8, pp. 116766–116780, 2020.

[99] M. R. AlRashidi and K. M. El-Naggar, "Long term electric load forecasting based on particle swarm optimization," *Applied Energy*, vol. 87, no. 1, pp. 320–326, 2010.

[100] M. Clerc and J. Kennedy, "The particle swarm - explosion, stability, and convergence in a multidimensional complex space," *IEEE Transactions on Evolutionary Computation*, vol. 6, no. 1, pp. 58–73, 2002.

[101] Available: http://www.IGMC.ir/Power-grid-status-report.

[102] M. T. Hagan and M. B. Menhaj, "Training feedforward networks with the Marquardt algorithm," *IEEE Transactions on Neural Networks*, vol. 5, no. 6, pp. 989–993, 1994.

[103] Z. Lv and L. Qiao, "Deep belief network and linear perceptron based cognitive computing for collaborative robots," *Applied Soft Computing*, Article ID 106300, 2020.

[104] H. Zhang, Z. Qiu, J. Cao, M. Abdel-Aty, and L. Xiong, "Event-Triggered synchronization for neutral-type semi-markovian neural networks with partial mode-dependent time-varying delays," *IEEE Transactions on Neural Networks and Learning Systems*, vol. 31, no. 11, pp. 4437–4450, 2020.

[105] B. Wang and L. Chen, "New results on the control for a kind of uncertain chaotic systems based on fuzzy logic," *Complexity*, vol. 2019, Article ID 8789438, 8 pages, 2019.

[106] H. Chen, H. Qiao, L. Xu, Q. Feng, and K. Cai, "A fuzzy optimization strategy for the implementation of RBF LSSVR model in vis-NIR analysis of pomelo maturity," *IEEE Transactions on Industrial Informatics*, vol. 15, no. 11, pp. 5971–5979, 2019.

Hindawi
Mathematical Problems in Engineering
Volume 2021, Article ID 5559475, 13 pages
https://doi.org/10.1155/2021/5559475

Research Article

Reliability Analysis of Dynamic Fault Tree Based on Binary Decision Diagrams for Explosive Vehicle

Guang-Jun Jiang,[1,2] Zong-Yuan Li,[1] Guan Qiao,[1,2] Hong-Xia Chen,[1,2] Hai-Bin Li,[1] and Hong-Hua Sun[1,2]

[1]*School of Mechanical Engineering, Inner Mongolia University of Technology, Hohhot 010051, Inner Mongolia, China*
[2]*Inner Mongolia Key Laboratory of Advanced Manufacturing Technology, Hohhot 010051, Inner Mongolia, China*

Correspondence should be addressed to Guan Qiao; qiaoguan@imut.edu.cn

Received 26 February 2021; Revised 24 March 2021; Accepted 29 March 2021; Published 10 April 2021

Academic Editor: Mohammad Yazdi

Dynamic fault tree is often used to analyze system reliability. The Markov model is a commonly used method, which can accurately reflect the relationship between the state transition process and the dynamic logic gate transfer in the dynamic fault tree. When the complexity or scale of system is increasing, the Markov model encountered a problem of state space explosion leading to increase troubles. To solve the above problems, a modular approach is needed. Based on the modular approach, a hybrid fault module was researched in this paper. Firstly, the stackable fault subtree containing complex static/dynamic logic gate is transformed into four common combinational logic gates through preprocessing of the dynamic gate in the module. Then, the complexity of the model was reduced by incorporating four common combinational logic gates and using the binary decision graph to solve variable ordering in the calculation of failure probability of static subtree. Moreover, the calculating process of complex mixed logic gate fault tree can be simplified. An example of the ammonium nitrate/fuel explosive production system for BCZH-15 explosive vehicle was used to verify the feasibility of the presented method.

1. Introduction

Fault tree analysis (FTA) is a common method for the reliability modeling and evaluating large safety-critical systems as discussed in [1, 2]. The classic fault tree is a static tool, and its primary objective is to improve the safety for the probabilistic safety assessment as discussed in [3, 4]. Dynamic fault tree is an extension of common fault tree, which adds many special logic gates to express the existing problems in specific systems. Mi et al. [5] studied system action of mechatronics systems through taking the advantages of the dynamic fault tree (DFT). Fault tree analysis is a risk assessment method widely used in the process industry. Yazdi et al. [6–8] improved the traditional fault tree analysis, mainly for the study of uncertainty handling in qualitative and quantitative risk assessment procedures. The Markov model is appropriate for modeling complex systems that have traits of timing, sequencing, repair, redundancy, and fault tolerance as discussed by Ericson [9]. However, the Markov model becomes unwieldy as the system size increases. It is difficult to construct and solve Markov models for the large systems as discussed in [10–12]. Li [13] used the Bayesian network method to avoid dealing with Markov state explosion problem. Li et al. [14–16] used multiple methods such as multisource information fusion and Bayesian networks in the process of studying the reliability of offshore wind turbines. Dugan et al. [17–19] utilized dynamic gates to discern independent dynamic subtrees and used the different Markov model for each subtree through the process of modularization. As discussed by Jiang et al. [20], in solving the problem of reliability analysis and analysis of dynamic systems, fuzzy set theory is used. Huang et al. [21] proposed an improved decomposition scheme, where the dynamic subtree can be further modularized (if there exist some independent subtrees). A huge fault tree may contain dynamic subtrees and static subtrees. Use the

binary decision diagram (BDD) method to calculate the failure rate of the top event of the fault tree. BDD was applied to efficiently realize synthesis of reversible functions as discussed by Mathias Soeken et al. [22]. The modularization for large fault trees before analysis can improve computational efficiency. The approach of dynamic innovative fault tree (DIF tree) as discussed in [23] exploited the modularization by combining static and dynamic analysis. Ge et al. [24] analyzed DFT using improved the sequential binary decision diagram (SBDD) method. Bandyopadhyay et al. [25] improved a design technique, where BDDs are used to construct optical circuits.

However, after the modularization, the applicability of the model should be considered for relatively complex systems. Zhang et al. [26] proposed a generalized dynamic reliability model to calculate reliability of system under complex load. In dynamic systems, the semi-Markov process (SMP) was applied to solve the problem that the lifetime of components follows nonexponential distributions as discussed by Li et al. [27]. Abimbola et al. [28] presented a risk assessment methodology for analyzing the safety of critical components based on BN as discussed in [28]. This paper studies how to use modular methods to solve system reliability problems.

In recent years, the focus on field mixed explosive vehicle research has been performed to improve or design new electrical control systems to enhance the safety of equipment; to study the advantages of equipment in special geographic locations; to improve the blasting efficiency by changing the composition of the mixed explosive. There are only a few literatures on the reliability of the equipment, and only the reliability of the equipment can meet the operating requirements and can the safety, superiority, and efficiency of the equipment be demonstrated. With the dynamic characteristics becoming more and more obvious, it is urgent to evaluate equipment reliability considering the dynamic characteristics.

The remainder of the paper is organized as follows: Section 2 introduces division method of fault tree modular and illustrates how to preprocess the dynamic fault tree's logical gates. Section 3 investigates the static subtree BDD theory solution method. The dynamic fault tree Markov theory solution method is described in Section 4. The proposed method was applied to calculate the reliability of the explosive production system for the BCZH-15 explosive vehicle in Section 5. Finally, the conclusion of the article is presented.

2. Fault Tree Modular Analysis Method

2.1. Modular Division for Fault Tree. Rauzy et al. [29] presented the fault tree depth traversal method, which can modularize the fault tree. This method is concise and highly effective to deal with fault tree modularization problem. The deep traversal node method is used to divide module for the fault tree, which is easy to discover modules and zone. The procedure is as follows:

(1) Calculate the traverse node for the fault tree and list the results

(2) Sort the root node, leaf nodes, and the intermediate nodes and perform depth-first leftmost traversal for them

(3) Collect the information of the internal event V for the third traversal node and collect the first and the last period of each subtime to provide strong evidence for modularizing the event.

Module division for the fault tree is shown in Figure 1, and the results are shown in Tables 1 and 2.

In Table 1, S indicates that the fault tree executes the left traversal node rule and then passes through the number of the node in turn, and V represents the name of each node in the fault tree. The sequence is given in Table 1.

Table 1 can summarize the target node numbers that each module can reach after executing the leftmost traversal node method, and then push out whether the modules are independent. In Table 2, Min is the node number that the module first arrives, and Max is the last module. Y means that the module is a separate module, and N means a nonindependent module. The division results are shown in Table 2.

From the operations given in Table 2, it can be concluded that the part of the fault tree modulo can be divided into T, M1, M4, M5, and M6.

2.2. Preprocessing of Logic Gate. After modularizing the fault tree, it is necessary to further determine the module state (dynamic or static). The BDD method is used to calculate the subtree for the static submodule. The Markov model is applied to mold for the dynamic submodule. Since the system is divided into small modules, state explosion problem will not occur during the model processing. Due to logic gate nesting, the static submodule may contain dynamic submodule after the module division in a complex fault tree. In this case, the corresponding algorithm cannot be applied to the fault tree submodule. Preprocessing of dynamic logic gate is required for the basic fault tree, and the complex hybrid dynamic logic gate is transformed into an easy solution model, which can greatly simplify the subsequent calculation.

2.2.1. Processing of Simple Logic Gate. Pretreatment of the logic gate includes the following: copretreatment of AND gate by OR gate, pretreatment of AND gate or PAND gate, pretreatment of two kinds of PAND gate stacking, and pretreatment of FDEP gate (Figures 2–5).

The above is the basic preprocessing process of logic gates.

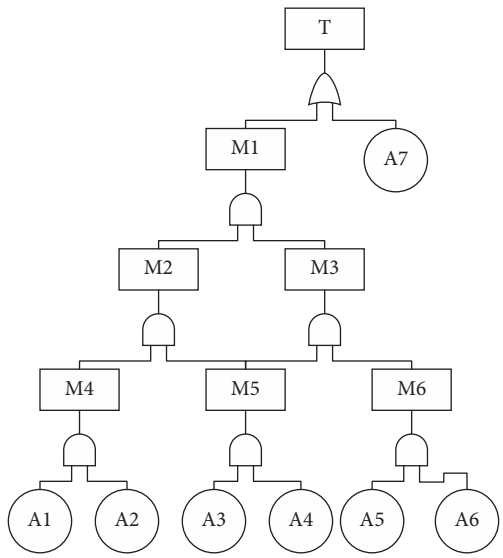

Figure 1: The fault tree.

Table 1: First traversal result.

S	1	2	3	4	5	6	7	8
V	T	M1	M2	M4	A1	A2	M4	M5
S	9	10	11	12	13	14	15	16
V	A3	A4	M5	M2	M3	M5	M6	A5
S	17	18	19	20	21	22		
V	A6	M6	M3	M1	A7	T		

Table 2: Final traversal result.

Module name	T	M1	M2	M3	M4	M5	M6
Min	2	3	4	8	5	9	16
Max	21	19	14	18	6	10	17
Y/N	Y	Y	N	N	Y	Y	Y

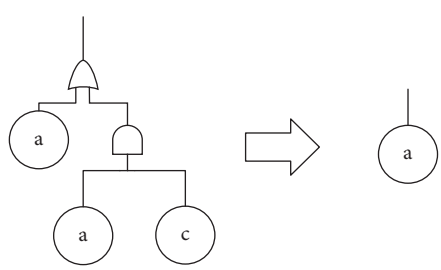

Figure 2: AND gate and OR gate preprocessing.

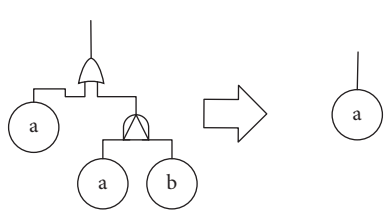

Figure 3: PAND gate and OR gate preprocessing.

3. BDD Subtree Calculation

The BDD method is generally applied to solve the problem of the static fault tree. The BDD method plays a great role in promoting the analysis of the static subtree. The BDD method was proposed by the American scholar Akers in 1978, as discussed in [30]. The method can transform the fault tree into a BDD only containing bottom events. The advantage of the BDD method is that the fault tree can be analyzed only using Weibull function expression without depending on intermediate events. Based on the BDD, disjoint Weibull function can be written down directly, and the minimum cut set can be obtained for qualitative analysis. The calculating amount of the method is linearly related to the scale of the graph. Therefore, it is an effective way to solve the problem that the calculating amount of the traditional FTA method increases exponentially with the scale of the fault tree.

3.1. Static Fault Tree Transformation. In the BDD conversion process, the main operation is based on the if-then-else (ite) structure of the Shannon decomposition, shown in the following equations:

$$f(X) = x_i f_i + \overline{x_i} f_0, \tag{1}$$

$$\begin{aligned} f_1 &= f_1(x_1, x_2, \ldots, x_{i-1}, 1, x_{i+1}, \ldots, x_n), \\ f_0 &= f_0(x_1, x_2, \ldots, x_{i-1}, 0, x_{i+1}, \ldots, x_n), \end{aligned} \tag{2}$$

where the parent node is x_i and the child nodes are f_0 and f_1.

3.1.1. Validation. Simple coding and index ordering are performed using ite for a simple fault tree. The influence of different index sorting on BDD generation is analyzed.

The fault tree is shown in Figure 6. The following equations represent the relationships among events:

$$\begin{aligned} T &= x_1 + G_1, \\ G_1 &= x_2 \cdot x_3, \\ &= ite(x_2, 1, 0) \cdot ite(x_3, 1, 0), \\ &= ite(x_2, ite(x_3, 1, 0), 0), \end{aligned} \tag{3}$$

$$\begin{aligned} T &= ite(x_1, 1, 0) + ite(x_2, ite(x_3, 1, 0), 0), \\ &= ite(x_1, 1, ite(x_2, ite(x_3, 1, 0), 0)). \end{aligned} \tag{4}$$

The BDD conversion graph of the fault tree is drawn by the above relationship.

3.1.2. Impact Analysis of Variable Ordering Results. At present, the optimal ordering of BDD is still under study. The mainstream BDD optimization algorithms are precise sorting algorithm and dynamic heuristic algorithm. The optimal index ranking is shown in Figure 6). When the variable order becomes index $(x_2) > index\ (x_3) > index\ (x_1)$, BDD would change (Figure 7).

Since the different ordering, the original six sides change to twelve sides. The calculation process is increased from two sets of equations to four groups, and variable ordering is especially critical when dealing with more complex models. It is shown that a good variable ordering is related to the complexity of the BDD.

3.2. BDD Probability Calculation. After sorting the variables, the path pointing to 0 or 1 can be obtained, where the point 1 represents the top event occurring and the point 0 represents not occurring.

3.2.1. Calculation of Top Event Probability. Determining all paths point to 1, the path is recorded as $P_i\,(i = 1, 2, 3, \ldots, m)$, where m is the number of paths. P_i is shown in the following equation:

$$P_i = \prod_{i=1}^{n_i} x_{ij}^{'}, x_{ij}^{'} \in \left\{x_{ij}, \overline{x_{ij}}\right\}, x_{ij} \in \{x_1, x_2, \ldots, x_n\}. \tag{5}$$

Disjoint expressions of the fault tree can be represented as follows:

$$P(T) = P\left(\sum_{i=1}^{m} P_i\right) = \sum_{j=1}^{m}\left(\prod_{j=1}^{n_i} x_{ij}^{'}\right). \tag{6}$$

The probability of occurrence of the top event can be calculated using probability formula of the mutual exclusion event as below:

$$P(T) = P\left(\sum_{i=1}^{m} P_i\right) = \sum_{j=1}^{m}\left(\prod_{j=1}^{n_i} P\left(x_{ij}^{'}\right)\right). \tag{7}$$

The probability of failure of the bottom event can be expressed as $P(x_{ij})$.

3.3. A Case of Study. The above content is verified by an example. A, B, C, D, and E are bottom events (Figure 8). The probability of failure of the bottom event is shown in Table 3.

After determining the probability of the leaf node, the fault tree can be modularly divided. The fault tree is divided into three parts: M1, M2, M3, where the submodules are M1 and M2. The submodule M1 is converted into BDD, as shown in Figure 9. Combining the transfer graph with the failure probability of variables B and C, probability of occurrence of module M1 can be obtained, which is 0.28.

The probability of occurrence of module M2 is calculated based on the following BDD (Figure 9). Combined with failure probability of variables D and E, the probability of occurrence of module M2 can be obtained, which is 0.405.

After obtaining the probability of occurrence of the modules M1 and M2, probability of occurrence for M3 can be further calculated (Figure 10). The BDD model of the fault tree, defined as module M3, is a combination of M1, A3, and M2.

Obtain the probability of M1, M2, and A, and the probability of M3 can be calculated as 0.657.

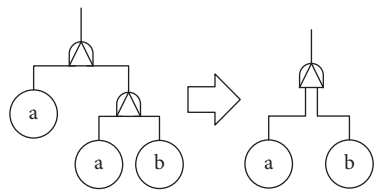

Figure 4: Priority and gate preprocessing.

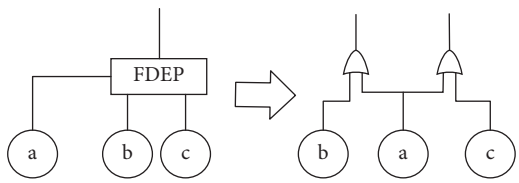

Figure 5: FDEP gate preprocessing.

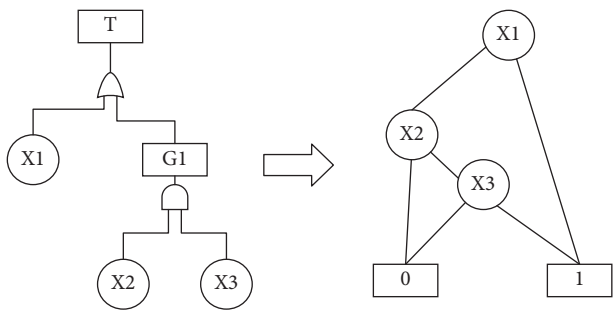

Figure 6: The fault tree transformation diagram.

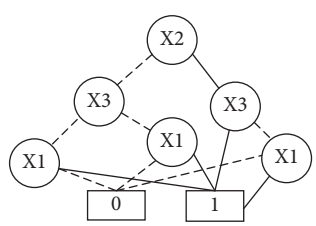

Figure 7: Reordering BDD.

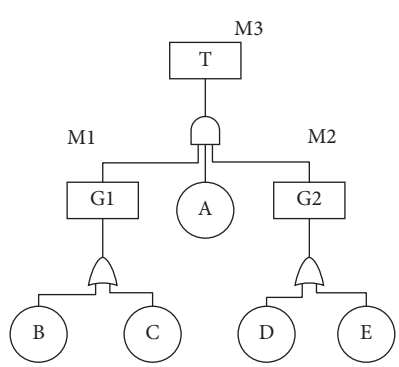

Figure 8: Modular fault tree.

Table 3: Bottom event failure probability.

Bottom event code	A	B	C	D	E
Failure probability	0.2	0.1	0.2	0.3	0.15

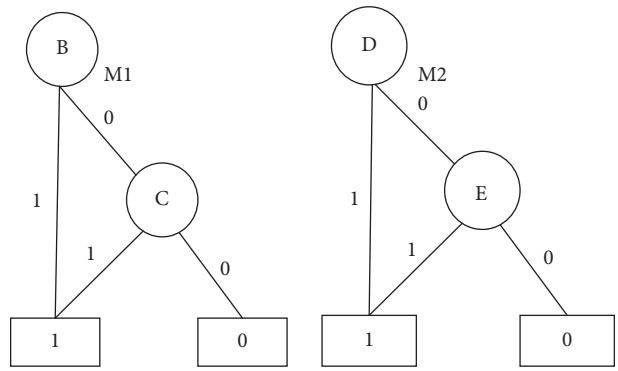

Figure 9: Model M1 and model M2.

4. Solution of Markov Model by Dynamic Fault Tree

4.1. Markov Model Theory. Continuous-time Markov decision processes provide a very powerful mathematical framework to solve widely used decision problems, as discussed by Bartocci [31]. The process can be defined as the following random process:

$$\begin{aligned} &\{X(t), t \in T\}, if \forall t_0 < t_1 < \ldots t_n < t_{n+1} \in T, \\ &P[X(t_{n+1}) \le x_{n+1} | X(t_0) = x_0, X(t_1) = x_1 \ldots X(t_n) = x_n], \\ &= P[X(t_{n+1}) \le x_{n+1} | X(t_n = x_n)], \end{aligned} \tag{8}$$

where A is a random variable event, which occurs before time t_n, and event B is an event that occurs afterwards. The Markov chain is shown in the following equation:

$$\begin{aligned} P[B|A, X(t_n) = x_n] &= P[B|X(t_n) = x_n], \\ P[AB|X(t_n) = x_n] &= P[A|X(t_n) = x_n] P[B|X(t_n) = x_n]. \end{aligned} \tag{9}$$

The sequence is shown as follows:

$$\begin{aligned} &P(X_{n+1} = i_{n+1} | X_0 = i_0, X_1 = i_1 \ldots X_n = i_n), \\ &= P(X_{n+1} = i_{n+1} | X_n = i_n). \end{aligned} \tag{10}$$

4.2. Markov and Dynamic Logic Gate Transformation. In order to make the fault tree model better deal with the sequential logical relationship between the parts in the dynamic system, Dugan et al. [17] proposed the dynamic gate to represent the dynamic working relationship of the system in 1992. The Markov chain can represent the conversion relationship between system states using graphics. This graphical structure provides a visual tool to solve problems. Dynamic fault trees (DFTs) introduce four basic (dynamic) gates: the priority AND (PAND), the sequence enforcing (SEQ), the standby or spare (SPARE), and the functional dependency (FDEP), as discussed by Dugan et al. [17]. The Markov transformation process of specific dynamic logic gates will be introduced.

4.2.1. Dynamic Logic Gate Transformation. The process of converting the four common dynamic logic gates into Markov chain will be described. The four common dynamic logic gates are PAND gate, SEQ, SPARE, and FDEP, and the relevant transition diagrams are shown in Figures 11–14.

4.3. Quantitative Analysis of Markov chain. The quantitative analysis method of the Markov model generally consists of five steps: first, define the system state; second, the transition probability matrix construction; third, solve the spherical transition probability matrix; fourth, solve the differential equations; fifth, solve the fault probability state at any time.

The system state set, the fault state set, and the working state set are defined as follows: $M = \{0, 1\}$, $F = \{1\}$, and $W = \{0\}$.

When defining the random process, the corresponding time point t should be set as shown below:

$$X(t) = \left\{ \begin{array}{ll} 1, & \text{system failure}, \\ 0, & \text{system working}. \end{array} \right\} \tag{11}$$

Defining $A = P\_E$, where A is the transition matrix and E is equal to the identity matrix of P. The equation of state is shown below:

$$\left\{ \begin{array}{l} P' = AP, \\ P(0) = E. \end{array} \right\} \tag{12}$$

The derivative column of the state probability and the column vector of the probability derivative are, respectively, expressed as $P$and P'. Equation (13) is C–K equation:

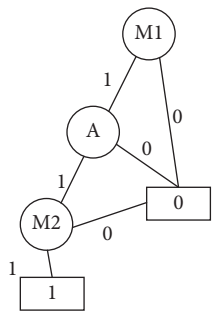

Figure 10: Model M3.

$$\left\{\begin{array}{c} P_{ij}'(t) = q_{ij}p_{ij}(t) + \sum_{k=j} q_{ik}p_{kj}(t), \\ p_{ij(t)} = 1, \quad i = j, \\ p_{ij}(t) = 0, \quad i \neq j. \end{array}\right\} \tag{13}$$

In the process of the Markov chain transfer, the complexity of state transition usually increases with the increase of chain length. The transition probability from i to j can be expressed as P_{ij} as follows:

$$P(t) = \begin{bmatrix} P_{00}(t) & P_{01}(t) & P_{0NF}(t) \\ P_{10}(t) & P_{11}(t) & P_{1NF}(t) \\ P_{NF0}(t) & P_{NF1}(t) & P_{NFNF}(t) \end{bmatrix}. \tag{14}$$

The transfer probability matrix can be written as follows:

$$Q = \begin{bmatrix} -(\lambda_{0,1} + \lambda_{0,NF}) & \lambda_{0,1} & \lambda_{0,NF} \\ 0 & 0 & 0 \\ 0 & 0 & 0 \end{bmatrix}, \tag{15}$$

when the chain length is 1, the state transition process can be represented as follows:

$$\begin{aligned} P^{T^1} &= P_{01}(t) = \frac{\lambda_{0,1}}{\lambda_{0,1} + \lambda_{0,NF}}\left(1 - e^{-(\lambda_{0,1}+\lambda_{0,NF})t}\right), \\ &= \lambda_{0,1}\left\{\frac{1}{\lambda_{0,1} + \lambda_{0,NF}} - \frac{1}{\lambda_{0,1} + \lambda_{0,NF}} e^{-(\lambda_{0,1}+\lambda_{0,NF})t},\right\} \\ \lambda_{0,1} &\geq 0\lambda_{0,NF} \geq 0. \end{aligned} \tag{16}$$

The state transition process of chain length 2 can be deduced by the formula of chain length 1. When the event from 0 to j requires two transfer processes, this process is defined as T^2, and $P(T)$ is the ultimate transition probability of each edge on T^2. This process can be seen as follows:

$$\begin{aligned} P^{T^2} = P_{02}(t) = \lambda_{0,1}\lambda_{1,2}\Bigg\{ & \frac{1}{(\lambda_{0,1} + \lambda_{0,NF}) + (\lambda_{1,2} + \lambda_{1,NF})} \\ & - \frac{1}{(\lambda_{0,1} + \lambda_{0,NF})(-\lambda_{0,1} - \lambda_{0,NF} + \lambda_{1,2} + \lambda_{1,NF})} e^{(-\lambda_{0,1}+\lambda_{0,NF})t} \\ & - \frac{1}{(\lambda_{1,2} + \lambda_{1,NF})(-\lambda_{1,2} - \lambda_{1,NF} + \lambda_{0,1} + \lambda_{0,NF})} e^{-(\lambda_{1,2}+\lambda_{1,NF})t}\Bigg\}. \end{aligned} \tag{17}$$

The following equation represents the state transition of chain length is n:

$$P^{T^n} = P_{0n}(t) = \prod_{i=1}^{n} \lambda_{i-1,i}\left\{\prod_{i=1}^{n} \frac{1}{\lambda_{i-1,i} + \lambda_{i-1,NF}} - \sum_{i=1}^{n} \frac{1}{(\lambda_{i-1,i} + \lambda_{i-1,NF}) \prod_{j=1, j\neq i}^{n} (-\lambda_{i-1,i} - \lambda_{i-1,NF} + \lambda_{j-1,j} + \lambda_{j-1,NF})} e^{-(\lambda_{i-1,i}+\lambda_{i-1,NF})t}\right\}, \tag{18}$$

where $\lambda_{i-1,i} > 0, \lambda_{i-1,NF} > 0$.

5. Fault Tree Modular Analysis

The main work of the pharmaceutical system of explosive vehicle is to manufacture explosives. The working environment of the explosive vehicle is harsh, and the failure rate is high. Through existing data, the failure probability of bottom event was obtained for the explosive vehicle.

5.1. Fault Tree Establishment and Module Division. Figure 15 shows the dynamic fault tree. It can be seen that the fault tree established includes several static and dynamic modules. The system is mainly divided into four types: flow display module, storage tank module, pump body module, and sensitizing agent system module. The storage tank module is mainly responsible for storing various liquids to ensure that the catalysts used in the preparation process are kept in a stable state. The main function of the chemical agent module is to filter to ensure that no impurities are mixed in during the configuration process. The pump body module controls the stable output of the ingredients during the preparation of explosives. The flow display module ensures that the flow output process can be observed by the outside world.

5.1.1. Preprocessing the Fault Tree. The FDEP gate exists under the OR gate of module N1. The FDEP gate transformation process is as follows: the subordinate modules of N2 are all static gates. The module M1 under N2 can be combined due to a static module. Fault tree after preprocessing is shown in Figure 16.

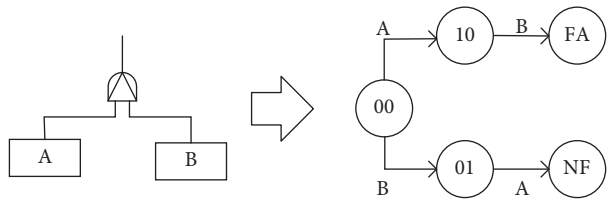

Figure 11: PAND logical gates transform to MC.

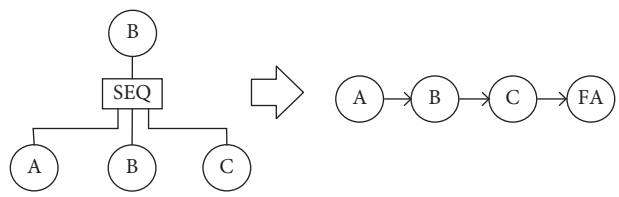

Figure 12: SEQ logical gates transform to MC.

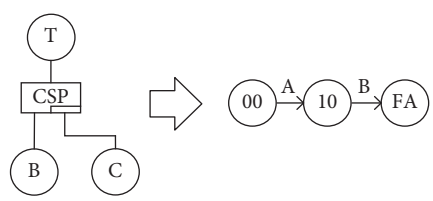

Figure 13: CSP logical gates transform to MC.

The fault tree can be divided into four basic modules S1, S2, S3, and S4. In module S1, there is a submodule C consisting of static logic gates, which can be divided into static module. Modules S2 and S3 are static modules. Module S4 is divided into dynamic submodule because its subtree root node is the spare parts gate.

5.2. Fault Tree Modular Calculation. According to BDD, its nodes are firstly divided. Sorting the bottom events uses a heuristic sorting method and defined the order $index(x_1) > index(x_2) > index(x_3)$. Get BDD (Figure 17).

For the transformation of the static module S2, the above method should be used. First, the heuristic algorithm is applied to determine the subunit sequencing:

$$in\ de\ x(x_7) > in\ de\ x(x_8) > in\ de\ x(x_9) > in\ de\ x(x_{10}) > in\ de\ x(x_{11}) > in\ de\ x(x_{12}) > in\ de\ x(x_{13}). \quad (19)$$

The BDD of module S2 is shown in Figure 18.

Similarly, module S3 was converted into BDD, where the sorting is defined as

$$in\ de\ x(x_{15}) > in\ de\ x(x_{16}) > in\ de\ x(x_{17}) > in\ de\ x(x_{18}). \quad (20)$$

The BDD of transformation is shown in Figure 19.

The module S4 contains the submodules C4 and C5, where C5 is the spare part of C4. BDD was established to solve the probability of C4 (Figure 13). The order has no succession, and Markov chain is shown in Figure 20.

The failure probability of parts in the bottom event is shown in Table 4. The following data sources are from the maintenance records of the BZ15 heavy-duty oil ammonia explosive vehicle and related experimental data in the factory.

The probability of failure of each module at 1000 hours is obtained by the bottom event probability, as shown in Table 5.

After obtaining the data failure probability of each module, the data are further integrated to obtain failure probability of the top event.

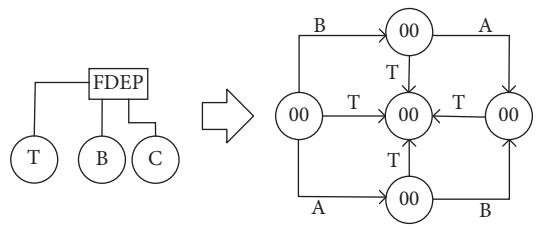

Figure 14: FDEP logical gates transform to MC.

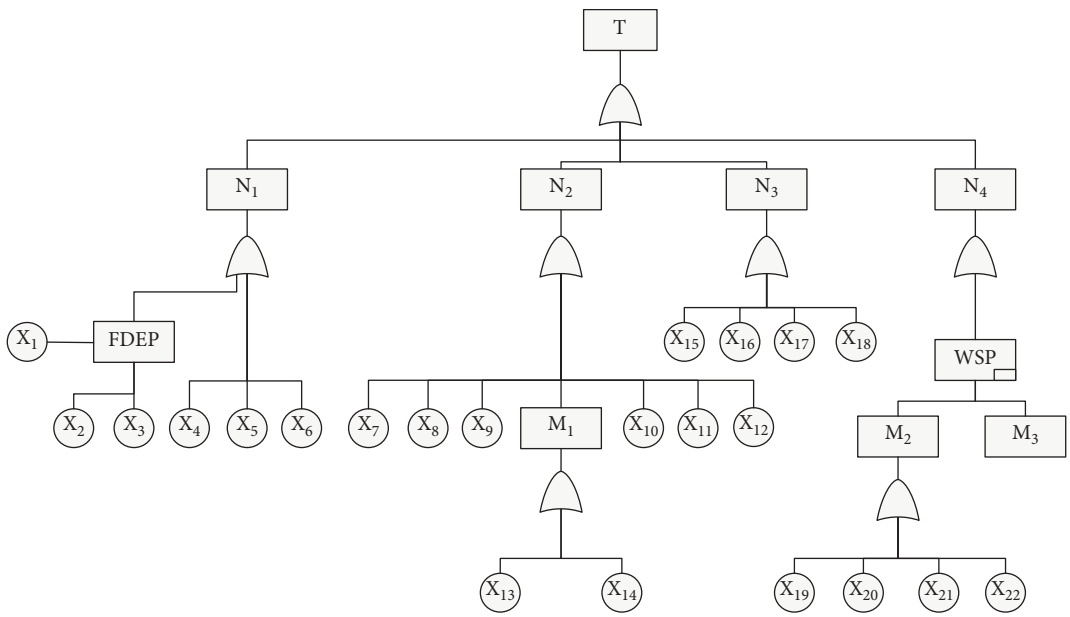

Figure 15: The model of dynamic fault tree.

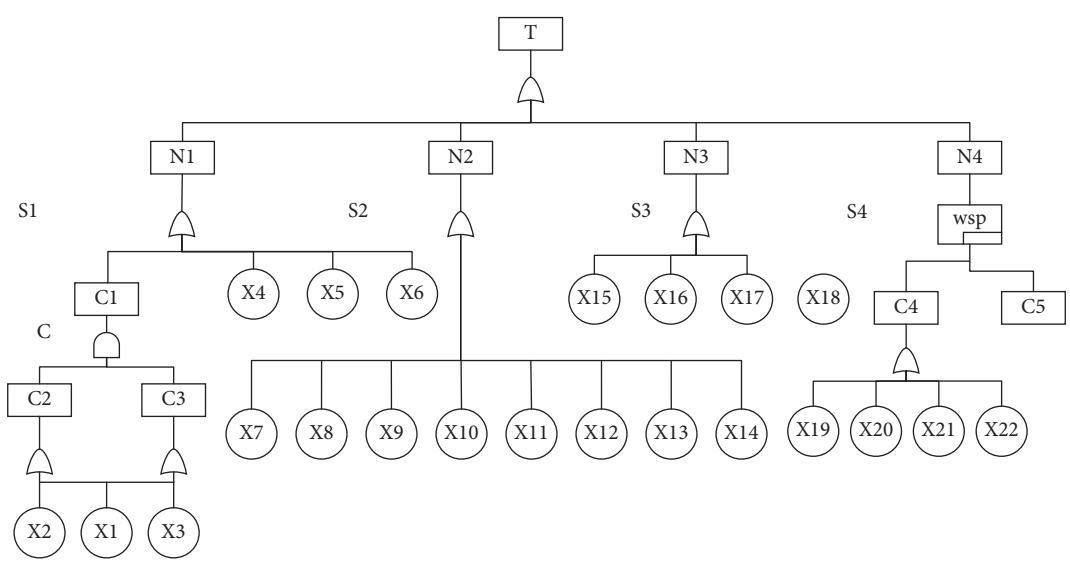

Figure 16: Dynamic fault tree module division.

According to the integration, the reliability of the system after one thousand hours of running time can be obtianed. The integration diagram is shown in Figure 21.

Finally, combining the failure probability of each module to evaluate the system reliability and failure rate can be obtained as 0.6292 and 0.3708, respectively.

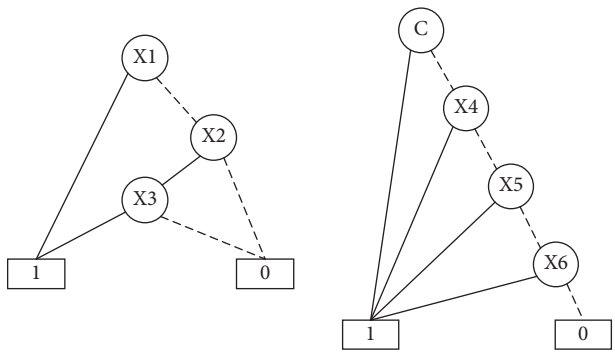

Figure 17: The binary decision diagrams.

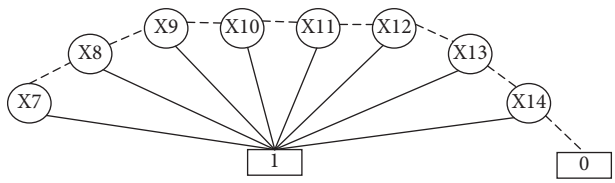

Figure 18: The binary decision diagrams.

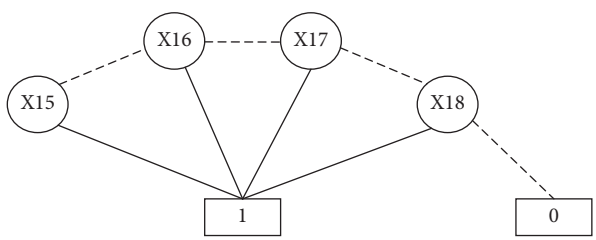

Figure 19: The binary decision diagrams.

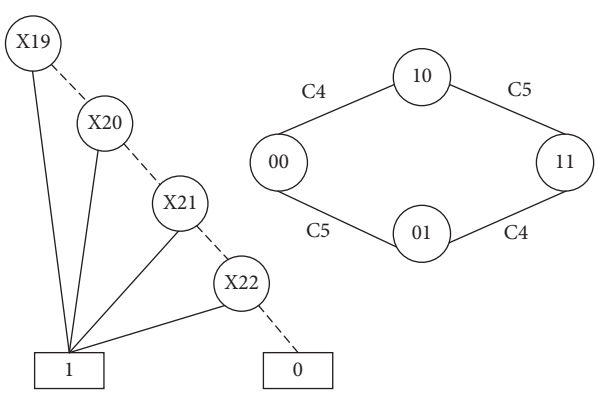

Figure 20: The BDD and Markov chain.

6. Discussion

The Markov model is usually used to solve the problem of dynamic fault tree. Complex systems are difficult to build using traditional Markov models. Due to the dynamic fault tree containing static subtrees, the BDD can be used to solve the problem of static subtree. The logic gate combination is simplified using the pretreatment method. For the simplified dynamic fault tree [32–35], BDD is used to solve the problem. The complexity of the solution is closely related to the construction of the binary decision graph model. The complexity of model construction is affected by the ordering

Table 4: Bottom event failure probability.

Encoding	Event	Probability ($10^{-4}h^{-1}$)
X_1	Line interface failure	0.5
X_2	Fuel flow-meter failure	0.4
X_3	Sensitizer flow-meter failure	0.2
X_4	Solenoid valve failure	0.3
X_5	Connection line failure	0.2
X_6	System display failure	0.1
X_7	The leakage of fuel tank	0.1
X_8	The leakage of oil pipe joints	0.5
X_9	Oil pipe failure	0.1
X_{10}	Oil filter element failure	0.8
X_{11}	Oil-pressure meter failure	0.2
X_{12}	One-way valve failure	0.2
X_{13}	Stator failure	0.45
X_{14}	Bearing failure	0.15
X_{15}	Emulsion matrix pump failure	0.3
X_{16}	Flexible pipe failure	0.7
X_{17}	Flexible pipe joint failure	0.2
X_{18}	Butterfly valve failure	0.4
X_{19}	Sensitizer pump failure	0.1
X_{20}	Water tube failure	0.5
X_{21}	Sensitizer filter element failure	0.2
X_{22}	Sensitizer tank failure	0.2

Table 5: Failure probability of each module.

Encoding	Model	Probability
C	Fuel flow module	0.1008
S1	Flow display module	0.1537
S2	Tank module	0.2261
S3	Pump body module	0.1513
S4	Sensitizing agent system module	0.3333

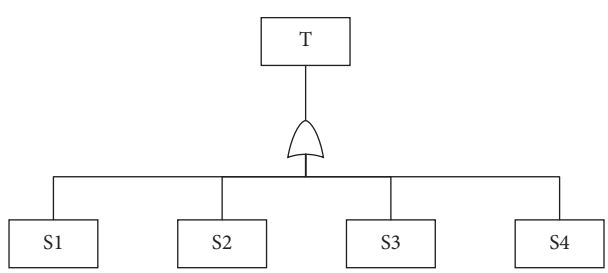

Figure 21: Integration diagram.

of variables. The complex structure of the fault tree is improved, and the difficulty of sorting the BDD variables is reduced by preprocessing the logic gate. Taking the subtree N1 in Figure 16 as an example, the FDEP gate is connected under the OR gate. If the variables are sorted directly without preprocessing, it is difficult to reasonably sort due to the various sorting of dynamic logic gate. The preprocessed module is shown in Figure 17. The preprocessed module S1 only contains two kinds of static gates. Sorting the variables is becoming easier, and difficulty of solving is reduced. The binary decision method can be directly used to solve the solution, and the result is as shown in Table 5. Using this method, the failure probability of each subtree can be obtained at the same time, and the dynamic fault tree can be rigorously analyzed.

The information obtained from the current research results is still very limited. Because of its influence by many factors, the accuracy of the failure probability still needs further research. Therefore, the subsequent researches should go along diversification. Since the amount of information that can be obtained using only one data source is small, in the future, a multisource information fusion

method will be used to more accurately evaluate the system reliability.

7. Conclusion

This article introduces how to use the modular approach to solve the probability density of basic events in the dynamic fault tree when the system has certain complexity and multiple subsystems. The module pretreatment method is adopted to simplify the submodule of the fault tree due to the excessive mixture and overlap of logic gates. This modular approach has two advantages: first the variables ordering for the module becomes easy to reduce the complexity of BDD and solve difficulty by pretreatment, and second the failure probability of the subsystem can be obtained for evaluating the reliability of the subsystem. The feasibility of the method was verified by analyzing dynamic fault tree of explosive production system for the BCZH-15 explosive vehicle. At present, due to the difficulty of individual data collection in the data collection process and the lack of a large amount of experimental data support, the failure rate of the collected products is not accurate enough. It may have an impact on the accuracy of the result evaluation. In the future, when the data are insufficient, fuzzy theory will be used to define the failure rate of the product, and the rationality of the final output result will be determined through the comparison of expert experience.

Data Availability

The data used to support the findings of this study are included within the article.

Conflicts of Interest

There are no conflicts of interest.

Acknowledgments

This work was partially supported by the National Natural Science Foundation of China under the contract no. 71761030 and the Graduate Teaching Program of Inner Mongolia University of Technology under the contract no. YJG2017013.

References

[1] E. J. Henley and H. Kumamoto, *Reliability Engineering and Risk Assessment*, Prentice-Hall, Englewood Cliffs, NJ, USA, 1981.

[2] N. G. Leveson, *Safeware: System Safety and Computers*, Addison-Wesley, Reading, MA, USA, 1995.

[3] Y. Ren and J. B. Dugan, "Optimal design of reliable systems using static and dynamic fault trees," *IEEE Transaction on Reliability*, vol. 47, pp. 234–244, 1998.

[4] N. Siu, "Risk assessment for dynamic systems: an overview," *Reliability Engineering and System Safety*, vol. 43, no. 1, pp. 43–73, 1994.

[5] J. Mi, Y. F. Li, Y. J. Yang, W. Peng, and H. Z. Huang, "Reliability assessment of complex electromechanical systems under epistemic uncertainty," *Reliability Engineering and System Safety*, vol. 152, pp. 1–15, 2016.

[6] M. Yazdi, S. Kabir, and M. Walker, "Uncertainty handling in fault tree based risk assessment: state of the art and future perspectives," *Process Safety and Environmental Protection*, vol. 131, pp. 89–104, 2019.

[7] M. Yazdi, F. Nikfar, and M. Nasrabadi, "Failure probability analysis by employing fuzzy fault tree analysis," *International Journal of System Assurance Engineering and Management*, vol. 8, no. 2, pp. 1177–1193, 2017.

[8] M. Yazdi, A. Nedjati, E. Zarei, and R. Abbassi, "A novel extension of DEMATEL approach for probabilistic safety analysis in process systems," *Safety Science*, vol. 121, pp. 119–136, 2020.

[9] C. A. Ericson, *Hazard Analysis Techniques for System Safety*, John Wiley & Sons, Hobokrn, NJ, USA, 2015.

[10] A. C. Torres-Echeverria, "Modeling and optimization of proof testing policies for safety instrumented systems," *Reliability Engineering and System Safety*, vol. 94, pp. 838–854, 2009.

[11] A. Lisnianski, "Extended block diagram method for a multi-state system reliability assessment," *Reliability Engineering and System Safety*, vol. 92, pp. 1601–1607, 2007.

[12] Y. Dutuit, F. Innal, A. Rauzy, and J.-P. Signoret, "Probabilistic assessments in relationship with safety integrity levels by using Fault Trees," *Reliability Engineering and System Safety*, vol. 93, no. 12, pp. 1867–1876, 2008.

[13] Y. F. Li, J. Mi, Y. Liu, Y. J. Yang, and H. Z. Huang, "Dynamic fault tree analysis based on continuous-time Bayesian networks under fuzzy numbers," *Proceedings of the Institution of Mechanical Engineers, Part O, Journal of Risk and Reliability*, vol. 229, no. 6, pp. 530–541, 2005.

[14] H. Li, H. Diaz, and C. Guedes Soares, "A developed failure mode and effect analysis for floating offshore wind turbine support structures," *Renewable Energy*, vol. 164, pp. 133–145, 2021.

[15] H. Li, A. P. Teixeira, and C. Guedes Soares, "A two-stage Failure Mode and Effect Analysis of offshore wind turbines," *Renewable Energy*, vol. 162, pp. 1438–1461, 2020.

[16] H. Li, C. G. Soares, and H. Z. Huang, "Reliability analysis of a floating offshore wind turbine using Bayesian Networks," *Ocean Engineering*, vol. 217, Article ID 107827, 2020.

[17] J. B. Dugan, S. J. Bavuso, and M. A. Boyd, "Dynamic fault-tree for fault-tolerant computer systems," *IEEE Transaction on Reliability*, vol. 41, no. 3, pp. 363–376, 1992.

[18] J. B. Dugan, K. J. Sullivan, and D. Coppit, "Developing a low-cost high-quality software tool for dynamic fault-tree analysis," *IEEE Transactions on Reliability*, vol. 49, no. 1, pp. 49–59, 2000.

[19] L. Meshkat, J. B. Dugan, and J. D. Andrews, "Dependability analysis of systems with on demand and active failure modes using dynamic fault trees," *IEEE Transaction Reliability*, vol. 51, no. 3, pp. 240–251, 2002.

[20] G.-J. Jiang and L. Gao, "Reliability analysis of martial arts arena robot systems based on fuzzy set theory," *Journal of Mechanical Science and Technology*, vol. 32, no. 11, pp. 5069–5077, 2018.

[21] C.-Y. Huang and Y.-R. Chang, "An improved decomposition scheme for assessing the reliability of embedded systems by using dynamic fault trees," *Reliability Engineering and System Safety*, vol. 92, no. 10, pp. 1403–1412, 2007.

[22] M. Soeken, L. Tague, G. W. Dueck, and R. Drechsler, "Ancilla-free synthesis of large reversible functions using binary decision diagrams," *Journal of Symbolic Computation*, vol. 73, pp. 1–26, 2016.

[23] J. B. Dugan, "DIF tree: a software package for the analysis of dynamic fault tree models," in *Proceedings of the Reliability and Maintainability Symposium*, pp. 64–70, Philadelphia, PA, USA, January 1997.

[24] D. Ge, M. Lin, Y. Yang, R. Zhang, and Q. Chou, "Quantitative analysis of dynamic fault trees using improved Sequential Binary Decision Diagrams," *Reliability Engineering and System Safety*, vol. 142, pp. 289–299, 2015.

[25] C. Bandyopadhyay, R. Das, R. Wille, R. Drechsler, and H. Rahaman, "Synthesis of circuits based on all-optical mach-zehnder interferometers using binary decision diagrams," *Microelectronics Journal*, vol. 71, pp. 19–29, 2018.

[26] X. Zhang, H. Gao, H.-Z. Huang, Y.-F. Li, and J. Mi, "Dynamic reliability modeling for system analysis under complex load," *Reliability Engineering and System Safety*, vol. 180, pp. 345–351, 2018.

[27] X.-Y. Li, H.-Z. Huang, and Y.-F. Li, "Reliability analysis of phased mission system with non-exponential and partially repairable components," *Reliability Engineering and System Safety*, vol. 175, pp. 119–127, 2018.

[28] M. Abimbola, F. Khan, N. Khakzad, and S. Butt, "Safety and risk analysis of managed pressure drilling operation using Bayesian network," *Safety Science*, vol. 76, pp. 133–144, 2015.

[29] Y. D. Rauzy, "A linear-time algorithm to find modules of fault tree," *IEEE Transaction on Reliability*, vol. 45, no. 3, 1996.

[30] S. B. Akers, "Binary decision diagrams," *IEEE Transaction on Computers*, vol. C-27, pp. 509–516, 1978.

[31] E. Bartocci, L. Bortolussi, T. Brázdil, D. Milios, and G. Sanguinetti, "Policy learning in continuous-time Markov decision processes using Gaussian Processes," *Performance Evaluation*, vol. 116, pp. 84–100, 2017.

[32] S. Reed, "An efficient algorithm for exact computation of system and survival signatures using binary decision diagrams," *Reliability Engineering and System Safety*, vol. 165, pp. 257–267, 2017.

[33] A. Toppila, A. Salo, Binary decision diagrams for generating and storing non-dominated project portfolios with interval-valued project scores," *European Journal of Operational Research*, vol. 260, no. 1, pp. 244–254, 2017.

[34] J. Mi, Y.-F. Li, W. Peng, and H.-Z. Huang, "Reliability analysis of complex multi-state system with common cause failure based on evidential networks," *Reliability Engineering and System Safety*, vol. 174, pp. 71–81, 2018.

[35] H. Li, H.-Z. Huang, Y.-F. Li, J. Zhou, and J. Mi, "Physics of failure-based reliability prediction of turbine blades using multi-source information fusion," *Applied Soft Computing*, vol. 72, pp. 624–635, 2018.

Hindawi
Mathematical Problems in Engineering
Volume 2021, Article ID 6636794, 12 pages
https://doi.org/10.1155/2021/6636794

Research Article

An Operational Safety Evaluation Method for Manned Transport Aircraft and Large UAV in Mixed Airspace

Xin Ma,[1] Xiaoqiang Zhang,[2] Huawei Wang,[1] Songbin Ding,[1] and Xia Li[2]

[1]*Nanjing University of Aeronautics and Astronautics, Nanjing 211106, China*
[2]*Civil Aviation Flight University of China, Guanghan 618307, Sichuan, China*

Correspondence should be addressed to Xiaoqiang Zhang; xqzhanguestc@163.com

Received 24 December 2020; Revised 13 February 2021; Accepted 12 March 2021; Published 9 April 2021

Academic Editor: Bosheng Song

To improve the predictive ability in trajectory of large unmanned aerial vehicle (UAV) and the calculation performance in complicated circumstances with mixed airspace, multiple aircraft types, and joint operations, the concept of phased trajectory deviation (PTD) is introduced and a corresponding minimal interval algorithm (PTD-MI) is set up. This algorithm is capable of deriving the minimal interval between various aircraft types according to the crosswind impacts and the UAV characteristics at different flight phases and thus achieves the effective safety evaluation in airspace operation. To demonstrate the rationality and generality of the proposed algorithm, several simulation experiments are conducted. Based on the experimental results, flight procedure protection area is plotted by PTD-MI algorithm and compared with that generated by Ground-Based Augmentation System (GBAS). Results indicate that the proposed algorithm is capable of deriving a more scientific basis for airspace assignment and outperform GBAS in dealing with wide-area space problems. And, compared with GBAS, PTD-MI algorithm shows a more stable calculation performance and is easier to output the results. PTD-MI algorithm is proposed under the flight safety regulation designed by the International Civil Aviation Organization (ICAO) and designed to provide effective technical supports for the safe and normal operations of aircrafts.

1. Introduction

At present, many older manned aircraft, because of the poor performances of the aircraft, the small commercial payload space of the aircraft, and the deficiency of aviation telecommunication equipment [1], have gradually been modified into large unmanned aircraft, which are used in low-altitude cargo transportation and general aviation flights [2, 3].

In the research field of UAV track prediction and operation safety assessment, the current research accumulation is as follows. First of all is the study of risk factors. By sorting out the unsafe incidents, we can conclude the causes of the accidents. Wang and Chen provided a hybrid optimization algorithm with directivity [4], Zhao et al. proposed a case study for diagnosis [5], Zhang used the learning model to supplement experiments and demonstrate the imperfections in the algorithm and case diagnosis [6, 7]. In this way, the graded management method of accident factors has been established. Second is the study of risk degree. According to the hierarchical management of accident factors, factor screening and weight design have become the focus of safety evaluation model [8]. In the preliminary studies, the evaluation schemes were mostly built around the SHELL model, which basically realized the accident risk assessment [9]. At this stage of the study, Chen proposed a Hawks optimization scheme based on the computer system [10, 11], Li et al. provide a global optimization strategy [12], and Xia et al. provided intelligent systems [13], and the results of their research explain and justify the implementation of the optimization scheme. Shen used a grasshopper optimizer to enhance the adaptability of previous studies [14, 15] so that the various levels of risk assessment parameters obtained a specific design basis. Third is the study of flight path prediction. According to the available data, the method of graded management of accident factors and the scheme of risk assessment have been initially established [16]. Chen

studied early accident diagnosis and provided research ideas for parameter selection and evaluation [17], Hu studied the defects of accident diagnosis and proposed the use of multiplicity selection method to carry out simulation experiments [18], and Zhang et al. established a method to show the application effect of experimental results by using Image Dehazing (ID) technology [19, 20]. The next step of research will mainly focus on the collection of original data of accident factors [21]. According to different research objects and evaluation criteria, flight path prediction research is mainly used for flight path planning [22]. Fourth is the study on the accuracy of evaluation results. Since all industries have accident evaluation programs, but the requirements for accuracy of evaluation results and quantitative methods are different, civil aviation flight safety assessment emphasizes precision and control [23]. In a study conducted in recent years, Zhao proposed the application of image segmentation and processed the evaluation results graphically [24], Zhang et al. proposed the concept of integer programming to make the evaluation results more accurate in the graphic display [25], and Zhao et al. proposed Improved Ant Colony Optimization (Improved ACO) to improve the display degree and scope of evaluation results [26, 27]. These research results make the simulation results and evaluation results more applicable to the real civil flight practice field. At present, a breakthrough has been made in the study of flight safety evaluation; however, in dealing with problems such as high precision, large scope, and complex airspace structure, the existing algorithms have low computational performance [28], or cannot carry out evaluation for specific environment, and lack a calculation method with high adaptability [29]. At the same time, the existing research lacks the countermeasures to the joint operation. Even so, in terms of algorithm and comparative experiment design, the research results are rich. In the future, experiments and argumentation can be carried out under the premise of optimal design, and evaluation basis and rules can be summarized.

In the current practical operation and production process, more and larger UAV and manned aircraft are carrying out joint operation missions [30]. In this mixed airspace, flight safety assessment is a difficult work, and the main difficulties lie in the choice of parameter types and the use of evaluation criteria [31]. At the same time, transform old manned aircraft into large UAV; it has been gradually realized at this stage, and this kind of transformation is more and more [32], and the number of old aircraft is also large [33]. As a result, general aviation missions at low altitudes will increasingly performed using large UAV; if a safety assessment method can be developed which is suitable for the joint operation of large UAV and manned aircraft in mixed airspace [34, 35], these findings can improve the flight safety of general aviation and promote the strategy of further opening up the low-altitude airspace [36].

This paper takes operational safety assessment as the research direction and tries to establish a trajectory prediction model. This model can be used to evaluate the operational safety trend in the low-altitude airspace, and the evaluation scope should cover the local airspace of the airport, and the evaluation results should meet the ICAO requirements for the accuracy of risk assessment.

2. Problem Description

First of all, because of the preflight planning stage, it is impossible to accurately obtain all kinds of conditions during the actual flight, such as airspace situation, meteorological information, and flight environment [37].Those differences in the preplanning and implementation leads to the result between the planned trajectory and the actual trajectory which is different [38]. According to the conflict probability value stipulated by ICAO [39], the navigation equipment accuracy of large UAV is used to analyze various influencing factors under the operating environment [40], and the fusion algorithm is established for the overall airspace to calculate and obtain the interval safety value that should be maintained between aircrafts, so as to complete the evaluation of flight conflict [41]. As described above, the current model lacks the analysis and processing of aircraft performance parameters and does not consider the turning radius trajectory deviation or the linear [42]. If the flight procedure design specification of transport aircraft is used for analysis, many unfavorable factors will be brought so that the calculated results cannot be used for correct evaluation [43]. Therefore, the design of PTD-MI algorithm needs to avoid the above adverse factors.

Secondly, the airport has a wide range of local airspace. If ground equipment is used for trajectory observation and prediction [44], the increase of observation distance will lead to the increase of evaluation error [45]. Therefore, the design of PTD-MI algorithm needs to consider the optimization of evaluation error.

Finally, the evaluation results derived from the algorithm can easily show the application effect.

3. Improved Computational Model

According to ICAO regulations, calculate flight envelope on the mission to carry out the plan, and all running implementation stages need to meet standards, including the conflict between aircraft probability which are restricted to 1.5×10^{-8} (accident/flight hours) [46]; the data can be seen as the flight safety guarantee value, and it can be used to represent the current conflict between the probability of aircraft operating. In the design of the improved model, the large UAV is used as the experimental object [47].

3.1. Established Model of Turning Stage. As experimental objects, large UAVs are generally equipped with Global Positioning System, which can autonomously and accurately search for preset airway points, and have the ability to fly along the preset path [48]. All of them have no flight technical tolerance and do not need to set the time margin for the pilot response. In the actual flight process, compared with the transport aircraft, the experimental subjects need to focus on the data such as lift-off point position, turning speed, turning slope, and flight mission altitude, which are the main parameters for the formation of flight trajectory of

large UAV. Assuming rated cruising speed v_1 and turning slope γ_1, there is a relationship between rated turning radius R_1 and flight parameters under current flight conditions:

$$R_1 = \frac{v_1^2}{g \tan \gamma_1}. \tag{1}$$

Assuming that the real slope is γ_2 and the cruising speed v_2 is arbitrary, the normal distribution relationship is established:

$$\begin{aligned} F_\gamma(\gamma_2) &= \frac{1}{\sqrt{2\pi\sigma_\gamma}} \exp\left(-\frac{(\gamma_1 - \gamma_2)^2}{2\sigma_\gamma^2}\right), \\ F_v(v_2) &= \frac{1}{\sqrt{2\pi\sigma_v}} \exp\left(-\frac{(v_1 - v_2)^2}{2\sigma_v^2}\right). \end{aligned} \tag{2}$$

Assuming that the center of the circle is O, the model expression of the turning trajectory is established:

$$\begin{cases} x_2 = x_1 + R_0 \cos \alpha, \\ y_2 = y_1 - R_0 \sin \alpha. \end{cases} \tag{3}$$

Assuming that the center of the allowed maximum turning trajectory is represented by $O_1(x_1, y_1)$ and the center of the real turning trajectory is represented by $O_2(x_2, y_2)$, it is assumed that the trajectory of the real flight overlaps with the preset trajectory, which is generated by the true course angle, represented by α. Because global positioning system is widely used for navigation and positioning in the field of civil aviation transportation, its civil precision is usually about 50 meters [49]. At the same time, equipment error, installation error, and aerodynamic error exist in real environment and experiment. After taking all kinds of errors into consideration, a normal distribution relationship is established. Assuming that the maximum permissible heading angle is α_1 and the true heading angle is α_2, then

$$F_\alpha(\alpha_2) = \frac{1}{\sqrt{2\pi\sigma_\alpha}} \exp\left(-\frac{(\alpha_1 - \alpha_2)^2}{2\sigma_\alpha^2}\right). \tag{4}$$

According to the relevant provisions of aircraft operation attached to ICAO Annex 6, the σ_α value is 2.58°, without considering the case of $\alpha_1 = \alpha_2$, and the expression of α is established as follows:

$$\alpha = \begin{cases} \pi - \arctan\left(\dfrac{y_1}{x_1}\right), \\ 2\pi - \arctan\left(\dfrac{y_1}{x_1}\right). \end{cases} \tag{5}$$

3.2. Established Model of Crosswind Influence. Assuming that the experimental object is affected by the crosswind with wind speed of WS, according to the conservative principle, omnidirectional wind is used to represent the crosswind; then,

$$R_2 = R_1 + \frac{WS}{\mu}, \tag{6}$$

where, under the omnidirectional wind, the true turning radius is R_2 and the angle to complete the turn is μ. Therefore, under the influence of the above turning slope, height, and other factors, the trajectory deviation component S_{rd} can be expressed as follows:

$$S_{rd} = x_L - x_2 + R_1, \tag{7}$$

where x_L is a known quantity. The value of x_L is the value of the actual flight position of the experimental object in the coordinate system O_2.

3.3. Established Model of Straight Flight. Generally, in the straight flight stage, due to the influence of navigation equipment precision and wind, there are differences between the actual flight path and the preflight planned path. In the total flight time of the experiment, the experimental subjects spent more flight time in the straight way and less flight time in the turning way. If, in the advance path planning stage, the deviation caused by straight flight and turn flight is calculated separately and integrated, then this approach will increase the workload of preflight preparation [50]. According to the conservative principle of ICAO in the way of safety assessment, the deviation value of the straight line segment and the turning segment can be calculated uniformly, to obtain the total amount of deviation satisfying the two modes of flight, thus ensuring the adaptability of the calculation results.

Assumptions exist in space plane position point $A_3(x_3(t,t\Delta), y_3(t,t\Delta))$, it means, in the preset trajectory points, to allow maximum deviation, there is a position point $A_4(x_4(t,t\Delta), y_4(t,t\Delta))\cos^{-1}\theta$, and it means the current real trajectory point position. Because the experiment task is to fly straight and then temporarily not consider height variation, d means the distance between the two points above, flight time for $t\Delta$; then, we can get the space position of expression:

$$\begin{cases} x_3(t,t_\Delta) = \varepsilon_{3x} + \left(-d_3 + \int_0^{t+t_\Delta} v_3(t)\mathrm{d}t\right)\cdot \cos\phi, \\ y_3(t,t_\Delta) = \varepsilon_{3y}, \end{cases} \begin{cases} x_4(t,t_\Delta) = \varepsilon_{4x}\cdot \cos\phi - \varepsilon_{4y}\cdot \sin\phi + \cos\beta\cos\phi\left(-d_4 + \int_{t_\Delta}^{t+t_\Delta} v_4(t)\mathrm{d}t\right), \\ y_4(t,t_\Delta) = \varepsilon_{4x}\cdot \sin\phi + \varepsilon_{4y}\cdot \cos\phi + \cos\beta\sin\phi\left(-d_4 + \int_{t_\Delta}^{t+t_\Delta} v_4(t)\mathrm{d}t\right), \end{cases} \tag{8}$$

where i is the number of the experimental subject, β is the position point with the maximum allowable deviation, ϕ is the real position point, there is an included angle between points β and ϕ and any point O on the preplanned trajectory in the flight direction, and ε is the coordinate system position tolerance. In the current case, the trigonometric relationship consisting of a line of points O, flight direction, and trajectory deviation values is established.

Suppose the time interval is $t\Delta$; then, $|x_{34}(t,t\Delta)|$ and $|y_{34}(t,t\Delta)|$, respectively, represent the position relationship of β and ϕ with respect to the position point O, and the relationship is as follows:

$$\begin{cases} x_{34}(t,t_\Delta) = \varepsilon_{3x} - \left(\varepsilon_{4x}\cos\phi - \varepsilon_{4y}\sin\phi\right) + S_{34x}(t,t_\Delta), \\ y_{34}(t,t_\Delta) = \varepsilon_{3y} - \left(\varepsilon_{4y}\sin\phi + \varepsilon_{4y}\cos\phi\right) + S_{34y}(t,t_\Delta), \end{cases} \begin{cases} S_{34x}(t,t_\Delta) = \cos\phi\left(-d_3 + \int_0^{t+t_\Delta} v_3(t)\mathrm{d}t\right) - \cos\phi\cos\beta\left(-d_4 + \int_{t_\Delta}^{t+t_\Delta} v_2(t)\mathrm{d}t\right), \\ S_{34y}(t,t_\Delta) = -\cos\beta\sin\phi\left(-d_4 + \int_{t_\Delta}^{t+t_\Delta} v_4(t)\mathrm{d}t\right), \end{cases} \tag{9}$$

where position point O is the initial point, the experimental subject and point O exist at points $S_{34x}(t,t\Delta)$ and $S_{34y}(t,t\Delta)$, and points $S_{34x}(t,t\Delta)$ and $S_{34y}(t,t\Delta)$ are symmetric with the preplanned trajectory, the three establish trigonometric relations. Then, when $t\Delta$ is a specific value that can be measured and obtained, the distance between two points can be obtained:

$$S_{34}(t,t_\Delta) = \sqrt{S_{34x}^2(t,t_\Delta) + S_{34y}^2(t,t_\Delta)}. \tag{10}$$

According to the above expression, the distance between the real flight trajectory position point and point O should be greater than the minimum safety distance, so the distance between the two points should be wider than 0, which is a positive number. If that is true, that means the mission can continue, in which the subject is at an appropriate range, and it satisfies the probability of safety collision and is not easy to have collision and conflict. If the conclusion is equal to 0 or less than 0, it means that the experimental subject is in the restricted range, or already in the dangerous area. According to the conservative principle, the expression of the minimum critical deviation component in the straight flight stage is obtained, and the relationship is as follows:

$$\left|S_{34}(t,t_\Delta)\right| = S_{L\min}. \tag{11}$$

After derivation, the total deviation M in the turning flight stage and the straight flight stage is obtained, and the expression is as follows:

$$S_{r\,d} + S_{L\min} = M. \tag{12}$$

3.4. Established Model of Safe Operation. The initial design of the model is as follows:

$$\begin{cases} w_1 = w_{mx} + w_{nx}, \\ w_2 = w_{my} + w_{ny}, \\ w_3 = w_{mz} + w_{nz}, \end{cases} \tag{13}$$

where w_{mx}, w_{my}, w_{mz} and w_{nz}, w_{ny}, w_{nz} are the dimensions of transport aircraft and experimental objects and the parameters are length, wingspan, and height in order. If the transport aircraft and the experimental subject regard each other as points, when their respective initial models are in contact, it can be considered that the operation conflict has been generated and the safety is affected (see Figure 1).

The improved model is established by comprehensively considering all the safe operation parameters, and the relationship is as follows:

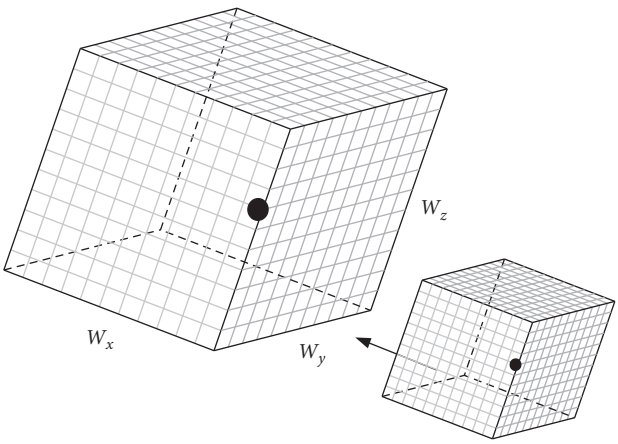

Figure 1: The initial model and model contact.

$$G = \frac{A}{M}\left(w_1 + \frac{U_s w_2}{V_s}\right)P\left(1 + \frac{W_s w_2}{V_s w_3}\right)\eta + \frac{B}{M}\left(w_3 + \frac{U_o w_2}{V_o}\right)P\left(1 + \frac{W_o w_2}{V_o w_3}\right)\eta, \tag{14}$$

where G is the value of conflict probability obtained through calculation by importing the security operation parameters into the improved model, η is the operating sorties of transport aircraft per hour, A represents for the number of experimental subjects (UAV), which is consistent with the flight direction and flight trend of transport aircraft in the current airspace, and B also represents for the number of experimental subjects (UAV), which is remains opposite with the transport aircraft in flight direction and trend within the current airspace. Assuming that when the conflict occurs if the flight trend of the experimental subject and the transport aircraft is consistent, then U_s,V_s, and W_s are used to represent the velocity data parallel to the flight direction, perpendicular to the flight direction, and above the flight direction. Similarly, U_o, V_o, and W_o are data under the trend of remaining relative flight. P is the probability that the transport aircraft and the experimental subject (UAV) fly over each other.

In order to make the experimental conclusion adaptable to civil aviation manned transport aircraft, the parameter composition and constant setting in the model should meet the requirements of ICAO on flight standards and safe operation, etc [51]. Computational and research objects mainly include experimental objects (UAV), other aircraft similar in type to experimental objects, and civil aviation manned transport aircraft. Assume that φ_1 is the quality of flight mission execution, φ_2 is the pilot operation technology, and φ_3 is the probability of operating failure per 100,000 hours, and statistics of real operation data in recent ten years is shown in Table 1 [52, 53]. Because the research objects are civil aviation manned transport aircraft and experimental objects (UAV), civil aviation transport flight has a strict set of retention barriers, as required by the law and regulations, and it is permissible for a civilian transport aircraft with a fault to fly missions; according to the conservative principle, the operation failure probability of transport aircraft can refer to the ICAO regulation, namely, the maximum number of failures per 100,000 hours allowed.

According to the preset data and real data in the table, the expression of φ_1 is obtained as follows:

$$\varphi_1 = \sum_{i=1}^{n} E_i T_i, \tag{15}$$

where E_i is the applicability of flight status and T_i is the number of aircraft in the experimental airspace. In addition, according to formula (15), E_i is used to represent the failure data per 100,000 hours and T_i is used to represent the failure interval data. So, the expression of φ_2 can be obtained.

Pilot's flying skills are mainly reflected in the civil aviation manned transport aircraft, and UAV is not affected by this factor and can directly use the former accident ratio 9.62%; then, $\varphi_3 = 1–0.0962 = 0.9$.

To sum up, according to the provisions of ICAO, one conflict in safe operation will be recorded as two accidents, and the evaluation model of safe operation conflict will be established. The expression RE is as follows:

$$RE = 2\left(1 - \varphi_1\right) \cdot \varphi_2 \cdot \left(1 - \varphi_3\right) \cdot G. \tag{16}$$

If the calculated result of RE is set as the probability value of safe operation conflict, which is constant and meets the requirements of ICAO for safe operation, the improved model is used for analysis and calculation. Assuming that the relative motion states of the transport aircraft and the experimental subject are unchanged, the structure of the airspace remains unchanged, the operating conditions remain unchanged, then $(A + B)$ can be regarded as the sum of the number of aircraft in the current airspace so that the airspace density data can be obtained. This calculation result is a quantified airspace management conclusion and meets the flight standard of safe operation conflict probability.

4. Design of Simulation Experiment

An airport in the south of China was selected for the simulation experiment, and the flight performance data of the research object were referred to Airbus 320 and AT200, as shown in Table 2 [54, 55]. Because the AT200 and the same class of UAV, which are large fixed-wing UAV, must take off from civilian airports, so, in flight, take-off climb and approach phase is more prone to conflict. The parameters were added into the improved calculation model, the influence of flight trajectory deviation is considered, and the conflict probability value of safe operation is considered, so the minimum interval value between the research objects can be calculated to obtain the turning flight stage and the straight flight stage. The above calculation results can be used as the capacity conclusion of the flight airspace, which is a quantitative result.

Considering the airport information, consider the route and route point information and then start the design of the simulation experiment. Normally, July and August are the busiest months for transport aircraft; select the hourly flight flow in the low-altitude airspace within the research airspace,

Table 1: The maintenance actions and costs corresponding to different maintenance levels.

Type	Number of serious failures per 100,000 flight hours	MTBF (hour)	Applicability of flight status (%)	Task completion schedule (%)
Airbus 320 (no statistical NEO)	0.20	48.5	12	85
Boeing 737NG (800)	0.20	49.2	12	85
AT-200	12	29.5	96	86
Y-5 (UAV)	9	23.4	87	78
Predator	34	44.1	73	79
Pioneer	248	19.2	77	83
Hunter	15	10.9	96	81

Table 2: Parameters of simulation experiment.

Type	Data	Type	Data
V (km/h)	650	w_{mx} (m)	37.57
Γ	45	w_{my} (m)	34.10
σ_v	15	w_{mz} (m)	11.76
σ_α	2	w_{nz} (m)	11.84
P	0.5	w_{ny} (m)	12.80
H	—	w_{nz} (m)	4.04
V_S or V_O	5.23	U_s	3
W_S or W_O	0.58	U_o	497
W_S (km/h)	30	Altitude (m)	3200

using this data as the value of η. According to the influence of the cutting angle and heading angle on the experimental design, three different angle relationships are established.

Design 1. When the two planes are flying in the same direction and the transport aircraft is in the departure and climbing stage, in this case, transport aircraft would travel from low-altitude airspace to medium altitude airspace, or higher altitude, so set the maximum $\beta = 15^\circ$ and $\varphi = 20^\circ$, and this is according to ICAO operating standard.

Design 2. When the two planes are flying face to face and the transport aircraft is in the arrived stage, in this case, the transport aircraft has a high speed, and set $\beta = 5^\circ$ and $\varphi = 20^\circ$.

Design 3. When the two planes are flying face to face and both planes are flying horizontally, in this case, the flight status of transport aircraft is relatively stable, and the possibility of sudden changes in operating conditions is low, and set $\beta = 0^\circ$ and $\varphi = 15^\circ$.

The above three conditions were established to simulate the situation where the transport aircraft and the UAV had a high probability of conflict, increase the redundancy of experimental results, and adhere to the conservative principle.

According to the design of the experiment, parameters are added into the model, and the conclusion can be obtained through equations (12) and (16):

(i) The first case, $M_{(1)} > 3.116$km, $(A+B)_1 = 1.203 \times 10^{-3}$ (frame/km^3)

(ii) The second case, $M_{(2)} > 4.214$km, $(A+B)_2 = 0.895 \times 10^{-3}$ (frame/km^3)

(iii) The third case, $M_{(3)} > 3.762$km, $(A+B)_3 = 1.054 \times 10^{-3}$ (frame/km^3)

The experimental results can be made into a graph to show the relationship between the conflict probability of safe operation and the interval between the aircraft, and the relation of density is obtained, as shown in Figures 2 and 3.

5. Description of Application and Innovation

According to three groups of experiments, when the experimental subjects are in the stage of arrival and departure flight, they will have a large space change and speed change for climbing. For this reason, the amount that can be used to adjust the heading angle is reduced, resulting in insufficient space for the flight path to be used for adjustment or avoidance in preflight preparation, and there will a high probability of collision, and it is very likely to happen to intrude into another airspace. At the same time, it also shows that, in this operating state, the density of joint operating aircraft needs to keep low, which conforms to the objective facts. It can be concluded that, in the low-altitude airspace, the adjustment variation of heading angle can provide data support for calculating the probability of collision.

Similar evaluation models mostly exist in the collaborative evaluation between ground operating equipment and aircraft, and the main reason is that both civil aviation and general aviation aircraft perform missions in low-altitude airspace using conventional or visual flight procedures, depending on the location of ground equipment, ground visual references, and route point setting points and lack of accurate positioning ability and monitoring equipment. As a result, the data of the evaluation model contains the positioning tolerance value, so the practical guiding significance is not sufficient, and does not apply to the evaluation of the mixed airspace for large UAV and manned aircraft [56].

In order to reflect the advantages of PTD-MI algorithm in dealing with wide-area space problems, according to the design of simulation experiment, the data in Table 2 were added into the evaluation model of GBAS, and the calculation results are shown in Table 3.

Among them, the experimental results under the GBAS model are divided into two situations: the results within 15 kilometers and the results outside 15 kilometers. Because

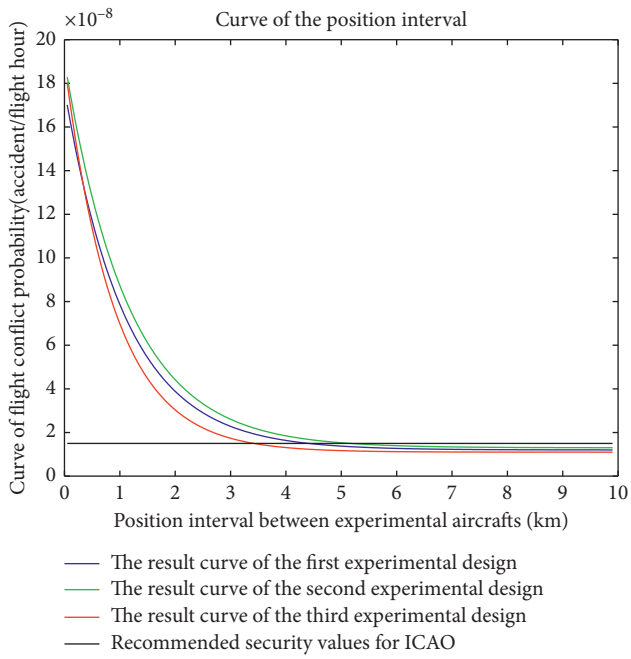

Figure 2: Curve of the position interval.

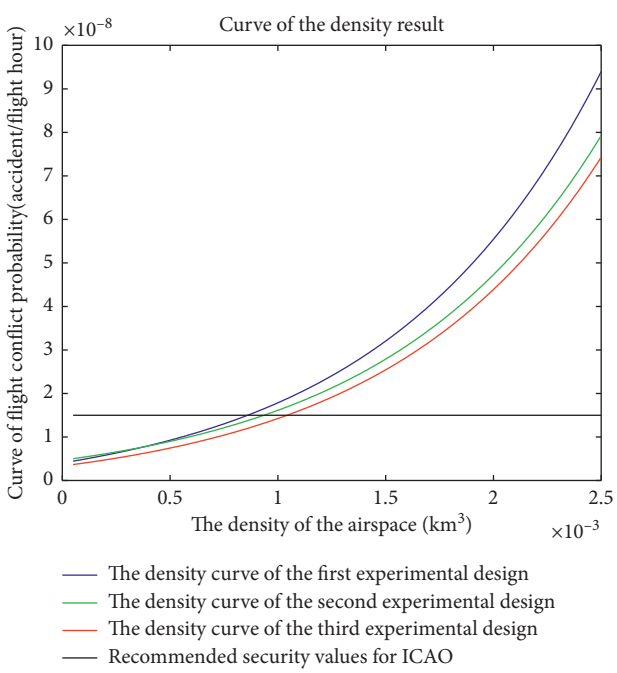

Figure 3: Curve of the density result.

the distance between ground equipment and aircraft increases, the positioning error of ground equipment also increases. According to the results of the third case of experiments, the flight procedure protection area is drawn, as shown in Figures 4 and 5.

As shown in the picture, there are three colors: white, gray, and black, and they represent the operating areas based on the above two evaluation conclusions. The operation area is divided into three layers: the first layer is the area where flight missions can be carried out, the second layer is the buffer area where the possibility of conflict needs to be carefully handled, and the third layer is the area where UAV is prohibited to fly. Taking the approach stage and low-altitude airspace as examples, the altitude of low-altitude airspace shall be calculated as below 6000 meters (inclusive), and the spatial planning quantity of simulation experiment results is shown in Table 4. In Figures 6 and 7, the parameters of simulation experiment are set as follows: the elevation of the airport is 1150 meters, and the average mountain height within the range of the approach stage is 1372.26 meters.

The application effect of the experimental results shows that due to the use of the PTD-MI model, the volume of the first layer airspace increases by 10.04%, 9.54%, and 8.09%, which indicates that the flight area of the large UAV is expanded, and the application effect is excellent.

The reasons for the above results can be summarized as three points. First, the GBAS evaluation model evaluates the working data of ground equipment [57]. Thie equipment uses 30 MHz–300 MHz electromagnetic wave for data transmission to realize navigation and positioning functions [58]. Therefore, there will be an attenuation of efficiency when information is transmitted in a large area, which leads to the fact that the M value is not a constant quantity. Its positioning tolerance value will increase with the expansion of the evaluation airspace [59], so it is not suitable for the research of position interval in the overall airspace. This method is suitable for evaluation in a small space such as near the runway. Second, the ground equipment cannot be built at the midpoint of the runway entrance, so the deviation of heading angle will inevitably occur [60], and when the flight value is smaller, the accuracy of the data is higher, so the error is very obvious due to the existence of deviation. Thirdly, relevant parameters

Table 3: Comparison of experimental results based on the two algorithms.

Experimental design sequence number	Types of experimental results	Model of GBAS (within 15 kilometers; outside 15 kilometers)	PTD-MI
The first case	The total deviation M, km	>2.588; >3.844	>3.116
	Total number of aircraft $(A+B)$, frame/km^3	1.281×10^{-3}; 0.982×10^{-3}	1.203×10^{-3}
The second case	The total deviation M, km	>3.602; >5.013	>4.214
	Total number of aircraft $(A+B)$, frame/km^3	0.962×10^{-3}; 0.615×10^{-3}	0.895×10^{-3}
The third case	The total deviation M, km	>3.116; >4.607	>3.762
	Total number of aircraft $(A+B)$, frame/km^3	1.138×10^{-3}; 0.807×10^{-3}	1.054×10^{-3}

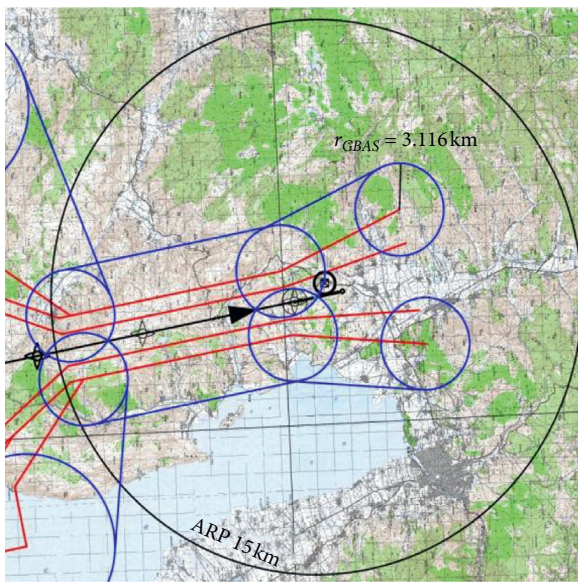

Figure 4: The result of approach phase based on the GBAS model.

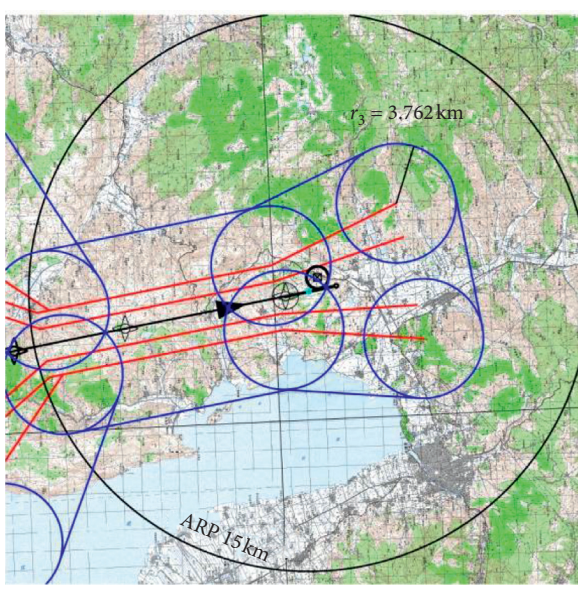

Figure 5: The result of approach phase based on PTD-MI.

Table 4: Spatial planning quantity based on simulation experiment results.

Layer number	Simulation experiment of the first case (km^3)		Simulation experiment of the second case (km^3)		Simulation experiment of the third case (km^3)	
	GBAS	PTD-MI	GBAS	PTD-MI	GBAS	PTD-MI
The first layer	8464.73	9409.55	8016.88	8863.63	8542.81	9288.82
The second layer	1092.78	910.38	1302.83	1059.76	1169.32	988.95
The third layer	2387.95	2387.95	2387.95	2387.95	2387.95	2387.95

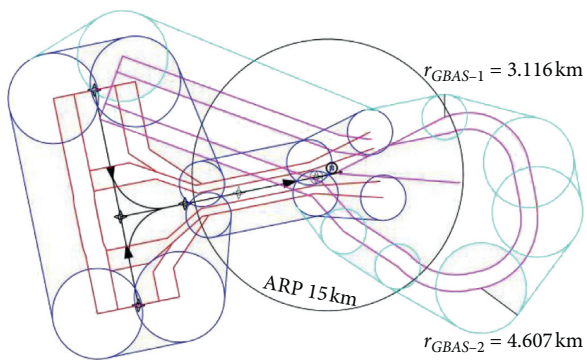

Figure 6: The results of mixed airspace based on the GBAS model.

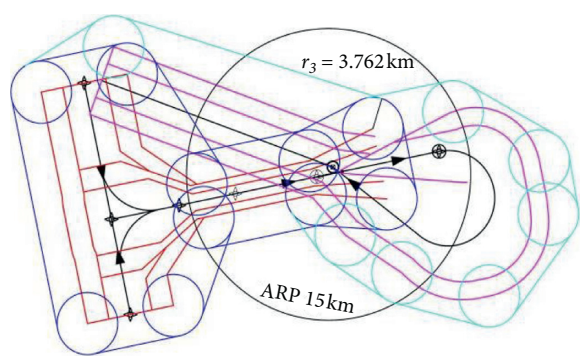

Figure 7: The result of mixed airspace based on PTD-MI.

based on satellite positioning are not included in the ground equipment evaluation model, which will greatly increase the inaccuracy of the calculation conclusions in the application of space problems. Based on the above three reasons, it can be found that the experimental design takes data accuracy, safety margin and mixed airspace operation into full consideration [61]. The conclusion obtained by the PTD-MI algorithm calculation makes the M value in a more reasonable range and improves the scientific nature of the density value.

There are two innovations about the PTD-MI algorithm. First, the model fully considers the flight characteristics of the turning stage and the straight stage and adds the flight attitude data into the evaluation model to obtain the results. This is the first time to study such a problem. Second, take the flight conflict safety value recommended by ICAO as the basis of experimental design [62], the first discussion of flight planning in the mixed airspace, including conflict assessment between large UAV and manned aircraft, and these conclusions are applicable to preflight planning of flight missions in the overall airspace.

6. Summary and Conclusions

In this paper, the concept of PTD is introduced, and a corresponding PTD-MI algorithm is set up. According to the actual operation and production situation, the simulation experiment is designed and the experimental results are shown, and the experimental results reflect the application effect of operation safety evaluation. In addition, the experimental results of the GBAS model are compared and analyzed, and the conclusions are as follows:

(1) The PTD-MI algorithm is consistent with the requirements of rationality and generality in the actual operation, which is conducive to maintaining the accuracy of the experimental results. The algorithm maintains the characteristics of large UAV at all flight stages and under the influence of crosswind, and it provides an optimal basis to deal with airspace planning problems and widens the application range of PTD-MI algorithm.

(2) In the simulation experiments, the PTD-MI algorithm shows excellent and effective computing performance. In the prediction of the flight path within the local airspace of the airport, the acceptable calculation results can be provided. By comparing and analyzing the results of PTD-MI algorithm and GBAS algorithm, the superiority of PTD-MI algorithm in dealing wide-area space problems is shown.

(3) Due to the reference of ICAO flight standard parameters, the calculation results derived from PTD-MI algorithm are applicable to the operation safety evaluation of civil aviation.

For future works, we recommend applications of the proposed method to other UAV systems [63–67], adaptive control techniques [68–72], applications of optimization methods such as differential evolution, particle swarm, whale optimizer, differential search, and other optimizers for optimizing parts of the process [73–78], distributed optimization [79], and other optimization forms such as robust, memetic, many objective, multiobjective, and fuzzy optimization [80–87].

Data Availability

The data used to support the findings of the study are available within the article.

Conflicts of Interest

The authors declare no conflicts of interest.

Authors' Contributions

X. M. and X.Z. conceptualized the study; X. M. developed methodology; X. Z. helped with software; H. W. and S. D. validated the study, X. M. carried out formal analysis; X. L. investigated the study; X. M. collected resources; X. M. carried out data curation; X. M. wrote the original draft; X. Z. reviewed and edited the article; X. M. visualized the study; H. W. and S. D. supervised the study; X. M. administrated the project; X. M. helped with funding acquisition. All authors have read and agreed to the published version of the manuscript.

Acknowledgments

This research was supported by Civil Aviation Administration of China, development foundation educational talents program (no.14002600100018J034) and general foundation of Civil Aviation Flight University of China (J2018067). The funders had no role in the design of the study, in the collection, analyses, or interpretation of data, in the writing of the manuscript, or in the decision to publish the results.

References

[1] X. Zhang, J. J. Zhang, and S. F. Wu, "Aircraft monitoring by the fusion of satellite and ground ADS-B data," *Acta Astronautica*, vol. 11, pp. 398–405, 2017.

[2] H. Li, A. P. Teixeira, and C. Guedes Soares, "A two-stage failure mode and effect analysis of offshore wind turbines," *Renewable Energy*, vol. 162, pp. 1438–1461, 2020.

[3] J. J. Sofonia, S. Phinn, C. Roelfsema, F. Kendoul, and Y. Rist, "Modelling the effects of fundamental UAV flight parameters on LiDAR point clouds to facilitate objectives-based planning," *ISPRS Journal of Photogrammetry and Remote Sensing*, vol. 149, pp. 105–118, 2019.

[4] M. Wang and H. Chen, "Chaotic multi-swarm whale optimizer boosted support vector machine for medical diagnosis," *Applied Soft Computing*, vol. 88, Article ID 105946, 2020.

[5] X. Zhao, X. Zhang, Z. Cai et al., "Chaos enhanced grey wolf optimization wrapped ELM for diagnosis of paraquat-poisoned patients," *Computational Biology and Chemistry*, vol. 78, pp. 481–490, 2019.

[6] Y. Zhang, "Towards augmented kernel extreme learning models for bankruptcy prediction: algorithmic behavior and comprehensive analysis," *Neurocomputing*, vol. 430, pp. 185–212, 2020.

[7] X. Zhang, "Robust feature learning for adversarial defense via hierarchical feature alignment," *Information Sciences*, vol. 10, p. 42, 2020.

[8] N. A. Golilarz, H. Gao, R. Kumar, L. Ali, Y. Fu, and C. Li, "Adaptive wavelet based MRI brain image de-noising," *Frontiers in Neuroscience*, vol. 14, p. 728, 2020.

[9] N. A. Golilarz, H. Gao, W. Ali, and M. Shahid, "Hyperspectral remote sensing image de-noising with three dimensional wavelet transform utilizing smooth nonlinear soft thresholding function," in *Proceedings of the 15th International Computer Conference on Wavelet Active Media Technology and Information Processing*, pp. 142–146, Chengdu, China, December 2018.

[10] H. Chen, A. A. Heidari, H. Chen, M. Wang, Z. Pan, and A. H. Gandomi, "Multi-population differential evolution-assisted Harris hawks optimization: framework and case studies," *Future Generation Computer Systems*, vol. 111, pp. 175–198, 2020.

[11] Y. Xu, H. Chen, J. Luo, Q. Zhang, S. Jiao, and X. Zhang, "Enhanced Moth-flame optimizer with mutation strategy for global optimization," *Information Sciences*, vol. 492, pp. 181–203, 2019.

[12] C. Li, L. Hou, B. Y. Sharma et al., "Developing a new intelligent system for the diagnosis of tuberculous pleural effusion," *Computer Methods and Programs in Biomedicine*, vol. 153, pp. 211–225, 2018.

[13] J. Xia, H. Chen, Q. Li et al., "Ultrasound-based differentiation of malignant and benign thyroid Nodules: an extreme learning machine approach," *Computer Methods and Programs in Biomedicine*, vol. 147, pp. 37–49, 2017.

[14] L. Shen, H. Chen, Z. Yu et al., "Evolving support vector machines using fruit fly optimization for medical data classification," *Knowledge-Based Systems*, vol. 96, pp. 61–75, 2016.

[15] C. Yu, "SGOA: annealing-behaved grasshopper optimizer for global tasks," *Engineering with Computers*, vol. 1, pp. 1–28, 2021.

[16] M. A. Lotufo, L. Colangelo, and C. Perez-Montenegro, "UAV quadrotor attitude control: an ADRC-EMC combined approach," *Control Engineering Practice*, vol. 11, pp. 13–22, 2018.

[17] H.-L. Chen, G. Wang, C. Ma, Z.-N. Cai, W.-B. Liu, and S.-J. Wang, "An efficient hybrid kernel extreme learning machine approach for early diagnosis of Parkinson′s disease," *Neurocomputing*, vol. 184, pp. 131–144, 2016.

[18] J. Hu, "Orthogonal learning covariance matrix for defects of grey wolf optimizer: insights, balance, diversity, and feature selection," *Knowledge-Based Systems*, vol. 213, Article ID 106684, 2020.

[19] X. Zhang, T. Wang, W. Luo, and P. Huang, "Multi-level fusion and attention-guided CNN for image dehazing," *IEEE Transactions on Circuits and Systems for Video Technology*, vol. 99, p. 1, 2020.

[20] X. Zhang, "Pyramid channel-based feature attention network for image dehazing," *Computer Vision and Image Understanding*, vol. 197–198, Article ID 103003, 2020.

[21] H. Li, H.-Z. Huang, Y.-F. Li, J. Zhou, and J. Mi, "Physics of failure-based reliability prediction of turbine blades using multi-source information fusion," *Applied Soft Computing*, vol. 72, pp. 624–635, 2018.

[22] H. Li, H. Diaz, and C. G. Soares, "A developed failure mode and effect analysis for floating offshore wind turbine support structures," *Renewable Energy*, vol. 164, pp. 133–145, 2020.

[23] J.. Marion, P. Letortu, and T.. Claire, "UAV survey of a coastal cliff face-Selection of the best imaging angle," *Measurement*, vol. 24, pp. 110–117, 2019.

[24] D. Zhao, "Chaotic random spare ant colony optimization for multi-threshold image segmentation of 2D Kapur entropy," *Knowledge-Based Systems*, vol. 216, Article ID 106510, 2020.

[25] X. Zhang, M. Fan, D. Wang, P. Zhou, and D. Tao, "Top-k feature selection framework using robust 0-1 integer programming," *IEEE Transactions on Neural Networks and Learning Systems*, vol. 31, p. 1, 2020.

[26] X. Zhao, D. Li, B. Yang, C. Ma, Y. Zhu, and H. Chen, "Feature selection based on improved ant colony optimization for

online detection of foreign fiber in cotton," *Applied Soft Computing*, vol. 24, pp. 585–596, 2014.

[27] X. Zhang, D. Wang, Z. Zhou, and Y. Ma, "Robust low-rank tensor recovery with rectification and alignment," *IEEE Transactions on Pattern Analysis and Machine Intelligence*, vol. 34, p. 1, 2019.

[28] R. U. Khan, X. Zhang, R. Kumar, A. Sharif, N. A. Golilarz, and M. Alazab, "An adaptive multi-layer botnet detection technique using machine learning classifiers," *Applied Sciences*, vol. 9, no. 11, p. 2375, 2019.

[29] N. K. Jain, U. Nangia, and J. Jain, "A review of particle swarm optimization," *Journal of The Institution of Engineers (India): Series B*, vol. 99, no. 4, pp. 407–411, 2018.

[30] S. Aggarwal and N. Kumar, "Path planning techniques for unmanned aerial vehicles: a review, solutions, and challenges," *Computer Communications*, vol. 149, pp. 270–299, 2020.

[31] W. Peng, Z. S. Ye, and N. Chen, "Bayesian deep-learning-based health prognostics toward prognostics uncertainty," *IEEE Tra. onInd. Ele.*vol. 67, no. 3, pp. 2283–2293, 2019.

[32] Z. Bai, L. Y. Ling, and T. Han, "Research on attiude stabilitu of small UAV," *Computer Simulation*, vol. 466, pp. 16–20, 2017.

[33] N. A. Golilarz, H. Gao, and H. Demirel, "Satellite image de-noising with harris hawks meta heuristic optimization algorithm and improved adaptive generalized Gaussian distribution threshold function," *IEEE Access*, vol. 7, pp. 57459–57468, 2019.

[34] N. A. Golilarz, M. Mirmozaffari, T. A. Gashteroodkhani et al., "Optimized wavelet-based satellite image de-noising with multi-population differential evolution-assisted harris hawks optimization algorithm," *IEEE Access*, vol. 8, pp. 133076–133085, 2020.

[35] G. Xiang and C. Guedes Soares, "Improved dynamical modelling of freely falling underwater cylinder based on CFD," *Ocean Engineering*, vol. 211, p. 107538, 2020.

[36] H. Li and C. G. Soares, "Reliability analysis of floating offshore wind turbines support structure using hierarchical Bayesian network," in *Proceedings of the 29th European Safety and Reliability Conference*, pp. 2489–2495, Hannover, Germany, September 2019.

[37] M. Riahi Manesh and N. Kaabouch, "Analysis of vulnerabilities, attacks, countermeasures and overall risk of the automatic dependent surveillance-broadcast (ADS-B) system," *International Journal of Critical Infrastructure Protection*, vol. 19, pp. 16–31, 2017.

[38] M. Wang, H. Chen, B. Yang et al., "Toward an optimal kernel extreme learning machine using a chaotic moth-flame optimization strategy with applications in medical diagnoses," *Neurocomputing*, vol. 267, pp. 69–84, 2017.

[39] L. Hu, G. Hong, J. Ma, X. Wang, and H. Chen, "An efficient machine learning approach for diagnosis of paraquat-poisoned patients," *Computers in Biology and Medicine*, vol. 59, pp. 116–124, 2015.

[40] X. Xu and H.-l. Chen, "Adaptive computational chemotaxis based on field in bacterial foraging optimization," *Soft Computing*, vol. 18, no. 4, pp. 797–807, 2014.

[41] Y. Zhang, "Boosted binary Harris hawks optimizer and feature selection," *Engineering with Computers*, vol. 25, p. 26, 2020.

[42] J. Tu, H. Chen, J. Liu et al., "Evolutionary biogeography-based whale optimization methods with communication structure: towards measuring the balance," *Knowledge-Based Systems*, vol. 212, p. 106642, 2021.

[43] N. A. Golilarz, N. Robert, J. Addeh, and A. Salehpour, "Translation invariant wavelet based noise reduction using a new smooth non-linear improved thresholding function," *Computational Research Progress in Applied Science and Engineering*, vol. 3, no. 3, pp. 104–108, 2017.

[44] M. Yazdi, F. Nikfar, and M. Nasrabadi, "Failure probability analysis by employing fuzzy fault tree analysis," *International Journal of Intelligent Engineering and Systems*, vol. 8, no. 2, pp. 1177–1193, 2017.

[45] M. Khatami and S. H. Zegordi, "Coordinative production and maintenance scheduling problem with flexible maintenance time intervals," *Journal of Intelligent Manufacturing*, vol. 28, no. 4, pp. 857–867, 2017.

[46] C. Liu, N. X. Luo, and L. B. Lu, "Rotorcraft route planning based on artificial potential field," *Construction Simulator*, vol. 81, pp. 101–105, 2017.

[47] C.-G. Huang, H.-Z. Huang, and Y.-F. Li, "A bidirectional LSTM prognostics method under multiple operational conditions," *IEEE Transactions on Industrial Electronics*, vol. 66, no. 11, pp. 8792–8802, 2019.

[48] Y. Liu, Y. Chen, and T. Jiang, "On sequence planning for selective maintenance of multi-state systems under stochastic maintenance durations," *European Journal of Operational Research*, vol. 268, no. 1, pp. 113–127, 2018.

[49] C. D. Dao and M. J. Zuo, "Optimal selective maintenance for multi-state systems in variable loading conditions," *Reliability Engineering & System Safety*, vol. 166, pp. 171–180, 2017.

[50] W. Shan, "Double adaptive weights for stabilization of moth flame optimizer: balance analysis, engineering cases, and medical diagnosis," *Knowledge-Based Systems*, vol. 13, Article ID 106728, 2020.

[51] H. Yu, "Dynamic Gaussian bare-bones fruit fly optimizers with abandonment mechanism: method and analysis," *Engineering with Computers*, pp. 1–29, 2020.

[52] X. Zhang, R. Jiang, T. Wang, and J. Wang, "Recursive neural network for video deblurring," *IEEE Transactions on Circuits and Systems for Video Technology*, vol. 99, p. 1, 2020.

[53] M. Yazdi, A. Nedjati, E. Zarei, and R. Abbassi, "A novel extension of DEMATEL approach for probabilistic safety analysis in process systems," *Safety Science*, vol. 121, pp. 119–136, 2020.

[54] T. Jiang and Y. Liu, "Selective maintenance strategy for systems executing multiple consecutive missions with uncertainty," *Reliability Engineering & System Safety*, vol. 193, Article ID 106632, 2020.

[55] K. B. Richard, B. H. Stephen, M. M. Douglas, and S. Eric, "Introduction to unmanned aircraft systems," 2014.

[56] N. A. Golilarz and H. Demirel, "Thresholding neural network (TNN) based noise reduction with a new improved thresholding function," *Computational Research Progress in Applied Science & Engineering*, vol. 3, no. 2, pp. 81–84, 2017.

[57] General Aviation Branch of China Air Transport Association, *China's Development Report on Civil Drones*, General Aviation Branch of China Air Transport Association, Taipei, Taiwan, 2019.

[58] M. Yazdi and S. Kabir, "A fuzzy Bayesian network approach for risk analysis in process industries," *Process Safety and Environmental Protection*, vol. 111, pp. 507–519, 2017.

[59] N. A. Golilarz, H. Demirel, and H. Gao, "Adaptive generalized Gaussian distribution oriented thresholding function for image de-noising," *International Journal of Advanced Computer Science and Applications*, vol. 10, no. 2, pp. 10–15, 2019.

[60] Z. Shao, F. Yan, and Z. Zhou, "Path planning for multi-UAV formation rendezvous based on distributed coopera- tive

particle swarm optimization," *Applied Sciences-Base*, vol. 16, 2019.

[61] C. Diallo, U. Venkatadri, A. Khatab, and Z. Liu, "Optimal selective maintenance decisions for large serial k-out-of-n: G systems under imperfect maintenance," *Reliability Engineering & System Safety*, vol. 175, pp. 234–245, 2018.

[62] H. Li, C. Guedes Soares, and H.-Z. Huang, "Reliability analysis of a floating offshore wind turbine using Bayesian Networks," *Ocean Engineering*, vol. 217, Article ID 107827, 2020.

[63] J. Hu, M. Wang, C. Zhao, Q. Pan, and C. Du, "Formation control and collision avoidance for multi-UAV systems based on Voronoi partition," *Science China Technological Sciences*, vol. 63, no. 1, pp. 65–72, 2020.

[64] J. Hu, H. Zhang, L. Liu, X. Zhu, C. Zhao, and Q. Pan, "Convergent multiagent formation control with collision avoidance," *IEEE Transactions on Robotics*, vol. 36, no. 6, pp. 1805–1818, 2020.

[65] J.-w. Hu, B.-y. Zheng, C. Wang et al., "A survey on multi-sensor fusion based obstacle detection for intelligent ground vehicles in off-road environments," *Frontiers of Information Technology & Electronic Engineering*, vol. 21, no. 5, pp. 675–692, 2020.

[66] J. Zhao, J. Liu, J. Jiang, and F. Gao, "Efficient deployment with geometric analysis for mmWave UAV communications," *IEEE Wireless Communications Letters*, vol. 9, no. 7, pp. 1115–1119, 2020.

[67] G. Zhu, S. Wang, L. Sun, W. Ge, and X. Zhang, "Output feedback adaptive dynamic surface sliding-mode control for quadrotor UAVs with tracking error constraints," *Complexity*, vol. 2020, Article ID 8537198, 23 pages, 2020.

[68] J. Wang, P. Zhu, B. He, G. Deng, C. Zhang, and X. Huang, "An adaptive neural sliding mode control with ESO for uncertain nonlinear systems," *International Journal of Control, Automation and Systems*, vol. 10, p. 1, 2020.

[69] Y. Huang, J. Wang, F. Wang, and B. He, "Event-triggered adaptive finite-time tracking control for full state constraints nonlinear systems with parameter uncertainties and given transient performance," *ISA Transactions*, vol. 108, pp. 131–143, 2020.

[70] J. Wang, Y. Huang, T. Wang, C. Zhang, and Y. h. Liu, "Fuzzy finite-time stable compensation control for a building structural vibration system with actuator failures," *Applied Soft Computing*, vol. 93, Article ID 106372, 2020.

[71] Z. Chen, J. Wang, K. Ma, X. Huang, and T. Wang, "Fuzzy adaptive two-bits-triggered control for nonlinear uncertain system with input saturation and output constraint," *International Journal of Adaptive Control and Signal Processing*, vol. 34, no. 4, pp. 543–559, 2020.

[72] X. Zhang, Y. Wang, X Chen et al., "Decentralized adaptive neural approximated inverse control for a class of large-scale nonlinear hysteretic systems with time delays," *IEEE Transactions on Systems, Man, and Cybernetics: Systems*, vol. 49, no. 12, pp. 2424–2437, 2018.

[73] J. Liu, C. Wu, G. Wu, and X. Wang, "A novel differential search algorithm and applications for structure design," *Applied Mathematics and Computation*, vol. 268, pp. 246–269, 2015.

[74] G. Sun, B. Yang, Z. Yang, and G. Xu, "An adaptive differential evolution with combined strategy for global numerical optimization," *Soft Computing*, vol. 68, pp. 1–20, 2019.

[75] G. Sun, C. Li, and L. Deng, "An adaptive regeneration framework based on search space adjustment for differential evolution," *Neural Computing and Applications*, pp. 1–7, 2021.

[76] B. Bai, Z. Guo, C. Zhou, W. Zhang, and J. Zhang, "Application of adaptive reliability importance sampling-based extended domain PSO on single mode failure in reliability engineering," *Information Sciences*, vol. 546, pp. 42–59, 2021.

[77] Y. Cao, Y. Li, G. Zhang, K. Jermsittiparsert, and M. Nasseri, "An efficient terminal voltage control for PEMFC based on an improved version of whale optimization algorithm," *Energy Reports*, vol. 6, pp. 530–542, 2020.

[78] N. Gao, D. Luo, B. Cheng, and H. Hou, "Teaching-learning-based optimization of a composite metastructure in the 0–10 kHz broadband sound absorption range," *The Journal of the Acoustical Society of America*, vol. 148, no. 2, pp. EL125–EL129, 2020.

[79] H.-J. Ma, G.-H. Yang, and T. Chen, "Event-Triggered optimal dynamic formation of heterogeneous affine nonlinear multiagent systems," *IEEE Transactions on Automatic Control*, vol. 66, no. 2, pp. 497–512, 2021.

[80] H. Chen, H. Qiao, L. Xu, Q. Feng, and K. Cai, "A fuzzy optimization strategy for the implementation of RBF LSSVR model in vis-NIR analysis of pomelo maturity," *IEEE Transactions on Industrial Informatics*, vol. 15, no. 11, pp. 5971–5979, 2019.

[81] S. Qu, Y. Han, Z. Wu, and H. Raza, "Consensus modeling with asymmetric cost based on data-driven robust optimization," *Group Decision and Negotiation*, pp. 1–38, 2020.

[82] B. Cao, S. Fan, J. Zhao, P. Yang, K. Muhammad, and M. Tanveer, "Quantum-enhanced multiobjective large-scale optimization via parallelism," *Swarm and Evolutionary Computation*, vol. 57, Article ID 100697, 2020.

[83] B. Cao, J. Zhao, Y. Gu, Y. Ling, and X. Ma, "Applying graph-based differential grouping for multiobjective large-scale optimization," *Swarm and Evolutionary Computation*, vol. 53, Article ID 100626, 2020.

[84] B. Cao, X. Wang, W. Zhang, H. Song, and Z. Lv, "A many-objective optimization model of industrial internet of things based on private blockchain," *IEEE Network*, vol. 34, no. 5, pp. 78–83, 2020.

[85] B. Cao, W. Dong, Z. Lv, Y. Gu, S. Singh, and P. Kumar, "Hybrid microgrid many-objective sizing optimization with fuzzy decision," *IEEE Transactions on Fuzzy Systems*, vol. 28, no. 11, pp. 2702–2710, 2020.

[86] B. Cao, J. Zhao, P. Yang et al., "Multiobjective 3-D topology optimization of next-generation wireless data center network," *IEEE Transactions on Industrial Informatics*, vol. 16, no. 5, pp. 3597–3605, 2019.

[87] X. Fu, P. Pace, G. Aloi, L. Yang, and G. Fortino, "Topology optimization against cascading failures on wireless sensor networks using a memetic algorithm," *Computer Networks*, vol. 177, Article ID 107327, 2020.

Hindawi
Mathematical Problems in Engineering
Volume 2021, Article ID 5597414, 11 pages
https://doi.org/10.1155/2021/5597414

Research Article

Hybrid Numerical Simulation of Jet Blast Distance of a Departing Aircraft

Xin He,[1] Yaqing Chen,[2] Yilong Ma,[1] Dengfeng Hu,[1] and Haoran Gao[3]

[1]*Air Traffic Management College, Civil Aviation Flight University of China, Guanghan 618307, China*
[2]*CAAC Key Laboratory of Flight Technology and Safety, Civil Aviation Flight University of China, Guanghan 618307, China*
[3]*Institute Office, Civil Aviation Flight University of China, Guanghan 618307, China*

Correspondence should be addressed to Yaqing Chen; chenyaqingmail@sina.com

Received 2 February 2021; Revised 1 March 2021; Accepted 14 March 2021; Published 31 March 2021

Academic Editor: Mohammad Yazdi

A hybrid numerical simulation method was established by combining the Spalart-Allmaras (SA) turbulence model and detached eddy simulation (DES). Numerical simulations were carried out to model cold and hot spray conditions of a nozzle without considering the internal flow of an engine to determine jet conditions. Analysis results show that the calculated hot spray results more in line with the reality. The jet effect of a typical aircraft engine was simulated numerically to determine the distance influenced by the jet blast from a departing aircraft engine.

1. Introduction

To address the strains created by an increasing number of flights and the lack of airport support capability, major airports in China have been reconstructed and expanded. At present, more than ten airports in China have adopted a multiple runway operation mode [1–3]. Most of China's multiple runway airports have adopted a parallel runway mode, making it difficult to avoid the problem of runway crossings during actual operation. China has the following runway-crossing protocols. First, "if one aircraft enters the runway, then other aircraft cannot cross the runway," such as at Shanghai Hongqiao International Airport and Shanghai Pudong International Airport. Second, "one can choose to cross the runway from the front side of a departing aircraft," such as at Chongqing Jiangbei International Airport. Third, "bypass the runway in a U-shaped path to achieve the purpose of crossing," such as at Beijing Capital Airport. The above methods for crossing a runway avoid threatening aircraft safety during ground operations but seriously restrict operational efficiency of the ground. Therefore, China has considered an operational mode that traverses the runway from the rear side of the departing aircraft, taxi-behind, as shown in Figure 1. The mode taxi-behind is to cross the runway behind the departing aircraft in order to reduce the operational conflict of the airport scene and improve operational efficiency, for example, O 'Hare Airport in the United States has used this model and demonstrated good safety and efficiency improvements.

The jet blast of the departing aircraft is the most important factor hindering the implementation of taxi-behind. Without adequate safety interval, an aircraft crossing a runway could be blown off course or even overturned by the strong aerodynamic load of the jet blast from the departing aircraft. The magnitude of the safety interval mainly depends on the strength of the jet blast of the departing aircraft and the bearing capacity of the runway-crossing aircraft, so it is necessary to study the influence distance of the jet blast of the departing aircraft engine. At present, computational fluid dynamics (CFD) numerical simulation and the real engine test are the main methods to analyze the impact of aircraft jet blast. Due to the difficulty, high cost, and great safety risk of the real engine test on the runway and aircraft engine data are highly confidential in countries, we can only get the limited data of jet velocity distribution from the engine manufacturer or the aircraft manufacturer, and it is not enough to be used in the research of the runway

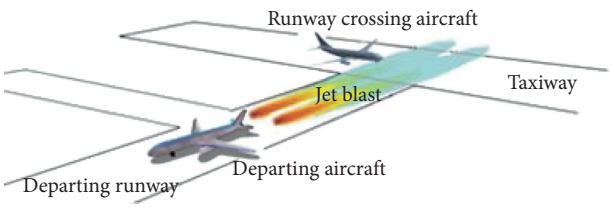

Figure 1: The taxi-behind mode schematic diagram.

operation mode. The hybrid numerical simulation method was adopted in this study for research.

Compared with domestic research, foreign research in this field was carried out earlier. In addition to the experimental method, the numerical simulation method was used to obtain the formation and evolution process of the jet as well as the parameters such as velocity, pressure, and temperature [4]. The influence of jet on landing aircraft is also analyzed in some literatures [5]. In 2006, Melber-Wilkending [6] established and verified the process chain based on the adaptive DLR TAU program, using CFD considering as example a Hangar and an AIRBUS A380 configuration, and gave the flow solver program for determining the jet wake of the rear engine. Slaboch in Volpe National Transportation Systems Center [7] presents an operational model for the prediction of jet blast, and the model was developed based upon three modules including a jet exhaust model, jet centerline decay model, and aircraft motion model. The final analysis was compared with data acquired during a jet blast study conducted by the Volpe Center in 1999. This analysis closely matched the data from the 1999 test. The analysis was then used to predict the jet blast evolution from aircraft that have been introduced since 1999, including the Boeing 777-300ER. Ishiko et al. [8] in order to examine the far-field velocity of jet blast by computational fluid dynamics (CFD) in this research, simulation using Reynolds-averaged Navier–Stokes (RANS) equation is carried out with very large computational domain. The velocity profiles obtained by numerical simulation agree well with those obtained by experiments. Then, they performed the parametric study of wind direction. It is found that the wind direction angle that has the most effect on the deflection of jet blast is lower than ninety degrees. Supported by theoretical and wind tunnel modeling, Bennett et al. [9] have experimented with an array of aerodynamic baffles on the surface behind a set of turbofan engines of 124 kN thrust. Lidar and point sampler measurements show that, as long as the intervention takes place within the zone where the Coanda effect holds the jet to the surface (i.e., within about 70 m in this case), quite modest surface-mounted baffles can rapidly lift the jet away from the ground. This was of potential benefit in abating both surface concentrations and jet blast downstream. There were also some modest acoustic benefits. The three-dimensional jet flow field of aircraft was simulated by Taguchi et al. [10]; they used a supersonic nozzle wall jet device, and the experimental results were compared with the calculation results of the SST turbulence model. The results show that the existing Reynolds stress database is of great significance to the establishment of the wall jet turbulence model. In recent decades, the RANS (Reynolds-averaged Navier–Stokes) method has been used to study jet flow fields in aviation. However, reliable numerical results have not been obtained [11]. Although the RANS method requires the minimal computational effort, the pulsating motion details are smoothed out by homogenizing the turbulent fluctuations [12]. Therefore, it is impossible to accurately simulate the growth rate of the shear layer and turbulence details such as the inviscid velocity of the jet, which is not affected by the shear layer [13–15]. Scholars at home and abroad have used the LES (large eddy simulation) method to carry out numerical simulations on jet blast. The basic concept has been to directly and numerically simulate large eddies by using the spatial sieve filtration method, Fourier function, or Gaussian function to separate large and small eddies [16–18]. The subgrid stress model has been used to calculate small eddies [19]. In [20], the LES method was used to simulate the aerodynamic noise and coaxial twin jet flow noise before and after installing a zigzag nozzle, and the effect of the zigzag nozzle on the flow field structure and sound field was studied. In [21], free flow and jet flow numerical simulations were carried out with the LES method. The results showed that the location and shape of large turbulence structures were consistent with the experimental images. Although the LES method has achieved good results, in an actual numerical simulation process, even the LES method needs a considerable grid support to capture small eddies near the engine walls [22]. Moreover, when assessing the complex flow of engine jets, the near-wall mode of the LES method cannot accurately separate the high Reynolds number near-wall turbulence, so it can only deal with low Reynolds number turbulent flows [23, 24].

At present, the DES (detached eddy simulation) method has been introduced to assist in the numerical simulation of jet engines. It is a numerical method used for the calculation of detached vortices [25, 26]. The basic concept employs the RANS method to simulate small-scale turbulent fluctuations near the engine wall. In the area far away from the boundary layer, a Smagorinsky large eddy simulation is used to simulate the detached vortex to enable the subgrid Reynolds stress model [27]. This method has two advantages. First, it avoids the problem of a larger grid size in the conventional boundary layer method (LES). The method also ensures that the large-scale detached vortex energy can be accurately simulated in a range far away from the surface of the object. Liu et al. [28] used a mixed unstructured grid and an SST turbulence model to simulate a jet engine with the DES method and compared it with experimental results. The rationality of the method was proven. Dietiker and Hoffmann [29] used the DES method to study a three-dimensional unsteady jet and compared it with experimental data to obtain relatively good numerical results. Gong et al. [30] proposed an improved delay separation vortex simulation (IDDES) method based on the SST model for a high-precision simulation of the jet engine effect and conducted a numerical study of the dynamic jet effect through a RANS/LES hybrid method. Their results showed that the velocity distribution in a jet blast can be predicted better [31, 32].

In summary, DES offers great advantages in the numerical simulation of jet blast, but domestic scholars have

seldom used this approach. At present, domestic and foreign scholars have performed more numerical simulations of near-field jet blasts [33–37]. However, for taxiing behind of the departing aircraft, more attention has been paid to the far-field flow of the jet [38–40]. The SA turbulence model, as a classic aviation field model, exhibits strong robustness and a rich experience value [41, 42]. Therefore, based on the SA turbulence model and the DES method, a DES-SA mixed numerical simulation method is built to simulate the far field of a jet blast. A nozzle model that does not consider internal engine flow is used. Two different jet states from a Boeing aircraft nozzle are calculated, and the calculated state, which is more consistent with the working conditions of the engine, is determined. On this basis, the influence distance of a typical jet blast is studied to provide the necessary theoretical and technical support for the implementation of a taxi-behind mode. At the same time, it provides a reference for the study of engine jet by the DES numerical simulation method.

2. Methodology

N-S equations are the most complete governing equations describing fluid motion so far and can be written in the form of Cartesian tensor using summation convention.

The continuity equation is

$$\frac{\partial \rho}{\partial t} + \frac{\partial}{\partial x_i}\left(\rho u_i\right) = 0. \tag{1}$$

The momentum equation is

$$\frac{\partial}{\partial t}\left(\rho u_i\right) + \frac{\partial}{\partial x_i}\left(\rho u_j u_i\right) = -\frac{\partial p}{\partial x_i} + \frac{\partial \sigma_{ij}}{\partial x_j} + \frac{\partial}{\partial x_j}\left(-\rho u_j' u_i'\right), \tag{2}$$

where u_i is the Reynolds average velocity component omitting the average sign; ρ is the density; p is the pressure; u_i' is the pulsating velocity; σ_{ij} is the stress tensor component.

Based on the SA turbulence model combining the DES method, the hybrid DES-SA numerical simulation method is used to simulate the far-field flow of a jet engine [43, 44]. The integral method for the DES-SA approach is as follows:

$$\frac{\partial}{\partial t}\int_{\Omega} \tilde{\nu}\, \mathrm{d}\Omega + \oint_{\partial\Omega}\left(F_{c,T} - F_{v,T}\right)\mathrm{d}S = \int_{\Omega} Q_T\, \mathrm{d}\Omega, \tag{3}$$

where $\tilde{\nu}$ is the viscosity coefficient; $F_{c,T}$ is the convective flux term; $F_{v,T}$ is the viscous flux term; Q_T is the source item which contains generation and destruction items.

The mixed model adopts a mixed length scale l_{DES} instead of the traditional SA turbulence model d to calculate the distance from the unit to the nearest wall; the following formula is adopted:

$$\tilde{d} = \min\left(d, C_{\mathrm{DES}}\Delta\right), \tag{4}$$

where C_{DES} is the adjustable coefficient, which is usually 0.65; Δ is the filter scale in the LES method.

Therefore, the DES-SA mixing method has $d \ll \Delta$ ($l_{\mathrm{DES}} = d$) in the near-wall region. The traditional SA turbulence model is used for numerical simulation, which has $d \gg \Delta$ ($l_{\mathrm{DES}} = \Delta$) far away from the wall area. When there is a balance between the production term and the dissipation term, $\tilde{\nu} \propto S\Delta^2$. At this point, the DES-SA mixing method is transformed into the LES method to simulate the jet flow.

At present, the main method for nozzle boundary condition construction depends on whether to consider the internal flow of the nozzle. For the case of internal nozzle flow, the boundary of the computational domain lies within the nozzle. The boundary conditions are usually set as the total pressure and total temperature inside the nozzle or the total pressure ratio of the internal combustion chamber (the combustion chamber) to the external atmosphere (P_0/P) and total temperature ratio (T_0/T) [45]. This method restricts the size and internal configuration of nozzle. It can fully consider the viscous effect of the inner wall in the engine nozzle [46]. The calculation accuracy is relatively high. However, considering that the nozzle is a highly proprietary product, the internal structure and size data are difficult to obtain. Therefore, the internal flow of the nozzle is not considered in this study. We only require the Mach number, static pressure, and static temperature at the outlet of the nozzle and regard the nozzle outlet condition as the entry condition for the solution domain of the flow field.

3. Example Verification Analysis

Considering the complex working state of the engine, scholars at home and abroad typically compare the two states of cold and hot spray when calculating a jet engine field and analyze the similarities and differences between the two states of cold and hot spray. Then, according to the actual situation, the conditions that are more suitable for the actual working conditions are determined for numerical simulation. In this study, the combined DES-SA method is used to study the two states of engine cold jetting and hot spraying. The setting of specific parameters is given in Table 1.

Taking a Boeing A320 aircraft (engine type is CFM56-5B) as an example, according to the actual engine size, the twin nozzle model in the calculation example is scaled down. The diameter of the CFM56-5B engine fan nozzle is 1.735 m; the specific structure is shown in Figures 2 and 3.

To investigate the ground effect, the calculation domain is chosen as follows: according to the assembly height of the A320 aircraft engine (the vertical height of the axis from the ground is approximately 1.68 m), the height distance from the ground is 1.7348 m and perpendicular to the direction of the incoming flow. The width of the flow field is 45.533 m, and the height is 24.5013 m along the streamline direction. The length of the flow field is 341.498 m. To obtain more accurate calculation results, the boundary conditions are set as follows: the ground is set as the boundary condition of the material surface, the outlet is set as the pressure outlet condition, and the three planes and the flow inlet surface parallel to the flow are set as the far-field pressure condition. The calculation domain size is shown in Figure 4.

During mesh processing, the mesh at the nozzle outlet is encrypted to better simulate the velocity change at the nozzle outlet, as shown in Figures 5(a) and 5(b). During the volume

Table 1: Calculation state of double-channel jet flow.

Case	M_{pj}	M_{sj}	TTR_p	TTR_s	M_{cf}
I	0.85	0.95	1.0	1.0	0.05
II	0.85	0.95	2.26	1.0	0.05

M_{pj}, the Mach number of the inner nozzle outlet; M_{sj}, the fan outlet Mach number; TTR, the total temperature ratio of the inner and outer flow fields of the nozzle; M_{cf}, the number of incoming Mach flows for the external flow field of the nozzle.

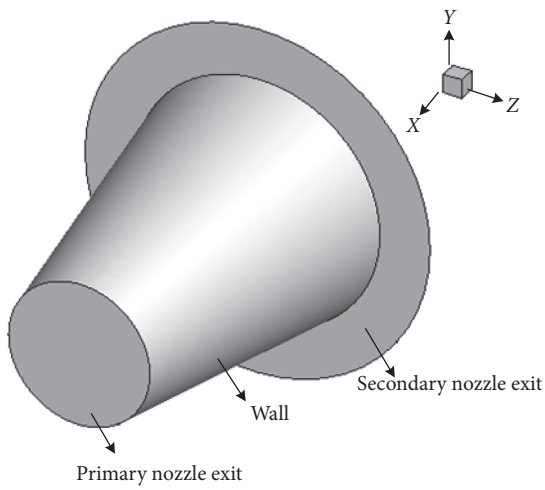

Figure 2: Three-dimensional structure of the nozzle (x, axial direction; y, radial direction; z, height direction).

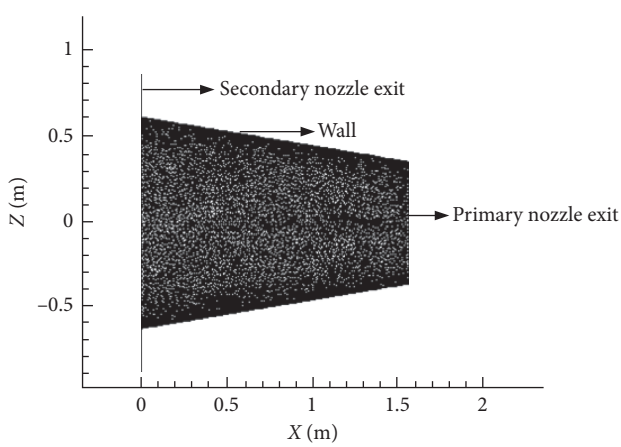

Figure 3: Top view of the nozzle structure.

mesh generation, in order to take the ground effect into account, the mesh at the ground and the nozzle is encrypted, as shown in Figures 5(c) and 5(d). The specific number of grid nodes and cells is shown in Table 2

The boundary conditions of the external flow field are as follows: static pressure $P = 101325$ Pa, static temperature $T = 298$ K, and working gas is the ideal gas. According to formula (5) and the total temperature ratio, the static temperature and static pressure at the outlet of the inner nozzle and outer nozzle can be determined.

$$\frac{T_0}{T} = \left(1 + \frac{\gamma - 1}{2} M^2\right). \tag{5}$$

Figures 6 and 7 show the results of the numerical simulation of the nozzle axis velocity varied with the nozzle distance obtained from the numerical simulation. In the graph, we can see that the axial velocity of the nozzle decreases rapidly within the distance from the front 100 m; regardless of whether the nozzle is heated or not, the velocity slows down from 100 m, and the axis velocity at 300 m is still approximately 60 m/s. Compared with the incoming velocity (16.6 m/s), the speed is still greater. There is a risk in crossing the runway at this distance. Therefore, it can be concluded that the static temperature at the outlet of the nozzle has a little effect on the speed drop in the range from 100 m to 300 m downstream.

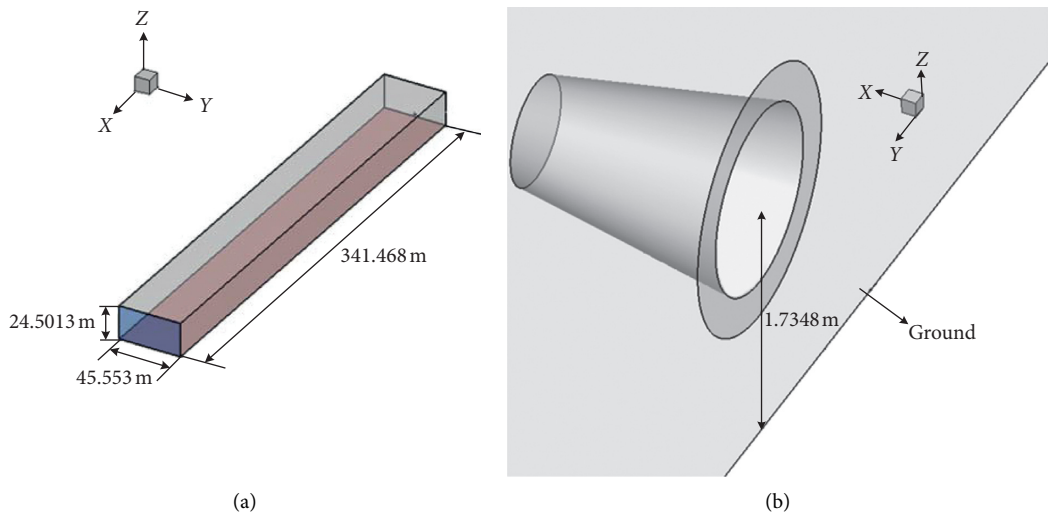

Figure 4: Calculation domain size (x, flow direction; y, direction; z, height direction).

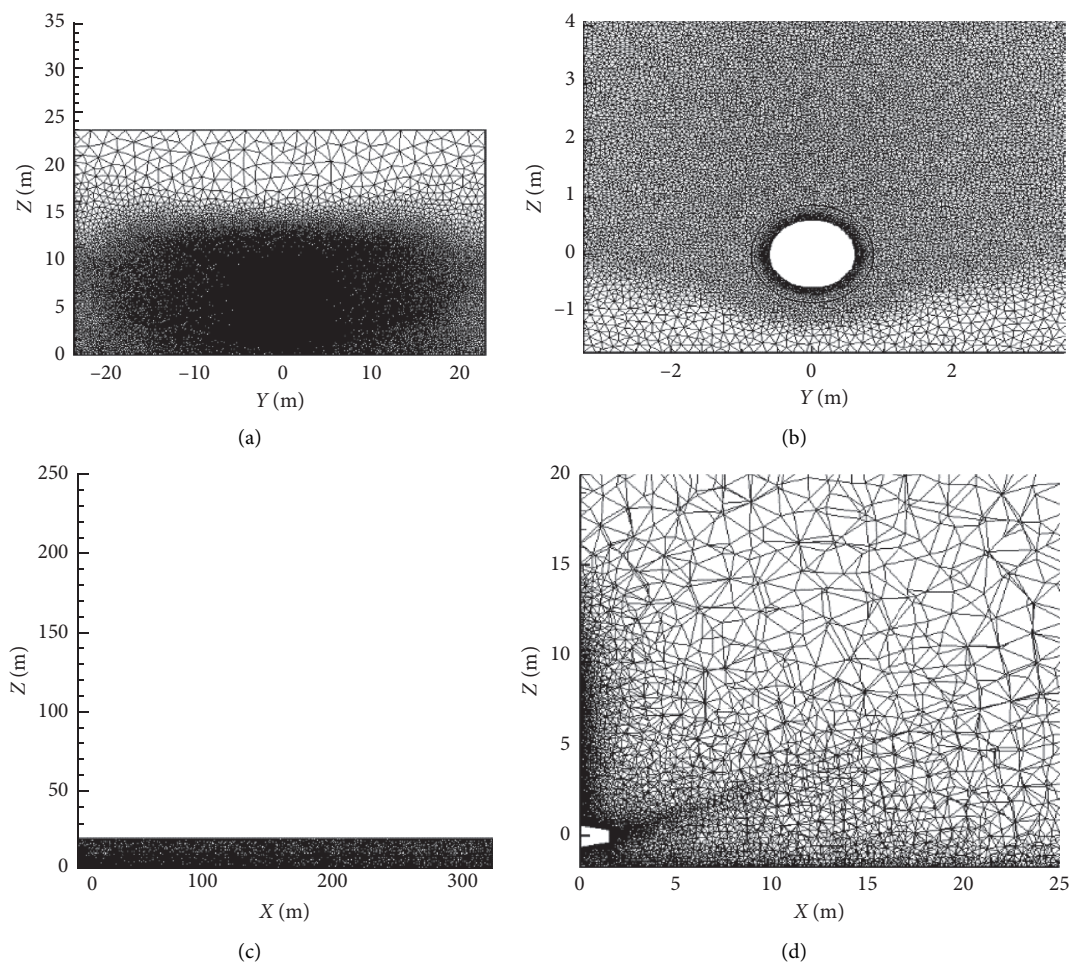

Figure 5: Grid details. (a) Nozzle outlet surface mesh. (b) Local surface mesh at nozzle outlet. (c) The symmetry plane of the flow field is the volume grid. (d) Section of the volume mesh at the nozzle exit.

Figures 8 and 9 show the velocity clouds of the nozzle outlet under cold spray and hot spray conditions, respectively. Figure 8 shows that the velocity at the outlet of the nozzle is the greatest. As the distance increases, the velocity decreases gradually due to the dissipation of energy, and the incoming gas flow also creates a shearing action with the tail

Table 2: Number of mesh nodes and mesh cells.

Grid nodes	Grid cell
942,325	5,131,569

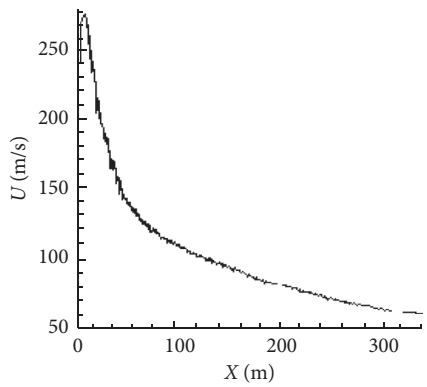

Figure 6: Axis velocity of the nozzle axis at $TTR_p = 1.0$.

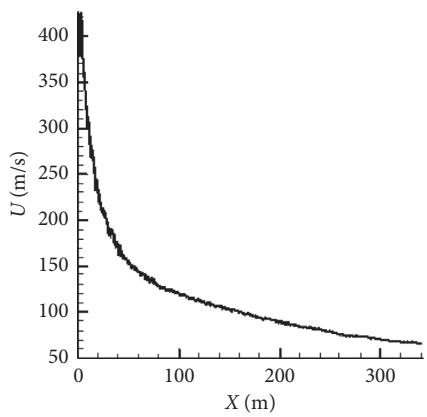

Figure 7: Axis velocity of the nozzle axis at $TTR_p = 2.26$.

jet stream at high speed, resulting in an increase in the gas flow velocity near the tail jet stream. It can be seen in Figure 9 that although the Mach number at the outlet is less than the Mach number at the culvert, the speed at the outlet is faster than that at the culvert. The reason is that the total temperature at the outlet is higher and the static temperature is higher than the static temperature at the culvert, so the corresponding sound speed is also faster. Although the Mach number is relatively low, the absolute velocity of the calculated airflow is still faster.

Figures 10 and 11 show the temperature cloud map at the outlet of the nozzle calculated under cold spray and hot spray conditions, respectively. In the figures, we can see that the influence range of the tail jet increases with increasing distance. The absolute value of the difference between the center and the ambient temperature decreases with increasing distance. However, the total temperature ratio is 1 under the cold spray condition, and the gas energy inside and outside the nozzle is the same. According to formula (5), when the total temperature is constant, the larger the Mach number is, the lower the static temperature is. Therefore, the static temperature at the outlet of the nozzle is lower than that of the outside atmosphere. It is obvious that this example is different from an actual engine situation.

During the heating state, the static temperature of the outlet is higher than the ambient temperature, while the static temperature of the outlet is lower than the ambient temperature. This is due to the heating at the outlets and the higher total gas temperature at the outlets. At a certain Mach number, the static temperature at the outlet of the inner nozzle is far higher than that of the environment. However, the Mach number is larger than the external atmosphere, so the static temperature at the outlet is lower. It is worth noting that the static temperature at the center of the tail gas jet is higher than that of the external atmosphere compared with the cold spray state, which is also due to the higher static temperature of the gas in the cones. From the above analysis, the hot injection state is more consistent with the real working situation of the engine.

4. Numerical Simulation Analysis of Typical Jet Engine Flow

The influence distance of a departing aircraft's jet blast is very important for determining the safe clearance of the rear crossing mode. Therefore, this section performs a numerical simulation analysis on the jet effect of a typical engine. According to CAAC data, as of February 2019, the proportion of Airbus and Boeing aircrafts in domestic airlines is 94.66%. Among them, the A320, B777, and B737-800 account for up to 78.18% of the total. The CRJ900, as a typical representative of the regional aircraft, is favored for its excellent flight performance and low fuel consumption. Therefore, the above four models are selected and categorized according to their wake ratings: light-duty (CRJ900), medium-duty (A320 and B737-800), and heavy-duty (B777). The thermal jet method is used to analyze and calculate the influence distance of the jet blast.

(1) Determine the shrinkage of the calculation model

When calculating the far-field tail jet flow due to the lack of actual size data, the model is scaled according to the actual engine's fan diameter

(2) Calculate the true flow of internal and external channels

The air flow in the ducts is calculated according to the bypass ratio and the total air flow rate. The formula is as follows:

$$\dot{m}_{\text{pilot\_duct}} = \frac{\dot{m}_{\text{total}}}{(\text{bypass\_ratio} + 1)}, \tag{6}$$

$$\dot{m}_{\text{external\_duct}} = \dot{m}_{\text{total}} - \dot{m}_{\text{pilot}_{\text{duct}}}. \tag{7}$$

(3) Calculate the speed of internal and external channels

For a turbofan engine, the ratio of internal and external ducts is 2 : 8. Therefore, the velocity of the internal and external ducts can be calculated according to the momentum theorem under the

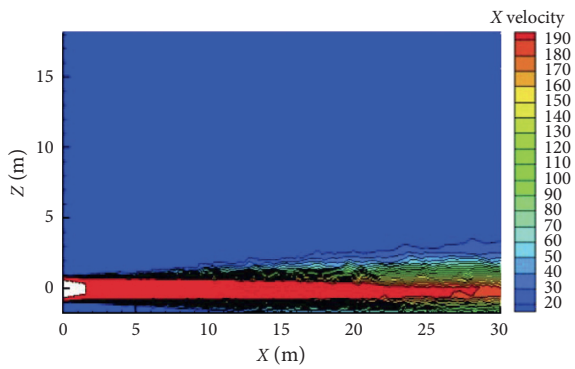

Figure 8: Velocity cloud map of the nozzle outlet at $TTR_p = 1.0$.

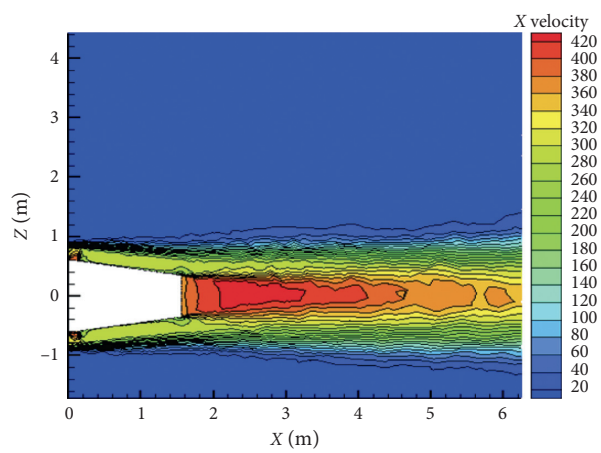

Figure 9: Velocity cloud map of the nozzle outlet at $TTR_p = 2.26$.

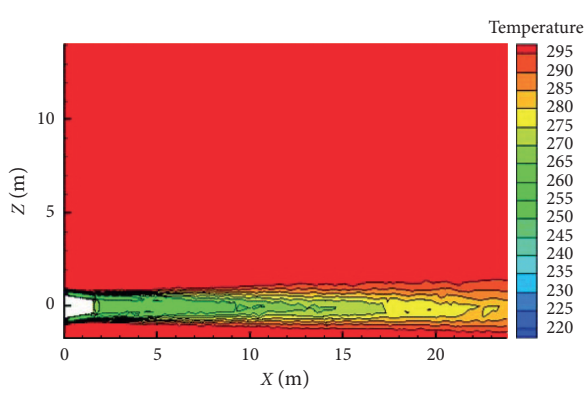

Figure 10: Temperature cloud map of the nozzle outlet at $TTR_p = 1.0$.

condition of known internal and external channel flows.

$$F\Delta t = \dot{m}\Delta V. \tag{8}$$

(4) Determine the Mach numbers inside and outside the culvert

To determine the speed and temperature inside and outside the culvert, the Mach number of the inner and outer ducts can be calculated according to the following formulas.

$$a = \sqrt{\gamma RT}, \tag{9}$$

$$Ma = \frac{V}{a}. \tag{10}$$

Taking A320 as an example, the real jet blast tail effect is calculated. The A320 mainly uses the CFM56-5B engine, and the relevant parameters are given in Table 3.

According to formulas (6)–(10), the boundary conditions at the nozzle outlet can be obtained, as given in Table 4.

Through numerical simulations of the above cases, the jet velocity distribution curve and the velocity profile of the jet XZ section are obtained (Figures 12 and 13). According to the limitations in the Flight Crew Operation Manual (FCOM), this study mainly analyzes jet engines at speeds of 44 m/s, 22 m/s, and 16 m/s. Figure 13 shows that the influence distances of A320 jet blast at speeds of 44 m/s, 22 m/s, and 16 m/s are 90 m, 296 m, and 451 m, respectively.

Similarly, numerical simulations for the B777, B737-800, and CRJ900 are carried out to obtain the velocity distributions of their jet blasts, as shown in Figures 14–16.

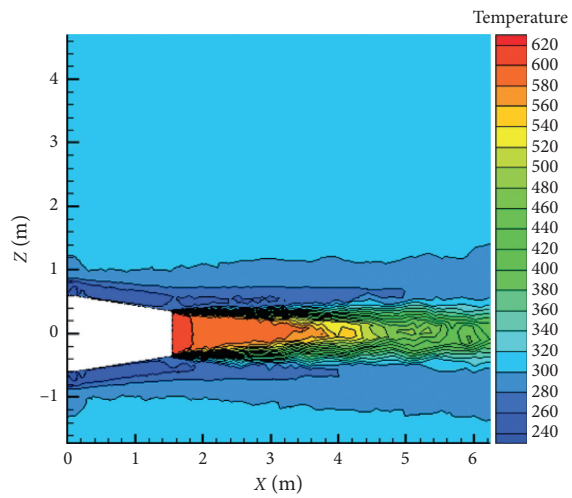

Figure 11: Temperature cloud map of the nozzle outlet at $TTR_p = 2.26$.

Table 3: A320 engine parameters.

Maximum take-off thrust (daN)	Air mass flow (kg/s)	Bypass ratio	Diameter (mm)	Engine outlet temperature (°C)
13360	390.5	5.0	1735	297

Table 4: Dynamic boundary conditions of the A320 engine.

Internal nozzle static pressure (Pa)	Internal nozzle static temperature (K)	Mach number of internal nozzle	External nozzle static pressure (Pa)	External nozzle static temperature (K)	Mach number of external nozzle
101325	570	0.8579	101325	328.15	0.9045

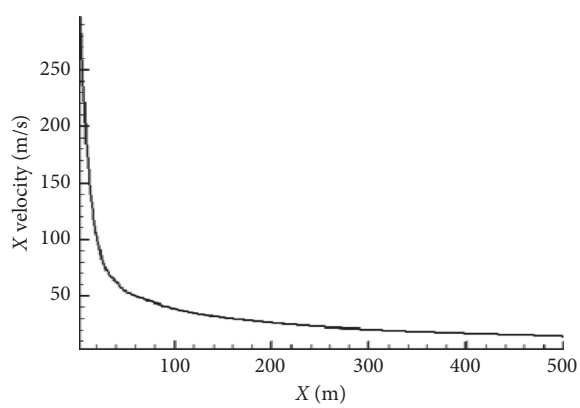

Figure 12: Velocity distribution curve of the A320 jet.

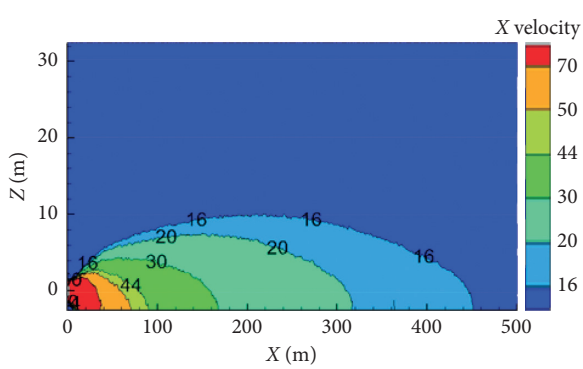

Figure 13: Velocity distribution cloud map of the XZ section of the A320 jet.

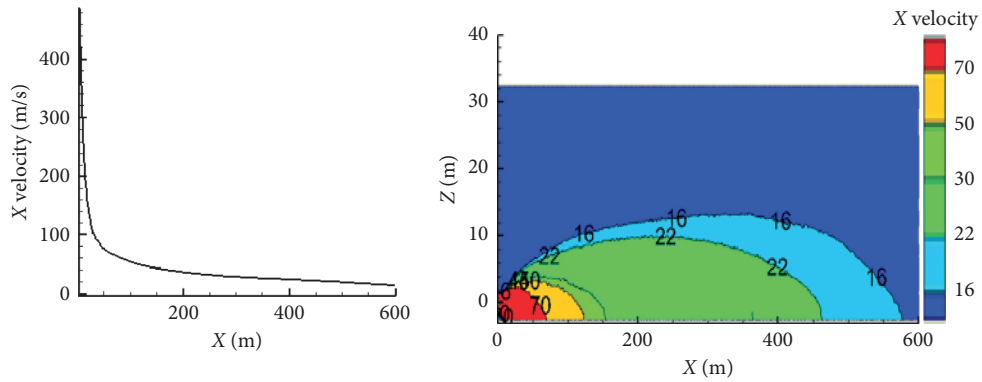

(a) (b)

Figure 14: B777 jet velocity distribution curve and XZ section velocity distribution cloud map.

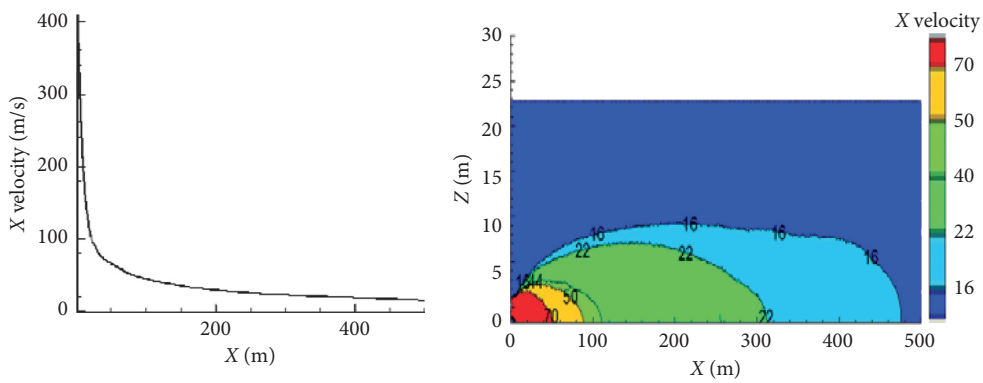

(a) (b)

Figure 15: B737-800 jet velocity distribution curve and XZ section velocity distribution cloud map.

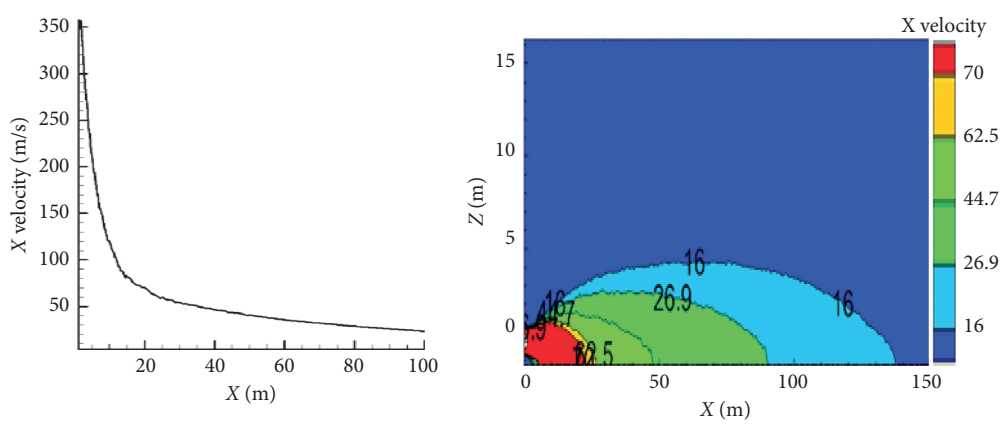

(a) (b)

Figure 16: CRJ900 jet velocity distribution curve and *XZ* section velocity distribution cloud map.

Table 5: Influence distance of a typical jet blast.

Aircraft type	Influence distance of 44 m/s	Influence distance of 22 m/s	Influence distance of 16 m/s
B777	153 m	462 m	576 m
A320	90 m	296 m	451 m
B737-800	86 m	312 m	475 m
CRJ900	47 m	125 m	157 m

In summary, the influence distances of the B777, A320, B737-800, and CRJ900 jet blast at speeds of 44 m/s, 22 m/s, and 16 m/s are given in Table 5.

5. Conclusion

Based on the safe operation of the taxi-behind mode, the influence distance of jet flow in aircraft engine under the taxi-behind mode is numerically simulated. Based on the SA turbulence model, the DES-SA hybrid method is constructed. Cold spray and hot spray conditions are calculated using a nozzle model without considering the internal flow of the engine, and the state of the engine's actual working condition is determined. According to the selection of four presently used typical aircraft models, the jet effect of the engine is numerically simulated, and the influence distance of the jet blast is determined.

(1) The numerical simulation results for two jet types under cold and hot spray conditions indicate the following: whether the coning channel is heated or not, the speed at the axis of the engine nozzle decreases with the increase of the nozzle distance, and the velocity decreases rapidly within 100 m of the engine nozzle and decreases slowly beyond 100 m. Compared with the unheated condition, the inner channel heating condition is more consistent with the actual working state of the engine.

(2) The numerical simulation results for a typical jet engine effect show the following: medium-duty and heavy-duty aircrafts typically use a more powerful engine with more horsepower than a light-duty aircraft. When the jet speed is 16 m/s, the influence distance is far greater than 300 m. When the jet velocity speed is 16 m/s, the impact distance of the light-duty aircraft is much less than 300 m. In the follow-up work of this study, a typical aircraft type will be selected to carry out the real engine jet effect experiment at the airport, and the corresponding parameters of the jet blast will be collected. The experimental data obtained will further verify the numerical simulation results in this study.

Data Availability

The data on engine parameters of typical aircrafts are derived from https://www.prattwhitney.com ~~~~~~~~ ~~~~~~~~~~~~~~amp and https://http://www.cfmaeroengines.com.

Disclosure

The funders had no role in the design of the study; in the collection, analyzes, or interpretation of data; in the writing of the manuscript; or in the decision to publish the results.

Conflicts of Interest

The authors declare that they have no conflicts of interest.

Authors' Contributions

X.H. and Y.C. conceptualized and supervised the study; X.H. developed methodology, performed formal analysis, collected data, and wrote the original draft; Y.M. developed software and investigated, edited, and reviewed the study; Y.C., X.H., D.H., and H.G. validated the study; Y.C. collected resources and fund; H.G. visualized the study; D.H. administered the project. All authors have read and agreed to the published version of the article.

Acknowledgments

The authors acknowledge the comments and suggestions from the editor and all the anonymous reviewers. This research was supported by CAAC Aviation Safety Capacity Building Fund Supported Project (TM2018-3-1/2).

References

[1] Y. Chen, Y. Ma, and Hexin, "Analysis and research process of paired approach mode," *Advances in Aeronautical Science and Engineering*, vol. 11, no. 6, pp. 767–773, 2020.

[2] M. Yazdi, S. Daneshvar, and H. Setareh, "An extension to fuzzy developed failure mode and effects analysis (FDFMEA) application for aircraft landing system," *Safety Science*, vol. 98, pp. 113–123, 2017.

[3] M. Yazdi, S. Kabir, and M. Walker, "Uncertainty handling in fault tree based risk assessment: state of the art and future perspectives," *Process Safety and Environmental Protection*, vol. 131, pp. 89–104, 2019.

[4] J. Chen, P. Zhang, N. Zhou, and Y. Deng, "Application of detached-eddy simulation based on Spalart-Allmaras turbulence model," *Journal of Beijing University of Aeronautics and Astronautics*, no. 7, pp. 56–60, 2012.

[5] Y. Zhang, R. P. Rudis, F. Y. Wang et al., "Simulation of jet blast effect on landing aircraf," *Air Traffic Control Quarterly*, vol. 9, no. 3, pp. 211–227, 2016.

[6] S. Melber-Wilkending, "Aerodynamic analysis of jet-blast using CFD considering as example a Hangar and an AIRBUS A380 configuration," in *New Results in Numerical and Experimental Fluid Mechanics V*, H. J. Rath, C. Holze, H. J. Heinemann, R. Henke, and H. Hönlinger, Eds., Springer, Berlin, Germany, 2006.

[7] P. Slaboch, "An operational model for the prediction of jet blast," in *Proceedings of the 50th AIAA Aerospace Sciences Meeting including the New Horizons Forum and Aerospace Exposition*, Nashville, TN, USA, January 2012.

[8] K. Ishiko, A. Hashimoto, Y. Matsuo, and S. Watanabe, "Numerical examination of the effect of cross-wind on jet blast," in *Proceedings of the 50th AIAA Aerospace Sciences Meeting including the New Horizons Forum and Aerospace Exposition*, Nashville, TN, USA, January 2012.

[9] M. Bennett, S. M. Christie, A. Graham et al., "Abatement of an aircraft exhaust plume using aerodynamic baffles," *Environmental Science & Technology*, vol. 47, no. 5, p. 2346, 2013.

[10] M. Taguchi, N. Semba, K. Mori et al., "Experimental study on jet blast at laboratory scale," *Journal of Energy and Power Engineering*, vol. 8, no. 8, pp. 1386–1392, 2014.

[11] L. P. Zhao, "Numerical simulation for high temperature and high pressure flow field of aircraft engine jet impingement," *Ship Science and Technology*, vol. 38, no. 1, pp. 145–149, 2016.

[12] X.-Q. Liu and Y.-Z. Wu, "The computation of the lateral jet turbulence flow using DES method," *Acta Aeronautica et Astronautica Sinica*, vol. 25, no. 3, pp. 209–213, 2004.

[13] G. Xiang, S. Wang, and C. G. Soares, "Study on the motion of a freely falling horizontal cylinder into water using OpenFOAM," *Ocean Engineering*, vol. 196, p. 106811, 2020.

[14] X. Yu, G. Xiang, H. Collopy et al., "Trajectory prediction of a model rocket falling into the towing tank: experimental tests versus numerical simulations," *Journal of Aerospace Engineering*, vol. 33, no. 5, p. 04020056, 2020.

[15] G. Xiang and C. Guedes Soares, "Incorporating irregular nonlinear waves in simulation of dropped cylindrical objects," *Proceedings of the Institution of Mechanical Engineers, Part M: Journal of Engineering for the Maritime Environment*, vol. 234, no. 1, pp. 272–283, 2020.

[16] H. Li and C. G. Soares, "Reliability analysis of floating offshore wind turbines support structure using hierarchical Bayesian network," in *Proceedings of the 29th European Safety and Reliability Conference*, pp. 2489–2495, Hannover, Germany, September 2019.

[17] H. Li, H.-Z. Huang, Y.-F. Li, J. Zhou, and J. Mi, "Physics of failure-based reliability prediction of turbine blades using multi-source information fusion," *Applied Soft Computing*, vol. 72, pp. 624–635, 2018.

[18] G. Xiang and C. Guedes Soares, "Improved dynamical modelling of freely falling underwater cylinder based on CFD," *Ocean Engineering*, vol. 211, p. 107538, 2020.

[19] Z. Yang, "Large-eddy simulation: past, present and the future," *Chinese Journal of Aeronautics*, vol. 28, no. 1, pp. 11–24, 2015.

[20] X. Liu, W. Huang, and H. Li, "The simulation of separated exhaust jet noise," *Science Technology and Engineering*, vol. 19, no. 22, pp. 338–342, 2019.

[21] Z. Zhu, X. Cheng, and H. Pan, "Large eddy simulation of supersonic jet mixing flow," *Journal of Aerospace Power*, vol. 34, no. 1, pp. 210–216, 2019.

[22] Y. Sun, *Separation Flow Study Based on RANS Method and RANS/LES Hybrid Method*, Huazhong University of Science, Wuhan, China, 2018.

[23] G. Xiang, X. Li, X. Yu, Y. Luo, and Y. Cao, "Motion dynamics of dropped cylindrical objects in flows after water entry," *Ocean Engineering*, vol. 173, pp. 659–671, 2017.

[24] G. Xiang, L. Birk, X. Yu, and H. Lu, "Numerical study on the trajectory of dropped cylindrical objects," *Ocean Engineering*, vol. 130, pp. 1–9, 2017.

[25] H. Tan, *The Numerical Simulation of Frigate Surface Flow Field with DES Method*, Nanjing University of Aeronautics and Astronautics, Nanjing, China, 2017.

[26] L. Davidson and S. Dahlström, "Hybrid LES-RANS: an approach to make LES applicable at high Reynolds number," *International Journal of Computational Fluid Dynamics*, vol. 19, no. 6, pp. 415–427, 2005.

[27] M. A. Pakhomov and V. I. Terekhov, "RANS modeling of flow structure and turbulent heat transfer in pulsed gas-droplet mist jet impingement," *International Journal of Thermal Sciences*, vol. 100, no. 2, pp. 284–297, 2016.

[28] X. Liu, Y. Wu, and K. Chen, "Computation of lateral turbulent jets using m-SST DES model I," *Acta Mechanica Sinica*, no. 4, pp. 401–406, 2004.

[29] J. F. Dietiker and K. Hoffmann, "Detached-eddy-simulation of supersonic jet flows," in *Proceedings of the 6th AIAA Aviation Technology, Integration and Operations Conference (ATIO)*, Wichita, KS, USA, September 2006.

[30] Z. Gong, J. Li, J. Shan, and H. Zhang, "Numerical investigation of powered jet effects by RANS/LES hybrid methods," *Xibei Gongye Daxue Xuebao/Journal of Northwestern Polytechnical University*, vol. 37, no. 3, pp. 565–571, 2019.

[31] F. D. Gao, D. X. Wang, H. D. Wang et al., "Numerical analysis and verification of the gas jet from aircraft engines impacting a jet blast deflector," *Chinese Journal of Mechanical Engineering*, vol. 31, no. 5, pp. 127–137, 2018.

[32] K. Yue, L. Cheng, H. Liu, and Y. Wang, "Analysis of jet blast impact of embarked aircraft on deck takeoff zone," *Aerospace Science and Technology*, vol. 45, no. 5, pp. 60–66, 2015.

[33] N. A. Buchmann, C. Atkinson, and J. Soria, "Ultra-high-speed tomographic digital holographic velocimetry in supersonic particle-laden jet flows," *Measurement Science & Technology*, vol. 24, no. 2, pp. 827–837, 2012.

[34] D. R. Brooks, T. Ecker, K. T. Lowe et al., "Experimental Reynolds stress spectra in hot supersonic round jets," in *Proceedings of the 52nd Aerospace Sciences Meeting*, pp. 1227–1245, National Harbor, MD, USA, January, 2014.

[35] H. Li, A. P. Teixeira, and C. Guedes Soares, "A two-stage failure mode and effect analysis of offshore wind turbines," *Renewable Energy*, vol. 162, pp. 1438–1461, 2020.

[36] H. Li, C. Guedes Soares, and H.-Z. Huang, "Reliability analysis of a floating offshore wind turbine using Bayesian Networks," *Ocean Engineering*, vol. 217, p. 107827, 2020.

[37] H. Li, H. Diaz, and C. G. Soares, "A developed failure mode and effect analysis for floating offshore wind turbine support structures," *Renewable Energy*, vol. 164, pp. 133–145, 2020.

[38] Y. Chen and X. Zhang, "A preliminary study on schemeson crossing runway behind takeoff aircraft at the chongqing Jiangbei airport," *Journal of Civil Aviation*, vol. 2, no. 4, pp. 25–30, 2018.

[39] M. Yazdi and S. Kabir, "A fuzzy Bayesian network approach for risk analysis in process industries," *Process Safety and Environmental Protection*, vol. 111, pp. 507–519, 2017.

[40] M. Yazdi, F. Nikfar, and M. Nasrabadi, "Failure probability analysis by employing fuzzy fault tree analysis," *International Journal of System Assurance Engineering and Management*, vol. 8, no. 2, pp. 1177–1193, 2017.

[41] R. Paoli, L. Nybelen, J. Picot et al., "Effects of jet/vortex interaction on contrail formation in supersaturated conditions," *Physics of Fluids*, vol. 25, no. 5, pp. 25–30, 2013.

[42] M. Yazdi, A. Nedjati, E. Zarei, and R. Abbassi, "A novel extension of DEMATEL approach for probabilistic safety analysis in process systems," *Safety Science*, vol. 121, pp. 119–136, 2020.

[43] P. R. Spalart, "Detached-eddy simulation," *Annual Review of Fluid Mechanics*, vol. 41, no. 41, pp. 181–202, 2009.

[44] ANSYS Inc, *ANSYS FLUENT User's Guide*, ANSYS Inc, Shanghai, China, 2011.

[45] M. Shives and C. Crawford, "Adapted two-equation turbulence closures for actuator disk RANS simulations of wind & tidal turbine wakes," *Renewable Energy*, vol. 92, pp. 273–292, 2016.

[46] A. Lopez, W. Nicholls, M. T. Stickland, and W. M. Dempster, "CFD study of jet impingement test erosion using Ansys fluent® and OpenFOAM®," *Computer Physics Communications*, vol. 197, no. 6, pp. 88–95, 2015.

Hindawi
Mathematical Problems in Engineering
Volume 2021, Article ID 5564269, 16 pages
https://doi.org/10.1155/2021/5564269

Research Article

Presentation of Analytical Methods for Better Decision Making about the Most Important Factor Influencing Rural Accidents

Seyed Mohsen Hosseinian,[1] Vahid Najafi Moghaddam Gilani,[1] Hossein Tahmasbi Amoli,[2] Mohammad Nikookar,[3] and Alireza Orouei[4]

[1]*School of Civil Engineering, Iran University of Science and Technology (IUST), Tehran, Iran*
[2]*School of Engineering and Technology, Shomal University, Amol, Iran*
[3]*School of Civil Engineering, University of Guilan, Rasht, Iran*
[4]*School of Civil Engineering, Islamic Azad University, Semnan, Iran*

Correspondence should be addressed to Vahid Najafi Moghaddam Gilani; vahid.moghaddam90@gmail.com

Received 29 January 2021; Revised 28 February 2021; Accepted 11 March 2021; Published 20 March 2021

Academic Editor: Mohammad Yazdi

Due to population growth and the increasing number of vehicles on rural roads, traffic accidents have become one of the most important problems in the transportation system, which greatly affects the social and economic situation of the people. The main purpose of this study was to apply the analytical method to investigate the factors affecting the severity of traffic accidents on rural roads of Guilan, Iran, in order to determine the most effective factor in the occurrence of these accidents. At first, the frequency analysis was used to evaluate the variables and their frequency, then the Friedman test (FT) was applied to prioritize the factors, and the exploratory factor analysis (EFA) was used to determine the most effective factor in the occurrence of vehicle accidents in Guilan rural roads. Based on the FT, weather condition was the most important factor effective in these accidents. According to the results of the EFA, five factors were identified as the main factors involved in accidents in which the first factor contributing to accidents was the environmental factor, including weather condition and road surface condition. This indicates that concurrent result of the FT and the EFA, weather condition as an environmental factor, was identified as the most important factor affecting vehicle accidents on rural roads of Guilan. Finally, safety strategies were proposed to increase safety and reduce accidents along these roads.

1. Introduction

Traffic accidents are now a worldwide problem that annually kills a large number of people and brings huge economic costs to society [1, 2]. Although the scientific growth and the advancement of technology in vehicles have created relative prosperity for humans, it has caused an important problem called road accidents [3] that has become one of the world's leading economic, social, and health hazards today and as one of the most important causes of mortality, disability, and damages in the world which is worryingly increasing [4, 5]. World statistics show that the economic and human casualties of road accidents are high. Approximately 3700 people die every day and 1.35 million a year from traffic accidents, and nearly 50 million are injured or disabled every year. Road accidents are the eighth leading cause of death in the world [6, 7].

Factor analysis is a kind of approach that we may see in deep view in machine learning models [8–13] and various hybrid, enhanced, and boosted optimization techniques [14–27], and intelligent model studies [28–32] as well. For example, there are many well-established enhanced optimizers that have a style of factor analysis and evaluation-based decisions such as particle swarm optimizer (PSO) [33],

Harris hawks optimizer (HHO) [34], whale optimizer algorithm (WOA) [35], differential search (DS) [36], ant colony optimizer (ACO) [37, 38], grey wolf optimizer (GWO) [25, 39], teaching-learning-based optimizer (TLBO) [40], differential evolution (DE) [41, 42], and other hybrid and enhanced methods [18, 20, 22, 26, 27]. Such techniques may also be applied to optimal control [43], analysis of machine learning models [44], optimal resource allocation [45], analysis of shuttlecock production [46], intelligent damage detection [47–49], image and video processing [50–55], and analysis of energy consumption [56]. They can also be applied to deep learning systems [57–61], adaptive control systems [62–65], and monitoring systems [66–69].

The safety of urban and rural roads depends on the behavior of road users, which is the result of each individual's beliefs and attitudes. So, knowing these can give a good understanding of traffic behaviors [70, 71]. In recent years, due to the unsuitable situation of traffic accidents in Iran, many steps have been taken to ensure traffic safety and improve transportation performance [72, 73]. Since driving accidents are a multifactorial cause, identifying the causes and carefully examining the current situation is an essential step in reducing and controlling accidents that without it, the need to plan and manage them cannot be resolved. Therefore, the primary priority of the organizations concerned should be the identification of the root causes of accidents [73–76].

On rural roads of Iran, casualties due to accidental injury are almost 4.33 per 1000 and deaths from unintentional injuries are 5213 [77]. These findings illustrate the need for research and investment in rural infrastructure to improve the safety of rural roads [78]. Rural residents have more traveling compared with urban residents [79]. Although rural accidents may seem minor based on road casualties than urban roads, studying rural roads should be a priority with a social equity approach in mind [80].

In recent years, various studies have been carried out on the subject area of traffic safety on rural roads. Ghaffar et al. [81] attempted to assess the burden of road traffic injuries (RTIs) in Pakistan. Results showed that most accidents occurred from 12 to 18. The incidence of RTI was the highest at the age of 16 to 45 and RTI in males was about three times greater than females. Labinjo et al. [82] conducted a population-based research to examine the RTI epidemiology in Nigeria. Results indicated that motorcycle accidents accounted for 54.33% of RTI. Increased risk of injury was associated with males among the age of 18 to 44. Hu and Xiang [83] investigated the properties of rural road accidents by quantitative analysis. Results showed that 92.68% and 5.42% of fatalities happened in straight and curved roads, respectively. Moreover, fatalities in the daytime were more serious than those in the night time and driving a motor vehicle was the significant reason of fatalities. Zangooei Dovom et al. [84] examined the distribution of fatal accidents in Iran. According to the result, the males had more casualties compared with the females and most accidents had a peak at 21 to 30 ages for both genders. Moreover, the male-to-female ratio was 3.41. They also indicated that the riskiest group was the male motorcyclist among all road users. López et al. [85] investigated the accident patterns and contributory factors on rural two-lane highways. Results of the study showed that the highest accident rate occurred in the condition of good weather, daylight, regular working day, the age group of 28–60, summer season, male gender, and from 12 to 18. Zimmerman et al. [86] aimed to survey all people living in households within 200 m of two low volume rural roads in Tanzania. Results showed that the majority of crashes contained motorcycles (71%) and the majority of victims were males (82%) with 27 mean age. Lee and Jeong [87] investigated the properties of road collisions between rural roads and expressways in truck drivers. Results indicated that the crash rates were greater in the middle of the week. On rural roads, the accident rates in the daytime were greater (81.7%) than those in the night time. Accidents mostly occurred in clear/cloudy weather (76.2%). Most accidents happened on the straight roads (62.2%), followed by intersections (15.4%) and curved roads (9.4%). Casado-Sanz et al. [80] considered various factors in rural road accidents. The results showed that driver's age 30–45 years old, male driver, the middle of the week, good weather condition, and daylight had the maximum percentage of accidents on rural roads in Spain. Kamboozia et al. investigated various factors affecting the severity of accidents on rural roads of Iran and indicated that male drivers had a significant contribution in the occurrence of vehicle accidents. Moreover, 12 to 6 pm had the highest accident rate (day time). They also revealed that the middle of the week recorded the greatest accident occurrence [88]. Recently, optimization algorithms are applicable for various engineering problems [20–26, 34, 89, 90].

Studies have shown the essential need to figure out the factors affecting accidents. The abundance of tourist and natural attractions, as well as the location of people living in the villages, has caused many traveling in the Guilan province. On the other hand, the distribution of urban and rural population centers has increased the traffic volume and, consequently, the number of traffic accidents in Guilan. So, this research aimed to explore the main features of road accidents and estimate that which of these factors become significant in affecting the probability of accident severity on rural roads of Guilan province to improve road safety and take the necessary safety measures.

2. Methodology

2.1. Data. The analytical methods used in this study included descriptive statistical surveys, Kolmogorov–Smirnov test (K-S), Friedman test (FT), and factor analysis (FA), and data used were 2481 road accidents resulting in fatal, injury, and damage accidents recorded from Guilan traffic police on rural roads from March 2014 to March 2019. Data included accident severity, accident time, accident day, accident season, road surface condition, geometry of accident location, daylight condition, type of vehicle accident, driver age, driver gender, weather condition, and reason of accident. The dependent variable in this study was different levels of accident severity, which initially were classified into three categories of injury and fatal and damage. Since the number

of fatal accidents was smaller than the total number of accidents, fatal accidents were combined with injury accidents and the dependent variable was classified into two categories of injury/fatal and damage accidents. Figure 1 indicates the process of this research.

2.2. Analytical Method

2.2.1. Kolmogorov–Smirnov Test. The K-S test is commonly applied to investigate the normality of data [91] and is a nonparametric experiment for the data distribution [92]. By comparing the approximate significance test with α, one can decide about the normality of data distribution. Considering $\alpha = 0/05$ (with 95% certainty), if p value $> 0/05$, the null hypothesis of normality rejects. It means that data distribution is not normal [93]. The null hypothesis (H_0) is that the data have a normal distribution, and the alternative hypothesis (H_a) is that they have not [94]. Indeed this test is a compliance test distribution for quantitative data [95].

2.2.2. Friedman Test. The Friedman rank sum is normally utilized to compare the classifiers over multiple datasets. It is an extensively utilized nonparametric technique to analyze various associated specimens in computational biology and other areas. For instance, it is used for comparing the performance consequences of a group of (expression-oriented) classifiers over multiple datasets that cover benchmark functions, case problems, or performance indicators. The Friedman examination process is to analyze variance by ranks, indeed, detected rank scores or rank scores found by making numerical or ordinal results in order. It is utilized in case one which is not enthusiastic for making robust distributional assumptions. Simultaneous examinations are also proposed in addition to the ordinary normal approximation that uses the covariance outline of the distribution of the values of the variances in rank sums [88, 96, 97].

2.2.3. Factor Analysis. The FA is one of the statistical methods for modeling the covariation among a dataset. It is used to determine the most influential variables when the number of variables is high and the relationships between them are unknown. The main purpose of using the FA is to reduce the dimensionality of a set of observed variables and determine the most important variables affecting the formation of phenomena. The FA is generally divided into two categories of the exploratory factor analysis (EFA) and the confirmatory factor analysis (CFA). The EFA is applied to identify the latent constructs when the structure of the relationships among variables is unknown and to generate hypotheses about their possible structures, while the CFA is used to identify variables by dimensions [98]. The EFA method was used in this research.

Since the sample size is a determining factor in the accuracy of element clustering by the FA technique, it must be assured that it is sufficient. In EFA, Kaiser–Mayer–Olkin (KMO) and Bartlett's test of sphericity are used to check the suitability of the data (sample size). The amount of KMO is between zero and one, and its small values (less than 0.5) indicate that the available correlations are not suitable for FA. The closer this value to one, the appropriate the data for the FA [99]. The output of Bartlett's test of sphericity can also be used to calculate chi-square amounts.

3. Results and Discussion

At first, using the K-S test, the parametric or nonparametric data were determined for the correct selection of statistical tests. Then, the FT was used to determine the priority of the factors, and the FA was applied to identify the underlying variables. Finally, by comparing different methods of analysis, the most important factors in increasing the likelihood of accidents were proposed to increase safety and reduce vehicle accidents on rural roads of Guilan.

3.1. Frequency Analysis

3.1.1. Investigating Accident Year. Analysis of accident statistics based on the years, as shown in Figure 2(a), showed that the highest number of accidents occurred in 2015-2016 ($n = 562$) and the least occurred in 2018-2019 ($n = 428$). Between 2014 and 2019, a total of 2481 vehicle accidents on rural roads were recorded; 84.92% of drivers were injured and dead, and 15.08% of vehicles were damaged, which is shown in Figure 2(b), indicating that rural vehicle accidents of Guilan often resulted in injuries/fatalities and there were few accidents resulted in damages. The highest percentage of injury/fatal and damage accidents occurred in 2017-2018 (19.99%) and 2014-2015 (4.19%), respectively. Figure 2(c) shows that the highest rates of male and female accidents occurred in 2015-2016 (21.28%) and 2017-2018 (1.81%), respectively, and the lowest accident rates for them occurred in 2018-2019 and 2014-2015 in the amount of 16.65% and 0.36%, respectively. On the other hand, male drivers generally were accounted for the highest percentage of vehicle accidents (about 95.32%). Male-to-female ratios indicated considerably higher male rates, maximum 50.88 times higher in 2014-2015, and on average 28.22.

3.1.2. Effect of Accident Time. Figure 3(a) shows that the highest percentage of vehicle accidents for both males and females (44.06%) occurred from 12 pm to 6 pm, of which 41.72% of these were males and only 2.34% were females. The lowest percentage of male and female drivers was 4.76% and 0.16% from 12 am to 6 am, respectively. Also, according to Figure 3(b), 37.36% of accidents as the highest percentage resulted in injuries and fatalities and only 6.69% resulted in damages between 12 pm and 6 pm. The lowest injury/fatal (3.67%) and damage (1.25%) accidents were recorded from 12 am to 6 am.

3.1.3. Effect of Accident Day. According to Figure 4(a), 40.67% of vehicle accidents (as the highest percentage) happened in the middle of the week, of which 38.90% were males and 1.77% were females. From these days, 34.46% of drivers were injured and dead and 6.21% resulted in vehicle

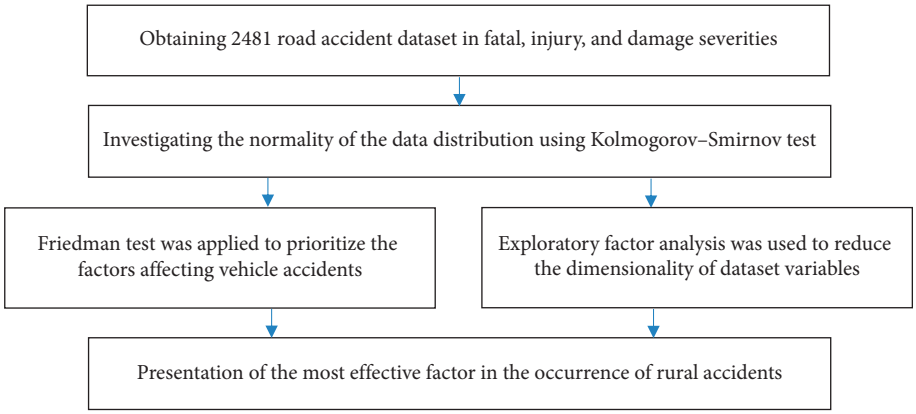

Figure 1: The steps of the research method.

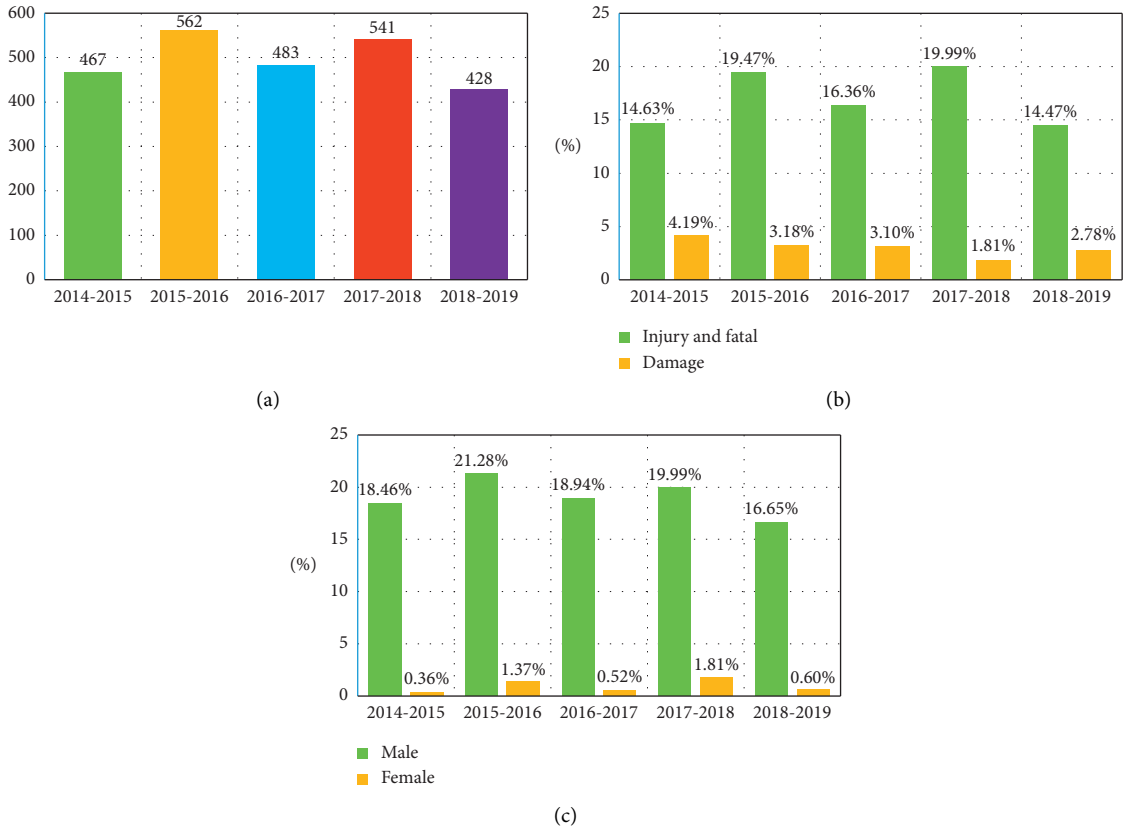

Figure 2: Accident statistics based on (a) accidents year; (b) accident severity and years; (c) driver gender and accidents year.

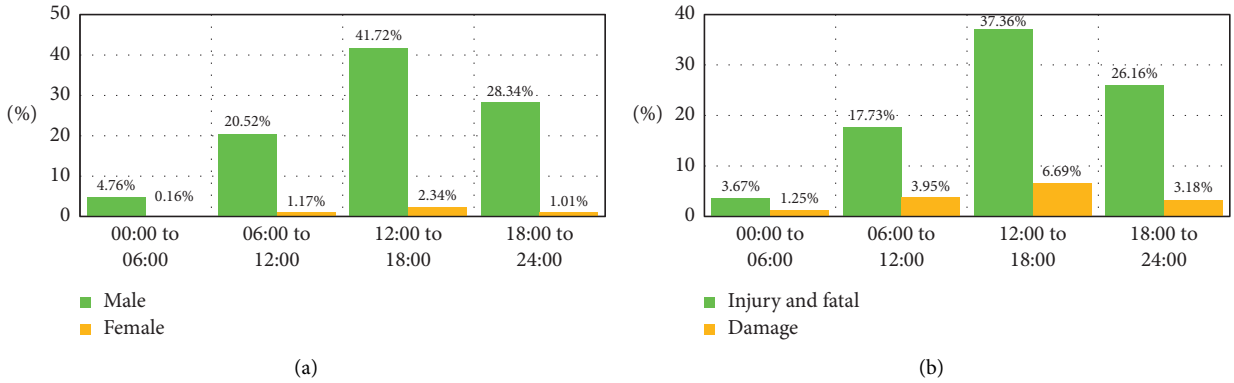

Figure 3: Accident statistics based on accident time and (a) driver gender; (b) accident severity.

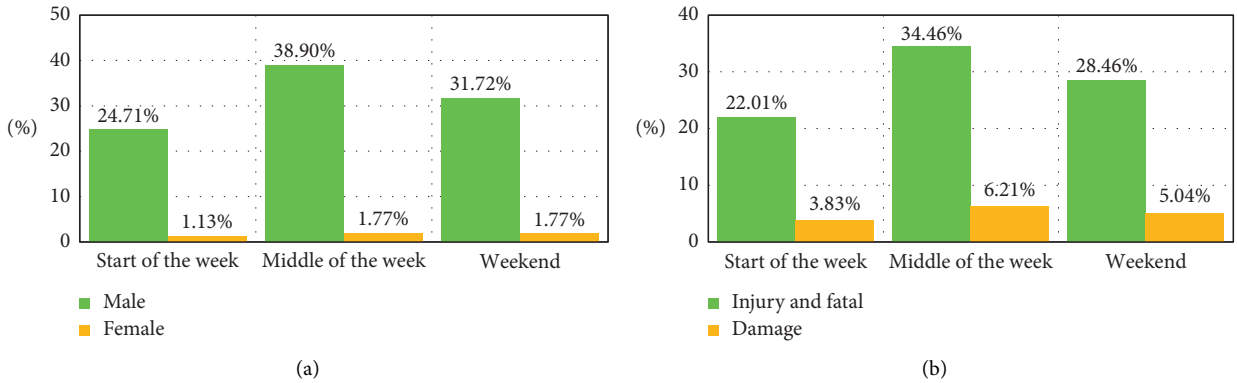

Figure 4: Accident statistics based on accident day and (a) driver gender; (b) accident severity.

damages by accidents, as shown in Figure 4(b). After that, most of the accidents were on weekends (33.49%), of which 31.72% were males and the rest were females. The lowest percentage of accidents occurred during the start of the week, with male drivers accounting for 24.71% of accidents and female drivers accounting for 1.13% of them. On the other hand, as shown in Figure 4(b), the first few days of the week had the lowest percentage of injuries/fatalities (22.01%) and damages (3.83%).

3.1.4. Effect of Accident Season. As shown in Figure 5(a), 30.17% of accidents occurred in the summer season as the highest percentage, of which 28.71% were males and 1.46% were females and the minimum accidents happened in autumn. Female drivers had the lowest percentage of accidents in the autumn, with a magnitude of 0.77%. According to Figure 5(b), the most serious and the lowest percentage of injury/fatal accidents occurred in summer (27.63%) and winter (15.91%), respectively, but it was the reverse for damage accidents (4.80% for winter and 2.54% for summer).

3.1.5. Effect of Road Surface Condition. Three road surface conditions of dry, wet, and snowy were considered in the research. According to Figure 6(a), male drivers had the highest portion of accidents, accounting for 83.19%, which occurred on the dry surface, 11.89% happened on wet surface, and the rest of male accidents (0.24%) happened on snowy surface condition. Female drivers had the least participation in traffic accidents. It should be noted that there were no female driver accidents on the snowy surface. Results of Figure 6(b) show that dry surface condition caused the highest percentage of injuries/fatalities (75.01%) and the lowest vehicle damage rate occurred in snowy pavement (0.12%).

3.1.6. Effect of Geometry of Accident Location. The straight road, as shown in Figure 7(a), caused the most accidents (74.57%), with the male and female drivers contributing 71.02% and 3.55%, respectively. The intersection also caused the least percentage of accidents, with male drivers contributing 0.48% and females accounting for 0.04%. According to Figure 7(b), the straight road accounted for the largest percentage of all injury/fatal accidents, 62.31% of rural road accidents, followed by accidents on the horizontal curve (22.25%), and the intersection (0.36). Also, the most damage accidents (12.25%) occurred on the straight road, with a small percentage of them (2.66%) on the horizontal curves and 0.16% on the intersection.

3.1.7. Effect of Daylight Condition. As shown in Figure 8(a), daylight condition was considered day, night, and sunrise/sunset in this study. 71.06% of accidents occurred on day, of which 67.39% were males and 3.67% were females, followed by 27.81% of night accidents. The lowest percentage of accidents was at sunrise/sunset time (1.13%). It should be noted that no female accidents occurred in sunrise/sunset. Results in Figure 8(b) show that among the accidents that occurred in the day, 59.77% resulted in injuries/fatalities and 11.29% resulted in damages, respectively. After that, 27.81% of accidents that happened at night resulted in injuries/fatalities (24.1%) and damages (3.71%), respectively, followed by 1.05% and 0.08% of sunrise/sunset accidents for them, respectively. So, the lowest percentage of accidents was during sunrise/sunset time.

3.1.8. Effect of Type of Vehicle Accident. Figure 9(a) shows that the largest type of vehicle accidents involved in a road traffic accident (RTA) was car-motorcycle/bike accidents that 41.15% of accidents were males and 1.98% were females, followed by getting off the road accidents (22.37% for males and 0.93% for females) and car-car accidents (24.02% for males and 1.21% for females). The lowest percentage of vehicle accidents was related to car-heavy truck accidents by male drivers (0.52%) and female drivers (0%). Results in Figure 9(b) shows that the highest percentage of injury/fatal vehicle accidents (42.52%) was car-motorcycle/bike accidents and the least in injuries/fatalities was car-heavy truck accidents (0.20%). Car-car accidents were also the leading cause of damages (5.93%), and the least damages were occurred in car-agricultural machinery accidents (0.12%).

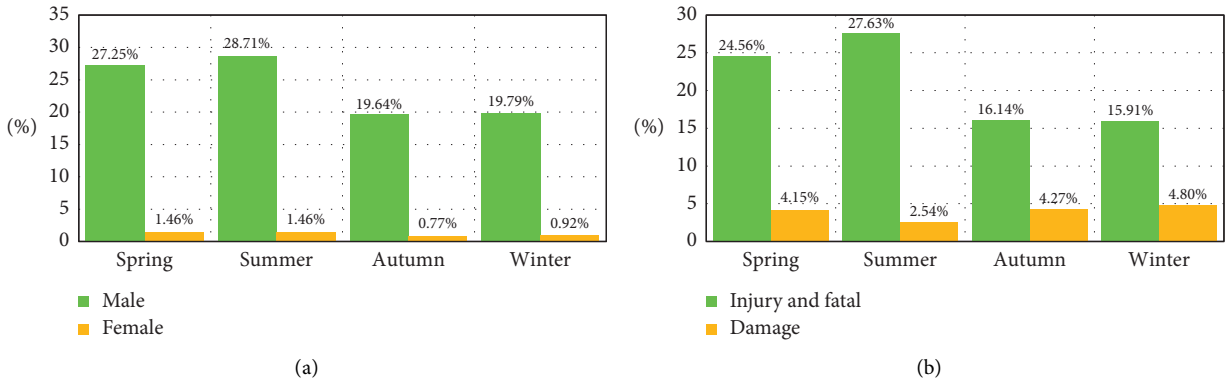

Figure 5: Accident statistics based on accident season and (a) driver gender; (b) accident severity.

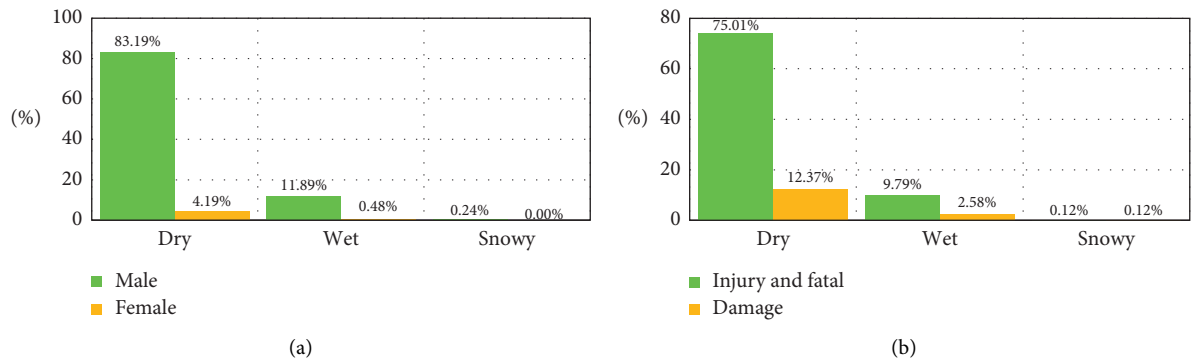

Figure 6: Accident statistics based on road surface condition and (a) driver gender; (b) accident severity.

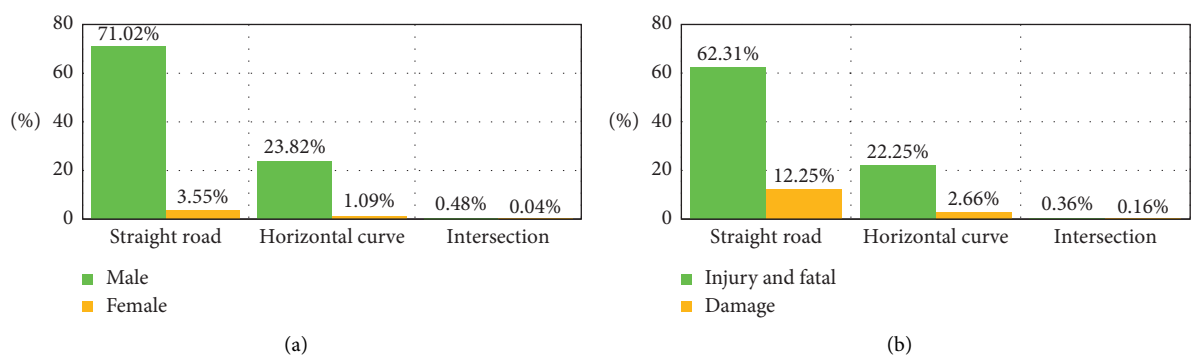

Figure 7: Accident statistics based on geometry of accident location and (a) driver gender; (b) accident severity.

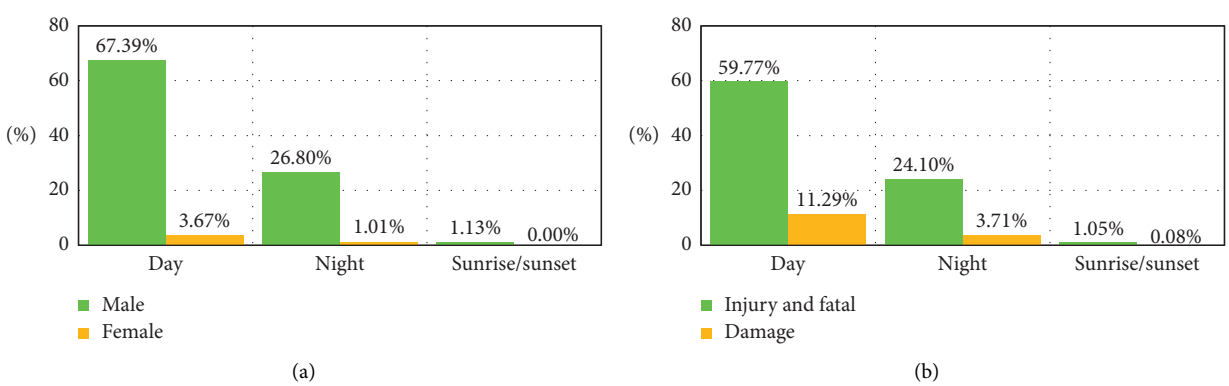

Figure 8: : Accident statistics based on daylight condition and (a) driver gender; (b) accident severity.

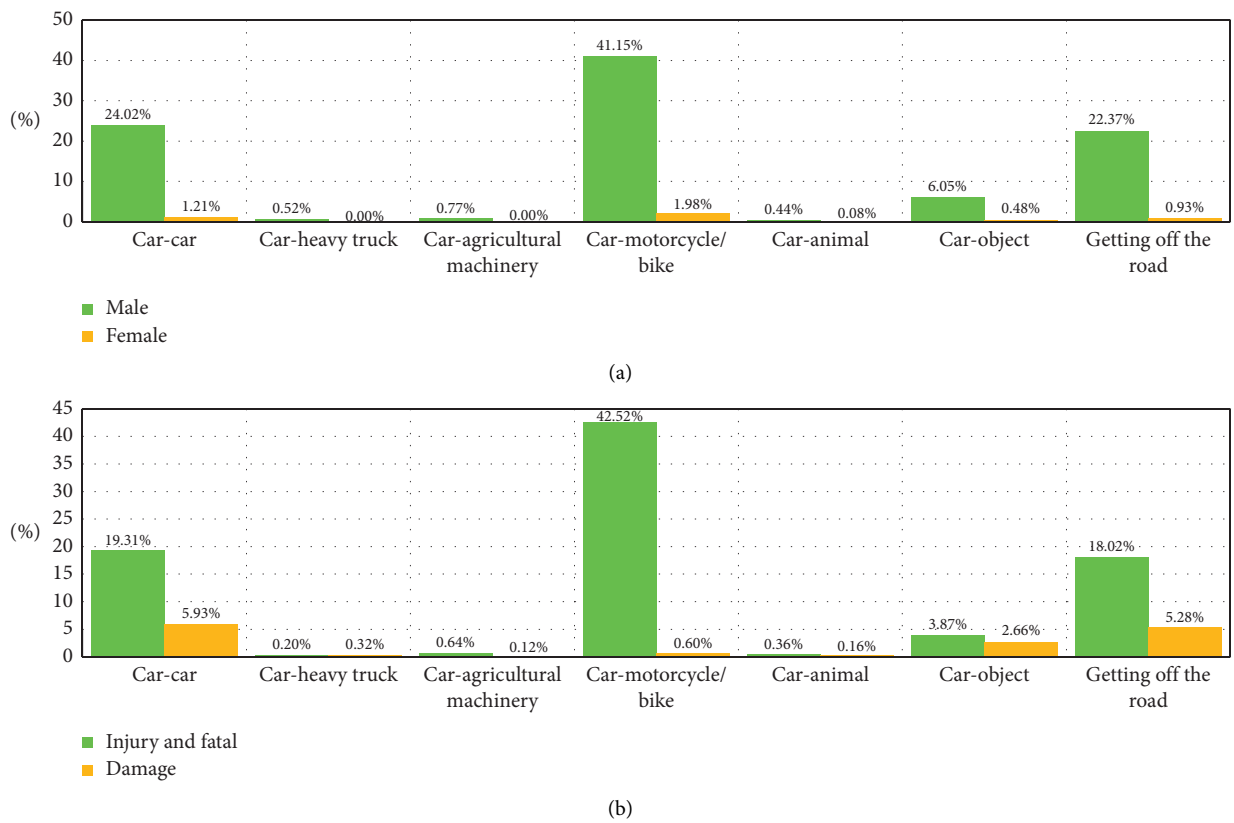

Figure 9: Accident statistics based on type of vehicle accident and (a) driver gender; (b) accident severity.

3.1.9. Effect of Driver Age and Gender. In this research, drivers were categorized into five age groups and both injury/fatal and damage accidents were higher among males than females, as shown in Figure 10(a). Percentages of accidents were prepared for the two genders for all age categories. Results indicated that greater male and female accident rates were in the age group of 30 to 45 (35.91% and 2.34%, respectively). The lowest male and female accident rates were 2.98% and 0.04%, with the age group less than or equal to 18, as shown in Figure 10(a). Also, the age groups of 60 and over had the lowest percentage of accidents in females. According to Figure 10(b), the most injury/fatal and damage accidents were in drivers at the age of 30 to 45 (31.76% and 6.49%, respectively) and the lowest age at which injury/fatal and damage accidents occurred (2.82% and 0.2%, respectively) was in the age group less than or equal to 18.

3.1.10. Effect of Weather Condition. Male and female accident rates were compared in four different weather conditions: clear/sunny, cloudy, rainy, and snowy. Results obtained on weather conditions for both male and female accidents are illustrated in Figure 11(a). The higher male and female accident percentages were observed in clear/sunny weather (76.78% for males; 3.67% for females), and snowy weather had the lowest percentage of accidents for both of them (0.52% and 0%, respectively). Statistics showed no female accidents on rural roads of Guilan in snowy weather. Clear/sunny weather had the highest percentage of both injury/fatal and damage accidents (68.8% and 11.65%, respectively), and the lowest percentage of these accidents was due to the snowy weather (0.28% and 0.24%, respectively), as shown in Figure 11(b).

3.2. Kolmogorov–Smirnov Test. For evaluating the normality of the data, first, the statistical distribution of the data should be ensured. So, the K-S test was applied to check the normality of the data distribution. Table 1 shows the results of this test.

As shown in Table 1, the significance level in the K-S test (represented by sig.) was less than 0.05 and considering 5% error, the null hypothesis (H_0) was rejected, which is the natural distribution of the variables, and H_1 was accepted. So, the distribution was not normal and nonparametric tests were used.

3.3. Friedman Test. In the research, 11 independent variables were presented that the rank of each of these variables was examined by the FT. The FT can be applied to evaluate the rank equality of variable levels. Table 2 shows the statistical significance in which the statistical sample volume, chi-square statistic, degrees of freedom, and the level of significance (α that represented by sig.) are represented.

As shown in Table 2, a lower level of significance of α than 5% indicated that H_0 was rejected, which shows that claiming the rank equal was not accepted. As a result, ratings

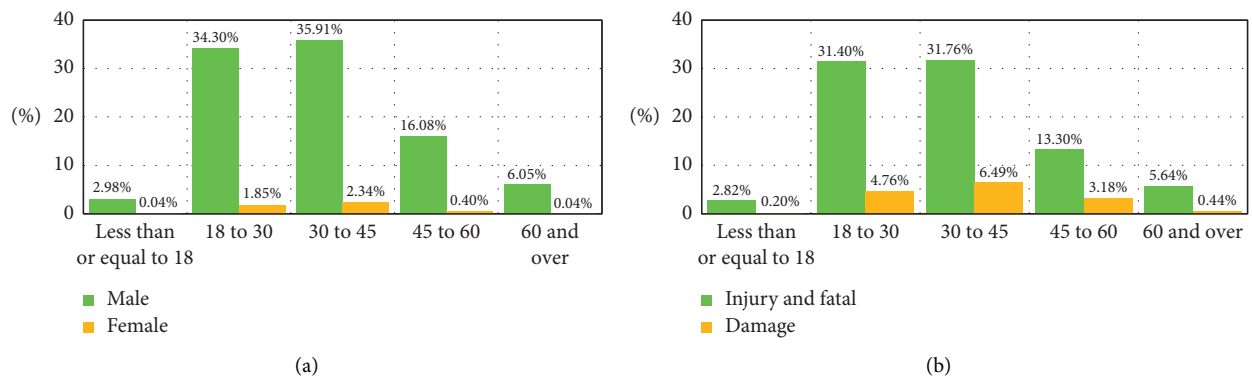

Figure 10: Accident statistics based on driver age and (a) driver gender; (b) accident severity.

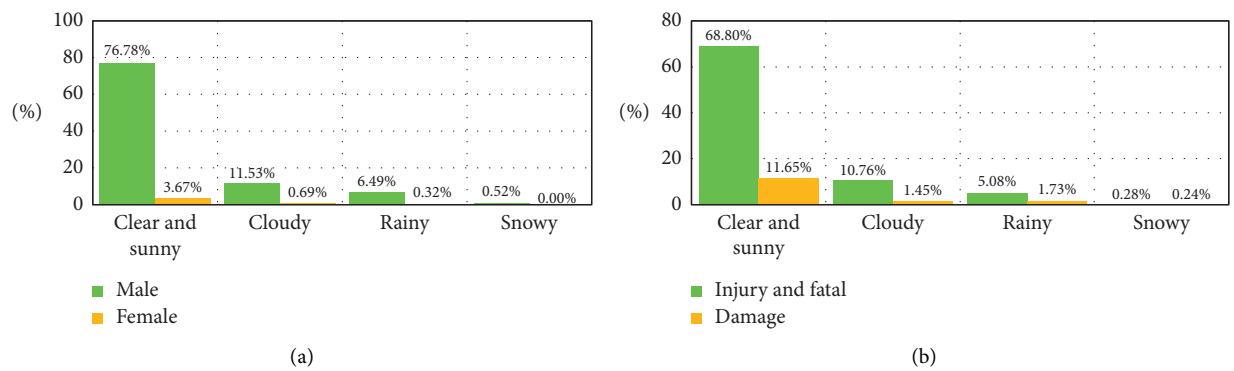

Figure 11: Accident statistics based on weather condition and (a) driver gender; (b) accident severity.

were not uniform. In Table 3, the ranking status of the independent variables is presented, indicating the mean rating of each variable. The smaller the mean rating, the greater the importance of the variable.

According to Table 3, the variables of weather condition, road surface condition, and type of vehicle accident had the highest rank, respectively, with the test score of 3.22, 3.48, and 3.99, respectively. On the other hand, the variables of geometry of accident location, accident day, and driver gender were the least important factors in the occurrence of accidents, showing that weather condition as an environmental factor had the greatest impact on the occurrence of vehicle accidents in the rural roads and then road surface condition as a road factor and the second most effective factor in increasing the occurrence of accidents. Type of vehicle accident also was identified as the third most influential factor in these accidents.

3.4. Factor Analysis. Table 4 indicates the result of the FA, including the KMO index and the Bartlett test.

According to Table 4, the KMO amount was 0.507, indicating that it was appropriate to use FA. Bartlett's test results showed that approximate chi-square was much larger than five. Also, the level of significance of the test statistic was less than 0.05, meaning that the alternative hypothesis was confirmed and there was a significant correlation between the variables. Therefore, all the factors of the research were effective in investigating the severity of accidents, and in other words, the relationship between all components was confirmed.

Table 5 shows the eigenvalues and variance corresponding to each component. Eigenvalues specify the components that remain in the analysis. Whatever the eigenvalue of a component is greater, that component indicates more variance. In fact, components with an eigenvalue of less than 1 are excluded from the analysis. In Table 5, three parameters of initial eigenvalues, eigenvalues of nonrotating, and postrotating extraction components are given.

In Table 5, components 1 to 5 had eigenvalues greater than one. So, they remained in the analysis. Due to the eigenvalues of nonrotating extraction components, five components could explain the variances and variability of variables and contained approximately 58% of the variance. In Table 6, the component matrix is presented before rotation, which shows the component loads of each variable in the remaining components.

Due to the difficulty of interpreting nonrotating component loads, the components were rotated to make interpretation easier. In other words, in the component matrix before rotation, the first component expressed a higher percentage of variation, whereas in the components rotation method, each of the remaining components represented an almost identical proportion of the total change explained by the three parameters mentioned. Table 7 shows the rotation matrix of the remaining components, which the extraction

Table 1: The K-S test result.

Number	Variables	Most extreme differences			Test statistic	Asymp. sig. (2-tailed)
		Absolute	Positive	Negative		
1	Accident time	0.242	0.194	−0.242	0.242	0.0
2	Accident day	0.222	0.204	−0.222	0.222	0.0
3	Accident season	0.207	0.207	−0.142	0.207	0.0
4	Road surface condition	0.520	0.520	−0.353	0.520	0.0
5	Geometry of accident location	0.467	0.467	−0.286	0.467	0.0
6	Daylight condition	0.444	0.444	−0.267	0.444	0.0
7	Type of vehicle accident	0.221	0.207	−0.221	0.221	0.0
8	Driver age	0.216	0.216	−0.166	0.216	0.0
9	Driver gender	0.541	0.541	−0.413	0.541	0.0
10	Weather condition	0.472	0.472	−0.318	0.472	0.0
11	Reason of accident	0.295	0.295	−0.219	0.295	0.0

Table 2: The FT results.

Number of data	Chi-square	Degrees of freedom	Asymp. sig.
2481	13965.319	10	0.0

Table 3: Mean rank in the FT.

Variables	Mean	Rank
Weather condition	3.22	1
Road surface condition	3.48	2
Type of vehicle accident	3.99	3
Accident time	4.57	4
Daylight condition	5.13	5
Accident season	5.53	6
Reason of accident	6.24	7
Driver age	6.83	8
Geometry of accident location	7.18	9
Accident day	7.51	10
Driver gender	7.97	11

Table 4: KMO and Bartlett's test.

KMO measure of sampling adequacy.		0.507
Bartlett's test of sphericity	Approx. chi-square	2156.045
	Df	55
	Sig.	0.0

method in both matrices was principal component analysis and the rotation technique was Equamax with Kaiser Normalization. The values in Tables 6 and 7 indicate the degree of correlation of the relevant variable with the relevant components.

In the FA, the influence of variables on the severity of accidents was expressed using the coefficients listed in the rotated component matrix table. The greater the absolute magnitude of the coefficients of each variable, the more effective the desired component in total changes of each variable. The FA was performed on 11 independent variables affecting vehicle accidents on rural roads of Guilan, which identified five components as the main components. The analysis showed that the variables of weather condition and road surface condition were under the first component that the significant coefficients between the first component and each variable were 0.899 and 0.892 and positive, respectively. Therefore, it can be said that weather condition and road surface condition were the first factors affecting the occurrence of vehicle accidents on these rural roads, which had a large impact (depending on the size of the coefficient) on the occurrence of accidents. Also, daylight condition and accident time were under the second most influential components in accidents with positive coefficients (0.808 and 0.793, respectively) that positively affected the occurrence of accidents. Similarly, type of vehicle accident and reason of accident variables were under the third component (with coefficients of 0.796 and 0.778, respectively), geometry of accident location and accident season (with coefficients of –0.783 and 0.632, respectively, in which negative coefficient indicates that the variable had a significant effect on reducing accidents) were under the fourth component, and finally, driver age and driver gender (with coefficients of –0.679 and 0.595, respectively) were considered as the fifth most effective factor in vehicle accidents on rural roads of Guilan.

3.5. Comparisons. The current study investigated the risk factors of accident severity in vehicle accidents on rural roads of Guilan by applying several analysis methods to determine more precisely the variables affecting the severity of vehicle accidents. Results provided insight regarding the relationship between the various risk factors and accident severity for enhancing traffic safety on these roads. Each of these methods, considering their own specific algorithms, investigated the effective variables. So, to summarize the results using different methods, the results should be compared with each other. In the FT, the variables of weather condition, road surface condition, and type of vehicle accident were among the first to third rankings that caused accidents. While in the FA, the variables of weather condition and road surface condition were identified as the first effective factor, and daylight condition and accident time were recognized as the second effective factor in vehicle accidents. This illustrates that the joint result of the FT and FA, weather condition as an environmental factor, was recognized as the most important factors effective in vehicle accidents on rural roads of Guilan.

Table 5: Total variance explained.

Component	Initial eigenvalues			Extraction sums of squared loadings			Rotation sums of squared loadings		
	Total	% of variance	Cumulative %	Total	% of variance	Cumulative %	Total	% of variance	Cumulative %
1	1.730	15.726	15.726	1.730	15.726	15.726	1.695	15.410	15.410
2	1.330	12.093	27.819	1.330	12.093	27.819	1.344	12.217	27.627
3	1.281	11.650	39.469	1.281	11.650	39.469	1.280	11.636	39.263
4	1.072	9.749	49.218	1.072	9.749	49.218	1.069	9.720	48.982
5	1.039	9.444	58.662	1.039	9.444	58.662	1.065	9.680	58.662
6	0.985	8.959	67.621						
7	0.969	8.806	76.426						
8	0.899	8.171	84.597						
9	0.727	6.610	91.207						
10	0.629	5.719	96.926						
11	0.338	3.074	100.000						

Table 6: Component matrix before rotation.

Variables	Component				
	1	2	3	4	5
Accident time	0.185	0.763	0.080	0.071	−0.110
Accident day	0.041	−0.059	−0.231	0.264	0.275
Accident season	0.250	0.077	−0.070	−0.315	0.543
Road surface condition	0.871	−0.146	−0.127	0.051	−0.029
Geometry of accident location	0.022	−0.128	−0.062	0.661	−0.439
Daylight condition	0.250	0.742	0.222	0.071	0.014
Type of vehicle accident	0.109	−0.129	0.751	0.271	0.062
Driver age	0.158	−0.179	0.075	−0.499	−0.448
Driver gender	−0.055	−0.125	−0.044	0.340	0.496
Weather condition	0.875	−0.187	−0.087	0.061	−0.012
Reason of accident	0.065	−0.227	0.754	−0.108	0.111

Table 7: Rotated component matrix.

Variables	Component				
	1	2	3	4	5
Accident time	0.008	0.793	−0.081	−0.016	−0.060
Accident day	0.100	−0.069	−0.136	−0.004	0.413
Accident season	0.187	0.043	−0.023	0.632	0.173
Road surface condition	0.892	0.047	−0.009	0.028	−0.019
Geometry of accident location	0.132	−0.012	−0.013	−0.783	0.141
Daylight condition	0.051	0.808	0.082	0.074	−0.001
Type of vehicle accident	0.045	0.076	0.796	−0.150	0.085
Driver age	0.151	−0.162	0.005	0.048	−0.679
Driver gender	−0.006	−0.120	0.089	0.075	0.595
Weather condition	0.899	0.018	0.041	0.029	−0.008
Reason of accident	−0.012	−0.080	0.778	0.137	−0.133

During the study period, 2481 vehicle accidents occurred on the rural roads of Guilan, which resulted in 84.92% injuries/fatalities and 15.08% damages, respectively. 2018-2019 had the lowest number of accidents with 428 cases and 2015-2016 had the highest number with 562 cases. In terms of gender, 95.32% of drivers in vehicle accidents were male and only 4.68% were females. 12 pm to 6 pm was identified as the most dangerous accident hours and 12 am to 6 am was recognized the safest. However, in general, considering the accidents at other times, most of the accidents happened in the daytime. The examination of the number of accidents on a weekly basis showed that the highest number was in the middle of the week. Summer and spring seasons, respectively, were the most dangerous seasons and autumn and then winter were the safest seasons. Most of the accidents in the province on rural roads occurred in dry surface condition, straight road, and in clear and sunny weather. Examination of the type of vehicle involved in accidents showed that car-motorcycle/bike accidents had the highest share. Also, based on the results of driver age, both male and female drivers aged 30 to 45 and then with a slight difference, drivers aged 18 to 30 had the highest accident rates. Finally, the results of reason of accident showed that invasion to left and right and then inability to control were identified as the most important reason of accidents.

Given that most accidents occurred from 12 pm to 6 pm and in the middle of the week, it can be said that these accidents were mostly due to return trips from work. Then, most of the accidents occurred on the weekends due to the increased travel to the province from elsewhere, and on the other hand, due to the high rate of motorcycle and bike accidents, high traffic of motorcycles and bicycles on these roads was one another major cause of accidents in these areas in which appropriate safety measures should be adopted. Given the high rate of accidents in the summer and after the spring and due to the favorable climate of the province, high rates of excursions were another reason for accidents along these roads. The least accidents occurred in the autumn and winter, respectively, which could be due to adverse climatic conditions for travel, particularly reduced the use of motorcycles and bicycles and agricultural activities in the colder months of the year.

The reasons for using motorcycles/bikes can be locals' livelihoods, cheapness compared with cars, easy learning, and accessibility for people of all ages, youth unemployment, and the proximity of the villages to each other, which make the use of motorcycles/bikes in the province more prosperous. This can increase the likelihood of car-motorcycle/bike accidents occurring.

The results of this study in comparison with the previous studies showed that the greatest multitude of accidents

happened during the daytime, similar to some studies [80, 81, 83, 85, 87, 100]. In opposition, Soltani et al., represented the highest number of accidents at night [101]. Results also showed that most accidents happened at 12 to 18, which confirms others [81, 83, 85]. Taking into account the days of the week, the results showed that most of the accidents occurred in the middle of the week that is in accordance with some previous studies [80, 85, 87], considering that the mid-week days also include working days. The maximum number of accidents was in summer and the minimum number of them occurred in autumn season probably because of more using of the vehicle in summer on rural roads of Guilan that is consistent with other studies that have shown that most accidents occurred in summer [77, 85] and is in contrast with some other studies which indicated more accident occurred in winter because of snowy and slippery roads [102]. This may be because that region had more snowfall than the study area of this research. Considering road surface conditions, the highest number of accidents occurred on dry surface and then most accidents were recorded on wet surface that confirms the study of Mayora and Piña [103], which showed that most accidents occurred on dry road conditions. The results also indicated that straight road had the highest accident rates among the other types which other studies confirm [83, 87]. This research indicated that RTAs involving a motorcycle/bike were most common, which is consistent with others [77, 82, 83, 86]. Motorcyclists/cyclists have been classified as vulnerable road users since they are not protected properly and share the road with high-speed vehicles and therefore are at greater risk [86]. The result that male motorcyclist/cyclist was more frequent than female ones is consistent with some research studies on road accidents [84, 104] and with some other research studies indicating that male riders were at the highest risk of the accidents [104, 105]. The highest male-to-female ratio was due to the fact that in Iran, females usually do not ride a motorcycle/bike alone legally. Generally, the study revealed that the proportion of male drivers was much greater than the proportion of female drivers in rural road accidents, which is in line with others [77, 80–86, 106]. It can be attributed to the fact that they are more prone to high-risk behaviors or unsafe road practices. The age group most affected by rural road accidents in this study was 30–45 [80], followed by 18–30, which affirms the findings from other surveys [77, 81, 82, 84–86, 106, 107]. With respect to weather condition, the highest accident rate occurred in the condition of clear and sunny weather that is in line with the results of other research studies [80, 85, 87]. Reason of accidents showed that invasion to left and right and then inability to control led to the highest number of accidents which is similar to Richter et al. results [108].

4. Conclusion

In this research, after analyzing the accident data to make a better decision, by statistical analysis of accidents, the causes of the risk of accident of Guilan have been concluded. Also, for the more practical use of this study, some suggestions have been made regarding the results. The most important results of the frequency analysis are as follows:

(i) The result of the K-S test indicated that the test was significant and therefore, the independent variables did not have a normal distribution. As a result, nonparametric tests were applied.

(ii) In the FT, the most important factors affecting vehicle accidents were weather condition, road surface condition, and type of vehicle accident, and this indicates that the most influential factor affecting these accidents on rural roads of Guilan was weather condition as an environmental factor and the second most important factor was road surface condition as an environmental factor (like weather condition) affecting the occurrence of accidents. Therefore, according to the FT results, environmental factor had the greatest impact on the occurrence of accidents.

(iii) Based on the FA, five factors were identified as the main factors affecting Guilan rural accidents. In other words, 11 effective variables in accidents have been reduced to five factors separately. The FA showed that the variables of weather condition and road surface condition were under the first factor affecting the occurrence of accidents. Therefore, the environmental factor (as the first factor) was the most important factor in the occurrence of accidents. The variables of daylight condition and accident time were under the second factor; type of vehicle accident and reason of accident were under the third factor; geometry of accident location and accident season were under the fourth factor; and driver age, driver gender, and accident day were under the fifth effective factor in occurrence of vehicle accidents in Guilan.

(iv) For the future work and analysis, we will deal with some state-of-the-art machine learning [14–19, 27, 37, 38, 109–112] and optimization algorithms [8, 11, 13, 113–115] to be incorporated with the proposed approach to attain more accuracy. Also, in future works, we will investigate factor analysis in more varieties of topics such as analysis of optimal water resources [116], analysis of multicriteria design of shale-gas-water supply chains [117], life cycle assessment of greenhouse gas emissions [118], coupling system dynamics analysis [119], assessing the global potential of aquifer thermal energy storage [120], analysis of process development [121], analysis of shape measurement [122], analysis of energy efficiency modeling [123], analysis of innovative oxidation processes [124–128], and pareto-based multiobjective optimization [129, 130].

5. Safety Approach

In order to decrease the number of accidents on rural roads of Guilan, it is necessary to consider all the factors together

that are effective in the occurrence of accidents and provide appropriate solutions according to their importance. According to the analysis results, executable solutions that can be used to decrease rural road accident risks are as follows:

(i) Motorcyclists and cyclists were more likely to be involved in accidents due to the insufficient visibility of drivers. Therefore, they need to be careful about how the vehicle is moving (invasion to left and right, right of way violation, and inability to control), especially in clear and sunny weather. Wearing bright clothes and using lamps are recommended for motorcyclists and cyclists at night.

(ii) In addition to advertising on the radio, television, and urban advertising, police, municipal, forensic, and health organizations are recommended to gift luminous stickers for motorcyclists and cyclists for free.

(iii) Increasing the resolution and the number of signs and using reflective signs on low-speed vehicles on rural roads are recommended.

(iv) Given the high accident rates on straight roads, more police presence and control on these roads, especially from 12 pm to 6 pm, are one of the best ways to reduce vehicle accidents. Also, considering most accidents occurring during the day and between 12 pm to 6 pm, police control is better than night time. On the other hand, because the accident rate is also high from 6 pm to 12 am (nights), it is recommended to use proper lighting on rural roads.

(v) Encouraging motorcyclists and cyclists to use helmets as well as enforcing stricter laws dealing with offenders and enacting laws that do not fully cover accident insurance for people without helmets may be appropriate measures to increase their willingness to use them.

(vi) Separating the path of motorcyclists and cyclists in hazardous areas by creating barriers between them and the road is an effective way to increase their safety.

(vii) Warning the drivers on straight road segments since geometry of accident location had effects on accidents. Warning signs or other pavement-based warning techniques, such as pavement marker and rumble strip, can help decrease the risk.

Data Availability

The data used to support the findings of this study are currently under embargo while the research findings are commercialized. Requests for data, 3 months after publication of this article, will be considered by the corresponding author.

Conflicts of Interest

The authors declare that they have no conflicts of interest.

References

[1] S. Hao and L. Yang, "Traffic network modeling and extended max-pressure traffic control strategy based on granular computing theory," *Mathematical Problems in Engineering*, vol. 2019, Article ID 2752763, 11 pages, 2019.

[2] A. Abdi, "Analysing the influence of encroachment angle and median parameters on safety of rural highways using vehicle dynamics performance," in *Proceedings of the IOP Conference Series: Materials Science and Engineering*, IOP Publishing, Bangkok, Thailand, May 2019.

[3] I. Bargegol, "Delay modeling of un-signalized roundabouts using neural network and regression," *Computational Research Progress in Applied Science & Engineering*, vol. 2, pp. 28–34, 2016.

[4] S. Li, "A short-term traffic flow reliability prediction method considering traffic safety," *Mathematical Problems in Engineering*, vol. 2020, Article ID 6682216, 9 pages, 2020.

[5] Y. Li, "MTGPLP approach for traffic signal intelligent control," *Mathematical Problems in Engineering*, vol. 2020, Article ID 8603598, 18 pages, 2020.

[6] World Health Organization, *Global Status Report on Road Safety 2018*, WHO, Geneva, Switzerland, 2018.

[7] S. Wang, "Macrolevel traffic crash analysis: a spatial econometric model approach," *Mathematical Problems in Engineering*, vol. 2019, Article ID 5306247, 10 pages, 2019.

[8] X. Zhang, "Robust feature learning for adversarial defense via hierarchical feature alignment," *Information Sciences*, vol. 560, pp. 256–270, 2020.

[9] X. Zhang, T. Wang, W. Luo, and P. Huang, "Multi-level fusion and attention-guided CNN for image dehazing," *IEEE Transactions on Circuits and Systems for Video Technology*, vol. 1, p. 1, 2020.

[10] X. Zhang, M. Fan, D. Wang, P. Zhou, and D. Tao, "Top-k feature selection framework using robust 0-1 integer programming," *IEEE Transactions on Neural Networks and Learning Systems*, vol. 38, pp. 1–15, 2020.

[11] X. Zhang, "Robust low-rank tensor recovery with rectification and alignment," *IEEE Transactions on Pattern Analysis and Machine Intelligence*, vol. 43, no. 1, pp. 238–255, 2019.

[12] X. Zhang, R. Jiang, T. Wang, and J. Wang, "Recursive neural network for video deblurring," *IEEE Transactions on Circuits and Systems for Video Technology*, vol. 1, p. 1, 2020.

[13] X. Zhang, T. Wang, J. Wang, G. Tang, and L. Zhao, "Pyramid channel-based feature attention network for image dehazing," *Computer Vision and Image Understanding*, vol. 197-198, Article ID 103003, 2020.

[14] H. Yu, "Dynamic Gaussian bare-bones fruit fly optimizers with abandonment mechanism: method and analysis," *Engineering with Computers*, vol. 7, pp. 1–29, 2020.

[15] C. Yu, "SGOA: annealing-behaved grasshopper optimizer for global tasks," *Engineering with Computers*, vol. 1, pp. 1–28, 2021.

[16] W. Shan, "Double adaptive weights for stabilization of moth flame optimizer: balance analysis, engineering cases, and medical diagnosis," *Knowledge-Based Systems*, vol. 214, Article ID 106728, 2020.

[17] J. Tu, H. Chen, J. Liu et al., "Evolutionary biogeography-based whale optimization methods with communication structure: towards measuring the balance," *Knowledge-Based Systems*, vol. 212, Article ID 106642, 2021.

[18] Y. Zhang, "Towards augmented kernel extreme learning models for bankruptcy prediction: algorithmic behavior and

comprehensive analysis," vol. 430, , pp. 185–212, Neurocomputing, 2020.

[19] Y. Zhang, "Boosted binary Harris hawks optimizer and feature selection," *Engineering with Computers*, vol. 23, pp. 1–30, 2020.

[20] H.-L. Chen, G. Wang, C. Ma, Z.-N. Cai, W.-B. Liu, and S.-J. Wang, "An efficient hybrid kernel extreme learning machine approach for early diagnosis of Parkinson's disease," *Neurocomputing*, vol. 184, pp. 131–144, 2016.

[21] L. Hu, G. Hong, J. Ma, X. Wang, and H. Chen, "An efficient machine learning approach for diagnosis of paraquat-poisoned patients," *Computers in Biology and Medicine*, vol. 59, pp. 116–124, 2015.

[22] L. Shen, H. Chen, Z. Yu et al., "Evolving support vector machines using fruit fly optimization for medical data classification," *Knowledge-Based Systems*, vol. 96, pp. 61–75, 2016.

[23] J. Xia, H. Chen, Q. Li et al., "Ultrasound-based differentiation of malignant and benign thyroid Nodules: an extreme learning machine approach," *Computer Methods and Programs in Biomedicine*, vol. 147, pp. 37–49, 2017.

[24] C. Li, L. Hou, B. Y. Sharma et al., "Developing a new intelligent system for the diagnosis of tuberculous pleural effusion," *Computer Methods and Programs in Biomedicine*, vol. 153, pp. 211–225, 2018.

[25] X. Zhao, X. Zhang, Z. Cai et al., "Chaos enhanced grey wolf optimization wrapped ELM for diagnosis of paraquat-poisoned patients," *Computational Biology and Chemistry*, vol. 78, pp. 481–490, 2019.

[26] M. Wang and H. Chen, "Chaotic multi-swarm whale optimizer boosted support vector machine for medical diagnosis," *Applied Soft Computing Journal*, vol. 88, 2020.

[27] X. Xu and H.-l. Chen, "Adaptive computational chemotaxis based on field in bacterial foraging optimization," *Soft Computing*, vol. 18, no. 4, pp. 797–807, 2014.

[28] R. U. Khan, X. Zhang, R. Kumar, A. Sharif, N. A. Golilarz, and M. Alazab, "An adaptive multi-layer botnet detection technique using machine learning classifiers," *Applied Sciences*, vol. 9, no. 11, p. 2375, 2019.

[29] A. Addeh, A. Khormali, and N. A. Golilarz, "Control chart pattern recognition using RBF neural network with new training algorithm and practical features," *ISA Transactions*, vol. 79, pp. 202–216, 2018.

[30] N. Amiri Golilarz, "Adaptive wavelet based MRI brain image de-noising," *Frontiers in Neuroscience*, vol. 14, p. 728, 2020.

[31] N. A. Golilarz, H. Gao, and H. Demirel, "Satellite image denoising with Harris hawks meta heuristic optimization algorithm and improved adaptive generalized Gaussian distribution threshold function," *IEEE Access*, vol. 7, pp. 57459–57468, 2019.

[32] N. A. Golilarz, A. Addeh, H. Gao et al., "A new automatic method for control chart patterns recognition based on ConvNet and Harris hawks meta heuristic optimization algorithm," *IEEE Access*, vol. 7, pp. 149398–149405, 2019.

[33] B. Bai, Z. Guo, C. Zhou, W. Zhang, and J. Zhang, "Application of adaptive reliability importance sampling-based extended domain PSO on single mode failure in reliability engineering," *Information Sciences*, vol. 546, pp. 42–59, 2021.

[34] H. Chen, A. A. Heidari, H. Chen, M. Wang, Z. Pan, and A. H. Gandomi, "Multi-population differential evolution-assisted Harris hawks optimization: framework and case studies," *Future Generation Computer Systems*, vol. 111, pp. 175–198, 2020.

[35] Y. Cao, Y. Li, G. Zhang, K. Jermsittiparsert, and M. Nasseri, "An efficient terminal voltage control for PEMFC based on an improved version of whale optimization algorithm," *Energy Reports*, vol. 6, pp. 530–542, 2020.

[36] J. Liu, C. Wu, G. Wu, and X. Wang, "A novel differential search algorithm and applications for structure design," *Applied Mathematics and Computation*, vol. 268, pp. 246–269, 2015.

[37] X. Zhao, D. Li, B. Yang, C. Ma, Y. Zhu, and H. Chen, "Feature selection based on improved ant colony optimization for online detection of foreign fiber in cotton," *Applied Soft Computing*, vol. 24, pp. 585–596, 2014.

[38] D. Zhao, "Chaotic random spare ant colony optimization for multi-threshold image segmentation of 2D Kapur entropy," *Knowledge-Based Systems*, vol. 216, Article ID 106510, 2020.

[39] J. Hu, H. Chen, A. A. Heidari et al., "Orthogonal learning covariance matrix for defects of grey wolf optimizer: insights, balance, diversity, and feature selection," *Knowledge-Based Systems*, vol. 213, Article ID 106684, 2021.

[40] N. Gao, D. Luo, B. Cheng, and H. Hou, "Teaching-learning-based optimization of a composite metastructure in the 0–10 kHz broadband sound absorption range," *The Journal of the Acoustical Society of America*, vol. 148, no. 2, pp. EL125–EL129, 2020.

[41] G. Sun, "An adaptive differential evolution with combined strategy for global numerical optimization," *Soft Computing*, vol. 24, no. 9, pp. 6277–6296, 2019.

[42] G. Sun, C. Li, and L. Deng, "An adaptive regeneration framework based on search space adjustment for differential evolution," *Neural Computing and Applications*, vol. 32, pp. 1–17, 2021.

[43] D. Yu, Y. Mao, B. Gu, S. Nojavan, K. Jermsittiparsert, and M. Nasseri, "A new LQG optimal control strategy applied on a hybrid wind turbine/solid oxide fuel cell/in the presence of the interval uncertainties," *Sustainable Energy, Grids and Networks*, vol. 21, Article ID 100296, 2020.

[44] B. Wang, "Parallel lstm-based regional integrated energy system multienergy source-load information interactive energy prediction," *Complexity*, vol. 2019, Article ID 7414318, 13 pages, 2019.

[45] J. Yan, W. Pu, S. Zhou, H. Liu, and M. S. Greco, "Optimal resource allocation for asynchronous multiple targets tracking in heterogeneous radar networks," *IEEE Transactions on Signal Processing*, vol. 68, pp. 4055–4068, 2020.

[46] H. Yue, H. Wang, H. Chen, K. Cai, and Y. Jin, "Automatic detection of feather defects using lie group and fuzzy Fisher criterion for shuttlecock production," *Mechanical Systems and Signal Processing*, vol. 141, Article ID 106690, 2020.

[47] H. Kordestani, C. Zhang, and M. Shadabfar, "Beam damage detection under a moving load using random decrement technique and Savitzky–Golay Filter," *Sensors*, vol. 20, no. 1, p. 243, 2020.

[48] H. Kordestani and C. Zhang, "Direct use of the savitzky-golay filter to develop an output-only trend line-based damage detection method," *Sensors*, vol. 20, no. 7, p. 1983, 2020.

[49] A. A. Mousavi, C. Zhang, S. F. Masri, and G. Gholipour, "Structural damage localization and quantification based on a ceemdan hilbert transform neural network approach: a model steel truss bridge case study," *Sensors*, vol. 20, no. 5, p. 1271, 2020.

[50] Q. Zhu, "Research on road traffic situation awareness system based on image big data," *IEEE Intelligent Systems*, vol. 35, no. 1, pp. 18–26, 2019.

[51] Q. Jiang, "Unified no-reference quality assessment of singly and multiply distorted stereoscopic images," *IEEE Transactions on Image Processing*, vol. 28, no. 4, pp. 1866–1881, 2018.

[52] M. Xu, C. Li, S. Zhang, and P. L. Callet, "State-of-the-Art in 360° video/image processing: perception, assessment and compression," *IEEE Journal of Selected Topics in Signal Processing*, vol. 14, no. 1, pp. 5–26, 2020.

[53] M. Yang and A. Sowmya, "An underwater color image quality evaluation metric," *IEEE Transactions on Image Processing*, vol. 24, no. 12, pp. 6062–6071, 2015.

[54] B. Wang, B. Zhang, and X. Liu, "An image encryption approach on the basis of a time delay chaotic system," *Optik*, vol. 225, Article ID 165737, 2021.

[55] S. Hinojosa, D. Oliva, E. Cuevas, G. Pajares, D. Zaldivar, and M. Pérez-Cisneros, "Reducing overlapped pixels: a multi-objective color thresholding approach," *Soft Computing*, vol. 24, no. 9, pp. 6787–6807, 2020.

[56] X. Zhao, Y. Ye, J. Ma, P. Shi, and H. Chen, "Construction of electric vehicle driving cycle for studying electric vehicle energy consumption and equivalent emissions," *Environmental Science and Pollution Research*, vol. 27, no. 30, pp. 37395–37409, 2020.

[57] T. Qiu, X. Shi, J. Wang et al., "Deep learning: a rapid and efficient route to automatic metasurface design," *Advanced Science*, vol. 6, no. 12, Article ID 1900128, 2019.

[58] T. Li, M. Xu, C. Zhu, R. Yang, Z. Wang, and Z. Guan, "A deep learning approach for multi-frame in-loop filter of HEVC," *IEEE Transactions on Image Processing*, vol. 28, no. 11, pp. 5663–5678, 2019.

[59] H. Chen, A. Chen, L. Xu et al., "A deep learning CNN architecture applied in smart near-infrared analysis of water pollution for agricultural irrigation resources," *Agricultural Water Management*, vol. 240, Article ID 106303, 2020.

[60] J. Qian, S. Feng, Y. Li et al., "Single-shot absolute 3D shape measurement with deep-learning-based color fringe projection profilometry," *Optics Letters*, vol. 45, no. 7, pp. 1842–1845, 2020.

[61] J. Qian, "Deep-learning-enabled geometric constraints and phase unwrapping for single-shot absolute 3d shape measurement," *APL Photonics*, vol. 5, no. 4, Article ID 046105, 2020.

[62] J. Wang, "An adaptive neural sliding mode control with ESO for uncertain nonlinear systems," *International Journal of Control, Automation and Systems*, vol. 2020, pp. 1–11, 2020.

[63] Z. Chen, J. Wang, K. Ma, X. Huang, and T. Wang, "Fuzzy adaptive two-bits-triggered control for nonlinear uncertain system with input saturation and output constraint," *International Journal of Adaptive Control and Signal Processing*, vol. 34, no. 4, pp. 543–559, 2020.

[64] J. Wang, Y. Huang, T. Wang, C. Zhang, and Y. h. Liu, "Fuzzy finite-time stable compensation control for a building structural vibration system with actuator failures," *Applied Soft Computing*, vol. 93, Article ID 106372, 2020.

[65] Y. Huang, J. Wang, F. Wang, and B. He, "Event-triggered adaptive finite-time tracking control for full state constraints nonlinear systems with parameter uncertainties and given transient performance," *ISA Transactions*, vol. 108, pp. 131–143, 2021.

[66] C. Li, L. Sun, Z. Xu, X. Wu, T. Liang, and W. Shi, "Experimental investigation and error analysis of high precision FBG displacement sensor for structural health monitoring," *International Journal of Structural Stability and Dynamics*, vol. 20, no. 06, Article ID 2040011, 2020.

[67] L. Sun, C. Li, C. Zhang, T. Liang, and Z. Zhao, "The strain transfer mechanism of fiber bragg grating sensor for extra large strain monitoring," *Sensors*, vol. 19, no. 8, p. 1851, 2019.

[68] C. Zhang, "Fibre Bragg grating sensor-based damage response monitoring of an asymmetric reinforced concrete shear wall structure subjected to progressive seismic loads," *Structural Control and Health Monitoring*, vol. 26, no. 3, p. e2307, 2019.

[69] L. Sun, C. Li, C. Zhang, Z. Su, and C. Chen, "Early monitoring of rebar corrosion evolution based on FBG sensor," *International Journal of Structural Stability and Dynamics*, vol. 18, no. 08, Article ID 1840001, 2018.

[70] I. Bargegol, V. N. M. Gilani, and F. Jamshidpour, "Relationship between pedestrians' speed, density and flow rate of crossings through urban intersections (case study: rasht metropolis) (RESEARCH NOTE)," *International Journal of Engineering-Transactions C: Aspects*, vol. 30, no. 12, pp. 1814–1821, 2017.

[71] H. Behbahani, "Analysis of crossing speed of the pedestrians in marked and unmarked crosswalks in the signalized and un-signalized intersections (case study: rasht city)," in *Proceedings of the IOP Conference Series: Materials Science and Engineering*, vol. 245, IOP Publishing, Kunming, China, October 2017.

[72] H. Behbahani, "Investigation of un-signalized roundabouts delay with adaptive-network-based fuzzy inference system and fuzzy logic," *Computational Research Progress in Applied Science & Engineering*, vol. 2, no. 04, pp. 1–7, 2016.

[73] S. M. Hosseinian, V. Najafi Moghaddam Gilani, P. Mehraban Joobani, and M. Arabani, "Investigation of moisture sensitivity and conductivity properties of inductive asphalt mixtures containing steel wool fiber," *Advances in Civil Engineering*, vol. 2020, no. 1, 9 pages, Article ID 8890814, 2020.

[74] A. Abdi, "Dynamic modelling of the effects of combined horizontal and vertical curves on side friction factor and lateral acceleration," in *Proceedings of the IOP Conference Series: Materials Science and Engineering*, IOP Publishing, Bangkok, Thailand, May 2019.

[75] V. Najafi Moghaddam Gilani, S. M. Hosseinian, H. Behbahani, and G. H. Hamedi, "Prediction and pareto-based multi-objective optimization of moisture and fatigue damages of asphalt mixtures modified with nano hydrated lime," *Construction and Building Materials*, vol. 261, Article ID 120509, 2020.

[76] N. Kamboozia, M. Ameri, and S. M. Hosseinian, "Statistical analysis and accident prediction models leading to pedestrian injuries and deaths on rural roads in Iran," *International Journal of Injury Control and Safety Promotion*, vol. 27, no. 4, pp. 493–509, 2020.

[77] S. T. Heydari, A. Hoseinzadeh, F. Ghaffarpasand et al., "Epidemiological characteristics of fatal traffic accidents in Fars province, Iran: a community-based survey," *Public Health*, vol. 127, no. 8, pp. 704–709, 2013.

[78] L. Shen, "Identification of accident blackspots on rural roads using grid clustering and principal component clustering," *Mathematical Problems in Engineering*, vol. 2019, Article ID 2151284, 12 pages, 2019.

[79] T. Litman and M. Hughes-Cromwick, "Public transportation's impact on rural and small towns: a vital mobility link," 2017.

[80] N. Casado-Sanz, B. Guirao, and D. Gálvez-Pérez, "Population ageing and rural road accidents: analysis of accident severity in traffic crashes with older pedestrians on Spanish

crosstown roads," *Research in Transportation Business & Management*, vol. 30, Article ID 100377, 2019.

[81] A. Ghaffar, A. A. Hyder, and T. I. Masud, "The burden of road traffic injuries in developing countries: the 1st national injury survey of Pakistan," *Public Health*, vol. 118, no. 3, pp. 211–217, 2004.

[82] M. Labinjo, C. Juillard, O. C. Kobusingye, and A. A. Hyder, "The burden of road traffic injuries in Nigeria: results of a population-based survey," *Injury Prevention*, vol. 15, no. 3, pp. 157–162, 2009.

[83] S. Hu and Q. Xiang, "Characteristics analysis of traffic accidents on rural roads," *CICTP 2012: Multimodal Transportation Systems-Convenient, Safe, Cost-Effective, Efficient*, vol. 1, pp. 2506–2513, 2012.

[84] H. Zangooei Dovom, Y. Shafahi, and M. Zangooei Dovom, "Fatal accident distribution by age, gender and head injury, and death probability at accident scene in Mashhad, Iran, 2006–2009," *International Journal of Injury Control and Safety Promotion*, vol. 20, no. 2, pp. 121–133, 2013.

[85] G. López, J. Abellán, A. Montella, and J. de Oña, "Patterns of single-vehicle crashes on two-lane rural highways in granada province, Spain," *Transportation Research Record: Journal of the Transportation Research Board*, vol. 2432, no. 1, pp. 133–141, 2014.

[86] K. Zimmerman, D. Jinadasa, B. Maegga, and A. Guerrero, "Road traffic injury on rural roads in Tanzania: measuring the effectiveness of a road safety program," *Traffic Injury Prevention*, vol. 16, no. 5, pp. 456–460, 2015.

[87] S. Lee and B. Y. Jeong, "Comparisons of traffic collisions between expressways and rural roads in truck drivers," *Safety and Health at Work*, vol. 7, no. 1, pp. 38–42, 2016.

[88] N. Kamboozia, M. Ameri, and S. M. Hosseinian, "Investigation of effective factors in the severity of rural road accidents in guilan to determine the most effective factors and provide safety solutions," *Road*, vol. 29, no. 106, pp. 115–128, 2021.

[89] Y. Xu, H. Chen, J. Luo, Q. Zhang, S. Jiao, and X. Zhang, "Enhanced Moth-flame optimizer with mutation strategy for global optimization," *Information Sciences*, vol. 492, pp. 181–203, 2019.

[90] M. Wang, H. Chen, B. Yang et al., "Toward an optimal kernel extreme learning machine using a chaotic moth-flame optimization strategy with applications in medical diagnoses," *Neurocomputing*, vol. 267, pp. 69–84, 2017.

[91] F. S. Nahm, "Nonparametric statistical tests for the continuous data: the basic concept and the practical use," *Korean Journal of Anesthesiology*, vol. 69, no. 1, p. 8, 2016.

[92] A. Rao, W. Han, and P. Senarathne, "A comparison of SLAM prediction densities using the Kolmogorov smirnov statistic," *Unmanned Systems*, vol. 04, no. 04, pp. 245–254, 2016.

[93] G. D. Ruxton, D. M. Wilkinson, and M. Neuhäuser, "Advice on testing the null hypothesis that a sample is drawn from a normal distribution," *Animal Behaviour*, vol. 107, pp. 249–252, 2015.

[94] C. N. Kroll, K. E. Croteau, and R. M. Vogel, "Hypothesis tests for hydrologic alteration," *Journal of Hydrology*, vol. 530, pp. 117–126, 2015.

[95] I. Bargegol, V. Gilani, and S. Farghedayn, "Analysis of the effect of vehicles conflict on pedestrian's crossing speed in signalized and un-signalized intersection," *Advances in Environmental Biology*, vol. 8, no. 21, pp. 502–510, 2014.

[96] R. Eisinga, "Exact p-values for pairwise comparison of Friedman rank sums, with application to comparing classifiers," *BMC Bioinformatics*, vol. 18, no. 1, p. 68, 2017.

[97] N. Kamboozia, M. Ameri, and S. M. Hosseinian, "Statistical analysis and presentation of accident prediction model leading to injuries and deaths of pedestrians in rural roads of Gilan," *Journal of Transportation Research*, vol. 17, pp. 493–509, 2020.

[98] D. L. Bandalos and S. J. Finney, *Factor Analysis: Exploratory and Confirmatory, in The Reviewer's Guide to Quantitative Methods in the Social Sciences*, Routledge, England, UK, 2018.

[99] H. F. Kaiser, "An index of factorial simplicity," *Psychometrika*, vol. 39, no. 1, pp. 31–36, 1974.

[100] H. Sadeghi-Bazargani, B. Samadirad, N. Shahedifar, and M. Golestani, "Epidemiology of road traffic injury fatalities among car users; a study based on forensic medicine data in East Azerbaijan of Iran," *Bulletin of Emergency and Trauma*, vol. 6, no. 2, p. 146, 2018.

[101] G. Soltani, "Investigating prevalence of deaths from traffic accidents and factors associated with it in yazd in 2009," *SSU_Journals*, vol. 21, no. 6, pp. 831–839, 2014.

[102] A. Razzaghi, A. Bahrampour, M. R. Baneshi, and F. Zolala, "Assessment of trend and seasonality in road accident data: an Iranian case study," *International Journal of Health Policy and Management*, vol. 1, no. 1, p. 51, 2013.

[103] J. M. Pardillo Mayora and R. Jurado Piña, "An assessment of the skid resistance effect on traffic safety under wet-pavement conditions," *Accident Analysis & Prevention*, vol. 41, no. 4, pp. 881–886, 2009.

[104] W. A. Harrison and R. Christie, "Exposure survey of motorcyclists in new south wales," *Accident Analysis & Prevention*, vol. 37, no. 3, pp. 441–451, 2005.

[105] F. L. Mannering and L. L. Grodsky, "Statistical analysis of motorcyclists' perceived accident risk," *Accident Analysis & Prevention*, vol. 27, no. 1, pp. 21–31, 1995.

[106] C. A. Butts, R. Gonzalez, L. Nguyen et al., "Twelve-year review of urban versus rural off-road vehicle injuries at a level 1 trauma center," *Journal of Surgical Research*, vol. 233, pp. 331–334, 2019.

[107] F. Mohtasham amiri, "Road traffic accidents, life-threatening phenomenon in guilan province: an epidemiologic study," *Journal of Guilan University of Medical Sciences*, vol. 23, no. 92, pp. 1–8, 2015.

[108] T. Richter, S. Ruhl, J. Ortlepp, and E. Bakaba, "Causes, consequences and countermeasures of overtaking accidents on two-lane rural roads," *Transportation Research Procedia*, vol. 25, pp. 1989–2001, 2017.

[109] J. Hu, "Orthogonal learning covariance matrix for defects of grey wolf optimizer: insights, balance, diversity, and feature selection," *Knowledge-Based Systems*, vol. 213, Article ID 106684, 2020.

[110] V. Najafi Moghaddam Gilani, "Investigation of the impact of deicer materials on thermodynamic parameters and its relationship with moisture susceptibility in modified asphalt mixtures by carbon nanotube," *Arabian Journal for Science and Engineering*, vol. 2020, 2020.

[111] G. H. Hamedi, "The effect of aggregate-forming minerals on thermodynamic parameters using surface free energy concept and its relationship with the moisture susceptibility of asphalt mixtures," *Advances in Civil Engineering*, vol. 2021, Article ID 8818681, 15 pages, 2021.

[112] V. Najafi Moghaddam Gilani, S. M. Hosseinian, and M. Nikookar, "Presentation of a new deicer with the least moisture and fatigue failures in asphalt mixtures," *Arabian Journal for Science and Engineering*, vol. 46, no. 2, 2021.

[113] X. Zhang, "Top-*k* feature selection framework using robust 0-1 integer programming," *IEEE Transactions on Neural Networks and Learning Systems*, vol. 1, pp. 1–15, 2020.

[114] X. Zhang, "Recursive neural network for video deblurring," *IEEE Transactions on Circuits and Systems for Video Technology*, vol. 99, no. 1, p. 1, 2020.

[115] X. Zhang, "Multi-level fusion and attention-guided CNN for image dehazing," *IEEE Transactions on Circuits and Systems for Video Technology*, vol. 99, p. 1, 2020.

[116] X. Cheng, L. He, H. Lu, Y. Chen, and L. Ren, "Optimal water resources management and system benefit for the Marcellus shale-gas reservoir in Pennsylvania and West Virginia," *Journal of Hydrology*, vol. 540, pp. 412–422, 2016.

[117] Y. Chen, L. He, J. Li, and S. Zhang, "Multi-criteria design of shale-gas-water supply chains and production systems towards optimal life cycle economics and greenhouse gas emissions under uncertainty," *Computers & Chemical Engineering*, vol. 109, pp. 216–235, 2018.

[118] Y. Chen, L. He, Y. Guan, H. Lu, and J. Li, "Life cycle assessment of greenhouse gas emissions and water-energy optimization for shale gas supply chain planning based on multi-level approach: case study in Barnett, Marcellus, Fayetteville, and Haynesville shales," *Energy Conversion and Management*, vol. 134, pp. 382–398, 2017.

[119] Y. Chen, J. Li, H. Lu, and P. Yan, "Coupling system dynamics analysis and risk aversion programming for optimizing the mixed noise-driven shale gas-water supply chains," *Journal of Cleaner Production*, vol. 278, Article ID 123209, 2021.

[120] H. Lu, P. Tian, and L. He, "Evaluating the global potential of aquifer thermal energy storage and determining the potential worldwide hotspots driven by socio-economic, geo-hydrologic and climatic conditions," *Renewable and Sustainable Energy Reviews*, vol. 112, pp. 788–796, 2019.

[121] X. Han, D. Zhang, J. Yan, S. Zhao, and J. Liu, "Process development of flue gas desulphurization wastewater treatment in coal-fired power plants towards zero liquid discharge: energetic, economic and environmental analyses," *Journal of Cleaner Production*, vol. 261, Article ID 121144, 2020.

[122] C. Zuo, Q. Chen, G. Gu et al., "High-speed three-dimensional shape measurement for dynamic scenes using bi-frequency tripolar pulse-width-modulation fringe projection," *Optics and Lasers in Engineering*, vol. 51, no. 8, pp. 953–960, 2013.

[123] C. Yang, F. Gao, and M. Dong, "Energy efficiency modeling of integrated energy system in coastal areas," *Journal of Coastal Research*, vol. 103, no. s1, pp. 995–1001, 2020.

[124] B. Wang, Z. Song, and L. Sun, "A review: comparison of multi-air-pollutant removal by advanced oxidation processes-industrial implementation for catalytic oxidation processes," *Chemical Engineering Journal*, vol. 409, no. 1, Article ID 128136, 2020.

[125] M. Yazdi, T. Saner, and M. Darvishmotevali, "Application of an artificial intelligence decision-making method for the selection of maintenance strategy," in *Proceedings 10th International Conference on Theory and Application of Soft Computing, Computing with Words and Perceptions - ICSCCW-2019*, pp. 246–253, Springer, Cham, Switzerland, August 2020.

[126] M. Yazdi, "Ignorance-aware safety and reliability analysis: a heuristic approach," *Qual Quality and Reliability Engineering International*, vol. 36, no. 2, pp. 652–674, 2020.

[127] M. Yazdi, S. Daneshvar, and H. Setareh, "An extension to fuzzy developed failure mode and effects analysis (FDFMEA) application for aircraft landing system," *Safety Science*, vol. 98, pp. 113–123, 2017.

[128] M. Yazdi, "Acquiring and sharing tacit knowledge in failure diagnosis analysis using intuitionistic and pythagorean assessments," *Journal of Failure Analysis and Prevention*, vol. 19, no. 2, pp. 369–386, 2019.

[129] H. Behbahani, G. H. Hamedi, and V. Najafi Moghaddam Gilani, "Predictive model of modified asphalt mixtures with nano hydrated lime to increase resistance to moisture and fatigue damages by the use of deicing agents," *Construction and Building Materials*, vol. 265, Article ID 120353, 2020.

[130] A. Ghasemzadeh Mahani, "Experimental investigation and multi-objective optimization of fracture properties of asphalt mixtures containing nano-calcium carbonate," *Construction and Building Materials*, vol. 285, Article ID. 122876, 2021.

Hindawi
Mathematical Problems in Engineering
Volume 2021, Article ID 6636955, 13 pages
https://doi.org/10.1155/2021/6636955

Research Article

Investigating the Effective Factors of Renewable Energy Development in Tehran Metropolis

Mohammad Reza Arasteh Taleshmekaiil,[1] **Seyed Mohammad Reza Khatibi**,[1,2] **Mona Mohemsaz**,[3] **Mohammad Hossein Azimi**,[2] **and Ali Sadeghpour**[4]

[1]*Faculty of Urbanism Engineering, Islamic Azad University of North Tehran, Tehran, Iran*
[2]*Department of Urbanism, Faculty of Architecture and Urbanism Engineering, Qazvin Branch, Islamic Azad University, Qazvin, Iran*
[3]*Faculty of Urban and Regional Planning, Science and Research Branch, Islamic Azad University, Tehran, Iran*
[4]*Faculty of Engineering, Varamin-Pishva Branch, Islamic Azad University, Tehran, Tehran Province, Iran*

Correspondence should be addressed to Seyed Mohammad Reza Khatibi; m_khatibi@qiau.ac.ir

Received 26 December 2020; Revised 7 February 2021; Accepted 18 February 2021; Published 8 March 2021

Academic Editor: Noorbakhsh Amiri Golilarz

To prepare for the urban development of 2.5 billion people by 2050, the development of low-carbon, resilient, and liveable urban settlements is crucial. Not only do metropolises contribute to global climate change by rapidly emitting and increasing emissions but they themselves are very fragile and vulnerable to these changes. The purpose of this study is to optimize a model for the development of renewable energies in Tehran City and its application in different sectors to achieve sustainability. The research method is according to the type of the applied-developmental study. Information is based on documentation and field methods. Data were collected using a questionnaire from 76 experts and analysed using MICMAC software. The results indicate the fact that the use of public and specific stimuli and incentives for electricity producers to use renewable energy will accelerate the development of renewable energy at the urban level. In order to improve the existing situation, the unsustainable model can be offered to change the situation in favour of the use of new energy at the regional level. Based on the research results, in general, patterns of deployment and development of renewable energies are grouped into five main groups: the use of financial instruments, the use of legal instruments, the development of technology, education and awareness-raising that urban sustainability in the energy sector can be considered based on these four pillars.

1. Introduction

The path taken today to use modern energy to achieve sustainable development goals can be seen as a scientific challenge for its realization in the modern age [1]. With their ever-expanding development, today's cities are large parts of Iran's metropolises' energy consumption and not exemplary. A metropolis like Tehran, accounting for only less than 12% of the country, accounts for 15% of its air pollution level [2]. Paying attention to new approaches in the field of energy can be a viable solution to many urban biodiversity problems in the future. There are many related areas and technologies that can be used for this aim, such as sensor fusion systems [3], intelligent damage detection [4–6], monitoring systems [7–10], parameters optimization [11], optimization [12], smart grid [13], computer vision systems [14], power allocation systems [15], image and video processing [16–21], and decision-making approaches [22–24].

According to the Tehran Electricity Distribution Company, Tehran city consumes about 20% of the country's total electricity. These statistics show that the need to pay attention to other energy production aspects can be an inevitable necessity. Tehran has serious problems with the supply and distribution of pollution in the energy production and consumption sector. Meanwhile, renewable energy as a sustainable solution in the field of energy

production and pollution of urban air in recent years has received much attention. Renewable energies are energies with a sustainable production process and continuous replacement capability, which according to this definition, the process of sustainable production is the use of natural or artificial cycles that can continuously convert raw materials into the desired energy and if there is any an operation or need for storage, can be capable of continuous replacement [25].

Urban development can be considered as a multidimensional concept that includes economic, social, and environmental approaches. Management problems in this process always exist between the urban space, stakeholders, and urban infrastructure. This complexity requires multidimensional approaches and specific quantitative or qualitative methods to analyse and synthesize various aspects of transformation processes, from environmental impacts on urban renewal to energy impacts, economic development, and development strategies. Sustainable energy systems are always in complex communication with the community and the development of technical infrastructure. The successful development of a sustainable energy system depends on social acceptance, market dynamics, regulations and policies, and different producer groups' support. Natural energy sources such as solar energy are increasing due to the high potential of exploitation and use as sources of heating, air conditioning, and electricity and can be reduced by developing fossil fuel consumption. As a major source of sustainable energy, benefits bring a lot to the community [26–28].

Energy production and consumption have some considerations, which directly affect the sustainability of the urban environment. In fact, the depletion of fossil fuels and greenhouse gas emissions due to the oil and coal-based model or the occupation of natural spaces for centralized reproduction models should be considered. Rather, energy production costs are also increasing. These costs affect the income statement, in economic activities, which may include variable value regarding the total cost of energy production, between 5 and 40 percent of total costs that are more in terms of cost of energy production and service delivery [29–32].

Generally, energy efficiency is defined as the relationship between production, services, and energy costs [33]. Therefore, through energy efficiency, energy saving by maintaining the same energy consumption as expected without reduction, production and comfort levels, guaranteed supply, sustainability, and environmental protection are also available as desirable targets. This sustainability process involves saving various energy sources used, such as oil, coal, and natural gas [34, 35].

Developing the application of renewable energy technologies is becoming a strategic option given the reduction of greenhouse gases as a global energy source. During the last two decades, the use of new energies has been considered in two parts. The first is related to the direct production of heat, and the second is related to the production of electricity [36]. According to the UN Environment Program in 2016, households consume about 40% of the world's energy. This volume of energy consumption in Iran is mainly from the consumption of seasonal resources that emit a large volume of greenhouse gases, which in large cities such as Tehran in Iran causes a lot of air pollution. Iran is one of the top 10 countries in carbon dioxide (CO_2) emissions, with rapid urbanization and migration. Industrial growth and socio-political developments are the main factors in the rapid growth of cities [37, 38].

The study on the energy consumption of urban households and CO_2 emissions in a country like Iran with a population of more than 80 million people and a neutralization rate of 3.5% is important [39]. Fossil fuel groups (coal, oil, and natural gas) are used worldwide as the main energy source, which also comprises a very high percentage of primary energy that includes the areas of scarcity and rising prices in this segment of resources. Therefore, it can be said that the current power system has problems on its own, which has uncontrollable environmental consequences and numerous negative environmental consequences (climate change, greenhouse effect, acid rain, and deforestation) and geopolitical instability [40, 41]. That change in this traditional system due to the existing problems such as cities' physical development, population growth, industrial development, and biological pollution can provide planners with a sustainable solution through the use of new energies.

Although fossil fuels are still a major source of energy in cities, the use of renewable energy as a fundamental solution to metropolitan areas' problems is becoming increasingly urgent [30]. Many renewable energy technologies, such as photovoltaic panels, small wind turbines, micro turbines, and gas engines, are increasingly being integrated into power distribution systems [42] and can be used in urban areas.

Extensive use of renewable energy is a new approach in urban planning in order to achieve sustainable urban development. The development of low-carbon cities is one of the most important executive approaches in this field. Depending on the resources available in each geographical area, the type of use of renewable energy is different and requires its own scenarios.

In a study by Child et al., two transition pathways towards a 100% renewable energy (RE) power sector by 2050 are simulated for Europe using the LUT energy system transition model. The first is a region scenario, whereby regions are modelled independently, and the second is an area scenario, which has transmission interconnections between regions [6].

Future technologies such as homogeneous systems and biomass heating in cities are characterized by energy saving and high energy efficiency. Developmental research on renewable energy models in urban areas has become a necessity for achieving a sustainable energy system. Many cities around the world have expressed their commitment to 100% energy use from these clean sources, and it is predicted that by 2025, cities like Copenhagen and Munich will be able to source electricity from renewable sources. As such, these cities can be considered as zero-carbon cities. According to the Tehran city council resolution, Tehran's municipality is obliged to change the use of electricity to 20% by using public energy. During this time, Tehran's waste incinerator

has been set up to generate 3 MWh (Megawatt hour) of electricity. In addition to equipping many of Tehran's public spaces with solar panels, Tehran's municipality has implemented extensive policies to provide 20% of the city's public electricity with renewable energy. Today, the use of green energy in urban areas reflects areas where the scientific community of large-scale urban renewable energy production is interested as a solution for sustainable energy development. Because it can be considered sustainable solutions to meet the growing demand for energy in cities and to reduce greenhouse gas emissions as an important principle of sustainability in energy issues, research is essential to achieving energy efficiency and profitability in sustainable renewables over time, and its use in urban areas can be considered one of the most important energies and urbanization challenges of today [42–49].

Today, the use of renewable energy in urban areas is a field that is considered by urban planners. Extensive use of renewable energy in urban areas on a large scale is assumed to be a solution for sustainable energy development, both to meet the growing energy needs of cities and to reduce carbon emissions. To access these efficient, profitable, and sustainable energy sources, it is necessary to increase the technical capabilities, investment, public awareness, and responsibilities of governments. Then, by considering an ideal condition for the development of these energies in urban areas, a model for its development can be presented.

The present study explores the potential for utilization and coverage of various renewable energy sources and the practical implementation of related technologies for the security of sustainable development in the Tehran metropolis. Many city-states face many problems in their metropolises, but commonalities can be found in the development of renewable energy. Research and development funds are allocated for the application of these energies in cities. However, this is not common and is not supported in many countries, which in turn slows down innovation in this area. In Iran, especially in metropolises such as Tehran, subsidies and incentive policies are often in conflict with each other. Contrary to conventional global policies, policies aimed at promoting renewable energy technologies in Iran are constantly changing, and despite the tendency to take this approach, the policies run counter to the public interest and discourage acceptance. When the incentives to use this type of energy in society are eliminated, private companies that provide services and develop the technical sector will also go bankrupt. Also, the ever-changing subsidies and legal barriers to employment are increasingly making it difficult to access renewable energy projects. In Tehran, excessive air pollution, greenhouse gas emissions, high energy consumption, and a high potential for renewable energy have always been an incentive to develop this type of energy. But so far, this has not happened due to the problems mentioned. Recognizing the challenges of this creature and providing appropriate solutions can overcome these obstacles.

2. Research Method

This study seeks to identify the factors affecting the utilization of new energy at urban levels, emphasizing Tehran's District 4. The research method is applied-developmental. This research tries to determine the potential of applying the new energy and presenting the most optimal strategies in the Tehran 4 area. Accordingly, the research data gathering tool, conducted in 1977, is based on documentary and field methods. To select the main and measurable variables for problem analysis, books, theses, and related articles were studied. Moreover, after identifying different metrics for utilizing and evaluating the potential of new energies, following the comments of professors and experts in the field, three main dimensions (solar, wind, and geothermal) were selected in the areas of applicability and productivity, which are analysed based on the MICMAC analytical method in statistical analysis. The research's statistical population is specialists and experts in the field of development and utilization of new energies. The selected sample is 76 people, that the questionnaire was developed to investigate the interrelationships of each of the indicators in relation to each other as a matrix and distributed among them. The target population is Ph.D. graduates in civil engineering, urban planning, energy economics, geography, and urban planning and experts with at least 8 years' experience in the field of modern energy development in Tehran municipality New Energy Organization of Tehran. Of the statistical sample, 76 have indicated their readiness to participate in this study. The sample survey comments were present at all stages of the research, and that is why the type of sampling is considered integer. The descriptive characteristics of the statistical sample in question are given in Table 1.

2.1. Study Area. Tehran Region 4 is located on the southern slope of Alborz Range and northeast of Tehran Metropolis and is the largest and most populous area among the 22 districts of Tehran. This area covers an area of 6123.9 hectares with a population of 917261 (in 2015). According to these figures, this specific area covers 7.2% of the total area and 10.5% of the population of Tehran metropolis. Tehran District 4 has 9 districts and 20 neighbourhoods, and after District 22, it has the largest privacy limit. This area is bounded on the north by Area 1 and on the west by Anchor Street at Area 1 and in the Pasdaran by Area 3, on the south by the Resalat Street border at Districts 7 and 8, and near Damavand St. by District 13, on the south. Thus, District 4 has zones 1, 3, 7, 8, and 13 in common and adjacent bodies (http://www.amar.org.ir). In terms of land use in Region 4, 11.1% and 10.5%, respectively, of the city's textured area and 18% of the open and green areas and its expandable lands are much more than other areas of Tehran, respectively. The existence of Sorkheh Hesar, Lawizan, and Lashkara Parks has added to the attractiveness of the area and its contribution to regional performance levels. The presence of East Tehran's industrial

Table 1: Descriptive characteristics of the statistical sample of the research.

Field of study/organ	Number
PhD of Civil	7
PhD of Urban Planning	21
PhD of Energy Economics	14
PhD of Geography and Urban Planning	13
Municipality experts	11
New energy organization experts	10

district has increased the possibilities for job creation, production, and added to the trans-regional physical mobility [50].

2.2. Data Analysis

2.2.1. The Pattern of Deployment of New Energy for Sustainable Development in the District 4 of Tehran. Looking at the future and its alternatives is very difficult for humankind to live in a society of constant change. Scriptwriting is perhaps the most crucial foresight methodology that can model the probable futures that are structured to reflect different organizations and systems' futures. Because of its efficiency in time uncertainty and complexity, this technique is a valuable tool that helps organizations prepare for possible futures, and it makes organizations more flexible and innovative.

In this research, after identifying the issue, the key factors and drivers related to modern energy application in the 4th district of Tehran 41 (with 76 experts of urban affairs and modern energy development) were investigated. Then, the key factors and driving forces were rated based on the degree of significance and uncertainty; the rating scale (0 = trivial, 1 = weak, 2 = moderate, 3 = strong, P = potential impact) was used to determine the significance of the responses. At the beginning of the discussion, we consider the title given that there are a large number of cases (41 cases) in the process of running the software and each one with a code which are illustrated in Table 2. Each of these factors is assigned codes from 1 to 41. The 41*41 matrix was formed and analysed in the MICMAC software based on the mean scores given to the propellants. Of the 1681 relationships evaluated in this matrix, 771 were zero. 549 number one relationships, 291 two relationships, and 51 three and 19 P relationships had a potential impact. Matrices based on a statistical index with data rotation twice were 100% desirable and optimized, which indicates the high validity of the questionnaire and its answers (Tables 3 and 4).

At the end of every matrix, the quantity of repetition must be aligned towards a certain limit. Based on the number of adjustments, the correct classification of criteria is formed. Finally, with the impact and dependence of these criteria, the MDI matrix is obtained.

3. Direct Indicator (MDI) and Indirect Impact Matrix (MII)

Indirect impact matrix (MII) is consistent with direct impact matrix (MDI), which increases with the power of repetition by continuous repetitions. From this matrix, the new classification of variables emphasizes the most important variables of the system. In fact, because of the matrix multiplication program applied to indirect classification, it detects a hidden variable. This program examines the effects of feedback by methods and loops of feedback and thus based on a hierarchical set of variables. In the order of influence, given the number of paths and loops of length 1, 2, ..., N created by any variable; given the number of paths and loops of length 1, 2, ..., N in each variable, respectively, dependence. In general, the classification is multiplied by 3, 4, or 5.

3.1. Direct Impact Matrix (MDI Matrix). As previously mentioned, 41 driving factors, each identified in the software as a code, form the study's basis. According to the cases mentioned earlier, each index's status can be distinguished by the position of the distribution of the indexes and their position in the influence-matrix of the direct effects matrix. Thus, the indicators' distribution map shows that eleven indicators (code 1, 10, 13, 15, 21, 24, 28, 30, 31, 37, and 38) are the impacts of the indicators on the system. Indicators in this area of the chart have the most impact and the least impact, and as the most critical indicators, the status of the system and its changes depend on them. The identified indicators are system inputs, and the system cannot control them because they are out of the system and act as stable indicators.

3.1.1. Bidirectional Indicators. Seven indicators (code 3, 4, 5, 11, 19, 32, and 41) are identifiable as bidirectional indicators in the system. It means that, at the same time, they are influential and effective, and their nature is unstable. So, every action and change on them will cause a reaction and change on another.

3.1.2. Risk Indicators. Risk indicators are indexes (code 4, 5, 11, and 32); that is, they have a very high capacity to become key players in the system, and because of their unstable nature, they have the potential to become a breakpoint of the system (application of new energy at the urban level).

3.1.3. Target Indicators. Code 3, 19, and 41 are introduced as target indicators. These indicators are more than influential and can be identified with acceptable certainty due to system evolution. The system changes and evolves in the desired direction. Therefore, these indicators represent the targets set in the system rather than displaying a predetermined result.

Table 2: Propulsion forces identified from the interviews and sources studied.

Code	Propulsion forces
1	The upward trend in the price of fossil energy
2	Power generation during peak hours
3	Reduce greenhouse gas emissions by using new energy
4	Competitiveness of renewable energy generation
5	Reliable investment in renewable energy due to the reliability of electricity generation from these sources
6	Providing clean power for specific applications with high area and consumption
7	Unlimited increase in energy consumption
8	The high cost of energy production in traditional ways
9	Dependence of renewable energies on geographical and environmental conditions at the regional level
10	Manufacturing technology of domestic types of equipment
11	Obtaining energy resources at a lower cost and higher productivity
12	Balance and justice accessible to energy at affordable prices
13	Liberalization and privatization of the energy sector
14	Increasing energy conversion efficiency and productivity
15	Change in the consumption process
16	Ensuring the security of energy supply, establishing competition, and protecting the environment
17	Continued optimization of energy supply and demand
18	Reforming the energy pricing system
19	Development of the use of renewable energies
20	Developing specific environmental standards for the clean energy industry
21	Energy sector restructuring
22	Action to economize technology in the use of new energy
23	Developing policies for the uptake, transfer of new technologies such as renewable technologies
24	Preparing energy consumption standards and guidelines for energy consumption by different sectors
25	Formulate and implement policies necessary to establish energy consumption standards
26	Energy consumption audit and monitoring
27	Preparation of energy management law and supervision of good enforcement of energy laws
28	Modification of existing technologies
29	Education, awareness, and information
30	Providing government facilities
31	Provision of technical facilities by the municipality and the organization of new energy
32	Development of new energy infrastructure at the regional level
33	Maximum efficiency of modern energy efficiency
34	Provision of legal facilities by the municipality for the development and use of modern energy
35	Cultivation and training in the use and importance of new energies
36	Public propaganda on the use of new energies
37	Having the knowledge of applying
38	Cooperation of various institutions in facilitating the use of modern energy in the private sector
39	Providing consulting services from the municipality and the organization of new energy
40	Creating employment in the field of modern energies
41	Development and application of clean transport

Table 3: Initial analysis of interaction matrix data.

Indicator	Value
Matrix size	41
Number of iterations	2
Number of zeros	771
Number of ones	549
Number of twos	291
Number of threes	51
Number of P	19
Total	910
Fill rate	54/13445%

Source: MICMAC software output, analysis of author's findings.

Table 4: Matrix utility and optimization.

Iteration	Influence (%)	Dependence (%)
1	99	95
2	100	101

3.1.4. Influential or Affiliate Indicators. Influential or affiliate indicators (codes 6 and 33), with low impact and high effectiveness, are system-dependent indicators that are very sensitive to the evolution of two-way variables. These indicators can be considered as system output.

3.1.5. Independent and Exempt Indicators. Independent and exempt indicators (codes 2, 7, 8, 9, 12, 16, 18, 23, 25, 26, 27, 29, 34, 35, 36, 37, 40) are identified as independent system indicators. That means, these indicators are not significantly affected by other system indicators, and they have little or no effect on them. These indicators have very little to do with the system. Thus, they do not stop the main indicator nor evolve a variable in the system.

3.1.6. Among These Indicators. Discrete indicators: the position of the power generation index at peak hours (code 2) indicates that it has nothing to do with the dynamics and current changes of the system in terms of applying new energy to sustain the region, and they can be logged out of the system.

3.1.7. Leverage and Secondary Indicators. The leverage and secondary indicators (codes, 8, 9, 12, 14, 16, 7, 18, 23, 26, 27, 29, 34, 35, 36, 39, 40) are more than influential since they have a strong influence on the system and have leverage in its dynamics, and they can be of particular interest as a starting point to start.

3.1.8. Regulatory Indicators. Regulatory indicators (codes 20, 17, and 22) in area 4 of the diagram can act as secondary leverage, weak targets, or secondary biomarkers. Finally, Figure 1 shows a graphical representation of the indicators studied concerning the pattern of renewable energy use in Tehran's District 4 area. In this figure, the direct effects of the indicators on other indicators of the system are specified. How indicators affect the weakest effects, weak effects, intermediate effects, strong effects, and potential effects is visible.

3.2. Indirect Impact Matrix (MII Matrix). By the application, indirect effects of each index have been raised to the powers of 2, 3, 4, 5, and so on. As a result, the indirect effects of each index were calculated using the renewable energy models. It has been measured at level 4 of Tehran city. The indicators' indirect interaction matrices (codes 3, 4, 10, 19, 28, and 32) have more influence and impact than other variables. The results show the high impact of these six indicators on the system. These indicators can have a greater impact on the use of new energy and make it one of the most influential indicators. The distribution of indexes and their position on the damage axis, the indirect effects of the Matrix on the condition of each index, with their position on the axis, are as follows.

3.2.1. Influential Indicators. The map of the index distribution indicates that the matrix of indirect effects with the codes of 1, 10, 13, 20, 24, 28, 30, 31, and 38 is the most effective indices.

3.2.2. Bidirectional Indicators. Nine indicators (codes 3, 4, 5, 19) are identifiable as bidirectional indicators in the system. It means that they are very effective at the same time, and their nature is mixed with instability. So, every action and change on them will cause a reaction and change on another.

3.2.3. Risk Indicators. The energy resource utilization indicator with lower cost and higher productivity (code 11) is known as the only risk indicator in the system; that is, they have a very high capacity to become key players in the system, and because of their unstable nature, they have the potential to become a breakpoint of the system (the application of new energy at the municipal level).

3.2.4. Target Indicators. Codes 32 and 41 are introduced as target indicators. This means that in this matrix no indicator can be identified with certainty as a result of the evolution of the system to achieve the desired pattern changes and evolution.

3.2.5. Affective or Dependent Indicators. As with the direct effects matrix, the matrices (codes 14, 33, and 40) have low-impact and high-impact indicators, which are very sensitive to the evolution of two-way variables. These indicators can be considered as system output.

3.2.6. Independent and Exempt Indicators. Independent and exempt indicators around the graph axis in area 1 are identified as independent system indicators. This means that these indicators are not significantly influenced by other system indicators and have little or no effect on them. These indicators have very little to do with the system because they do not stop the main indicator nor evolve a variable in the system.

3.2.7. Discrete Indicators. The position of the power output indicator at peak hours (code 2) indicates that the position of the power output index at peak hours (code 2) has nothing to do with the current dynamics and changes of the system in the application of modern energy in order to sustain the region, and they can be logged out of the system.

3.2.8. Leverage and Secondary Indicators. Leverage and secondary indicators (codes 7, 8, 9, 12, 16, 18, 23, 25, 27, 28, 31, 35, 36 and 39) have a strong impact on the system, rather than being effective and have leverage role in its dynamics, and they can be of particular interest as a starting point to start.

3.2.9. Regulatory Indicators. Regulatory indicators (codes 6, 15, 17, 21, and 22) can actually act as secondary leverage, weak targets, or secondary risk indicators around the centre of the chart.

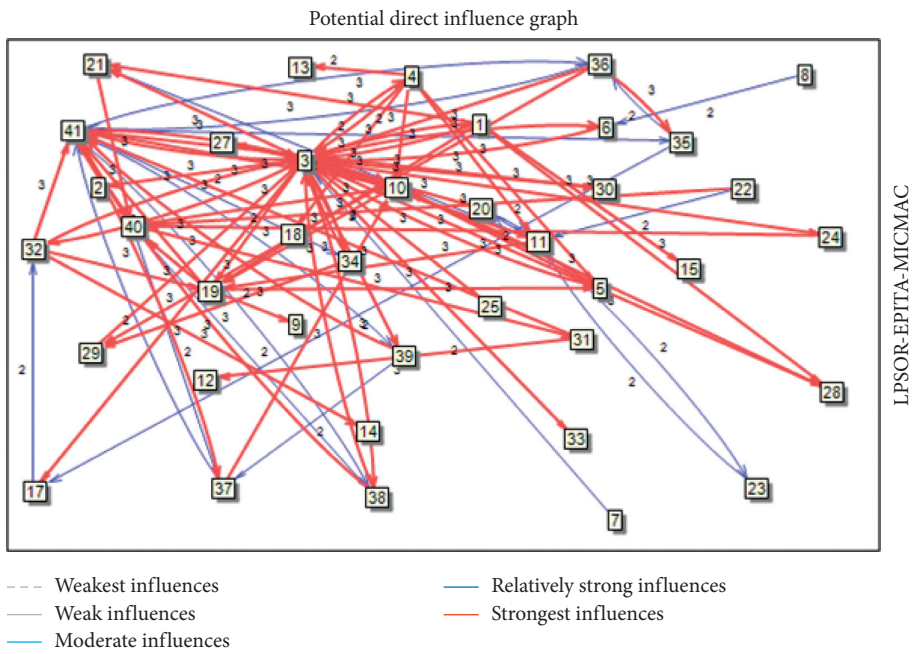

Figure 1: Direct effects between indicators and relationships between them (MICMAC software output).

Finally, Figure 2 shows a graphical representation of the indicators studied in relation to new energy utilization pattern in the Tehran area 4 based on the indirect matrix. Indirect effects of indicators on other system indicators are illustrated in this figure. How indicators affect the weakest effects, weak effects, intermediate effects, strong effects, and potential effects is visible.

Figure 3 shows the potential direct and indirect effects of the indicators evaluated. As can be seen, in addition to the relationships between the indices, there are also potential relationships between them that can be used in the final analysis to develop a model for the use of modern energy for sustainable development. As can be seen, the indicators (code 4) (code 3) (code 6) (code 41) (code 19) are assigned. As mentioned, these codes have the highest priority.

3.3. Identify the Strategic Variables in the Chart. Strategic variables can be manipulated and affect the dynamics and change of the system. With this description, variables that have a very high impact but cannot be controlled cannot be considered a strategic variable. Assuming the status chart of variables as a coordinate network, the variables in zone 2 have such a situation, and planners can rarely change these variables. As shown in the diagram, variables located in zone 3 of the coordinate network have a very low impact on the system, and they cannot be considered strategic variables. Zone 4 variables also have no strategic relevance due to their strong dependence on other variables, and they are often the result of other variables. However, the coordinate network's zone 1 variables are strategic variables because they are both manageable by the management system and have an acceptable impact on the system. The closer we get from the end of zone 3 to the end of zone 1 of the coordinate network, the greater the variable's importance and strategic importance. Thus, by providing explanations and examining the indicators related to the research's nature, identifying the influential indicators in presenting the proposed model of application of modern energy in District 4 of Tehran is discussed. According to the explanation of Figure 4, in the matrix, the direct effects of indices (codes 3, 5, 11, 19, 32, and 41), are almost the priorities of the direct matrix which are key indicators of the model.

3.4. System Stability and Instability. The distribution of variables within the graph indicates the degree of stability or instability of the system. If the variables are in the form of L in the graph, the system is stable, and this state of the system indicates the stability of the influencing variables and their persistence over the other variables. If the variables are scattered from the coordinate axis to the bottom of the graph, the system is unstable, and the lack of effective variables threatens the system. Figure 5 shows the schematic representation of stable and unstable systems.

As can be seen, Figure 6 illustrates the unstable situation of District 4 of Tehran in the current situation for the use of new energy at the urban level. In order to improve the status situation, considering the results of this study and the software outputs and taking into account the factors driving and prioritizing them, a sustainable model can be put in place to change the situation in favour of the use of new energy at the regional level.

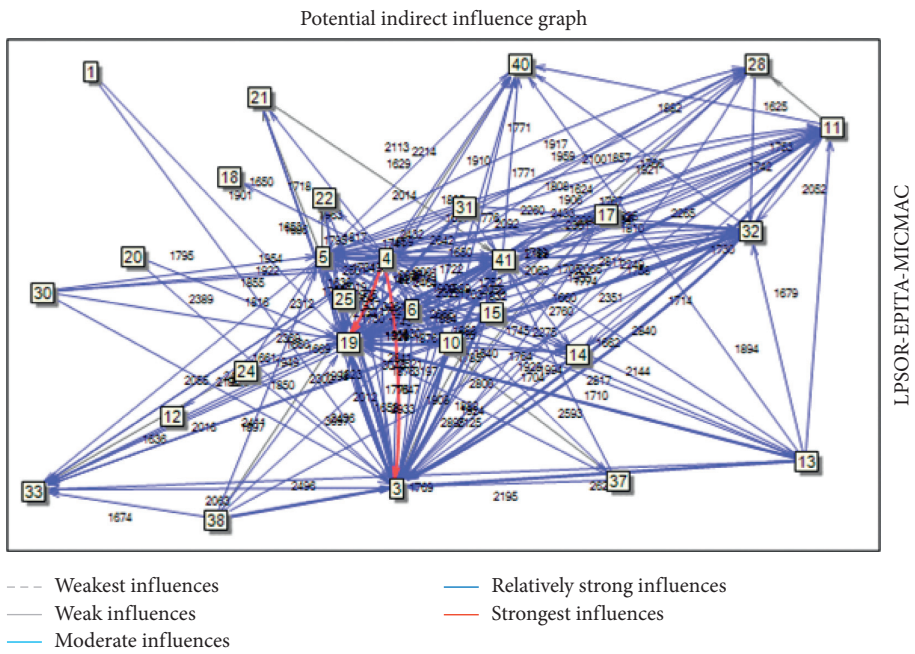

Figure 2: Indirect effects between indicators and their interactions (MICMAC software output).

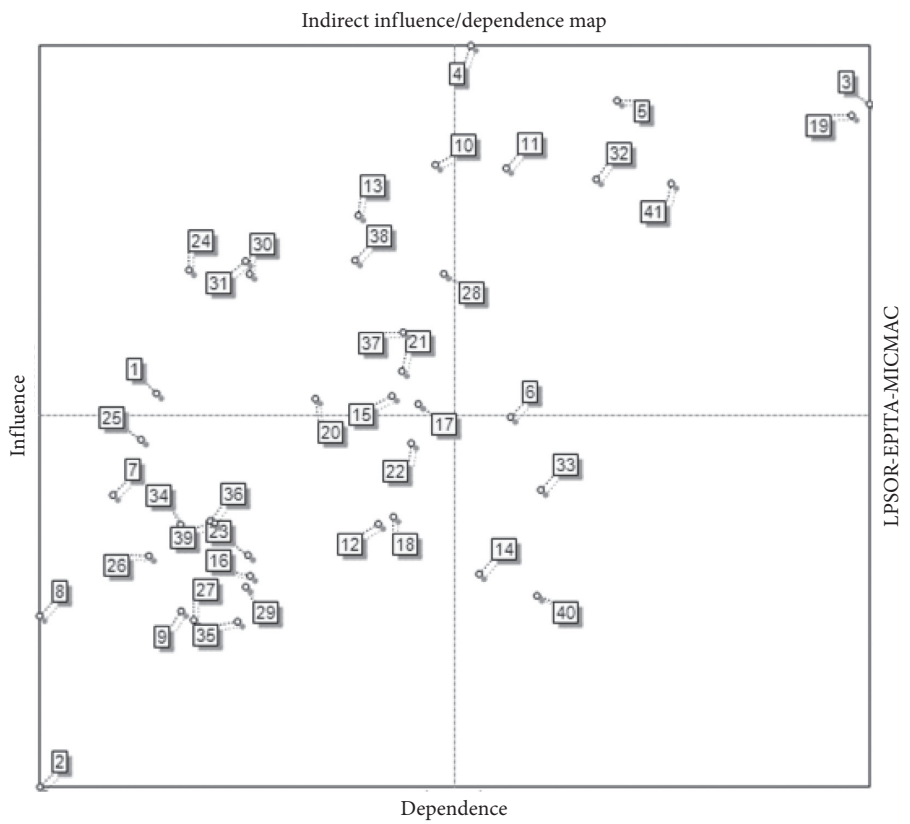

Figure 3: Distribution of indicators and their position in the influence—impact matrix of potential impacts (MICMAC software output).

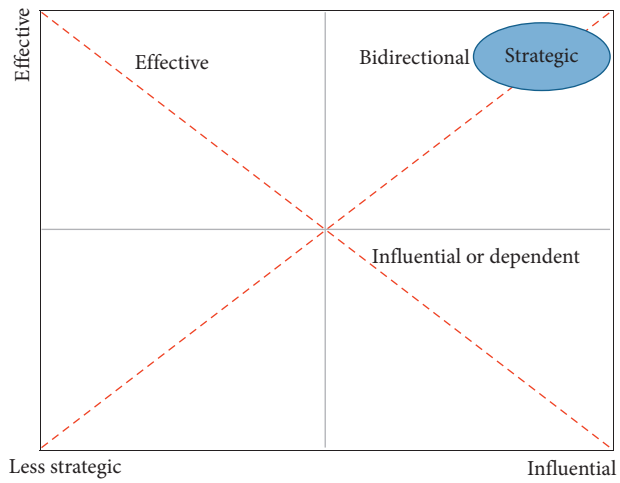

Figure 4: Positioning of strategic variables in graphs [51].

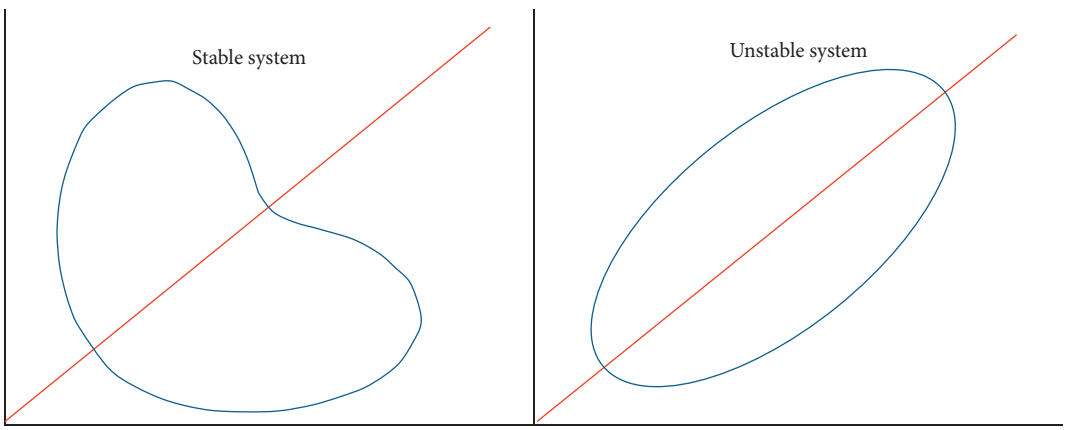

Figure 5: Schematic representation of stable and unstable systems [52].

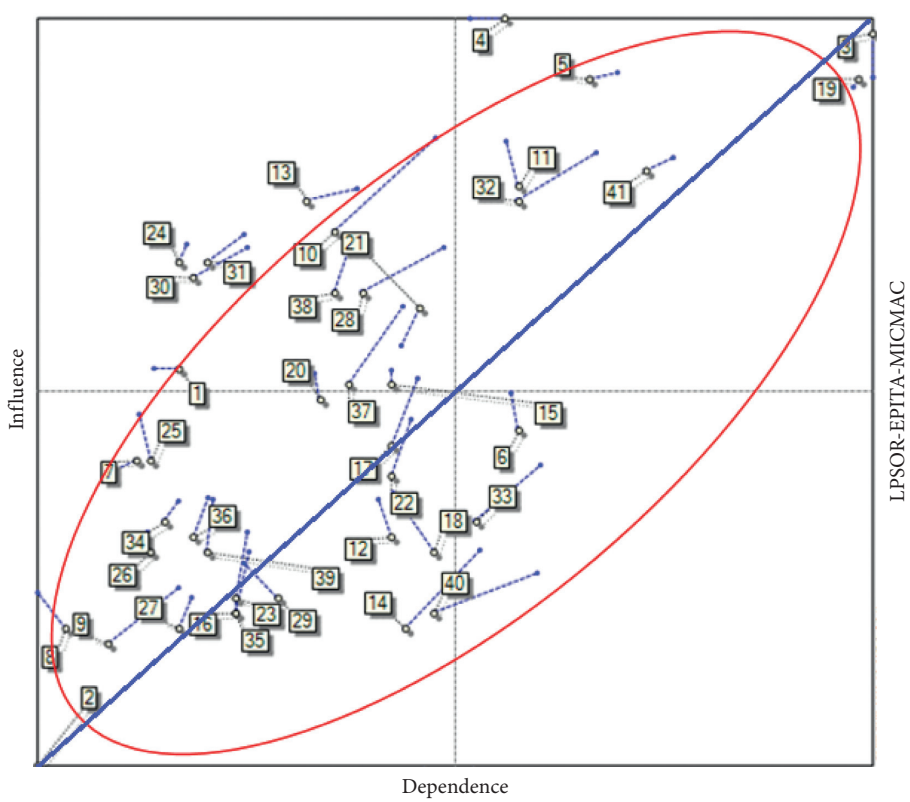

Figure 6: Stability of the system under study (MICMAC software output).

4. Conclusion

Patterns have so far been proposed for modern energy use at different levels, based on existing approaches. In this study, MICMAC software was used to provide a model for applying renewable energies in District 4 of Tehran to provide a precise model based on sound strategies. The general and significant results of this model show that the development of renewable energies is not a path that an organ or government can implement alone, and it requires the involvement of the whole community. Here are two types of short-term planning in which more emphasis is placed on competitiveness in the use of renewable energy technologies and the development of the market for distributed electricity generation from renewable energies. Also, in long-term planning, renewable energy finds its main path and will be completely integrated into the national energy planning process. Renewable energy producers will increasingly be competing with other alternative energy sources based on the cost of the product. Based on the research results, generally, the pattern of utilization and development of renewable energies can be classified into five main groups: financial instruments utilization, use of legal tools, technology development, education and awareness-raising.

The use of appropriate financial instruments provides an appropriate level of investment in newer technologies to develop renewable and sustainable energy programs, which will be compared with the potential of national renewable resources. In this regard, together with international resources, public resources will be guided appropriately in meeting these objectives. Furthermore, the right investment space will attract foreign and local investors. International financial institutions can guarantee the creation of new power plants and facilities around the world by providing resources and credits. These institutions play an important role in determining the future composition of energy sources through direct lending, credit guarantees, or policy guidance.

The purpose of applying legal instruments is to develop, implement, and maintain an effective legal system to develop renewable energy, which has been emphasized in this study. In this regard, an appropriate legal framework for pricing and tariff structure should be designed to support the renewable energy coalition in the energy economy and to attract investors. Furthermore, this legal framework should be able to encourage independent power producers and local producers of liquid and gas fuels to use renewable resources in their systems. In Iran, parliament as the legislator's reference in the creation of national laws related to renewable energies and in the energy, debate at national and international level plays a fundamental role that the most important of these are as follows:

(i) Adopting laws to increase the share of renewable energy in the country's energy basket

(ii) Ensuring that new government commitments to increase the share of renewable energy are announced

(iii) Eliminating fossil fuel subsidies

(iv) Trying to reform the tax system

(v) Moreover, promoting energy efficiency programs

The development of sustainable renewable energy technologies with appropriate standards is another important strategy in developing renewable energy use. In this regard, local research and development and production should be encouraged to promote renewable energy technology's optimal use. Also, the application of machine learning, such as models in [53–55], and neural network models such as models in [56–61] is welcomed to detect the relation among the crucial components for developing renewable energy.

Public awareness, empowerment, and education strategy require the use of mechanisms to raise public awareness of the benefits and opportunities of renewable energy to increase its use and develop its market by disseminating information on the economic, environmental, social, and commercial benefits of renewable energy technologies. The government and related government institutions should be encouraged to promote educational programs in this field. Communication between national, provincial, and local government agencies on renewable energy policies can play a decisive role in this relationship. Meantime, the mass media determine the quality of information presentation and dissemination. In this regard, the mass media in the field of renewable energies perform the following tasks: taking into account the social and environmental aspects of reporting, introducing the benefits of renewable energies and environmental damage and human health from fossil fuels, news coverage of renewable energies and its introduction as an appropriate solution to the climate change problem, and an effective factor in sustainable development.

There are several future directions that we recommend for other researchers. The optimization approaches such as methods in [62–70] can be applied to address the efficacy and detecting the most effective sustainable development factors for a case study. Also, feature selection methods are required as a preprocessing step [71–78] for detecting the most effective and sustainable development factors. Another direction that we will investigate is an exploratory analysis using optimized prediction tasks as developed in [79–83] and optimization algorithms as proposed in [84–88].

Data Availability

The data used to support the findings of this study are available from the corresponding author upon request.

Conflicts of Interest

The authors declare that they have no conflicts of interest.

Acknowledgments

This study did not take any specific grant from funding organisations in the public, commercial, or not-for-profit sectors.

References

[1] J. Yan, W. Pu, S. Zhou, H. Liu, and M. S. Greco, "Optimal resource allocation for asynchronous multiple targets tracking in heterogeneous radar networks," *IEEE Transactions on Signal Processing*, vol. 68, pp. 4055–4068, 2020.

[2] A. A. S. A. Ghareh Gozloo, "A major conceptual analysis of traffic pollution control in urban management in order to provide a framework consistent with the sustainability paradigm in financing municipalities," *Geography and Urban Planning of the Zagros Vision Quarterly*, vol. 9, 2013.

[3] J.-W. Hu, "A survey on multi-sensor fusion based obstacle detection for intelligent ground vehicles in off-road environments," *Frontiers of Information Technology & Electronic Engineering*, vol. 21, no. 5, pp. 675–692, 2020.

[4] H. Zheng, C. Zhang, and M. Shadabfar, "Beam damage detection under a moving load using random decrement technique and Savitzky–Golay filter," *Sensors*, vol. 20, no. 1, p. 243, 2020.

[5] H. Kordestani and C. Zhang, "Direct use of the savitzky-golay filter to develop an output-only trend line-based damage detection method," *Sensors*, vol. 20, no. 7, p. 1983, 2020.

[6] A. A. Mousavi, C. Zhang, S. F. Masri, and G. Gholipour, "Structural damage localization and quantification based on a ceemdan hilbert transform neural network approach: a model steel truss bridge case study," *Sensors*, vol. 20, no. 5, p. 1271, 2020.

[7] C. Li, L. Sun, Z. Xu, X. Wu, T. Liang, and W. Shi, "Experimental investigation and error analysis of high precision FBG displacement sensor for structural health monitoring," *International Journal of Structural Stability and Dynamics*, vol. 20, no. 6, Article ID 2040011, 2020.

[8] L. Sun, C. Li, C. Zhang, T. Liang, and Z. Zhao, "The strain transfer mechanism of fiber bragg grating sensor for extra large strain monitoring," *Sensors*, vol. 19, no. 8, p. 1851, 2019.

[9] C. Zhang, Z. Alam, L. Sun, Z. Su, and B. Samali, "Fibre bragg grating sensor-based damage response monitoring of an asymmetric reinforced concrete shear wall structure subjected to progressive seismic loads," *Structural Control and Health Monitoring*, vol. 26, no. 3, Article ID e2307, 2019.

[10] L. Sun, C. Li, C. Zhang, Z. Su, and C. Chen, "Early monitoring of rebar corrosion evolution based on FBG sensor," *International Journal of Structural Stability and Dynamics*, vol. 18, no. 8, Article ID 1840001, 2018.

[11] C. Cai, X. Wu, W. Liu et al., "Selective laser melting of near-α titanium alloy Ti-6Al-2Zr-1Mo-1V: parameter optimization, heat treatment and mechanical performance," *Journal of Materials Science & Technology*, vol. 57, pp. 51–64, 2020.

[12] C. Cai, X. Gao, Q. Teng et al., "Hot isostatic pressing of a near α-Ti alloy: temperature optimization, microstructural evolution and mechanical performance evaluation," *Materials Science and Engineering: A*, vol. 802, Article ID 140426, 2020.

[13] X. Wang, Y. Liu, and K.-K. R. Choo, "Fault tolerant multi-subset aggregation scheme for smart grid," *IEEE Transactions on Industrial Informatics*, vol. 848, p. 1, 2020.

[14] S. Xu, J. Wang, W. Shou, T. Ngo, A.-M. Sadick, and X. Wang, "Computer vision techniques in construction: a critical review," *Archives of Computational Methods in Engineering*, 2020.

[15] J. Yan, W. Pu, S. Zhou, H. Liu, and Z. Bao, "Collaborative detection and power allocation framework for target tracking in multiple radar system," *Information Fusion*, vol. 55, pp. 173–183, 2020.

[16] Q. Zhu, "Research on road traffic situation awareness system based on image big data," *IEEE Intelligent Systems*, vol. 35, no. 1, pp. 18–26, 2019.

[17] Q. Jiang, F. Shao, W. Gao, Z. Chen, G. Jiang, and Y.-S. Ho, "Unified no-reference quality assessment of singly and multiply distorted stereoscopic images," *IEEE Transactions on Image Processing*, vol. 28, no. 4, pp. 1866–1881, 2018.

[18] M. Xu, C. Li, S. Zhang, and P. L. Callet, "State-of-the-art in 360° video/image processing: perception, assessment and compression," *IEEE Journal of Selected Topics in Signal Processing*, vol. 14, no. 1, pp. 5–26, 2020.

[19] M. Yang and A. Sowmya, "An underwater color image quality evaluation metric," *IEEE Transactions on Image Processing*, vol. 24, no. 12, pp. 6062–6071, 2015.

[20] B. Wang, B. Zhang, and X. Liu, "An image encryption approach on the basis of a time delay chaotic system," *Optik—International Journal for Light and Electron Optics*, vol. 225, Article ID 165737, 2020.

[21] S. Hinojosa, D. Oliva, E. Cuevas, G. Pajares, D. Zaldivar, and M. Pérez-Cisneros, "Reducing overlapped pixels: a multi-objective color thresholding approach," *Soft Computing*, vol. 24, no. 9, pp. 6787–6807, 2020.

[22] C. Wu, P. Wu, J. Wang, R. Jiang, M. Chen, and X. Wang, "Critical review of data-driven decision-making in bridge operation and maintenance," *Structure and Infrastructure Engineering*, pp. 1–24, 2020.

[23] S. Liu, W. Yu, F. T. S. Chan, and B. Niu, "A variable weight-based hybrid approach for multi-attribute group decision making under interval-valued intuitionistic fuzzy sets," *International Journal of Intelligent Systems*, vol. 36, no. 2, 2020.

[24] S. Liu, F. T. S. Chan, and W. Ran, "Decision making for the selection of cloud vendor: an improved approach under group decision-making with integrated weights and objective/subjective attributes," *Expert Systems with Applications*, vol. 55, pp. 37–47, 2016.

[25] A. R. A. M. M. K. G. Kazemian, "The place of renewable and renewable energies in the biodiversity of cities case study of Tehran," *Journal of Urban Research and Planning*, vol. 8, no. 22, pp. 99–188, 2016.

[26] M. Bottero, C. D'Alpaos, and A. Oppio, "Decision-making for urban planning and regional development," *Advances in Operations Research*, vol. 2019, Article ID 5178051, 2 pages, 2019.

[27] Z. Lukszo, E. Bompard, P. Hines, and L. Varga, "Energy and complexity," *Complexity*, vol. 2018, Article ID 6937505, 2 pages, 2018.

[28] J. A. León, G. Montero, M. A. Coronado et al., "Renewable energy integration: economic assessment of solar energy to produce biodiesel at supercritical conditions," *International Journal of Photoenergy*, vol. 2018, Article ID 8769582, 9 pages, 2018.

[29] Y. Shen, R. Wei, and L. Xu, "Energy consumption prediction of a greenhouse and optimization of daily average temperature," *Energies*, vol. 11, no. 1, p. 65, 2018.

[30] A.-J. Perea-Moreno, M.-Á. Perea-Moreno, Q. Hernandez-Escobedo, and F. Manzano-Agugliaro, "Towards forest sustainability in Mediterranean countries using biomass as fuel for heating," *Journal of Cleaner Production*, vol. 156, pp. 624–634, 2017.

[31] A.-J. Perea-Moreno, M.-J. Aguilera-Ureña, and F. Manzano-Agugliaro, "Fuel properties of avocado stone," *Fuel*, vol. 186, pp. 358–364, 2016.

[32] M. J. Sorgato, K. Schneider, and R. Rüther, "Technical and economic evaluation of thin-film CdTe building-integrated

photovoltaics (BIPV) replacing façade and rooftop materials in office buildings in a warm and sunny climate," *Renewable Energy*, vol. 118, pp. 84–98, 2018.

[33] D. La Cruz-Lovera, A.-J. Perea-Moreno, D. La Cruz-Fernández, J. A. Alvarez-Bermejo, and F. Manzano-Agugliaro, "Worldwide research on energy efficiency and sustainability in public buildings," *Sustainability*, vol. 9, no. 8, p. 1294, 2017.

[34] B. Marchi and S. Zanoni, "Supply chain management for improved energy efficiency: review and opportunities," *Energies*, vol. 10, no. 10, p. 1618, 2017.

[35] L. Zhao and Z. Zhou, "Developing a rating system for building energy efficiency based on in situ measurement in China," *Sustainability*, vol. 9, no. 2, p. 208, 2017.

[36] J. Aggarwal and M. L. Aggarwal, "Harnessing solar energy for every home: energy saving applications," *Conference Papers in Science*, vol. 2014, Article ID 628294, 3 pages, 2014.

[37] M. Soltani, O. Rahmani, A. Beiranvand Pour, Y. Ghaderpour, I. Ngah, and S. H. Misnan, "Determinants of variation in household energy choice and consumption: case from Mahabad city, Iran," *Sustainability*, vol. 11, no. 17, p. 4775, 2019.

[38] O. Rahmani, S. Rezania, A. Beiranvand Pour et al., "An overview of household energy consumption and carbon dioxide emissions in Iran," *Processes*, vol. 8, no. 8, p. 994, 2020.

[39] L. D. D. Harvey, "Resource implications of alternative strategies for achieving zero greenhouse gas emissions from light-duty vehicles by 2060," *Applied Energy*, vol. 212, pp. 663–679, 2018.

[40] A.-J. Perea-Moreno and Q. Hernandez-Escobedo, "Solar resource for urban communities in the Baja California Peninsula, Mexico," *Energies*, vol. 9, no. 11, p. 911, 2016.

[41] C. Filippín, S. Flores Larsen, and F. Ricard, "Improvement of energy performance metrics for the retrofit of the built environment. Adaptation to climate change and mitigation of energy poverty," *Energy and Buildings*, vol. 165, pp. 399–415, 2018.

[42] H. M. Munir, R. Ghannam, H. Li et al., "Control of distributed generators and direct harmonic voltage controlled active power filters for accurate current sharing and power quality improvement in islanded microgrids," *Inventions*, vol. 4, no. 2, p. 27, 2019.

[43] Z. Xu, Y. Gao, M. Hussain, and P. Cheng, "Demand side management for smart grid based on smart home appliances with renewable energy sources and an energy storage system," *Mathematical Problems in Engineering*, vol. 2020, Article ID 9545439, 20 pages, 2020.

[44] S. K. Murthy, A. Goyal, N. Rajasekar, K. Pareek, T. T. Nguyen, and A. Garg, "Predictive modelling and surface analysis for optimization of production of biofuel as A renewable energy resource: proposition of artificial neural network search," *Mathematical Problems in Engineering*, vol. 2020, Article ID 4065964, 13 pages, 2020.

[45] A. Sadeghpour and G. Ozay, "Evaluation of reinforced concrete frames designed based on previous Iranian seismic codes," *Arabian Journal for Science and Engineering*, vol. 45, no. 10, pp. 8069–8085, 2020.

[46] A. Addeh, A. Khormali, and N. A. Golilarz, "Control chart pattern recognition using RBF neural network with new training algorithm and practical features," *ISA Transactions*, vol. 79, pp. 202–216, 2018.

[47] A. Curreli, G. Serra-Coch, A. Isalgue, I. Crespo, and H. Coch, "Solar energy as a form giver for future cities," *Energies*, vol. 9, no. 7, p. 544, 2016.

[48] E. Laiola and P. Giungato, "Wind characterization in Taranto city as a basis for innovative sustainable urban development," *Journal of Cleaner Production*, vol. 172, pp. 3535–3545, 2018.

[49] J. Z. Thellufsen and H. Lund, "Roles of local and national energy systems in the integration of renewable energy," *Applied Energy*, vol. 183, pp. 419–429, 2016.

[50] Tehran center for studies and planning, "Detailed Plan of Tehran District 4." Municipality of Tehran, 2006.

[51] N. Zali, T. Rabbani, and V. V. Motti, "Application of prospective structural analysis for identification of strategic variables in the future development of Baneh City in Iran," *European Spatial Research and Policy*, vol. 22, no. 1, pp. 153–171, 2015.

[52] J. Arcade, M. Godet, F. Meunier, and F. Roubelat, "Structural analysis with the MICMAC method & actor's strategy with MACTOR method," *Futures Research Methodology*, vol. 3, 1999.

[53] X. Zhang, T. Wang, W. Luo, and P. Huang, "Multi-level fusion and attention-guided CNN for image dehazing," *IEEE Transactions on Circuits and Systems for Video Technology*, p. 1, 2020.

[54] X. Zhang, D. Wang, Z. Zhou, and Y. Ma, "Robust low-rank tensor recovery with rectification and alignment," *IEEE Transactions on Pattern Analysis and Machine Intelligence*, vol. 43, no. 1, pp. 238–255, 2019.

[55] X. Zhang, R. Jiang, T. Wang, and J. Wang, "Recursive neural network for video deblurring," *IEEE Transactions on Circuits and Systems for Video Technology*, vol. 8, p. 1, 2020.

[56] D. Zhao, L. Liua, F. Yua et al., "Chaotic random spare ant colony optimization for multi-threshold image segmentation of 2D Kapur entropy," *Knowledge-Based Systems*, vol. 216, Article ID 106510, 2020.

[57] H.-L. Chen, G. Wang, C. Ma, Z.-N. Cai, W.-B. Liu, and S.-J. Wang, "An efficient hybrid kernel extreme learning machine approach for early diagnosis of Parkinson's disease," *Neurocomputing*, vol. 184, pp. 131–144, 2016.

[58] L. Hu, G. Hong, J. Ma, X. Wang, and H. Chen, "An efficient machine learning approach for diagnosis of paraquat-poisoned patients," *Computers in Biology and Medicine*, vol. 59, pp. 116–124, 2015.

[59] J. Xia, H. Chen, Q. Li et al., "Ultrasound-based differentiation of malignant and benign thyroid Nodules: an extreme learning machine approach," *Computer Methods and Programs in Biomedicine*, vol. 147, pp. 37–49, 2017.

[60] C. Li, L. Hou, B. Y. Sharma et al., "Developing a new intelligent system for the diagnosis of tuberculous pleural effusion," *Computer Methods and Programs in Biomedicine*, vol. 153, pp. 211–225, 2018.

[61] X. Xu and H.-L. Chen, "Adaptive computational chemotaxis based on field in bacterial foraging optimization," *Soft Computing*, vol. 18, no. 4, pp. 797–807, 2014.

[62] H. Yu, W. Li, C. Cheng et al., "Dynamic Gaussian bare-bones fruit fly optimizers with abandonment mechanism: method and analysis," *Engineering with Computers*, pp. 1–29, 2020.

[63] J. Hu, H. Chen, A. A. Heidari et al., "Orthogonal learning covariance matrix for defects of grey wolf optimizer: insights, balance, diversity, and feature selection," *Knowledge-Based Systems*, vol. 213, Article ID 106684, 2021.

[64] C. Yu, M. Chen, K. Cheng et al., "SGOA: annealing-behaved grasshopper optimizer for global tasks," *Engineering with Computers*, pp. 1–28, 2021.

[65] W. Shan, Z. Qiao, A. A. Heidari, H. Chen, H. Turabieh, and Y. Teng, "Double adaptive weights for stabilization of moth flame optimizer: balance analysis, engineering cases, and

medical diagnosis," *Knowledge-Based Systems*, vol. 214, Article ID 106728, 2020.

[66] J. Tu, H. Chen, J. Liu et al., "Evolutionary biogeography-based whale optimization methods with communication structure: towards measuring the balance," *Knowledge-Based Systems*, vol. 212, Article ID 106642, 2021.

[67] H. Chen, A. A. Heidari, H. Chen, M. Wang, Z. Pan, and A. H. Gandomi, "Multi-population differential evolution-assisted Harris hawks optimization: framework and case studies," *Future Generation Computer Systems*, vol. 111, pp. 175–198, 2020.

[68] X. Zhao, X. Zhang, Z. Cai et al., "Chaos enhanced grey wolf optimization wrapped ELM for diagnosis of paraquat-poisoned patients," *Computational Biology and Chemistry*, vol. 78, pp. 481–490, 2019.

[69] Y. Xu, H. Chen, J. Luo, Q. Zhang, S. Jiao, and X. Zhang, "Enhanced Moth-flame optimizer with mutation strategy for global optimization," *Information Sciences*, vol. 492, pp. 181–203, 2019.

[70] M. Wang and H. Chen, "Chaotic multi-swarm whale optimizer boosted support vector machine for medical diagnosis," *Applied Soft Computing Journal*, vol. 88, Article ID 105946, 2020.

[71] X. Zhao, D. Li, B. Yang, C. Ma, Y. Zhu, and H. Chen, "Feature selection based on improved ant colony optimization for online detection of foreign fiber in cotton," *Applied Soft Computing*, vol. 24, pp. 585–596, 2014.

[72] Y. Zhang, R. Liu, A. A. Heidari et al., "Towards augmented kernel extreme learning models for bankruptcy prediction: algorithmic behavior and comprehensive analysis," *Neurocomputing*, vol. 430, 2020.

[73] Y. Zhang, R. Liu, X. Wang, H. Chen, and C. Li, "Boosted binary Harris hawks optimizer and feature selection," *Engineering with Computers*, pp. 1–30, 2020.

[74] L. Shen, H. Chen, Z. Yu et al., "Evolving support vector machines using fruit fly optimization for medical data classification," *Knowledge-Based Systems*, vol. 96, pp. 61–75, 2016.

[75] M. Wang, H. Chen, B. Yang et al., "Toward an optimal kernel extreme learning machine using a chaotic moth-flame optimization strategy with applications in medical diagnoses," *Neurocomputing*, vol. 267, pp. 69–84, 2017.

[76] X. Zhang, J. Wang, T. Wang, R. Jiang, J. Xu, and L. Zhao, "Robust feature learning for adversarial defense via hierarchical feature alignment," *Information Sciences*, vol. 560, 2020.

[77] X. Zhang, M. Fan, D. Wang, P. Zhou, and D. Tao, "Top-k feature selection framework using robust 0-1 integer programming," *IEEE Transactions on Neural Networks and Learning Systems*, pp. 1–15, 2020.

[78] X. Zhang, T. Wang, J. Wang, G. Tang, and L. Zhao, "Pyramid channel-based feature attention network for image dehazing," *Computer Vision and Image Understanding*, vol. 197198 pages, 2020.

[79] W. Zhu, C. Ma, X. Zhao et al., "Evaluation of sino foreign cooperative education project using orthogonal sine cosine optimized kernel extreme learning machine," *IEEE Access*, vol. 8, pp. 61107–61123, 2020.

[80] G. Liu, W. Jia, M. Wang et al., "Predicting cervical hyperextension injury: a covariance guided sine cosine support vector machine," *IEEE Access*, vol. 8, pp. 46895–46908, 2020.

[81] Y. Wei, H. Lv, M. Chen et al., "Predicting entrepreneurial intention of students: an extreme learning machine with Gaussian barebone harris hawks optimizer," *IEEE Access*, vol. 8, pp. 76841–76855, 2020.

[82] H. Tang, Y. Xu, A. Lin et al., "Predicting green consumption behaviors of students using efficient firefly grey wolf-assisted K-nearest neighbor classifiers," *IEEE Access*, vol. 8, pp. 35546–35562, 2020.

[83] A. Lin, Q. Wu, A. A. Heidari et al., "Predicting intentions of students for master programs using a chaos-induced sine cosine-based fuzzy K-nearest neighbor classifier," *IEEE Access*, vol. 7, pp. 67235–67248, 2019.

[84] Y. Fan, P. Wang, A. A. Heidari et al., "Rationalized fruit fly optimization with sine cosine algorithm: a comprehensive analysis," *Expert Systems with Applications*, vol. 157, Article ID 113486, 2020.

[85] E. Rodríguez-Esparza, L. A. Zanella-Calzada, D. Oliva et al., "An efficient Harris hawks-inspired image segmentation method," *Expert Systems with Applications*, vol. 155, Article ID 113428, 2020.

[86] S. Jiao, G. Chong, C. Huang et al., "Orthogonally adapted Harris hawks optimization for parameter estimation of photovoltaic models," *Energy*, vol. 203, Article ID 117804, 2020.

[87] Z. Xu, Z. Hu, A. A. Heidari et al., "Orthogonally-designed adapted grasshopper optimization: a comprehensive analysis," *Expert Systems with Applications*, vol. 150, Article ID 113282, 2020.

[88] A. Abbassi, R. Abbassi, A. A. Heidari et al., "Parameters identification of photovoltaic cell models using enhanced exploratory salp chains-based approach," *Energy*, vol. 198, Article ID 117333, 2020.

Hindawi
Mathematical Problems in Engineering
Volume 2021, Article ID 5534659, 10 pages
https://doi.org/10.1155/2021/5534659

Research Article

Optimal Selective Maintenance Decision-Making for Consecutive-Mission Systems with Variable Durations and Limited Maintenance Time

Huiying Gao, Xiaoqiang Zhang, Xiaoqiang Yang, and Bo Zheng

Aviation Engineering Institute, Civil Aviation Flight University of China, Deyang 618307, China

Correspondence should be addressed to Xiaoqiang Zhang; xqzhanguestc@163.com

Received 4 February 2021; Revised 16 February 2021; Accepted 19 February 2021; Published 2 March 2021

Academic Editor: Mohammad Yazdi

Maintenance is inevitable for repairable components or systems in modern industries. Since the maintenance effectiveness has a great influence on the subsequent operations and in addition, different maintenance options are possible for the components of the system during the break between any two successive missions, the optimal selective maintenance strategy needs to be determined for a system performing successive missions. A number of selective maintenance models were set up on the basis that the durations of each mission are predetermined, the maintenance time is negligible, and the states of the components at the end of the previous mission can be accurately obtained. However, in the actual industrial and military missions, these premises may not always hold. In this paper, a novel selective maintenance model under uncertainties and limited maintenance time is proposed to improve these deficiencies. The genetic algorithm is selected to solve the optimization problem, and an illustrative example is presented to demonstrate the proposed method. The optimal selective maintenance decision without the constraint of maintenance time is used for comparison.

1. Introduction

Equipment maintenance refers to the technical activities to restore the function of the equipment after deterioration or failures, and it is a key factor affecting the development of industrial, military, aviation, and so on. In general, the maintenance of a component or system can be divided into planned maintenance and unplanned maintenance. The former, also known as preventive maintenance (PM), is usually a maintenance policy formulated in advance. In case of a PM, maintenance activities will be conducted at a preset time or under a predetermined system state. For unplanned maintenance, it is a maintenance policy taken after the system failure occurs and also called corrective maintenance (CM). What the decision-makers usually concern most contains two aspects: one is the reliability of the system after a maintenance activity and the other is the optimal maintenance strategy under limited maintenance time to minimize the maintenance cost. From the early 1960s, academia and industrial community have shown a strong interest in the optimization of maintenance strategies. In the past few decades, a large amount of research works with respect to maintenance have been reported. Scholars have built a number of maintenance models based on the assumption that the components are updated after repairs [1–3]. However, the assumption that the components become brand new after repairs is usually far from the truth. To describe the maintenance situation in the real world, the concept of imperfect maintenance is published. An imperfect maintenance (IM) refers to a maintenance activity after which the system returns to a state between minimal repair and replacement. Alaswad and Xiang [4], Wu and Zuo [5], and Nakagawa [6] have made several comprehensive reviews on imperfect maintenance. In these reviews, some IM models including (p, q) model [7], $(p(t), q(t))$ model [8], Kijima I and Kijima II models [9, 10], age reduction models [11], intensity reduction model [12], quasirenewal process model [13], and so on are remarkable. How to

choose a proper model is an application-dependent and thorny problem and has been recently discussed by Liu et al. [14].

For the moment, the imperfect maintenance has been well studied but how to identify the optimal maintenance strategy under limited maintenance budget and time is still a hot potato for the decision-makers, especially, with the addition of uncertainties. The first reported work with respect to selective maintenance should date back to Rice et al. [15]. Immediately after that, Cassady et al. [16, 17] proposed some selective maintenance problems and a general selective maintenance model was constructed by considering different maintenance actions. In management science, selective maintenance is a class of optimization problems in nature. Rice et al. [15] and Rajagopalan and Cassady [18] proposed several enumerating methods to resolve the selective maintenance models, but they become computationally inefficient as the crescent complexity of selective maintenance models. Therefore, some heuristic algorithms such as simulated annealing algorithm [19], genetic algorithm [20, 21], ant colony optimization [22], and artificial neural networks [23] have been applied to identify an optimal maintenance strategy under acceptable computational efficiency.

In practice, components or systems may be connected to each other in an arbitrary form and the components may be multistate. Therefore, Liu and Huang [24], Pandey et al. [25], and Liu et al. [26] studied the optimal selective maintenance strategy for a multistate system consisting of binary-state components or multistate components, respectively. Dao and Zuo [27] proposed a selective maintenance model of multistate systems based on the load-dependent degradation model. Besides, some selective maintenance optimizations based on various IM models such as the Kijima I model [28], the Kijima II model [24], and the hybrid model [29] have also been studied.

Although a lot of research with respect to selective maintenance models have be done, but most of the models were set up on the basis that the durations of each mission were predetermined and the states of the components at the end of the previous mission can be accurately obtained. In the actual industrial tasks and military missions, these premises may not always hold. For example, an airplane may change the flight course according to the weather or the commands from air traffic controllers. In these situations, the mission duration will be variable. Jiang and Liu [30] and Khatab et al. [31] set up some selective maintenance models considering the uncertainties associated with the durations of missions but they do not concern the constraint of maintenance time. In this paper, a novel selective maintenance model is proposed under variable mission durations and limited maintenance time.

The remainder of this paper is organized as follows. Section 2 lists some hypotheses on which the selective maintenance model is set up, and imperfect maintenance based on the Kijima II model is introduced. Section 3 discusses the selective maintenance model under uncertainties. Section 4 presents an illustrative example. Conclusions are finally summarized in Section 5.

2. Model Hypotheses and Imperfect Maintenance Based on Kijima II Model

In military operations, a weapon may change mission mode according to the actual situation and the mission durations are correspondingly variable. To maintain the warfare capability, the maintenance activities must maximize the reliability of the system within limited maintenance time. In this paper, to set up the novel selective maintenance model, some basic hypotheses are made as follows:

(1) The system for selective maintenance is composed of n repairable components in any combination ways. The states of all the components as well as the system can be identified at any time and under a binary-state (functioning or failed).

(2) As shown in Figure 1, the maintenance activities can be only conducted in the break between any two successive missions and the duration of each break is a limited constant, denoting as T^M.

(3) Several maintenance options are available for components during the breaks, including do nothing (DN), minimal repair (MR), replacement maintenance (RM), and imperfect preventive/corrective maintenance (IPM/ICM).

(4) The state of element i at the beginning and the end of the kth mission can be described by binary variables $S_{i,k}^B$ and $S_{i,k}^E$, respectively. Moreover, it has

$$S_{i,k}^B = \begin{cases} 1, & \text{if component is functioning,} \\ 0, & \text{otherwise,} \end{cases}$$
$$S_{i,k}^E = \begin{cases} 1, & \text{if component is functioning,} \\ 0, & \text{otherwise.} \end{cases} \tag{1}$$

(5) All the components are brand new before the first mission and the duration of the first mission is a given constant t_1, the state of element i ($i \in \{1, 2, \cdots, n\}$) at the end of the first mission is known as $S_{i,1}^E$, and the virtual age of each element at the end of the first mission is also predetermined, whereas it is uncertain for the subsequent missions.

(6) The duration of each future mission (except the first mission) can be denoted as a discrete variable T_k ($k \in \{2, \cdots, N\}$) in this paper, which has w_k possible values and the probability for the jth ($j \in \{1, 2, \cdots, w_k\}$) possible value t_k^j is p_k^j.

For component i ($i \in \{1, 2, \cdots n\}$), it is assumed that the virtual ages at the beginning and the end of the kth mission are $V_{i,k}^B$ and $V_{i,k}^E$, respectively; the virtual age after the kth ($k \in \{1, 2, \cdots, N-1\}$) maintenance is $V_{i,k}^M$ (obviously, $V_{i,k+1}^B = V_{i,k}^M$ and the minimum is zero); the failure time of component i from the beginning of the kth mission is represented by $T_{i,k}^F$ ($T_{i,k}^F \in [0, +\infty)$); the actual service time of component i in the kth mission can be denoted by a random variable $T_{i,k}^\Theta$ ($T_{i,k}^\Theta \in [0, t_k]$), where t_k is the duration of the kth mission. Then, it is obvious that $T_{i,k}^\Theta \in (0, t_k)$ in the case that the component fails in the kth mission; otherwise,

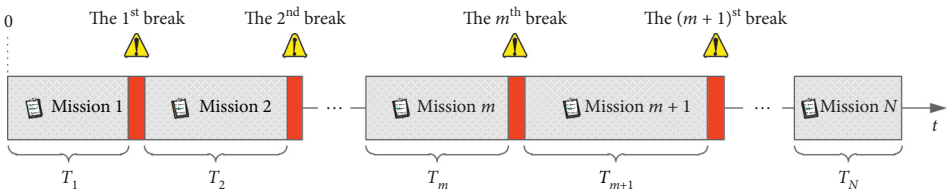

Figure 1: The successive missions and breaks.

the component works properly all through the kth mission and it has $T_{i,k}^{\Theta} = t_k$. In addition, since the maintenance activity can only be conducted during the break between the two successive missions, it is easy to gain the following:

$$V_{i,k}^{E} = V_{i,k}^{B} + T_{i,k}^{\Theta}. \tag{2}$$

According to the Kijima II model and equation (2), the virtual age of component i after the kth maintenance can be defined as follows:

$$V_{i,k+1}^{B} = \beta_{i,k} V_{i,k}^{E} = \beta_{i,k}\left(V_{i,k}^{B} + T_{i,k}^{\Theta}\right), \tag{3}$$

where $\beta_{i,k}$ ($\beta_{i,k} \in [0,1]$) is the age reduction factor, and it is closely related to the maintenance effectiveness.

In maintenance activities, the maintenance cost can be roughly divided into the fixed maintenance cost and the reparative maintenance cost. As a result, the total maintenance cost of component i allocated in the kth break can be expressed as

$$C_{i,k} = C_{i,k}^{0} + C_{i,k}^{M}, \tag{4}$$

where $C_{i,k}^{0}$ represents the inevitable fixed cost such as the payment for the serviceman and $C_{i,k}^{M}$ represents the reparative maintenance cost used to reduce the virtual age of component i and it is controllable.

Generally, the more reparative maintenance cost is, the better or more effective the maintenance will be. A great number of studies with respect to the age reduction factor can be found. Diallo et al. [32] indicated that the reparative maintenance cost and the current virtual age of the component were the two principal factors affecting the degree of system repair. For convenience, the maintenance cost for performing an minimal repair (MR), an maximum imperfect maintenance (MIM), and a replacement maintenance (RM) are denoted by $C_{i,k}^{\text{MR}}$, $C_{i,k}^{\text{MIM}}$, and $C_{i,k}^{\text{RM}}$ hereinafter, respectively. An ICM procedure for a failed component can be split up into an MR and a further maintenance to reduce the virtual age. Therefore, performing an MIM to a failed component is more expensive compared with a functioning component. When $C_{i,k}^{M} = C_{i,k}^{\text{MR}}$, MR is performed, the degree of repair of the component is zero, and the repaired component is restored to "as bad as old (ABAO)"; if $C_{i,k} = 0$, then it corresponds to DN. Particularly, if $C_{i,k}^{M} = C_{i,k}^{\text{RM}}$, the repaired component is restored to "as good as new (AGAN)." It is easy to understand that when the virtual age of the component is small, the reparative cost of maintenance is relatively low and it can achieve a good maintenance effect, whereas, as the virtual age of the component continues to increase, the cost of reparative maintenance will increase and the corresponding maintenance effect will gradually decrease meanwhile. Nguyen et al. [33] described the relationships among preventive maintenance cost, replacement maintenance cost, and the degree of rejuvenation after system repair. Pandey et al. [29] defined the age reduction factor as a function related to maintenance cost as follows:

$$\beta_{i,k} = \begin{cases} 1 - \left(\dfrac{C_{i,k}^{M} - C_{i,k}^{\text{MR}}}{C_{i,k}^{\text{MIM}}}\right)^{\left(1/m_{i,k}\right)}, & \text{for } S_{i,k}^{E} = 0 \text{ and } C_{i,k}^{M} \in \left[C_{i,k}^{\text{MR}}, C_{i,k}^{\text{MR}} + C_{i,k}^{\text{MIM}}\right], \\ 1 - \left(\dfrac{C_{i,k}^{M}}{C_{i,k}^{\text{MIM}}}\right)^{\left(1/m_{i,k}\right)}, & \text{for } S_{i,k}^{E} = 10 \text{ and } C_{i,k}^{M} \in \left[0, C_{i,k}^{\text{MIM}}\right], \end{cases} \tag{5}$$

where $m_{i,k}$ is the characteristic constant and it determines the exact relationship between the reparative maintenance cost $C_{i,k}^{M}$ and the age reduction factor $\beta_{i,k}$. As shown in Figure 2, if the component is in functioning state, when the ratio between $C_{i,k}^{M}$ and $C_{i,k}^{\text{MIM}}$ is a constant, the variable $m_{i,k}$ will lead to different age reduction factors.

From Figure 2, it can be found that the larger the value of $m_{i,k}$ is, the more obvious the maintenance effect is. As discussed in [26, 34], this scenario corresponds to the component with smaller virtual age; whereas, the value of $m_{i,k}$ decreases as the component aging and the effect would be decreased for even a large amount of maintenance cost. Pandey et al. [29] defined the characteristic constant $m_{i,k}$, the mean residual life (MRL) $T_{i,k}^{\text{MRL}}$, and the virtual age $V_{i,k}^{E}$ and discussed the relationship of the three, and it has the following:

$$m_{i,k} = \frac{T_{i,k}^{\text{MRL}}}{V_{i,k}^{E}}. \tag{6}$$

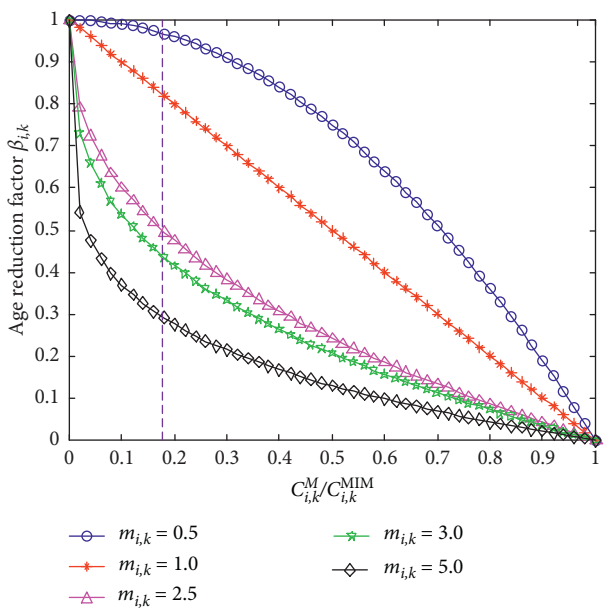

FIGURE 2: The relationship between $\beta_{i,k}$ and $(C_{i,k}^{M}/C_{i,k}^{\mathrm{MIM}})$.

Assuming that the virtual age $V_{i,k}^{B}$ at the beginning of the kth mission is a given constant $v_{i,k}^{b}$, the actual service time in the kth mission is t^{Θ}, then the mean residual life $T_{i,k}^{\mathrm{MRL}}$ can be calculated as follows:

$$T_{i,k}^{\mathrm{MRL}} = \frac{\int_{t^{\Theta}}^{+\infty} R_{i,k}\left(x|v_{i,k}^{b}\right)\mathrm{d}x}{R_{i,k}\left(t^{\Theta}|v_{i,k}^{b}\right)}, \tag{7}$$

where $R_{i,k}(t^{\Theta}|v_{i,k}^{b})$ is a conditional probability, and it represents the survival probability of component i at the end of the kth mission under the condition that $V_{i,k}^{B} = v_{i,k}^{b}$.

Substituting equation (7) into equation (6),

$$m_{i,k} = \frac{T_{i,k}^{\mathrm{MRL}}}{V_{i,k}^{E}} = \frac{\int_{t^{\Theta}}^{+\infty} R_{i,k}\left(x|v_{i,k}^{b}\right)\mathrm{d}x}{\left(v_{i,k}^{b} + t^{\Theta}\right)R_{i,k}\left(t^{\Theta}|v_{i,k}^{b}\right)}. \tag{8}$$

In equation (8), if $T_{i,k}^{\mathrm{MRL}} \geq V_{i,k}^{E}$, i.e., $m_{i,k} \geq 1$, the virtual age at the end of the kth mission is less than half of the mean residual life under the condition that $V_{i,k}^{B} = v_{i,k}^{b}$, then component i is young; whereas, if $T_{i,k}^{\mathrm{MRL}} < V_{i,k}^{E}$, i.e., $m_{i,k} < 1$, then component i is in aging state and the performance of the component will not be significantly improved even more maintenance cost is allocated.

3. The Proposed Selective Maintenance Model under Uncertainties and Limited Maintenance Time

The survival probability and the virtual age of component i at the end of the kth mission are closely related to its state at the beginning of the kth mission. The detailed evaluation method will be discussed in the following:

(a) $S_{i,k}^{B} = 0$.

In this case, component i is failed at the beginning of the kth mission. Since the maintenance activities can only be conducted in the breaks between any two successive missions, as a result, component i does not work in reality during this mission, and the survival probability at the end of the kth mission as well as the incremental virtual age of component i throughout this mission are both zero.

(b) $S_{i,k}^{B} = 1$.

In this case, component i is in functioning state at the beginning of the kth mission. According to the state of component i at the end of the kth mission, two cases can be subdivided further.

(b1) $S_{i,k}^{B} = 1, S_{i,k}^{E} = 1$.

In this case, component i is operating smoothly during the kth mission and it remains in functioning state at the end of the kth mission. Therefore, the survival probability of component i in the kth mission, under the condition that $V_{i,k}^{B} = v_{i,k}^{b}$, can be denoted as a conditional probability $R_{i,k}(t \mid v_{i,k}^{b})$, which satisfies the following:

$$R_{i,k}\left(t|v_{i,k}^{b}\right) = \frac{R_{i}\left(t + v_{i,k}^{b}\right)}{R_{i}\left(v_{i,k}^{b}\right)}, \tag{9}$$

where t is the time interval since the beginning of the kth mission and $R_{i}(v_{i,k}^{b})$ is the survival probability of component i in the case that the virtual age is $v_{i,k}^{b}$. Since component i is in functioning state at the end of the kth mission, the actual service time for component i throughout the kth mission satisfies $T_{i,k}^{\Theta} = T_{k} = t_{k}$. The virtual age and the survival probability at the end of the kth mission can be expressed as $V_{i,k}^{E} = v_{i,k}^{b} + t_{k}$ and $R_{i,k}(t_{k}|v_{i,k}^{b})$, respectively.

(b2) $S_{i,k}^{B} = 1, S_{i,k}^{E} = 0$.

On the contrary, component i may fail within the kth mission. In this case, the value of failure time $T_{i,k}^{\Theta}$ lies in the time interval $(0, t_{k})$, i.e., $T_{i,k}^{\Theta} \in (0, t_{k})$. The probability density function (PDF) of $T_{i,k}^{\Theta}$ under the condition that $V_{i,k}^{B} = v_{i,k}^{b}, T_{k} = t_{k}$ can be calculated by the following:

$$f_{T_{i,k}^{\Theta}|V_{i,k}^{B},T_{k}}\left(t|v_{i,k}^{b}, t_{k}\right) = \frac{f_{T_{i,k}^{\Theta}|V_{i,k}^{B}}\left(t|v_{i,k}^{b}\right)}{1 - R_{i,k}\left(t_{k}|v_{i,k}^{b}\right)}, \quad 0 < t < t_{k}, \tag{10}$$

where $f_{T_{i,k}^{\Theta}|V_{i,k}^{B}}(t|v_{i,k}^{b})$ is the PDF of failure time $T_{i,k}^{\Theta}$. Then, the virtual age of component i at the end of the kth mission is $V_{i,k}^{E} = V_{i,k}^{B} + T_{i,k}^{\Theta}$; furthermore, the cumulative distribution function (CDF) and PDF of $V_{i,k}^{E}$ can be derived as follows:

$$F_{V_{i,k}^E|V_{i,k}^B,T_k}\left(v_{i,k}^e|v_{i,k}^b,t_k\right)=F_{T_{i,k}^\Theta|V_{i,k}^B,T_k}\left(v_{i,k}^e-v_{i,k}^b|v_{i,k}^b,t_k\right), \tag{11}$$

$$f_{V_{i,k}^E|V_{i,k}^B,T_k}\left(v_{i,k}^e|v_{i,k}^b,t_k\right)=\frac{\mathrm{d}F_{T_{i,k}^\Theta|V_{i,k}^B,T_k}\left(v_{i,k}^e-v_{i,k}^b|v_{i,k}^b,t_k\right)}{\mathrm{d}v_{i,k}^e}=f_{T_{i,k}^\Theta|V_{i,k}^B,T_k}\left(v_{i,k}^e-v_{i,k}^b|v_{i,k}^b,t_k\right), \tag{12}$$

where $F_{T_{i,k}^\Theta|V_{i,k}^B,T_k}(v_{i,k}^e-v_{i,k}^b|v_{i,k}^b,t_k)$ and $f_{T_{i,k}^\Theta|V_{i,k}^B,T_k}(v_{i,k}^e-v_{i,k}^b|v_{i,k}^b,t_k)$ are the CDF and PDF of $T_{i,k}^\Theta$, respectively; $F_{V_{i,k}^E|V_{i,k}^B,T_k}(v_{i,k}^e|v_{i,k}^b,t_k)$ and $f_{V_{i,k}^E|V_{i,k}^B,T_k}(v_{i,k}^e|v_{i,k}^b,t_k)$ are the CDF and PDF of $V_{i,k}^E$, respectively.

If ICM is selected for a failed component i, it will be restored to functioning state after the maintenance activity and it has $S_{i,k+1}^B=1$, $V_{i,k+1}^B=\beta_{i,k}(V_{i,k}^B+T_{i,k}^\Theta)$, $(\beta_{i,k}\in[0,1))$; in this scenario, the CDF and PDF of $V_{i,k+1}^B$ under the condition that $V_{i,k}^B=v_{i,k}^b$, $T_k=t_k$ can be expressed as follows:

$$F_{V_{i,k+1}^B|V_{i,k}^B,T_k}\left(v_{i,k+1}^b|v_{i,k}^b,t_k\right)=F_{T_{i,k}^\Theta|V_{i,k}^B,T_k}\left(v_{i,k+1}^b/\beta_{i,k}-v_{i,k}^b|v_{i,k}^b,t_k\right), \tag{13}$$

$$f_{V_{i,k+1}^B|V_{i,k}^B,T_k}\left(v_{i,k+1}^b|v_{i,k}^b,t_k\right)=\frac{\mathrm{d}F_{T_{i,k}^\Theta|V_{i,k}^B,T_k}\left(v_{i,k+1}^b/\beta_{i,k}-v_{i,k}^b|v_{i,k}^b,t_k\right)}{\mathrm{d}v_{i,k+1}^b}=\frac{f_{T_{i,k}^\Theta|V_{i,k}^B,T_k}\left(v_{i,k+1}^b/\beta_{i,k}-v_{i,k}^b|v_{i,k}^b,t_k\right)}{\beta_{i,k}}, \tag{14}$$

where $F_{V_{i,k+1}^B|V_{i,k}^B,T_k}(v_{i,k+1}^b|v_{i,k}^b,t_k)$ and $f_{V_{i,k+1}^B|V_{i,k}^B,T_k}(v_{i,k+1}^b|v_{i,k}^b,t_k)$ are the CDF and PDF of $V_{i,k+1}^B$, respectively.

In a number of actual industrial and military environments, the durations are variables, together with the inherent randomness of the failure time $T_{i,k}^F$; as a result, the actual service time $T_{i,k}^\Theta$ is a random variable. In addition to these uncertainties, the virtual age at the beginning of the kth mission and the age reduction factor $\beta_{i,k}$ associated with the maintenance options are uncertain; thus, the virtual age at the beginning of the $(k+1)^{\text{st}}$ mission is stochastic. The propagation of a variety of uncertainties between the successive missions is illustrated in Figure 3.

The survival probability of component i in the kth mission under the condition that $\mathbf{T}_{k-1}=\mathbf{t}_{k-1}=(t_1,t_2,\cdots,t_{k-1})$ can be expressed as follows:

$$R_{i,k}(t|\mathbf{t}_{k-1})=\Pr\left\{T_{i,k}>t\mid T_1=t_1,T_2=t_2,\cdots,T_{k-1}=t_{k-1}\right\}. \tag{15}$$

Similarly, the reliability for component i in successfully completing the kth mission under the condition that $\mathbf{T}_k=\mathbf{t}_k=(t_1,t_2,\cdots,t_k)$ can be denoted as follows:

$$\begin{aligned}R_{i,k}(\mathbf{t}_k)&=\Pr\left\{S_{i,k}^E=1|T_1=t_1,T_2=t_2,\cdots,T_k=t_k\right\}\\&=R_{i,k}(t_k|\mathbf{t}_{k-1}),\end{aligned} \tag{16}$$

where t is the elapsed time since the beginning of the kth mission.

In case of $\mathbf{T}_k=\mathbf{t}_k=(t_1,t_2,\cdots,t_k)$, the reliability of the system in successfully completing the kth mission satisfies the following:

$$\begin{aligned}R_{s,k}(\mathbf{t}_k)&=R_{s,k}(t_1,t_2,\cdots,t_k)\\&=\Pr\left\{S_{s,k}^E=1|T_1=t_1,T_2=t_2,\cdots,T_k=t_k\right\},\end{aligned} \tag{17}$$

where $S_{s,k}^E=1$ indicates that the system is in functioning state at the end of the kth mission.

According to the sixth hypothesis in Section 2, the durations in this study are assumed to be discrete variables. Consequently, the reliability of the system in successfully completing the kth mission can be derived on the basis of equation (17) as follows:

$$\begin{aligned}R_{s,k}^D&=\Pr\left\{S_{s,k}^E=1\right\}\\&=\sum_{j_1=1}^{w_1}p_1^{j_1}\sum_{j_2=1}^{w_2}p_2^{j_2}\cdots\sum_{j_k=1}^{w_k}p_k^{j_k}R_{s,k}\left(t_1^{j_1},t_2^{j_2},\cdots,t_k^{j_k}\right)\\&=\sum_{j_1=1}^{w_1}\sum_{j_2=1}^{w_2}\cdots\sum_{j_k=1}^{w_k}\left[\left(\prod_{v=1}^{k}p_v^{j_v}\right)R_{s,k}\left(t_1^{j_1},t_2^{j_2},\cdots,t_k^{j_k}\right)\right],\end{aligned} \tag{18}$$

where $w_v\,(v\in\{1,2,\cdots,k\})$ and $t_v^{j_v}\,(j_v\in\{1,2,\cdots,w_v\})$ are the number of possible values and the j_vth possible value for t_v, respectively, and $p_v^{j_v}$ is the corresponding probability mass.

The purpose of the selective maintenance is to maximize the probability for completing all the missions subject to the total maintenance budget. According to the Hypothesis 2, the first maintenance activity is conducted after mission 1 is over. In other words, the maintenance activities have nothing to do with $R_{s,1}^D$. Thus, the selective optimization model can be simplified as follows:

$$\begin{aligned}\max R_s&=\prod_{k=2}^{N}R_{s,k}^D,\\&\sum_{j=1}^{N-1}\sum_{i=1}^{n}C_{i,j}\le C^\delta;\\\text{s.t.}\quad&0\le C_{i,j}\le C_{i,j}^0+C_{i,j}^{\mathrm{RM}};\\&\sum_{i=1}^{n}t_{i,j}^M\le T^M;\\&\quad i\in\{1,2,\cdots,n\};\ j\in\{1,2,\cdots,N-1\}.\end{aligned} \tag{19}$$

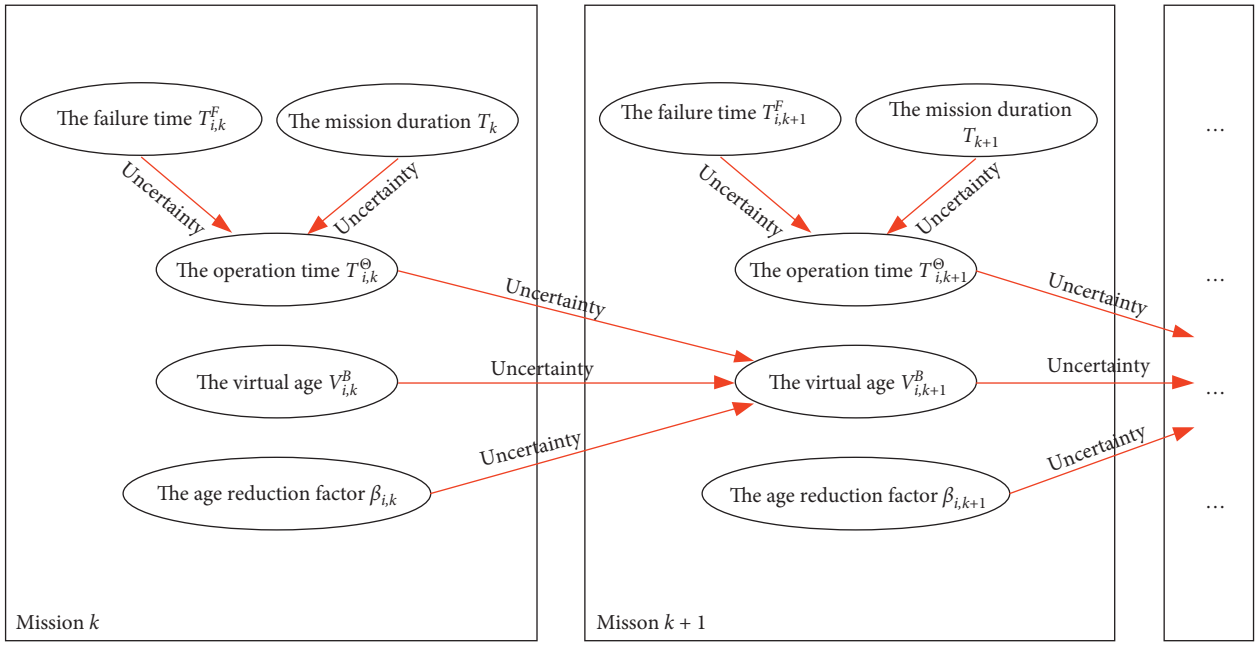

Figure 3: The propagation of uncertainty between the successive missions.

where $C_{i,k}$ is the maintenance cost allocated to component i in the kth ($k \in \{1, 2, \cdots, N-1\}$) break, and C^δ is the limited maintenance budget for all the maintenance activities.

According to equation (19), the selective maintenance decision is a complex nonlinear programming problem with continuous decision variables. It is scarcely possible to solve the problem within the limited time by traditional reliability analysis methods or optimization algorithms [35–40]. However, some advanced intelligent optimization algorithms such as genetic algorithm, simulated annealing algorithm, Bayesian networks [41–43], and ant colony algorithm can find the global approximate optimal solution in a reasonable amount of time. Without loss of generality, the widely used genetic algorithm is selected in this study.

The key point to solve optimization problems with the genetic algorithm lies in how to convert the feasible solutions into population individuals in the genetic algorithm. Theoretically, the maintenance cost allocated to each component can be any real number in the feasible region. To reduce the computational complexity, the decision variables are converted into integer variables and the feasible solutions corresponding to the population individuals are expressed as an integer vector $\mathbf{L}$ composed of $n \times (N-1)$ elements and yields the following:

$$\mathbf{L} = \left(\underbrace{l_{1,1}, l_{2,1}, \cdots, l_{n,1}}_{\text{the } 1^{\text{st}} \text{ break}}, \cdots, \underbrace{l_{1,k}, l_{2,k}, \cdots, l_{n,k}}_{\text{the } k^{\text{th}} \text{ break}}, \cdots, \underbrace{l_{1,N-1}, l_{2,N-1}, \cdots, l_{n,N-1}}_{\text{the } (N-1)^{\text{th}} \text{ break}} \right), \tag{20}$$

where $l_{i,k}\,(0 \le l_{i,k} \le W_L)$ is the maintenance level for component i in the kth break and W_L is the number of maintenance levels determined by decision-makers. It is easy to understand that the larger W_L is, the more accurate the optimal solutions will be while more computation complexity. Therefore, the decision-makers need to make a compromise between the accuracy and the computation complexity. The different values of W_L correspond to various maintenance costs and maintenance times. The detailed information with respect to maintenance activities is tabulated in Table 1.

The process of the optimization for selective maintenance based on the genetic algorithm is illustrated with Figure 4. It contains mainly six steps, and the pseudoprogram can described as follows.

Step 1. Initialization: set $k = 1$; determine the system structure as well as the initial state and the virtual age of each component at the end of the first mission;

Step 2. Feasible population: generate initial feasible individuals according to the number of population individuals set by the genetic algorithm;

Step 3. Virtual age and survival probability for component: convert the population individuals into the maintenance cost allocated to each component; calculate the virtual age $V^E_{i,k}$ and the survival probability $R_{i,k}(\mathbf{t}_k)$ for each component;

Step 4. Survival probability and maintenance cost for the system: evaluate the survival probability $R^\Delta_{s,k}$

Table 1: The maintenance actions and relevant information corresponding to different maintenance levels.

Levels ($l_{i,k}$)	Costs ($C_{i,k}$)	Time ($t_{i,k}^M$)	Maintenance activities $V_{i,k}^E = 0$	$V_{i,k}^E = 1$
0	0	0	DN	DN
1	$C_{i,k}^0 + C_{i,k}^{\mathrm{MR}}$	$t_{i,k}^M(1)$	MR	IPM
⋮	⋮	⋮	⋮	⋮
$l_{i,k}$	$C_{i,k}^0 + C_{i,k}^{\mathrm{MR}} + (l_{i,k} - 1)(C_{i,k}^{\mathrm{MIM}} - C_{i,k}^{\mathrm{MR}})/(W_L - 3)$	$t_{i,k}^M(l_{i,k})$	ICM	IPM
⋮	⋮	⋮	⋮	⋮
$W_L - 2$	$C_{i,k}^0 + C_{i,k}^{\mathrm{MIM}}$	$t_{i,k}^M(W_L - 2)$	ICM	MIM
$W_L - 1$	$C_{i,k}^0 + C_{i,k}^{\mathrm{MR}} + C_{i,k}^{\mathrm{MIM}}$	$t_{i,k}^M(W_L - 1)$	MIM	MIM
W_L	$C_{i,k}^0 + C_{i,k}^{\mathrm{RM}}$	$t_{i,k}^M(W_L)$	RM	RM

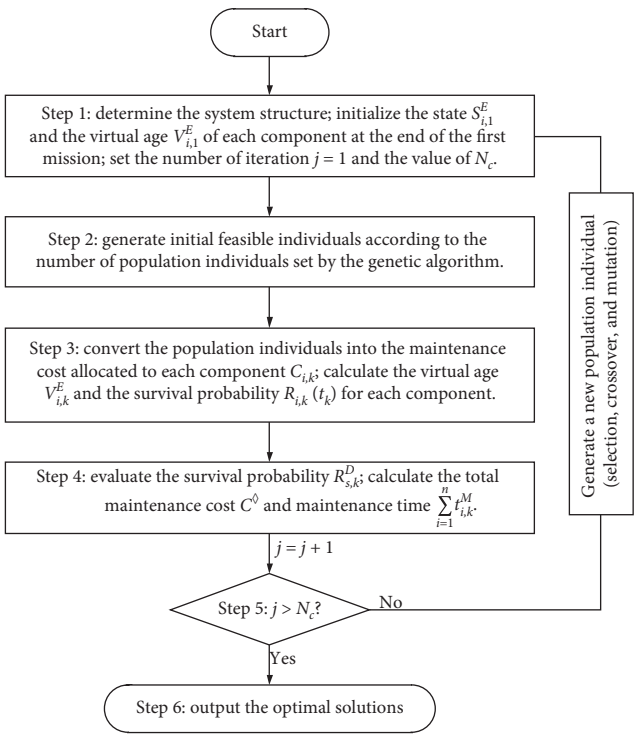

Figure 4: The process of the genetic algorithm.

according to the system structure; calculate the actual total maintenance cost C^{δ};

Step 5. Stopping criterion: if the number of iteration optimizations is less than the specified value N_c, a new population individual will be generated according to the selection, crossover, and mutation operation rules of the genetic algorithm, and the process goes to step 3; otherwise, the process proceeds to step 6;

Step 6. End: output the optimal solutions.

4. An Illustrative Example

To demonstrate the feasibility of the proposed method, an illustrative example with respect to selective maintenance will be studied in this section. The hydraulic system of an airplane is composed of three components, as shown in Figure 5, and it is going to perform four different flights (four successive missions). Assuming that all the components are in brand new state at the beginning of the first mission, the lifetime of each component follows a Weibull distribution, the scale parameter $\eta_i\,(i \in \{1, 2, 3\})$, and the shape parameter $\gamma_i\,(i \in \{1, 2, 3\})$ as well as the maintenance cost, and the state and the virtual age at the end of the first mission are tabulated in Table 2. The maintenance times corresponding to different maintenance levels are tabulated in Table 3. The durations of the four missions are discrete variables, and the probability distributions are tabulated in Table 4. In this study, the maximum maintenance level W_L is set as $W_L = 5$, the total budget for maintenance cost C^{δ} is 240,000 CNY, and the maximum allowable maintenance time is 6 hour. The optimal maintenance decision can be obtained, and it is tabulated in Table 5. Scenario 1 denotes that the limited maintenance time is considered in the optimal selective maintenance decision, whereas Scenario 2 does not. The optimal selective maintenance decisions in Scenario 2 are used for comparison.

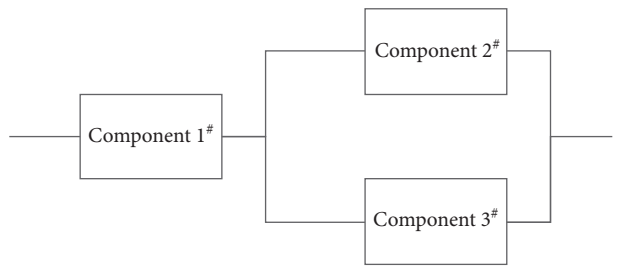

Figure 5: The reliability logic block diagram for the hydraulic system.

Table 2: The parameters of each component (unit of maintenance cost: ¥1,000; unit of time: day).

i	η_i	γ_i	$S_{i,1}^B$	$S_{i,1}^E$	$V_{i,1}^B$	$T_{i,1}^{\Theta}$	$C_{i,k}^0$	$C_{i,k}^{\mathrm{MR}}$	$C_{i,k}^{\mathrm{MIM}}$	$C_{i,k}^{\mathrm{RM}}$
1	22	2.5	1	1	0	6.5	0.28	1.6	28	37
2	16	1.8	1	1	0	6.5	0.31	2.6	32	40
3	18	3.2	1	0	0	3.5	0.42	2.2	24	35

It can be seen from Table 5 that there are three selective maintenance decisions need to be made for the four missions. Empirically, the more maintenance cost is allocated to a component, the more reliable it is. The maximal reliability of the system in successfully completing the missions under two different scenarios is 0.8497 and 0.8883, respectively. It is easy to see that the maintenance cost in Scenario 1 is larger than the cost in Scenario 2, but the reliability is worse. The main reason for this result is the limited maintenance time.

Table 3: The maintenance time corresponding to different maintenance levels (unit of time: hour).

Component ID	Maintenance level	Time
$1^{\#}$	0	0
	1	0.50
	2	3.20
	3	4.40
	4	5.10
	5	0.60
$2^{\#}$	0	0
	1	0.20
	2	3.20
	3	4.80
	4	5.31
	5	0.42
$3^{\#}$	0	0
	1	0.35
	2	1.25
	3	1.80
	4	3.45
	5	0.80

Table 4: The probability distributions of the durations (unit of time: day).

T_1	6.5	—	—
p_1	1	—	—
T_2	9.5	10	10.5
p_2	0.2	0.6	0.2
T_3	8.8	9.6	—
p_3	0.5	0.5	—
T_4	9.3	10.2	10.8
p_4	0.3	0.4	0.3

Table 5: The optimal selective maintenance decisions (unit of maintenance cost: ¥1,000; unit of time: hour).

i	Scenario 1 Maintenance cost (level $l_{i,k}$)			Scenario 2 Maintenance cost (level $l_{i,k}$)		
	$k = 1$	$k = 2$	$k = 3$	$k = 1$	$k = 2$	$k = 3$
1	14.08 (2)	1.88 (1)	37.28 (5)	14.08 (2)	14.08 (2)	29.88 (4)
2	40.31 (5)	40.31 (5)	17.61 (2)	34.91 (4)	32.31 (3)	17.61 (2)
3	35.42 (5)	26.62 (4)	24.42 (3)	35.42 (5)	13.52 (2)	24.42 (3)
$R^D_{s,k+1}$	0.9846	0.8923	0.9672	0.9832	0.9357	0.9656
$C_{s,k}$	89.81	68.81	79.31	84.41	59.91	71.91
$\sum_{i=1}^{n} t^M_{i,k}$	4.22	4.37	5.6	9.31	9.25	10.1
$C^{\diamond}$	—	237.93	—	—	216.23	—
R_s	—	0.8497	—	—	0.8883	—

*$C_{s,k}$ represents the total maintenance budget allocated to the kth maintenance activity; $C^{\diamond}$ represents the actual maintenance cost for all the missions.

5. Summary and Conclusions

In this paper, the conception of virtual age is used for the repairable components and the durations of the missions are regarded as discrete random variables, and a novel selective maintenance model under uncertainties and limited maintenance time is proposed. The imperfect maintenance based on the Kijima II model is introduced firstly, and then, the CDFs and PDFs of the virtual ages of components after a maintenance activity are derived. Subsequently, the survival probability of each component in different mission and the reliability of the system in successfully completing the missions are derived. Finally, the optimal selective maintenance decisions based on the genetic algorithm under limited maintenance budget and limited maintenance time are obtained. The proposed selective maintenance model takes the maintenance time into consideration, which is more consistent with the actual situation. In case of a limited maintenance time, the maintenance cost is larger and the reliability is worse, but they are sacrificed for saving time. The decision-maker must make a compromise between the three.

In this paper, the states of each component are assumed to be binary variables and the durations of the missions are crisp values. It should be noted that the computation complexity will increase rapidly as the missions increase. Selective maintenance issues with respect to multistate

systems as well as fuzzy durations will be studied in our future works.

Data Availability

The data used to support the findings of this study are included within the article.

Disclosure

The funders had no role in the design of the study; in the collection, analyses, or interpretation of data; in the writing of the manuscript; or in the decision to publish the results.

Conflicts of Interest

The authors declare that they have no conflicts of interest.

Authors' Contributions

H. G. and X. Z. conceptualized the study; H. G. developed the methodology; X. Z. provided software; H. G., X. Z., X. Y., and B. Z. validated the study; H. G. performed formal analysis; H. G. investigated the study; H. G. provided the resources; X. Z. was responsible for data curation; H. G. wrote and prepared the original draft; H. G. wrote, reviewed, and edited the article; X. Z. visualized the study; X. Y. and B. Z. supervised the study; H. G. was involved in project administration; H. G. was responsible for funding acquisition. All authors have read and agreed to the published version of the manuscript.

Acknowledgments

This research was supported by the Sichuan Science and Technology Program, grant nos. 2019YJ0395 and 2021YJ0519 and General Aviation Special Research Project of Civil Aviation Flight University of China, grant no. THZX2018-09.

References

[1] B. D. Jonge and P. A. Scarf, "A review on maintenance optimization," *European Journal of Operational Research*, vol. 285, no. 3, pp. 805–824, 2019.

[2] X. Zhou, C. Wu, Y. Li, and L. Xi, "A preventive maintenance model for leased equipment subject to internal degradation and external shock damage," *Reliability Engineering & System Safety*, vol. 154, pp. 1–7, 2016.

[3] Q. Qiu, L. Cui, and D. Kong, "Availability and maintenance modeling for a two-component system with dependent failures over a finite time horizon," *Proceedings of the Institution of Mechanical Engineers, Part O: Journal of Risk and Reliability*, vol. 233, no. 3, pp. 200–210, 2019.

[4] S. Alaswad and Y. Xiang, "A review on condition-based maintenance optimization models for stochastically deteriorating system," *Reliability Engineering & System Safety*, vol. 157, pp. 54–63, 2017.

[5] S. Wu and M. J. Zuo, "Linear and nonlinear preventive maintenance models," *IEEE Transactions on Reliability*, vol. 59, no. 1, pp. 242–249, 2010.

[6] T. Nakagawa, *Maintenance Theory of Reliability*, Springer, Berlin, Germany, 2006.

[7] S.-H. Sheu, C.-C. Chang, Y.-L. Chen, and Z. George Zhang, "Optimal preventive maintenance and repair policies for multi-state systems," *Reliability Engineering & System Safety*, vol. 140, pp. 78–87, 2015.

[8] J. H. Cha, M. Finkelstein, and G. Levitin, "Optimal mission abort policy for partially repairable heterogeneous systems," *European Journal of Operational Research*, vol. 271, no. 3, pp. 818–825, 2018.

[9] W. Si and Q. Yang, "A generalized mixed effect kijima model and application in optimal maintenance planning," *IEEE Transactions on Reliability*, vol. 65, no. 3, pp. 1551–1561, 2016.

[10] A. Yevkin and V. Krivtsov, "A generalized model for recurrent failures prediction," *Reliability Engineering & System Safety*, vol. 204, p. 107125, 2020.

[11] L. Doyen, O. Gaudoin, and A. Syamsundar, "On geometric reduction of age or intensity models for imperfect maintenance," *Reliability Engineering & System Safety*, vol. 168, pp. 40–52, 2017.

[12] Q. Qiu and L. Cui, "Optimal mission abort policy for systems subject to random shocks based on virtual age process," *Reliability Engineering & System Safety*, vol. 189, pp. 11–20, 2019.

[13] A. Knezevic, L. Vasov, S. Vlacic, and C. Kostic, "Imperfect maintenance model for estimating aircraft fleet availability," *Aircraft Engineering and Aerospace Technology*, vol. 89, no. 2, pp. 338–346, 2017.

[14] Y. Liu, H. Z. Huang, and X. Zhang, "A data-driven approach to selecting imperfect maintenance models," *IEEE Transactions on Reliability*, vol. 61, pp. 101–112, 2011.

[15] W. F. Rice, C. R. Cassady, and J. A. Nachlas, "Optimal maintenance plans under limited maintenance time," in *Proceedings of the 7th Industrial Engineering Research Conference*, Banff, Canada, May 1998.

[16] C. R. Cassady, E. A. Pohl, and W. Paul Murdock, "Selective maintenance modeling for industrial systems," *Journal of Quality in Maintenance Engineering*, vol. 7, no. 2, pp. 104–117, 2001.

[17] C. R. Cassady, W. P. Murdock Jr., and E. A. Pohl, "Selective maintenance for support equipment involving multiple maintenance actions," *European Journal of Operational Research*, vol. 129, pp. 252–258, 2001.

[18] R. Rajagopalan and C. R. Cassady, "An improved selective maintenance solution approach," *Journal of Quality in Maintenance Engineering*, vol. 12, no. 2, pp. 172–185, 2006.

[19] C. M. La Fata and G. Passannanti, "A simulated annealing-based approach for the joint optimization of production/inventory and preventive maintenance policies," *The International Journal of Advanced Manufacturing Technology*, vol. 91, no. 9–12, pp. 3899–3909, 2017.

[20] F. Moinian, H. Sabouhi, J. Hushmand, A. Hallaj, H. Khaledi, and M. Mohammadpour, "Gas turbine preventive maintenance optimization using genetic algorithm," *International Journal of System Assurance Engineering and Management*, vol. 8, no. 3, pp. 594–601, 2017.

[21] X. Chen, Y. An, Z. Zhang, and Y. Li, "An approximate nondominated sorting genetic algorithm to integrate optimization of production scheduling and accurate maintenance based on reliability intervals," *Journal of Manufacturing Systems*, vol. 54, pp. 227–241, 2020.

[22] M. Khatami and S. H. Zegordi, "Coordinative production and maintenance scheduling problem with flexible maintenance

time intervals," *Journal of Intelligent Manufacturing*, vol. 28, no. 4, pp. 857–867, 2017.

[23] Z. Zhao, B. Xiao, N. Wang, X. Yan, and L. Ma, "Selective maintenance optimization for a multi-state system with degradation interaction," *IEEE Access*, vol. 7, pp. 99191–99206, 2019.

[24] Y. Liu and H. Z. Huang, "Optimal selective maintenance strategy for multi-state systems under imperfect maintenance," *IEEE Transactions on Reliability*, vol. 59, pp. 356–367, 2010.

[25] M. Pandey, M. J. Zuo, and R. Moghaddass, "Selective maintenance modeling for a multistate system with multistate components under imperfect maintenance," *IIE Transactions*, vol. 45, no. 11, pp. 1221–1234, 2013.

[26] Y. Liu, Y. Chen, and T. Jiang, "On sequence planning for selective maintenance of multi-state systems under stochastic maintenance durations," *European Journal of Operational Research*, vol. 268, no. 1, pp. 113–127, 2018.

[27] C. D. Dao and M. J. Zuo, "Optimal selective maintenance for multi-state systems in variable loading conditions," *Reliability Engineering & System Safety*, vol. 166, pp. 171–180, 2017.

[28] T. Jiang and Y. Liu, "Selective maintenance strategy for systems executing multiple consecutive missions with uncertainty," *Reliability Engineering & System Safety*, vol. 193, p. 106632, 2020.

[29] M. Pandey, M. J. Zuo, R. Moghaddass, and M. K. Tiwari, "Selective maintenance for binary systems under imperfect repair," *Reliability Engineering & System Safety*, vol. 113, pp. 42–51, 2013.

[30] T. Jiang and Y. Liu, "Robust selective maintenance strategy under imperfect observations: a multi-objective perspective," *IISE Transactions*, vol. 52, no. 7, pp. 751–768, 2020.

[31] A. Khatab, E. H. Aghezzaf, I. Djelloul, and Z. Sari, "Selective maintenance optimization for systems operating missions and scheduled breaks with stochastic durations," *Journal of Manufacturing Systems*, vol. 43, pp. 168–177, 2017.

[32] C. Diallo, U. Venkatadri, A. Khatab, and Z. Liu, "Optimal selective maintenance decisions for large serial k-out-of-n: G systems under imperfect maintenance," *Reliability Engineering & System Safety*, vol. 175, pp. 234–245, 2018.

[33] D. T. Nguyen, Y. Dijoux, and M. Fouladirad, "Analytical properties of an imperfect repair model and application in preventive maintenance scheduling," *European Journal of Operational Research*, vol. 256, no. 2, pp. 439–453, 2017.

[34] A. Khatab and E.-H. Aghezzaf, "Selective maintenance optimization when quality of imperfect maintenance actions are stochastic," *Reliability Engineering & System Safety*, vol. 150, pp. 182–189, 2016.

[35] H. Li, H.-Z. Huang, Y.-F. Li, J. Zhou, and J. Mi, "Physics of failure-based reliability prediction of turbine blades using multi-source information fusion," *Applied Soft Computing*, vol. 72, pp. 624–635, 2018.

[36] M. Yazdi, S. Daneshvar, and H. Setareh, "An extension to fuzzy developed failure mode and effects analysis (FDFMEA) application for aircraft landing system," *Safety Science*, vol. 98, pp. 113–123, 2017.

[37] M. Yazdi, S. Kabir, and M. Walker, "Uncertainty handling in fault tree based risk assessment: state of the art and future perspectives," *Process Safety and Environmental Protection*, vol. 131, pp. 89–104, 2019.

[38] H. Li, H. Diaz, and C. G. Soares, "A developed failure mode and effect analysis for floating offshore wind turbine support structures," *Renewable Energy*, vol. 164, pp. 133–145, 2020.

[39] M. Yazdi, F. Nikfar, and M. Nasrabadi, "Failure probability analysis by employing fuzzy fault tree analysis," *International Journal of System Assurance Engineering and Management*, vol. 8, no. 2, pp. 1177–1193, 2017.

[40] M. Yazdi, A. Nedjati, E. Zarei, and R. Abbassi, "A novel extension of DEMATEL approach for probabilistic safety analysis in process systems," *Safety Science*, vol. 121, pp. 119–136, 2020.

[41] H. Li, A. P. Teixeira, and C. Guedes Soares, "A two-stage failure mode and effect analysis of offshore wind turbines," *Renewable Energy*, vol. 162, pp. 1438–1461, 2020.

[42] H. Li, C. Guedes Soares, and H.-Z. Huang, "Reliability analysis of a floating offshore wind turbine using Bayesian networks," *Ocean Engineering*, vol. 217, p. 107827, 2020.

[43] M. Yazdi and S. Kabir, "A fuzzy Bayesian network approach for risk analysis in process industries," *Process Safety and Environmental Protection*, vol. 111, pp. 507–519, 2017.

Hindawi
Mathematical Problems in Engineering
Volume 2021, Article ID 6657459, 12 pages
https://doi.org/10.1155/2021/6657459

Research Article

Optimization of Layout and Pipe Sizes for Irrigation Pipe Distribution Network Using Steiner Point Concept

Preeti Walmik Gajghate,[1] **Ashwini Mirajkar**,[1] **Uzma Shaikh**,[1] **Neeraj Dhanraj Bokde**,[2] **and Zaher Mundher Yaseen**[3]

[1]*Visvesvaraya National Institute of Technology, Nagpur 440010, India*
[2]*Department of Mechanical and Production Engineering—Renewable Energy and Thermodynamics, Aarhus University, Aarhus 8000, Denmark*
[3]*Faculty of Civil Engineering, Ton Duc Thang University, Ho Chi Minh City, Vietnam*

Correspondence should be addressed to Zaher Mundher Yaseen; yaseen@tdtu.edu.vn

Received 5 December 2020; Revised 16 February 2021; Accepted 20 February 2021; Published 27 February 2021

Academic Editor: Noorbakhsh Amiri Golilarz

In tropical countries like India, irrigation is necessary to grow crops in the nonmonsoon period. The conventional methodology for conveying irrigation water from the source to the field is through open canals. However, considering huge losses due to evaporation and percolation, a modern system of irrigation like pipe irrigation network (PIN) is desired. Advancement in technology has led to the progress in the PIN as they are compatible with modern irrigation facilities such as sprinkler and drip irrigation systems. In the present study, the layout of the PIN is designed and optimized in two phases. Initially, the looped network is traced out for the Bakhari distributary of the Kanhan Branch Canal, India. Minimum spanning tree (MST) network is obtained from the looped network using Prim's algorithm to calculate the nodal demands. The layout optimization of the MST is carried out using the Steiner concept to obtain the initial Steiner tree (IST). The steady-state hydraulic analysis and design are carried out for the looped and IST network. The results show that the percentage of length decreasing from the looped network to the MST network is 51.58%. The IST network is the optimized network having the minimum length showing a 12.21% length reduction compared to the MST network. The total reduction in the cost of the Steiner tree is found to be 4.25% compared to the looped network. Steiner concept application to large irrigation networks can reduce the length of the network thereby minimizing the total project cost.

1. Introduction

Freshwater is a finite and vital resource that is essential for maintaining the life cycle on Earth. India constitutes 2.4% of the world's surface area and supports 16.7% of the world's population. It possesses only 4% of the world's water resources [1]. The estimated population of India is 1,210 million with a growth rate of 17.64% [2]. With the increase in population, the requirement for agricultural products would increase and the scarcity of water would certainly affect the production from agriculture [3, 4]. Moreover, in the last three decades, the annual and summer precipitation showed a decreasing trend of 5%, while a positive trend is observed for the temperature with a significant value of 5% [5]. This concludes that precipitation has been declining with the rapid warming in the last 30 years [6]. This indicates that the growing demands are to be satisfied with limited resources as the rainfall is also decreasing over the period. India accounts for 7.39% of total global agricultural output and as per the Economy Survey of India 2018–19, the agricultural sector contributes around 15–17% to the country's gross domestic product (GDP), which necessitates irrigation [7]. Therefore, to support the country's economy, it is necessary to save water and use it sustainably. In ancient times, the principal irrigation practice was conveying the flow of springs and streams by constructing temporary

barriers across them and irrigating the adjoining fields by the canal system. The major drawback of the conventional canal systems is the loss of water due to percolation, evaporation, and sometimes thefts in between the reaches. Besides, the issue of land acquisition also persists. Small traditional conventional earthen channels (200 m) exhibit a conveyance efficiency of around 75.07%, which indicates the extent of seepage loss in large irrigation networks [8, 9]. In the case of open canals, the overall project efficiency ranges from 41 to 48%, which further falls to 20 to 35% making Pipe Irrigation Network (PIN) a necessity [10]. A buried pipeline system may reduce the water demand to a significant extent with the use of a pumped irrigation system as compared to the earthen channels [11, 12]. Considering the huge seepage and evaporation losses in irrigation water conveyance through the canal system, it is the need of the hour to shift to another efficient system as far as Indian practices are concerned. Irrigation technology made rapid strides in the 21st century in terms of overall cost and water use efficiency. Using computer simulation, a reliable water network can be developed by forming the hydraulic models if a sufficient head is available [13, 14]. The underground pipes in an open field give an opportunity to freely design the layout and thus making PIN a better choice in terms of both water use efficiency and overall cost. Also, it requires less execution time for undulating fields as compared to the canal distribution system. The branching (tree) water distribution networks are popular for supplying water, where the demand is very high such as irrigation and industries as they are simple in comparison to the complicated loop networks [15, 16]. The irrigation sector is the one that requires a large amount of water in a calculated manner. An effective irrigation water supply system is required to satisfy all the demands. This is accomplished by providing an optimized pipe irrigation network.

For a given layout, an optimized PIN is the one which satisfies all the demands as well as constraints with the minimum possible cost. The cost may further be reduced if there is freedom of variation in layout as well [17]. The issue of the simultaneous layout with the design of water distribution network (WDN) optimization has been dealt with by many researchers from the last few decades. Bhave and Lam suggested a two-step approach to obtain a minimum cost WDN layout. The concept gives a minimum length layout. The lengths of the links are considered in the Steiner tree approach while the nodal discharges or hydraulic gradient level (HGL) are not given weightage for determining the optimized layout [15]. A minimum cost layout including design of WDN wherein linear programming (LP) was used to design pipe diameters and the hydraulic network solver addressed the flow through the pipes and pressures at the nodes [18]. A model of the optimized layout of WDNs with single loading was presented in which a zero-one integer model selected the pipes considering the hydraulic properties and redundancy and in the following step, design models were used to optimize the pressures and diameters resulting in an optimized layout and design of WDN [19]. Comparison of the twin genetic algorithm (GA) with binary and integer coding for the optimized layout of the branched network was carried out with dynamic programming (DP) based on time and storage requirement in both approaches [20]. An evolution program was developed in GA to optimize the looped WDN for the first time [21]. A maximum entropy-based method was developed in which the optimized cost along with reliability could be achieved for the optimized layouts [22]. A heuristic method was proposed based on reliability for the simultaneous layout and design of WDN. The network layout with the maximum number of pipes is considered initially, followed by a design float method to obtain the final least costly network [23]. An empirically derived objective function was developed for the optimal layout of the tree network using mixed integer linear programming (MILP). The data used for MILP was the location and demands of the users [24]. GIS was used in the backdrop as the classical graph theory (CGT) algorithm was used to find out the minimum length of the spanning tree [25]. A method was presented in which the pipes are removed sequentially to reach the minimum cost network to obtain the optimal layout and design of branched WDN. The design flows were obtained using Clements's method [26]. A six-looped water distribution system having seventeen links was used to demonstrate the multicriteria maximum entropy method for the optimization of link size, reliability, and network layout. The chief criterion being network, therefore, a compromise between entropy, redundancy, reliability, and network cost were observed sequentially within the population of the best solutions. As a smaller part of the network has been considered for layout and design, the efficiency of the method was improved [27]. For the optimal layout of the urban drainage network, loop-by-loop cutting algorithm based on graph theory and GA has been used [28]. A multiobjective evolutionary method was presented for the optimization of the design and layout of WDN [29]. Particle swarm optimization (PSO) technique was linked with MATLAB for irrigation WDN layout and cost optimization [30]. A fusion method of tree growing-jumping particle swarm optimization (TG-JPSO) was proposed which is a blend of layout and pipe size optimizers to achieve an optimal layout and design of WDN. A modified version of Labye's iterative discontinuous method (LIDM) was used which gives several solutions that finally converge to an optimized design [31]. Max-min ant system (MMAS) algorithm has been used to obtain the minimum cost design considering layout and pipe diameters of the network simultaneously [32]. The accuracy of various methods and their comparative studies were also carried out in the past. It was found that the ant algorithm (AA) application to the branched WDN gives better results as compared to GA [33], whereas recently developed Physarum algorithm performs better than the ant colony algorithm for optimization of branched WDNs [34]. A heuristic method based on a uniform flow network was suggested to achieve minimum variance in the pipe flows for increased reliability of the network. The system was evaluated through a variance of flow series and the obtained optimal layout network was designed using linear programming [35]. Thevenin theorem (TT) applied for electric circuits was applied for the model reduction and analysis of large WDN [36]. Recently

developed population-based Harris hawks algorithm (HHO) was developed for the WDN optimization of the Homashahr city in Iran [37]. A novel heuristic targeted path search algorithm (TPSA) based on the determination of optimal paths followed by the flow of water in a WDN was developed for three benchmark networks. In the process of optimization, the targeted trial of decrease in pipe diameters of the network was guided by two individual subroutines, thus exploring the search space [38]. Some of the hydraulic simulation software is also coupled with these heuristic techniques to obtain the optimized design of WDN [39]. The basics of hydraulic simulation and interoperability of the water distribution network were presented and a hydraulic WDN model was prepared for scheduling and science operations of WDN with the help of SCADA data and GIS data in WaterGEMS to optimize the network effectively [40]. Steiner point concept is coupled with LP for a small 8-node example to obtain an optimized layout [41].

In the present study, a layout optimization model is developed in a stepwise manner. The approach starts with the development of a looped network for calculating the demands which are further designed and optimized using WaterGems connect. The second step consists of the conversion of the looped network into the minimum spanning tree (MST) network using Prim's algorithm. The final step is the application of the Steiner concept to the MST to obtain the Steiner tree (ST), which gives the optimized layout and design of the network. A comparison of the looped network and the ST network shows a reduction of 4.25% in the total network cost. A flowchart depicting the methodology is shown in Figure 1. The abbreviations used in this paper are tabulated in Table 1.

2. Characterization of the Study Area

The area selected for the present study is Bakhari distributary of the Pench irrigation project, located in Parseoni, a small town and a municipal council in Nagpur district in the state of Maharashtra, India. The study area with latitude $21^{\circ}19'34.15''$ N and longitude $79^{\circ}11'15.55''$ E is well-connected via state and national highway. Bakhari distributary offtakes from Left Bank Canal (LBC) of Pench irrigation project having discharge capacity of 1.58 cumecs to irrigate 2057.17 Ha culturable command area (CCA). The schematic sketch of the study area is presented in Figure 2.

3. Materials and Methods

3.1. Looped Network. Looped networks are complex compared to the branched networks but are more reliable. On the other hand, for large irrigation networks branched networks are more economical. For the present study, the looped gravity-fed network is traced out in AutoCAD Map 3D along the road lines of the study area as shown in Figure 3.

The pipeline along the roads avoids the problem of land acquisition, while for layout optimization, some of the field area may be covered. The underground pipe system suffices for the utilization of the complete field area. The looped network consists of 1 source reservoir, 60 nodes, and 87 pipes to supply irrigation water to the field. It covers a total length of 59.17 Km to irrigate 2057.17 Ha CCA with a discharge capacity of 1.578 cumecs. For the PIN, the seepage and evaporation losses are almost eliminated. However, leakage losses may be present. Considering 10% leakage losses, the gross irrigation requirement (GIR) and net irrigation requirement (NIR) for the different crops in the area are calculated as shown in Table 2.

The looped network consists of 27 polygons and the demand for each of the polygon is calculated as the percentage of the total demand (GIR) as per the area of each polygon as shown in Table 3.

The nodal demands are found out by using the Thiessen polygon tool in WaterGEMS. Pipe sizing of the PIN is carried out followed by steady-state simulation by taking a set of designed commercial diameters to optimize the total cost of the looped network as shown in Figure 3.

3.2. Minimum Spanning Tree (MST) Network. The looped PIN is converted to a branch network known as MST which is a network consisting of a set of pipes resulting in a tree connecting each node in the system. Prim's algorithm (PA) is used to obtain the MST for the study area. In the field of computer science, PA is used to find the minimum spanning tree for a connected weighted undirected graph. This means it obtains a subset of the edges forming a tree that includes every vertex, keeping into account that the total weight of all the edges in the tree is minimized. Czech mathematician Vojtèch Jarnik developed this algorithm in 1930. It was later independently developed by computer scientist Robert C. Prim in 1957 and rediscovered by Edsger Dijkstra in 1959. Therefore, it is also sometimes called the Jarnik algorithm, the DJP algorithm, or the Prim–Jarnik algorithm [42]. PA is a greedy algorithm that finds a set of the pipes forming a tree, which includes each node, where the total length of all the links in the tree is minimum. This algorithm is directly based on the MST property, which finds the global optimum solution for the minimum length. The obtained MST consists of 1 reservoir, 60 nodes, and 60 pipes with a total length of 28.65 Km to irrigate 2057.17 Ha CCA as shown in Figure 4.

3.3. Initial Steiner Tree (IST). Further layout optimization is carried out with the concept of the Steiner tree (ST). Steiner points are the additional nodal points in an existing system to produce an optimal layout. The connecting links between different nodes and the Steiner points are considered as straight lines with link diameters as a continuous variable. The characteristics of the Steiner tree for a multinode network are as follows. (i) ST for an N-node network can have a maximum of up to N-2 Steiner points; however, it may be less when some of the given nodes also act as junction nodes. (ii) Each Steiner point is connected to three points (given nodes or other Steiner points) such that the angle between the connecting link is 120°. Computer algorithms and several methodologies are there to obtain the Steiner tree [43–45]. Additional Steiner points are obtained for the already existing system of nodes to obtain optimal layout using

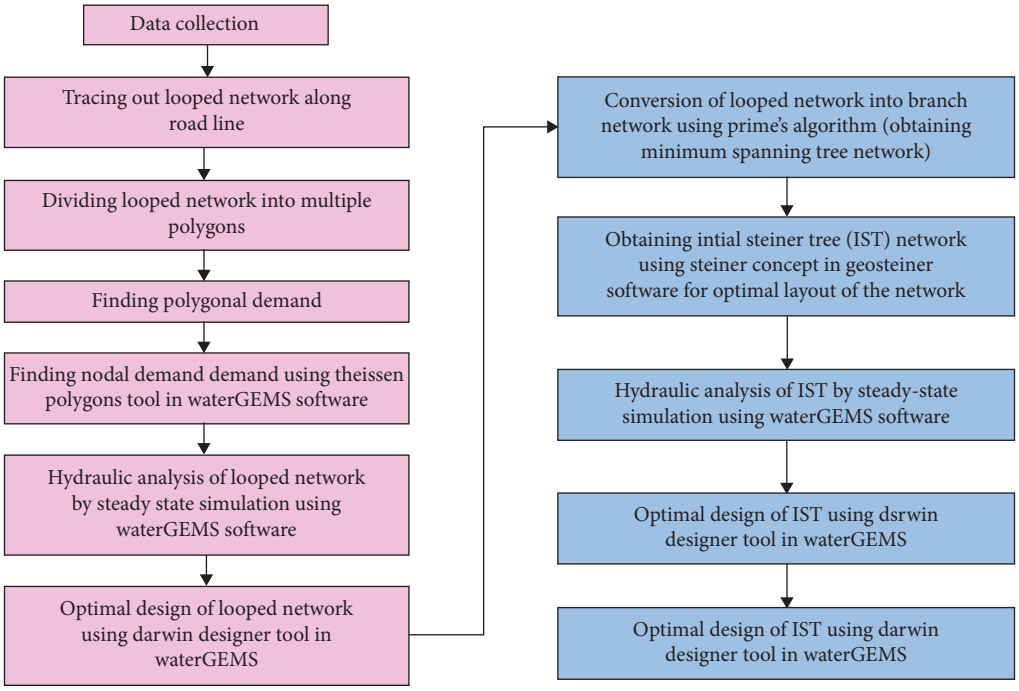

Figure 1: Flow chart depicting the methodology of the study.

Table 1: List of abbreviations.

Abbreviations	
AA	Ant algorithm
CCA	Culturable command area
CGT	Classical graph theory
DP	Dynamic programming
GA	Genetic algorithm
GDP	Gross domestic product
GIR	Gross irrigation requirement
HHO	Harris Hawks algorithm
HGL	Hydraulic gradient level
IST	Initial Steiner tree
LBC	Left bank canal
LIDM	Labye's iterative discontinuous method
LP	Linear programming
MILP	Mixed integer linear programming
MMAS	Max-min ant system
MST	Minimum spanning tree
MST	Minimum spanning tree
NIR	Net irrigation requirement
PA	Prim's algorithm
PIN	Pipe irrigation network
PSO	Particle swarm optimization
ST	Steiner tree
TPSA	Targeted path search algorithm
TG-JPSO	Tree growing-jumping particle swarm optimization
TT	Thevenin theorem
WDN	Water distribution network

GeoSteiner software. The computation of the exact solutions to the Steiner tree problems is obtained with the help of the GeoSteiner software package which has a very fast (publicly available) program [46]. A complete written programmed code which is with a clear method to generate the Steiner tree is recorded [47]. For the present study, a new initial Steiner tree network is formulated in ArcMap which consists of 60 nodes, 21 Steiner points, 81 pipes, and 1 source reservoir as shown in Figure 5 to convey the irrigation water to all demand nodes. The total length of the network is reduced to 25.15 Km to irrigate the same CCA. After layout optimization pipe sizing of the initial Steiner tree is carried out for the same set of designed diameters, the same network is then optimized for pipe sizing by using the Darwin designer tool in WaterGEMS, which works on GA parameters.

The optimized design study has no true optimality and only knows the best solution relative to other solutions already found during computation. In general, population size and random number seed are the common parameters to change in computing the model under consideration. The sensitivity of the existing model is tested by a random number of seeds for the model being optimized. With GA optimization having a stochastic nature, it might be beneficial to change population size up or down. Faster runs are obtained using a smaller population size, but the model is less diverse and potentially optimized results with the population being less [48]. Pressure constraints are set to maintain positive pressure at the nodes.

4. Results and Discussion

The initial looped network consists of 87 links and 60 nodes with a total length of 56.17 km. The analysis of the network is carried out by considering the minimum and maximum pressure of 0.17 m and 20 m, respectively. Based on these pressures, a set of designed diameters are selected in which minimum and maximum diameters are 50 mm and 1600 mm, respectively. After optimizing the network, it is

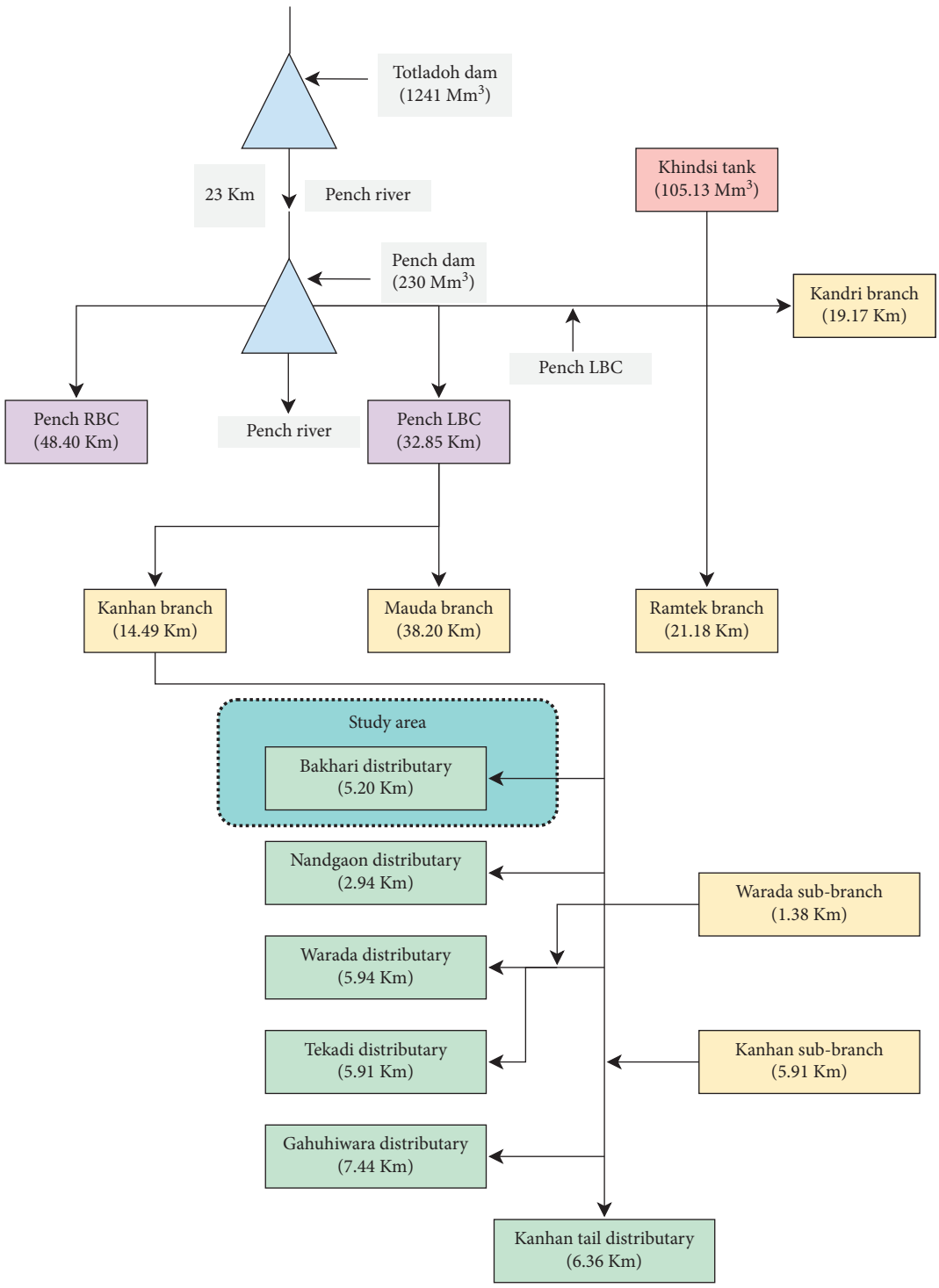

Figure 2: Schematic sketch of study area.

observed that out of 87 pipe diameters, 25 pipes (3, 7, 10, 12, 17, 18, 20, 27, 32, 33, 34, 36, 45, 50, 51, 55, 59, 68, 71, 72, 73, 74, 79, 85, 87) diameters have a value less than the designed diameter and 2 pipes (25, 77) are having a diameter equal to the designed diameter as shown in Figure 6. The cost reduction is brought about as a result of the reduction in the pipe sizes of the optimized design.

Pipe sizing is carried out by considering pressure constraints in which minimum and maximum pressures are set to 0.17 and 20 m. It is found that all the simulated pressures are positive which are well within the minimum and maximum pressure limits as shown in Figure 7. However, for only one junction (17), the pressure exceeds the upper pressure limit which is 20.95 and can be neglected.

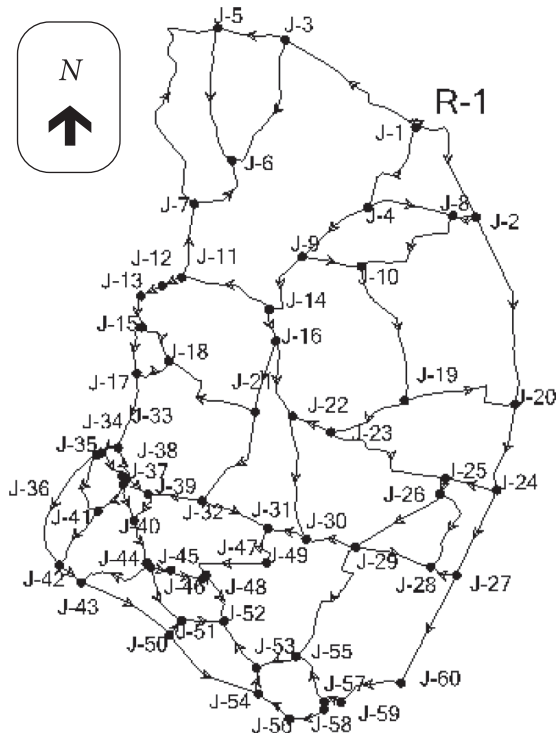

Figure 3: Looped network for Bakhari.

Table 2: NIR and GIR for 90% efficiency.

		Demand (approved) in m^3			
Crop	%	Area (m^2)	Delta (m)	NIR at field (m^3)	GIR at field (m^3)
Sugar cane	6	3464944.26	1.17	4042758.36	4447034.19
Other perennial crops	2	1154981.42	0.9	1039541.03	1143495.13
Paddy (Kharif)	70	40424349.64	0.31	12588950.96	13847846.06
Cotton	10	5774907.09	0.26	1497722.15	1647494.37
Wheat	12	6929888.51	0.25	1728175.6	1900993.16
Total	**100**		**57749070.91**		**22986862.91**

Table 3: Areawise demand for 90% efficiency.

Polygon no.	Area (m^2)	% Area	GIR (m^3)	Demand (m^3/s)
1	1392956.3	2.41	554462.5	0.11
2	1186152.14	2.05	472144.7	0.09
3	759288.51	1.31	302232.8	0.06
4	1138073.57	1.97	453007.1	0.09
5	776647.09	1.34	309142.3	0.06
6	1171101.22	2.03	466153.7	0.09
7	1748101.88	3.03	695827.3	0.13
8	292008.07	0.51	116233	0.02
9	347877.22	0.6	138471.6	0.03
10	261804.95	0.45	104210.8	0.02
11	224658.3	0.39	89424.64	0.02
12	446383.18	0.77	177681.6	0.03
13	258386.8	0.45	102850.2	0.02
14	60371.55	0.1	24030.73	0
15	145458.28	0.25	57899.28	0.01
16	39453.71	0.07	15704.44	0
17	1217991.22	2.11	484818.1	0.09
18	122548.94	0.21	48780.28	0.01
19	283491.6	0.49	112843.1	0.02

Table 3: Continued.

Polygon no.	Area (m^2)	% Area	GIR (m^3)	Demand (m^3/s)
20	1071211.4	1.85	426392.8	0.08
21	1874704.24	3.25	746221	0.14
22	560513.73	0.97	223111	0.04
23	706984.8	1.22	281413.4	0.05
24	784147.43	1.36	312127.8	0.06
25	488044.43	0.85	194264.8	0.04
26	2873835.73	4.98	1143923	0.22
27	339504.17	0.59	135138.7	0.03
Total		**20571700.46**		**1.58**

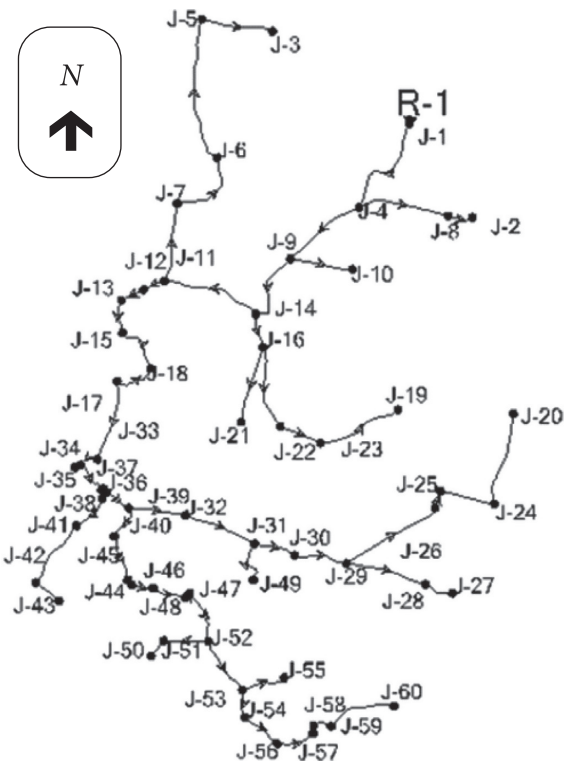

Figure 4: Minimum spanning tree network.

Steiner tree network consists of 81 pipes, 60 nodes, 21 Steiner points, and 1 source reservoir with a total length of 25.15 km. Out of 81 pipes, it is observed that 23 pipes (1, 2, 3, 5, 18, 26, 28, 29, 30, 34, 35, 41, 46, 49, 50, 66, 70, 71, 72, 76, 77, 79, 80) are having a diameter less than the designed diameter and 6 pipes (4, 10, 36, 40, 47, 81) have diameters equal to the designed diameter, as shown in Figure 8. The cost of the network is reduced due to the reduction in the pipe size of 23 pipes.

Steady-state simulation analysis of the Steiner tree model is carried out which results in pressure values within the permissible limit. On optimizing the network for pipe sizing, it is observed that all pressure heads are positive with simulated value ranges from 0.85 to 21.72 m having zero violation in pressure at each node. The obtained optimized solution is for pressure constraints of 0.65 to 23 m. Figure 9 indicates pressure variation at each node for the initial Steiner tree. It is clear from Figure 9 that the simulated pressures are well within the considered limits.

The overall comparison between the initial looped WDS and IST is shown in Table 4 which indicates the comparison parameters as length, area, material, number of nodes and pipes, discharge capacity, and total cost of both the networks. Along with these parameters, the comparison based on hydraulic properties such as minimum and maximum

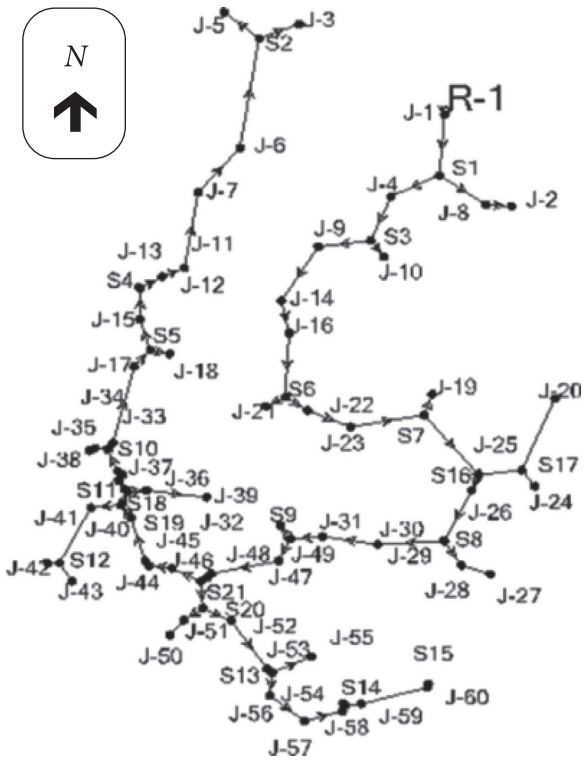

Figure 5: Steiner tree.

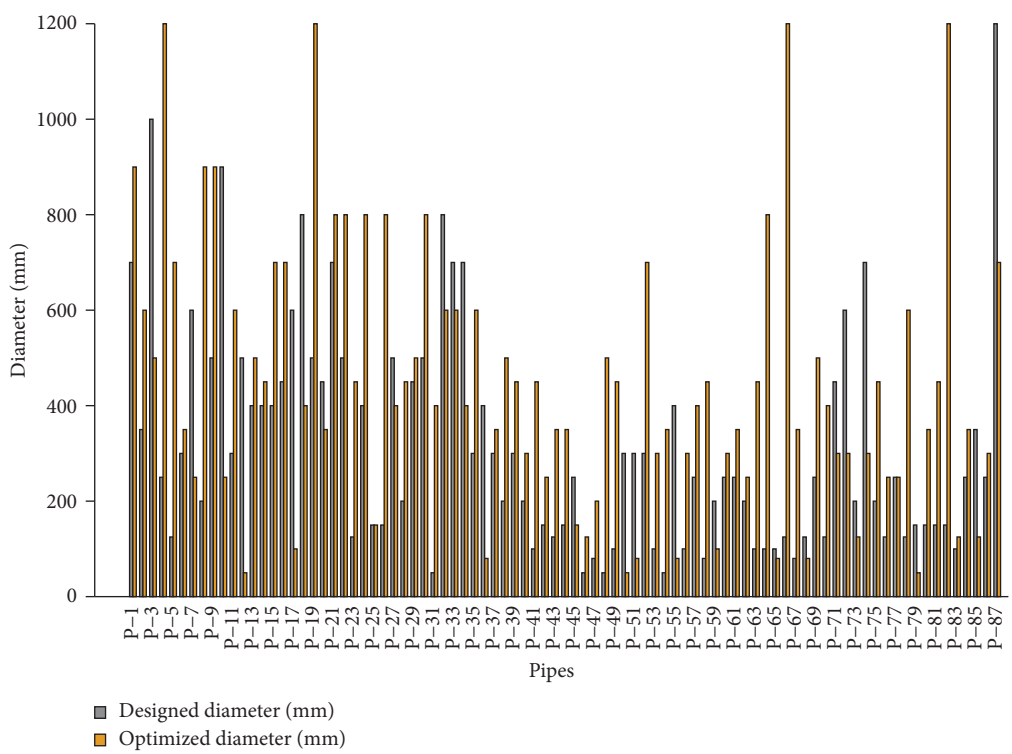

Figure 6: Designed diameter versus optimized diameter of the looped network.

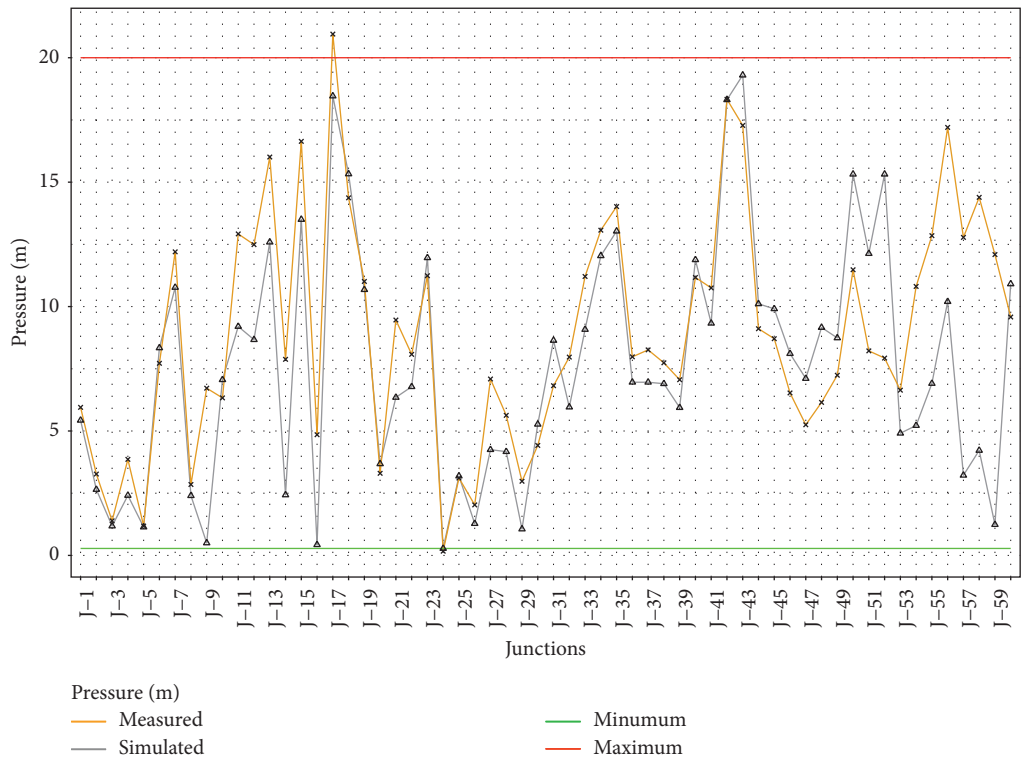

Figure 7: Pressure variation at each junction of looped network.

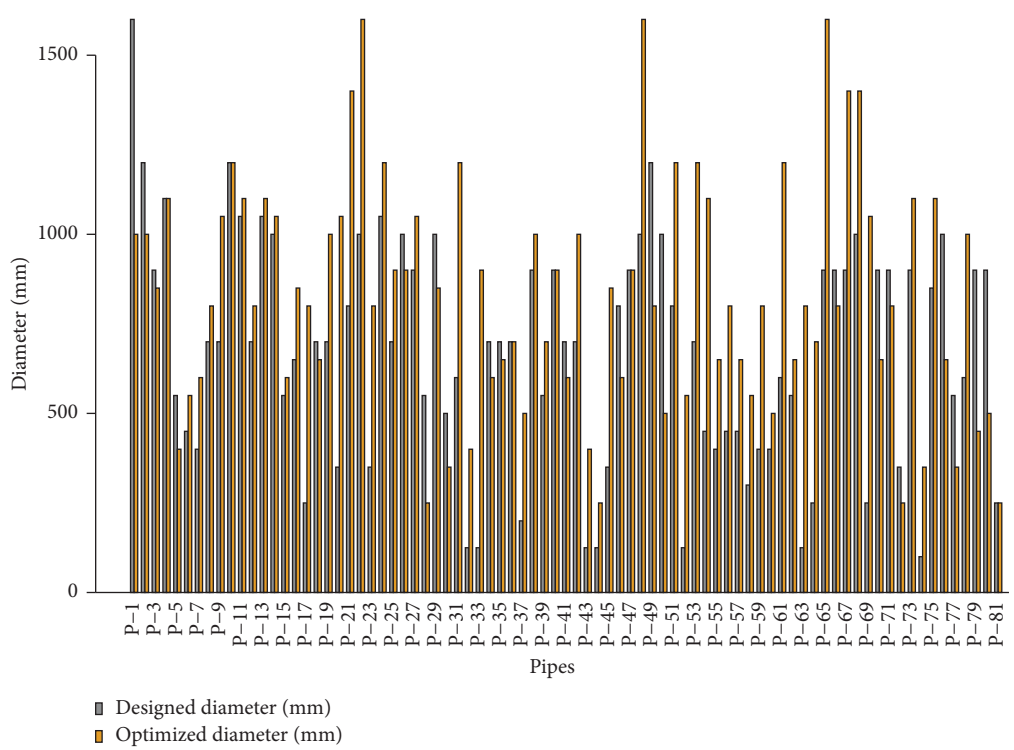

Figure 8: Designed diameter versus optimized diameter of initial Steiner tree network.

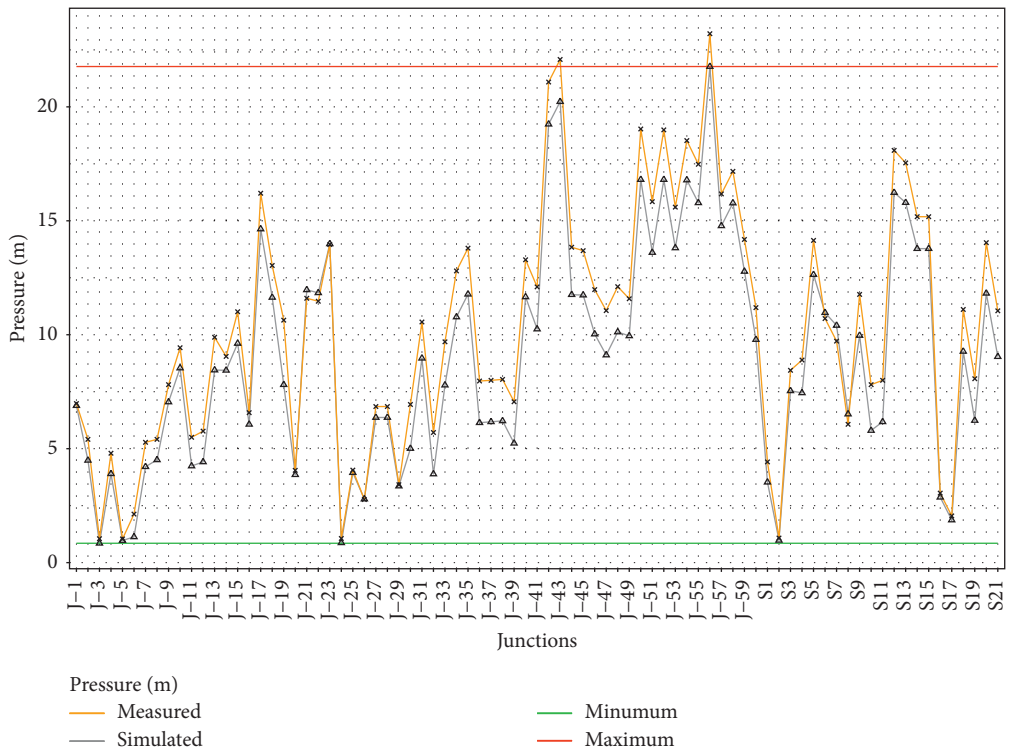

Figure 9: Pressure variation at each node for initial Steiner tree.

Table 4: Comparison between looped network and initial Steiner tree network.

Parameter	Looped network		IST network	
Length (km)	59.17		25.151	
Area (km^2)	2057.17		2057.17	
Material	PVC		PVC	
Source reservoir	1		1	
Node	60		81 (60 + 21 Steiner points)	
Pipe	87		81	
Discharge capacity (cumecs)	1.578		1.578	
Total cost (rs.)	25.86 crores		24.76 crores	
Cost per km length (rs./km)	0.437 crores		0.984 crores	
	Minimum	Maximum	Minimum	Maximum
Designed diameters (mm)	50	1200	250	1600
Optimized diameter (mm)	50	1200	250	1600
Pressures (m)	0.17	20	0.65	23
Simulated pressures (m)	0.28	19.3	0.85	21.72

designed and optimized diameters and pressures and simulated pressures of both the networks is also presented.

5. Conclusion

As the network is buried underground, therefore the location of the nodes does not create any hindrance to on-land farming. Moreover, the increment in the number of nodes also has little effect on the functionality of the network. In the present study, initially, a looped network is analyzed and design is carried out for the total length of 59.17 Km. The total cost of looped PIN is found to be 25.86 crores, that is, 0.45 crores per Km length. After converting the looped network to a branch network (MST) using PA, it is observed that number of links reduced to 60 from the 87 for the same nodal demand. The length of the looped network decreases to 28.65 Km from 59.17 Km, that is, 51.58%. The final step in which the MST is converted to IST using the Steiner concept shows the reduction in network length from 28.65 to 25.151 Km, that is, 12.21% although the number of links and nodes were increased to 81 and 81 (60 already existing nodes and 21 Steiner points), respectively. The total cost of the Steiner network is 24.76 crores, that is, 0.987 crores per km length. The total reduction in the cost of the Steiner tree is found to be 4.25% compared to the looped network. Results highlight that though the per meter cost of the ST is higher than the initial looped network, but the two-step optimization of layout reduced the total cost of the network. Hence,

the method proposed in the present study can be certainly utilized for the layout and pipe size optimization. As the pipes are underground, the Steiner point junctions are feasible, as no on-field problems are faced. The present work can be extended for further cost reduction, which may be possible if different pipe materials are used for different lengths of the network.

Data Availability

Data are available upon request to the corresponding author.

Conflicts of Interest

The authors declare that they have no conflicts of interest.

Acknowledgments

The data for the present study is provided by the Pench Irrigation Division, Nagpur, Maharashtra, India, under Vidarbha Irrigation Development Corporation, for which the authors extend a sincere thanks to the department.

References

[1] S. K. Jain, P. K. Agarwal, and V. P. Singh, *Inter-basin Water Transfer, in Hydrology and Water Resources of India*, pp. 1065–1109, Springer, Berlin, Germany, 2007.

[2] C. Chandramouli and R. General, "Census of India," *Provisional Population Totals*, New Delhi: Government of India, New Delhi, India, 2011.

[3] U. Surendran, C. M. Sushanth, E. J. Joseph, N. Al-Ansari, and Z. M. Yaseen, "FAO CROPWAT model-based irrigation requirements for coconut to improve crop and water productivity in Kerala, India," *Sustainability (Switzerland)*, vol. 11, p. 18, 2019.

[4] M. Maghrebi, R. Noori, R. Bhattarai et al., "Iran's agriculture in the anthropocene," *Earth's Future*, vol. 8, no. 9, Article ID e2020EF001547, 2020.

[5] S. A. Salman, S. Shahid, H. A. Afan, M. S. Shiru, N. Al-Ansari, and Z. M. Yaseen, "Changes in climatic water availability and crop water demand for Iraq region," *Sustainability*, vol. 12, no. 8, p. 3437, 2020.

[6] K. Radhakrishnan, I. Sivaraman, S. K. Jena, S. Sarkar, and S. Adhikari, "A climate trend analysis of temperature and rainfall in India," *Climate Change and Environmental Sustainability*, vol. 5, no. 2, p. 146, 2017.

[7] M. Ronit and P. Divya, "The relationship between the growth of exports and growth of gross domestic product of India," *International Journal of Business and Economics Research*, vol. 3, no. 3, pp. 135–139, 2014.

[8] R. C. Srivastava, S. Mohanty, R. B. Singandhupe, A. K. Biswal, L. I. P. Ray, and D. Sahoo, "Studies on canal water based pressurized irrigation system in a minor irrigation command," *Journal of Agricultural Engineering*, vol. 43, no. 4, pp. 28–35, 2006.

[9] R. C. Srivastava et al., "Feasibility evaluation of pressurized irrigation in canal commands," *Water Resources Management*, vol. 24, no. 12, pp. 3017–3032, 2010.

[10] M. Satpute, P. Khandve, and M. Gulhane, "Pipe distribution nerwork for irrigation–an alternative to flow irrigation," in *Proceedings of 99th Indian Science Congress Environmental Sciences*, 99th Indian Science Congress, Part II, Odisha, India, January 2012.

[11] R. v. Bentum, I. K. Smout, and X. Z. Ci, "Use of pipelines to improve surface irrigation in hebei province, China," *Journal of Irrigation and Drainage Engineering*, vol. 121, no. 6, pp. 405–410, 1995.

[12] I. K. Smout, "Use of low-pressure pipe systems for greater efficiency," *Agricultural Water Management*, vol. 40, no. 1, pp. 107–110, 1999.

[13] A. M. Michael, *Irrigation: Theory and Practice*, Vikas Publishing House, Chennai, TN, India, 1978.

[14] Z. M. Yaseen, P. Sihag, B. Yusuf, and A. M. S. Al-Janabi, "Modelling infiltration rates in permeable stormwater channels using soft computing techniques," *Irrigation and Drainage*, vol. 70, 2020.

[15] P. R. Bhave and C. F. Lam, "Optimal layout for branching distribution networks," *Journal of Transportation Engineering*, vol. 109, no. 4, pp. 534–547, 1983.

[16] B. Karimi, P. Mohammadi, H. Sanikhani, S. Q. Salih, and Z. M. Yaseen, "Modeling wetted areas of moisture bulb for drip irrigation systems: an enhanced empirical model and artificial neural network," *Computers and Electronics in Agriculture*, vol. 178, Article ID 105767, 2020.

[17] P. W. Gajghate and A. Mirajkar, "Irrigation pipe network planning at tertiary Level: an Indian case study," *KSCE Journal of Civil Engineering*, vol. 24, no. 1, pp. 322–335, 2019.

[18] I. C. Goulter and D. R. Morgan, "An integrated approach to the layout and design of water distribution networks," *Civil Engineering Systems*, vol. 2, no. 2, pp. 104–113, 1985.

[19] K. Awumah, S. K. Bhatt, and I. C. Goulter, "AN integer programming model for layout design OF water distribution networks," *Engineering Optimization*, vol. 15, no. 1, pp. 57–70, 1989.

[20] G. A. Walters and T. Lohbeck, "Optimal layout OF tree networks using genetic algorithms," *Engineering Optimization*, vol. 22, no. 1, pp. 27–48, 1993.

[21] J. W. Davidson, "Evolution program for layout geometry of rectilinear looped networks," *Journal of Computing in Civil Engineering*, vol. 13, no. 4, pp. 246–253, 1999.

[22] T. Tanyimboh and C. Sheahan, "A maximum entropy based approach to the layout optimization of water distribution systems," *Civil Engineering and Environmental Systems*, vol. 19, no. 3, pp. 223–253, 2002.

[23] M. H. Afshar, M. Akbari, and M. A. Mariño, "Simultaneous layout and size optimization of water distribution networks: engineering approach," *Journal of Infrastructure Systems*, vol. 11, no. 4, pp. 221–230, 2005.

[24] R. P. Lejano, "Optimizing the layout and design of branched pipeline water distribution systems," *Irrigation and Drainage Systems*, vol. 20, no. 1, pp. 125–137, 2006.

[25] A. G. Prats and S. G. Picó, "Layout design of irrigation networks in highly parcelled territories using geographical information system," *Journal of Irrigation and Drainage Engineering*, vol. 133, no. 6, pp. 573–582, 2007.

[26] P. P. Alandí, J. F. O. Álvarez, and J. M. T. Martín-Benito, "Optimization of irrigation water distribution networks, layout included," *Agricultural Water Management*, vol. 88, no. 1–3, pp. 110–118, 2007.

[27] T. T. Tanyimboh and Y. Setiadi, "Joint layout, pipe size and hydraulic reliability optimization of water distribution systems," *Engineering Optimization*, vol. 40, no. 8, pp. 729–747, 2008.

[28] A. Haghighi, "Loop-by-Loop cutting algorithm to generate layouts for urban drainage systems," *Journal of Water*

Resources Planning and Management, vol. 139, no. 6, pp. 693–703, 2013.

[29] S. H. A. Saleh and T. T. Tanyimboh, "Coupled topology and pipe size optimization of water distribution systems," *Water Resources Management*, vol. 27, no. 14, pp. 4795–4814, 2013.

[30] S. Bao-Feng and M.-Y. Du Xue, "Optimization of tree pipe networks layout and size, using particle swarm optimization," *WSEAS Transactions on Computers*, vol. 13, pp. 219–230, 2014.

[31] M. J. Monem and B. S. Kashkooli, "New discrete particle swarm optimization applied to the design of pressurized irrigation networks," *Journal of Irrigation and Drainage Engineering*, vol. 143, no. 1, Article ID 04016071, 2017.

[32] M. Masoumi, B. S. Kashkooli, M. J. Monem, and H. Montaseri, "Multi- objective optimal design of on- demand pressurized irrigation networks," *Water Resources Management*, vol. 30, no. 14, pp. 5051–5063, 2016.

[33] M. H. Afshar and M. A. Mariño, "Application of an ant algorithm for layout optimization of tree networks," *Engineering Optimization*, vol. 38, no. 3, pp. 353–369, 2006.

[34] E. Koritsas, E. Sidiropoulos, and C. Evangelides, "Optimization of branched water distribution systems by means of a physarum-inspired algorithm," *Proceedings*, vol. 2, no. 11, p. 598, 2018.

[35] R. Gupta and S. Rathi, "Joint consideration of layout and pipe sizes for water distribution network design with reliability," *Procedia Engineering*, vol. 186, pp. 357–363, 2017.

[36] R. Balireddy, A. Chakravorty, S. N. Kuiry, and S. M. Bhallamudi, "Application of Thevenin Theorem for model reduction and analysis of large water distribution networks," *World Environmental and Water Resources Congress 2020*, American Society of Civil Engineers, Virginia, USA, 2020.

[37] S. Khalifeh, S. Akbarifard, V. Khalifeh, and E. Zallaghi, "Optimization of water distribution of network systems using the Harris Hawks optimization algorithm (Case study: Homashahr city)," *MethodsX*, vol. 7, p. 100948, 2020.

[38] A. Manolis, E. Sidiropoulos, and C. Evangelides, "Targeted path search algorithm for optimization of water distribution networks," *Urban Water Journal*, pp.1–13, 2021, in Press.

[39] D. F. Ahmed and M. Y. Nawaf, "Design of multivariable control system of a distillation tower via simulation using MATLAB/simulink," *Tikrit Journal of Engineering Sciences*, vol. 26, no. 3, pp. 43–50, 2019.

[40] B. Jiang, F. Zhang, J. Gao, and H. Zhao, "Building a water distribution network hydraulic model by using WaterGEMS," *ICPTT 2012*, American Society of Civil Engineers, Virginia, USA, 2012.

[41] R. Gupta, V. Upadhyaya, and V. K. Sudhan, "Optimal layout and sizing of pipe distribution network considering steiner points," *World Environmental and Water Resources Congress 2019*, American Society of Civil Engineers, Virginia, USA, 2019.

[42] E. O. Frimpong, *Minimum Connection of Pipes for Water Distribution Network in Agric Nsima*, Springer, Berlin, Germany, 2012.

[43] F. C. Harris, "Steiner minimal trees: their computational past, present, and future," *Journal of Combinatorial Mathematics and Combinatorial Computing*, vol. 30, pp. 195–220, 1999.

[44] W. M. Boyce, "An improved program for the full steiner tree problem," *ACM Transactions on Mathematical Software*, vol. 3, no. 4, pp. 359–385, 1977.

[45] P. Winter and M. Zachariasen, "Euclidean Steiner minimum trees: an improved exact algorithm," *Networks*, vol. 30, no. 3, pp. 149–166, 1997.

[46] D. Juhl, D. M. Warme, P. Winter, and M. Zachariasen, "The GeoSteiner software package for computing Steiner trees in the plane: an updated computational study," *Mathematical Programming Computation*, vol. 10, no. 4, pp. 487–532, 2018.

[47] M. Z. do Nascimento, V. R. Batista, and W. R. Coimbra, "An interactive programme for weighted Steiner trees," *Journal of Physics: Conference Series*, vol. 574, p. 12073, 2015.

[48] T. M. Walski, D. V Chase, and D. A. Savic, *Water Distribution Modeling*, Springer, Berlin, Germany, 2001.

Hindawi
Mathematical Problems in Engineering
Volume 2021, Article ID 6613332, 18 pages
https://doi.org/10.1155/2021/6613332

Research Article

Multiobjective Route Selection Based on LASSO Regression: When Will the Suez Canal Lose Its Importance?

Jingmiao Zhou,[1,2] **Yuzhe Zhao**,[2] **and Jiayan Liang**[2]

[1]*Business School, Dalian University of Foreign Languages, Dalian 116044, China*
[2]*Collaborative Innovation Center for Transport Studies, Dalian Maritime University, Dalian 116026, China*

Correspondence should be addressed to Yuzhe Zhao; zhaoyuzhe@dlmu.edu.cn

Received 13 December 2020; Revised 21 January 2021; Accepted 24 January 2021; Published 19 February 2021

Academic Editor: Mohammad Yazdi

With coronavirus disease 2019 reshaping the global shipping market, many ships in the Europe-Asia trades that need to sail through the Suez Canal begun to detour via the much longer route, the Cape of Good Hope. In order to explain and predict the route choice, this paper employs the least absolute shrinkage and selection operator regression to estimate fuel consumption based on the automatic identification system and ocean dataset and designed a multiobjective particle swarm optimization to find Pareto optimal solutions that minimize the total voyage cost and total voyage time. After that, the weighted sum method was introduced to deal with the route selection. Finally, a case study was conducted on the real data from CMA CGM, a leading worldwide shipping company, and four scenarios of fuel prices and charter rates were built and analyzed. The results show that the detour around the Cape of Good Hope is preferred only in the scenario of low fuel price and low charter. In addition, the paper suggests that the authority of Suez Canal should cut down the canal toll according to our result to win back the ships because we have verified that offering a discount on the canal roll is effective.

1. Introduction

Despite bleak prospects of worldwide market amid the coronavirus disease 2019 (COVID-19) pandemic, shipping remains the backbone of the global economy [1]. However, shipping companies must reconsider their decision-making of ship operations in order to survive the crisis. Suddenly, Europe-Asia sailing via the Cape of Good Hope rather than the shorter route via the Suez Canal looks like an attractive option. As shown in Figure 1 [2], since the end of March 2020, at least 32 such sailings took place via the Cape of Good Hope. Many ships operated by the three major shipping alliances, 2M, Ocean Alliance, and THE Alliance, have all chosen the longer route.

Sailing around the Cape of Good Hope, more than 3,000 nautical miles and at least 5 days longer than transiting through the Suez Canal, may seem to be a strange move. But the preference of this sailing option is not unprecedented. When fuel price nosedived in late 2015, many ships sailing from the US east coast to Asia did the same until the Suez Canal slashed the transit charge. Apparently, bypassing the Suez Canal is driven by external factors like fuel price, charter rate, and canal transit charge.

The additional fuel and charter costs of switching to the longer route are negligible, owing to the drop of fuel prices and charter rates. More importantly, the growing costs can be largely offset by the benefits of avoiding the expensive canal transit charge. It is reported that Maersk shells out approximately 350,000 USD per ship for transiting through the Suez Canal [4]. Under the combined effects of external factors, the detour around the Cape of Good Hope offers shipping companies an effective measure to minimize total voyage cost.

In practice, however, the minimal cost is not the only object in the decision-making of ship operations. The detour via the longer route inevitably increases the total voyage time, which will lower the service level and may annoy shippers. In fact, some shippers are weighing up whether to stop booking slots from shipping companies making the detour [5]. To maintain market share, shipping companies

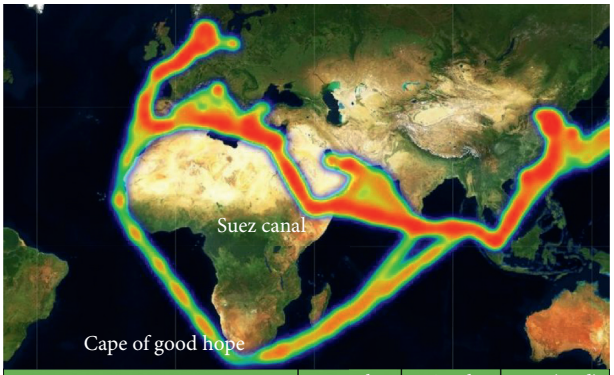

Route	March	April	May (mid)
Asia-Europe (westbound)	1	7	0
Europe-Asia (eastbound)	0	7	8
US EastCost-Asia (eastbound)	0	7	7

Figure 1: Number of containerships switched to the route via the Cape of Good Hope. Note: the data are collected from BIFA [2]; the heat map is from [3].

must work to improve the service level, i.e., minimizing the total voyage time. Hence, the decision of whether to detour is a multiobjective problem aimed at trading off minimal total voyage cost against minimal total voyage time.

Considering the growing popularity of detouring around the Cape of Good Hope, this paper aims to disclose how external factors influence the decision of whether to detour. To clarify the mechanism of influence, the main obstacle lies in the difficulty in precisely estimating the total voyage cost. For instance, it is very difficult to estimate fuel consumption, which is impacted by various factors, such as sailing speed, draft, wind direction, and current direction. Most scholars only roughly estimated fuel consumption with a cubic function of sailing speed. Other scholars, namely, Fagerholt et al. [6] and Yao et al. [7], proposed a fuel consumption function based on empirical data from a shipping company but did not consider the impact of external factors on fuel consumption. The inaccurate estimation of fuel consumption will lead to errors in predicting the decision-making of shipping companies. To solve the problem, this paper employs the least absolute shrinkage and selection operator (LASSO) regression model to examine the correlations between eigenvariables and solve the problem of fuel consumption estimation.

Therefore, this paper employs the LASSO regression model to reflect the relationships among different eigenvariables. In addition, a particle swarm optimization (PSO) technique-based solver is proposed to solve this multiobjective problem. Finally, since the decision-making of ship operations is an immediate choice, the weighted sum (WS) method is introduced. Striving to solve an emerging and valuable issue, this paper makes the following contributions:

(1) This paper analyzed the determinants of the ship detouring behavior from Suez Canal to the Cape of Good Hope, which is a realistic problem with critical significance for the shipping industry but only investigated by few scholars so far.

(2) Some cutting-edge big data techniques and optimization methods were applied in combination to solve the problem. Specifically, the data preparation, training LASSO regression model, multiobjective particle swarm optimization (MOPSO) algorithm, and WS method were integrated into a novel optimization framework of sailing speed and sailing route.

(3) Four scenarios reflecting the fluctuation of shipping market conditions were proposed and analyzed for the ship detouring problem. For each scenario, the paper also calculated the suggested Suez Canal toll that is able to win back the ships detouring around the Cape of Good Hope.

The remainder of this paper is organized as follows: Section 2 makes a thorough review of the related literature; Section 3 establishes a LASSO regression model to estimate fuel consumption, introduces a multiobjective optimization model, describes the solving algorithm MOPSO, and introduces the WS method; Section 4 presents and analyzes the optimization results through a case study; and Section 5 puts forward the conclusions.

2. Literature Review

Ship operations decision-making mainly includes fleet management, ship scheduling, route planning, and speed setting. Christiansen et al. [8] summarized the studies on ship scheduling and route planning. Mansouri et al. [9] provide a survey of existing research on sustainable decision-making of ship operations. Fuel consumption is an important variable in the decision-making of sailing speed and route. Fagerholt et al. [10] obtained fuel consumption through linear interpolation and optimized the sailing speed and route. Zhen et al. [11] also relied on linear interpolation to ascertain fuel consumption and proposed a tabu search (TS) algorithm to minimize the fuel cost. Zhen et al. [12] combined two-stage iterative algorithm and fuzzy logic method with ε-constraint into a novel approach to solve the sailing speed and route decision problem subjected to changing fuel price. Lee et al. [13] optimized the speed of liner shipping under the weather impact, revealing that the sailing speed affects the transit time between ports and, in turn, impacts the service level. To optimize the sailing route, Gkerekos and Lazakis [14] presented a novel framework based on a data-driven model, which plans the ship routes in view of historical ship performance and current weather conditions.

Most speed optimization models assume that fuel consumption is the cubic formula of the sailing speed [15]. In real-world scenarios, fuel consumption is affected by various factors other than sailing speed. Characterizing fuel consumption by sailing speed and load, Wen et al. [16] optimized the route and speed of multiple ships under time, cost, and environmental constraints. Wang and Meng [17] explored the deterministic speed optimization problem, a subproblem of container routing problem: the relationship between sailing speed and fuel consumption was analyzed

based on historical data, and the fuel consumption was found to depend on voyage legs, for the weather varies from leg to leg. Kim and Lee [18] introduced the optimization-based decision support system (DSS) to ship scheduling and used the Linear, Interactive, Discrete Optimizer (LINDO) to maximize the profit of cargo transport. Windeck and Stadtler [19] also developed a DSS for low-carbon shipping network design problem under weather factors.

In recent years, big data analytics begin to be concerned in operations research [20]. For example, Lee et al. [13] implemented the method of big data in meteorological archives and predicted fuel consumption based on the massive weather data at different points of the sea, creating a systematic strategy to extract the weather information from massive archive data for route planning. However, their research is not sufficiently comprehensive, for the fuel consumption of ships is not only affected by weather but also influenced by the state of the sea and various other external factors.

Many other scholars have developed big data-driven models for ship fuel consumption by considering the complicated impacts of external factors. Zheng et al. [21] used artificial neural network (ANN) to predict fuel consumption and optimize the sailing speed. Based on the noon report data, ANN is also applied by Beşikçi et al. [22] to predict fuel consumption of a tanker according to eigenvariables including ship speed, mean draft, and cargo load. Drawing on the wavelet neural network (WNN), Wang et al. [23] established a model to optimize energy efficiency in real time and used the model to determine the optimal engine speeds based on the data collected from GPS receiver, wind speed sensor, water depth sensor, and other technologies. In addition, some relevant regression approaches were developed by Lepore et al. [24], Wang and Yang [25], and Wang et al. [23]. For example, Wang et al. [26] discovered the close correlations between various eigenvariables that affect fuel consumption and selected these eigenvariables with the LASSO regression algorithm. In this paper, the LASSO regression, which has been proven to be effective by Wang et al. [26] in analyzing the impacts of multiple eigenvariables, is adopted to predict fuel consumption during navigation.

For the decision-making of sailing speed and route, many intelligent algorithms have been adopted to solve the optimization model. With the aid of the PSO algorithm, Zheng et al. [21] minimized the total fuel consumption by determining the sailing speed between every two stations; the global optimal sailing speed was acquired through comparison between different improved PSO algorithms. Moore et al. [27], as the first to apply the PSO algorithm in multiobjective optimization, highlighted the importance of individual and swarm searches but ignored the maintenance of swarm diversity. Lee et al. [13] introduced the MOPSO algorithm to minimize the fuel cost and maximize the service level and obtained the Pareto optimal solution. Cariou et al. [28] developed a heuristic approach based on a genetic algorithm (GA) and then solved the problem of large-scale combinatory optimization of speed, route, and cargo flow. Gkerekos et al. [14] modified Dijkstra's shortest path algorithm through heuristics fittings and applied the algorithm recursively until finding the optimal route.

To sum up, the PSO algorithm has not been widely applied with data-driven estimation of fuel consumption. Table 1 compares the few relevant studies in terms of fuel consumption estimation, number of objectives, and solving algorithm. To solve the decision-making of ship speed and route amid the COVID-19, this paper selects the LASSO regression model proposed by Wang et al. [26] and the MOPSO algorithm proposed by Nguyen and Kachitvichyanukul [31].

3. Methodology

The methodology in this paper consists of four parts. Section 3.1 introduces the LASSO regression that can predict fuel consumption precisely. In Section 3.2, a mathematical model is put forward. Then, in Section 3.3, a MOPSO algorithm is designed to solve the mathematical model. Finally, the WS method is introduced to deal with route selection.

3.1. Fuel Consumption Estimation Based on LASSO Regression

3.1.1. Z-Score Normalization. The dimensionality of the original data tends to vary with data fields. For instance, some eigenvariables contain positive and negative values. To prevent solver instability, the original data should be normalized before being imported to the training model. Here, the original data is preprocessed through Z-score normalization.

The Z-score normalization with the mean of zero and standard deviation of one can be expressed as

$$Z_i = \frac{x_i - \overline{x}}{\sqrt{\left(\sum_{i=1}^{n} \left(x_i - \overline{x}\right)^2 / n - 1\right)}}, \tag{1}$$

where $X = \{x_i\}$, $i = 1, 2, \ldots, n$ is the original dataset and $\overline{x}$ is the mean of the original values.

3.1.2. LASSO Regression Model. The LASSO is a parsimonious model that adds a penalty equivalent to absolute magnitude of regression coefficients and tries to minimize them [32]. The model can be described as minimizing the residual sum of squares (RSS), also known as the sum of squared residuals, where the residual in statistics refers to the deviation of the predicted data from the actual value. If the penalty or constraint is sufficiently large, all coefficients are decreased towards zero. If the penalty or constraint decreases to zero, the coefficients not strongly associated with the outcome are decreased to zero, which is equivalent to removing these variables from the model. Therefore, the LASSO is an excellent tool for processing data with complex collinearity.

Suppose there is a set of N samples, and the ith sample consists of the vector $x_i = (x_{i1}, x_{i2}, \ldots, x_{ip})$ composed of p covariates and the response variable y_i. Then, optimize the model:

Table 1: Comparison between the relevant literature.

Authors	Fuel consumption	Single/multiple objectives	Algorithm
Wen et al. [16]	A function of speed and payload	Multiple	Heuristic branch-and-price
Fagerholt et al. [10]	Linear interpolation	Single	The commercial optimization software Xpress MP
Sheng et al. [29]	The third power of speed	Single	Formula derivation
Zhen et al. [11]	Linear interpolation	Single	A TS-based solving method
Zhen et al. [12]	Linear interpolation	Multiple	A hybrid strategy coupling the two-stage iterative algorithm and fuzzy logic method with ε-constraint
Cariou et al. [28]	The third power of speed	Single	A GA-based heuristic
Lee et al. [13]	Weather archive data parser and weather impact miner	Multiple	MOPSO
Zheng et al. [21]	ANN	Single	PSO
Gkerekos and Lazakis [14]	Deep neural network	Single	Dijkstra's algorithm
Ma et al. [30]	The third power of speed	Single	Dijkstra's algorithm
...	...	...	...
Our research	LASSO regression model	Multiple	MOPSO

$$\arg \min_{\beta_0, \beta \in \Re^p} \frac{1}{N} \sum_{i=1}^{N} \left(y_i - \beta_0 - x_i^T \beta \right)^2, \tag{2}$$

$$\text{s.t.} \sum_{j=1}^{p} \left| \beta_j \right| \leq t, \tag{3}$$

where $\beta = (\beta_1, \beta_2, \ldots, \beta_p)$ is the regression coefficient vector under sparse assumption.

Without loss of generality, the covariates can be normalized so that $\sum_i x_{ij}/N = 0$ and $\sum_i y_i/N = 0$. Letting $\overline{y}$ and $\overline{x}$ be the mean values of y_i and x_i and the unbiased estimation $\widehat{\beta}_0 = \overline{y} - \overline{x}^T \beta = 0$. Then, by supposing the sample $X = (x_1, x_2, \ldots, x_N)^{\mathrm{T}}$ and the output vector $y = (y_1, y_2, \ldots, y_N)^{\mathrm{T}}$ and adopting the L^p norm of the vectors ($\|x\|_p = (\sum_{i=1}^{m} |x_i|^p)^{1/p}$), formulas (2) and (3) can be simplified as

$$\begin{aligned} &\arg \min_{\beta \in \Re^p} \left\{ \frac{1}{N} \left\| y - X\beta^T \right\|_2^2 \right\} \\ &\text{s.t.} \|\beta\|_1 \leq t. \end{aligned} \tag{4}$$

The model can be further transformed into the Penalized Least Squares Function, which is also known as the Lagrangian form [33, 34]:

$$L(\beta, \lambda) = \min_{\beta \in \Re^p} \left\{ \frac{1}{N} \left\| y - X\beta^T \right\|_2^2 + \lambda \|\beta\|_1 \right\}, \tag{5}$$

where λ is the regularization parameter ($\lambda \geq 0$). According to the Lagrangian Duality, λ has a data-dependent relationship with t.

3.1.3. Solving the LASSO Regression Model. The LASSO regression model is generally solved by the combination of the k-fold cross-validation and the least angle regression (LARS) algorithm (LassoLarsCV) [30, 35]. In this research, λ or t is estimated by using 10-fold cross-validation. λ, a constant parameter, was estimated by minimizing formula (5), while β was solved with the LARS algorithm so that the residual error was reduced continuously until it was less than a constant.

3.1.4. Fuel Consumption Estimation. Through the above analysis, a LASSO regression model was built to predict fuel consumption. Following the multiple linear regression formulation [36], the fuel consumption F is represented as follows:

$$F = \beta X + b, \tag{6}$$

where b are intercepts.

3.2. Mathematical Model. This paper focuses on the decision of whether to detour around the Cape of Good Hope amid COVID-19. The objective is to minimize to total voyage cost, while the voyage time is not strictly restricted. The total voyage cost was broken down into the sailing fuel cost, the berthing fuel cost, the charter cost, and the transit charge of the Suez Canal.

The sailing fuel cost accounts for a large proportion of the total voyage cost. Hence, it is important to predict the sailing fuel consumption. During the voyage, the fuel consumption of the ship is affected by various eigenvariables, including but not limited to sailing speed, draft, weather conditions, and sea conditions. Some eigenvariables are strongly correlated, such as wind speed and wind force. The strong correlations make the fuel consumption estimation a typical multicollinearity problem. Hence, this paper employs the LASSO regression method proposed by Wang et al. [26] to select the eigenvariables and improve the interpretability and accuracy of the fuel consumption estimation.

After the LASSO regression model was determined, the mathematical model of our problem was established to describe the total cost and total time of voyage and to reveal the correlation between fuel consumption, sailing speed, and other factors. The two objectives of our problem are

conflicting with each other: the total voyage cost is positively correlated with the sailing speed, while the total voyage time is negatively correlated with the sailing speed. To rationalize the decision of whether to detour, it is necessary to find the Pareto optimal solution of the tradeoff relationship between the two objectives. The model, aiming to minimize the total cost and total time of voyage, was solved by the MOPSO algorithm.

Our research considers a liner ship operating on a given route with a set of ports of call. Here, the mandatory time window of arrival of each port is considered. However, the sailing speed between the two ports visited in sequence is variable due to navigation environment and other factors. Therefore, we set up the nodes $N = \{1, 2, \ldots, n\}$ including ports that can be visited by the ship.

Each node has the arrival time t_i^{arrive} and the departure time t_i^{leave} of the ship. For the node that is not port, we can set $t_i^{\text{leave}} - t_i^{\text{arrive}} = 0$. Additionally, the trip from port i to port $i+1$ was defined as a leg i. The parameters of the optimization model are explained in Table 2.

The total voyage cost of the ship consists of three parts: the sailing fuel cost, berthing fuel cost, charter cost, and the Suez Canal toll. The sailing fuel consumption for leg i was described as the LASSO regression model $f(v_i, E_i)$, where E_i denotes the various eigenvariables at leg i. The berthing fuel cost per hour at port was fixed because only the auxiliary engine of the ship operates during port call. Let k be the mean amount of fuel consumed per hour at port. Then, the fuel cost per hour (α) at port can be expressed as $\alpha = kP_{\text{fuel}}$. The charter cost depends on the total voyage time and is indirectly affected by fuel price: the falling fuel price will change the supply-demand relationship of the shipping market, which in turn changes the ship's charter rate. Finally, if the ship sails through the Suez Canal, the operator must pay an expensive toll at once. Therefore, the first objective of the model, seeking to minimize the total voyage cost of the ship on the given route (M_1), can be expressed as

$$\begin{aligned}\min M_1 = &\sum_{i=1}^{n} P_{\text{fuel}} f(v_i, E_i) + \sum_{i=1}^{n} \alpha\left(t_i^{\text{leave}} - t_i^{\text{arrive}}\right) \\ &+ \gamma \sum_{i=1}^{n}\left(\frac{l_i}{v_i} + t_i^{\text{leave}} - t_i^{\text{arrive}}\right) + P_{\text{pass}} y.\end{aligned} \tag{7}$$

On the given route, the voyage time of the ship should be as short as possible. Therefore, the second objective is to minimize the total voyage time (M_2) and can be expressed as

$$\min M_2 = \sum_{i=1}^{n}\left(\frac{l_i}{v_i} + t_i^{\text{leave}} - t_i^{\text{arrive}}\right), \tag{8}$$

subject to

$$t_n^{\text{arrive}} - t_1^{\text{leave}} \geq \sum_{i=1}^{n}\left(\frac{l_i}{v_i} + t_i^{\text{leave}} - t_i^{\text{arrive}}\right), \tag{9}$$

$$V_{\min} \leq v_i \leq V_{\max}, \quad i = 1, \ldots, n. \tag{10}$$

The objective (7), minimizing the total voyage cost, conflicts with the objective (8), minimizing the total voyage time. Constraint (9) sets a limit on the total voyage time. Constraint (10) ensures that the sailing speed of the ship falls between the lower and upper limits in all legs.

3.3. MOPSO Algorithm. The PSO is a metaheuristic algorithm that has been successfully applied to many real-world scenarios [37]. In the algorithm, each particle in the swarm is treated as a possible solution to the problem, and the optimal solution is searched for based on the behaviors of particles and the interaction between particles.

Considering only one objective, the original PSO proposed by Kennedy and Eberhart [38] cannot be directly applied to multiobjective problems. The MOPSO, aimed at solving problems with different priorities, has been developed in recent years, for example, handling multiobjective optimization problems with a multiswarm cooperative particle swarm optimizer [39], a bare-bones multiobjective particle swarm optimization algorithm [40], and variable-size cooperative coevolutionary particle swarm optimization for feature selection on high-dimensional data [41]. This paper selects the MOPSO framework developed by Nguyen and Kachitvichyanukul [31] as it is one of the most classical MOPSO and has proven efficiency for this problem. The MOPSO can memorize the current search situation and make timely adjustment to the search strategy, resulting in excellent global convergence and robustness.

To solve the multiobjective problem, the MOPSO mainly combines Pareto sorting mechanism to find the historical optimal solution of particles and update the noninferior solution set. The noninferior solutions are searched for in parallel using efficient clusters. In multiobjective optimization, the MOPSO iteratively outputs a set of noninferior solutions that are dominated by each other. Then, the global optimal position can be obtained by randomly screening the noninferior solution set. The steps of the MOPSO framework are summarized as follows:

Step 1. Z-score normalization was adopted to normalize the two objective functions of our problem, i.e., total voyage cost and total voyage time:

Table 2: Notations.

Parameters	Definitions
N	Set of nodes $N=\{1, 2, \ldots, n\}$, node $i \in N$
y	A binary variable equal to 1 if the ship passes through the Suez Canal
P_{fuel}	Fuel price per ton consumed during sailing and berthing (USD/ton)
P_{pass}	The toll to pass through the Suez Canal (USD)
t_i^{arrive}	Arrival time of the ship at port i (hour), $t_1^{\text{arrive}} = 0$ is not considered
t_i^{leave}	Departure time of the ship at port i (hour), $t_n^{\text{arrive}}$is large enough, and t_n^{leave} is not considered
l_i	Sailing distance of leg i, the trip from port i to port $i+1$ (nautical mile)
k	Fuel consumption per hour at port (ton/hour)
γ	Charter rate of the ship (USD/day)
$f(v_i, E_i)$	Fuel consumption per unit time in leg i
v_i	Speed decision on leg i (knot)
$V_{\min}$	Minimum sailing speed (knot)
$V_{\max}$	Maximum sailing speed (knot)

$$M_1'(v_i) = \frac{M_1(v_i) - \overline{M_1(v_i)}}{\sqrt{\left(\sum_{i=1}^{n}\left(M_1(v_i) - \overline{M_1(v_i)}\right)^2/n-1\right)}}, \quad i = 1, \ldots, n,$$
$$M_2'(v_i) = \frac{M_2(v_i) - \overline{M_2(v_i)}}{\sqrt{\left(\sum_{i=1}^{n}\left(M_2(v_i) - \overline{M_2(v_i)}\right)^2/n-1\right)}}, \quad i = 1, \ldots, n, \tag{11}$$

where $M_1'(v_i)$ and $M_2'(v_i)$ are the normalized values of M_1 and M_2 under speed v_i, respectively, and $\overline{M_1(v_i)}$ and $\overline{M_2(v_i)}$ are the mean values of M_1 and M_2 under speed v_i, respectively.

Step 2. The initial swarm was set up, and each particle was given an initial speed and position. The other parameters, such as learning rate, upper and lower limits of inertia weight, maximum number of iterations, and swarm size, were also initialized.

Step 3. The fitness of each particle, depending on the two objectives, was calculated as

$$\begin{cases} M_1 = \sum_{i=1}^{n} P_{\text{fuel}} f(v_i, E_i) + \sum_{i=1}^{n} \alpha\left(t_i^{\text{leave}} - t_i^{\text{arrive}}\right) \\ + \gamma \sum_{i=1}^{n}\left(\frac{l_i}{v_i} + t_i^{\text{leave}} - t_i^{\text{arrive}}\right) + P_{\text{pass}} y, \\ M_2 = \sum_{i=1}^{n} \frac{l_i}{v_i} + \left(t_i^{\text{leave}} - t_i^{\text{arrive}}\right). \end{cases} \tag{12}$$

After the algorithm was initialized and updated, the constraints of the two objective functions were satisfied by limiting the control variables to the specified range.

Step 4. The fitness of particles was compared. The optimal position (P-best) and noninferior solution set of particles were updated according to the dominance relations. The global optimal position (G-best) of particles was randomly selected from the noninferior solution set.

Step 5. The speed and position vectors of each of the N particles in the swarm were, respectively, updated as

$$\begin{aligned} x_i &= \left(x_{i,1}, x_{i,2}, \ldots, x_{i,D}\right) \in R^D, \\ v_i &= \left(v_{i,1}, v_{i,2}, v_{i,D}\right) \in R^D, \quad i = 1, 2, \ldots, n, \end{aligned} \tag{13}$$

where x_i denotes the position of particle i, v_i denotes the velocity of particle i, and D is the number of decision variables. In the evolution process, the position and velocity of each particle were, respectively, updated as

$$\begin{aligned} v_{\text{id}}^{k+1} &= \omega v_{\text{id}}^{k} + c_1 r_1\left(p_{\text{id}}^{k} - x_{\text{id}}^{k}\right) + c_2 r_2\left(p_{\text{gd}}^{k} - x_{\text{gd}}^{k}\right), \\ x_{\text{id}}^{k+1} &= x_{\text{id}}^{k} + v_{\text{id}}^{k+1}, \end{aligned} \tag{14}$$

where ω is the inertia weight, k denotes the iteration number, r_1 and r_2 are uniform random variables in the interval [0, 1], $d \in D$ is the dimension of the vector, p_{id}^{k} and p_{gd}^{k} denote the acceleration constants for its personal best (P-best) and the global best position (G-best), respectively, x_{id}^{k} is previous position of the particle I, and v_{id}^{k+1} is new velocity of the particle i.

Step 6. If the maximum number of iterations was reached, the set of Pareto optimal solutions was outputted; otherwise, steps 3–6 were repeated.

Step 7. The upper and lower bounds of sailing speed were determined according to the actual situation and ship performance. Then, the minimum values of the two objectives (M_1^L and M_2^L), i.e., the positive ideal point A, and the maximum values of the two objectives B ($M_1^U$and M_2^U), i.e., the negative ideal point B, were obtained.

Step 8. In the set of Pareto optimal solutions, the solution with the minimum relative distance from positive and negative ideal points was screened out as the optimal tradeoff solution $C(M_1^*, M_2^*)$, and the

corresponding speed was taken as the optimal sailing speed. Formula (15) shows the line connecting positive ideal point A and negative ideal point B, and the intersection of this line and Pareto frontier is the optimal tradeoff solution $P(M_1^*, M_2^*)$:

$$P(M_1^*, M_2^*) = \frac{M_2^U - M_2^L}{M_1^U - M_1^L}\left(x - M_1^L\right) + M_2^L, \tag{15}$$

where $P(M_1^*, M_2^*)$ is the optimal tradeoff solution, M_1^L and M_2^L are the minimum values of the two objectives, and M_1^U and M_2^U are the maximum values of the two objectives, respectively.

The selection of the best tradeoff solution from Pareto frontier is shown in Figure 2.

3.4. Weighted Sum (WS) Method. After getting the optimal tradeoff solution of the total voyage cost and the total voyage time though the MOPSO algorithm, the WS method [42] is used to evaluate two routes under specific fuel prices and charter rates in this paper. The purpose is to provide a decision reference for operators. The idea of the WS method is to convert the multiobjective optimization into a single objective optimization problem by using a convex combination of objectives. The steps of the WS framework are summarized as follows:

Step 1: the total voyage cost gap Δ_{M_1} and the total voyage time gap Δ_{M_2} between the two routes in given scenario are, respectively, calculated as

$$\begin{aligned} \Delta_{M_1} &= M_1(1) - M_1(2), \\ \Delta_{M_2} &= M_2(1) - M_2(2), \end{aligned} \tag{16}$$

where Δ_{M_1} is the total voyage cost gap, Δ_{M_2} is the total voyage time gap, $\Delta_{M_2}^c$ is the loss of economic value, U is a single objective utility function, and ω is the weight of cost.

Step 2: the total voyage time gap Δ_{M_2} is converted into the loss of economic value $\Delta_{M_2}^c$ due to the delayed delivery of the cargo in this period [16]:

$$\Delta_{M_2}^c = \frac{\tau}{24}\Delta_{M_2}, \tag{17}$$

where τ is the market price of the cargo at the destination.

Step 3: the multiobjective is transformed into a single objective utility function U by introducing the weight of cost ω, which shows the route decision of operators when they have different preferences for voyage cost and voyage time. The WS method solves the scalar optimization problem:

$$\min U = \omega\Delta_{M_1} + (1-\omega)\Delta_{M_2}^c, \tag{18}$$

where $1 \geq \omega \geq 0$.

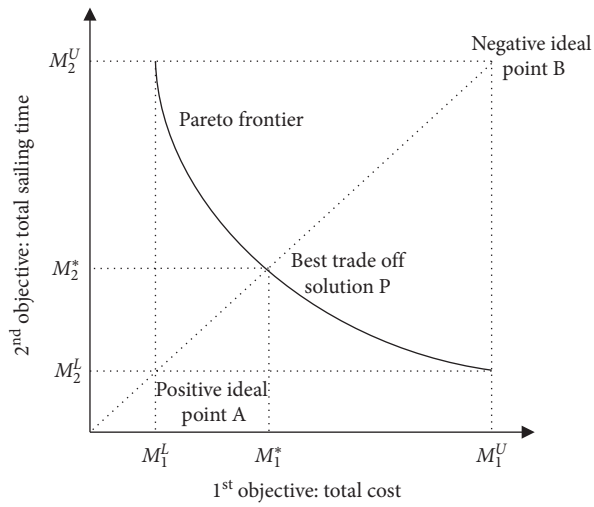

Figure 2: The selection of the optimal solution from the Pareto frontier.

In summary, the objective of the mathematical model in Section 3.2 is to minimize the total fuel consumption predicted by the LASSO regression model in Section 3.1. The model was solved by the MOPSO algorithm in Section 3.3. Route selection was obtained through the WS method in Section 3.4. As shown in Figure 3, the algorithm is implemented in four phases: data preparation, training LASSO regression model, finding the optimal solution with the MOPSO algorithm, and the route selection with the WS method.

4. Case Study

The data selection and preparation are introduced in Section 4.1. The fuel consumption estimation process is presented in Section 4.2. The setting of MOPSO parameters is shown in Section 4.3. Finally, Section 4.4 gives a comprehensive analysis on the route choice.

4.1. Data Selection and Preparation. The case study uses the parameters of a real container ship named "CMA CGM Chile," which transports dry cargoes from the Indian Ocean to Le Havre, France. According to the records of the automatic identification system (AIS) provided by Elane Inc., the ship passed through the Suez Canal (Route SC, Figure 4) during the voyage from December 23rd, 2019, to January 25th, 2020, departing from Qingdao, then visiting Ningbo, Daqu, Yangshan, Yantian, Pasir Panjiang, and Sokhna in sequence, and finally arriving at Le Havre. However, the ship detoured around through the Cape of Good Hope (Route CGH, Figure 5) during another voyage from March 16th, 2020, to April 25th, 2020. The order of ports visited by the ship was Qingdao, Ningbo, Daqu, Yangshan, Yantian, Pasir Panjiang, and Le Havre. Although the ship detoured around through the Cape of Good Hope, the ports visited in actual voyage did not change. Therefore, it is appropriate for this paper to select such a range of ship navigation for calculation. In addition,

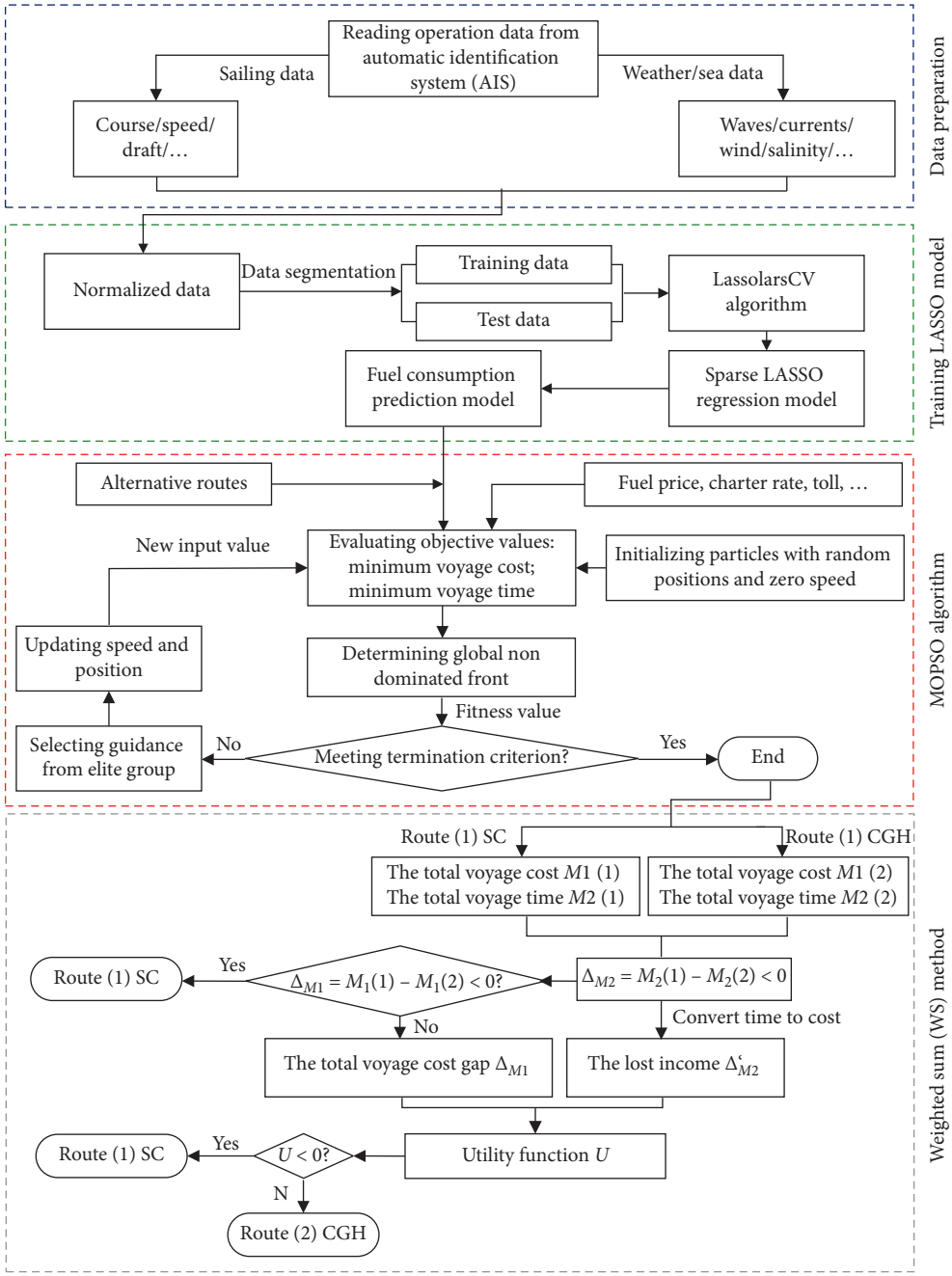

Figure 3: The workflow of the method in the paper.

several legs except the legs between the ports of call in actual voyage are given in the figures to prove the fuel consumption estimation model proposed.

Here, the fuel costs of the two routes were estimated based on two different fuel prices: $P_{\text{fuel}} = 365.5$ USD/ton (the fuel price in March 20, 2019) and $P_{\text{fuel}} = 190.6$ USD/ton (the fuel price in December 27, 2019). The berthing fuel consumption per hour is set as $k = 5.2$ ton/hour [28]. The detour will increase the total voyage time, incurring more charter cost, and the charter rate is affected indirectly by the fuel price. Here, the charter cost is set to 20,833.3 USD/day at the fuel price of 190.6 USD/ton [43]. The toll to pass through the Suez Canal is set to 450,000 USD (the toll in January 4th, 2020). In addition, the arrival time t_i^{arrive} and the departure time t_i^{leave} of the ship at node i were obtained from AIS data. Here, the market price of the cargo at the destination $\tau = 10000$ USD/day. Finally, the maximum and minimum sailing speeds were taken from the shipping logs. The values of the related parameters are listed in Table 3.

4.2. Fuel Consumption Estimation. The main dataset available from AIS and ocean dataset includes mean speed, mean draft, course, current speed, wind speed, wind force, seawater temperature, seawater salinity, and effective wave height. Among them, the weather data like current speed,

Figure 4: Route SC before the falling of fuel price (sailing from December 23rd, 2019, to January 25th, 2020, passing through the Suez Canal).

Figure 5: Route CGH after the outbreak of COVID-19 (sailing from March 16th, 2020, to April 25th, 2020, around the Cape of Good Hope).

Table 3: The values of relevant parameters.

Parameters	Value
Fuel consumption per hour at port, k	5.2 tons/hour
Charter rate, γ	20,833.3 USD/day at the fuel price of 190.6 USD/ton
Maximum sailing speed, $V_{\max}$	22 knots
Minimum sailing speed, $V_{\min}$	10 knots
The toll to pass through the Suez Canal, P_{pass}	450,000 USD

wind speed, wind force, and seawater temperature were extracted from the nc.file obtained from the Copernicus Marine Environment Monitoring Service [44]. Part of the original dataset is presented in Table 4.

The original dataset, involving 490 samples and 10 eigenvariables, was used to train our model. Table 5 shows the original dataset after being processed by Z-score normalization. The normalized dataset was randomly divided into a training set and a test set at the ratio of 4 : 1 and used to verify the effectiveness and reliability of our estimation model.

Taking fuel consumption as the response and other eigenvariables as inputs, our estimation model was optimized by computing the best λ conforming to the least RSS. As mentioned in Section 3.1.3, 10 equal subsets were divided from the training set and conducted for validation. In this way, the optimal values of λ and b were determined as 0.020955 and 0.0000928, respectively.

In this case study, the five eigenvariables (as marked by $*$ in Table 6) corresponding to the nonzero regression coefficients were selected for fuel consumption estimation. As shown in Table 6, the eigenvariables were loosely correlated with fuel consumption, except for sailing speed. The eigenvariables like current speed, wind speed, and wind force had very small effects on fuel consumption. The sailing

Table 4: Part of the original dataset of the ship.

Number	Fuel consumption (ton)	Sailing speed (knot)	Draft (m)	Wind speed (m/s)	Wind force (Pa)	Seawater salinity (0.001)	...
1	4.14	11.88	11.7	3.47	0.02	28.12	
2	4.74	12.42	11.7	4.09	0.03	29.22	
3	5.01	12.64	11.7	4.22	0.03	31.51	
4	6.51	13.1	11.7	5.23	0.04	32.63	...
5	6.33	13.5	11.7	5.15	0.04	32.42	
...	...	...	...	...	...	...	

Table 5: Part of the normalized dataset of the ship.

Number	Fuel consumption	Sailing speed	Draft	Wind speed	Wind force	Seawater salinity	...
1	−2.2605	−2.5564	−4.8435	−1.0858	−0.8543	−3.6283	
2	−2.1378	−2.3163	−4.8435	−0.8737	−0.7193	−3.0492	
3	−2.0846	−2.2185	−4.8435	−0.8292	−0.7193	−1.8437	
4	−1.7787	−2.0140	−4.8435	−0.4835	−0.5844	−1.2541	...
5	−1.8170	−1.8361	−4.8435	−0.5109	−0.5844	−1.3647	
...	...	...	...	...	...	...	

Table 6: Regression coefficient vector of our estimation model.

Features	β_i
Sailing speed	0.9591*
Draft	0.0022*
Course	0
Wind speed	0
Wind force	−0.0018*
Current direction (east)	0
Current direction (north)	−0.2678*
Wave height	0
Seawater salinity	−0.0366*
Seawater temperature	0

speed makes the greatest impact on the fuel consumption. As a result, the fuel consumption cost increases significantly with sailing speed, which can also increase the total voyage cost. The correlations of the selected eigenvariables are also illustrated in Figure 6. The LASSO regression model solves the multicollinearity between variables, as evidenced by the strong correlation between wind speed and wind force.

A comparison between our estimation model and a general linear regression estimation is provided to verify the performance. The estimation effects of the two models on the same test set were measured by the mean absolute percentage error (MAPE) and root mean square error (RMSE) (Table 7). The fitting performance of the two methods is compared in Figure 7. Apparently, our model outperformed the general linear regression model in the estimation of fuel cost and achieved lower RMSE and MAPE than that model.

Compared with Wang et al. [26], another study utilizes LASSO-based model for ship fuel consumption and achieves a RMSE of 7.4, and the performance of our model seems better. While the workflows of LASSO algorithm in two papers are similar, the RMSE value depends on the data selection. Wang et al. [26] collected data from 97 ships with different sizes. In contrast, our paper focuses on only one ship (CMA CGM Chile), in order to achieve the best accuracy on this ship and precisely simulate the routing decision. Our aim is not to develop a general fuel consumption that can be applied to all ships, indeed, which is even impossible. Now, it can be shown that the LASSO algorithm is able to estimate the fuel consumption of the test ship with considerable precision. The rest of the case study is to apply the MOPSO algorithm based on the estimated fuel consumption model.

4.3. Setting of MOPSO Parameters. The MOPSO parameters were configured as follows: the swarm size N is 200, and the maximum number of iterations is 100. Under this setting, the program took 47 seconds on average in 30 repeated runs. In 24 out of the 30 runs, the results were basically consistent, indicating the stability of the MOPSO algorithm. Figure 8 shows the convergence curves of the two objective functions. It can be seen that the MOPSO algorithm had converged to the optimal values of the two objectives at the 100th iteration.

4.4. Results and Discussion

4.4.1. Analysis on the Current Situation: Why Detour? Recall the phenomenon introduced in Section 4.1 that the ship "CMA CGM Chile" sailed through Route SC at a fuel price of 365.5 USD/ton and detoured to Route CGH at a fuel price of 190.6 USD/ton. By using our proposed algorithms, we are able to explain why the ship chose to detour. As shown in Figure 9, the optimal solutions of both Route SC (depicted in green) and Route CGH (depicted in red) follow the pattern that the total voyage cost decreases with the total voyage time rising. Since the decision-maker has to choose from the optimal solutions, it is clear that the two objectives, minimizing the total voyage cost and minimizing the total voyage time, conflict with each other. In order to make comparison among the optimal solutions in Route SC and Route CGH, we applied the principle of selecting the optimal solution from the Pareto frontier in Section 3.3.

Figure 9(a) displays the total voyage cost and total voyage time of Route SC at the fuel price of 365.5 USD/ton. It can be seen that the total voyage cost of the Pareto optimal solution was 2,711,000 USD, and the total voyage time was 793.3

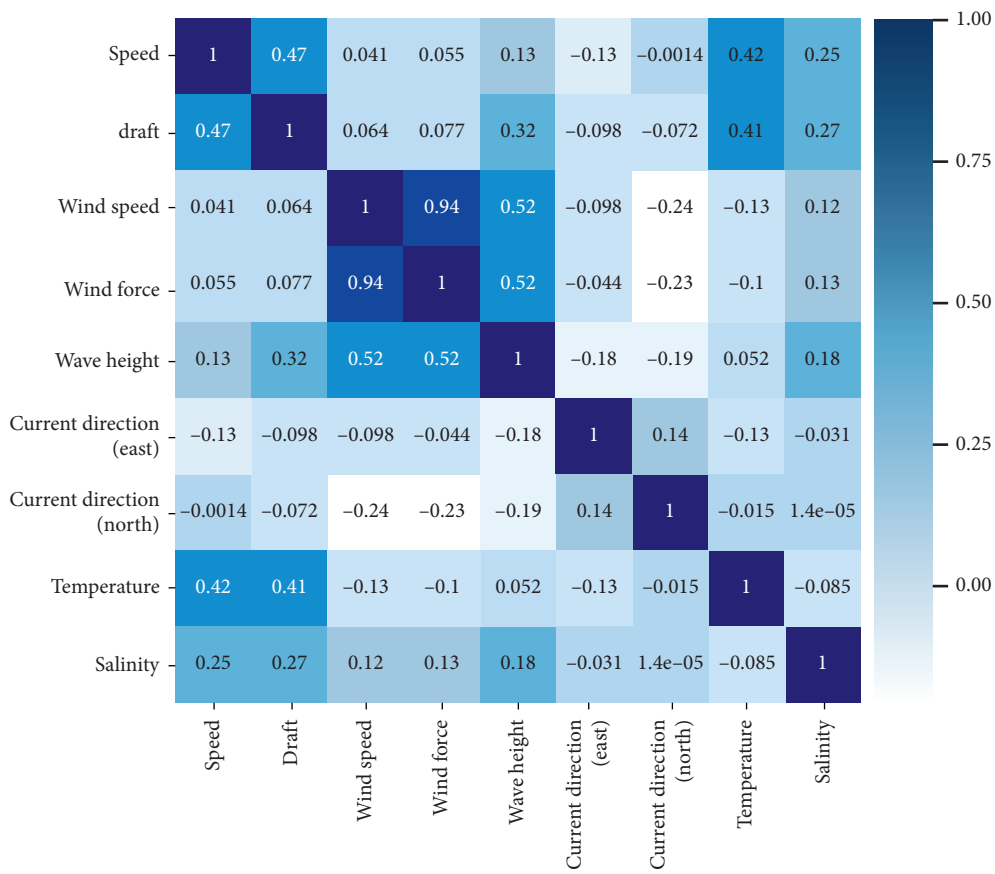

Figure 6: The correlations between eigenvariables.

Table 7: Comparison of MAPE and RSME values of the two models.

Model	MAPE (%)	RMSE
Our model	9.2482	1.6458
General linear regression model	19.9612	3.1275

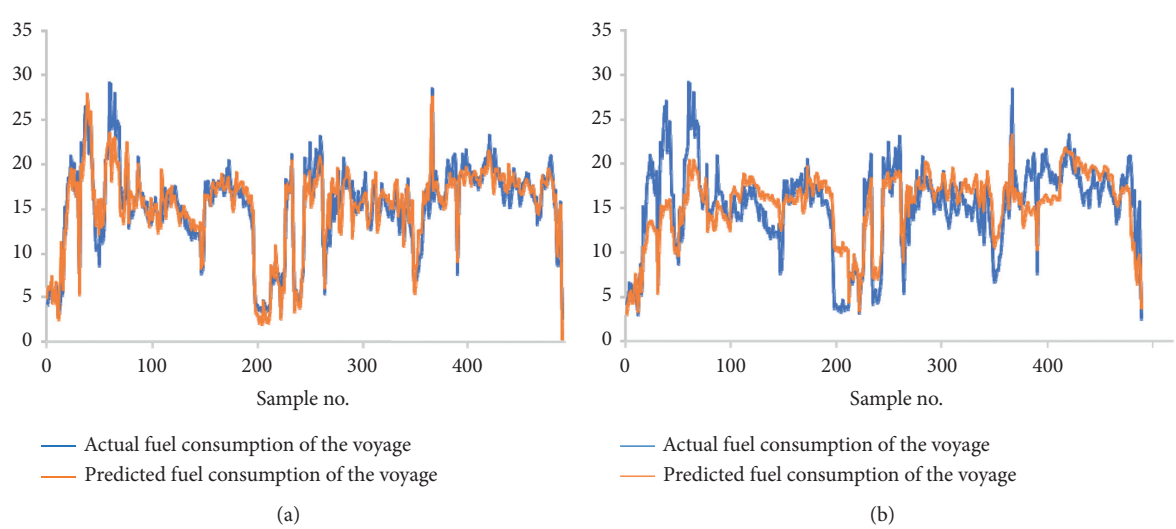

Figure 7: Comparison of estimation results of the two models: (a) our model; (b) general linear regression model.

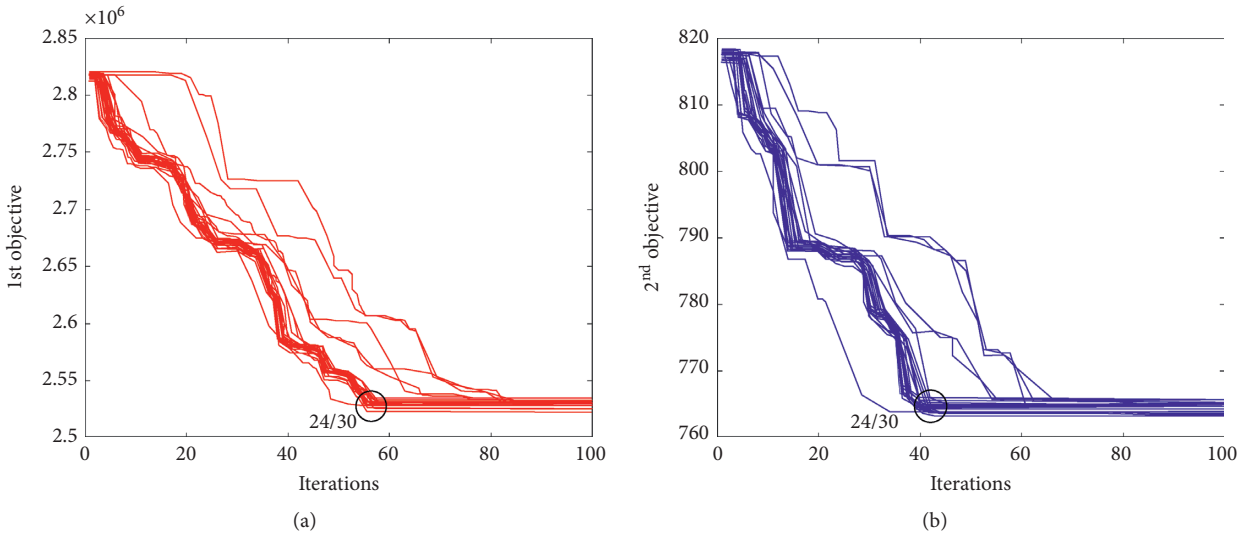

Figure 8: Convergence curves of the two objective functions: (a) first objective; (b) second objective.

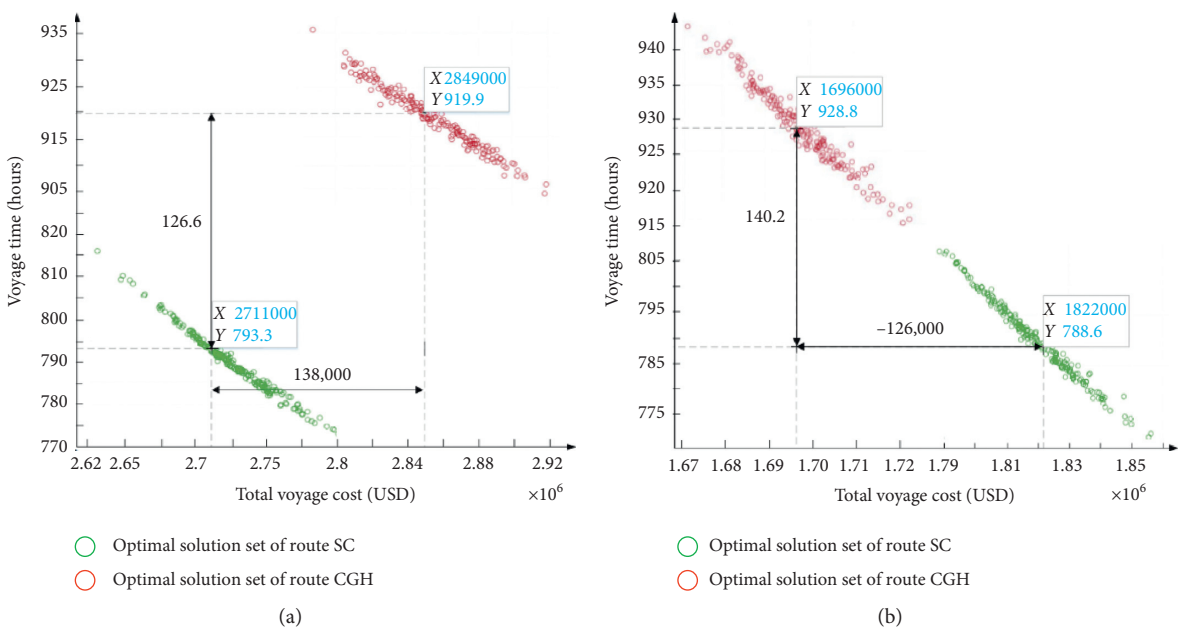

Figure 9: The distribution charts of total voyage cost and total voyage time of the two routes at the fuel price of (a) 365.5 USD/ton and (b) 190.6 USD/ton.

hours. As shown in Figure 9(a), the total voyage cost of Route CGH stood at 2,849,000 USD, and the total voyage time lasted 919.9 hours. Route CGH had a greater total voyage cost and total voyage time than Route SC. Hence, it is more cost-effective to choose Route SC at the fuel price of 365.5 USD/ton.

After the outbreak of COVID-19, the global fuel price plunged deeply. Figure 9(b) displays the total voyage cost and total voyage time of Route SC at the fuel price of 190.6 USD/ton. The total voyage cost was 1,822,000 USD, much smaller than that in the scenario of 365.5 USD/ton. And the total voyage cost of Route CGH was 1,696,000 USD, down by 1,153,000 USD/ton from that at the fuel price of 365.5 USD/ton and 126,000 USD lower than that of Route SC. Although the total voyage time of Route CGH at the fuel price of 190.6 USD/ton was 140.2 hours (about 5.8 days) longer than that of Route SC, by balancing the different objectives, the ship chose the longer route at the fuel price of 190.6 USD/ton.

Table 8 compares the voyage time and speed of each leg on two routes that were estimated by using the methodology proposed in this paper, and the actual values collected from AIS data. The relative error of voyage time and speed was limited to less than 9%, except for Leg 7 of Route CGH in the scenario of 190.6 USD/t. It also can be seen that the sailing speed fluctuated during

Table 8: Estimation and actual values of the variables of each leg on two routes.

	Leg i	Actual voyage time (hour)	Estimated voyage time (hour)	Relative error of voyage time (%)	Actual speed (knot)	Estimated speed (knot)	Relative error of speed (%)
Fuel price of 365.5 USD/t, Route SC	Leg 1	22.13	21.39	**−3.37**	12.19	12.62	**3.49**
	Leg 2	24.70	24.45	**−1.03**	10.98	11.09	**1.04**
	Leg 3	9.33	10.10	**8.18**	12.32	11.39	**−7.56**
	Leg 4	3.88	3.64	**−6.24**	7.21	7.69	**6.65**
	Leg 5	21.63	22.60	**4.48**	17.23	16.49	**−4.28**
	Leg 6	23.37	25.34	**8.47**	18.24	16.82	**−7.80**
	Leg 7	35.03	37.66	**7.49**	19.10	17.77	**−6.97**
	Leg 8	46.97	47.39	**0.90**	17.09	16.94	**−0.89**
	Leg 9	77.65	75.81	**−2.37**	18.73	19.18	**2.42**
	Leg 10	69.92	71.95	**2.90**	17.97	17.46	**−2.82**
	Leg 11	68.58	68.26	**−0.46**	17.90	17.98	**0.47**
	Leg 12	60.95	59.41	**−2.52**	16.76	17.19	**2.59**
	Leg 13	66.80	67.94	**1.70**	16.67	16.39	**−1.67**
	Leg 14	46.75	46.67	**−0.16**	19.03	19.06	**0.16**
	Leg 15	40.33	37.90	**−6.04**	17.74	18.88	**6.43**
	Leg 16	48.65	44.72	**−8.08**	10.64	11.57	**8.79**
Fuel price of 190.6 USD/t, Route CGH	Leg 1	13.32	14.17	**6.40**	13.37	12.57	**−6.01**
	Leg 2	31.12	31.46	**1.11**	11.14	11.02	**−1.09**
	Leg 3	9.17	8.62	**−5.93**	12.44	13.22	**6.30**
	Leg 4	3.83	3.67	**−4.20**	7.72	8.06	**4.38**
	Leg 5	28.68	29.87	**4.12**	17.11	16.43	**−3.96**
	Leg 6	26.47	24.31	**−8.14**	11.97	13.03	**8.86**
	Leg 7	38.05	44.11	**15.93***	18.66	16.10	**−13.74***
	Leg 8	42.92	41.81	**−2.57**	17.84	18.31	**2.64**
	Leg 9	66.82	65.91	**−1.35**	18.15	18.40	**1.37**
	Leg 10	63.57	64.05	**0.77**	18.07	17.93	**−0.76**
	Leg 11	89.60	88.15	**−1.62**	17.80	18.09	**1.65**
	Leg 12	89.23	86.99	**−2.51**	17.29	17.73	**2.57**
	Leg 13	87.42	90.91	**3.99**	18.83	18.11	**−3.84**
	Leg 14	96.78	95.09	**−1.75**	19.35	19.70	**1.78**
	Leg 15	79.60	74.90	**−5.90**	18.70	19.87	**6.27**
	Leg 16	64.22	65.66	**2.25**	17.61	17.22	**−2.20**

Leg 1~16 of the voyage. When sailing for a short distance on Leg 1~4, the speed obtained by the model is basically consistent with the actual speed. Similarly, when sailing for a long distance on Leg 5~16, the estimated values is also close to the actual values. In a word, the estimations and the actual values are basically the same. The results again prove that our methodology can precisely predict the actual voyage.

4.4.2. Scenario Analysis: When to Detour? The fuel prices and charter rates are time-varying factors. Figure 10 shows the change in fuel price and charter rate from December 20th, 2019, to July 3rd, 2020, collected from Clarksons [43]. According to the actual distributions of fuel price and charter rate, four scenarios were designed (Figure 11): high fuel price and high charter rate (HFHC), high fuel price and low charter rate (HFLC), low fuel price and high charter rate (LFHC), and low fuel price and low charter rate (LFLC). Although the HFLC scenario happens occasionally in reality, this scenario was simulated to provide more comprehensive results. The combinations of fuel price and charter rate in HFLC were generated randomly within the range of HFLC and represented by yellow rectangles in Figure 11. The actual combinations of fuel price and charter rate were represented by blue dots. Then, the total voyage cost and the relationship between the four scenarios were analyzed in details.

Table 9 provides the total voyage costs and the total voyage time of Route SC and Route CGH in Scenarios HFHC, HFLC, LFHC, and LFLC, respectively. In Scenarios HFHC, LFHC, and HFLC, the total voyage cost of Route SC was at least 120,700 USD, 83,700 USD, and 130,300 USD lower than that of Route CGH, as shown in the inputs that were marked by $*$ in Table 9, and Route SC remains an absolute advantage on the total voyage time due to the sailing distance. Therefore, the operator will naturally choose Route SC in the above three scenarios. By contrast, in Scenario LFLC, the total voyage cost of Route SC was higher than that of Route CGH for all fuel price and charter rate although the total voyage time of Route SC took less time, as shown in the inputs corresponding to LFLC in Table 9, marked by $*$. In this case, it should analyze the operator's preference to find out which route will be more competitive. And if let the operator select Route SC in Scenario LFLC, how does the authority of the Suez Canal need to adjust its canal toll?

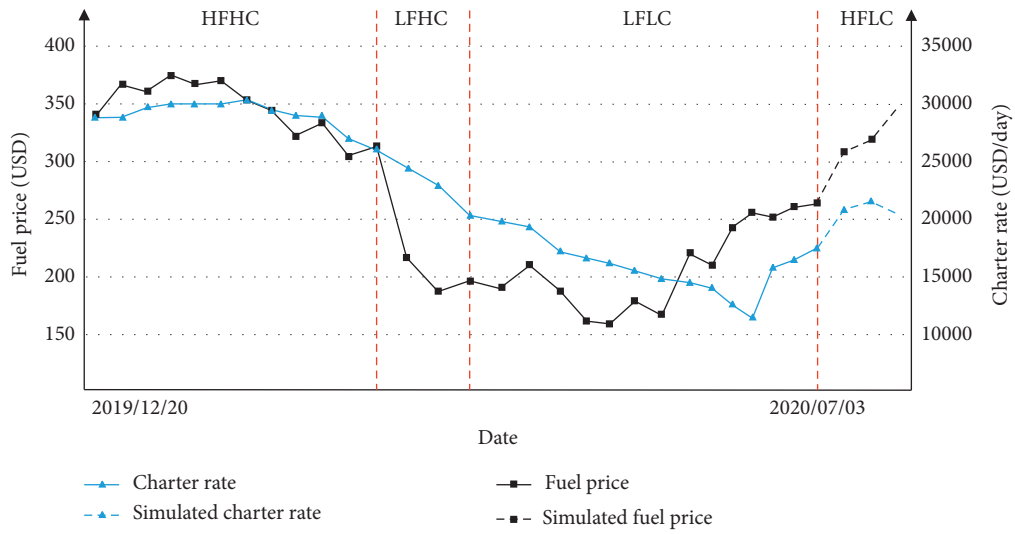

Figure 10: The change trend of fuel price and charter rate.

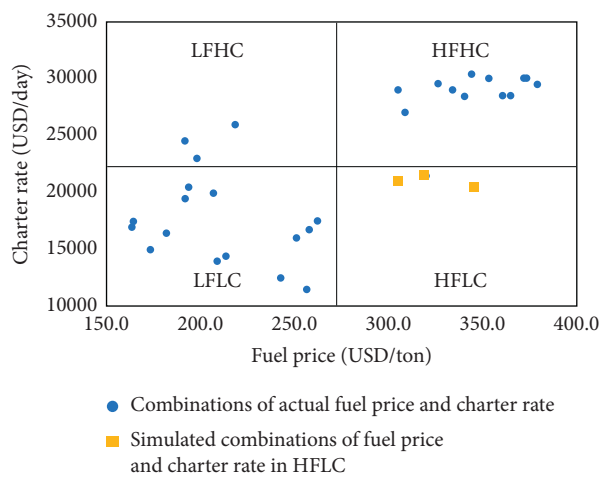

Figure 11: The four scenarios.

Actually, the canal toll is a significant factor influencing the route choice when fuel price and charter rate are fixed. On April 1st, 2020, the authority of the Suez Canal once announced a 6% discount for European ships [45], but it is evident with many ships including the CMA ship that this discount is not sufficient to prevent the detour around the Cape of Good Hope. Here, taking the fuel price of 193.58 USD/ton and the charter rate of 20,500 USD/day in April 3rd, 2020, as an example in the Scenario LFLC set, we attempted to test the impact of different discounts on the original canal toll (450,000 USD) on the choice between Route SC and Route CGH using the WS method in Section 3.4. The route choice decision-making is complicated by the fact that the adjustment of canal toll impacts both the total voyage cost gap Δ_{M_1} and the total voyage time gap Δ_{M_2} between the two routes. Therefore, we used utility (U) to represent the satisfactory degree of the decision-maker. The values of utility can be calculated by the WS method, as mentioned in Section 3.4. The higher the value of U, the more attractive the Route SC. The results of Δ_{M_1}, Δ_{M_2}, and U are shown in Table 10. We also calculated the Suez Canal toll (P_{pass}) and the toll discount corresponding to $U = 0$, which can make sure the attractiveness of Route SC and Route CGH are the same, by linearly interpolating a value between the Suez Canal tolls with utilities very close to zero. In Table 10, the positive U that was closest to zero and the negative U that was closest to zero under any cost preference were marked by $*$, and the Ppass corresponding to U=0 was derived from these values.In order to avoid the ships from detouring to Route CGH, the Suez Canal Authority needs to keep $U \geq 0$ when adjusting P_{pass} and the toll discount.

From the results in Table 10, we can find two implications. First, if the operator does not pay so much attention to the voyage cost, even if the canal toll does not need to be discounted, that is, when it is still 450000 USD,

Table 9: The total voyage cost and total voyage time of two routes in the four scenarios.

Scenarios	Fuel price (USD/ton)	Charter rate (USD/day)	The total voyage cost of Route SC (10^4 USD)	The total voyage cost of Route CGH (10^4 USD)	The total voyage cost gap between Route SC and Route CGH (10^4 USD)	The total voyage time of Route SC (hour)	The total voyage time of Route CGH (hour)	The total voyage time gap between Route SC and Route CGH (hour)
HFHC	340.50	28,500	266.17	279.03	−12.87	792.1	925.3	−133.2
	365.50	28,500	271.11	284.90	−13.80	793.3	919.9	−126.6
	361.42	28,500	268.17	280.87	−12.70	791	920.5	−129.5
	379.75	29,500	283.23	302.20	−18.97	786.9	921.0	−134.1
	372.25	30,000	293.60	312.93	−19.33	788.2	922.3	−134.1
	374.00	30,000	297.17	316.63	−19.47	790.2	922.4	−132.2
	353.50	30,000	276.83	294.60	−17.77	784.5	921.0	−136.5
	344.17	30,500	274.00	289.63	−15.63	781.0	923.0	−142
	326.50	29,500	263.20	278.17	−14.97	782.1	925.6	−143.5
	334.00	29,000	266.10	279.87	−13.77	788.5	930.1	−141.6
	305.08	29,000	256.77	268.83	−12.07*	778.3	926.1	−147.8
	309.00	27,000	250.07	262.60	−12.53	774.6	936	−161.4
LFHC	218.17	26,000	214.87	223.23	−8.37*	757.1	931.2	−174.1
	191.42	24,500	200.20	209.93	−9.73	773.2	917.5	−144.3
	197.75	23,000	197.00	205.53	−8.53	763.3	916.9	−153.6
LFLC	193.58	20,500	189.53	175.97	13.56*	775.8	928.5	−152.7
	206.33	20,000	191.83	174.03	17.80*	780.4	921.0	−140.6
	191.17	19,500	185.97	167.13	18.84*	788.6	928.8	−140.2
	163.42	17,500	169.27	156.17	13.10*	782.5	912.5	−130
	163.25	17,000	164.50	154.27	10.23*	780.6	920.0	−139.4
	181.17	16,500	170.50	149.77	20.73*	779.4	908.5	−129.1
	173.08	15,000	160.47	147.83	12.64*	777	905.0	−128
	213.00	14,500	162.57	154.63	7.94*	771	893.1	−122.1
	208.75	14,000	172.93	150.30	22.63*	781.2	900.3	−119.1
	242.50	12,500	180.17	162.10	18.07*	780.9	921.5	−140.6
	256.50	11,500	185.37	162.57	22.80*	791.5	924	−132.5
	251.00	16,000	193.47	168.17	25.30*	786.5	915.8	−129.3
	257.50	16,750	199.50	175.53	23.97*	779.8	916.4	−136.6
	261.83	17,500	208.50	185.93	22.57*	786.6	915.2	−128.6
HFLC	305.00	21,000	235.10	248.13	−13.03	790.2	926.5	−136.3
	319.50	21,500	245.70	259.37	−13.67	791.5	928.0	−136.5
	345.40	20,500	232.67	248.40	−15.73	796.1	931.8	−135.7

Route SC still has obvious competitiveness. For example, we can clearly observe that when the operator's cost preference is reduced to 0.3, that is, when the operator pays more attention to the loss of economic value caused by the delayed delivery of the cargo, the operator will undoubtedly choose Route SC. That is to say, if the arrival time of the ship at the destination becomes very important, that is, when the operator is not allowed to violate the delivery agreement, the ship will not detour Route CGH. However, April 2020 is in a relatively special time window. COVID-2019 triggered many chain reactions in the global shipping market. Factor in some operators had no time to pay attention to delivery of the cargo in transit, many ports were closed down, and the fluctuation of fuel price and charter rate was abnormal. Route CGH became a cost-saving choice for some operators at that time.

The second implication is that if the authority of the Suez Canal is willing to discount the canal toll, it will certainly have an effect on the route selection, regardless of the operator's preference. Only when the operator pays more attention to the cost preference, the authority of the Suez Canal needs to have more discount for the canal toll if the operator wants to choose Route SC. For example, when the cost preference equals 1, the authority of the Suez Canal needs to give a discount of more than 30.13% (as marked by $*$ in the bottom of Table 10) on the canal toll to make a difference in the route choice of the operator. As previously analyzed, the cost preference of 0.3 can no longer be discounted. So, for the cost preference of 0.4, the authority of the Suez Canal only needs to reduce the canal toll to 40830USD; that is, 9.27% discount (as marked by $*$ in the bottom of Table 10) is enough to enable the ship to re-enter Route SC.

Finally, we do a computational experiment on the canal toll discounts which should be made by the authority of the Suez Canal for the operator with different preferences under all possible fuel prices and charter rates in the Scenario LFLC set. The results in Table 11 show that when the operator's cost preference is higher than 0.5, the canal toll discount

Table 10: The canal toll discounts at the fuel price of 193.58 USD/ton and the charter rate of 20,500 USD/day.

Fuel price (USD/ton)	Charter rate (USD/day)	The toll (10^4 USD)	Δ_{M_1} (10^4 USD)	Δ_{M_2} (hours)	$\Delta^c_{M_2}$ (10^4 USD)	The total utility U of voyage cost and voyage time (10^4 USD)								
					ω	1	0.9	0.8	0.7	0.6	0.5	0.4	0.3	...
					$1-\omega$	0	0.1	0.2	0.3	0.4	0.5	0.6	0.7	...
193.6	20500	45	13.56	−152.7	−6.36	13.56	11.57	9.58	7.58	5.59	3.60	1.61	−0.39 *	
		44	12.28	−153	−6.38	12.28	10.41	8.55	6.68	4.82	2.95	1.09	−0.78	
		43	11.6	−153.6	−6.40	11.60	9.80	8.00	6.20	4.40	2.60	0.80	−1.00	
		42	10.58	−153.7	−6.40	10.58	8.88	7.18	5.48	3.79	2.09	0.39	−1.31	
		41	9.97	−154.7	−6.45	9.97	8.33	6.69	5.05	3.40	1.76	0.12 *	−1.52	
		40	8.25	−155.5	−6.48	8.25	6.78	5.30	3.83	2.36	0.89	−0.59 *	−2.06	
		39	7.04	−155.7	−6.49	7.04	5.69	4.33	2.98	1.63	0.28 *	−1.08	−2.43	
		38	6.45	−155.7	−6.49	6.45	5.16	3.86	2.57	1.27	−0.02 *	−1.31	−2.61	
		37	5.62	−156.8	−6.53	5.62	4.40	3.19	1.97	0.76	−0.46	−1.67	−2.89	
		36	5.19	−157.5	−6.56	5.19	4.01	2.84	1.66	0.49 *	−0.69	−1.86	−3.04	
		35	3.83	−157.7	−6.57	3.83	2.79	1.75	0.71 *	−0.33 *	−1.37	−2.41	−3.45	
		34	1.65	−158.2	−6.59	1.65	0.83	0.00 *	−0.82 *	−1.65	−2.47	−3.30	−4.12	
		33	0.87	−159.5	−6.65	0.87	0.12 *	−0.63 *	−1.38	−2.14	−2.89	−3.64	−4.39	
		32	0.38	−159.2	−6.63	0.38 *	−0.32 *	−1.02	−1.72	−2.43	−3.13	−3.83	−4.53	
		31	−0.3	−159.7	−6.65	−0.30 *	−0.94	−1.57	−2.21	−2.84	−3.48	−4.11	−4.75	
		30	−2.29	−160.1	−6.67	−2.29	−2.73	−3.17	−3.60	−4.04	−4.48	−4.92	−5.36	
		29	−4.05	−160.6	−6.69	−4.05	−4.31	−4.58	−4.84	−5.11	−5.37	−5.64	−5.90	
		28	−6.15	−161.5	−6.73	−6.15	−6.21	−6.27	−6.32	−6.38	−6.44	−6.50	−6.56	
P_{pass} with $U=0$ (10^4 USD)						31.44	32.73	34.00	34.54	35.40	38.06	40.83	—	—
The toll discount with $U=0$ (%)						30.13 *	27.27	24.45	23.25	21.33	15.41	9.27 *	—	—

Table 11: The canal toll discounts with different preferences in the Scenario LFLC set.

Fuel price (USD/ton)	Charter rate (USD/day)	The toll discount (%)									
		$\omega=1$	$\omega=0.9$	$\omega=0.8$	$\omega=0.7$	$\omega=0.6$	$\omega=0.5$	$\omega=0.4$	$\omega=0.3$	$\omega=0.2$	$\omega=0.1$
193.58	20500	30.13	27.27	24.45	23.25	21.33	15.41	9.27	—	—	—
206.33	20000	39.47	37.96	35.50	33.87	31.56	27.62	21.00	9.33	—	—
191.17	19500	41.63	40.19	37.28	34.71	31.97	27.83	20.70	10.43	—	—
163.42	17500	29.25	28.18	27.06	25.53	23.05	20.29	15.42	1.45	—	—
163.25	17000	23.83	22.34	19.96	17.87	15.68	11.47	4.77	—	—	—
181.17	16500	46.14	45.02	43.65	41.89	39.33	35.64	30.69	17.19	—	—
173.08	15000	30.04	28.92	27.50	25.24	21.93	17.93	9.07	0.50	—	—
213	14500	15.29	13.98	12.48	10.52	7.46	4.60 *	—	—	—	—
208.75	14000	50.21	49.08	47.61	45.86	43.90	41.63	36.63	28.19	7.59	—
242.5	12500	40.10	39.27	38.22	36.91	35.25	33.30	30.83	25.22	12.54	—
256.5	11500	50.72	49.41	48.38	47.41	44.67	41.71	36.57	27.60	10.67	—
251	16000	56.32 *	54.99	52.90	49.88	47.05	41.49	35.84	25.75	6.48	—
257.5	16750	53.11	51.84	50.21	47.52	45.65	43.70	37.72	25.70	8.63	—
261.83	17500	50.08	48.79	47.86	46.65	44.50	42.34	38.19 *	30.87	14.76	—

should be at least 4.60% (as marked by $*$ in Table 11), and the ship will return to Route SC. Of course, only when the authority of the Suez Canal needs to adjust a large discount to 56.32% (as marked by $*$ in Table 11) on the canal toll, the ships will not detour Route CGH. On the other hand, when the operator's cost preference is less than 0.5, there is no need to reduce the canal toll in some cases, such as $\omega = 0.1$ or 0.2. Even for the operators with time preference, if the authority of the Suez Canal expects all of them to choose Route SC, a 38.19% discount (as marked by $*$ in Table 11) is still required.

5. Conclusions

We observed that, in a period of time after the outbreak of COVID-19, some ships in the Europe-Asia trades chose to detour the Cape of Good Hope to transport cargos, which caused us to explore the reasons behind it. In view of the different factors that need to be considered in the operations of a real container ship, including external factors like fuel price, charter rate, canal transit charge, and navigation environments, as well as the controllable factors like sailing speed and sailing route, a research framework including data preparation, training LASSO regression, MOPSO algorithm, and WS method is constructed. First, LASSO regression is used to build a ship fuel consumption estimation model, which can effectively select variables from multiple eigenvariables with strong multicollinearity. Next, a mathematical model was established to minimize total voyage cost and total time of voyage and solved by the MOPSO algorithm. After that, the WS method was introduced to deal with the route selection. Finally, a case study on a real container ship named "CMA CGM Chile" was carried out to verify the

feasibility of our method. The results show that the proposed method can be used as a decision support tool for route planning.

In the case study, the optimal decisions were obtained for different combinations of fuel price and charter rate. In most cases, the Suez Canal was found to be the more attractive option. Four scenarios (HFHC, HFLC, LFHC, and LFLC) were designed based on actual fuel prices and charter rates. The detour around the Cape of Good Hope is preferred only in the LFLC scenario. Therefore, in the LFLC scenario, the authority of the Suez Canal needs to reduce the canal toll, which always has an effect on winning back ships. Our computational experiment shows that the authority of the Suez Canal has to offer a 4.60% discount for those operators who are sensitive to the cost. For those who have time preference, the canal toll should not be adjusted in some cases. However, if the authority of the Suez Canal wants to win back all the ships, a huge discount of 56.32% is required for the canal toll.

The limitation of this paper lies in the neglect of accidents and piracy, which might also affect the route planning. To better reflect the actual situation, the future research will take the occurrence probability of accidents and piracy in the voyage into account. In addition, the emission cost may need to be considered if authority of Suez Canal or the Cape of Good Hope puts forward environmental policies.

Data Availability

The data used to support the findings of this study are available from the corresponding author upon request.

Conflicts of Interest

The authors declare that there are no conflicts of interest regarding the publication of this paper.

Acknowledgments

The authors are thankful for the following dataset providers: Elane Inc., who provided us the AIS data of CMA CGM Chile; Clarksons, who provided us the fuel prices and charter rates; and Copernicus Marine Environment Monitoring Service, who offered us the weather data generously. This research was funded by the National Natural Science Foundation of China (Grant nos. 72072017, 71902016, and 71831002), the Foundation for Humanities and Social Sciences of the Ministry of Education of China (Grant no. 18YJC630261), the Natural Science Foundation of Liaoning Province of China (Grant nos. 2020-hylh-41 and 2020-BS-213), and the Social Science Foundation of Liaoning Province of China (Grant nos. L19AGL012, 2020JYT20, and 20211s1qnkt-020).

References

[1] P. Sand, "Suez canal ship transits rise amidst the Covid-19 pandemic," 2020, https://www.bimco.org/news/market_analysis/2020/20200616_suez_canal_ship_transits.

[2] BIFA, "Cape routings increase despite shipper fury," 2020, https://www.bifa.org/news/articles/2020/may/cape-routings-increase-despite-shipper-fury.

[3] MarineTraffic, "Heat map of containerships," 2020, https://t.co/EJ8vHkL0Jo.

[4] K. Vishal, "Is Suez canal losing its importance?" 2018, http://themarineexpress.com/is-suez-canal-losing-its-importance/.

[5] Lloyd, "Cape routings increase despite shipper fury," 2020, https://www.lloydsloadinglist.com/freight-directory/news/Cape-routings-increase-despite-shipper-fury/76670.htm#.XzmP4TW-vIU.

[6] K. Fagerholt, G. Laporte, and I. Norstad, "Reducing fuel emissions by optimizing speed on shipping routes," *Journal of the Operational Research Society*, vol. 61, no. 3, pp. 523–529, 2010.

[7] Z. Yao, S. H. Ng, and L. H. Lee, "A study on bunker fuel management for the shipping liner services," *Computers & Operations Research*, vol. 39, no. 5, pp. 1160–1172, 2012.

[8] M. Christiansen, K. Fagerholt, B. Nygreen, and D. Ronen, "Ship routing and scheduling in the new millennium," *European Journal of Operational Research*, vol. 228, no. 3, pp. 467–483, 2013.

[9] S. A. Mansouri, H. Lee, and O. Aluko, "Multi-objective decision support to enhance environmental sustainability in maritime shipping: a review and future directions," *Transportation Research Part E: Logistics and Transportation Review*, vol. 78, pp. 3–18, 2015.

[10] K. Fagerholt, N. T. Gausel, J. G. Rakke, and H. N. Psaraftis, "Maritime routing and speed optimization with emission control areas," *Transportation Research Part C: Emerging Technologies*, vol. 52, pp. 57–73, 2015.

[11] L. Zhen, M. Li, Z. Hu, W. Lv, and X. Zhao, "The effects of emission control area regulations on cruise shipping," *Transportation Research Part D: Transport and Environment*, vol. 62, pp. 47–63, 2018.

[12] L. Zhen, Z. Hu, R. Yan, D. Zhuge, and S. Wang, "Route and speed optimization for liner ships under emission control policies," *Transportation Research Part C: Emerging Technologies*, vol. 110, pp. 330–345, 2020.

[13] H. Lee, N. Aydin, Y. Choi et al., "A decision support system for vessel speed decision in maritime logistics using weather archive big data," *Computers and Operations Research*, vol. 98, pp. 330–342, 2017.

[14] C. Gkerekos and I. Lazakis, "A novel, data-driven heuristic framework for vessel weather routing," *Ocean Engineering*, vol. 197, Article ID 106887, 2020.

[15] H. N. Psaraftis and C. A. Kontovas, "Speed models for energy-efficient maritime transportation: a taxonomy and survey," *Transportation Research Part C: Emerging Technologies*, vol. 26, pp. 331–351, 2013.

[16] M. Wen, D. Pacino, C. A. Kontovas, and H. N. Psaraftis, "A multiple ship routing and speed optimization problem under time, cost and environmental objectives," *Transportation Research Part D: Transport and Environment*, vol. 52, pp. 303–321, 2017.

[17] S. Wang and Q. Meng, "Sailing speed optimization for container ships in a liner shipping network," *Transportation Research Part E: Logistics and Transportation Review*, vol. 48, no. 3, pp. 701–714, 2012.

[18] S. H Kim and K. K. Lee, "An optimization-based decision support system for ship scheduling," *Computers & Industrial Engineering*, vol. 33, no. 3-4, pp. 689–692, 1997.

[19] V. Windeck and H. Stadtler, *A Liner Shipping Network Design—Routing and Scheduling Impacted by Environmental Influences*, Springer, Berlin, Heidelberg, 2011.

[20] R. Agarwal, V. Dhar, and Vasant, "Editorial-big data, data science, and analytics: the opportunity and challenge for IS research," *Information Systems Research*, vol. 25, no. 3, pp. 443–448, 2014.

[21] J. Zheng, H. Zhang, L. Yin et al., "A voyage with minimal fuel consumption for cruise ships," *Journal of Cleaner Production*, vol. 215, pp. 144–153, 2019.

[22] E. B. Beşikçi, O. Arslan, O. Turan et al., "An artificial neural network based decision support system for energy efficient ship operations," *Computers & Operations Research*, vol. 66, pp. 393–401, 2016.

[23] K. Wang, X. Yan, Y. Yuan, and F. Li, "Real-time optimization of ship energy efficiency based on the prediction technology of working condition," *Transportation Research Part D: Transport and Environment*, vol. 46, pp. 81–93, 2016.

[24] A. Lepore, M. S. dos Reis, B. Palumbo, R. Rendall, and C. Capezza, "A comparison of advanced regression techniques for predicting ship CO_2 emissions," *Quality and Reliability Engineering International*, vol. 33, no. 6, pp. 1281–1292, 2017.

[25] S. Wang and J. Yang, "A probabilistic model for latent least squares regression," *Neurocomputing*, vol. 149, pp. 1155–1161, 2015.

[26] S. Wang, B. Ji, J. Zhao et al., "Predicting ship fuel consumption based on lasso regression," *Transportation Research Part D: Transport and Environment*, vol. 65, pp. 817–824, 2017.

[27] J. Moore, R. Chapman, and G. Dozier, "Multiobjective particle swarm optimization," in *Proceedings of the 38th Annual on Southeast Regional Conference*, pp. 56-57, Clemson, SC, USA,, April 2000.

[28] P. Cariou, A. Cheaitou, R. Larbi, and S. Hamdan, "Liner shipping network design with emission control areas: a genetic algorithm-based approach," *Transportation Research Part D: Transport and Environment*, vol. 63, pp. 604–621, 2018.

[29] D. Sheng, Q. Meng, and Z.-C. Li, "Optimal vessel speed and fleet size for industrial shipping services under the emission control area regulation," *Transportation Research Part C: Emerging Technologies*, vol. 105, pp. 37–53, 2019.

[30] D. Ma, W. Ma, S. Jin et al., "Method for simultaneously optimizing ship route and speed with emission control areas," *Ocean Engineering*, vol. 202, Article ID 107170, 2020.

[31] S. Nguyen and V. Kachitvichyanukul, "Movement strategies for multi-objective particle swarm optimization," *International Journal of Applied Metaheuristic Computing*, vol. 1, no. 3, pp. 59–79, 2010.

[32] R. Tibshirani, "Regression shrinkage and selection via the lasso," *Journal of the Royal Statistical Society: Series B (Methodological)*, vol. 58, no. 1, pp. 267–288, 1996.

[33] A. Belloni, V. Chernozhukov, and L. Wang, "Square-root lasso: pivotal recovery of sparse signals via conic programming," *Biometrika*, vol. 98, no. 4, pp. 791–806, 2011.

[34] H. Zou, "The adaptive lasso and its oracle properties," *Journal of the American Statistical Association*, vol. 101, no. 476, pp. 1418–1429, 2006.

[35] M. R. Osborne, B. Presnell, and B. A. Turlach, "On the lasso and its dual," *Journal of Computational and Graphical Statistics*, vol. 9, no. 2, pp. 319–327, 2000.

[36] D. Montgomery, E. Peck, and G. Vining, *Introduction to Linear Regression Analysis*, Wiley & Sons, vol. 40, no. 12, pp. 2775-2776, Hoboken, NJ, USA, 5th edition, 2012.

[37] T. J. Ai and V. Kachitvichyanukul, "A particle swarm optimization for the vehicle routing problem with simultaneous pickup and delivery," *Computers & Operations Research*, vol. 36, no. 5, pp. 1693–1702, 2009.

[38] J. Kennedy and R. Eberhart, "Particle swarm optimization," in *Proceedings of the IEEE International Conference on Neural Networks*, vol. 4, pp. 1942–1948, Perth, Australia, November 1995.

[39] Y. Zhang, D. Gong, and Z. Ding, "Handling multi-objective optimization problems with a multi-swarm cooperative particle swarm optimizer," *Expert Systems with Applications*, vol. 38, no. 11, pp. 13933–13941, 2011.

[40] Y. Zhang, D.-W. Gong, and Z. Ding, "A bare-bones multi-objective particle swarm optimization algorithm for environmental/economic dispatch," *Information Sciences*, vol. 192, pp. 213–227, 2012.

[41] X.-F. Song, Y. Zhang, Y.-N. Guo, X.-Y. Sun, and Y.-L. Wang, "Variable-size cooperative coevolutionary particle swarm optimization for feature selection on high-dimensional data," *IEEE Transactions on Evolutionary Computation*, vol. 24, no. 5, pp. 882–895, 2020.

[42] J. L. Cohon, *Multi-objective Programming and Planning*, Academic Press, New York, NY, USA, 1978.

[43] Clarksons, "Fuel prices and charter rates," 2020, http://sin.clarksons.net.

[44] CMEMS, "Marine environment monitoring service," 2020, http://marine.copernicus.eu/services-portfolio/access-to-products/.

[45] SCA, "Suez canal authority," 2020, https://www.suezcanal.gov.eg/English/Pages/default.aspx.

Hindawi
Mathematical Problems in Engineering
Volume 2021, Article ID 5539245, 7 pages
https://doi.org/10.1155/2021/5539245

Research Article

A Laboratory Approach to Measure Carbonate Rocks' Adsorption Density by Surfactant and Polymer

Hamid Esfandyari,[1] Abdorrahman Moghani,[1] Feridun Esmaeilzadeh,[2] and Afshin Davarpanah[3]

[1]*Department of Petroleum Engineering, Abadan Faculty of Petroleum Engineering, Petroleum University of Technology (PUT), Abadan, Iran*
[2]*Department of Chemical and Petroleum Engineering, School of Chemical and Petroleum Engineering, Enhanced Oil and Gas Recovery Institute, Enhanced Gas Condensate Recovery Research Group, Shiraz University, Shiraz, Iran*
[3]*Department of Petroleum Engineering, Science and Research Branch, Islamic Azad University, Tehran, Iran*

Correspondence should be addressed to Hamid Esfandyari; esfandyari_shirazu@yahoo.com

Received 9 January 2021; Revised 3 February 2021; Accepted 8 February 2021; Published 18 February 2021

Academic Editor: Mohammad Yazdi

Chemical recovery techniques have always been considered as one of the efficient secondary and tertiary recovery methods to enhance the oil recovery factor. Regarding the diversity of reservoir heterogeneity and rock properties for each field, various chemical agents were taken into consideration to provide a feasible process that has the best agreement with the reservoir characterization. The objective of this paper is to investigate the considerable influence of a set of chemical agents and temperature impact on the surfactant adsorption density of carbonate rocks. According to the results of this experiment, higher temperatures provide lower surfactant adsorption density. The lowest adsorption carbonate rocks' adsorption density had occurred at 80°C. Furthermore, it was witnessed that hydrolyzed polyacrylamide addition to the surfactant would cause a dramatic decrease in the adsorption density in comparison with the surfactant or polymer individually.

1. Introduction

Nowadays, many kinds of research studies have been complimented on the tertiary oil recovery field in order to enhance oil recovery (EOR) and make stable oil production after the primary and secondary oil recovery [1–7]. The use of a surfactant as a surface-active agent is one of the new techniques for growing oil extraction by changing the wettability of carbonate reservoirs from oil-wet to water-wet [8–13]. This chemical agent, by reducing IFT and/or altering surface wettability, causes the movement of trapped oils to boost and so to enhance oil recovery [14–18]. In recent decades, chemical injections have been extensively used in enhancing oil recovery, aiming at increasing the displacement coefficient in heterogeneous reservoirs and hence reducing residual oil saturation [19–24].

In petroleum engineering, the polymer is used as an additive in the petroleum reservoir to sweeping oil to increase oil recovery. Chemical flooding has subcategories such as polymer flooding, surfactant flooding, alkali/polymer flooding, and alkali/surfactant/polymer (ASP) flooding [25–31].

Injection of a surfactant and/or a polymer is one of the essential chemical injection mechanisms, especially in reservoirs with high water salinity in which alkaline is not suggested due to the deposition of salty compounds in the formation. ASP flooding can improve oil production more than water flooding noticeably; however, it causes new problems due to the attendance of high amount of alkali, for instance, the mixture of the oil-in-water emulsion has harmful effects of the shell and the corrosion of the oil production tools [32–35]. Therefore, the new surfactant

combinations without alkali are of crucial importance in the EOR process, particularly in oil reservoirs with high temperature gradient and high salinity. In this method, the surfactant can be used for two reasons: decreasing the interfacial tension between water and oil and changing rock wettability [36–39]. Additionally, using the polymer can be exploited to reduce the water and oil mobility ratio. Since a surfactant enables to bond with the strands of a polymer, the combination of surfactants and polymers creates different properties and performances than when used individually [17, 40].

Ahmed et al. (2014) evaluated the adsorption of a cationic surfactant, namely, C12 on carbonate minerals. They investigated the adsorption of this surfactant in carbonate formations and stated that its adsorption ability depends on different parameters including pH, electrolyte composition of formation water, and mineral types present in carbonate formations. The amount of its adsorption on calcite at a low level of pH (5–6.5) is 0.5 mg/m^2. However, the adsorption capacity increases when carbonate formations possess silica or clay compounds. Wang et al., in 2015, worked on the adsorption of chemical surfactants on carbonate reservoirs via the injection of the surfactant/polymer in three ways: injection of the surfactant alone, injection of the polymer after the surfactant, and injection of the polymer and surfactant together. They used Betaine, an amphoteric surfactant, and hydrolyzed polyacrylamide polymer sulphonate. Results showed that the adsorption capacity of the carbonate rock was found to be 0.163 mg/g of the rock, during surfactant flooding alone, and if the injection of the surfactant along with the polymer would be fulfilled, the average capacity of adsorption was found to be 0.079 mg/g of the rock; otherwise, when the combination of the surfactant and polymer was injected, the average capacity of adsorption would be 0.083 mg/g of the rock [41]. Feng et al. in 2012 stated that the mixture of the polymer to the surfactant solution accelerated the reduction of surface tension between water and oil. They showed that the injection of chemicals containing polymer and alkaline led to increasing the oil recovery rate from 13% to 20%. This value is much larger than that when the injection of the polymer was applied alone under the same conditions [17].

Ahmed F. Belhaj et al. (2021) investigated the adsorption behavior of two chemical surfactant nanionic alkyl polyglucoside (APG) and anionic alkyl ether carboxylate (AEC) on the carbonate surfactant using static adsorption experiments and artificial neural network (ANN) prediction. The static experiment indicated that the nanionic surfactant has more adsorption density with respect to the anionic surfactant. The ANN model revealed good agreement with the experimental result, and also, the results showed that adsorption density for both surfactants decreases as temperature increases [42]. Das et al. (2020) measured the adsorption density of a nanionic surfactant with two different types of hydrophobic units and hydrophilic polyethoxylate units ranging from 15 to 40 mers on Indiana limestone. The results showed that adsorption increased by temperature increasing and decreased with more hydrophilic groups [43]. Saha et al. (2017) investigated the effect of mineralogy on the adsorption characteristics of the surfactant-reservoir rock system. Cationic Triton X-100 was used as the chemical surfactant, and the results indicated that adsorption capacity of the surfactant is strongly dependent on the mineral content of the rock in the order of illite > feldspar > montmorillonite > kaolinite [44].

The adsorption and preservation of polymers and surfactants on reservoir rock surfaces are notable factors in the injection process due to decreasing fluid viscosity, leading to the reduction of final oil recovery. This indicates loss of chemicals from the solution and hence reduction in the amount of chemical injection. Executive and, especially, economic aspects can influence the efficiency of chemical injection operation. Therefore, the lower the absorption of the polymer and surfactant is, the lower the amount of the injectable chemical and final cost would be. Since surfactants have a high potential to reduce the surface tension between water and oil and to change the wettability of the rocks to water-wetting, the main objectives of this study are as follows:

(i) Investigation of the adsorption ability of different concentrations of Triton X-100 as a surfactant on a carbonate rock

(ii) Investigation of the impact of using the hydrolyzed acrylamide polymer on the adsorption capacity of Triton X-100 in critical concentration

(iii) Investigation of the effect of temperature on the adsorption capacity of the assessed surfactant

2. Materials and Methods

The core plug used in experiments is from the Binak oil field located in the south of Iran. The properties of the used core plug are given in Table 1.

The aqueous phase used in this study includes distilled water along with sodium chloride with the concentration of 10,000 ppm. The Triton X-100 is a nonionic surfactant with a water-wet polyethene oxide chain (5 units of ethylene oxide) and an aromatic lipophilic or hydrophobic chain and was created by Merck Company. The general properties of this material are given in Table 2.

Nonionic polyacrylamide provides a neutral solution when solved in distilled water. Table 3 and Figure 1 show the characteristics and form of this compound, respectively.

2.1. Experimental Method. The experimental procedure which was done in this investigation is as follows:

(1) Cleaning the core plug in a soxhlet by combining toluene and methanol

(2) Drying the core in the oven and powdering it with milling

(3) Prepare different concentrations of Triton X-100 (50–1000 ppm) and polymer (250–2500 ppm) in a brine solution with a concentration of 10000 ppm

(4) Separation of 3 gr of the rock powder and mixing with 60 gr of the surfactant and polymer solution

Table 1: The properties of the used core sample.

Material	Porosity (%)	Pore volume (cm^3)	Absolute permeability (md)	Gas permeability (md)	Diameter (cm)	Length (cm)
Anhydrite + dolomite	13.39	12.10	4.76	10.60	3.67	**8.54**

Table 2: The chemical and physical characteristics of the used surfactant.

Chemical formula	$C_{14}H_{22}O$ (C_2H_4O) n (n = 9-10)
Molecular weight	647 gr/mol
Physical state	Viscous and colorless fluid
Density	1.07 gr/cm^3
Melting point	6°C
Vapour pressure	Less than1 mmHg
Flammability point	251°C

Table 3: Properties of the used polymer.

Name	Partially hydrolyzed polyacrylamide
Physical state	White granule powder
Solubility	Soluble in water
Molecular weight	15–25 g/mol
Insoluble impurities	%<2.0
Hydrolization degree	20–30%
Solving time	Less than 60 min
Chemical formula	[-CH_2CH ($CONH_2$)-]
Kind	Nonionic
Free monomers and partially hydrolyzed polyacrylamide	Up to a maximum of 0.05%

(5) Perform the adsorption test in different concentrations and different temperatures

(6) Measure CMC of the surfactant solutions and polymer by electrical conductivity and pH

(7) Preparing CMC and retesting at 25, 40, 60, and 80°C

(8) Adding polyacrylamide to the surfactant solution in CMC concentration and retesting in four different temperatures and salt concentration of 10000 ppm

(9) Evaluating the results and the curves and giving recommendations

3. Results and Discussion

The adsorption of the surfactant at the salt concentration of 10000 ppm in different surfactant concentrations and four temperature ranges is primarily investigated. The critical concentration of the solutions containing Triton X-100 surfactant and hydrolyzed polyacrylamide is then calculated with pH and electrical conductivity methods, and their CMCs were used to perform adsorption tests.

3.1. Temperature Impact. The impact of temperature on the absorption capacity of the surfactant was examined at 25, 40, 60, and 80°C. In these experiments, 3 gr of the powdered rock was placed in a beaker, and 60 g of the surfactant and brine solution with the concentration of 10000 ppm was added. Ten experiments were conducted in 24 hours with different concentrations of the surfactant in the range of 50 to 1000 ppm. After 12 hours, the solution reached the equilibrium, and then, the adsorption density was measured using the following equation:

$$\tau = \left(\frac{(C_1 - C_e) * M_s}{M_c} \right) * 10^{-3}, \quad (1)$$

where τ is the adsorption density (mg/g), C_i is the initial concentration, C_e is the equilibrium concentration (ppm), M_s is the solution weight, and M_c is the rock powder weight (gr). The data obtained in the ambient temperature are illustrated in Figure 2. As to be seen in this graph, increasing the surfactant concentration elevates the adsorption density. The increasing rate was extremely ascending to 400 ppm and remained fairly stable. Ultimately, the adsorption density would be 3.91 mg/g at this temperature.

Previous experiments were repeated at the same concentrations at 40°C, and their results are shown in Figure 2. An increase of about 15°C has led to a decrease in density. As the data show, the concentration of the remaining surfactant in the solution has increased. The density of adsorption at this temperature has decreased to 3.556 mg/g. The experiments were conducted at 60°C, and the amount of surfactant remaining in the test container was slightly higher than that at 40°C, which means that an increase of 20°C has been able to reduce the adsorption density. The data from the experiments are shown in Figure 2. The adsorption density is reduced to 3.44 mg/g. The last tested temperature is 80°C. All tests were repeated at this temperature, and their results are shown in Figure 2. The temperature increase has a positive effect on the absorption of the surfactant. Absorption density at this temperature at the final concentration of the surfactant is 3.37 mg/g. Electrical conductivity and pH measurements were employed to obtain the critical concentration of the surfactant and polymer used in this study. In these methods, pH and electrical conductivity of different concentrations of the surfactant and polymer were measured and sketched versus concentration on a graph. The data drawn on the graph have two different trends. The trends were first regretted linearly using the linear method. Then, the critical concentration of the solutions corresponding to the intersection of the two lines was obtained. In this research, the critical concentrations of the surfactant and polymer were found to be 450 ppm and 1300 ppm, respectively.

3.2. Hydrolyzed Polyacrylamide Addition Impact. In order to investigate the hydrolyzed polyacrylamide impact on the surfactant adsorption, 1300 ppm of this polymer was added to the surfactant solution with a concentration of 450 ppm. The obtained solution was placed on a magnetic stirrer at ambient temperature for 24 hours. It was then kept at room

Figure 1: Hydrolyzed polyacrylamide.

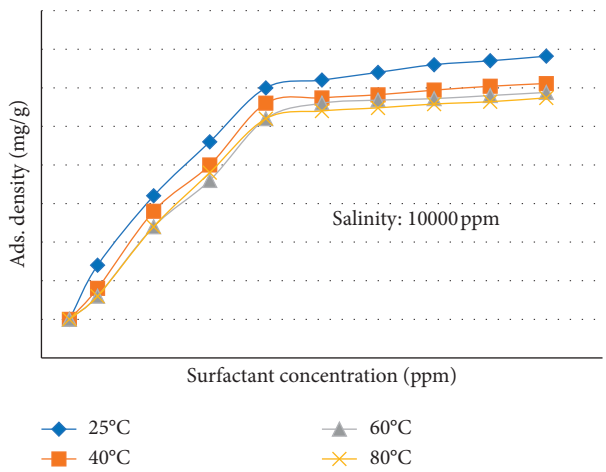

Figure 2: The surfactant adsorption density vs. Triton X-100 surfactant concentration at different temperatures and salt concentration of 10000 ppm.

Table 4: Initial and residual values of the surfactant/polymer at ambient temperature and 40°C with a concentration of 10000 ppm.

Test no.	Used material	Initial amount of surfactant + polymer (ppm)	Residual amount of surfactant/polymer (ppm) at 25°C	Adsorption density of surfactant/polymer (mg/g) at 25°C	Residual amount of surfactant/polymer (ppm) at 40°C	Adsorption density of surfactant/polymer (mg/g) at 40°C
1	S	450	285	3.30	297.60	3.048
2	P	1300	1154	2.92	1167	2.660
3	$S+P$	875	757	2.36	765	2.200

S : surfactant and P : polymer.

Table 5: Initial and residual values of the surfactant/polymer at 60°C and 80°C with a concentration of 10000 ppm.

Test no.	Used material	Initial amount of surfactant + polymer (ppm)	Residual amount of surfactant/polymer (ppm) at 60°C	Adsorption density of surfactant/polymer (mg/g) at 60°C	Residual amount of surfactant/polymer (ppm) at 80°C	Adsorption density of surfactant/polymer (mg/g) at 80°C
1	S	450	303.70	2.926	310	2.80
2	P	1300	1174	2.520	1186	2.28
3	$S+P$	875	771	2.080	774	2.02

S : surfactant and P : polymer.

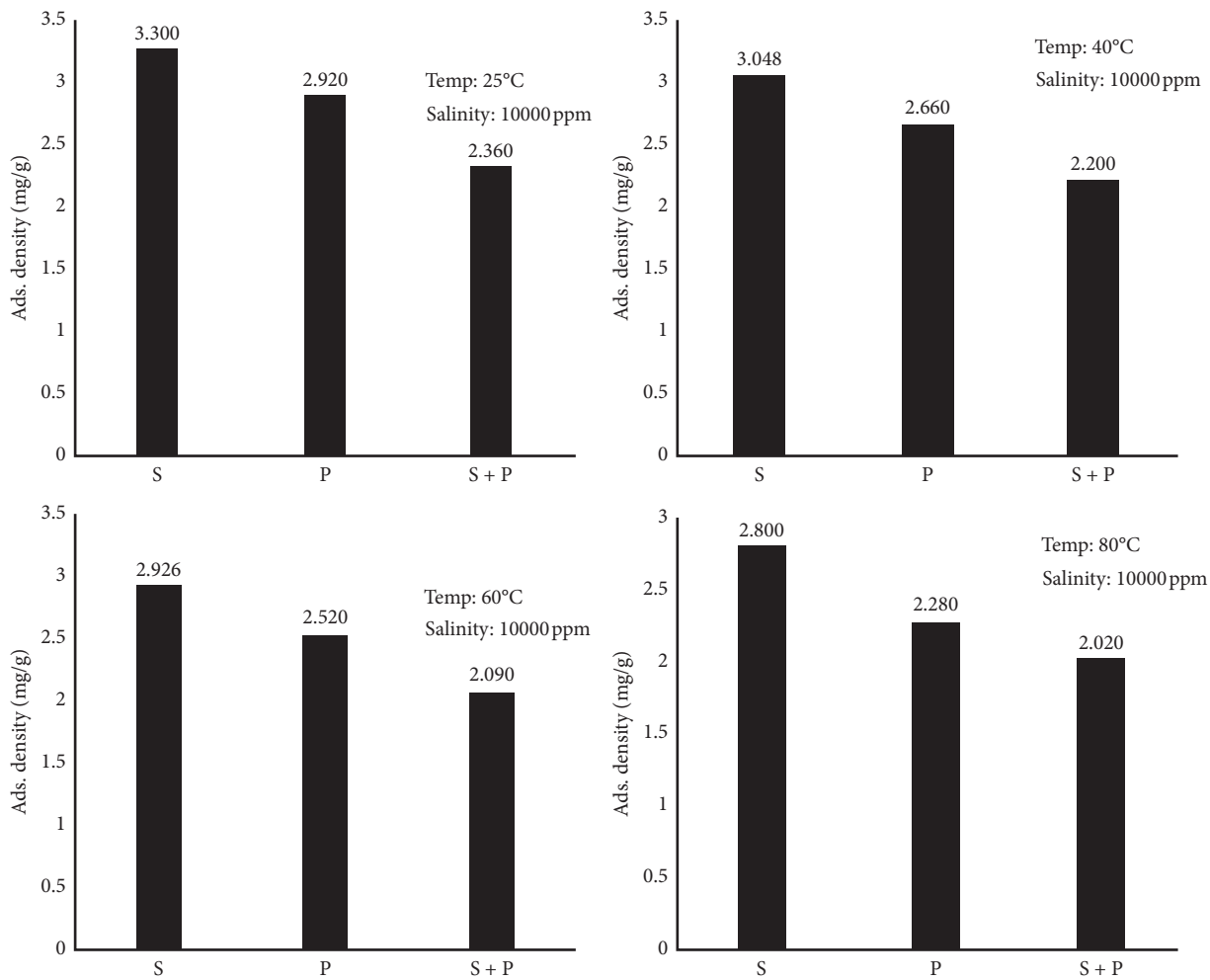

Figure 3: Polyacrylamide effect on the surfactant adsorption at different temperatures.

temperature for 12 hours to reach the equilibrium. After the equilibrium, some of the solutions were taken to measure the concentration of the surfactant by a spectrophotometer. The following tables and graphs show the results of these tests. It is concluded from the obtained data that the mixture of the polymer and surfactant could decrease the surfactant adsorption on the rock powder. Moreover, it could decrease the adsorption density from 3.3 to 2.92 mg/g at ambient temperature, 3.048 to 2.66 mg/g at 40°C, 2.926 to 2.25 mg/g at 60°C, and 2.8 to 2.28 mg/g at 80°C. The results are shown in Tables 4 and 5 as well as in Figure 3.

4. Conclusions

The main findings of this study are as follows:

(i) The adsorption density of the surfactant or polymer reduced with increasing temperature. The maximum reduction in adsorption density was attained at 80°C for both additives.

(ii) The polymer was prepared in 1300 ppm and added to the surfactant solution with 450 ppm. The results showed that hydrolyzed polyacrylamide had a positive effect on the reduction of the surfactant adsorption.

(iii) The adsorption rate of Triton X-100 and/or hydrolyzed polyacrylamide alone on carbonate rock was higher than that of both compounds in a mixture of 0.027 gr surfactant and 0.078 gr polymer.

(iv) As the temperature rises from 25°C to 80°C, the rate of adsorption of the surfactant and polymer on the carbonate rock surface decreases, and this trend is likely to continue at temperatures above 80°C; therefore, using of these compounds as a mixture (Triton X-100 and polyacrylamide) in oil reservoirs with a high temperature gradient (i.e., more than or equal to 80°C) would be suitable in terms of the economic view.

(v) The adsorption density increases with increasing surfactant concentration up to CMC at a constant temperature, and then, it remained approximately stable.

In addition, different type probabilistic methods can be used to deal with objective uncertainties such as but not limited to [45–51].

Data Availability

The data used to support the findings of this study are available from the corresponding author upon request.

Conflicts of Interest

The authors declare that they have no conflicts of interest.

Acknowledgments

The authors are grateful to Shiraz University for supporting this research.

References

[1] H. Esfandyari, A. Haghighat Hoseini, S. R. Shadizadeh, and A. Davarpanah, "Simultaneous evaluation of capillary pressure and wettability alteration based on the USBM and imbibition tests on carbonate minerals," *Journal of Petroleum Science and Engineering*, 2020.

[2] X. Hu, J. Xie, W. Cai, R. Wang, and A. Davarpanah, "Thermodynamic effects of cycling carbon dioxide injectivity in shale reservoirs," *Journal of Petroleum Science and Engineering*, vol. 195, Article ID 107717, 2020.

[3] A. Davarpanah and B. Mirshekari, "Experimental investigation and mathematical modeling of gas diffusivity by carbon dioxide and methane kinetic adsorption," *Industrial and Engineering Chemistry*, vol. 58, no. 27, pp. 12392–12400, 2019.

[4] A. Davarpanah, "Parametric study of polymer-nanoparticles-assisted injectivity performance for axisymmetric two-phase flow in EOR processes," *Nanomaterials*, 2020.

[5] Y. Hu, Q. Cheng, J. Yang, L. Zhang, and A. Davarpanah, "A laboratory approach on the hybrid-enhanced oil recovery techniques with different saline brines in sandstone reservoirs," *Processes*, vol. 8, no. 9, 1051 pages, 2020.

[6] A. Davarpanah, "Feasible analysis of reusing flowback produced water in the operational performances of oil reservoirs," *Environmental Science and Pollution Research*, vol. 25, pp. 35387–35395, 2018.

[7] A. Davarpanah and B. Mirshekari, "Mathematical modeling of injectivity damage with oil droplets in the waste produced water re-injection of the linear flow," *European Physical Journal - Plus*, vol. 134, Article ID 12546, 2019.

[8] H. Esfandyari, S. R. Shadizadeh, F. Esmaeilzadeh, and A. Davarpanah, "Implications of anionic and natural surfactants to measure wettability alteration in EOR processes," *Fuel*, vol. 278, Article ID 118392, 2020.

[9] H. Esfandyari, A. Moghani Rahimi, F. Esmaeilzadeh, A. Davarpanah, and A. H. Mohammadi, "Amphoteric and cationic surfactants for enhancing oil recovery from carbonate oil reservoirs," *Journal of Molecular Liquids*, vol. 322, Article ID 114518, 2020.

[10] Z. Haiyan and A. Davarpanah, "Hybrid chemical enhanced oil recovery techniques: a simulation study," *Symmetry (Basel)*, vol. 12, no. 7, Article ID 1086, 2020.

[11] F. Pan, Z. Zhang, X. Zhang, and A. Davarpanah, "Impact of anionic and cationic surfactants interfacial tension on the oil recovery enhancement," *Powder Technology*, vol. 373, pp. 93–98, 2020.

[12] M. Mazarei, A. Davarpanah, A. Ebadati, and B. Mirshekari, "The feasibility analysis of underground gas storage during an integration of improved condensate recovery processes," *Journal of Petroleum Exploration and Production Technology*, vol. 9, pp. 397–408, 2019.

[13] A. Davarpanah, R. Shirmohammadi, B. Mirshekari, and A. Aslani, "Analysis of hydraulic fracturing techniques: hybrid fuzzy approaches," *Arabian Journal of Geosciences*, vol. 12, no. 13, 402 pages, 2019.

[14] G. Houjian, X. Guiying, Z. Yanyan et al., "Influencing factors on the properties of complex systems consisting of hydrolyzed polyacrylamide/triton X-100/cetyl trimethylammonium bromide: viscosity and dynamic interfacial tension studies," *Energy and Fuels*, vol. 23, pp. 300–305, 2009.

[15] M. J. Rosen, H. Wang, P. Shen, and Y. Zhu, "Ultralow interfacial tension for enhanced oil recovery at very low surfactant concentrations," *Langmuir*, vol. 21, no. 9, pp. 3749–3756, 2005.

[16] A. Davarpanah, "A feasible visual investigation for associative foam >\ polymer injectivity performances in the oil recovery enhancement," *European Polymer Journal*, vol. 105, pp. 405–411, 2018.

[17] A. Davarpanah and B. Mirshekari, "Numerical simulation and laboratory evaluation of alkali–surfactant–polymer and foam flooding," *International Journal of Environmental Science and Technology*, vol. 17, pp. 1123–1136, 2020.

[18] S. Nesic, A. Zolotukhin, V. Mitrovic, D. Govedarica, and A. Davarpanah, "An analytical model to predict the effects of suspended solids in injected water on the oil displacement efficiency during waterflooding," *Processes*, vol. 8, p. 659, 2020.

[19] A. Davarpanah, R. Shirmohammadi, and B. Mirshekari, "Experimental evaluation of polymer-enhanced foam transportation on the foam stabilization in the porous media," *International Journal of Environmental Science and Technology*, vol. 16, pp. 8107–8116, 2019.

[20] Z. Zhao, Z. Li, W. Qiao, and L. Cheng, "Dynamic interfacial behavior between crude oil and octylmethylnaphthalene sulfonate surfactant flooding systems," *Colloids and Surfaces A: Physicochemical and Engineering Aspects*, vol. 259, no. 1, pp. 71–80, 2005.

[21] F. Li, L. Sun, Y. Wang, T. Wu, and Y. Li, "Effect of laponite particles on the emulsion stability of produced water from polymer flooding," *Journal of Petroleum Science and Engineering*, vol. 10, no. 1, pp. 49–61, 2014.

[22] A. Davarpanah, B. Mirshekari, T. Jafari Behbahani, and M. Hemmati, "Integrated production logging tools approach for convenient experimental individual layer permeability measurements in a multi-layered fractured reservoir," *Journal of Petroleum Exploration and Production Technology*, vol. 8, pp. 743–751, 2018.

[23] X. Hu, M. Li, C. Peng, and A. Davarpanah, "Hybrid thermal-chemical enhanced oil recovery methods; an experimental study for tight reservoirs," *Symmetry (Basel)*, vol. 12, no. 6, 947 pages, 2020.

[24] A. Davarpanah and B. Mirshekari, "Experimental study of CO_2 solubility on the oil recovery enhancement of heavy oil reservoirs," *Journal of Thermal Analysis and Calorimetry*, vol. 139, 2019.

[25] A. Mandal, "Chemical flood enhanced oil recovery: a review," *International Journal of Oil, Gas and Coal Technology*, vol. 9, no. 3, 241 pages, 2015.

[26] S. M. Hosseini-Nasab, C. Padalkar, E. Battistutta, and P. L. J. Zitha, "Mechanistic modeling of the alkaline/surfactant/polymer flooding process under sub-optimum salinity conditions for enhanced oil recovery," *Industrial and Engineering Chemistry*, vol. 24, pp. 6875–6888, 2016.

[27] X. Han, I. Kurnia, Z. Chen, J. Yu, and G. Zhang, "Effect of oil reactivity on salinity profile design during alkaline-surfactant-polymer flooding," *Fuel*, 2019.

[28] F. Li, L. Ye, Y. Li, and T. Wu, "Investigation into the adsorption of partially hydrolyzed polyacrylamide onto in situ formed magnesium hydroxide particles," *RSC Advances*, 2016.

[29] F. Li, W. He, D. Sun, T. Wu, and Y. Li, "Effect of sodium-montmorillonite particles on the stability of oil droplets in produced water from alkali/surfactant/polymer flooding," *Journal of Cleaner Production*, vol. 104, pp. 468–474, 2015.

[30] J. Guo, Q. Liu, M. Li, Z. Wu, and A. A. Christy, "The effect of alkali on crude oil/water interfacial properties and the stability of crude oil emulsions," *Colloids and Surfaces A: Physicochemical and Engineering Aspects*, vol. 273, pp. 213–218, 2006.

[31] A. Davarpanah and B. Mirshekari, "A simulation study to control the oil production rate of oil-rim reservoir under different injectivity scenarios," *Energy Reports*, vol. 4, pp. 664–670, 2018.

[32] L. Zhang, H. Xiao, H. Zhang, L. Xu, and D. Zhang, "Optimal design of a novel oil-water separator for raw oil produced from ASP flooding," *Journal of Petroleum Science and Engineering*, vol. 59, pp. 213–218, 2007.

[33] Z. Zhao, C. Bi, W. Qiao, Z. Li, and L. Cheng, "Dynamic interfacial tension behavior of the novel surfactant solutions and Daqing crude oil," *Colloids and Surfaces A: Physicochemical and Engineering Aspects*, vol. 294, pp. 191–202, 2007.

[34] C. Negin, S. Ali, and Q. Xie, "Most common surfactants employed in chemical enhanced oil recovery," *Petroleum*, vol. 3, pp. 197–211, 2017.

[35] P. Druetta, P. Raffa, and F. Picchioni, "Chemical enhanced oil recovery and the role of chemical product design," *Applied Energy*, vol. 252, Article ID 113480, 2019.

[36] X. Wu, M. Han, B. H. Zahrani, and L. Guo, "Effect of surfactant-polymer interaction on the interfacial properties for chemical EOR," *SPE Middle East Oil Gas Show Conf MEOS*, 2015.

[37] J. J. Sheng, "Modern chemical enhanced oil recovery," *Modern Chemical Enhanced Oil Recovery*, 2011.

[38] L. Cui, K. Ma, A. A Abdala et al., "Adsorption of a switchable cationic surfactant on natural carbonate minerals," *SPE Journal*, 2015.

[39] M. V. Bennetzen, K. Mogensen, S. Frank, and K. Mohanty, "Dilute surfactant flooding studies in a low-permeability oil-wet Middle East carbonate," in *Social Petroleum Engineering - International Peteroleum Technology Confeference 2014, IPTC 2014 Unlocking Energy through Innovative Technology Capability*, Doha, Qatar, January 2014.

[40] S. S. Riswati, W. Bae, C. Park, A. K. Permadi, I. Efriza, and B. Min, "Experimental analysis to design optimum phase type and salinity gradient of Alkaline Surfactant Polymer flooding at low saline reservoir," *Journal of Petroleum Exploration and Production Technology*, vol. 173, pp. 1005–1019, 2019.

[41] J. Wang, M. Han, A. B. Fuseni, and D. Cao, "Surfactant adsorption in Surfactant-Polymer flooding for carbonate reservoirs," in *Proceedings of the SPE Middle East Oil Gas Show Conference MEOS*, Manama, Bahrain, March 2015.

[42] A. F. Belhaj, K. A. Elraies, M. S Alnarabiji et al., "Experimental investigation, binary modelling and artificial neural network prediction of surfactant adsorption for enhanced oil recovery application," *Chemical Engineering Journal*, vol. 406, Article ID 127081, 2021.

[43] S. Das, A. Katiyar, N. Rohilla, Q. Nguyen, and R. T. Bonnecaze, "Universal scaling of adsorption of nonionic surfactants on carbonates using cloud point temperatures," *Journal of Colloid and Interface Science*, vol. 577, pp. 431–440, 2020.

[44] R. Saha, R. V. S. Uppaluri, and P. Tiwari, "Effect of mineralogy on the adsorption characteristics of surfactant—reservoir rock system," *Colloids and Surfaces A: Physicochemical and Engineering Aspects*, vol. 531, pp. 121–132, 2017.

[45] S. Kabir, M. Yazdi, J. I. Aizpurua, and Y. Papadopoulos, "Uncertainty-Aware dynamic reliability analysis framework for complex systems," *IEEE Access*, vol. 6, pp. 29499–29515, 2018.

[46] M. Yazdi, "Introducing a heuristic approach to enhance the reliability of system safety assessment," *Quality and Reliability Engineering International*, pp. 1–27, 2019.

[47] M. Yazdi, "Footprint of knowledge acquisition improvement in failure diagnosis analysis," *Quality and Reliability Engineering International*, vol. 35, no. 1, pp. 405–422, 2018.

[48] M. Yazdi, "Ignorance-aware safety and reliability analysis: a heuristic approach," *Quality and Reliability Engineering International*, vol. 36, pp. 652–674, 2020.

[49] M. Yazdi, "A perceptual computing – based method to prioritize intervention actions in the probabilistic risk assessment techniques," *Quality and Reliability Engineering International*, pp. 1–27, 2019.

[50] M. Yazdi, S. Kabir, and M. Walker, "Uncertainty handling in fault tree based risk assessment: state of the art and future perspectives," *Process Safety and Environmental Protection*, vol. 131, pp. 89–104, 2019.

[51] S. Kabir, T. K. Geok, M. Kumar, M. Yazdi, and F. Hossain, "A method for temporal fault tree analysis using intuitionistic fuzzy set and expert elicitation," *IEEE Access*, vol. 8, pp. 980–996, 2020.